

IN-SPACE PROPULSION



WHO

WE ARE

WHAT

WE DO

WHY

WE DO WHAT WE DO

WHEN

THINGS WILL HAPPEN

HOW

WE DO IT

Innovative space transportation systems now in development by NASA and its partners promise a new era of scientific discovery in space. But the struggle to unlock the secrets of our solar system presents unique new challenges. Central among them: faster access throughout the solar system, and the ability to rendezvous with, orbit and conduct in situ exploration of planets, satellites and other solar system bodies.

These are the missions of NASA's In-Space Propulsion program: to enable science at new destinations; to significantly reduce the time and cost required for spacecraft to reach their destinations; and to allow mission planners to shift their focus from the difficulty of the journey to the science challenges at the destination. To read more about the planned missions of the Science Mission Directorate, click [HERE](#).

To read more on the objectives, approach and status of In-Space Propulsion technologies read the [In Space Propulsion Overview](#) and [NASA's In-Space Propulsion Technology Program: Overview and Update](#) presented here by the Project Manager and Technical Area Managers.

NASA Engineers Test Propulsion System Aimed at Enabling Deep Space Exploration

August 23



NASA engineers have begun testing unique propulsion hardware that could enable more ambitious, cost effective exploration of deep space. The technology, a High Voltage Hall Accelerator, or HiVHAC, is a rocket thruster that could reduce fuel load and spacecraft mass, decrease transit times and launch costs, and allow for larger scientific payloads -- key elements to the

Business Opportunities

Science Mission Directorate

-ROSS-2004 NRA

-ROSES-2005 NRA

On Going Business

Request for Information (RFI)

Previous NRA Awardees

ISP -

Education and Public Outreach (EP&O) for educators & students grades 5-8

TECH ISP -

In-depth technical information about space propulsion technologies

exploration of Earth's neighboring planets and our Solar System.

[Read More](#)

Marshall's Solar Sail Propulsion Team, Industry Partner Deploy Solar Sail System

July 27



Marshall engineers and their industry partners at L'Garde Inc. of Tustin, Calif., recently reached a milestone in the testing of solar sails -- a unique propulsion technology that uses the Sun's energy to propel robotic spacecraft. The team successfully deployed a 20-meter solar sail and boom system at NASA Glenn Research Center's Plum Brook facility in Sandusky, Ohio.

Brook facility in Sandusky, Ohio.

[Read More](#)

NASA Engineers, Tennessee College Students Successfully Demonstrate Catch Mechanism for Future Space Tether

July 8



NASA engineers and college students at Tennessee Technological University in Cookeville, Tenn., recently reached a milestone in the development of a tether-based propulsion system. The team "launched" a spacecraft model and caught it in mid-air with a unique catch mechanism that could be used in the future to grab a payload or craft traveling in space. Engineers from the In-Space Propulsion Technology Office at the Marshall Center closely participated in the design and development of the technology.

Image: A Momentum-Exchange Electrodynamic Reboost, or MXER, tether system in Earth orbit prepares to catch a payload as it travels in space. As the fast-moving

tether spins, it catches the payload via a mechanism at the tether's tip, and then throws the payload toward its final destination.

[Read More](#)

Aerocapture Team Successfully Completes Test of Ablative Thermal Protection System Panels

May 18

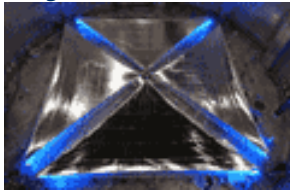


NASA engineers recently used a "field of mirrors" to successfully test a panel of a Thermal Protection System (TPS) for Aerocapture technologies. The tests were conducted at the National Solar Thermal Test Facility at the Sandia National Labs in Albuquerque, N.M. The test facility includes a 200-foot-tall tower and 212 large mirrors or heliostats to track the Sun and focus sunlight on a target. The tests were sponsored by the In-Space Propulsion Technology Project at the Marshall Space Flight Center in Huntsville, Ala.

[Read More](#)

Solar Sails/ATK Space Systems Sail Photos

May 5

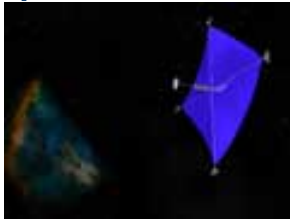


Engineers at the Marshall Space Flight Center in Huntsville, Ala., and their industry partner, ATK Space Systems of Goleta, Calif., recently reached a milestone in the testing of solar sails -- a unique propulsion technology that uses the Sun's energy to propel robotic spacecraft.

[Read More](#)

NASA to Begin Testing Two Solar Sail Systems

April 18



On April 18, 2005 NASA's Solar Sail Propulsion team and industry partners will begin testing two 20-meter solar sail systems in a simulated space environment -- a critical milestone in developing the unique, solar-driven propulsion technology that could enable future deep space missions. Solar sail research is led by the In-Space Propulsion Technology Office at the Marshall Center.

In the artist's rendition above, a concept design of an interstellar probe driven by a solar sail propulsion system travels through space on its way out of the Solar System

[Read More](#)

[Contact Us](#)

Owner: Space Transportation Directorate Curator: [Sherry Wallace](#)
Web Services Provided by: [A&WS \(Applications & Web Services\)](#) - SAIC
[NASA Privacy Statement](#)



IN-SPACE PROPULSION

WHO

WE ARE

WHAT

WE DO

WHY

WE DO WHAT WE DO

WHEN

THINGS WILL HAPPEN

HOW

WE DO IT

ISP -

Education and Public Outreach (EP&O) for educators & students grades 5-8

TECH ISP -

In-depth technical information about space propulsion technologies

WHO WE ARE -

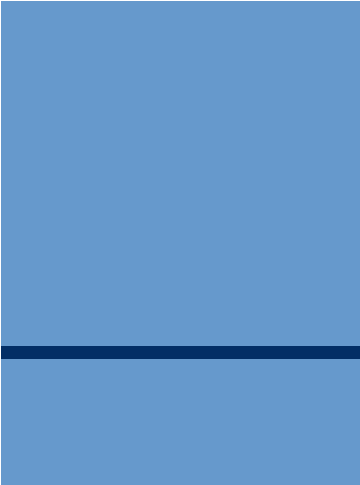
We are the men and women of NASA's In-Space Propulsion Program - - a broad collaborative team of scientific and engineering researchers and technologists at NASA field centers, university laboratories, and other government and commercial facilities across America - - managed by NASA's Science Mission Directorate in Washington, D.C.

NASA's Marshall Space Flight Center in Huntsville, AL., which is responsible for implementing the program for the Science Mission Directorate, is bringing together all the in-space propulsion talents and resources NASA and its partners have to offer. The In-Space Transportation Investment Area at Marshall is intended to serve as a focal point for technology development and integration.

Further information may be found through the Science Mission Directorate homepage on the World Wide Web (WWW) at <http://science.hq.nasa.gov/>

The Marshall Center maintains the In-Space Propulsion Web presence for NASA scientists, stakeholders and others interested in learning more about in-space propulsion technologies, programs and partnering opportunities. For more information, contact:

webmaster@inspacetransportation.com



[Home](#) ~ [Who](#) ~ [What](#) ~ [Why](#) ~ [When](#) ~ [How](#)
[ISP for Teachers & Students](#) ~ [Technical ISP](#)
[Space Transportation Web Site](#)



IN-SPACE PROPULSION

WHO

WE ARE

WHAT

WE DO

WHY

WE DO WHAT WE DO

WHEN

THINGS WILL HAPPEN

HOW

WE DO IT

ISP -

Education and Public Outreach (EP&O) for educators & students grades 5-8

TECH ISP -

In-depth technical information about space propulsion technologies

WHAT WE DO -

Aerocapture systems to slow a ship down at its destination without the use of significant on-board propellant...

Electric thrusters that can run not just for minutes but for years, enabling a spacecraft to accelerate continuously through space, rather than merely coast...

Space sails powered by sunlight, capable of quickly pushing spacecraft to the very outskirts of the solar system - or enabling satellite to "hover" at a specific point in space...

These are just a few examples of the technologies now being investigated and developed by NASA's In-Space Propulsion Program.

Together with leading propulsion researchers from academia, industry and other government organizations, we seek to identify, fund and fly those technologies that promise to enable a new era of scientific discovery throughout our solar system.

ISP technologies now in development include:

[Aerocapture](#)

[Ion Propulsion](#)



Momentum-Exchange Electrodynamic Reboost (MXER) Tether

Solar Sails

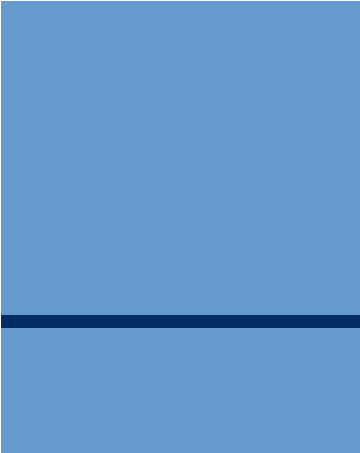
Infinite Journeys

Solar Thermal
Not Available

Advanced Chemical

Ultra-Light Tank Technology for In-Space Application

Solar Electric Propulsion



[Home](#) ~ [Who](#) ~ [What](#) ~ [Why](#) ~ [When](#) ~ [How](#)
[ISP for Teachers & Students](#) ~ [Technical ISP](#)
[Space Transportation Web Site](#)



IN-SPACE PROPULSION

WHO

WE ARE

WHAT

WE DO

WHY

WE DO WHAT WE DO

WHEN

THINGS WILL HAPPEN

HOW

WE DO IT

ISP -

Education and Public Outreach (EP&O) for educators & students grades 5-8

TECH ISP -

In-depth technical information about space propulsion technologies

WHY WE DO WHAT WE DO -

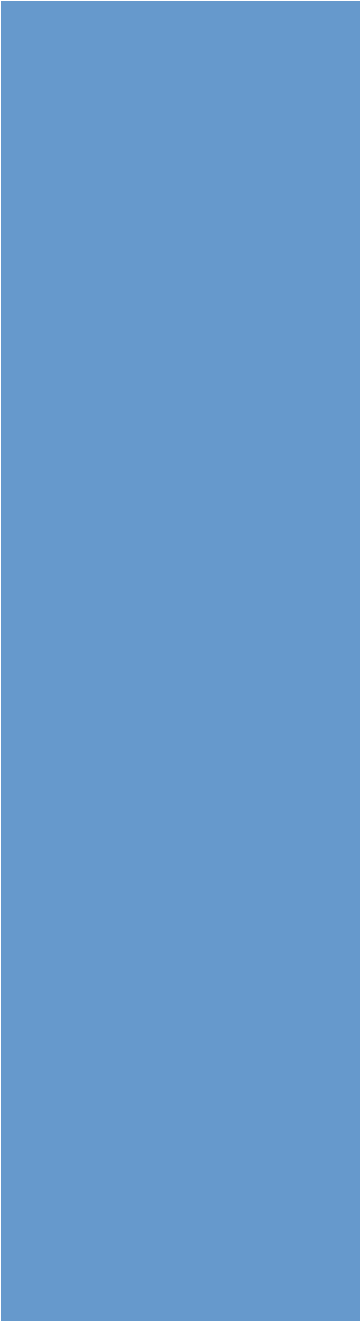
Historically, the only way to deliver a scientific probe to one of our neighboring planets - or to any other object of interest in space - has been to launch it aboard a rocket capable of boosting it to sufficient speed, then waiting while it coasts toward its destination. Then, often many years later, it arrives on the scene, where it must use a substantial amount of chemical propellant - carried at the expense of added science payload - to enter orbit. If it is physically impossible to carry enough fuel to stop, the craft typically might zip right on past its target - gathering as much information as it can in the days or weeks of its passage.

There has to be a better way...

True, trip times often can be reduced by conducting well-timed planetary flybys, catching a gravity boost en route to the final destination. But even so, the wait for scientific returns is excruciatingly long in career terms. Moreover, what science data is returned is all too often limited in its richness by constraints on craft size and power - constraints imposed by the limitations of conventional propulsion systems.

It is our view that scientists should be enabled to expect much more; more plentiful and more powerful instruments; more comprehensive and more detailed data capture and more timely return of data - for more bounty of discovery.

Imagine a deep-space mission enabled by a spacecraft with a high-energy power source capable of high-fidelity data gathering and transmission back to Earth.



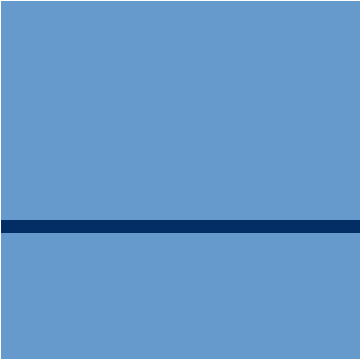
<http://nmp.nasa.gov/ds1>

Imagine that the same craft can slow down, achieve orbit and serve as a platform for long-duration observation of planet or celestial body - before powering up thrusters and heading to another research destination.

This is the vision for next-generation space science that informs and motivates the work of the In-Space Propulsion Program.

It is the propulsion technologies we intend to deliver over the next 10-15 years that will significantly further our efforts to turn this vision into reality. <http://earth.nasa.gov>

The In-Space Propulsion Program established a systems analysis office to drive out and substantiate technology investment needs, which consequently brought about the formulation of a multi-center NASA and contractor systems analysis team. The team performs systematic and periodic analyses and studies to provide critical data for the technology area managers to use in determining their funding priorities and program direction. Efforts of the team provide quantitative data necessary to measure the benefits of each technology area, and thus contribute to identifying and understanding technology requirements, gaps and shortfalls.



[Home](#) ~ [Who](#) ~ [What](#) ~ [Why](#) ~ [When](#) ~ [How](#)
[ISP for Teachers & Students](#) ~ [Technical ISP](#)
[Space Transportation Web Site](#)



IN-SPACE PROPULSION

WHO

WE ARE

WHAT

WE DO

WHY

WE DO WHAT WE DO

WHEN

THINGS WILL HAPPEN

HOW

WE DO IT

ISP -

Education and Public Outreach (EP&O) for educators & students grades 5-8

TECH ISP -

In-depth technical information about space propulsion technologies

WHEN THINGS WILL HAPPEN -

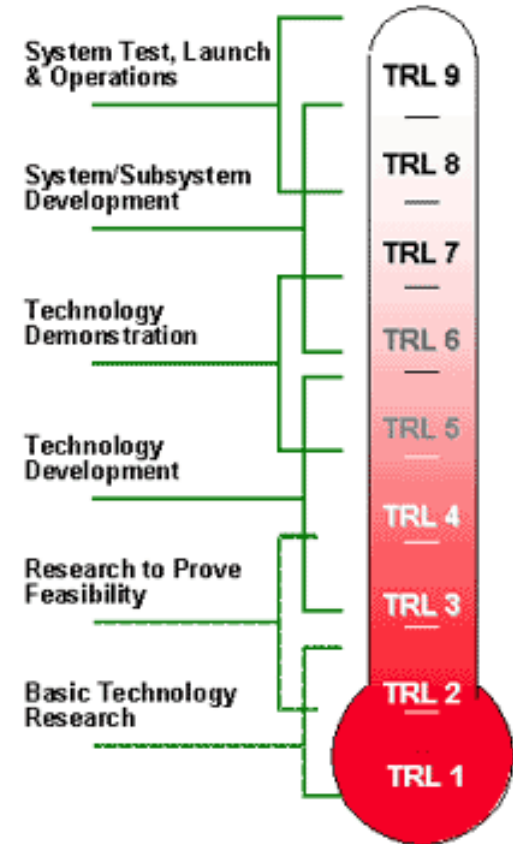
Some of the technologies now being pursued by the In-Space Propulsion Program may not be ready to fly until well into the next decade. But others may fly sooner... In some cases, much sooner.

Click [HERE](#) for ISP Timelines

The potential flight readiness of each technology depends on its maturity, as determined via a series of investigations validating the scientific principles involved, application of a prototype in a laboratory environment, and eventually flight-testing in an operating environment simulating the conditions faced by sustained exposure to space.

NASA calls this process the "Technology Readiness Level" scale, which is broken down as follow:

- TRL 9: Actual system "flight proven" via successful mission operations
- TRL 8: Actual system completed and "flight qualified" via test and demonstration (ground or space)
- TRL 7: System prototype demonstration in a space environment
- TRL 6: System/subsystem model or prototype demonstration in a relevant environment (ground or space)
- TRL 5: Component and/or breadboard validation in relevant environment
- TRL 4: Component and/or breadboard validation in laboratory environment
- TRL 3: Analytical and experimental critical function and/or characteristic proof-of-concept
- TRL 2: Technology concept and/or application formulated
- TRL 1: Basic principles observed and reported





IN-SPACE PROPULSION

WHO

WE ARE

WHAT

WE DO

WHY

WE DO WHAT WE DO

WHEN

THINGS WILL HAPPEN

HOW

WE DO IT

ISP -

Education and Public Outreach (EP&O) for educators & students grades 5-8

TECH ISP -

In-depth technical information about space propulsion technologies

HOW WE DO IT -

We've got a lot of tricks in our bag and a proposed technology to drive every science mission imaginable.

Each in-space propulsion technology has singular advantages, unique strengths, making them candidates for a host of interplanetary science missions with specific payload requirements or destination parameters. And every propulsion technology has variations - one space sail concept may provide a more cost-effective solution than another, for example.

As a rule, the In-Space Propulsion Program will compete technologies to determine which are most deserving of NASA's time and resources. The program will issue public NRAs for phased research intended to further development of each technology. And NASA will solicit talent and input everywhere -without pushing "favorite" technologies, dismissing alternatives, or failing to seek out innovations from the academic community, the private sector and other sources. More information can be found on the research opportunities of Space Science on the NRAs homepage at:

http://research.hq.nasa.gov/code_s/open.cfm

It is our intention to deliver technologies that best support each mission's parameters. That means partnering with the brightest and most dedicated propulsion researchers in the country, providing them with the finest resources NASA can offer, and working together toward a single purpose: rewriting the

20th century space flight paradigm.

The stated mission of the Solar Science Division of the Science Mission Directorate is to solve the mysteries of the universe, to explore the solar system, to discover planets around other stars, and to search for life beyond Earth. To carry out this mission, NASA's Science Mission Directorate sponsors a broad range of research programs relevant to its four Science Themes, defined as:

- Astronomical Search for Origins and Planetary Systems (ASO) that addresses the origins of galaxies, stars, proto-planetary and extra-solar planetary systems, Earth-like planets, and the origin of life;
- Solar System Division that seeks to understand all aspects of our Solar System, including the planets, satellites, small bodies, and solar system materials, and the search for possible habitats of life beyond Earth;
- Structure and Evolution of the Universe (SEU) that involves the study of cosmology, the large scale structure of the universe, the evolution of stars and galaxies, including the Milky Way and objects with extreme physical conditions and an examination of the ultimate limits of gravity and energy in the Universe;
- The Sun-Earth Connection (SEC) that concerns the Sun as a typical star and as the controlling agent of the space environment of the Solar System, especially the Earth.

Further information about these themes, as well as access to the most recent Strategic Plans (as of late 2001) for both NASA and Science Mission Directorate, may be found through the Science Mission Directorate homepage on the World Wide Web (WWW) at <http://science.hq.nasa.gov/>



[Home](#) ~ [Who](#) ~ [What](#) ~ [Why](#) ~ [When](#) ~ [How](#)
[ISP for Teachers & Students](#) ~ [Technical ISP](#)
[Space Transportation Web Site](#)

In Space Propulsion Overview

14-17 January 2003



Les Johnson
Manager, In Space Propulsion
Technology Projects Office



In-Space Propulsion Program Overview



◆ Objective

- Develop in-space propulsion technologies that can enable and/or benefit near and mid-term NASA science missions by significantly reducing cost, mass, and/or travel times.

Technology areas include:

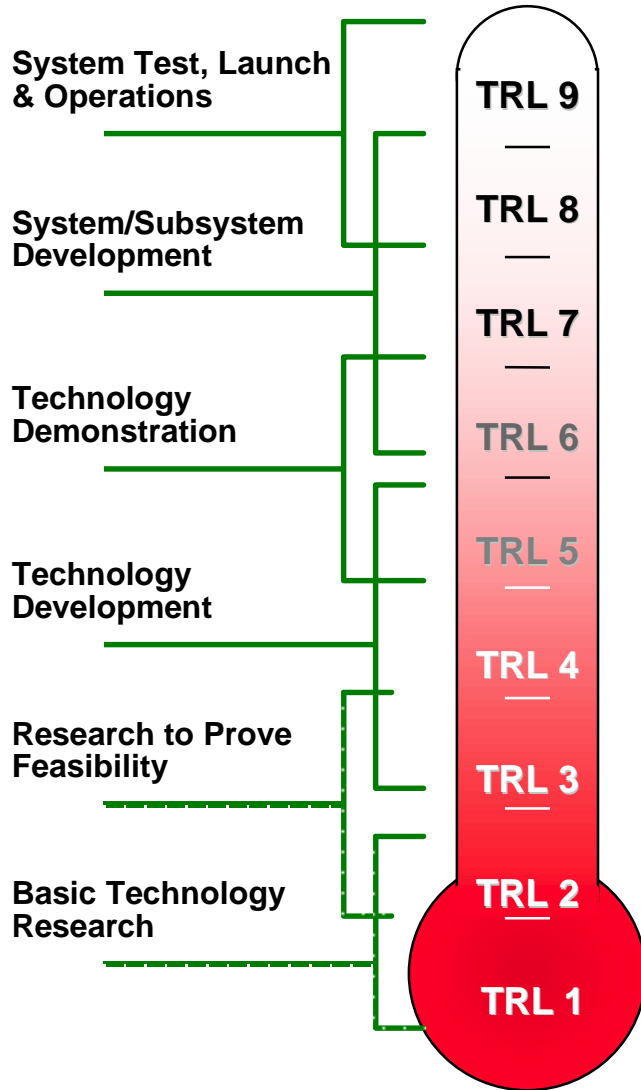
- Solar Electric Propulsion (nuclear electric is now part of Nuclear Systems Initiative)
- Propellantless Propulsion (aerocapture, solar sails, tethers, etc.)
- Advanced Chemical Propulsion

◆ Approach:

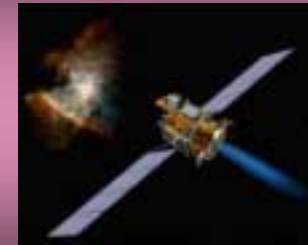
- Identify and prioritize the most promising technologies using systems analysis and peer review.
- Develop mid-TRL technologies to TRL 6 for incorporation into mission planning within 3-5 years of initiation.
 - Maximize use of open competition to seek best solutions



In-Space Propulsion Program Will Advance Mid-TRL Technologies to Support NASA Mission Applications



NASA Implementation: (Deep Space One Ion Engine Example)



In-Space Propulsion Technologies

Aeroassist



Adv. Electric Propulsion



Solar Thermal



Adv. Chemical



Tethers



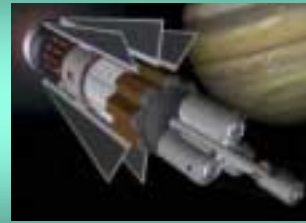
Solar Sails



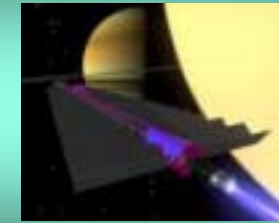
Plasma Sails



Low-TRL Technologies For the Future



External Pulsed Plasma



Fusion & Antimatter



Beamed Energy



In-Space Propulsion Program Status

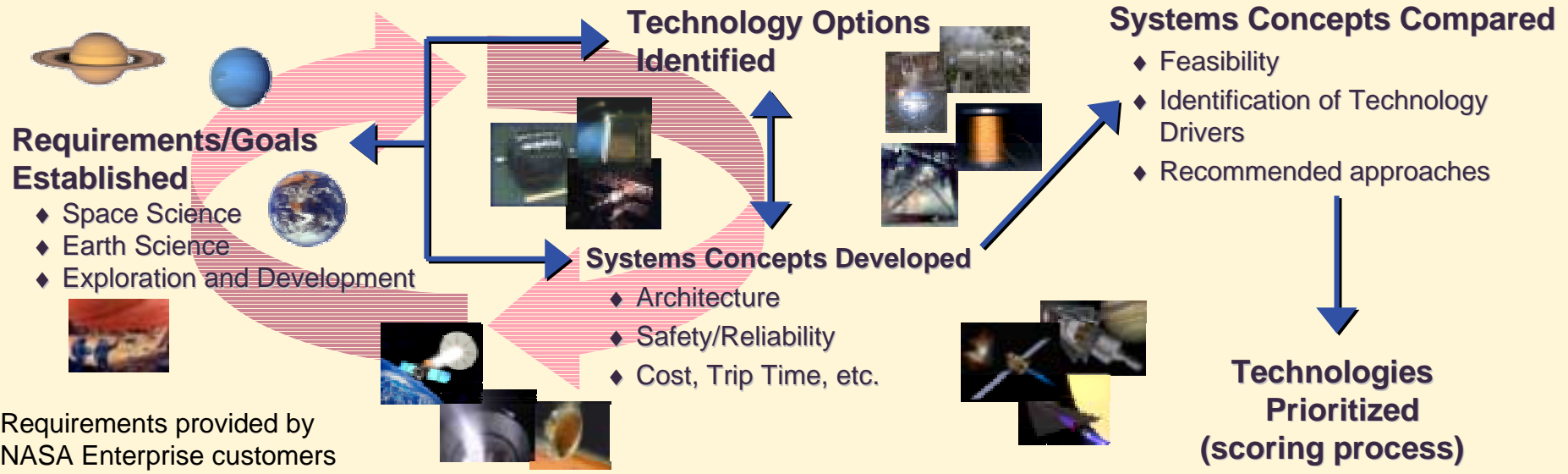


◆ Status

- In Space Propulsion is a HQ, Space Science, managed program
 - Dr. Colleen Hartman, Program Manager
 - MSFC is the implementing organization for ISP
- Competed efforts
 - Two awards made under an NRA specific to the Next Generation of Ion Electric Propulsion technologies.
 - Released In Space Propulsion Technologies, Cycle 1 solicitation (Aerocapture, Solar Sails, Electric Propulsion for NEP and Power Conversion) under the Research Opportunities in Space Sciences (ROSS) NRA. Selections announced in late August, 2002.
 - In Space Propulsion Technologies NRA, Cycle 2 (Aerocapture, Advanced Chemical, kW Solar Electric Propulsion, Momentum Exchange Tethers, Plasma Sails and Solar Sails) amendment to the ROSS NRA currently open - http://research.hq.nasa.gov/code_s/nra/current/NRA-02-OSS-01/appendA4_4.html.
- Directed efforts
 - FY02 directed tasks included Systems Analysis and continuation of NSTAR life test.
 - Eight directed tasks underway for FY03.
- All Nuclear technologies moved under the Nuclear Systems Initiative



FY02 In Space Propulsion Technology Prioritization Process



High Priority	Medium Priority	Low Priority	High Payoff/High Risk
Aerocapture	Advanced Chemical	Solar Thermal	Solar Sails 1 g/m ²
NGI (5/10 kW)	Solar Electric		Momentum Exchange Tethers
Solar Sails	SEP Hall (100 kw)		Plasma Sails

**Cross-Enterprise
In-Space
Propulsion
Priorities**



In-Space Transportation Technology Products

High Priority Technologies



◆ Aerocapture

- Low-mass aeroshell with integrated TPS
- Aerocapture flight-like instrumentation
- Advanced Aerodynamic Decelerators (trailing ballutes, attached ballutes and inflatable aeroshells)

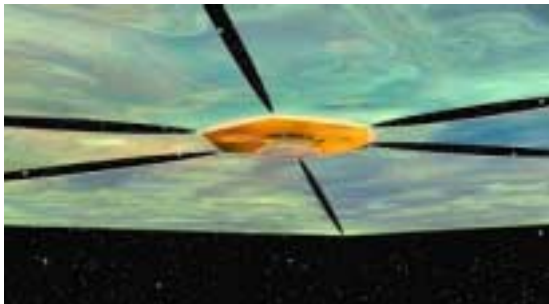
◆ Next Generation Ion Thruster

- Next generation integrated ion engine thruster technology
 - NASA's Evolutionary Xenon Thruster
 - Carbon Based Ion Optics



◆ Solar Sails

- Sail subsystem design and fabrication and ground demonstration
- Structural testing of sail booms
- Long term environmental evaluation of ultra-thin sail material





In-Space Transportation Technology Products Medium / Low Priority Technologies



◆ **Advanced Chemical**

- Fuels development
- Cryogenic Fluid Management
- Lightweight components

◆ **kW Solar Electric Propulsion**

- Laboratory demonstration of 50kW Hall thrusters
- Competitively select thruster technology advancement based on application

◆ **Solar Thermal Propulsion**

- Technology investments under further study
- Directed tasks focused toward fundamental performance questions

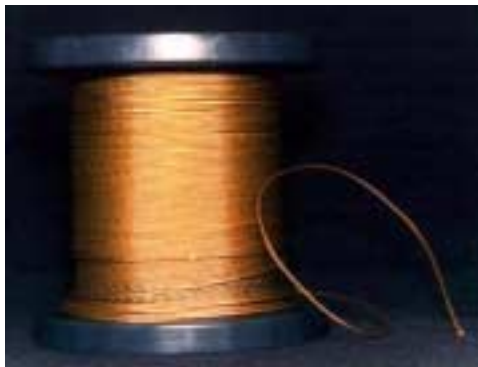


In-Space Transportation Technology Products High Risk/High Payoff & Lower Priority Technologies



◆ Plasma Sails

- Thrust measurement and validation
- Compare analytical model results vs. Laboratory test data



◆ Momentum Exchange Tethers

- Model development and evaluation
- Catch Mechanism concept
- High strength tether

◆ Solar Sails < 1g/m²

- Ultra-lightweight sail materials
- Large area lightweight structures and mechanisms



NASA's In-Space Propulsion Technology Program: Overview and Update

Les Johnson,^{*} Leslie Alexander,[†] Randy M. Baggett,[‡] Joseph A. Bonometti,[§] Melody Herrmann,[¶]
Bonnie F. James,[#] and Sandy E. Montgomery^{**}
*NASA Marshall Space Flight Center
Huntsville, Alabama 35812*

NASA's In-Space Propulsion Technology Program is investing in technologies that have the potential to revolutionize the robotic exploration of deep space. For robotic exploration and science missions, increased efficiencies of future propulsion systems are critical to reduce overall life-cycle costs and, in some cases, enable missions previously considered impossible. Continued reliance on conventional chemical propulsion alone will not enable the robust exploration of deep space—the maximum theoretical efficiencies have almost been reached and they are insufficient to meet needs for many ambitious science missions currently being considered. The In-Space Propulsion Technology Program's technology portfolio includes many advanced propulsion systems. From the next-generation ion propulsion system operating in the 5- to 10-kW range to aerocapture and solar sails, substantial advances in spacecraft propulsion performance are anticipated. Some of the most promising technologies for achieving these goals use the environment of space itself for energy and propulsion and are generically called “propellantless” because they do not require onboard fuel to achieve thrust. Propellantless propulsion technologies include scientific innovations such as solar sails, electrodynamic and momentum transfer tethers, aeroassist, and aerocapture. This paper will provide an overview of both propellantless and propellant-based advanced propulsion technologies, as well as NASA's plans for advancing them as part of the In-Space Propulsion Technology Program.

I. Introduction

The In-Space Propulsion Technology Program is entering its third year and significant strides have occurred in the advancement of key transportation technologies that will enable or enhance future robotic science and exploration missions. At the program's inception, a set of technology investment priorities were established using an Agencywide prioritization process and, for the most part, has changed little, thus allowing a consistent framework in which to fund and manage technology development. The technology priorities are listed in Table 1. High-priority technologies are those considered enabling for a set of high-value midterm science targets. Medium-priority technologies are those that will enhance or enable missions that are not perceived as critical as those benefiting from the high-priority technologies, but are still important and need significant funding. Low-priority technologies will be matured as funding is available. The high-payoff/high-risk technologies are those that are the most immature, yet have the potential to be considered high priority once some key science and engineering feasibility questions are answered.

^{*} Manager, In-Space Propulsion Technology Projects Office, TD05

[†] Technology Area Manager, Chemical and Thermal Propulsion Project, TD05

[‡] Technology Area Manager, Next-Generation Electric Propulsion Project, TD05

[§] Technology Area Manager, Emerging Propulsion Technologies, TD05

[¶] Manager, Technology Planning and System Analysis, TD05

[#] Technology Area Manager, Aerocapture Technology Project, TD05

^{**} Manager, Solar Sail Propulsion Project, TD05

Technology development within the In-Space Propulsion Technology Program is funded primarily through competitive NASA Research Announcements and with industry, universities, and NASA field Centers eligible to bid. The result has been a national effort focused on maturing in-space propulsion technologies to technology readiness level (TRL) 6 for transition to flight at the earliest possible date.

Table 1. In-Space Propulsion Technology Program Priorities

High Priority	Medium Priority	Low Priority	High Payoff/High Risk
Aerocapture	Advanced chemical	Solar thermal	Momentum exchange electrodynamic reboost tethers
Next-generation solar electric propulsion	Solar electric propulsion (including Hall thrusters)		Very low areal density solar sails
Solar sails			

II. Aerocapture

A. General Description

Aerocapture uses a planet’s atmosphere to accomplish a quick, near-propellantless orbit capture—the placement of a space vehicle in its proper orbit. The atmosphere is used as a brake to slow down a spacecraft, transferring the energy associated with the vehicle’s high speed into thermal energy.

The aerocapture maneuver starts with a hyperbolic trajectory into the atmosphere of the target body. The atmosphere’s density creates friction, slowing the craft and placing it into an elliptical orbit. Onboard thrusters are then used to circularize the orbit.

This nearly fuel-free method of decelerating a space vehicle could reduce the typical mass of an interplanetary spacecraft by more than half, allowing for a smaller and less expensive vehicle—one better equipped to conduct long-term science at its destination and to enable greater scientific return—and for faster trip times. In fact, aerocapture, when combined with solar electric propulsion technology, enables missions to outer planet destinations that would be impractical using conventional propulsion.

The requirement to slow down a spacecraft nonpropulsively can be achieved in two ways. The craft can be enveloped by a structure with heat shielding applied to the external surfaces. Such rigid “aeroshells” were used during entry and descent into Mars’ atmosphere by the Mars Pathfinder in 1997 and the Mars Exploration Rovers in early 2004. However, one distinction is that these missions were direct entry into a planetary atmosphere while aerocaptured systems will remain in orbit. Another option is for the vehicle to deploy an aerocapture inflatable deceleration system as an inflatable ballute—a combination parachute and balloon made of thin, durable material.

B. Technical Approach

Four different technology concepts are under consideration or development for aerocapture use: (1) blunt body, rigid aeroshell design; (2) slender body, rigid aeroshell design; (3) trailing ballute design; and (4) attached ballute design.

The blunt body, rigid aeroshell system encases a spacecraft in a protective shell. This shell provides an aerodynamic control surface and a means of protection from the high heating experienced during high-speed atmospheric flight. Once a space vehicle is captured into a planet’s orbit, the aeroshell is jettisoned.

An aeroshell consists of three main parts: (1) the external thermal protection material; (2) adhesives, which are used to bond the thermal protection system (TPS) to the aeroshell; and (3) an underlying structure to which the internal spacecraft and the external thermal protection material are attached. The challenges with this approach are to customize the design and thickness of the thermal protection material to accommodate different heating characteristics endured during aerocapture, and to develop adhesives capable of withstanding extremely high temperatures.

The slender body configuration looks much like an elongated capsule, with a hard shell surrounding the spacecraft. The design could provide increased volume in the interior of the spacecraft when compared to the blunt body design, allowing for improved packaging of larger crafts. Because of its slender body shape, the system also could provide increased tolerance for navigational and atmospheric uncertainties.

The trailing ballute features an inflated toroidal volume that is much larger than the spacecraft it is towed behind, much like a parachute, to slow the vehicle down. The trailing ballute design allows for easy detachment and minimizes interference with the spacecraft's operation. The ballute itself is made of a lightweight, thin-film material.

The trailing ballute design may have performance advantages over the aeroshell design. One such advantage is not enclosing the payload in a rigid shell during interplanetary cruise. Not having an enclosure around the spacecraft allows it to take full advantage of the volume available in the launch vehicle shroud. Also, in an aeroshell design, the shell takes all the force and heating of reentry. But with the trailing ballute design, the ballute would incur most of the aerodynamic forces and heat, allowing any protection around the payload to be very lightweight.

The attached forebody ballute looks much like the aeroshell or blunt body. The attached ballute is often referred to as a hybrid system, with a rigid foreshell and an inflated, attached ballute extending from either the front or back of the spacecraft.

The inflatable, attached ballute extends from a rigid nosecone and works much like a parachute, providing a large surface area to slow the spacecraft down to allow for an aerocapture maneuver to occur. As the spacecraft approaches a planet's atmosphere, the ballute is inflated and then jettisoned once the craft is captured into orbit.

Made of thin, lightweight material, such as DuPont Kapton[®], the inflatable, attached ballute design offers many of the same advantages and functionality as trailing ballute designs. The challenge facing researchers is to create a flexible, inflatable TPS to protect the spacecraft from the intense heat experienced during atmospheric entry.

C. Status

Aerocapture has never been flight tested. Relevant experience, however, exists from ablative entry capsules. Ablative entry technologies have been used throughout the history of the U.S. Space Program, including the Apollo return capsule and the Galileo probe.

D. Recent Accomplishments

In 2003 and 2004, several aerocapture TPS candidate materials, both ablative and nonablative, have undergone extensive arcjet testing. Advanced, lightweight structures have also been developed and are currently undergoing testing. Applied Research Associates, NASA Ames Research Center, NASA Langley Research Center (LaRC), and Lockheed Martin are involved in TPS/structures development for rigid aeroshell aerocapture applications. Both heat flux and recession sensors are also being developed at Ames Research Center. These sensors have been integrated into TPS and arcjet tested.

In 2003, Ball Aerospace made significant progress in the design, development, and testing of a trailing ballute system. Progress was made in the areas of ballute shape, survivability, flow stability, aeroelastic response and separation. Lockheed Martin won a contract to develop an inflatable aeroshell concept and Ball Aerospace won a contract for an inflatable attached afterbody concept. In 2002, the In-Space Propulsion Technology Program completed a systems definition study of aerocapture at Saturn's moon, Titan. Results showed significant reductions in trip time and overall system mass by utilizing aerocapture versus all-propulsive capture. The aerothermal analyses also uncovered that radiative heating accounted for a significant portion of the overall heating to the aerocapture vehicle. Technology development tasks were then initiated to accommodate those findings. In 2003, a systems definition study of aerocapture at Neptune was completed. Results of that study showed that aerocapture was a feasible approach and would save trip time and overall mass. In 2004, the In-Space Propulsion Technology Program is conducting a systems study of aerocapture at Venus.

In the summer of 2003, aerocapture was selected as one of five candidate technologies for the New Millennium Program ST-9 mission. ST-9 would provide an opportunity to flight validate aerocapture computational modeling and design tools and would provide for an opportunity to flight validate an integrated aerocapture system for future mission applications.

III. Next-Generation Solar Electric Propulsion

A. General Description

Solar electric propulsion (SEP) uses solar array power to ionize and accelerate heavy propellants, such as xenon, as inputs to a low-thrust, fuel-efficient, ion propulsion system (IPS). The typical IPS consists of ion thrusters, power processor units, and a propellant storage and management subsystem. The low thrust level of ion engines means that they have to run for a long time to accelerate the spacecraft to its desired velocity. For example, if the ion engine on Deep Space 1 (DS 1), NASA Solar Electric Propulsion Technology Application Readiness (NSTAR), was continuously operated at its maximum thrust, the spacecraft would accelerate from zero to 60 mph in ≈ 40 hr. However, after a year of thrusting at this level the spacecraft would be traveling more than 10,000 mph ($>4,500$ m/s). In addition, ion engines are the most fuel-efficient rockets used in space today. They are roughly 10 times more fuel-efficient than conventional chemical rocket engines.

B. Technical Approach

The simplest form of SEP, electrothermal thrusters, uses the heat produced from electric current passing through resistance heaters or the propellant itself to energize the propellant. Electrothermal thrusters have seen broad application on commercial satellites in recent years for stationkeeping and attitude control. It is a mature technology and has a rich future for applications involving orbit transfer and relatively high thrust.

The second type of SEP, electrostatic thrusters, relies on application of an electric field to accelerate the propellant directly. The propellant is initially ionized and then injected across a voltage potential established between an anode and cathode. The resulting force on the charged propellant ions accelerates them to high exhaust velocities. This type of device can achieve very high specific impulse (3,000 to 12,000 s and above) and is ideal for missions in which propellant mass must be minimized. These devices are generally limited to very low thrusts, but can achieve extremely high vehicle velocities due to their efficient propellant utilization. Ion propulsion and Hall thrusters fall into this category.

The third type of SEP, electromagnetic thrusters, employs a combination of electric and magnetic fields to accelerate ionized propellant and produce thrust. There is a wide variety of options available involving steady and pulsed modes of operation. All rely on the Lorentz force arising from the flow of ions (current) through a magnetic field to accelerate the propellant. These devices are more limited in terms of specific impulse than ion propulsion, but they are able to process higher amounts of power. These types of systems are ideal for applications where higher thrust levels are required. Magnetoplasmadynamic thrusters, Lorentz force accelerators, and pulsed inductive thrusters fall into this category.

The emphasis of the In-Space Propulsion Technology Program is on ion thrusters, though Hall thrusters are also part of the technology portfolio.

C. Status

Ion engines have been demonstrated in space and are the primary propulsion system for NASA's Dawn mission. The first use of an ion propulsion system for primary propulsion was on the DS 1 mission in 1998.

The ion engine on DS 1, jointly developed by NASA Glenn Research Center (GRC), Boeing, and the NASA Jet Propulsion Laboratory (JPL), was designed to operate for 1 yr at its maximum power level of 2.5 kW (≈ 3.4 hp). Over this time NSTAR used ≈ 83 kg of xenon, the propellant of choice for ion thrusters. Xenon is found naturally in Earth's atmosphere, is chemically inert, and environmentally safe. Several long duration tests were performed to make sure the ion engine for DS 1 would last long enough to perform the mission. These included a 1,000-hr test, a 2,000-hr test, and an 8,000-hr test, all performed at the engine's maximum power level. The maximum power level is believed to be the most stressing condition for the engine. Beginning in the fall of 1998, the DS 1 flight spare engine was placed in a long duration test at JPL with the objective of demonstrating that the engine could be run for 150% of its design life. At the end of the JPL extended life test in June 2003, the NSTAR flight spare engine had operated for more than 30,352 hr and processed more than 235.1 kg of xenon. This is by far the longest any rocket engine has ever been operated and corresponds to 283% of its original design life.

D. Recent Accomplishments

The next-generation electric propulsion (NGEP) focus is to advance electric propulsion system and component technologies. In the past year under NGEP, GRC completed phase I of NASA's evolutionary xenon thruster (NEXT) development. NEXT phase I objectives included definition of the NEXT propulsion system requirements

and a successful demonstration of system level performance at power levels in excess of 7 kW using an engineering model NEXT thruster with a breadboard power processing unit and breadboard propellant management system. GRC also operated the NEXT 40-cm thruster for more than 2,000 hr and identified several design improvements for the prototype thruster currently under development in phase 2. JPL's extended life test (ELT) of the DS 1 flight spare NSTAR thruster exceeded 30,000 hr of operation before completing a planned shutdown. At its conclusion in June 2003, the NSTAR ELT was the longest life test ever performed on an ion thruster. Following the ELT, thruster life test data and hardware evaluation significantly contributed to improving the NEXT thruster design. Under the NGEF carbon-based ion optics effort, JPL successfully completed design, fabrication, vibration and performance testing of 30-cm carbon-carbon ion optics. Boeing Electron Dynamic Devices completed fabrication and vibration test of 30-cm pyrolytic graphite grids. If flight qualified, these grids will significantly improve the life/throughput capability of ion thrusters. Other NGEF significant technology advancements were made by GRC in high power Hall thruster and high current hollow cathode designs. GRC completed performance testing on the NASA-457M Hall thruster up to 90 kW supporting further development of an engineering model thruster.

IV. Solar Sails

A. General Description

Solar sail propulsion uses sunlight to propel vehicles through space by reflecting solar photons from a large, mirror-like sail made of a lightweight, reflective material. This source of propulsion is not to be confused with the solar wind, which does not provide any significant level of thrust. The continuous photonic pressure provides propellantless thrust to hover indefinitely at points in space or conduct orbital maneuver planes changes much more efficiently than conventional chemical propulsion. Eventually, it might propel a space vehicle to tremendous speeds—theoretically much faster than any present-day propulsion system. Because the Sun supplies the necessary propulsive energy, solar sails also require no onboard propellant, thus reducing payload mass.

First-generation sails will vary in size from 100 to 200 m, depending on mission destination, and typically would be three-axis stabilized. It would be compacted and stowed for launch. Once deployed, the sails would be supported by ultra-lightweight trusses.

Solar sails are composed of flat, smooth material covered with a reflective coating and supported by lightweight structures attached to a central hub. Near-term sails likely will use aluminized DuPont Mylar[®] or CP1. Both materials have previously flown in space. More robust sails might use a meshwork of interlocking carbon fibers.

B. Technical Approach

A solar sail could fly in low-Earth orbit, but it would need to be robust enough to withstand significant gravity and environmental loads. Missions to the outer solar system and beyond require further innovations in architectures and materials. While an interstellar probe is a notable potential future mission application for sails, it is a far-term vision. The most near-term applications are for heliocentric missions in the Earth's neighborhood (the Earth-Sun L1 libration point for example). This class is the current focus of the In-Space Propulsion Technology Program's effort. It will lead to the next generation of solar sails which will enable a close approach to the Sun (<0.25 au) where thermal and radiation environments will be more stressing.

NASA is concentrating its development effort on the three-axis stabilized, square sails. This sail looks much like a kite. Four booms extend from a central hub that houses the four triangular sail quadrants during launch.

C. Status

Two teams have been selected by NASA to lead hardware development activities that will culminate in ground demonstrations of key solar sail technology systems. L'Garde, Inc., of Tustin, CA, is developing a solar sail system that employs booms that are flexible at ambient temperatures but "rigidize" at temperatures below -35 °C. Their concept uses articulated vanes located at the corners of the square to control the solar sail attitude and thrust direction. Able Engineering Company of Goleta, CA, is developing a coilable longeron that deploys in space much the way a spring-loaded screw is rotated to remove it from an object. Their concept for attitude control is to twist the booms and possibly shift the center of mass.

Both hardware development activities began with a 3-mo concept study for a design reference mission. This was followed by a 12-mo phase to design, fabricate, and test 10-m subscale solar sails to drive out design issues in the spring of 2004. The next phase focuses on scaling the design and fabrication processes followed in early 2005 by the demonstration of a 20-m subscale solar sail system at the Plum Brook facility at GRC near Sandusky, OH.

D. Recent Accomplishments

In the summer of 2003, solar sail technology was selected as one of the candidate technologies for the New Millennium Program ST-9 mission. In January 2004, LaRC presented a conceptual design for an optical diagnostic system (ODS) to provide on-orbit characterization of solar sail shape. An ODS breadboard exercise was conducted in conjunction with the following activity. In March and April 2004, the 10-m system ground demonstrators were tested in NASA's thermal vacuum chambers. Tests included deployment functionality demonstrations and static and dynamic structural characterizations.

V. Advanced Chemical Propulsion

A. General Description

Though it has its limitations, chemical propulsion will be the workhorse of in-space transportation for many years to come. Those technologies that reduce the mass fraction of the propulsion system in favor of science will be the focus of in-space propulsion technology investments in this area.

B. Technical Approach

Planned investments in this area are currently under review.

VI. Solar Thermal Propulsion

A. General Description

Solar thermal propulsion makes use of sunlight to directly heat and expel a propellant, in lieu of either chemical combustion or electromagnetic acceleration of it. The heated propellant is fed through a conventional rocket nozzle to produce thrust. The engine thrust is directly related to the surface area of the solar collector and to the local intensity of the solar radiation.

B. Technical Approach

Most proposed designs for solar thermal rockets use hydrogen as their propellant due to its low molecular weight, but many other propellants are being considered. There are two basic solar thermal propulsion concepts, differing primarily in the method by which they use solar power to heat the propellant.

Indirect solar heating involves pumping the propellant through passages in a heat exchanger that is heated by solar radiation. The windowless heat exchanger cavity concept is a design taking this radiation absorption approach.

Direct solar heating involves exposing the propellant directly to solar radiation. The rotating bed concept is one of the preferred concepts for direct solar radiation absorption; it offers higher specific impulse than other direct heating designs by using a retained seed (tantalum carbide or hafnium carbide) approach. The propellant flows through the porous walls of a rotating cylinder, picking up heat from the seeds, which are retained on the walls by centrifugal force. The carbides are stable at high temperatures and have excellent heat transfer properties.

VII. Momentum Exchange Electrodynamic Reboost Tethers

A. General Description

Momentum-exchange tether propulsion transfers momentum from one object to another by briefly linking a slow-moving object with a faster one. Much the same way ice skaters play "crack the whip," the slower object's speed could be dramatically increased as momentum and energy is transferred to it from the faster object. Similarly, a rotating tether facility in an elliptical Earth orbit might snare slower moving spacecraft in low-Earth orbit and throw them into much higher energy orbits.

The momentum-exchange electrodynamic reboost (MXER) tether propulsion system could use momentum-exchange to transfer satellites from low-Earth orbit to geosynchronous transfer orbit and beyond. After throwing the payload, the MXER tether would then use energy collected from solar panels to drive electrical current through the tether. This electrical current would push against the Earth's magnetic field and reboost the tether's orbit, restoring the energy that was transferred to the payload.

Once launched to low-Earth orbit by a rocket, the MXER tether system is intended to deploy a tether roughly 60 to 90 mi (100 to 150 km) in length. This tether would be made of lightweight, high-strength material, coated

for protection from the space environment. Part of the tether would also incorporate an insulated conductive material, like aluminum, to carry the electrical current needed to reboost the tether.

Payloads bound for high-Earth or escape orbits, such as communications satellites and interplanetary spacecraft, would be launched by rocket to low-Earth orbit. There, they would rendezvous with the tip of the spinning MXER tether, which would snare them via a net-like catch mechanism and then throw them toward their final destination. The process would eliminate or reduce the need for the upper-stage booster rocket usually associated with these high-energy orbits. And because the MXER tether could reboost its own orbit without propellant, it could repeat its orbital transfer duties for the duration of its lifespan. Also, since the need for an expendable upper-stage rocket—normally used only once—is eliminated or reduced, this capability would mean smaller, less expensive rockets could be used to launch the payloads.

VIII. Technology Planning and Systems Analysis

A. General Description

The In-Space Propulsion Technology Program established a technology planning and systems analysis team to identify technology investment needs. The main objective of the systems analysis team is to support the program with appropriate systems analysis studies to provide critical data to use in determining funding priorities and program direction. The In-Space Propulsion Technology Program has assembled a core systems analysis team that can support quick turnaround studies and will create and/or utilize a database of tools and simulations in each technology area to support systems analysis studies.

IX. Conclusion

Progress is being made toward the delivery of high-priority, first- and second-generation in-space propulsion technologies for potential space science applications within the next 2–3 yr. The next-generation electric (ion) propulsion system is moving toward an integrated ground demonstration in FY 2006. The first generation rigid aeroshell is comparably headed toward ground validation in the same timeframe. Solar sail technology, while impossible to completely validate to TRL 6 on the ground, will be matured sufficiently for flight validation as early as FY 2006/2007.



IN-SPACE PROPULSION

WHO

WE ARE

WHAT

WE DO

WHY

WE DO WHAT WE DO

WHEN

THINGS WILL HAPPEN

HOW

WE DO IT

ISP -

Education and Public Outreach (EP&O) for educators & students grades 5-8

TECH ISP -

In-depth technical information about space propulsion technologies

Ongoing Work

Requests for Information (RFI)

Presently all Requests for Information are closed
See below Request for Information Archives for previous RFI's

Research Opportunities of Space Science NRA ROSS- 2002

[ROSS-2002 NRA Summary](#)

[ROSS-2002 Appendix A4.2 In-Space Propulsion Technologies](#)

[Previous NRA Awardees](#)

Request for Information Archives:

Emerging Propulsion RFI (closed)

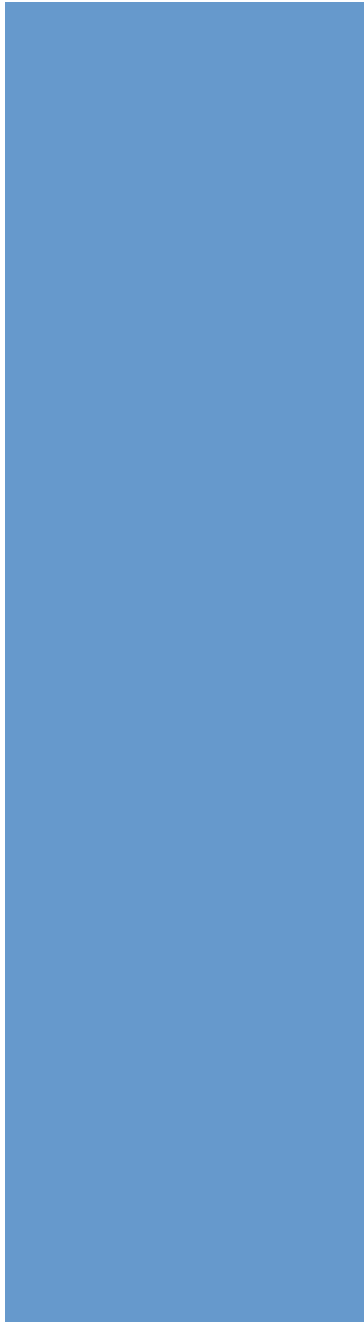
The Request for Information (RFI), Solicitation Number: NNM04AA02L, seeks information on new, innovative in-space propulsion technologies. Following receipt of submissions, a multi-center team will evaluate the submissions and make recommendations to the Emerging Propulsion Technologies Manager in the In-Space Propulsion Technology Projects Office at Marshall Space Flight Center for possible solicitation in the recommended area(s) under Cycle 4 NRA. For more complete information, follow the link below to the announcement.

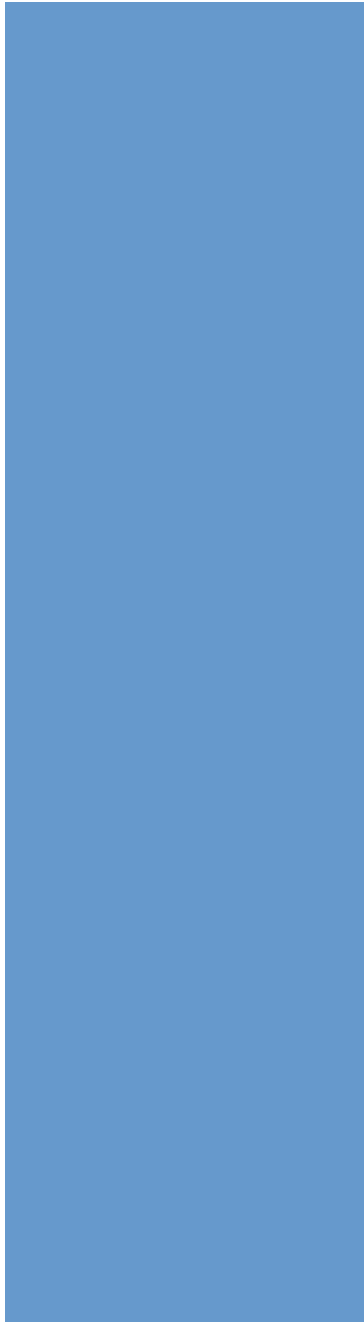
<http://prod.nais.nasa.gov/cgi-bin/eps/synopsis.cgi?acqid=111458>

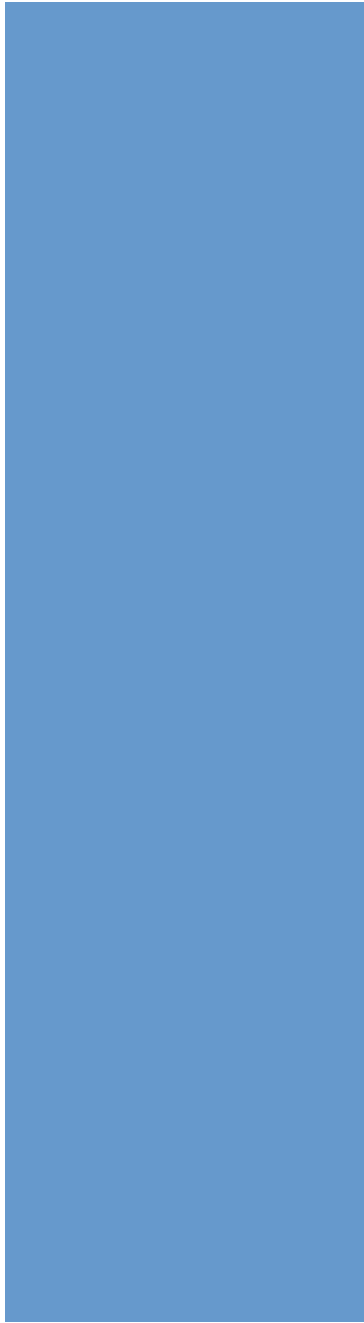
Advanced Chemical RFI (closed)

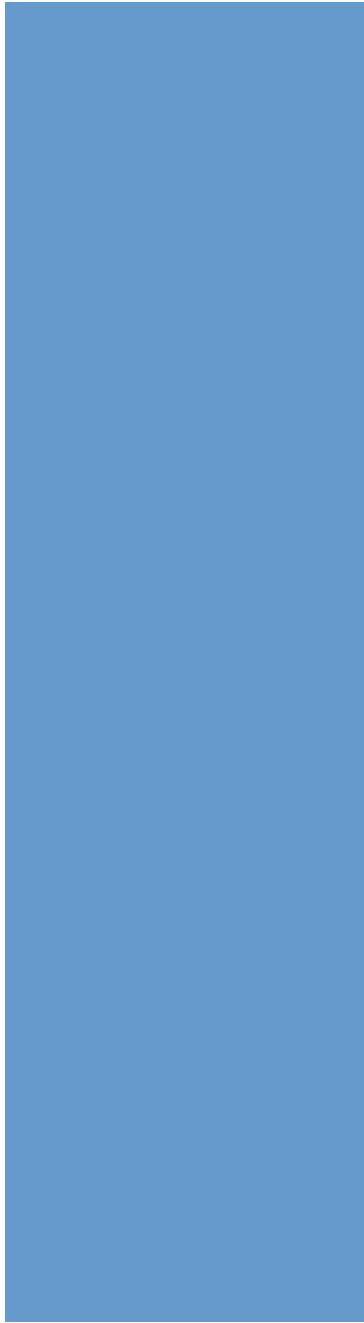
The Request for Information (RFI), Solicitation Number: NNM04AA01L, is seeking information from organizations that have flown chemical propulsion systems on deep space missions, ideas for improving the performance, reliability, cost, and operability of those systems based on their experiences for the In-Space Propulsion Technology Project. In addition to "lessons-learned", this solicitation also seeks the identification of mid-TRL technologies that, if matured appropriately, would improve performance, reliability, cost, and operability. For more complete information, follow the link below to the announcement.

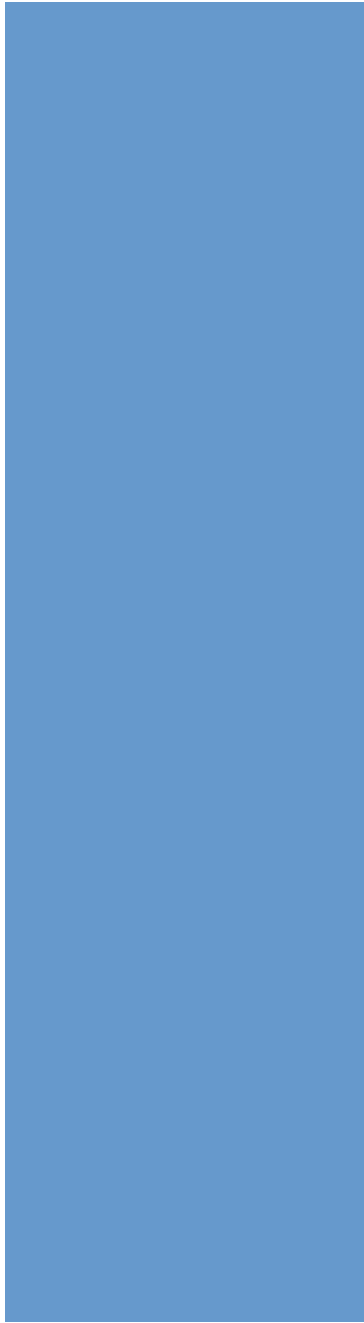
<http://prod.nais.nasa.gov/cgi-bin/eps/synopsis.cgi?acqid=111914>

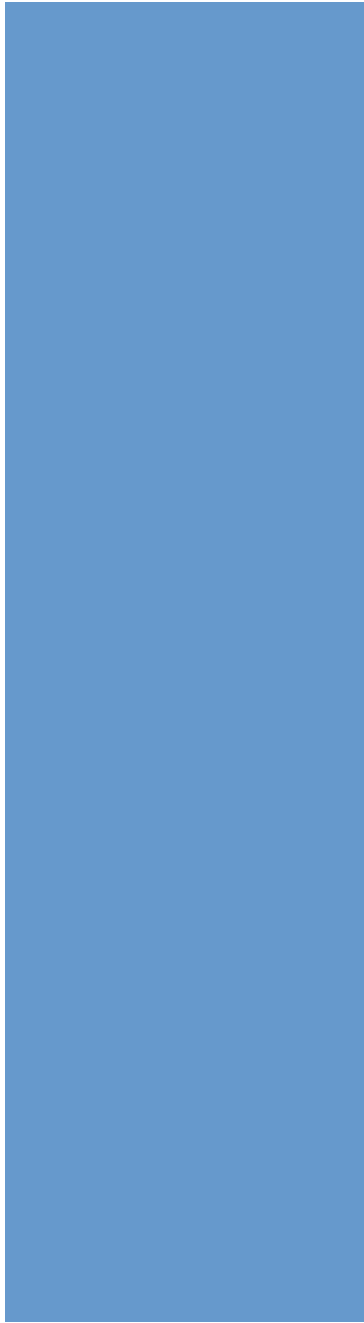


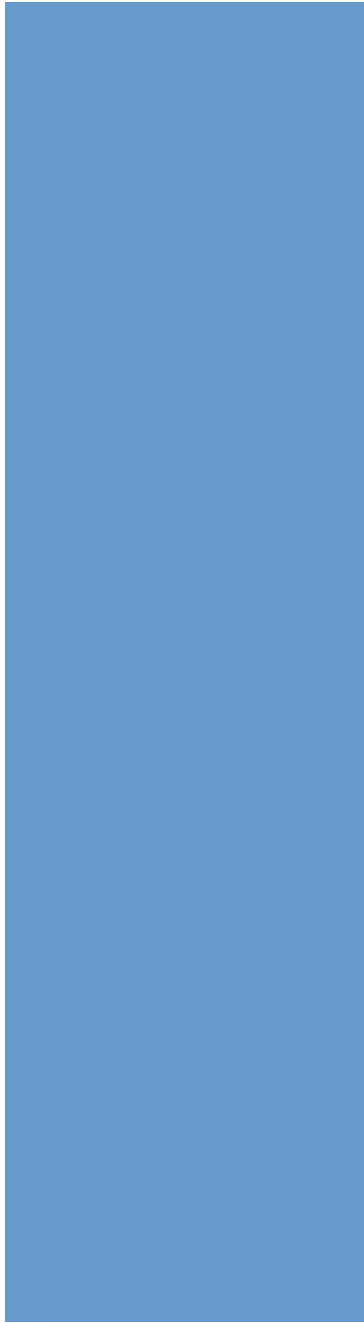














[Home](#) ~ [Who](#) ~ [What](#) ~ [Why](#) ~ [When](#) ~ [How](#)
[ISP for Teachers & Students](#) ~ [Technical ISP](#)
[Space Transportation Web Site](#)

In-Space Propulsion Technologies Proposal Information Package (PIP)

	<p>ROSES 2005 NRA More info coming soon</p>
--	---



IN-SPACE PROPULSION

WHO

WE ARE

WHAT

WE DO

WHY

WE DO WHAT WE DO

WHEN

THINGS WILL HAPPEN

HOW

WE DO IT

ISP -

Education and Public Outreach (EP&O) for educators & students grades 5-8

TECH ISP -

In-depth technical information about space propulsion technologies

New Business Opportunities:

[Research Opportunities in Space Science ROSS-2004 NRA](#)

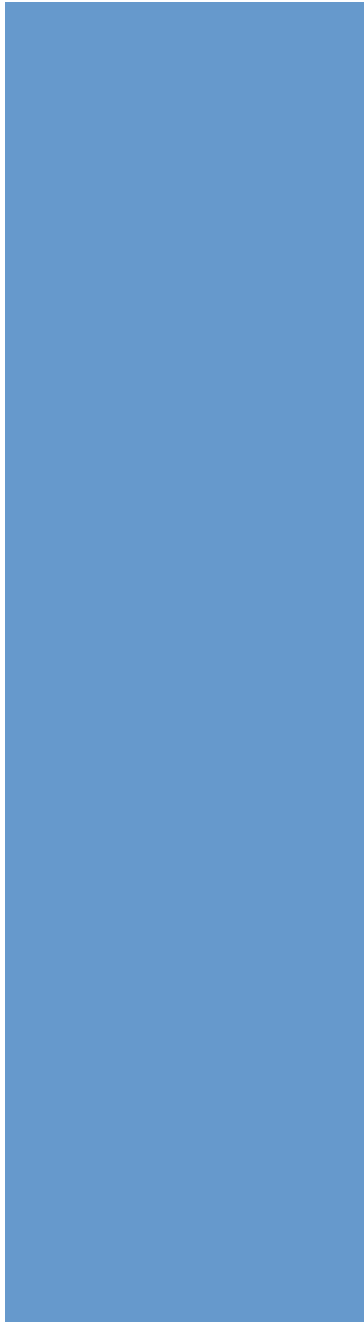
[ROSS-2004-Cycle 3A Proposal Information Package](#)

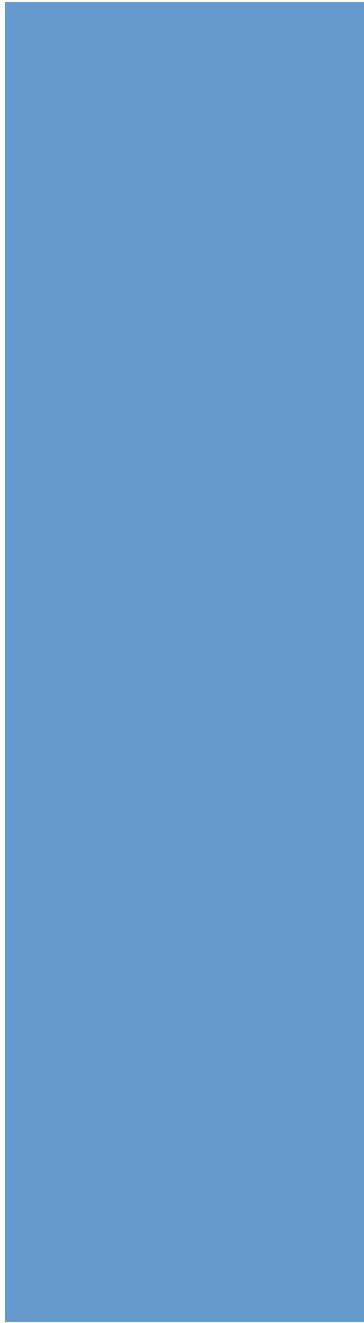
[ROSS-2004 Electronic Submission of Notice of Intent](#)

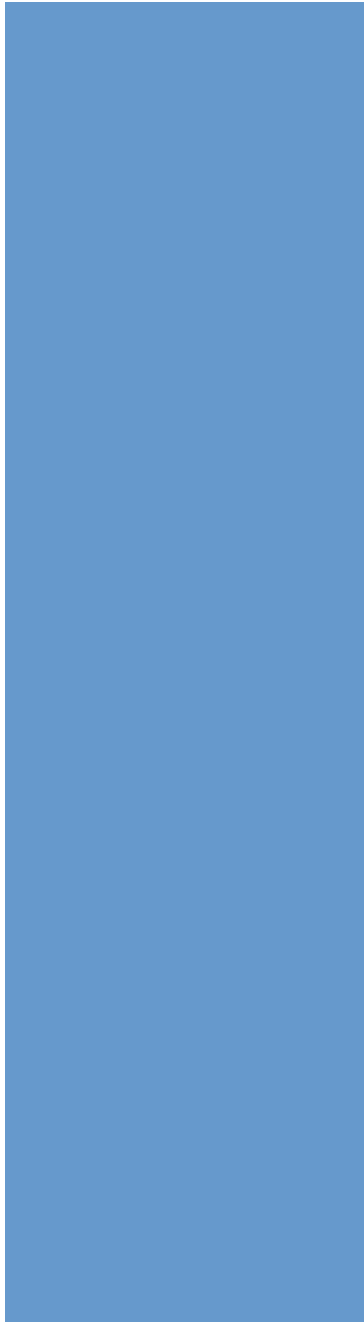
[2004 NRA Proposer's Guidebook](#)

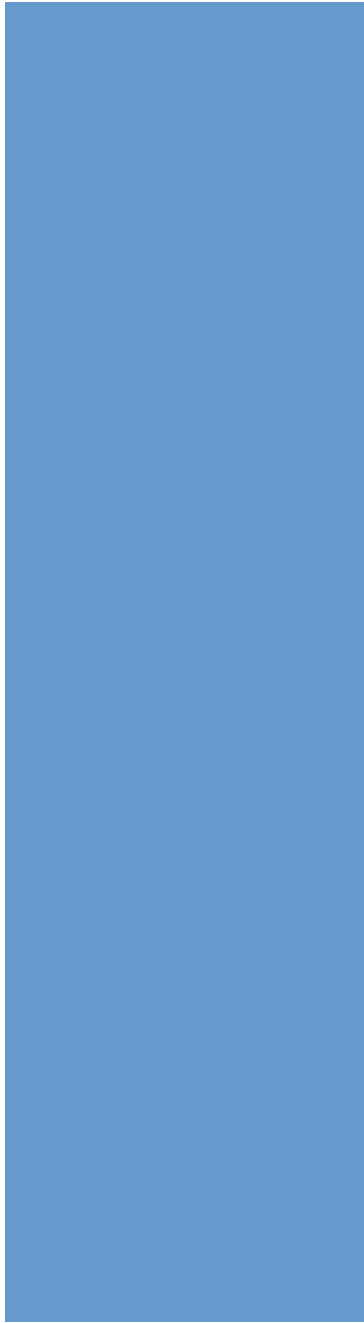
To read more on the objectives, approach and status of In-Space Propulsion technologies read NASA's In-Space Propulsion Technology Program: [Overview and Update](#) and [An Overview of NASA's Solar Sail Propulsion Project](#) presented here by the Project Manager and Technical Area Managers.

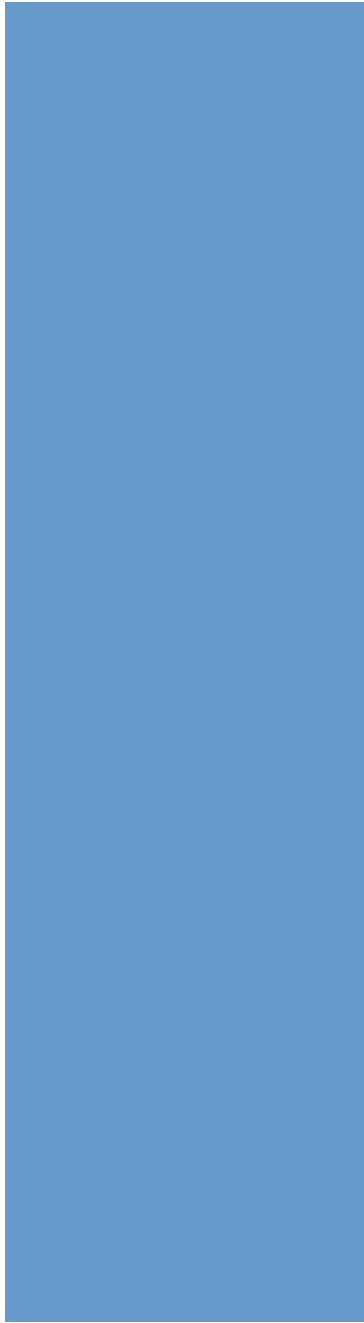
To read more about the interests for In-Space Propulsion on going work click [here](#).

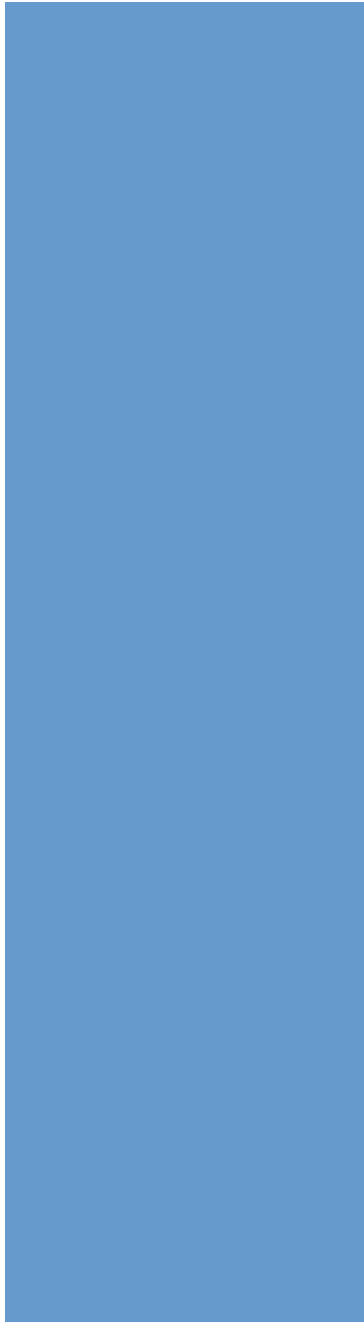


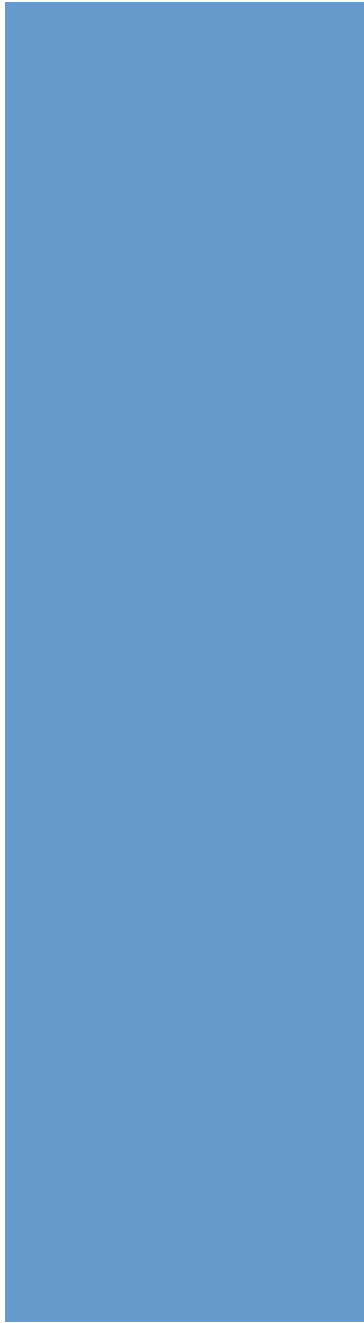


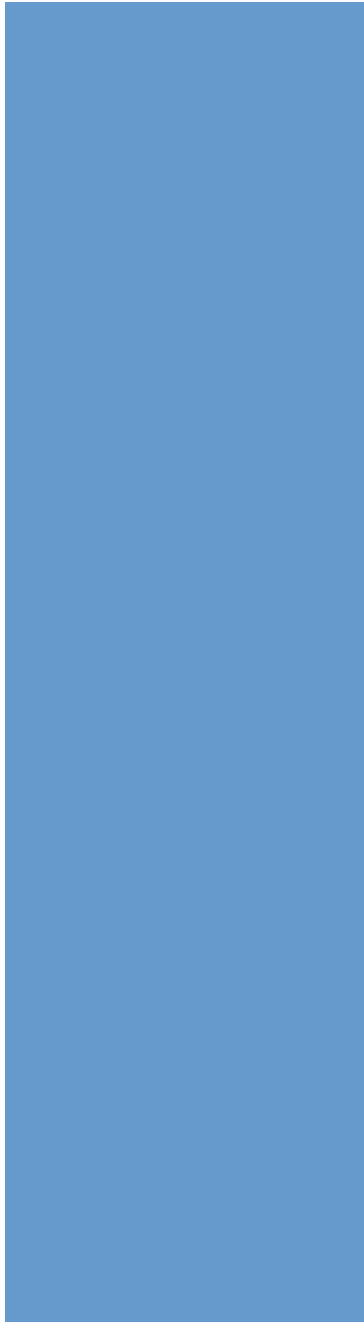














[Home](#) ~ [Who](#) ~ [What](#) ~ [Why](#) ~ [When](#) ~ [How](#)
[ISP for Teachers & Students](#) ~ [Technical ISP](#)
[Space Transportation Web Site](#)



IN-SPACE PROPULSION



WHO

WE ARE

WHAT

WE DO

WHY

WE DO WHAT WE DO

WHEN

THINGS WILL HAPPEN

HOW

WE DO IT

ISP -

Education and Public Outreach (EP&O) for educators & students grades 5-8

TECH ISP -

In-depth technical information about space propulsion technologies

NRA Cycle 1 Awards - In Space Propulsion

Topics/Technology Area: Spacecraft / Solar Sails

Program Manager: Edward (Sandy) Montgomery - NASA/MSFC

Three Selections:

1. Able Engineering Company - Scalable Solar Sail System Development and Ground Demonstration

The ABLE-SRS team proposes a disciplined systems engineering development program that culminates in a ¼-scale demonstration of a 100-m class solar sail system. ABLE's kinematically determinant large-system design and test approach produces a solar sail system amenable to credible flight qualification via practical ground testing. This assertion is backed by ABLE's 100% success rate in developing and ground-test-qualifying very large space structures for flight. Our proposed design and system demonstration test approach will prove solar sails are ready for Sentinel class (100-m) and future larger missions. We propose a phased technology validation effort begins in phase one with detailed design studies to identify technical issues arising at the system level. In phase two we develop detailed designs, validate analytical models and begin validating selected element and subassembly hardware. In phase three we integrate our validated subassemblies into a sail system, and demonstrate the flight-worthiness of our sail system design approach with detailed and system-wide ground tests. Under the systems engineering leadership of ABLE Engineering, our team joins leading NASA and industry solar sailing technologists, flight-seasoned engineers, and private consultants to focus a wealth of aerospace engineering and solar sailing program experience on the solar sail system demonstration task. The program, over three phases, builds a solid engineering basis for the solar sail system demonstrator. A detailed series of tests are

performed to demonstrate and measure performance, and correlations with pre-test modeling validate our tools for future missions. Our ground-testable sail system will meet required sail performance with good margins and high reliability. Our system design and demonstration of this technology under NASA funding will ready sail technology not only for the critical Sentinel missions, but also for a series of progressively more challenging missions planned by NASA, NOAA, and the DoD.

2. L'Garde Inc. - Development of an ultra-light weight and eminently scalable inflatable deployed and supported Solar Sail Subsystem

L'Garde, Inc. shall use its space-flight experience in inflatable, rigidizable and membrane space structures to develop a scalable, lightweight and cost-effective solar sail subsystem to TRL-6. We propose a carefully planned program, based on Solar Sail Design, Manufacturing and Tests we have done since 1994, and are doing now for the Team Encounter mission. We have also brought to the effort a strong team of experts in (a) Structures, Materials and Dynamic testing (NASA-LaRC), (b) Mission/Orbit Definition, Systems Engineering and GNC (JPL and Ball Aerospace); and (c) Team Encounter for the Outreach Program. The NASA requirements and the systems analysis results will flow down to the design analyses of the Solar Sentinel Solar Sail subsystem concept design. This will result, after the scaling analyses, to the design of three ground-test items proposed to bring the Solar Sail SOA to TRL-6: The first will be a sub-scale, 10mX10m test unit for ambient deployment and design shake-down tests. The second will also be a 10mX10m unit for vacuum deployment, rigidization and dynamics testing. Based on the results of these two tests, the third test item, the 20mX20m full-scale test item design will be updated. The proposed effort culminates in the fabrication and test of the 20X20m unit at the NASA/GRC's Plum Brook facility. This final test unit shall be shown to meet or exceed all solar sail requirements by analysis and test results, followed by the Solar Sentinel Mission Concept design update. The proposed solar sail structure consists of four ultra-light, inflatable-rigidizable booms in a cruciform configuration, controllably deployed within a narrow geometric envelope, via a patented L'Garde process. The proposed rigidization is the Sub-Tg (or cold) rigidization method. The proposed sail material is 2-micron Mylar, metalized on both sides, proven by space-environment analyses and test to amply withstand the environments of most solar sail missions. L'Garde, however, is totally open to the use of any NASA-preferred materials. The sail will be reinforced against tearing and tear propagation and will be attached to

the cruciform structure in a following-load configuration. This results in the lightest possible scalable structure and virtually eliminates bending loads and long-column buckling. Based on our analytical and experimental results to date, we believe this is the most efficient path to an operational solar sail for NASA.

3. JPL - Solar Sails GNC Took Kit

The technology needed to accurately predict realistic flight performance estimates for solar sail missions does not yet exist. A team comprised of technical experts from the Jet Propulsion Laboratory, California Institute of Technology and Ball Aerospace & Technologies Corp. in Boulder, Colorado proposes to develop an integrated set of simulation tools to predict, re-calibrate, and optimize the trajectory, maneuvers, and propulsive performance of a sail during a representative flight mission. These trajectory optimization and sail-craft guidance, navigation and control (GNC) simulation tools are necessary for realistic studies of solar sail missions. Additional professional participants from government, industry and universities will add strategic expertise in modeling and simulation. This team is uniquely capable of developing a realistic solar sail GNC toolset owing to their actual low-thrust flight experience on New Millennium DS1 and development of a commercial sail-craft. The toolset will advance the technology readiness level to that needed for rapid design and planning of solar sail flight mission concepts. In addition, the toolset will be designed so that it can be easily integrated into an optimal GNC system for the flight of future sail missions. The toolset will include analytical models for (1) solar radiation pressure acting on the sail, (2) disturbance forces acting on the sail from gravitation and thermal torques, (3) orbital mechanics, (4) sail structural dynamics, (5) attitude control system dynamics, (6) navigation sensors, and (7) environmentally induced changes to sail properties. A mission concept from the class of Solar Wind Sentinels will also be modeled, and the integrated simulation tools will be demonstrated on that candidate mission.

Topics/Technology Area: Spacecraft / Aerocapture

Program Manager: Bonnie James - NASA/MSFC

Six Selections:

1. Langley Research Center - High Temperature Composites and Adhesives for Reduced-Mass Aeroshells

The objective of the work proposed here is to leverage several emerging structures and materials technologies to significantly reduce the mass of aeroshell systems. Because reduced mass translates directly into larger payloads and increased science, the importance of accomplishing this goal is common to nearly all planetary missions that utilize aerocapture. Current aeroshell designs typically use metallic structure. Sometimes conventional composite materials are incorporated into the design. The amount of thermal protection required for these materials is relatively great, and the resulting aeroshells are relatively massive. There are now new families of high-temperature resins and composite material manufacturing techniques that have the potential to significantly reduce mass and improve aeroshell design. The proposed effort is intended to demonstrate that the use of these technologies can result in significant mass reductions (approaching 30%) for the primary aeroshell structure and its associated thermal protection system (TPS). An additional goal is to show that these mass reductions can be obtained at relatively low cost, and without the high risk often associated with alternative aeroshell designs or planetary entry systems. The program will determine optimized aeroshell system masses for a range of planetary entry environments (including Titan and Neptune) with acceleration loads of 3-20g and peak structural temperatures ranging from 400-700 degrees Fahrenheit (for the primary structure that lies behind the TPS). The optimized systems should result in a significant mass savings for relatively less challenging missions (such as Titan aerocapture), and will hopefully go further to become enabling for more difficult missions (such as Neptune aerocapture). The approach will be to determine optimized aeroshell concepts through analysis of several exploration mission scenarios. State-of-the art high-temperature composite materials, resins, and adhesives will then be examined for incorporation into these concepts. The program will verify fabrication methods for lightweight compound curvature aeroshells through the fabrication of representative coupon samples, structural elements, and finally system level subcomponents, all of which will be tested in relevant environments. This effort will be a natural extension of work that has already been done to incorporate high-temperature materials into NASA aircraft and reusable launch vehicle (RLV) programs. The effort will build on the heritage of existing aeroshell design, and will use a building-block approach that begins with the identification and testing of coupon-sized material and adhesive specimens. Once appropriate materials

and adhesives have been verified for aerocapture in relevant environments, larger scale system-level components and finally a representative aeroshell prototype will be demonstrated. The goal will be to advance the TRL of high-temperature structural systems to a TRL of 6, and to maximize their impact on all aspects of aeroshell design.

2. NASA Ames Research Center - Development of Aeroshell Technologies for Aerocapture Missions to the Outer Planets

NASA Ames Research Center (ARC) and our team members propose to develop the critical aeroshell technologies to enable aerocapture missions in support of Solar System Exploration. The critical technologies that enable aerocapture are guidance, navigation and control (GN&C) and the thermal protection system (TPS). If the Aerocapture Flight Test Experiment (AFTE) was selected for the New Millennium Program ST7 mission (and was successful), much of the GN&C risk for aerocapture could have been retired. Unfortunately, AFTE was not selected for ST7. Independently, however, the TPS issues for outer planet exploration have not been adequately addressed and require a significant development effort. An aerocapture mission to Titan can be accomplished in the near-term utilizing existing TPS materials, some of which are flight proven. There are other materials, not yet at TRL 6, which offer potential cost savings and/or an enhanced opportunity to acquire valuable flight test data. These will require modest further development to reach TRL 6. Our proposed developmental efforts will offer a range of TPS options for a Titan aerocapture mission. An aerocapture mission to Neptune cannot be accomplished with existing TPS materials at acceptable aeroshell mass fractions. The Neptune aerocapture flight environment will expose the TPS to both very high heat fluxes and extremely large total heat loads (factors of 2 - 5 higher than Galileo). We propose to develop a new class of TPS concepts (utilizing existing materials) that will provide reliable, efficient performance for such severe environments. TPS selection, performance, and sizing for any atmospheric entry mission is governed by definition of the aerothermal environment it will be exposed to. Existing uncertainties in current capabilities to model several flowfield characteristics result in aeroshell designs incorporating significant margins. Some of these uncertainties can only be mitigated with flight data due to limitations of existing ground test facilities. We propose to improve the aerothermal environment modeling in those areas that can be supported with focused ground tests. Our primary methodology to develop the above mentioned aeroshell technologies is utilization of arc jet, ballistic range and wind tunnel testing. The

technology developed will focus on the two reference missions but will have broad application for future missions.

3. ELORET - MicroSensor and Instrumentation Technology for Aerocapture

Eloret Corp. and our partners NASA Ames Research Center (ARC), JPL, and SRI International, proposes to develop instrumentation technology for risk reduction of aerocapture for Solar System Exploration. This effort falls under the critical technology of Thermal Protection Systems. Current technology of sensors applied in flight for aeroshell flowfield or TPS response is based on 1960s technology. This effort will focus on raising the TRL from 3 to 6 for two instruments with the potential to have large impact on risk reduction and science payload mass fraction: heat flux/temperature; and recession. The recession sensor is proposed as an option to modernize the recession depth sensor flown on the Galileo mission. Direct measurement of heat flux will enable the quantification of time and location of transition to turbulence: a critical parameter in the conservative sizing of aftshell TPS mass. Both measurements will allow for direct verification of physics models used for TPS sizing, and atmospheric conditions. The baseline effort is the heat flux/temperature sensor, followed in priority by modernization of the Galileo ablation sensor option.

4. Applied Research Associates - Advanced Ablator Families for Aeroassist Missions

NRA 02-OSS-1 - In-Space Propulsion Technologies (Aerocapture) Notice of Intent to Propose Engineering Optimization, Testing and Analysis of Advanced Families of Charring Ablators for Aeroassist Missions to the Outer Planets and their Moons William M. Congdon Ablatives Laboratory Applied Research Associates, Inc. 14824 E. Hinsdale Ave., Ste. C Englewood, Colorado 80112 303/699-7737 - bcongdon@msn.com Donald M. Curry Structures and Mechanics Division NASA Johnson Space Center Houston, Texas 77058 281/483-8865 - donald.m.curry1@jsc.nasa.gov Timothy J. Collins Structures and Materials Division NASA Langley Research Center Hampton, VA 23681 757/864-3113 - t.j.collins@larc.nasa.gov Missions to the outer planets and their moons involving aeroassist technologies pose stringent thermal protection system requirements for high-performance, very lightweight ablative materials. Over the past three years, ARA, Inc. has developed family systems of advanced ablators that can meet these requirements. Now at a TRL of 4 to 5, these ablator families consist of flexible, filled silicones and

phenolics with densities from 11 lb/ft³ to 28 lb/ft³, and include formulations of still higher density for the most severe entry-heating environments. The new silicone-based materials are suitable for entry environments with peak heating up to about 200 Btu/ft²-sec (227 w/cm²). One advanced formulation, Hyperlite-A at 13 lb/ft³, shows good performance and the potential for significant weight savings for a Titan aerocapture or entry mission. Lightweight flexible phenolics, such as PhenCarb-28 at 28 lb/ft³, look promising for Neptune missions with peak heating in the range from about 1,000 to 2,000 Btu/ft²-sec (~1.1 to 2.3 kw/cm²). A Phencarb-32 or -36 should have more optimal performance and efficiency for still higher heating. All of these materials in the advanced ablator families use a new, state-of-the-art manufacturing process known as the Strip-Collar Bonding Approach, or "SCBA." This involves CAD/CAM and CNC laser milling to produce high-tolerance, reliable heat shields with greatly reduced labor requirements compared to the traditional method of honeycomb bonding and packing. Demonstration, subscale manufacturing to date has shown that SCBA offers cost savings in the range of 33% compared to the honeycomb method as used on Pathfinder and MER missions. Having developed these ablator materials to an intermediate TRL, and demonstrated their efficacy for advanced planetary missions, it is now important to increase their TRL to 6 by engineering optimization, testing and analysis. Thus, we have defined a joint ARA and NASA/JSC and NASA/LaRC program under ROSS-2002 to accomplish this goal. ARA will lead this two-year project and ARA's W.M.Congdon will be the Principal Investigator. In short, ARA's role will be centered on advanced TPS materials and their manufacture, and understanding how changes in formulation and constituents produce the desired changes in performance and weight. ARA will also have leadership for understanding and correlating ablator test results and for the refining of critically-important thermal-response models (math models) for predicting TPS performance in a flight environment. NASA/JSC's project responsibility will be based on its many unique capabilities for the systems and structures engineering aspects of spacecraft heat-shield development. JSC engineering will collaborate with other NASA centers (particularly LaRC) to define entry environments for key missions as they are evolved, will address aeroshell shapes and structures, and will conduct flight analyses to evaluate/define thermal protection system performance and requirements for advanced optimization of materials and models. JSC engineering will also define the material testing required for advanced ablator systems to demonstrate a technology maturity equivalent to a TRL 6 and prescribe the database needed to extend the TRL to an 8-9 value. NASA/LaRC will be responsible for investigating and defining suitable aeroshell

structures and structural materials for Titan/Neptune missions. This joint ARA/JSC/LaRC project will involve a substantial amount of arc-jet testing of advanced ablative materials. The purpose of this testing is fourfold: 1) to understand how existing advanced ablaters perform for defined and simulated mission environments; 2) to rank performance and select a best candidate for each specific mission; 3) to develop data that might lead to advanced optimization of a specific candidate as needed; and 4) to generate high-fidelity thermal response data for enhancement of material response models in a closely simulated environment of specific flight missions. Arc-jet testing will use the NASA/ARC facilities, in particular the 60 MW Interaction Heating Facility. Approximately 160 ablator samples will be arc-jet tested during this two-year project.

5. Lockheed Martin Astronautics - Aerocapture Technologies

In response to the NRA 02-OSS-01, Lockheed Martin with its extensive experience in design, manufacturing and test of aeroshell, is formally submitting this proposal toward the Aerocapture Technology of the NRA. Our experiences in design and manufacturing of many NASA's planetary entry vehicles, such as Mars Pathfinder, Galileo Probe and aeroshells for the Mars Exploration Program, will help advance the entry heatshield technology to highly mass-efficient systems for outer planet aerocapture. In addition to our in-house IR&D in Entry Systems, we will rely on our flight vehicle development experience to establish an efficient set of test programs, with structural and high-energy thermal testing facilities, to improve the level of aerocapture technology. These tests will include material properties definition, system mechanical definition and high-energy arcjet testing. Only by improving the mass efficiency, effective Thermal Protection Systems of the entry aeroshells, can the Titan and Neptune Aerocapture Missions be realized. This reentry technology also has direct application to other missions such as advanced Mars landers, Earth sample return missions and the like; will benefit many other NASA missions. Our proposal concentrates on the requested four technical areas associated within Section A, the Aeroshell Technologies task. These areas are collected into technical disciplines as follows: 1) Aeroshell System Requirements, 2) Aeroshell Design, 3) TPS Materials, and 4) Structural Materials and Adhesives. The first two areas provide aerocapture technical support and aeroshell design parameters that feed the last two areas, which perform development and test of candidate systems. We have identified three specific Structure/TPS systems that we believe to be highly promising for the large range of heating conditions specified in the Titan and Neptune reference

aerocapture missions: 1) Graphite composite/SLA-561V ablator system, 2) Carbon-carbon (C-C) monocoque system, 3) Option 3 advances the C-C design that incorporates high efficiency thermal insulation technology.

6. Ball Aerospace and Technologies Corp. - Technology Development of Ballute Aerocapture

Our team (Ball Aerospace & Technologies Corp., Langley Research Center, ILC Dover and the Jet Propulsion Lab) proposes to advance the critical technologies of system level trailing ballute aerocapture design from TRL 3 to TRL 6. Our core team has over 48 years of experience with aeroassist mission and technology development and 13 years of involvement with inflatable lightweight film assemblies. Our team has a mature working relationship based on current ballute aerocapture work being performed under a Gossamer NRA contract. Our trailing ballute aerocapture concepts offer payload mass fractions of more than 80%, nearly a 3 to 1 improvement over chemical orbit insertion for missions such as Titan and Neptune. The investments proposed not only retire risk and maturity issues for Titan and Neptune, but offer technology advancement and verification approaches that are scalable to many other missions. Our concepts provide complimentary technology to low-thrust advanced propulsion systems such as electric and solar sail, resulting in mass savings that enables lower cost, higher science return missions to most of the solar system. We propose a combination of design, analysis, process development and test that will retire the critical risks recognized by the aerocapture community. The critical risks addressed include: hypersonic/rarefied flow stability including wake shock focusing, aeroelasticity and structural dynamics including ballute deformation/ flowfield interactions, mission design and robust trajectory modulation including ballute separation algorithm development, tether design and ballute attachment, packaging, storage, inflation and deploy dynamics and materials assessments including strength, thermal capability, density, maturity, seaming, and fabrication. Analyses proposed include CFD/DSMC, FEA, and trajectory (3-dof and 6-dof Monte Carlo). Testing will include materials properties tests, hypersonic wind tunnel and under expanded free jet testing, along with the construction of prototypes for hypersonic tests, and deployment and inflation testing. At the end of the proposed effort we will deliver an optimized ballute configuration with minimum system mass and a roadmap for the next step: a low cost Earth flight demonstration minimizing mission and developmental risk.



[Home](#) ~ [Who](#) ~ [What](#) ~ [Why](#) ~ [When](#) ~ [How](#)
[ISP for Teachers & Students](#) ~ [Technical ISP](#)
[Space Transportation Web Site](#)



ISP IN-SPACE PROPULSION

(for students and teachers grades 5 thru 12)



EDUCATORS
Grades 5-8

STUDENTS
Grades 5-8

SCIENCE FAIRS

LINKS

ISP HOME

JUST FOR FUN

**EDUCATIONAL
OPPORTUNITIES**

...IMAGINE EDUCATORS

...igniting students' minds with all the thunderous power of a NASA rocket. And imagine doing it with NASA's help.

For many of you, the World Wide Web must sometimes wear the twin faces of Janus.

From one vantage point, it is a crucial resource for the classroom, offering an unprecedented wealth of access to information and learning materials. But from the opposite viewpoint, the Web can be as frustrating and tiresome a maze as any ever devised, fraught with dead ends, unexpected detours and untrustworthy guideposts.

Hard to inspire a classroom full of bright young minds with screen after screen of broken links and 404 error codes.

At NASA's In-Space Propulsion Web site, we strive to maximize the value of NASA's Web-based educational resources, while always seeking to minimize the frustrations of the online maze. One of the primary goals of the ISP Web presence is to be a clearinghouse

STUDENTS IMAGINE...

...driving an old car -- one with a clunky engine, lousy gas mileage, poor brakes and no antenna -- all the way from New York or Baltimore or some other East Coast city to the Grand Canyon in Arizona, one of the most breathtaking wonders of the natural world. You're excited about the trip... but it's an awfully long journey. And you can't stop anywhere along the way. There isn't much room for luggage. You can't even get much on the radio.

Now... imagine if, when you finally get to the Grand Canyon, you can't even stop! You can only lean out the window as you drive past, snapping pictures with your handheld camera, hoping you get at least a glimpse of the spectacle you came so far to see...

Sounds like a pretty lousy trip to us. But it's actually quite similar to the way past space missions into our solar system have been conducted.

Because of the heavy weight of the fuel

**Visit the NASA
explorers
website**

for teaching resources related to innovative propulsion technologies, space exploration, and the wonders of our solar system.

Here, thanks to [NASAexplores](#) and [NASA Spacelink](#), you'll find ways to inspire your students to start thinking like rocket scientists. We'll direct you to tools that can turn your classroom into a space laboratory, and to teaching packages that will transform your curriculum into a space-based journey of discovery that will challenge your students, broaden their horizons, and show them the potential for rewarding careers in math, science and engineering.

To better accomplish these goals, we need your feedback! [Contact us](#) with your ideas for new and better education tools, packages and links. Make us aware of your specific classroom needs, and the manner in which we can best serve them.

Like Dr. Robert H. Shaffer, dean and professor emeritus of Indiana University, we at ISP see young people "not as empty bottles to be filled, but as candles to be lit."

For NASA, "lighting the candle" is -- as it has ever been -- our primary focus. Launching missions to further humanity's exploration of the cosmos, to expand our scientific knowledge and improve life here on Earth, and to seek new inspiration and new

needed to drive a spaceship, because it's very difficult to carry enough fuel to run an engine that could slow down and put a vehicle into orbit around other worlds, and because traveling to our neighboring planets is just so slow... modern space travel needs a new solution. A solution that can provide space vehicles with more efficient engines and more powerful fuel, enabling them to reach their destinations faster and to stop and visit awhile -- not just flash past and snap a few pictures.

That's the job of the In-Space Propulsion Program, NASA's new team of scientists and engineers who are finding alternative methods of sending spaceships on science missions to other planets.

Missions you might someday have a hand in creating.

The purpose of this educational Web site is to interest students just like you in new propulsion technologies and the future of the space program. Here, you'll find helpful explanations that will allow you to think just like a rocket scientist -- and your teachers will find education packages that will turn your classroom into a space laboratory!

Some of these technologies and programs may sound a lot like science fiction to you at first, but trust us -- by the time you're out of

adventure out among the stars.

That's a pursuit worth sharing with every young American.

Come explore the future with us.

school, one or two of them will be as common as school buses. And the others will be right around the corner.

Can you imagine that?

Good. Come inside -- and let's explore the solar system!



Owner: Space Transportation Directorate Curator: [Sherry Wallace](#)
Web Services Provided by: [A&WS \(Applications & Web Services\)](#) - SAIC
[NASA Privacy Statement](#)



TECH ISP

IN-SPACE PROPULSION TECHNOLOGIES



"The earth is a cradle of the mind, but one cannot live in a cradle forever."

**Konstantin E. Tsiolkovsky,
Father of Russian Astronautics,
1896**

What if you could conduct science at the far reaches of the solar system - routinely, thoroughly, and without regard for the complex mechanics of getting there and back again?

The vast gulf of space and the limitations of traditional propulsion technologies are the primary obstacles inhibiting the efforts of scientists like you... and it's time to make a change. Important science can no longer wait for decades or more while conventional spacecraft undertake arduous, years-long journey across the solar system - only to return mere weeks or months' worth of data.

This 20th century flight paradigm need no longer apply.

This Web site is intended to provide you with the contacts, program status and detailed technology information necessary to help you join us in developing, maturing and flying alternative propulsion systems that will one day carry science

- **LINKS**
- **TECHNICAL PUBLICATIONS**
- **WORKING WITH NASA**

- **ISP MAIN**

**CURRENT
TECHNOLOGIES****Aeroassist**

*Aerocapture -
Aerobraking -*

**Solar Electric
Propulsion**

*Next Generation
Electric Propulsion -
SEP Hall -*

Solar Sails**Advanced
Chemical****Tethers**

*Momentum Exchange -
Electrodynamic -*

Solar Thermal

**EMERGING
TECHNOLOGIES**

Aerogravity Assist -

missions to any point in the solar system - faster than ever before and with an exponentially greater return on investment.

By partnering with the most capable minds in academia, industry and government, NASA seeks to overcome the obstacles inherent to the journey, and improve scientific discovery at the destination.

Together, we look forward to a lifetime of successful work - measured not in weeks or months...but in true lifetimes.



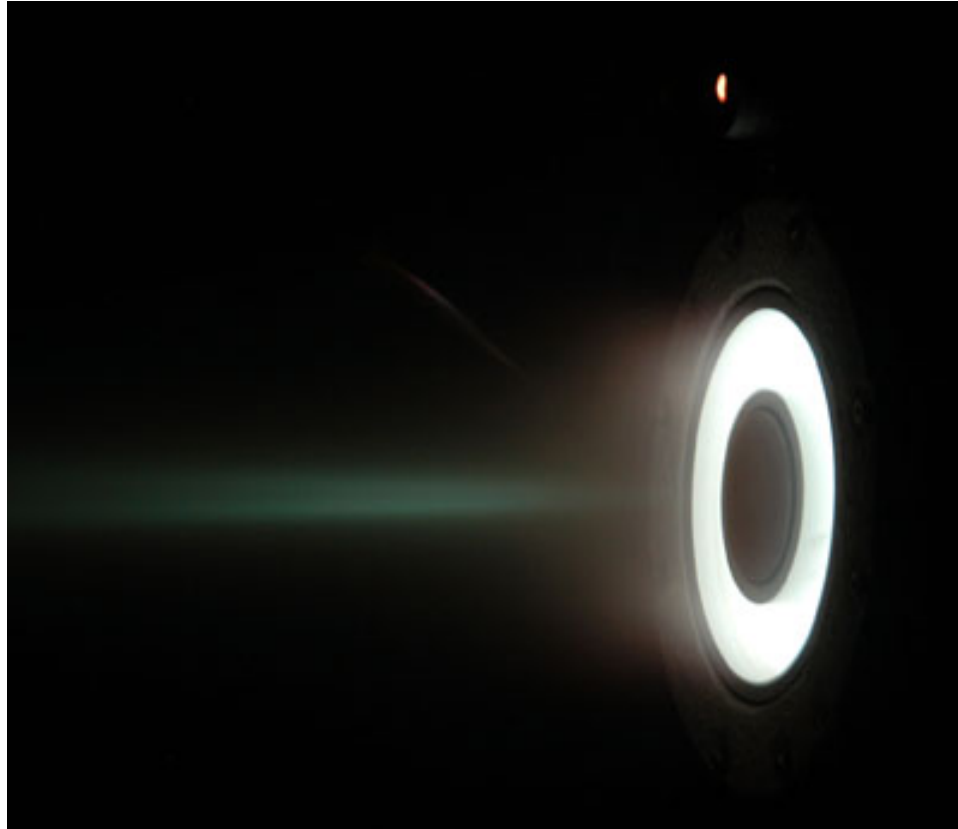
Owner: Space Transportation Directorate Curator: [Sherry Wallace](#)
Web Services Provided by: [A&WS \(Applications & Web Services\)](#) - SAIC
[NASA Privacy Statement](#)



[Back](#)

NASA Engineers Test Propulsion System Aimed at Enabling Deep Space Exploration

NASA engineers have begun testing unique propulsion hardware that could enable more ambitious, cost effective exploration of deep space. The technology, a High Voltage Hall Accelerator, or HiVHAC, is a rocket thruster that could reduce fuel load and spacecraft mass, decrease transit times and launch costs, and allow for larger scientific payloads -- key elements to the exploration of Earth's neighboring planets and our Solar System.



The High Voltage Hall Accelerator (HiVHAC) thruster during testing at NASA's Glenn Research Center.

Performance testing on the HiVHAC thruster began in early May. The thruster, built by Aerojet Corp., of Redmond, Wash., is being tested at varying power levels -- from 0.2 to 2.8 kilowatts -- in a vacuum chamber at NASA's Glenn Research Center in Cleveland, Ohio. The 10-by-33 foot (3-by-10-meter) cylindrical chamber simulates the vacuum and temperature extremes of space.



The High Voltage Hall Accelerator (HiVHAC) thruster in the vacuum chamber before testing at NASA's Glenn Research Center.



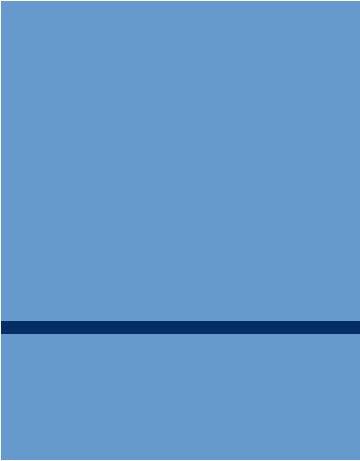
The purpose of the testing is to verify the HiVHAC thruster can operate efficiently over a wide range of input powers, as would be provided by a photovoltaic power source during a deep space mission. Photovoltaic power sources -- commonly referred to as solar cells -- convert sunlight into electricity.

Successful operation of the thruster over a wide range of input power could enable this type of propulsion to be used for missions throughout the Solar System, including trips to explore asteroids, comets and the outer planets. Low power operation is particularly important because it allows spacecraft to continue thrusting in space far from the Sun, where there is little solar power available to be absorbed by a craft's solar arrays. This capability -- to operate efficiently at low power levels -- is not possible with the majority of state-of-the-art propulsion technologies.

This type of propulsion is categorized as solar electric propulsion, because it converts solar radiation to electrical power, which is then used to create and accelerate ions in a propellant -- a very small flow of xenon gas -- to produce thrust.

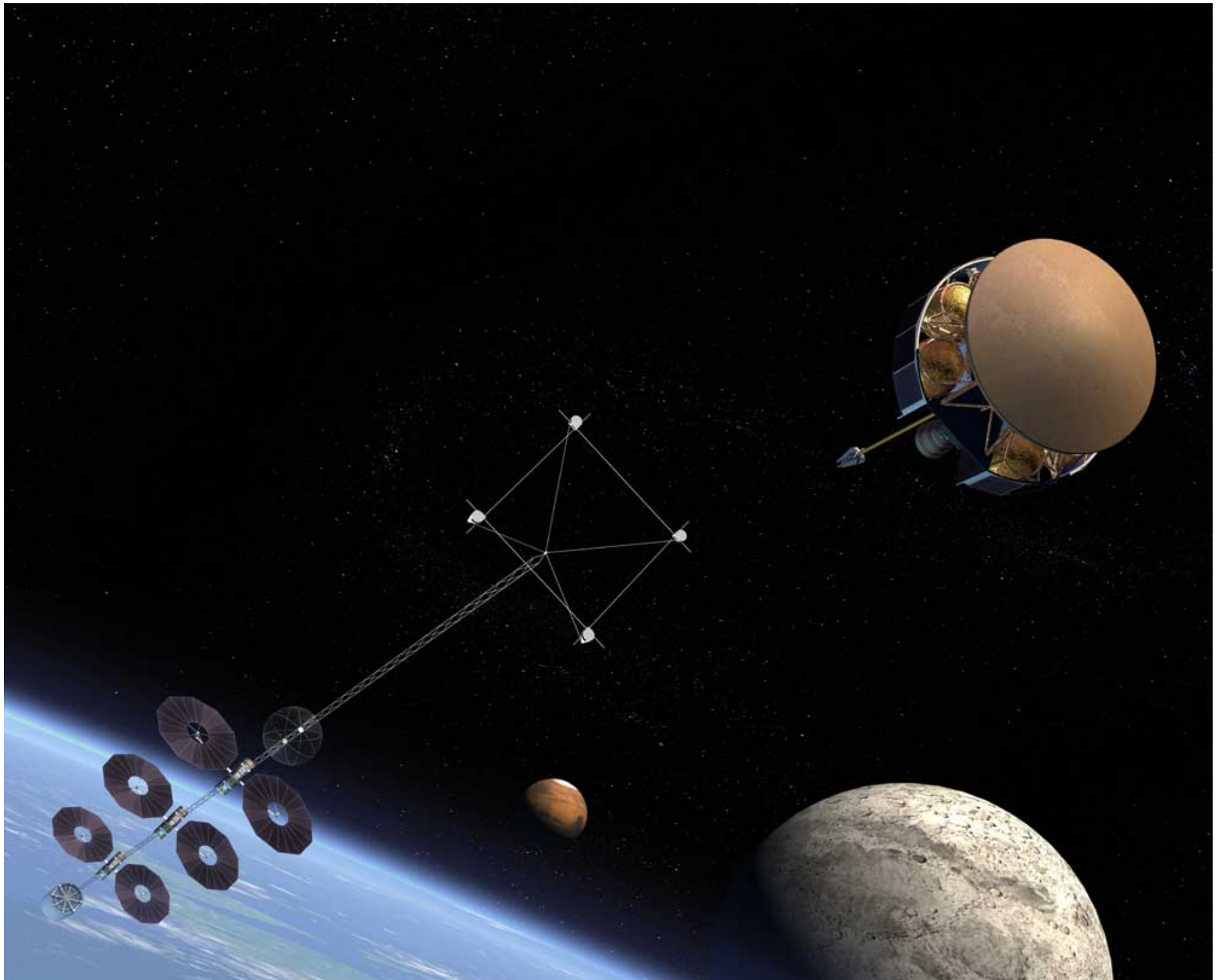
The thrust generated by this propulsion technology is much smaller than that of state-of-the-art chemical alternatives -- comparable to the force exerted by a sheet of paper resting on the palm of your hand. However, unlike chemical systems that may only burn for a few minutes, a solar electric propulsion engine can thrust continuously for years. Velocities more than 10 times those possible with chemical systems also can be achieved by spacecraft accelerating over a long period of time using this propulsion technology.

Additional tests on the HiVHAC thruster are planned through 2005. The HiVHAC project is managed by the In-Space Propulsion Technology Office at NASA's Marshall Space Flight Center in Huntsville, Ala. The project is being conducted by NASA's Glenn Research Center in Cleveland, Ohio. The In-Space Propulsion Technology Office implements the In-Space Propulsion Technology Program on behalf of NASA's Science Mission Directorate in Washington.



For more information on solar electric propulsion technology:
[Fact Sheet](#)

[Home ~ Who ~ What ~ Why ~ When ~ How](#)
[ISP for Teachers & Students ~ Technical ISP](#)
[Space Transportation Web Site](#)







IN-SPACE PROPULSION

Aerocapture Team Successfully Completes Test of Ablative Thermal Protection System Panels

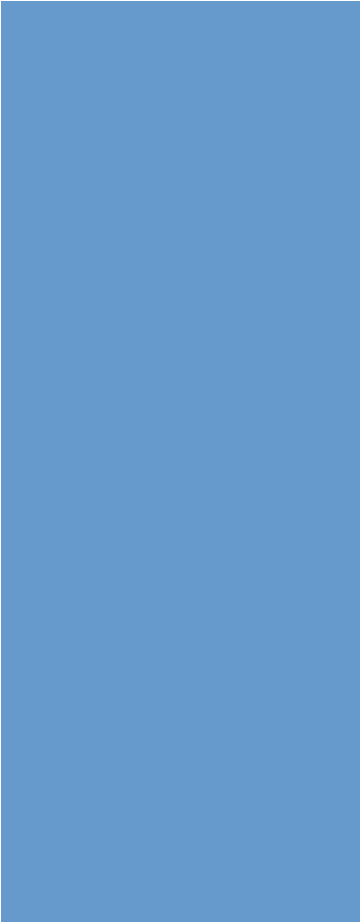
NASA engineers recently used a "field of mirrors" to successfully test a panel of a Thermal Protection System (TPS) for Aerocapture technologies.

Aerocapture is a flight maneuver that uses a planet's atmosphere as a "brake" to place the vehicle in its proper orbit, also called orbit capture. Friction created as a spacecraft briefly dips into the dense atmosphere slows the craft, placing it into an elliptical orbit.

For an Aerocapture maneuver to succeed, a thermal protection system is needed to shield the spacecraft from the high heat generated during an orbit capture in an atmosphere.

The test supports Aerocapture rigid aeroshell systems currently being developed by the Aerocapture Technology Area of the In-Space Propulsion Technology Project at NASA's Marshall Space Flight Center in Huntsville, Ala. Such rigid aeroshells were used by the Mars Exploration Rover during its entry and descent into Mars' atmosphere and its landing on the planet's surface in 2003, as well as by the Mars Pathfinder in 1997.

Similar ablative entry technologies have been used throughout the history of the U.S. Space Program -- including the capsules used from 1963 until 1972 to return humans from space; and the Galileo Probe, launched in October 1989 on a 14-year mission to explore the planet Jupiter and its surrounding moons. "Ablative" means the top layer burns off or recedes at very high



temperatures, thus preventing the high heat from entering a spacecraft. To be effective, materials and designs of ablative thermal protection systems are carefully "matched" to a planet's atmosphere and the intended entry maneuver.

The test was sponsored by the In-Space Propulsion Technology Project at Marshall and conducted by Applied Research Associates of Englewood, Colo., a NASA contractor for the In-Space Project. Testing was performed at the National Solar Thermal Test Facility at the Sandia National Labs in Albuquerque, N.M. The solar tower, built in 1978 for solar energy research, includes 212 large mirrors or heliostats, and a 200-foot-tall tower used to accommodate targets as large as 300 square feet. The tower can generate heat fluxes 2,500 times more intense than the Sun. The 20-by-20-foot heliostats, which are computer-controlled, track the Sun and focus sunlight on a target in the tower, and can be used to simulate the intense heat encountered during an aerocapture maneuver.

[Back](#)



National Solar Thermal Test Facility site of solar panel test in April 2005

On April 6, engineers tested one ablative thermal protection system panel at the solar tower. The 12-inch-square panel was placed in a special test fixture designed to hold the panel perpendicular to the beam generated by the heliostats. The Sun's radiation, or heat, was then focused on the panel for approximately 100 seconds.

The proof-of-concept test was conducted to verify test procedures and conditions prior to full-scale testing on 24-inch panels. The full-scale tests, to

be conducted in 2005, will be used to study the effects of differences in thermal expansion between the protective system and the underlying structure.

Engineers hope to use data from the panel tests to determine the overall suitability of certain thermal protection system, adhesives and structure combinations for a rigid aeroshell system. The Aerocapture group plans to conduct aeroshell system testing in late 2006, to demonstrate the performance of new, lighter-weight aeroshell materials that could be used for future science missions.

Aerocapture technology research is part of NASA's In-Space Propulsion Technology Program, managed by the Science Mission Directorate in Washington and implemented by the Marshall Center in Huntsville. The program's objective is to develop in-space propulsion technologies that can benefit near and mid-term NASA space science missions by significantly reducing cost, mass and travel times.

For more information, visit:

National Solar Thermal Test Facility - http://www.sandia.gov/Renewable_Energy/solarthermal/nsttf.html

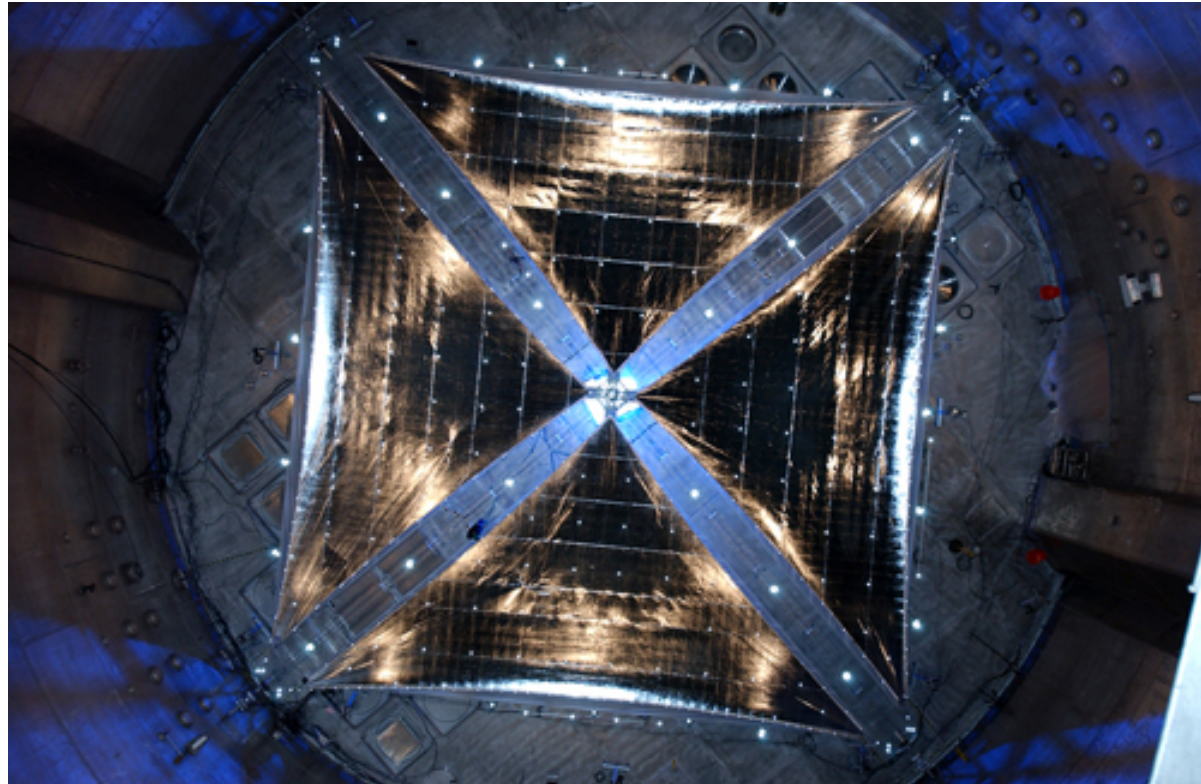
[Home](#) ~ [Who](#) ~ [What](#) ~ [Why](#) ~ [When](#) ~ [How](#)
[ISP for Teachers & Students](#) ~ [Technical ISP](#)
[Space Transportation Web Site](#)



IN-SPACE PROPULSION

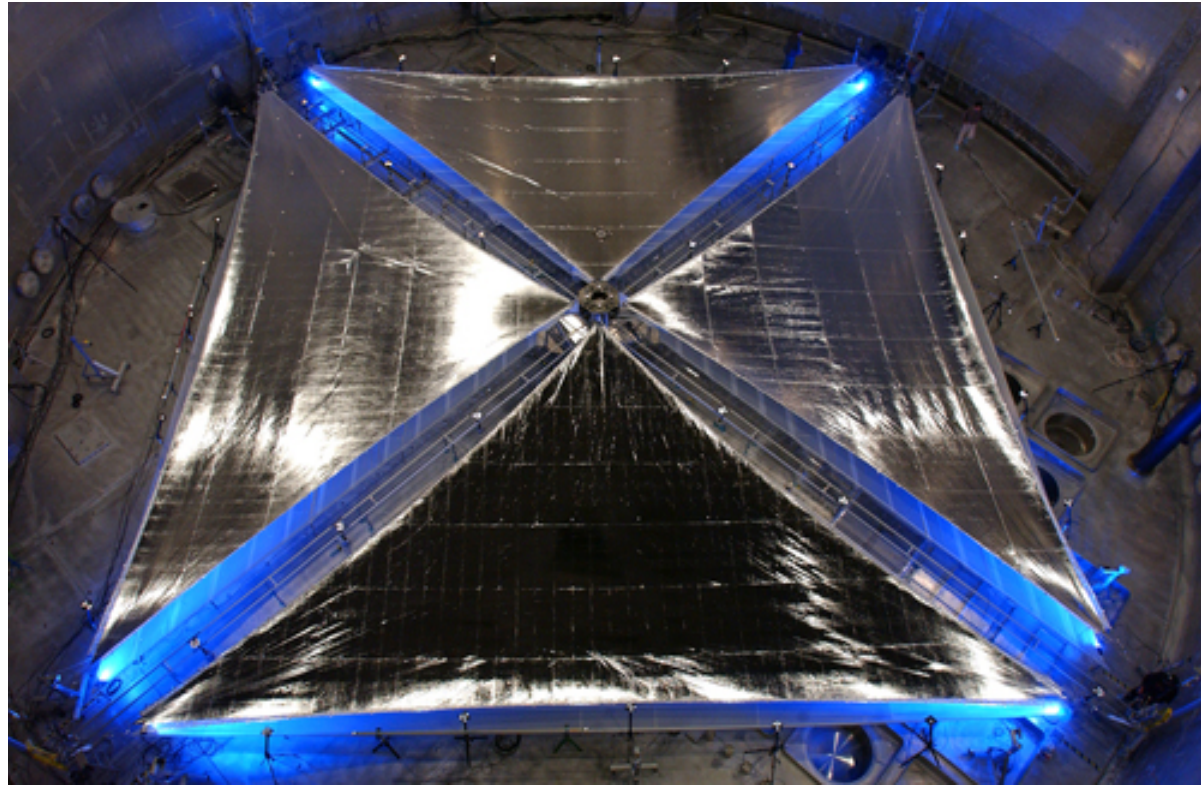
Marshall's Solar Sail Propulsion Team Deploys Solar Sail System at NASA Research Center

Engineers at the Marshall Space Flight Center in Huntsville, Ala., and their industry partner, ATK Space Systems of Goleta, Calif., recently reached a milestone in the testing of solar sails -- a unique propulsion technology that uses the Sun's energy to propel robotic spacecraft. The team successfully deployed a four-quadrant, 20-meter solar sail and boom system at NASA Glenn Research Center's Plum Brook facility in Sandusky, Ohio. The deployment was conducted in Plum Brook's Space Power Facility -- the world's largest space environment simulation chamber. It was the first in a series of tests, which began April 18, on the 20-meter sail concept. ATK Space Systems is one of two companies conducting tests at the facility. The companies were selected in 2002 by NASA to lead hardware design and development of solar sail system concepts for the In-Space Propulsion Technology Program. The program is implemented by the In-Space Propulsion Technology Office at the Marshall Center on behalf of NASA's Science Mission Directorate in Washington. L'Garde, Inc. of Tustin, Calif., is expected to begin testing of its 20-meter sail design in June.



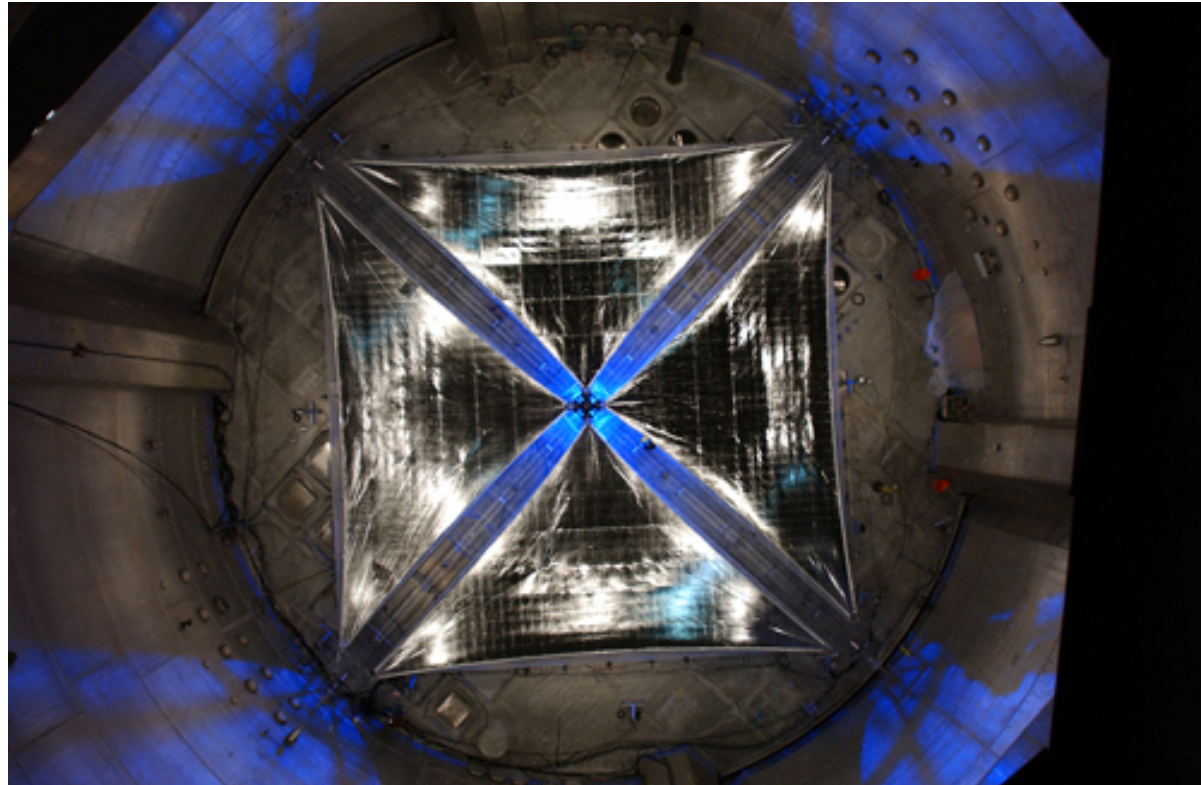
A 20-meter solar sail and boom system, developed by ATK Space Systems of Goleta, Calif., is fully deployed during testing at NASA Glenn Research Center's Plum Brook facility in Sandusky, Ohio. Blue lights help illuminate the four triangular sail quadrants as they lie outstretched in Plum Brook's Space Power Facility -- the world's largest space environment simulation chamber. The sail material is supported by a series of coilable booms, which are extended via remote control from a central stowage container about the size of a suitcase, and is made of an aluminized, plastic-membrane material called CP-1. The material is produced under license by SRS Technologies of Huntsville, Ala. The deployment, part of a series of tests that began April 18, is a critical milestone in the development of solar sail propulsion technology that could lead to more ambitious inner Solar System robotic exploration. (NASA/MSFC)

[Back](#)



A 20-meter solar sail and boom system, developed by ATK Space Systems of Goleta, Calif., is fully deployed during testing at NASA Glenn Research Center's Plum Brook facility in Sandusky, Ohio. Blue lights positioned beneath the system help illuminate the four triangular sail quadrants as they lie outstretched in Plum Brook's Space Power Facility -- the world's largest space environment simulation chamber. The sail material is supported by a series of coilable booms, which are extended via remote control from a central stowage container about the size of a suitcase, and is made of an aluminized, plastic-membrane material called CP-1. The material is produced under license by SRS Technologies of Huntsville, Ala. The deployment, part of a series of tests that began April 18, is a critical milestone in the development of solar sail propulsion technology that could lead to more ambitious inner Solar System

robotic exploration. (NASA/MSFC)



A 20-meter solar sail and boom system, developed by ATK Space Systems of Goleta, Calif., is fully deployed during testing at NASA Glenn Research Center's Plum Brook facility in Sandusky, Ohio. The lightweight sail material is supported by a series of coilable booms, which are extended via remote control from a central stowage container about the size of a suitcase. Blue lights help illuminate the four triangular sail quadrants as they lie outstretched in Plum Brook's Space Power Facility, the world's largest space environment simulation chamber, which measures 100-feet in diameter and 122-feet high. The facility was designed and constructed to test nuclear and non-nuclear space hardware in a simulated low-Earth-orbit environment. The 20-meter system deployment, part of a series of tests that began April 18, is a critical



milestone in the development of solar sail propulsion technology that could lead to more ambitious inner Solar System robotic exploration. (NASA/MSFC)

[Home](#) ~ [Who](#) ~ [What](#) ~ [Why](#) ~ [When](#) ~ [How](#)
[ISP for Teachers & Students](#) ~ [Technical ISP](#)
[Space Transportation Web Site](#)

National Aeronautics and
Space Administration

Marshall Space Flight Center
Huntsville, Alabama 35812



Aerocapture Technology

NASA technologists are working to develop ways to place robotic space vehicles into long-duration, scientific orbits around distant Solar System destinations without the need for the heavy, on-board fuel loads that have historically inhibited vehicle performance, mission duration and available mass for science payloads.

Aerocapture—a flight maneuver that inserts a spacecraft into its proper orbit once it arrives at a planet—is part of a unique family of “aeroassist” technologies under consideration to achieve these goals and enable robust science missions to any planetary body with an appreciable atmosphere. NASA fuels discoveries that make the world smarter, healthier and safer.

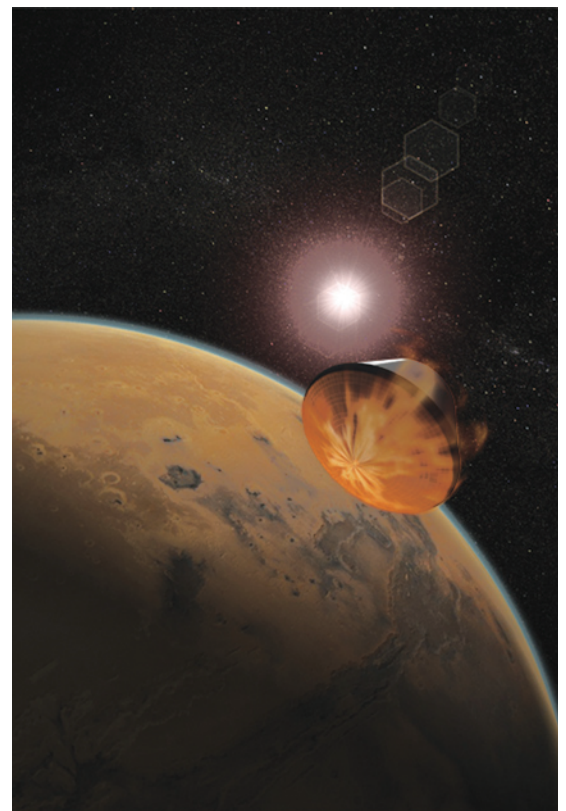
Aerocapture technology is just one of many propulsion technologies being developed by NASA technologists and their partners in industry and academia, led by NASA’s In-Space Propulsion Technology Office at the Marshall Space Flight Center in Huntsville, Ala. The Center implements the In-Space Propulsion Technology Program on behalf of NASA’s Science Mission Directorate in Washington.

Aerocapture uses a planet’s or moon’s atmosphere to accomplish a quick, near-propellantless orbit capture to place a space vehicle in its proper orbit. The atmosphere is used as a brake to slow down a spacecraft, transferring the energy associated with the vehicle’s high speed into thermal energy.

The aerocapture maneuver starts with an approach trajectory into the atmosphere of the target body. The dense atmosphere creates friction, slowing the

craft and placing it into an elliptical orbit—an oval shaped orbit.

This nearly fuel-free method of decelerating a space vehicle could significantly reduce the mass of an interplanetary spacecraft. Less spacecraft mass allows for more science instrumentation to be added to the mission or allows for a smaller and less-expensive vehicle.



Aerocapture entering Mars Orbit.

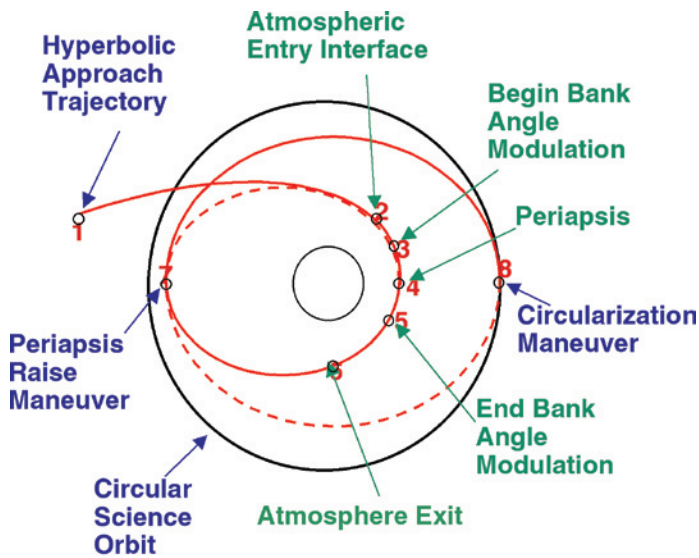


Diagram of Aerocapture maneuver overview.

The requirement to slow down a spacecraft for orbit insertion and to protect it from the heating environment of a planet's atmosphere—the gaseous area surrounding a planet that can vary greatly in temperature—could be achieved in two ways. The craft could be enveloped by a structure with heat shielding applied to the external surfaces. Such rigid “aeroshells” were used during the entry and descent into Mars’ atmosphere, and the landing on the planet’s surface by the Mars Exploration Rover mission launched in 2003 and the Mars Pathfinder in 1997. Another option could be for the vehicle to deploy an aerocapture device, such as an inflatable heat shield or an inflatable, trailing ballute—a combination parachute and balloon made of thin, durable material and towed behind the vehicle after deployment.

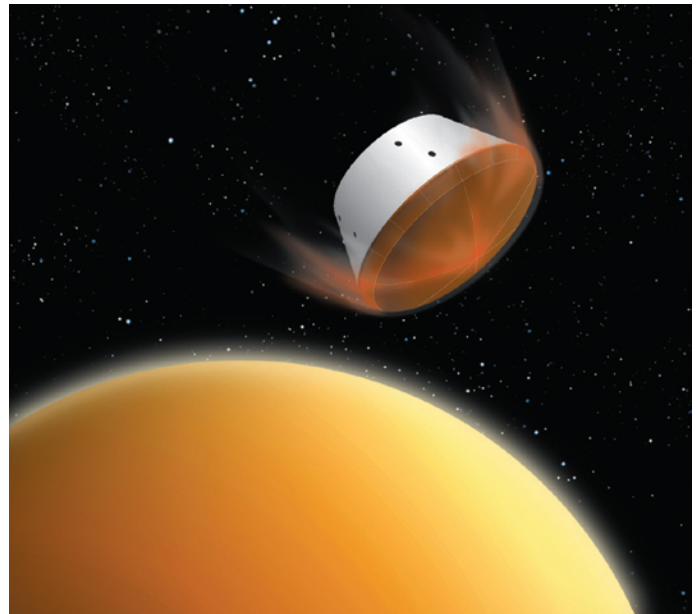
Four different aerocapture concepts under consideration for development are:

- Blunt body, rigid aeroshell design
- Slender body, rigid aeroshell design
- Trailing ballute design
- Attached ballute design

Blunt body, rigid aeroshell design

The blunt body, rigid aeroshell system encases a spacecraft in a protective shell. This shell could provide an aerodynamic surface and protection from the intense heating experienced during high-speed atmospheric flight. Once a space vehicle is captured into a planet’s orbit, the aeroshell could then be jettisoned.

The aeroshell would consist of three main parts: the external thermal protection material; adhesives, used to bond the thermal protection system to the aeroshell; and an underlying structure, to which the internal spacecraft and the outside thermal protection material would be attached. The challenges facing researchers are to customize the design and thickness of the thermal protection material to accommodate different heating characteristics endured during aerocapture, develop adhesives capable



Conceptual design of blunt body, rigid aeroshell.

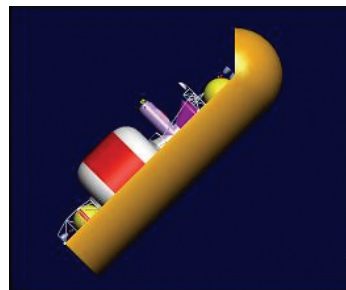
of withstanding extremely high temperatures, and supporting structures that are lightweight, yet very durable.

NASA has used this aeroshell system design in the past for atmospheric entry missions. The most recent example is the Mars Exploration Rovers—Spirit and Opportunity—which launched in June and July 2003, and landed on the Martian surface in January 2004.

Another example is the Apollo Command Module. The module was used for six unmanned space flights from February 1966 to April 1968 and continued through the final manned Apollo 17 lunar mission in December 1972.

Slender body, rigid aeroshell design

The slender body configuration looks much like an elongated capsule, with a hard shell surrounding the spacecraft.



Conceptual design of slender, rigid aeroshell.

The enhanced controllability of a slender body shape could provide increased tolerance for navigational and atmospheric uncertainties during the aerocapture maneuver. Preliminary studies indicate the slender body design may be required for robotic missions to Neptune and possibly other outer planetary destinations.

Trailing ballute design

One of NASA's investments in inflatable, deceleration technology is a trailing ballute configuration. The design features a toroidal, or donut-shaped, ballute that is much larger than the spacecraft and is towed behind the craft—much like a parachute—to slow a vehicle down. The “trailing” design also could allow for easy detachment after the aerocapture maneuver is complete. The ballute itself could be made of a lightweight, thin-film material.

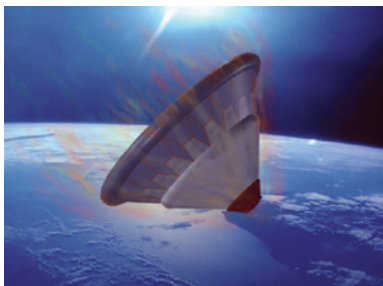


Conceptual design of trailing ballute.

The trailing ballute design may have performance advantages over the rigid aeroshell design. In an aeroshell design, the shell takes all the force and heating of re-entry. However, with the trailing ballute design, the ballute would incur most of the aerodynamic forces and heat, possibly allowing any protection around the payload to be very lightweight. The design configuration also could be applied to various size and shape payloads.

Attached ballute design

The attached ballute design looks much like the aeroshell or blunt body design. The attached ballute is often referred to as a hybrid system, with a rigid foreshell and an inflated, attached ballute extending from either the front or back of the spacecraft.



Conceptual design of inflatable re-entry and descent technology at Earth orbit.

The inflatable, attached ballute would extend from a rigid nose-cap and work much like a parachute, providing a large surface area to slow the spacecraft down to allow for an aerocapture maneuver to occur. As the spacecraft approaches a planet's atmosphere, the ballute would inflate and then jettison once the craft is captured into orbit.

Made of thin lightweight material, such as Kapton—a material often used in multi-layered insulating (MLI) blankets—the inflatable,

attached ballute design could offer many of the same advantages and functionality as trailing ballute designs. The challenge facing researchers is to create a flexible, inflatable thermal protection system that could protect the spacecraft from the high heat conditions experienced during entry into a planet's atmosphere.

Researchers currently are assessing the benefits and application of this concept for potential, future missions.

Potential aerocapture missions

NASA researchers are considering aerocapture technologies for a broad range of future mission objectives.

The aerocapture maneuver has never been flight-tested. Relevant experience, however, exists from ablative entry capsules, so named because the top layer of the craft's heat shield is designed to burn away. Ablative entry technologies have been used throughout the history of the U.S. Space Program—including the Apollo return capsule, used from 1963 until 1972 to return humans from the Moon and Earth orbits; and the Galileo Probe, launched in October 1989 on a 14-year mission to explore the planet Jupiter and its surrounding moons.

Aerocapture is a systems technology in which many of the elements already exist, or are evolved from developments in other aeroentry applications. The aeroshell and thermal protection systems have heritage to those developed for past Earth, Venus, Mars and Jupiter missions. The ability to guide and control a blunt body through an atmospheric exit maneuver was human-rated for the Apollo- Earth return capsule as a weather-contingency plan, but was never exercised in flight.

NASA's aeroassist technology development team includes Langley Research Center in Hampton, Va.; Ames Research Center in Moffett Field, Calif.; the Jet Propulsion Laboratory in Pasadena, Calif.; Johnson Space Center in Houston, Texas; and the Marshall Space Flight Center.

Aerocapture technology is being developed by the In-Space Propulsion Technology Program, which is managed by NASA's Science Mission Directorate in Washington and implemented by the In-Space Propulsion Technology Office at the Marshall Space Flight Center in Huntsville, Ala. The program objective is to develop in-space propulsion technologies that can enable or benefit near and mid-term NASA space science missions by significantly reducing cost, mass and travel times.

For more information about NASA's In-Space Propulsion program and aerocapture research, visit:

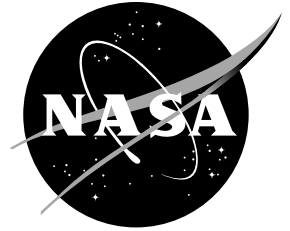
<http://www.nasa.gov>

<http://www.inspacepropulsion.com>

Explore. Discover. Understand.

National Aeronautics and
Space Administration

Marshall Space Flight Center
Huntsville, Alabama 35812



In-Space Propulsion

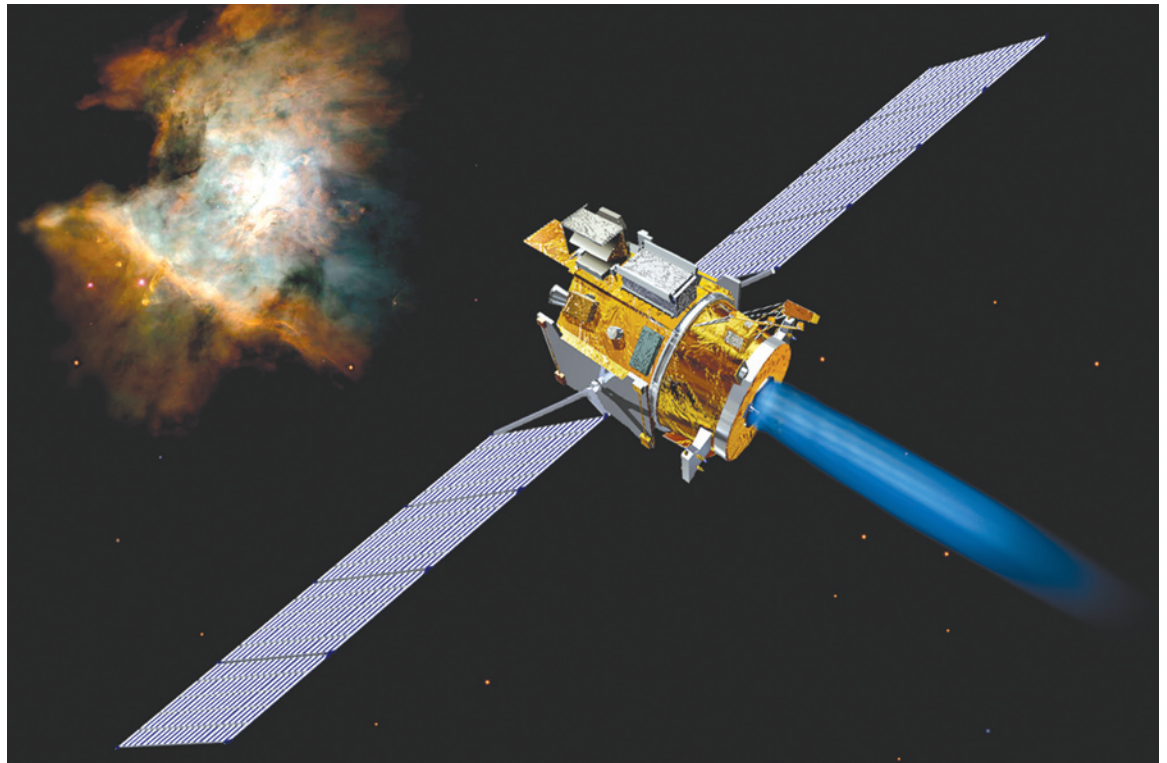
Ion Propulsion

Ion propulsion—a futuristic technology that for decades catapulted spacecraft through the pages of science fiction novels—is now a reality. An ion engine, developed by NASA and measuring just 12 inches (30 centimeters) in diameter, was the main propulsion source for Deep Space 1, a 20th Century spacecraft that completed—in December 2001 – its primary mission: to validate technologies for 21st century spacecraft.

An ion propulsion system converts spacecraft power into the kinetic energy of an ionized gas jet. As the ionized gas exits the spacecraft, it propels

the craft in the opposite direction. An ion engine is fueled by xenon, a colorless, odorless, tasteless and chemically inert gas. The xenon fuel fills a chamber ringed with magnets. When the ion engine is running, electrons emitted from a cathode strike xenon atoms, knocking away an electron orbiting each atom's nucleus and turning it into an ion.

The spacecraft contains a pair of electrically charged metal grids. The force of the electric field generated by the grids exerts a strong, electrostatic pull on the xenon ions, much the way bits of lint are pulled to a pocket comb that has been given a static



electric charge by rubbing it on wool. The xenon ions shoot past the grids at speeds of more than 88,000 mph (146,000 kilometers), continuing out the back of the engine and into space. These exiting ions produce the thrust that propels the spacecraft.

Ion propulsion is 10 times more fuel efficient than on-board chemical propulsion systems. This greater efficiency means less propellant is needed for a mission. In turn, the spacecraft can be smaller and lighter, and launch costs lower.

Deep Space 1 carried 178 pounds (81 kilograms) of xenon propellant, capable of fueling engine operation at one-half throttle for more than 20 months. Ion propulsion increased the craft's speed by 7,900 mph (12,700 kilometers) over the course of the mission.

NASA has studied ion engines since the 1950s. Dr. Harold Kaufman, a technologist at NASA's Glenn Research Center (formerly Lewis Research Center) in Cleveland, Ohio, designed and built the first broad-beam electron-bombardment ion engine in 1959, using mercury as fuel. Suborbital ion engine tests were under way by the early 1960s.

In the early 1990s, NASA identified improved electric propulsion as an enabling in-space propulsion technology for future deep space missions. Glenn Research Center and the Jet Propulsion

Laboratory in Pasadena, Calif., partnered on the NASA Solar Electric Power Technology Application Readiness project, or NSTAR. Its purpose: to develop a xenon-fueled ion propulsion system for deep space missions.

Ion engines with extended performance and higher-power, NSTAR-type engines—in the 10-kilowatt and 0.08 pound-thrust range—are candidates for propelling future spacecraft to visit Pluto, the moons of Jupiter and other large bodies in the outer solar system. Low-power (100 to 500 watt) systems also could be used to deliver miniaturized robot spacecraft to visit and study comets, asteroids and other smaller bodies. Laboratory tests to develop high- and low-power, light-weight ion propulsion system components and subsystems are now under way.

NASA fuels discoveries that make the world smarter, healthier and safer.

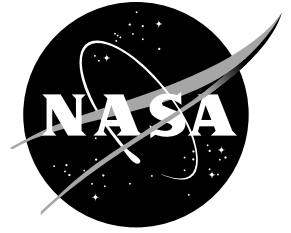
For more information about the Deep Space 1 mission, visit:
<http://nmp.jpl.nasa.gov/ds1/>

For more information about ion propulsion and other in-space propulsion technology systems, visit:
<http://www.nasa.gov>
<http://www.inspacepropulsion.com>

Explore. Discover. Understand.

National Aeronautics and
Space Administration

Marshall Space Flight Center
Huntsville, Alabama 35812



In-Space Propulsion

Momentum-Exchange Electrodynamic Reboost (MXER) Tether

NASA's In-Space Propulsion Technology Program is developing experiments to demonstrate tether-based propulsion—which draws power from the Sun and uses the magnetic field surrounding the Earth to propel spacecraft without the use of on-board propellant. The innovative technology could dramatically reduce the cost of raising the orbits of other spacecraft, including those destined for deep-space missions.

Momentum-exchange tether propulsion transfers momentum from one object to another by briefly

linking a slow-moving object with a faster one. Much the same way ice skaters play “crack the whip,” the slower object’s speed could be dramatically increased as momentum and energy is transferred to it from the faster object. Similarly, a spinning tether facility in an elliptical Earth orbit might snare slower-moving spacecraft in low-Earth orbit and throw them into much higher-energy orbits.

NASA researchers currently are developing the technologies needed to realize this advanced form of propulsion. The “Momentum-Exchange Electro-



dynamic Reboost” tether propulsion system, or MXER tether, could use momentum-exchange to transfer satellites from low-Earth orbit to geosynchronous transfer orbit—an elliptical orbit stretching from 200 miles out to 22,300 miles above the equator—and beyond. After throwing the payload, the MXER tether would then use energy collected from solar panels to drive electrical current through the tether. The Earth’s magnetic field would push against the current and reboost the tether’s orbit, restoring the energy that was transferred to the payload.

Once launched to low-Earth orbit by a rocket, the MXER tether system is intended to deploy a tether roughly 100 to 150 kilometers (62 to 93 miles) in length. This tether would be made of lightweight, high-strength material, coated for protection from the space environment. Part of the tether would also incorporate an insulated conductive material, like aluminum, to carry the electrical current needed to reboost the tether.

Payloads bound for high-Earth or escape orbits, such as communications satellites and interplanetary spacecraft, would be launched by rocket to low-Earth orbit. There, they would rendezvous with the tip of the spinning MXER tether, which would “snare” them via a net-like catch mechanism, then throw them toward their final destination. The process would eliminate or reduce the need for the upper-stage booster rocket usually associated with these high-energy orbits. And because the MXER tether could reboost its own orbit without propellant, it could repeat its orbital transfer duties for the duration of its lifespan. Also, since the need for an expendable upper-stage rocket—normally used only once—is eliminated or reduced, this capability would mean smaller, less expensive rockets could be used to launch the payloads.

All these capabilities make MXER tether technology extremely beneficial to NASA’s space science missions. The tether system could tremendously enhance most current and future launch

missions, becoming an economical “gateway to space”—much as the Panama Canal serves today as a passageway from the Atlantic to the Pacific for ocean shipping.

NASA researchers are already studying ways to expand the technology’s potential, such as also deploying a tether into orbit around the Moon. This two-tether system—one in orbit around the Earth and the other around the Moon—could enable cheap, efficient two-way transport of payloads to and from the surface of the Moon, paving the way for future utilization of lunar resources and permanent human colonization, as well as robotic journeys to Mars and the outer planets.

NASA’s MXER tether technology development team presently includes Tennessee Technological University in Cookeville, Tenn.; Lockheed Martin Astronautics in Denver, Colo.; and Tethers Unlimited of Lynnwood, Wash. Several other organizations and businesses are expected to join in the near future.

MXER tether technology is being developed by the In-Space Propulsion Technology Program, which is managed by NASA’s Science Mission Directorate in Washington and implemented by the In-Space Propulsion Technology Office at Marshall Space Flight Center in Huntsville, Ala. The program objective is to develop in-space propulsion technologies that can enable or benefit near and mid-term NASA space science missions by significantly reducing cost, mass and travel times. NASA fuels discoveries that make the world smarter, healthier and safer.

For more information about NASA’s Space Transportation Systems, visit:

<http://www.nasa.gov>

For more information about the In-Space Propulsion Technology Program, visit:

<http://inspacepropulsion.com>

Explore. Discover. Understand.

National Aeronautics and
Space Administration

Marshall Space Flight Center
Huntsville, Alabama 35812



Advanced Chemical Propulsion

Chemical propulsion has provided the basis for rocket system transportation since Dr. Robert Goddard, known as the father of modern rocket propulsion, successfully launched the first liquid fuel rocket in 1926. As NASA prepares for future space exploration, the Agency must continue to improve and develop new chemical propulsion systems. In doing so, there is the opportunity to reduce the mass of launch vehicle systems and the cost of space exploration and provide greater opportunities for science investigations.

Seeking to fulfill these goals, researchers are investigating and developing advanced forms of in-space propulsion technologies to meet future space exploration needs and to enable more ambitious deep space exploration. The In-Space Propulsion Technology Office at NASA's Marshall Space Flight Center in Huntsville, Ala., is investigating innovative chemical formulations and the benefits of new cryogenic systems that capitalize on the potentially high specific impulse (Isp), or performance, of cryogenic propellants; and developing advanced propulsion systems with lightweight materials and optimized components.

The Marshall Center implements the In-Space Propulsion Technology Program on behalf of NASA's Science Mission Directorate in Washington. NASA fuels discoveries that make the world smarter, healthier and safer.

Advanced Propellant Formulations

NASA scientists and engineers are continually seeking methods to develop high-energy pro-

pellants and improve propulsion systems. The challenge facing these researchers is the ability to further improve current chemical formulations that are already approaching their theoretical limits of performance.

Development of innovative gelled propellant formulations is underway. By adding a gelling agent to an appropriate liquid propellant, the requirements for handling, conditioning and storage of the propellant could be reduced, resulting in a more compact system. This also may reduce the number of system components and the amount of power required to maintain the propellant in a useable state.

However, researchers face additional challenges, such as a reduction of propellant performance, when



Artist concept of spacecraft powered by advanced chemical propulsion.

adding gelling agents. To offset this loss in fuel efficiency, energetic particles—usually in the form of metal powders—are added. Unfortunately, additional wear on the fuel injectors and engine is introduced, warranting the need for new engineering designs.

NASA researchers are addressing these issues by investigating and developing new system concepts to produce a useable gelled propellant system with reduced complexity and weight.

Cryogenic Propellants

The development of cryogenic systems and propellants—ones requiring extremely low temperatures for storage—offers the potential for a significant increase in specific impulse. The In-Space Propulsion Technology Office at the Marshall Center is currently investigating cryogenic propellant performance and system concepts that may be beneficial to long-duration science missions. The study is looking at proposed innovative system concepts that will significantly reduce or eliminate the boil-off—loss of vapor from cryogenic propellants during long duration storage in space—avoiding the need to carry excessive amounts of propellant in large tanks.

Advancements in subsystems and components required to contain, thermally condition and deliver these propellants for long-term durations must be accomplished before cryogenic propellants are practical for in-space propulsion applications. Mass optimization through lightweight and improved materials is being pursued in concert with systems and components advancement. Innovative refrigeration and insulation systems also are being identified and advanced, resulting in a reduction in the power and the number of system components required.

Future cryogenic systems may enable some of NASA's most ambitious outer planet investigations, as well as provide in-space support systems for Mars or lunar destinations.

Lightweight/Optimized Propulsion Systems and Components

Most rocket propulsion is accomplished by mixing two liquid chemical propellants. In the space environment, maintaining the propellants in a liquid state requires efficient systems that condition and maintain the fuel and oxidizer at suitably low temperatures.

Active systems—valves, gauges or regulators—are required for refrigeration and thermal control of the propellants. Passive insulation systems such as multi-layer blankets are used as well. Both insulation systems add hardware complexity and weight to the space transportation system. New and improved systems will be required to maintain propellants in the long-term. NASA scientists are addressing these needs.

In the area of lightweight and optimized components and systems, NASA scientists are researching ways to advance component, material and manufacturing technology. This work includes advancing composite materials for propellant tanks to greatly reduce the weight of these essential propulsion system elements, possibly by as much as 50 percent as compared to state-of-the-art titanium tanks, as well as improvements in shield and insulation technology with the potential to replace heavier multi-layer insulation blankets, while also providing optimum meteoroid protection.

Improvements in these areas could result in substantial reduction of the overall systems weight and allow for more payload and scientific instrumentation, resulting in greater scientific return.

More about the Advanced Chemical Propulsion Program

Research for advanced chemical and thermal propulsion for in-space applications focuses on near-term products that can build on the long and proven heritage of state-of-the-art chemical propulsion systems. In-space technologists aim to optimize current technology, such as pressurization and mixture-ratio control, to improve propulsion systems performance—yielding more cost-efficient exploration of the space frontier.

The Marshall Space Flight Center in Huntsville is partnering with other NASA centers—Jet Propulsion Laboratory in Pasadena, Calif.; Glenn Research Center in Cleveland, Ohio; Ames Research Center in Moffett Field, Calif.; and Johnson Space Center through its White Sands Test Facility in Las Cruces, N.M.—for advanced chemical and thermal propulsion research. Industry partners include Boeing Space Systems in Huntington Beach, Calif., and Carleton Technologies Inc., Pressure Technology Division in Glenn Burnie, Md.

Research in the technology area is being funded by the In-Space Propulsion Technology Program, which is managed by NASA's Science Mission Directorate in Washington and implemented by the In-Space Propulsion Technology Office at the Marshall Space Flight Center in Huntsville, Ala. The program's objective is to develop in-space propulsion technologies that can enable or benefit near and mid-term NASA space science missions by significantly reducing cost, mass and travel times.

For more information, visit:

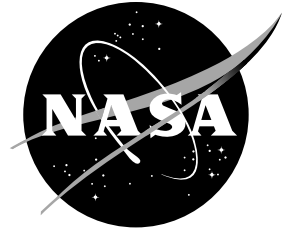
<http://www.nasa.gov>

<http://www.inspacepropulsion.com>

Explore. Discover. Understand.

National Aeronautics and
Space Administration

Marshall Space Flight Center
Huntsville, Alabama 35812



In-Space Propulsion

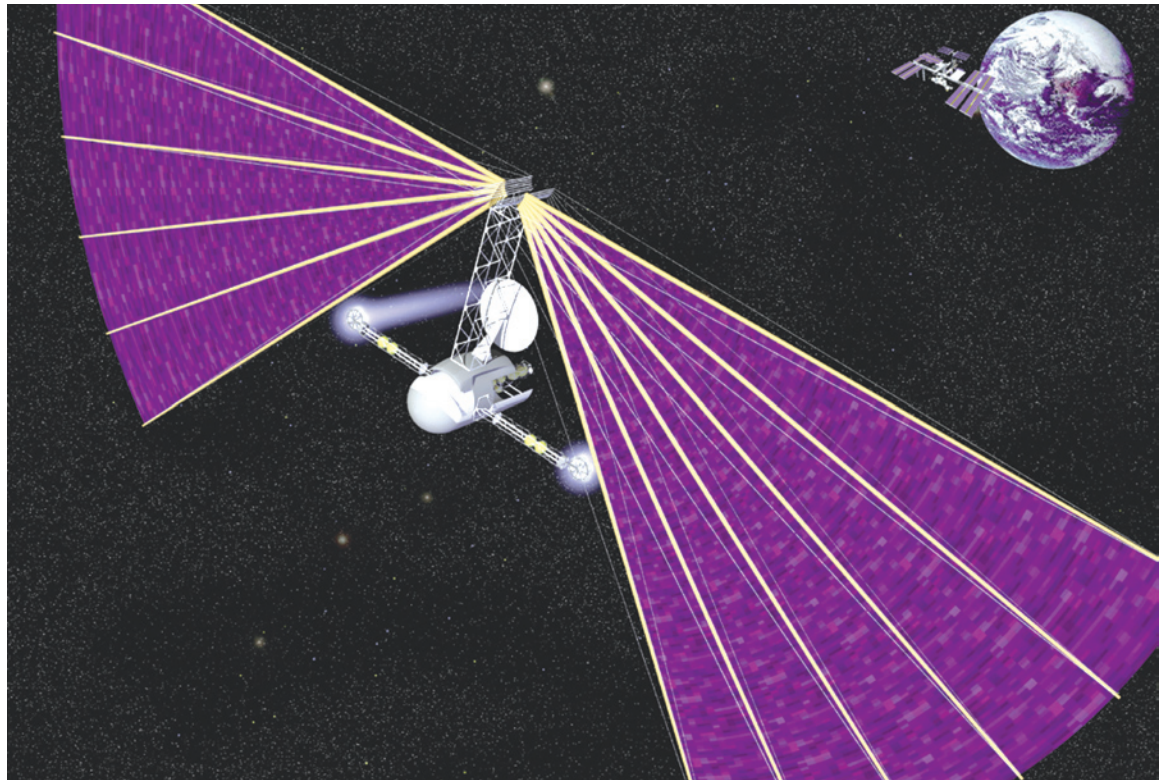
Solar Electric Propulsion

In the early 1990s, NASA identified electric propulsion as a key in-space propulsion technology for possible future deep space missions and began developing and testing various electric propulsion technologies. Intended to reduce fuel mass, decrease travel times and permit larger payloads, electric propulsion technologies may be one of the keys to our continued exploration of Earth's neighboring worlds.

Electric propulsion technologies generate thrust via electrical energy derived from a solar source, such as solar arrays, which convert solar radiation to electrical power.

This energy is used to accelerate an on-board propellant by one of three processes:

- Electrostatic: accelerating a propellant by applying a force to a charged particle in an electric field
- Electromagnetic: using a current to induce a magnetic field to accelerate propellant
- Electrothermal: accelerating a propellant by electrically heating and expanding it through a nozzle



Among the more mature solar electric propulsion technologies typically considered for in-space use in Earth orbit and beyond are:

- Hall thrusters
- Ion thrusters
- Pulsed plasma thrusters
- Arcjet thrusters
- Resistojets

The NASA Solar Technology Application Readiness (NSTAR) thruster was the first ion thruster used for primary propulsion on Deep Space 1, NASA's successful ion propulsion demonstrator launched in October 1998. Deep Space 1 cruised the Solar System up to 158 million miles (254 million kilometers) from Earth, testing in-space hardware and electric propulsion capabilities. It encountered Comet Borrelly near the completion of its mission in December 2001.

Spacecraft powered by typical electric propulsion systems may eject propellant at up to 20 times the speed of conventional chemical systems, delivering a much higher specific impulse, or the amount of thrust obtained for the weight of fuel burned. Electric-based systems also require far less propellant mass than a state-of-art, chemical-propellant craft.

Another benefit of electric propulsion is that deep-space missions would no longer be constrained by narrow and rare launch window opportunities dictated by planetary alignment. Traditionally, chemical-propelled spacecraft move from planet to planet as they travel, using "gravity-assist" maneuvers in each world's orbit to increase their own velocity and "sling-shot" toward their final destination. A mission to Neptune or Pluto using electric propulsion, for example, could make straight for its intended target, rather than "touring" other planets to help boost its velocity as it travels.

NASA's Solar Electric Propulsion team includes researchers from Glenn Research Center in Cleveland; the Jet Propulsion Laboratory in Pasadena, Calif.; Marshall Space Flight Center in Huntsville, Ala.; and leading-edge partners in other government agencies, industry and academia. The Marshall Center implements the In-Space Propulsion Technology Program, which is managed by the Science Mission Directorate in Washington. NASA fuels discoveries that make the world smarter, healthier and safer.

For more information about NASA In-Space Propulsion Technology systems, visit:

<http://www.nasa.gov>

<http://www.inspacepropulsion.com>

Explore. Discover. Understand.

In-Space Propulsion Technologies Proposal Information Package (PIP)



[Proposal Information Package \(PIP\)](#)

This Proposal Information Package describes the technical goals and objectives and other related information in support of the NASA Research Announcement for In-Space Propulsion Technologies (NNH04ZSS001N, Amendment 13 Section B.22). Section 1.0 provides the program scope for each technology area. Section 2.0 provides the programmatic information.

Questions about material in this Proposal Information Package should be submitted in writing to:

Ms. Marlyce Alexander
Mail Stop: PS50
NASA
Marshall Space Flight Center, AL 35812
Voice: 256-544-8344 / Fax: 256-544-6062
Email: marlyce.alexander@msfc.nasa.gov

39th AIAA Joint Propulsion Conference
 Huntsville, AL
 July 20-23, 2003

An Overview Of NASA's Solar Sail Propulsion Project
Gregory Garbe, Edward E. Montgomery IV
 NASA/MSFC
In-Space Propulsion Technologies Projects

Abstract

Research conducted by the In-Space Propulsion (ISP) Technologies Projects is at the forefront of NASA's efforts to mature propulsion technologies that will enable or enhance a variety of space science missions. The ISP Program is developing technologies from a Technology Readiness Level (TRL) of 3 through TRL 6. Activities under the different technology areas are selected through the NASA Research Announcement (NRA) process. The ISP Program goal is to mature a suite of reliable advanced propulsion technologies that will promote more cost efficient missions through the reduction of interplanetary mission trip time, increased scientific payload mass fraction, and allowing for longer on-station operations. These propulsion technologies will also enable missions with previously inaccessible orbits (e.g., non-Keplerian, high solar latitudes).

The ISP Program technology suite has been prioritized by an agency wide study¹. Solar Sail propulsion is one of ISP's three high-priority technology areas. Solar sail propulsion systems will be required to meet the challenge of monitoring and predicting space weather by the Office of Space Science's (OSS) Living with a Star (LWS) program. Near-to-mid-term mission needs include monitoring of solar activity and observations at high solar latitudes. Near-term work funded by the ISP solar sail propulsion project is centered around the quantitative demonstration of scalability of present solar sail subsystem designs and concepts to future mission requirements through ground testing, computer modeling and analytical simulations.

This talk will review the solar sail technology roadmap, current funded technology development work, future funding opportunities, and mission applications.

This work is declared a work of the United States Government and is not subject to copyright protection in the United States.

Introduction

The ever increasing technological demands of civilization (Global Positioning System usage, space based weather observations, satellite telecommunications, etc.) have placed increased importance on space based assets. A high level of service reliability requires the ability to place additional assets in orbits that are not practically accessible via chemical propulsion. The In-Space Propulsion Program mandate is to mature innovative propulsion technologies that will enable or enhance a variety of NASA space science missions and thereby guarantee their performance and reliability for commercial usage. The Solar Sail Propulsion (SSP) Project is one of ISP's three high priority projects whose objective is the near term verification and development of solar sail system level technology through ground testing and the development of subsystems, operations tools and computational models. NASA's Office of Space Science (OSS) funds research based on the results of peer reviewed proposals submitted to Topics in the Research Opportunities in Space Science (ROSS) of NASA Research Announcements (NRA). All ISP solicitations are contained within the ROSS In-Space Propulsion Technologies (ISTP) Topic. OSS also firmly believes that the ROSS solicitations should be guided by input from the technology community and this is best achieved through the periodic convening of a Technology Assessment Group (TAG).

The first ISP Solar Sail TAG was held over two days in January 2002. The TAG participants formed three discussion groups (Structures, Trajectory and Attitude Control, and Materials) to define what ground based testing and tools were needed in order to advance solar sail's Technology Readiness Level (TRL). The groups represented the highest priority solar sail subsystems and or components as well as the technical expertise of the TAG participants. Figure 1 is the Solar Sail technology

development roadmap that was synthesized from the respective discussion group worksheets² and has been used by the SSP office develop all of the subsequent research solicitations.

ISTP Cycle 1 Solicitation

System Level Ground Demonstration

The first of two SSP research elements in the ISTP cycle 1 called for a prototype solar sail system for use in ground test that would be used to validate design concepts for sail packaging and deployment, to verify attitude control

subsystem function, and to characterize the structural mechanics and dynamics of the deployed sail in a simulated space environment. The solicitation called for a square sail configuration consisting of a reflective sail membrane, a deployable sail support structure, an attitude control subsystem, and all hardware needed to stow the sail for launch. In addition this system was required to meet the characteristics given in Table 1. A sub-L₁ solar monitoring mission concept was also provided as a reference mission for guidance in design and scalability issues.

**Solar Sail Technology Assessment Group Roadmap
In-Space Propulsion Program**

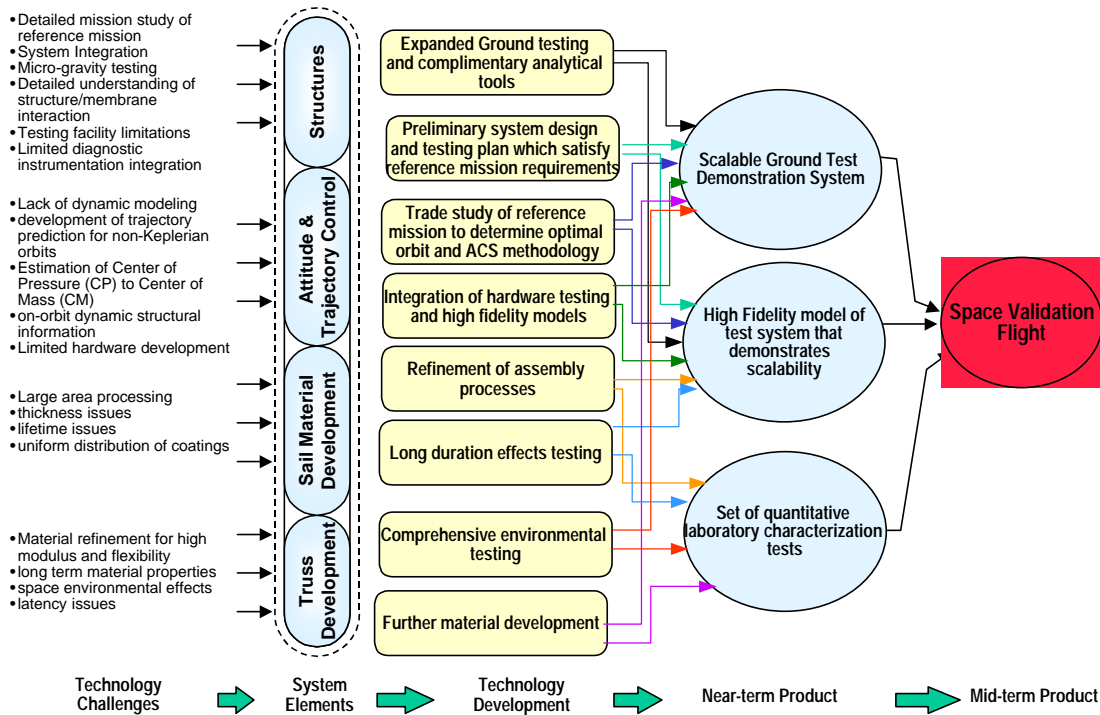


Figure 1: 2002 Solar Sail Technology Assessment Group (TAG) Roadmap

Solar Sail Integrated Software Tools

The second of two SSP research elements in the ISTP cycle 1 called for a set of integrated simulation tools to predict the trajectory, maneuvers, and propulsive performance of a solar sail during a representative flight profile. The solicitation encouraged that these tools should be able to be integrated into an optimal GNC subsystem on a future flight mission. In addition, the tools were required to be applicable to a solar sail mission of characteristics given in Table 2 and incorporate the following analytical models:

- Solar radiation pressure acting on the sail as a function of sail orientation and distance from the Sun.
- Disturbance forces acting on the sail such as gravitational torques and thermal deformation of the support structure.
- Orbital mechanics
- Sail structural dynamics
- Attitude control system dynamics
- Navigational sensors

Dimensions:	20 meters x 20 meters or greater
Sail Subsystem Areal Density	< 20 g/m ² (with scalability to 12 g/m ² for 10 ⁴ m ²)
Stowed Volume	< 0.5 m ³ (with scalability to 1.5 m ³ for 10 ⁴ m ²)
Thrust Vector Turning Rate about roll axis:	> 1.5°/hr
Effective Sail Reflectance	> 0.75
Anti-sunward Emissivity	> 0.30
Thrust Vector Pointing Range	± 22.5° (centered on the solar vector, thrusting anti-sunward)
Membrane Characteristics	space-durable, tear-resistant material designed for an operational lifetime of at least 1 year in the near-GEO environment.
System Flatness	Effective for Propulsion
ACS	3-axis, minimize propellant usage

Table 1: Cycle 1 System Level Ground Demonstration Required Characteristics

Dimensions:	100 meters x 100 meters or greater
Sail Subsystem Mass	120 kg
Spacecraft Mass	80 kg
Total Flight Mass	200 kg
Characteristic Acceleration @ 1 Au	0.35 mm/s ²
Sail Reflectivity	0.85
Mission Class	Sub L ₁
Thrust Vector Pointing Range	Cone angle of 40°
Pitch Rates	1.5°/hr.

Table 2: Cycle 1 Integrated Software Tools Required Mission Characteristics

ISTP Cycle 1 Hardware Work

SSP awarded ground demonstration contracts to two separate companies that had proposed two separate types of technologies in order to achieve the project objective. ABLE Engineering Company's (AEC) proposed work, based on their prior ST 7 work³, incorporate their rigid coilable boom, a C_p/C_M ACS subsystem and partner SRS' CPI for a sail membrane. L'GARDE Inc. proposed work, based on the experience they gained on ST 5⁴ and as the sail provider for Team Encounter⁵, incorporate their

inflatable and sub-T_g rigidizable boom, a control vane based ACS and Mylar for the sail membrane. A technical description of work being performed by AEC⁶ and L'GARDE⁷ is found in the respective teams papers at this conference. The parallel testing and development of these two system level demonstrations that have varied technologies in the three major components removes the risk of this technology development from encountering a single point failure. The system level ground

demonstration work has been divided into three phases. A six month concept refinement phase was completed in May 2003. During this Phase, the two teams provided analysis of their system's performance when scaled to the Design Reference Mission given in Table 3 and a preliminary test plan for the following two twelve month phases.

The 12-month hardware development phase began in June 2003. In this phase both team are building and testing components and subsystems with 10-m quadrants. The most comprehensive of these tests will be when the respective teams deploy their integrated boom and sail subsystem in the LaRC 14-m vacuum facility in the first half of 2004.

Following a successful second phase the teams will culminate their work in a twelve month system verification phase. In this phase both teams will build and test fully integrated 20-m sail systems that will be comprised of its launch packaging container, and an operational ACS subsystem. In the first half of 2005, the respective teams will test their system in the 30-m thermal vacuum system at Glenn Research Center's Plumbrook Space Power Facility.

Applicability to OSS Missions

The Sun Earth Connection (SEC) division of OSS has identified solar sail propulsion as an enabling technology⁸ because it is the only propulsion system that can deliver several SEC mission payloads to their desired destinations. Figure 2 shows a roadmap of these missions and

the Solar sail performance characteristics required. The axis on the left is the solar sail system areal density which is shown decreasing as the axis moves towards the top of the plot while the bottom axis is time. The first two missions shown on this chart (Flight Validation and Geostorm) are missions that would provide the space validation and confidence that would enable the last four roadmap missions [Solar Polar Imager (SPI), L1-Diamond (L1D), Particle Acceleration Solar Observatory, and Interstellar Probe]. The missions requirements and performance of SPI and L1D have strongly influenced the formulation and implementation of the previous described SSP work.

Future Directions

The SSP Project approach of providing near term verification of solar sails through the development of system level technology using ground testing and the development of subsystems, operations tools and computational models has begun building a technological foundation that can be readily used by future programs (e.g., New Millennium Program) in their pursuit of providing space validation of this technology. In so doing, this work will bring the technology to a readiness level such that it will minimize the exposure to risk of future flight programs.

Launch Mass(kg)	Payload Mass(kg)	Payload Power(W)	Total Power(W)	TM Dish(m)	TM Band	TM Rate(Kb/s)	S/C Dia(m)	Launch Vehicle
250	50	100	750	1.5	X	100	<2.3	Delta 2425-9.5

Table 3: Cycle 1 Design Reference Mission Characteristics

Figure 2: 2003 Sun Earth Connection Solar Sail Mission Roadmap

References:

[1] Integrated I-Space Transportation Plan, In-Space Propulsion Program, NASA, 2000.

[2] G. Garbe, 2002 Solar Sail Technical Assessment Group Report, NASA, 2002.

[3] D. Murphy et al., "Scaleable Solar Sail Subsystem Considerations", 43rd AIAA,

Structures, Structural Dynamics, and Materials Conference, AIAA 2002-1703.

[4] West, J. L. and B. Derbes, “Solar Sail Vehicle Design for the Geostorm Warning Mission”, Structures, Structural Dynamics, and Materials Conference, AIAA 2000-5326.

[5] B. Derbes et al., “Team Encounter Solar Sails”, 39th AIAA Joint Propulsion Conference, AIAA 2003-4797.

[6] D. Murphy et al., “Progress and Plans for a System Level Demonstration of a Scaleable Square Solar Sail”, 39th AIAA Joint Propulsion Conference, AIAA 2003-4794.

[7] D. Lichodziejewski et al., “Bringing an Effective Solar Sail Design to TRL 6”, 39th AIAA Joint Propulsion Conference, AIAA 2003-4659.

[8] Sun Earth Connections Roadmap 2003 – 2008, NASA, September 2002.



ISP IN-SPACE PROPULSION

(for students and teachers grades 5 thru 12)



EDUCATORS
Grades 5-8

STUDENTS
Grades 5-8

SCIENCE FAIRS

LINKS

ISP HOME

JUST FOR FUN

**EDUCATIONAL
OPPORTUNITIES**

Educational Opportunities

As much as we enjoy providing tools and resources for the classroom, we're equally determined to get students and teachers out of the hallowed halls of learning -- and bring them here to NASA!

Educational opportunities at NASA Field Centers -- from educator fellowships and research grants to student co-ops and summer internship programs -- are a key source of new ideas and fresh vision, helping NASA realize its goals for the U.S. Space Program. It's also a key source for finding the men and women who may become tomorrow's NASA workforce.

In other words, for finding **YOU**.

Explore these opportunities, and [contact us](#) to learn more.

Educators & Students

[NASA's Education Programs](#)

[<http://education.nasa.gov/>]

[NASA's Cooperative Education Program](#)

[<http://eodd.msfc.nasa.gov/coop/>]

[NASA Space Grant College and Fellowship Program](#)

[<http://calspace.ucsd.edu/spacegrant/>]



[Women in Science and Engineering \(WISE\) scholars program](#)

[<http://education.msfc.nasa.gov/docs/064.htm>]

[Future Assets, Student Talent \(FAST\) program](#)

[<http://education.msfc.nasa.gov/docs/024.htm>]

[Graduate Student Researchers Program](#)

[<http://education.nasa.gov/gsrp/>]

Owner: Space Transportation Directorate Curator: [Sherry Wallace](#)

Web Services Provided by: [IDS \(Internet Delivery Services\)](#) - CSC

[NASA Privacy Statement](#)



ISP IN-SPACE PROPULSION

(for students and teachers grades 5 thru 12)



EDUCATORS
Grades 5-8

STUDENTS
Grades 5-8

SCIENCE FAIRS

LINKS

ISP HOME

JUST FOR FUN

**EDUCATIONAL
OPPORTUNITIES**

Just For Fun

Whysville

Have you ever wondered what makes some rockets fly in space, or why the stars don't fall out of the sky? If the answers are yes then get your parents permission to join [Whysville](#).

After signing in at Whysville, hop on the Destination Bus to WASA by choosing WASA from the drop down list. When arriving at WASA hop off and let your imagination carry you to the stars and planets by designing an Ion Engine at the Ion Engine Office or learn about gravity at SIRT Zero Gravity.

Fun Java Programs

Basic Instructions:

The applets on this page are written in Sun Microsystems' [Java](#) language. On Windows systems, most Netscape and Internet Explorer browsers only support a primitive level of Java applets (version 1.1.8) but Sun has made available a free plug-in that users can download. The plug-in enables browsers to run applets written with the latest level of Java technology (version 1.4.1). It is highly recommended that Windows users download the plug-in before attempting to run the applets on this page.

For Mac users, the Java language is embedded within the Mac OS system, but only Mac OS X supports a high-enough level of Java (version 1.3.1) to run these applets. Currently, Apple has no plans to make higher-level (version 1.2 and higher) Java available to Mac

OS 9 users and below.

Download the [Java plug-in](#) for Windows.

Read [Apple's statements](#) on Java technology for the Mac.

Java Applets:

● [Trajectory Simulation](#)

This applet displays and animates the trajectories of a variety of spacecraft, both historical and current. Due to limitations in the applet, some trajectories cannot yet be displayed, such as Magellan, and others can only have a portion of their trajectories displayed, such as Mariner 10, Galileo, and Cassini. Most of the data for this applet was taken from the [JPL Missions](#) and the [NSSDC Planetary Sciences](#) sites.

● [Mars Mission Trajectory Planner](#)

This applet allows the user to plan a round-trip mission to Mars. The applet displays contour plots of departure and arrival dates from Earth to Mars, and Mars to Earth. These contour plots are sometimes known as "[porkchop](#)" plots. The "porkchop" plot enables a mission planner to quickly see when a spacecraft can be sent to Mars for the least amount of energy. By clicking a location in the "porkchop" plot, the applet will calculate and display the transfer orbit corresponding to those departure and arrival days, which can then be animated. Mission opportunities for different years can be selected from the pull-down menu. Clicking and dragging on the "porkchop" allows the planner to explore different regions of the launch opportunity.

● [Main Asteroid Belt Simulation](#)

This applet displays and animates the first 1000 numbered asteroids. Most of these asteroids occupy the Main Asteroid Belt, a region between Jupiter and Mars. Among the largest are the asteroids Ceres and Vesta, which are targets of the upcoming [Dawn](#) spacecraft mission. When the animation is stopped, users can click on an individual asteroid to see its particular name and orbit. Asteroids of particular interest are displayed with their names.

- [MPC Plot of the Inner Solar System](#)

● [Kuiper Belt Object Simulation](#)

This applet displays and animates the objects that form the [Kuiper Belt](#), an recently-discovered asteroid field in the outer solar system that is of great interest to planetary scientists. The planned [New Horizons](#) mission will fly by Pluto and several Kuiper Belt objects. When the animation is stopped, users can click on an individual asteroid to see its particular name and orbit. KBOs of particular interest (such as [Quaoar](#) and [Varuna](#)) are displayed with their names.

- [MPC Plot of the Outer Solar System](#)

● [Potentially Hazardous Asteroids](#)

This applet displays and animates the objects that are considered [potentially hazardous](#) to the Earth. PHAs are hazardous because they cross through the Earth's orbit as they orbit the Sun, and if the Earth and the PHA are in the same location at the same time, this is a [risk of impact](#). Therefore, search and monitoring programs worldwide seek to discover and track PHAs. However, because of their proximity to Earth's orbit, PHAs are probably the first asteroids that we will exploit in the future for resources. A small asteroid holds potentially trillions of dollars worth of materials!

● [The Closest Stars to the Sun](#)

This applet creates a three-dimensional display of the [nearest stars](#) to the Sun. The



information used to display them comes from the [RECONS](#) database of nearby stars.

- [Radial Thrust Simulation](#)
- [Catch Mechanism Simulation](#)
- [Brayton Cycle Simulation](#)

Owner: Space Transportation Directorate Curator: [Sherry Wallace](#)

Web Services Provided by: [IDS \(Internet Delivery Services\)](#) - CSC

[NASA Privacy Statement](#)



ISP IN-SPACE PROPULSION

(for students and teachers grades 5 thru 12)



EDUCATORS
Grades 5-8

STUDENTS
Grades 5-8

SCIENCE FAIRS

LINKS

ISP HOME

JUST FOR FUN

**EDUCATIONAL
OPPORTUNITIES**

Links

[Text Only Version - Click Here](#)

Educators Grades 5-8:

[Air Breathing Rockets](#)

[Building Blocks to Space](#)

[Designing Tomorrow's Space Ships Today](#)

[Destination Mars](#)

[Escape Velocity: Fun and Games](#)

[Flying on the Ground](#)

[Galaxies Galore, Games and More](#)

[Liftoff to Learning: The Mathematics of Space-Rendezvous](#)

[Mega-Magnetism](#)

[NASA Central Operation of Resources for Educators](#)

[NASAexplores](#)

[NASA Education](#)

[NASA Spacelink](#)

[Patterns, Functions, and Algebra: Wired for Space](#)

[Sling Shot to Space](#)

[Slow and Steady Wins the Race...to Distant Space](#)

[Space Games Gallery Homepage](#)

[The First-Ever Space Rescue Vehicle](#)

[The Space Elevator](#)



[What is Orbit?](#)

Educators Grades 9-12:

[Air-Breathing Rockets](#)

[Building Blocks to Space](#)

[Designing Tomorrow's Space Ships Today](#)

[Destination Mars](#)

[Escape Velocity: Fun and Games](#)

[Flying on the Ground](#)

[Interactive Plasma Physics Education Experience](#)

[Liftoff to Learning: The Mathematics of Space-Rendezvous](#)

[Liftoff to Learning: Tethered Satellites](#)

[Mega-Magnetism](#)

[NASA Central Operation of Resources for Educators](#)

[NASAexplores](#)

[NASA Education](#)

[NASA Spacelink](#)

[Sling Shot to Space](#)

[Slow and Steady Wins the Race...to Distant Space](#)

[The First-Ever Space Rescue Vehicle](#)

[The Space Elevator](#)

[What is Orbit?](#)

Students 5-8:

[Design a Spacecraft](#)

[Electrons](#)

[Falling Into a Black Hole](#) (board game)

[Galaxies Galore, Games and More](#)

[History of the Electron](#)



[Magnetic Field Lines](#)
[Magnetic Field Lines: A History](#)
[Magnetic Fields](#)
[Magnetic Fields: A History](#)
[NASA Qwhiz!](#)
[Space Games Gallery Homepage](#)
[Ultra-Efficient Engine Technology: Fun and Games](#)

Students 9-12:

[History of the Electron](#)
[Interactive Plasma Physics Education Experience](#)
[Magnetic Field Lines](#)
[Magnetic Field Lines: A History](#)
[Magnetic Fields](#)
[Magnetic Fields: A History](#)
[Space Research Fun & Learning Games](#)
[The Earth's Magnetosphere: A History](#)
[The Magnetosphere](#)

Science Fair Resources:

[Experimental Science Projects: An Intermediate Level Guide](#)
[Links to Science Project Sites](#)
[Looking for a Science Fair Project Topic?](#)
[Science Fair Primer](#)
[Science Project Guidelines](#)
[S'COOL : Science Project/Science Fair Ideas](#)
[Space Science/Astronomy Projects](#)



The Ultimate Science Fair Resource

Owner: Space Transportation Directorate Curator: [Sherry Wallace](#)

Web Services Provided by: [IDS \(Internet Delivery Services\)](#) - CSC

[NASA Privacy Statement](#)



ISP IN-SPACE PROPULSION

(for students and teachers grades 5 thru 12)



EDUCATORS
Grades 5-8

STUDENTS
Grades 5-8

SCIENCE FAIRS

LINKS

ISP HOME

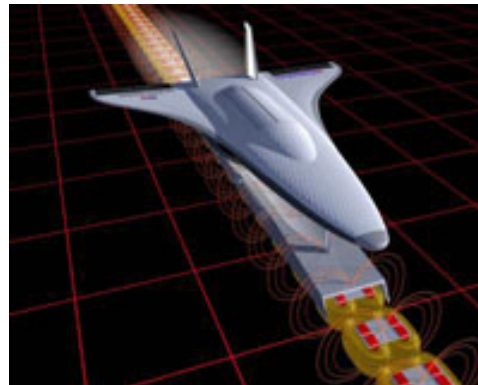
JUST FOR FUN

**EDUCATIONAL
OPPORTUNITIES**

Students Grades 5 - 8

Wired for Space

Electricity is the lifeblood of a spacecraft or launch system. Without electricity, important instruments, computers, radio transmitters, and other systems will not work. The scientists and engineers working with magnetic levitation launch system research and the ProSEDS

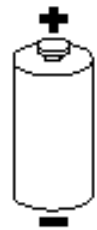


electrodynamics experiment must have a thorough knowledge of electricity. They rely on electrical engineers (engineers who have completed specialized study in the design and building of electrical systems and electronic components) for expert assistance. The concepts of electrical circuits, resistors, and current are at the heart of all electrical systems in any launch system or space vehicle.

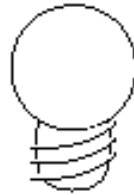
Safety First!! Do not experiment with electric outlets and appliances at home or in school. The high voltage (we will explain this later) can kill you. The batteries that you will use for the experiments will not give a shock (unless you put a LOT of them together.)

Prediction

Using the shapes on the diagram below, make a drawing of an arrangement that you think will light up the bulb and one that does not. Keep this paper for future reference.



BATTERY



BULB



WIRE

Make a circuit!

Using a D-cell battery, a flashlight bulb, and a piece of insulated wire, find out how they should be arranged to make the bulb light up.

1. Make drawings of 3 ways that work and one that does not.
2. Compare this to the predictions that you made.
3. What do you think is happening in the wire when the path is complete? (This is called a closed circuit.)
4. What happens when the path is broken? (We call this an open circuit.)

A Shocking Event

Do you ever remember getting a shock after you walked across a carpet and then touched a metal doorknob? That electric shock was caused by the build-up of an electric charge in your body. When you touched the metal doorknob the charge jumped from you to the door. Why? You were full of extra electrons (a charge) after you walked across the carpet in your shoes or slippers. When your hand moved close to the doorknob, some of the electrons jumped across to the metal. We say that your body and the doorknob had a potential difference which caused the flow of electrons from your body to the doorknob. A constant potential difference or voltage causes a steady flow of electrons, called an electric current. Think of voltage as a push and the bigger the push, the more voltage. This electrical push is measured in volts. The amount of current is measured in amperes.

The [Theatre of Electricity](http://www.mos.org/sln/toe/toe.html) [http://www.mos.org/sln/toe/toe.html] has information about the Van de Graaff generator, the equipment that is used to generate a surge of charge and

make your hair stand on end.

5. Compare your little shocking events in the past to lightning strikes. How might they be similar? How are they different? Find out how lightning is formed in clouds and what you should do to protect yourself from strikes.

NASA's [Marshall Space Flight Center](http://www.msfc.nasa.gov) [http://www.msfc.nasa.gov] has played an important role in the collections of lightning data from space and on the ground. Check it out!

[National Geographic](http://www.nationalgeographic.com/lightning/) [http://www.nationalgeographic.com/lightning/] shares stories from survivors of lightning strikes and teaches the science of lightning.



Add a Battery!

Your battery is the energy source and gives electricity its push through the circuit with about 1.5 volts. The amount of charge that is being pushed is measured in amperes. Add another battery to your circuit with more wire to see what happens when you add another battery (more push). Connect the two batteries together by placing a wire from the positive end of one to the negative of the other and then connecting to the bulb. This creates a "series" arrangement and the voltages are added together giving more push. It will also cause your battery to lose power more quickly, so don't leave it connected for long!

Caution! Don't add more than one battery. You may burn out the flashlight bulb.

6. Draw a diagram of the most successful arrangement.

7. What was the effect of 2 batteries on the brightness of the bulb?

Batteries produce their energy with chemical reactions that take place inside the battery. Power utilities use electric generators to provide 110 volts to home outlets. Power lines may carry 20,000 volts along the length of the wire. While most of us depend on electricity from local power plants, emergency services like hospitals usually have a back-up generator to produce some electricity for their needs if there is a power outage.

8. What are some ways you can prepare for a power outage at your home?

Resistance

9. Using a regular straw and a smaller diameter cocktail straw, compare how easy it is to blow air through them.

The flow of electricity through a circuit is similar to the flow of air in the 2 straws. If it takes more work to push the air, or the current, then we say that the object has more resistance. When you hook up a bulb in a circuit, the bulb resists the current causing the thin filament to heat and light up.

10. Compare the resistance of thin wire and thick wire. (Remember the straw example?) Which one would allow current to pass more easily?

11. Resistance is measured in ohms. A typical light bulb has a resistance of about 100 ohms. A toaster or iron may only have a resistance of about 15 ohms. Think back to the straw activity again. If there is not much resistance a lot of current is permitted, which produces heat. Hypothesize how resistance is related to the amount of current.

Possible web resources about electricity and magnetism:

<http://web66.coled.umn.edu/hillside/franklin/jummy/Project.html>

<http://www.eia.doe.gov/kids/>

<http://www.howstuffworks.com/electromagnet.htm>

Additional NASA web resources:

[NASA Education](#)

[NASA Spacelink](#)



Owner: Space Transportation Directorate Curator: [Sherry Wallace](#)
Web Services Provided by: [IDS \(Internet Delivery Services\)](#) - CSC
[NASA Privacy Statement](#)



ISP IN-SPACE PROPULSION

(for students and teachers grades 5 thru 12)



EDUCATORS
Grades 5-8

STUDENTS
Grades 5-8

SCIENCE FAIRS

LINKS

ISP HOME

JUST FOR FUN

**EDUCATIONAL
OPPORTUNITIES**

Educators Grades 5 - 8

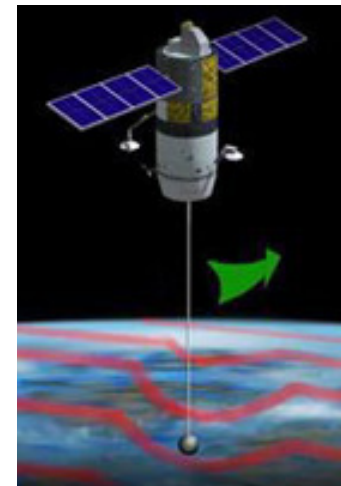
Mega-Magnetism

One of the key rules of magnetism-that opposites attract and similarities repel-is behind a no-fuel method of space propulsion. When you're trying to move space objects, you need to think big, and there aren't many magnets larger than the Earth!

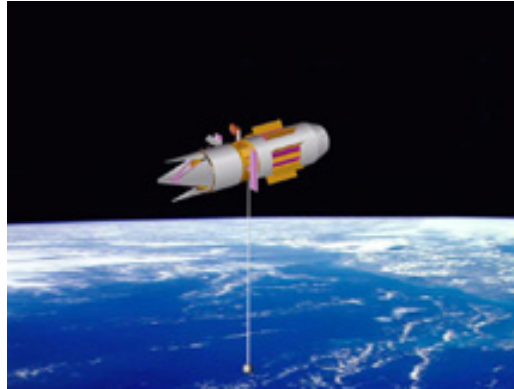
The Propulsive Small Expendable Deployer System experiment-called ProSEDS-uses what is called an electrodynamic tether, to produce thrust. Electrodynamic tether thrusters work by using the force of a magnetic field on a wire carrying an electrical current. When the tether moves through a magnetic field, it makes an electric current. The magnetic field around the tether will push against the much stronger magnetic field around Earth. That push-pull, which is what magnetism is all about, will be used to move satellites and other spacecraft.

If that sounds a bit hard to understand, think about how the alternator in a car works. Moving a coil of wire around a magnet creates electrical energy. ProSEDS moves a wire tether around the Earth-a very large magnet-and voltage is produced through the tether.

The positive end of the tether attracts electrons and sends them down the wire to the negative end, where a rocket is attached. Magnetic force presses down on the electrons, moving them, and they push the tether-and anything else in the way-along with them.



Since the rocket is in the way, it goes along, too. At the negative end, the electrons are released.



This thrust isn't the type of thrust that would launch a space vehicle, but it would give a craft already in space a boost of power. That power could change the orbit of a satellite, adjust the orbit of the International Space Station, or power satellites already in orbit-and it would all be done without using any fuel. It would be sort of like driving your car and never having to stop for gas.

ProSEDS will lower its orbit by sending electrons in only one direction. Reversing the electrons in the tether would allow spacecraft to move up as well as down, but in order to do that it would need a power source.

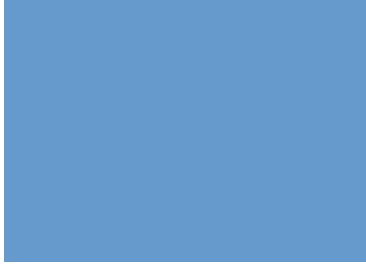
Once a satellite reaches low-Earth orbit, the next stage of the craft usually contains fuel to boost it into higher orbit. That fuel is heavy and expensive, and the vehicle has to be built to carry that extra weight. When ProSEDS is able to provide that thrust, it will mean those spacecraft no longer need to carry fuel. That will save both money and fuel.

ProSEDS will launch on a Delta II rocket. The 9.3-mile tether it deploys will be about as thin as dental floss and will move a rocket stage weighing thousands of pounds!

Published by [NASAexplores](http://NASAexplores.com) [http://NASAexplores.com]: August 23, 2001

[Express Lessons and Online Resources](http://www.nasaexplores.com/lessons/01-055/5-8_index.html)

[http://www.nasaexplores.com/lessons/01-055/5-8_index.html]



Owner: Space Transportation Directorate Curator: [Sherry Wallace](#)
Web Services Provided by: [IDS \(Internet Delivery Services\)](#) - CSC
[NASA Privacy Statement](#)



TECH ISP

IN-SPACE PROPULSION TECHNOLOGIES



Working With NASA

PARTNERING with NASA and the In-Space Propulsion program...

*Coming together is a beginning,
staying together is progress,
and working together is success.*

-- Henry Ford

"No bucks," the old adage says, "no Buck Rogers." But whereas funding is certainly a key to our success, NASA truly thrives on the relationships that guarantee that success.

Contract teams. Research fellowships. Student Co-ops. Joint endeavors with the brightest minds and the boldest innovators in American industry, academia and government.

From all these invaluable partnerships spring the true "Buck Rogers" -- inspiration, determination, vision.

Success.

- **LINKS**
- **TECHNICAL PUBLICATIONS**
- **WORKING WITH NASA**

- **ISP MAIN**

CURRENT TECHNOLOGIES**Aeroassist**

Aerocapture -
Aerobraking -

Solar Electric Propulsion

Next Generation
Electric Propulsion -
SEP Hall -

Solar Sails**Advanced Chemical****Tethers**

Momentum Exchange -
Electrodynamic -

Solar Thermal

EMERGING TECHNOLOGIES

Aerogravity Assist -

The In-Space Propulsion program is a prime example. We seek to ramp up the nation's mission to explore the solar system faster, safer and more affordably. We can't do it alone.

Opportunities to partner with NASA are plentiful. New grants, fellowships, contracts and teaming prospects are constantly on the horizon. Whether you are an established aerospace firm, a new business, an academic researcher, an engineering student or a high school science or math teacher, NASA has opportunities for you. Take a look:

Research Funding Opportunities**[NASA Research Announcements \(NRAs\)](#)**

[http://spacetransportation.com/isp1/tech/working_with_nasa.pdf]

Industry & Academia**[Business Opportunities with NASA](#)**

[<http://ec.msfc.nasa.gov/hq/library/biz.html>]

[Central Contractor Registration](#)

[<http://www.ccr.gov/>]

[NASA Center Procurement Sites](#)

[<http://procurement.nasa.gov/cgi-bin/nais/nasaproc.cgi>]

[NASA Research Opportunities](#)

[<http://research.hq.nasa.gov/research.cfm>]

[Faculty Research Awards](#)

[<http://education.msfc.nasa.gov/docs/055.htm>]

[NASA's Office of Small and Disadvantaged
Business Utilization](#)

[<http://www.hq.nasa.gov/office/codek/>]

[SBIR/STTR](#)

[<http://sbir.nasa.gov/>]

[Minority University- Space Interdisciplinary
Network \(MU-SPIN\) Program](#)

[<http://muspın.gsfc.nasa.gov/>]

Educators & Students

[NASA's Education Programs](#)

[<http://education.nasa.gov/>]

[NASA's Cooperative Education Program](#)

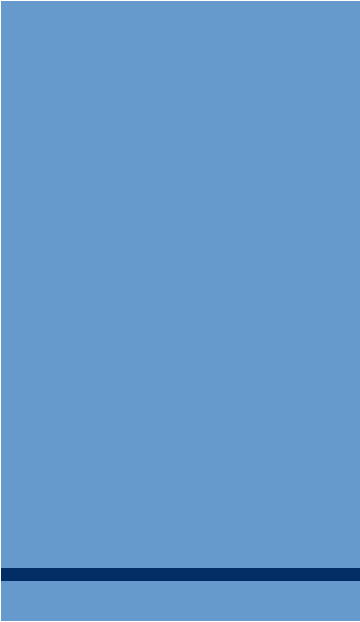
[<http://eodd.msfc.nasa.gov/coop/>]

[NASA Space Grant College and Fellowship Program](#)

[<http://calspace.ucsd.edu/spacegrant/>]

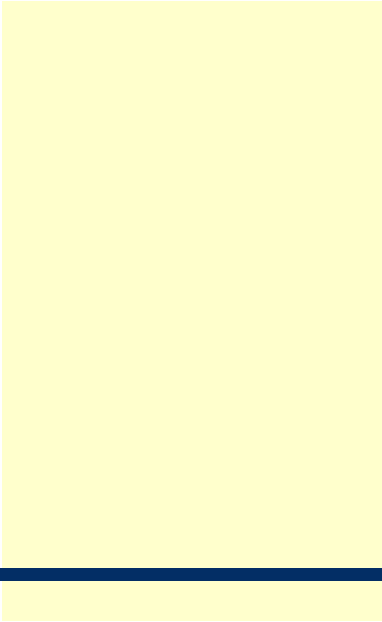
[Women in Science and Engineering \(WISE\)
scholars program](#)

[<http://education.msfc.nasa.gov/docs/064.htm>]



[Future Assets, Student Talent \(FAST\) program](http://education.msfc.nasa.gov/docs/024.htm)
[<http://education.msfc.nasa.gov/docs/024.htm>]

[Graduate Student Researchers Program](http://education.nasa.gov/gsrp/)
[<http://education.nasa.gov/gsrp/>]





TECH ISP

IN-SPACE PROPULSION TECHNOLOGIES



Technical Publications

GENERAL TECHNICAL REFERENCES

[AIAA 2004-3834 A Comparison of Transportation Systems for Human Missions to Mars](#) - PDF format

[AIAA 2003-4803 Engineering Level Model Atmospheres for Titan & Neptune](#) - PDF format

Niehoff, J.C. and Friedlander, A.F., "Comparison of Advanced Propulsion Capabilities for Future Planetary Missions," *Journal of Spacecraft and Rockets*, Vol. 11, No. 8, Aug. 1974, pp. 566-573.

Frisbee, R., "Advanced Propulsion," *Transportation Beyond 2000: Engineering Design for the Future Workshop*, NASA Conference Proceedings 10184, Part 2, Hampton, VA, Sep. 1995, pp. 693-702.

Curran, F.M., Sovey, J.S., and Myers, R.M., "Electric Propulsion: An Evolutionary Technology," *Acta Astronautica*, Vol. 29, No. 9, 1993, pp. 651-665.

McInnes, C.R., "Near-Term Mission Applications For

- **LINKS**
- **TECHNICAL PUBLICATIONS**
- **WORKING WITH NASA**

- **ISP MAIN**

**CURRENT
TECHNOLOGIES****Aeroassist**

*Aerocapture -
Aerobraking -*

**Solar Electric
Propulsion**

*Next Generation
Electric Propulsion -
SEP Hall -*

Solar Sails**Advanced
Chemical****Tethers**

*Momentum Exchange -
Electrodynamic -*

Solar Thermal

**EMERGING
TECHNOLOGIES**

Aerogravity Assist -

Low Performance Solar Sails," Space Technology and Applications International Forum-2001, edited by M. El-Genk, AIP Conference Proceedings 552, Albuquerque, NM, Feb. 2001, pp. 379-384.

Leipold, M., "Solar Sail Technology Development And Application To Fast Missions To The Outer Heliosphere," Space Technology and Applications International Forum-2001, edited by M. El-Genk, AIP Conference Proceedings 552, Albuquerque, NM, Feb. 2001, pp. 385-392.

Gavit, S.A., Liewer, P.C., Wallace, R.A., Ayon, J.A., Frisbee, R.H., "Interstellar Travel - Challenging Propulsion and Power Technologies for the Next 50 Years," Space Technology and Applications International Forum-2001, edited by M. El-Genk, AIP Conference Proceedings 552, Albuquerque, NM, Feb. 2001, pp. 716-726.

Houts, M., Van Dyke, M., Godfroy, T., Pedersen, K., Martin, J., Dickens, R., Salvail, P., and Hrbud, I., "Options for Development of Space Fission Propulsion Systems," Space Technology and Applications International Forum-2001, edited by M. El-Genk, AIP Conference Proceedings 552, Albuquerque, NM, Feb. 2001, pp. 822-827.

Sukhodolsky, A., "On New Generations of Solar Propulsive Systems for Space," Space Technology and Applications International Forum-2001, edited by M. El-Genk, AIP Conference Proceedings 552, Albuquerque, NM, Feb. 2001, pp. 944-949.

Johnson, L., "The NASA In-Space Transportation Area," NASA JPL/MSFC/UAH 12th Annual Advanced Space Propulsion Workshop, Huntsville, AL, April 2001.

Cole, J., "An Overview of the Advanced Propulsion Research Project Office," NASA JPL/MSFC/UAH 12th Annual Advanced Space Propulsion Workshop, Huntsville, AL, April 2001.

Polk, J., "An Overview of JPL's Advanced Propulsion Concepts Research Program," NASA JPL/MSFC/UAH 12th Annual Advanced Space Propulsion Workshop, Huntsville, AL, April 2001.

Dunning Jr., J.W., Benson, S., and Oleson, S., "NASA's Advanced On-Board Propulsion Program: Activities at John H. Glenn Research Center," NASA JPL/MSFC/UAH 12th Annual Advanced Space Propulsion Workshop, Huntsville, AL, April 2001.

Garner, C., and Price, H., "A Summary of Recent Activities in Solar Sail Propulsion," NASA JPL/MSFC/UAH 12th Annual Advanced Space Propulsion Workshop, Huntsville, AL, April 2001.

Horodyskyj, U., "Sailing Into Space: Steering Towards Mars," NASA JPL/MSFC/UAH 12th Annual Advanced Space Propulsion Workshop, Huntsville, AL, April 2001.

Taylor, T.S., "Solar Sail Propelled Outer Planet Probes," NASA JPL/MSFC/UAH 12th Annual Advanced Space Propulsion Workshop, Huntsville, AL, April 2001.

Borowski, S.K., "2001: A Space Odyssey Revisited - The Feasibility of 24 Hour Commuter Flights to the Moon Using Lox-Augmented NTR Propulsion," NASA JPL/MSFC/UAH 12th Annual Advanced Space Propulsion Workshop, Huntsville, AL, April 2001.

Litchford, R., Bitteker, L., Jones, J., and Poston, T., "Prospects for Nuclear Electric Propulsion Using Closed-Cycle Magnetohydrodynamic Energy Conversion," NASA JPL/MSFC/UAH 12th Annual Advanced Space Propulsion Workshop, Huntsville, AL, April 2001.

Millis, M.G., "Emerging Possibilities for Space Propulsion Breakthroughs," Interstellar Propulsion Society Newsletter, Vol.1, No.1, July 1995.

Woodcock, G., "Solar Electric Propulsion (SEP) Independent Assessment," White Paper, Gray Research, Inc., Huntsville, AL, 2001.

Woodcock, G., "Nuclear Electric Propulsion (NEP) Independent Assessment," White Paper, Gray Research, Inc., Huntsville, AL, 2001.

Woodcock, G., "Nuclear Thermal Propulsion (NTP) Independent Assessment," White Paper, Gray Research, Inc., Huntsville, AL, 2001.

Noca, Frisbee, Johnson, Kos, Gefert, and Dudzinski, "Evaluating Advanced Propulsion Systems for the Titan Explorer Mission," IEPC-01-175, 27th IEPC, 2001.

Noca, Polk and Lennard, "Evolutionary Strategy for Use of Nuclear Electric Propulsion in Planetary Exploration,"

Cole, J., "Really Advanced Propulsion Research," Presentation to the Florida Chapter of the AIAA, January 2000.

L. Friedmann, Starsailing, Wiley, NY (1988).

E. Mallove and G. Matloff, The Starflight Handbook, Wiley, NY (1989).

G. L. Matloff, Deep-Space Probes, Springer-Praxis, Chichester, UK (2000).

C. R. McInnes, Solar Sailing, Springer-Praxis, Chichester, UK (2000).

J. L. Wright, Space Sailing, Gordon and Breach, Philadelphia, PA (1992).

SYSTEMS ANALYSIS

[AIAA 2004-3643 Controllability of Large SEP for Earth Orbit Raising](#)

[AIAA 2004-3804 Application of Solar Electric Propulsion to a Comet Surface Sample Return Mission](#)

CURRENT TECHNOLOGIES TECHNICAL

REFERENCES

Aeroassist

Aerocapture

AIAA-2003-4655 [Trailing Ballute
Aerocapture: Concept and
Feasibility Assessment](#)

AIAA-2003-4952 [Preliminary
Aerothermodynamics of Titan
Aerocapture Aeroshell](#)

AIAA-2003-4951 [Aerocapture
Simulation and Performance for
the Titan Explorer Mission](#)

AIAA-2003-4956 [Planetary Probe
Mass Estimation Tool
Development and its Application
to Titan Aerocapture](#)

AIAA-2003-4799 [Titan
Aerocapture Systems Analysis](#)

AIAA-2003-4955 [Structural
Design of the Titan Aerocapture
Mission](#)

[AIAA-2003-4953 An Analysis of the Radiative Heating Environment for Aerocapture at Titan](#)

[AIAA-2003-4954 Thermal Protection Concepts and Issues for Aerocapture at Titan](#)

[AIAA-2004-0484 The Impact of Flowfield-Radiation Coupling on Aeroheating for Titan Aerocapture](#)

[AIAA-2004-0486 Aeroheating Analysis for the Afterbody of a Titan Probe](#)

[Comparison of Methods to Compute High-Temperature Gas Viscosity](#)

[Collision Integrals for Ion-Neutral Interactions of Nitrogen and Oxygen](#)

[AIAA-2004-2456 Analysis of Afterbody Heating Rates on the Apollo Command Modules, Part 1: AS-202](#)

AIAA-2004-2469 N2-CH4-AR

Chemical Kinetic Model for
Simulations of Atmospheric Entry
to Titan

Lemmerman, L., Wercinski, P.,
"Small Neptune Orbiter Using
Aerocapture," Space Technology
and Applications International
Forum, (STAIF-97), Albuquerque,
NM, Jan. 1997

[http://www.hq.nasa.gov/office
/codez/plans /SSE00plan.pdf](http://www.hq.nasa.gov/office/codez/plans/SSE00plan.pdf)

Kos, L. et. al., "In-space
Integrated Space Transportation
Activity - Neptune Orbiter Mission
Briefing," NASA Marshall Space
Flight Center, April 2001

Tauber, M., Wercinski, P.,
Henline, W., Paterson, J., and
Yang, L., "Uranus and Neptune
Atmospheric Entry Probe Study,"
Journal of Spacecraft and
Rockets, Vol. 31, No. 5, pp. 799-
805, Sept-Oct., 1994.

Lasher, L., Wilson, K. and Greif,
R., "Radiation From an Isothermal
Hydrogen Plasma at
Temperatures Up To 40,000 K,"
Lockheed Palo Alto Research

Laboratory 6-76-66-17 Revised
July 1967.

Nelson, F. and Goulard, R.,
"Equilibrium Radiation From
Isothermal Hydrogen-Helium
Plasmas," Journal of Quantitative
Spectroscopy and Radiative
Transfer, Vol. 8, 1968, pp. 1351-
1372.

Tauber, M. and Wakefield, R.,
"Heating Environment and
Protection During Jupiter Entry,"
Journal of Spacecraft and
Rockets, Vol. 8, No. 6, June 1971,
pp. 630-636.

Marvin, J. and Pope, R., "Laminar
Convective Heating and Ablation
in the Mars Atmosphere," AIAA
Journal, Vol. 5, No. 2, 1967, pp.
240-248.

Wright, M. J., Candler, G. V., and
Bose, D., "A Data-Parallel Line
Relaxation Method for the Navier-
Stokes Equations," AIAA Journal,
Vol. 36, No. 9, 1998, pp. 1603-
1609.

Olynick, D. R., Henline, W. D.,
Hartung-Chambers, L., and
Candler, G. V., "Comparisons of

Coupled Radiative Navier-Stokes Flow Solutions with the Project Fire II Flight Data," AIAA Paper No. 94-1955, June 1994.

MacCormack, R.W. and Candler, G.V., "The Solution of the Navier-Stokes Equations Using Gauss-Seidel Line Relaxation," Computers and Fluids, Vol. 17, No. 1, 1989, pp. 135-150.
Yee, H.C., "A Class of High-Resolution Explicit and Implicit Shock Capturing Methods," NASA TM 101088, 1989.

Olejniczak, J. and Fletcher, D.G., "An Experimental and Computational Study of the Freestream Conditions in an Arc-Jet Facility," AIAA Paper No. 2000-2567, June 2000.

Wright, M. J., Sinha, K., Olejniczak, J., Candler, G. V., Magruder, T. D., and Smits, A. J., "Numerical and Experimental Investigation of Double-Cone Shock Interactions," AIAA Journal, Vol. 38, No. 12, 2000, pp. 2268-2276.

Wright, M. J., Loomis, M., and Papadopoulos, P., "Aerothermal

Analysis of the Project Fire II
Afterbody Flow," AIAA Paper No.
2001-3065, June 2001.

Baulch, D.L., et. al., "Evaluated
Kinetic Data for Combustion
Modeling," Journal of Physical
and Chemical Reference Data,
Vol. 21, No. 3, 1992, pp. 411.

Chen, Y.-K. and Milos, F., "Implicit
Ablation and Thermal Response
Program for Spacecraft
Heatshield Analysis", Journal of
Spacecraft and Rockets, Vol. 36,
No. 3, May-June 1999, pp 475-
483.

Laub, B. and Beck, R. A. S.,
"Development of Baseline
Response Model for Carbon
Phenolic", Contract No. GS-23F-
010K, ITT Aerotherm, Mountain
View, CA 94043, Oct. 2000.

Aerobraking

Solar Electric Propulsion

Next Generation Electric Propulsion

SEP Hall

Solar Sails

[AIAA 2004-3996 Study of Possible Solar Sail Applications for Mars Missions](#)

[AIAA 2003-5275 Solar Sail Application to Comet Nucleus Sample Return](#)

[AIAA 2003-4659 Bringing an Effective Solar Sail Design Toward TRL 6](#)

[AIAA 2004-1506 The Development of Solar Sail Propulsion for Inner Solar System, NASA Science Mission](#)

[AIAA 2003-4654 Aerocapture Technology Project Overview](#)

[NASA/TM-2004-213511, Optical Diagnostic System for Solar Sails: Phase 1 Final Report - PDF Format \(1.9MB\)](#)

[NASA's In-Space Propulsion Technology Program: Overview and Update - PDF format](#)

[Dr. Garbe AIAA 2003-5274b](#) -
PDF format

Advanced Chemical

General Advanced Chemical

Guernsey, Carl, Baker, Ray, and
Miyake, Robert, "Space Storable
Propulsion Advanced Chemical
Propulsion Final Report", Report
No. JPL D-27810, Jet Propulsion
Laboratory, Pasadena, CA
February 17, 2004

[Advanced Space Storable Propellants for Outer Planet Exploration](#)

Thunnissen, Daniel P., Guernsey,
Carl S., Baker, Raymond, S., and
Miyake, Robert N., "Advanced
Space Storable Propellants for
Outer Planet Exploration", 40th
AIAA/ASME/SAE/ASEE Joint
Propulsion Conference and
Exhibit 11-14 July 2004, Fort
Lauderdale, FL

[Advanced Chemical Propulsion Study](#)

Woodcock, G., Byers, D.,
Alexander, L., Krebsbach, A.,
“Advanced Chemical Propulsion
Study,” AIAA 2004-3494, 40th
AIAA/ASME/SAE/ASEE Joint
Propulsion Conference and
Exhibit 11-14 July 2004, Fort
Lauderdale, FL

Modeling of Spacecraft Advanced
Chemical Propulsion Systems

Benfield, M., and Belcher, J.,
“Modeling of Spacecraft
Advanced Chemical Propulsion
Systems”, AIAA 2004-4195, 40th
AIAA/ASME/SAE/ASEE Joint
Propulsion Conference and
Exhibit 11-14 July 2004, Fort
Lauderdale, FL

Advanced Fuels

Cryogenic Fluid Management

An Updated Zero Boil-Off
Cryogenic Propellant Storage
Analysis Applied to Upper Stages
or Depots in an LEO Environment

Plachta, David and Kittel, Peter
“An Updated Zero Boil-Off
Cryogenic Propellant Storage

Analysis Applied to Upper Stages
or Depots in an LEO
Environment”, NASA/TM-2003-
211691, also identified as AIAA-
2002-3589

Spray Bar Zero-Gravity Vent
System for On-Orbit Liquid
Hydrogen Storage

Hastings, L., Flachbart, J.,
Hedayat, M., Fazah, M., Lak, T.,
Nguyen, H., Bailey, L., ”Spray Bar
Zero-Gravity Vent System for On-
Orbit Liquid Hydrogen Storage”,
NASA/TM-2003-212926

Results of an Advanced
Development Zero Boil-Off
Cryogenic Propellant Storage
Test

Plachta, D., “Results of an
Advanced Development Zero Boil-
off Cryogenic Propellant Storage
Test”, AIAA-2004-3837, Glenn
Research Center, Cleveland,
Ohio. 40th AIAA/ASME/SAE/
ASEE Joint Propulsion
Conference and Exhibit 11-14
July 2004, Fort Lauderdale, FL

Lightweight & Optimized Components

Tethers

[MXER TAG 2003 Final Report](#)

Electrodynamic

Momentum Exchange

Solar Thermal

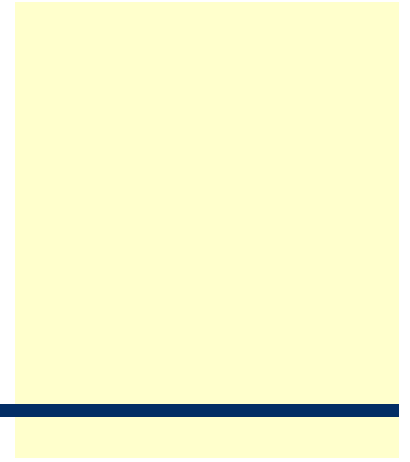
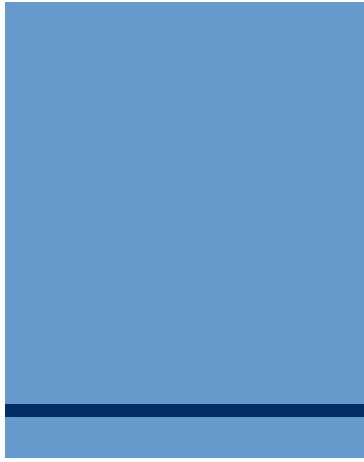
[AIAA 2003-5029 Results of
Evaluation of Solar Thermal
Propulsion](#)

[Results of Evaluation of Solar
Thermal Propulsion](#)

Woodcock, G., Byers, D., "Results
of Evaluation of Solar Thermal
Propulsion", AIAA 2003-5029,
39th Annual Joint Propulsion
Conference, Huntsville, AL July
2003

EMERGING TECHNOLOGIES TECHNICAL REFERENCES

Aerogravity Assist





TECH ISP

IN-SPACE PROPULSION TECHNOLOGIES



Links

CURRENT TECHNOLOGIES

Aeroassist

Aerocapture
Aerobraking

Solar Electric Propulsion

Next Generation Electric
Propulsion

- [NASA's Evolutionary Xenon Thruster \(NEXT\)](#)

SEP Hall

Solar Sails

[Project Overview \(pdf\)](#)

-
-

- **LINKS**
- **TECHNICAL PUBLICATIONS**
- **WORKING WITH NASA**

- **ISP MAIN**

**CURRENT
TECHNOLOGIES**

Aeroassist

Aerocapture -
Aerobraking -

**Solar Electric
Propulsion**

Next Generation
Electric Propulsion -
SEP Hall -

Solar Sails

**Advanced
Chemical**

Tethers

Momentum Exchange -
Electrodynamic -

Solar Thermal

**EMERGING
TECHNOLOGIES**

Aerogravity Assist -

[Solar Sail, Mission Classes
Supported Charts \(pdf\)](#)

Advanced Chemical

Advanced Fuels
Cryogenic Fluid Management
Lightweight Components

Tethers

Electrodynamic

- [NASA Space
Transportation Systems](#)
- [Space Tethers and
Their Potential
Applications](#)

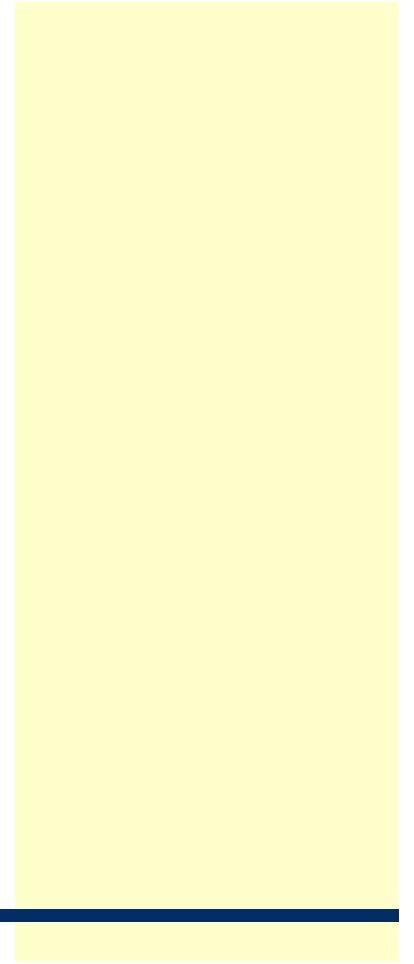
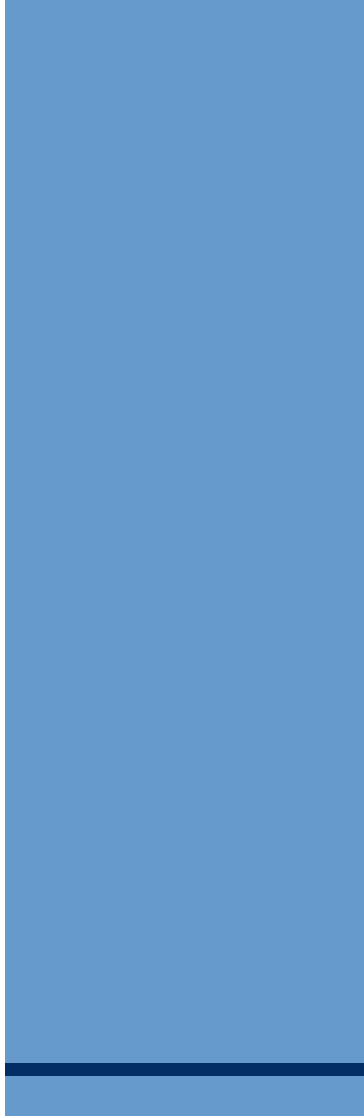
Momentum Exchange

Solar Thermal

EMERGING TECHNOLOGIES

Aerogravity Assist







TECH ISP

IN-SPACE PROPULSION TECHNOLOGIES



Under Construction

The page you are seeking is currently under constructions.

Please check back for more information.

- **LINKS**
- **TECHNICAL PUBLICATIONS**
- **WORKING WITH NASA**

- **ISP MAIN**

**CURRENT
TECHNOLOGIES**

Aeroassist

*Aerocapture -
Aerobraking -*

**Solar Electric
Propulsion**

*Next Generation
Electric Propulsion -
SEP Hall -*

Solar Sails

**Advanced
Chemical**

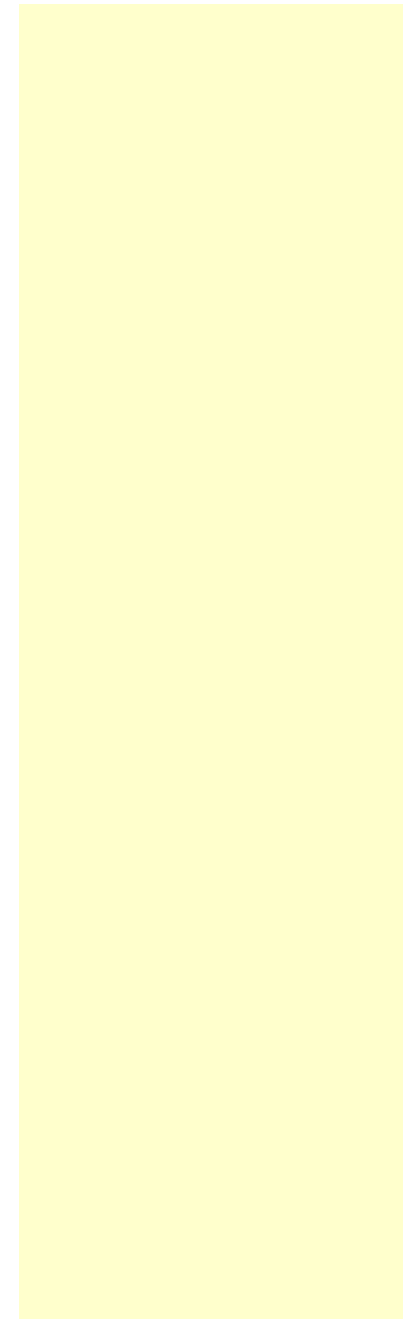
Tethers

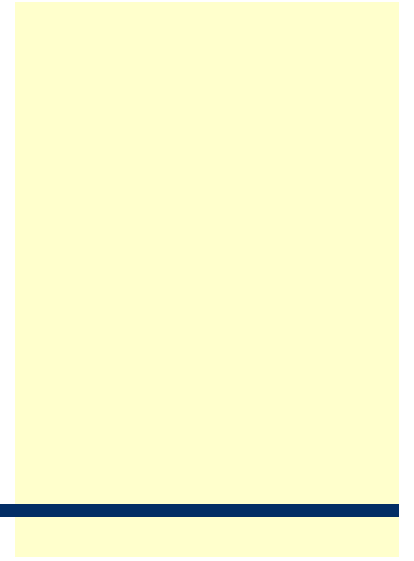
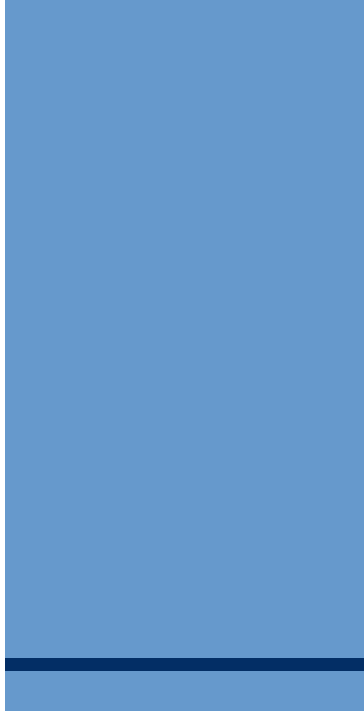
*Momentum Exchange -
Electrodynamic -*

Solar Thermal

**EMERGING
TECHNOLOGIES**

Aerogravity Assist -







TECH ISP

IN-SPACE PROPULSION TECHNOLOGIES



Aeroassist

Aeroassist Overview:

General Description

As NASA continues to send robotic missions into the Solar System, with plans for humans eventually to follow, a key challenge is to decrease mission costs and risks. One of the key propulsion areas under consideration to meet these needs is aeroassist -- a family of unique technologies that could enable future planetary exploration in deep space.

Aeroassist maneuvers encompass the various ways in which a flight vehicle may make use of a planet's atmosphere and aerodynamic forces to alter its orbit or travel velocity.

Aeroassist technologies now in use or in development include direct entry, aeroentry, aerobraking, aerocapture and aerogravity assist.

Direct Entry

Direct entry involves the passage of an entry probe -- a spacecraft designed to enter an atmosphere from a hyperbolic orbit and transmit data back to Earth. To date, only "ballistic," or unguided, direct entries have been performed because of the intense speed associated with the maneuver.

- **POTENTIAL MISSION APPLICATIONS**
- **FUNDAMENTAL PHYSICS**
- **TECHNICAL PUBLICATIONS**
- **LINKS**
- **ISP MAIN**
- **TECH MAIN**

CURRENT TECHNOLOGIES**Aeroassist**

Aerocapture -
Aerobraking -

Solar Electric Propulsion

Next Generation
Electric Propulsion -
SEP Hall -

Solar Sails**Advanced Chemical****Tethers**

Momentum Exchange -
Electrodynamic -

Solar Thermal

EMERGING TECHNOLOGIES

Aerogravity Assist -

The Galileo mission successfully conducted a direct entry maneuver during its 14-year mission to explore Jupiter and its moons, when the spacecraft released a probe into Jupiter's atmosphere in December 1995.

Direct entry technology could also be used for landing on a planet's surface. The Pioneer Venus Multi-probe mission was launched in August 1978 to investigate the atmosphere of the planet Venus and take measurements all the way to the planet's surface. Another example of a direct entry landing was the Mars Pathfinder, which launched in December of 1996 to study the Red Planet's surface and atmosphere. Pathfinder last sent data back to Earth on Sept. 27, 2003.



Galileo Probe

Aeroentry

Aeroentry is a more common flight maneuver than aerocapture or aerobraking. It is conducted whenever a spacecraft enters a planet's atmosphere from orbit. The Space Shuttle performs aeroentry every time it returns from orbit around the Earth. The Viking Landers used this aeroassist technology when the twin spacecraft landed on Mars in 1976 to gather atmospheric and surface data.

There are substantial differences between aeroentry and direct entry. Aeroentry requires a slower entry velocity and also typically involves guided entry -- a precision landing in a designated area -- such as the Space Shuttle's landings.

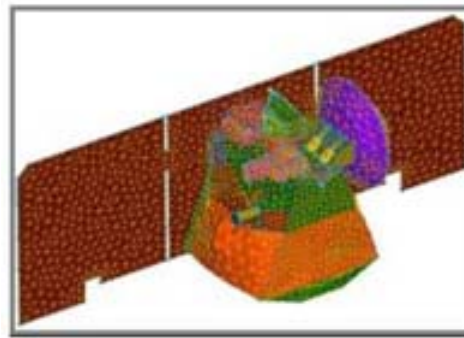


Viking Lander

Aerobraking

Aerobraking uses onboard fuel to capture a spacecraft into orbit but, then, utilizes drag from a planet's atmosphere to

slow down and place a spacecraft into its final orbit. This technique involves dipping into the uppermost portion of the atmosphere to adjust a craft's orbital altitude. This process can take several months to perform, as in the case of the Mars Global Surveyor, which launched in November of 1996. The spacecraft's mission was to analyze and send data back to Earth about the planet's magnetic field, atmosphere and surface. The Mars Global Surveyor made a series of aerobraking maneuvers over a nine-month period to gradually reduce its altitude and achieve its intended orbit.



Aerobraking Model



Mars Global Surveyor

A more recent mission -- the Mars Odyssey -- launched in April 2001 to study the Red Planet's composition, search for water and ice, and measure solar and cosmic radiation. The craft also made a series of aerobraking maneuvers but, this time, over a 77-day period to gradually reduce its altitude and achieve its intended orbit. The Odyssey spacecraft remains in orbit around the Red Planet today, sending vital data back to Earth.



Mars Odyssey

Aerocapture

Aerocapture is the next step in aeroassist technology development and is currently being developed within NASA.

Aerocapture is a technique whereby a spacecraft uses a planet's atmosphere to slow down and achieve orbit. An aerocapture vehicle approaching a planet is captured into orbit as it passes through the atmosphere, without the use of onboard propulsion. This fuel-free method could reduce the mass of an interplanetary spacecraft by more than half, allowing for smaller and less expensive launch vehicles or increasing the science payload capacity available on same size vehicles.

To conduct an aerocapture maneuver, a spacecraft requires adequate drag to slow its speed and also needs adequate protection from the heating environment. These functions could be accomplished in several ways. One option is with a rigid aeroshell like that used during the entry and descent of the [Mars Pathfinder](#) --in 1997 -- a mission that explored the

planet's surface and sent pictures and data back to Earth. Other farther-term alternatives would be a potentially lighter, inflatable aeroshell or a large, trailing ballute -- a combination parachute and balloon made of durable, thin material and stowed behind the vehicle for deployment.



Inflatable Aeroshell Aerocapture



Aerocapture at Titan



Rigid Aerocapture

Aerogravity Assist

Aerogravity assist combines the use of a planet's atmosphere,

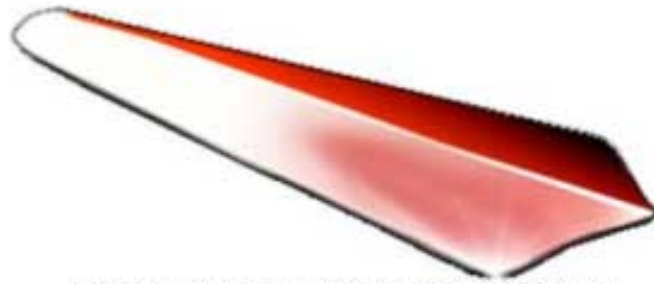
gravity and onboard vehicle propulsion to modify a spacecraft's orbit. The technique is much like a "gravity assist" maneuver where a spacecraft flies near a planet and uses the planet's gravitational force to bend the craft's trajectory. With aerogravity assist, the vehicle flies very close to the planet, basically within the atmosphere.

This use of gravity and aerodynamics could help the spacecraft turn more sharply, or bend at an increased angle, around the planet than with gravity alone, giving a greater "slingshot" effect. This technique has been studied by NASA researchers over the past decades and has significant potential to reduce interplanetary trip times.

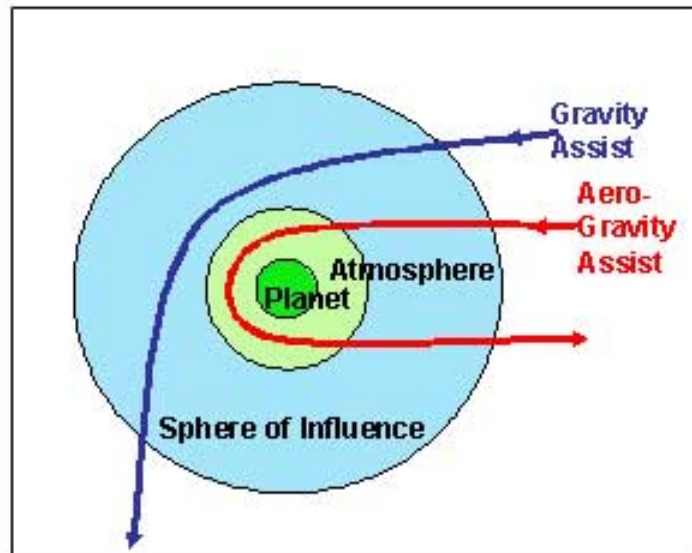
The technique has significant technology development challenges. Aerogravity assist requires these key components:

- Long, thin vehicle shapes -- more like a "flying wing" than a capsule -- to minimize drag on the spacecraft and provide better maneuvering capability
- A high-performance thermal protection system that accommodates high heating conditions of the space vehicle's sharp leading edge
- Efficient packaging of payloads within the spacecraft

The primary benefits of aerogravity assist is that it could reduce overall system mass and significantly shorten trip times to the Outer Planets.



Aerogravity Assist Concept Vehicle



Aerogravity Assist Benefit



Wave Rider Vehicle Testing



TECH ISP

IN-SPACE PROPULSION TECHNOLOGIES



Tethers

Momentum eXchange / Electrodynamic Reboost (MXER) Tethers:

Introduction

The development of tether technology has opened up an exciting new possibility for spacecraft-completely propellantless propulsion. Rockets push against their own exhaust, but a conducting, electrodynamic tether allows a spacecraft to push against the Earth's magnetic field, transferring the rotational angular momentum of the Earth to the orbital angular momentum of the spacecraft. In order to understand the merits of this technology, we must first understand the advantages and limitations of momentum-exchange and electrodynamic tethers.

- **POTENTIAL MISSION APPLICATIONS**
- **FUNDAMENTAL PHYSICS**
- **TECHNICAL PUBLICATIONS**
- **LINKS**
- **ISP MAIN**
- **TECH MAIN**

CURRENT TECHNOLOGIES

Aeroassist

Aerocapture -
Aerobraking -

Solar Electric Propulsion

Next Generation
Electric Propulsion -
SEP Hall -

Solar Sails

Advanced Chemical

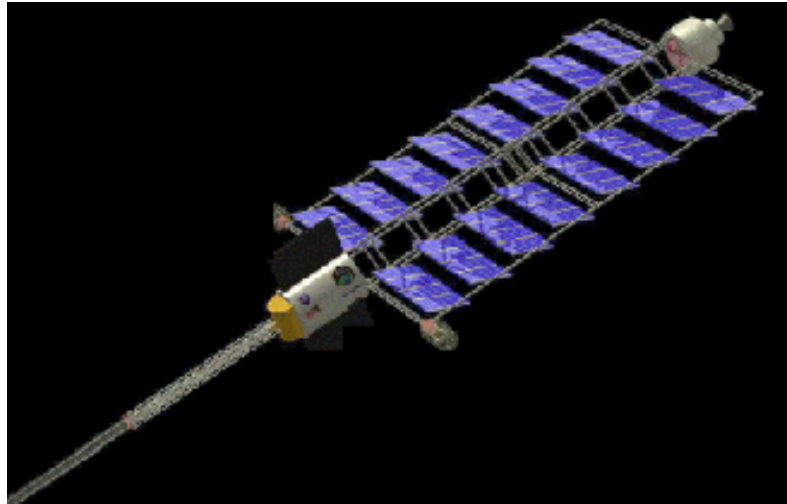
Tethers

Momentum Exchange -
Electrodynamic -

Solar Thermal

EMERGING TECHNOLOGIES

Aerogravity Assist -



The endmass of an MXER tether station. The tether deployer, plasma contactors, and solar arrays are all visible. The upper stage of the launch vehicle has been retained for ballast mass.

A pure **momentum-exchange (MX) tether** does not create orbital energy; it only exchanges it. This exchange of momentum takes place very quickly (within a few minutes), and it increases the orbital energy of the payload dramatically. This dramatic increase in the payload's orbital energy comes at the expense of the tether station. As it catches and throws a payload, its orbital energy is reduced, and it assumes a lower orbit. Without reboost, it will soon lose enough orbital energy to burn up in the atmosphere. Hence, without reboost, the MX tether would soon be useless.

Any type of propulsion system, in theory, could be used to reboost an MX tether. Chemical, nuclear, and electric are all options, but if rocket reboost is used, the MX tether station will have to be refuelled regularly, and the entire tether system will be no more efficient than the reboost rocket. A propellantless

form of tether rebost would be ideal.

A purely **electrodynamic (ED) tether** is a propellantless system, but it is limited to the regions above the Earth where the ionosphere and magnetic field are relatively strong (<1000 km). It collects current from the ionosphere to flow through its conductive tether. That tether acts like a wire moving through the field lines of the Earth's magnetic field; consequently a $\mathbf{J} \times \mathbf{B}$ force is exerted on the system. The ED tether can passively generate power (at the expense of orbital energy) or use a power supply to drive current through the tether and create thrust (increasing orbital energy).

In theory, an ED tether could dock with a payload and slowly spiral up to a higher orbit, then release it and spiral back down. However, the ED tether is limited to altitudes less than 1000 km, and achieves performance similar to other low-thrust, high-power propulsion systems (such as ion engines) which have very low thrust-to-weight ratios.

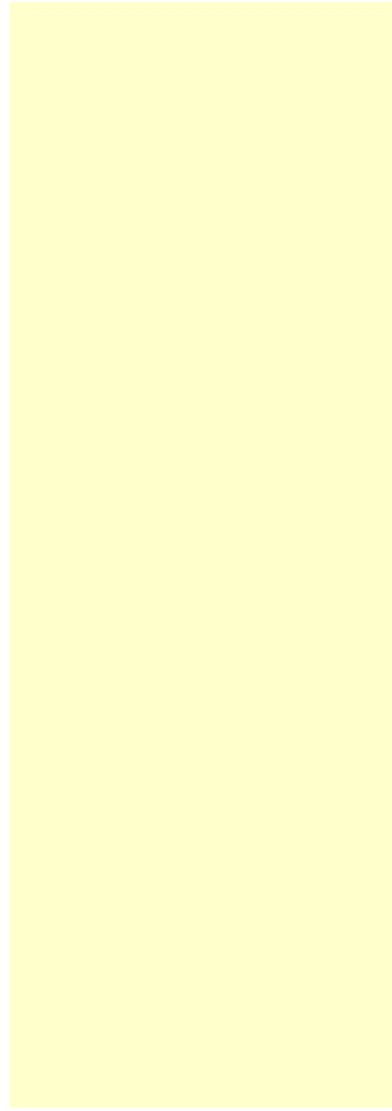
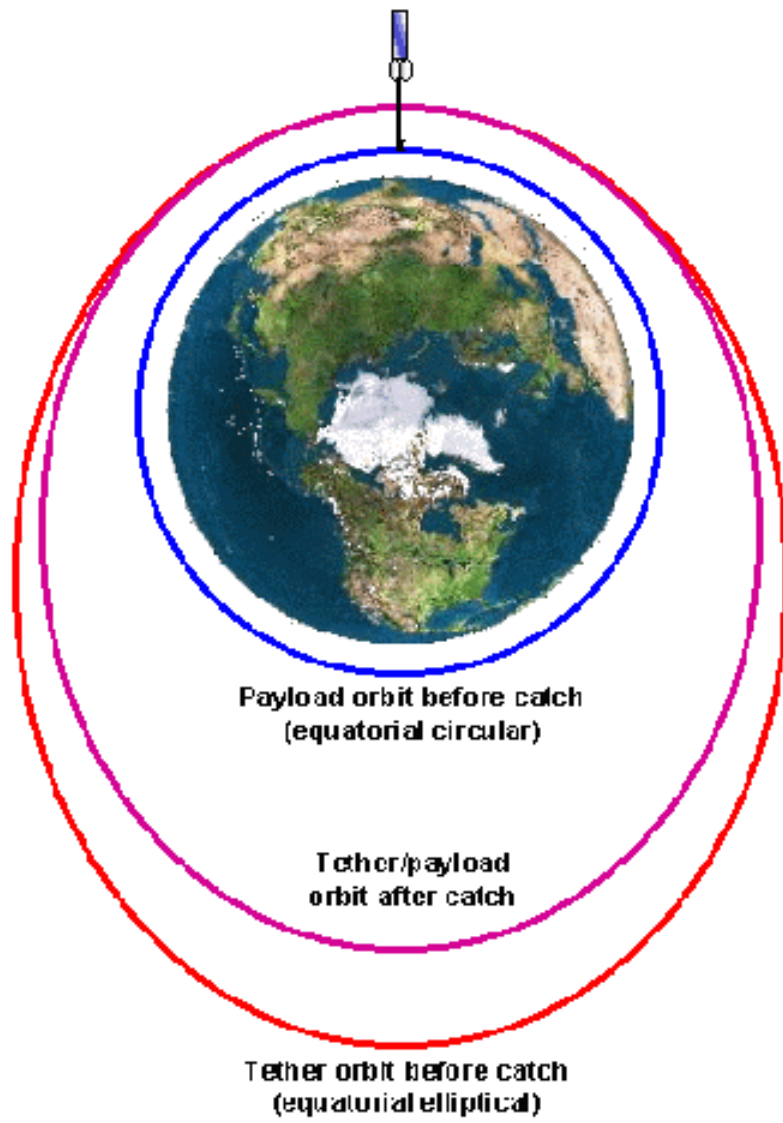


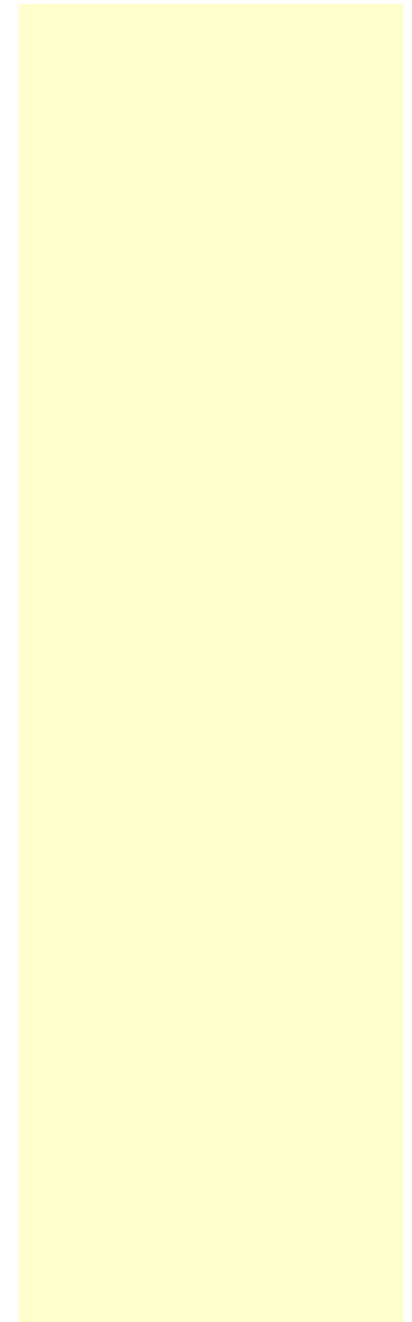
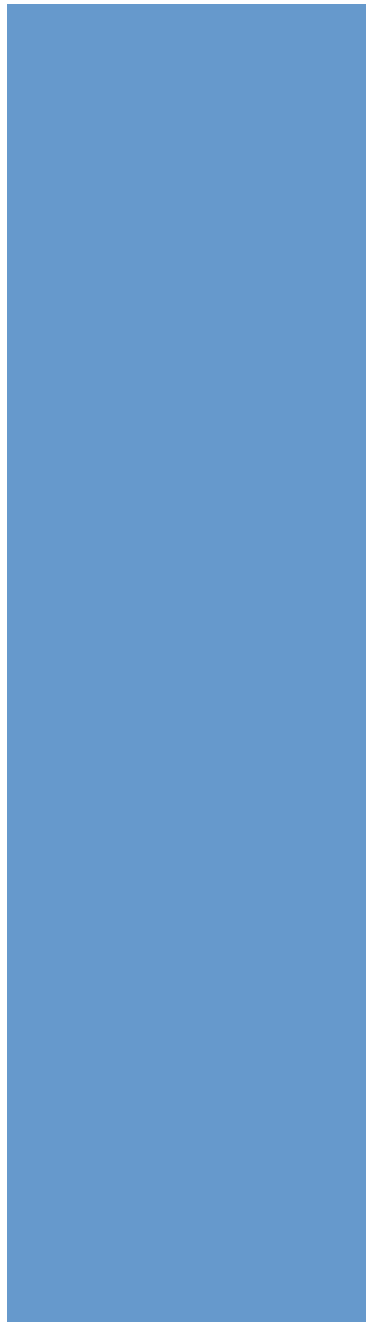
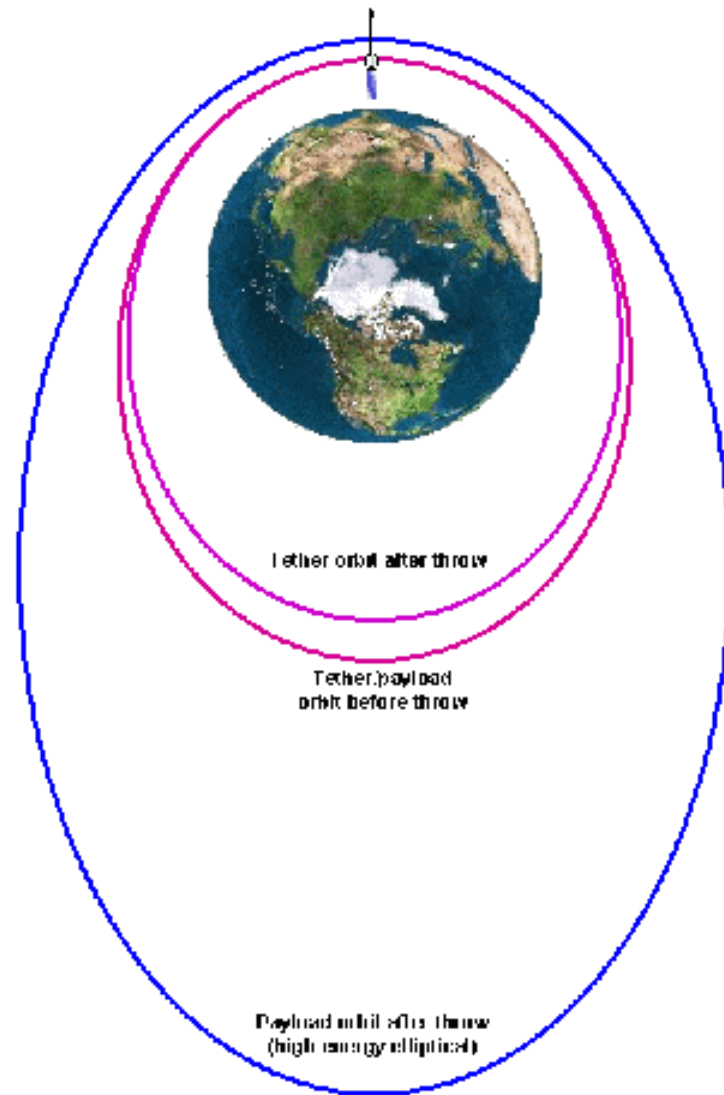
An electrodynamic tether tug.

The MX and ED tethers, by themselves, do not achieve exceptional improvements in performance over existing technologies. The MX tether is hobbled by a rebost

requirement, and the ED tether is constrained to operate at low orbital altitudes. However, a hybrid of the two, the **Momentum eXchange / Electrodynamic Reboost (MXER) tether**, may be capable of breaking through these limitations and enabling a *powerful, propellantless system for orbital transfer*.

In principle, a MXER tether in an elliptical orbit could catch a payload in a low Earth orbit, carry it for an orbit, and then throw it into a higher energy orbit. The entire procedure would only take a few hours. It can then employ electrodynamic reboost over a much longer period to restore the orbital energy it gave to the payload. Hence, the tether system can give the payload all of the efficiencies of a "high-thrust", impulsive orbit transfer, but slowly reboost itself using only electricity.









TECH ISP

IN-SPACE PROPULSION TECHNOLOGIES



Next Generation Electric Propulsion

General Description:

The ion thruster is one of the most promising [solar electric propulsion \(SEP\)](#) technologies currently being developed to support future outer planet missions for NASA's Science Mission Directorate. Typically, ion thrusters are used in high-ISP (specific impulse)/low thrust applications that require longer lifetimes and higher efficiency than state-of-the-art (SOA) chemical propulsion systems (for description of how ion propulsion works - see fundamental physics.)

Click [HERE](#) for a Solar Electric Propulsion Quicktime movie.
Viewing this movie requires Quicktime, you can download it here if required.
<http://www.apple.com/quicktime/downloading/index.html>

Today, the standard for ion thrusters is the NASA SEP Technology Application Readiness thruster, or NSTAR thruster. In October 1998, NASA's Jet Propulsion Laboratory initiated an extended life test of the NSTAR thruster - a flight spare thruster identical to one flown on the successful Deep Space 1 mission. This test was concluded on June 30, 2003, after 30,352 continuous hours of operation, providing a solid basis for ion thruster selection for near-term science missions.

- **POTENTIAL MISSION APPLICATIONS**
- **FUNDAMENTAL PHYSICS**
- **TECHNICAL PUBLICATIONS**
- **LINKS**
- **ISP MAIN**
- **TECH MAIN**

CURRENT TECHNOLOGIES

Aeroassist

Aerocapture -
Aerobraking -

Solar Electric Propulsion

Next Generation
Electric Propulsion -
SEP Hall -

Solar Sails

Advanced Chemical

Tethers

Momentum Exchange -
Electrodynamic -

Solar Thermal

EMERGING TECHNOLOGIES

Aerogravity Assist -

For additional information regarding NSTAR extended life test, click [HERE](#).



NEXT 40 cm Thruster
Operating at 6 kW



NEXT Engineering Model
20 cm Thruster

The focus of Next Generation Electric Propulsion effort is to advance ion propulsion system technologies through development of NASA's Evolutionary Xenon Thruster, or NEXT. Successful NEXT development will more than double the SOA ion thruster power capability and lifetime throughput -- or the total amount of propellant that can be processed -- while increasing the specific impulse by 32 percent and thrust by 156 percent. A comparison of the NSTAR performance and the NEXT performance goals are shown in the following table:

Beginning of Life at Full Power	NSTAR	NEXT
PPU Input	2.47	7.31
Thruster Input Power (kW)	2.30	6.85

Thrust (mN)	92.4	237
ISP (sec)	3120	4050
Throughput (kg)	83 design	270 design
	235 ground demo	TBD
Thruster/PPU Efficiency (kg/kW)	57%	65%
Thruster Specific Mass (kg/kW)	3.6	1.8
PPU Specific Mass (kg/kW)	6.0	3.5

The primary objective of the NEXT project is to develop a multi-engine ground system demonstrator to a high level of maturity (Technology Readiness Level 5, with significant progress toward TRL-6) and validate capabilities required for long-life deep-space electric propulsion missions. Specifically, NEXT development activities will address three main subsystems of the ion propulsion system: the ion thruster, the power processor unit (PPU) and the propellant management system (PMS). At the end of Phase 1 in August 2003, NASA's Glenn Research Center (GRC) had successfully demonstrated system level performance of an engineering model thruster, a PPU and a PMS at power levels in excess of 7.0 kW. In addition, the GRC has operated a 40-cm NEXT engineering model thruster for more than 2000 hours. GRC is continuing to evaluate grid erosion from this Phase 1 test and identify potential design improvements to the proto-type thruster being developed in Phase 2.



Single String Integration Test at GRC: EM2 Thruster



Diagnostic Equipment for Vacuum Facility # 6 at GRC



Diagnostic Equipment for Vacuum Facility # 6 at GRC





TECH ISP

IN-SPACE PROPULSION TECHNOLOGIES



Solar Thermal

General Description:

Solar Thermal propulsion operates in space by capturing solar energy with inflatable concentrator mirrors that focus the sunlight inside a high-temperature engine cavity to heat propellant. The concept is a simple and safe method for taking spacecraft from low Earth orbit to geosynchronous orbit or Earth escape. The propulsion system of a solar thermal-powered spacecraft consists of three basic elements: a Concentrator which focuses and directs incident solar radiation, an Absorber/Thruster which receives solar energy, heats and expands propellant (hydrogen) to produce thrust, and a Propellant system which stores cryogenic propellant for extended periods and passively feeds it to the absorber/thruster.



- **POTENTIAL MISSION APPLICATIONS**
- **FUNDAMENTAL PHYSICS**
- **TECHNICAL PUBLICATIONS**
- **LINKS**
- **ISP MAIN**
- **TECH MAIN**

CURRENT TECHNOLOGIES

Aeroassist

*Aerocapture -
Aerobraking -*

Solar Electric Propulsion

*Next Generation
Electric Propulsion -
SEP Hall -*

Solar Sails

Advanced Chemical

Tethers

*Momentum Exchange -
Electrodynamic -*

Solar Thermal

EMERGING TECHNOLOGIES

Aerogravity Assist -

Technology Benefits:

- Use of in situ resources to provide high efficiency at potentially low cost
- Higher payload fraction than chemical
- Solar derived electric power
- Concentrator & high-gain antenna or aeroassist system
- Higher Isp (> 700 s) than chemical options (300 -500 s)
- Higher thrust-to-weight ratios than electric systems
- Space solar power
- Synthetic Aperture radar
- Sunshield for space telescopes
- High temperature materials

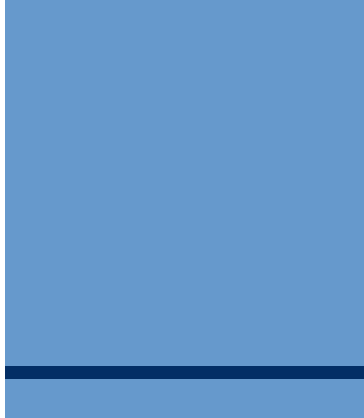
Technology Status:

- Component level hardware developed
- Limited System integration activity
- Isp currently slated to perform investment study to evaluate technology
- Isp demonstrated between 700-750 sec

Future Plans / Challenges:

- Ground test of existing full-scale STP engine designs
- Provide relevant environment demonstration of critical components







TECH ISP

IN-SPACE PROPULSION TECHNOLOGIES



Hall Thruster

General Description:

Hall thrusters use an axial electric field to accelerate ions, similar to Ion thrusters. Combining a radial magnetic field with this generates an azimuthal Hall current. This current interacts with the radial magnetic field producing a volumetric ($\mathbf{j} \times \mathbf{B}$) accelerating force on the plasma. As with grid ion thrusters, Hall thrusters can be categorized according to their respective power sources.



Technical Benefits:

- Significantly reduces required refueling flights for orbital transfer applications
- Four times the Payload of chemical Systems using

- **POTENTIAL MISSION APPLICATIONS**
- **FUNDAMENTAL PHYSICS**
- **TECHNICAL PUBLICATIONS**
- **LINKS**
- **ISP MAIN**
- **TECH MAIN**

CURRENT TECHNOLOGIES**Aeroassist**

*Aerocapture -
Aerobraking -*

Solar Electric Propulsion

*Next Generation
Electric Propulsion -
SEP Hall -*

Solar Sails**Advanced Chemical****Tethers**

*Momentum Exchange -
Electrodynamic -*

Solar Thermal

EMERGING TECHNOLOGIES

Aerogravity Assist -

next generation power levels

- High power Hall thruster systems can utilize large onboard power to enable range of missions by reducing trip times and mass while increasing payload
- Successful FY03 50 kW task will validate Hall thruster design methodology for intermediate power levels

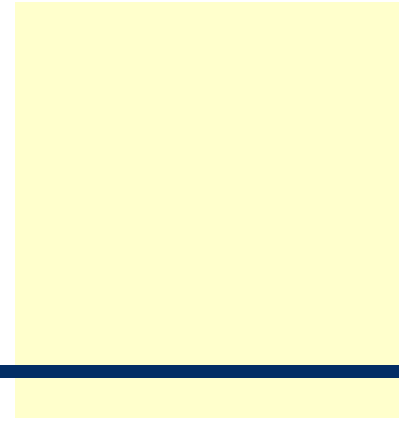
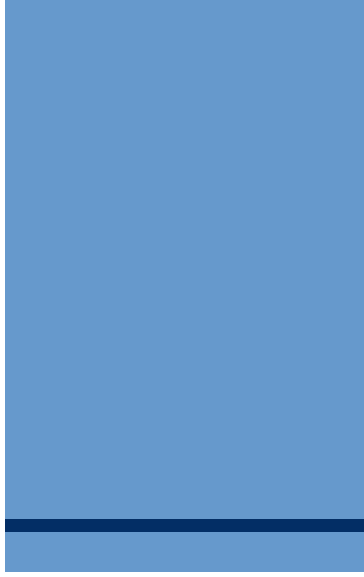
Technology Status:

- State of the art - 4.5 kW developments for flight
- Scalability to larger power levels for Primary propulsion
- 10 kW ground test complete

Future Plans:

- Investigate critical spacecraft integration issues
- Investigate lifetime capability of 50 kW Hall thruster
- Develop and test engineering model thruster system







TECH ISP

IN-SPACE PROPULSION TECHNOLOGIES



Solar Electric Propulsion

General Description:

A solar electric propulsion (SEP) system uses electrical energy from a solar array to accelerate a propellant to much higher exhaust jet velocities (v_j) than those that can be realized from chemical reactions. Because of these significantly higher exhaust velocities, SEP systems can impart much more total impulse to a spacecraft per mass of propellant, referred to as specific impulse, I_{sp} , providing the potential for significant propellant mass savings. If the solar array and power conditioning hardware can be made light enough, this results in a net reduction in mass for a SEP vehicle vs. a chemical vehicle.

There are three types or categories of electric propulsion; electrothermal, electromagnetic, and electrostatic. These are compared in Table 1 and Figure 1. Each category has a different range of I_{sp} as shown in the figure below. Note that as the I_{sp} increases resulting in lighter propellant mass, the thrust to power ratio decreases, generally requiring longer trip times. As a result, each type of electric propulsion is best suited for different classes of missions. For most interplanetary and orbit raising missions, the electrostatic thruster is of most interest because of its inherent high I_{sp} . These are discussed in detail in the [Next Generation Electric](#)

- **POTENTIAL MISSION APPLICATIONS**
- **FUNDAMENTAL PHYSICS**
- **TECHNICAL PUBLICATIONS**
- **LINKS**
- **ISP MAIN**
- **TECH MAIN**

CURRENT TECHNOLOGIES

Aeroassist

Aerocapture -
Aerobraking -

Solar Electric Propulsion

Next Generation
Electric Propulsion -
SEP Hall -

Solar Sails

Advanced Chemical

Tethers

Momentum Exchange -
Electrodynamic -

Solar Thermal

EMERGING TECHNOLOGIES

Aerogravity Assist -

Propulsion section.

ELECTROTHERMAL:

- ACCELERATION BY ELECTRICALLY HEATING PROPELLANT AND EXPANDING THROUGH NOZZLE;
Isp TENDS TO BE LOW AND LIMITATIONS SIMILAR TO CHEMICAL EXIST
 - RESISTOJET
 - ARCJET

ELECTROMAGNETIC:

- ACCELERATION BY FORCE ON CURRENT PASSING THROUGH THE PROPELLANT INDUCED BY MAGNETIC FIELD;
 - MAGNETOPLASMA DYNAMIC (MPD)
 - PULSED PLASMA THRUSTER (PPT)

ELECTROSTATIC (ION):

- ACCELERATION BY FORCE ON CHARGED PARTICLE IN ELECTRIC FIELD
 - ELECTRON BOMBARDMENT
 - HALL EFFECT

Electric propulsion is being used by commercial telecommunication satellites and has been demonstrated as a primary spacecraft propulsion system by the NSTAR demonstration on the Deep Space 1 (DS-1) mission. The successful demonstration of electric propulsion for DS-1 enabled the DAWN mission, recently selected in the Discovery Program,

to baseline electric propulsion. The ISP Program is pursuing technologies to increase the performance of electrostatic thrusters by going to higher power levels and by increasing the Isp on a system level.

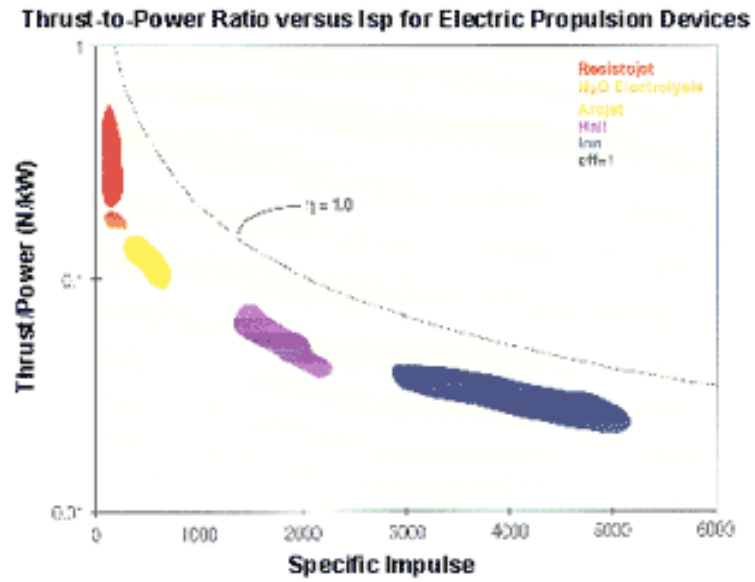


Figure 1



TECH ISP

IN-SPACE PROPULSION TECHNOLOGIES



Advance Chemical Propulsion

General Description:

Chemical propulsion systems have historically been the primary means for transportation of payloads in space because they generate the very large amounts of thrust required to overcome the effect of Earth's gravity.



Technology Benefits:

Increased performance and safety

- Application of high Isp storable cryogenic propellants to enable long-term missions in space
- Accommodate extended missions without propellant losses
- Advanced fuels with improved performance (increased Isp) could minimize need for aerobraking

- **POTENTIAL MISSION APPLICATIONS**
- **FUNDAMENTAL PHYSICS**
- **TECHNICAL PUBLICATIONS**
- **LINKS**
- **ISP MAIN**
- **TECH MAIN**

CURRENT TECHNOLOGIES

Aeroassist

*Aerocapture -
Aerobraking -*

Solar Electric Propulsion

*Next Generation
Electric Propulsion -
SEP Hall -*

Solar Sails

Advanced Chemical

Tethers

*Momentum Exchange -
Electrodynamic -*

Solar Thermal

EMERGING TECHNOLOGIES

Aerogravity Assist -

Reduced propellant storage uncertainties

- Reduced launch mass, or
- Increased payload capability to enhance science missions

Improve overall system efficiency (Thermal/ Pressure control)

- Pressure control / venting without auxiliary propulsion resettling
- Better vehicle cooling and reduced cryogenic boil-off
- Cross-benefits for other propulsion systems

Technology Status:

Many advanced chemical propellants are being analyzed and tested to determine their performance and applicability to in-space propulsion. Chemical rocket systems include solid, cryogenic liquid, and storable liquid propellants, as well as hybrid and cold gas rockets. The number of compounds used in the reactions typically categorizes these propellants. Researchers are investigating ways to increase Isp, lifetime and overall performance of state-of-the-art chemical systems.

Future Plans / Challenges:

- **Advanced Fuels**

Evaluate high-energy storable propellants that will enhance performance for in space application

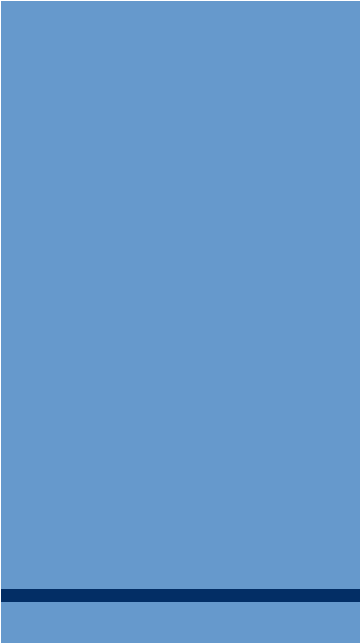
- **Cryogenic Fluid Management**

There are many aspects in the loading, storage, and pumping of cryogenic fluids currently being analyzed and augmented in order to improve the efficiency and safety of handling these materials. Some of the major areas of investigation are:

- Zero-G pressure control/Capillary Liquid Acquisition Devices
- On-orbit Propellant transfers, including filling the vehicle upper stage during ascent
- Liquid Mass Measurement
- Cryogenic Storage with both passive and active heat removal
- Zero Boil-Off Tank Pressure Control

Typically, these efforts concentrate on conducting analysis, building simulations, constructing test fixtures, building scaled and full-size equipment, and finally verification of the analysis and simulations through testing. The safe and efficient utilization of cryogenic fluids for engines, thrusters, and life support systems continues to be a major investment area for the IISTP.

- **Lightweight Components**



Reducing the weight and complexity of the structures used to carry chemical propellants is also vital in increasing payload capabilities. Liquid propellants all require holding vessels along with complex piping and mixing apparatus. The combination and combustion chambers tend to be large and heavy. Advanced materials are being developed that will reduce the size and weight of the components, thus directly increasing payload capability.



TECH ISP IN-SPACE PROPULSION TECHNOLOGIES



Aerocapture

General Description:

Aerocapture technology uses a planetary atmosphere to alter the velocity of a vehicle. The incoming spacecraft makes a single pass deep into the atmosphere, using drag to establish a captured orbit, without the use of propellant. This fuel-free method could reduce the typical mass of an interplanetary spacecraft by half, allowing for a smaller cheaper vehicle - one better equipped to conduct robust, long-term science at its destination. Aerocapture technologies and system requirements now under investigation by NASA and its partners span a broad spectrum of mission needs. In addition to design and testing of ballutes and other aerocapture systems themselves, flight vehicles also are being studied to determine how use of aerocapture technologies impact vehicle aerodynamics, heat shielding and on-board guidance and controls. MSFC researchers are working to develop and improve engineering-level atmospheric models for Titan,



- **POTENTIAL MISSION APPLICATIONS**
- **FUNDAMENTAL PHYSICS**
- **TECHNICAL PUBLICATIONS**
- **LINKS**
- **ISP MAIN**
- **TECH MAIN**

CURRENT TECHNOLOGIES

Aeroassist

*Aerocapture -
Aerobraking -*

Solar Electric Propulsion

*Next Generation
Electric Propulsion -
SEP Hall -*

Solar Sails

Advanced Chemical

Tethers

*Momentum Exchange -
Electrodynamic -*

Solar Thermal

EMERGING TECHNOLOGIES

Aerogravity Assist -

Neptune, and other outer planets as required. Engineering-level atmospheric models are an enabling technology for systems design and analysis of all types of aerocapture technology, ballutes and other inflatable systems, (Low-Mid-High L/D vehicle, etc.).

More detailed information can be found at URL: http://www.spacetransportation.com/code_s/inspace_aerocapture.html

Technology Benefits:

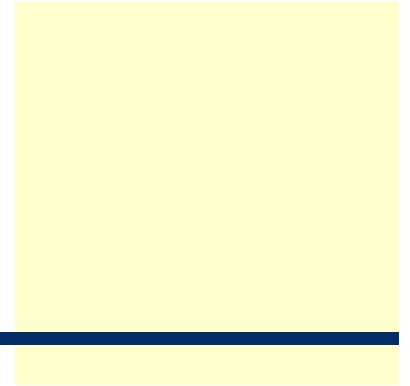
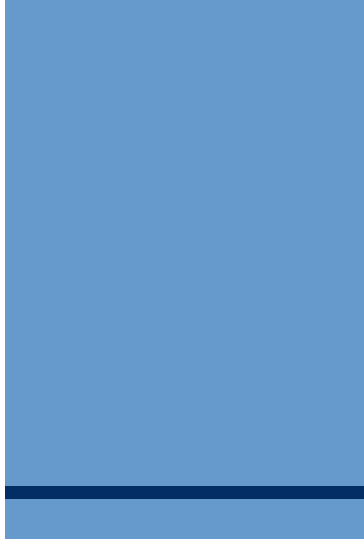
- Capable of high Delta V impulsively at target arrival (multi-g deceleration)
- Shortens trip times to outer planets (by using aerogravity assist or allowing higher Earth departure energies)
- No or very little propellant required for orbit insertion/entry
- Enables precision landing

Technology Status:

- Aerocapture has never been flight demonstrated
- Relevant experience exists from ablative entry capsules, Magellan, +MGS aerobraking, Odyssey

Future Plans / Challenges:

- Directed:
 - Aerocapture performance modeling
 - High temperature composites
 - Sensor





TECH ISP

IN-SPACE PROPULSION TECHNOLOGIES



Solar Sails

General Description:

Propellantless propulsion system that utilizes solar photon pressure to obtain thrust. Sail film is compactly stowed for launch and deployed and supported by ultra-light weight trusses.

Click [HERE](#) for a Solar Sail Quicktime movie.

Viewing this movie requires Quicktime, you can download it here if required. <http://www.apple.com/quicktime/download/index.html>

Technology Benefits:

- No propellants required
- Straightforward concept (challenge is scaling to large area with ultra-low density)
- No environmental impact
- Ideal for station keeping and fixed reference applications

Technology Status:

- **POTENTIAL MISSION APPLICATIONS**
- **FUNDAMENTAL PHYSICS**
- **TECHNICAL PUBLICATIONS**
- **LINKS**
- **ISP MAIN**
- **TECH MAIN**

CURRENT TECHNOLOGIES

Aeroassist

Aerocapture -
Aerobraking -

Solar Electric Propulsion

Next Generation
Electric Propulsion -
SEP Hall -

Solar Sails

Advanced Chemical

Tethers

Momentum Exchange -
Electrodynamic -

Solar Thermal

EMERGING TECHNOLOGIES

Aerogravity Assist -

Sail Project	Root Area	Areal ρ (g/m ²)	GNC	Orbit	Start
ST7	40	19.1	Gimbaled C_m/C_p	SGTO (N/A)	N/A
Encounter	70	<20	Tub C_m/C_p	Extra-Solar	3Q '04
FY02 NRA	20 (100)	20 (15)	TBD	N/A	1Q '04
GeoStorm	80	16	TBD	Sub L ₁	TBD
SPI	150	12.9	TBD	60° solar inclination	'09

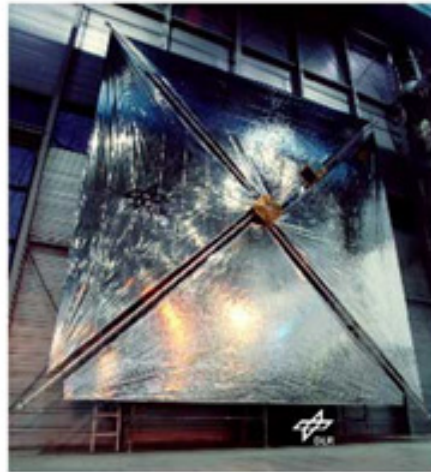
Future Plans / Challenges:

- Technology development towards flight validation
 - 15 g/m² (system level)
 - Propellantless Guidance, Navigation & Control
 - Deployment validation & verification
- Further advances in materials and lightweight structures
- Ground validation & testing of quarter-scale model
- Develop high fidelity computational models

Sail Samples:



DLR 20 m Sail



AEC-Able Coillable Boom (TRL 8, 3 g/m²)





**Proposal Information Package (PIP)
For the
In-Space Propulsion Technology Office,
Cycle 3A
ROSS 2004 NRA Amendment**

DESCRIPTION OF THE PROGRAM OPPORTUNITY:

The In-Space Propulsion (ISP) Program of NASA's Science Mission Directorate (SMD) solicits proposals for basic supporting research and technology investigations in multiple areas associated with advanced in-space propulsion technologies. The ISP Program is responsible for the development of technologies that support the following goals: reduced trip times, increased payload capabilities, and integrated/combined passive and active propulsion systems for enabling certain science missions and to reduce propulsion system and system operation costs. These goals apply to earth orbital, planetary and deep space applications. The In-Space Propulsion Program develops technologies from a Technology Readiness Level (TRL) of 3 through a TRL of 6. Definitions for TRLs 3-6 include:

- A) TRL 3 - Analytical and experimental critical function and/or characteristic proof-of-concept.
- B) TRL 4 - Component and/or breadboard validation in laboratory environment.
- C) TRL 5 - Component and/or breadboard validation in relevant environment.
- D) TRL 6 -System/subsystem model or prototype demonstration in a relevant environment (Ground or Space).

Simply stated, the primary goal of this NRA is to solicit proposals for research that will define requirements and advance/mature technologies that will enable or enhance NASA scientific exploration missions within the solar system and beyond. The intent of this NRA is not to provide flight hardware for specific missions, but to enhance propulsion technologies that may be used by NASA in the future. Research related to improving system performance, extending lifetime, developing critical technologies, and optimizing operation are some of the activities that support this solicitation.

Proposals are being solicited under this NRA for the technical areas and related objectives provided within this proposal information package (PIP). It is anticipated that at least one award will be made for each task. Proposers should reference the ROSS 2004 Announcement Summary at

http://research.hq.nasa.gov/code_s/nra/current/NNH04ZSS001N/index.html and the In-Space Propulsion Program – Cycle 3A Amendment at http://research.hq.nasa.gov/code_s/nra/current/NNH04ZSS001N/AppendB_22.html which will provide designated base period and option period(s) for each technology area listed below. Proposers or teams of proposers may submit proposals for multiple technology areas. However, each proposal shall address only one task area under the following technology topics.

1.0 Solar Sails

Task 1.1 Scaling Law Development

Task 1.2 Thrust Measurement in a Simulated Solar Energy Facility

2.0 Advanced Chemical Technology

Task 2.1 Advanced In-Space Chemical Thrusters capable of operating in higher temperatures

3.0 Momentum-eXchange/Electrodynamic Reboost (MXER) Tether Technology

Task 3.1 Development of a MXER Hybrid Tether

1.0 Solar Sails

Introduction

Solar sails have been studied for a variety of missions and have the potential to provide cost effective, propellantless propulsion that enables longer on-station operation, increased scientific payload mass fraction, and access to previously inaccessible orbits (e.g. non-Keplerian, high solar latitudes, etc.). These missions and others support the strategic objectives of the Science Mission Directorate. The goal of Solar Sail Propulsion (SSP) is to demonstrate a system in a relevant ground environment by the end of FY06. Two major on-going efforts to design, build and test a 20m sail were initiated through a previous NRA solicitation. The two efforts are being performed by teams led by L'Garde and Able Engineering companies, respectively. Information on these efforts and others currently in progress under the In-Space Propulsion Program may be found at <http://www.inspacepropulsion.com/nra3.html>. To address specific technical issues associated with the development of solar sail technology, the following task topics are being solicited under this amendment to the ROSS 2004 NRA:

Task 1.1 Scaling Law Development

Task 1.2 Thrust Measurement in a Simulated Solar Energy Facility

Description of Tasks and Products

Task 1.1 Scaling Law Development

The largest System Ground Demonstrators that will be tested under ongoing tasks for the In-Space Propulsion Technology Program are 20m on edge. Testing of larger sails, perhaps 40m on edge, have been considered, however the 20m solar sails will most likely be the largest that can be tested under thermal-vacuum conditions on the ground. Consequently, modeling, analyses, and scaling law development will be critical to determining the performance of various solar sail designs requiring sizes many times greater than what can be ground tested.

This task shall provide a review of the state-of-the-art in solar sail scaling law research, define and produce needed improvements in current scaling law methodology and develop new methods for scaling laws that can be applied to solar sail systems. Additionally, a plan shall be developed addressing the method by which scaling laws can be validated from the results of ground and/or flight experiments.

The baseline phase shall include:

- Review and documentation of the state-of-the-art solar sail scaling law research.
 - Cite source of data
 - Summary report of research conducted
 - Research of gaps
- A detailed plan, including schedule and cost, of the Optional Phase effort.
- A final report documenting the key results and conclusions from the Baseline Phase.

The option phase shall include activities to:

- Define and produce needed improvements in current scaling law methodology.
- Develop new methods for scaling laws that can be applied to solar sail systems.
- Develop a viable methodology by which scaling laws can be validated from the results of ground and/or flight experiments.
- Provide a final report as specified in the Amendment.

Task 1.2 Thrust Measurement in a Simulated Solar Energy Facility

Several proposals selected under the two previous In-Space Propulsion NRAs are focused on developing and validating analytical tools which can be used to determine the performance of any solar sail design and move the technology toward TRL 6. Deployment, static shape, dynamics and attitude control are the main areas of performance that are being addressed. Another key performance parameter that has not yet been fully studied is the thrust developed by a solar sail.

Proposals submitted on this topic are to assess the feasibility and design of an experiment to allow performance testing of a solar sail in a simulated solar energy facility. A solar sail system test article provided by a proposer is to be mounted in a solar simulator that can provide conditions replicating a 1 AU condition for various solar sail angles. The thrust produced by the solar sail is to be measured using a low thrust measurement system.

The baseline period shall include:

- A thrust measurement experiment design to include facility requirements and the preliminary design of test articles.
- Identification and assessment of a solar energy simulation and thrust measurement facility that could be used to measure the thrust produced on the test article(s).
- A detailed plan, including schedule and cost of the optional phase effort.
- A final report as specified in the Amendment.

The option period shall include:

- Performance of thrust measurements and supporting tests using the facility identified in the base period.
- Analyses of measurement and test data.
- A final report as specified in the Amendment.

2.0 Advanced Chemical Technology

Introduction

Primary propulsion for space exploration is generally accomplished by state-of-the-art chemical propulsion systems that use solid, cryogenic liquid and storable liquid propellants. Earth storable propellants are used on most scientific and commercial spacecraft because they offer appropriate performance levels with minimum integration issues. However, as conventional chemical propellants approach their theoretical limits, new and innovative concepts for

improving the performance of chemical propulsion systems are being sought. Technologies are needed that provide opportunities for increased payload capacity and decreased trip time for the science community to realize greater experimental return. To support innovations in these areas, this NRA solicits proposals for the application of advanced materials to propulsion components and systems, as described herein.

This NRA is specifically focused on the identification, rapid evaluation and development of bipropellant thrusters that fully exploit the potential offered by advanced materials. Thrusters appropriate for delta V functions for NASA planetary spacecraft (including maneuvers near planetary bodies) are desired. Although subject to detailed analyses and risk assessments, pressure-fed thrusters with the following characteristics are of special interest:

- High potential to provide data from the rapid evaluation of the proposed concept(s) to meet the performance requirements of typical NASA outer planets science missions. (Typical outer planet missions spend about 2 - 3 years in the inner solar system for gravity assist or Solar Electric Propulsion (SEP) operations. Closest approach to the Sun is usually Venus' orbit. Transfer times in the outer solar system are 3 - 10 years. Scientific spacecraft payloads of interest are a few hundred kg, and chemical propulsion delta Vs range from about 2 to about 5 km/s.)
- Specific impulse greater than 335 seconds with NTO/N₂H₄ propellant at nominal operating conditions
- Specific impulse greater than 330 seconds with NTO/MMH propellant at nominal operating conditions
- The ability to operate for a minimum time of one hour (or longer if demanded by high-priority scientific missions) with significant margins in all operating conditions typically required by scientific and commercial applications

Description of Tasks and Products

Until recently, Earth-storable bipropellant performance was constrained by temperature limitations of the standard material (columbium), which is used world-wide for thrust chambers. The use of more advanced materials (iridium coated rhenium) in Earth-storable thrust chambers has resulted in specific impulse gains of approximately ten seconds. The mission benefits of this increased performance have led to immediate adoption of low-risk versions of the iridium/rhenium (Ir/Re) chambers. However, the operating temperature of initial thruster designs has been limited to approximately 2050K or less, which does not exploit the full potential of iridium/rhenium. More recent tests have indicated that

iridium/rhenium thrust chambers can be operated at 2500K in oxidizing atmospheres. This represents an opportunity to rapidly exploit the recent advancements in materials technology. Successful demonstration of higher-temperature thrust chambers could also open the path to use higher-energy propellants with even higher combustion temperatures.

Proposals from offerers who possess innovative concepts or advanced materials with more promise than the iridium/rhenium chambers solicited are also encouraged. They must be consistent with the budget and schedule guidelines for technology advancement specified in this NRA.

Task 2.1 Advanced In-Space Chemical Thrusters capable of operating in higher temperatures

Proposals are sought that contain a baseline phase and up to two option periods of performance as described below.

A Baseline Phase that includes:

- A spacecraft system study to demonstrate:
 - Benefit of the proposed concept
 - system level impacts (e.g., operational issues and thermal impact upon other spacecraft subsystems)
 - The ability to meet the performance requirements of typical NASA outer planets science mission
 - The prudent technical path to mature the technology to a TRL of 6
 - Address program and technical risk in a plan that features off-ramps with hard decision criteria
- A laboratory-version thruster that will:
 - Demonstrate the promise of rapidly validating the critical technologies required by the performance goals
 - Evaluate by test the ability to explore the full potential of these advanced materials (Ir/Re) (Some limits testing should be performed).
 - Provide a strong basis for the selection of final injector and chamber designs for the option period
 - Address key technology issues as early as possible to minimize overall programmatic risk
- A plan for the validation and transfer of technology for near-term use.
- A detailed plan, including schedule and cost, of the Option Phases.

- A final report, as specified by the Amendment, documenting the key results and conclusions from the Baseline Phase.

Up to two option phases shall include (neither option to exceed 12 months):

- Detailed designs of thrusters that can meet the performance and interface goals for at least two propellant options. The designs shall include analyses and other considerations that support the selected approaches.
- Fabrication of at least one thruster concept for operation with a selected propellant. Fabrication of two or more thrusters is preferred.
- Tests over the range of operating and environmental conditions that are required to evaluate and validate the selected concept, including sufficient limits testing to permit the realization of the performance offered by iridium-coated rhenium thrust chambers. The tests, and any required analyses, shall be such as to enable prudent adoption of the selected concept for immediate transition to full-scale development for flight.
- The identification of hardware inventory available for limit testing, and of facilities and support hardware for testing.
- A final report, as specified by the Amendment, documenting the key results and conclusions from each proposed Option Phase.

3.0 Momentum-eXchange/Electrodynamic Reboost (MXER) Tether Technology

Introduction

The Momentum-eXchange/Electrodynamic Reboost (MXER) tether concept is a reusable, space-based transportation system that could boost spacecraft payloads from low Earth orbits (LEO) to high-energy orbits, such as geosynchronous transfer orbit (GTO) and beyond. In so doing, the MXER tether could provide most of the increase in velocity currently provided by a launch vehicle's upper stage. This would allow spacecraft payloads to be launched on smaller rockets or allow spacecraft to carry larger scientific payloads.

The MXER tether facility consists of a high-strength tether approximately 100 to 150 kilometers in length, with a number of spacecraft-like control nodes arranged along a portion of the tether. At the "tip" is a specially designed "catch" mechanism. At the other end is ballast mass, typically the upper stage retained from the tether's launch vehicle. The tether facility operates in an elliptical orbit about the Earth, with a perigee of 300 to 500 kilometers and an apogee of 6,000 to 10,000 kilometers. It has a significant rotation rate, such that its tip moves at a velocity of

approximately 1,200 meters per second. This high rotation rate generates large centrifugal tension forces along the tether's length, thus requiring the tether to be constructed of a material that possesses high tensile strength with minimal mass. (The numbers given here are representative ranges. Specific orbital and rotational parameters for the tether are mission, payload, and configuration-dependent.)

The rotation of the tether allows its tip to instantaneously match the position and velocity of a payload in much lower energy orbit than that of the tether. The payload links with the catch mechanism, remains attached to it for approximately half of a tether-rotation, and is then released into a much higher-energy orbit than the tether. During this interaction, significant orbital energy and angular momentum is transferred from the tether to the payload.

To restore the energy and momentum transferred by the tether, electrical current (estimated to be 40 amperes) collected from the ionosphere at low altitudes is driven through the tether using energy collected by solar panels. This flow of current through the tether in the presence of the Earth's magnetic field generates a body force across the tether (the Lorentz force) that adds orbital energy. Continued operation of this electrodynamic reboost over a period of weeks restores the energy and momentum transferred to the payload, and prepares the tether to catch and throw another payload. Electrodynamic reboost does not consume any propellant since the Earth itself serves as the reaction mass, via magnetic interaction between the tether and the Earth's field.

To provide a conductive path for this electrical current, a significant portion of the length of the overall MXER tether must incorporate electrically conductive materials, in addition to the high tensile-strength material. Furthermore, these conductive materials must be heavily insulated against the plasma, due to the large electrical potential that will exist between the tether and the ambient environment. Substantial cross-sectional areas of conductive materials will be required to minimize resistive losses in the conductive material. This combination high-strength/conductive tether is referred to as the hybrid tether.

Since no material exists that has both high specific tensile strength (tensile strength divided by density) and high specific electrical conductivity (conductivity divided by density), it is anticipated that each of these needs will be accomplished by a dedicated material. Currently, there exists three polymeric materials that have the highest specific tensile strengths. They are UHMWPE (Spectra), PBO (Zylon), and PIPD (M5). Aluminum has more than twice the specific conductivity of its nearest competitors, copper and silver. Superconductive materials are not considered feasible due to the extreme difficulty of maintaining low temperature via passive

radiation, and the tremendous mass penalty of active cooling across the tether's length.

The hybrid tether must also have a long lifetime in its operational environment. Tether survivability manifests itself in two distinct ways -- environmental survivability and structural survivability.

The hybrid tether will be under attack from atomic oxygen, ultraviolet radiation and charged-particle radiation throughout its lifetime (nominally 10 years). This is a consequence of the orbital parameters of the tether facility, which are in turn a function of the orbital transfer desired for the spacecraft payload. Atomic oxygen fluxes at low altitudes could severely oxidize unprotected polymeric materials. The tether facility could be damaged by charged-particle radiation at higher altitudes as it passes in and out of portions of the Van Allen radiation belts. Also, while illuminated, the tether facility could be subjected to damage from solar ultraviolet radiation. Therefore, proposals for the hybrid tether shall discuss and delineate their strategies for environmental survivability.

Additionally, at lower altitudes there is a significant flux of micrometeoroids and orbital debris (MMOD), primarily consisting of the latter. These particles -- large and small -- could strike the tether at extreme velocities, and damage or sever the fibers. The number of particles passing through a region at any given time is exponentially dependent on the size of the particle. Thus, small particles are much more common than large particles. Additionally, small particles cannot be tracked by ground-based radars, whereas larger particles can.

The most likely mitigation against the damage caused by debris strikes is to arrange the cross-section of the tether over a large area so only a large debris strike can completely sever the tether at any one location. In addition to spreading out the cross-section, the configuration must be able to "cross-strap" tension loads and electrical current around damaged sections of the tether back into undamaged sections. This multi-path design, however, is complicated significantly by the presence of insulated conductor that must be insulated from the ambient plasma at all times. Proposals for the hybrid tether shall discuss and delineate their strategies for structural survivability, with special mention of the issues of tensile and electrical cross-linking.

It is noted that structural survivability and environmental survivability are competing requirements. Structural survivability drives the tether design to a distributed cross-section over the maximum area to minimize the damage of any individual debris strike. Environmental survivability drives the tether design to a minimum cross-section to minimize damage from atomic oxygen, and ultraviolet

and ionizing radiation. This solicitation seeks a systemic solution that achieves the best compromise between both requirements.

In addition to survivability issues, the design of the tether must be capable of rejecting the heat generated internally by ohmic heating, and must minimize the absorptance of heat from the Sun and Earth reflection. Ohmic heating could be minimized by including large amounts of conductive material and minimizing the temperature of the aluminum, since its resistance is temperature-dependent. The emissivity and absorptivity/emissivity ratio of the outermost layer of tether material is a key consideration in rejecting heat and minimizing absorption. Proposals for the hybrid tether shall discuss and delineate their strategies for heat rejection.

Finally, an operational MXER tether facility will require significant lengths of hybrid tether. Therefore, concept(s) proposed should be amenable to automated manufacture and inspection. Manufacture of coupons and samples for proof-of-concept testing (in the base and option one period) may be produced under batch processes or "hand" labor. However, selected processes shall have traceability to automated, continuous manufacturing techniques. Proposals for the hybrid tether shall discuss and delineate, to whatever degree understood, their strategies for tether manufacture and testing.

Description of Tasks and Products

Proposers should describe in detail their concept(s) for a tether design that meets the criteria described herein. They shall include as much technical data and analysis as available to support their design basis. In areas where there is an absence of data and analysis, they shall include a clear rationale why they believe their proposed concept(s) would be successful.

In the base period of the proposed effort, a series of preliminary tests, models and analyses shall be delineated that shall address technical questions to their proposed design(s). These should be followed, as soon as appropriate, with manufacturing of proof-of-concept samples that shall be tested and analyzed in the first option period. The second option period shall require a continuous fabrication and inspection process(s) of a representative MXER hybrid tether section.

Task 3.1 Development of a MXER Hybrid Tether

The Base Phase (9 months) shall include:

- A literature search, review and assessment of materials, coatings and processes applicable to a hybrid MXER tether design.

- Development of a thermal model of the MXER tether system to be used to determine the specific thermal environment in which the MXER tether system must operate.
- A trade study to determine candidate hybrid tether materials and designs that simultaneously meet the requirements stated above. The study should address each of the multiple MXER tether performance, lifetime and environmental constraints discussed above; and provide objective criteria as the basis for recommending specific tether designs. It is acceptable to recommend more than one tether design concept for development testing.
- A detailed plan, including schedule and cost, of the Option One Phase effort.
- A final report, as specified in the Amendment.

The Option One Phase, not to exceed 12 months, shall include:

- Fabrication and testing of candidate hybrid tether material samples (identified and recommended in the baseline phase) in a relevant, simulated space environment (thermal, vacuum, and plasma) to demonstrate expected performance (simultaneously in current, voltage, tension, and mechanical redundancy at a minimum). Samples tested must be at least 25 centimeters in total length.
- A detailed plan, including schedule and cost, of the Option Two Phase effort, including as a minimum:
 - Recommendation of a specific tether material and design for further development testing, based on the outcome of the sample testing and applicable analysis.
 - Documentation outlining the processes required for manufacturing continuous lengths of the selected hybrid tether.
- A final report, as specified in the Amendment.

Option Two Phase, not to exceed 12 months, shall include:

- The manufacture and delivery to NASA of a continuous, 1-kilometer sample of the selected tether that has been inspected in a continuous fashion for quality and consistency.
- A detailed analysis, demonstrating that the selected tether can survive the expected environment (in manner and performance required for an operational MXER tether station) for a minimum of ten years.
- A Final report, as specified in the Amendment.

4.0 Software Standards

The following software standards shall be used for all reports, tools and databases resulting from proposed efforts:

- ANSI standard programming languages or Sun Microsystems Java.
- A web-ready, browser client model designed to run on cross-platforms using Internet Information Server (IIS). It shall be compatible with Netscape/Internet Explorer 5.0 or greater. The models must be delivered via CD-ROM.
- A second deliverable as a stand-alone model that will run on a 98/NT Platform.
- Computer software deliverables that can be reproduced, used to prepare derivative works, performed publicly, and displayed publicly, by or on behalf of the Government. Thus, the proposal must clearly indicate how and the extent to which the proposed computer software will meet these goals.
- Source and executable codes that will be delivered, including any necessary scripts. This includes any codes that are derived or a by-product from a selected proposal and shall be included as a part of that proposal.
- Complete written documentation of delivered programs or databases that includes a final report, as specified by the Amendment, and user's manual ready for publication (examples can be provided upon request). Online documentation and a Help Menu are highly recommended.
- A two-month (minimum) beta testing schedule before delivery of product. The beta test must finish at least one month prior to final delivery. This allows for any adjustments that may be identified in the code. Additional information will be discussed in the kickoff meeting.

Final Report, User's Manual and Guidelines Document

- All documents shall be developed in PC format Microsoft Word 2000 or later, or an equivalent software format approved by NASA before submission.
- An electronic copy (CD-ROM) and one hardcopy are required.

All documents shall be required for delivery at least one month in advance of the final product for product review and ISP Program comment.

Educators Grades 5-8

Air Breathing Rockets [http://www.nasaexplores.com/lessons/01-047/5-8_index.html]

Building Blocks to Space [http://www.nasaexplores.com/lessons/01-043/5-8_index.html]

Designing Tomorrow's Space Ships Today [http://www.nasaexplores.com/lessons/02-007/5-8_index.html]

Destination Mars [http://www.nasaexplores.com/lessons/01-060/5-8_index.html]

Escape Velocity: Fun and Games [http://www.nasaexplores.com/lessons/01-049/5-8_index.html]

Flying on the Ground [http://www.nasaexplores.com/lessons/01-059/5-8_index.html]

Galaxies Galore, Games and More [<http://amazing-space.stsci.edu/galaxies-galore/>]

Liftoff to Learning: The Mathematics of Space-Rendezvous [<http://quest.arc.nasa.gov:80/space/teachers/liftoff/math.html>]

Mega-Magnetism [http://www.nasaexplores.com/lessons/01-055/5-8_index.html]

NASA Central Operation of Resources for Educators [<http://CORE.NASA.gov>]

NASAexplores [<http://nasaexplores.com>]

NASA Education [<http://education.nasa.gov>]

NASA Spacelink [<http://Spacelink.nasa.gov>]

Patterns, Functions, and Algebra: Wired for Space [http://connect.larc.nasa.gov/pdf/00_3.pdf]

Sling Shot to Space [http://www.nasaexplores.com/lessons/01-027/5-8_index.html]

Slow and Steady Wins the Race...to Distant Space [http://www.nasaexplores.com/lessons/01-069/5-8_index.html]

Space Games Gallery Homepage [<http://vesuvius.jsc.nasa.gov/er/seh/games.html>]

The First-Ever Space Rescue Vehicle [http://www.nasaexplores.com/lessons/01-026/5-8_index.html]

The Space Elevator [http://www.nasaexplores.com/lessons/01-015/5-8_index.html]

What is Orbit? [http://www.nasaexplores.com/lessons/01-079/5-8_index.html]

Educators Grades 9-12:

Air-Breathing Rockets [http://www.nasaexplores.com/lessons/01-047/9-12_index.html]

Building Blocks to Space [http://www.nasaexplores.com/lessons/01-043/9-12_index.html]

Designing Tomorrow's Space Ships Today [http://www.nasaexplores.com/lessons/02-007/9-12_index.html]

Destination Mars [http://www.nasaexplores.com/lessons/01-060/9-12_index.html]

Escape Velocity: Fun and Games [http://www.nasaexplores.com/lessons/01-049/9-12_index.html]
Flying on the Ground [http://www.nasaexplores.com/lessons/01-059/9-12_index.html]
Interactive Plasma Physics Education Experience [<http://ippex.pppl.gov/>]
Liftoff to Learning: The Mathematics of Space-Rendezvous [<http://quest.arc.nasa.gov:80/space/teachers/liftoff/math.html>]
Liftoff to Learning: Tethered Satellites [<http://quest.arc.nasa.gov:80/space/teachers/liftoff/tether.html>]
Mega-Magnetism [http://www.nasaexplores.com/lessons/01-055/9-12_index.html]
NASA Central Operation of Resources for Educators [<http://CORE.NASA.gov>]
NASAexplores [<http://nasaexplores.com>]
NASA Education [<http://education.nasa.gov>]
NASA Spacelink [<http://Spacelink.nasa.gov>]
Sling Shot to Space [http://www.nasaexplores.com/lessons/01-027/9-12_index.html]
Slow and Steady Wins the Race...to Distant Space [http://www.nasaexplores.com/lessons/01-069/9-12_index.html]
The First-Ever Space Rescue Vehicle [http://www.nasaexplores.com/lessons/01-026/9-12_index.html]
The Space Elevator [http://www.nasaexplores.com/lessons/01-015/9-12_index.html]
What is Orbit? [http://www.nasaexplores.com/lessons/01-079/9-12_index.html]

Students 5-8

Design a Spacecraft [http://oops.gsfc.nasa.gov/speakers_bureau/EdGoodies/]
Electrons [<http://www-spof.gsfc.nasa.gov/Education/welect.html>]
Falling Into a Black Hole (board game) [http://spaceplace.jpl.nasa.gov/svlbi_do1.htm]
Galaxies Galore, Games and More [<http://amazing-space.stsci.edu/galaxies-galore/>]
History of the Electron [<http://www-spof.gsfc.nasa.gov/Education/whelect.html>]
Magnetic Field Lines [<http://www-spof.gsfc.nasa.gov/Education/wfldline.html>]
Magnetic Field Lines: A History [<http://www-spof.gsfc.nasa.gov/Education/whfldlns.html>]
Magnetic Fields [<http://www-spof.gsfc.nasa.gov/Education/wmfield.html>]
Magnetic Fields: A History [<http://www-spof.gsfc.nasa.gov/Education/whmfield.html>]
NASA Qwhiz! [<http://prime.jsc.nasa.gov/Qwhiz/>]
Space Games Gallery Homepage [<http://vesuvius.jsc.nasa.gov/er/seh/games.html>]
Ultra-Efficient Engine Technology: Fun and Games [<http://www.ueet.nasa.gov/StudentSite/funandgames.html>]

Students 9-12

History of the Electron [<http://www-spof.gsfc.nasa.gov/Education/whelect.html>]

Interactive Plasma Physics Education Experience [<http://ippex.pppl.gov/>]

Magnetic Field Lines [<http://www-spof.gsfc.nasa.gov/Education/wfldline.html>]

Magnetic Field Lines: A History [<http://www-spof.gsfc.nasa.gov/Education/whfldlns.html>]

Magnetic Fields [<http://www-spof.gsfc.nasa.gov/Education/wmfield.html>]

Magnetic Fields: A History [<http://www-spof.gsfc.nasa.gov/Education/whmfield.html>]

Space Research Fun & Learning Games [http://spaceresearch.nasa.gov/fun_learning/games.html]

The Earth's Magnetosphere: A History [<http://www-spof.gsfc.nasa.gov/Education/whms1.html>]

The Magnetosphere [<http://www-spof.gsfc.nasa.gov/Education/wms1.html>]

Science Fair Resources

Experimental Science Projects: An Intermediate Level Guide [<http://www.isd77.k12.mn.us/resources/cf/SciProjInter.html>]

Links to Science Project Sites [<http://globalchange.nasa.gov/Resources/Learning/madscientist.html>]

Looking for a Science Fair Project Topic?

[http://lws-edu.gsfc.nasa.gov/playground/science_fair_proj/science_fair.htm]

Science Fair Primer [<http://users.rcn.com/tedrowan/primer.html>]

S'COOL : Science Project/Science Fair Ideas

[<http://asd-www.larc.nasa.gov/SCOOOL/scifair.html>]

Space Science/Astronomy Projects

[http://lws-edu.gsfc.nasa.gov/playground/science_fair_proj/science_fair_2.htm]

The Ultimate Science Fair Resource [<http://www.scifair.org/>]



ISP IN-SPACE PROPULSION

(for students and teachers grades 5 thru 12)



EDUCATORS
Grades 5-8

STUDENTS
Grades 5-8

SCIENCE FAIRS

LINKS

ISP HOME

JUST FOR FUN

**EDUCATIONAL
OPPORTUNITIES**

COMING SOON



Owner: Space Transportation Directorate Curator: [Sherry Wallace](#)
Web Services Provided by: [IDS \(Internet Delivery Services\)](#) - CSC
[NASA Privacy Statement](#)



Advanced Space Transportation Program

Research Funding Opportunities NASA Research Announcements(NRAs)

- ◆ **ROSS 2002 In-Space Propulsion Technologies Solicitation (NRA-02-ISPT)**
Solicitation address:
http://research.hq.nasa.gov/code_s/nra/current/NRA-02-OSS-01/index.html

- ◆ **Amendment to the ROSS 2002 is expected in August 2002**
Includes the following technical areas:
 - Solar Sails
 - Aerocapture
 - Electric Propulsion
 - Hall Thrusters
 - Advanced Chemical Propulsion
 - MXER Tethers
 - Plasma and Magnetic Sails
 - Solar Thermal Propulsion

A Comparison of Transportation Systems for Human Missions to Mars

Brand Griffin^{*}, Brent Thomas[†], Diane Vaughan[‡]
Gray Research, Inc Huntsville, AL 35806

Bret Drake[§]
NASA Johnson Space Center, Houston, TX 77058

Les Johnson^{**}
NASA Marshall Space Flight Center

and

Gordon Woodcock^{††}
Gray Research, Inc Huntsville, AL 35806

There are many ways to send humans to Mars. Credible technical reports can be traced to the 1950's. More recently, NASA has funded major studies that depict a broad variety of trajectories, technologies, stay times, and costs. Much of this data is still valid with direct application to today's exploration planning. This paper presents results comparing these studies with particular emphasis on the in-space transportation aspects of the mission. Specifically, comparisons are made on propulsion systems used for getting the crew and mission equipment from Earth orbit to Mars orbit, descending and ascending from the surface, and returning to Earth orbit. Areas of comparison for each of these phases include crew size, mission mass, propellant mass, specific impulse, transit time, surface stay time, aerobraking, and others. Data is analyzed to demonstrate either strong trends toward particular technologies or diverging solutions.

I. Purpose/Introduction

A. Purpose

The purpose of this paper is to provide mission planners and analysts with a comparison of in-space transportation characteristics found in key Mars studies.

B. Introduction

Today, engineers are asked to conduct Mars analysis but have little understanding of the breadth and depth of previous work (see Fig. 1). One annotated bibliography refers to over 243 citations through December, 2000. Studies are available through conventional literature searches; however, others are buried in filing cabinets at NASA Centers and in offices of Aerospace Contractors. The documentation is inconsistent and material comes in many different formats. Some are recorded as formal documents, others as interim study reports. Technical conference papers provide a valuable source of published data, whereas, the latest work is not in the public domain and only available in presentation chart form. Regardless, the work is impressive and because many of the technical and

^{*} Manager, Systems Analysis and Space Architecture, Gray Research Inc., Huntsville, AL, Senior Member

[†] Engineer, In-Space Propulsion, Gray Research Inc., Huntsville, AL, Member

[‡] Systems Engineer, In-Space Propulsion, Gray Research Inc., Huntsville, AL

[§] Requirements Lead, Office of Exploration Systems/EX, NASA-JSC, Member

^{**} Manager, In-Space Propulsion Technology Projects Office, Marshall Space Flight Center TD05

^{††} Chief Technologist, Gray Research, Huntsville, AL, Associate Fellow

planning issues are the same today, it represents an enormous resource for future Mars mission planning. Few engineers have ready access to these studies let alone the time to dig through 1000's of pages for a particular data point. This paper represents the process used to identify key studies, collect the documentation, conduct comparison analyses and present results as they apply to in-space transportation. While the comparisons are useful, it is important to note that because the underlying mission objectives, ground rules, and assumptions vary widely, the results do not represent a true apples-to-apples comparison.

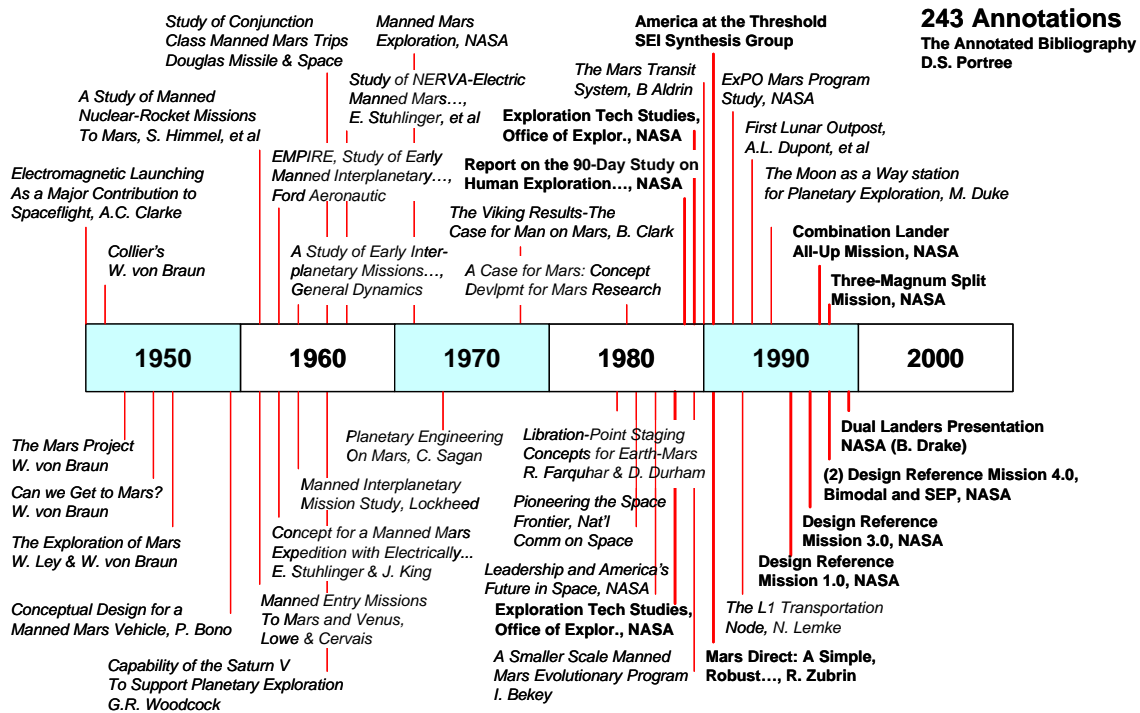


Figure 1 Timeline for Mars studies (bold type represents selected studies)

II. Approach

A. Survey of Studies, Reports and Technical Papers

The process began with a comprehensive search to identify studies, reports, and technical papers for human missions to Mars. Because there is no single repository of documentation on this subject, this process included research through NASA and contractor technical libraries, internet searches, and copying material from personal collections. A large volume of material was collected both in hard copy and electronic form. For this research, 21 studies were selected for comparison. Some are alternatives created within the same study, but because they represent a different approach, they were compared separately. The rationale for selecting the 21 studies is shown in Fig. 2.

Study	Options within Study	Acronym	Selection Rationale
1988/1989 Case Studies	5	Exp-P, Exp-M, Evo88, Evo89, Exp89	Agency-wide analysis of exploration options; provide focused program for human exploration of solar system
90 Day Study	1	90D	Large integrated NASA/Contractor effort, results well documented, includes design, schedule and cost
Synthesis Study – America at Threshold	1	Syn	Chartered by National Space Council – “major study”; Explore Mars & provide significant science return
Mars Direct	2	MDCh/MDNTR	Low cost; no orbital rendezvous or assembly; dependent upon ISRU propellant production for return; Chemical and NTR options
Mars Semi-Direct	1	MSD	Concept bridge between Mars Direct and Design Reference Mission 1.0; low cost
STCAEM	1	S-C/A	Major NASA funded study produced by Boeing in 1991; focus on in-space propulsion
STCAEM NTR	1	S-NTR	Major NASA funded study produced by Boeing in 1991; focus on in-space propulsion
STCAEM NEP	1	S-NEP	Major NASA funded study produced by Boeing in 1991; only study chosen using Nuclear Electric Propulsion as in-space propulsion
STCAEM SEP	1	S-SEP	Major NASA funded study produced by Boeing in 1991; focus on in-space propulsion
DRM 1.0	1	DRM1	NASA’s “Design Reference Mission” based upon previous studies; good focus on operations and science return
DRM 3.0	1	DRM3	Refine DRM 1.0 systems concepts and design; smaller class launch vehicle (80mt);source data from Borowski paper
DRM 4.0	2	DRM4N/DRM4S	Refine DRM 3.0; SEP Prop Option; NTR Bimodal “all-propulsive” option; source data from Borowski NTR
Combo Lander	2	CLA/CLS	Focus on single Mars lander to transport crew & also support on surface; all-up and split mission scenarios
Dual Lander	1	DUL	Follow-on of combo lander study – back to 2 landers; no formal report, presentation charts only
Total Studies	21		

Figure 2 Rationale for study selection

B. Rationale for Selecting Key Studies

Mars studies are complex with many interrelated variables. “An Overview of Recent Coordinated Human Exploration Studies” and “Key Findings from Previous NASA Exploration Mission Studies” are two NASA presentations that provide a good comparison of many of these variables. The analysis discussed in this paper builds upon this work while focusing on the attributes of in-space transportation.

A consideration for selecting key studies was to determine the technological relevance. The first credible study was von Braun’s “Das Marsprojekt” of 1952. NASA funded studies from 1963 to 1972. There was very limited study work from 1972 to 1988. All of the basic themes of Mars architectures (except perhaps solar electric propulsion (SEP)) were pioneered in the old studies and repeated in the later studies. Studies that were published from 1988 to the present were chosen to include modern technology development. Also, 1988 was the year that President George H. Bush appointed NASA to form the Mars Office of Exploration, which resulted in plans for a number of reports on manned missions to Mars and the Moon. These reports started a series of credible studies that would be produced over the following ten years.

Another guideline that was used in the selection of key studies was quality and quantity of documentation. There was a strong preference for published studies, in particular those resulting in formal documentation authored by NASA Headquarters. Published reports from NASA funded contractors were also considered an important source of information and, in some cases, a technical society paper was used because it best described the in-space transportation portion of a study. When no other documentation was available, presentations were accepted only because they represented the latest work. Documents were screened for credible concepts that included enough information to be used in comparison. NASA and NASA funded aerospace contractors’ studies were chosen because of the consensus process leading to an integrated architecture versus an emphasis on particular technologies.

Presidential support and new approaches to accomplish manned lunar and Mars missions were additional criteria for the selection of the key studies. Also, studies were selected based on the significant benefits produced from new approaches to get to Mars such as split missions (sending the equipment first then the crew) and Venus swingby trajectories (using the gravity of Venus to reduce propulsion system mass).

It is important to note that cost was not a consideration for selecting or comparing key studies. Typically, any cost analysis was based on different assumptions, schedules, and risk. Although cost was not considered for selection it is often related to mass. Most costing models use mass as the primary input for system cost, and thus mission designers typically strive to reduce overall system masses.

C. Traceability of Data

Early in the process, studies were collected and reviewed. It would be easy to lose track of the source of pertinent data, so a concerted effort was made to trace each piece of data back to a page and volume number within the study. Although time consuming, the benefit of this approach allowed revisits to the source material for verification. Millions, if not hundreds of millions, of dollars of analysis is represented in these reports and having a means of access to this data affords significant cost savings for future mission planners.

D. Different Ground Rules and Assumptions

It is difficult to compare one study to the next because each study had its own ground rules and assumptions. Some were motivated by scientific objectives and others by “flags and footprints”. Some were constrained by schedule, cost, or technology readiness. Others created very large launch vehicles, and some relied on making return propellant on the surface of Mars.

The common primary objective of each study was to safely send and return humans to Mars. The secondary objective varied among the different studies reviewed. Some studies yielded more defined information in specific areas than others. Specific areas included in-space propulsion and operations. In-space propulsion was better defined in Space Transfer Concepts and Analysis for Exploration Missions (STCAEM) reports which yielded four types of in-space propulsion applications using the same ground rules and assumptions. The Design Reference Mission 1.0 focused not only on landing a crew safely on Martian surface but on providing them with the tools to accomplish science and exploration objectives.

Technology advancement was assumed in all Mars studies. Propulsion and in-situ resource utilization (ISRU) for propellant production made a significant difference in architecture studies. Studies assumed different technology development and readiness for the Mars mission in the launch opportunity investigated. Perhaps the greatest assumption in these studies was payload capacity for heavy lift launch vehicles (HLLV). Assumed launch vehicle lift capability ranged from 80 metric tonne (mt) to as large as 240mt across the board. Overall capacity of the launch vehicle affected the transportation system definition which drove the complexity of comparing the studies. By comparison, the Saturn V vehicle had over a 100mt lift.

III. Mars Mission Planning

A. Trajectories

Trajectories employed in each mission dictate different requirements for the mission ranging from launch opportunity dates to requirements for initial mass in low earth orbit (IMLEO). Trajectory options for studies generally fall into two types of trajectory classes: opposition or “short-stay” and conjunction or “long-stay”.

The first Mars mission class consists of short stay times (typically 40 days) and round trip mission times ranging from 365-660 days. This is referred to as an opposition class mission, although the exploration community has adopted the more descriptive terminology “short-stay” mission. Most opposition class missions try to use a Venus swingby trajectory as the nominal approach. A swingby maneuver uses a planet’s gravity to modify the trajectory change in velocity (Δv) and reduce trip time. Deep space maneuvers are used when Venus swingbys are not available for specific mission dates/trip times. Trajectory profiles for typical short-stay missions are shown in Fig. 3. This class of mission has high propulsive requirements even when employing a gravity assisted swingby of Venus or performing a deep space maneuver to reduce the total mission energy. Short-stay missions always have one short transit leg, either outbound or inbound, and one long transit leg, the latter requiring close passage by the Sun (0.7 AU or less). After arrival at Mars, rather than wait for a near-optimum return alignment, the spacecraft initiates the return after a brief stay and the return leg cuts well inside the orbit of the Earth to make up for the “negative” alignment of the planets that existed at Mars departure. Distinguishing characteristics of a short-stay mission are: 1) short stay at Mars, 2) short to medium total mission duration, 3) perihelion passage inside the orbit of Venus on either the outbound or inbound legs, and 4) large total energy (propulsion) requirements.

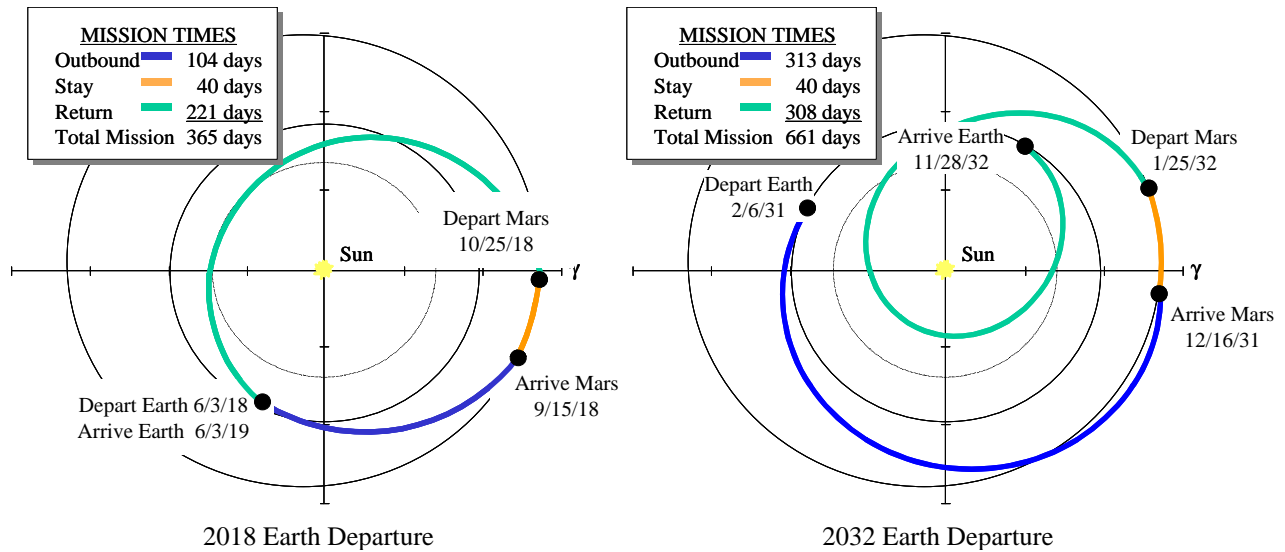


Figure 3 Short-stay (opposition class) mission profile examples

The short-stay mission approach has some distinct disadvantages. First, the total energy requirement varies greatly for each mission opportunity to Mars, repeating across the synodic cycle. (The 15 year synodic cycle is the period of time required for the orbital phasing between Earth and Mars to repeat itself). The total energy is also dependent on total round trip mission time and it can vary by as much as 88% across the synodic cycle. For all Mars mission classes, as trip time decreases, the required injection velocity and Mars arrival velocity both increase. This is important because higher total energies require exponentially greater propellant quantities, and higher approach velocities place excessive demand on technology development. In addition, total round trip mission time can be up to 660 days, with only 40 days at Mars. These long periods in deep space environment increase human radiation exposure, as well as physiological degradation due to the weightless environment and human performance issues that must be considered during the mission design process.

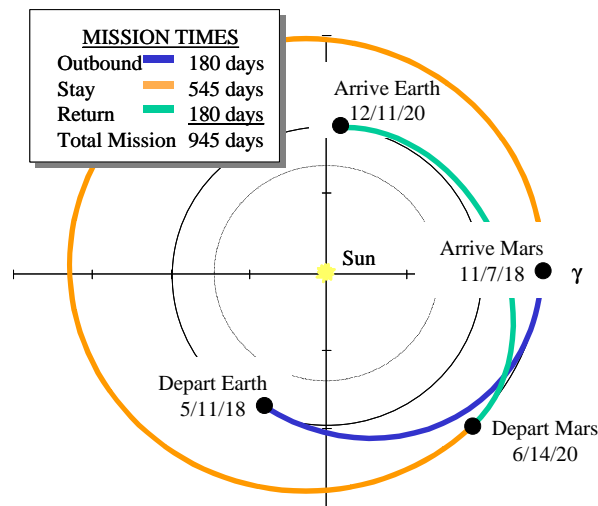


Figure 4 Trajectory profile for typical fast-transit, long-stay (conjunction class) mission

The second Mars mission class is typified by long-duration stay-times (as much as 600 days) and long total round trip times (approximately 900 days). This mission type is referred to as conjunction class, although the exploration community has adopted the more descriptive terminology “long-stay” mission. These missions represent global minimum-energy solutions for a given launch opportunity. Unlike short-stay mission approaches, departure

timing is based on a lower energy return. A variation of this long-stay mission has a total round trip time comparable to those of the minimum-energy mission, but the one-way transits are substantially reduced. Distinguishing characteristics of long-stay missions include: 1) long total mission durations, 2) long-stays at Mars, 3) relatively little energy change between opportunities, 4) bounding of both transfer arcs by the orbits of Earth and Mars (closest perihelion passage of 1 AU), and 5) relatively short transits to and from Mars (less than 200 days). The mission flight profile for a typical fast-transit mission is shown in Fig. 4.

B. Propulsion Options

The major propulsion options for human Mars missions are summarized in Fig. 5.

Propulsion Option	Description	Advantages	Disadvantages
Chemical	Conventional cryogenic rocket engines, usually one stage for each major maneuver (TMI, MOI, TEI). Insulated tanks with vapor-cooled shields to reduce boiloff. Start T/W 0.1 to 0.25. Isp ~ 460s.	-Mature technology -High thrust, short burn times -Ballistic interplanetary transfers facilitate implementing artificial gravity	-Low performance leads to high IMLEO except for conjunction profile with long transfer times -Cryogenic with hydrogen, low density, needs heat leak control -Expendable system
Chemical/ Aerocapture	Same as chemical except aerocapture used for MOI. Large aeroshell needed requiring either intact launch or in-space assembly. Lander may capture separately to simplify configuration.	-Reduces IMLEO by replacing one major maneuver with aerocapture	-Performance still marginal for "hard year" opportunities -Aerocapture risk: TPS/thermal, GN&C -Mars Vhp limited to ~ 6 for safe aerocapture -Expendable system
NTR	Nuclear thermal rocket engine, hydrogen propellant, Isp ~ 900s. Usually drop tanks utilized for each major maneuver. Insulated tanks as above; start T/W <= 0.1 to reduce nuclear engine size.	-Known technology -Twice the Isp of chemical propulsion reduces IMLEO and sensitivity to opportunity -High thrust, short burn times -Ballistic interplanetary transfers facilitate implementing artificial gravity	-Nuclear costs and risks -Engine test protocols not resolved (how to contain radioactive products) -Cryogenic with hydrogen, low density, needs heat leak control (exacerbated because propellant is all hydrogen) -Expendable system
SEP	Large (multi-megawatt) solar electric propulsion system, performs all major maneuvers. Isp typically 3000s; MPD or comparable thrusters.	-Known technology with flight experience in small size -High Isp reduces IMLEO and sensitivity -No hydrogen propellant -Reusable system	-Large size may require more space assembly than other options -High-power electric thrusters not mature (TRL 2 - 3) -Achievable power-to-mass ratio may not permit opposition-class profiles
NEP	Large (multi-megawatt) nuclear electric propulsion system, probably Brayton or liquid metal Rankine power generation, performs all major maneuvers. Isp typically 3000s; MPD or comparable thrusters.	-Known technology (no space experience or experimental prototypes except thermoelectric and thermionic conversion) -High Isp reduces IMLEO and sensitivity -No hydrogen propellant -Potentially reusable system	-Nuclear costs and risks -Large size may require more space assembly than other options -High-power electric thrusters and space configuration power conversion not mature (TRL 2 - 3) -Achievable power-to-mass ratio may not permit opposition-class profiles
SEP/Chem	Large SEP "tug" system ~ 1 mega-watt delivers chemical propulsion interplanetary vehicle to highly elliptic Earth orbit (perhaps in major sections with berthing for assembly). Chemical propulsion system departs from this orbit; otherwise same as chemical option.	-Placement in elliptic orbit reduces chemical delta-v by ~ 3 km/s, reducing IMLEO and sensitivity to opportunity -Other advantages same as Chemical Option	-Cost and mission complexity added by use of SEP "tug" -Cryogenic with hydrogen, low density, needs heat leak control -Expendable system

Figure 5 Propulsion option advantages and disadvantages

C. Mission Approach

Two approaches to mission design were researched: the all-up mission and the split mission. The all-up mission requires both cargo and crew to leave Earth's orbit at the same time. In split mission design, the cargo is flown to Mars prior to crew departure for Mars. The reason for the split mission is to send cargo and perhaps even return propellant on a low-energy trajectory which requires much less propellant.

Another feature of the transportation system is the method of orbit insertion. Studies have proposed both propulsive and aerocapture alternatives. The propulsive option uses the vehicle’s propulsion system to reduce the delta-v while aerocapture uses the planet’s atmosphere to slow the vehicle down.

In-situ resource utilization is another mission variable. ISRU is another way of saying “live off the land”. ISRU can involve propellant production on the surface of Mars or one of its moons, using Martian resources for oxygen production, and/or setting up a habitat on the surface where food can be grown. The type of ISRU employed will determine what the mass requirement for the mission will be, as well as other mission parameters.

Another mission approach was artificial gravity to counter physiological degradation during long periods of weightlessness. This, of course, has a significant impact on the design and location of propulsive elements. Some architectures use artificial gravity but none are included in the list of 21 missions used for this comparison.

IV. Areas of Comparison and Results

Common areas of comparison (see Fig. 6) were identified so the differences across the Mars studies could be seen. Most areas related directly to the transportation system, but several areas such as crew size were included to provide context and indicator of mission scale.

In missions requiring on-orbit assembly, different Mars vehicle elements are launched into Low Earth Orbit (LEO) on separate HLLV launches. Assembly may consist of a “simple” automated rendezvous and dock between elements or it can be much more complex requiring use of a space station or construction facility.

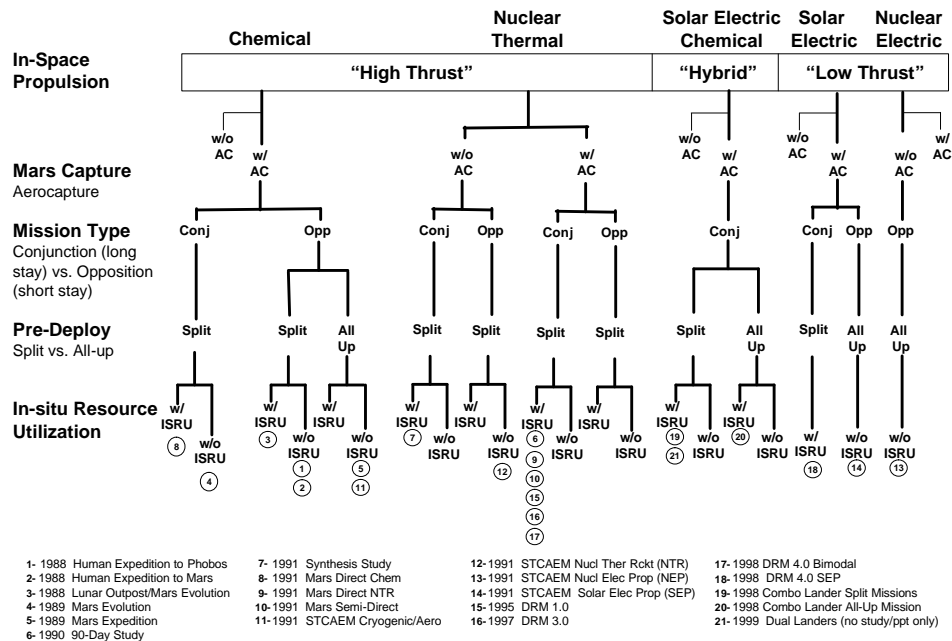


Figure 6 Mission design options for Mars studies

Most studies described the type of propellant used for Mars ascent and descent including the dependence on in-situ propellant production.

For this research, a Mars mission is considered to be one round trip from Earth. This is important because some transportation schemes send the cargo ahead with the crew to follow. In this case, all crew and cargo launches required for a single round trip would be book-kept against the mission.

A. Earth Departure Date

The Earth departure date or launch window opportunity is the first date when a cargo and/or piloted vehicle leaves LEO. In an all-up mission approach, the piloted vehicle with relevant cargo departs LEO and travels to Mars; thus, the mission will be accomplished during the designated opportunity window (i.e. CLA 2011). Alternatively, the split mission requires two Earth departure dates. The cargo departs LEO on the first opportunity and the piloted vehicle follows on the second opportunity (i.e. DRM1 2009/2011).

Mars mission planning is sensitive to the 15 year synodic cycle. Within the synodic period, some launch dates are “easier” than others due to planetary positions at departure and return. The difference between easy and hard mission opportunities has an impact on design of a transportation system. Some studies documented (i.e. DRM1) took a conservative approach of designing to the hardest opportunity year (2009) in the synodic cycle. The philosophy behind this rationale is that excess system capability may be available on the easier departure dates such that additional payload mass in the form of cargo or crew members may be afforded.

Launch opportunities for the 21 studies ranged from 1997 to 2018 for the LEO departures. The latest initial launch refers to the 90-Day Study in 2018. The information shown in Fig. 7 is based on the first crew departure date from LEO and shows the Mars Direct 1997 mission as the earliest. Some studies included multiple departure dates across the entire synodic cycle as part of a process of building a self-sufficient Mars outpost.

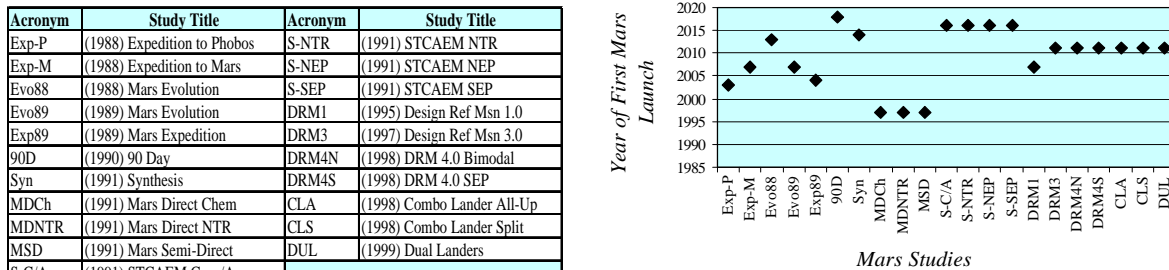


Figure 7 Study legend and Earth departure dates for chosen Mars studies

B. Crew Size

Human missions to Mars are more complex than the robotic missions. Increased system reliability along with adequate consumables and travel accommodations will drive the mission design and transportation system. After departure from LEO, the crew is committed to the Mars journey without re-supply from Earth. As a result, trade-offs are usually made between cost and comfort, as well as performance and risk. Few studies presented material on the relationship between crew size and mission assurance. Crew size determines mass of the habitat and the corresponding space transportation system as well. STCAEM performed an analysis and concluded seven or eight was the minimum crew size to have an adequate skill/training mix with allowance for one disabled crew person.

Many studies concentrated on an optimal skill mix for choosing crew members while others were concerned with the overall mission cost. Requirements for the crew size and composition of the crew would require considerable effort for future studies. Operational tasks would need to be well-defined along with safety and risk considerations. Crew dynamics would also be an important consideration. Figure 8 shows the variance in crew size from three crew members to as many as eight.

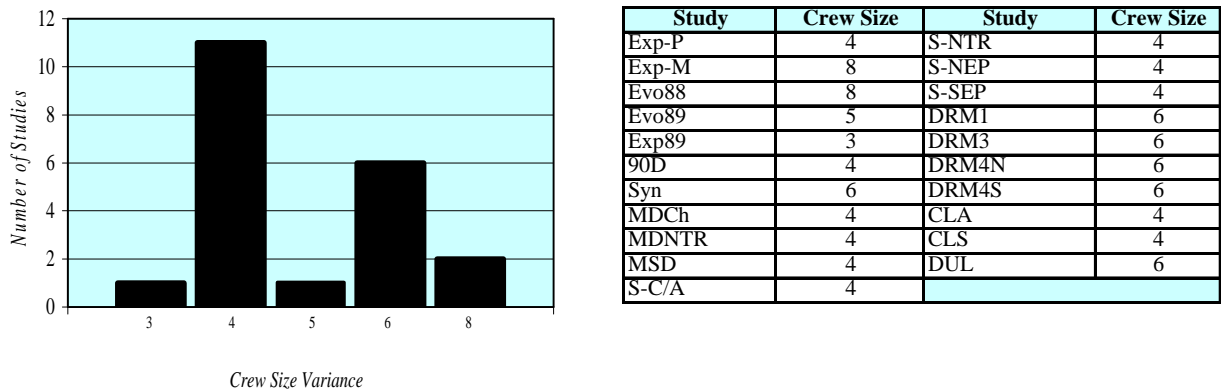
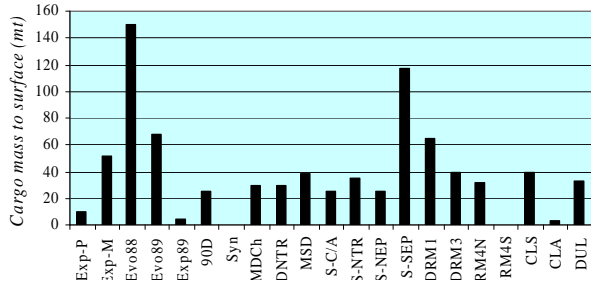


Figure 8 Crew size variance for chosen Mars studies

C. Cargo Mass to Surface

Missions were compared for cargo that reached the surface of the planet. (See Fig. 9.) Mars Evolution (1988) delivered the greatest amount of cargo while Combination Lander All-up (1998) delivered the least. Payload cargo mass is the amount of cargo delivered to the surface of Mars by the transportation system on a single opportunity from Earth. This cargo may consist of consumables such as crew supplies and food, power systems, and possibly a surface habitat. Generally, cargo remains on the planet surface as a building block for a Mars outpost.



*No data found for Synthesis Study & DRM4S

Figure 9 Cargo mass payload to Mars surface

missions generally provide for redundant consumables and/or abort options in the event that the piloted mission is unable to rendezvous with their cargo on the Mars surface.

D. Split/All-Up Mission Approach

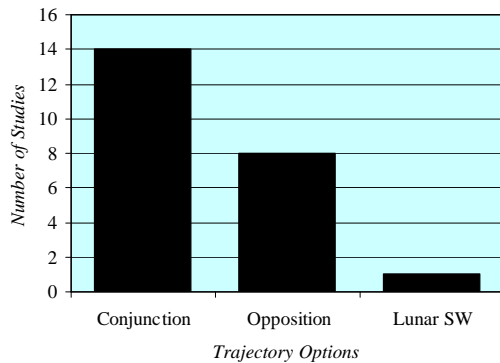
A split mission sends cargo ahead of the crew. Launches occur at sequential launch opportunities (i.e. 2009/2011). In contrast, the all-up mission approach includes both cargo and crew on the same flight opportunity.

Of the 21 studies researched, 5 used the all-up mission approach. The remaining use variations on split mission approach.

All-up mission design involves less risk because the crew is not separated from their cargo. Split

E. Trip Time and Trajectory

A trip is the time it takes for a flight, either cargo or manned, to complete a mission. Mars missions include an outbound leg and inbound leg. Nested in between the outbound and inbound legs is the Mars surface stay time in which the crew performs exploration and science.



Conjunction	Opposition	Lunar Swingby
Evo88-in	Exp-P	S-NEP
Evo89	Exp-M	S-SEP
90D	Evo88-out	
Syn	Exp89	
MDCh	S-C/A	
MDNTR	S-NTR	
MSD	S-NEP	
DRM1	S-SEP	
DRM3		
DRM4N		
DRM4S		
CLA		
CLS		
DUL		

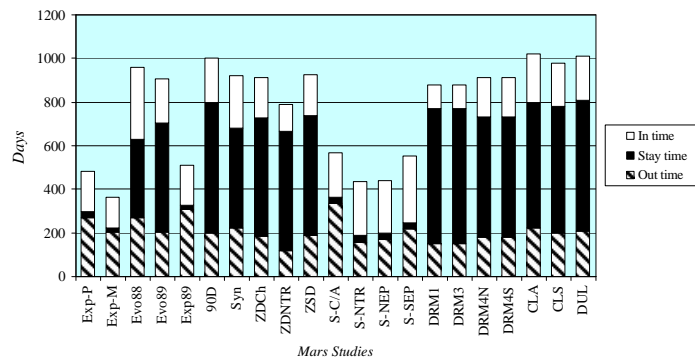


Figure 10 Trajectory selections and Mars mission trip time

Most opposition class missions try to use Venus swingby's; deep space maneuvers are used when Venus swingbys are not available for specific mission dates and associated trip times. The STCAEM Nuclear Electric Propulsion (NEP) opposition trajectory includes a lunar swingby leg.

Mission outbound times were 80 days (Mars Direct) to 335 days (STCAEM Cryo/Aero). In general, inbound times were the same or somewhat quicker. Of the studies surveyed, the 90-Day Study had the longest duration stay of 600 days. Figure 10 shows the trajectory options and mission trip times.

F. In-Situ Resource Utilization

For transportation studies, ISRU translates into propellant made from the atmosphere or soil. Since propellant is a large portion of overall mission mass, ISRU provides an attractive option to transporting return propellant. Many studies assumed that ISRU would be a developed and available technology when the mission took place.

For many studies, ISRU utilization was viewed as necessary for mission success. A clear two-thirds of the studies incorporated ISRU in their mission design.

Many of the studies viewed ISRU as a technology requirement that would, at a minimum, produce propellant using seed-hydrogen from Earth. The hydrogen would catalytically react with Martian CO₂ to produce methane and water eliminating the need to store cryogenic hydrogen. The methane and water would be stored and liquefied then chemically combined to produce a methane/oxygen bipropellant.⁸ This bipropellant would be used to refuel a Mars ascent vehicle upon departure.

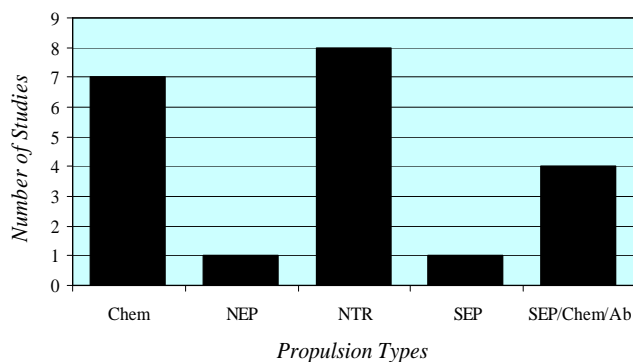
The Mars Direct Study is 100% dependent upon ISRU propellant production. Some of the other studies view ISRU as a technology development that would be a critical component especially for a long-term Mars outpost establishment. Its greatest potential is to provide self-sufficiency, providing greater resources for a broader range of transportation, habitation, life sciences, construction, energy production and other long term activities.⁵

G. Propulsion Type

The types of propulsion used in the 21 studies were Chemical, Nuclear Thermal Rocket (NTR), Nuclear Electric, Solar Electric or a hybrid of Solar Electric and Chemical using an aerobrake (Ab) referred to as SEP/Chem/Ab. (See Fig. 11.)

Almost an even split occurs between Chemical propulsion (7 studies) and NTR propulsion (8 studies). The remaining 6 studies used SEP with a chemical stage for Trans-Mars Injection (TMI) with only one study using NEP.

Mars studies tend to be transportation studies. The selection of propulsion systems includes important trades that compares key parameters, such as trip time and radiation exposure. The danger of radiation from an NTR or NEP was traded with the benefits of a fast-transit trajectory. Faster trips decrease the danger of crew exposure to in-space radiation caused by solar particle events and galactic cosmic radiation. On the other hand, chemical propulsion is generally slower with added exposure to in-space radiation. Figure 5 presents advantages and disadvantages for using different types of propulsion.



Chem	NEP	NTR	SEP	SEP/Chem/Ab
Exp-P	S-NEP	90D	S-SEP	DRM4S
Exp-M		Syn		CLA
Evo88		MDNTR		CLS
Evo89		MSD		DUL
Exp89		S-NTR		
S-C/A		DRM1		
MDCh		DRM3		
		DRM4N		

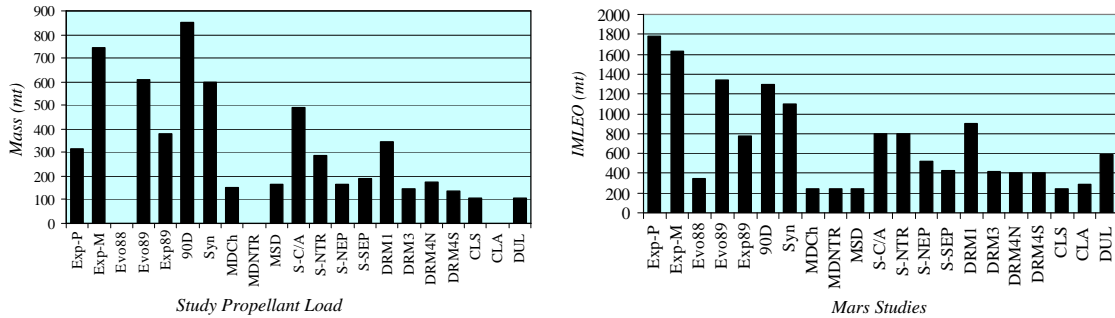
Figure 11 Mars study propulsion selection

H. Propellant Load

The propellant load is the amount of propellant required to perform a complete mission (includes cargo flights and one manned flight). Propellant is the largest item contributing to the overall mission mass in LEO. Reduction in propellant mass is assumed to reduce overall mission cost. Figure 12 shows the amount of propellant required for each Mars mission and the corresponding overall mission mass. The propellant load is a significant contributor to

IMLEO. No propellant mass numbers were found for Mars Direct NTR, Lunar Outposts/Mars Evolution (1988), or the Combination Lander All-up studies.

The Human Expedition to Phobos published in 1988 yielded the greatest IMLEO as compared to the other studies. Mars Direct scenarios came in at the lowest IMLEO essentially 7.4 times less than Human Expedition to Phobos. It should be noted that the main goal of the Mars Direct scenario was low cost hence low IMLEO. It should be observed that the degree of design optimism varies widely among the studies and one should be cautious about drawing too many conclusions from IMLEO comparisons.



*Propellant Load numbers for MDNTR, CLA, and Evo88 not found.

Figure 12 Propellant Mass and IMLEO for One Mars Mission

I. Aeroassist at Mars Descent to Mars Surface

Aerocapture uses the atmosphere for deceleration thus avoiding additional propellant. Most of these studies use aerocapture and aerobraking interchangeably. Since then, aerobraking has come to mean the slow process of gradually circularizing a parking orbit by repeated skims of the upper atmosphere.

Some studies used an aerobrake for capture into Mars orbit and for the Mars descent maneuver. Others used the descent lander propulsion and parachutes. Still, 5 studies of the 21 studies used all-propulsive capture into Mars orbit while 16 employed the use of aeroassist.

J. Heavy Lift Launch Capability and Number of Launches per Mission

All studies use a HLLV to place Mars mission elements into LEO. The lift capability of the launch vehicle determines the number of launches. The DRM1 mission had a launch vehicle size of 240mt intended to avoid in-space assembly. Each element was directly launched into LEO, and following system checkout, proceeded with the outbound leg of the journey to Mars. Other studies chose smaller, HLLV's and more in-space assembly (i.e. STCAEM NEP). Results comparing the size of the HLLV and the number of launches per mission are presented in Fig. 13.

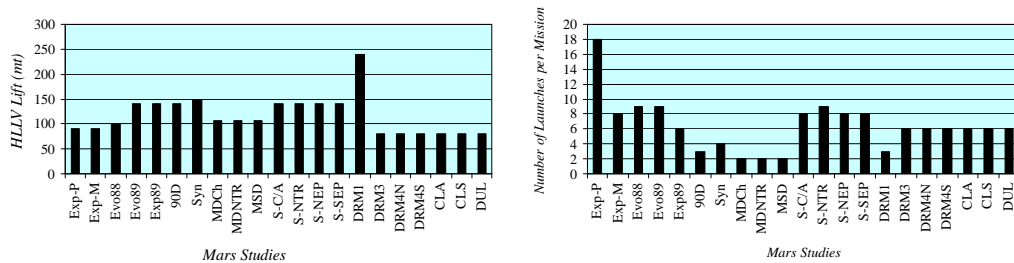


Figure 13 Assumed Mars launch vehicle capability and number of launches for one Mars mission

K. Summary

In summary, there are many ways to conduct a Mars mission as seen throughout this paper. The common areas of comparison among the researched Mars studies reveal differences in mission approach, as well as in ground rules and assumptions. The comparisons are presented not to select a favored scheme, but to show the extensive work that has been done and to create an enormous resource for future Mars mission planning.

Supporting Data

Supporting Personnel

Mary Ellen Harris SAIC Library (Archives)
Ben Donahue Boeing (Mars Studies + Archives)
Vance Houston NASA MSFC Archives

Acronyms and Abbreviations

90D Report of the 90-Day Study on Human Exploration of the Moon and Mars
CLA Combination Lander All-Up
CLS Combination Lander Split
delta v delta velocity; change in velocity
DRM Design Reference Mission
DRM1 Design Reference Mission version 1.0
DRM3 Design Reference Mission version 3.0
DRM4N Design Reference Mission version 4.0 – NTR Bimodal “all propulsive option”
DRM4S Design Reference Mission version 4.0 – SEP option
DUL Dual Landers Presentation
ETO Earth To Orbit
Evo88 Exploration Studies Technical Report: Lunar Outpost to Early Mars Evolution
(Case Study 4)
Evo89 Exploration Studies Technical Report: Mars Evolution Case Study
Exp89 Exploration Studies Technical Report: Mars Expedition Case Study
Exp-M Exploration Studies Technical Report: Human Expedition to Mars (Case Study 2)
Exp-P Exploration Studies Technical Report: Human Expedition to Phobos (Case Study 1)
HEO High Earth Orbit
HLLV Heavy-lift Launch Vehicle
IMLEO Initial Mass in Low Earth Orbit
ISRU In-situ Resource Utilization
LEO Low Earth Orbit
L2 Libration Point 2
MDCh Mars Direct Study: Chemical Propulsion option
MDNTR Mars Direct Study: Nuclear Thermal Rocket option
MSD Mars Semi Direct Study
NEP Nuclear Electric Propulsion
NTR Nuclear Thermal Rocket
RCS Reaction Control System
S-C/A Space Transfer Concepts and Analysis for Exploration Missions,
Volume 2: Cryo/Aerobrake Vehicle
SEP Solar Electric Propulsion
S-NEP Space Transfer Concepts and Analysis for Exploration Missions,
Volume 5: Nuclear Electric Propulsion Vehicle
S-NTR Space Transfer Concepts and Analysis for Exploration Missions,
Volume 3: Nuclear Thermal Rocket Vehicle
S-SEP Space Transfer Concepts and Analysis for Exploration Missions,
Volume 4: Solar Electric Propulsion Vehicle
STCAEM Space Transfer Concepts and Analysis for Exploration Missions
Syn Synthesis Group Study – “America at the Threshold”
TMI Trans-Mars Injection

References

- ¹ Soldner, J.K., “Round-Trip Mars Trajectories – New Variations on Classic Mission Profiles,” AIAA Paper No. 90-2932, *AIAA/AAS Astrodynamics Conference*, Portland, OR, August 20-22, 1990.
- ² NASA. “Exploration Studies Technical Report.” NASA-TM-4075, 1988.
- ³ NASA. “Exploration Studies Technical Report.” NASA-TM-4170, 1989.

- ⁴NASA. "Report of the 90 Day Study on Human Exploration of the Moon and Mars." NASA internal report. 1989.
- ⁵NASA. "America at the Threshold: America's Space Exploration Initiative." Report of the Synthesis Group. 1991.
- ⁶"Space Transfer Concepts and Analysis for Exploration Missions," The Boeing Co., Volumes 2 - 5, NAS8-37857, Huntsville, AL, March 1991.
- ⁷Reference Mission Version 3.0 Addendum to the Human Exploration of Mars: The Reference Mission of the NASA Mars Exploration Study Team, edited by B. G. Drake, Exploration Office document EX13-98-036, June 1998.
- ⁸Zubrin, R., and Weaver, D., "Practical Methods for Near-Term Piloted Mars Missions", AIAA 93-2089, presented at 29th Joint Propulsion Conference and Exhibit, Monterey, Calif., June 28-30, 1993.
- ⁹Larson, Wiley J., and Pranke, Linda K., *Human Spaceflight: Mission Analysis and Design*, 2nd ed., McGraw-Hill, New York, 2000.
- ¹⁰Borowski, Stanley K., Dudzinski, Leonard A., and McGuire, Melissa L., "Vehicle and Mission Design Options for the Human Exploration of Mars/Phobos Using "Bimodal" NTR and LANTR Propulsion," NASA TM-1998-208834, 1998.
- ¹¹Zubrin, R., Baker, D., and Gwynne, Owen, "Mars Direct: A Simple, Robust, and Cost Effective Architecture for the Space Exploration Initiative," 29th Aerospace Sciences Meeting, AIAA 91-0328, Reno, Nevada, January 7-10, 1991.
- ¹²Human Exploration of Mars: The Reference Mission of the NASA Mars Exploration Study Team, edited by B.G. Drake, Exploration Office document EX13-98-036, June 1998.
- ¹³NASA. "Mars Architecture Study Dual Lander Scenario." "Presentation of the Mars Architecture Study Team, Bret Drake. 1999.

ENGINEERING-LEVEL MODEL ATMOSPHERES FOR TITAN AND NEPTUNE

C.G. Justus* and Aleta Duvall†
Computer Sciences Corporation, Huntsville, AL

D.L. Johnson‡
NASA Marshall Space Flight Center, Marshall Space Flight Center, AL

ABSTRACT

Global reference atmospheric models for Titan and Neptune have been newly developed for utilization in NASA's aerocapture systems analysis studies. Their applicability to the engineering design of guidance, navigation and control, and thermal protection systems is discussed. The legacy and key features of Titan-GRAM and Neptune-GRAM are presented, with emphasis on the characterization of quasi-random atmospheric density perturbations. Sample Monte Carlo output for each model is presented.

INTRODUCTION

Engineering-level atmospheric models for Titan and Neptune have been newly developed for use in NASA's

systems analysis studies of aerocapture applications in missions to the outer planets. Analogous to highly successful Global Reference Atmospheric Models for Earth (GRAM)¹ and Mars (Mars-GRAM)^{2,3}, the new models are called Titan-GRAM and Neptune-GRAM. Like GRAM and Mars-GRAM, an important feature of Titan-GRAM and Neptune-GRAM is their ability to simulate quasi-random perturbations for Monte Carlo analyses in developing guidance, navigation and control algorithms, and for thermal systems design. Figure 1 compares density-height profiles for Earth, Mars, Titan, and Neptune. Relatively low scale heights (~10 km) make densities for Earth and Mars drop rather rapidly with altitude. Significantly higher scale height values for Titan and Neptune (~40 km) make these atmospheres considerably "thicker". Titan's large density scale height is due to its low gravity (~0.14 x

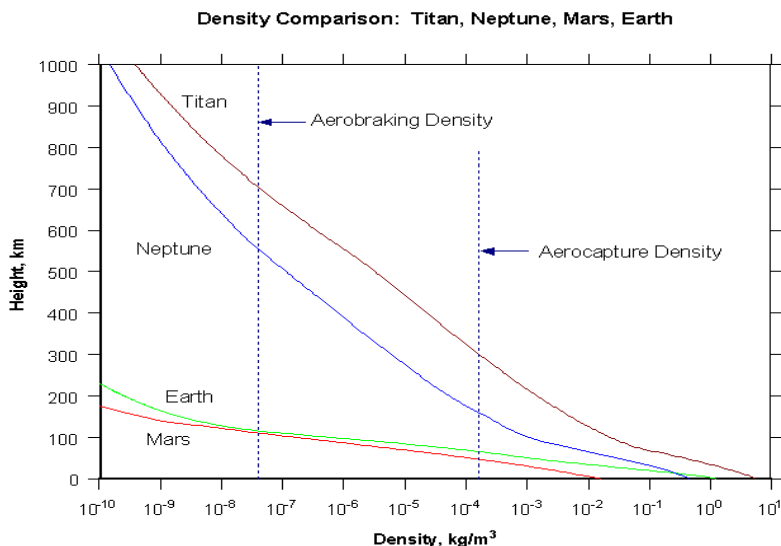


Figure 1 - Typical density versus altitude on Earth, Mars, Titan, and Neptune.

*Member, Principal Computer Scientist.

†Member, Computer Scientist.

‡Member, Aerospace Engineer.

Earth gravity), while that for Neptune is due to its low atmospheric mean molecular weight (~2.3 versus ~29 for Earth). Vertical dotted lines in Figure 1 show density values and altitudes at which aerocapture or aerobraking maneuvers would occur on these planets.

BASIS FOR THE ATMOSPHERIC MODELS

In GRAM and Mars-GRAM, input values for date, time, latitude, longitude, etc. are used to calculate planetary position and solar position, so that effects of latitude variation, and seasonal and time-of-day variations can be computed explicitly.

A simplified approach is adopted in Titan-GRAM and Neptune-GRAM whereby these effects (as well as effects of relatively large measurement uncertainties for these planets) are represented within a prescribed envelope of minimum-average-maximum density versus altitude. Figure 2(a) shows this envelope for Titan, for which engineering atmospheric profiles of Yelle et al.⁴ are used. For Neptune, data from Cruikshank⁵ were employed to generate a comparable envelope, shown in Figure 2(b).

A single model input parameter (Fminmax) allows the user of Titan-GRAM or Neptune-GRAM to select

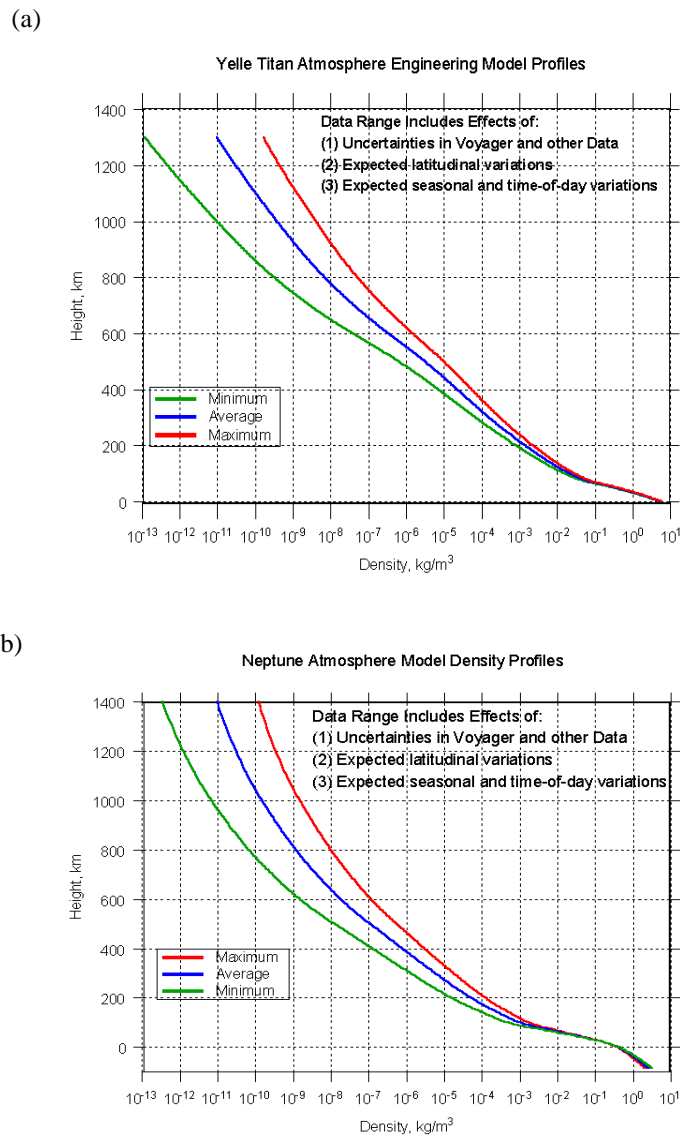


Figure 2 – Minimum, average, and maximum density versus altitude for (a) Titan⁴ and (b) Neptune (developed from data in Cruikshank⁵).

where within the min-max envelope a particular simulation will fall. $F_{minmax} = -1, 0, \text{ or } 1$ selects minimum, average, or maximum conditions, respectively, with intermediate values determined by interpolation (i.e. F_{minmax} between 0 and 1 produces values between average and maximum). Effects such as variation with latitude along a given trajectory path can be computed by user-selected representations of variation of F_{minmax} with latitude.

Yelle et al. assumed methane mole fractions of 5%, 3%, and 1% for minimum, average, and maximum density Titan atmospheres, respectively. Aerothermal analyses (other papers in this session) showed very strong radiational heating by CN radicals produced from methane and nitrogen reactions in the high-temperature aerocapture entry shock layer. Because of the importance of methane concentration in this process, an option was added in Titan-GRAM to allow the user to select any amount of methane (up to 5%), while retaining the original Yelle et al. profiles of mean

molecular weight versus height and density versus height. Atmospheric density perturbations are computed by methods similar to those used in GRAM and Mars-GRAM. Perturbation magnitudes in Titan-GRAM and Neptune-GRAM are estimated from a methodology similar to that of Strobel and Sicardy⁶, based on expected wave saturation effects.

In particular, perturbation magnitudes are modeled from an approximate fit to the wave saturation condition relation

$$\rho'_{max} / \rho_0 = [L / (2 \pi H)] (1 + [L / (2 \pi H)]^2)^{1/2} (dT_0 / dz + g / C_p) / (g / R) \quad (1)$$

where H is pressure scale height ($R T_0 / g$), R is gas constant, g is acceleration of gravity, T_0 is background mean temperature, and C_p is specific heat at constant pressure. Model perturbation magnitudes are illustrated in Figures 3(a) and 3(b).

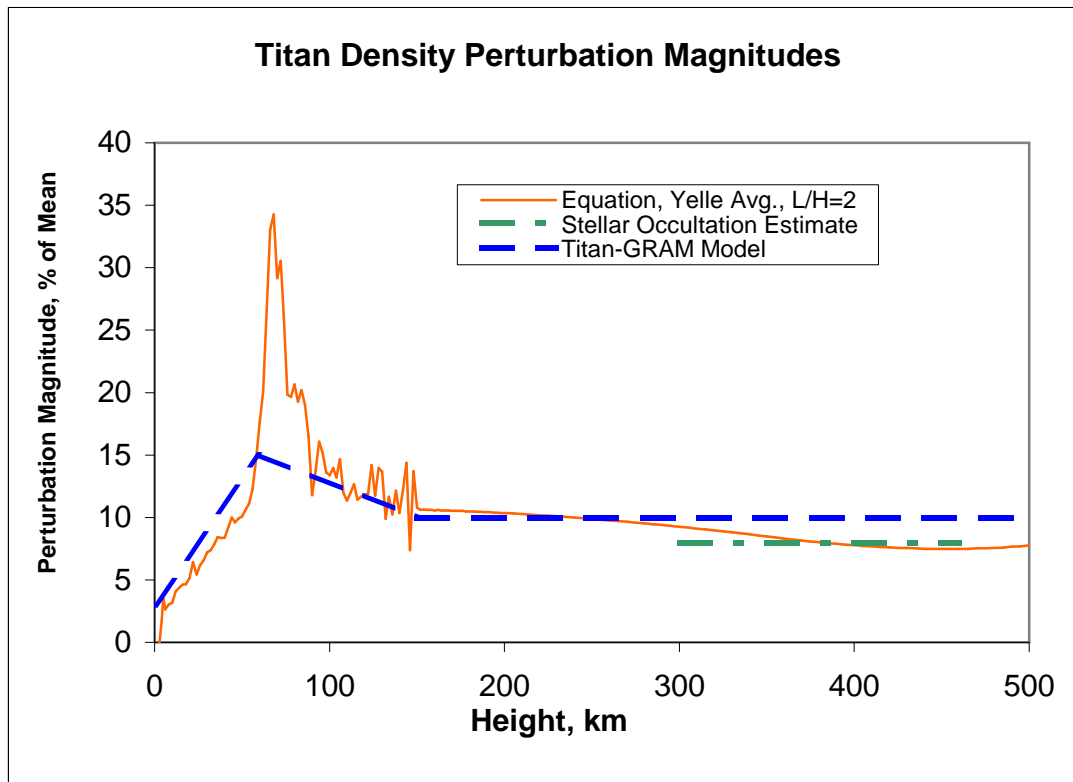


Figure 3(a) – Perturbation magnitudes in Titan-GRAM. Model values approximate equation (1), with ratio $L/H=2$ and dT_0/dz from respective average atmospheres. Textured line is estimated value from Figure 1(a) of Strobel and Sicardy⁶.

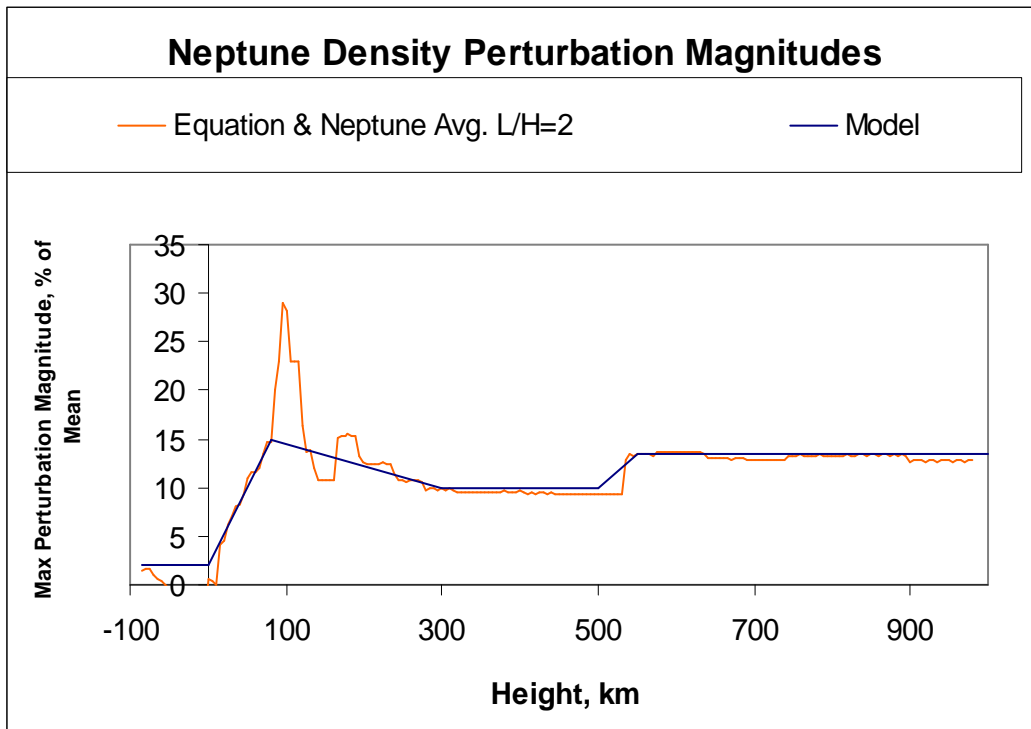


Figure 3(b) – Perturbation magnitudes in Neptune-GRAM. Model values approximate equation (1), with ratio $L/H=2$ and dT_0/dz from respective average atmospheres.

SAMPLE MODEL RESULTS

Sample Monte Carlo outputs from Titan-GRAM and Neptune-GRAM are shown in Figure 4.

CONCLUSIONS

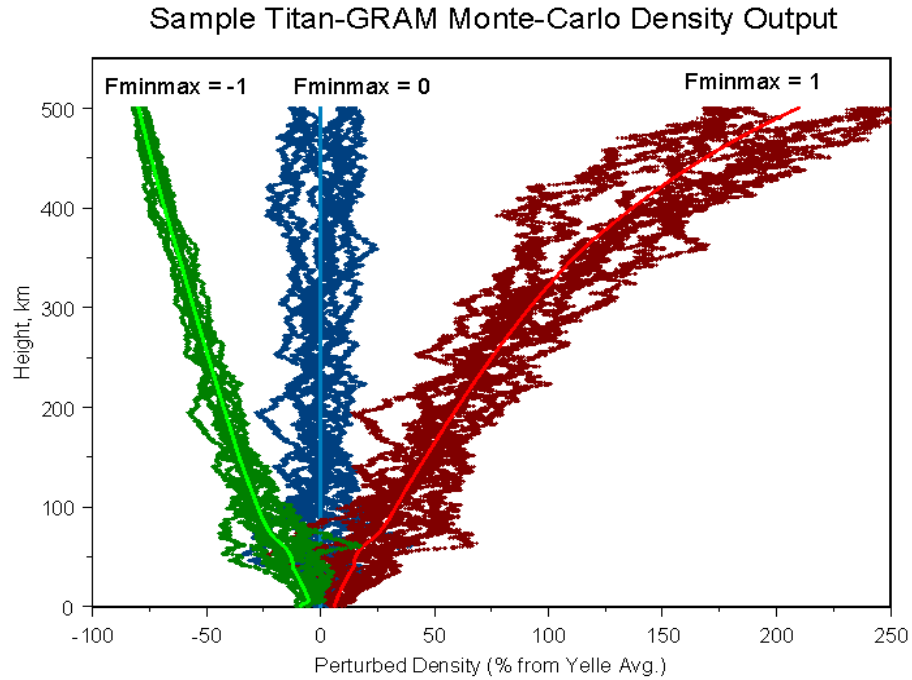
Titan-GRAM and Neptune-GRAM are engineering-level atmospheric model for Titan and Neptune, suitable for a wide range of mission design, systems analysis, and operations tasks. For orbiter missions, Titan-GRAM and Neptune-GRAM applications include analysis for aerocapture or aerobraking operations, analysis of station-keeping issues for science orbits, analysis of orbital lifetimes for end-of-mission planetary protection orbits, and atmospheric entry issues for accidental break-up and burn-up scenarios. For Titan lander missions, Titan-GRAM applications include analysis for entry, descent and landing (EDL), and guidance, navigation and control analysis for precision landing. Using Titan-GRAM or Neptune-

GRAM perturbation models in Monte Carlo mode make them especially suited for design and testing of guidance, navigation, and control algorithms and for heat loads analysis of thermal protection systems.

ACKNOWLEDGEMENTS

The authors gratefully acknowledge support from the NASA/Marshall Space Flight Center In-Space Propulsion Program. Particular thanks go to Bonnie James (MSFC), Manager of the Aerocapture Technology Development Project, to Michelle M. Munk (LaRC/MSFC), Lead Systems Engineer for Aerocapture, and to Ann Trausch and Melody Herrmann (MSFC), team leads and Mary Kae Lockwood (LaRC), technical lead for the Titan/Neptune Systems Analysis study. Model user feedback and suggestions from the following individuals are also greatly appreciated: Dick Powell, Brett Starr, and David Way (NASA LaRC), and Claude Graves and Jim Masciarelli (NASA JSC).

(a)



(b)

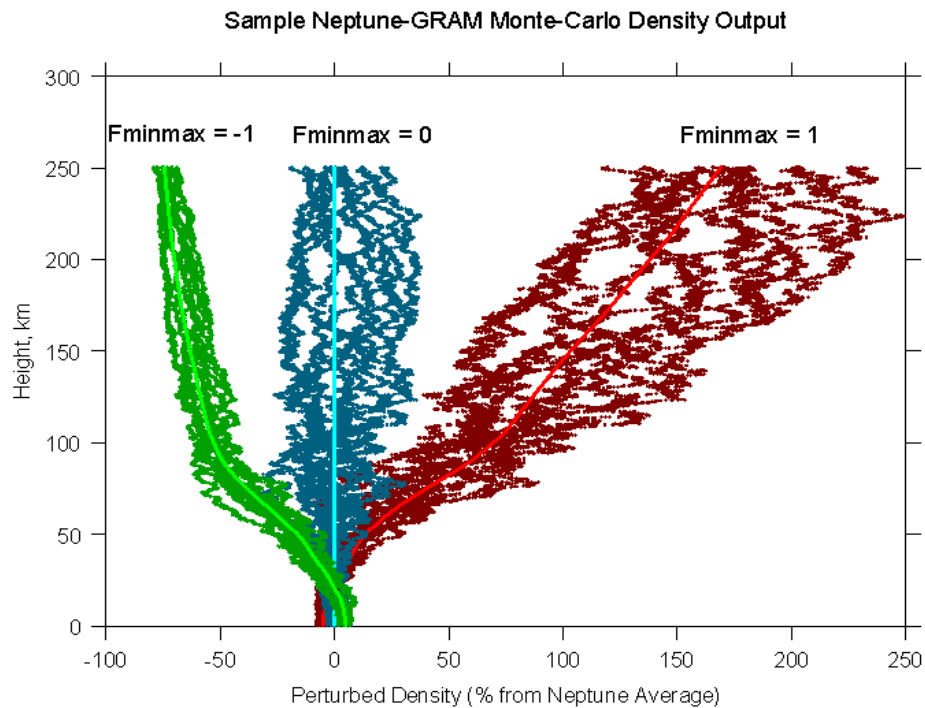


Figure 4 - Sample Monte Carlo perturbation profiles from (a) Titan-GRAM and (b) Neptune-GRAM for $F_{minmax} = -1, 0$ and 1 . Density values are expressed as percentage deviation from average density ($F_{minmax} = 0$) profile value.

REFERENCES

¹Justus, C.G., Johnson, D.L., and James, B.F., "New Global Reference Atmospheric Model (GRAM-99) and Future Plans", COSPAR 33rd General Assembly, Warsaw, Poland, Invited Paper C4.2-0003, July 2000.

²Justus, C.G., and Johnson, D.L., *Mars Global Reference Atmospheric Model 2001 Version (Mars-GRAM 2001) Users Guide*, NASA/TM-2001-210961, April 2001.

³Justus, C.G., James, B.F., Bougher, S.W., Bridger, A.F.C., Haberle, R.M., Murphy, J.R., and Engel, S., "Mars-GRAM 2000: A Mars Atmospheric Model for Engineering Applications", *Advances in Space Science*, Vol. 29, No. 2, 2002, pp. 193202.

⁴Yelle, R.V., Strobel, D.F., Lellouch, E., and Gautier, D., "Engineering Models for Titan's Atmosphere", *Huygens Science, Payload and Mission*, ESA SP-1177, Aug 1997.

⁵Cruikshank, D.P., Ed., *Neptune and Triton*, University of Arizona Press, Tucson, 1995.

⁶Strobel, D.F., and Sicardy, B., "Gravity Waves and Wind Shear Models", *Huygens Science, Payload and Mission*, ESA SP-1177, Aug. 1997.

Controllability of Large SEP for Earth Orbit Raising

Gordon Woodcock

Gray Research, 655 Discovery Drive, Suite 300, Huntsville, AL 35806 USA, grw33@comcast.net

A six-degree-of-freedom (6DOF) simulation was constructed and exercised for a large solar electric propulsion (SEP) vehicle operating in low Earth orbit. Nominal power was 500 kWe, with the large array sizes implied. Controllability issues, including gravity gradient, roll maneuvering for Sun tracking, and flexible arrays, and flight control methods, were investigated. Initial findings are that a SEP vehicle of this size is controllable and could be used for orbit raising of heavy payloads. This research was sponsored by the In-Space Propulsion organization of the NASA Marshall Space Flight Center.

I. Purpose

The research reported investigated controllability of large solar electric propulsion (SEP) systems operating in low Earth orbit. Controllability factors included gravity gradients and roll control requirements. This paper presents a status report on the work, with initial results.

II. Introduction

Large solar electric propulsion systems are one option for moving large payloads from low Earth orbit (LEO) to geosynchronous orbit (GEO) or beyond^{1,2}. Examples of such payloads are cargo elements of a logistics system for supporting human lunar exploration, and very large space optical or infrared telescopes. SEP electric power levels for these missions may range from tens to hundreds of kilowatts, with correspondingly large solar arrays. Thrust may be provided by gridded ion or Hall thrusters; in the future other thruster candidates may become competitive.

Large objects in low Earth orbit are subject to significant gravity gradient torques. Some, such as the International Space Station (ISS), are designed to fly a gravity gradient stable or neutral attitude strategy to minimize the problem. This strategy imposes on the ISS a need for two-axis solar array articulation so that the main body of the ISS remains in a local-horizontal-local-vertical (LVLH) attitude.

Another possible strategy is to control the SEP body and solar arrays to inertially face the Sun, placing thruster installations at the four corners of the (nominally square) array on two-axis gimbals. Thruster pointing controls gravity gradients and is directed to maximize available thrust for orbit raising. Restrictions on thruster pointing are applied to prevent plume impingement on the body of the vehicle. (This is a shortcoming as it will reduce the duty cycle of the thrusters and will reduce Isp and thrust due to thrust vector diversion.) Chemical propulsion provides attitude stabilization during occultation periods. This strategy was investigated several years ago during solar power satellite studies. It was concluded that multi-megawatt SEP systems could be controlled for LEO-GEO transfers by this method. The subject SEP systems were assumed constructed on orbit; it appears these configurations might be difficult for autonomous deployment.

For a SEP, it is important to minimize mass in order to minimize trip time from LEO to the destination. Given this consideration, plus a need for autonomous deployment, the attitude strategy is often single-axis solar array articulation, with roll maneuvering of the SEP body around the thrust axis, to provide Sun-pointing capability. Roll maneuvers place the solar array tilt axis perpendicular to the Sun line. Array tilt aims the array to face the Sun. This design and maneuver approach permits a conventional SEP arrangement with thrusters aft, payload forward, and arrays extended to the sides; deployment is relatively straightforward. However, this design does not permit gravity gradient stable or neutral attitude. Thrust is available for attitude control, but thrust directed to attitude control causes at least some reduction in performance. Roll maneuvers at relatively high roll rates may be needed for precise Sun-pointing, but some loss in precision may be preferable to providing the control authority for high rates.

The SEP will at times be in Earth shadow (typically ½ hour or less) such that electric thrust power is not available. Battery power for main propulsion operation during shadow periods represents a significant mass penalty (alpha contribution = duration/[Wh/kg], typically 5 to 10 kg/kWe). The options are to provide chemical propulsion

attitude control during shadow periods, or to permit attitude drift during these periods, with recovery when main power is turned on again.

Large solar arrays can be stiff, massive and difficult to deploy, or flexible, light and easier to deploy. There is concern about the influence of flexible arrays on SEP controllability.

In order to assess these issues, an existing six-degree-of-freedom satellite orbital simulation was modified to model the SEP problem.

III. Mission and System Geometry; Coordinate Systems

Requirements on the Analysis ... The SEP is in Earth orbit, and must (nominally) thrust in the direction of flight. If plane change is needed during the ascent, yaw steering (out of the orbit plane) may also be needed. The orbit must be propagated as a result of thrust, drag, and Earth oblateness effects. Gravity gradient acts on the vehicle, and its torque must be computed. The SEP needs to track the Sun, and can only generate thrust when sunlit. The location of the Sun relative to the maneuvering SEP must be determined, as well as whether or not the SEP is in Earth's shadow. The SEP configuration must permit three-axis control in order to execute roll maneuvers to track the Sun, and to maintain control of pitch and roll. The computations must be able to deal with large attitude variations, especially in roll. The SEP array tilt needed to track the Sun must be determined, and tilt control simulated. In the flexible array case, the effects of the flexible array must also be modeled.

This analysis starts with the SEP on standby in a low Earth orbit. To minimize drag and control requirements, the SEP is positioned with the solar arrays in the orbit plane and in a gravity gradient stable or neutral LVLH attitude. This is illustrated in Figure 1, which also shows some of the coordinate systems used.

Coordinate Systems ... Analysis begins in the heliocentric system, using ephemeris equations to locate the Earth according to the selected analysis start date. Since the analysis is Earth-centered, the direction of the Sun from Earth, in helio coordinates, is transformed to Earth coordinates to get the Sun vector re Earth inertial coordinates. The orbit is initialized with altitude, eccentricity, line of nodes, inclination, argument of periapsis, and initial true anomaly for the SEP. The local path coordinate system moves with the SEP. The SEP has its own coordinates which move relative to local path coordinates according to satellite maneuvers. SEP attitude is described in terms of roll, pitch and yaw in that sequence.

The mission is transfer from low Earth orbit to geosynchronous orbit and return. A payload of 50,000 kg is delivered, and the SEP returns itself, with no payload, for reuse.

The Earth coordinate system is x towards spring equinox, z north pole, y RHCS

The orbit coordinate system is the usual. X points to periapsis, Y 90 deg in motion direction, Z rhcs (north for posigrade orbit). Z is the orbit vector O.

Satellite control strategy is roll to place array tilt axis psl, tilt to orient arrays to Sun.

The initial rate is about the z axis, y->x negative with attitude as shown (roll -90), or x->y positive if z axis points other way.

The local coordinate system along the path is x flight direction, y right facing in flight direction, z nadir. The satellite initial attitude is 90 deg roll (to the left or right), with zero array tilt, to place it in gravity gradient neutral attitude

Array tilt is pos z -> x, zero in x-y plane

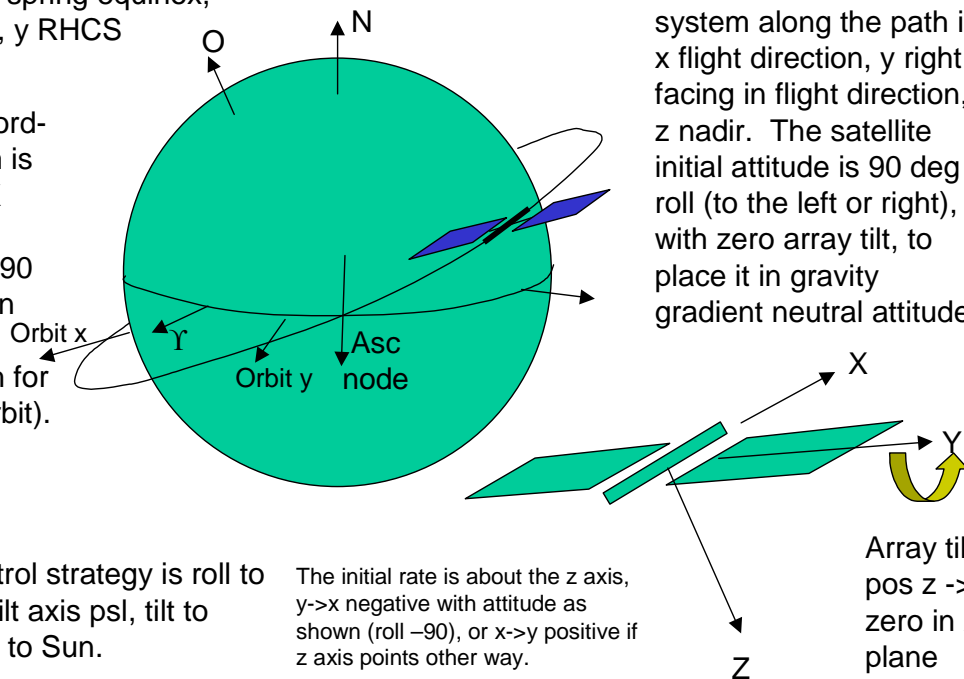


Figure 1: Coordinate Systems and SEP Axes

IV. Estimating SEP Characteristics; SEP Representative Description

For this analysis I chose a 500-kWe SEP in order to make the control problem potentially difficult. SEP input and calculated parameters are given in Table 1. The SEP alpha is about 30 kg/kWe based on dry mass not including propellant tanks, and total electric power. Array geometry and the thruster roll control offsets were varied. Rigid arrays similar to the “square riggers” of reference 2 used a width/height ratio of 1.2. Width is in the y direction (transverse from the thrust axis) and height is along the thrust axis. A flexible deployable array used w/h 10, which gives it a packaged length of 10+ m compatible with typical EELV payload fairing length, and an extension length of 100 m (each wing). Rigid analysis of this configuration was done for comparison, The flexible array was assumed to be a fan-fold assembly of rigid hinged panels 2 x 20 m with ½ meter diameter Astromast deployable trusses forward and aft of the panels. Each panel is supported at two points (one fore, one aft) by the masts. First-mode flexible beam natural frequency was calculated based on representative mast stiffness. Total mass per unit length was masts plus panels, with result 0.0018 Hz. For simulation development, a simpler flexible structure was also used, a rigid panel supported by a short flexible section; this had a natural frequency 0.0024 Hz.

Description Item	Value and Units	Description Item	Value and Units
- Input Values -		- Calculated Values -	
Payload	50000 kg	Up trip time	240 d
Payload length	10 m	Return trip time	61 d
Power kWe	500	Array area	2000 sq m
Isp	2000 sec	Array height	10 m @ w/h=10
Delta V up	6700 m/s	Array width	100 m (ea wing)
Delta V down	6700 m/s	Jet power	325 kW
Trip Time Up (Limit)	270 days	Thrust	33.14 N
Thruster alpha	2 kg/kWe	Propellant flow	0.001689 kg/s
PPU/cabling alpha	4 kg/kWe	Payload x offset	9.93 m
Propulsion efficiency	65%	Payload accomm x offset	4.93 m
Run time fraction	90%	Array x offset	-2.57 m
Array W/kg	143	Thruster x offset	-7.5 m
Array W/sq m	250	PPU x offset	-7.5 m
Array w/h	1.2 to 10	Avionics/flt control x offset	-2.57 m
Body diameter	4.5 m	Propellant x offset	-10.07 m
Initial beta tilt	0 deg	Structures x offset	-5.06 m
Beta tilt rate	1 deg/sec	Payload accomm mass	5000 kg
Thrust lateral offset	2.5 or 5 m, + & - y for total of 5 or 10 m	Array mass	2500 kg
Avionics & flight control mass	250 kg	Thruster mass	1000 kg
		PPU & cabling mass	2000 kg
		Propellant tank mass	2060 kg
Payload accomm. fraction	10% of payload mass	Structures mass	4483 kg
Propellant tank fraction	5% of loaded propellant	Inert mass	19,255 kg
		Return cutoff mass	19,255 kg
Structural fraction	35% of other inert mass	Up propellant	31,394 kg
		Return propellant	7841 kg
		Unusable propellant	1962 kg
Unused and reserve propellant	5% of impulse propellant	Total propellant	41,196 kg
		Total initial mass	110,451 kg

Figure 2 illustrates the 500 kWe SEP with the flexible deployable array. The tank is sized for xenon or krypton; with krypton some cooling is needed to achieve desirable densities. The thrusters are on a simple deployment assembly to increase the roll control moment arm to +/- 5 m. Rigid body control analysis showed that in the case of large w/h (long narrow arrays) that +/- 2.5 m was not enough. Propulsion power processors are located close to the thrusters. Arrays and their deployment systems are forward of the tank. Avionics are included in the array area, and forward of that is the payload, assumed 5 m diameter by 10 m length.

V. Simulation Description

Coordinate systems were described above. The simulation is run in either rigid body or flexible body mode. In the flexible case, additional inputs are required to describe the flexibility of the arrays. The simulation calculates an inertia tensor for the SEP based on input data. Except for the solar arrays, point masses and offsets are used for all inertia contributions. In the rigid array case, array inertia contribution is computed for each wing from a flat rectangle approximation; lateral offsets are added, and a transform of the form \mathbf{AIA}^{-1} is used to account for array tilt. In the flexible array case, array inertia is not calculated because it is simulated. (Simulation includes calculation of inertia contributions.) A nominal 1-sec time step is used. Because the large SEP is not very maneuverable, this appears to provide adequate fidelity. Large pitch gimbal angles (45 degrees) are permitted so that +/- pitch gimbal can exert substantial control authority.

In principle, this type of simulation is simple. Calculate the parameters needed in the appropriate coordinate system, and numerically integrate the equations of motion. There is a lot of switching back and forth between coordinate systems because changes in attitude rate are easiest to integrate in the body axis coordinate system, while the translational equations of motion and the quaternion need to be integrated in an inertial frame. Another complication is that one needs a control law to maintain correct attitude. The control law must orient the solar arrays to track the Sun and maintain body axis orientation as dictated by the desired thrust vector.

Because attitude changes can be large, SEP motion is calculated by integrating the quaternion that describes SEP attitude relative to Earth inertial coordinates. The quaternion is initialized by (1) specifying the initial date (transform from helio to Earth coordinates), the orbit parameters, the SEP initial true anomaly and initial attitude, (2) stepping through the coordinate transforms from Earth inertial to SEP coordinates, thus generating the transform matrix for Earth inertial to SEP coordinates, and (3) extracting the initial quaternion from the matrix.

The simulation begins as soon as the SEP is illuminated; the SEP is initially positioned in a feathered, gravity gradient stable attitude as described above. Upon illumination, thrust is switched on and the SEP begins to maneuver to full-power attitude. Array tilt and vehicle roll occur simultaneously. Array tilt is limited to a set rate, 1 degree per second in the cases presented.

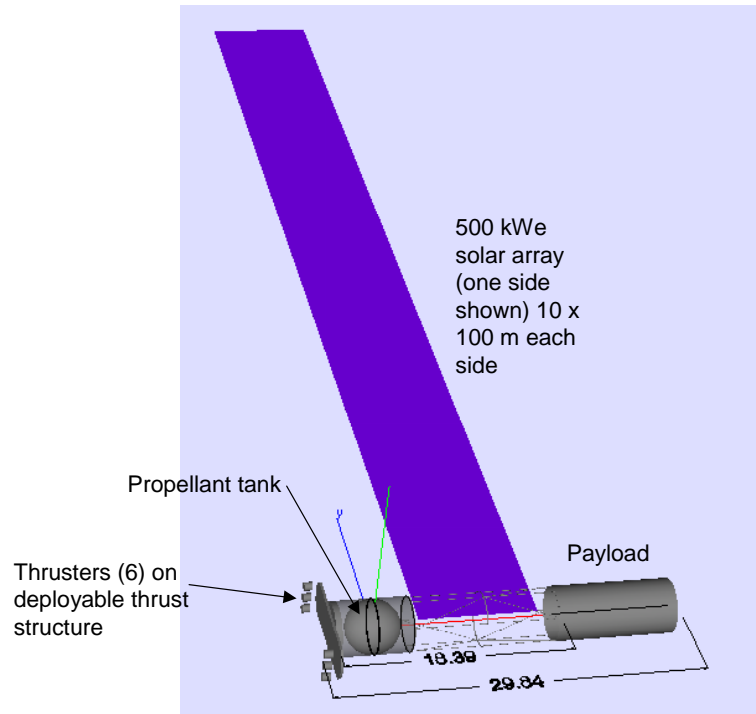


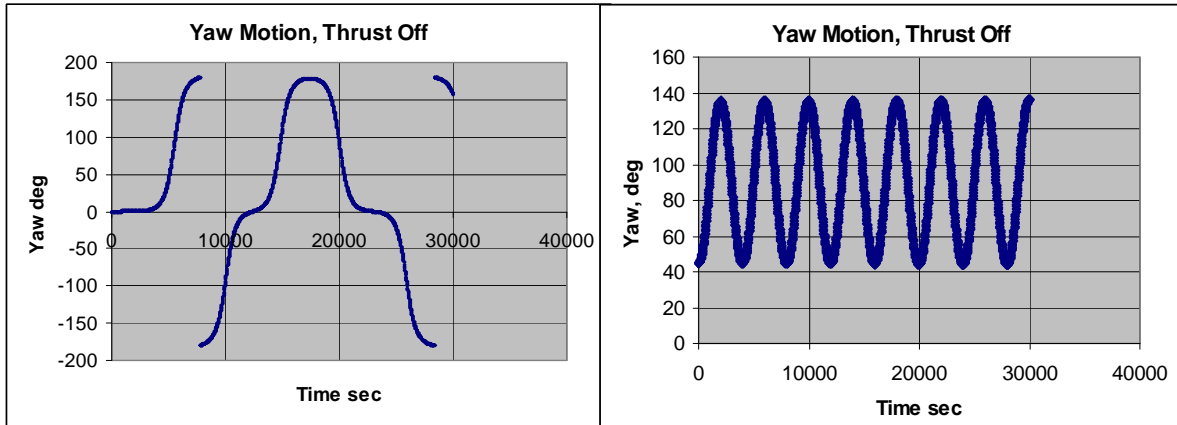
Figure 2: 500 kWe SEP, Flexible Array Geometry

The simulation begins as soon as the SEP is illuminated; the SEP is initially positioned in a feathered, gravity gradient stable attitude as described above. Upon illumination, thrust is switched on and the SEP begins to maneuver to full-power attitude. Array tilt and vehicle roll occur simultaneously. Array tilt is limited to a set rate, 1 degree per second in the cases presented.

VI. Rigid Results

The first rigid tests were without power and array motion, to test the integrator. These used a SEP configuration with approximately square arrays (not the high aspect ratio depicted above). The SEP was placed in its nominal start attitude and integrated for a few orbits. This original SEP concept was not actually gravity gradient stable in the start attitude, it was gravity gradient neutral. Because of large moments of inertia about the y and z axes compared to the x axis, due to the distribution of large masses along the x axis, the gravity gradient stable attitude is with the x axis vertical. Figure 3 shows simulation test results. The first case started with the SEP in normal start attitude, and the second with an initial yaw of about 45 degrees. The first case eventually falls out of the gravity gradient neutral attitude and rotates or oscillates depending on rotating motion coupling with the slightly elliptic orbit. The second exhibits a normal gravity gradient oscillation.

The next tests, after some debugging, simulated powered flight for about one orbit. Some adjustment of gains was necessary to obtain reasonable behavior. The thrust vector control laws were very ordinary, attitude error with negative attitude rate feedback. Array tilt used an on/off algorithm for simulated array drive at 1 degree per second, with a +/- 1.5 degree deadband. At this point the roughly square array was still being used. Two cases are of interest: (1) during periods of occultation, no thrust is provided, and (2) during periods of occultation, chemical propulsion is used, but only for roll rate damping. These are shown in Figure 4.



Initial yaw = 0 (gg neutral)

Initial yaw 45 degrees

Figure 3: Initial Tests with No Thrust

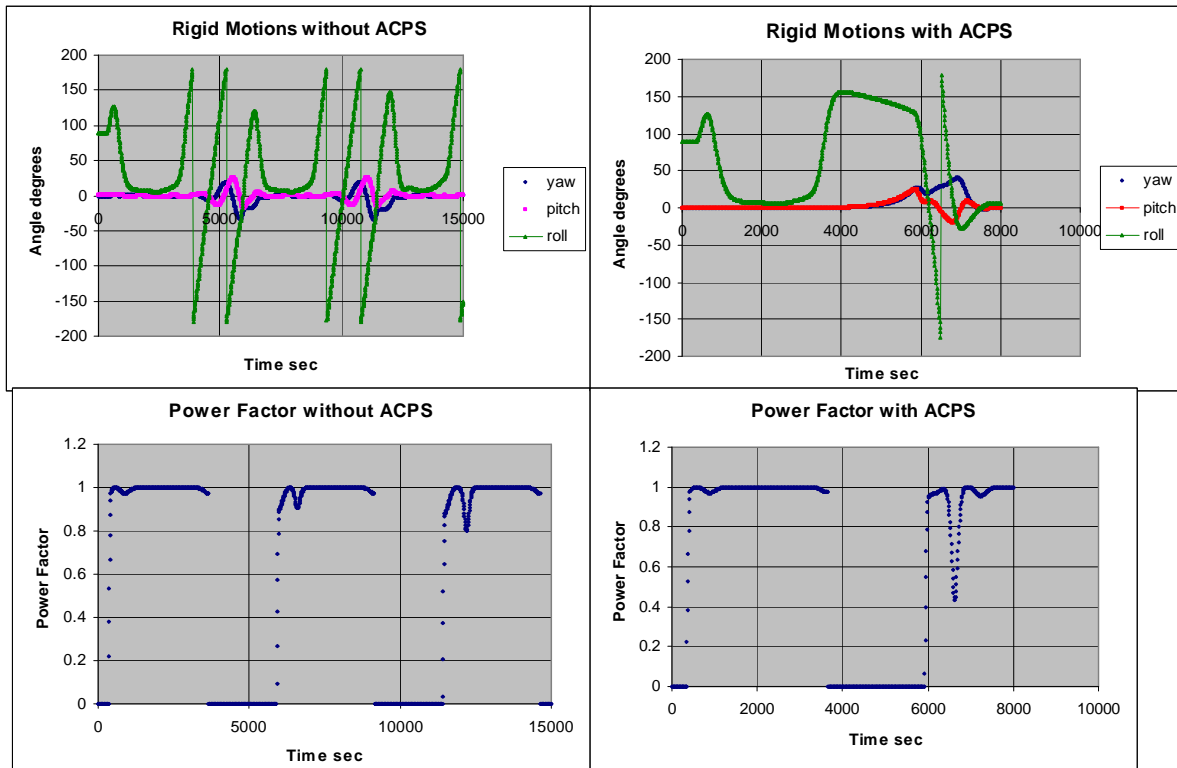


Figure 4: Effects of Attitude Control (Chemical) Propulsion on Flight Motions

On the left, command roll rate increases rapidly just before the vehicle goes into occultation. High roll rate commands occur when the vehicle is flying nearly towards or nearly away from the Sun. Array Sun orientation is mainly handled by array tilt, so roll errors have little effect on power factor, and power factor remains high despite considerable roll errors. However, upon entering Earth's shadow, thrust is discontinued and the high roll rate continues unaffected by commanded roll rate. The vehicle experiences approximately a complete spurious revolution. To reduce this motion, simulated chemical thrust was added. This thrust comes on whenever electric thrust is off, and is commanded only by roll rate negative feedback. The high roll rate is therefore attenuated upon entering shadow as seen on the right. Upon re-entering sunlight, the vehicle is flying nearly towards the Sun and another high roll rate occurs. There is some coupling with other axes and pitch and yaw excursions occur, but are damped out when the high roll rate is discontinued. Further adjustment of axis gains might reduce this effect. Power factor is relatively good in either case. The use of chemical propulsion, even though limited, results in significant propellant consumption. Figure 5 shows a typical mass history over several orbits.

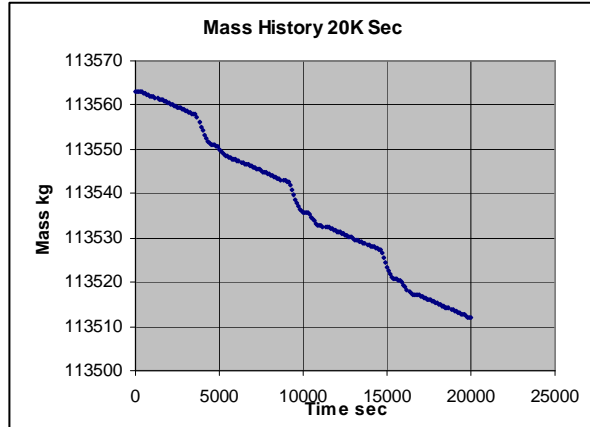


Figure 5: Mass History with ACPS

For comparison with flexible cases, further rigid runs were made with the long, narrow W/H = 10 array. In this case, the thruster lateral offset was set at +/- 5 m rather than 2.5 used for the "square rigger" configuration. A 2+ day case was run to assess whether control could be retained over a large number of orbits. Orbit altitude results are shown in Figure 6. Increase in eccentricity occurs because occultation is occurring during the apogee pass.

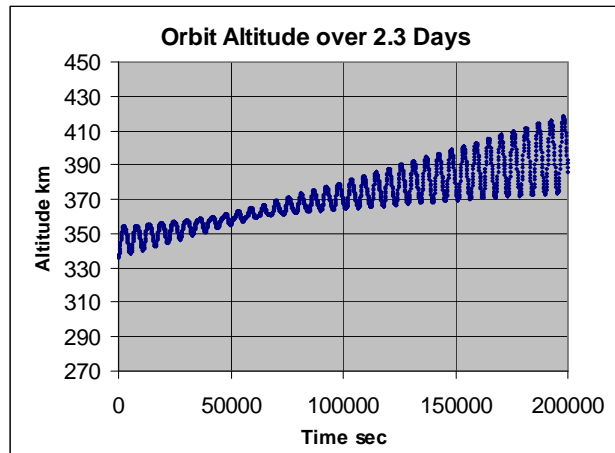


Figure 6: Orbit Altitude (Rigid Case)

VII. Flexible Array Simulation Description

A simplified model of a flexible array was used to develop the flexible simulation and is reported here. Later, a fully flexible model will be constructed. The simplified model had a 10-meter section of flexible array as a "spring" and a 90-meter rigid section as the "mass", as illustrated in Figure 7. The flexible section had the same mass stiffness as the fully flexible array. This simplified array model had a calculated natural frequency, attached to a fixed object, of 0.0024 Hz. This array was attached to a rigid core body. Motion of the array in the presence of core body rotation was visualized and modeled. Tests of the model were run to confirm the modeling before complete SEP simulations.

VIII. Flexible Array Simulation Tests

The first test did a single integration step of body roll, after which the body was fixed and the array allowed to respond. As shown in Figure 8, the numerically integrated response (after the usual debugging) exhibited the same natural frequency as analytically predicted.

Further tests were conducted to determine the response of the array to a constant applied body torque. The body begins to rotate, the flexible array lags, and torque on the rigid section of array builds up as the flexible section is bent by body motion. The array undergoes an oscillation about an overall body plus array rotation.

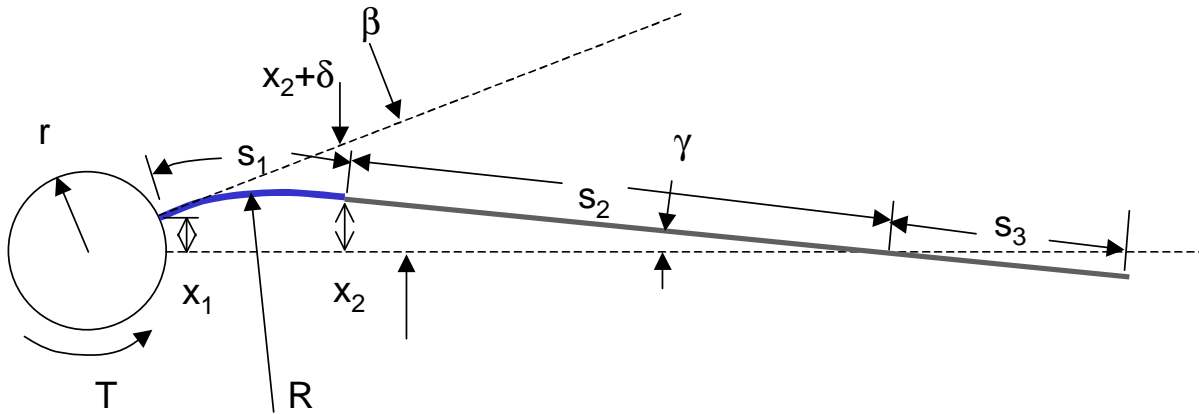


Figure 7: Diagram of Flexible Array Motion in Response to a Roll Increment. Flex Section in Blue. $S_2 = 2 S_3$

The frequency of this oscillation is much higher than that of the array attached to a rigid object. This was not anticipated, but should have been. The x-axis (rotational) moment of inertia of the rigid array section is about 20 times that of the rigid core body. Therefore, the oscillatory motion may be viewed as the rigid core body oscillating on the flexible spring sections of array, attached to a nearly fixed outer section of array. This motion is illustrated in Figure 9. The average roll position advances with the applied torque, and the instantaneous body roll position oscillates about the average. The oscillatory motion is greatly attenuated on the large rigid array section.

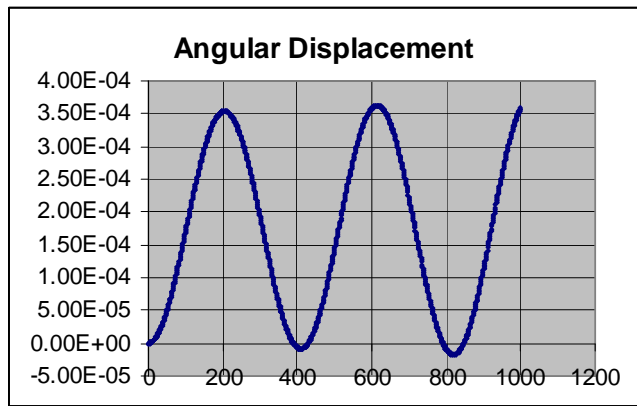


Figure 8: Oscillation Test

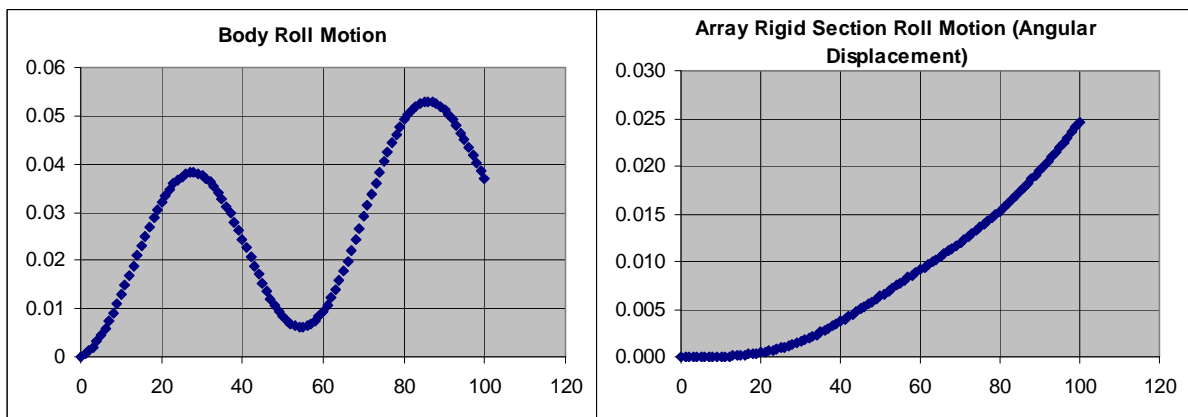


Figure 9: Test of Body and Array Roll Motion

IX. Flexible Array SEP Control Results

The simulated flexible array was then connected to the 6DOF simulation to analyze controllability of the large SEP. In addition to the simplification of the array flexibility, a further simplification was added in that the flexible motion simulation assumes the array is always in the x-y plane, whereas the array actually rotates about the y axis to track the Sun. This means that the flexible response is always maximum, since roll motion is about the x axis. Pitch and yaw motions in this current simulation are small compared to roll motions.

In the case of orbit raising with plane change, yaw motion can be more significant, since yaw steering is required to change the plane. The yaw motion in that case is like a sinusoidal oscillation in yaw attitude with one oscillation per orbit.

Figure 10 shows motions for the rigid case and the flexible case, for the same flight conditions. Figure 11 shows the motion of the rigid body and the flexible array; note that the array lags as would be expected but not greatly. Oscillations are not present and are apparently damped out by the negative rate feedback in the control law.

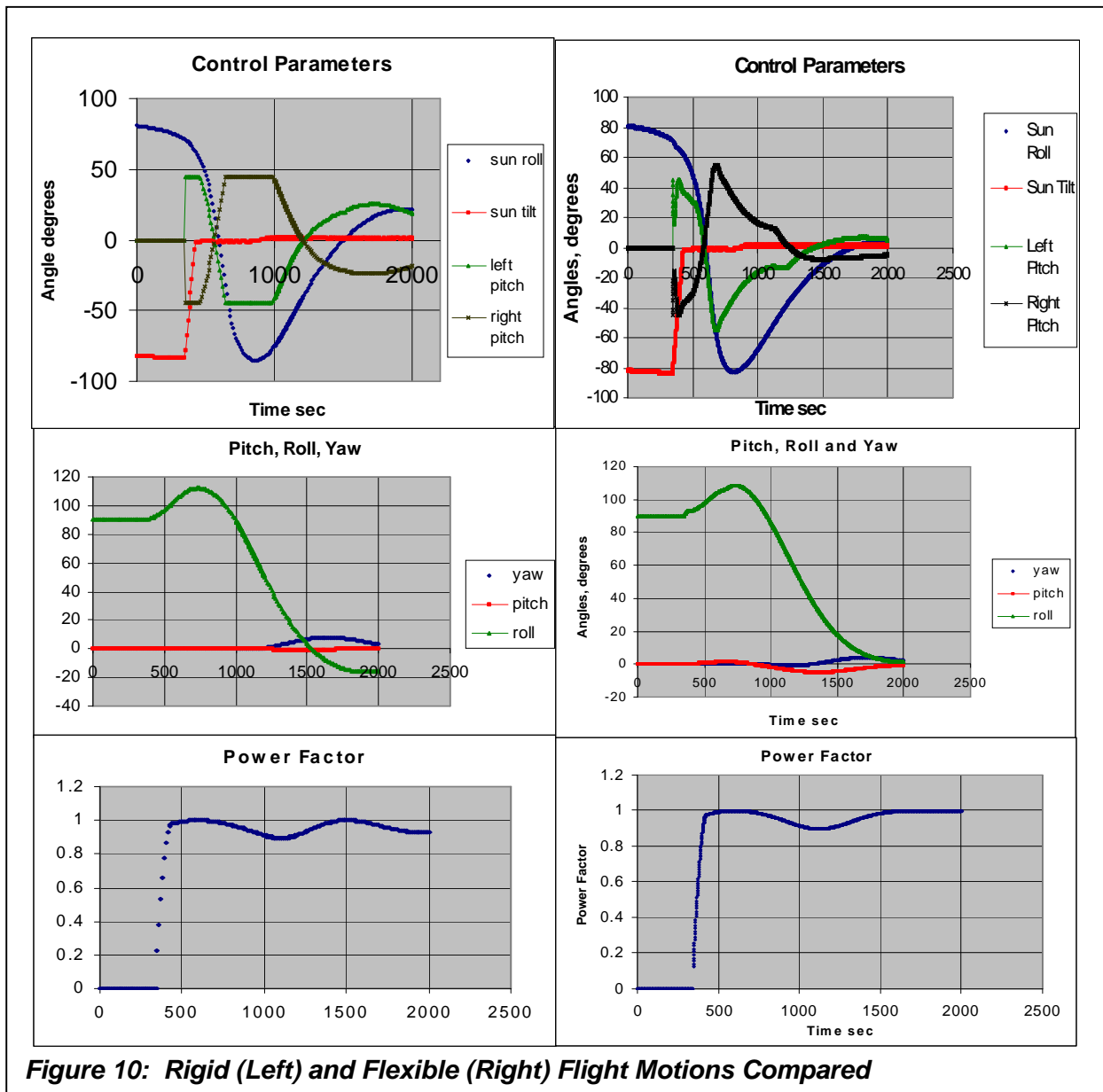


Figure 10: Rigid (Left) and Flexible (Right) Flight Motions Compared

X. Findings to Date

Results of this study at this point are tentative; it is a work in progress. The main results are three:

(1) Large SEP vehicles are controllable in low Earth orbit, at least enough so to perform orbit raising. The main control problem is roll maneuvers of large vehicles.

(2) Use of some chemical attitude control propulsion during occultation periods may be needed. Our results were somewhat inconclusive and need more investigation. If needed, the performance impact will be significant, due to propellant consumption at low Isp. See below regarding an anticipatory control scheme that could reduce or eliminate this problem. Also note that all control problems are ameliorated with altitude, since the orbit period is longer and maneuver rates are reduced.

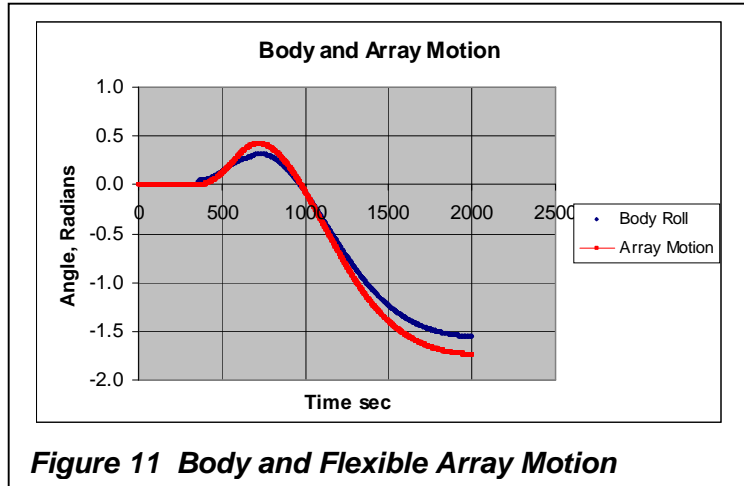


Figure 11 Body and Flexible Array Motion

(3) Large flexible arrays, at least up to about 500 kWe, even with very low natural frequencies, are controllable. The actuators (thrusters) and attitude sensors are on a central relatively rigid body, and flexible motions of large arrays appear as an external disturbance, which is controlled by negative rate feedback. The electric thrusters are feeble actuators, and even with very flexible arrays, do not introduce array attitude errors more than a few degrees. Electric propulsion systems do not require precise attitude control. Trajectory errors introduced by thrust vector errors can be compensated by GN&C. Array solar-pointing attitude is only a power function, and since the power loss is a cosine of the attitude error, errors of a few degrees are negligible.

(3) Large flexible arrays, at least up to about 500 kWe, even with very low natural frequencies, are controllable. The actuators (thrusters) and attitude sensors are on a central relatively rigid body, and flexible motions of large arrays appear as an external disturbance, which is controlled by negative rate feedback. The electric thrusters are feeble actuators, and even with very flexible arrays, do not introduce array attitude errors more than a few degrees. Electric propulsion systems do not require precise attitude control. Trajectory errors introduced by thrust vector errors can be compensated by GN&C. Array solar-pointing attitude is only a power function, and since the power loss is a cosine of the attitude error, errors of a few degrees are negligible.

XI. Issues and Future Work

Gain Tuning – Very little gain tuning was performed. Further effort could improve controllability and performance. Gains on the 3 axes were the same; variations here might prove fruitful.

Fully Flexible Array; Array Configuration – The flexible array model was crude. A fully flexible array needs to be modeled and simulated. Only two array configurations were tried. Concept design studies relating ease of array deployment and array mass versus configuration and stiffness should be performed, with simulation of the most promising concepts to ensure that they are controllable and provide adequate overall flight performance.

Correct Modeling of Flexible Array Attitude – The flexible array was modeled as always in the x-y plane. This appears to be a worst case. It is not, of course, accurate, since the array is tilted to face the Sun. A higher fidelity model needs to be constructed and exercised to account for actual array attitude versus time, its actual flexible response to body torques applied by the thrusters, and overall influence on flight control and performance.

Anticipatory Controller – The typical proportional-differential controller simulated here is designed to respond reactively to unpredictable disturbances. Command roll attitude in an orbit is, of course, highly predictable. In this situation of a large vehicle hard to maneuver, a better control system would anticipate required maneuvers, especially where high rates are demanded, and initiate response to the anticipated requirement before the requirement appears as an attitude error. Maximum rates and overshoots could be reduced, and better overall attitude performance achieved.

Yaw Steering – Orbit raising with plane change requires yaw steering to accomplish the plane change. This complicates the attitude control problem by adding another degree of freedom to required maneuvers. (The simulation already has all the degrees of freedom, but attitude commands, except to control pitch and yaw at zero, appear only for the roll axis.) Orbit raising with plane change needs to be simulated to determine whether the

additional degree of freedom on commands leads to attitude rate coupling on the various axes. Some of this is observed even in the present simulation.

Performance – Orbit raising performance was explored very little. There are potentially significant loss mechanisms, including off-pointing of the Sun and the thrust vector, and losses due to chemical propulsion used to control attitude during occultation periods. These need to be explored to obtain estimating relations and rules of thumb for overall performance prediction for large SEP vehicles, so that realistic performance analysis can be performed without necessity for detailed simulations.

Exploration of the Analysis Space – Finally, the large and complex analysis space (all the parameters, mission requirements, flight conditions, configurations, etc.) was only glimpsed. First, a reasonable plan for exploration of the analysis space needs to be created in order to do the important exploration as economically as practicable, and to neglect areas of exploration without significant impact. The plan needs to be executed to the level needed to obtain design guidelines for SEP mission analysis and design. When a specific system is designed and built, detailed simulation will be performed in depth for that system. What is needed now is enough work to facilitate performance estimates for conceptual and preliminary design, with reasonable confidence in results.

X. References

1. Gefert, Leon P., Hack, Hurt J., & Kerslake, Thomas W., “Options for the Human Exploration of Mars using Solar Electric Propulsion”, CP458, *Space Technology and Applications International Forum – 1999*, The American Institute of Physics.
2. Sarver-Verhey, Timothy R., Kerslake, Thomas W., Rawlin, Vincent K., Falck, Robert, Dudzinski, Leonard J., and Oleson, Steven R., Solar Electric Propulsion Vehicle Design Study for Cargo Transfer to Earth-Moon L1”, AIAA paper 2002-3791, *Joint Propulsion Conference 2002*.

Application of Solar Electric Propulsion to a Comet Surface Sample Return Mission

Mike Cupples[†]

*Science Applications International Corporation
Huntsville, Alabama 35806*

Victoria Coverstone* and Byoungsam Woo**

*University of Illinois at Urbana-Champaign,
Urbana, Illinois 61801*

Current NSTAR (planned for the Discovery Mission: Dawn) and NASA's Evolutionary Xenon Thruster based propulsion systems were compared for a comet surface sample return mission to Tempel 1. Mission and systems analyses were conducted over a range of array power for each propulsion system with an array of 12 kW EOL at 1 AU chosen for a baseline power level. Engine configurations investigated for NSTAR included 4 operational engines with 1 spare and 5 operational engines with 1 spare. The NEXT configuration investigated included 2 operational engines plus 1 spare, with performance estimated for high thrust and high Isp throttling modes. Figures of merit for this comparison include Solar Electric Propulsion dry mass, average engine throughput, and net non-propulsion payload returned to Earth flyby.

Introduction

With the success of the Deep Space 1 mission^{1,2}, the potential of Solar Electric Propulsion Systems (SEPS) was clearly demonstrated, making SEPS a strong candidate for various interplanetary missions. The long-duration, high-efficiency operation of SEPS allows new ways to explore the inner and outer solar system, and enables missions that can be difficult and expensive to reach with chemical propulsion systems. NASA has undertaken an ion propulsion system development program to create a new ion propulsion system based on NASA's Evolutionary Xenon Thruster³ (NEXT). This thruster is being developed through the NEXT Generation Electric Propulsion (NGEP) Technology Area⁴ office under the auspices of the In-Space Propulsion Technology Projects at Marshal Space Flight Center (MSFC). The NEXT based propulsion system has a higher maximum design power than NSTAR along with advances in both the power processing and the propellant management systems.

This paper provides a parametric comparison of NSTAR and NEXT propulsion systems based on a typical comet surface sample return (CSSR) mission^{5,6}. Specifically, the study compares SEPS based on the current NEXT and NSTAR thruster system designs. The NSTAR thruster chosen for this analysis is the thruster planned for NASA's Discovery Mission Dawn. A summary of mission and system assumptions is provided in the following sections. The primary Figures of merit (FOMs) employed to distinguish the NEXT and NSTAR propulsion system are the non-propulsion system mass returned to earth after completing all mission requirements, average engine throughput,

[†] Systems Engineer, In-Space Technology Assessment Lead, Science Applications International Corporation, 6725 Odyssey Drive, Huntsville, AL 35806

* Associate Professor, Department of Aeronautical and Astronautical Engineering, 306 Talbot Laboratory, 104 S. Wright Street, Urbana, IL 61801, Member AAS, Associate Fellow AIAA

** Graduate Student, Department of Aeronautical and Astronautical Engineering, 306 Talbot Laboratory, 104 S. Wright Street, Urbana, IL 61801

and SEP system dry mass. Other key FOMs, not considered in this study but expected to in general favor NEXT, are cost and complexity of the SEPS.

Previous studies have investigated the application of NEXT to flagship class missions^{7,8,9} such as Titan Explorer and Neptune Orbiter. A recent study¹⁰ provides an analyses summary of current applications of the NEXT thruster to deep space missions. The study herein compares the NSTAR and NEXT propulsion systems within the context of a New Frontiers class mission¹¹. A comet sample return mission to Tempel 1 was chosen for this study because it is a challenging mission that could probably be performed within the New Frontiers cost cap and should demonstrate the efficiency of SEPS.

Current electric propulsion (EP) technologies were applied to the CSSR mission. The parametric study consisted of investigating the performance of the propulsion systems over a range of power levels, number of operational thrusters, and thruster throttling modes. For the NSTAR system, cases investigated included four and five operational thrusters with one spare. This variation in thruster number allowed a determination of best performance based on a baseline array power of 12 kW. For this same baseline power, cases with two NEXT thrusters were explored. High thrust throttling and high Isp throttling were investigated in the NEXT cases to provide an evaluation of performance over the projected operational throttling envelope of the thruster.

Mission Assumptions.

A summary of mission assumptions are as follows:

- 1) Mission Type – Comet surface sample return
- 2) Target – comet Tempel 1
- 3) Launch Date – 2008 Earth Departure
- 4) Stay Time @ Target – 60 days
- 5) Sample returned to Earth – SEPS delivers sample return capsule to Earth direct entry

The payload is defined in this study as two parts: 1) 50 kg of mass that remains at the comet and 2) the net non-propulsive mass that is returned to Earth. This net return mass consists of the comet sample, comet sample return capsule with concomitant mechanisms, and the remaining spacecraft mass (e.g. subsystem including navigation instruments, communication instruments, science instruments, structure, power, and thermal).

Figure 1 depicts orbits of the Earth and comet Tempel 1 around the sun. The primary objective of the mission is for the spacecraft to rendezvous with Tempel 1, collect a sample, and return the sample to Earth. A launch vehicle will place the SEPS spacecraft on an optimal Earth escape trajectory, and the SEPS propulsion will provide an optimal transfer to rendezvous with Tempel 1 and also provide return propulsion for a flyby of Earth at sample delivery.

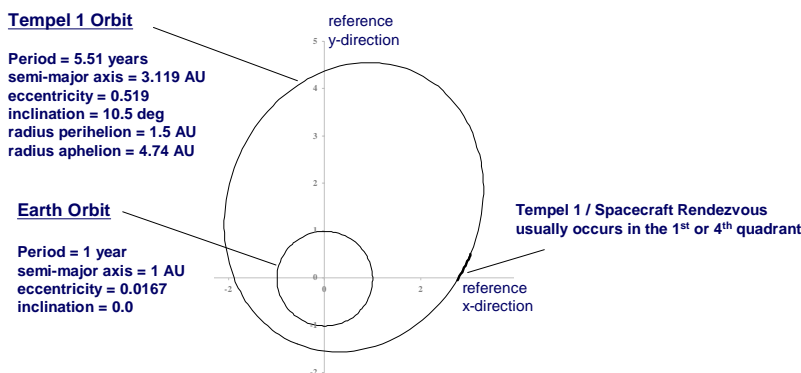


Figure 1 Earth and Tempel 1 Solar System Orbit Depiction

Systems Assumptions

Launch Vehicle. The launch vehicle¹² (LV) chosen for this investigation was the Delta IV 4040. This LV is the smallest Delta medium class LV, and matches well the low cost objective of a New Frontiers class sample return mission. The LV modeling details that were included in the trajectory optimization process are provided below in Figure 2. This study assumed a LV margin of 0%.

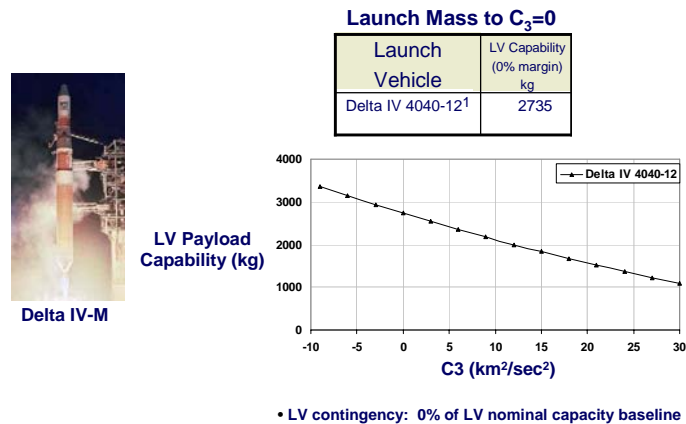


Figure 2 LV performance model

Solar Electric Propulsion. Detailed SEP system models were developed and utilized to perform the analyses conducted in this study. The system models for each case of this study include power and power conversion/distribution, thrusters, power processing units, propellant management and tank, structures, and thermal control. SEP system models are either physics based models or models derived from scaling of actual spacecraft data. For example the SEPS structure model was derived from a spacecraft database including Cassini, Galileo, Mars Global Surveyor, Near, Odyssey, and Mars Climate Orbiter. A detailed summary of the system models is provided in Figure 3.

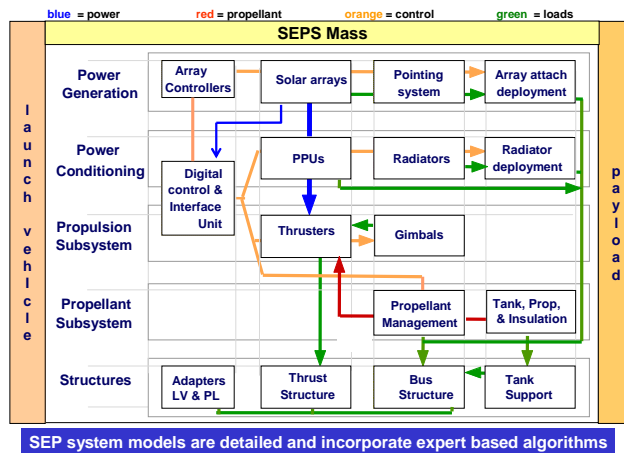


Figure 3 SEP System Model Depiction

The propulsion configurations investigated are shown in Figure 4 below. The propulsion system duty cycle of 90% implies that the propulsion system will be thrusting for 90% of the total time of the transfer to and from the comet. This transfer time does not include the 60 day comet stay.



Figure 4 Thruster, PPU, and PMS systems analysis assumptions

The NSTAR thruster, sometimes termed the Qmod-NSTAR, is based on Molybdenum gridded ion optics. The NEXT thruster is based on Molybdenum gridded ion optics as well.

System Power. The solar arrays were assumed as the only source of propulsion power for the system (other than battery power during solar array deployment). The array power model employed in the trajectory optimization task is multi-junction GeAs array technology¹³ with Ultraflex light weight array design¹⁴. The performance of this solar array technology is slightly below $1/r^2$ solar insolation.

The Ultra-Flex array concept is depicted in Figure 5. Other necessary power system modeling assumptions are shown in Figure 5 as well.



Figure 5 Solar array system modeling assumptions

Other Assumptions. Several other systems assumptions including Xe propellant contingency, systems dry mass contingency, redundancy, and ACS are summarized in Table 1.

Table 1 Miscellaneous systems analysis assumptions

Contingency	Propellant: 10% of Xe deterministic, NSTAR (Dawn Mission Assumption) 8.6% of Xe deterministic, NEXT (NGEP Program Assumption) Dry Mass: 30% of current best estimate
Redundancy	One extra ion system (thruster, PPU, propellant distribution string, and DCIU)
ACS	ACS provided by IPS during low thrust burn ACS provided by RCS during periods when IPS is not active

In this phase of analysis, work to delineate the spacecraft mass with the concomitant instruments and mechanisms to make a successful comet sample return is incomplete. Further spacecraft definition is expected to be performed in the near future to address this need.

Trajectory Optimization

Trajectory optimization with variable thrust and thrust direction has been previously investigated^{15,16,17}. The solution typically requires the optimization a number of parameters. For the case investigated, the final delivered mass to Earth return is maximized.

Trajectory optimization was performed using Solar Electric Propulsion Trajectory Optimization Program (SEPTOP)¹⁸. SEPTOP is a two-body, Sun-centered, low-thrust trajectory optimization program for preliminary mission feasibility studies that provides relatively accurate performance estimates. The program determines a numerical solution to a two point boundary value problem that satisfies intermediate boundary constraints. In SEPTOP, the user estimates initial conditions, and then uses a shooting method to integrate the trajectory from an initial time to final time. SEPTOP computes an error at the final time and uses it to correct the estimate of the initial conditions. This process is repeated until the error becomes smaller than the prescribed tolerance. The required inputs are Time-of-flight, nominal Earth departure, array power at Earth departure, maximum power into Power Processing Unit (PPU), intermediate rendezvous body (in this case comet Tempel 1), and LV specifications. SEPTOP can model variable thrust and mass flow rate as a function of power into the PPU. The power generated from a solar array is modeled as a function of the spacecraft's distance from the Sun. Thruster and solar array models are therefore also required as inputs.

Performance Comparison

Figure 6 shows a typical Tempel 1 roundtrip comet sample return trajectory. This trajectory, based on an optimized NEXT high thrust throttling mode, required approximately 8 years in total transfer time. The salient trajectory features include the following:

- 1) LV assisted Earth departure to a C3 of $\sim 14.3 \text{ km}^2/\text{sec}^2$
- 2) SEPS assisted transfer to rendezvous with Tempel 1 ~ 1276 days
- 3) 60 day stay at Tempel 1, during which a sample is taken from the comet and returned to the spacecraft
- 4) SEPS assisted return to an Earth flyby to allow sample return to Earth ~ 1687 days

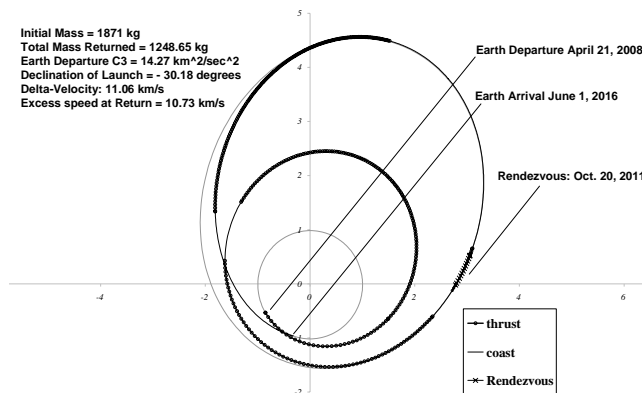


Figure 6 Typical comet surface sample return trajectory

Derived results for this example trajectory are as follows: SEPS wet mass = 1249 kg, SEPS dry mass = 623 kg, total payload (not including the 50 kg remaining at the comet) = 622 kg and the average engine throughput = 308 kg.

Variation in Performance Due to Array Power and Operational Thrusters. Two case studies of payload vs array power are depicted in Figures 7 and 8. For the first case, Figure 7 shows the result of varying the number of operational propulsion strings (thruster, ppu, and propellant distribution and control). Given that five thrusters at a maximum power each of 2.567 kW implies a maximum power usage of over 12.8 kW at 1 AU, the 5+1 configuration allows the system to utilize all of the available array power (minus housekeeping) at 1 AU. Four thrusters at a maximum power each of 2.567 kW implies a maximum power usage of less than 10.3 kW at 1 AU which implies that the 4+1 configuration does not permit the full array power to be utilized at 1 AU. Yet as Figure 7 shows, the NSTAR 4+1 configuration performed modestly better than the 5+1 configuration due to the overpowering increase in dry mass for the 5+1 case.

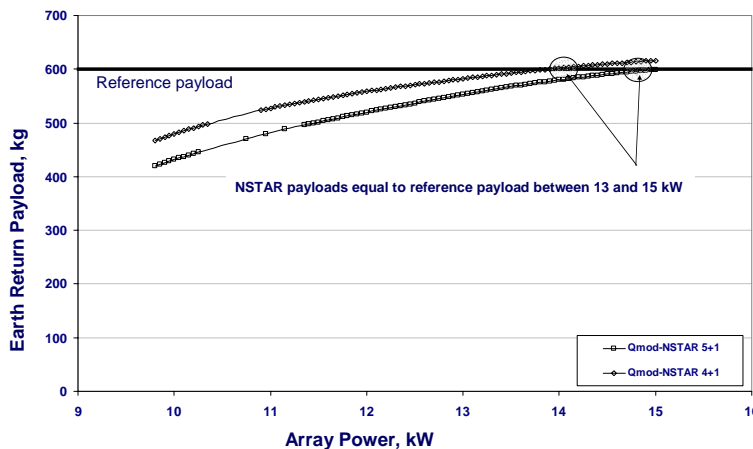


Figure 7 NSTAR payload for a range of array power and engine configuration

The second case study investigated the difference in performance between the NEXT high thrust and high Isp throttling modes, with further comparison to the NSTAR thruster. Notice from Figure 8 that the NSTAR and NEXT performance begins to diverge at 10 kW of array power. The High thrust throttling mode and the high Isp throttling mode show a crossover in performance at approximately 12 kW, with the high thrust throttling mode providing a slight performance benefit over the high Isp mode at power levels above 12 kW. Hence the choice of 12 kW as a baseline power level to perform much of the analyses of this study. In general, the NEXT thruster

performed better than NSTAR over the range of power investigated in this study, with NEXT providing ~ 60 kg more payload over NSTAR at 12 kW array power.

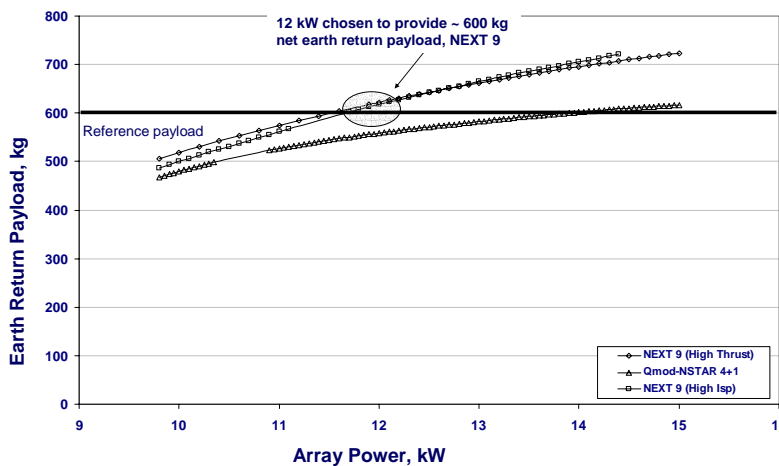


Figure 8 NEXT and NSTAR payload comparison over a range of array power

Detailed Comparison of Payload Delivery Performance at Baseline Array Power. A comparison of NSTAR and NEXT was performed at a power level of 12 kW. 12 kW was chosen as a baseline power to perform this analysis for two reasons: the first is that this power level corresponds to a little more than 600 kg of Earth return payload for NEXT and is near a cross-over in payload between high thrust throttling and high Isp throttling; the second reason for the 12 kW baseline array power is that a NEXT phase 1 study was performed at 12 kW, thus allowing the study herein to relate to earlier studies with some continuity.

An overall stack mass comparison is shown in Figure 9. The case of NSTAR with a 4+1 engine configuration delivers over ~ 559 kg to Earth, as compared to 520 for the 5+1 engine configuration. The NEXT cases using the high thrust throttling mode deliver about 622 kg to Earth return, and the cases utilizing the high Isp throttling mode deliver approximately 618 kg to Earth return. Thus, for the Tempel 1 CSSR mission, both NEXT cases showed significant improvement over NSTAR in payload delivery capability. Also this NEXT payload delivery was realized with a 2+1 engine configuration that may imply significant cost and complexity benefits over the 4+1 NSTAR configuration.

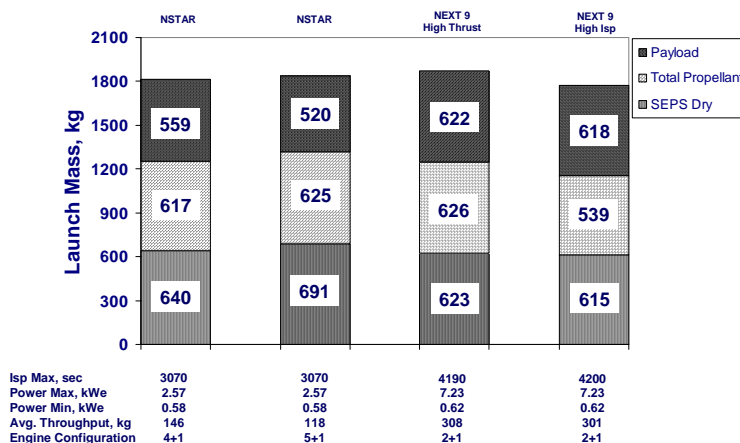


Figure 9 Comparison of mission stack mass for NEXT and NSTAR

In addition to the payload FOM, SEPS dry mass and average engine throughput is shown in Figure 9. In general, the NEXT SEPS is less massive than NSTAR SEPS because of the lower number of propulsive strings required to perform the mission. In all NSTAR cases and in the NEXT high Isp case, the average engine throughput is less than the engine design requirements of 150 kg and 300 kg respectively. The NEXT high thrust throttling mode case exceeded the throughput design requirement by approximately 8 kg.

Multi-Engine Operation and Power Available to IPS Time Histories. Figures 10, 11, and 12 show engine on-off time histories with their corresponding ion propulsion system power levels for each of the cases identified in Figure 9 above. For each case, the array power level is 12 kW at 1 AU, and the transfer time is approximately 8.1 years. These graphs provide power profiles as a function of mission time, and facilitate a determination of how well the ion propulsion system is utilizing the power during the course of the mission.

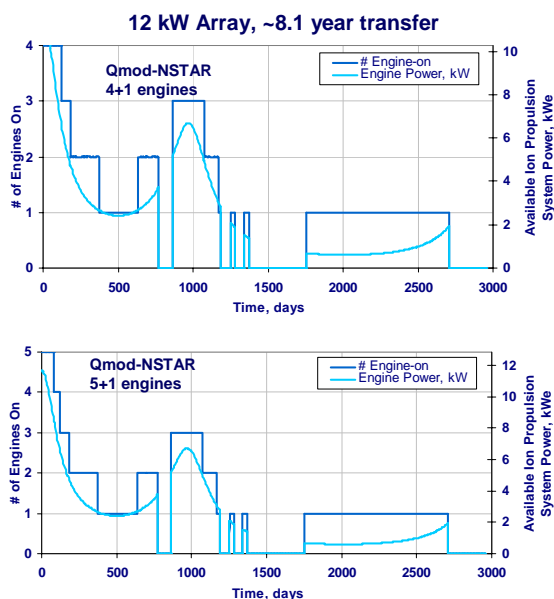


Figure 10 NSTAR engine operation and propulsion system power time history

NSTAR 4+1 and 5+1 engine configurations are compared in Figure 10. During most of the mission, three or less thrusters are required, and for only a short time during the beginning of the mission, 4 or 5 thrusters are in operation. Thus, Figure 11 provides some corroborating evidence for the better performance seen earlier for the 4+1 configuration, given that for the 5+1 configuration the very small increase in overall power utilization improvement is overcome by the relatively large increase in system dry mass. In addition, given that 4 thrusters (or 5 thrusters, depending on the case) are needed for only a short time during the beginning of the transfer, it would be possible to eliminate the spare thruster (along with the related mass) and operate without a spare during the first part of the mission. This operation would, however, significantly increase the mission risk. A similar argument could be made for the NEXT 2+1 configuration shown in Figures 11 and 12, but mission risk would increase as well.

A comparison of the NSTAR 4+1 configuration with the NEXT high thrust and high Isp throttling modes are provided in the following graphs, Figures 11 and 12. . In general, the NEXT and NSTAR engines can operate at high AU because the minimum thruster power level for each thruster is 0.62 kW and 0.58 kW respectively. This high AU operation can be seen in Figures 11 and 12 for the mission phase between approximately 2000 sec and 3000 sec.

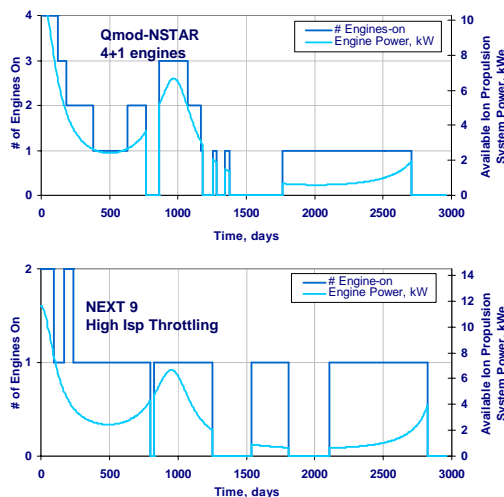


Figure 11 Engine and power time history comparison for NEXT high Isp Throttling and NSTAR

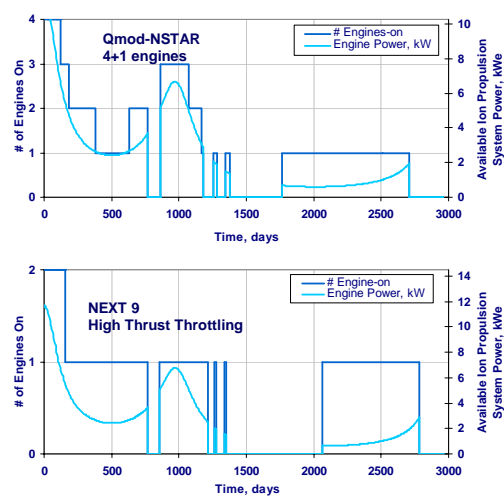


Figure 12 Engine and power time history comparison for NEXT high thrust throttling and NSTAR

As seen in the previous results of Figure 9, the performance of NEXT high thrust throttling is somewhat better than NEXT high Isp throttling. A clue to the performance difference can be found in a comparison of NEXT high thrust throttling and high Isp throttling as seen in Figure 11 and 12. Figures 11 and 12 indicate one obvious difference in overall mission profile. The difference occurs before approximately 250 days into the mission, and can be seen in Figure 11 as a transitioning of the high Isp system from two thrusters to one thruster to two again, and then back to one thruster; for the remainder of the mission, the thrusters transitioned between one and zero thrusters. During this same time in the mission and shown in Figure 12, the high thrust system transitions from two thrusters to one thruster, and then transitions between one or zero thrusters throughout the remainder of the mission. In terms of available power to the ion propulsion system, the high thrust throttling case shows a smooth transitioning of thrusters from two to one as the available power varies from higher to lower power; the high Isp case demonstrates a less smooth transitioning of thrusters over the same power level changes. To understand the difference in operation between the thrusters, it must be understood that for a given power level, an engine operating in the high thrust throttling mode generates a higher thrust level than the same engine operating in the high Isp throttling mode. It is also true that for a given power level (where that power level is low enough that either one or two engines can operate simultaneously) the thrust generated by two engines equally dividing the total available power can be more

than the thrust generated by one engine alone operating at the same total available power. Thus, during the first 250 days of the high Isp mission, the trajectory optimizer found that during a part of the trajectory two thrusters operating at higher thrust was more critical in maximizing the earth return payload than one thruster operating at higher efficiency. During the same 250 days of the high thrust mission, the higher thrust provided by the high thrust throttling mode was adequate, and thus the optimizer found that throttling back to two thrusters was not required.

Summary and Conclusions

NSTAR and NEXT based propulsion systems were compared for a comet surface sample return mission to Tempel 1. A range of array power was investigated for each propulsion system, and 12 kW EOL at 1AU was chosen as a baseline array power for this analysis. Engines configurations investigated for NSTAR included 4+1 and 5+1 engines, and the NEXT configuration only included a 2+1 case. For NSTAR, it was found that the 4+1 engine configuration provided modest performance advantage over the 5+1 configuration. The NEXT 2+1 configuration was then compared to the NSTAR 4+1, with a small performance advantage going to the NEXT thruster. It should be noted, however, that the NEXT 2+1 SEPS configuration is lighter in dry mass and less complex in hardware implementation, resulting in an expected significantly less costly SEPS vehicle than the NSTAR 4+1 SEPS vehicle. In both the NEXT and NSTAR cases, a power/engine-on time history showed smooth variation in thruster on-off sequences following the available power to the IPS. Due to the rather low minimum throttle points of 0.62 kW and 0.58 kW for NEXT and NSTAR respectively, the thrusters performed effectively at the higher AU points of the trajectories. It was found for NSTAR that 4 thrusters are needed for only a short time during the beginning of the transfer. Thus, it would be possible to eliminate the spare thruster (along with the related mass) for the mission, but the mission risk would increase significantly. A similar argument could be made for the NEXT 2+1 configuration, but mission risk would increase as well. Finally, engine throughput for NEXT and NSTAR are within the accepted assumed limits of 300 kg for NEXT and 150 kg for NSTAR for all cases investigated except for the NEXT high thrust throttling case.

Acknowledgements

The work described in this paper was performed by Science Applications International Corporation (SAIC) under contract with the NASA Marshall Space Flight Center (MSFC). Special thanks go to Les Johnson, manager of NASA MSFC In-Space Propulsion Technology Investment Projects, and Randy Baggett, manager of NASA MSFC Next Generation Electric Propulsion Technology Area, for providing direction for this work.

References

- ¹ Rayman, M. D., and Williams, S. N., "Design of the First Interplanetary Solar Electric Propulsion Mission," *Journal of Spacecraft and Rockets*, Vol. 39, No. 4, 2002, pp. 589-595
- ² Rayman, M. D., Chadbourne, P. A., Culwell, J. S., and Williams, S. N., "Mission Design for Deep Space 1: A Low-Thrust Technology Validation Mission," International Academy of Astronautics, Paper L98-0502, April 1998.
- ³ Michael J. Patterson, John E. Foster, Thomas W. Haag, and George C. Soulas, "Next: NASA'S Evolutionary Xenon Thruster Development Status," 39th Joint Propulsion Conference, AIAA 2003-4862, Huntsville, AL, July 2003.
- ⁴ Johnson, C.L., Alexander, L., Baggett, R.M., Bonometti, J.A., Herrmann, M., James, B.F., Montgomery, S.E., "NASA's In-Space Propulsion Technology Program: Overview and Status," 2004 JANNAF, Las Vegas, NV, May 2004.
- ⁵ Tan, G.H., Sims, J.A., "Mission Design for the Deep Space 4/Champlion Comet sample Return Mission," AAS 98-187, AAS/AIAA Space Flight Mechanics Meeting, Monterey, CA, February, 1998.
- ⁶ Sims, J.A., "Trajectories to Comets Using Solar Electric Propulsion," AAS 2000-134, AAS/AIAA Space Flight Mechanics Meeting, Clearwater, FL., January 2000.
- ⁷ Cupples, M.L., Green, S.H., Coverstone, V., "Factors Influencing Solar Electric Payload Delivery to Outer Planet Missions," 2003 AAS/AIAA Space Flight Mechanics Conference, AAS 03-123.
- ⁸ Cupples, M., Green, S., Donahue, B., Coverstone, V., "Solar Electric and Chemical Propulsion for a Titan Mission," 39th Joint Propulsion Conference, AIAA 2003-4728, July 2003.

-
- ⁹ Byoungsam, W., Coverstone, V., Hartmann, J., Cupples, M., "Trajectory and Systems Analysis for Outer Planet Solar Electric Propulsion Missions," *Journal of Spacecraft and Rockets*, pending publication, 2004.
- ¹⁰ Oh, David., Sims, J., Benson, S., Gefert, L., Witzberger, K., Cupples, M., "Deep Space Applications of the NEXT Thruster," 40th Joint Propulsion Conference, AIAA 2004- , Ft. Lauderdale, FL., July 2004.
- ¹¹ <http://centauri.larc.nasa.gov/newfrontiers/>
- ¹² <http://elvperf.ksc.nasa.gov>
- ¹³ T. Kerslake, "Photovoltaic Array Performance during an Earth-to-Jupiter Heliocentric Transfer," NASA Glenn Research Center, PS-496, Aug. 2000.
- ¹⁴ <http://www.aec-able.com/arrays/ableultraflex.html>
- ¹⁵ Sauer, C. G., "Optimization of Multiple Target Electric Propulsion Trajectories," AIAA 11th Aerospace Sciences Meeting, AIAA Paper 73-205, Washington, DC, Jan. 1973
- ¹⁶ Melbourne, W. G., Richardson, D. E., and Sauer, C. G., "Interplanetary Trajectory Optimization with Power-Limited Propulsion Systems," Jet Propulsion Laboratory, TR No. 32-173, Pasadena, CA, 1962.
- ¹⁷ Williams, S. N., and Coverstone, V. L., "Mars Missions Using Solar Electric Propulsion," *Journal of Spacecraft and Rockets*, Vol. 37, No. 1, 2000, pp. 71–77.
- ¹⁸ Williams, S. N., "An Introduction to the use of VARITOP A general purpose low-thrust trajectory optimization program," Jet Propulsion Laboratory, JPL D-11475, Pasadena, CA, 1994.

Trailing Ballute Aerocapture: Concept and Feasibility Assessment

Kevin L. Miller[‡], Doug Gulick^{**}, Jake Lewis[†], Bill Trochman
Ball Aerospace & Technologies Corp., Boulder, CO

Jim Stein*
ILC Dover, Inc., Frederica, DE

Daniel T. Lyons *
Jet Propulsion Laboratory, California Institute of Technology, Pasadena, CA

Richard G. Wilmoth*
NASA Langley Research Center, Hampton, VA

Trailing Ballute Aerocapture offers the potential to obtain orbit insertion around a planetary body at a fraction of the mass of traditional methods. This allows for lower costs for launch, faster flight times and additional mass available for science payloads. The technique involves an inflated ballute (balloon-parachute) that provides aerodynamic drag area for use in the atmosphere of a planetary body to provide for orbit insertion in a relatively benign heating environment. To account for atmospheric, navigation and other uncertainties, the ballute is oversized and detached once the desired velocity change (ΔV) has been achieved. Analysis and trades have been performed for the purpose of assessing the feasibility of the technique including aerophysics, material assessments, inflation system and deployment sequence and dynamics, configuration trades, ballute separation and trajectory analysis. Outlined is the technology development required for advancing the technique to a level that would allow it to be viable for use in space exploration missions.

keywords: aerocapture, inflatable, thin-film structures, rarefied flow, direct simulation monte carlo (DSMC)

[†] Member AIAA

* Co-Investigator, Member AIAA

** Currently at Lockheed Martin, Member AIAA

[‡] Principal Investigator, Member AIAA

Nomenclature

Kn	Knudsen number
M	Mach number
p	pressure
q	heating rate

Introduction

The application of inflatable film systems for aeroassist maneuvers has been employed in system concepts for about 40 years¹. However, recent advances in inflatables technologies promise significant improvements in system performance and substantial reductions in risk. These advances provide the basis for renewed interest in ballute system technology development. A team consisting of Ball Aerospace & Technologies Corp., ILC Do-

ver, Inc., Jet Propulsion Lab, and Langley Research Center has been engaged over the past 2 years developing critical technologies and analyses for the use of balloon-parachutes (ballutes) for capture in a planetary orbit using the atmosphere to generate aerodynamic drag, thus slowing the system to capture into a desired orbit. Using specific impulse as a means of illustrating performance relative to other technologies, such as chemical propulsion, ballutes provide up to 1200 s impulse, yet retain scalability over a large range of spacecraft size without significantly constraining the spacecraft operations or configuration. For an orbital mass of 1000 kg and a delta V of 1 km/s, this results in an increase in payload mass (or a reduction of launch mass) of over 350 kg.

This paper addresses critical issues for implementation of the technology, mission design constraints, configuration concepts and overall performance characteristics, including results of aerothermal and aerostability analyses, guidance algorithm design and performance,

Copyright © 2003 by Ball Aerospace & Technologies Corp. Published by the American Institute of Aeronautics and Astronautics, Inc. with permission.

and overall system characteristics. The efforts to date have focused on capture at Mars and Titan. Future efforts will include detailed analysis of Neptune mission options.

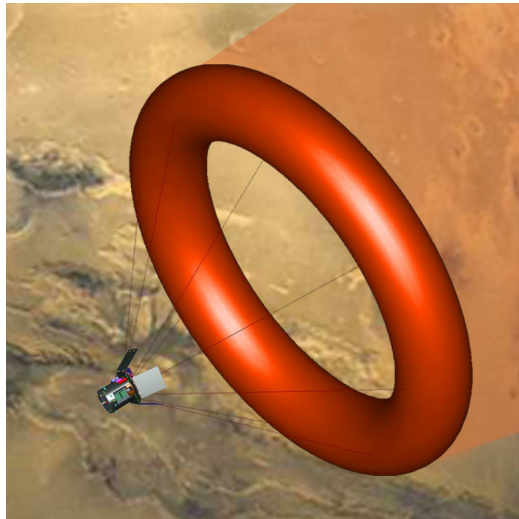


Fig. 1: Ballute aerocapture provides orbit insertion with small influence on spacecraft design and a mass fraction of less than 25 percent, saving hundreds of kilograms as contrasted with traditional techniques.

Mission Concept

Ballute technology can be applied with many configuration options and design approaches, but the overall mission concept investigated in this paper begins with the material limitations of the ballute system, and establishes mission designs that are compatible with these limitations. More specifically, the design logic illustrated in Figure 1 is employed to define primary characteristics and limitations of the flight system.

The flight system is launched with the inflatable system stowed, and remains in this configuration throughout most of cruise. A candidate aerocapture sequence for a Titan mission is illustrated in Table 1 and Figure 2. As shown, a day or so prior to the projected atmospheric entry interface, the ballute system is deployed and inflated, allowing ample time for damping of deployment dynamics and verification of the entry configuration. A final trajectory correction maneuver may be conducted shortly before entry to minimize the delivery error term. Although attitude error and atmospheric instabilities perturb the flight system, the restoring moment with the trailing ballute is so large that static aerodynamic stability is not a major issue. The periapsis is targeted to keep peak heating rates within the ballute material limits for the drag modulated atmospheric pass. The ballute drag area is sized to provide sufficient delta velocity to capture in the desired orbit. As discussed in Guidance and Separation Performance, the on-board computer and

accelerometers are used to calculate a point for separation of the ballute system based on the projected delta V of the towing spacecraft at atmospheric exit. After commanding a pyro-initiated separation, the towing spacecraft completes a ballistic trajectory to the atmospheric exit point. A propulsive burn is conducted at apoapsis to raise periapsis out of the atmosphere.

Three of the key challenges to be faced in the development of an aerocapture mission are: (1) navigation, trajectory management, and atmospheric characteristics, (2) aerostability of the spacecraft during the aeropass, including deployments and aeroelastic response of the system to hypersonic environments, and (3) development of spacecraft systems capable of sustaining the very high heating rates and aerodynamic forces of aerocapture, without sustaining excessive impact on the overall mission.

Table 1: Aerocapture Event Timeline

	Event	Time*	Comment
	TCM-3		Target Entry Probe
	Release Probe	E-30 days	
	TCM-4		Target Orbiter Arrival
Approach	Tracking & Orbit Determination		
	Data Cutoff	E-2 days	
	TCM-5	E-1 day	Correct Orbiter Arrival
	Tracking & Orbit Determination		
	TCM-6 (optional)	E-6 hrs.	Orbiter "Tweak"
	Deploy Ballute	E-5 hrs.	
	Data Cutoff	E-3 hrs.	
	Final Uplink	E-1 hr.	
Drag Pass	Enter Atmosphere	E-0	
	Max Heat Rate	E+169 sec.	On Ballute
	Max Dynamic Pressure	E+185 sec.	On Ballute
	Release Ballute	E+231 sec.	
	Lowest Altitude	E+783 sec.	405 km
	OA-0 (optional)		Drag Makeup Maneuver
	Exit Atmosphere	E+3263 sec.	
In Orbit	OA-1	E+8000 sec.	Periapsis Raise
	OA-2	E+17185 sec.**	Circularize Orbit

* - Times after atmosphere entry are representative and are taken from the `frmm_high` case.

** - Time of burn is highly variable due to variation in apoapsis and is only performed if necessary.

Aerocapture offers significant benefit for eight planetary bodies in the solar system: Venus, Earth, Mars, Jupiter, Saturn, Titan, Neptune and Uranus. The following figures show a comparison between two representative aerocapture trajectories: one for Mars and one for Titan. The 5.5 km/sec entry speed for the Mars trajectory is representative for a direct Earth to Mars type 1 trajectory launched in 2005. The 6.5 km/sec entry speed for the Titan trajectory is representative of a Solar Electric Propulsion trajectory with a single Venus flyby and a flight time of about 7 years². Table 2 specifies the key parameters for each trajectory.

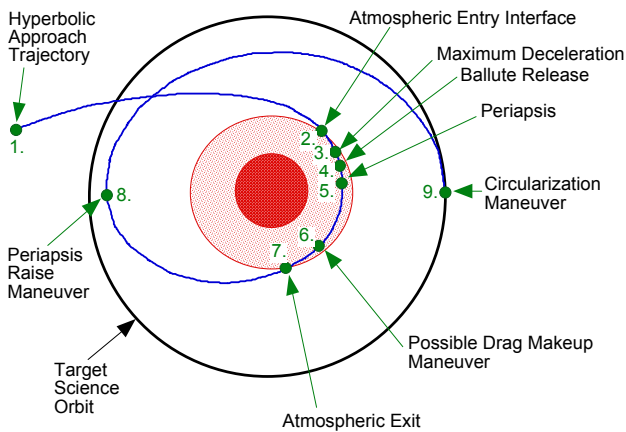


Figure 2: Sequence of Events for a Representative Ballute Aerocapture

Table 2: A Comparison of Key Mission Parameters

Parameter	Mars	Titan
Entry Mass (kg)	400	500
Ballute Mass (kg)	25	41
Area with Ballute (m ²)	300	751
Area without Ballute (m ²)	2	3.8
Entry C _d	1.7	1.7
S/C C _d	1.8	2.3
Entry Speed (km/sec)	5-6	6-8
Max. Allowable Qdot (W/cm ²)	3.0	3.0
Entry Flight Path Angle (°)	-22	-39
Entry Altitude (km)	200	1000
Atmospheric Scale Height (km)	7.6	41
Pass duration (s)	~60	~3600
Ballistic Ratio	~135	~150

The periapsis altitude of the hyperbolic approach trajectories was targeted low enough to accommodate reasonable uncertainties in entry conditions due to Nav errors as well as reasonable uncertainties in the atmospheric density. Thus, a high periapsis altitude (equivalent to a shallow Flight Path Angle at entry) and a low density atmosphere would require drag from the ballute for the entire pass through the atmosphere. For the nominal entry conditions and atmospheres used for these representative trajectories, sufficient delta-V is achieved before the spacecraft reaches periapsis, so the ballute must be released to minimize the drag during the remainder of the flight through the atmosphere.

Figure 2.0 shows a typical sequence of events during the ballute aerocapture phase. The spacecraft approaches the planet or moon on a hyperbolic approach trajectory (1) that has been carefully targeted to enter the atmosphere (2) at the desired speed and flight path angle. The large drag from the ballute system causes the spacecraft to experience a maximum deceleration of several g's (3) shortly after entry. When the spacecraft has been slowed sufficiently the ballute is released (4) and the spacecraft proceeds through the remainder of the atmospheric segment (5-7) with minimal drag. If too much energy is removed from the orbit before leaving the atmosphere, a drag makeup maneuver (6) might be required to raise apoapsis out of the atmosphere. A maneuver at the first apoapsis (8) is essential for raising periapsis out of the atmosphere. If the on-board orbit determination is sufficiently accurate, the periapsis raise maneuver can be targeted very close to the desired final altitude so that a single, final maneuver can be made to circularize the orbit (9). The alternative is to command several "clean-up" maneuvers from the ground after tracking the spacecraft after the automated maneuvers have put the spacecraft close to its final, science orbit.

Figure 3 shows the time history of the altitude during the atmospheric flight segment of the representative trajectories. The initial state is 100-200 sec before entry, which is defined at a particular altitude for each body. The entry and release times are noted by dashed lines on the plots, where Titan entry (and Release) occurs before Mars entry (and Release) only because the time from entry for the initial states were arbitrarily specified. The ballutes are released before periapsis is reached for both examples because the nominal trajectory is targeted low enough to accommodate uncertainties. Note that the Titan atmosphere is much thicker than for Mars, since entry is at 1000 km altitude for Titan and at 200 km for Mars.

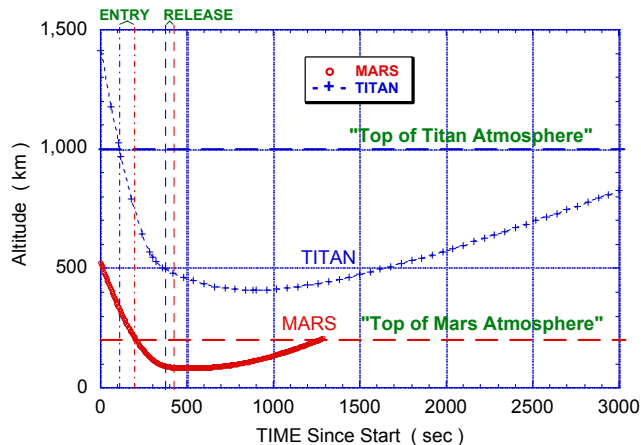


Figure 3: Altitude versus Time for Representative Ballute Aerocapture at Mars & Titan

Figure 4 shows the velocity history during the atmospheric flight segment. Trajectories for Titan are expected to have a higher entry speed and Delta V than for Mars. The velocity decreases rapidly early in the trajectory when the velocity is high and the density is increasing rapidly. For both of these cases, ballute release may be at a relatively high altitude well before periapsis, so there is enough towing spacecraft drag during the remainder of the trajectory to have a noticeable effect on the velocity. This effect must be estimated by the on-board separation algorithm in order to release the ballute at the correct time. (These trajectories were the result of a computer search for the right time to separate, so both hit their respective apoapsis targets exactly.) In the real world there is some chance that the ballute will be released a little too soon, in which case drag will not provide enough velocity change and propellant will be used to lower the apoapsis altitude later in the mission. There is also a chance that the ballute will be released late, in which case drag will extract too much energy from the orbit, and propellant will be used to raise the apoapsis later in the orbit. If release is significantly later than the perfect release time (i.e., ~3-5 sec), propellant will be needed during the pass to raise apoapsis. This burn is pre-programmed and selected based on on-board sensing.

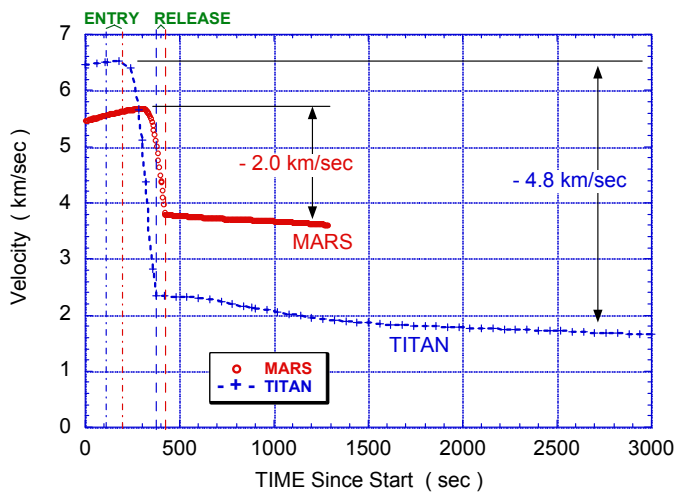


Figure 4: Velocity versus Time for Representative Ballute Aerocapture at Mars & Titan

A basic assumption for this study was that the ballute would be made out of existing materials, such as Kapton. Kapton has a rated temperature of about 500°C, which corresponds with a heating rate of about 3 W/cm². The size of the ballute is selected based on this. Figure 5 shows maximum Qdot prior to ballute release. In these examples, there is a secondary peak near periapsis, where the density is highest. If the entry flight path angle is decreased (undershoot, i.e. the approach

hyperbola is targeted to a lower altitude), then the ballute will be released earlier than for these reference trajectories, and the secondary peak will be larger. If the entry path is steep enough, then the secondary peak can be larger than the primary peak. Steeper entries have a much more noticeable effect on the secondary peak than they do on the primary peak, since the ballute can still be attached. Although the ballute does not have to survive the secondary peak, because it has already been released, the spacecraft does have to survive both peaks. Higher peaks require more thermal protection of the spacecraft. An atmospheric density that is significantly higher than nominal has the same effect on the shape and magnitudes of the peaks as a steeper entry. Conversely, a shallower entry, or a thinner than expected atmosphere have the opposite effect in that both the Qdot peaks before and after ballute release are reduced. Better knowledge of the atmosphere and better navigation both enable the approach trajectory to be targeted higher in the atmosphere, where both Qdot and uncertainties due to separation errors are minimized.

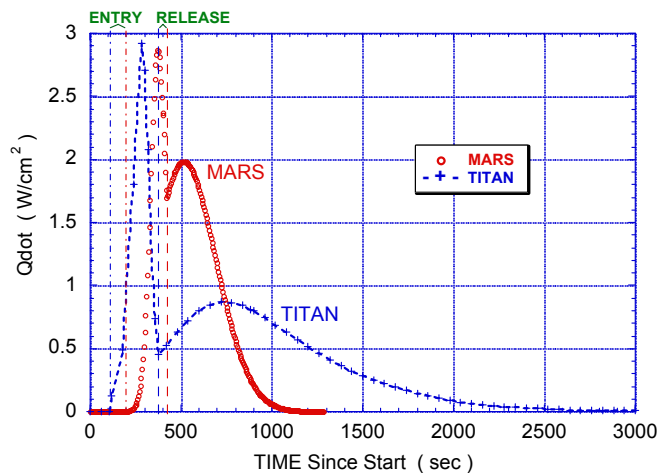


Figure 5: "Qdot" versus Time for Representative Ballute Aerocapture at Mars & Titan

Figure 6 shows the Dynamic Pressure (defined as 0.5 * Density * Velocity²). The dynamic pressure is useful for computing inflation pressure required to maintain the shape of the ballute during capture, and for computing aeroelastic effects and tether loads. After separation, the potentially higher values of dynamic pressure are useful for determining dynamic loads on the towing spacecraft.

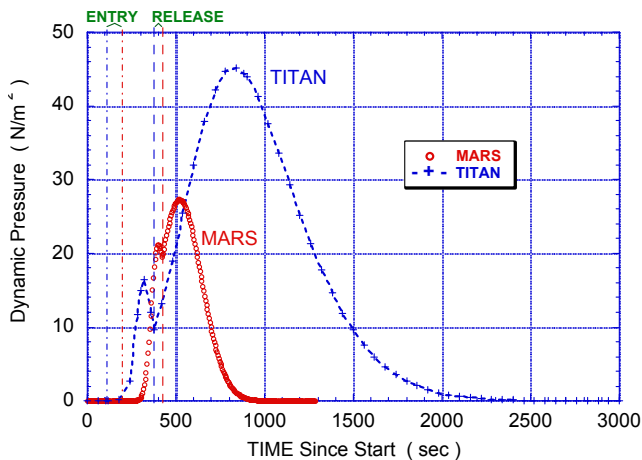


Figure 6: Dynamic Pressure versus Time for Representative Ballute Aerocapture at Mars & Titan

When the system enters the atmosphere, the large drag area results in a rapid deceleration that can reach several g's before the spacecraft has decelerated enough, as shown in Figure 7. The rate of increase and the magnitude of the peak always occur before separation, so they are useful measurements that can improve the performance of the separation algorithm. Once the ballute is released, the deceleration drops dramatically because the drag area is typically reduced by up to a factor of 150, or the ratio of the ballistic number of the towing spacecraft and the towing spacecraft plus ballute. The deceleration usually remains very low after ballute release even though the maximum dynamic pressure is largest near periapsis.

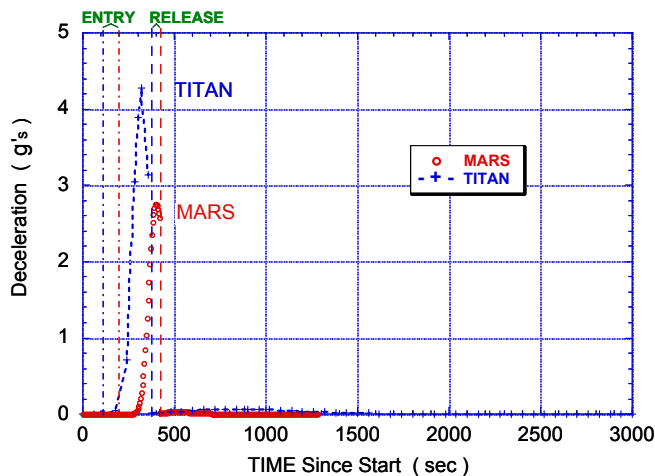


Figure 7: Deceleration versus Time for Representative Ballute Aerocapture at Mars & Titan

Figure 8 shows the history of the atmospheric density during the atmospheric flight segment. While the ballute is attached, the densities are very comparable between Mars and Titan. After ballute release, the density

at periapsis of the Titan trajectory is significantly higher than for the Mars trajectory. Even though the density is larger for this Titan trajectory, the secondary peak for Qdot is less than for the Mars trajectory, because the velocity is lower.

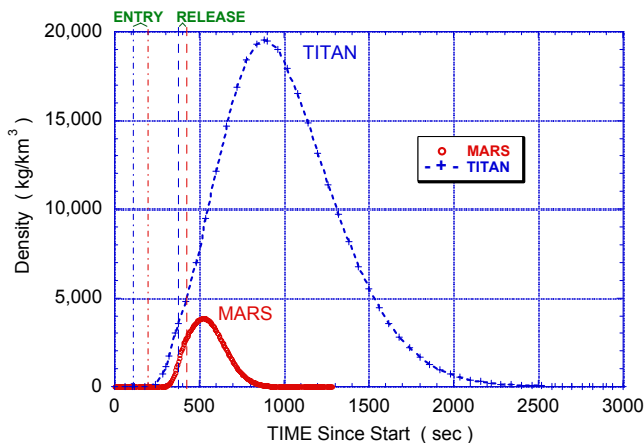


Figure 8: Density versus Time for Representative Ballute Aerocapture at Mars & Titan

Figure 9 shows the log of the density plotted versus altitude for these two reference trajectories. The significantly steeper slope for the Mars example represents the much smaller scale height for the Mars atmosphere (7.6 km) than that for Titan (41 km).

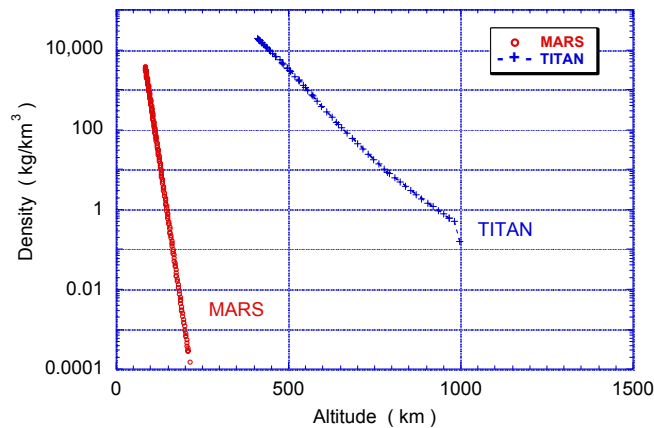


Figure 9: Density versus Altitude for Representative Ballute Aerocapture at Mars & Titan

Configuration Concept

A variety of configuration concepts employing ballute technology can be applied for planetary aerocapture missions, but this paper is focused on the use of trailing toroidal ballutes. As presented by Masciarelli and Westhelle³, ballistic ratio is a key design parameter. In order to minimize the size and mass of the ballute assembly,

the towing spacecraft ballistic number is maximized. General logic for sizing of a ballute system is illustrated in Figure 10.

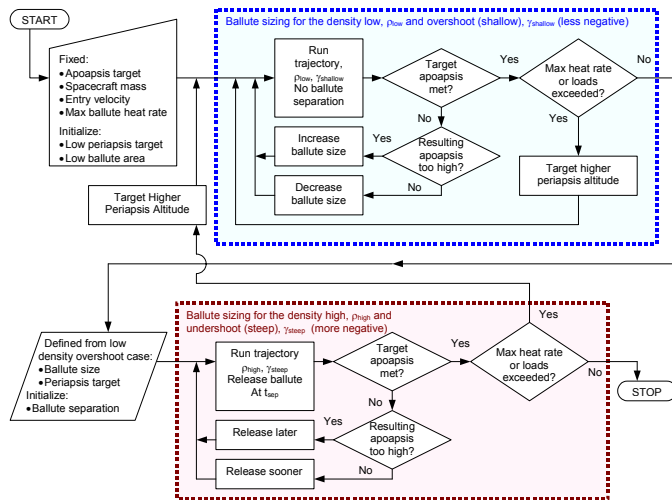


Figure 10 Ballute Sizing Logic

The frontal area of the ballute is determined by the delta V requirement of the mission. For a toroidal ballute the remainder of the geometry is then dependent on the aspect ratio (major diameter/minor diameter). For a given frontal area the surface area of the ballute remains constant. Thus the weight of the thin film comprising the ballute is independent of the aspect ratio. However, the gas volume decreases with increasing aspect ratio, so the more the ballute resembles a bicycle tire instead of a truck tire, the lighter the ballute will be⁴. This mass savings is somewhat offset by the additional weight of longer tethers used to support a large aspect ratio ballute. For a 750 m² frontal area ballute with an aspect ratio of 5:1 the inflation gas mass is 1/3 of the thin film mass of the ballute.

Toroidal ballutes provide critical aerodynamic advantages for aerocapture. More specifically, since the trajectory is outside of the continuum regime, the volume in the wake of the spacecraft is not efficient for creating drag. Furthermore, the towing spacecraft creates a bow shock, and this shock expands behind the spacecraft. The inside diameter and trailing distance of the toroid are designed to eliminate interaction with the bow shock. However, other shapes have also been investigated. For example, a double torus, which is two toroids with a flat span of material between them, is also a possible candidate. This geometry does not tend to produce significant film mass savings but can substantially reduce the required mass of the inflation gas. The double torus is a more complicated geometry and would also probably require more mass for seaming.

The tether angle is sized by determining the distance the ballute needs to trail behind the spacecraft for the spacecraft wake to be swallowed by the hole in the torus. This is also a function of ballute aspect ratio. Lower tether angles result in lower tether and ballute loads but are also longer which increases tether mass.

Tethers can be grouped into two primary categories, strings and columns. String tethers provide stiffness in tension only whereas columns provide both tension and compression stiffness. Column tethers are desirable because they provide a stable and verifiable configuration before entering the atmosphere. String tethers introduce the risk of recontact between the ballute and spacecraft and uncontrolled attitude upon atmospheric entry. Deployment of the ballute during the drag pass, like a parachute deployment, is possible but riskier. With drag deployment it might not be necessary to have column tethers because string tethers would always be in tension. A mix of string and column tethers may be the best option. String tethers provide a greater range of material possibilities and can probably be more efficient in tension than column tethers which are likely to be inflated tubes of the same material as the ballute.

Risk and Critical Issues

Performing aerocapture using inflatables offers significant mass savings over competing orbit insertion technologies enhancing, and, in some cases, enabling planetary orbiter science missions. However, before ballute aerocapture missions can be considered, many potential risk items need to be identified and retired. Some risk items may be easily addressed, whereas, some items might require stepping back and rethinking of a conceptual solution. The greatest technical risks for the thin-film, trailing, tethered torus, baselined in this study as the best balance of performance, risk, and feasibility, are presented here:

Seaming - Large thin-film inflatables have already been constructed and deployed in space, however, aerocapture will require very high thermal and dynamic pressure load requirements. The trade between thin-films and higher weight, higher heating/loading capable fabrics/aramids favors thin-films. This is due to the much lower aerial densities of thin films allowing much larger drag areas, thereby achieving the flying higher altitude, less stressing trajectories. However, these studies have assumed that high-thermal capable seaming technologies can be developed, such as adhesives, ultrasonic welding, stitching with cover tape, etc. A solution if seaming represents a thermal limitation is to try to keep it in low heating areas and/or protect the seams with local thermal treatments, however this will impact the mass of the system.

Tethers - Tethers that can withstand the multiple g deceleration of aerocapture exist (braided PBO is base-lined); however, attachments to the ballute concepts are conceptual. Currently, patch fan or stirrup concepts are being considered (see seaming above).

Trajectory - The trajectory risk is whether the trajectory can be controlled using drag modulation only (i.e., critical timing of ballute separation) to accommodate atmospheric, navigation and performance uncertainties. Initial modeling efforts indicate that relatively simple guidance algorithms accommodate uncertainties with generous margins on the timing of separation.

Packing and Storage - The ten year+ transits for some of the outer planet missions puts a requirement on the ballute to work after being stowed for a very long time. There is limited data on the properties of some of the candidate materials after long term storage. Blocking, creasing and pinholes due to packing may present problems for the inflatable as well.

Deployment - Controlled deployment and inflation are critical. To mitigate any risk of tethers getting tangled and to avoid re-contact between the spacecraft and ballute, the baseline design concept includes inflatable columns in some tether locations to provide some compressive stiffness in the system. Other concepts are also being considered.

Aeroelasticity - Interactions between the hypersonic, rarefied flow and the ballute could present a problem. This is very complex to assess analytically, and facility limitations make testing very difficult. It can be argued that the rates between the very high speed, low density flow and the lower resonance of the inflatable make aeroelasticity at the altitudes that are being considered for the thin-film ballute concept incompatible; however, verification of this is challenging.

Material - Thermal, aerial density, tensile strength, material maturity, ballute manufacturability, and seaming characteristics are all critical factors in the design. Candidate materials⁵ (Kapton, PBO, etc.) are under evaluation; however, more detailed analyses and test need to be performed for a full assessment trade.

Flow Stability - The potential exists for the toroidal concept for choked flow through the torus. The subsonic flow in the wake of the spacecraft provides a means of back flow that can disrupt the flow stability. A series of CFD analyses and expansion jet/windtunnel tests have been planned for assessing this risk.

Analysis Tool Discussion

The aerothermodynamic design objectives for an inflatable aerocapture system are to maximize the drag while minimizing the aerodynamic heating so as to

minimize the non-payload weight. Approximate design tools are used to initially size the aerocapture device, but the complexity of the flow around ballute geometries requires that these designs be verified and design margins be established through detailed aerothermodynamic analyses. Furthermore, an initial review of the trade space for Neptune and Titan aerocapture suggests that peak heating could occur over a wide range of flow regimes ranging from hypersonic continuum to transitional rarefied flow. Therefore, analysis techniques are required that can fully address the issues associated with each of these regimes.

In the continuum regime, the LAURA (Langley Aerothermodynamic Uppwind Relaxation Algorithm) code⁶ provides the capability to model hypersonic, high-temperature real-gas flows based on the Navier-Stokes equations. LAURA has been previously applied to computations of toroidal geometries for nominal aerocapture conditions for several different planetary atmospheres including Neptune and Titan⁷. The thermochemical models developed for these earlier studies include finite-rate chemistry and are used in the present work.

At lower densities, flow around the spacecraft and ballute transitions to rarefied flow, and aerothermodynamic simulations require the Direct Simulation Monte Carlo (DSMC) technique developed by Bird⁸. DSMC simulates gas flows by modeling the motion and collisions of millions of representative molecules based on the kinetic theory of gases. For this study, the DAC code (DSMC Analysis Code) of LeBeau⁹ is used. DAC treats complex three-dimensional geometries as well as simple axisymmetric shapes while simulating the discrete molecular behavior of the flow with multiple species including chemistry. DAC chemistry models were developed based on the same reaction sets and rates used in the LAURA continuum calculations.

The Navier-Stokes and DSMC simulations are supplemented with rapid-design, engineering methods based on free-molecular and Newtonian models, continuum-to-rarefied bridging relations, and stagnation heating correlations^{10,11,12}. The detailed results obtained from the Navier-Stokes and DSMC simulations allow an assessment of the error margins that should be applied to the engineering methods as well as providing more detailed predictions of force and heating distributions.

Performance Analysis Results

Aeroanalysis Results

Navier-Stokes (LAURA) and DSMC (DAC) simulations have been performed for a 750 m² ballute at several points along a typical Titan aerocapture trajectory to provide aerodynamic drag and heating environments.

The LAURA simulations were performed with no-slip, radiative equilibrium, and fully-catalytic wall boundary conditions. Thermal nonequilibrium was treated with a two-temperature gas model. The DSMC simulations were performed using fully diffuse wall boundaries with complete thermal accommodation and fully catalytic recombination of atomic species⁹.

A sample DSMC flowfield prediction is shown in Fig. 11^{9,13}. (Since the flow is axisymmetric, only the region from the axis to the outer computational boundary is shown.) The bow shock created by the toroid focuses to a triple point above the axis formed at the intersection with a normal shock (Mach disk) and reflected shock. For trajectory conditions where both LAURA and DAC were run, similar flow structures were obtained, and the variation in the size and location of the Mach disk over the trajectory was similar for the two methods.

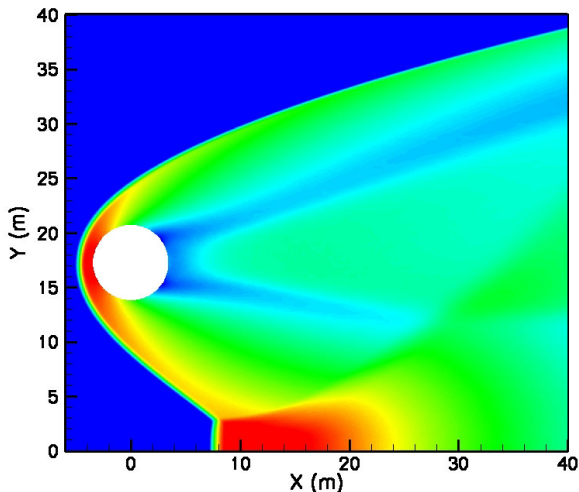


Figure 11 - Pressure Contours for DSMC Prediction Near Peak Heating Condition. $V_\infty=5.52$ km/s, $\rho_\infty=9.04 \times 10^{-7}$ kg/m³, $T=168$ K

Aerodynamic drag predictions are shown as a function of Knudsen number in Fig. 12 where the Knudsen number is based on the maximum ballute diameter. The predictions are compared to a traditional bridging relation based on a sine-squared variation in drag between the continuum and free-molecular limits. The bridging relation was developed prior to the computational simulations and used to predict ballute drag in the initial trajectory determination. The bridging relation could likely be improved by basing the Knudsen number on the minor diameter rather than the maximum diameter of the toroid. However, the LAURA and DAC predictions show that the original bridging relation gives a conservative (lower) prediction of the drag effectiveness of the ballute¹³.

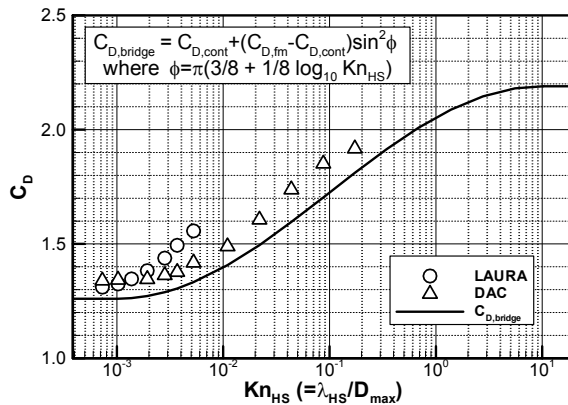


Figure 12 - Ballute Drag Coefficient - Comparison of CFD/DSMC Predictions to Bridging Relation

The stagnation heat transfer on the ballute is shown as a function of density along the trajectory in Fig. 13. The peak heating condition occurs at a condition where rarefaction effects become increasingly important. The predictions correlate well with $\rho_\infty^{0.5} V_\infty^3$ as expected for these hypersonic flow conditions, and this correlation is extended to very low densities using a bridging relation similar to that used for drag. LAURA predicts higher heating than DAC at densities less than 10^6 kg/m³ in part due to lack of slip boundary conditions in the LAURA calculations. However, assessment of these differences should be made with caution since there are differences in the details of the thermal and chemical modeling between the two methods whose effects have not been fully investigated.

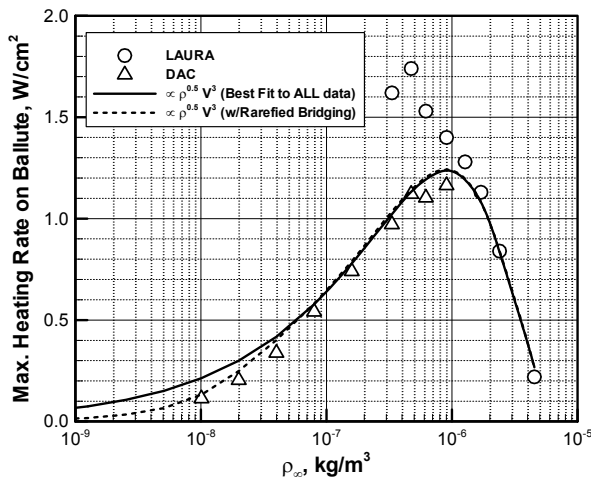


Figure 13 - Correlation of Stagnation Heating Rate Using DAC and LAURA Codes

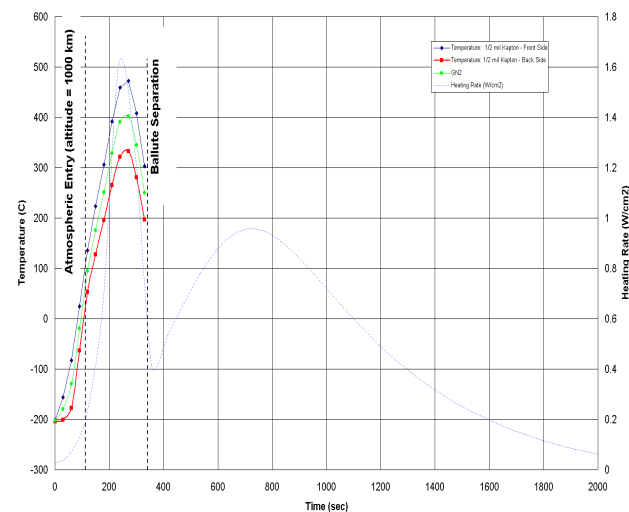
Aeroheating/Thermal Response

Analyses have been developed to ensure that the ballute system is maintained within limits of the inflatable

system¹⁴. A temperature response curve for maximum aerocapture heating at Titan is illustrated in Figure 14. Although the majority of the system is comprised of lightweight films 0.5 mil thick and less, in some localized areas, due to reduced nose radii and consequently, increased local heating, somewhat heavier materials with higher temperature limits will be employed.

Manufacturing and Material Performance Considerations

The driving constraint for ballute aerocapture is the ballute material property limits. Aero-thermal analyses have been used to create a configuration that meets the performance requirements for the ballute and achieves a thermal environment that is near the limits of state-of-the-art materials. For several of the materials discussed



below, the thermal environment is beyond their
Figure 14 - The ballute trajectory has been selected based on material thermal performance limits

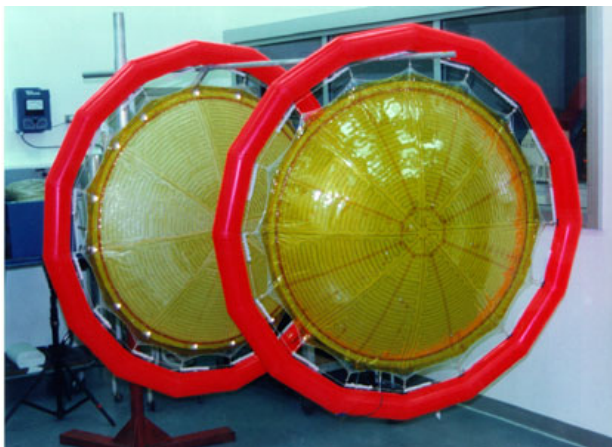


Figure 15 - ILC Dover Inflatable Parabolic Antenna Reflector Dish Demonstrates Capability for 3 Dimensional Forming of Kapton Film Structures

published glass-transition temperatures (T_g). However, due to the transient nature of the aerocapture event, these materials remain viable candidates because they support the loading conditions during the event. With these candidates, manufacturing, provides the greatest materials challenge.

To begin, a broad range of potential materials were identified. For the toroid and inflatable tethers, candidates include thin films, "rigidizable" composites, elastomer-coated structural fabrics, and ceramic fabrics. Operating temperature limits for these materials range from 125°C to 1250°C. The two leading candidate materials identified were thin films: Kapton and Polyboxoxazole (PBO). Both Kapton and PBO offer relatively high temperature capabilities—around 500 °C⁵. PBO is reported to perform at even higher temperatures, however further material study is required. PBO film is currently produced at the research and development level, and is produced in small areas. PBO remains flexible at cryogenic temperatures, unlike other high-temperature film candidates. In contrast, Kapton film is cast and is very mature from a manufacturing standpoint. It is relatively inexpensive, available off-the-shelf, has flight heritage (TRL 9), and has similar performance characteristics as PBO.

For tensile tethers, high strength materials such as PBO and Twaron are available; more advanced materials such as MSI's M5, will be monitored as they are developed. These materials are typically capable of operating at temperatures up to 650°C for limited periods of time. To increase tether performance at temperature, a ceramic jacketing is a viable option, if necessary, to protect the tether during aerocapture.

To identify viable materials for a ballute, a variety of mechanical tests of candidate materials are currently being performed using a Dynamic Mechanical Analyzer (DMA). This equipment provides a means to compare Modulus (both stored and loss), creep performance (both isothermal and ramping temperature), and tensile performance. The DMA allows testing at temperatures of up to 650°C and in a controlled atmosphere. For the current effort, a nitrogen purge is being used because it is representative of aerocapture targets and it is non-oxidizing. Additional optical testing will also be performed to determine emissivity properties of the candidates. This trade will identify those films that are more likely to radiate thermal energy away from the ballute and reduce surface temperatures⁵.

The material trade extends beyond material maturity and temperature performance. Seaming these materials will require development for this type of application. Temperature survivability of the ballute assembly depends on the capability of seam construction more so than that of the base material. Several techniques currently exist and have been employed on thin film structures. For example, pressure sensitive adhesive (PSA)

tapes are commonly employed due to their ease of use with thin films. PSA's do not operate at high environmental temperatures without thermal protection.

To maintain low-mass seams, polyimide adhesives and high temperature silicone adhesives are being investigated for seam construction. Polyimide adhesives are of the same polymer family as Kapton, only in liquid form. These require a high temperature and moderate pressure to create the bond. The resulting bond is at (or near) the full strength of the base material. Silicone adhesives are available in many forms from room temperature vulcanized (RTV) to platinum/heat cured. This system relies on a mechanical bond to the film to achieve its strength. However, many films are not overly receptive to a silicone bond so special candidates must be selected. Coated films have been identified that are high temperature-compatible. These include vapor-deposited aluminum (VDA) films, copper coated films, and germanium coated films. These metalized films will improve emissivity and ESD protection.

Another manufacturing issue that must be considered is the material patterning approach¹⁵. Since materials are not available in a width of the scale of the ballute, it must be broken into smaller seamed sections. The typical approach for an inflatable torus is to pattern it as segments. The smaller (and more numerous) the segments, the less faceted and more ideal shaped of the torus will be achieved. However, the greater the number of segments, the more seams exist, increasing manufacturing time and cost as well as mass. To alleviate this problem, thermal forming of films is being assessed. Kapton films have been successfully 3-dimensionally formed to create a more conformal shape for inflatables such as a parabolic antenna reflector dish. This forming process involves moderate effort to develop molds that produce high quality formed parts. Ultimately, the patterned shape will be traded against the predicted aero/thermal performance to determine the design and manufacturing approach.

Guidance and Separation Performance

A successful ballute aerocapture, which leaves the towing spacecraft in the desired orbit, requires release of the ballute after sufficient energy loss is achieved. The timing of the ballute separation must be robust enough to handle atmospheric density uncertainties, entry trajectory delivery and knowledge errors and spacecraft and ballute ballistic coefficient uncertainties. Ballute separation timing is performed on-board by comparing the desired and estimated orbital energy. Orbital energy is estimated by propagating the trajectory using a central force gravity model and accelerometer measurements. Energy loss due to atmospheric drag acting on the spacecraft after separation is significant for steep entry cases and must be accounted for in the release tim-

ing. An exponential atmospheric density model is carried on-board and refined by filtering accelerometer measurements using an EKF. The atmospheric density model is used to propagate the spacecraft trajectory to the atmospheric exit point to estimate energy loss after ballute separation. When the current orbital energy minus the predicted post-separation energy loss is less than the energy of the desired orbit, the ballute is released. The separation algorithm block diagram and flow chart are presented in figures 16 and 17.

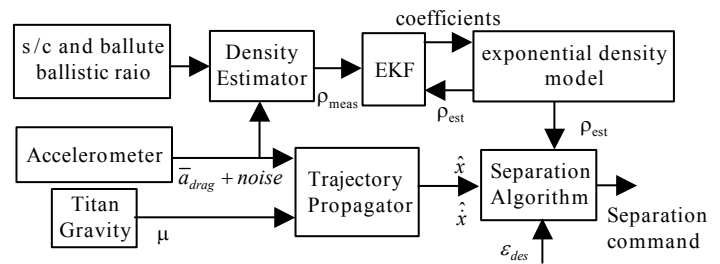


Figure 16. Ballute separation system block diagram

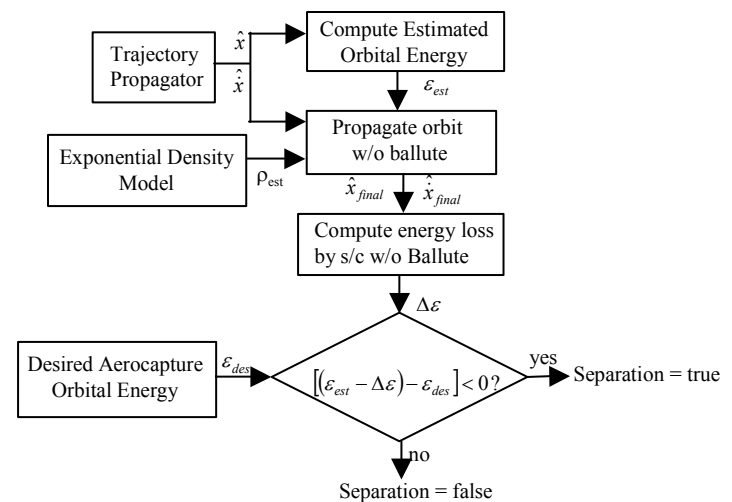


Figure 17. Ballute separation system flow chart

Separation algorithm performance was investigated for a Titan mission. Performance is evaluated in terms of the aerocapture success rate and the 3σ ΔV required to circularize the orbit after aerocapture completion. The circularization ΔV and success rate were determined from the results of a Monte Carlo simulation. Atmospheric density uncertainty, trajectory delivery and knowledge errors, spacecraft and ballute drag coefficient uncertainties and accelerometer errors were randomized in the Monte Carlo simulation. Titan's atmospheric density was modeled using TitanGRAM, which includes random density perturbations superimposed on the mean density which can be varied over the 3σ range by setting the Fminmax parameter from -1 to 1 with a value

of 0 representing the nominal atmosphere. The density variation with latitude at the expected arrival date was modeled using the following expression for Fminmax

$$F_{minmax} = 0.46 \cdot \sin(\text{lat}) \pm 0.54$$

Trajectory error analysis results³ indicate an entry FPA delivery error of 0.9 degrees (3σ) and an entry FPA knowledge error of 0.3 degrees (3σ). Spacecraft and ballute ballistic coefficient errors of 5% (3σ) and accelerometer errors consistent with the Honeywell QA3000-30 specification were also used in the Monte Carlo simulation. The spacecraft and ballute physical properties are given in table 3. The Monte Carlo results are shown in figures 18-21 and corresponding 3σ values are listed in table 4. It is clear from figures 4 and 5 that the mean apoapsis altitude is significantly higher than the target value of 1700 km especially for low periapsis altitude cases. This is a result of over-estimation of density by the on-board density model (EKF), which causes a slightly early ballute release to occur. Options for im-

Minimum Circularization ΔV	125 m/sec
Maximum Circularization ΔV	376 m/sec
Mean Circularization ΔV	186 m/sec
Mean + 3-sigma Circularization ΔV	285 m/sec
Mean Heating Rate	1.9 W/cm ²
Mean + 3-sigma Heating Rate	2.1 W/cm ²

Table 4. Monte Carlo Simulation Results

proving this aspect of the separation algorithm are under investigation.

Summary

System level analysis efforts conducted for NASA’s Gossamer and In Space Propulsion programs illustrate the enormous performance benefits available for missions to planetary bodies with an atmosphere. Using ballutes for aerocapture results in an improvement of the effective specific impulse by more than a factor of three, when compared with typical bi-propellant chemical systems used for orbit insertion. Even as compared with structural aeroshells, design, operational and mass performance benefits are significant. More specifically, mass savings come from elimination of the aeroshell system. Additional savings are available by simplifying the spacecraft structure by removing many of the constraints placed upon it by the aeroshell architecture, such as thermal control system required to route heat out of the aeroshell. Additionally, ballutes are significantly less demanding on packaging and configuration for the system. While those for a Titan orbiter a mass savings of ~300 kg or 40% of the spacecraft dry mass is possible by using a ballute instead of a hard aeroshell to perform aerocapture.

Future efforts for advancing this technology will require definition of technology validation via an Earth flight test.

Acknowledgments

Funding for this study was provided by the NASA Office of Space Science under contract NAS8-02130. The authors would like to thank Bonnie James and Michelle Munk at the MSFC In Space Propulsion Program office for their sponsorship and direction of these efforts, as well as Jennifer Dooley at JPL, who managed the Gossamer study (NASA contract number 1205966) that was a basis for some of the cited efforts. The authors would like to thank George Sapna, ILC Dover, Peter Gnoffo, Langley Research Center, Scott Inlow, Ball Aerospace & Technologies, Corp., and Reuben Rohrschneider, Ball Aerospace & Technologies, Corp., who made significant and substantial contributions to the body of work used for development of this paper.

Parameter	Value
Titan Entry Velocity	6.5 km/sec
Apoapsis of Aerocapture Orbit	1700 km
Ballute Frontal Area	750 m ²
Spacecraft Frontal Area	3 m ²
Spacecraft Mass	1000 kg
Ballute Mass	42 kg
Spacecraft Drag Coefficient	0.75 continuum 2.2 free molecular
Ballute Drag Coefficient	1.3 continum 2.38 free molecular

Table 3. Input Parameters for Monte Carlo Run

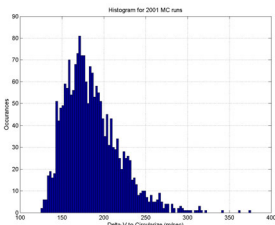


Fig 18 Circularization ΔV

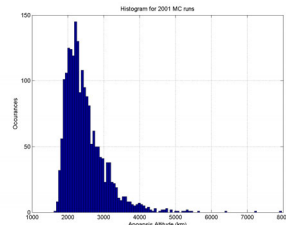


Fig 19 Apoapsis Altitude

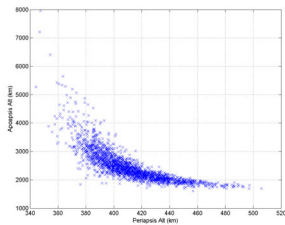


Fig 20 Apoapsis Vs Periapsis

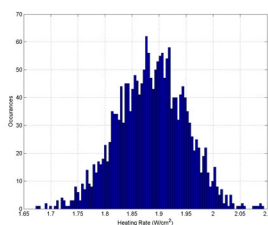


Fig 21 Peak Heating Rate

Parameter	Value
Success Rate	100 %

References

¹ Jay Musil, Goodyear Aerospace Corporation, Contract NAS7-100, "Study of Expandable, Terminal Decelerators for Mars Atmosphere Entry", 21 Oct 1966.

² Noca, M., and Bailey, R., "Titan Explorer Mission Trades from the Perspective of Aerocapture," AIAA 2003-4801, July, 2003.

³ Masciarelli, J., and Westhelle, C., Advanced Mission Design Branch, Johnson Space Center, "Entry Corridors for Ballute Aerocapture", dated 11/25/2002 and "Atmospheric Profile Effects on Navigation Error Sensitivities", dated 12/20/2002.

⁴ Hornung, H.G., "Hypersonic Flow Over Bodies in Tandem and its Relevance to Ballute Design," AIAA 2001-2776, 31st AIAA Fluid Dynamics Conference, Anaheim, CA, June, 2001.

⁵ Hall, J.L., "A Review of Ballute Technology for Planetary Aerocapture," IAA-L-1112, 4th IAA Conference on Low Cost Planetary Missions, Laurel, MD, May, 2000.

⁶ Gnoffo, P. A., "An Upwind-Biased, Point-Implicit Relaxation Algorithm for Viscous, Compressible Perfect-Gas Flows," NASA TP-2953, Feb. 1990.

⁷ Gnoffo, P. A., "Computational Aerothermodynamics in Aeroassist Applications," AIAA 2001-2632, 15th AIAA Computational Fluid Dynamics Conference, Anaheim, CA, June 2001.

⁸ Bird, G. A., "Molecular Gas Dynamics and the Direct Simulation of Gas Flows," Clarendon Press, Oxford, 1994.

⁹ LeBeau, G. J., and Lumpkin II, F.E., "Application Highlights of the DSMC Analysis Code (DAC) Software for Simulating Rarefield Flows," Computer Methods in Applied Mechanics and Engineering, Vol. 191, Issue 6-7, 2001, pp. 595-609.

¹⁰ DeJarnette, F. R., Hamilton, H. H., Weilmuenster, K. J., Cheatwood, F. M., "A Review of Some Approximate Methods Used in Aerodynamic Heating Analyses," J. of Thermophysics, Vol. 1, No. 1, Jan. 1987

¹¹ Wilmoth, R. G., "DACFREE - A Free-Molecular / Newtonian Code for Hypersonic Flow"

¹² Gnoffo, P.A. and Anderson, B.P., "Computational Analysis of Towed Ballute Interactions," AIAA 2002-2997.

¹³ Wang, W., Sun, Q., and Boyd, I.D., "Towards Development of a Hybrid DSMC-CFD Method for Simulating Hypersonic Interacting Flows," AIAA 2002-309, 8th AIAA/ASME Joint Thermophysics and Heat Transfer Conference, St. Louis, MO, June 2002.

¹⁴ Hall, J.L., and Le, A.K., "Aerocapture Trajectories for Spacecraft with Large, Towed Ballutes," AAS 01-235, AAS/AIAA Space Flight Mechanics Meeting, San Diego, CA, February 2001.

¹⁵ Grahne, M., Cadogan, D., "Revolutionary Design Concepts for Inflatable Space Structures," (1999-01-5520), World Aviation Congress, San Francisco, CA, Oct., 1999.

Preliminary Aerothermodynamics of Titan Aerocapture Aeroshell

Naruhisa Takashima*
AMA Inc.
Hampton, VA 23666

Brian R. Hollis† and E. Vincent Zoby‡
NASA Langley Research Center
Hampton, VA 23681

Kenneth Sutton§
National Institute of Aerospace
Hampton, VA 23666

Joe Olejniczak**
NASA Ames Research Center
Moffett Field, CA 94035

Michael J. Wright†† and Dinesh Prabhu‡‡
ELORET Corporation
Sunnyvale, CA 94087

Abstract

Aeroheating environments for a Titan aerocapture mission were computed for the Titan Aerocapture Systems Analysis study funded through the In-Space Propulsion Program Office at NASA Marshall Space Flight Center. In this work, the convective heating environments for a candidate Titan probe (70 deg. sphere-cone geometry) are presented. The sensitivities of these environments to the computational grids, mass diffusion models, and reaction rates are examined in the context of axisymmetric flow using two different flow solvers. The lessons learned are applied to the forebody of the probe at an angle of attack of 16 deg. Results of computations from two different flow solvers are compared to reduce uncertainties in the predicted aerothermal environments. At the peak convective heating condition, the convective heating rate at the stagnation point is 28 W/cm^2 and the maximum heating rate, which occurs at the nose of the axisymmetric aeroshell is 46 W/cm^2 . A smooth-wall transition criterion of Re_θ of 200 is used in determining the likelihood of flow transition on the forebody and shown to occur on the leeside. Turbulent flow calculations show that the level of heating on the leeside increases by 250%, and the location of the maximum heating point moves from the nose to the leeside shoulder. Finally, aerodynamic force coefficients extracted from the computed solutions are shown to be in good agreement with those assumed in the generation of flight trajectories. The three-dimensional aerothermal environments, along with the predicted radiative heating environments, are used in the selection and sizing of the Thermal Protection System for the forebody of the probe.

Nomenclature

* Senior Project Engineer, Member, AIAA.

† Aerospace Engineer, Aerothermodynamics Branch, Senior Member, AIAA.

‡ Research Engineer, Aerothermodynamics Branch, Fellow, AIAA.

§ Senior Research Fellow, Associate Fellow, AIAA.

** Senior Research Scientist, Reacting Flow Environments Branch, Senior Member, AIAA.

†† Senior Research Scientist, Senior Member, AIAA

‡‡ Senior Research Scientist, Associate Fellow, AIAA

Alt	Altitude (km)
AoA	Angle of attack (deg)
CL	Lift coefficient
CD	Drag coefficient
D	Reference diameter (3.75 m)
L/D	Lift-to-Drag Ratio
Mach	Mach number
P	Pressure (Pa)
Re_θ	Momentum thickness Reynolds number.
ρ and Rho	Density (kg/m^3)
T	Translational temperature (K)

T_v	Vibrational temperature (K)
TPS	Thermal Protection System
V	Velocity (m/s)

Introduction

Titan, the largest moon of Saturn, is the only known moon in the solar system that has a fully developed atmosphere. The density of the atmosphere of Titan is actually greater than that of the Earth with a surface pressure 50% greater than that of Earth. The atmosphere is composed mainly of nitrogen, which accounts for approximately 94% by volume, with balance of argon and significant traces of hydrocarbon elements. Hydrocarbon elements are the building blocks for amino acids, a necessary ingredient for formation of life. For this reason, Titan is of significant interest to the scientific community for the understanding of early formation of life here on Earth. Voyager 1 was the first mission to Titan taking pictures of its dense atmosphere. Currently, the Cassini spacecraft with Huygens probe on board is en route to Titan. The joint NASA/ESA mission expects the spacecraft to arrive at Saturn on July 1st, 2004 and release its probe on December 25th, 2004.

As a potential follow-on mission to the Cassini-Huygens mission, a systems analysis study of an aerocapture mission to Titan was initiated by the NASA In-Space Propulsion Program Office at the NASA Marshall Space Flight Center (MSFC). Past studies have shown a vehicle mass saving of up to 66% can be realized using aerocapture technology compared to an all-propulsive mission to Titan. However, by design, these past analyses were of low fidelity and many assumptions were made to reach the conclusions. Hence, the goals for the present study include providing higher fidelity systems definition and sensitivities for Titan aerocapture mission that can be used by scientists, mission planners, technology planners, technologists and future mission managers; and to perform higher fidelity analyses for validating and updating previous assumptions. The system analysis study was performed by a multi-center NASA team with participation from NASA Ames Research Center (ARC), Jet Propulsion Laboratory, Johnson Space Center, Marshall Space Flight Center, and led by Langley Research Center (LaRC).¹

This paper will present the results of the computations performed by LaRC and ARC to determine the aeroheating environments and will focus on the convective heating portion of these environments. A companion paper will present the results of the radiative heating analyses.² Prior to the

work, extensive analyses, both numerical and experimental, were performed to determine the aeroheating environment of the Huygens probe.^{3,4,5,6} Analyses have shown that significant radiative emission of mainly CN violet system can occur within the shock layer due to non-equilibrium condition, and the amount of the CN radiation is sensitive to the freestream gas composition. For the worst case condition, the level of radiative heat flux was determined to be twice that of the convective heating flux.⁴

Titan Aerocapture Reference Concept

The forebody design of the aeroshell used by the study is shown in Fig. 1. The design is based on the Mars Smart Lander (MSL) aeroshell design,⁷ which has a 70 deg. sphere cone forebody and a bi-conic aftbody. For the Titan aeroshell, the MSL design was geometrically scaled to a diameter of 3.75 m, and the aftbody shape was altered to meet the packaging requirements. The overall length of the vehicle is 2.096 m, and the center of gravity is located such that an L/D of 0.25 is achieved at a trim angle of attack of 16 deg. The study defined six reference trajectories for an entry speed of 6.5 km/s with a ballistic coefficient of 90 kg/m². Trajectories were created for combinations of three atmospheric density profiles: minimum, nominal and maximum, with lift vector directions of up (undershoot) and down (overshoot). The three density profiles are shown in Fig. 2, which were obtained with Titan atmosphere model, TitanGRAM, developed by Justus and Duvall.⁸ The reference trajectories were computed using the Program for Optimization of Simulated Trajectories (POST).⁹

For the present study, aerothermodynamic analyses were performed primarily for conditions along the minimum atmosphere lift-up trajectory. Engineering analyses showed that the maximum stagnation point convective heating rate on a sphere occurs along the minimum atmosphere lift-up trajectory. Fig. 3 shows the points along the reference trajectory that the computations were performed and Table 1 lists the freestream at each trajectory point. Based on equilibrium engineering analysis, cases 3 (t=253 s), 4 (t=281 s) and 5 (t=308 s) were predicted to be the peak convective heating, the peak dynamic pressure and the peak radiative heating, respectively.

There are many uncertainties in the composition of the Titan atmosphere.⁸ The relative amounts of nitrogen, argon and methane will impact the overall heating rate on the vehicle. For radiative heating conservatism, the atmospheric composition was chosen as 95% N₂ and 5% CH₄ by volume along the entire reference trajectory.

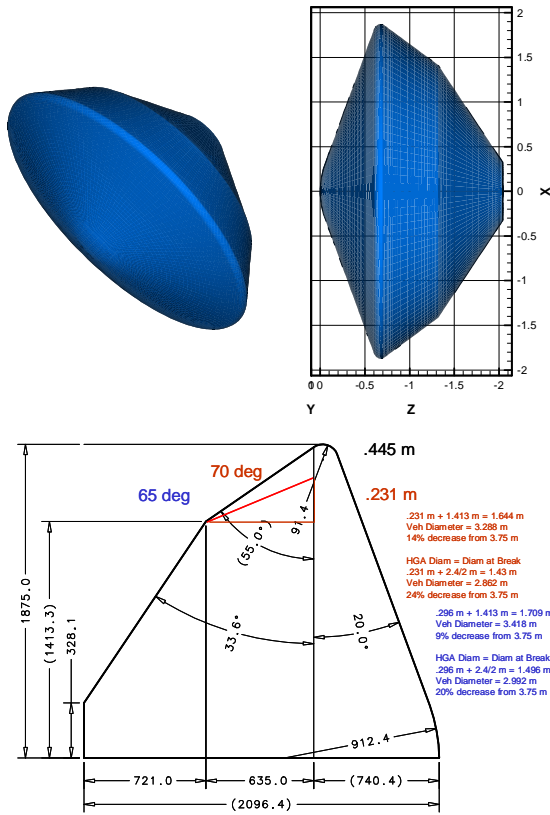


Fig. 1. Titan aeroshell design.

Titan Atmospheric Density Versus Altitude

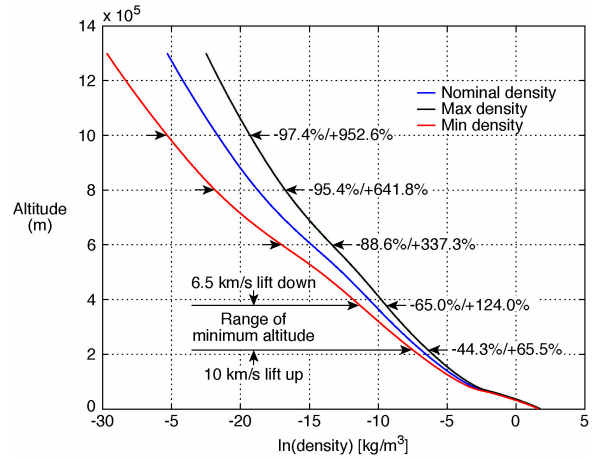


Fig. 2. Titan atmosphere density profiles.

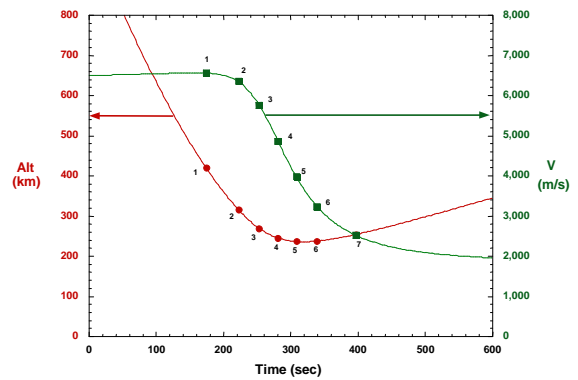


Fig. 3. Minimum atmosphere lift-up aeroheating reference trajectory.

Table 1. Freestream conditions along minimum atmosphere lift-up reference trajectory.

CASE	Time (sec)	Alt (km)	V (m/s)	AoA (deg)	rho (kg/m ³)	P (Pa)	T (K)	Mach
1	174	420	6558	16	4.697E-06	0.188	131.9	27.8
2	222	316	6348	16	5.070E-05	2.293	149.9	25.3
3	253	269	5761	16	1.491E-04	6.910	152.7	22.7
4	281	245	4859	16	2.665E-04	12.350	152.6	19.2
5	308	237	3978	16	3.305E-04	15.250	152.4	15.7
6	339	238	3239	16	3.212E-04	14.840	152.4	12.8
7	397	255	2521	16	2.138E-04	9.893	152.7	9.9

Computational Analyses

As mentioned previously, the aeroheating environment computations were performed simultaneously during the course of the study by two teams from NASA Langley and Ames Research centers. Each team performed the calculations independently using different Computational Fluid Dynamics (CFD) programs. Once a set of calculations was made, the results were compared and analyzed by the two teams. If differences were observed, the causes were investigated and analyzed to the satisfaction of both teams. The purpose of having two totally independent parties calculating identical problems was to minimize the uncertainties in the results and gain greater confidence in the level of physical and numerical modeling in the codes.

During the course of the study, computational analyses were performed in two stages. During the first stage, computations were performed on the forebody at a zero degree angle of attack, i.e., axisymmetric flow, for the peak convective heating condition (Case 3) to perform sensitivity analyses with respect to transport/kinetic models. After the completion of the first stage, the second stage involved computing three-dimensional flow on the forebody for all seven trajectory points. The results from the second stage were delivered to the TPS team for TPS sizing purpose.

Sensitivity analyses were performed using two different CFD codes: Langley Aerothermodynamic Upwind Relaxation Algorithm (LAURA),¹⁰ developed at LaRC, and the Data Parallel Line Relaxation (DPLR) program,¹¹ developed at ARC. Both CFD codes solve the three-dimensional Navier-Stokes equation using finite volume method with finite rate chemistry and thermal nonequilibrium. LAURA uses Roe's flux difference splitting with Yee's second-order symmetric total variation diminishing scheme to model the inviscid fluxes. Steady state solution is obtained using either point or line relaxation. The code supports MPI with multi-block structured grid to decrease computing time. DPLR uses third-order modified Steger-Warming flux vector splitting to calculate the inviscid fluxes and data-parallel line relaxation method to reduce the time to steady state convergence. Both codes use second order central differencing for the viscous fluxes and turbulent flow is modeled with the Baldwin-Lomax turbulence model. Both codes have been widely used in predicting aerothermal environments for several planetary probes.^{7,10,12} Each code was executed by its respective center during the course of the study.

Results

Sensitivity Analyses

To gain insight and reduce the uncertainties in the numerical results, sensitivity analysis on the diffusion model and chemical kinetic rates were made by performing calculations for the peak convective heating condition (Case 3) at zero degree of angle attack. For all the runs, the codes were executed with finite rate chemistry and thermal nonequilibrium using Park's two-temperature model.¹³ For the nominal case, a total of 18 species was assumed to be present in the gas mixture: N, N⁺, N₂, N₂⁺, C, C⁺, C₂, CH, CH₂, CH₃, CH₄, H, H⁺, H₂, CN, CN⁺, NH and e⁻. "Super catalytic" surface boundary condition was chosen where the species fraction is fixed at freestream values of 95% N₂ and 5% CH₄ at the wall. Forcing the gas mixture to recombine to the freestream composition causes the chemical energy to be released back into the flow, which results in conservative wall heating rates. The wall temperature was assumed to be at radiative equilibrium with surface emissivity of 0.90, and the boundary layer was assumed to be laminar.

Fig. 4. shows the grid and the temperature contour for the axisymmetric solution using LAURA. The grid for the solution was obtained using the built-in grid alignment capability of LAURA. The capability allows for grid clustering within the boundary layer and near the shock, as well as, adaptation of the outer boundary to the bow shock. The degree of adaptation is controlled through user-defined parameters.

Proper cell spacing near the wall is essential for calculating accurate heating rates. The wall cell spacing in LAURA is controlled by specifying the wall cell Reynolds number:

$$Re_w = \left(\frac{\rho a \Delta \eta}{\mu} \right) \quad (1)$$

where a is the local sound speed, $\Delta \eta$ is the cell height at the wall and μ is the local viscosity. Grid sensitivity analysis showed that, as seen in Fig. 5, $Re_w = 10$ is sufficient to resolve the laminar boundary heating rate. Requirements for DPLR are similar. The LAURA solutions presented in this work was obtained using $Re_w = 1$.

Fig. 6 shows comparison of convective heating rates along the surface using different diffusion model and chemical species. 12 species mixture is simply the 18 species mixture mentioned above without the ions and electron. The figure shows a variation of approximately 25% in stagnation point heating rate depending on the diffusion model and the chemical species. The two LAURA solutions with 18 species show that a higher stagnation heating rate of 50 W/cm^2 is predicted with the multi-component diffusion model, compared to the stagnation heating rate of 42 W/cm^2 computed with constant Schmidt number. Note the good agreement in the heating rate distribution between the two codes when the same diffusion model of constant Schmidt number of 0.5 and the total number of species are used.

Fig. 7 shows the variation of the translational temperature profile along the stagnation streamline calculated for the nominal case by DPLR and LAURA with three different chemical kinetic models. The forward reaction rate coefficients for each model are listed in Table 2. The backward reaction rates were calculated with equilibrium constants for both codes. Although all the solutions shown predicted the same stagnation point heating rate of approximately 50 W/cm^2 , the plot shows that the shock stand off distance and the peak post shock temperature vary with different chemical kinetic models. The profile labeled LAURA (Nelson '91) was computed with LAURA, assuming heavy particles as the collision partner for the ionization reactions, as listed by Nelson.³ During the study, it was confirmed through a private conversation with the author that the ionization reactions in the article were not appropriate, and that the collision partner should be electrons and not heavy particles. The profile labeled LAURA (Park '85) was computed with the same reaction rates as Nelson '91 but with the correct electron ionization reactions. Comparison of the two profiles shows that the heavy particle ionization reactions contribute to a decrease in both the post shock temperature and shock stand off distance, which is caused by the greater ionization of particles. Comparison of two profiles labeled LAURA (Park '85) and LAURA (Park '89), which are taken from rates published by Chul Park,^{13,14} shows the influence of nitrogen dissociation rates on the shock stand off and temperature. The faster nitrogen dissociation rates for Park '89, as shown in Table 2, causes greater dissociation of nitrogen molecules. This decreases the energy within the shock layer that results in slightly lower post shock temperature and shock stand off distance. Lastly, as with the diffusion model comparison, when the same

chemical kinetic model Park '85 is used, the stagnation line temperature profiles calculated by the two codes are in relatively good agreement.

Table 3 lists the convective and radiative heating rates at the axisymmetric stagnation point calculated using the three chemical kinetic models. The radiative heating rates were calculated using LORAN¹⁵ with the flow field results from the LAURA calculations. The existence of Cyano radical, CN, contributes to the large values of radiative heating rates, which are approximately twice the amount of convective heating rates. The table shows that the convective heating rates are insensitive to the kinetic models, whereas, the radiative heating rates vary by approximately 225%. The results indicate that, as expected, the radiative heating rate is sensitive to the different post shock temperature and shock stand off distance computed by the different models. A difference in shock stand off distance of just 1 cm can result in a radiative heating rate difference of approximately 30%. Similar results were calculated using NEQAIR¹⁶ and DPLR. Details of the radiation calculations are presented in the companion paper.²

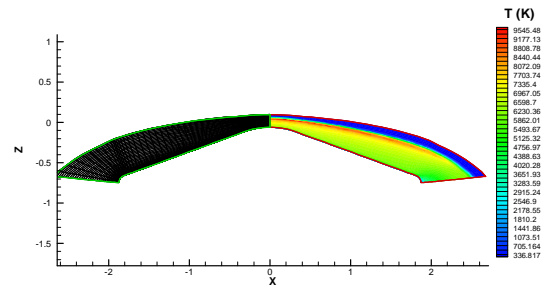


Fig. 4. Temperature contour at peak heating condition.

Table 2. Forward reaction rates.

Reaction	Forward reaction rate coefficient k_f [$\text{cm}^3/\text{mole}\cdot\text{s}$]
Dissociation Reactions $T_a = (T T_v)^{0.5}$	
<u>Nelson '91, Park '89, Park '85</u>	
$\text{C}_2 + \text{M} \rightarrow \text{C} + \text{C} + \text{M}$	$9.68 \times 10^{22} T_a^{-2.0} \exp(-71,000/T_a)$
$\text{CH} + \text{M} \rightarrow \text{C} + \text{H} + \text{M}$	$1.13 \times 10^{19} T_a^{-1.0} \exp(-40,193/T_a)$
$\text{CN} + \text{M} \rightarrow \text{C} + \text{N} + \text{M}$	$1.00 \times 10^{23} T_a^{-2.0} \exp(-90,000/T_a)$
$\text{CH}_4 + \text{M} \rightarrow \text{CH}_3 + \text{H} + \text{M}$	$2.25 \times 10^{27} T_a^{-1.87} \exp(-52,900/T_a)$
$\text{CH}_3 + \text{M} \rightarrow \text{CH}_2 + \text{H} + \text{M}$	$2.25 \times 10^{27} T_a^{-1.87} \exp(-54,470/T_a)$
$\text{CH}_2 + \text{M} \rightarrow \text{CH} + \text{H} + \text{M}$	$2.25 \times 10^{27} T_a^{-1.87} \exp(-50,590/T_a)$
$\text{NH} + \text{M} \rightarrow \text{N} + \text{H} + \text{M}$	$1.13 \times 10^{19} T_a^{-1.0} \exp(-41,820/T_a)$
$\text{H}_2 + \text{M} \rightarrow \text{H} + \text{H} + \text{M}$	$1.47 \times 10^{19} T_a^{-1.23} \exp(-51,950/T_a)$
<u>Nelson '91, Park '85</u>	
$\text{N}_2 + \text{M} \rightarrow \text{N} + \text{N} + \text{M}$	$3.70 \times 10^{21} T_a^{-1.6} \exp(-113,200/T_a)$
<u>Park '89</u>	
$\text{N}_2 + \text{N}_2 \rightarrow \text{N} + \text{N} + \text{N}_2$	$7.0 \times 10^{21} T_a^{-1.6} \exp(-113,200/T_a)$
$\text{N}_2 + \text{N} \rightarrow \text{N} + \text{N} + \text{N}$	$3.0 \times 10^{22} T_a^{-1.6} \exp(-113,200/T_a)$
Exchange Reactions ($T_a = T$)	
<u>Nelson '91, Park '89, Park '85</u>	
$\text{C} + \text{N}_2 \rightarrow \text{CN} + \text{N}$	$1.11 \times 10^{14} T_a^{-0.11} \exp(-23,000/T_a)$
$\text{CN} + \text{C} \rightarrow \text{C}_2 + \text{N}$	$3.00 \times 10^{14} T_a^{0.0} \exp(-18,120/T_a)$
$\text{C}_2 + \text{N}_2 \rightarrow \text{CN} + \text{CN}$	$7.10 \times 10^{13} T_a^{0.0} \exp(-5,330/T_a)$
$\text{H} + \text{N}_2 \rightarrow \text{NH} + \text{N}$	$2.20 \times 10^{14} T_a^{0.0} \exp(-71,370/T_a)$
$\text{H}_2 + \text{C} \rightarrow \text{CH} + \text{H}$	$1.80 \times 10^{14} T_a^{0.0} \exp(-11,490/T_a)$
$\text{CN}^+ + \text{N} \rightarrow \text{CN} + \text{N}^+$	$9.80 \times 10^{12} T_a^{0.0} \exp(-40,700/T_a)$
$\text{C} + \text{N} \rightarrow \text{CN}^+ + \text{e}^-$	$1.00 \times 10^{15} T_a^{1.5} \exp(-164,400/T_a)$
$\text{C}^+ + \text{N}_2 \rightarrow \text{N}_2^+ + \text{C}$	$1.11 \times 10^{14} T_a^{-0.11} \exp(-50,000/T_a)$
Associative Ionization Reactions ($T_a = T$)	
$\text{N} + \text{N} \rightarrow \text{N}_2^+ + \text{e}^-$	$1.79 \times 10^{09} T_a^{0.77} \exp(-67,500/T_a)$
Ionization Reactions ($T_a = T_v$)	
<u>Nelson '91</u>	
$\text{N} + \text{M} \rightarrow \text{N}^+ + \text{e}^- + \text{M}$	$2.50 \times 10^{34} T_a^{-3.82} \exp(-168,600/T_a)$
$\text{C} + \text{M} \rightarrow \text{C}^+ + \text{e}^- + \text{M}$	$3.90 \times 10^{33} T_a^{-3.78} \exp(-130,000/T_a)$
$\text{H} + \text{M} \rightarrow \text{H}^+ + \text{e}^- + \text{M}$	$5.90 \times 10^{37} T_a^{-4.0} \exp(-157,800/T_a)$
$\text{Ar} + \text{M} \rightarrow \text{Ar}^+ + \text{e}^- + \text{M}$	$2.50 \times 10^{34} T_a^{-3.82} \exp(-181,700/T_a)$
<u>Park '85, Park '89</u>	
$\text{N} + \text{e}^- \rightarrow \text{N}^+ + \text{e}^- + \text{e}^-$	$2.50 \times 10^{34} T_a^{-3.82} \exp(-168,600/T_a)$
$\text{C} + \text{e}^- \rightarrow \text{C}^+ + \text{e}^- + \text{e}^-$	$3.90 \times 10^{33} T_a^{-3.78} \exp(-130,000/T_a)$
$\text{H} + \text{e}^- \rightarrow \text{H}^+ + \text{e}^- + \text{e}^-$	$5.90 \times 10^{37} T_a^{-4.0} \exp(-157,800/T_a)$
$\text{Ar} + \text{e}^- \rightarrow \text{Ar}^+ + \text{e}^- + \text{e}^-$	$2.50 \times 10^{34} T_a^{-3.82} \exp(-181,700/T_a)$

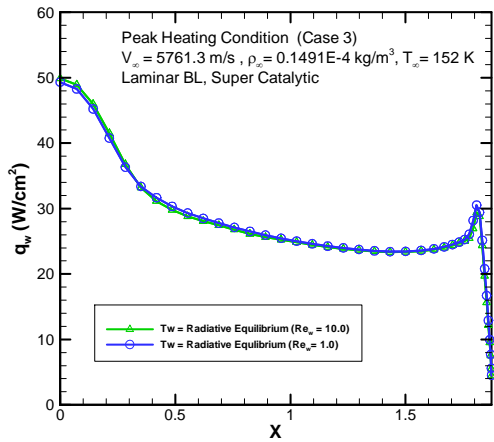


Fig. 5. Wall cell Reynolds number sensitivity.

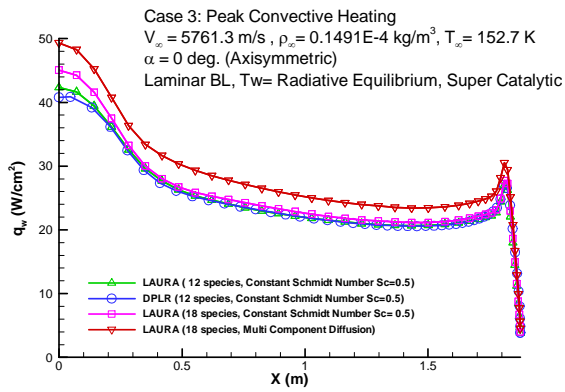


Fig. 6. Variation of convective heating rate along the forebody surface.

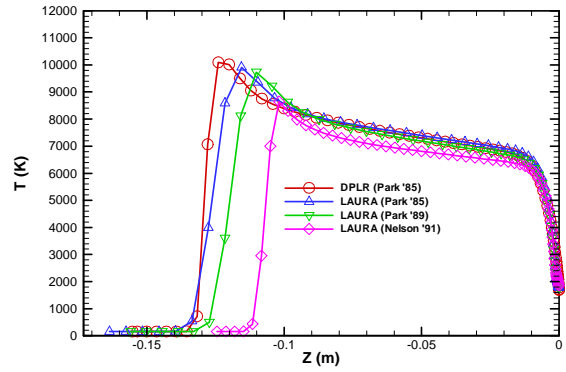


Fig. 7. Translational temperature profile along the stagnation streamline.

Table 3. Axisymmetric stagnation point heating rates for peak heating condition.

	Convective (W/cm ²)	Radiative (W/cm ²)
LAURA (Nelson '91)	49.32	60.93
LAURA (Park '89)	51	107.81
LAURA (Park '85)	51.86	138.52

Three-dimensional Results

Three-dimensional calculations were performed along the minimum atmosphere lift-up trajectory for the entry speed of 6.5 km/s using LAURA with 18 chemical species. Multi-component diffusion model with Park '89 chemical kinetic rates were used for the calculation. Fig. 8 shows the multi-block structured grid used for the LAURA calculations. Fig. 9 shows the shock structure in the pitch plane for the freestream conditions along the 6.5 km/s reference trajectory listed in Table 1. All computations were made for an angle of attack of 16 deg., which is the design trim angle for the aeroshell. Fig. 10 shows the variation of convective heating rate along the surface in the pitch plane for all seven trajectory points, and Fig. 11 shows the variation of convective heating rate at the nose along the trajectory. The maximum heating rate along the trajectory is 46 W/cm^2 , which transpire at the Case 3 peak heating condition. For all cases, the maximum heating rate occurs not at the flow stagnation point, which is located approximately at $X = -0.98 \text{ m}$, but at the windward side shoulder and the nose/geometric stagnation point. Fig. 12 shows the variation of Re_θ along the forebody pitch plane for all seven cases. Based on a conservative engineering transition criterion of Re_θ of 200, the flow will likely transition to turbulent on the leeward side of the forebody some time before $t=253 \text{ s}$ (Case 3) and remain turbulent until after $t=339 \text{ s}$ (Case 6).

Fig. 13 shows variation of convective heating rate along the forebody pitch plane for fully laminar and turbulent flows for Cases 3 and 5. Turbulent flow

was modeled using the algebraic turbulence model of Baldwin and Lomax.¹⁷ The figure shows that the turbulent heating rate is 2.5 times that of the laminar heating rate on the leeward side, and the location of maximum heating rate has shifted from the nose and the windward side shoulder to the leeward side shoulder. Although the engineering criterion predicts the flow will be laminar on the windward side, a 10% increase in heating level is observed due to turbulent flow for both cases.

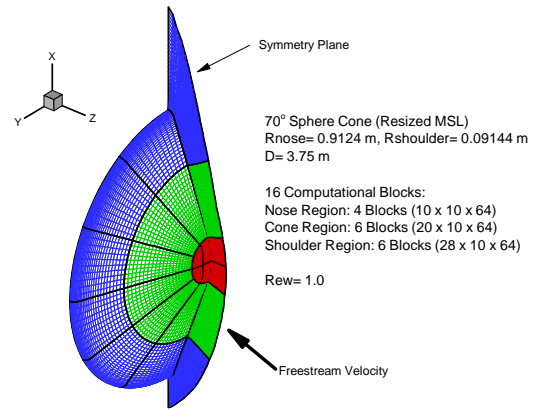


Fig. 8. Computational grid for the forebody calculation

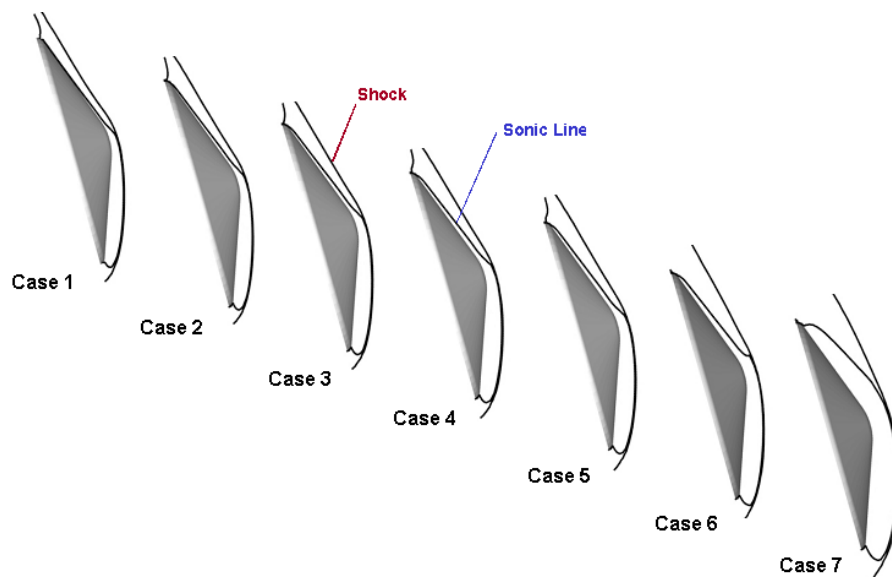


Fig. 9. Shock structure in the pitch plane.

Table 4 lists the lift and drag coefficient, as well as the lift-to-drag ratio of the forebody at each trajectory point. Case 1 data is excluded from the table based on the finding that condition is above the limits for continuum Navier-Stokes calculation. The table shows that the configuration meets the preliminary L/D design requirement of 0.25 along the trajectory. The CG location at the 16° trim angle of attack is at $z/D = 0.3$ and $x/D = 0.0197$.

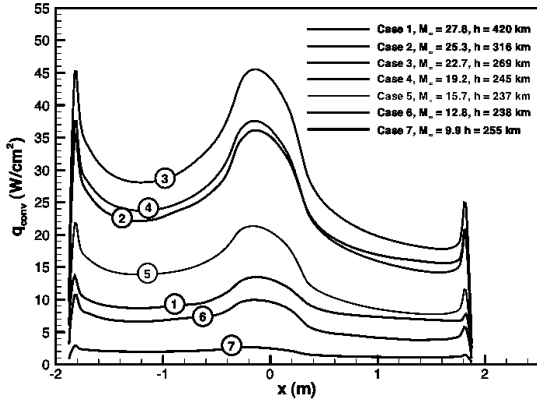


Fig. 10. Variation of convective heating rate on the forebody for the seven trajectory points.

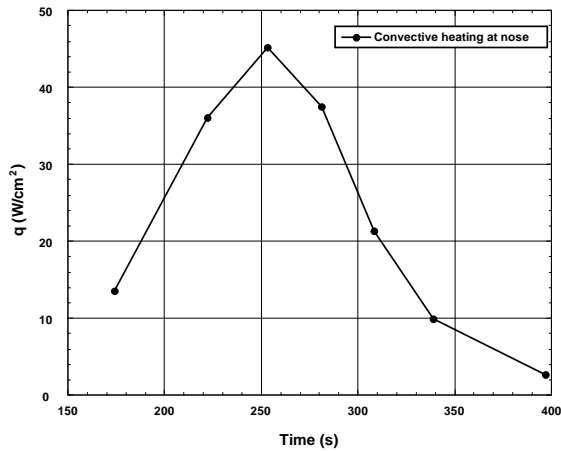


Fig. 11. Variation of convective heating rate along the reference trajectory.

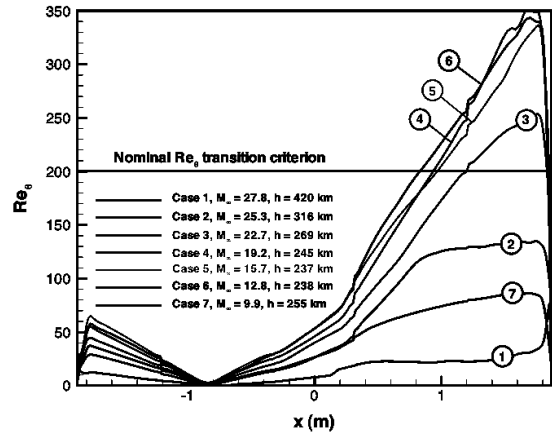


Fig. 12. Variation of Re_0 along the forebody for each trajectory point.

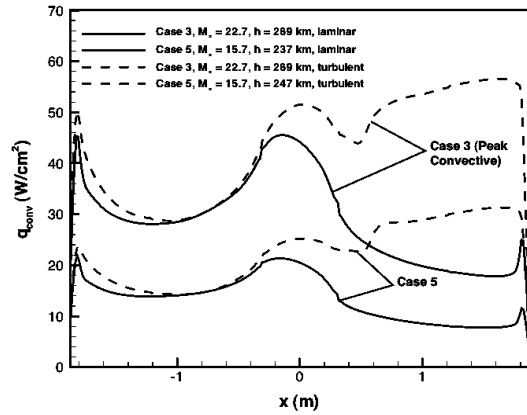


Fig. 13. Turbulent and laminar convective heating rates for Case 3 and 5.

Table 4. Vehicle aerodynamics.

	Case 1	Case 2	Case 3	Case 4	Case 5	Case 6	Case 7
CL	*	0.360	0.360	0.357	0.357	0.360	0.362
CD	*	1.446	1.437	1.421	1.420	1.427	1.429
L/D	*	0.249	0.251	0.252	0.251	0.252	0.254

Summary and Conclusions

Aeroheating environments along a reference trajectory were calculated for the Titan Aerocapture System Analysis study. The environment was calculated using two different CFD codes by two teams from different NASA Research centers for the purpose of reducing uncertainties through direct comparison of results. Sensitivity analyses showed that two codes are in good agreement when identical transport/chemical kinetic models are used. Axisymmetric flow calculations showed that while insensitive to the chemical kinetic rates, convective heating rates are sensitive to the diffusion model and the choice of chemical species. In contrast, the radiative heating rates calculated using the CFD solutions are sensitive to the shock stand off distance and the post shock temperature profile, which are influenced by the chemical kinetic model as expected. Radiation calculations using the CFD results showed that the majority of the heating on the aeroshell will be due to radiative heating, which will drive not only the TPS sizing but also the material selection due to the nature of radiative heating. For this reason, careful reexaminations of the chemistry models are needed to reduce the uncertainties in the radiative heating.

Three dimensional forebody calculations showed that the reference configuration meets the design L/D requirement of 0.25 along the reference trajectory. Momentum thickness Reynolds number along the forebody indicates that the flow is likely to transition to turbulent on the leeward side. Turbulent calculations show that the convective heating level on the leeside is increased by 250%, and the location of the maximum heating moves from the nose and the windward shoulder to the leeside shoulder.

Acknowledgments

The authors would like to acknowledge Peter Gnoffo for his valuable contribution towards the sensitivity analyses and assistance with the LAURA CFD program. In addition, the authors would like to acknowledge Lin Chambers for her assistance with the LORAN radiation program.

Naruhisa Takashima is supported under NASA Langley Research Center SAMS contract NAS1-00135. Ken Sutton is supported under contract NAS1-02117 from NASA Langley Research Center to National Institute of Aerospace. Michael Wright and Dinesh Prabhu were supported under contract NAS2-99092 from NASA Ames Research Center to ELORET Corp.

References

- ¹ Lockwood, M., "Titan Aerocapture Systems Analysis," AIAA 2003-4799, July 2003.
- ² Olejniczak, J., et al., "An Analysis of the Radiative Heating Environment for Aerocapture at Titan," AIAA 2003-4953, July 2003.
- ³ Nelson, H. F., Park, C. and Whiting, E. E., "Titan Atmospheric Composition by Hypervelocity Shock-Layer Analysis," *Journal of Thermophysics*, Vol. 5, No. 2, April-June 1991, pp 157-165.
- ⁴ Baillion, M., Pallegoix, J. F. and Soler, J., "Huygens Probe Aerothermodynamics," AIAA 97-2476, June 1997.
- ⁵ Park, C. and Bershader D., "Determination of the Radiative Emission of a Hypersonic Flow Simulating the Cassini-Titan Atmospheric Entry Probe Environment," AIAA 90-1558, June 1990.
- ⁶ Baillion, M., "Aerothermodynamic Requirements and Design of the Huygens Probe," *Capsule Aerothermodynamics*, AGARD-R-808, May 1997.
- ⁷ Edquist, K. T., et al., "Aeroheating Environments for a Mars Smart Lander," AIAA 2002-4505, Aug. 2002.
- ⁸ Justus, C. and Duvall, A., "Engineering- Level Model Atmospheres for Titan and Neptune," AIAA-2003-4803, July 2003.
- ⁹ Way, D., Powell, R. and Edquist, K., "Aerocapture Simulation and Performance for the Titan Explorer Mission," AIAA 2003 4951, July 2003.
- ¹⁰ Gnoffo, P. A., "Computational Aerothermodynamics in Aeroassist Applications," AIAA 2001-2632, 2001.
- ¹¹ Wright, M. J., Candler, G. v. and Bose, D., "Data-Parallel Line Relaxation Method for Navier-Stokes Equations," *AIAA Journal*, Vol. 36, No. 9, Sept. 1998.
- ¹² Wright, M.J., Loomis, M., and Papadopoulos, P., 'Aerothermal Analysis of the Project Fire II Afterbody Flow,' *Journal of Thermophysics and Heat Transfer*, Vol. 17, No. 2, pp. 240-249, 2003.
- ¹³ Park, C. "On Convergence of Chemically Reacting Flows" AIAA 85-0247, Jan. 1985.
- ¹⁴ Park, C. "A Review of Reaction Rates in High Temperature Air" AIAA 89-1740, June 1989.
- ¹⁵ Chambers, L. H., "Predicting Radiative Heat Transfer in Thermochemical Nonequilibrium Flow Fields," NASA TM-4564, Sept. 1994.
- ¹⁶ Whiting, E. E., et al., "NEQAIR96, Nonequilibrium and Equilibrium Radiative Transport and Spectra Program: User's Manual," NASA RP-1389, Dec. 1996.
- ¹⁷ Cheatwood, F. M. and Thompson, R., A., "The Addition of Algebraic Turbulence Modeling to Program Laura," NASA TM 107758, April 1993.

Aerocapture Simulation and Performance for the Titan Explorer Mission

David W. Way*
Richard W. Powell*
Karl T. Edquist*
James P. Masciarelli†
Brett R. Starr*

Abstract

A systems study for a Titan aerocapture orbiter has been completed. The purpose of this study was to determine the feasibility and potential benefits of using aerocapture technologies for this destination. The Titan Explorer design reference mission is a follow-on to the Cassini/Huygens exploration of the Saturnian system that consists of both a lander and an orbiter. The orbiter uses aerocapture, a form of aeroassist, to replace an expensive orbit insertion maneuver with a single guided pass through the atmosphere. Key environmental assumptions addressed in this study include: the uncertainty in atmospheric density and high frequency atmospheric perturbations, approach navigation delivery errors, and vehicle aerodynamic uncertainty. The robustness of the system is evaluated through a Monte Carlo simulation. The Program to Optimize Simulated Trajectories is the basis for the simulation, though several Titan specific models were developed and implemented including: approach navigation, Titan atmosphere, hypersonic aeroshell aerodynamics, and aerocapture guidance. A navigation analysis identified the Saturn/Titan ephemeris error as major contributor to the delivery error. The Monte Carlo analysis verifies that a high-heritage, low L/D, aeroshell provides sufficient performance at a 6.5 km/s entry velocity using the Hybrid Predictor-corrector Aerocapture Scheme guidance. The current mission design demonstrates 3-sigma success without additional margin, assuming current ephemeris errors, and is therefore not dependent on the success of the Cassini/Huygens mission. However, additional margin above 3-sigma is expected along with the reduced ephemeris errors in the event of a successful Cassini mission.

Nomenclature

BOC Beginning of Cassini
c.g. Center of Gravity
CAD Computer Aided Design
CFD Computational Fluid Dynamics
DoF Degree of Freedom
EDL Entry, Descent, and Landing
EOC End of Cassini
GRAM Global Reference Atmospheric Model

HYPAS Hybrid Predictor-corrector Aerocapture Scheme
IRIS Infrared Interferometer Spectrometer
L/D Lift to Drag Ratio
LAURA Langley Aerodynamic Upwind Relaxation Algorithm
MER Mars Exploration Rover
MGS Mars Global Surveyor
MPF Mars Pathfinder
MRO Mars Reconnaissance Orbiter
POST Program to Optimize Simulated Trajectories
SEP Solar Electric Propulsion
UVS Ultraviolet Spectrometer
□DOR Delta Differential One-way Ranging
□V Velocity Addition
□ Standard Deviation

* Aerospace Engineer, NASA Langley Research Center

† Aerospace Engineer, NASA Johnson Space Center

Background

Aerocapture description

Aerocapture, a form of aeroassist, is a propellant-less alternative to the currently requisite all-propulsive planetary capture. Using drag to decelerate the vehicle, aerocapture replaces the expensive orbit insertion maneuver with a single guided pass through the atmosphere. To date, aerocapture has not been demonstrated in flight.

In contrast, aerobraking uses many passes through the atmosphere to reduce the period of an elliptical orbit. This reduces, but does not eliminate, the propulsive capture requirement. Aerobraking has been used successfully in the Martian atmosphere by Mars Global Surveyor (MGS), and Mars Odyssey, and is planned for Mars Reconnaissance Orbiter (MRO).

A nominal drag profile associated with the aerocapture pass is designed to remove all of the hyperbolic excess velocity and enough additional orbital energy to place the spacecraft in an elliptical orbit with the desired apoapsis. Because of the larger energy requirements, aerocapture occurs at altitudes much lower than aerobraking. A guidance system is used to target the desired exit conditions by reacting to changes in the atmosphere. Bank angle modulation is used to control the rate of ascent/descent, which indirectly affects the drag. The flight path angles required to fly full lift-up and full lift-down form a theoretical entry corridor.

Figure 1 diagrams the sequence of aerocapture events. At the first apoapsis after the aerocapture pass, a small propulsive maneuver must be completed to raise the periapsis to the desired altitude. The periapsis must be raised during the first orbit in order to prevent the vehicle from re-entering the atmosphere a second time. Another small propulsive burn is typically performed at periapsis to clean-up any residuals in the desired science orbit apoapsis.

Titan Explorer Mission

The Titan Explorer design reference mission is a follow-on to the Cassini/Huygens exploration of the Saturnian system that consists of both a lander and an orbiter.¹ Both spacecraft

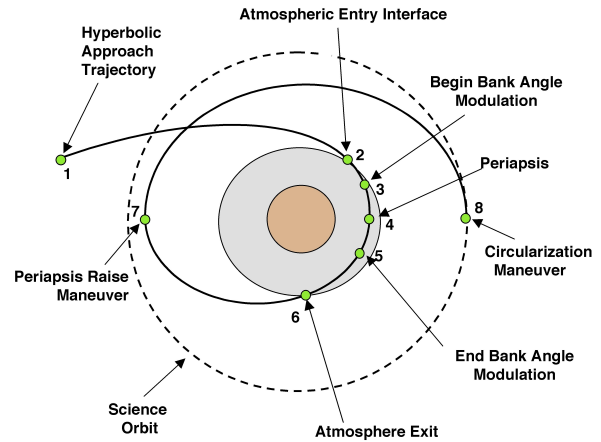


Figure 1: Aerocapture into Circular Orbit

are launched together on a single Delta IV-class launch vehicle in 2010. Figure 2 shows a Computer Aided Design (CAD) model of the stack packaged in a 4 m launch fairing. A Solar Electric Propulsion (SEP) module and a single Venus gravity assist provide a 6.25 year interplanetary cruise to the Saturn system.²

Both the orbiter and the lander are initially targeted for a direct entry to Titan. Thirty days prior to arrival, the orbiter releases the lander and executes a divert maneuver to the desired aerocapture approach trajectory.

The orbiter provides a telecom link for the lander during Entry, Descent, and Landing (EDL) then completes an aerocapture to the desired science orbit (a near-polar 1700 km circular orbit). Following aerocapture, the heatshield and backshell are jettisoned, and the orbiter begins a three-year science mission.

Study Goals

A systems study for a Titan aerocapture orbiter has been completed as part of the NASA In-space Propulsion Program.³ The purpose of this study was to determine the feasibility and potential benefits of using aerocapture technologies for this destination.^{4,5} The products of this study are a reference mission, baseline systems definition, and technology requirements that may be used by scientists, systems engineers, technology developers, and mission managers in planning future missions. This study provides additional value over previous systems studies because of the higher fidelity of

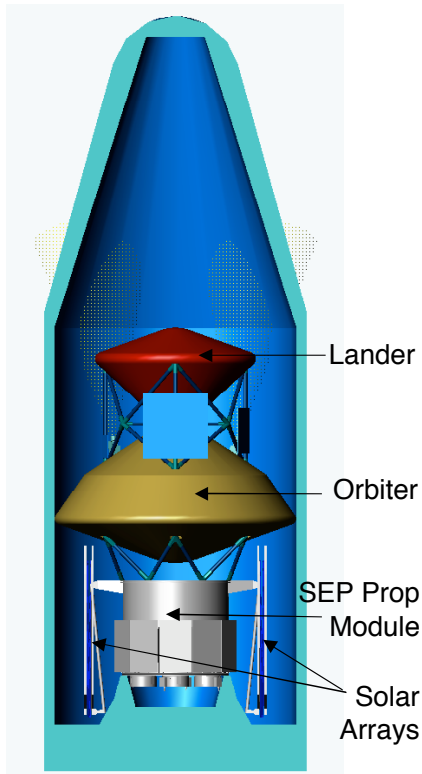


Figure 2: Launch Configuration

the analyses and environmental models that were employed.

Key environmental assumptions, central to successful aerocapture, are addressed in this study. These assumptions include the uncertainty in atmospheric density, high frequency atmospheric variability, approach navigation delivery errors, and vehicle aerodynamic uncertainty. Aerocapture risk is mitigated by quantifying the atmospheric uncertainty based on all available measurements, designing the vehicle to provide adequate aerodynamic control authority, developing a robust guidance system, and incorporating sufficient margins. The robustness of the system is evaluated through Monte Carlo simulation.

Simulation Heritage

The heritage of the Monte Carlo simulation used in this study is based upon previous Langley Research Center work on many diverse planetary missions that involve phases of atmospheric flight. These missions

include aerobraking orbiters: MGS, Mars Odyssey, and MRO (scheduled for launch in 2005); direct lander entries: Mars Pathfinder (MPF), Genesis, Stardust, Mars 2001 Surveyor Lander (cancelled), Mars Exploration Rovers (MER), and Mars Science Laboratory (MSL) (planned for launch in 2009); and aerocapture proposals: Mars Surveyor 2001 Orbiter (cancelled) and Mars Premier Orbiter (aerocapture option not adopted). The current simulation leverages this experience in atmospheric flight and applies it to a new destination, Saturn's largest moon, Titan.

Simulation Development

Trajectory Simulation

To aid in the systems study activity, a high fidelity Monte Carlo trajectory simulation has been developed to simulate flight through the Titan atmosphere during aerocapture. This simulation provides data and statistics used to quantify mission success probabilities, evaluate candidate guidance algorithms, and provide the technical feedback required for mission and aeroshell design (aerodynamic loads, maximum heat rate, integrated heat loads, orbit circularization fuel, etc.).

The Program to Optimize Simulated Trajectories (POST) is the basis for this simulation.⁶ However, several Titan specific models were developed and implemented to support this work. These models include: approach navigation, Titan atmosphere, hypersonic aeroshell aerodynamics, and aerocapture guidance. These models are discussed in more detail.

Atmosphere

An engineering-level atmosphere model, denoted Titan-GRAM, was developed for this study.⁷ Titan-GRAM is similar to and based upon the Mars Global Reference Atmosphere Model, Mars-GRAM, which has been used for in the design and operations support for many Mars exploration projects.

Titan-GRAM atmospheric density predictions are based on minimum, nominal, and maximum density vs. altitude profiles predicted by Yelle et al.⁸ The Yelle models are based on

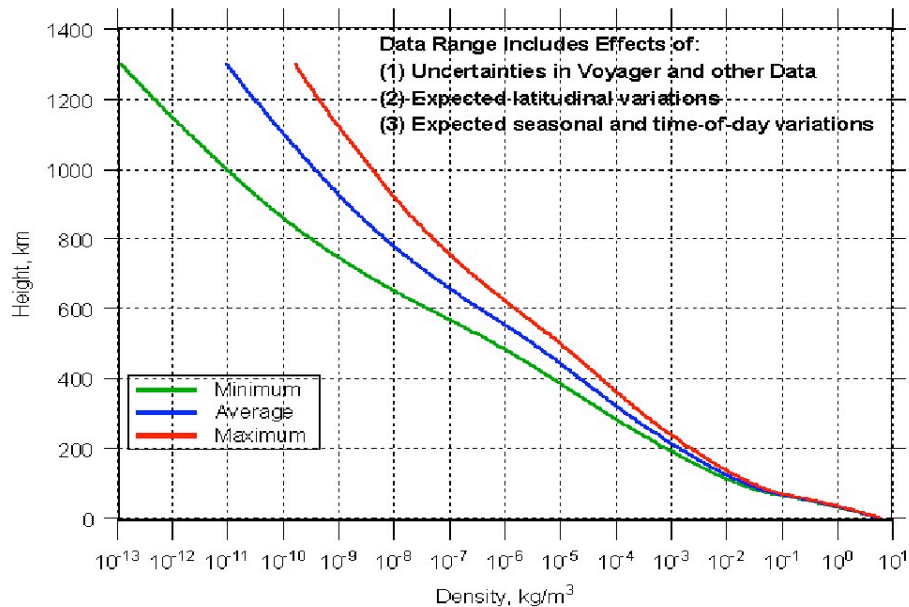


Figure 3: Yelle et al. Titan Atmospheric Density Profiles

observations from Voyager 1 radio science, Infrared Interferometer-Spectrometer (IRIS), and Ultraviolet Spectrometer (UVS). Shown in Figure 3, the Yelle density profiles include density variation due to latitude, season, and diurnal effects as well as measurement uncertainty.

Within Titan-GRAM, an atmospheric density control parameter, $f_{\min\max}$, is used to linearly interpolate between the Yelle profiles. An $f_{\min\max}$ of 1.0 corresponds to the maximum expected density for a given altitude, while $f_{\min\max}$ of -1.0 corresponds to the minimum expected density. A sinusoidal variation of $f_{\min\max}$ with latitude was implemented to simulate latitudinal density gradients during an aerocapture pass.

Within the trajectory simulation, $f_{\min\max}$ is varied as a function of latitude to capture the expected latitudinal gradients. A perturbation model, based on gravity wave theory, is also included for use in the Monte Carlo analysis with a maximum perturbation (1 σ) of 10% the mean density. Figure 4 shows a sample of perturbed density profiles generated by Titan-GRAM.

Aerodynamics

An aerodynamic model for the reference spacecraft has been developed using high-fidelity computations. The reference spacecraft has a 70 deg sphere-cone heatshield, similar to the Viking Mars Lander entry vehicle, and a bi-conic backshell. The configuration is shown in Figure 5.

Constant normal and axial force aerodynamic coefficients are used for the aerocapture pass simulation and are based on Langley Aerodynamic Upwind Relaxation Algorithm (LAURA) Computational Fluid Dynamics (CFD) results in the hypersonic regime. LAURA solves the viscous fluid dynamic equations on a structured grid with built-in adaptation.⁹ Thermal and chemical non-equilibrium models are used to calculate the high-temperature flowfield behind the bow shock.

The high heritage, $L/D = 0.25$, aeroshell configuration provides 3.5 degrees of theoretical corridor width at a 6.5 km/sec entry velocity. A higher entry velocity of 10 km/s results in a 4.7 degree theoretical corridor.

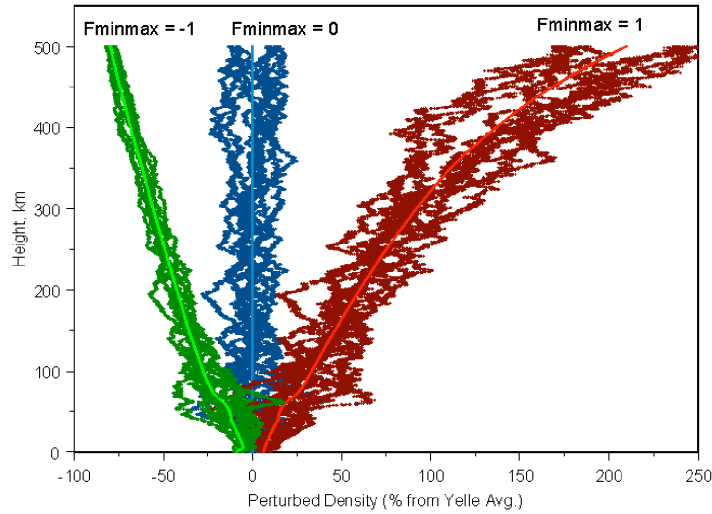


Figure 4: Sample Titan-GRAM Density Perturbations

Guidance

A Hybrid Predictor-corrector Aerocapture Scheme (HYPAS) aerocapture guidance algorithm was developed and included in the simulation.¹⁰ The HYPAS algorithm uses an analytic method, based on deceleration due to drag and altitude rate error feedback, to predict exit conditions and then adjust the bank angle command in order to achieve a target apoapsis altitude and orbit inclination at atmosphere exit.

The HYPAS guidance consists of two phases: the “capture phase”, in which the guidance establishes pseudo-equilibrium glide conditions; and an “exit phase”, in which exit conditions are predicted, assuming a constant altitude rate, and the lift vector is adjusted to null the error between predicted and target apoapsis. Figure 6 shows the guidance phases during an aerocapture pass.

Bank reversals maintain inclination error within desired limits. All reference values are computed and updated during flight. The HYPAS algorithm was adapted for use at Titan, and two sets of guidance initialization parameters were developed: one for the 6.5 km/s entry, and one for the 10.0 km/s entry. Monte Carlo trajectory simulations were run with this guidance to determine overall aerocapture performance.

A pseudo bank controller was developed to mimic the dynamics of a flight control system in a Three Degree-of-Freedom (3-DoF) simulation. These effects include a control system time lag and a finite system response, limited by a maximum angular acceleration and a maximum angular velocity. The bank angle controller analytically calculates the time required, and resulting angular travel necessary, to complete the maneuver to the commanded attitude. It has been found that including this type of controller in a 3-DoF simulation provides a good approximation to Six Degree-of-Freedom (6-DoF) dynamics.

Because the aerocapture spacecraft performs bank reversals to maintain inclination accuracy, and because these reversals could take as much as 15 seconds to complete, the trajectory simulation must model the effects of an attitude controller. These bank reversals force the

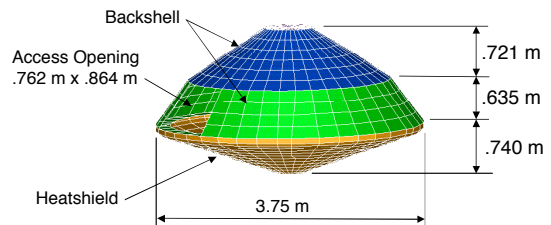


Figure 5: Aeroshell Configuration

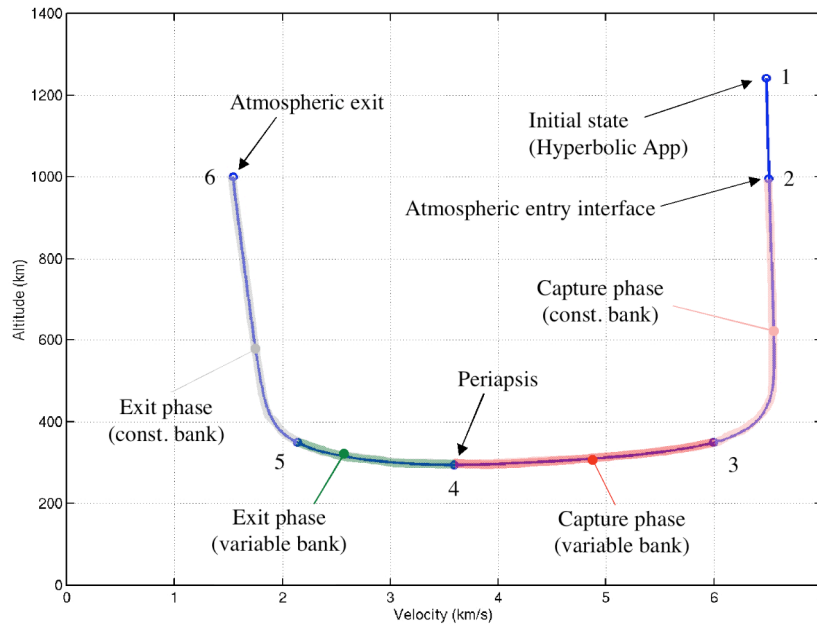


Figure 6: Phases of HYPAS Aerocapture Guidance

spacecraft off of the optimum flight profile that the guidance is trying to follow. Not including the error produced during this maneuver would result in overly optimistic conclusions regarding the vehicle's targeting ability and the required circularization ΔV .

Navigation

Initial states were provided by a JPL navigation assessment that assumed post-Cassini ephemeris knowledge and the following data sources: two-way Doppler and ranging, ΔDOR , and optical navigation.¹¹ These assumptions resulted in a 3σ delivery flight path angle dispersion of ± 0.93 deg. Figure 7 shows the delivery footprint in the B-plane. The dashed line in this figure is a radius vector to the nominal aim-point.

The three dominant contributors to this delivery error were Saturn and Titan ephemerides, maneuver execution error, and optical data measurement error. The current Cassini mission is expected to improve the ephemeris errors by a factor of six. However, this improved navigation is not guaranteed, but rather contingent upon the successful completion of the Cassini mission. Therefore, both Beginning of Cassini (BOC) and End of Cassini (EOC) states were evaluated. For the purposes of this study, it was assumed that the flight path

angle dispersions would degrade by approximately 52% with the use of BOC states.

Since Titan is a moon of Saturn with an orbital period of approximately 16 days, the mission designer has a wide choice in approach velocities for any mission opportunity (Titan's velocity could either add or subtract from the nominal Saturn approach velocity). Intercepting Titan at different true anomalies easily tailors the entry velocity, with only small changes in the

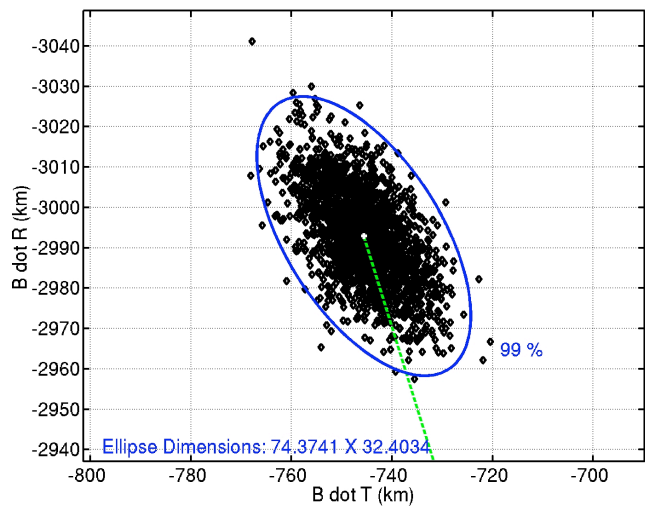


Figure 7: Delivery Error in the B-plane

incoming hyperbolic approach trajectory. Entry velocities of 6.5 km/s and 10.0 km/s were considered. A 15% increase in flight path angle dispersions was levied on the higher entry velocity.

The Table 1 summarizes the entry flight path angle dispersions assumed in this study along with the theoretical corridor for an L/D = 0.25. Further navigational assessment is required to validate these assumptions.

Table 1: Entry Flight Path Angle Uncertainties

Entry Velocity	EOC Ephemeris	BOC Ephemeris	Theoretical Corridor
6.5 km/s	± 0.93 deg	± 1.42 deg	3.5 deg
10 km/s	± 1.07 deg	± 1.63 deg	4.7 deg

Results

Monte Carlo Analysis

System performance, risk, and robustness are measured by generating statistics from Monte Carlo simulations of the Titan aerocapture. Many (generally 2000) individual aerocapture trajectories are simulated with random perturbations applied to initial entry conditions, vehicle aerodynamics, vehicle mass properties, and Titan atmospheric conditions. This flight simulation is composed of three main parts: a POST2 trajectory simulation, which integrates all of the models discussed above; an executive Monte Carlo script, which coordinates the generation and execution of 16 parallel simulations; and various supporting scripts for sampling random distributions, compiling and formatting output data, evaluating metrics and statistics, and producing plots and figures. Table 2 lists the uncertainties used in this study.

Table 2: Monte Carlo Uncertainties

Category	Variable	Nominal	$\pm 3\sigma$ or min/max	Distribution
Initial Conditions	x- position	603.3 km	From covariance	Correlated
	y- position	-390.8 km	From covariance	Correlated
	z- position	3502 km	From covariance	Correlated
	x- velocity	-3.363 km/s	From covariance	Correlated
	y- velocity	-4.123 km/s	From covariance	Correlated
	z- velocity	-3.734 km/s	From covariance	Correlated
Atmosphere	Perturbation seed	1	1/9999	Uniform (integer)
	Fminmax bias	0	-0.53/+0.53	Uniform
Aerodynamics	Trim angle-of-attack	-16 deg	± 2.0 deg	Normal
	C_A (axial force)	1.48	$\pm 3\%$	Normal
	C_N (normal force)	-0.05	$\pm 5\%$	Normal
Mass Properties	Axial c.g.(Zcg/D)	0.1979	± 0.00848	Normal
	Radial c.g.(Xcg/D)	0.0231714	± 0.00184	Normal

Beginning of Cassini

The first scenario examined is for a navigation ephemeris uncertainty consistent with knowledge prior to the Cassini mission. This combination of large navigation uncertainty and low entry velocity, 6.5 km/s, results in the most challenging conditions. Statistics for apoapsis altitude and circularization ΔV are presented in Table 3.

Figure 8 shows the aerocapture corridor (flight path angle) as a function of f_{minmax} (density). The theoretical corridor is bounded by the full lift-down and full lift-up cases. The plus (+) symbols show the range of f_{minmax} during the active guidance portion of the aerocapture pass, due to latitudinal variation of f_{minmax} . The circles indicate the f_{minmax} at periapsis. The bias in the data towards the higher values of f_{minmax} is again due to the latitudinal variation of f_{minmax} , since the aerocapture pass occurs over northern latitudes. The target flight path angle was chosen to capture as many of the cases as possible into the theoretical corridor. The large spread in entry flight path angle, compared to the theoretical corridor, suggests small margins.

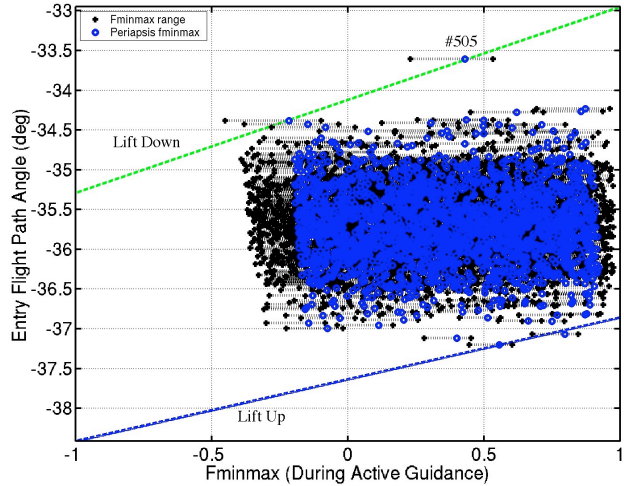


Figure 8: Entry Corridor, BOC 6.5 km/s

Table 3 Performance Statistics, BOC 6.5 km/s

	Apoapsis altitude (km)	Circularization ΔV (m/s)
Minimum	1240.5	157.2
Maximum	2166.3	293.3
Mean	1691.3	179.6
1 σ	± 63.9	± 11.1
3 σ	± 191.8	± 33.2

Figure 9 shows a histogram of the final apoapsis altitude. The mean apoapsis of 1691.3 km, with a standard deviation of ± 63.9 km, compares well with the 1700 km target altitude. Additionally, the 3 σ range of ± 191.8 km is within the target range of < 200 km, which indicates that the guidance can be tuned to capture a large percentage of the theoretical corridor. Only one case (#505) failed to capture. However, this case represents a 4.5-sigma case for entry flight path angle, which has a probability of occurrence of only 1 in nearly 15,000.

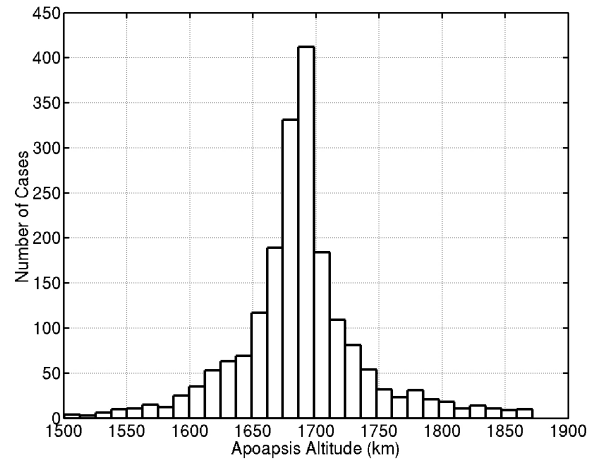


Figure 9: Apoapsis Altitude, BOC 6.5 km/s

Figure 10 shows the histogram for the required ΔV . This ΔV includes both the periapsis raise maneuver and the final circularization burn. The 3-sigma (99.86 %-tile) value is 212.9 m/s.

End of Cassini

These Monte Carlo results are representative of navigation ephemeris uncertainty post-Cassini for a 6.5 km entry velocity. Statistics for apoapsis altitude and circularization ΔV are presented in Table 4.

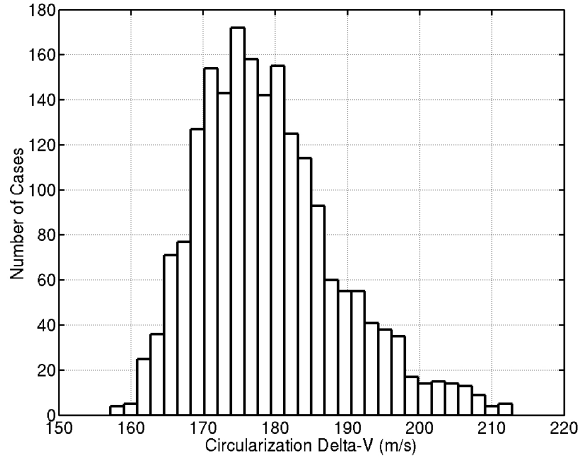


Figure 10: Circularization ΔV , BOC 6.5 km/s

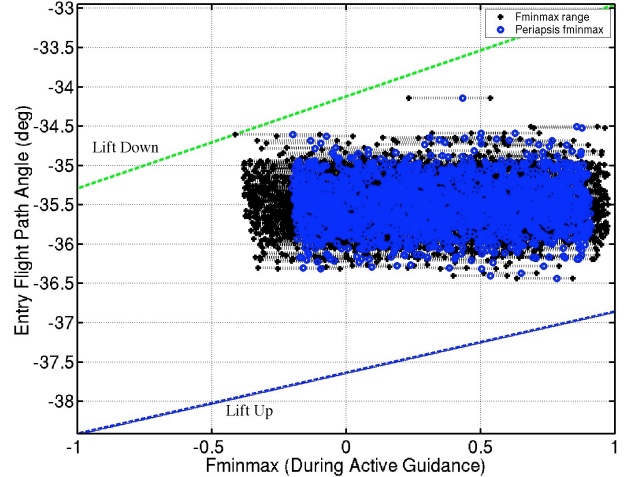


Figure 11: Entry Corridor, EOC 6.5 km/s

Figure 11 shows the aerocapture corridor (flight path angle) as a function of f_{minmax} (density). The effect of the improved (reduced) uncertainty expected from the Cassini mission is evident by the tighter grouping in flight path angle as compared to Figure 8. The size of the flight path angle dispersions, compared to the theoretic corridor, suggests increased margins for this scenario. Because of the arrival geometry, the aerocapture pass occurs over northern latitudes – entering over the northern pole and exiting near the equator. Therefore, the mean f_{minmax} (~ 0.3) is positive. The target flight path angle was chosen to bring this mean to the center of the theoretical corridor.

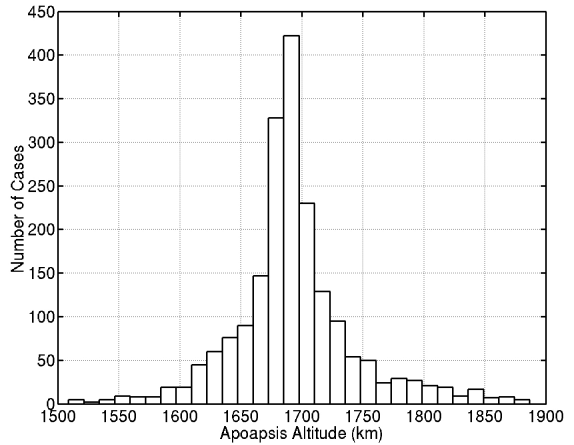


Figure 12: Apoapsis Altitude, EOC 6.5 km/s

Table 4 Performance Statistics, EOC 6.5 km/s		
	Apoapsis altitude (km)	Circularization ΔV (m/s)
Minimum	1327.8	156.0
Maximum	2196.6	252.8
Mean	1697.7	177.7
1 σ	± 63.5	± 9.5
3 σ	± 190.4	± 28.6

Figure 12 shows a histogram of the final apoapsis altitude. The mean apoapsis is 1697.7 km, with a standard deviation of 63.5 km. The 3-sigma range of ± 190.4 km is within the target range of < 200 km. All cases captured within 500 km of the target apoapsis.

Figure 13 shows the histogram and statistics for the required ΔV . The 3-sigma (99.86 %-tile) value is 206.3 m/s. The maximum ΔV was 252.8 m/s.

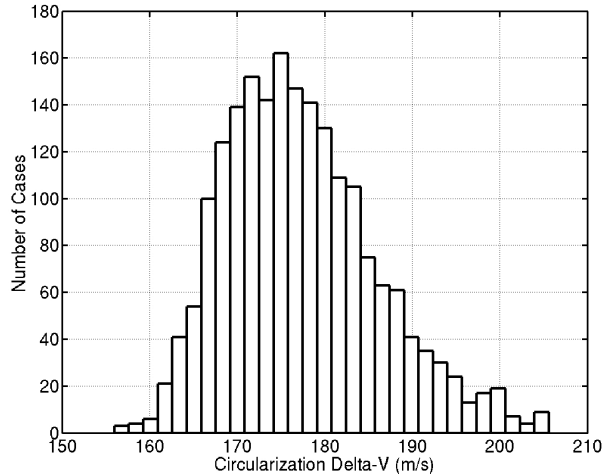


Figure 13: Circularization ΔV , EOC 6.5 km/s

Conclusions

1. The JPL navigation analysis identified the Saturn/Titan ephemeris error as major contributor the delivery error. The current mission design demonstrates 3-sigma success, without additional margin, assuming BOC ephemeris errors, and is therefore not dependent on the success of the Cassini/Huygens mission. However, additional margin above 3-sigma is expected along with the reduced EOC ephemeris errors in the event of a successful Cassini mission.
2. Uncertainty in the Titan atmospheric density, including high frequency perturbations, is the single largest unknown. To mitigate this risk, sufficient margin and conservatism are carried in the design of the entry conditions, aeroshell, and guidance system. While arrival during a particular season would reduce the expected density range, the full density range was used in the Monte Carlo analysis.
3. The Monte Carlo analysis verifies that a high-heritage, low L/D, aeroshell provides sufficient performance at a 6.5 km/s entry velocity. A mid L/D aeroshell technology development is not required. Additional aerocapture performance is also available at higher entry velocities, 10 km/s, but must be

traded against increased Thermal Protection System requirements.

4. The Monte Carlo analysis demonstrates that the HYPAS guidance is robust and provides acceptable performance. Approximately 92% of the theoretical corridor is captured using this algorithm while requiring only slightly more than 200 m/s of on-orbit ΔV to achieve the target science orbit.

References

1. Bailey, R., Hall, J., and Spilker, T., "Titan Aerocapture Mission and Spacecraft Design Overview," AIAA-2003-4800, Conference Proceedings of the 39th AIAA/ASME/SAE/ASEE Joint Propulsion Conference and Exhibit, Huntsville, AL, July 2003.
2. Noca, M., Bailey, R., and Dyke, R., "Titan Explorer Mission Trades from the Perspective of Aerocapture," AIAA-2003-4801, Conference Proceedings of the 39th AIAA/ASME/SAE/ASEE Joint Propulsion Conference and Exhibit, Huntsville, AL, July 2003.
3. James, B. and Munk, M., "Aerocapture Technology Development Within the NASA In-Space Propulsion Program," AIAA-2003-4654, Conference Proceedings of the 39th AIAA/ASME/SAE/ASEE Joint Propulsion Conference and Exhibit, Huntsville, AL, July 2003.
4. Hall, J., Noca, M., and Bailey, R., "Cost-Benefit Analysis of the Aerocapture Mission Set," AIAA-2003-4658, Conference Proceedings of the 39th AIAA/ASME/SAE/ASEE Joint Propulsion Conference and Exhibit, Huntsville, AL, July 2003.
5. Lockwood, M. K., "Titan Aerocapture Systems Analysis," AIAA-2003-4799, Conference Proceedings of the 39th AIAA/ASME/SAE/ASEE Joint Propulsion Conference and Exhibit, Huntsville, AL, July 2003.

6. Bauer, G. L., Cornick, D. E., and Stevenson, R., "Capabilities and Applications of the Program to Optimize Simulated Trajectories (POST)," NASA CR-2770, February 1977.
7. Justus, C. and Duvall, A., "Engineering-Level Model Atmospheres for Titan and Neptune," AIAA-2003-4803, Conference Proceedings of the 39th AIAA/ASME/SAE/ASEE Joint Propulsion Conference and Exhibit, Huntsville, AL, July 2003.
8. Yelle, R. V., Strobel, D. F., Lellouch, E., and Gautier, D., "Engineering Models for Titan's Atmosphere," in ESA report SP-1177, "Huygens Science, Payload and Mission," August 1997.
9. Cheatwood, F. M. and Gnoffo, P. A., "User's Manual for the Langley Aerodynamic Upwind Relaxation Algorithm (LAURA)," NASA TM-4674, April 1996.
10. Masciarelli, J. and Queen, E., "Guidance Algorithms for Aerocapture at Titan," AIAA-2003-4804, Conference Proceedings of the 39th AIAA/ASME/SAE/ASEE Joint Propulsion Conference and Exhibit, Huntsville, AL, July 2003.
11. Haw, R., "Approach Navigation for a Titan Aerocapture Orbiter," AIAA-2003-4802, Conference Proceedings of the 39th AIAA/ASME/SAE/ASEE Joint Propulsion Conference and Exhibit, Huntsville, AL, July 2003.

39th AIAA/ASME/SAE/ASEE Joint Propulsion Conference and Exhibit
Huntsville, AL
July 22, 2003

PLANETARY PROBE MASS ESTIMATION TOOL DEVELOPMENT AND ITS APPLICATION TO TITAN AEROCAPTURE

R. Eric Dyke*
Swales Aerospace
Hampton, VA 23681

ABSTRACT

An integrated mass properties estimation and aeroshell structural sizing design tool, called PROBECODES, is being developed for quick sizing of conceptual, atmospheric-entry planetary exploration vehicles. This tool will eventually integrate EDS PLM Solutions I-deas[®] entry system geometry models, Microsoft[®] Excel-based entry system mass properties estimation spreadsheets, CFD generated aerothermodynamic loads, and structural sizing/optimizing software such as EDS PLM Solutions I-deas[®] or Collier Research's HyperSizer[™] in order to create preliminary vehicle mass estimates, with particular emphasis on aeroshell structural sizing estimates. The Microsoft[®] Excel-based spreadsheet portion of the tool, called ProbeMAASS1 is currently being developed. It contains a mass properties/design database of previous planetary exploration vehicles and design studies; a mass properties breakdown and design description of these vehicles' major subsystems; mass estimation methods for the major subsystems of new vehicles using combinations of analytical techniques, empirical relationships, and user-specified data; and an automatic aeroshell structural finite element mesh generator. Currently this tool is limited to sphere-cone and ellipsled type vehicles, but future versions will include other types as they are developed. Though still under development, parts of this tool were successfully used to help quickly estimate Orbiter aerocapture system masses for a wide variety of TPS material/thickness and aeroshell size combinations for

the Titan Aerocapture Systems Analysis study of 2002. In addition this tool was used to help estimate total launch wet mass for ten different Titan mission/launch vehicle configurations. This paper will present an overview of the full tool (PROBECODES) and an overview of the mass properties estimation spreadsheets (ProbeMAASS1). Lastly, it will present the mass sensitivity results from the Titan Aerocapture study.

NOMENCLATURE/ABBREVIATIONS

CBE	Current Best Estimate
CFD	Computational Fluid Dynamics
CG's	Centers of Gravity
EGA	Earth Gravity Assist
GDTL	Geometric Data Transfer Link
GUI	Graphical User Interface
L/D	Lift divided by Drag
LMDTL	Lumped Mass Data Transfer Link
LV	Launch Vehicle
MEL	Master Equipment List
MEM's	Mass Estimation Methods
MPD	Mass Properties Database
MPB	Mass Properties Breakdown
SEP	Solar Electric Propulsion
TPS	Thermal Protection System
VVGA	Venus-Venus-Venus Gravity Assist
VGA	Venus Gravity Assist
ΔV	Velocity change

INTRODUCTION

As part of the ongoing exploration of the solar system, there is a need for an atmospheric-entry probe design tool that takes conceptual probe design data and provides quick-turnaround probe mass estimates and aeroshell structural sizing. To fulfill this need, an integrated mass properties estimation and aeroshell structural sizing design tool is currently being developed. This tool, called PROBECODES (Probe Conceptual Design Software), is comprised of several different components, including commercially available software, as shown in Figure 1. Current methods for

* Aerospace Engineer

probe mass estimation and aeroshell sizing often involve using separate, non-integrated historical data, mass estimation methods, and finite element modeling/structural sizing tools. Often the geometry models, mass estimations, and finite element modeling are done by different individuals using different tools which may or may not share data easily. The ultimate goal of PROBECODES is to integrate mission-driven payload requirements, EDS PLM Solutions I-deas^{®1} entry system geometry models, Microsoft[®] Excel²-based entry system historical databases, Microsoft[®] Excel-based mass properties estimation spreadsheets, CFD-generated aerothermodynamic loads (pressure and/or temperature distributions), structural materials data, and structural sizing/optimizing software such as MSC/NASTRAN³, EDS PLM Solutions I-deas[®] or Collier Research's HyperSizer^{TM 4} into a seamless end-to-end tool in order to produce preliminary vehicle mass and aeroshell structural sizing estimates. The primary benefit of PROBECODES, when completed, over previous methods will be to allow a single user to quickly create conceptual probe geometry, estimate component masses, and size the aeroshell structure all within a single tool in a short time.

PROBECODES and the mass estimation component, ProbeMAASS1 (Probe Mass Approximations & Automeshing for Structural Sizing, version 1), are currently limited to sphere-cone and ellipsed shaped entry vehicles. Future entry vehicle shapes, such as bi-conics, bent bi-conics, and other configurations will be addressed in later versions. This tool also assumes a general payload packaging layout has been established. Lastly, the automated structural sizing aspects of the tool are currently limited to the aeroshell. Sizing for the wide variety of possible internal structural components such as payload support structure (decks, rings, etc.) is not currently supported. Such items must be handled in an "offline" manner, with the resulting finite element meshes and masses then being used as input to this tool.

While still in the development stages, portions of ProbeMAASS1 were successfully used for mass sensitivity studies for the Titan Aerocapture Systems Study of 2002⁵. Aeroshell mass sensitivities were developed for a range of provided TPS materials and aeroshell size/TPS material combinations. In addition, the tool was used to help estimate total (full stackup) launch wet masses for ten different mission architectures. The results of these studies are presented later in this paper.

OVERVIEW OF PROBECODES TOOL

The baseline requirements in developing PROBECODES are that preliminary aeroshell structural design and probe mass estimate results be produced from the conceptual data in a relatively short time (2 to 3 days), and that these results be produced with a minimum of special hardware and software. The current tool architecture primarily uses EDS PLM Solutions I-deas[®], Microsoft[®] Excel, and Collier Research's HyperSizerTM. I-deas[®] is used for aeroshell solid modeling and surface area/volume calculations and for aeroshell structural finite element model editing and solving. Microsoft[®] Excel is used for the probe mass properties database of historical probes and probe studies, the mass estimation methods, aeroshell surface area calculations, and aeroshell structural finite element model generation. Though not yet integrated into PROBECODES, Collier Research's HyperSizerTM will be used to optimize the aeroshell structure. As newer, better methods become available, or as the tool components allow themselves to be combined or separated, the tool architecture as shown in Figure 1 will be modified to incorporate those changes to produce a more efficient product.

Payload Requirements, Mission Design

The user must start with a given or assumed mission profile. The mission profile determines the payload components required to meet the mission objectives, including scientific instrumentation and their associated support subsystems (telecom, navigation, command and data handling, power, etc.). The mission profile also determines the delivery time and atmospheric entry profile, including entry speed, entry angle, maximum deceleration, and aeroheating rates and total heat loads. The aerodynamic performance requirements, such as vehicle L/D, ballistic coefficient, etc., necessary to ensure the proper entry profile help determine the general class of entry vehicle. Currently, the low L/D vehicles are represented by the axisymmetric sphere-cone shapes, and the mid L/D vehicles are represented by the ellipsed shape. Together, the general vehicle shape required and the volume necessary to accommodate the proposed payload determine the overall aeroshell size.

Solid Modeling (EDS PLM Solutions I-deas[®])

EDS PLM Solutions I-deas[®] is used as the entry vehicle solid modeler. Multiple axisymmetric sphere-cone solid models have been created within an I-deas[®] model file, including a stand-alone forebody, stand-alone backshells (conic, bi-conic, multi-conic,

hemispheric, and spherical cap), and combined forebody/backshell models for bi-conic and hemispheric cap backshells. These models are parametrically dimensioned such that the user may edit one or all of the cross section dimensions and the solid model is automatically updated. An axisymmetric ellipsled solid model has also been created with a single backshell separation configuration. Additional solid models will be created for more general (non-axisymmetric) ellipsled shapes with more general backshell separation geometries.

Geometric Data Transfer Link (GDTL)

The GDTL transfers the solid model geometry data from I-deas[®] to the ProbeMAASS1 spreadsheets. With the appropriate solid model opened, an I-deas[®] program file is used to list and save the model dimensions and surface areas. The program file is then transferred (if necessary) to the PC platform where ProbeMAASS1 resides. A macro within ProbeMAASS1 then reads the file and uploads the dimensions and surface areas for use in later calculations.

Entry System Database

The entry system database is a compilation of planetary exploration probe and probe study design data. It is in Excel spreadsheet form, with separate sheets for the sphere-cone and ellipsled vehicle types. These databases, described in more detail in a later section, are part of the ProbeMAASS1 spreadsheets, and contain probe geometry, entry environment definition, subsystem and component masses, and structural materials and construction methods. The data are used to develop mass estimation methods in ProbeMAASS1, and allow the user to make quick initial guesses for subsystem or component masses based on similarity to previous designs.

User Input Parameters

User input parameters are values entered into the ProbeMAASS1 spreadsheets. They include such wide-ranging details as probe destination, number of propellant tanks, or parachute diameter. They are input in a “linear” fashion on each spreadsheet from top to bottom, as each spreadsheet is filled out for each probe system. ProbeMAASS1 uses the historical database, user input, and mass estimation methods (MEM’s) discussed later to calculate component masses. The user can also override any or all calculated values in the spreadsheets. Since the ProbeMAASS1 spreadsheets will calculate aeroshell surface areas that are used in aeroshell structure and TPS mass estimation, the user may also input probe dimensions separate from the

imported I-deas[®] geometry. This allows the user to take quick looks at the impact dimension changes have on aeroshell mass.

Entry Systems Mass Properties Tool (ProbeMAASS1)

ProbeMAASS1 is the heart of this mass estimation tool. It will be discussed in more detail in a later section.

Mass Properties Output

The mass properties output currently consists of three items: the lumped mass data, the aeroshell mesh, and the probe mass summary. The lumped mass data consists of point masses and their associated centers of gravity (CG’s) for larger components. They are either calculated by the ProbeMAASS1 spreadsheets or entered directly by the user, and are added to the aeroshell mesh file. While the spreadsheets currently determine the point masses, the CG calculations have not yet been fully integrated into ProbeMAASS1. The aeroshell mesh is a structural finite element mesh created by internal macros in the ProbeMAASS1 spreadsheets and is described in more detail in a later section. The probe mass summary sheet lists current best estimate (CBE) masses for each probe component. Component masses are also added to give associated subsystem masses and total probe mass. The user may also specify separate uncertainty factors to be applied to each component CBE to determine the growth mass. In the first pass through ProbeMAASS1, before aeroshell structural sizing has been completed, the aeroshell mass is calculated parametrically from historical probe data. Due to the wide variety of probe configurations, this first aeroshell mass estimate is considered low fidelity and must be updated after the structural sizing has been completed on the aeroshell.

Inertial, Aero & Thermal Loads

These loads are determined by external analyses. Simple inertial loads (gravity and body accelerations) and uniform aerodynamic pressures can be applied to the mesh within the ProbeMAASS1 spreadsheets and macros. Thermal loads/temperature distributions and more complex aerodynamic pressure distributions must be applied within I-deas[®] or some other pre/post processor at this time.

Material Data

The material data for finite element analysis is typically specified by the user within a finite element pre/post processor. Since the aeroshell structure is to be optimized using Collier Research's HyperSizer™ (see below), the current tool architecture assumes the aeroshell will be optimized using a HyperSizer™ material database.

Finite Element Modeling/Structural Sizing

The aeroshell mesh is imported into I-deas® or other appropriate pre-processor. There the mesh is edited/modified, lumped masses are added, and secondary or payload support structure is added as necessary. The model is then solved in I-deas® or MSC/NASTRAN. The mesh input and results files are then submitted to HyperSizer™ for structural optimization of the aeroshell.

HyperSizer™ is a windows-based, commercially available structural sizing/weight estimation/weight optimization software tool⁴. A plate and/or beam element finite element model and its results file are first read into HyperSizer™. A graphical interface allows the user specify a range of structural "families" (i.e., unstiffened panels, sandwich panels, uniaxially stiffened panels), a range of structural "concepts" (i.e. "C" or "I" stiffeners), and a range of materials for various regions of the finite element model. HyperSizer™ then steps through each combination of designs for each region from lightest to heaviest until a successful design is created. The major advantage of HyperSizer™ is that it performs numerous user specified closed-form failure checks on each region for each design (family/concept combination) using the initial finite element model. This eliminates the need to create multiple finite element models.

Once aeroshell optimization is complete, the aeroshell mass is entered into the probe summary spreadsheet. Future enhancements will include automatic updates of the probe mass summary spreadsheet after aeroshell optimization.

Structural Design and Mass Estimate (Preliminary)

As part of the HyperSizer™ optimization routine, several structural concepts can be evaluated, including sandwich construction, blade stiffened panels, isogrids, etc. Thus, an aeroshell mass and structural design are produced as part of the HyperSizer™ optimization process.

OVERVIEW OF PROBEMAASS1

ProbeMAASS1 is the main component of PROBE CODES. It is a series of Excel spreadsheets which act as the "clearing house" for all probe design data, and is the primary user interface for probe mass estimation. It contains an import interface for aeroshell solid model dimensions and surface areas created in I-deas®. It also contains Visual Basic macros for generating aeroshell structural finite element meshes for sphere-cone and ellipsled geometries. The approach in developing ProbeMAASS1 was to use a linear progression through the series of Excel spreadsheets with a minimum of user inputs in order estimate the entry probe mass. Early on in the tool development, the Excel spreadsheet format was chosen over various "GUI" formats so that all historical data, references, supporting notes, and equations could easily be viewed by the user. Figure 2 shows the major functional features of ProbeMAASS1. These features are discussed in more detail in the following sections.

Mass Properties Database (MPD)

The Mass Properties Database (MPD) is a collection of historical probe (flight) and probe study (paper) data. It contains a limited amount of data for European, Soviet, and Japanese probes, but is primarily a collection of data from NASA-directed probes. There are separate database spreadsheets for the sphere-cone and ellipsled type entry vehicles. The probe data are grouped according to probe destination (i.e. Venus, Mars, etc.), and are subdivided into the major categories shown in Figure 3. The first four categories are probe overviews: Mission Overview (destination, launch date, launch vehicle), Total Mass Properties (mass, moments of inertia), Geometry (overall forebody and backshell dimensions), and Entry Environment (speed, angle, maximum deceleration, maximum heat rate and heat load). Next come the probes major systems: Forebody System, Aftbody System, Deceleration Systems, and Payload. Each system is further broken down into the subsystems shown in Figure 3, which are described in more detail in the next section. This general breakdown is followed for both sphere-cone and ellipsled type entry vehicles. There is considerably less data in the ellipsled database simply due to the limited amount of ellipsled flight and study data available.

As with all other spreadsheets in ProbeMAASS1, the database spreadsheets follow a color-coding convention. For the database sheets, cells containing flight data are colored turquoise, while cells containing paper study data are colored light turquoise. Some values, like probe ballistic coefficient, which are not

found specifically in the literature, are calculated from other data, and the resulting cells are colored tan. Once the color conventions are understood, they help the user understand at a glance the type of data he or she is dealing with.

Every cell or every line of cells in the MPD contains a cell comment that lists a reference for the data shown. For cases where no data was found, the associated cell was left blank. In other cases, conflicting values were found, such as for a heat load or entry deceleration. In such cases, the most recent data value was entered into the cell, and other conflicting values, with references, were listed in the cell comment. Cell comments are also used to include more in-depth information beyond what is showable in the given cell, such as facesheet or honeycomb thicknesses for sandwich panel aeroshells.

Mass Properties Breakdown (MPB)

The probes' major system masses are further refined by the Mass Properties Breakdown (MPB). The MPB is not a separate spreadsheet, but is embedded in and part of the MPD. The actual refinement is also shown in Figure 3. For the forebody and aftbody systems, the probe mass is broken down to thermal protection, structure, separation system, thermal control, and miscellaneous subsystems and their components. The deceleration systems are further broken down into the pilot, main, and terminal parachutes and terminal descent (airbag) subsystems. Even within these subsystems is more detailed information such as parachute deploy speed, deploy altitude, etc. The payload system is further broken down into structure, science instrument, power, guidance/navigation, telecom, command and data handling, thermal control, harness, propulsion, and miscellaneous subsystems. Again, within these subsystems is considerable detailed component mass such as propellant tank size and material, etc. Some of the more detailed information is shown in the cells, while other is contained in the cell comments.

Mass Estimation Methods (MEM's)

The bulk of ProbeMAASS1 is devoted to the Mass Estimating Methods (MEM's). These are the individual spreadsheets, as shown schematically in Figure 4, which are used to estimate the component, subsystem, system, and total probe mass. A separate spreadsheet is devoted to each major system and its associated subsystems and components. The MEM's take several forms, depending on the system or component being estimated. In some cases, the user may simply refer to the MPD and use an historical component mass which is most similar to the current design, and which may be

independent of probe size. An example would be aeroshell separation fittings. While the number of fittings may vary, the basic fitting design may be relatively constant, thus allowing the user to apply the historical mass to the current design for a quick mass estimate.

In other cases, simple parametric scaling is used to estimate a new component mass. For example, a new parachute mass may be estimated by scaling a closely similar historical parachute mass by the ratio of the diameter squared. Such scaling assumes a constant areal density (kg/m^2) between the historical design and the new design. Areal densities are also used to estimate masses for aeroshell structure and TPS. Using the aeroshell surface areas either from the geometry imported from the I-deas[®] solid model or calculated by the ProbeMAASS1 spreadsheets, in conjunction with areal densities from historical data, the aeroshell structure and TPS masses can be calculated. The historical areal densities are generally curve fits of previous probe design data. Figure 5 shows an example of a curve fit used to give a first-pass estimate of forebody aeroshell structural areal density for sphere-cone type probes.

The highest fidelity mass estimation uses closed form solutions. For this tool, closed form solutions are primarily used to calculate sphere-cone surface areas, and to estimate mass for the propulsion system and its components. Standard textbook equations⁶ are used to estimate propellant mass, pressurant mass, and propellant and pressurant tank masses. While this closed form method may produce higher fidelity mass estimates, it requires more user input than the other two methods.

As with any tool, care must be used to ensure that correct and reasonable input is being used, and that the output is reasonable. While historical masses may be used for some components, technological advancements often reduce the size and mass of these components. Such mass reductions are not currently predicted in the MEM's. In addition, several of the MEM's in this tool use curve fitting from only a few historical data points to develop scaling parameters. Such curves are often based on a very limited number of data points. The MEM's are updated to incorporate new data as it becomes available. To that end, this tool has been designed with a great deal of flexibility to allow the user to override estimated masses at any level in the process (component, subsystem, full probe).

Validation of the MEM's is an ongoing process. Closed form solutions for sphere-cone surface areas and propulsion component masses have been checked by

hand to verify their accuracy. The surface area calculations for ellipsled geometry using the internal macros have been compared with I-deas[®] calculated values and match to within 0.05%. Curve fits of historical data and parametric mass scaling laws are constantly being reviewed to ensure the most accurate mass estimation methods.

Aeroshell Automesher

The last major feature of ProbeMAASS1 is the automatic aeroshell structural finite element mesh generator and its associated surface area calculators for the sphere-cone and ellipsled aeroshells. The sphere-cone probe dimensions and surface areas can be imported through the GDTL discussed earlier. In order to provide more flexibility and to quickly evaluate the impact dimensional changes have on probe mass, the user may also enter override dimensions for the forebody and aftbody in their respective spreadsheets. Figure 6 shows generic sphere-cone forebody and aftbody cross-sections and dimensions. The spreadsheets then calculate surface areas using standard equations⁷. The I-deas[®] or override dimensions are then carried into the Sphere-Cone Aeroshell Mesh Generator spreadsheet (See Figure 4.) where the user then enters values to control the mesh density. Once all mesh control variables are entered, the internal macro generates a plate element structural finite element mesh with dummy material properties. The user may specify whether the forebody only, backshell only, or combined forebody and backshell meshes are created. For the sphere-cones, there is only one separation configuration: the backshell separating from the forebody at a given horizontal plane. The sphere-cone macro supports forebodies with hemispherical, spherical cap, conic, bi-conic, or multi-conic backshells. Figure 7 shows a typical mesh for a sphere-cone aeroshell with forebody and bi-conic backshell. The resulting mesh file is output as an MSC/NASTRAN .dat bulk data file. This format allows for easy model import into a wide variety of finite element pre/post processors (FEMAP, PATRAN, I-deas[®], etc.). After import into the pre-processor, the user may edit the model as necessary to incorporate lumped masses and/or secondary structure or modify material properties, then solve the model. The user then sends the model and solution files to HyperSizer[™] for structural optimization. Currently, the link to HyperSizer[™] is a manual transfer. Future enhancements will include automated links.

For ellipsled entry vehicles, dimensions and surface areas can also be brought in through the GDTL. At this time, the GDTL only supports axisymmetric ellipsled vehicles with horizontal aft and canted forward

backshell/forebody separation configurations. The GDTL will be updated later to transfer geometry data for more general ellipsled configurations. The ProbeMAASS1 Ellipsled Surface Area Calculator spreadsheet currently allows the user to enter dimensions for more general ellipsled geometries. Figure 8 shows a generic ellipsled with associated dimensions. Ellipsleds may be non-axisymmetric (upper and lower halves with different ellipse semi-axis ratios), and may have one of eighteen different backshell separation configurations. Similar to the sphere-cones, the dimensions here are carried into the Ellipsled Aeroshell Mesh Generator spreadsheet where the user enters all the required mesh control values, and the internal macro creates the aeroshell plate element structural mesh. The mesh control values allow the user to specify creation of the ellipsled forebody only, backshell only, base only, or all three. Figure 9 shows a typical ellipsled plate element mesh generated by the automesher. The resulting mesh can then be imported into a pre/post processor for editing and solving, then sent to HyperSizer[™] for structural optimization.

Future Enhancements

ProbeMAASS1 is continually being updated. As new historical data becomes available, it is added to the database. This new data is then used to update the MEM's where applicable. Currently, the automatic mesh generators only create plate elements for the aeroshell. Future enhancements include a lumped mass data transfer link (LMDTL). Within the spreadsheets, centers of gravity (CG's) will be estimated for various point masses such as fuel tanks, electronics boxes, parachutes, etc. The user will also be able to override these estimates by inputting the desired CG's. The point masses and their associated CG's will be added to the finite element model when it is generated. In addition, more automated links are planned to open and transfer geometric data from the I-deas[®] solid model files into the ProbeMAASS1 spreadsheets, and to access and run the structural finite element codes such as I-deas[®] and HyperSizer[™].

APPLICATION TO TITAN AEROCAPTURE SYSTEMS STUDY (2002)

Though still under development, parts of this tool were successfully used in conjunction with other subsystem mass estimates⁸ provided by the Jet Propulsion Laboratory (JPL) and TPS sizing^{9,10,11,12} provided by Ames Research Center (ARC), Langley Research Center (LaRC), and Applied Research Associates (ARA) to help estimate Titan orbiter masses for a wide variety of TPS material/thickness and aeroshell size/TPS combinations and to help quickly

estimate total wet launch masses for the Titan Aerocapture Systems Analysis study of 2002.

Impact of TPS Selection

The goal of the TPS selection sensitivity study was to determine the impact of aeroheating levels and, hence, TPS material selection and thickness on the total Titan orbiter mass, the aerocapture system mass, and the orbiter forebody TPS mass. In addition, the impact on aerocapture system mass fraction and orbiter ballistic coefficient were also investigated. This study required separate detailed aeroheating and TPS analyses for a 6.5 km/s Titan atmosphere entry to determine aeroheating rates and loads (both radiative and convective), and TPS material selection and thickness. For this study, several assumptions were made:

1. The orbiter aeroshell was held at a constant 3.75 meter maximum diameter.
2. The backshell TPS material (SLA) and areal density (1.87 kg/m²) were held constant⁹.
3. The orbiter wet mass (without aerocapture system)⁸ was held constant.
4. The aeroshell structural areal density (kg/m²)¹³ was held constant.
5. The forebody TPS thicknesses and areal densities, shown in Table 1 below, were held constant for each case. All values except C-C data are from References 9-11. C-C data is from Reference 12.

Material	Thermal Load Case	Thick-ness (cm)	Areal Density (g/cm ²)
SRAM-14	Nominal lift down	1.55	0.348
SRAM-17	Nominal lift down	1.93	0.526
SLA-561V	Nominal lift down	2.43	0.622
SRAM-20	Nominal lift down	2.08	0.667
SRAM-20	0.8 conv, 1.8 rad	2.54	0.814
SRAM-20	0.6 conv, 2.6 rad	3.76	1.204
PhenCarb-20	Nominal lift down	2.34	0.711
PhenCarb-20	0.8 conv, 1.8 rad	2.71	0.868
PhenCarb-20	0.6 conv, 2.6 rad	2.91	0.931
TUFROC	Nominal lift down	5.13	1.181
TUFROC	0.8 conv, 1.8 rad	5.70	1.289
TIFROC	0.6 conv, 2.6 rad	6.12	1.371
C-C (Genesis-style) +15%	Nominal lift down	5.51	1.493
C-C (Genesis-style) +15%	0.8 conv, 1.8 rad	5.99	1.587
C-C (Genesis-style) +15%	0.6 conv, 2.6 rad	6.39	1.665

Table 1. Titan Aerocapture TPS Sizing Data

The nominal orbiter dimensions were adjusted for each material and thickness in order to calculate surface areas at the mid-thickness of the forebody TPS. These dimensions were entered into the Sphere-Cone Forebody spreadsheet in ProbeMAASS1 (See Figure 4.) as user input, and the spreadsheet calculated the associated surface areas. TPS areal densities were also entered later as user input, and the TPS mass was

calculated by the spreadsheet. Fifteen TPS material/thickness combinations were evaluated and TPS masses calculated in just a couple hours. The resulting masses were added to other previously calculated orbiter system masses to determine total orbiter wet launch mass, aerocapture system mass, aerocapture system mass fraction, forebody TPS mass, and aerocapture ballistic coefficient as a function of TPS. The above items were also calculated for TPS

with 30% and 50% mass margin. The results were plotted as bar graphs¹⁴ as shown in Figures 10 through 14. The TPS material TUFROC was chosen as the baseline. ProbeMAASS1 allowed the user to show the orbiter mass sensitivity for a wide variety of TPS materials and thicknesses in a very short time. For this particular study, the lightest candidate investigated (SRAM-14) showed a potential 128 kg mass savings over the baseline TUFROC TPS material.

Impact of Orbiter Diameter/TPS Combination

The goal of the orbiter diameter/TPS combination sensitivity study was to determine the impact of aeroshell diameter/forebody TPS combination on total Titan orbiter mass, aerocapture system mass and mass fraction, orbiter forebody TPS mass, and orbiter aerocapture ballistic coefficient. Several assumptions were made for this study:

1. The 3.75 meter diameter aeroshell was photographically scaled down by 5%, 10%, 15%, and 20%. Payload packaging was not re-evaluated.
2. The backshell TPS material (SLA) and areal density (1.87 kg/m^2)⁹ were held constant.
3. All Titan orbit dry mass subsystem masses were held constant except structure, which was reduced linearly with diameter.
4. The aeroshell structural areal density (kg/m^2)¹³ was held constant.
5. The orbiter separation ring and payload pallet ring structure masses¹³ were scaled linearly with diameter.

Similar to the study of mass sensitivity to TPS material alone, the modified aeroshell dimensions and TPS areal densities were input into the ProbeMAASS1 spreadsheet which calculated TPS masses. The TPS masses and orbiter system masses scaled per items 4 and 5 above were added to other previously calculated orbiter system masses to determine total orbiter wet

launch mass, aerocapture system mass, aerocapture system mass fraction, forebody TPS mass, and aerocapture ballistic coefficient for the various diameter/TPS combinations. The results for the five aeroshell diameters and six TPS materials under nominal aeroheating loads were plotted as bar graphs¹⁴ as shown in Figures 15 through 19. The 3.75 meter diameter aeroshell with TUFROC TPS material was chosen as the baseline. Again, ProbeMAASS1 allowed the user to show the orbiter mass sensitivity for a wide variety of aeroshell diameter/TPS combinations in a very short time. This particular study showed the potential mass savings associated with reducing aeroshell diameter and showed significant mass variations with respect to aeroshell diameter and TPS, with the 3.0 m aeroshell/SRAM-14 TPS combination having 19.2% of the TPS mass of the baseline 3.75 m/TUFROC combination.

Impact of Mission Configuration/Launch Vehicle on Total Launch Growth Wet Mass

The goal of this sensitivity study was to determine the impact mission configuration/launch vehicle had on total launch growth wet mass. Several assumptions were made for this study:

1. Two all-chemical missions and eight aerocapture mission architectures, with either chemical or SEP (Solar Electric Propulsion) cruise propulsion systems¹⁵, were evaluated. See Table 2 below.
2. For the aerocapture missions, a constant 515 kg aerocapture system growth mass and a constant 875 kg payload growth mass (in Titan orbit) was assumed.
3. For the all-chemical missions, a constant 937 kg payload growth mass (in Titan orbit) was assumed.
4. The EGA mission with SEP and aerocapture and a Delta 4450 launch-vehicle was the baseline.

Mission	Launch Vehicle	Gravity Assist	Propulsion System	Cruise Time (yrs.)	V _{entry} (km/s)	ΔV _{trajectory} (km/s)
1	Delta 4450	VVVGA	Chemical	9.3	6.2	1.5
2	Delta 4450	VGA	SEP	5.7	6.5	8.3
3	Delta 4450	EGA	Chemical	7.5	5.3	1.6
4	Delta 4450	EGA	SEP	5.9	6.5	6.7
5	Delta IV H	VVVGA	Chemical	9.3	6.2	1.5
6	Delta IV H	VGA	SEP	5.7	6.5	6.9
7	Delta IV H	EGA	Chemical	7.1	6.6	0.5
8	Delta IV H	EGA	SEP	6.1	6.5	4.6
9	Delta IV H	VVVGA	All chemical	~11.3	6.2	4.8
10	Delta IV H	VVVGA	All chemical	~11.9	5.9	3.5

Table 2. Mission Profiles¹⁵

ProbeMAASS1 was used to a lesser extent for this sensitivity study, but still proved valuable for producing the desired mass estimations in a very short time. For this study, the payload mass was assumed a constant 1390 kg for the aerocapture missions, and a constant 937 kg for the all-chemical missions. The trajectory ΔV's were used in the ProbeMAASS1 Propulsion spreadsheet to estimate required propellant mass (fuel and oxidizer for the assumed bi-propellant, pressure regulated system) and propellant tank size. The pressurant mass and pressurant tank size were estimated in the spreadsheet from the propellant tank sizes and user input for pressurant molecular weight and system pressure. The actual propellant and pressurant tank masses were estimated by using the tank areal density (kg/m²) for similar radius tanks¹⁶. Thruster masses were estimated from user input for number and size of thrusters, and a thruster mass trend curve⁶. Miscellaneous propulsion system fitting mass was estimated as a user-specified mass fraction of the other propulsion system mass. Propulsion module dry mass was estimated by a simple linear scaling of a baseline chemical or SEP propulsion module, as appropriate. The propulsion system and propulsion module dry masses were then combined with other previously determined stackup component masses. Figure 20¹⁴, shows the resulting total launch growth wet mass vs. mission configuration for the ten different configurations listed above. ProbeMAASS1 allowed the user to show the mass-saving benefits of aerocapture missions to Titan for a variety of missions in a very short time. These particular results show that the aerocapture missions to Titan provide significant mass savings over all-chemical missions primarily due to the large propellant and propulsion module dry masses required for the all-propulsive ΔV maneuvers.

CONCLUDING REMARKS

The PROBE CODES tool and its major component, ProbeMAASS1, are still in development. The goal is to have a near-seamless end-to-end tool for taking conceptual atmospheric entry probe designs, estimating system, subsystem, and component masses, and performing structural sizing optimizations on the probe aeroshells to produce a preliminary probe aeroshell structural design, all in a relatively short time. While not yet completed, great strides have been made towards completing this process, and portions of the tool have been successfully used to support mass sensitivity trade studies for the 2002 Titan Aerocapture Systems Analysis study. Enhancements will continue to be made as the tool develops.

ACKNOWLEDGEMENTS

The author wishes to thank Dr. Mary Kae Lockwood of the NASA LaRC Vehicle Analysis Branch for her guidance in developing the tool architecture and tool focus. The author would also like to thank K. Chauncey Wu of the NASA LaRC Vehicle Analysis Branch for his inputs during the initial stages of the tool development, and Glenn A. Hrinda, also of the NASA LaRC Vehicle Analysis Branch, for his inputs for future tool enhancements.

REFERENCES

1. EDS PLM Solutions I-deas[®] software versions 9 and higher, Electronic Data Systems Corporation, Plano, TX
2. Microsoft[®] Excel User's Guides 1 and 2, Microsoft Corporation, 1994.
3. MSC/NASTRAN Quick Reference Guide, The MacNeal-Schwendler Corporation, 1992.

4. Collier Research Corporation, HyperSizer™ Structural Sizing Software, Book 1: Tutorial & Applications, Second Edition, Collier Research Corporation, October 1998.
5. Lockwood, M.K., et al, Titan Aeroshell Aerocapture Systems Analysis Review, Jet Propulsion Laboratory, Pasadena, CA, August 29-30, 2002.
6. Brown, C.D., Spacecraft Propulsion, AIAA Education Series, 1996.
7. Staff of Research and Education Association, Handbook of Mathematical, Scientific, and Engineering Formulas, Tables, Functions, Graphs, Transforms, Research and Education Association, 1997.
8. Bailey, R.W., *Spacecraft Design*, Titan Aeroshell Aerocapture Systems Analysis Review, Jet Propulsion Laboratory, Pasadena, CA, August 29-30, 2002.
9. Laub, B., *Thermal Protection (TPS)*, Titan Aeroshell Aerocapture Systems Analysis Review, Jet Propulsion Laboratory, Pasadena, CA, August 29-30, 2002.
10. Congdon, W.M. and Curry, D.M., *2007 Titan Mission Analysis of ARA Ablators to Define Required Thickness and Weights*, Analysis Results of July 11, 2002.
11. Congdon, W.M., “Titan Ablator Thickness”, Analysis Results of August 23, 2002, e-mail from W.M. Congdon (Applied Research Associates) to M.K. Lockwood (NASA LaRC).
12. Dec, J., “Genesis TPS for Titan Aerocapture”, Analysis Results of September 27, 2002, e-mail from J. Dec (NASA LaRC) to M.K. Lockwood (NASA LaRC).
13. Hrinda, G.A., *Aeroshell Structure*, Titan Aeroshell Aerocapture Systems Analysis Review, Jet Propulsion Laboratory, Pasadena, CA, August 29-30, 2002.
14. Dyke, R.E., *Mass Sensitivities*, Titan Aeroshell Aerocapture Systems Analysis Review, Jet Propulsion Laboratory, Pasadena, CA, August 29-30, 2002.
15. Noca, M.A., *Mission Analysis*, Titan Aeroshell Aerocapture Systems Analysis Review, Jet Propulsion Laboratory, Pasadena, CA, August 29-30, 2002.
16. Sweetser, T.H., et al, “Titan Lander Conservative Science 01-06”, JPL Team-X Report, June 15, 2001.

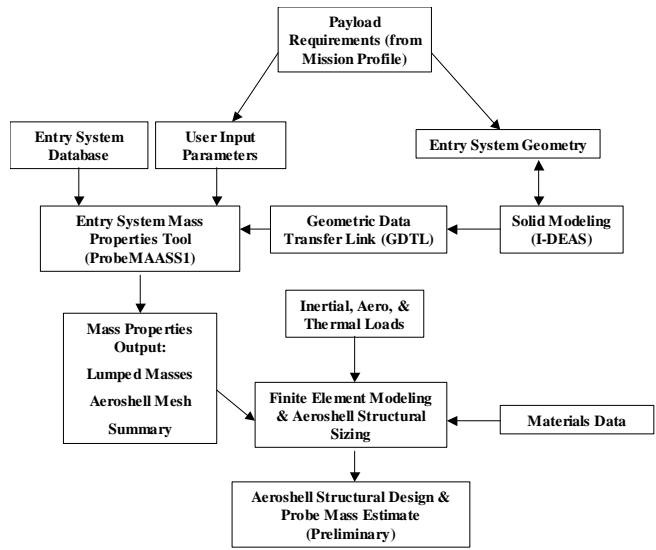


Figure 1. PROBECODES Entry System Mass Properties & Structural Design Tool Architecture

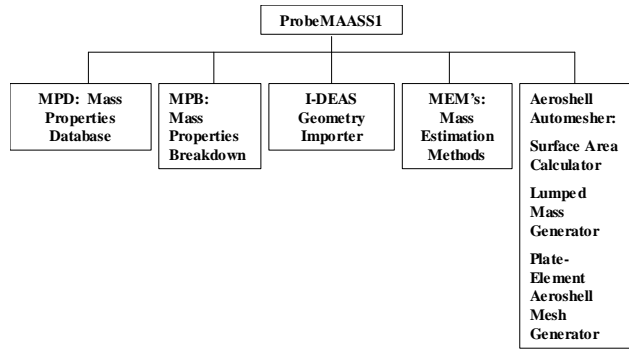


Figure 2. ProbeMAASS1 Functional Features

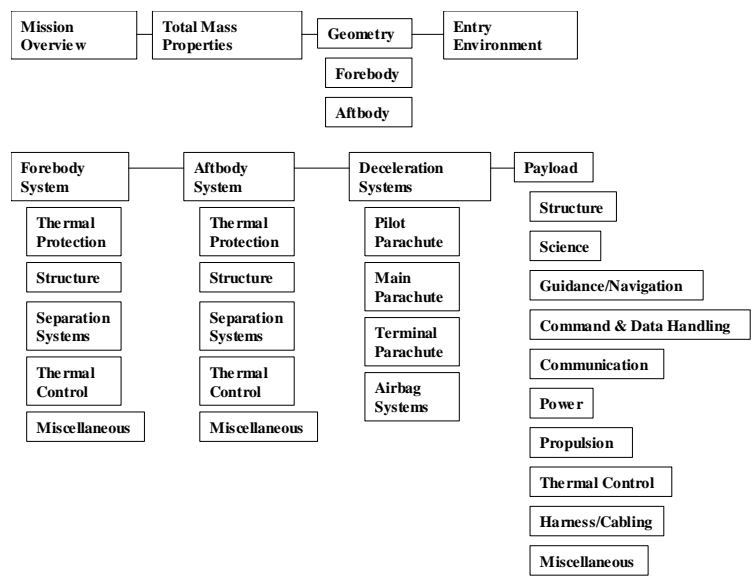


Figure 3. MPD/MPB Breakdown

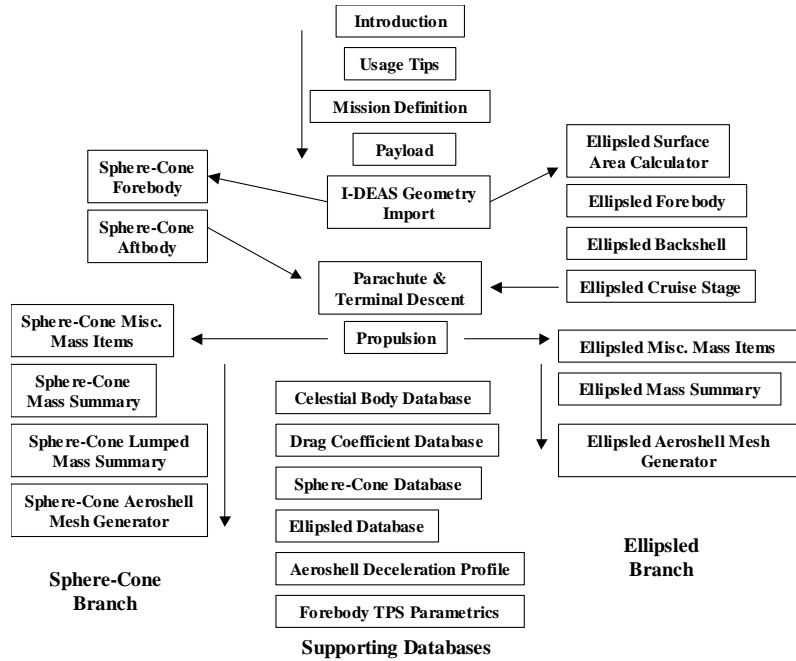


Figure 4. ProbeMAASS1 Component Spreadsheets

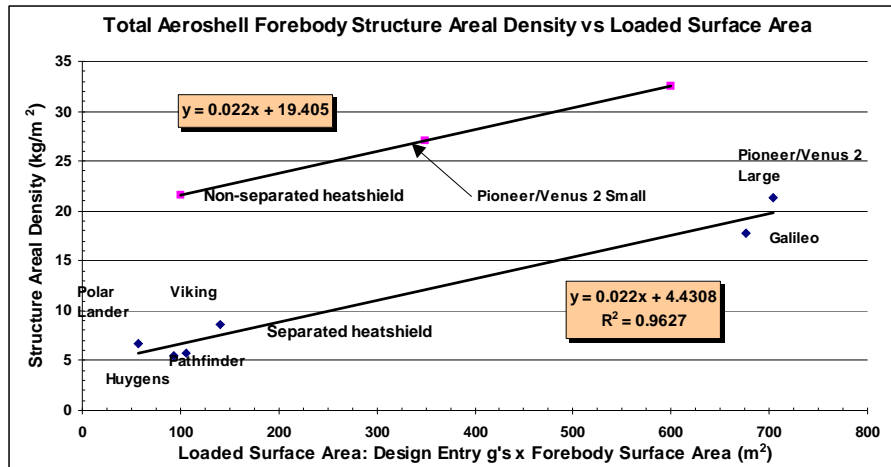


Figure 5. Sample MEM Curve from Historical Data

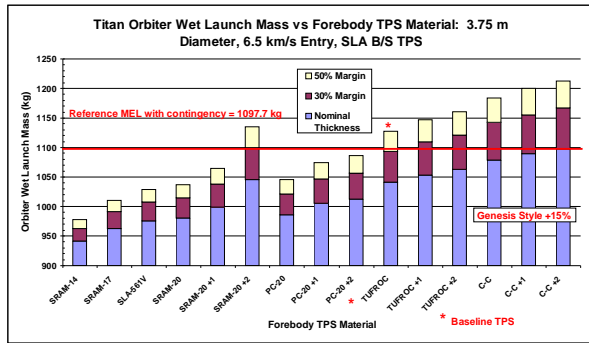


Figure 10. Orbiter Wet Launch Mass vs. TPS Material

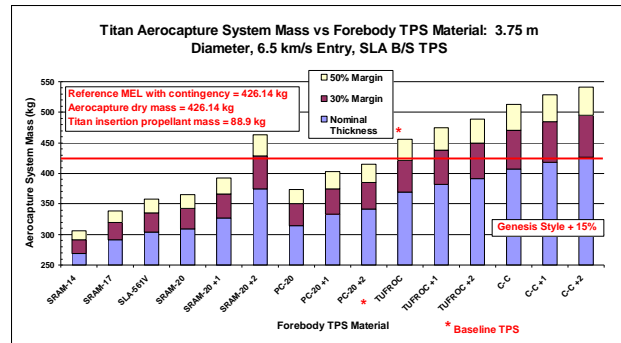


Figure 11. Aerocapture System Mass vs. TPS Material

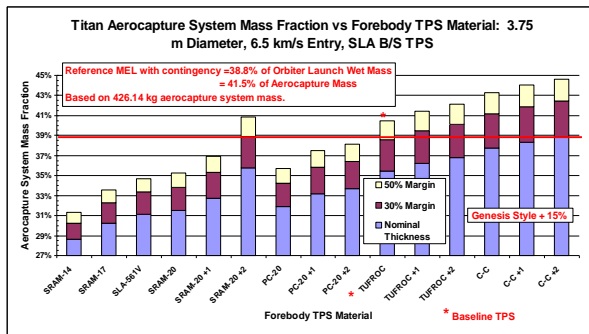


Figure 12. Aerocapture System Mass Fraction vs. TPS Material

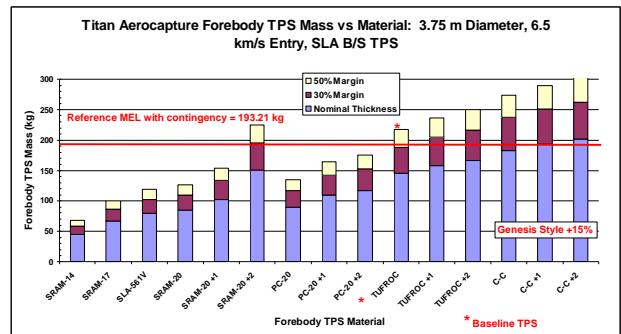


Figure 13. Forebody TPS Mass vs. TPS Material

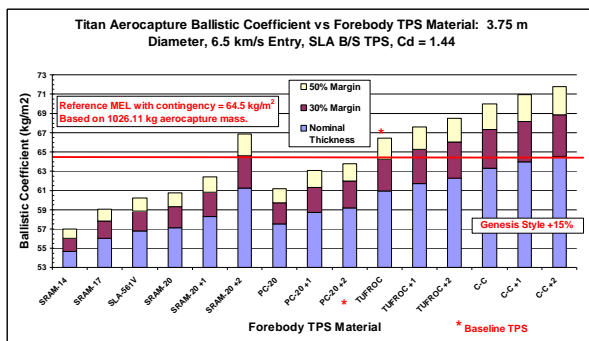


Figure 14. Aerocapture Ballistic Coefficient vs. TPS Material

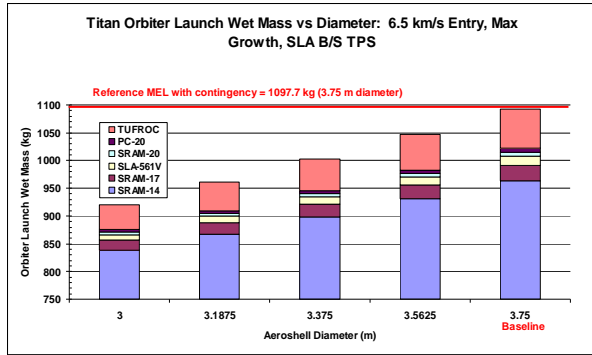


Figure 15. Orbiter Launch Wet Mass vs. Diameter and TPS

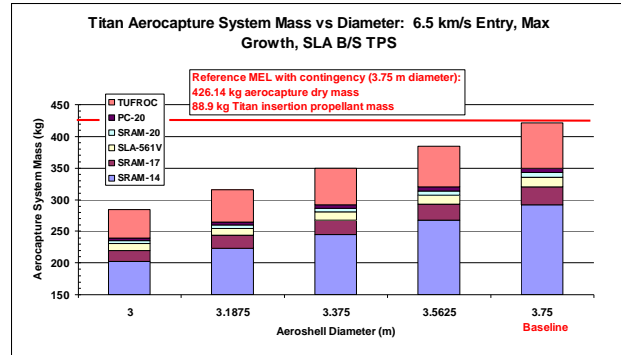


Figure 16. Aerocapture System Mass vs. Diameter and TPS

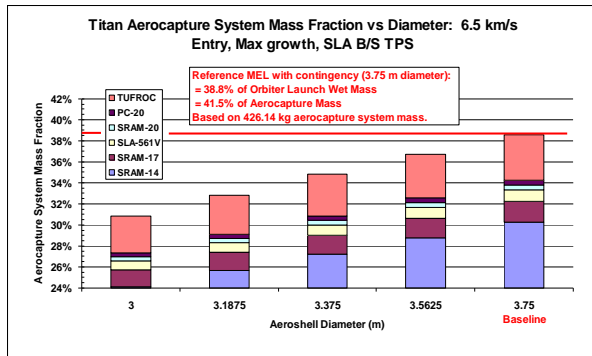


Figure 17. Aerocapture System Mass Fraction vs. Diameter and TPS

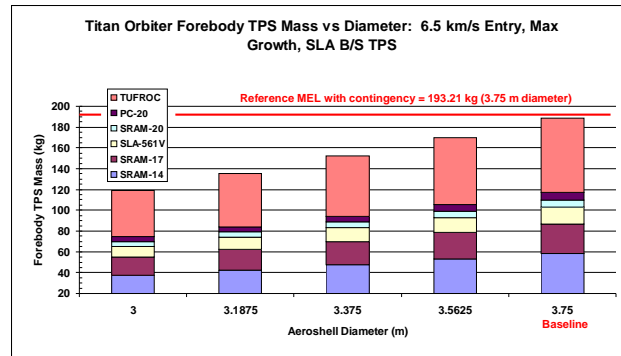


Figure 18. Forebody TPS Mass vs. Diameter and TPS

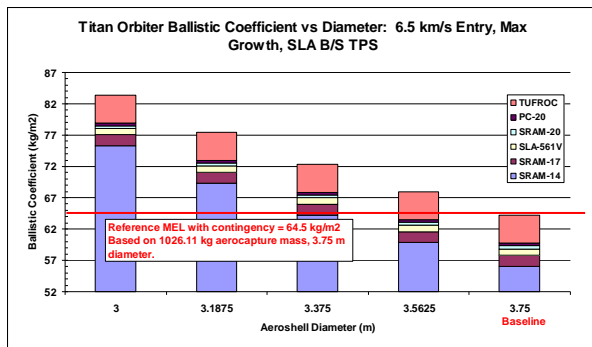


Figure 19. Orbiter Ballistic Coefficient vs. Diameter and TPS

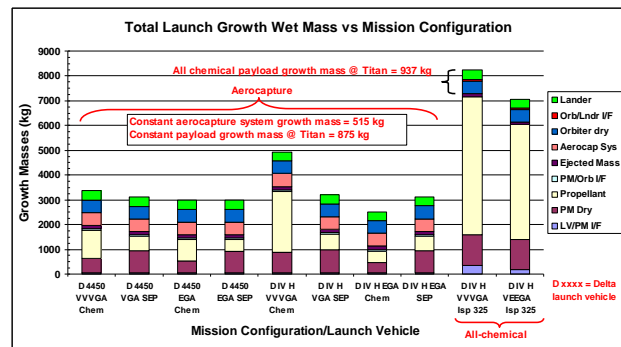


Figure 20. Total Launch Growth Wet Mass vs. Mission Configuration

TITAN AEROCAPTURE SYSTEMS ANALYSIS

Mary Kae Lockwood*
 NASA Langley Research Center

INTRODUCTION

Performance projections for aerocapture show a vehicle mass savings of between 40 and 80%, dependent on destination, for an aerocapture vehicle compared to an all-propulsive chemical vehicle. In addition aerocapture is applicable to multiple planetary exploration destinations of interest to the NASA Office of Space Science. These results led to the identification of aerocapture as one of the top three propulsion technologies for solar system exploration missions during the 2001 NASA In-Space Propulsion Program (ISP) technology prioritization effort, led by Marshall Space Flight Center, to rank current ISP propulsion technologies. An additional finding was that aerocapture needed a better system definition and that supporting technology gaps needed to be identified.

An aerocapture systems analysis effort was kicked off in late February and completed in September 2002. The focus of the effort was on aerocapture at Titan with a rigid aeroshell system. Titan was selected as the initial destination for the study due to potential interest in a follow-on mission to Cassini/Huygens. The systems analysis is being completed by a multi-center NASA team including scientists and engineers from Ames Research Center, the Jet Propulsion Laboratory, Johnson Space Center, Langley Research Center, and Marshall Space Flight Center, led by Langley Research Center. Continued aerocapture systems analysis work is in progress with a Neptune aerocapture systems analysis study. Neptune is representative of the gas giant planets. Additional destinations and further work will be defined based on NASA Office of Space Science roadmap updates and ISP technology development. Plans in FY04 include Mars and Venus.

*Member AIAA.

Copyright © 2003 by the American Institute of Aeronautics and Astronautics, Inc. No copyright is asserted in the United States under Title 17, U.S. code. The U.S. Government has a royalty-free license to exercise all rights under the copyright claimed herein for Governmental Purposes. All other rights are reserved by the copyright owner.

SYMBOLS/NOMENCLATURE

A	Area (m ²)
AFE	Aeroassist Flight Experiment
α_{trim}	Trim Angle of Attack
BOC	Beginning of Cassini
CA	Axial Force Coefficient
CBE	Current Best Estimate
CD	Coefficient of Drag
CFD	Computational Fluid Dynamics
CG, cg	Center of Gravity
CL	Coefficient of Lift
CN	Normal Force Coefficient
D	Drag
EGA	Earth Gravity Assist
EOC	End of Cassini
HGA	High Gain Antennae
L	Lift
L/D	Lift-to-Drag ratio
M/CDA	Ballistic Coefficient (kg/m ²)
SEP	Solar Electric Propulsion
TPS	Thermal Protection System
VGA	Venus Gravity Assist

BACKGROUND

An aerocapture flight profile schematic is shown in Figure 1. The vehicle approaches the planet/moon from a hyperbolic approach trajectory, shown at point 1, designed to achieve state conditions including flight path

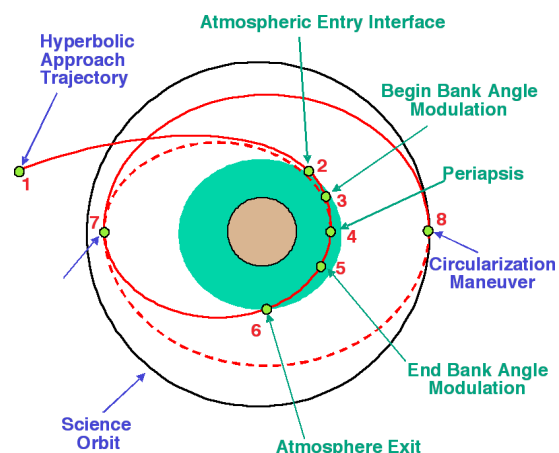


Figure 1. Aerocapture flight schematic.

angle at atmospheric interface, point 2, within a predetermined range. Bank angle modulation, rotation of the lift vector about the velocity vector is initiated by the guidance at point 3. The drag on the vehicle as it passes through the atmosphere provides the delta V required to capture the vehicle into the desired orbit. The amount of delta V imparted to the vehicle is controlled by the on-board guidance by modulating bank angle, i.e. the direction of the vehicle's lift vector. A command of lift up during an atmospheric pass results in increasing altitudes, nominally decreasing atmospheric density, reduced drag and reduced delta V imparted. A command of lift down results in decreasing altitudes, nominally increasing atmospheric density, increased drag and increased delta V imparted. Bank angle modulation is commanded throughout the atmospheric pass from point 3 to point 5. By point 5, where the influence of aerodynamic forces is no longer significant, the energy depleted from the initial hyperbolic trajectory is that required to capture the vehicle into the desired orbit. At apoapsis, point 7, a small delta V burn is performed to raise the periapsis.

AEROCAPTURE CORRIDOR

The aerocapture theoretical corridor is bounded by the full lift up trajectory and the full lift down trajectory for a nominal atmosphere and vehicle aerodynamics. (The theoretical corridor width is defined by the difference between the entry flight path angle corresponding to a full lift down trajectory and the entry flight path angle corresponding to a full lift up trajectory for a nominal atmosphere and aerodynamics.) If the vehicle enters the atmosphere at a flight path angle steeper than defined by the full lift up trajectory the vehicle lands. If the vehicle enters the atmosphere at a flight path angle shallower than that defined by the full down trajectory the vehicle is not captured. Figure 2 illustrates the theoretical corridor and the effects of navigation, atmosphere and aerodynamic uncertainties on the theoretical corridor. The plot shows entry flight path angle for a full lift up and full lift down trajectory as a function of the atmosphere variable F_{minmax} , where $F_{minmax}=0$ is the nominal atmosphere, $F_{minmax}=-1$ is the lowest density atmosphere, $F_{minmax}=+1$ is the maximum density atmosphere. The plot is shown for a given vehicle, entry velocity, and target orbit. To first order, the aerocapture corridor required to accommodate atmospheric dispersions, navigation errors (delivery flight path angle), and aerodynamic uncertainties can be root sum squared to determine the total corridor required. If the theoretical corridor is significantly greater than the corridor width required, then the vehicle control authority is adequate and the aerocapture is robust. The ap-

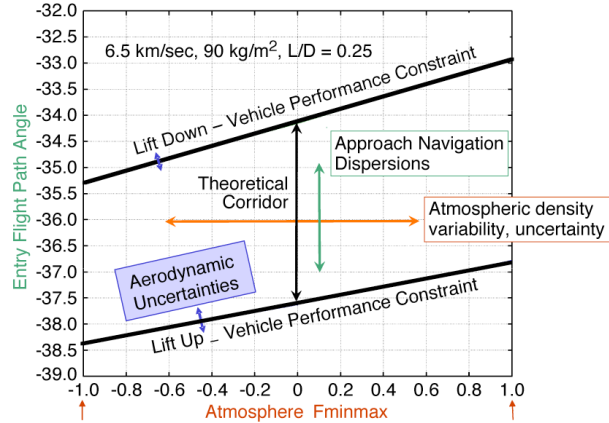


Figure 2. Aerocapture flight corridor, effect of uncertainties and dispersions.

proach is only an estimate. For example factors such as high frequency atmospheric density perturbations are not included in this approach and can affect the results. Monte Carlo simulation analyses must be completed to assess feasibility and robustness.

Concerns expressed regarding the risk of aerocapture have largely been in three areas. 1) Atmosphere variability and uncertainty; 2) Approach navigation delivery errors; 3) Aerodynamics utilized to control capture. To address these concerns, the following approach can be taken in the design of the aerocapture system.

- Based on available atmospheric measurements, quantify and model the physical range of atmosphere variability and uncertainty.
- Quantify the approach navigation delivery errors, and incorporate navigation systems into the vehicle design to reduce errors.
- Quantify the aerodynamic uncertainties including margin.
- Select a vehicle L/D to provide adequate control authority.
- Provide adequate vehicle control responsiveness to accommodate perturbations, including atmospheric perturbations.
- Develop a robust guidance.
- Evaluate aerocapture robustness through Monte Carlo simulation incorporating all variability, uncertainty, errors and dispersions.
- Design the aerocapture system to provide margin *above* 3- σ success, in particular for first time flights and for high value payloads.

PREVIOUS AEROCAPTURE ASSUMPTIONS

Previous aerocapture mission analysis work has demonstrated significant benefit of aerocapture for outer planet missions. However, due to the broad nature of the work, the analysis was low fidelity. Many assumptions were made, and it was noted that higher fidelity analyses would be needed to address the assumptions.

Assumptions made in previous aerocapture mission analyses were that the available aerocapture corridor width at a given destination was adequate to accommodate all of the dispersions and uncertainties, such as atmosphere uncertainties, navigation dispersions, and aerodynamic uncertainties. And that these uncertainties and dispersions could be quantified. It was assumed that guidance algorithms could be designed to successfully capture the vehicle over the range of uncertainties/dispersions. For Titan, the aerocapture subsystem mass, including structure and TPS, was estimated to be 27% of entry mass. It was assumed that aeroheating environments for aerocapture could be quantified and accommodated by TPS systems within the mass allocation. With entry velocities at Titan of 6-10 km/sec and the Titan atmosphere being predominantly Nitrogen, aeroheating rates were expected to be modest and convective heating dominated. As a result, TPS materials such as SLA 561 were expected to be applicable. All of the earlier studies assumed that the spacecraft could be packaged in the aeroshell; that volume is available, subsystems can be located to meet center of gravity (cg) restrictions, thermal and communication issues can be solved. It was assumed that the selected science orbits are feasible and that technology, including analysis tools would be ready in time to meet a project schedule. It was also estimated that the benefit of aerocapture at Titan compared to an all-propulsive capture provides a mass savings of 66%.

All of the assumptions made were to be addressed in the systems analysis study described here.

OBJECTIVES

The objectives for the Titan aerocapture systems analysis were therefore to provide higher fidelity analyses for validation and update to aerocapture assumptions made in mission studies, including performance, environments, mass properties, etc. The results of the analysis were to be provided to scientists, mission planners, technology planners, technologists and future mission managers. The feasibility, benefit and risk of aeroshell aerocapture system and technologies for Titan destination were to be defined. Technology gaps were

to be identified and performance goals of key technologies defined.

APPROACH

A multi-center aerocapture systems analysis team was formed, including NASA engineers and scientists from Ames Research Center, the Jet Propulsion Laboratory, Johnson Space Center, Langley Research Center, and Marshall Space Flight Center, led by Langley Research Center. The team kicked off the study in late February and completed the work in September 2002.

The analysis included top level sensitivity studies to identify a reference concept for higher fidelity analysis and to provide sensitivities through a broader range of possible aerocapture mission scenarios. The reference concept was to provide a higher fidelity reference to address the previous assumptions noted above, to provide a reference for higher fidelity component level trades, and to provide a benchmark to the top-level sensitivities.

The mission objectives and initial spacecraft design for the reference concept was based on JPL's TeamX study¹ of the Titan Explorer mission.

TITAN AEROCAPTURE REFERENCE CONCEPT

The level one objectives for the Reference Concept were defined based on a modified set of those used in the TeamX study. The Titan Explorer consisted of an Orbiter and a Lander, each delivered to Titan. The Orbiter delivers the Lander to its Titan entry trajectory. The Lander performs a direct entry. The Orbiter aerocaptures into a near polar orbit about Titan.

One of the goals is to minimize trip time to Titan. The science mission is to be three years, with three years of Orbiter operations at Titan. In addition, the Orbiter serves as a relay for the Lander for the first year. The Orbiter science instruments include a Microwave spectrometer, SAR, Multispectral imager, USO as described in more detail in Ref 4. The launch date selected is 2010. This requires technologies to be at a technology readiness level (TRL) of six by 2006. Other launch dates are also considered. A SEP propulsion module is selected for the Reference Concept with comparisons made to the chemical propulsion module. Given the relatively near-term launch date, as much heritage hardware as possible is utilized. The mission is defined as a Class A mission with a fully redundant design. The team was funded to study the aerocapture Orbiter only. The Lander had to be

treated as a “black box” such that most of the TeamX analysis for the Lander was taken as is. The Lander mass allocation is 400 kg.

Concept Selection

Selection of a Reference Concept is a balance between providing reduced trip time to the destination, adequate delivered mass, adequate aerocapture flight corridor width to provide a robust system, all while meeting the science objectives.

Mission analyses were conducted for the Titan aerocapture mission with various launch vehicles, gravity assist options, chemical propulsion vs. solar electric propulsion (SEP), and various launch dates as described in Reference 3. Figure 3 shows the delivered mass vs. flight time for various launch dates for a Venus Gravity Assist (VGA) and a SEP propulsion module. Note that for flight times greater than six years, the maximum mass that can be delivered remains nearly constant. Delivered mass decreases significantly as trip time is reduced from six to five years or less. Figure 4 shows the inertial entry velocity for the same missions as Figure 2. Six to eight year trip times result in entry velocities of less than ~7 km/sec for most launch opportunities. Also, entry velocity increases rapidly for trip times less than five to six years.

Since convective heating increases approximately with the cube of entry velocity as shown in Figure 4, trip times greater than six years were expected to reduce the mass of the required thermal protection system allowing more of the delivered mass to be allocated to meet science requirements.

Selection of a 6.5 km/sec entry velocity with an approximately 6 year trip time, dependent on opportunity, resulted in a balance between trip time and mass. From Figure 5, the stagnation point convective aeroheating on a one meter nose radius at 6.5 km/sec is approximately 40 W/cm². SLA 561 was expected to be adequate for the aeroheating environment.

Note that due to the Titan orbit about Saturn, entry velocity can be increased for given flight time without loss in delivery mass capability. The velocities in Figure 4 are each minimum inertial entry velocity.

To determine the theoretical corridor width leading to determination of the vehicle lift to drag ratio required, full lift up and full lift down aerocapture trajectories were developed over the range of entry velocities of interest, and for a range of lift to drag ratio vehi-

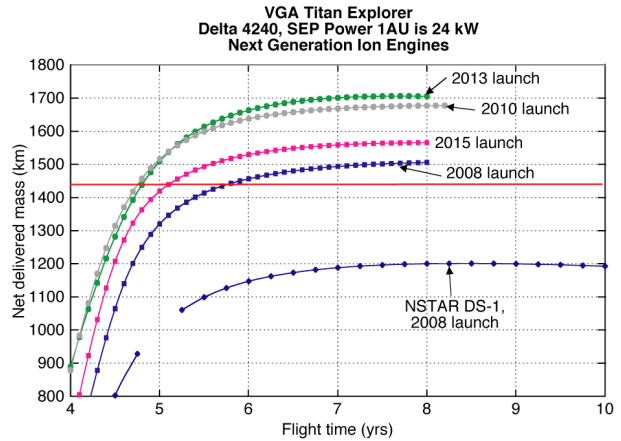


Figure 3. Delivered mass vs. mission flight time. Ref 3.

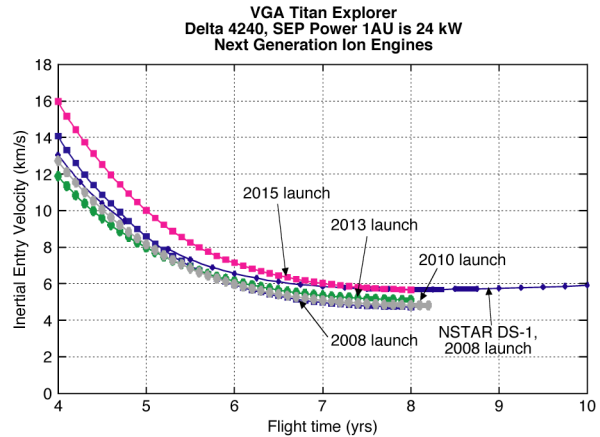


Figure 4. Inertial entry velocity vs. mission flight time. Ref 3.

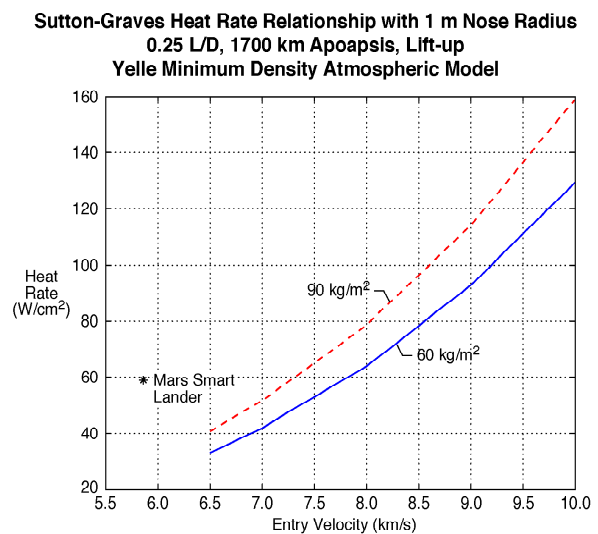


Figure 5. Convective stagnation point heat rate vs. entry velocity. Ref 7.

cles. Initial analysis had shown that ballistic coefficient and target apoapsis were secondary variables in the determination of corridor width. From Figure 6, for a vehicle with $L/D = 0.25$, a 3.5 deg theoretical corridor width with 6.5 km/sec entry velocity is achieved. (With a 10 km/sec entry and the same L/D , 4.7 deg theoretical corridor width is achieved.) The 3.5 deg corridor width was expected to be more than adequate to accommodate $3\text{-}\sigma$ navigation delivery errors, atmosphere dispersions and aerodynamic uncertainties with 99.7% or greater success. This allowed a high heritage low L/D sphere cone configuration to be selected. If increased corridor were required, mid L/D configurations are viable alternatives.

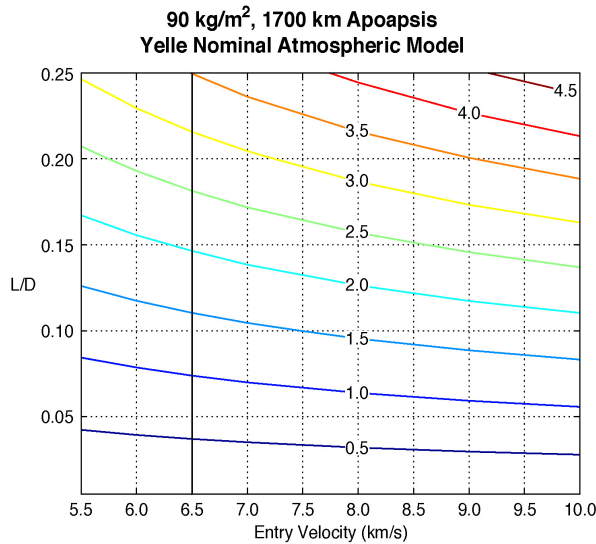


Figure 6. Aerocapture corridor width as a function of vehicle lift to drag ratio. Ref 7.

Navigation

Several navigation approaches were analyzed for Titan as described in Reference 2. The approach selected for the Reference Concept is based on the Cassini optical navigation camera capability, Δ DOR (utilized on Odyssey), and Dopler and Range combined. The $3\text{-}\sigma$ flight path angle dispersions, based on a Beginning of Cassini (BOC) Titan ephemeris is $\pm 1.42^\circ$. Significant improvements in knowledge of the location of Saturn, Titan will result from Cassini mission. $3\text{-}\sigma$ sets of entry states, BOC and EOC, were utilized in the Monte Carlo analyses described below. This detailed navigation analysis was required to assess feasibility and robustness of Titan aerocapture. Further reduction in the flight path angle dispersions can be achieved with the resolution of the Mars Reconnaissance Orbiter camera, as noted in Reference 2.

Atmosphere Modeling

TitanGRAM, discussed in detail in Reference 5, includes a model of measurement uncertainties, residual uncertainties (turbulence, waves, etc); variation with latitude, altitude, time of day, season. This model fidelity is required to assess mission feasibility and robustness. Figure 7 shows the Titan atmospheric density with altitude.

The arrival date of the current study results in the maximum variation of density with latitude. Since the science orbit is near polar, aerocapture occurs over a wide range of latitudes. Figure 8 represents a simulation of the expected variability of F_{minmax} with latitude.

Figures 7 and 8 show the mean variation of the Titan atmosphere. Also included in TitanGRAM are the atmosphere perturbations. Both the mean variations and perturbations are utilized in the Monte Carlo analysis described below.

Cassini-Huygens data will reduce measurement uncertainty as discussed further below.

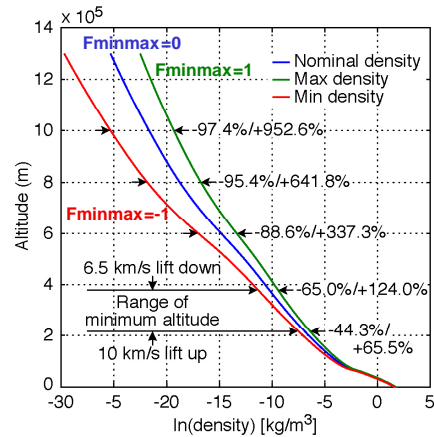


Figure 7. TitanGRAM atmospheric density as a function of altitude.

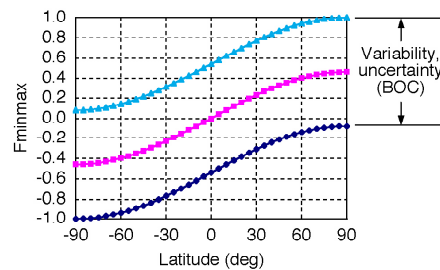


Figure 8. Simulated variation of F_{minmax} TitanGRAM parameter with Titan latitude.

Aerodynamics

Aerodynamic uncertainties included in the Monte Carlo are based on LAURA CFD for blunt bodies at hypersonic velocities.⁷ The uncertainties include $\pm 3\%$ uncertainty in CA; $\pm 5\%$ uncertainty in CN; and a trim angle of attack (α_{trim}) uncertainty of ± 2 deg used to represent uncertainty in Cm. The CG uncertainty used is ± 0.0318 m in axial, Z_{cg} and ± 0.0069 m in radial X_{cg} . Figure 9 (Ref 7) shows the effect of these uncertainties on vehicle lift to drag ratio.

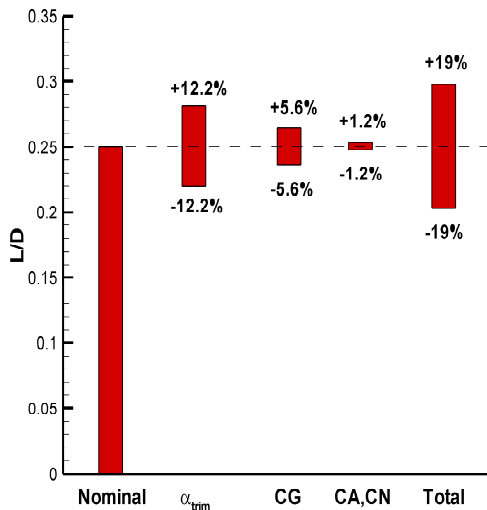


Figure 9. Effect of aerodynamic uncertainties on L/D. Ref 7.

Guidance

HYPAS guidance (ref 6) was chosen for the Titan aerocapture systems analysis. (Other guidance algorithms are planned for future consideration.) HYPAS was originally developed for the Aeroassist Flight Experiment (AFE). However the current version includes several improvements since AFE.

HYPAS utilizes vehicle lift and bank angle control through the atmosphere to target the desired exit orbit apoapsis and inclination (or plane). It is an analytically derived algorithm based on deceleration due to drag and altitude rate error feedback. This analytic, non-iterative, on-the-fly approach leads to efficient code (~320 source lines in Fortran), minimal storage requirements, and fast and consistent execution times.

HYPAS consists of two phases as illustrated in Figure 10: 1) Capture Phase: Establishes pseudo-equilibrium glide conditions; 2) Exit Phase: Exit condi-

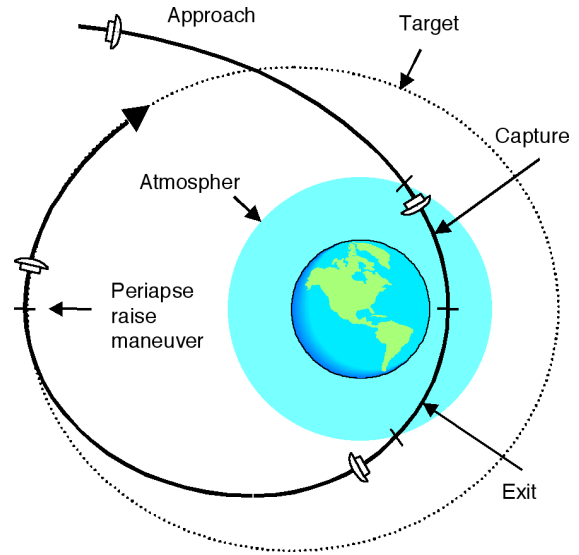


Figure 10. Aerocapture guidance phases. Ref 6.

tions are predicted analytically assuming a constant altitude rate. The lift vector is adjusted to null the error between predicted and target apoapsis, and bank reversals are used to keep inclination errors within the desired limits. Results show excellent performance and an ability to capture ~98% of the theoretical corridor.

Performance/Simulation

A Titan aerocapture simulation and Monte Carlo have been developed. All uncertainties critical to aerocapture robustness are included in the parameters varied in the Monte Carlo simulations. These parameters are the initial states with corresponding delivery errors at atmospheric interface; the atmosphere variability and uncertainty; including mean range and perturbations; aerodynamic uncertainties in CA, CN, α_{trim} , and cg uncertainties.

During a Monte Carlo analysis, Monte Carlo parameters are each randomly varied over a specified range and distribution defined by the subsystem/model engineer. Two thousand trajectory simulations are completed in one Monte Carlo analysis. Results from these simulations provide aerocapture performance statistics to determine robustness, margin, risk; guidance development, stress case identification (control algorithm development – future); statistical distributions of critical parameters, design trajectories, for subsystem design.

Monte Carlo analyses are completed for six Titan aerocapture mission scenarios. The first three are completed for the inertial arrival velocity of 6.5 km/sec with no updates assumed from Cassini/Huygens. This

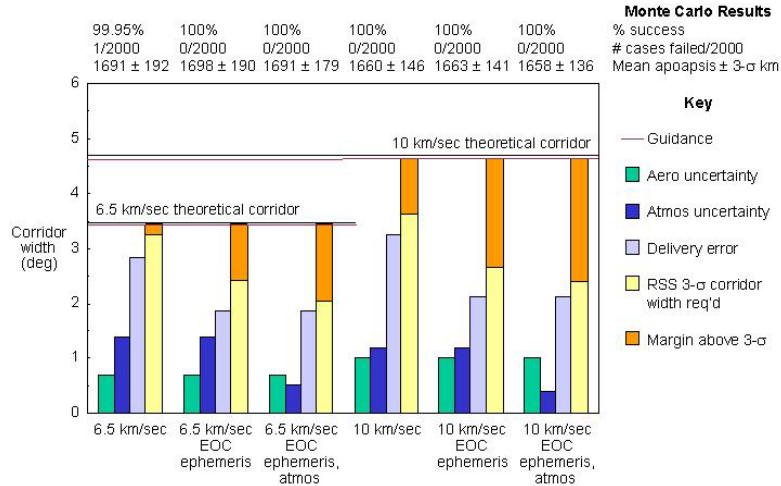


Figure 11. Titan aerocapture robustness.

analysis is labeled “6.5 km/sec” on the chart in Figure 11. As shown at the top of the figure, for this Monte Carlo 99.95% of the cases successfully aerocaptured at Titan; one of 2000 cases failed. The first set of bars in Figure 11 show the corridor width required to accommodate aero uncertainty, atmosphere uncertainty, and delivery error, as well as the root sum square used to estimate total corridor width required for the 6.5 km/sec case. A comparison of the corridor width required and the theoretical corridor minus the loss in corridor due to guidance (only 2% loss), indicates that the 6.5 km/sec case with no update from Cassini/Huygens will be successful 3-sigma, but that there is not significant margin over and above a 3-sigma success.

Adding the expected improvement in ephemeris from Cassini/Huygens in the next Monte Carlo analysis, labeled “6.5km/sec EOC ephemeris” shows the reduction in corridor required to accommodate delivery errors, and a corresponding reduction in the RSS 3-sigma corridor width required. The result is a significant increase in margin over and above a 3-sigma success. These results are confirmed by the Monte Carlo analyses, where 100%, or 2000 of 2000, cases successfully aerocaptured. Further improvement results from the expected reduction in atmospheric uncertainty resulting from the Cassini/Huygens mission, labeled “6.5km/sec EOC ephemeris, atmos.”

The next set of Monte Carlo’s completed is for 10km/sec inertial entry velocity. The same three scenarios are completed for the 10km/sec entries as for the 6.5 km/sec entries. For each scenario, 100% of the Monte Carlo cases are successfully captured. Note that with increased velocity, the theoretical corridor increases

faster than the net change in corridor width required due to aero, delivery and atmosphere errors and dispersions. Thus aerocapture performance robustness increases with velocity. The simulation, Monte Carlo analysis and results are discussed further in reference 7.

Aeroheating Environments

Conservative aeroheating design trajectories were selected for the reference concept. Design trajectories were based on the maximum atmospheric concentration of CH₄, 5% by volume. The atmospheric CH₄ concentration estimate is expected to either remain or be decreased with Cassini/Huygens data.

A conservative ballistic coefficient, 90 kg/m², was assumed for the design trajectories. The resulting reference concept ballistic coefficient is 69kg/m², with a possible range of 56 – 84 kg/m² for variation in vehicle diameter, aeroheating rates/loads, TPS selection and sizing (shown later in the paper). In addition, initial analyses show a decrease in aeroheating with decreasing ballistic coefficient, making 90 kg/m² conservative for the design trajectories.

Lift-up trajectories were utilized to define the maximum heat rates; lift-down trajectories were used to define the maximum heat loads. These selections result in the most conservative trajectories for aeroheating environment definition.

Based on the design trajectories and vehicle configuration, the peak laminar convective aeroheating rates are ~46 W/cm² for 6.5 km/sec lift up, minimum atmosphere, alpha = 16 deg, stagnation point. Transi-

tion to turbulence is likely prior to peak convective heating on heatshield lee side based on an $Retheta = 200$ transition criteria and CFD results for the 6.5 km/sec lift up, minimum atmosphere, 16 deg angle-of-attack trajectory. This will likely increase the maximum convective heating on the heatshield beyond the above 46 W/cm^2 .⁹

For the maximum Titan CH₄ concentrations, 5% by volume, all aeroheating predictions from the study have shown that the radiative aeroheating from CN is greater than the convective aeroheating. For the wind-side of the heatshield at $\alpha = 16$ deg, the maximum radiative aeroheating is predicted to occur at the stagnation point. Radiative heating rates range from the “low end” $\sim 93 \text{ W/cm}^2$ to the “conservative” $\sim 280 \text{ W/cm}^2$ for 6.5 km/sec lift up, minimum atmosphere, $\alpha = 16$ deg, stagnation point. These results, completed during the study, were known to be preliminary. One of the recommendations from the study was to develop improvements in the radiative aeroheating environments analysis methods. This work is currently on going and discussed further in References 8 and 9.

Based on the preliminary estimates, a range of radiative and convective heat rates and loads are estimated to provide a sensitivity of TPS selection and sizing to potential aeroheating environments for Titan aerocapture as shown in Figure 12.

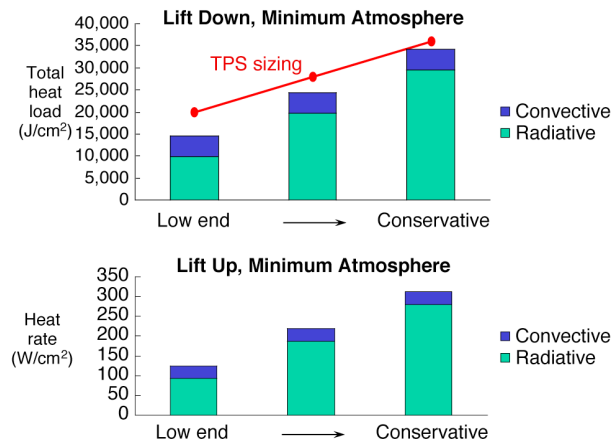


Figure 12. Aeroheating environments.

TPS

Candidate TPS materials are identified, and several sized,^{10,11,12,13} for the range of Titan aeroheating environments expected. The ability of low density TPS materials (ex. SRAMs) to absorb radiation is currently unknown and requires testing. TUFROC, PhenCarb20, C-C Genesis-type are expected to absorb radiation. How-

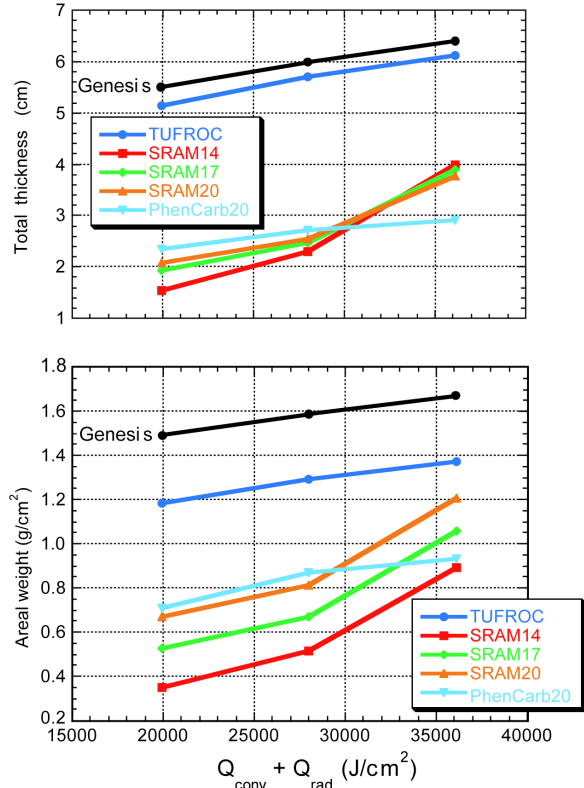


Figure 13. TPS thickness and mass vs. TPS type, aeroheating load. Ref 10.

ever these materials must also be tested in the radiative environments. In the TPS sizing analyses shown in Figure 13,¹⁰ it was assumed that the materials could absorb the radiation.

Low-density silicone-based ablators are predicted to experience significant recession at the highest heating conditions. However they provide the lowest mass at lowest heating conditions. TUFROC and PhenCarb20 exhibit less sensitivity to heating variations than low density silicone-based ablators, but with increased mass. PhenCarb 20 exhibits small surface recession in the inert Titan atmosphere. TUFROC is non-ablating. C-C foam Genesis-type concept is also non-ablating.

For the Reference Concept, TUFROC (with the low end heat load sizing + 30%) was utilized in the MEL for two reasons. The TUFROC is expected to absorb radiation, and TUFROC TPS results in a conservative mass estimate compared to other candidate materials.

TPS testing is needed to determine the ability of TPS materials to absorb CN radiation and to provide a family of TPS materials to accommodate a range of potential aeroheating environments at reduced mass.

Aeroshell Structure

The aeroshell structure was designed to be a current technology concept.¹⁴ Figure 14¹⁴ illustrates the structural components of the aeroshell. The loads are launch dominant with launch loads of 7 G axial, 3 G lat; and entry loads of 4 G axial with 3146 Pa on the heatshield for the 6.5 km/s entry. TPS masses used in the structure design are 1.181 g/cm² for the heatshield TUFROC TPS, and .187 g/cm² for the backshell SLA TPS.

The aeroshell was sized using HyperSizer/NASTRAN with the following results. The heatshield is 25.4 mm thick Hexcell 5052 Alloy Hexagonal Al Honeycomb core, with Graphite Polyimide facesheets. The backshell is 12.7 mm thick Hexcell 5052 Alloy Hexagonal Al Honeycomb core, with Graphite Polyimide facesheets.

The aeroshell mass is summarized in Figure 15.¹⁴ The total aeroshell current best estimate mass (structure + TPS + non structural) is 327.80 kg.

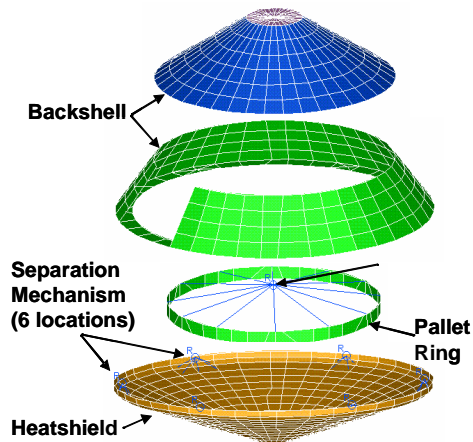


Figure 14. Aeroshell structural components. Ref 14.

Component	Area (m ²)	Structure Mass (kg)	TPS Mass (kg)	Non Structural Mass (kg)
Heatshield	12.58	41.58	148.62*	0
Backshell	15.01	43.27	28.69**	2.38
Pallet Ring	1.20	42.47	0	1.20
Sep Ring	1.79	11.35	0	.89
Sep Ring Attachments	0.45	2.85	0	4.50
Totals		141.52	177.31	8.97

Figure 15. Aeroshell structure mass. Ref 14.

Mass Properties, Packaging

Figure 16 shows the stack and orbiter packaging design.⁴ Note that the aeroshell size and packaging efficiency are governed by the 2.4 m diameter high gain antennae (HGA) packaging.

Figure 17 shows a system level mass summary for the Delta 4450, SEP, Earth Gravity Assist (EGA), aerocapture concept. The concept has 30% system level margin, and greater than 10% system reserve. A VGA option with a Delta 4450, SEP, VGA, aerocapture has 6% system reserve. The aerocapture mass fraction is 41.5% of orbiter entry mass. These results are not possible without this level of detail in packaging, s/c design, structure, and TPS.

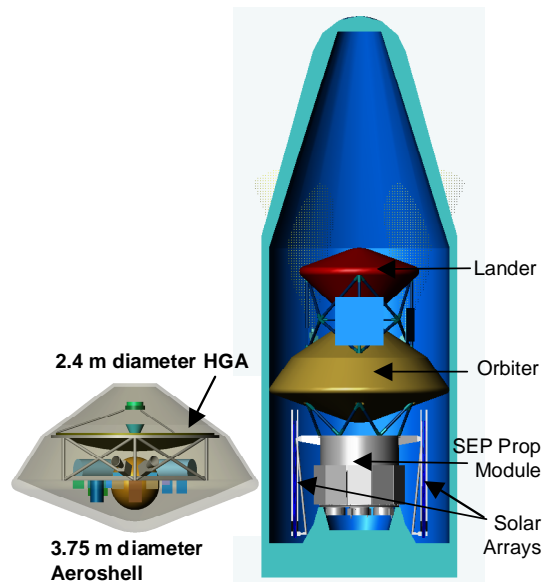


Figure 16. Reference mission packaging. Ref 4.

Component	Mass (kg)			
	Current Best Estimate	% Contingency	Growth	System Allocation
Lander	280.2	29.8%	363.8	400.0
Orbiter/Lander Interface	47.5	30.0%	61.8	61.8
Orbiter	883.6	24.2%	1097.7	1200.0
Prop Mod/Orbiter Interface	47.3	30.0%	61.4	61.4
SEP Prop Module	1084.0	21.4%	1316.5	1450.0
Launch/Prop Mod Interface	60.0	30.0%	78.0	78.0
Stack Total	2402.6	24.0%	2979.2	3251.2
Launch Vehicle Capability	3423			
System Level Mass Margin	29.8%	(LV Cap - CBE) / LV Cap		
System Reserve	13.0%	(LV Cap - Growth) / LV Cap		

Figure 17. System level mass properties for Reference Titan Explorer aerocapture mission. Ref 4.

MASS PROPERTY SENSITIVITIES

Several mass property sensitivity analyses were completed to determine aerocapture mass fraction, aeroshell mass, system mass sensitivity to aeroheating environment assumptions, TPS candidates and aeroshell size.¹⁵ An assessment of aerocapture system mass to an all propulsive mass system was also completed to determine the mass savings for an aerocapture system.^{15,3}

The aerocapture system mass fraction as a function of aeroheating environment and TPS concept is shown in Figure 18.¹⁵ For example, SRAM-20 is sized for three levels of aeroheating environments. Results are labeled SRAM-20, SRAM-20 +1, SRAM-20 +2, for the low, medium and conservative aeroheating levels respectively. The potential savings in mass for alternate

TPS concepts, compared to the baseline, is evident. In addition, the effect of aeroheating environment on TPS mass is also shown. The ballistic coefficient range is 56 – 72 kg/m² over this range of aeroheating environments and TPS materials for the 3.75 m diameter aeroshell.

Based on the orbiter packaging, a reduction in the aeroshell diameter may be possible. The minimum diameter would be approximately 3 m. Further reduction would preclude packaging of the spacecraft with the 2.4 m HGA. A maximum of 20% reduction in aerocapture system mass fraction results for a minimum 3 m diameter aeroshell. The ballistic coefficient range for aeroshell size range of 3 – 3.75 m diameter and range of TPS is 56 – 84 kg/m², all lower than the design trajectory ballistic coefficient of 90 kg/m².

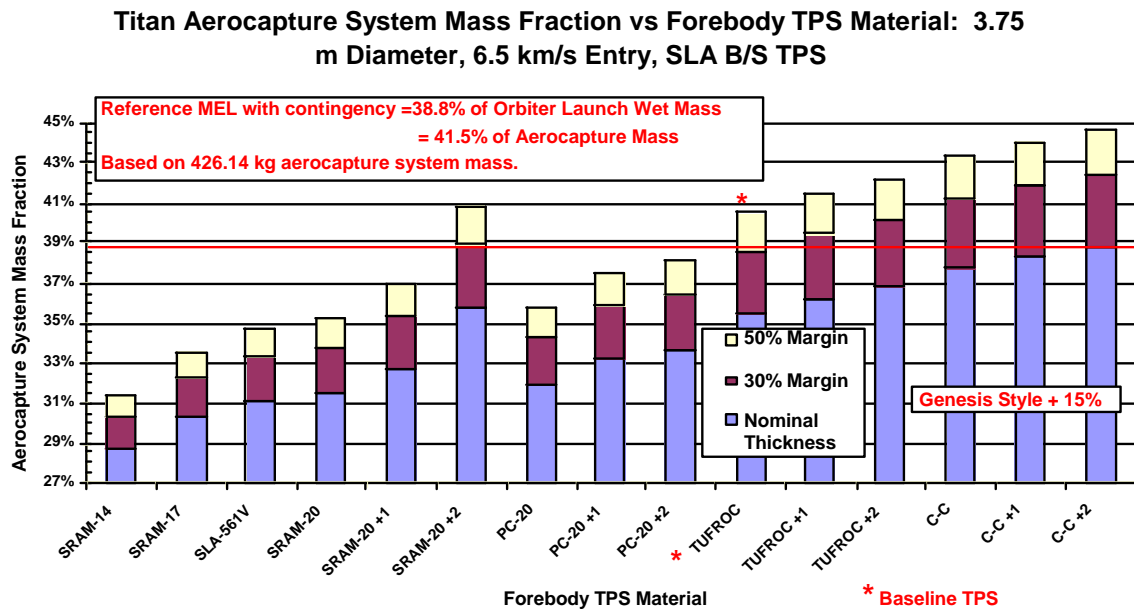


Figure 18 Aerocapture system mass fractions vs. forebody TPS material and aeroheating environments.

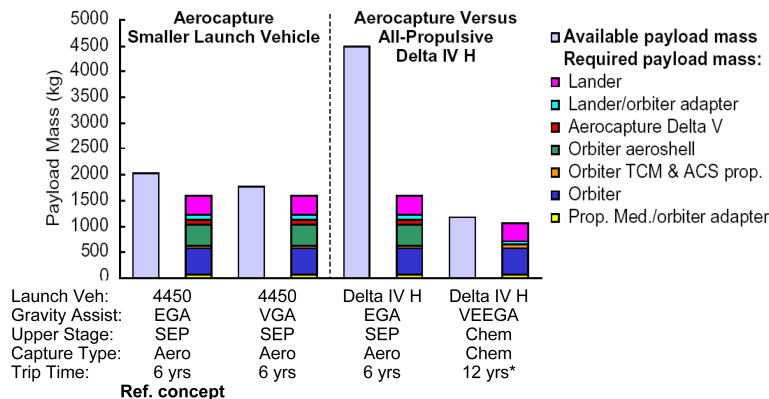


Figure 19 Aerocapture vs. All-Propulsive. *Includes 2 year moon tour used to reduce the propellant requirements for all propulsive capture.

Figure 19 shows a comparison of the Titan Explorer mission with aerocapture compared to an all-propulsive option. For the Titan Explorer payload mass, the all-propulsive option was not feasible with a Delta 4450, while aerocapture enables a feasible mission on the 4450. On a Delta IV Heavy an all-propulsive option is marginal, but potentially feasible. However trip times are 12 years for an all propulsive option compared to 6 years for an aerocapture mission. In addition the aerocapture mission is capable of delivering 2.4 times more payload to Titan compared to the all-propulsive mission for the same launch vehicle. Dependent on mission requirements including required payload mass and trip time, for example, aerocapture is enabling to strongly enhancing compared to an all-propulsive mission.

SUMMARY

Aerocapture is feasible, and the performance is adequate, for the Titan mission with the high heritage low L/D configuration and no improvements from the Cassini/Huygens mission. 99.95% success results for a 6.5 km/sec entry with the low L/D configuration, but with low margin above 3- σ . 100% success results for a 10 km/sec entry with the low L/D configuration, with margin above 3- σ success. Cassini/Huygens results in an increase in margin and robustness significantly above 3- σ , for 6.5 km/sec and 10 km/sec entry aerocapture at Titan with the high heritage low L/D configuration.

Aerocapture can deliver 2.4 times more mass to Titan than an all-propulsive system for the same launch vehicle.

TECHNOLOGIES

Technologies identified in the study as needing development were grouped into three categories; enabling technologies, strongly enhancing technologies and enhancing technologies. As noted earlier, aerocapture is enabling to strongly enhancing for the Titan missions, dependent on the mission requirements. However aerocapture is ready for an Earth or Mars flight experiment without additional technology development. An aerocapture flight experiment may be desirable to demonstrate aerocapture technology to reduce risk/cost for science mission acceptance.

The strongly enhancing technologies identified include

- Aeroheating methods development and validation. Large uncertainties currently exist, improved pre-

diction capability could result in reduced TPS mass, as well as support configuration trades and further mission design trades.

- TPS material testing. TPS materials proposed and other TPS options exist today, but have not been tested against the expected radiative heating at Titan.
- Atmosphere Modeling. Titan General Circulation Model output is needed to represent the “true” natural variability of the atmosphere.

The enhancing technologies identified include

- Aeroshell lightweight structures for reduced aerocapture mass.
- Guidance – Existing guidance algorithms have been demonstrated to provide acceptable performance, improvements could provide increased robustness.
- Simulation – Huygens trajectory reconstruction, statistics and modeling upgrades.
- Mass properties/structures tool for systems analysis capability improvement, concept trades.
- Deployable high gain antennae for increased data return.

The following technologies provide significant benefit to the mission but are already in a funded development cycle for TRL 6 by 2006.

- MMRTG (JPL sponsored AO in proposal phase, First flight Mars '09)
- SEP engine (Glenn Research Center engine development complete in '0#)
- Second Generation AEC-Able UltraFlex Solar Arrays (175W/kg)
- MRO optical navigation camera to be demonstrated in MRO.

ADDENDUM

Aerocapture Characteristics: Titan vs. Mars

Since much of the higher fidelity aerocapture work has been done for Mars missions, Figure 20 provides a

comparison of a representative Mars aerocapture mission to the Titan aerocapture reference mission described in this paper for reference.

Destination/ Reference Parameter	Titan	Mars
Entry Velocity (km/sec)	6.5*	5.7
Nom. Entry Flight Path Angle (deg)	-36	-14.2
Apoapsis/Science Orbit (km)	1700	1400
Atmosphere Composition	95%N ₂ , 5%CH ₄ **	95.3% CO ₂ , 2.7%N ₂
Atmos Scale Height at Aerocapture Altitude (km)	~40	10.5
Atmospheric Interface Altitude (km)	1000	250
Aerocapture Altitude (km)	200-400	40
L/D	.25	.25
M/CDA (kg/m ²)	90***	148
Theoretical Corridor (deg)	3.5	~1.4
Time from Atmos Entry to Atmos Exit (min)	42	10
Convective Stagnation Point Heat Rate (W/cm ²)	46 (.91m nose rad)	30 (1.9m nose radius)
Radiative Aeroheating Rate (W/cm ²)	93-280	negligible
Max g's During Aerocapture (Earth g's)	3.5	2.5 - 3

Figure 20. Representative aerocaptures at Titan compared to Mars. *Titan aerocapture entry velocity 6.5 – 10km/sec, comparison given for 6.5km/sec. **Max CH₄ atmosphere. *For design trajectory & comparison; range: 56–84 kg/m² dependent on aeroheating, TPS, vehicle diameter**

REFERENCES

1. "Titan Lander Conservative Science 01-06" results dated 4,5,8,15 June, 2001.
2. Haw, R. "Approach Navigation for a Titan Aerocapture Orbiter," AIAA-2003-4802.
3. Noca, M., Bailey, R., "Titan Explorer Mission Trades from the Perspective of Aerocapture," AIAA-2003-4801.
4. Bailey, R., Hall, J., Spilker, T., "Titan Aerocapture Mission and Spacecraft Design Overview," AIAA-2003-4800.

5. Justus, J., Duvall, A., "Engineering-Level Model Atmospheres for Titan and Neptune", AIAA-2003-4803.
6. Masciarelli, J., "Guidance Algorithms for Aerocapture at Titan," AIAA-2003-4804.
7. Way, D., Powell, R., Edquist, K., "Aerocapture Simulation and Performance for the Titan Explorer Mission," AIAA-2003-4951.
8. Olejniczak, J., Prabhu, D., Wright, M., Takashima, N., Sutton, K., "An Analysis of the Radiative Heating Environment for Aerocapture at Titan," AIAA-2003-4953.
9. Takashima, N., Hollis, B., Olejniczak, J., Wright, M., Sutton, K., "Preliminary Aerothermodynamics of Titan Aerocapture Aeroshell," AIAA-2003-4952.
10. Laub, B., "Thermal Protection Concepts and Issues for Aerocapture at Titan," AIAA-2003-4954.
11. Curry, D.M., Congdon, W.M., "2007 Titan Mission Analysis of ARA Ablators to Define Required Thickness and Weights," Report presented to Titan Aerocapture Systems Analysis Team, Report Date 11July2002.
12. Congdon, W.M., "TPS-Table-Titan," e-mail to M.K.Lockwood, 23Aug2002.
13. Dec, J.A., "Titan Orbiter Heatshield Sizing Study," e-mail to M.K.Lockwood, 27Sep2002.
14. Hrinda, G., "Structural Design of the Titan Aerocapture Mission," AIAA-2003-4955.
15. Dyke, R. E., "Planetary Probe Mass Estimation Tool Development and Its Application to Titan Aerocapture," AIAA-2003-4956.

Acknowledgements: The author would like to acknowledge and thank the team members of the NASA Aerocapture Systems Analysis Team for their work and contributions to the Titan Aerocapture Systems Analysis Study and to this paper. Thank you to Carol Carroll, Aerocapture Systems Analysis Study Review Panel Chair, and the review panel members for review of this work and helpful comments and recommendations. Thank you to Anne Costa for preparing this paper for publication.

STRUCTURAL DESIGN OF THE TITAN AEROCAPTURE MISSION

Glenn A. Hrinda*

NASA Langley Research Center, Hampton VA

Abstract

A major goal of NASA's planetary exploration efforts is to create affordable spacecraft capable of delivering science experiments for long duration periods. To help achieve this goal the aerocapture technique for slowing a spacecraft has been investigated and appears to produce less vehicle mass than an all-propulsive mission. A conceptual spacecraft was designed and studied for an aerocapture mission to Titan, Saturn's largest moon. The spacecraft is an Orbiter/Lander combination that separates prior to aerocapture at Titan. The structural challenges faced in the design will be discussed as well as optimization sizing techniques used in the Orbiter's aeroshell structure. Design trades required to optimize the structural mass will be presented. Member sizes, concepts and material selections will be presented with descriptions of load cases and spacecraft structural configurations. Areas of concern will be highlighted for further investigation. This study involved the collaboration efforts of NASA representatives from Langley Research Center (LARC), Jet Propulsion Lab (JPL) and Ames Research Center (ARC). The concept design borrowed from existing flight hardware as much as possible.

Introduction

The structural sizing for a conceptual aerocapture spacecraft to Titan was required to obtain mass estimates based on current sizing methods. Finite element analysis (FEA) and HyperSizerTM sizing

software was used to model the launch stack assemble that included the Propulsion Module (PM), the Orbiter and the Lander. The Orbiter spacecraft performs aerocapture at Titan and is designed to withstand atmospheric heating. The Lander is a sphere-cone and was considered as a concentrated mass. No aeroshell design analysis was performed on the Lander. The launch vehicle used was a Boeing Delta IV heavy with a 4 meter fairing. The spacecraft integration into a Delta IV heavy launch vehicle was achieved through trade studies focusing on mission performance necessary for an aerocapture mission. Three primary design objectives were: minimum structural mass, dynamic modes at launch were met or exceeded and stress levels were within margin with minimal deflections. Load cases and frequency minimums at launch came from the Boeing Payload Planners Guide. Maximum loading at launch and during entry at Titan was used to design the spacecraft structure. The lowest predicted natural dynamic modes were investigated to identify any low frequency problems with the spacecraft.

The structural design used composites for the Orbiter aeroshell and a truss system to join the stack components. Modeling efforts were kept as simple as possible to shorten modifications occurring as the design progressed. HyperSizerTM sizing software was found beneficial in sizing the Orbiter's aeroshell. The software's ability to optimize composite sections without refining mesh densities and geometry was demonstrated throughout the design's progress.

Nomenclature/Abbreviations

CG	Center of Gravity
FEA	Finite Element Analysis
FEM	Finite Element Model
HGA	High Gain Antenna
NSM	Non-structural mass
PM	Propulsion Module
TPS	Thermal Protection System

**Structural Engineer, Vehicle Analysis Branch,
Aerospace Systems Concepts and Analysis
Competency*

Copyright © 2003 by the American Institute of Aeronautics and Astronautics, Inc. No copyright is asserted in the United States under Title 17, U.S. Code. The U.S. Government has a royalty-free license to exercise all rights under the copyright claimed herein for Governmental Purposes. All other rights are reserved by the copyright owner.

Conceptual Titan Design

The Titan aerocapture spacecraft is a stacked configuration requiring a three component stack consisting of a Propulsion Module (PM), an Orbiter and Lander. The three separate spacecraft were combined to form a launch stack capable of fitting into a 4 meter Delta IV fairing. Each vehicle must be able to separate during the Titan aerocapture mission sequence. The PM provides all thrust maneuvering to get the Orbiter and Lander near Titan. The Orbiter and Lander will then separate from the PM and then from each other. The Lander descends to the Titan surface in a Huygens type aeroshell. The Orbiter continues through the thin Titan atmosphere and begins aerocapture until achieving its mission orbit. The Orbiter was the only vehicle designed to take advantage of aerocapture. Once in orbit around Titan, the Orbiter will support an on orbit relay station for the Lander.

The conceptual spacecrafts were used as a baseline to test design and analysis methods used among the various NASA centers involved with aerocapture vehicle designs. This study focused on the weight reduction and strength requirements of the major load carrying structural members. The design attempts to maintain an axial load path direction starting with the Lander, into the Orbiter through its payload pallet and heatshield and final into the PM.

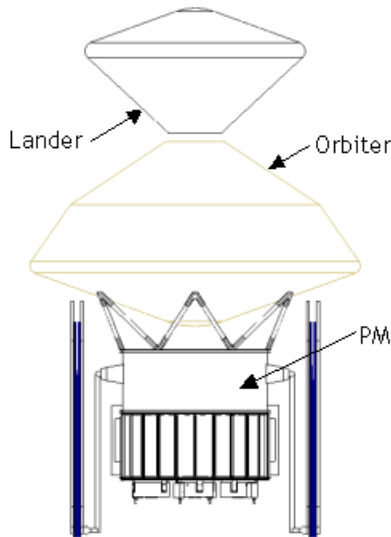


Figure 1. Launch Stack

The structural analysis performed in this study helped verify the stack arrangement and size the Orbiter aeroshell and support structure for the generic Lander. Investigating various stack arrangements showed that a truss would provide the lightest structure for supporting the Lander. A truss was also used for the PM to Orbiter adapter structure. The study used a launch load envelop for the Delta IV heavy. The Orbiter maximum diameter was set to 3.75 meters and used a heatshield cone and biconic backshell as shown in figure 1. The PM was modeled to include its stiffness contribution in determining overall stack frequency during launch. Launch loads were taken from the Boeing Delta IV Payload Designers manual (ref. 1).

Stack Configurations

The stacking sequence of the PM, Orbiter and Lander was decided upon after several trials of the three components arranged in different configurations. Each configuration had its abilities compared with each other until the stack shown in figure 1 was chosen. This arrangement was used after various stack sequences were attempted to find a stack able to meet strength, dynamics and center-of-gravity (CG) requirements. The diagrams in figure 2 represent a sample of the many stack sequences of the PM, Orbiter and Lander attempted during the design trade studies. The final stack configuration used in the design placed the Lander on top of the Orbiter.

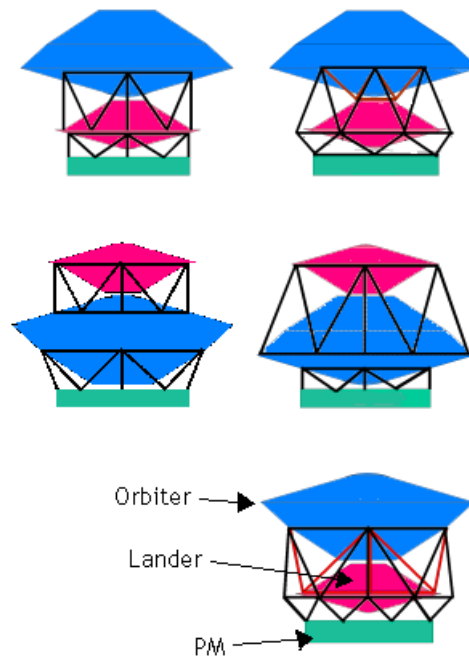


Figure 2. Trial Launch Stack Configurations

The configurations placing the Orbiter on top were dismissed because of the large mass of the Orbiter and low lateral stack bending frequency that is created during launch. The configurations produced heavy structures due to the increased stiffness requirements necessary for raising the lateral bending frequency above 10 Hz. One of the design goals was to minimize structural mass and maintain a minimum frequency of 10Hz lateral and 27Hz axial. These values were taken from the design guide in reference 3. The final configuration produced the minimal structural mass and maintained design stiffness requirements.

A generic sphere-cone Lander with a mass of 400 kg was assumed in the study and was modeled as a lumped mass with rigid connections to its outer diameter. A truss is used to create a load path from the Lander, through the Orbiter and into the PM. During the mission the Orbiter and Lander separate from the PM. The truss adapter to the PM is jettisoned with the PM and the six attachment points to the Orbiter heatshield are plugged. The method for plugging the heatshield penetrations will require further study. One possibility is to mechanically activate panels to cover the attach points. The Lander will separate from the Orbiter and head directly for the Titan surface. The upper truss supporting the Lander will then separate from the Orbiter. Aerocapture of the Orbiter will then commence at Titan.

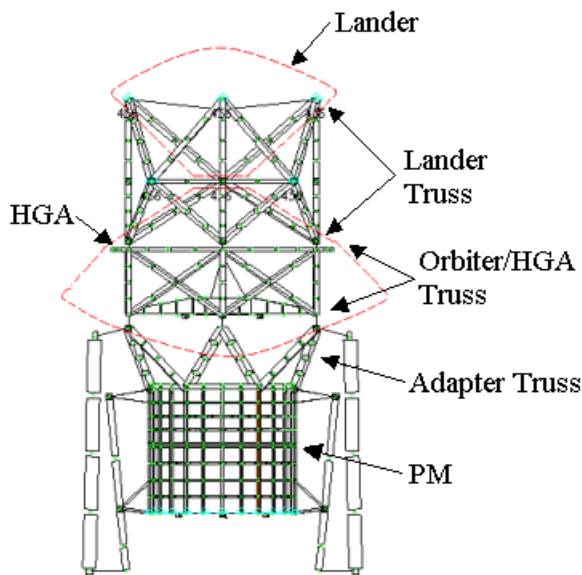


Figure 3. Stack Truss

Orbiter Aeroshell Design

The Orbiter spacecraft structure consists of the fore body heatshield, biconic backshell, cap plate and internal support structure supporting the Orbiter's payload. The largest payload components in the Orbiter are the 2.75m High Gain Antenna (HGA) and the spherical hydrazine tank. Figure 4 shows these components plus the arrangement of other internal components carried by the Orbiter. The payload deck is a hexagonal shaped aluminum honeycomb panel that extends to the aeroshell at six separation points. All payload deck items are modeled as concentrated masses with their CG offset made using rigid elements as required. The Orbiter aeroshell is supported by the adapter truss attached to the heatshield. The Lander is supported by a tube truss system that penetrates the Orbiter backshell at four locations. The load path continues straight down through an internal structure that also supports the HGA.

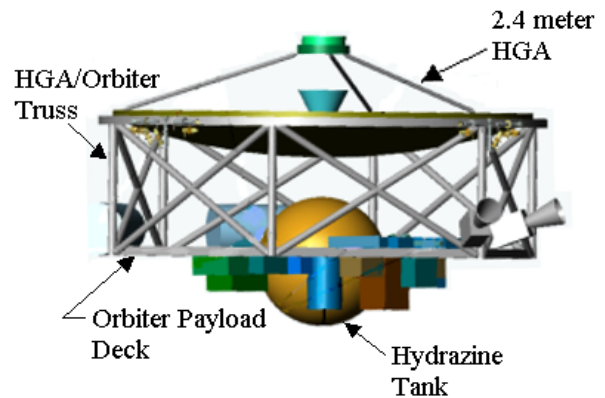


Figure 4. Orbiter HGA and payload deck (Lander not shown)

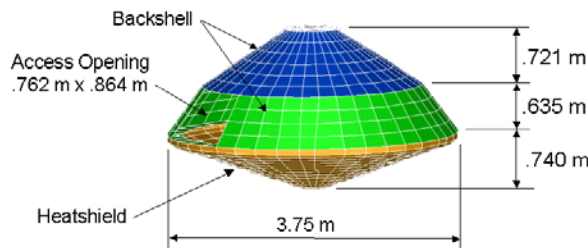
A payload pallet ring is used to transfer the loads coming from the Lander as well as the payload deck to six hard points on the Orbiter's heatshield. The six hard points are equally spaced around the perimeter of the payload ring and represent penetrations through the heatshield. The Orbiter aeroshell FEM is pinned at the six hard points. Concentrated masses were used to model the internal payloads along with rigid elements to properly locate CG's.

The load contribution from the Lander and Orbiter is carried into an adapter truss through the six points on the heat shield. The adapter truss tapers down to fit the front of the PM completing the load path. The choice of allowing the load path to continue through the heat shield raises obvious concerns with the

thermal protection system (TPS) being compromised. The mass of the Orbiter was reduced by not using its aeroshell to support the Lander mass. The stack concept relied on keeping load paths running axially through a tubular space truss. The six penetrations in the heatshield were accepted in this study and referred to as a detail requiring further investigation.

The Orbiter was analyzed using a combination of nastran finite element analysis (fea) and Hypersizer™ commercial sizing and optimization software. In order to utilize Hypersizer™, a coarse grid nastran fea was created with all non-structural masses (NSM) and mission loads of interest. The major NSM contribution was the heatshield and backshell TPS. Other NSM included Orbiter payload and aeroshell separation mechanisms as well as allocations for the six attach points through the heatshield. Figure 5 shows an exploded view of the FEM used to create a HyperSizer™ model of the Orbiter’s aeroshell.

Orbiter Model



Orbiter Model

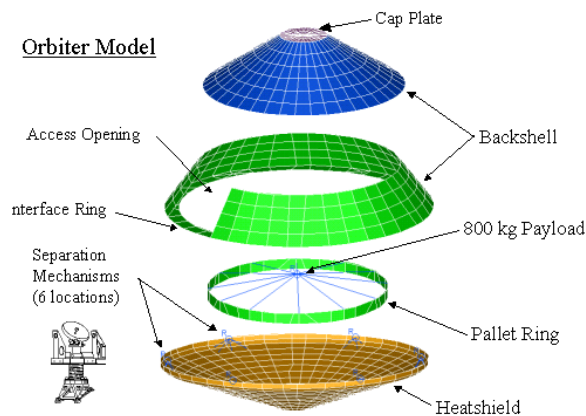


Figure 5. Orbiter Aeroshell FEM

The mesh size was kept coarse, however included enough detailing of the aeroshell geometry to accurately calculate the element forces required in Hypersizer™. An opening in the backshell was

modeled to represent an access panel to the Orbiter payload. No attempt was made to stiffen the opening by modeling the door or method of attachment to the backshell. The mass of the door was treated as a NSM with smearing at the nodes. The nastran finite element model (FEM) of the Orbiter was created only with basic nastran elements: quad4, tria3, conm2 and rbe2’s. These elements are easily supported by Hypersizer™ and were imported to form a Hypersizer™ model of the Orbiter aeroshell.

Several model configurations and load cases were used to find worse case conditions on the Orbiter aeroshell. The first configuration studied was the Orbiter in the launch mode with accelerations based on the Delta IV payload guide (ref. 3). The loads used were 3 g’s lateral and 7 g’s axial. The combined loads were the absolute maximums in the Delta IV launch load envelope. No assessment of acoustic energy and shock spectra on the total payload was attempted during the design.

The next load cases investigated were aerocapture entry loads of the Orbiter through the Titan atmosphere. Two load cases were investigated for different entry velocities. A 6.5 km/s and 10 km/s entry load cases were analyzed. The peak aero loads were obtained from CFD analysis based on the two trajectory cases. The loads were assumed to act normal to the heatshield and evenly distributed. The following loads were used:

6.5 km/s Entry loads: 4 G axial with 3146 Pa on heatshield

10 km/s Entry loads: 10.3 G axial with 8997 Pa on heatshield

The launch load forces were imported into Hypersizer™ to start sizing of the aeroshell. The Orbiter’s Hypersizer™ model was divided into different components for sizing. The approach was to size the heatshield as one uniform thickness as well as the lower and upper backshell and cap plate. The optimization concepts used were: honeycomb core with face sheets, blade stiffened panels and isogrids. Each concept had dimension variables that were used to find the optimal aeroshell geometry such as: blade separation distances, core and face sheet thickness, blade depths and thickness.

The TPS non-structural mass was added inside Hypersizer™. The mass could easily be changed on one of Hypersizer’s™ user input screens. This feature of the software was helpful for modifying the model to suit different TPS trial materials and thickness. The final TPS material used in the design of the Orbiter was TUFROC on the heatshield with

an aerial density of 1.181 g/cm². This density was held constant over the heatshield. The backshell and cap plate used SLA with an aerial density of .187 g/cm². The density was also constant over both surfaces. The TPS masses were exported as nastran conmm2's and evenly distributed at the element nodes.

Why use HyperSizer?

Spacecraft structures contain complex geometry and load distributions that are highly indeterminate and historically demanded finite element analysis (FEA) to solve. Performing structural analysis and sizing optimization has required large degree-of-freedom models with long solution run times. A software product called HyperSizer™ can help simplify structural sizing and reduce design analysis time. HyperSizer™ helps to automate the sizing of structures by reducing launch acceleration and entry loads into force and moment components on panels and beams throughout the spacecraft. The sizing includes finding the optimal material combinations, panel and beam dimensions such as thickness, depths and spacing. The code is not a finite element analysis or computer aided design package. HyperSizer™ adds to the capabilities of these tools to allow the engineer to design, size and perform detailed failure analysis on a complete vehicle.

The Orbiter's aeroshell design was used to demonstrate the software's composite design capability and use in conceptual designs. A new mass-sizing tool is under development for planetary spacecraft at LARC. The tool will have the ability to link spreadsheet user inputs into HyperSizer™ for composite structure sizing. This will greatly improve structural mass estimates and lessen analysis time usually dominated by FEM creation and modifications.

Optimization Capabilities

Optimization capabilities within HyperSizer™ include finding minimum weight panel or beam concepts, material selections, cross sectional dimensions, thickness and lay-ups from a database of 50 different stiffened and sandwich panel designs as well as a database of composite, metallic, honeycomb and foam materials. The database is used to define structural families inside HyperSizer™. The structural families include definitions for panels and beams such as the "uniaxial stiffened family", the "unstiffened plate/sandwich family" and the "open beam family".

The panels shown in figure 6 below represent some of the typical families of structural panels available in HyperSizer™. The panels may be stiffened with typical aerospace shapes or corrugated. The grid-stiffened family of panels has recently been added to HyperSizer™. This allows for the sizing optimization of isogrids, orthogrids and general grid rib-stiffened panel concepts with either isotropic or composite materials

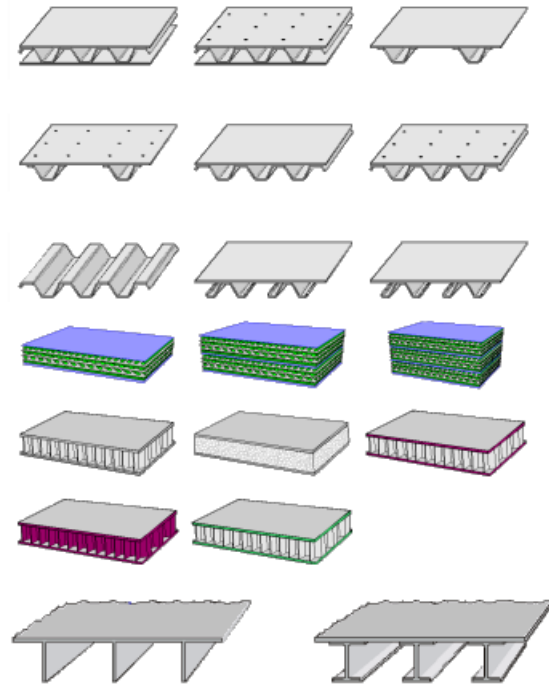


Figure 6. Typical HyperSizer™ panels

Orbiter payload deck and HGA support

The Orbiter payload deck and HGA support were modeled with plate and beam elements. The payload deck was a flat hexagonal shaped plate with a large hole cutout for a hydrazine tank carried into aerocapture orbit. The six corners of the hexagon platform extend to the outer diameter of the Orbiter. The platform lies in the same plane as the backshell/heatshield separation plane. The HGA is supported by an internal truss that also connects to the Lander truss. Loads from the Lander travel through the HGA support and into the payload ring located below the payload deck. Loads are then transferred through the heatshield structure and into the Orbiter/PM adapter.

Propulsion Module

The PM was modeled as shown in figure 7. The bulk of the module was made of aluminum channels and distributed lumped masses. Two solar arrays were also modeled and appear on the module sides. The solar arrays were modeled as beams having an approximate stiffness of the array panels. The modeling effort attempted to accurately capture the correct stiffness and mass of the module without fine detailing of the meshes. A concentrated mass with rigid elements was used for the propellant tank. Support structure for the tank was also provided with a truss system tying into a ring frame. A cylindrical wall stiffened with beam elements form the main thrust tube. The aft end of the tube was pinned with the forward end attaching to the Orbiter/PM adapter truss. The PM was modeled to help determine overall stack frequency at launch. By including the stiffness from the PM in the dynamic analysis, better determinations of the lowest modes were found.

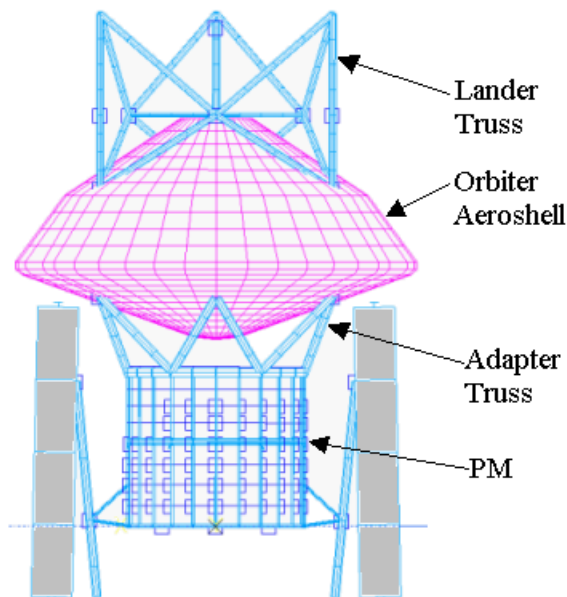


Figure 7. Orbiter FEM Components

Results

A dynamic analysis was performed on the Orbiter and launch stack to check for low natural frequencies. The suggested launch frequency minimums from the Boeing design guide (ref. 3) of 10 Hz lateral and 27 Hz axial were used. The launch stack minimum modes, shown in figures 8 and 9, were 10.5 Hz lateral and 27.8 Hz axial respectively. Figure 10 is the first mode shape of the Orbiter aeroshell at 54.6 Hz. No dynamic magnification factors were considered during launch.

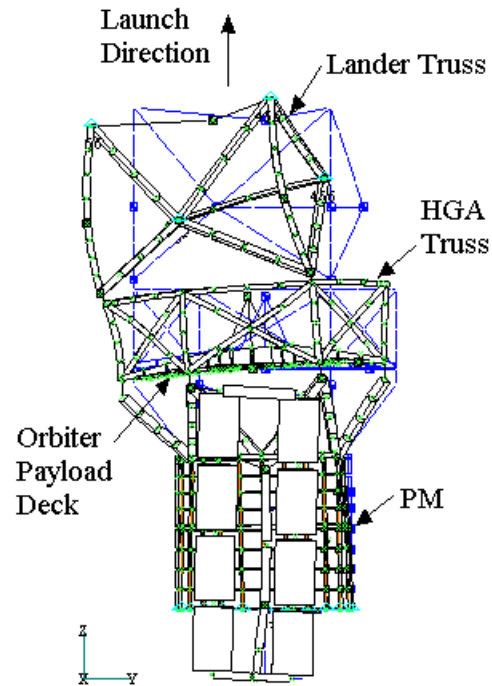


Figure 8. Lateral 10.5 Hz Launch Stack Mode

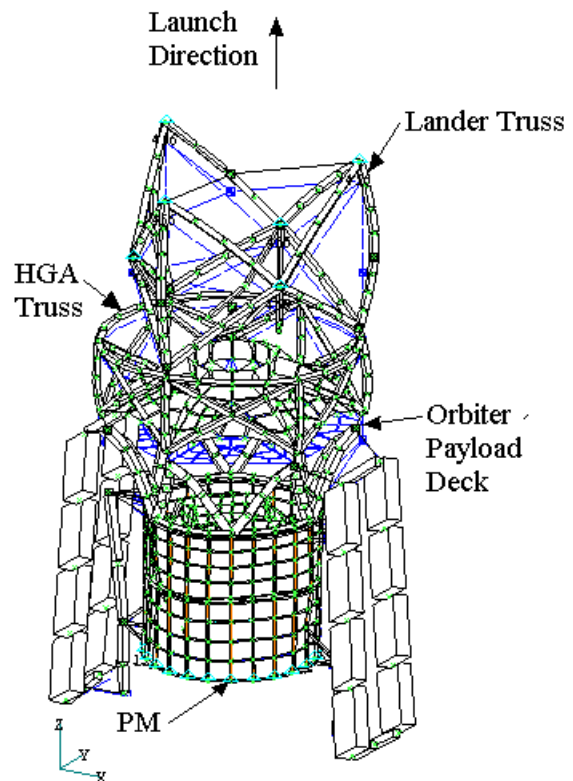


Figure 9. Axial 27.8 Hz Launch Stack Mode

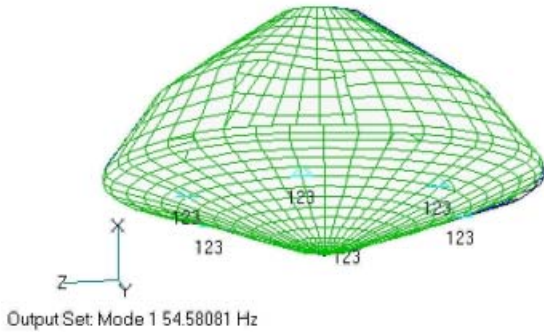


Figure 10. Orbiter 1st mode

The overall maximum deflections on the heatshield were checked at launch and during entry. The largest deflections occurred on the heatshield during launch and were less than 1 mm. The exaggerated deflected shape of the heatshield is shown in figure 11. Double curvature exists where the six adapter truss points attach through the heatshield. The deflections were small and not considered a concern for TPS bonding.

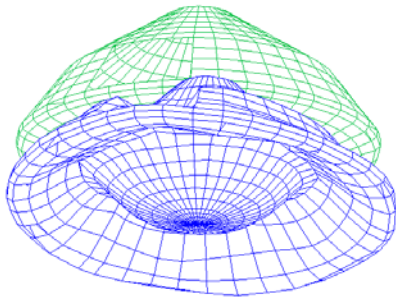


Figure 11. Orbiter Deflections at Launch

The Orbiter's aeroshell was sized after several iterations between nastran and HypersizerTM. The dominant load case was found to be during launch. The process optimized the aeroshell structure and indicated which materials and structural concept would produce the lightest aeroshell. Honeycomb core with face sheets were shown to be the best structural concept. The final core material for the heatshield was a 25.4mm thick Hexcell 5052 alloy hexagonal aluminum honeycomb with 1.7mm graphite polyimide face sheets. This design was similar to the Mars Exploration Rover (MER) heatshield except for the six hard points used in attaching the Orbiter heatshield to the PM. The backshell sizing done within HyperSizerTM showed a honeycomb core face sheet concept produced the

minimum structural mass. The core was a 12.7mm thick Hexcell 5052 alloy hexagonal aluminum honeycomb and graphite polyimide face sheets of varying thickness. The cap plate design was similar to the backshell.

Results from analyzing the HGA and Lander trusses showed the optimal material was 2" OD, 0.12" wall M55J/954 tubes. The Orbiter/PM adapter truss was similarly made with 3.2" OD, 0.2" wall M55J/954 tubes. The sizes were driven by finding sections large enough to prevent buckling.

A summary of the final Orbiter aeroshell mass is given in table 1 and the total launch stack mass summary is shown in table 2. The total spacecraft mass for the launch configuration was 3173.2 kg and included the Lander, Orbiter and PM. TPS and non-structural masses were included plus allowances for miscellaneous items such as heatshield to backshell separation components. The design relies on a system of composite M55J trusses that form a load path into the PM. This system produced minimal displacements during launch and held stresses within safety limits that were: 1.4 on ultimate, 1.25 on yield limit and 1.5 for buckling.

Part	Area	Structure Mass	TPS Mass	NSM
Heatshield (TufRoc)	12.58 m ²	41.58 kg	148.62 kg	0
Backshell (SLA-561V)	15.01m ²	43.27 kg	28.69 kg	2.38 kg
Pallet Ring	1.20m ²	42.47 kg	0	1.20 kg
Separation Ring	1.79m ²	11.35 kg	0	.89 kg
Separation Ring Attachments	.45m ²	2.85 kg	0	4.50 kg
Totals		141.52 kg	177.31kg	8.97 kg

Total Aeroshell (structure + TPS + NSM) = **327.80 kg**

Table 1. Orbiter Aeroshell Mass

Lander	400 kg
Lander Truss	61.8 kg
Orbiter Aeroshell + Payload	1200 kg
Orbiter/PM Truss	61.4 kg
PM	1450 kg
Total spacecraft	3173.2 kg

Table 2. Launch Stack Mass

Conclusion

The success of an aerocapture mission at Titan greatly depends on the mass reduction of the structure and the configuration of the launch stack. The design efforts encountered during this conceptual study showed the importance of defining the configuration in reducing spacecraft mass. The final launch configuration used an unconventional method of attaching the Orbiter heatshield to the PM. This method allowed a continuous load path from a 400kg Lander, into the Orbiter, through the Orbiter heatshield and into the PM. Maintaining a load path through the trusses that avoided the Orbiter aeroshell from supporting the Lander minimized the Orbiter aeroshell. The stacking arrangement also minimized the buckling lengths of the truss members as well as the number of required members. HyperSizer™ was used to perform optimization sizing of the Orbiter aeroshell without a detailed mesh and extensive remodeling effort. The results indicated a honeycomb face sheet composite could produce a light structure while providing the necessary stiffness to meet minimum dynamic frequency requirements at launch. The results from this study have established a starting point for a detailed fea of the Orbiter aeroshell. Such an analysis could include varying core and lay-up thickness and detailed analysis of attachment connections and separation mechanisms. The structural mass for this design was within the mass margin estimated for a successful Titan mission.

Acknowledgements

The author recognizes the following for their contribution to the Titan structural analysis: Jonathan Lam (JPL) for his nastran modeling of the PM and Orbiter payload structure, Rob Bailey (JPL) for packaging the Orbiter and detailing payload requirements, Bernie Laub (ARC) for TPS sizing on the Orbiter heatshield and backshell, and Eric Dyke (Swales Aerospace-LARC) for investigation of the Orbiter/Lander truss and stacking configurations.

References

1. G. A. Hrinda, "Integrated Structural Analysis of the X-43 Using HyperSizer Sizing Software", CS/PSHS/APS Joint Meeting, November 2000.
2. G. A. Hrinda, "Structures For the 3rd Generation Reusable concept Vehicle", Space 2001 Conference
3. "Delta IV Payload Planners Guide", The Boeing Company, Huntington Beach, CA, 2000.
4. Collier Research Corporation, "HyperSizer Tutorial & Applications", 2nd edition, Collier Research Corporation, 1998.
5. C. S. Collier, P. W. Yarrington and M. Pickenheim, "Design Optimization Using HyperSizer", Collier Research Corporation, The 1998 MSC Americas Users 'Conference', Universal City, CA, Oct 5-8, 1998.
6. C. S. Collier, P. W. Yarrington and M. Pickenheim, "Next Generation Optimization Today", The 1997 MSC Aerospace Users Conference', Newport Beach, CA, November 18-20, 1997.

An Analysis of the Radiative Heating Environment for Aerocapture at Titan

Joseph Olejniczak*

NASA Ames Research Center, Moffett Field, CA 94035

Michael Wright,† Dinesh Prabhu‡

ELORET Corp., 690 W. Fremont Ave., Suite 8, Sunnyvale, CA 94087

Naruhisa Takashima§

AMA Inc., 303 Butler Farm Road, Suite 104A, Hampton, VA 23666

Brian Hollis,** E. Vincent Zoby,††

NASA Langley Research Center, Hampton, VA 23681

and

Kenneth Sutton‡‡

National Institute of Aerospace, Hampton, VA 23666

Abstract

Details of the radiative heating analysis for the forebody of a candidate Titan aerocapture orbiter are presented. The radiative heating rates are obtained through a *posteriori* analysis of high-fidelity thermochemical nonequilibrium flow fields computed using modern techniques of computational fluid dynamics. Results from axisymmetric and three-dimensional analysis are presented at several points on candidate aerocapture trajectories in various model atmospheres of Titan. The radiative heating rates are found to be up to five times the peak convective heating rates, indicating that an accurate knowledge of the uncertainty of the radiative heating predictions is critical for a Titan aerocapture mission. The results also show that – (1) the radiative heating rates are dominated by the violet band system of CN, and (2) the gas mixture is optically thin. The predicted radiative heating is found to be very sensitive to the dissociation rate of molecular nitrogen – a factor of two increase in the rate, which is within the experimental uncertainty, results in a 25% decrease in the radiative heating.

Introduction

A one-year system analysis design study^{1,2} of an aerocapture mission to the Saturn moon Titan was recently completed. The purpose of the systems study was to identify the critical issues for an aerocapture mission, not necessarily to provide a complete mission design. The purpose of the radiation calculations presented in this paper was likewise to assess the impact of radiative heating on the system design and identify the further work needed before a Titan aerocapture mission could be launched.

Aerocapture uses a single pass through an atmosphere to dissipate excess energy and enter a stable orbit.

Aerocapture missions offer a mass savings over traditional propulsive capture missions if the mass fraction of the Thermal Protection System (TPS) needed to protect the vehicle during the atmospheric pass is less than the mass fraction of the propulsion system needed to slow the vehicle and enter orbit. The results of the systems analysis study¹ demonstrated that aerocapture missions at Titan provide a significant mass benefit compared to propulsive capture missions.

A 70-degree sphere-cone with a 1.875 m maximum radius was selected as the baseline design for the orbiter, as shown in Fig. 1. The geometry is a scaled version of the proposed Mars Smart Lander vehicle.³ For the nominal entry trajectory, the vehicle enters the atmosphere with a relative velocity of 6.5 km/s and flies at a constant 16° angle-of-attack. For comparable velocities and altitudes at Earth, the corresponding radiative heating level would be insignificant.

However, studies of the heating environment of the Titan probe Huygens indicated that radiative heating rates were 2-3 times greater than convective heating rates.^{4,6} The Huygens probe, part of the Cassini mission to Saturn, is a 2.70 (m) diameter 60-degree sphere cone that will enter the Titan atmosphere on a direct, ballistic trajectory. Since the proposed aerocapture orbiter is larger than Huygens and flies a longer, lifting trajectory, it was expected that the aerocapture orbiter would experience even higher radiative heating rates than the Huygens probe.

Titan has an atmosphere of nitrogen, methane, and argon. This gas composition leads to non-intuitive thermochemical nonequilibrium effects in the shock layer. The methane in the atmosphere dissociates in the nonequilibrium shock layer and CN forms. The CN molecule is a strong radiator. Therefore, even though the

* Senior Research Scientist, Reacting Flow Environments Branch. Senior Member AIAA

† Senior Research Scientist. Senior Member AIAA

‡ Senior Research Scientist. Associate Fellow AIAA

§ Senior Research Scientist. Senior Member AIAA

** Research Scientist, Aerothermodynamics Branch. Senior Member AIAA

†† Research Scientist, Aerothermodynamics Branch. Fellow AIAA

‡‡ Research Scientist, Aerothermodynamics Branch. Fellow AIAA

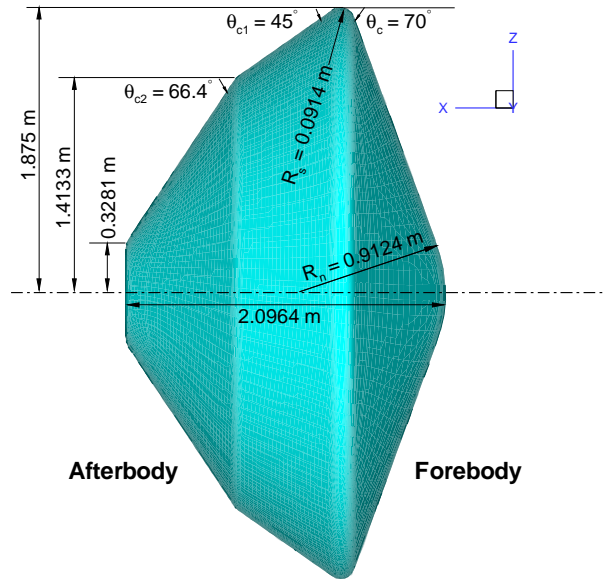


Figure 1. Schematic view of the Titan aerocapture orbiter.

entry velocity and post-shock temperatures are relatively low compared to Earth entry, there is the potential for significant nonequilibrium radiation.

The gas kinetic and radiation models used in this work are based on the work of Nelson *et al.*,⁷ which was developed using shock tube data from Park.⁸ The Park data are from only one velocity-pressure condition. A detailed

collisional-radiative model based on extensive shock tube data was developed to design the Huygens probe,^{4,6} but details of the experimental data and the model have not been published.

Because the radiative heating has a first order impact on the TPS material selection and mass, even a preliminary design of an aerocapture vehicle requires reliable estimates of the radiative heating. As a result, high fidelity CFD and radiation calculations using the best available thermophysical models were made to support the system design study.

This paper discusses these radiative heating predictions for the forebody of the Titan aerocapture orbiter. First, a description of the methods used to compute the radiative heating rates is given. Second, radiative heating results for axisymmetric and three-dimensional cases along candidate aerocapture trajectories are presented. Finally, the status of the ongoing efforts is reported. A series of companion papers describes the details and results of the mission design.⁹⁻¹⁶ Takashima *et al.*¹⁷ discusses the convective aeroheating environment for the aerocapture vehicle.

Methodology

The flow field and radiation production and transport were calculated in an uncoupled manner. In other words, Computational Fluid Dynamics (CFD) was used to compute

the flow field properties used as input to the radiation solvers, but the effect of the radiation on the flow field was neglected. Previous authors^{18,19} have used loosely or fully-coupled methods for strongly radiating flows. However, the uncoupled approach is appropriate for systems analysis trade studies because it provides a conservative estimate of the radiative heating at a much lower computational cost than a loosely or fully coupled approach, allowing a large number of candidate designs to be rapidly analyzed. The degree to which the uncoupled approach over-predicts the total radiative heating for this application will be discussed in a later section.

The radiation calculations are made by computing the radiative flux that reaches a location on the surface of the vehicle along a line-of-sight normal to that surface location. The calculations required as inputs the species number densities, translational temperature, and vibrational temperature at each point in the flow field along the line-of-sight. The radiation solvers compute the amount of radiation produced and the transport of that radiation along each line-of-sight.

CFD

Two different CFD solvers were used to compute the flow fields: DPLR¹⁹ and LAURA.²⁰ Briefly, both codes solve the Navier-Stokes equations including finite rate chemistry and vibrational nonequilibrium. DPLR and LAURA have been shown to give essentially the same results when using identical thermophysical models.¹⁷

The chemical reaction rates used were from Nelson *et al.*⁷ The rate model in Nelson *et al.* was developed for application to Titan entry and was based on a combination of shock tube data from Park⁸ and existing reaction rate models. Because the amount of nitrogen dissociation has a direct impact on the amount of CN formed, some calculations were made substituting the newer nitrogen dissociation rates from Park²² in order to test the sensitivity of the radiative heating to the reaction rate model. The rates in Park²² are approximately twice as fast as those in the Nelson *et al.* model. The effect of reaction rate choice on radiative heating will be discussed in detail in a later section. Most calculations were made using a twelve species model (CH₄, CH₃, CH₂, N₂, C₂, H₂, CH, NH, CN, N, C, and H). Calculations were also made using an eighteen species (CH₄, CH₃, CH₂, N₂, N₂⁺, C₂, H₂, CH, NH, CN, CN⁺, N, N⁺, C, C⁺, H, H⁺, and e) to confirm that ionization effects were unimportant.

Radiation

Similarly, two radiation transport codes were used: NEQAIR96²³ and LORAN.²⁴ Both of these radiation solvers calculate the emission and transport of radiation in the flow field using the tangent slab approximation. In this approximation radiation is assumed to be emitted from infinitely thin parallel planes perpendicular to the absorbing surface. NEQAIR96 performs the calculations line-by-line, computing an absorption coefficient for each atomic line

Table 1. Methane mass fractions for the three different Titan atmosphere models.

Atmosphere	CH ₄ Mass Fraction
Minimum	0.0293
Nominal	0.0173
Maximum	0.0055

and molecular rotational line in the vibrational bands. LORAN uses a smeared band model with a smoothly varying absorption coefficient for the molecular band. Comparisons of NEQAIR96 and LORAN results will be presented later.

The tangent slab results computed in either NEQAIR96 or LORAN need to be reduced to account for surface curvature effects. The exact value of this reduction factor depends on the surface geometry and the absorption in the flow field. For a spherical stagnation point in air, values from 0.75 to 0.85 have been previously used.^{25,26} In this work, a value of 0.80 was chosen.

The specific molecular bands considered were N₂ 1+ (B 3Π_g->A 3Σ_u⁺), N₂ 2+ (C 3Π_u->B 3Π_g), N₂ Lyman-Birge-Hopfield (a 1Π_g->X 1Σ_g⁺), CN violet (B 2Σ⁺->X 2Σ⁺), CN red (A 2Π->X 2Σ⁺), H₂ Werner (C 1Π_u->X 1Σ_g⁺), and H₂ Lyman (B 1Σ_u⁺->X 1Σ_g⁺). Also computed was radiation from atomic lines of N, C, and H. Updated molecular spectroscopic data from Laux²⁷ and atomic spectroscopic data from NIST²⁸ were used in NEQAIR96.

While CFD calculates the number of molecules and atoms in the ground electronic state, radiation is emitted from excited electronic states of molecules and atoms. Therefore, a collisional-radiative excitation model is needed to compute the number of electronically excited molecules and atoms and their distribution among vibrational and rotational states.

Since no validated excitation model was available for a nitrogen, methane, and argon gas mixture, the excited electronic states of the molecules and atoms were assumed to be in equilibrium, and therefore populated in a Boltzmann distribution governed by the vibrational temperature of the gas. While such an assumption is inappropriate for air mixtures, it is a reasonable approximation when CN is the main radiator emitting in the violet and red bands. Since the ground (X 2Σ⁺), first excited (A 2Π), and second excited (B 2Σ⁺) states of the CN molecule lie close together and are distinct with no crossings, it is a reasonable first approximation to assume that gas collisional rates will be sufficiently high to maintain a Boltzmann distribution among the first three electronic states.

Trajectories

The systems analysis group provided four different design trajectories, V6.5.² The aerothermal environments were computed at seven to nine specific points along each trajectory. Freestream conditions were taken from an atmospheric model⁸ developed as part of the Titan mission study. Both axisymmetric and three-dimensional CFD

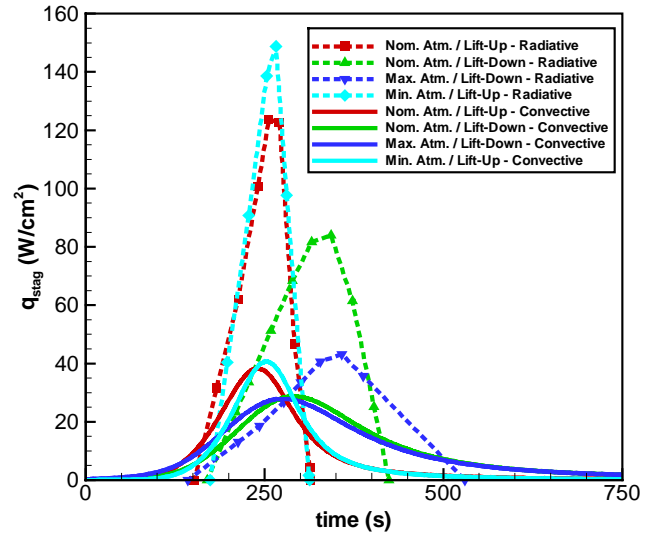


Figure 2. Predicted axisymmetric convective and radiative heating rates for four entry trajectories.

calculations were made. Radiative heating values were computed at selected points on the body including the stagnation point.

Results

For aerocapture missions to Titan with entry velocities below about 8.5 km/s, our results show that over 90% of the radiative heating is from the CN[v] band. The remaining radiation is from the CN red band (CN[r]), various N₂ molecular systems, and N atomic lines. Because the radiation from CN[v] is relatively short-wavelength, 340–430 nm, there is a concern that it will penetrate a low density TPS material and heat the material in-depth.⁸ The NEQAIR96 radiation calculations also showed that over the entire range of conditions of interest for Titan aerocapture the gas is optically thin; i.e. there is no absorption of the radiation by the gas in the flow field.

Axisymmetric Cases

Even though the aerocapture vehicle flow field is three-dimensional, initial calculations were made on the orbiter geometry assuming an axisymmetric flow field. In this way, a large number of trajectory points can be analyzed to provide radiative heating sensitivities to the design variables being studied by the systems analysts. Figure 2 shows the computed axisymmetric stagnation point convective and radiative heating rates for four entry trajectories corresponding to three different atmosphere models and two different flight path angles.

Since the exact composition of the Titan atmosphere is unknown, three different atmospheric models are considered: minimum, nominal, and maximum, where the nomenclature refers to the atmospheric density at a given altitude.¹⁰ It is further assumed that the different atmospheric models predict differing amounts of methane.

Table 2. Predicted axisymmetric peak radiative heating rates and radiative heat loads for four entry trajectories.

Trajectory	Peak Radiative Heating (W/cm ²)	Radiative Heat Load (J/cm ²)	Peak Convective Heating (W/cm ²)	Convective Heat Load (J/cm ²)
Nominal Atm. Lift-Up	124	10200	39	5500
Nominal Atm. Lift-Down	84	12090	29	7500
Maximum Atm. Lift-Down	43	8400	28	7700
Minimum Atm. Lift-Up	149	10580	41	5200
Minimum Atm. Lift-Down	100	12480	30	7600

The atmosphere-specific methane mass fractions are listed in Table 1. Lift-up indicates a steep entry angle requiring full lift to capture to the desired orbit. Lift-down indicates a shallow entry angle requiring full lift-down to capture to the desired orbit. The lift-up and lift-down trajectories thus define the boundaries of the entry corridor. The lift of the vehicle is controlled by roll modulation while at constant angle-of-attack.

The corresponding stagnation point heat loads and values of peak convective and radiative heating rates are given in Table 2. The convective heating rates are below 50 W/cm², however the radiative heating rates are up to 150 W/cm² for the minimum atmosphere, lift-up trajectory. Peak radiative heating occurs after peak convective heating. For the minimum atmosphere, lift-up trajectory peak convective heating is at $t=253$ s and peak radiative heating is at approximately $t=266$ s. The largest radiative heat load occurs on the minimum atmosphere, lift-down trajectory, and the largest total heat load is for the nominal atmosphere, lift-down trajectory.

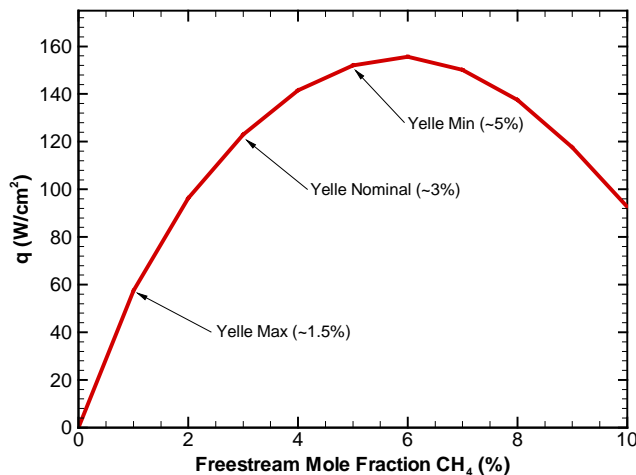


Figure 3. Effect of assumed freestream methane mole fraction on axisymmetric stagnation point radiative heating predictions for the $t = 253$ s point of the $v = 6.5$ km/s entry minimum atmosphere, lift-up trajectory.

Interestingly, the trajectory with the peak convective heating rate is the trajectory with the peak radiative heating rate, yet the trajectory with the maximum convective heat load is not the trajectory with the maximum radiative heat load. This surprising result is because the convective heating depends on the freestream enthalpy, while the radiative heating depends on temperature and CN concentration distributions through the entire shock-layer.

Although not shown, the predicted radiative heating rates are higher along the conical flank of the orbiter than at the stagnation point. The peak value is about 230 W/cm². The post-shock temperatures and CN mass fractions are similar in the two regions, and the heating is higher in the flank region simply because there is a larger volume of radiating gas.

The results shown here are from the DPLR CFD code and the NEQAIR96 radiation code using the Nelson *et al.* rate model. The results using the LAURA CFD code and the LORAN radiation code with the Nelson *et al.* rate model are within 5% of the DPLR/NEQAIR96 results. The radiative heating rates are from CN[v] only. The impact of including CN[r], molecular nitrogen bands, and atomic nitrogen lines is discussed below.

Because of chemical nonequilibrium in the shock layer, the amount of CN radiation depends strongly on the freestream methane concentration. At equilibrium, the shock-layer temperatures would be too high for CN to exist since the dissociation energy is only 7.65 eV. Figure 3 shows the calculated radiative heating rates as a function of assumed freestream methane concentration for the $t=253$ s point on the minimum atmosphere, lift-up trajectory. The freestream velocity is 5761 m/s and the density is $1.491e-4$ kg/m³. The amounts of methane corresponding to the three atmosphere models discussed above are indicated on the figure. The amount of methane predicted by the minimum atmosphere model happens to result in nearly the peak amount of radiative heating, indicating that designing the vehicle using the minimum atmosphere is the conservative choice for radiative heating.

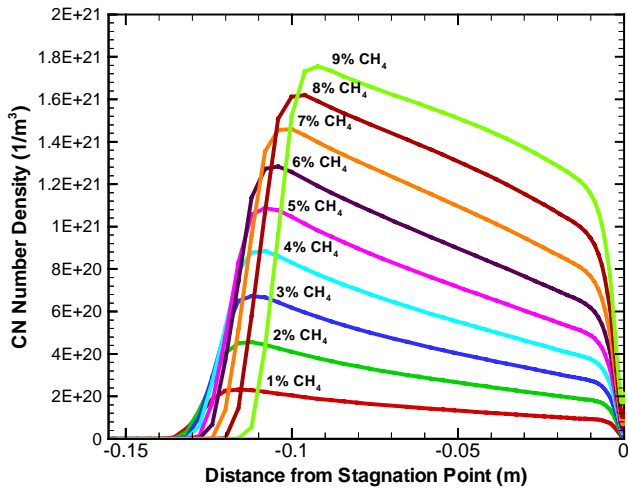


Figure 4. Effect of assumed freestream methane mole fraction on post-shock CN number density.

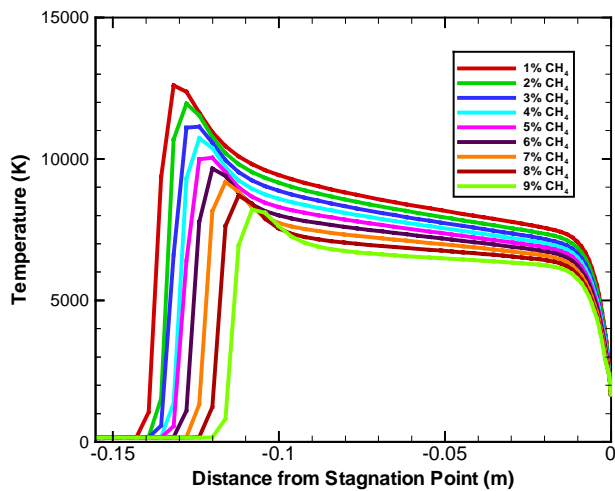


Figure 5. Effect of assumed freestream methane mole fraction on post-shock translational temperature.

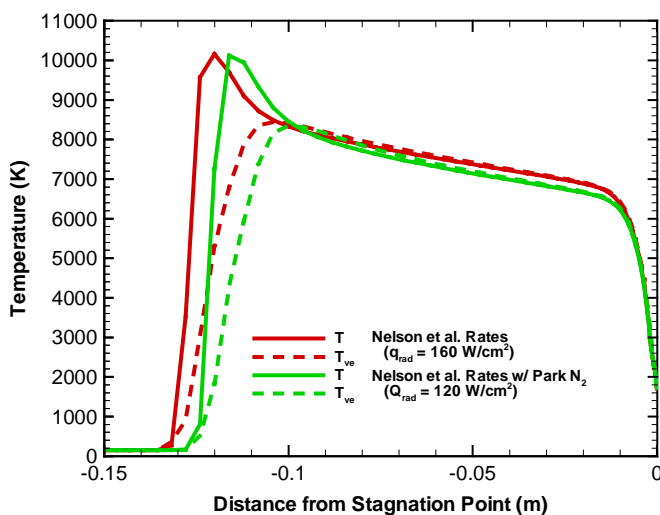


Figure 6. Computed axisymmetric stagnation line temperature profiles for two different reaction rate models.

The methane dissociates into its constituent atoms immediately downstream of the shock and quickly forms CN through various exchange reactions with the atmospheric nitrogen. More methane available means more CN is produced, as shown in Fig. 4. Therefore, at low methane concentrations the amount of radiation is proportional to the amount of methane in the atmosphere. As the amount of methane increases another effect becomes important, namely that the increased amount of methane dissociation decreases the post-shock temperature (Fig. 5). Even though there are more CN molecules, the effective temperature at which the CN radiates is lower. The net effect is to decrease the amount of CN radiation since the radiation intensity depends linearly on the number of radiating molecules but exponentially on the vibrational temperature. The vibrational temperature is in equilibrium with the translational temperature for about 70% of the shock layer.

There is some uncertainty in the thermophysical models for the Titan atmosphere. One important rate is the nitrogen dissociation rate. Figure 6 shows the effect of the value of the nitrogen dissociation rate on the shock stand-off distance and the resulting effect on the computed radiative heating rate. The two rates differ only by a constant factor of about two, and yet the predicted radiative heating rates differ by 25%. Additional data are needed to reduce this uncertainty.

Three-dimensional Cases

Three-dimensional calculations were also made for the lift-up, minimum atmosphere trajectory, which has the highest radiative heating rates. The distributed radiative heating on the forebody of the vehicle is shown in Fig. 7 for the $t=253$ s point of the lift-up minimum atmosphere trajectory with $\alpha=16^\circ$. Because the gas is optically thin, the radiative heating at the surface is given by the sum of

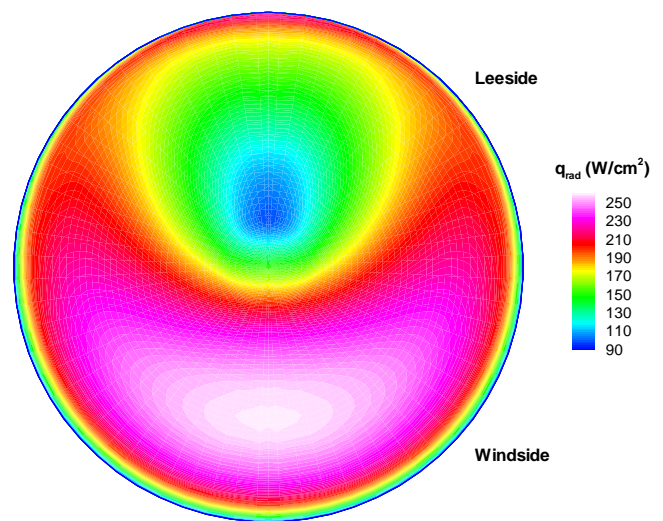


Figure 7. Computed three-dimensional forebody radiative heating rate for the $t = 253$ s point of the $v = 6.5$ km/s entry minimum atmosphere, lift-up trajectory.

Table 3. Three-dimensional stagnation point radiative heating rates for the $t = 253$ s point of the $v = 6.5$ km/s entry minimum atmosphere, lift-up trajectory.

CFD Code	# of Species	Kinetics	q_{rad} (CN Violet) (W/cm ²)	
			NEQAIR96	LORAN
DPLR	12	Nelson <i>et al.</i>	278	246
DPLR	12	Nelson <i>et al.</i> & Park N ₂	214	
DPLR	18	Nelson <i>et al.</i>	289	
LAURA	18	Nelson <i>et al.</i> & Park N ₂	202	175

the contributions of the individual radiating volumes of gas along a line-of-sight perpendicular to the surface. The peak radiative heating value is about 260 W/cm² is near the flow stagnation point where there is the largest volume of radiating gas. In the axisymmetric case, the largest volume of gas was in the conical flank region and the radiative heating rate is about 230 W/cm². The axisymmetric stagnation point heating rate of about 150 W/cm² is similar to the value at the center of the spherical nose for the three-dimensional calculation.

Figure 8 shows a comparison of the convective and radiative heating rates along the pitch-plane of the forebody for the $t=253$ s point of the lift-up minimum atmosphere trajectory. The flow stagnation point is at approximately $y=0.8$ m. The radiative heating is significantly larger than the convective heating over the entire forebody.

Table 3 gives the three-dimensional stagnation point heating rates for the $t=253$ s point of the lift-up minimum atmosphere trajectory for various combinations of CFD code, radiation code, and kinetic model. Using DPLR/NEQAIR96 the difference between the 12 species

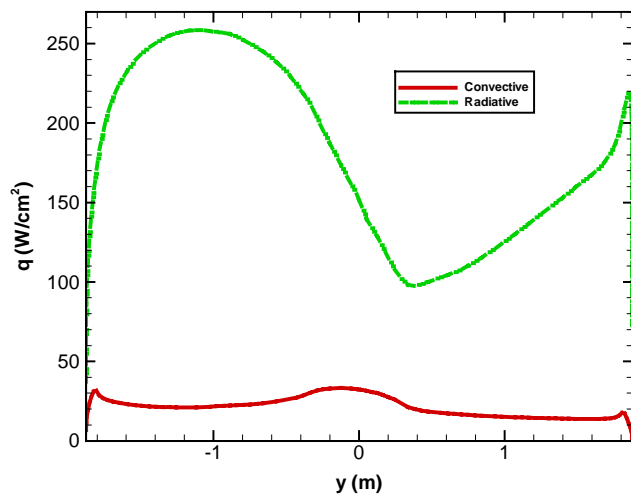


Figure 8. Computed pitch-plane forebody convective and radiative heating rate for the $t = 253$ s point of the minimum atmosphere, lift-up trajectory.

and 18 species radiative heat transfer is only 4%, indicating that ionization effects can be ignored for the systems studies. Using the DPLR flow field solution and the Nelson *et al.* model, LORAN predicts approximately 13% less radiation than NEQAIR96. Considering that LORAN uses a lumped band model as opposed to the detailed line-by-line method of NEQAIR96, there is reasonable agreement between the two codes. For this case, the use of the Park nitrogen dissociation rates reduces the radiative heating by almost 30%. The results from DPLR/NEQAIR96 and LAURA/LORAN are within 20% when the same kinetics model is used.

Figure 8 shows that the highest radiative heating occurs near the stagnation point of the vehicle. Since at higher entry velocities the post-shock temperature in the stagnation region will eventually become too high for CN to form, it was thought that increasing the entry velocity might reduce the amount of radiative heating. Figure 9 shows the computed radiative heating on the forebody for an entry velocity of 10 km/s at the peak heating point. The radiative heating levels in the stagnation region are indeed reduced from about 250 W/cm² to about 160 W/cm².

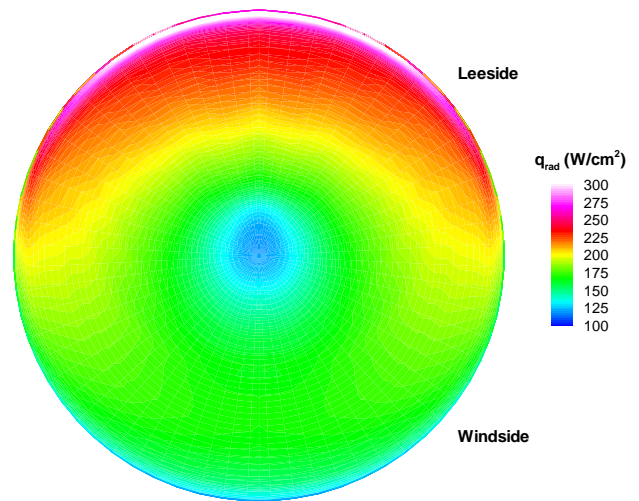


Figure 9. Computed three-dimensional forebody radiative heating rate for the peak convective heating point ($t = 152$ s) of the $v = 10$ km/s minimum atmosphere, lift-up trajectory

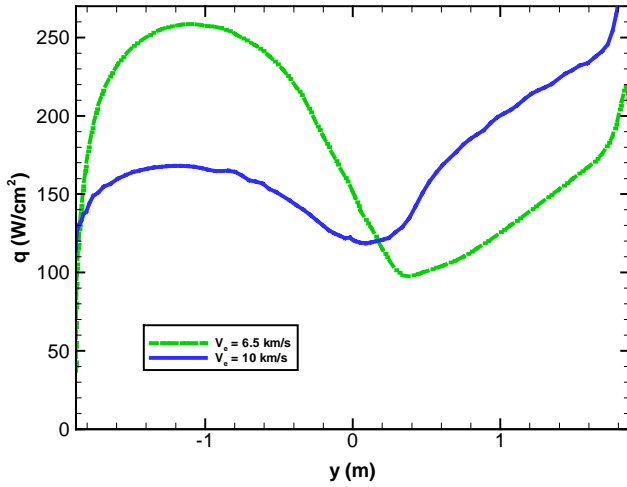


Figure 10. Computed pitch-plane forebody radiative heating rate for the $t = 253$ s point of the minimum atmosphere, lift-up trajectory and the $t = 152$ s point of the $v = 10$ km/s minimum atmosphere, lift-up trajectory.

However, for the 10 km/s entry the leeside of the vehicle has post-shock conditions similar to the 6.5 km/s stagnation point, and the radiative heating rate is as high as 220 W/cm^2 . A comparison of the radiative heating rates for the two entry velocities along the pitch-plane is shown in Fig. 10. In fact, the total integrated surface heating rate over the orbiter surface increases by 5%. Furthermore, this analysis does not include the contribution of the other radiators such as N_2 and N , which will contribute to the radiative heating at this entry velocity. Additionally, the convective heating will also be about 3.5 times higher compared to the 6.5 km/s entry trajectory. Therefore, increasing the entry velocity does not reduce the amount of heating to the vehicle.

Future Work

The prior analyses all assumed that the radiation calculation could be separated (decoupled) from the flow field calculation. This assumption is appropriate if the flow field is adiabatic and the energy lost from radiation is small. However, given the high levels of radiative heating predicted at relatively low entry velocities, it was decided to examine the impact of radiation-fluid coupling on the aerothermal heating predictions.

It is possible to estimate the amount of coupling between the radiation and fluid by evaluating the radiative loss parameter²⁹, Γ :

$$\Gamma = 2q_{\text{rad}} / \frac{1}{2} \rho_{\infty} V_{\infty}^3 \quad (1)$$

where q_{rad} is the stagnation point radiative heat flux, ρ_{∞} is the freestream density, and V_{∞} is the freestream velocity. When Γ becomes large ($> 1\%$), the flow is considered to be non-adiabatic and coupled to the radiation field. If a large amount of flow energy is converted to radiation, the shock-layer is cooled and there is a potentially significant impact on the fluid dynamics and chemical kinetics of the

flow. The net effect of the coupling would be to reduce the amount of radiative heating.

The radiative loss parameter for the reference Titan aerocapture vehicle was found to exceed 40% near peak radiative heating, indicating that the flow is non-adiabatic and coupled. By comparison, Γ is about 1% for the Fire-II flight experiment, and about 15% for Galileo. Further work investigating the effect of coupling is ongoing and will be presented in an upcoming paper. Preliminary results show that the coupled radiative heating rates are still 2-3 times greater than the convective heating rates.

Preliminary uncoupled afterbody calculations have also been made in order to assess the amount of radiative heating on the afterbody. The radiative heating analysis is still in progress and will be reported in an upcoming paper.

Finally, because the work presented in this paper identified that radiative heating is a significant design issue for Titan missions, experiments in the NASA Ames EAST shock tube are about to begin. The tests will provide data over a range of velocity and pressure conditions that will be used to either validate the existing chemical kinetic and radiation model or construct a new collisional-radiative model for application to the Titan atmosphere. The development of this new model will allow greater confidence in radiative heating predictions and quantified uncertainty estimates for Titan entry missions.

Summary and Concluding Remarks

Axisymmetric and three-dimensional thermochemical nonequilibrium Navier-Stokes calculations using DPLR and LAURA were made for a candidate Titan aerocapture orbiter along four design trajectories. The computed flow fields were used as inputs to the radiation solvers NEQAIR96 and LORAN. The combinations DPLR/NEQAIR96 and LAURA/LORAN gave similar answers.

Radiative heating was found to be a significant design issue for Titan aerocapture missions. The current results are conservative since they do not account for the radiative cooling effect, but this work has identified the key issues and sensitivities for the radiative heating environment.

The radiation results from the nonequilibrium formation of CN in the shock layer around the vehicle created in the nitrogen-methane atmosphere. In fact, if the flow field were in equilibrium, the radiative heating would be negligible compared to the convective heating. The radiation field was found to be optically thin for all conditions relevant to the aerocapture orbiter.

It was found that the peak radiative heating rate is five times greater than the peak convective heating rate, and the radiative heat load is twice as great as the convective heat loads for the minimum atmosphere, lift-up trajectory. Three-dimensional calculations showed that there was significant radiation on the entire forebody.

The predicted radiative heating was found to be sensitive to the choice of the nitrogen dissociation rate. A factor of two change in the rates produced a 25% change in the predicted heating rate. The factor of two difference in the rates is well within the experimental uncertainty of the data, indicating more accurate knowledge of the nitrogen dissociation rate is needed to reduce the uncertainty in the radiative heating predictions.

This work was performed as part of a preliminary system analysis study, and as expected it raised as many questions as it answered. Two of these questions, the effects of strongly coupled radiation and the impact of radiative heating on the afterbody, were mentioned in this paper. This work also identified the need for additional shock tube data in order to develop the collisional-radiative model necessary for a detailed mission design.

Acknowledgments

M. Wright and D. Prabhu were supported by NASA Ames Research Center, through contract NAS2-99092 to ELORET. N. Takashima was supported by NASA Langley Research Center, through contract to AMA, Inc. K. Sutton was supported by NASA Langley Research Center, through the National Institute of Aerospace, contract number NAS1-02117.

References

- ¹ Lockwood, M.K., "Titan Aerocapture Systems Analysis," AIAA Paper No. 2003-4799, Jul. 2003.
- ² Lockwood, M.K., Sutton, K., Prabhu, R., *et al.* "Entry Configurations and Performance Comparisons for the Mars Smart Lander," AIAA Paper No. 2002-4407, Aug. 2002.
- ³ Bailey, R., Hall, J., and Spilker, T., "Titan Aerocapture Mission and Spacecraft Design Review," AIAA Paper No. 2003-4800, Jul. 2003.
- ⁴ Baillion, M., Pallegoix, J.F., and Soler, J., "Huygens Probe Aerothermodynamics," AIAA Paper No. 97-2476, Jul. 1997.
- ⁵ Baillion, M., Taquin, G., and Soler, J., "Huygens Probe Radiative Environment," *Proceedings of the 19th International Symposium on Shock Waves, Shock Waves at Marseille II: Physico-Chemical Processes and Nonequilibrium Flow*, Springer-Verlag, 1995, p. 339-346.
- ⁶ Baillion, M. and Taquin, G., "Radiative Heat Flux: Theoretical and Experimental Predictions for Titan Entry Probe," *Capsule Aerothermodynamics*, AGARD Report No. 808, May 1997.
- ⁷ Nelson, H.F., Park, C., and Whiting, E.E., "Titan Atmospheric Composition by Hypervelocity Shock-Layer Analysis," *J. Thermophysics & Heat Transfer*, Vol. 5, No. 2, pp. 157-165, Apr.-Jun. 1991.
- ⁸ Park, C.S., "Studies of Radiative Emission from the Simulated Shock Layer of the Huygens Probe" *Ph.D. Thesis*, Stanford U., 1991.
- ⁹ Noca, M., Bailey, R., and Dyke, R., "Titan Explorer Mission Trades from the Perspective of Aerocapture," AIAA Paper No. 2003-4801, Jul. 2003.
- ¹⁰ Haw, R., "Approach Navigation for a Titan Aerocapture Orbiter," AIAA Paper No. 2003-4802, Jul. 2003.
- ¹¹ Justus, C. and Duvall, A., "Engineering-Level Model Atmospheres for Titan and Neptune," AIAA Paper No. 2003-4803, Jul. 2003.
- ¹² Masciarelli, J. and Queen, E., "Guidance Algorithms for Aerocapture at Titan," AIAA Paper No. 2003-4804, Jul. 2003.
- ¹³ Way, D., Powell, R., Masciarelli, J., and Starr, B., "Aerocapture Simulation and Performance for the Titan Explorer Mission," AIAA Paper No. 2003-4951, Jul. 2003.
- ¹⁴ Laub, B., "Thermal Protection Concepts and Issues for Aerocapture at Titan," AIAA Paper No. 2003-4954, Jul. 2003.
- ¹⁵ Hrinda, G., "Structural Design of the Titan Aerocapture Mission," AIAA Paper No. 2003-4955, Jul. 2003.
- ¹⁶ Dyke, R., "Planetary Probe Mass Estimation Tool Development and Its Application to Titan Aerocapture," AIAA Paper No. 2003-4956, Jul. 2003.
- ¹⁷ Takashima, N., Hollis, B., Olejniczak, J., Wright, M., and Sutton, K., "Preliminary Aerothermodynamics of Titan Aerocapture Aeroshell," AIAA Paper No. 2003-4952, Jul. 2003.
- ¹⁸ Olynick, D., Chen, Y.K., Tauber, M.E., "Aerothermodynamics of the Stardust Sample Return Capsule," *J. of Spacecraft and Rockets*, Vol. 36, No. 3, May-June 1999, p. 442-461.
- ¹⁹ Hartung, L.C., Mitcheltree, R.A., and Gnoffo, P.A., "Coupled Radiation Effects in Thermochemical Nonequilibrium Shock-Capturing Flowfield Calculations," *J. of Thermophysics and Heat Transfer*, Vol. 8, No. 2, Apr.-Jun. 1994, p. 244-250.
- ²⁰ Wright, M.J., G.V. Candler, and D. Bose, "Data-Parallel Line Relaxation Method for the Navier-Stokes Equations," *AIAA Journal*, Vol. 36, No. 9, pp. 1603-1609, Sep. 1998.
- ²¹ Gnoffo, P.A., "An Upwind-Biased Point-Implicit Relaxation Algorithm for Viscous, Compressible Perfect-Gas Flows," NASA TP-2953, Feb. 1990.
- ²² Park, C., *Nonequilibrium Hypersonic Aerothermodynamics*, Wiley & Sons, 1990.
- ²³ Whiting, E.E., Yen, L., Arnold, J.O., and Paterson, J.A., "NEQAIR96, Nonequilibrium and Equilibrium Radiative Transport and Spectra Program: User's Manual," NASA RP-1389, Dec. 1996.
- ²⁴ Hartung-Chambers, L., "Predicting Radiative Heat Transfer in Thermochemical Nonequilibrium Flow Fields, Theory and User's Manual for the LORAN code," NASA TM-4564, Sep. 1990.
- ²⁵ Reid, R.C., Jr., Rochelle, W.C., and Milhoan, J.D., "Radiative Heating to the Apollo Command Module: Engineering Predictions and Flight Measurements," NASA Tm X-58091, April 1972.

²⁶ Park, C., “Stagnation-Point Radiation for Apollo 4,” AIAA Paper No. 2001-3070, Jun. 2001.

²⁷ Laux, C.O., “Optical Diagnostics and Radiative Emission of Air Plasmas,” HTGL Report No. T-288, Stanford University, Aug. 1993.

²⁸ NIST, Washington, DC, “Atomic Spectra Database,” (http://physics.nist.gov/cgi-bin/AtData/main_asd), 2003.

²⁹ Anderson, J.D., Jr., *Hypersonic and High Temperature Gas Dynamics*, McGraw-Hill, 1989.

THERMAL PROTECTION CONCEPTS AND ISSUES FOR AEROCAPTURE AT TITAN

Bernard Laub
NASA Ames Research Center
Moffett Field, CA 94035

Abstract

A study to develop a conceptual design for an aerocapture mission at Titan was conducted by a NASA systems analysis team comprised of technical experts from several of the NASA centers. Multidisciplinary analyses demonstrated that aerocapture could be accomplished at Titan with a blunt 70° (half angle) rigid aeroshell entering the Titan atmosphere at an inertial entry velocity of ≈ 6.5 km/s. Aerothermal analyses demonstrated that the peak convective heating rates are relatively mild but the radiative heating rates, due to shock layer radiation from CN, are significantly larger and lie totally in the narrow UV band from 3500 to 4200 Å. TPS sizing analyses were conducted for a broad range of candidate TPS materials and, as expected, low density materials are the most attractive from a TPS mass standpoint. However, there is significant uncertainty associated with the interaction of low-density TPS materials with UV radiation (i.e., the potential for in-depth absorption). Consequently, the preliminary conceptual design adopted a higher mass TPS solution until the performance of low-density TPS materials can be investigated.

Introduction

Aerocapture is a flight maneuver executed by a spacecraft upon arrival at a planet in which atmospheric drag is used to decelerate the spacecraft into orbit during one atmospheric pass. This contrasts with the conventional alternatives of propulsive orbit insertion directly into the desired orbit or propulsive insertion into a large elliptical orbit followed by a long period of aerobraking to reduce the apoapsis altitude. The elements of aerocapture to establish a circular science orbit are illustrated in Figure 1.

Although aerocapture has never been attempted in any mission to date, it has long been recognized that this maneuver can greatly reduce the amount of propellant carried by the spacecraft, thereby enabling either larger payload mass fractions or smaller launch vehicles from

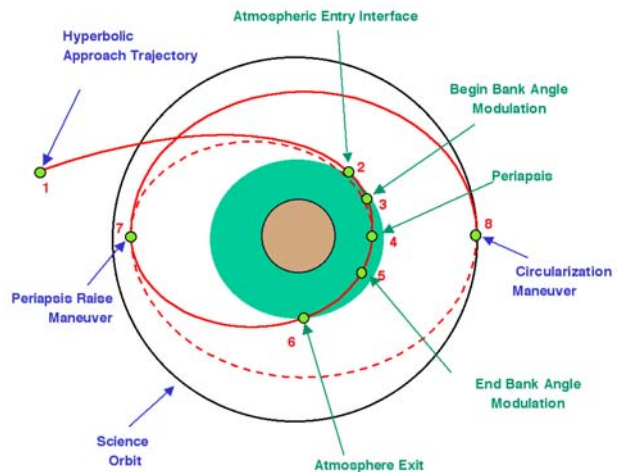


Fig. 1. The use of aerocapture to establish a circular science orbit about a planetary body¹

Earth. The propellant mass savings of aerocapture become especially significant for missions requiring large velocity changes for orbit insertion, either because a low circular orbit is required or because the approach velocity is high. In this context, several missions in NASA's Space Science Strategic Plan are either enabled or greatly enhanced by the propellant savings afforded by aerocapture technology. These missions include Mars Sample Return, Titan Explorer, Neptune Orbiter and Venus Surface Sample Return. Other severely mass-constrained planetary missions in the Discovery Program and any secondary payload programs would also clearly benefit from the availability of aerocapture technology.

Through detailed trade studies, the mission analysis team determined that aerocapture at Titan could be accomplished with a rigid aeroshell configured as a 70 degree half-angle blunt cone forebody with a lift-to-drag (L/D) ratio of 0.25 and a ballistic coefficient ($M/C_D A$) of ≈ 90 kg/m². The configuration is illustrated in Figure 2. Extensive mission analysis studies³ determined that a viable Titan mission, delivering an orbiter with a mass of 590 kg, could be launched around December 2010 and, with use of an Earth Gravity Assist (EGA) and Solar Electric Propulsion (SEP), flight time to Titan could be reduced to 5.9 years with an inertial entry velocity of ≈ 6.5 km/s at an altitude of 1000 km.

*Project Manager, Thermal Protection Materials
& Systems Branch, Associate Fellow, AIAA

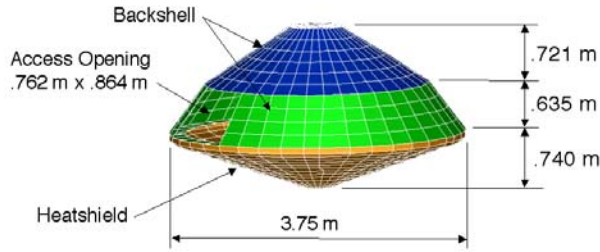


Fig. 2. Aeroshell configuration for Titan aerocapture²

Titan Atmosphere

The atmosphere around Titan is composed primarily of nitrogen with some argon and methane. There is some uncertainty about the concentrations of argon and methane, which leads to uncertainties in the density distribution through the atmosphere. Yelle⁴ developed engineering models for atmospheric density shown in Figure 3.

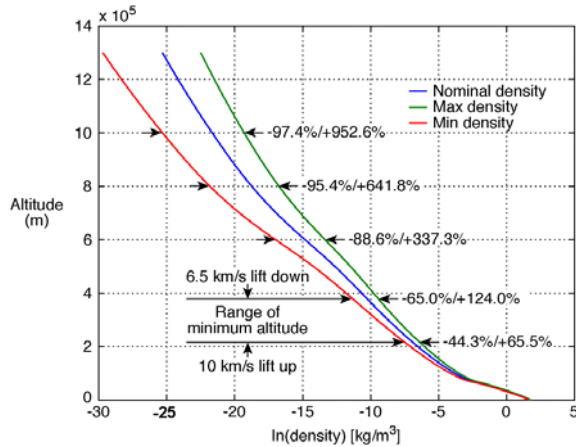


Fig. 3 Yelle engineering models for the density of the Titan atmosphere[†]

The variations in density are attributed to different models for methane concentration. The figure indicates the range of density variation of the minimum and maximum density models relative to the nominal model at selected altitudes. The figure also shows the minimum altitude range for candidate aerocapture trajectories. In these models the methane concentration is inversely proportional to mean density. As shown in Figure 4, the molar percent CH₄ is nearly constant over

[†]The term “lift down” employed in the figure is associated with the overshoot trajectory and indicates that the lift vector is in the trajectory plane and is always pointing downward during the entire aerocapture trajectory. Conversely, “lift up” is associated with the undershoot trajectory and indicates that the lift vector is always pointing up.

the altitude range where the energy of 6.5 km/s and 10 km/s aerocapture entries would be dissipated. Furthermore, the composition does not vary with density perturbations. The minimum density atmosphere’s methane content drops 50% between the surface and 6 km due to CH₄ condensation. However, CH₄ concentrations in the nominal and maximum density atmospheres are below the saturation level and thus remain constant to the surface.

Aerocapture Trajectories

Starr & Powell⁵ evaluated potential aerocapture trajectories at Titan with consideration of a range of ballistic coefficients and the uncertainties in atmospheric density. Guidance, navigation and control (GN&C) were limited to controlling the lift vector through bank angle modulation. The limiting cases are undershoot trajectories, where the lift vector is always pointing up, and overshoot trajectories, where the lift vector is always pointing down. Four trajectories,

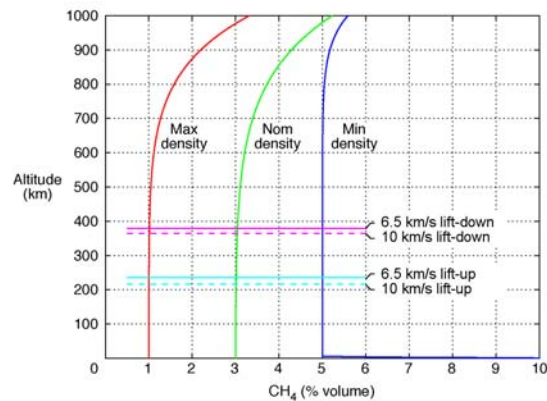


Fig 4. Models for methane concentration in Titan atmosphere

shown in Figure 5, were selected that bound the limits of peak heating rate and maximum total heat load

Convective and Radiative Heating

Convective and radiative heating rates[‡] at the stagnation point were calculated⁶ for the aeroshell configuration described previously and the four limiting trajectories presented in Figure 5. Stagnation point convective heating was calculated using the Fay-Riddell correlation⁷ and later confirmed with axisymmetric Computational Fluid Dynamics (CFD) solutions performed with the DPLR code.⁸ Non-equilibrium radiation calculations were performed with the NEQAIR code.⁹ As shown in Figure 6, the peak

[‡] Without consideration of the effects of ablation

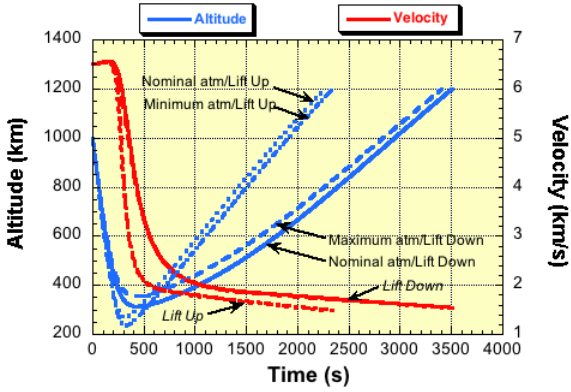


Fig. 5. Limiting aerocapture flight trajectories

stagnation point convective heating rates are less than 50 W/cm^2 and the undershoot trajectories (lift up) result in higher peak heating rates in comparison to the overshoot (lift down) trajectories. However, the peak stagnation point radiative heating rates are substantially larger. For the undershoot trajectories (lift up), peak stagnation point radiative heating rates are in the $120\text{-}150 \text{ W/cm}^2$ range. For the overshoot trajectories (lift down), peak stagnation point radiative heating rates are in the $45\text{-}85 \text{ W/cm}^2$ range.

It is worth noting that the convective heating is relatively insensitive to the concentration of methane assumed in the atmosphere. However, the radiative heating is very sensitive to methane concentration as all of the radiative heating is from CN formed in the shock layer from the interaction of dissociated methane with nitrogen. Consequently, the higher the methane concentration in the atmospheric model is (see Fig. 4), the higher are the radiative heating rates. While the non-equilibrium radiation environment was calculated with the most up-to-date chemistry and radiation models available, it should be recognized that there is significant uncertainty associated with these predictions. Shock tunnel tests at NASA Ames are planned within the next year to measure CN radiation at relevant conditions to enable validation and/or update of existing radiation heating models for Titan entry.

It must also be noted that the overshoot trajectories spend a longer time in the atmosphere than the undershoot trajectories. Consequently, the total convective heat load is typically larger for the overshoot trajectories in comparison to the undershoot trajectories. That is not necessarily true for the radiative heating due to the significant differences in the heat flux levels predicted for the range of trajectories and atmospheric models considered. This is demonstrated in Table 1, which summarizes the total convective and

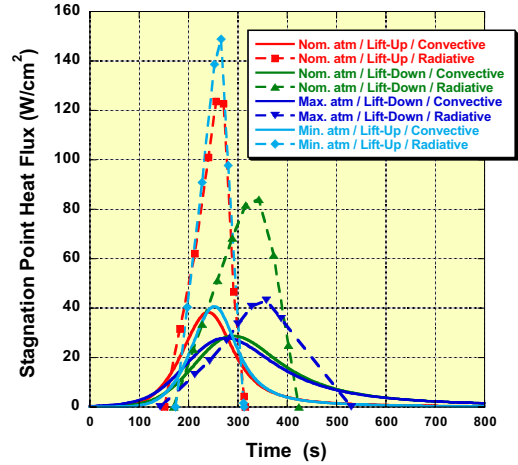


Fig. 6. Stag point heating for limiting trajectories

radiative heat loads for the four limiting trajectories considered. Note the similarities in the convective heat loads for the two overshoot and two undershoot trajectories. However, the radiative heat loads exhibit a dependence on methane concentration, that is, the minimum density atmosphere model has the highest methane concentration (see Fig. 4) while the maximum density atmosphere model has the lowest methane concentration. Table 1 suggests that total radiative heat load is dependent on time in the atmosphere (for example, compare the values for the lift up and lift down trajectories for the nominal density atmosphere) but a stronger dependence on the atmospheric model (e.g., compare the values for the maximum atmosphere on a lift up (undershoot) trajectory with the values for the minimum atmosphere on a lift down (overshoot) trajectory).

Table 1. Total heat loads for limiting aerocapture trajectories

Atmosphere model/ aerocapture trajectory	Convective heat load (J/cm^2)	Radiative heat load (J/cm^2)
Nominal atm/Lift up	5,500	10,021
Nominal atm/Lift down	7,500	12,090
Maximum atm/Lift down	7,700	8,393
Minimum atm/Lift up	5,200	15,769

Candidate TPS Materials

Given the range of convective and radiative heating described above, a range of thermal protection materials was identified as candidates for Titan aerocapture applications. The candidate TPS materials are summarized in Table 2.

Table 2. Candidate forebody TPS materials for Titan aerocapture[§]

Material	Shuttle tiles	SLA-561V	SRAM 14 (ARA)	SRAM 17 (ARA)
Density (g/cm³)	0.192-0.352	0.256	0.224	0.272
Description	Low-density, glass-based ceramic tile with glass-based coating.	Low-density cork silicone composite in Flexcore honeycomb.	Low-density cork silicone composite fabricated w/strip collar bonding technique.	Low-density cork silicone composite fabricated w/strip collar bonding technique.
Optical properties Solar absorptance Total hemis. emittance		≈ 0.50 ≈ 0.78	≈ 0.50 ≈ 0.78	≈ 0.50 ≈ 0.78
Performance limits	44 W/cm ² (certified)	Ablative. Char spall at p > 0.25 atm. No (little) recession at $\dot{q} < 100$ W/cm ² .	Ablative. No (little) recession at $\dot{q} < 100$ W/cm ² . Differential recession between composite ad interface strips may cause boundary layer transition. Other limits (if any) unknown.	Ablative. No (little) recession at $\dot{q} < 100$ W/cm ² . Differential recession between composite ad interface strips may cause boundary layer transition. Other limits (if any) unknown.
Uncertainties	May not be adequate for current estimates of peak convective heating. Will probably be transparent to CN radiation; a show-stopper	Low density, porous material. In-depth radiant transmission may be important.	Low density, porous material. In-depth radiant transmission may be important.	Low density, porous material. In-depth radiant transmission may be important.

The list encompasses well-characterized materials such as the Shuttle tiles, SLA-561V (used on Mars Viking, Mars Pathfinder, and Mars Exploration Rover) and fully dense carbon phenolic (used on the Pioneer Venus and Galileo entry probes). It also includes some more recent TPS materials such as PICA (used as the forebody TPS on Stardust), SIRCA (used as the Backshell Interface Plate on Mars Pathfinder and Mars Exploration Rover), and the Genesis Concept (employed by Lockheed-Martin as the forebody TPS on

the Genesis spacecraft). The list has some developmental materials such as low-density silicone and phenolic-based composites being developed by Applied Research Associates (ARA), TUFROC, a multilayer, non-ablative concept being developed by NASA Ames Research Center, and Acusil I, a moderate density silicone in honeycomb developed by ITT Aerotherm.

Most of these materials are organic resin-based composites that will pyrolyze when heated leaving a carbonaceous char at the surface. Table 2 provides the virgin density of these materials, a general description of their composition and construction, important optical properties (where known or can be estimated), some comments on their performance limits (where known or can be estimated), and some comments on performance uncertainties as perceived by the author.

[§] The list of candidate materials was assembled based on predictions of convective heating for Titan aerocapture but prior to the availability of predicted radiative heating. The magnitude of the predicted peak radiative heating rates would eliminate some of the candidate materials from serious consideration.

Table 2. Candidate forebody TPS materials for Titan aerocapture (continued)

Material	SIRCA	PICA	TUFROC	SRAM 20 (ARA)
Density (g/cm³)	0.192-0.352	0.256	Varies with layer sizing	0.32
Description	Low-density ceramic tile impregnated with silicone resin.	Low-density carbon fiberform partially filled with phenolic resin.	Multilayer composite: carbon fiberform/AETB tile with high emissivity, high temperature surface treatment	Low-density cork silicone composite fabricated w/strip collar bonding technique.
Optical properties Solar absorptance Total hemis. emittance	≈ 0.28 ≈ 0.92	≈ 0.90 ≈ 0.80	≈ 0.90 ≈ 0.90	≈ 0.50 ≈ 0.78
Performance limits	Ablative. No (little) recession at $q < 100 \text{ W/cm}^2$. Rapid recession (melting) at higher heat fluxes. Fabricated as tiles.	Ablative. No recession in non-oxidizing atmosphere at $q < 1000 \text{ W/cm}^2$. Excellent low density ablator, but not best insulator.	Non-ablative. May be usable to $q \sim 300 \text{ W/cm}^2$. Has to be fabricated as tiles.	Ablative. No (little) recession at $q < 100 \text{ W/cm}^2$. Differential recession between composite ad interface strips may cause boundary layer transition. Other limits (if any) unknown.
Uncertainties	Low-density, glass-based material. In-depth radiant transmission may be important.	Low density, porous material. In-depth radiant transmission may be important.	Heat flux limit currently uncertain. Spectral emittance data on coating shows very high emittance at CN violet wavelengths. Will absorb (not transmit) UV radiation.	Low density, porous material. In-depth radiant transmission may be important.

From the TPS standpoint, total heat loads for aerocapture are typically much larger than for direct entry. Consequently, the lowest mass TPS solutions will be good insulators, a characteristic that is usually associated with low-density materials. However insulation performance must be balanced with ablation performance, for example, too much surface recession can lead to alterations in shape that can affect aerodynamic performance. High-density materials are usually employed to minimize surface recession. However, the peak heating rates predicted for Titan aerocapture are within the capabilities of several of the low-density candidate materials, that is, they can provide good insulation performance with minimal

surface recession. Consequently, they are considered the most attractive candidate materials from the standpoint of minimizing TPS mass.

TPS Mass Estimates

To provide an estimate of TPS mass, preliminary forebody TPS sizing analyses were done for the four limiting aerocapture trajectories shown in Figure 5 for many (but not all) of the candidate materials listed in Table 2. The analyses were limited to the stagnation point heating shown in Figure 6 and, for purposes of estimating TPS mass, it was assumed that the nominal (without margin) stagnation point TPS thickness is

Table 2. Candidate forebody TPS materials for Titan aerocapture (concluded)

Material	PhenCarb-20 (ARA)	Acusil I	Carbon phenolic	Genesis concept
Density (g/cm³)	0.32	0.48	1.45	Varies with layer sizing
Description	Low-moderate density phenolic composite fabricated w/strip collar bonding technique.	Moderate density filled silicone in Flexcore honeycomb.	Fully dense tape-wrapped or chopped molded heritage material.	Carbon-carbon facesheet over carbon fiberform insulator.
Optical properties Solar absorptance Total hemis. emittance	≈ 0.50 ≈ 0.78	0.54 0.95	≈ 0.90 ≈ 0.90	≈ 0.90 ≈ 0.90
Performance limits	Ablative. No recession in non-oxidizing environment. Differential recession between composite and interface strips may cause boundary layer transition. Other limits (if any) unknown.	Ablative. No recession (in air) at $q < 100 \text{ W/cm}^2$. Will recede in air at higher heat fluxes (assumed by oxidation).	Ablative. No recession expected for Titan aerocapture environment.	Ablative. No recession expected for Titan aerocapture environment.
Uncertainties	Higher density and higher char yield of phenolics may mitigate in-depth radiant absorption at the penalty of higher thermal conductivity.	Higher density and good char yield may mitigate in-depth radiant absorption. Not as good an insulator as lower density materials. Difficult to fabricate in thicknesses > 2 inches.	High density and high char yield will mitigate in-depth radiant absorption. Not a very good insulator. Without recession, will be very heavy (a poor choice for this application).	High-density carbon facesheet will mitigate in-depth radiant absorption. Carbon fiberform not the best insulator, but better than fully dense carbon phenolic.

applied uniformly on the forebody. It was also assumed that the TPS is adhesively bonded to a rigid substructure consisting of 0.0376 mm thick graphite polyimide facesheets (front and back) on a 31.75 mm thick aluminum honeycomb. The density for the honeycomb and graphite polyimide facesheets is 0.069 g/cm³ and 1.0 g/cm³, respectively. It was assumed that all materials are at a uniform temperature of -74.8°C at atmospheric interface. It was also assumed that all candidate materials absorb CN radiation at the surface and perform as thermochemical ablators, that is, no spall or melt runoff. Analyses were performed to determine the thickness required for each candidate material to limit the maximum bondline temperature to 250°C. It should be noted that different individuals did the analyses for different materials, but all used comparable analysis tools that address the fundamental

physical and chemical mechanisms associated with the thermal/ablation performance of these materials in the Titan atmosphere. Some of the materials models are very mature and have been validated with extensive laboratory and arc jet test data. In contrast, some of the other materials are relatively new and their models are based on limited laboratory and arc jet test data.

The results of the analyses demonstrated that, for the four trajectories considered, the TPS thickness is significantly larger for the overshoot trajectories (lift down) than for the undershoot trajectories (lift up). This was the case for all of the candidate materials considered. Furthermore, maximum bondline temperature is attained during heat soak, that is, after the end of aerodynamic heating.

Table 3. Preliminary forebody TPS sizing for Titan aerocapture

Candidate TPS Material	Maximum atmosphere - Lift Down Convective Heat Load = 7,700 J/cm ² Radiative Heat Load = 8,393 J/cm ²		Nominal atmosphere – Lift Down Convective Heat Load = 7,500 J/cm ² Radiative Heat Load = 12,090 J/cm ²	
	Thickness (cm)	Areal weight (g/cm ²)	Thickness (cm)	Areal weight (g/cm ²)
SLA-561V	2.44	0.626	2.43	0.622
SRAM 14	1.57	0.353	1.55	0.348
SRAM 17	1.93	0.526	1.93	0.526
SRAM 20	2.08	0.667	2.08	0.667
PhenCarb-20	2.29	0.696	2.34	0.711
TUFROC	4.88	1.117	5.13	1.181
Genesis	---	---	5.51	1.298
PICA	5.94	1.591	5.82	1.557
Carbon phenolic	8.70	13.084	8.76	13.167

The results of the TPS sizing analyses are summarized in Table 3 which only shows the thickness and areal weight requirements for the overshoot trajectories because, as stated previously, they exceeded the requirements for the undershoot trajectories.

Table 3 illustrates that the thickness and areal weight for any candidate TPS material is similar for the two overshoot trajectories despite the significant difference in the total radiative heat load. Examination of Figure 6 will illustrate that the predicted radiative heating for the nominal atmosphere model results in higher peak heat fluxes in comparison to the maximum atmosphere model, but for a shorter period of time. As it was assumed that all of these materials are surface absorbers, the higher heat fluxes result in higher surface temperatures. As surface re-radiation is the predominant energy accommodation mechanism for all of these candidate materials, they are all more “efficient” at higher heat fluxes as long as they do not experience significant surface recession.

Table 3 also illustrates that, in general, TPS areal weight increases with material density. This is clearly evident by comparing the areal weight requirements between the candidates in the SRAM family where the composition and construction are similar but the virgin densities are different. Also, note that the areal weight of PhenCarb 20 is similar to SRAM 20. However, that is coincidental; the materials have the same virgin density but different compositions, as SRAM uses a silicone resin binder and PhenCarb, a phenolic resin binder. The thermal conductivity of the PhenCarb family should be higher than that of the SRAM family, but that is compensated for by the smaller surface

recession experienced by the PhenCarb in comparison to the SRAM.

This tradeoff is clearly demonstrated when one compares the areal weight of PICA with SRAM17 where the virgin densities are similar. PICA, composed primarily of carbon, has a much higher thermal conductivity than SRAM17 and this is reflected in the areal weights, with the areal weight of PICA approximately three times that of SRAM17. The fully dense carbon phenolic result clearly makes the point because, from the standpoint of composition, it is similar to PICA. Yet the almost six-fold increase in virgin density is accompanied by a significant increase in thermal conductivity, which is reflected in the areal weight requirements. The key point is that the materials that are primarily carbonaceous are excellent “ablaters” but not good insulators. They are best used in environments with very high heating rates because they are most efficient when they ablate. The heating rates for Titan aerocapture trajectories are not sufficiently severe to allow these materials to perform efficiently. The low density, low thermal conductivity materials are better choices.

The Genesis and TUFROC candidates need to be viewed differently. The Genesis TPS employs a thin carbon-carbon facesheet over a carbon fiberform insulator. The carbon-carbon is robust and will not experience any recession for the range of Titan aerocapture heating environments. Although the carbon fiberform is not the best insulator, it is one of the few materials that can be employed in contact with the carbon-carbon because such a material must be stable at the surface temperatures that the C-C facesheet will

attain. The TUFROC concept is different in some aspects. It is comprised of a carbon fiberform insulator bonded to an AETB low-density ceramic insulator. The two-layer composite has a high temperature, high emissivity, low catalytic efficiency surface treatment. The assembly is intended to be non-ablative, but the upper limit of the surface treatment is yet to be demonstrated. The sizing of TUFROC, a two-step process as defined by the carbon fiberform thickness, is governed by the upper temperature limit of the AETB ceramic. Once that is defined, the AETB thickness is sized to limit bondline temperature.

As a consequence of the carbon fiberform minimum thickness requirement for TUFROC, the areal weight of this concept is larger than for most of the other candidate materials. Existing data suggest that the coating can handle the range of heat fluxes anticipated for the range of Titan aerocapture trajectories considered. Furthermore, existing optical properties data on the coating indicate that it will absorb UV radiation. The results for the Genesis concept indicate that its areal weight will be slightly larger than that for TUFROC, primarily because the carbon fiberform is not as good an insulator as a composite of carbon fiberform over a low-density AETB ceramic.

TPS Performance Uncertainties

Of some concern is the interaction of CN radiation with low density, porous TPS materials. Figure 7 illustrates the spectral distribution of the predicted^j CN radiation where it is seen that almost all the radiation lies in a relatively narrow band in the ultraviolet (UV) with the peak at $\approx 3800\text{\AA}$ ($0.38\mu\text{m}$). Studies conducted during the 1980s, evaluated the performance of dozens of ablative materials exposed to high-energy lasers. The types of materials evaluated spanned the range from low-density organic resin composites to fully dense carbon-carbon composites. Materials were tested with both continuous wave (CW) and repetitively pulsed (RP) lasers at wavelengths from the visible ($0.53\mu\text{m}$) to the infrared ($10.6\mu\text{m}$). While material performance was strongly dependent on the type of material and the irradiance (heat flux) it was exposed to, the data also suggested a general trend where material performance degraded at the shorter wavelengths. Further studies demonstrated that the materials did not become semi-transparent at the shorter wavelengths, but rather the absorption length became larger as the wavelength got shorter. It should be noted that none of the materials that are TPS candidates for Titan aerocapture were evaluated under these laser studies.

^j Nonequilibrium NEQAIR calculations

Based on the trend observed in the laser studies, the performance of the most attractive TPS candidates for Titan aerocapture is, at best, uncertain. If these low-density materials have significant absorption lengths to radiation at UV wavelengths, there is the potential that the materials may spall (blow off the surface layer due to in-depth pyrolysis). It can be argued that when these materials pyrolyze they will form a carbonaceous

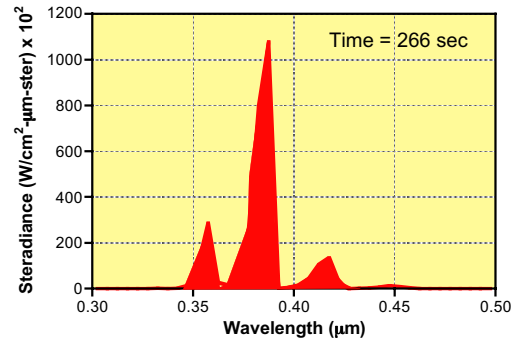


Fig. 7 Spectral distribution of CN radiation

surface char with different absorption characteristics than the virgin material; the char will be a surface absorber and/or scatter the incident radiation. That is certainly possible and, in fact, anticipated if the char has sufficient time to form and stays attached. That is the major issue because it is possible that in-depth absorption leading to periodic spall would continually remove whatever surface char is in the process of being formed.

It is also possible that pyrolysis gases injected into the boundary layer could scatter the incoming CN radiation or absorb it and re-radiate at longer wavelengths. Again, that is possible but it is very difficult to demonstrate, even analytically, due to uncertainties in the composition of the pyrolysis products and their absorption characteristics.

The only way to evaluate the performance of these materials when exposed to UV radiation is through experiments. Unfortunately, a good experimental simulation is not simple. The ideal experiment would expose these candidate materials to a radiation source at the wavelengths of interest and at relevant heat fluxes. All of the high-energy CW lasers operate in the infrared. There are excimer lasers that operate at the wavelengths of interest, but they are pulsed lasers that produce extremely high heat fluxes over a very short duration. There are some CW Argon-ion and Krypton lasers that produce radiation in the range of interest, but they are very low power.

It has been suggested that the materials be tested with a solar source. Examination of the black body spectral distribution of solar radiation illustrates that only a small fraction (<15%) of the energy lies in the UV band of interest with a significant fraction in the IR. Furthermore, the atmosphere filters out much of the UV radiation. Testing with a solar source would expose the materials to broadband radiation and the potential for in-depth absorption of UV radiation could be masked by char formation promoted by surface absorption of IR radiation.

Tests could also be done with a high power xenon lamp that simulates a 5800 K source. Examination of the black body spectral distribution from such a source illustrates that only a small fraction ($\approx 15\%$) lies in the band of interest. It is possible to filter the radiation from this lamp to allow only the UV radiation to reach the material sample, but at the sacrifice of much of the power.

The best option is the use of a commercially available Mercury-Xenon Lamp, which will allow the testing of 2.54 cm (1 inch) square specimens at the required energy flux levels. Mercury-Xenon short arc lamps are dosed with an exact amount of mercury and xenon gas. Due to the high operating pressure of mercury-xenon, the spectrum shows only traces from the broad, visible and infrared dominated xenon gas spectrum. The four main mercury lines dominate the spectrum, as shown in Figure 8. The first three lines provide an excellent simulation of the predicted CN radiation at Titan. The visible lines between 500 and 600 nm are easily filtered out, and can be included or not as desired. A simple cold filter can eliminate the visible and infrared lines.

A more fundamental approach would measure the relevant optical properties of the virgin (and char) candidate materials using a spectrophotometer and an integrating sphere. Such data would be very valuable but would require making (some) measurements on very thin samples. Slicing low-density materials into thin sections (≈ 1 mm) would be a challenge.

From the above discussion it should be apparent that validating adequate performance of the best TPS candidates for Titan aerocapture would not be simple due to experimental limitations. Some combination of the aforementioned tests must be done and the resultant data will need to be carefully evaluated before one can design a TPS for Titan aerocapture with confidence. If adequate performance of the most attractive candidate materials when exposed to CN radiation cannot be

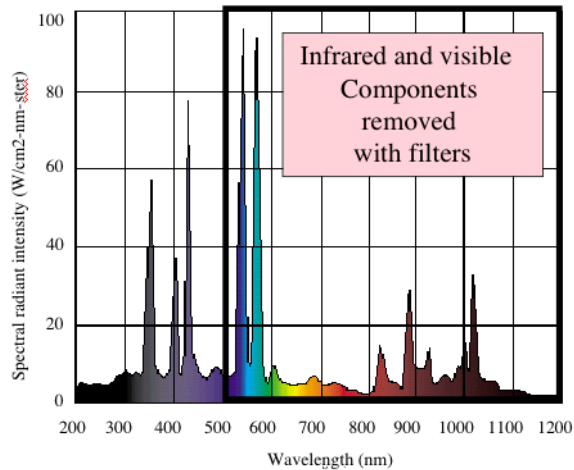


Fig. 8. Spectral output of Mercury-Xenon lamp shows good simulation of CN lines.

experimentally demonstrated, any TPS design employing these materials will have to include significant “margin” to mitigate the risk.

Preliminary TPS Conceptual Design

The charter of the NASA aerocapture systems analysis team is focused on identifying and prioritizing the most critical technology gaps to enable aerocapture to be utilized for Solar System Exploration (SSE) missions. The benefits of employing aerocapture for Titan Explorer can only be quantified through comparison with a design that employs chemical propulsion for orbit insertion. To enable that comparison, the aerocapture systems analysis team developed a preliminary conceptual design of an aerocapture “system” for Titan Explorer so that comparisons could be made of launch mass, payload mass, and system complexity. An estimate of TPS mass was required to support this conceptual design. For this purpose the systems analysis team preliminarily selected TUFROC for the forebody TPS. As seen in Table 3, the nominal areal weight of TUFROC (only sized at the stagnation point) is ≈ 1.18 g/cm² for the worst-case trajectory (nominal atmosphere, lift down). The surface area of the forebody aeroshell is ≈ 12.59 m², which results in a nominal forebody TPS mass of ≈ 149 kg. The TPS sizing studies identified several candidate materials that, potentially, would provide lower TPS mass solutions, in some cases by factors of 2-3. However, all of these attractive candidate materials need to be experimentally evaluated to ensure that potential in-depth radiant absorption will not significantly degrade material performance.

Summary

A NASA systems analysis team developed a rigid aeroshell conceptual design for orbit insertion around Titan using aerocapture. Candidate TPS materials were identified and preliminary TPS sizing studies were conducted using predicted stagnation point convective and radiative heating for limiting aerocapture trajectories. The results of these analyses demonstrated that existing low-density organic resin composites provide low TPS mass solutions for this mission. However, the potential for in-depth absorption of CN radiation can degrade the performance of these materials. The interaction of these materials with UV radiation needs to be experimentally evaluated, but the options for conducting the appropriate ground test experiments simulating UV radiation at relevant heat fluxes are limited. Therefore, the preliminary conceptual design incorporated a TPS concept (TUFROC) that has been demonstrated to absorb UV radiation at the surface, but requires a significantly larger TPS mass.

Acknowledgements

The author wishes to express his appreciation to Dr. Y. -K. Chen (NASA Ames Research Center) who conducted the TPS sizing analyses for SLA-561V, PICA, and TUFROC, to Dr. Gary A. Allen (ELORET/NASA Ames Research Center) who conducted the TPS sizing analyses for fully-dense carbon phenolic, to Mr. William M. Congdon (Applied Research Associates) who conducted the TPS sizing analyses for SRAM14, SRAM17, SRAM20 and PhenCarb20, and to Mr. John A. Dec (NASA Langley Research Center) who conducted the TPS sizing analyses for the Genesis TPS concept. The author also wishes to acknowledge Dr. Donald M. Curry (NASA Johnson Space Center) and Dr. F. Neil Cheatwood (NASA Langley Research Center) who were consulted in assembling the list of candidate TPS materials for Titan aerocapture. The author also wishes to acknowledge the special contributions of Dr. Susan M. White (NASA Ames Research Center) who researched available devices to simulate the Titan radiation environment and identified the Mercury-Xenon lamp.

References

1. Lockwood, M.K. "Titan Aerocapture Systems Analysis Overview," NASA Langley Research Center, Aerocapture Systems Analysis Review, Jet Propulsion Laboratory, Pasadena, California. August 29-30, 2002.
2. Hrinda, G.A., "Aeroshell Structure," NASA Langley Research Center, Aerocapture Systems Analysis Review, Jet Propulsion Laboratory, Pasadena, California. August 29-30, 2002.
3. Noca, M., "Mission Analysis," Jet Propulsion Laboratory, Aerocapture Systems Analysis Review, Jet Propulsion Laboratory, Pasadena, California. August 29-30, 2002.
4. Yelle et al.: "Engineering Models for Titan's Atmosphere", in *Huygens Science, Payload and Mission*, ESA SP-1177, 1997.
5. Starr, B.R. and Powell, R., "Titan/Neptune Aerocapture System Study," NASA Langley Research Center, Hampton, VA, March 29, 2002.
6. Olejniczak, J. and Allen, G.A., Jr., "Radiative Heating/TPS Sizing Results," NASA Ames Research Center, May 2, 2002.
7. Fay, J.A. and F.R. Riddell, "Theory of Stagnation Point Heat Transfer in Dissociated Air," *J. Aero. Sci.*, 25, (2), 73-85, 1958.
8. Wright, M.J., G.V. Candler, and D. Bose, "Data-Parallel Line Relaxation Method for the Navier-Stokes Equations," *AIAA Journal*, Vol. 36, No. 9, pp. 1603-1609, Sep. 1998.
9. Whiting, E.E., Park, C., Liu, Y., Arnold, J.O., and Paterson, J.A., "NEQAIR96, Nonequilibrium and Equilibrium Radiative Transport and Spectra Program: User's Manual," NASA RP-1389, Dec. 1996.

THE IMPACT OF FLOWFIELD-RADIATION COUPLING ON AEROHEATING FOR TITAN AEROCAPTURE

Michael J. Wright[†]

NASA Ames Research Center, Moffett Field, CA 94035

Deepak Bose*

ELORET Corporation, Sunnyvale, CA 94087

Joe Olejniczak[†]

NASA Ames Research Center

ABSTRACT

A methodology is developed that enables fully coupled computation of 3D flow fields including radiation assuming an optically thin shock layer. The method can easily be incorporated into existing CFD codes and does not appreciably increase the cost or the robustness of the resulting simulations. In addition, a view-factor based approach is demonstrated for the computation of radiative heating in optically thin gases that provides a significant accuracy improvement over the standard tangent-slab approach. These techniques are applied to the Titan aerocapture aeroheating problem, which is dominated by strong radiative heating. For this application, neglecting the non-adiabatic effects caused by radiation coupling results in an overprediction of radiative heating levels by about a factor of two. Radiative coupling effects also significantly lower predicted convective heating by reducing boundary layer edge temperatures. In addition, it is shown that the tangent slab approximation overpredicts radiative heating levels by a minimum of 20% in the stagnation region for this application. Over an entire design trajectory, correctly modeling radiative heat transfer results in a more than a factor of two reduction in total stagnation region heat load over an uncoupled analysis.

INTRODUCTION

The NASA In-Space Propulsion (ISP) program is currently investigating aerocapture as a means of enabling or improving the cost-efficiency of several planetary missions. During an aerocapture maneuver, the actively controlled vehicle decelerates into the target orbit by dissipating energy aerodynamically during a single pass through the atmosphere. In this manner, the large mass of a propulsive deceleration system is replaced by the potentially much smaller mass of an aeroshell to protect the vehicle from aerodynamic heating during the maneuver. One candidate destination for which aerocapture looks attractive is Saturn's largest moon Titan. A recent systems analysis study¹ was performed to examine the benefits of aerocapture at Titan. The resulting baseline Titan aerocapture vehicle would be proposed as a follow-on to the joint NASA/ESA Cassini mission, which is scheduled to arrive at Saturn in 2004 and release the Huygens Titan entry probe.

As a part of the systems study,¹ a preliminary aerothermal analysis of the baseline Titan aerocapture vehicle was performed, assuming an entry velocity of 6.5 km/s.²⁻³ These calculations showed that the predicted maximum stagnation point convective heating was moderate (40-45 W/cm² peak). However, this work also concluded that the heating due to

shock layer radiation will be much larger than the convective component. The Titan atmosphere at aerocapture altitudes consists primarily of nitrogen, with small amounts of argon and methane. The atmospheric methane (up to 3% by volume) dissociates in the nonequilibrium shock layer, leading to the formation of cyanogen, or CN. The CN molecule is a strong radiator in both the violet [B-X] and red [A-X] bands, and is responsible for more than 99% of the total predicted shock layer radiation at low entry velocities (below about 8 km/s). Preliminary analyses³ indicated that the radiative heating from CN at the stagnation point could be as high as 300 W/cm², or seven times as large as the convective component. These results were qualitatively consistent with previous analysis of the ballistic Huygens probe entry.⁴⁻⁶ The previous systems analysis study also looked at the effects of chemical kinetics, entry state variations, and uncertainties in atmospheric composition on the computed convective and radiative heating levels.

The high radiative heat flux predicted during this analysis was the primary driver in determining thermal protection system (TPS) material selection and sizing.⁷ However, the uncertainties in the predicted radiative heating levels were quite large, predominantly due to several simplifying assumptions that were made during the systems-level analysis. As a result of this study,¹⁻³ it was determined that

[†] Aerospace Engineer, Reacting Flow Environments Branch, Senior Member AIAA.

* Senior Research Scientist, Reacting Flow Environments Branch.

reducing the uncertainties in the prediction of radiative aeroheating was of primary importance for the design of any future Titan entry mission.

The prior analyses made three major assumptions:

1. The chemical-kinetic mechanism employed accurately predicted the amount of CN formed in the shock layer, and the electronic states of the resulting CN molecules were in a Boltzmann distribution at the mixture vibrational-electronic temperature.
2. The shock layer radiation was not coupled to the fluid dynamics and chemical kinetics in the flowfield (i.e. the flow was adiabatic). Therefore, shock layer radiation predictions could be performed as a post-processing step after the CFD was completed.
3. The distributed radiative heating on the vehicle could be adequately estimated via a tangent slab approximation with an appropriate scale factor to account for body curvature effects.

This paper presents a methodology for the computation of fully coupled convective and radiative heating for radiation in an optically thin gas, which will effectively eliminate the last two of these assumptions. This methodology is then applied to the Titan aerocapture problem. Results are shown only for the forebody of the Titan aerocapture vehicle. Afterbody results will be presented in a companion paper.⁸ An assessment of the validity of the first assumption is still under investigation.

TITAN AEROCAPTURE REFERENCE CONCEPT

The baseline configuration from the systems analysis study is a 3.75 m diameter 70-degree sphere cone, shown in Fig. 1.¹ The vehicle will fly at a constant angle of attack of 16 degrees to achieve a lift-to-drag ratio of 0.25, which was found to be sufficient to enable robust guidance and control during the aerocapture maneuver. The ballistic coefficient was set at 90 kg/m². This vehicle would enter the atmosphere of Titan at a nominal relative velocity of 6.5 km/s, although alternate trajectories with entry velocities up to 10 km/s were also considered. Aeroheating analysis and mission design were conducted using a series of lift-up and lift-down design trajectories.⁹ Trajectories were generated using three atmospheric density profiles,¹⁰ which bounded the uncertainty in atmospheric density as a function of altitude. The atmosphere was assumed to consist primarily of nitrogen, with small amounts of methane and argon. The relative abundance of these trace species as a function of altitude was determined using an engineering level atmospheric model (TitanGRAM),¹⁰ which predicted methane mole fractions between 1-5% at aerocapture altitudes.

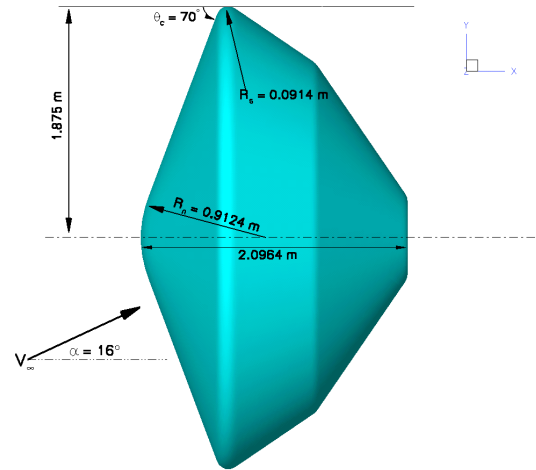


Fig. 1. Aeroshell configuration for the Titan aerocapture concept.

PHYSICAL AND NUMERICAL MODELS

The flowfield computations are performed using the computational fluid dynamics (CFD) code DPLR.¹¹⁻¹² DPLR is a parallel multiblock finite-volume code that solves the reacting Navier-Stokes equations including finite-rate chemistry and the effects of thermal nonequilibrium. The Euler fluxes are computed using a modified (low-dissipation) form of Steger-Warming flux vector splitting,¹³ with third-order spatial accuracy obtained via MUSCL extrapolation coupled with a minmod limiter.¹⁴ Viscous fluxes are computed to second-order accuracy using a central difference approach. Time advancement to a steady-state solution is achieved using the data-parallel line relaxation method.¹¹ DPLR has been used previously for several other planetary entry simulations.^{2,12,15}

A detailed description of the relevant equations for atmospheric entry flows has been presented in a number of sources¹⁶⁻¹⁷ and will not be repeated here. For typical Titan entry conditions thermal nonequilibrium effects will greatly influence the amount of predicted shock layer radiation. Therefore, two energy equations are solved; a total energy equation and a vibro-electronic energy equation. In this formulation it is assumed that the vibrational and electronic modes of the gas are in equilibrium with each other, but not with the translational-rotational component.¹⁷ This model was originally developed for air flows, but should be a reasonable approximation for the N₂-dominated Titan atmosphere (89-97% by mole) as well. The energy exchange between the translational-rotational and vibrational-electronic modes is modeled using a Landau-Teller formulation, where relaxation times are obtained from Millikan and White,¹⁸ assuming simple harmonic oscillators. Characteristic vibrational temperatures for the simple harmonic oscillator approximation are taken from Gurvich et al.¹⁹

Table 1. Reaction rates for the Titan kinetic mechanism (Rate = $CT_a^{\square} \exp(\square/T_a)$, M is a generic collision partner).

Reaction	C	\square	\square
	($\text{m}^3/\text{kmol}\cdot\text{s}$)		(K)
<u>Dissociation Reactions ($T_a = \sqrt{TT_v}$)</u>			
$\text{C}_2 + \text{M} \square \text{C} + \text{C} + \text{M}$	9.68E+19	-2.0	71000
$\text{N}_2 + \text{M} \square \text{N} + \text{N} + \text{M}$	3.70E+18	-1.6	113200
$\text{CH} + \text{M} \square \text{C} + \text{H} + \text{M}$	1.13E+16	-1.0	40913
$\text{CN} + \text{M} \square \text{C} + \text{N} + \text{M}$	1.00E+20	-2.0	90000
$\text{CH}_4 + \text{M} \square \text{CH}_3 + \text{H} + \text{M}$	2.25E+24	-1.87	52900
$\text{CH}_3 + \text{M} \square \text{CH}_2 + \text{H} + \text{M}$	2.25E+24	-1.87	54470
$\text{CH}_2 + \text{M} \square \text{CH} + \text{H} + \text{M}$	2.25E+24	-1.87	50590
$\text{NH} + \text{M} \square \text{N} + \text{H} + \text{M}$	1.13E+16	-1.0	41820
$\text{H}_2 + \text{M} \square \text{H} + \text{H} + \text{M}$	1.47E+16	-1.23	51950
<u>Exchange Reactions ($T_a = T$)</u>			
$\text{C} + \text{N}_2 \square \text{CN} + \text{N} + \text{M}$	1.11E+11	-0.11	23000
$\text{CN} + \text{C} \square \text{C}_2 + \text{N} + \text{M}$	3.00E+11	0.0	18120
$\text{C}_2 + \text{N}_2 \square \text{CN} + \text{CN}$	7.10E+10	0.0	5330
$\text{H} + \text{N}_2 \square \text{NH} + \text{N}$	2.20E+11	0.0	71370
$\text{H}_2 + \text{C} \square \text{CH} + \text{H}$	1.80E+11	0.0	11490
$\text{CN}^+ + \text{N} \square \text{CN} + \text{N}^+$	9.80E+09	0.0	40700
$\text{C} + \text{N} \square \text{CN}^+ + \text{e}$	1.00E+12	1.50	164440
$\text{C}^+ + \text{N}_2 \square \text{N}_2^+ + \text{C}$	1.11E+11	-0.11	50000
$\text{N} + \text{N} \square \text{N}_2^+ + \text{e}$	1.79E+06	0.77	67500
<u>Electron Impact Ionization Reactions ($T_a = T_v$)</u>			
$\text{N} + \text{e} \square \text{N}^+ + \text{e} + \text{e}$	2.50E+31	-3.82	168200
$\text{C} + \text{e} \square \text{C}^+ + \text{e} + \text{e}$	3.70E+28	-3.00	130720
$\text{H} + \text{e} \square \text{H}^+ + \text{e} + \text{e}$	2.20E+27	-2.80	157800

At the entry velocities considered, previous analysis² indicates that the flow is weakly ionized. However, this analysis also determined that the amount of ionization is small enough that the effect on convective and radiative heating predictions is negligible. Therefore a 13-species (CH_4 , CH_3 , CH_2 , N_2 , C_2 , H_2 , CH , NH , CN , N , C , H , Ar) 15-reaction finite-rate chemistry model is used in this paper. However, for completeness some cases were run using a 19-species 22-reaction model, including the ions N_2^+ , CN^+ , N^+ , C^+ , and H^+ as well as free electrons. In both cases the chemical source terms are modeled using rates collected for the Titan entry problem by Nelson et al.,⁵ with the exception that the heavy particle impact ionization reactions in Nelson et al. have been changed to electron impact ionization reactions as originally intended,² and the rates for those reactions have been updated to currently accepted values.²⁰ The complete reaction mechanism is given in Table 1. Following the work of Park,²¹ the governing temperature for all dissociation reactions is assumed to be $T_a = \sqrt{TT_v}$ where

T is the translational-rotational temperature, and T_v is the vibrational-electronic temperature. Equilibrium constants are computed using a minimized Gibbs free energy approach,²² which eliminates the need to generate curve fit expressions for each reaction. Species thermodynamic properties are modeled using the curve fit expressions of Gordon and McBride.²²

Viscosity and thermal conductivity are modeled using the species expressions and mixing rules presented by Gupta et al.²³ Collision integrals are taken from Park et al.²⁰ for most binary interactions. Collision integrals for all other interactions were computed using a modified Lennard-Jones potential²⁰ for the neutral-neutral interactions and a polarization potential for the ion-neutral interactions. The self-consistent effective binary diffusion (SCEBD) method²⁴ is used to model diffusion fluxes. The diffusion velocity of the electrons is computed from the requirement of zero current density in the flow. Either a laminar or fully turbulent flow model is used, depending on the case. For turbulent flows, the compressible Baldwin-Lomax algebraic model²⁵ is implemented with a turbulent Schmidt number of 0.5 and a turbulent Prandtl number of 0.9. The surface is assumed to be fully catalytic (diffusion limited) to all ions as well as N_2 and H_2 recombination, and non-catalytic to all other species. More rigorous surface boundary conditions could be applied if necessary, but the chemical energy contained in the trace carbonaceous species produced by methane decomposition is small compared to the total flow enthalpy, so little error is introduced by neglecting possible catalytic reactions of these species. A radiative equilibrium boundary condition is applied, with a constant emissivity of 0.85, which is a representative value for the type of carbonaceous ablator typically used for such applications.²⁶

The baseline computational grid for these simulations is a two-block non-degenerate topology, with a total of 125,000 grid points distributed around the 70-degree sphere-cone geometry. The grid for each computation was adapted using the Self Adaptive Grid code (SAGE)²⁷ to ensure that the outer boundary of the grid was aligned with the bow shock. Wall spacing was chosen to ensure that the cell Reynolds number at the wall was less than five, and 65 total points were used in the wall-normal direction. This grid topology and density was shown previously² to provide grid converged heating predictions for Titan aerocapture simulations, and direct comparisons between DPLR and the NASA Langley CFD code LAURA showed good agreement at that time.

Shock layer radiation is calculated using the radiation transport code NEQAIR,²⁸ which computes the emission, absorption, and transport of radiation line-by-line using a tangent slab approximation. Based on previous analysis, at the entry velocities considered in this paper essentially all of the radiation comes from the CN violet [B-X] (about 90% of the total) and red [A-X] (about 10%) bands. The radiating

species are assumed to be in a Boltzmann distribution at the mixture vibro-electronic temperature of the gas, which was found to be a reasonable approximation in previous work.^{2,29} Detailed radiation calculations³ have shown that, for the cases considered here, the radiative emission from CN is not significantly absorbed (the shock layer is optically thin), due in part to the relatively low shock layer pressures. Therefore essentially all of the radiation produced at each point in the flowfield is emitted isotropically to space over a solid angle of 4π steradians.

When using NEQAIR, the total amount of radiation reaching the surface is integrated along each line of sight using a tangent slab approximation. In the tangent slab approximation, it is assumed that the input line of sight represents an infinite slab of gas parallel to the surface at that point. However, in reality the shock layer is curved due to body curvature. Therefore, a correction factor must be applied to the tangent slab result to account for surface curvature effects. The net radiative heating to the body then becomes

$$q_{rad} = \bar{C}_r q_{ts} \quad (1)$$

where q_{rad} is the net radiative heat flux, \bar{C}_r is the correction factor for surface curvature, and q_{ts} is the tangent slab result. The value of this correction factor is a complex function of the surface geometry and shock layer conditions. For the stagnation region in blunt body air flows, values between 0.75-0.85 are typically used.^{28,30} The appropriate value to use away from the stagnation point is not well understood. Because of this, a value of $\bar{C}_r = 1.0$ is frequently applied to the entire vehicle in an attempt to ensure conservatism in the radiative heating prediction. The accuracy of this approximation will be discussed later in the paper. A more detailed description of the application of NEQAIR to Titan entry radiative heating can be found in the work of Olejniczak et al.³

For the case of an optically thin gas, it is possible to eliminate the tangent-slab approximation and use a view-factor based approach to compute the radiative heating at each body point without simplification. In a finite-volume approximation assuming an optically thin gas, the radiative heat flux at any point on the surface of the vehicle is the sum of radiative fluxes due to each emitting computational cell in the flowfield. Once the total emission, $I\Delta V$, from a volume element, ΔV , is determined from the CFD calculation, the heat flux contribution of this volume at a surface element, ΔA , on the body can be written as³¹

$$\begin{aligned} q_{rad} &= \frac{I\Delta V}{\Delta A} \left[\frac{\cos\theta}{4r^2} \right] \Delta A(r) \\ &= \frac{I\Delta V}{\Delta A} f(r, \theta, \Delta A) \Delta A(r) \end{aligned} \quad (2)$$

where r is the distance between the emitting volume and the target surface element, θ , is the angle between r and the surface normal, ΔA is the transmission factor, and f is the view factor that determines the fraction of radiative intensity that reaches the target surface element. The transmission factor ΔA ranges from zero for a completely optically thick gas to one for an optically thin gas. Since f is a purely geometrical quantity, it can be determined for each grid cell-surface element pair once and then stored. Eq. (2) explicitly assumes that r and θ are constant over the cell volume, and thus is applicable only when r is much larger than the dimensions of the emitting volume element. However, for typical CFD grids r may be comparable to the cell size in the shock layer and may even be smaller than the cell size in the boundary layer. Therefore each CFD grid cell must be sliced into smaller sub cells to compute the view factor. All the sub cells have the same volumetric emission, I , but the geometrical parameters r and $\cos\theta$ differ. The required number of sub cells is determined through grid resolution; i.e. the sub cell size must be small enough so that any further subdivision of the CFD cell does not affect the computed view factor. The computational load required to compute the view factor rises linearly with the number of sub cells. Therefore if a grid cell is subdivided once in each direction, the calculation becomes eight times more expensive. This is of particular concern in the boundary layer where several cell subdivisions may be needed. Fortunately, since the boundary layer cells do not emit strongly, it can be shown that a tangent slab approximation can be used for these cells without losing accuracy.

The advantage of using an exact method over the tangent slab approximation is evident if we consider a sample blunt body of radius R_b and a concentric spherical shock layer of radius R_s that is uniformly emitting around the body. The exact stagnation point radiative heat flux for this case can be written as:

$$q_{rad} = q_{ts} \left[\frac{R_s}{R_b} \right]^2 \sqrt{1 - \left[\frac{R_b}{R_s} \right]^2} \quad (3a)$$

or

$$\bar{C}_r = \left[\frac{R_s}{R_b} \right]^2 \sqrt{1 - \left[\frac{R_b}{R_s} \right]^2} \quad (3b)$$

For a shock layer very close to the body, $R_s \approx R_b$ and $q_{rad} \approx q_{ts}$. However, if the shock radius is only 10% larger than the body radius, Eq. (3) shows that q_{rad} falls by 30% compared to q_{ts} ($\bar{C}_r = 0.7$), which indicates that the value of \bar{C}_r is a strong function of the shock standoff distance. Since in reality the shock about a blunt body is neither

concentric nor uniformly emitting, $\bar{\mu}_r$ can be even smaller than predicted by this expression.

RADIATION COUPLING

For the uncoupled simulations, the flowfield is first computed with DPLR, and the resulting solution is post-processed to extract lines of sight for the radiation analysis. Lines of sight are generated normal to every surface grid point on the vehicle forebody, which yields an estimate of distributed surface radiative heating with the same spatial resolution as the convective heating estimates.

The amount of coupling between the shock-layer radiation and fluid can then be estimated by evaluating the radiative cooling parameter, or Goulard number,³² $\bar{\mu}$:

$$\bar{\mu} = 2q_{rad} / (\frac{1}{2} \bar{\rho} V^3) \quad (4)$$

where q_{rad} is the stagnation point radiative heat flux, $\bar{\rho}$ is the freestream density, and V is the freestream velocity. The factor of two in the numerator of Eq. (4) accounts for the fact that emission is isotropic; as much radiation is directed away from the surface as is directed towards it, and thus the total radiation flux along the stagnation line is twice that intercepted by the body. The radiative cooling parameter is essentially the ratio of the radiation energy flux to the total energy flux, and for optically thin gases is a direct measure of the amount of flow energy converted to radiation. When $\bar{\mu}$ becomes large ($\bar{\mu} > 0.01$) the flowfield is considered to be coupled, because the amount of flow energy converted to radiation has a significant impact on the fluid dynamics and chemical kinetics of the flow. The flowfield in this case can also be described as non-adiabatic, since energy can leave the computational domain via radiation transport.

The radiative cooling parameter was evaluated for the reference Titan aerocapture mission profile, based on the uncoupled aeroheating predictions from Refs. 2 and 3. At the peak convective heating point on the minimum atmosphere lift-up reference trajectory, the velocity was 5760 m/s and the freestream density was 1.49×10^{-4} kg/m³. The uncoupled radiation analysis predicted 290 W/cm² of radiative heating at the 3D stagnation point. By inserting these numbers into Eq. (4), we see that the Goulard number for this flow is approximately 0.4, indicating that the flow is strongly coupled. By comparison, $\bar{\mu} \approx 0.01$ for the Fire II flight experiment,³³ and for the Galileo probe $\bar{\mu}$ ranges from 0.03 assuming a fully coupled flowfield with ablation product blockage³⁴ to 0.1 for an uncoupled analysis.³⁵ The comparatively large values of $\bar{\mu}$ predicted for Titan aerocapture are due to the fact that CN is a strong radiator, and the atmospheric composition of Titan is ideal for CN formation behind a relatively low speed shock wave.

The effect of modeling radiative cooling is to reduce the predicted net amount of shock layer radiation. Tauber and Wakefield³⁶ have developed an engineering relation between $\bar{\mu}$ and the reduction in predicted stagnation point radiative heating:

$$q_{coup} / q_{unc} = 1 / (1 + \bar{\mu}^{0.7}) \quad (5)$$

where q_{coup} is the net radiative heating including coupling effects, q_{unc} is the radiative heating assuming an uncoupled flowfield, and $1/$ is a gas-mixture specific empirical constant. Although Eq. (5) was originally developed for the optically thick shock layer encountered during Jupiter entry ($\bar{\mu} = 3$),³⁶ it has been shown to provide reasonable results for strongly coupled air radiation by setting $1/ \approx 3.45$, and thus should provide a reasonable first estimate of the effect of radiation coupling for this problem. For $\bar{\mu} \approx 0.4$, Eq. (5) predicts a reduction in net radiative heating of more than 60% over the uncoupled result.

Weakly coupled flows have been computed previously using a loosely coupled approach,³⁷⁻³⁸ in which flowfield and radiation solutions are alternated until convergence is reached. However, this method becomes intractable for cases with strong coupling due to the number of iterations between the CFD and radiation solvers required to achieve convergence. In the general case, simulation of a fully coupled flowfield requires the simultaneous solution of the reacting Navier-Stokes and the radiative transport equations. The result is a set of integro-differential equations in which emission at any point in the flowfield has essentially instantaneous effect on all other points. In addition, resolution of frequency space and solid angle (emission direction) space greatly increase the dimensionality and complexity of the problem. Solution of this coupled equation set has been demonstrated previously,³⁹⁻⁴¹ but the resulting algorithms are extremely complex and time consuming, particularly in three spatial dimensions. However, since the shock layer produced during Titan aerocapture was found to be optically thin to CN radiation in previous analysis,³ it is possible to greatly simplify the coupled problem for Titan entries. In the case of an optically thin gas the analysis reduces to a pointwise computation of emission per unit volume. All radiation produced is assumed to either impact the body surface or leave the computational domain without interacting with the rest of the flow. Thus, radiation coupling in an optically thin gas acts as a volumetric sink term in the relevant energy conservation equations.

The emission rates for CN red and CN violet radiation can be readily computed from known spectroscopic constants.⁴² Assuming a Boltzmann distribution of the excited states, emission per unit volume is a function (to first-order) only of the number density of CN molecules available to radiate and the vibro-electronic temperature of the gas. Although in

principle the emission rates could be computed directly within DPLR, it was decided to curve fit these rates in order to improve the overall computational efficiency of the resulting algorithm. Therefore, analytical fits of the NEQAIR-computed optically thin emission for CN red and CN violet emission are generated. For convenience, a curve fit form used by Park⁴³ for equilibrium constants is borrowed:

$$E_{is} = N_s \exp(A_{1,is}/z + A_{2,is} + A_{3,is} \ln(z) + A_{4,is}z + A_{5,is}z^2) \quad (6)$$

where E_{is} is the total radiative emission for molecular band i of species s in $\text{W}/(\text{m}^3 \cdot \text{sr})$, N_s is the number density of the radiating species in particles/ m^3 , $z = 10000/T_w$, and $A_1 \square A_5$ are curve fit constants. Values of the constants in Eq. (6) for CN red and CN violet emission were obtained via a least-squares fitting process, and are given in Table 2. These expressions are accurate to within 2% over the temperature range of interest. The resulting curve-fit expressions are summed over the number of radiating species and the number of molecular bands for each species to compute the total emission in each cell (E_{tot})

$$E_{tot} = \sum_s \sum_i E_{is} \quad (7)$$

The result is inserted into DPLR as a sink term in the total and vibro-electronic energy equations to simulate the non-adiabatic energy loss due to conversion of flow energy to radiation. Note that, since the radiative emission is isotropic, a multiplicative factor of 4π steradians is required to convert from $\text{W}/(\text{m}^3 \cdot \text{sr})$ to W/m^3 such that the resulting source term has the correct units in a finite-volume scheme of energy per unit volume per unit time. The resulting source term (Q_{rad}) in the total and vibrational-electronic energy equations is then

$$Q_{rad} = -4\pi E_{tot} \quad (8)$$

where the negative sign indicates a sink of energy. In this manner, tight coupling between the flowfield and the radiation can be modeled with little performance penalty. It is important to point out that, even if the radiation were non-Boltzmann this approach would still be possible, although the functional form of the expressions for E_{is} would be considerably more complex.

In addition to the volumetric sink terms, that portion of the shock layer radiation that strikes the surface must be accounted for in the radiative equilibrium energy balance at the wall:

$$q_{conv} + q_{rad} = \epsilon \sigma T_w^4 \quad (9)$$

Table 2. Curve fit parameters for CN violet [B-X] and red [A-X] emission.

	A_1	A_2	A_3	A_4	A_5
CN violet	-0.24820	-28.088	1.2171	-4.2147	0.02354
CN red	-0.51122	-33.016	0.1590	-1.4679	0.00661

where q_{conv} is the convective heat flux to the wall (including surface catalysis), ϵ is the wall emissivity, $\sigma = 5.6691 \times 10^{-8} \text{ W}/(\text{m}^2 \cdot \text{K}^4)$ is the Stefan-Boltzmann constant, and T_w is the wall temperature. Note that conduction into the surface is assumed to be zero in Eq. (9), which is a standard conservative assumption used during preliminary design CFD analysis. The effects of conduction into the solid, as well as possible pyrolysis gas injection and ablation are typically accounted during response modeling and sizing of the TPS material. Possible interactions between ablation product gases and the boundary layer are beyond the scope of the current work.

In order to account for the effects of radiative heating in the surface energy balance (SEB) it is necessary to compute the integrated radiative heat flux at each surface point in the computational grid, which can become complicated in a multiple-block grid topology on a distributed memory parallel machine. Because the surface temperature varies as the fourth root of the heat flux (Eq. 9), it was expected that radiative surface heating would have only a small impact on the flowfield. Therefore, for the purposes of this paper it was decided to implement this effect in a loosely coupled manner. In this approach, a simulation is first performed in which the volumetric effects of radiation coupling are accounted for in the manner discussed above, but the surface heating effects are neglected (all of the emitted radiation is assumed to leave the flowfield and q_{rad} is set equal to zero in Eq. (9)). Radiative surface heating is then computed at each surface grid point in the initial solution. This pointwise radiative heating distribution is read into DPLR as a boundary condition for the solver and a new solution is generated that accounts for radiative heating in the SEB. This process is repeated until convergence is reached. The net result of including radiative heating in the surface energy balance will be to increase the radiative equilibrium wall temperature over that predicted with only convective heating included. This increase in surface temperature will tend to decrease the thermal gradient between the wall and the boundary layer edge, and thus should slightly further reduce the net convective heating to the wall. The effects of including radiative heating in the SEB will be quantified in the ‘‘Results’’ section.

Once a solution has been computed in DPLR, the radiative heating at each body point is obtained via a post-processing step using either a tangent slab approach or the view-factor method discussed above. It is important to note that in either

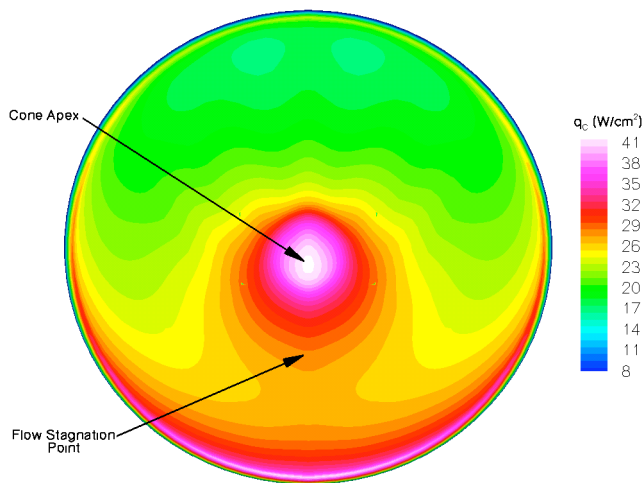


Fig. 2. Convective heating on the forebody of the Titan aerocapture vehicle, assuming uncoupled radiation. Peak heating point (t=253s) on the minimum atmosphere lift-up trajectory.

case the volumetric emission of the gas is fixed; the difference between the methods is in how the transport of that radiation to the surface is computed. Therefore either method is applicable to both uncoupled and coupled flowfield solutions.

RESULTS

Several Titan aerocapture trajectories were generated during the previous systems analysis study. However, much of the aerothermal analysis was performed on the minimum atmosphere lift-up trajectory, which was predicted to yield the highest radiative heat fluxes.³ The term “minimum atmosphere” refers to the use of the lower bound prediction for density as a function of altitude, as defined by Justus and Duvall.¹⁰ The atmospheric composition for this trajectory was 95% N₂ and 5% CH₄ by volume, and was assumed to be constant at aerocapture altitudes.² Peak convective heating was predicted to occur at t=253s on this trajectory, which corresponds to $\rho = 1.49 \times 10^{-4}$ kg/m³, $V = 5.76$ km/s, and $T = 152.7$ K. This trajectory point will be the focus of the parametric analysis presented here. Maximum radiative heat loads were predicted to occur on the minimum atmosphere lift-down trajectory.³

Figure 2 shows the computed uncoupled laminar convective heating on the forebody of the Titan aerocapture vehicle at this trajectory point. The computation was performed with a 13-species gas model, i.e. ionization was neglected. The effect of ionization on the results will be discussed below. The flow stagnation point is below the cone apex (at approximately $y = -0.8$ m) due to the 16° angle of attack. As shown in Fig. 2, peak convective heating is 41 W/cm² and occurs at the sphere-cone apex rather than the flow stagnation point, due to flow expansion and the resulting

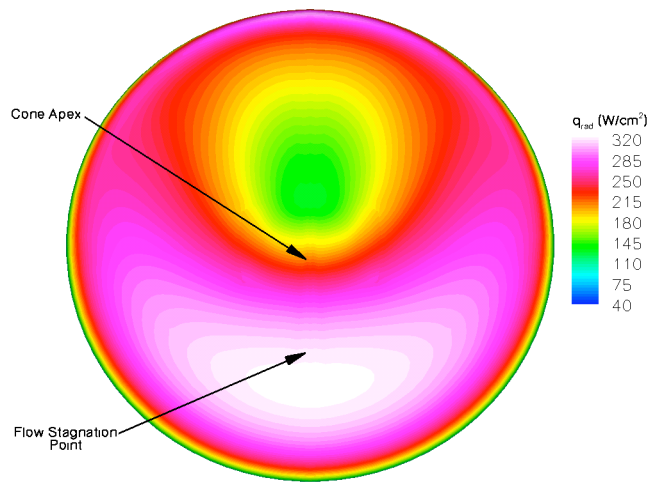


Fig. 3. Uncoupled radiative heating on the forebody of the Titan aerocapture vehicle, computed assuming a tangent slab approximation. Peak heating point (t=253s) on the minimum atmosphere lift-up trajectory.

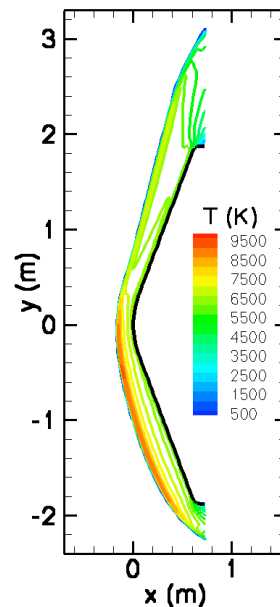


Fig. 4. Temperature contours in the symmetry plane. Peak heating point (t=253s) on the minimum atmosphere lift-up trajectory.

boundary layer thinning around the apex. Figure 3 shows the computed uncoupled radiative heating on the forebody at this trajectory point, assuming tangent slab with the correction factor $\bar{\mu}_r = 1.0$. Figure 4 shows computed translational temperature in the symmetry plane for this case. From these figures we see that the peak radiative heating is 323 W/cm² and occurs near the flow stagnation point, since this is where the post-shock temperatures are highest (larger emission per unit volume) and the shock standoff distances are largest (greater volume of radiating gas).

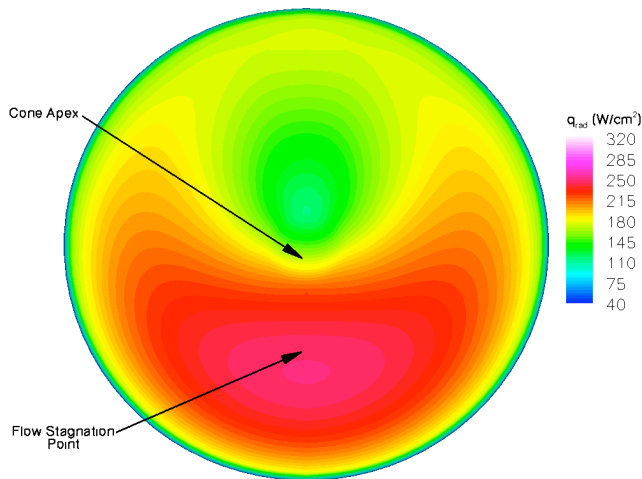


Fig. 5. Uncoupled radiative heating on the forebody of the Titan aerocapture vehicle, computed using a view factor method. Peak heating point ($t=253s$) on the minimum atmosphere lift-up trajectory.

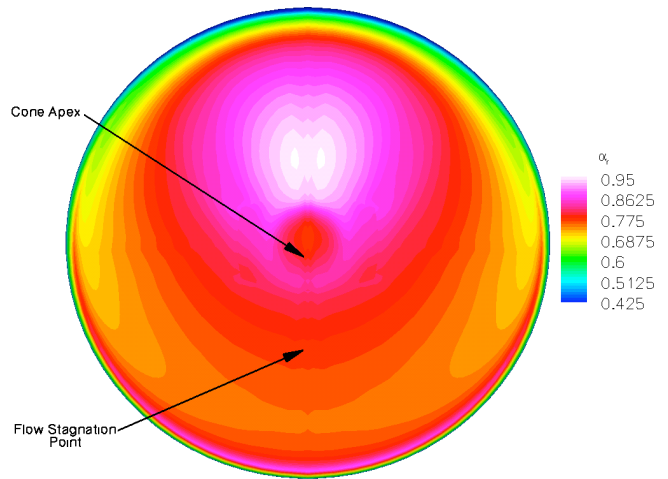


Fig. 6. Computed tangent slab correction factor ($\bar{\Omega}_r$) on the forebody of the Titan aerocapture vehicle. Peak heating point ($t=253s$) on the minimum atmosphere lift-up trajectory.

View Factor Based Analysis

As stated previously, the tangent slab assumption will tend to over predict radiative heating near the stagnation point, but it is not obvious *a priori* what the impact will be to other areas of the surface. In order to quantify the impact of using the tangent slab approach, Fig. 5 plots the uncoupled radiative heating for the solution shown in Fig. 3, computed with the more accurate view factor approach. By using view factors, the peak radiative heating is reduced to 246 W/cm^2 , which gives a stagnation point correction factor $\bar{\Omega}_r = 0.76$, meaning that the actual surface heating is 24% lower than the tangent slab result. Figure 6 shows the computed value of $\bar{\Omega}_r$ on the entire forebody for this case. From Fig. 6 we see that $\bar{\Omega}_r$ is fairly constant on the entire wind side, which is not surprising since the vehicle is blunt and lateral gradients are not large. $\bar{\Omega}_r$ is larger on the lee side (reaching a maximum value of about 0.95), because the shock standoff distance is smaller on the leeside and the shock itself is more planar (see Fig. 4), which better approximates the assumption of tangent slab. The area where the tangent slab assumption is the least accurate is the lee side shoulder, where the flow is expanding rapidly and the tangent slab assumption fails to account for the small radius of curvature of the surface. Because the view factor approach is more accurate than tangent slab, view factors will be used to compute all remaining radiative heating results in this paper.

The fact that $\bar{\Omega}_r$ is always less than 1.0 in Fig. 6 means that the total amount of radiative energy reaching the surface is significantly less when view factors are used. The reasons for this result are clear if we think about the amount of radiation that reaches the surface from a given volume element. In the tangent slab approximation, it is assumed that exactly one half of the isotropically emitted radiation

eventually reaches the surface. However, in the view factor approach, the actual subtended solid angle of the surface is computed for each volume element. Because of the fairly large shock standoff distance on the wind side, the strongest emitting volumes “see” a solid angle subtended by the surface that is about 30% smaller than the 2π steradians assumed by tangent slab. Emitting volumes closer to the body direct more of their energy to the surface, until at very close distances the tangent slab approximation becomes nearly exact. The difference between the actual solid angle subtended by the surface and the 2π steradian maximum, when integrated over all emitting volumes, accounts for the reduction in total energy reaching the surface. Finally, it should be noted that at the very top of the shoulder the results presented here are not accurate, since the computational solution space ends at a plane perpendicular to the maximum radius point on the aeroshell, and any radiation emitted beyond this point is not included in the view factor summation. However, this effect should be fairly small because of the rapidly expanding and cooling gas in this region, and will be localized to the top of the shoulder. A companion paper⁸ that includes a full wake grid addresses the problem of radiative heating to the shoulder.

Effects of Radiation Coupling

In order to evaluate the effects of radiation coupling on this flowfield, it is interesting to separate the volumetric (non-adiabatic) effects from the surface energy balance effects, as discussed in the previous section. Therefore, we first simulate the same trajectory point, accounting for non-adiabatic flow coupling via Eq. (7), but neglecting the radiative heating in the surface energy balance ($q_{rad} = 0$ in Eq. (8)). As a check, the volumetric emission sink term at each computational cell from the converged DPLR solution for this case was compared to that computed in NEQAIR as

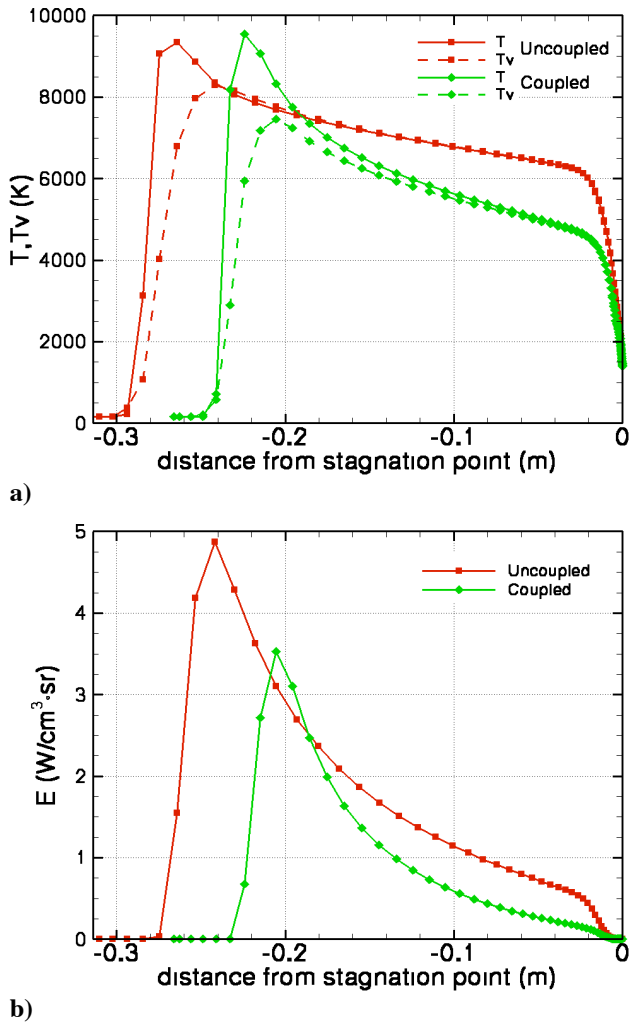


Fig. 7. Stagnation line a) temperatures and b) volumetric emission for the uncoupled and coupled simulations. Peak heating point ($t=253s$) on the minimum atmosphere lift-up trajectory.

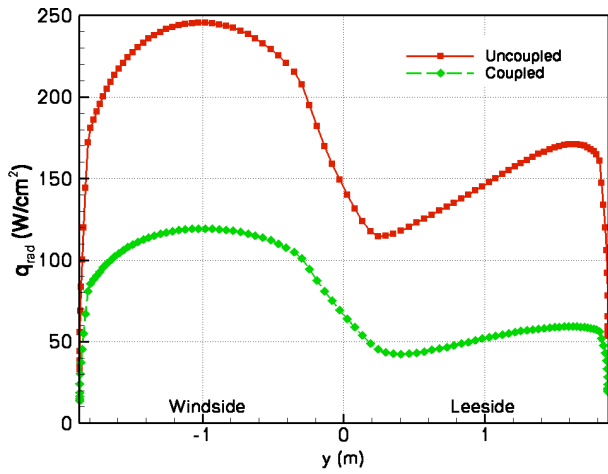
a post-processing step, and was found to agree to within 2% at most grid points, indicating that the term was modeled correctly and was properly incorporated into the code. Larger errors were observed in cool regions of the flow (such as the freestream), where the vibro-electronic temperature was outside of the bounds of the curve fit, but since the emission from these areas is orders of magnitude below peak levels, this error was considered acceptable.

Figure 7a shows the impact of radiative coupling on the stagnation line translational and vibro-electronic temperature profiles. The radiative energy sink term has two main effects. First, removing energy from the flowfield causes the shock to move closer to the body, which decreases the total volume of radiating gas. For this case the shock standoff distance decreases from 29 cm to 24 cm. Second, by depleting energy from the vibro-electronic energy pool, the maximum post-shock vibro-electronic

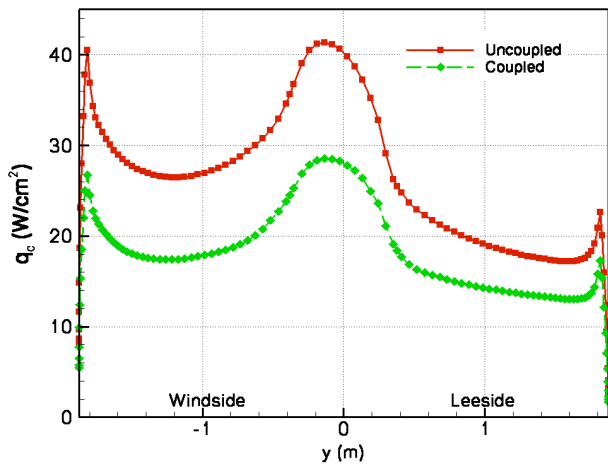
temperature is decreased by about 850 K, from 8300 K to 7450 K. This temperature decrease also decreases the amount of radiation emitted, since emission is a strong function of electronic temperature. Additionally, the depletion of vibro-electronic energy decreases the translational-rotational energy in the shock layer as well due to the energy coupling terms between the translational and vibrational modes of the gas. Although the majority of the emission occurs in the hottest gas immediately behind the shock, the flow continues to lose energy to radiation as it convects down the stagnation streamline, and as a result the total temperature decrease between the shock and the boundary layer edge is greater for the coupled flow case. Figure 7a also shows that the maximum post-shock translational temperature is essentially unaffected by coupling, because the peak translational temperature is reached immediately behind the shock wave before the vibro-electronic temperature has risen enough to generate excited CN molecules. At the boundary layer edge the flow reaches thermal equilibrium in both solutions, but the edge temperature is about 2000 K lower for the coupled flow. This decrease in edge temperature reduces the thermal gradient through the boundary layer, which will decrease convective heating as well.

Figure 7b shows the computed volumetric emission along the stagnation streamline for the uncoupled and coupled simulations. In a tangent slab approximation, this emission would be directly integrated along the stagnation streamline to compute the stagnation point radiative heat flux. From Fig. 7b we see immediately that the peak emission for both cases occurs at the location of peak vibrational, as opposed to translational, temperature. While the peak emission occurs immediately behind the shock wave, in both cases Fig. 7b shows that there is significant emission from the entire volume of gas between the shock and the boundary layer edge, and thus the typical radiating shock layer assumption of a thin layer of emitting gas is not valid for this flow. Finally, the figure also shows clearly that the coupled solution has less peak emission behind the shock wave (3.5 vs. 4.9 $W/cm^3 \cdot sr$), due to the decrease in peak vibrational temperature.

Figure 8a compares the coupled and uncoupled radiative heating along the centerline of the forebody of the Titan aerocapture vehicle for this case, computed with view factors. The stagnation point is at $y \sim -0.8$ m from the apex. By including the volumetric radiative coupling terms, the stagnation region radiative heating is reduced by slightly more than a factor of two, with a maximum of 119 W/cm^2 near the flow stagnation point as opposed to 246 W/cm^2 for the uncoupled case. By comparison, Eq. (5) with $\beta = 3$ predicts a maximum radiative heating of about 101 W/cm^2 . This indicates that using Eq. (5) to estimate the impact of radiation coupling is reasonable, but can be non-conservative for strongly coupled radiation in an optically thin medium, unless an appropriate value of β is selected.



a)



b)

Fig. 8. Coupled vs. uncoupled a) radiative and b) convective heating along the centerline of the Titan aerocapture vehicle. Peak heating point ($t=253s$) on the minimum atmosphere lift-up trajectory.

This same conclusion holds true if applied to the tangent slab predictions, where the uncoupled solution (Fig. 3) predicts 323 W/cm^2 maximum and a coupled solution (not shown) predicts 156 W/cm^2 , while Eq. (5) with $\bar{\Gamma}=3$ predicts a net tangent slab radiative heating of 119 W/cm^2 . From these results it is apparent that a universal value of $\bar{\Gamma}$ in Eq. (5) does not exist for Titan CN radiation; selecting a value of $\bar{\Gamma}=2.25$ would accurately reproduce the CFD results for the coupled case, but $\bar{\Gamma}=1.87$ would be required for the uncoupled case.

The computed convective heating for the coupled calculation is compared with the uncoupled result in Fig. 8b. As expected, the convective heating is significantly reduced as a consequence of flow coupling, reaching a peak value of 28.5 W/cm^2 at the apex, as compared to 41 W/cm^2 for the uncoupled case. However, since laminar convective heating is still only a small portion of the total predicted surface

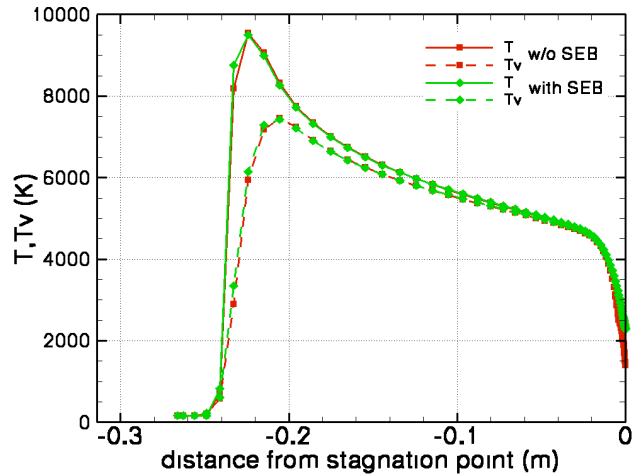


Fig. 9. Stagnation line temperatures for the coupled simulation, showing the impact of including radiative heating in the surface energy balance (SEB). Peak heating point ($t=253s$) on the minimum atmosphere lift-up trajectory.

heating, the TPS design impact of this reduction would be small. Interestingly, the surface shear stress (not shown) is nearly the same for the coupled and uncoupled solutions. This is not surprising, since the volumetric coupling terms directly reduce the internal energy of the gas, but have only an indirect effect on momentum.

The results in Fig. 8 were computed with full coupling in the volumetric sense, but with the impact of radiation on the surface energy balance neglected. In order to assess the impact of including radiative heating in the SEB, the case was simulated using the loosely coupled methodology discussed previously. Fig. 9 shows the computed translational and vibro-electronic temperatures along the stagnation line for these simulations. We see from Fig. 9 that including radiative heating in the SEB increases the radiative equilibrium wall temperature by about 700 K , but the shock layer is essentially unaffected. Because including radiation in the SEB does not alter shock layer temperatures, it has no impact on volumetric emission or computed radiative heating. Therefore, only a single loosely coupled iteration is required to achieve a final solution. Figure 10 shows the impact of the surface energy balance on the computed convective heating. Three lines are shown in Fig. 10: an uncoupled solution, a solution with volumetric coupling only, and a fully coupled solution including surface energy effects. Since the computed convective heating rate is not very sensitive to changes in wall temperature, including radiative heating in the SEB has a small impact on the computed convective heating. At the apex, the convective heating rate is reduced by 31% due to the volumetric effects of radiation coupling, and only an additional 6% due to the surface energy balance terms.

Including radiation in the SEB significantly increases the cost of a simulation. Even if only a single loosely coupled

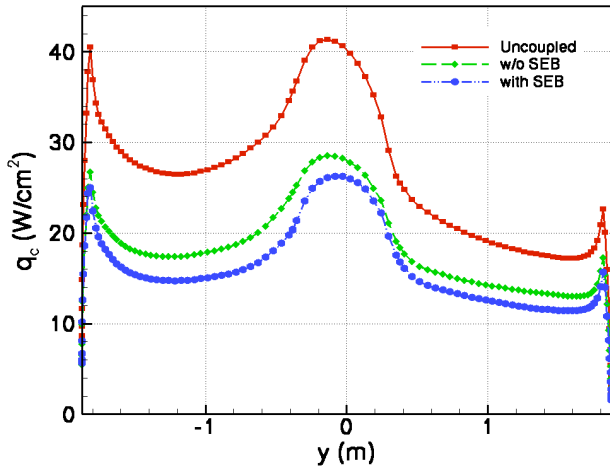


Fig. 10. Convective heating along the centerline of the Titan aerocapture vehicle, showing the impact of including radiative heating in the surface energy balance (SEB). Peak heating point (t=253s) on the minimum atmosphere lift-up trajectory.

iteration is required the computer time is still approximately doubled, since two computations are required to arrive at the final result. Developing a completely coupled method would be even more expensive, since the relatively expensive view factor computation would then need to be performed each iteration or the geometrical factors would need to be stored as an additional array of dimension number of surface points times number of volume cells. In addition, the energy balance presented in Eq. (9) also neglects conduction into the surface, which is typically taken into account (together with convective and radiative heating) by a material response model uncoupled from (or loosely coupled to) the CFD. Since, as shown in Figs. 9 & 10, including radiative heating in the SEB has no impact on the computed radiation and only a small impact on computed convective heating, the remaining results shown in this paper will neglect this effect.

Effects of Flow Ionization

A simulation was also performed to investigate the effect of ionization on the results presented here. For the uncoupled flow, the maximum ionization level was found to be only about $\beta \approx 3 \times 10^{-4}$, where β is the fraction of atoms or molecules that are ionized. At this low level of ionization, there was essentially no change in the convective heating to the body (about 0.3 W/cm² difference at the apex) or the radiative heating (about 2 W/cm² difference at the maximum heating point). The maximum ionization level for the coupled flowfield was reduced more than an order of magnitude to $\beta \approx 4 \times 10^{-5}$, due to the amount of energy lost to radiation. For this case there was no visible difference in either convective or radiative or surface heating for the ionized vs. non-ionized flowfield. In general, radiation

coupling will tend to suppress ionization. Therefore, if the effects of ionization are small for an uncoupled analysis, it can usually be safely neglected in the coupled analysis. However, ionization will become important at higher entry velocities.

Effects of Turbulence

Given the large size of the Titan aerocapture vehicle, engineering correlations predict that transition to turbulence will occur on the leeside of the vehicle somewhere near the peak heating point on the trajectory.² The effects of turbulence on convective heating were discussed in Ref. 2, but it is important to reexamine these results in the context of coupled radiation. Therefore, simulations of the t=253s point were also performed assuming that the flow was fully turbulent from the stagnation point, using a Baldwin-Lomax turbulence model. Before running a turbulent flow solution it is important to analyze the turbulence model to ensure its applicability to this problem. For example, the Baldwin-Lomax variant in DPLR by default relies on an enthalpy ratio search to locate the boundary layer edge, which is typically assumed to lie at the point away from the wall where the total enthalpy reaches 99% of the freestream value. However, the coupled flowfield is non-adiabatic and thus total enthalpy is not conserved. Therefore, such a method will tend to locate the “boundary layer edge” at the shock location, which is clearly not correct. For the coupled case shown here the boundary layer edge was located via a wall-normal search for the local maximum vorticity on each grid line. In order to ensure that the search never selected the shock, a manually selected maximum body-normal index was enforced based on the boundary layer location in the uncoupled solution.

Figure 11a compares convective heating along the centerline for four computations including all combinations of laminar and turbulent flow, and uncoupled and coupled radiation. The flow stagnation point is on the wind side at about $y = -0.8$ m from the apex. If we first look at the uncoupled results, we see that, as shown in Ref. 2, turbulent convective heating levels on the leeside of the forebody are as much as 2.5 times the laminar heating level, and even exceed the apex heating rate. There is also significant augmentation of wind side heating levels away from the stagnation region ($y < -0.8$ m), although the laminar and turbulent results are nearly the same at the stagnation point. When radiation coupling is included in the simulation, the laminar heating rate falls by 25-35% on the entire forebody, as discussed previously. Turning now to the coupled turbulent solution shown in Fig. 11a, a similar reduction in convective heating rate is observed in the stagnation area, but elsewhere the trend is quite different. In particular, on the leeside the turbulent convective heating is actually slightly higher for the coupled flow solution. However, the Baldwin-Lomax turbulent convective heating levels are sensitive to the computed boundary layer edge location. Therefore, because

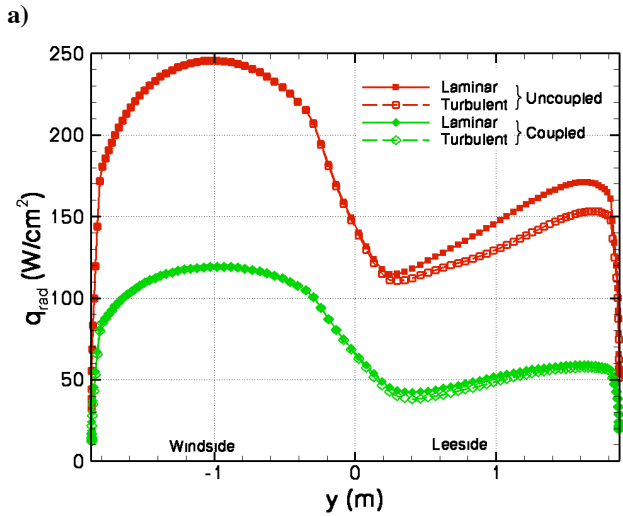
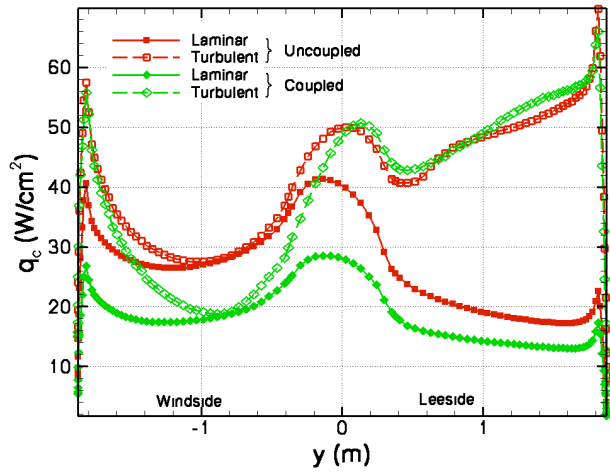


Fig. 11. a) Convective and b) radiative heating along the centerline of the Titan aerocapture vehicle, showing the effect of turbulence. Peak heating point ($t=253s$) on the minimum atmosphere lift-up trajectory.

of the problems discussed in the previous paragraph, accurate simulations of the turbulent convective heating levels for the coupled flowfield will likely require a more accurate turbulence model.

Radiative heating is primarily a function of shock-layer conditions, and thus should not be affected by the modeling issues discussed above. Figure 11b compares radiative heating along the centerline for the same cases shown in Fig. 11a. For both the laminar and turbulent solutions the effect of coupling is to reduce radiative heating levels by more than a factor of two. Flow turbulence has essentially no effect on predicted radiative heating levels on the wind side, which is not surprising since the effects of turbulence are confined to the boundary layer where the gas is cool and not radiating. However, on the lee side the turbulent solutions show a small decrease (about 10%) in radiative heating. This decrease is likely due to the slight increase in

Table 3. Selected points on the minimum atmosphere lift-up trajectory.

t (s)	ρ (kg/m^3)	V (m/s)	T (K)	P_{stag} (Pa)
174	4.697×10^6	6558	131.9	190
198	1.697×10^5	6512	143.2	680
228	6.414×10^5	6273	150.9	2400
253	1.491×10^4	5761	152.7	4700
266	2.051×10^4	5371	152.7	5610
281	2.665×10^4	4859	152.6	5960
312	3.338×10^4	3862	152.3	4730
339	3.212×10^4	3239	152.4	3320

shock standoff distance caused by the thicker turbulent boundary layer, but it was not explored in detail since the net effect is small.

Design Impact for Titan Aerocapture

The previous analysis concentrated on the impact of radiation coupling at a single trajectory point where shock layer radiation is significant. In order to understand the design impact of the improvements to CN radiation modeling presented here, the effect along an actual design trajectory must be evaluated. Therefore a series of cases are run at eight points along the minimum atmosphere undershoot trajectory, shown in Table 3. At each point a laminar uncoupled and coupled solution are computed so that the effects of radiation coupling can be quantified. Table 4 and Fig. 12 show the results for the point on the body in the stagnation region that experiences the maximum radiative heating. As can be seen from Fig. 12, radiation coupling has a significant impact on both convective and radiative heating levels throughout the trajectory. Computed heat loads for each case are shown in Table 5. For this trajectory, including radiation coupling in the simulation results in a 30% reduction in the convective heat load and a 57% reduction in radiative heat load. The combined heat load is slightly more than a factor of two lower when radiation coupling is modeled, which highlights the importance of accurate modeling for this type of strongly coupled problem.

Finally, it is interesting to note that the tangent slab correction factor $\bar{\Delta}_r$ varies little with time as shown in Table 4. In fact, to a good approximation a constant value of $\bar{\Delta}_r = 0.77$ could be used in the stagnation region for all trajectory points, for both the uncoupled and coupled solutions. A similar comparison was performed at the apex of the sphere cone, and again a fairly constant value of $\bar{\Delta}_r$ (0.78) was found to be sufficient for all trajectory points. This result is a little surprising at first, since the shock standoff distance varies considerably between the coupled and uncoupled solutions, and also varies with time during

Table 4. Stagnation region heating rates along the minimum atmosphere lift-up trajectory.

t (s)	Uncoupled			Coupled		
	q_c (W/cm ²)	q_{rad} (W/cm ²)	$\bar{\square}_r$	q_c (W/cm ²)	q_{rad} (W/cm ²)	$\bar{\square}_r$
174	8.4	24.4	0.81	6.2	4.0	0.78
198	14.1	78.7	0.78	8.9	21.5	0.78
228	23.8	166	0.77	15.1	72.8	0.78
253	28.2	246	0.76	18.7	119	0.76
266	27.1	270	0.76	18.0	121	0.77
281	23.6	213	0.77	16.1	86.6	0.76
312	11.8	13.6	0.79	10.5	10.5	0.77
339	5.5	0.2	-	5.5	0.0	-

Table 5. Stagnation region heat loads along the minimum atmosphere lift-up trajectory.

Uncoupled		Coupled	
Q_c (J/cm ²)	Q_{rad} (J/cm ²)	Q_c (J/cm ²)	Q_{rad} (J/cm ²)
3000	20700	2100	8900

the entry. As shown in Eq. (3) the value of $\bar{\square}_r$ for a thin emitting shock layer is a strong function of the shock standoff distance. Therefore, it seems logical to assume that, for example, the coupled solutions would have a larger value of $\bar{\square}_r$ due to the decrease in shock standoff distance. However, this analogy is misleading for these flows, because significant emission is produced in the entire region between the shock wave and boundary layer edge, which violates the assumption of a thin emitting layer in Eq. (3). In fact, the shock layer appears to be roughly self-similar for these flowfields, which results in a nearly constant value of $\bar{\square}_r$ at each point on the surface. Given the small amount of variability in $\bar{\square}_r$ with time, it is clear that a simple geometrically based constant value, based on the results of a single view-factor solution, would be a reasonable design assumption for this problem.

CONCLUSIONS

A new methodology is presented to enable the computation of fully coupled 3D flow fields including the non-adiabatic effects of strong radiative emission in an optically thin shock layer. The method can easily be incorporated into existing CFD codes and does not appreciably increase either the cost or the stability of the resulting simulations. Using this method, the volumetric effects of radiation coupling were shown to be much more important than the impact of radiative heating on the surface energy balance. In addition, a view-factor based approach was presented for computing radiative heating in optically thin gases. This approach,

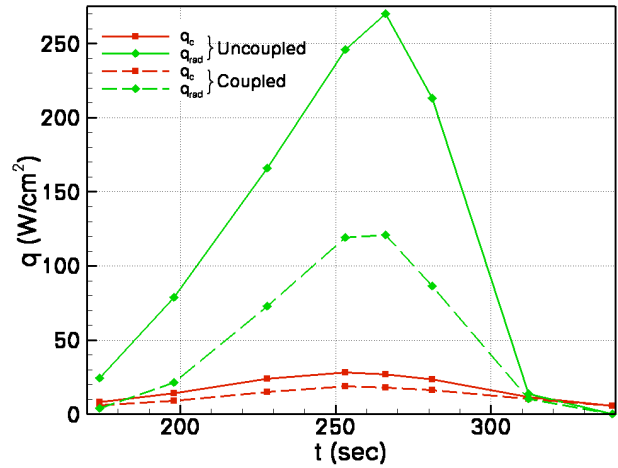


Fig. 12. Stagnation point convective and radiative heating for the Titan aerocapture vehicle as a function of time on the minimum atmosphere lift-up design trajectory.

while not new, does provide a significant accuracy improvement over the standard approach of using a tangent slab assumption.

These tools are applied to aeroheating simulations for a Titan aerocapture vehicle, which is an ideal demonstration case since Titan aeroheating is dominated by CN radiation produced in the optically thin shock layer. For this concept, previous uncoupled analysis predicted radiative heating rates of over 300 W/cm² at the stagnation point of the probe, as compared to convective heating rates of about 40 W/cm². By modeling the volumetric effects of radiation coupling on this flowfield, the net radiative heating rates were shown to be more than a factor of two below the uncoupled estimates. In addition, use of the view factor approach demonstrated that peak radiative heating in the stagnation region was about 25% less than that predicted using tangent slab at peak heating. The combination of these effects result in nearly a factor of three reduction in predicted maximum radiative heating levels for the Titan aerocapture vehicle. The energy lost from the flowfield due to radiation also reduces convective heating to the body by as much as 30% near peak heating, since boundary layer edge temperatures are considerably lowered. Comparison at multiple trajectory points demonstrated that the total heat load is reduced by a factor of two when coupling is properly modeled. Finally it was shown that the ratio of radiative heating predicted by the view factor and tangent slab methods is about $\bar{\square}_r = 0.77$ in the stagnation region and does not vary significantly with time during the entry. Therefore, it appears feasible to use a tangent slab approach with an approximate “universal” correction factor for a given vehicle geometry.

Although most other planetary entry problems of interest are not characterized by strong radiation and an optically thin shock layer, the methodology presented herein should prove useful for other simulations as well, since similar curve fits

can be generated for any radiating species of interest. Many entry problems have a mix of important radiators, some of which are heavily absorbed, but others that are optically thin. By modeling the optically thin (or nearly optically thin) components of the shock layer radiation in a coupled fashion, the resulting solution will be a better representation of the fully coupled result. At the least, such a solution will serve as a better starting point for a loosely coupled analysis, reducing the number of expensive iterations required for convergence.

ACKNOWLEDGEMENTS

The authors would like to thank Dr. Dinesh Prabhu (ELORET) for his invaluable inputs into modeling techniques and aerothermal analysis of strongly radiating flowfields, Dr. Chul Park (ELORET) for clarification of the appropriate reaction rates for the electron impact ionization reactions, Michael Tauber (ELORET) for discussions on engineering relations for coupling effects on radiative heating in air, and Drs. Prabhu and Ellis Whiting (ELORET) for their assistance in updating NEQAIR for Titan entry shock layer analysis. The work performed by the 2nd author was supported by the prime contract NAS2-99092 to ELORET.

REFERENCES

- ¹ Lockwood, M., "Titan Aerocapture Systems Analysis," AIAA Paper No. 2003-4799, Jul. 2003.
- ² Takashima, N, Hollis, B., Olejniczak, J., Wright, M., and Sutton, K., "Preliminary Aerothermodynamics of Titan Aerocapture Aeroshell," AIAA Paper No. 2003-4952, Jul. 2003.
- ³ Olejniczak, J., Prabhu, D., Wright, M., Takashima, N., Hollis, B., Sutton, K., and Zoby, V., "An Analysis of the Radiative Heating for Aerocapture at Titan," AIAA Paper No. 2003-4953, Jul. 2003.
- ⁴ Park, C.S. and Bershader, D., "Studies of Radiative Emission from the Simulated Shock Layer of the Huygens Probe," *Proceedings of the 18th International Symposium on Shock Waves*, 1991, pp. 671-676.
- ⁵ Nelson, H.F., Park, C., and Whiting, E.E., "Titan Atmospheric Composition by Hypervelocity Shock Layer Analysis," *Journal of Thermophysics and Heat Transfer*, Vol. 5, No. 2, 1991, pp. 157-165.
- ⁶ Baillion, M., Taquin, G., and Soler, J., "Huygens Radiative Probe Environment," *Proceedings of the 19th International Symposium on Shock Waves*, 1993, pp. 339-346.
- ⁷ Laub, B., "Thermal Protection System Concepts and Issues for Aerocapture at Titan," AIAA Paper No. 2003-4954, Jul. 2003.
- ⁸ Olejniczak, J., Prabhu, D.K., Bose, D., and Wright, M.J., "Aeroheating Analysis for the Afterbody of a Titan Probe," AIAA Paper No. 2004-0486, Jan. 2004.
- ⁹ Way, D., Powell, R., and Edquist, K., "Aerocapture Simulation and Performance for the Titan Explorer Mission," AIAA Paper No. 2003-4951, Jul. 2003.
- ¹⁰ Justus, C. and Duvall, A., "Engineering Level Model Atmospheres for Titan and Neptune," AIAA Paper No. 2003-4803, Jul. 2003.
- ¹¹ Wright, M.J., Candler, G.V., and Bose, D., "Data-Parallel Line Relaxation Method for the Navier-Stokes Equations," *AIAA Journal*, Vol. 36, No. 9, 1998, pp. 1603-1609.
- ¹² Wright, M.J., Loomis, M.A., and Papadopoulos, P.E., "Aerothermal Analysis of the Project Fire II Afterbody Flow," *Journal of Thermophysics and Heat Transfer*, Vol. 17, No. 2, 2003, pp. 240-249.
- ¹³ MacCormack, R.W. and Candler, G.V., "The Solution of the Navier-Stokes Equations Using Gauss-Seidel Line Relaxation," *Computers and Fluids*, Vol. 17, No. 1, 1989, pp. 135-150.
- ¹⁴ Yee, H.C., "A Class of High-Resolution Explicit and Implicit Shock Capturing Methods," NASA TM 101088, Feb. 1989.
- ¹⁵ Wercinski, P., Chen, Y.-K., Loomis, M., Tauber, M., McDaniel, R., Wright, M., Papadopoulos, P., Allen, G., and Yang, L., "Neptune Aerocapture Entry Vehicle Preliminary Design," AIAA Paper No. 2002-4812, Aug. 2002.
- ¹⁶ Lee, J.H., "Basic Governing Equations for the Flight Regimes of Aeroassisted Orbital Transfer Vehicles," *Thermal Design of Aeroassisted Orbital Transfer Vehicles*, ed. H.F. Nelson, Vol. 96, Progress in Astronautics and Aeronautics, AIAA, New York, 1985, pp. 3-53.
- ¹⁷ Gnoffo, P.A., Gupta, R.N., and Shinn, J.L., "Conservation Equations and Physical Models for Hypersonic Air Flows in Thermal and Chemical Nonequilibrium," NASA TP 2867, Feb. 1989.
- ¹⁸ Millikan, R.C. and White, D.R., "Systematics of Vibrational Relaxation," *Journal of Chemical Physics*, Vol. 39, No. 12, 1963, pp. 3209-3213.
- ¹⁹ Gurvich, L., Veyts, I., and Alcock, C., eds., Thermodynamic Properties of Individual Substances, 4th Edition, Hemisphere Publishing Corporation, New York, 1991.
- ²⁰ Park, C., Jaffe, R., and Partridge, H., "Chemical-Kinetic Parameters of Hyperbolic Earth Entry," *Journal of Thermophysics and Heat Transfer*, Vol. 15, No. 1, 2001, pp. 76-90.
- ²¹ Park, C., "Assessment of Two-Temperature Kinetic Model for Air," *Journal of Thermophysics and Heat Transfer*, Vol. 3, No. 3, 1989, pp. 233-244.
- ²² Gordon, S. and McBride, B.J., "Computer Program for Calculation of Complex Chemical Equilibrium Compositions and Applications," NASA RP 1311, Oct. 1994.
- ²³ Gupta, R.N., Yos, J.M., Thompson, R.A., and Lee, K., "A Review of Reaction Rates and Thermodynamic and Transport Properties for an 11-Species Air Model for Chemical and Thermal Nonequilibrium Calculations to 30,000 K," NASA RP 1232, Aug. 1990.

- ²⁴ Ramshaw, J.D., "Self-Consistent Effective Binary Diffusion in Multicomponent Gas Mixtures," *Journal of Non-Equilibrium Thermodynamics*, Vol. 15, No. 3, 1990, pp. 295-300.
- ²⁵ Brown, J.L., "Turbulence Model Validation for Hypersonic Flows," AIAA Paper No. 2002-3308, Jun. 2002.
- ²⁶ Stewart, D.A., "Surface Catalysis and Characterization of Proposed Candidate TPS for Access to Space Vehicles," NASA TM 112206, Jul. 1997.
- ²⁷ Davies, C.B. and Venkatapathy, E.V., "SAGE: The Self-Adaptive Grid Code, Version 3," NASA TM 1999-208792, Aug. 1999.
- ²⁸ Whiting, E.E., Yen, L., Arnold, J.O., and Paterson, J.A., "NEQAIR96, Nonequilibrium and Equilibrium Radiative Transport and Spectra Program: User's Manual," NASA RP-1389, Dec. 1996.
- ²⁹ Labracherie, L., Billiotte, M., and Houas, L., "Shock Tube Analysis of Argon Influence in Titan Radiative Environment," *Journal of Thermophysics and Heat Transfer*, Vol. 10, No. 1, 1996, pp. 162-168.
- ³⁰ Park, C., "Stagnation Point Radiation for Apollo 4," AIAA Paper No. 2001-3070, Jun. 2001.
- ³¹ Hottel, H.C. and Sarofim, A.F., Radiative Transfer, McGraw-Hill Book Company, New York, 1967, pg. 258.
- ³² Goulard, R., "The Coupling of Radiation and Convection in Detached Shock Layers," *Journal of Quantitative Spectroscopy and Radiative Heat Transfer*, Vol. 1, 1961, pp. 249-257.
- ³³ Cauchon, D.L., "Radiative Heating Results from the Fire II Flight Experiment at Reentry Velocity of 11.4 km/s," NASA TM X-1402, Jul. 1967.
- ³⁴ Tauber, M.E., Wercinski, P., Yang, L., and Chen, Y.-K., "A Fast Code for Jupiter Atmospheric Entry Analysis," NASA TM 1999-2208796, Sep. 1999.
- ³⁵ Moss, J.N. and Simmonds, A.L., "Galileo Probe Forebody Flowfield Predictions During Jupiter Entry," AIAA Paper No. 82-0874, Jan. 1982.
- ³⁶ Tauber, M. and Wakefield R., "Heating Environment and Protection During Jupiter Entry," *Journal of Spacecraft and Rockets*, Vol. 8, No. 3, 1971, pp. 630-636.
- ³⁷ Hartung, L., Mitcheltree, R.A., and Gnoffo, P.A., "Coupled Radiation Effects in Thermochemical Nonequilibrium Shock Capturing Flowfield Calculation," AIAA Paper No. 92-2868, Jul. 1992.
- ³⁸ Olynick, D.R., Henline, W.D., Hartung-Chambers, L., and Candler, G.V., "Comparison of Coupled Radiative Flow Solutions with Project Fire II Flight Data," *Journal of Thermophysics and Heat Transfer*, Vol. 9, No. 4, 1995, pp. 586-594.
- ³⁹ Gokcen, T. and Park, C., "The Coupling of Radiative Transfer to Quasi 1D Flows with Thermochemical Nonequilibrium," AIAA Paper No. 91-0570, Jan. 1991.
- ⁴⁰ Sakai, T., Tsuru, T., and Sawada, K., "Computation of Hypersonic Radiating Flowfield over a Blunt Body," *Journal of Thermophysics and Heat Transfer*, Vol. 15, No. 1, 2001, pp. 91-98.
- ⁴¹ Matsuyama, S., Sakai, T., Sasoh, A., and Sawada, K., "Parallel Computation of Fully Coupled Hypersonic Radiating Flowfield Using Multiband Model," *Journal of Thermophysics and Heat Transfer*, Vol. 17, No. 1, 2003, pp. 21-28.
- ⁴² Laux, C.O., "Optical Diagnostics and Radiative Emission of Air Plasmas," HTGL Report No. T-288, Stanford University, Stanford, CA, Aug. 1993.
- ⁴³ Park, C., Nonequilibrium Hypersonic Aerothermodynamics, Wiley, New York, 1990.

Aeroheating Analysis for the Afterbody of a Titan Probe

Joseph Olejniczak*

NASA Ames Research Center, Moffett Field, CA 94035

Dinesh Prabhu,[†] Deepak Bose,[‡]

ELORET Corp., 690 W. Fremont Ave., Suite 8, Sunnyvale, CA 94087

and

Michael J. Wright,[§]

NASA Ames Research Center, Moffett Field, CA 94035

Abstract

Convective and radiative aeroheating results for the afterbody of a candidate aerocapture vehicle for Titan are presented. The aeroheating environment is dominated by radiation from the CN radical that is formed in the nonequilibrium shock layer. Accurate prediction of the radiative heating rates requires accounting both for the non-adiabatic radiative cooling of the flow field and multi-dimensional radiation transport in the flow field. Since the flow field is optically thin to CN radiation, fully coupled flowfield-radiation solutions can be generated and then post-processed to yield the radiative surface heating accounting for three-dimensional radiation transport. The rear stagnation point convective heating rates are found to be less than 0.5 W/cm^2 and less than 3% of the forebody stagnation point heating rates. The rear stagnation point radiative heating is less than 1 W/cm^2 , however large areas of the conical afterbody experience radiative heating levels in the range of $2 - 7 \text{ W/cm}^2$ while the convective heating rates in the same areas are less than 1 W/cm^2 .

Introduction

There is renewed interest at NASA in exploring outer planets and their moons – specifically Titan, a moon of the planet Saturn. An important part of the technology development to enable such exploration missions is aerocapture, in which the space probe is “captured” into orbit after it decelerates aerodynamically using a single pass through the planet’s atmosphere. The high entry speeds associated with an aerocapture trajectory imply that the thermal protection system (TPS) is a key subsystem. Defining the aeroheating environments both in terms of peak heating rate and total heat load is critical for the design of this subsystem.

A one-year system analysis design study¹ of such an aerocapture mission to Titan was recently completed. The study demonstrated that aerocapture missions at Titan provide a significant mass benefit compared to propulsive capture missions, and also identified some of the critical issues for the mission design.²⁻¹² A 70-degree sphere-cone with a 1.875 m maximum radius was selected as the

baseline design for the orbiter, as shown in Fig. 1. For the nominal entry trajectory, the vehicle enters the atmosphere with a relative velocity of 6.5 km/s and flies at a constant 16° angle-of-attack.

For comparable velocities and altitudes at Earth, the corresponding convective heating level would be modest compared to heating on entry vehicles such as the Apollo capsules, the Stardust probe, or the Genesis probe. The radiative heating level would be insignificant. However, Titan has an atmosphere of nitrogen, methane, and argon. The methane in the atmosphere dissociates in the nonequilibrium shock layer and CN forms. The CN molecule is a strong radiator. Therefore, even though the entry velocity and post-shock temperatures are relatively low compared to typical Earth entry, there is significant nonequilibrium radiation from the CN violet [B-X] and CN red [A-X] bands.

Analysis in Olejniczak *et al.*¹² indicated that the radiative heating from CN at the stagnation point would be as high as 300 W/cm^2 , or seven times as large as the convective component of 45 W/cm^2 given by Takashima *et al.*¹¹ These results were consistent with previous analysis.¹³⁻¹⁷ of the ballistic probe Huygens, scheduled to enter the Titan atmosphere as part of the Cassini mission to Saturn.

Therefore, a major finding of the study was that accurate prediction of the aeroheating environment was a significant design issue because the predicted high levels of radiative heating drove the selection and amount of the TPS material required.^{8,12} The aeroheating analysis^{11,12} done as a part of the systems design study was preliminary in the sense that its objectives were 1) to provide rapid, conservative estimates of the aeroheating environment for use by the mission designers, and 2) to identify technical areas that require additional analysis before a mission could be undertaken. Because of the identified importance of quantifying the radiative heating environment for a Titan mission, work has continued on improving the predictions of the aeroheating environment. This paper and a companion paper¹⁷ describe the additional analysis that has been done since the conclusion of the systems study.

* Senior Research Scientist, Reacting Flow Environments Branch. Senior Member AIAA

[†] Senior Research Scientist, Associate Fellow AIAA

[‡] Senior Research Scientist, Senior Member AIAA

[§] Senior Research Scientist, Reacting Flow Environments Branch. Senior Member AIAA

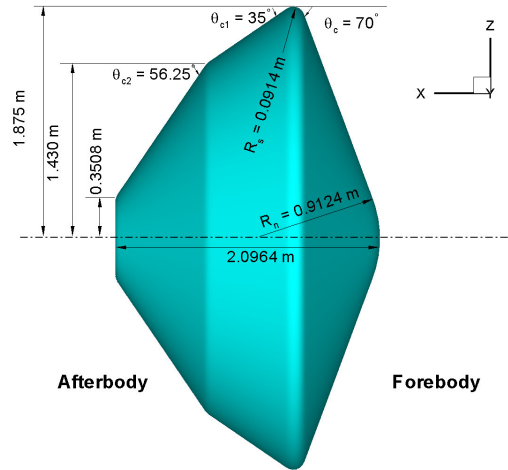


Fig. 1. Candidate configuration of a Titan aerocapture probe.

Specifically, this paper addresses three aspects of the aeroheating analysis that were neglected during the initial work. First, three-dimensional CFD calculations are used to define the convective and radiative heating levels on the probe afterbody. Second, the distributed radiative heating on the afterbody is computed accounting for fully three-dimensional radiation transport in the flow field. Third, non-adiabatic radiative cooling effects on the afterbody flow field are computed using the methodology described in Wright *et al.*¹⁷ While this paper focuses on the afterbody aeroheating environment, Wright *et al.*¹³ focuses on the forebody environment and the development of the radiation-flowfield coupling methodology accounting for radiative cooling effects.

Below, the methodology for computing the three-dimensional flow field is described. After a description of the physical and numerical models used for the CFD computations and the radiation production and transport calculations, the distributed heating results along one design trajectory are presented. Detailed results at seven afterbody surface locations are also shown.

Methodology

The flow field and radiation production and transport are calculated in a tightly coupled manner. In general, fully coupled flowfield-radiation computations require the solution of integro-differential equations. The computational resources required are prohibitive since the transport of radiation from each computational volume must be traced throughout the flow field, accounting for possible absorption by the gas. For the case of Titan aerocapture missions, Olejniczak *et al.*¹² showed two key results: 1) only the CN red and CN violet bands contributed significantly to the surface heating, and 2) those bands are optically thin, meaning that the photons are not absorbed in the flow field. These two results greatly simplify the radiation calculations, and allow an efficient fully coupled methodology to be developed by Wright *et al.*¹⁷ This methodology is compared to the standard loosely-coupled approach and described below. Prior to presenting the results, the trajectory points selected for analysis, the grid generation process, the CFD code and themophysical models used, and the radiation models are described.

Trajectory

In the present work, seven points along the nominal undershoot trajectory¹ using the Yelle minimum atmosphere model⁵ have been selected to compute. Although several design trajectories for different atmosphere models were studied, the above trajectory was selected to use for this work because it yielded the highest radiative heat fluxes and was analyzed in detail in the previous aerothermal analyses.^{11,12} The altitude-velocity map and reference convective heating rate (stag. point) are shown in Figs. 2a and 2b, respectively. Also shown as open symbols in the figures, are the points selected for high-fidelity computational analysis. The points are selected so as to adequately resolve the convective heat pulse, shown in Fig. 3b. The freestream conditions corresponding to the seven selected points are given in Table 1 and are taken from Justus.⁵ The atmospheric composition for the minimum atmosphere model is 95% N₂ and 5% CH₄ by volume, and is modeled to be constant

Table 1. Undershoot aerocapture trajectory points selected for computational analysis. The atmospheric composition is constant at 95% N₂ and 5% CH₄ by volume.

Case #	Time (s)	Altitude (km)	Velocity (km/s)	Density (kg/m ³) x10 ⁴	Pressure (Pa)	Temperature (K)	M
1	174	420	6.558	0.047	0.19	131.9	27.8
2	222	316	6.348	0.507	2.29	149.9	25.3
3 ^a	253	269	5.761	1.491	6.91	152.7	22.7
4	281	245	4.859	2.665	12.35	152.6	19.2
5	308	237	3.978	3.305	15.25	152.4	15.7
6	339	238	3.239	3.212	14.84	152.4	12.8
7	397	255	2.521	2.138	9.89	152.7	9.9

^a Peak convective heating point

at aerocapture altitudes.⁵ Of particular interest is the peak convective heating point ($t = 253$ s). Note that the angle of attack is held constant at 16° throughout the trajectory.

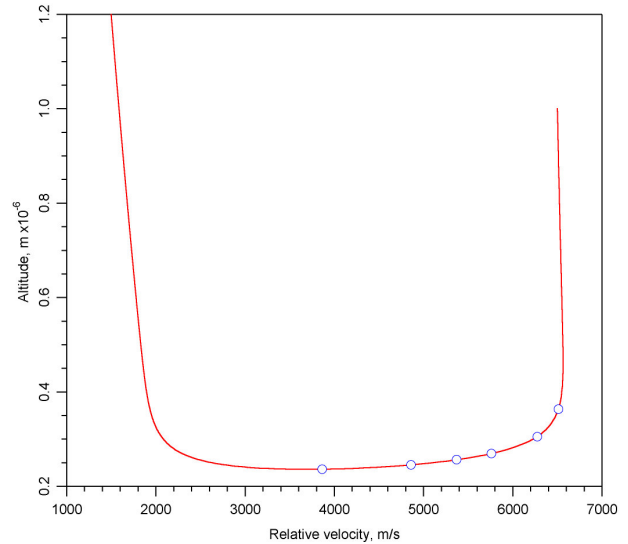
Volume Grid Generation

The volume grid for the configuration is very easily generated using *GridPro*.¹⁸ The basic topology consists of 13 blocks and has two “layers” (Fig. 3a). The advantage of the inner layer is that the grid clustering is confined to it and does not propagate into the outer layer. Another feature of the volume grid is that it is geometrically non-singular, thereby avoiding numerical artifacts in the solution in the stagnation region. The 13-block elementary topology can be reduced to a 4-block topology (Fig. 3b) by merging some of the blocks. This 4-block volume grid with appropriate wall spacing forms the basis for all initial calculations. The initial grid was then easily tailored using the adaptive grid code *SAGE*¹⁹ to align the shape of the outer boundary with the shock wave.

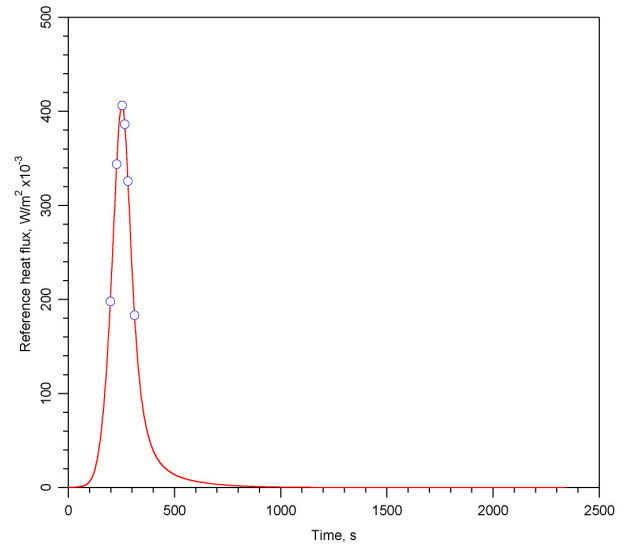
Numerical and Thermophysical Flow Field Modeling

The aerothermal environments at the selected trajectory points are computed using DPLR.^{20,21} DPLR is a parallel multiblock finite-volume code that solves the reacting Navier-Stokes equations including finite-rate chemistry and vibrational nonequilibrium. The Euler fluxes are computed using a modified (low-dissipation) form of Steger-Warming flux vector splitting,²² with third-order spatial accuracy obtained via MUSCL extrapolation coupled with a minmod limiter.²³ Viscous fluxes are computed to second-order accuracy using a central difference approach. Time advancement to a steady-state solution is achieved using the data-parallel line relaxation method.²⁰ Two recent applications of the code were the computation of the Fire II afterbody flow²⁴ and the computation of aerothermal heating for Neptune aerocapture.²⁵

A detailed description of the relevant equations for reentry flows has been presented in a number of sources^{26,27} and will not be repeated here. For typical Titan entry conditions thermal nonequilibrium effects will greatly influence the amount of predicted shock layer radiation. Therefore, two energy equations are solved; a total energy equation and a vibro-electronic energy equation. In this formulation it is assumed that the vibrational and electronic modes of the gas are in equilibrium with each other, but not with the translational-rotational component.²⁶ This model was originally developed for air flows, but should be a reasonable approximation for the nitrogen-dominated Titan atmosphere as well. The energy exchange between the translational-rotational and vibrational-electronic modes is modeled using a Landau-Teller formulation, where relaxation times are obtained from Millikan and White,²⁸ assuming simple harmonic oscillators. Characteristic vibrational temperatures for the simple



(a) Altitude-Velocity map

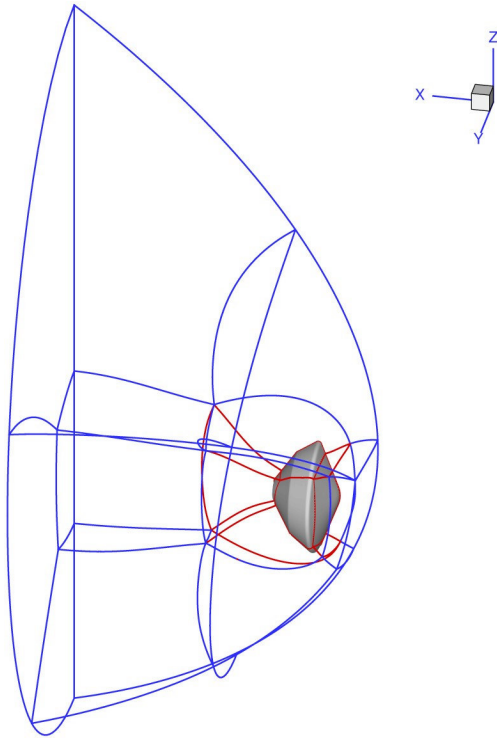


(b) Reference heating rate at stagnation point

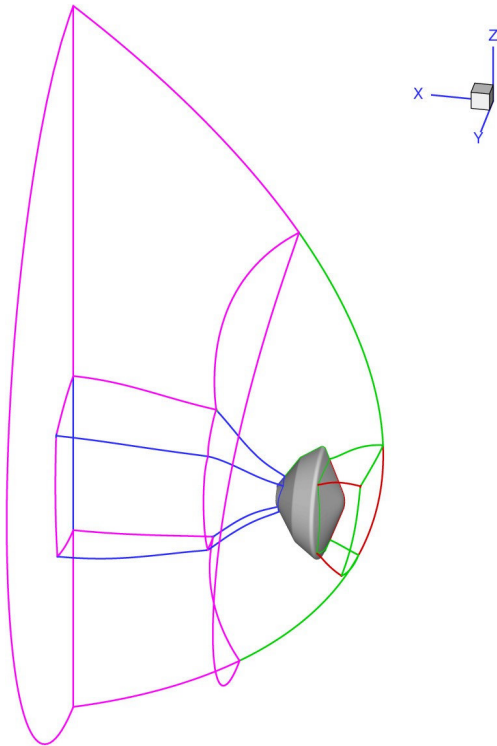
Fig. 2. Undershoot aerocapture trajectory for the Titan probe – (a) altitude-velocity map in a Yelle minimum atmosphere, and (b) reference heating rate at the stagnation point. The relative entry velocity is 6.5 km/s and the ballistic coefficient is 90 kg/m². The angle of attack is held constant at 16° throughout the trajectory. The open symbols are points at which CFD simulations are performed.

harmonic oscillator approximation are taken from Gurvich *et al.*²⁹

For the present work, a 12-species (CH_4 , CH_3 , CH_2 , N_2 , C_2 , H_2 , CH , CN , NH , N , C , H) gas model is used. The chemical kinetics/reaction mechanism for this species set is primarily the same as that developed by Nelson *et al.*³⁰ for application to Titan entry, based on a combination of shock tube data from Park³¹ and pre-existing reaction rate models. The exception is that the heavy particle impact



(a) Elementary Topology – 13 blocks



(b) Merged Topology – 4 blocks

Fig. 3. Volume grid - (a) elementary block, and (b) merged block grid topologies.

ionization reactions in Nelson *et al.* have been changed to electron impact ionization reactions as originally

Table 2. Reaction rates for the Titan kinetic mechanism (Rate = $CT_a^\eta \exp(-\theta_r/T_a)$, M is a generic collision partner).

Reaction	C ($\text{m}^3/\text{kmol}\cdot\text{s}$)	η	θ_r (K)
Dissociation Reactions ($T_a = \sqrt{TT_v}$)			
$\text{C}_2 + \text{M} \leftrightarrow \text{C} + \text{C} + \text{M}$	9.68E+19	-2.0	71000
$\text{N}_2 + \text{M} \leftrightarrow \text{N} + \text{N} + \text{M}$	3.70E+18	-1.6	113200
$\text{CH} + \text{M} \leftrightarrow \text{C} + \text{H} + \text{M}$	1.13E+16	-1.0	40913
$\text{CN} + \text{M} \leftrightarrow \text{C} + \text{N} + \text{M}$	1.00E+20	-2.0	90000
$\text{CH}_4 + \text{M} \leftrightarrow \text{CH}_3 + \text{H} + \text{M}$	2.25E+24	-1.87	52900
$\text{CH}_3 + \text{M} \leftrightarrow \text{CH}_2 + \text{H} + \text{M}$	2.25E+24	-1.87	54470
$\text{CH}_2 + \text{M} \leftrightarrow \text{CH} + \text{H} + \text{M}$	2.25E+24	-1.87	50590
$\text{NH} + \text{M} \leftrightarrow \text{N} + \text{H} + \text{M}$	1.13E+16	-1.0	41820
$\text{H}_2 + \text{M} \leftrightarrow \text{H} + \text{H} + \text{M}$	1.47E+16	-1.23	51950
Exchange Reactions ($T_a = T$)			
$\text{C} + \text{N}_2 \leftrightarrow \text{CN} + \text{N} + \text{M}$	1.11E+11	-0.11	23000
$\text{CN} + \text{C} \leftrightarrow \text{C}_2 + \text{N} + \text{M}$	3.00E+11	0.0	18120
$\text{C}_2 + \text{N}_2 \leftrightarrow \text{CN} + \text{CN}$	7.10E+10	0.0	5330
$\text{H} + \text{N}_2 \leftrightarrow \text{NH} + \text{N}$	2.20E+11	0.0	71370
$\text{H}_2 + \text{C} \leftrightarrow \text{CH} + \text{H}$	1.80E+11	0.0	11490
$\text{CN}^+ + \text{N} \leftrightarrow \text{CN} + \text{N}^+$	9.80E+09	0.0	40700
$\text{C} + \text{N} \leftrightarrow \text{CN}^+ + \text{e}$	1.00E+12	1.50	164440
$\text{C}^+ + \text{N}_2 \leftrightarrow \text{N}_2^+ + \text{C}$	1.11E+11	-0.11	50000
$\text{N} + \text{N} \leftrightarrow \text{N}_2^+ + \text{e}$	1.79E+06	0.77	67500

intended,³² and the rates for those reactions have been updated to currently accepted values.³³ The complete reaction mechanism is given in Table 2. Following the work of Park,³⁴ the governing temperature for all dissociation reactions is assumed to be $T_a = \sqrt{TT_v}$ where T is the translational-rotational temperature, and T_v is the vibrational-electronic temperature. Equilibrium constants are computed using a minimized Gibbs free energy approach,³⁵ that eliminates the need to generate curve fit expressions for each reaction. Species thermodynamic properties are modeled using the curve fit expressions of Gordon and McBride.³⁵ At the entry velocities considered, Takashima *et al.*¹¹ indicate that the flow is weakly ionized. However, the amount of ionization is small enough that the effect on convective and radiative heating predictions is negligible.

The aeroshell surface is assumed to be fully catalytic and in radiative equilibrium ($\varepsilon = 0.85$). No conduction into the surface is considered. The resulting convective heating estimates provide an excellent starting point for a loosely coupled approach to surface material response.

Radiation Modeling

Given a CFD solution as input, the radiation code NEQAIR96³⁶ is used to calculate the emission and transport of radiation in the flow field along lines-of-sight using the tangent slab approximation. In this approximation radiation is assumed to be emitted from infinitely thin parallel planes perpendicular to the absorbing surface. NEQAIR96 performs the calculations line-by-line, computing an absorption coefficient for each atomic line and molecular rotational line in the vibrational bands.

The radiation calculations are made by computing the radiative flux that reaches a location on the surface of the vehicle along a line-of-sight normal to that surface location. The calculations require as inputs the species number densities, translational temperature, and vibrational temperature at each point in the flow field along the line-of-sight. NEQAIR96 computes the amount of radiation produced and the transport of that radiation along each line-of-sight

For most calculations, radiation is computed only from the molecular bands CN violet ($B^2\Sigma^+ \rightarrow X^2\Sigma^+$) and CN red ($A^2\Pi \rightarrow X^2\Sigma^+$). For a few cases, other radiation sources were also modeled. Specifically, the molecular bands considered were $N_2 1+$ ($B^3\Pi_g \rightarrow A^3\Sigma_u^+$), $N_2 2+$ ($C^3\Pi_u \rightarrow B^3\Pi_g$), and N_2 Lyman-Birge-Hopfield ($a^1\Pi_g \rightarrow X^1\Sigma_g^+$). The atomic lines considered were N, C, and H. In all cases, radiation from CN red and CN violet accounted for greater than 97% of the total radiation. Updated molecular spectroscopic data from Laux³⁷ and atomic spectroscopic data from NIST³⁸ were used in NEQAIR96.

While CFD calculates the number of molecules and atoms in the ground electronic state, radiation is emitted from excited electronic states of molecules and atoms. Therefore, a collisional-radiative excitation model is needed to compute the number of electronically excited molecules and atoms and their distribution among vibrational and rotational states.

Since no validated excitation model is available for a nitrogen, methane, and argon gas mixture, the excited electronic states of the molecules and atoms were assumed to be in equilibrium, and therefore populated in a Boltzmann distribution governed by the vibrational temperature of the gas. While such an assumption is inappropriate for air mixtures, it is a reasonable approximation when CN is the main radiator emitting in the violet and red bands. Since the ground ($X^2\Sigma^+$), first excited ($A^2\Pi$), and second excited ($B^2\Sigma^+$) states of the CN molecule lie close together and are distinct with no crossings, it is a reasonable first approximation to assume that gas collisional rates will be sufficiently high to maintain a Boltzmann distribution among the first three electronic states. Since the rotational and translational temperatures are assumed to be in equilibrium, the

rotational populations of the vibrational states are governed by the translational temperature of the gas.

Flowfield-Radiation Coupling

Typically, radiation calculations are either uncoupled from or loosely-coupled to the flow field calculations. In an uncoupled approach, the radiation solver essentially post-processes the CFD results to compute the radiative heating on the surface along lines-of-sight normal to the surface. Implicit in this methodology is the assumption that the flow is adiabatic. In other words, the amount of energy that is lost due to radiation is negligible compared to the total energy in the flow field.

This adiabatic assumption can be evaluated by examining the radiative cooling parameter, or Goulard number³⁹

$$\Gamma = 2q_{rad} / \frac{1}{2}\rho_{\infty}V_{\infty}^3 \quad (1)$$

where q_{rad} is the stagnation point radiative heat flux, ρ_{∞} is the freestream density, and V_{∞} is the freestream velocity. The factor of two in the numerator of Eqn. (4) accounts for the fact that emission is isotropic; as much radiation is directed away from the surface as is directed towards it, and thus the total radiation flux along the stagnation line is twice that intercepted by the body. The radiative cooling parameter is essentially the ratio of the radiation energy flux to the total energy flux, and for optically thin gases is a direct measure of the amount of flow energy converted to radiation. When Γ becomes large ($\Gamma > 0.01$) the amount of flow energy converted to radiation has a significant impact on the fluid dynamics and chemical kinetics of the flow.

Using the results of Takashima *et al.* and Olejniczak *et al.*, the Goulard number at the peak convective heating point ($t = 253$ s) of the minimum atmosphere undershoot trajectory is $\Gamma = 0.4$. The large values of Goulard number predicted for Titan aerocapture are due to the peculiar conditions of Titan entry. The atmospheric composition of Titan is ideal for CN formation behind a relatively low speed shock wave. Furthermore, CN is very strong radiator even at the moderate post-shock temperatures typical of Titan entries.

This large value of the Goulard number makes it clear that accurate prediction of the aeroheating environment requires accounting for flowfield-radiation coupling. Previously, a loosely-coupled methodology has been used.^{40,41} In this approach the amount of radiative energy in each computational volume computed with the radiation solver is input back into the CFD computation as a sink term in the energy equation. The flow field is re-computed, and the solution is again processed by the radiation solver. This procedure is repeated iteratively until the solutions converge. However, this method becomes intractable for cases with strong coupling, due to the large number of iterations between the CFD and radiation solvers required to achieve convergence.

Another approach is to directly solve the coupled equation set,^{42,43,44} but the resulting algorithms require enormous computational resources and largely intractable for problems in three spatial dimensions.

Wright *et al.*¹⁷ have developed a tightly coupled methodology that applies to any flow field that is optically thin (no absorption), such as for Titan aerocapture. With no absorption in the flow field, it is possible to greatly simplify the coupled problem. The analysis reduces to a pointwise computation of emission per unit volume. All radiation produced is assumed to leave the computational domain without interacting with the rest of the flow or the surface. Thus, radiation coupling in an optically thin gas acts as a volumetric sink term in the relevant energy conservation equations, depending only on the local flow field properties. Assuming a Boltzmann distribution of the excited states, emission per unit volume is a function (to first-order) only of the number density of CN molecules available to radiate and the vibro-electronic temperature of the gas. Therefore, analytical fits of the NEQAIR96-computed optically thin emission for CN red and CN violet emission as a function of CN number density and vibro-electronic temperature are generated and incorporated into DPLR. The curve fit is of the form:

$$E_{is} = N_s \exp(A_{1,is} / z + A_{2,is} + A_{3,is} \ln(z) + A_{4,is} z + A_{5,is} z^2) \quad (2)$$

where E_{is} is the total radiative emission for molecular band i of species s in $W/(m^3 \cdot sr)$, N_s is the number density of the radiating species in particles/ m^3 , $z = 10000/T_v$, and $A_1 - A_5$ are curve fit constants. Values of the constants in Eqn. (2) for CN red and CN violet emission are given in Table 3. Further details are given in Wright *et al.*¹⁷ While it is expected that the radiative cooling will have a large effect on the forebody flow field, its effect on the afterbody flow field is examined in this paper.

Radiation Transport

When using NEQAIR, the total amount of radiation reaching the surface is integrated along each line of sight using a tangent slab approximation. In the tangent slab approximation, it is assumed that the input line of sight represents an infinite slab of gas parallel to the surface at that point. However, in reality the shock layer is curved due to body curvature. Therefore, a correction factor must be applied to the tangent slab result to account for surface curvature effects. The net radiative heating to the body then becomes

$$q_{rad} = \alpha_r q_{ts} \quad (3)$$

where q_{rad} is the net radiative heating, α_r is the correction factor for surface curvature, and q_{ts} is the tangent slab result. The value of this correction factor is a function of the surface geometry and the amount of absorption in the flow field. For the stagnation region in blunt body air

Table 3. Curve fit parameters for CN violet [B-X] and red [A-X] emission.

	A_1	A_2	A_3	A_4	A_5
CN violet	-0.24820	-28.088	1.2171	-4.2147	0.02354
CN red	-0.51122	-33.016	0.1590	-1.4679	0.00661

flows, values between 0.75-0.85 have been used.^{45,46} The appropriate value to use away from the stagnation point is not well understood. One of the objectives of this paper is to determine what values of α_r are appropriate for optically thin afterbody flow fields.

Determining these α_r values is possible because the radiative transport equations can be simplified for the case of optically thin radiation. The tangent-slab approximation can be discarded and a view-factor based approach to computing the radiative heating at each body point can be used. In a finite-volume approximation, the radiative heat flux at any point on the surface of the vehicle is the sum of radiative fluxes due to each emitting computational cell in the flowfield. The total heat flux at each surface point can be computed simply from the radiation intensity from each computational volume and the view factor that determines the amount of that radiation that reaches a given surface cell. Details of the method are given in Wright *et al.*¹⁷

Results

Three-dimensional flow field computations have been made at the seven trajectory points listed in Table 1. At each trajectory point except $t = 174$ s, there are calculations both with and without tightly-coupled radiation. A tightly coupled solution at $t = 174$ s could not be obtained. This point is a low density condition that is at the edge of applicability of the Navier-Stokes equations, and a DSMC solution is most likely required. The uncoupled results, described in detail below, predict that the radiative heating on the afterbody at $t = 174$ s is higher than at $t = 222$ s. This interesting result needs to be further investigated using DSMC methods.

For each of the uncoupled and coupled solutions, NEQAIR96 was used to compute the radiative heating at ten points on the surface of the vehicle using the tangent slab approximation along a line-of-sight normal to the surface. The location of these surface points is shown in a later figure. The line-of-sight data was extracted at equispaced points using version 9.2 of the visualization software Tecplot.⁴⁷

First, some general results will be discussed. Then, the convective heating results on the afterbody will be presented for the uncoupled and coupled calculations. Finally, comparisons will be presented among the results for the four different methods of computing radiative heating: uncoupled, tangent slab; coupled tangent slab;

Table 4. Computed aerodynamic coefficients for the uncoupled solutions.

	t=174 s	t=222 s	t=253 s	t=281 s	t=308 s	t=339 s	t=397 s
C_L	0.330	0.349	0.351	0.349	0.349	0.353	0.353
C_D	1.440	1.423	1.420	1.412	1.414	1.427	1.410
L/D	0.230	0.245	0.247	0.247	0.247	0.247	0.250

uncoupled, view factor; and coupled view factor. The forebody aeroheating results are presented in the companion paper Wright *et al.*¹⁷

The aerodynamic coefficients extracted from the computed solutions provide a good first check on the quality of the results. The lift and drag coefficients, and the L/D ratios at the seven trajectory points for the uncoupled solutions are shown in Table 4. The computed values are in good agreement with the L/D value of 0.25 assumed in the trajectory/mission studies. The value of L/D at $t=174$ s is less than the nominal value of 0.25 due to viscous effects at high altitudes. The computed coefficients for the coupled solutions are within 3% of the coefficients for the uncoupled solutions.

Some general features of the solutions can be seen by

examining the results from the uncoupled peak convective heating trajectory point, $t = 253$ s. Figures 4a and 4b show the pitch-plane contours of translational/rotational and vibrational/electronic temperatures, respectively. The interesting feature to note is that the vibrational/electronic temperatures remain high in the expanding portion of the flow immediately past the shoulder of the probe. These elevated temperatures will have significant impact on the radiative heating. The ten lines-of-sight at which radiative heating was computed using NEQAIR96 are also shown in the figure.

A detailed examination of the heating contribution from the wavelength range of 500-15000 Å showed that greater than 97% of the radiation is from CN. The violet band system contributes approximately 90% of the

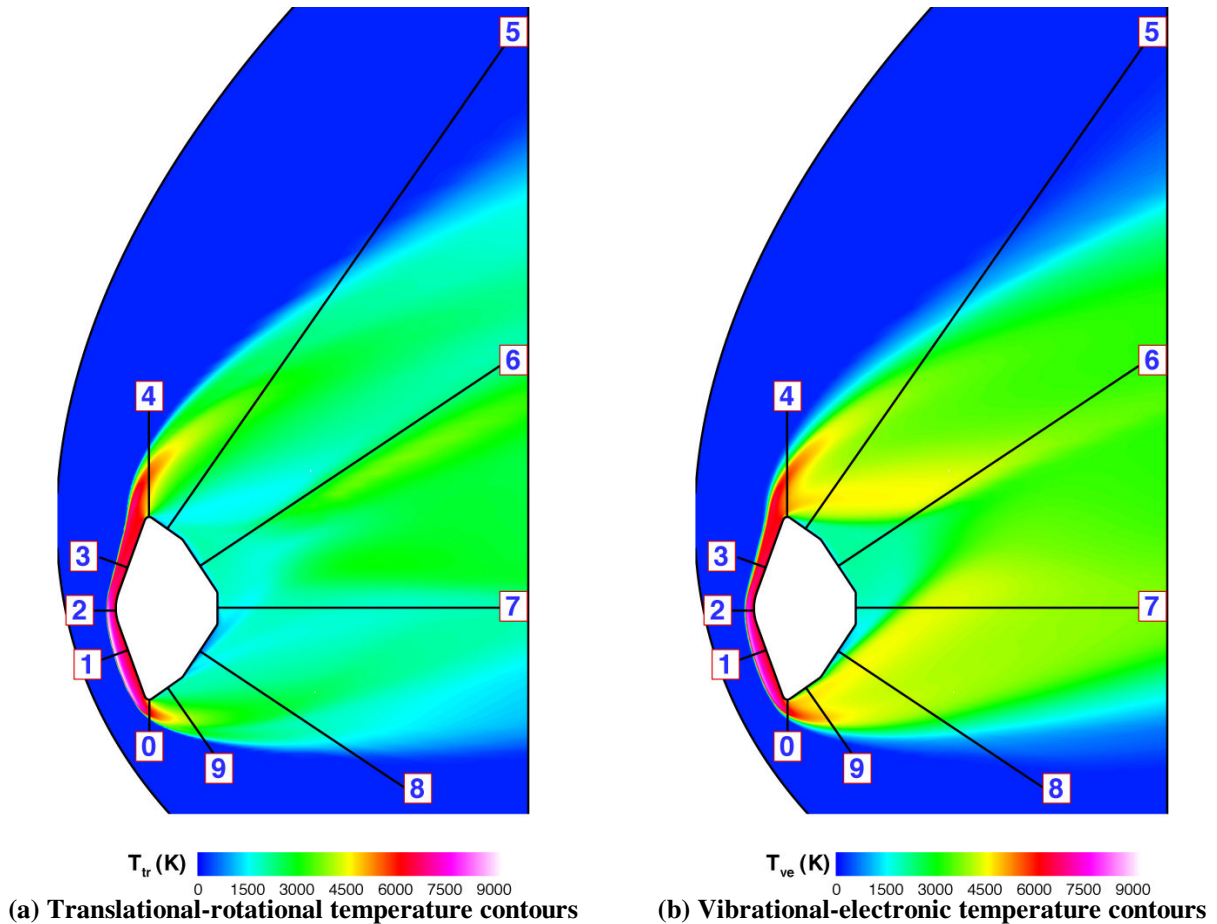


Fig. 4. Pitch plane contours of – (a) trans-rotational temperatures, and (b) vibrational electronic temperatures for the $t = 253$ s trajectory point. Also shown are the 10 pitch-plane lines of sight for radiative heating calculations.

radiation, and the red system the remaining 10%. While some variation in this split may occur for different trajectory points and at different surface points, no attempt was made to quantify this ratio. Figure 5 shows the pitch plane contours of mole fractions of potential radiating species. Note the different scale for each species. Even though there are significant amounts of N, H, and C, the temperature is too low for the atomic species to contribute to the radiative heating. It should be noted that even in the forebody region the temperatures are too low for any radiative heating from nitrogen molecular bands.

Most of the NEQAIR96 calculations were done using Voigt line shape profiles and by spreading 50000 points over 1000 Å regions. Because the flow is optically thin to CN red and violet, this resolution was believed to be adequate. Selected lines-of-sight were also computed using 50000 points spread over 50 Å regions. The results on the coarser intervals were consistently 2-3% higher than the results on the finer intervals, justifying the use of the coarse intervals.

Figure 6 shows the fore and aft views of the surface streamtraces. The streamline pattern on the forebody is simple and consists of one stagnation point. The interesting feature is that the fore stagnation point is on the frustum rather than on the spherical portion. This is despite the fact that the angle of attack of 16° is less than 20° sweepback of the frustum generator. The aft streamtrace pattern clearly shows multiple stagnation poi

Convective Heating

Radiative cooling effects have a significant impact on the convective heating. Figure 7 shows the afterbody convective surface heat transfer rates for the uncoupled (left) and coupled (right) solutions. The heating reduction due to radiative cooling at the aft stagnation point is almost a factor of three. Compared to the coupled solution, the uncoupled solution shows a large area of high heating rates around the shoulder on the lower, windward side of the probe. By removing energy from the forebody region of the flow, the radiative cooling moves the bow shock closer to the body, and reduces the temperatures in the wake region, lowering the heat

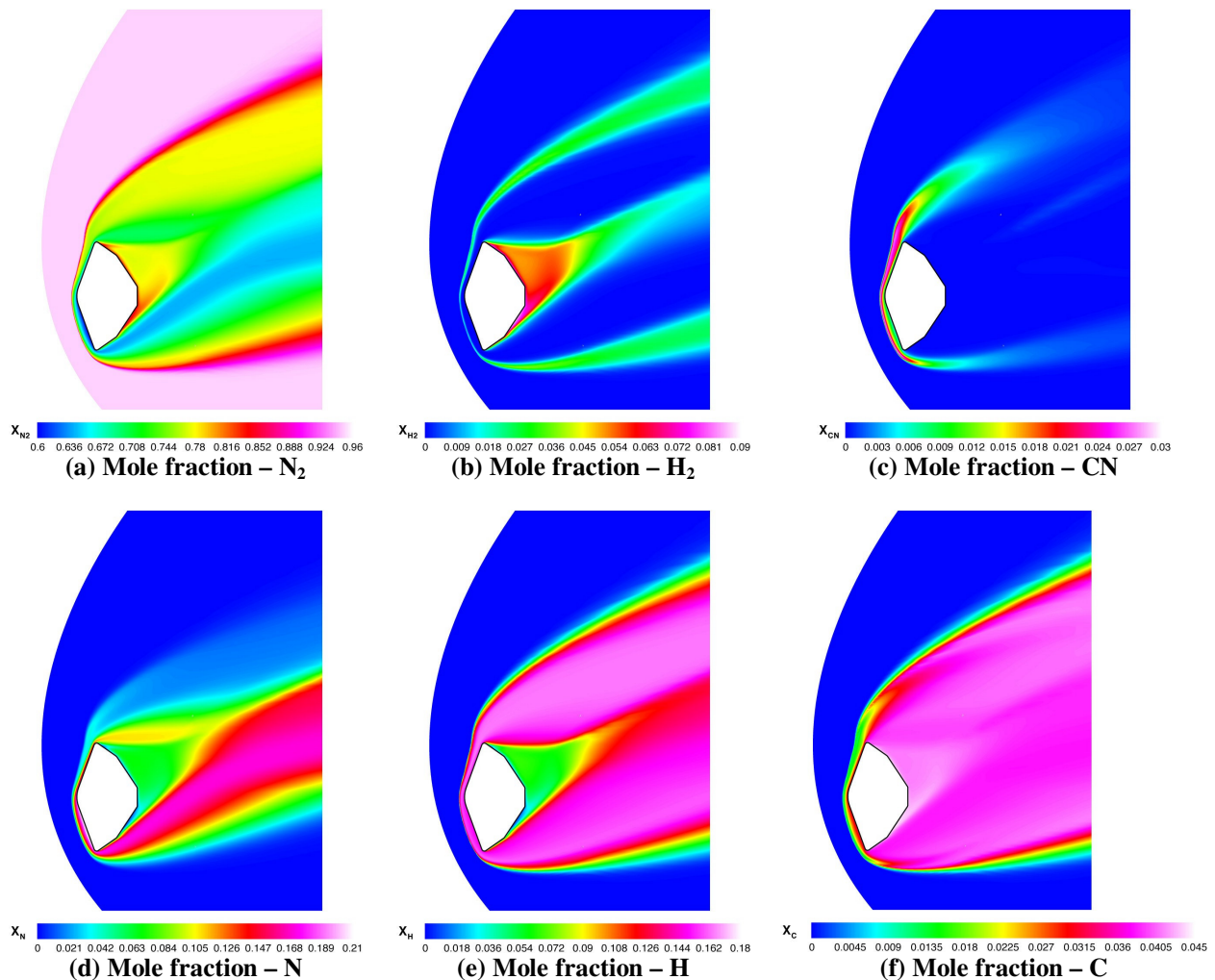


Fig. 5. Pitch plane contours of mole fractions of select species. Note different contour scales for each species.

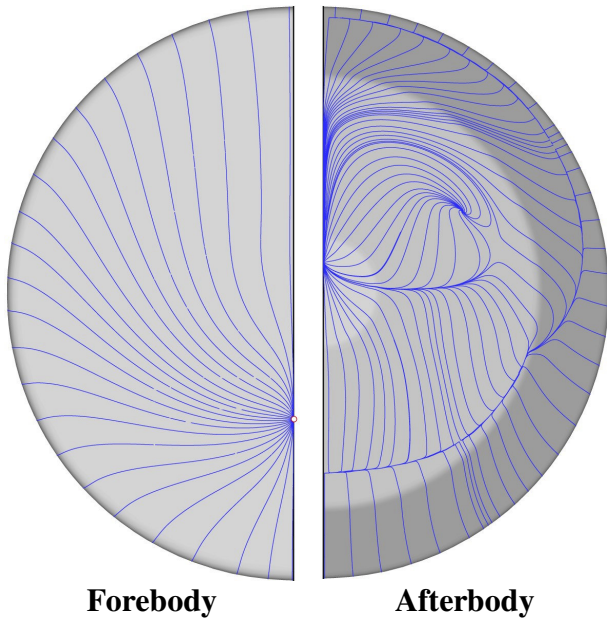


Fig. 6. Surface streamtraces for the fore and afterbody

transfer. Results for the other trajectory points are similar, although the reduction in heating rate due to radiative cooling is not as large.

Figure 8 shows the distributed convective heating along the pitch plane of the afterbody for the six trajectory points including coupled radiation. The heating distributions for the uncoupled cases are similar, but have higher levels. The stagnation point is located at $z = 0.32$ m for all the trajectory points and for both the uncoupled and coupled solutions. The heating rates on the first conical section of the lower part of the afterbody ($z < -1.43$ m) are highest for the $t = 253$ s trajectory point, not the $t = 281$ s trajectory point which has the highest stagnation point heating rate.

The afterbody stagnation point heating rate is shown in Fig. 9 as a function of time along the trajectory. Radiation coupling causes peak afterbody stagnation point heating to occur later in the trajectory compared to the uncoupled cases. The radiation coupling does not directly affect the afterbody flow field, but rather the coupling changes the forebody shock location and shape in the shoulder region, which in turn alters the afterbody flow field. Radiative cooling effects are strong for the times up to $t = 308$ s. At $t = 308$ s the amount of radiation is small, and so is the corresponding effect on the flow field. The ratio of afterbody stagnation point heating to forebody stagnation point heating varies from about 0.007 early in the trajectory to 0.031 late in the trajectory for both the uncoupled and coupled computations.

For the uncoupled computations, the maximum convective afterbody heating rate is 0.7 W/cm^2 . For the coupled computations, the maximum value drops to 0.4 W/cm^2 . Considering only the convective heating, these

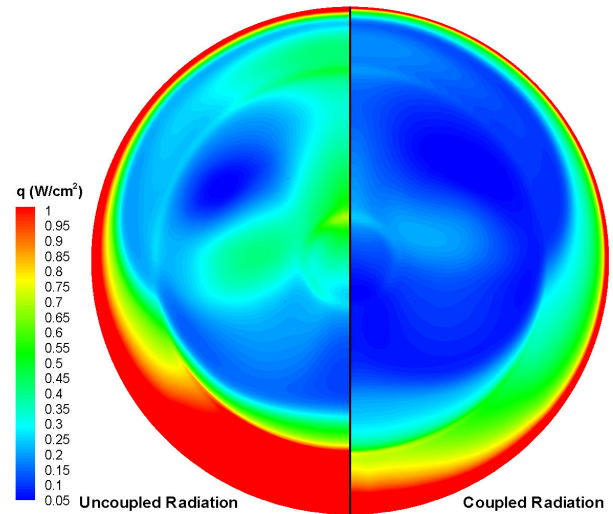


Fig. 7. Afterbody convective heating for the $t=253$ s trajectory point. Left: uncoupled solution. Right: coupled solution.

values correspond to radiative equilibrium surface temperatures of 620 K and 540 K, respectively.

Radiative Heating

In this section the radiative heating results are presented. Two sets of comparisons are shown: the uncoupled vs. coupled predictions, and the tangent slab vs. view factor predictions.

First, results comparing radiative heating levels using the view factor approach for uncoupled and coupled radiation are presented. Figure 10 shows the radiative heating on the afterbody for the $t = 253$ s trajectory point. The effect of radiative coupling is to reduce the radiative heating on the afterbody by 25 to 75%. The results are similar for the other trajectory points and are not shown.

Figure 11 shows a comparison of the distributed convective and radiative heating rates along the afterbody pitch plane for both the coupled and uncoupled solutions for the $t = 253$ s trajectory point. The radiative heating levels are significantly higher than the convective heating levels on the conical sections of the afterbody. For the coupled case, at the lower shoulder the radiative heating is 21 W/cm^2 compared to a convective heating rate of 6 W/cm^2 . On the upper shoulder, the radiative heating level is 23 W/cm^2 compared a convective heating level of 3 W/cm^2 . The radiative heating level on the flat section of the afterbody is lower than on the conical section because it does not have a view of the bow shock. In other words, there is no direct line-of-sight from the strongly radiating regions of the flow field to the flat section of the afterbody. Only radiation from the cooler regions of the wake reaches this surface, and the radiative heating levels are about the same as the convective heating levels. These results clearly show that just like for the forebody, the afterbody TPS selection and design are driven by the radiative heating levels.

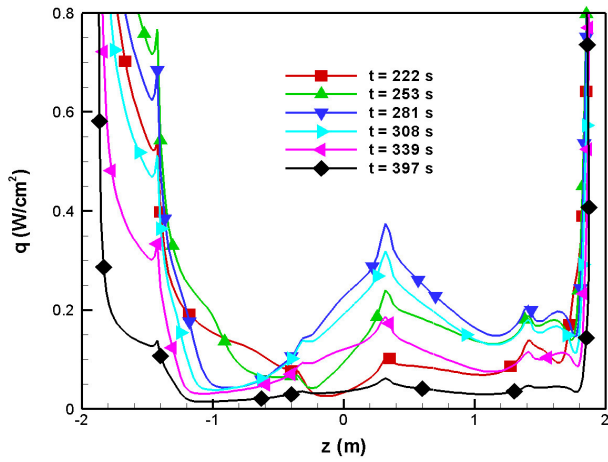


Fig. 8. Afterbody convective heating including coupled radiation.

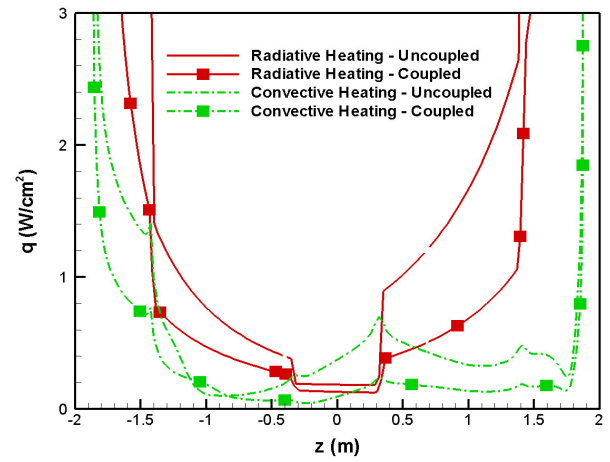


Fig. 11. Distributed afterbody convective and radiative heating at t=253 s

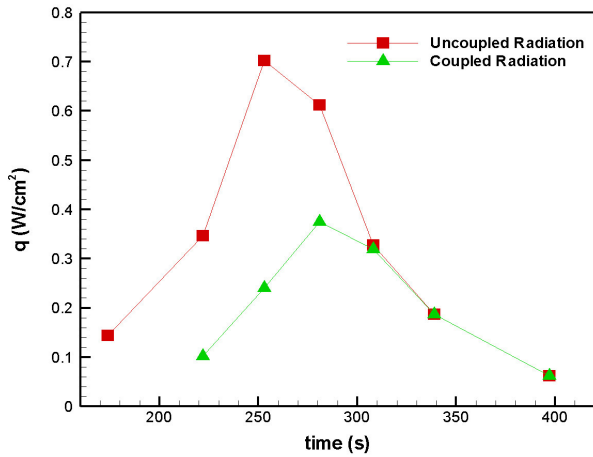


Fig. 9. Afterbody stagnation point convective heating

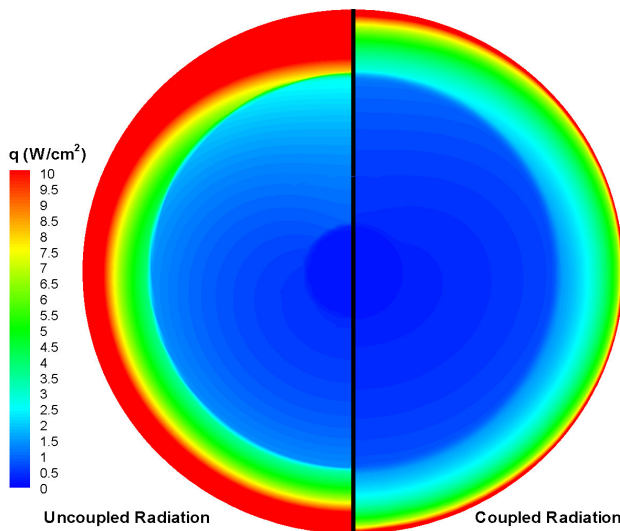


Fig. 10. Afterbody radiative heating at t=253 s.

Figures 12, 13, and 14 show the radiative heating rates computed using the view factor methodology at seven afterbody surface locations. Uncoupled and coupled results are shown. In Fig. 12 the heating rates on the surface at the bottom shoulder (labeled LOS0) and top (labeled LOS4) shoulder are shown. The heating rates on the both shoulders are about the same for the coupled solutions, unlike in the uncoupled case. Figure 13 shows the heating rates at the mid-point of the first conical sections after the shoulders. Not shown, at $t = 308$ s the convective and radiative heating rates are about the same, and at the later two trajectory points considered the radiative heating rates are negligible compared to the convective heating rates. Figure 14 shows the radiative heating rates on the second conical sections and the flat portion of the afterbody. The coupled radiative heating levels are less than 1 W/cm^2 . Although small, these heating rates are about the same as the convective afterbody stagnation point heating rates for $t < 308$ s. The uncoupled radiative heating rates for $t = 174$ s are higher than for $t = 222$ s. No coupled solution is available. While the magnitude of the radiative heating is small, this result should be investigated. The DSMC calculations needed to perform such an investigation are beyond the scope of the current work.

Radiative heating rates have also been generated using the tangent slab approximation. Tangent slab is a convenient, widely-used approximation that reduces the radiation transport problem to be 1-dimensional. Tangent slab assumes a flat surface with uniform, parallel planes of radiating gas above the surface. The radiative heating rate is computed by considering a line-of-sight normal to the surface at the point of interest. The radiative heating only depends on the gas directly above the surface point of interest. In blunt body stagnation regions, tangent slab overpredicts the amount of radiative heating. For optically thin flow fields there is a simple geometric reason for the overprediction. While the stagnation region flow is

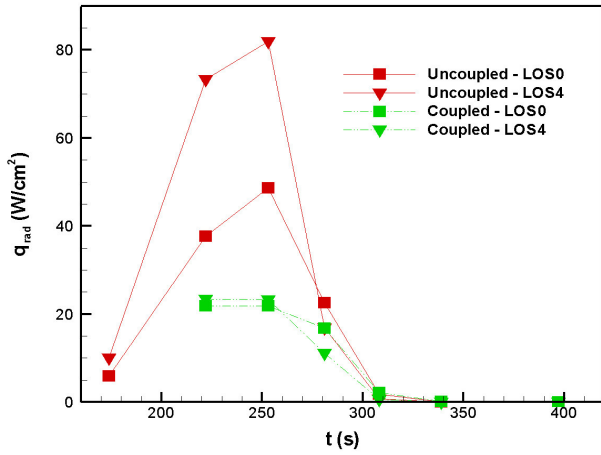


Fig. 12. Afterbody radiative heating at the top shoulder (LOS0) and the bottom shoulder (LOS4).

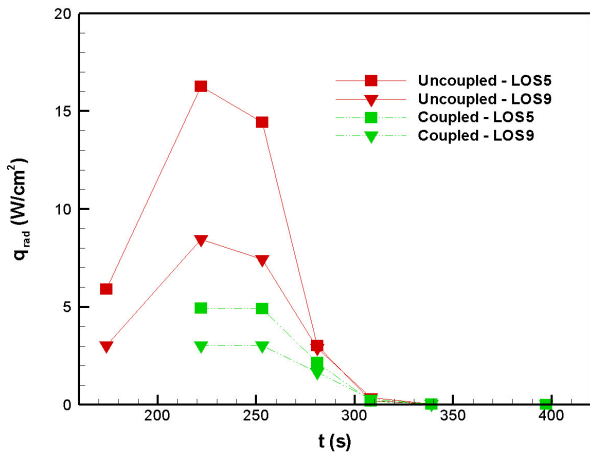


Fig. 13. Afterbody radiative heating on the top conical flank (LOS5) and on the bottom conical flank (LOS9).

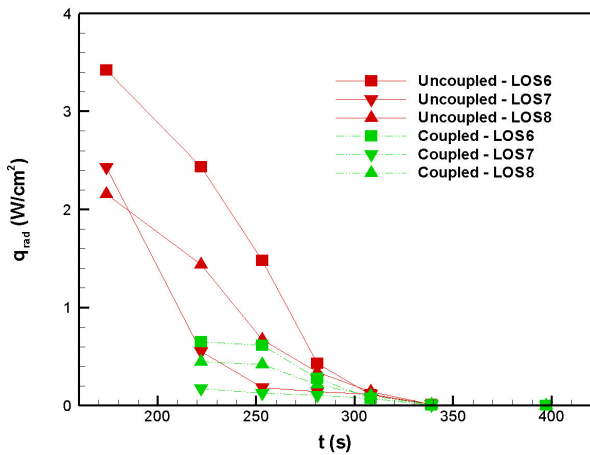


Fig. 14. Afterbody radiative heating at the second top conical flank (LOS6), the rear section (LOS7), and the second bottom conical flank (LOS8).

approximately uniform, the actual surface is curved and therefore has less view of the radiating volume than a straight surface. A reduction factor of between 0.75 and 0.85 has been shown to give good results over a range of freestream conditions and blunt body geometries.^{45,46} For non-stagnation regions, there is no reason to expect that a constant correction factor will be appropriate. The value of the correction factor will vary both with the surface curvature and the freestream conditions that determine the shock shape and location. In the afterbody region of a blunt probe, both the flat surface assumption and the uniform flow field assumption are violated. Even though we do not expect tangent slab to be valid in the afterbody region, it is instructive to compare the view factor results to the tangent slab results since the tangent slab approximation is so widely used.

Tables 5 and 6 show the tangent slab correction factors for the seven afterbody surface points shown in Fig. 4. A quick glance at the tables show that the correction factor is not constant neither at a surface point throughout the trajectory, nor at a time in the trajectory for all surface points. The correction factor even differs considerably between the uncoupled and coupled cases. The values range from 0.37 to over 75 for the uncoupled LOS7 case. This high value is somewhat misleading since the radiative heating predicted using the view factor methodology is only 0.18 W/cm².

Nevertheless, these results show that tangent slab is not always conservative, particularly for the flat region of the afterbody around the rear stagnation point. This region sees a portion of the wake that contains more CN and is

Table 5. Correction factors to tangent slab uncoupled radiative heating rates.

	LOS0	LOS4	LOS5	LOS6	LOS7	LOS8	LOS9
t=174s	0.65	0.52	0.43	0.33	0.33	0.66	0.67
t=222 s	0.58	0.45	1.26	3.98	16.82	0.75	0.81
t=253 s	0.61	0.52	2.47	10.59	75.28	1.24	1.21
t=281 s	0.70	0.56	1.57	0.73	1.64	0.82	1.15
t=308 s	0.74	0.58	0.89	0.40	0.37	0.68	0.85
t=339 s	0.71	0.53	0.79	0.41	0.41	0.72	0.78
t=397 s	0.73	0.70	0.82	0.43	0.37	0.78	0.74

Table 6. Correction factors to tangent slab coupled radiative heating rates.

	LOS0	LOS4	LOS5	LOS6	LOS7	LOS8	LOS9
t=222 s	0.90	0.45	1.31	1.26	5.96	0.70	1.01
t=253 s	0.63	0.37	2.05	2.61	52.45	1.63	1.34
t=281 s	1.08	0.54	1.76	0.63	0.71	0.77	1.31
t=308 s	1.10	0.56	0.96	0.40	0.35	0.68	0.95
t=339 s	0.95	0.51	0.83	0.40	0.39	0.74	0.83
t=397 s	0.74	0.71	0.78	0.40	0.34	0.76	0.74

hotter than the line-of-sight normal to the midpoint of this region. At the lower shoulder (LOS0), since the shock is close to the surface, the radiative heating is very sensitive to the shock shape and exact distance from the surface. The tangent slab approximation cannot accurately model this behavior because it only considers one line normal to the surface. The view factor results show that the correction factor varies from 0.58 to 0.69 for the uncoupled solutions while there is significant radiative heating ($222 \text{ s} < t < 281 \text{ s}$), and from 0.89 to 1.07 for the coupled solutions over the same time range. At the top shoulder (LOS4) the shock is further from the body, and the correction factor is closer to being constant and is always conservative.

Summary and Concluding Remarks

The afterbody aeroheating environment for a candidate Titan aerocapture vehicle is dominated by radiation from the CN radical formed in the nonequilibrium shock layer. Considering the undershoot design trajectory using the minimum atmosphere model, convective heating rates are generally less than 1 W/cm^2 on the entire afterbody, while the radiative heating rates on large areas of the afterbody are up to 7 W/cm^2 . Radiative heating rates at the shoulders are up to 20 W/cm^2 compared to a maximum convective heating of 6 W/cm^2 .

Accurate prediction of the radiative heating rates requires modeling the non-adiabatic radiative cooling of the flow field. Because the CN radiation is optically thin, it is possible to tightly couple the radiation calculations to the flow field calculation. The radiation-flowfield coupling removes energy from the flow field and reduces both the convective and radiative heating on the afterbody by 25 to 70%, depending on the specific surface location and time along the trajectory. The effect of the coupling is to reduce the forebody shock stand-off distance, and thereby alter the afterbody flow field.

Additionally, multi-dimensional radiation transport in the flow field is modeled by using a view factor approach to compute the radiative surface heating. Since the gas is optically thin, the radiative heating at any surface point is the sum of the radiation from all of the gas volumes that the surface point sees. It is found that accurate radiative heating rate predictions at the shoulder and on the afterbody require such a view factor approach. The usual tangent slab approximation is shown to be non-conservative for many points on the surface, and no constant correction factor can be applied to the tangent slab results to approximate the view factor results.

Acknowledgments

Ellis Whiting provided invaluable assistance in using the NEQAIR96 code. Dinesh Prabhu and Deepak Bose

were supported by NASA Ames Research Center, through contract NAS2-99092 to ELORET.

References

- ¹ Lockwood, M.K., "Titan Aerocapture Systems Analysis," AIAA Paper No. 2003-4799, Jul. 2003.
- ² Bailey, R., Hall, J., and Spilker, T., "Titan Aerocapture Mission and Spacecraft Design Review," AIAA Paper No. 2003-4800, Jul. 2003.
- ³ Noca, M., Bailey, R., and Dyke, R., "Titan Explorer Mission Trades from the Perspective of Aerocapture," AIAA Paper No. 2003-4801, Jul. 2003.
- ⁴ Haw, R., "Approach Navigation for a Titan Aerocapture Orbiter," AIAA Paper No. 2003-4802, Jul. 2003.
- ⁵ Justus, C. and Duvall, A., "Engineering-Level Model Atmospheres for Titan and Neptune," AIAA Paper No. 2003-4803, Jul. 2003.
- ⁶ Masciarelli, J. and Queen, E., "Guidance Algorithms for Aerocapture at Titan," AIAA Paper No. 2003-4804, Jul. 2003.
- ⁷ Way, D., Powell, R., Masciarelli, J., and Starr, B., "Aerocapture Simulation and Performance for the Titan Explorer Mission," AIAA Paper No. 2003-4951, Jul. 2003.
- ⁸ Laub, B., "Thermal Protection Concepts and Issues for Aerocapture at Titan," AIAA Paper No. 2003-4954, Jul. 2003.
- ⁹ Hrinda, G., "Structural Design of the Titan Aerocapture Mission," AIAA Paper No. 2003-4955, Jul. 2003.
- ¹⁰ Dyke, R., "Planetary Probe Mass Estimation Tool Development and Its Application to Titan Aerocapture," AIAA Paper No. 2003-4956, Jul. 2003.
- ¹¹ Takashima, N., Hollis, B., Olejniczak, J., Wright, M., and Sutton, K., "Preliminary Aerothermodynamics of Titan Aerocapture Aeroshell," AIAA Paper No. 2003-4952, Jul. 2003.
- ¹² Olejniczak, J., Prabhu, D., Wright, M., Takashima, N., Hollis, B., Sutton, K., and Zoby, V., "An Analysis of the Radiative Heating for Aerocapture at Titan," AIAA Paper No. 2003-4953, Jul. 2003.
- ¹³ Baillion, M., Pallegoix, J.F., and Soler, J., "Huygens Probe Aerothermodynamics," AIAA Paper No. 97-2476, Jul. 1997.
- ¹⁴ Baillion, M., Taquin, G., and Soler, J., "Huygens Probe Radiative Environment," *Proceedings of the 19th International Symposium on Shock Waves, Shock Waves at Marseille II: Physico-Chemical Processes and Nonequilibrium Flow*, Springer-Verlag, 1995, p. 339-346.
- ¹⁵ Baillion, M. and Taquin, G., "Radiative Heat Flux: Theoretical and Experimental Predictions for Titan Entry Probe," *Capsule Aerothermodynamics*, AGARD Report No. 808, May 1997.
- ¹⁶ Nelson, H.F., Park, C., and Whiting, E.E., "Titan Atmospheric Composition by Hypervelocity Shock-Layer Analysis," *J. Thermophysics & Heat Transfer*, Vol. 5, No. 2, pp. 157-165, Apr.-Jun. 1991

- ¹⁷ Wright, M.J., "The Impact of Flowfield-Radiation Coupling on Aeroheating for Titan Aerocapture," AIAA 2004-0484, Jan. 2004.
- ¹⁸ Program Development Corp., 300 Hamilton Avenue, Suite 409, White Plains, NY 10601, GridPro/az3000 User's Guide and Reference Manual, 1996.
- ¹⁹ Davies, C.B., "SAGE The Self-Adaptive Grid codE: Version 3," NASA/TM-1999-208792, August 1999.
- ²⁰ Wright, M.J., Candler, G.V., and Bose, D., "Data-Parallel Line Relaxation Method for the Navier-Stokes Equations," AIAA Journal, Vol. 36, No. 9, 1998, pp. 1603-1609.
- ²¹ Wright, M.J., Loomis, M.A., and Papadopoulos, P.E., "Aerothermal Analysis of the Project Fire II Afterbody Flow," Journal of Thermophysics and Heat Transfer, Vol. 17, No. 2, 2003, pp. 240-249.
- ²² MacCormack, R.W. and Candler, G.V., "The Solution of the Navier-Stokes Equations Using Gauss-Seidel Line Relaxation," Computers and Fluids, Vol. 17, No. 1, 1989, pp. 135-150.
- ²³ Yee, H.C., "A Class of High-Resolution Explicit and Implicit Shock Capturing Methods," NASA TM 101088, Feb. 1989.
- ²⁴ Wright, M.J., Loomis, M.A., and Papadopoulos, P.E., "Aerothermal Analysis of the Project Fire II Afterbody Flow," Journal of Thermophysics and Heat Transfer, Vol. 17, No. 2, 2003, pp. 240-249.
- ²⁵ Wercinski, P., Chen, Y.-K., Loomis, M., Tauber, M., McDaniel, R., Wright, M., Papadopoulos, P., Allen, G., and Yang, L., "Neptune Aerocapture Entry Vehicle Preliminary Design," AIAA Paper No. 2002-4812, Aug. 2002.
- ²⁶ Gnoffo, P.A., Gupta, R.N., and Shinn, J.L., "Conservation Equations and Physical Models for Hypersonic Air Flows in Thermal and Chemical Nonequilibrium," NASA TP 2867, Feb. 1989.
- ²⁷ Lee, J.H., "Basic Governing Equations for the Flight Regimes of Aeroassisted Orbital Transfer Vehicles," Thermal Design of Aeroassisted Orbital Transfer Vehicles, ed. H.F. Nelson, Vol. 96, Progress in Astronautics and Aeronautics, AIAA, New York, 1985, pp. 3-53.
- ²⁸ Millikan, R.C. and White, D.R., "Systematics of Vibrational Relaxation," Journal of Chemical Physics, Vol. 39, No. 12, 1963, pp. 3209-3213.
- ²⁹ Gurvich, L., Veyts, I., and Alcock, C., eds., Thermodynamic Properties of Individual Substances, 4th Edition, Hemisphere Publishing Corporation, New York, 1991.
- ³⁰ Nelson, H.F., Park, C., and Whiting, E.E., "Titan Atmospheric Composition by Hypervelocity Shock-Layer Analysis," J. Thermophysics & Heat Transfer, Vol. 5, No. 2, pp. 157-165, Apr.-Jun. 1991.
- ³¹ Park, C.S., "Studies of Radiative Emission from the Simulated Shock Layer of the Huygens Probe" Ph.D. Thesis, Stanford U., 1991
- ³² Park, C., private communication, NASA Ames Research Center, Oct. 2001.
- ³³ Park, C., Jaffe, R., and Partridge, H., "Chemical-Kinetic Parameters of Hyperbolic Earth Entry," Journal of Thermophysics and Heat Transfer, Vol. 15, No. 1, 2001, pp. 76-90.
- ³⁴ Park, C., "Assessment of Two-Temperature Kinetic Model for Air," Journal of Thermophysics and Heat Transfer, Vol. 3, No. 3, 1989, pp. 233-244
- ³⁵ Gordon, S. and McBride, B.J., "Computer Program for Calculation of Complex Chemical Equilibrium Compositions and Applications," NASA RP 1311, Oct. 1994.
- ³⁶ Whiting, E.E., Yen, L., Arnold, J.O., and Paterson, J.A., "NEQAIR96, Nonequilibrium and Equilibrium Radiative Transport and Spectra Program: User's Manual," NASA RP-1389, Dec. 1996.
- ³⁷ Laux, C.O., "Optical Diagnostics and Radiative Emission of Air Plasmas," HTGL Report No. T-288, Stanford University, Aug. 1993.
- ³⁸ NIST, Washington, DC, "Atomic Spectra Database," (http://physics.nist.gov/cgi-bin/AtData/main_asd), 2003.
- ³⁹ Goulard, R., "The Coupling of Radiation and Convection in Detached Shock Layers," Journal of Quantitative Spectroscopy and Radiative Heat Transfer, Vol. 1, 1961, pp. 249-257.
- ⁴⁰ Olynick, D., Chen, Y.K., Tauber, M.E., "Aerothermodynamics of the Stardust Sample Return Capsule," *J. of Spacecraft and Rockets*, Vol. 36, No. 3, May-June 1999, p. 442-461.
- ⁴¹ Hartung, L.C., Mitcheltree, R.A., and Gnoffo, P.A., "Coupled Radiation Effects in Thermochemical Nonequilibrium Shock-Capturing Flowfield Calculations," *J. of Thermophysics and Heat Transfer*, Vol. 8, No. 2, Apr.-Jun. 1994, p. 244-250.
- ⁴² Gokcen, T. and Park, C., "The Coupling of Radiative Transfer to Quasi 1D Flows with Thermochemical Nonequilibrium," AIAA Paper No. 91-0570, Jan. 1991.
- ⁴³ Sakai, T., Tsuru, T., and Sawada, K., "Computation of Hypersonic Radiating Flowfield over a Blunt Body," Journal of Thermophysics and Heat Transfer, Vol. 15, No. 1, 2001, pp. 91-98.
- ⁴⁴ Matsuyama, S., Sakai, T., Sasoh, A., and Sawada, K., "Parallel Computation of Fully Coupled Hypersonic Radiating Flowfield Using Multiband Model," Journal of Thermophysics and Heat Transfer, Vol. 17, No. 1, 2003, pp. 21-28.
- ⁴⁵ Reid, R.C., Jr., Rochelle, W.C., and Milhoan, J.D., "Radiative Heating to the Apollo Command Module: Engineering Predictions and Flight Measurements," NASA Tm X-58091, April 1972.
- ⁴⁶ Park, C., "Stagnation-Point Radiation for Apollo 4," AIAA Paper No. 2001-3070, Jun. 2001.
- ⁴⁷ Amtec Engineering, Inc., PO Box 3633, Bellevue, WA 98009-3633, "Tecplot® Version 9 User's Manual," NASA/RP 1389, December 1996.

Comparison of Methods to Compute High-Temperature Gas Viscosity

Grant E. Palmer* and Michael J. Wright†
 Eloret Corporation, Sunnyvale, California 94087

A review of the basic equations for computing the viscosity of neutral and ionized species is presented. Four commonly used methods for determining viscosity of a gas mixture are discussed. The performance and accuracy of these methods are tested for 11-species air and hydrogen–helium gas mixtures for temperatures ranging from 200 to 20,000 K. The Gupta–Yos mixing rule gives acceptable results for weakly or nonionized flows and requires half the computer time of solving the full multicomponent equations. The Armaly–Sutton mixing rule is applicable to higher temperature, more strongly ionized flows as long as the tuning parameters for the method are appropriately set. The Wilke mixing rule is the least-accurate method, is actually slower than the Gupta–Yos mixing rules, and should be used only as a method of last resort.

Nomenclature

$b_{i0}(1)$	=	Sonine polynomial expansion coefficient, sec/cm ³
e	=	electron charge, 4.803e−10 esu
esu	=	gm ^{1/2} cm ^{3/2} /s
g	=	relative molecular velocity, cm/s
k_b	=	Boltzmann's constant, 1.38054e−16 erg/K
M	=	molar mass, g/mole
m	=	molar mass, g/particle
N_A	=	Avogadro's number, 6.0225e+23 mol ^{−1}
n	=	number density, cm ^{−3}
$Q^{(l)}$	=	total interaction cross section
r	=	intermolecular separation
T	=	temperature, K
x	=	mole fraction
Z	=	charge number
η	=	viscosity coefficient, g/(cm · s)
Λ	=	shielding parameter
λ	=	Debye shielding length
μ_{ij}	=	reduced mass
σ^2	=	rigid sphere collision diameter, Å ²
$\Omega_{ij}^{(1,1)}, \Omega_{ij}^{(2,2)}$	=	collision integrals, cm ³ /s
$\Omega_{ij}^{(1,1)*}, \Omega_{ij}^{(2,2)*}$	=	reduced collision integrals, dimensionless
<i>Subscripts</i>		
e	=	electron
f	=	field
i, j, k	=	species

Introduction

ACCURATE modeling of the transport of momentum, energy, and mass in high-temperature shock layers is required to obtain an accurate description of the aerothermal environments needed for

thermal protection system design. There are two aspects to modeling transport: 1) transport properties of each species and 2) transport of the gaseous mixture as a whole. In the present paper, the transfer of momentum is examined. Specifically, the present paper details the methods to compute the coefficient of viscosity of individual species and gas mixtures.

Literally hundreds of papers have been written on the subjects of species and mixture viscosity, for example, Refs. 1–27. These papers commonly use different, and often conflicting, nomenclatures and systems of units. Much of the substantive theoretical work on computing transport properties was performed in the 1950s and 1960s. These references can be difficult to find. The purpose of this paper is to provide in one source the details of computing the viscosity of both neutral and ionized species. This paper also presents and compares the mixture viscosity relations most commonly used for hypersonic flow simulations using a consistent nomenclature and system of units for each method.

The computation of the viscosity of a pure species depends on the type of species considered. Short-range intermolecular forces (valence and chemical forces) are the primary drivers of neutral species interactions, especially at higher temperatures. These types of forces decrease rapidly with distance, so that distant encounters do not contribute significantly to the viscosity coefficient. Neutral species viscosity is a function of temperature only.

Ionized species viscosity is different from neutral species viscosity in that both long-range (electrostatic) and short-range intermolecular forces influence interactions between ionized species. Electrostatic forces decrease much more slowly with distance than do short-range forces. Because the number of distant encounters is so great, electrostatic forces due to distant encounters between charged particles can have a significant, even dominant, effect on the transport properties of a molecule. In addition, Coulomb shielding by free electrons plays a key role in determining the effective interaction cross section. Therefore, ionized species viscosity is a function of both temperature and electron number density. The first part of this paper presents a brief review of the general expressions for computing neutral and ionized species viscosity.

The viscosity of a multicomponent gas mixture can be obtained by solving the Boltzmann equation. This is generally accomplished using a Sonine polynomial expansion. The determination of the Sonine expansion coefficients requires the solution of a system of equations equal to the number of species present in the gas mixture. A number of simplified methods have been developed over the years to approximate multicomponent gas viscosity.^{1–7} These approximate methods try to address the dual requirements of computational efficiency and physical accuracy. Generally speaking, the approximate methods were designed for low-to-moderate temperature, neutral gas mixtures. They may or may not be applicable to

Presented as Paper 2002-3342 at the AIAA/ASME 8th Joint Thermophysics and Heat Transfer Conference, St. Louis, MO, 24–26 June 2002; received 7 July 2002; revision received 7 October 2002; accepted for publication 8 October 2002. Copyright © 2002 by the American Institute of Aeronautics and Astronautics, Inc. The U.S. Government has a royalty-free license to exercise all rights under the copyright claimed herein for Governmental purposes. All other rights are reserved by the copyright owner. Copies of this paper may be made for personal or internal use, on condition that the copier pay the \$10.00 per-copy fee to the Copyright Clearance Center, Inc., 222 Rosewood Drive, Danvers, MA 01923; include the code 0887-8722/03 \$10.00 in correspondence with the CCC.

*Senior Research Scientist, Reacting Flow Environments Branch, Mail Stop 230-2, Moffett Field, CA 94035. Associate Fellow AIAA.

†Senior Research Scientist, Reacting Flow Environments Branch, Mail Stop 230-2, Moffett Field, CA 94035. Member AIAA.

higher temperature gas mixtures where ionized species are present in significant amounts.

Three of the approximate mixture viscosity methods most commonly used in computational fluid dynamics (CFD) are evaluated in terms of efficiency and accuracy for an 11-species air mixture at temperatures ranging from 200 to 20,000 K. The approximate method results are compared against those obtained solving the multicomponent viscosity equations. Calculations are also performed using a hydrogen–helium gas mixture that approximates the Jovian atmosphere.

Viscosity of Neutral Species

The viscosity coefficient for a gas mixture can be obtained by solving the Boltzmann equation using a Sonine polynomial expansion (see Refs. 8 and 9). Because of the rapid convergence of the expansion, an accurate representation of the viscosity coefficient can be acquired by including only the first term. The equation for a single-species gas in grams per centimeter second reduces to

$$\eta_i = \frac{1}{2} k_b T b_{10}(1) = \frac{5}{8} (k_b T / \Omega_{ii}^{(2,2)}) \quad (1)$$

In Eq. (1), the $b_{10}(1)$ term is one of a series of Sonine expansion coefficients, which are discussed in more detail later. The viscosity collision integral $\Omega^{(2,2)}$ is one of a linear combination of integrals that are used to represent the Sonine polynomial expansion coefficients. As will be shown, an additional collision integral $\Omega^{(1,1)}$ will be required to compute the viscosity of a gas mixture. The collision integrals have units of cubic centimeter per second and take the following general form:

$$\Omega_{ij}^{(l,s)}(T) = \sqrt{\frac{k_b T}{2\pi\mu_{ij}}} \int_0^\infty \exp(-\gamma^2) \gamma^{2s+3} Q^{(l)}(g) d\gamma \quad (2)$$

$$\mu_{ij} = \frac{m_i m_j}{m_i + m_j} \quad (3)$$

$$\gamma^2 = \frac{1}{2} \frac{\mu_{ij} g^2}{k_b T} \quad (4)$$

The total interaction cross section $Q^{(l)}$ is computed by integrating the differential cross sections.⁸ Thus, the collision integral represents an orientationally and thermally averaged collision probability between two particles. The calculation of collision integrals from differential cross sections depends on the potential energy model. To simplify comparisons, Hirschfelder et al. presented the concept of a reduced collision integral⁸ that is the ratio of the collision integral evaluated using a given potential energy model divided by the collision integral evaluated using the rigid sphere model:

$$\Omega_{ij}^{(l,s)*} = \Omega_{ij}^{(l,s)} / [\Omega_{ij}^{(l,s)}]_{\text{rigid sphere}} \quad (5)$$

The expressions for the commonly used collision integrals $\Omega^{(1,1)}$ and $\Omega^{(2,2)}$ can be reexpressed in terms of the reduced collision integrals as

$$\begin{aligned} \Omega_{ij}^{(1,1)} &= \sigma^2 \sqrt{\pi k_b T / 2\mu_{ij}} (\Omega_{ij}^{(1,1)*}) \\ \Omega_{ij}^{(2,2)} &= 2\sigma^2 \sqrt{\pi k_b T / 2\mu_{ij}} (\Omega_{ij}^{(2,2)*}) \end{aligned} \quad (6)$$

Substituting Eq. (6) into Eq. (1) yields the commonly cited expression for the viscosity coefficient of a pure, neutral gas species:

$$\begin{aligned} \eta_i &= \frac{\frac{5}{8} k_b T \sqrt{m_i}}{2\sigma^2 \Omega_{ii}^{(2,2)*} \sqrt{\pi k_b T}} = \frac{\frac{5}{16} \sqrt{M_i / N_A} (k_b T)}{1.0e - 16 \sqrt{\pi} \sigma^2 \Omega_{ii}^{(2,2)*}} \\ &= 2.6693e - 5 \frac{\sqrt{M_i T}}{\sigma^2 \Omega_{ii}^{(2,2)*}} \end{aligned} \quad (7)$$

Note that Eq. (7) is a function of temperature only, which is consistent with kinetic theory. The factor of 10^{-16} is used to convert σ^2 from square angstrom to square centimeters.

Values of $\sigma^2 \Omega_{ii}^{(2,2)*}$ have been tabulated for many simplified intermolecular potentials and are available in the literature. Data for many neutral species interactions can be found in a variety of sources.^{1,10–15} A general discussion of the various interaction potential models can be found in Ref. 8. An evaluation of some of the sources of collision integral data is contained in Refs. 14 and 15.

Viscosity of Ionized Species

The nature of encounters between charged particles is different than that of neutral particles. Neutral particle encounters are governed primarily by short-range intermolecular forces. The effect of an encounter falls off rapidly with increasing distance such that distant encounters between neutral particles do not contribute significantly to the transport properties of a molecule. On the other hand, charged particle encounters are governed by both short-range and long-range (electrostatic) forces. Electrostatic forces decrease much more slowly with separation than do intermolecular forces. Because the number of distant encounters is so great, the electrostatic forces due to distant encounters between charged particles can have a significant, even dominant, effect on the transport properties of an ionized molecule. To a first approximation, the viscosity of an ionized gas can be obtained by solving the Boltzmann equation using the Debye potential (see Ref. 16)

$$V(r) = (1/r) \exp[-(r/\lambda)] \quad (8)$$

The Debye shielding length λ is discussed in the next paragraph. The Debye potential function represents the Coulomb interaction of ions and electrons. At very high temperatures, ion–ion interaction energies can be considerably different from a Coulomb potential energy. However, for most aerospace applications, the quantum mechanical deviation from a Coulomb potential will be small, and this effect can be neglected. For example, even at 10,000 K, the quantum mechanical correction for the $\sigma^2 \Omega_{ii}^{(2,2)*}$ value for atomic nitrogen ion is less than 0.05% of the screened Coulomb potential value (see Ref. 16).

As was already stated, electrostatic forces play a dominant role in determining the viscosity of an ionized species. However, because of the charge neutrality of most undriven ionized gases, the electrical charge of a particle beyond a certain distance is effectively neutralized by nearby particles of opposite charge. Another way of describing the situation is that, beyond a certain distance, charged particles are shielded from each other by intervening charges. In practice, this shielding effect has the effect of cutting off the integration of the collision cross section at a large distance known as the Debye shielding length. Interactions beyond this distance are ignored. The value of the Debye shielding length (in centimeters) can be obtained from¹⁷

$$\lambda = \sqrt{k_b T / 4\pi n_e e^2} = 6.905 \sqrt{T/n_e} \quad (9)$$

For the viscosity of an ionized gas species, in the absence of a magnetic field the coefficient of viscosity (in grams per centimeter second) for a fully ionized gas is given by¹⁸

$$\eta_i = 0.406 \frac{m_i^{\frac{1}{2}} (k_b T)^{\frac{5}{2}}}{Z^4 e^4 \ln \Lambda} = 2.207e - 15 \frac{M_i^{\frac{1}{2}} T^{\frac{5}{2}}}{Z^4 \ln \Lambda} \quad (10)$$

The charge number Z is 1 for a mixture of singly ionized gas molecules. The shielding parameter Λ is given by¹⁸

$$\Lambda = (3/2 Z Z_f e^3) \sqrt{k_b^3 T^3 / \pi n_e} = 12143 (T^{\frac{3}{2}} / Z Z_f \sqrt{n_e}) \quad (11)$$

The charge number of the field, Z_f , is 1 for a singly ionized gas. The viscosity of a fully ionized gas is due primarily to the positive ions. Viscous stresses due to electrons are generally negligible,¹⁸ but the electron number density must be obtained to calculate the shielding parameter.

Although Eq. (10) is useful in computing the viscosity of a fully ionized gas, it is necessary to develop an expression for the collision integrals of an ion–ion interaction to compute the mixture viscosity

of a gas containing both neutral and ionized species. When Eqs. (10) and (7) are compared, it is possible to derive an expression for $\sigma^2\Omega_{ij}^{(2,2)*}$ (in square angstrom) for an ionized species interaction:

$$\sigma^2\Omega_{ij}^{(2,2)*} = 1.209e + 10(\ln \Lambda / T^2) \quad (12)$$

Gupta et al.¹ used a slightly modified form of Eq. (12) to compute the ion-ion viscosity collision integral. His results are in generally good agreement with Spitzer.¹⁸ In addition, Mason et al.¹⁷ have presented tables of ionized species collision integral data using both attractive and repulsive screened potentials as a function of a normalized temperature. More recently, Stallcop et al.¹⁶ presented an expression to compute the repulsive shielded Coulomb collision integral in terms of a reduced temperature. Their expression, which closely reproduces the data of Ref. 17, was a curve fit to their detailed computational chemistry calculations of the potential energies and transport cross sections of ions:

$$\sigma^2\Omega_{ij}^{(N,-N)*} = 5.0e + 15(\lambda / T^*)^2 \ln\{D_N T^* [1 - C_N \exp(-c_N T^*)] + 1\} \quad (13)$$

The reduced temperature T^* is defined by the following expression:

$$T^* = 4132.5(T^{\frac{3}{2}} / \sqrt{n_e}) \quad (14)$$

The values for the constants in Eq. (13) for the repulsive potential are reproduced from Ref. 16 in Table 1. In addition, new curve fits for the attractive (ion-electron) potential have been generated from the data in Ref. 17 and are also given in Table 1. Strictly speaking, the values in Table 1 are valid for $T^* > 4$; however, this condition will be met except at very high temperatures and/or densities. For example, the T^* value for 11 species equilibrium air at 25,000 K and 100 kPa is 43.

Table 2 shows computed values of $\sigma^2\Omega_{ij}^{(2,2)*}$ using both Eq. (13) (Spitzer¹⁸ and Gupta et al.¹) and Eq. (14) (Mason et al.¹⁷ and Stallcop et al.¹⁶). The results are based on an equilibrium electron number density computed using an 11-species air chemistry model at a reference pressure of 100 kPa. The results show that Eq. (13) gives somewhat higher values for $\sigma^2\Omega_{ij}^{(2,2)*}$ than Eq. (14). However, the values are within 10% of each other, which is a smaller uncertainty than exists for most binary interactions; therefore, in practice both methods of evaluating $\sigma^2\Omega_{ij}^{(2,2)*}$ are acceptable.

Of greater concern is the approximation made by Gupta et al.¹ in the computation of $\sigma^2\Omega_{ij}^{(2,2)*}$ for ionized species pairs. They assume

Table 1 Shielded Coulomb collision integral curve-fit coefficients

n	Attractive potential			Repulsive potential		
	C_n	c_n	D_n	C_n	c_n	D_n
1	-0.476	0.0313	0.784	0.138	0.0106	0.765
2	-0.146	0.0377	1.262	0.157	0.0274	1.235

Table 2 Shielded Coulomb collision integral $\sigma^2\Omega_{ij}^{(2,2)*}$ for ion-ion interactions, assuming an equilibrium electron number density at a pressure of 100 kPa

Temperature, K	n_e, cm^{-3}	Stallcop et al., ¹⁶	Spitzer, ¹⁸
		Eq. (15)	Eq. (13)
5,000	6.115×10^{13}	3040	3051
6,000	2.556×10^{14}	1939	1970
7,000	6.923×10^{14}	1347	1382
8,000	2.198×10^{15}	947	986
9,000	6.805×10^{15}	678	721
10,000	1.711×10^{16}	506	548
11,000	3.572×10^{16}	391	430
12,000	6.378×10^{16}	313	348
13,000	9.905×10^{16}	258	289
14,000	1.353×10^{17}	220	247
15,000	1.646×10^{17}	192	215

that the ratio of viscosity and momentum transfer collision integrals for ionized species pairs is given by¹

$$A_{ij}^* = \frac{\Omega_{ij}^{(2,2)*}}{\Omega_{ij}^{(1,1)*}} = \frac{1.36Z^4 Q_c}{0.795Z^4 Q_c} = 1.71 \quad (15)$$

Thus, they assume the collision integral ratio for ionized species pairs has a constant value of 1.71 for all temperatures and electron number densities. However, the screened Coulomb potential results of Mason et al.¹⁷ and Stallcop et al.¹⁶ clearly show a temperature dependence of this ratio, for both attractive and repulsive potentials. Furthermore, the value of 1.71 given by Gupta et al.¹ appears unrealistically high at all temperatures and electron number densities. Both Mason et al.¹⁷ and Stallcop et al.¹⁶ indicate values of this ratio for repulsive potentials ranging from 1.02 to 1.26.

Collisions Between Ions and Neutrals

Collisions between ions and neutrals can be a significant contributor to the mixture viscosity of a partially ionized mixture. Although it is beyond the scope of this paper to discuss the details of such interactions, in practice they are governed by similar types of short-range forces that govern neutral interactions, coupled with several long-range forces, including polarizability and dispersion effects. Once an acceptable model for the intermolecular potential is selected, calculation of the collision integrals proceeds as for neutral interactions, and the resulting binary viscosity coefficient is a function of temperature only. Mason and McDaniel¹⁹ provide a detailed discussion of the relevant collision theory.

Viscosity of Multicomponent Gas Mixtures

The viscosity coefficient of a multicomponent gas mixture can be obtained by solving the Boltzmann equation using a Sonine polynomial expansion. Because of the rapid convergence of the Sonine polynomials, an accurate representation of the mixture viscosity coefficient can be acquired by including only the first term in the expansion⁸

$$\eta = \frac{1}{2} k_b T \sum_{j=1}^{NS} n_j b_{j0}(1) \quad (16)$$

In Eq. (16), NS is the number of species in the mixture and $b_{j0}(1)$ are Sonine expansion coefficients. The definition of the expansion coefficients consists of a complicated combination of bracket integrals, details of which are provided in Ref. 8. Chapman and Cowling²⁸ demonstrated that the bracket integrals could be replaced by a linear combination of collision integrals. When this simplification is used, the expansion coefficients can be determined from the following system of equations:

$$\sum_{j=1}^{NS} \frac{Q_{ij}^{00}}{R_{i0}} b_{j0}(1) = -1, \quad i = 1, 2, \dots, NS \quad (17)$$

where

$$\frac{Q_{ij}^{00}}{R_{i0}} = \frac{16 m_i}{15 m_j} \sum_{k=1}^{NS} \frac{n_k m_k}{(m_i + m_k)^2} \times \left[5m_j(\delta_{ij} - \delta_{jk})\Omega_{ik}^{(1,1)} + \frac{3}{2}m_k(\delta_{ij} + \delta_{jk})\Omega_{ik}^{(2,2)} \right] \quad (18)$$

The Kronecker delta δ_{mn} is 1 if $m = n$ and 0 otherwise. Thus, the determination of multicomponent viscosity requires the solution of a system of equations whose size is equal to the number of species in the gas mixture. The cost of computing multicomponent viscosity increases rapidly as the number of species in the gas mixture increases.

Equation (16) can be recast in terms of mole fractions x_j , and the leading term can be pulled inside the Sonine polynomial expression yielding the expression

$$\eta(1) = \sum_{j=1}^{NS} \frac{1}{2} x_j n_k k_b T b_{j0}(1) = \sum_{j=1}^{NS} x_j \bar{b}_{j0}(1) \quad (19)$$

In Eq. 19, $\eta(1)$ indicates that this is a first-order mixture viscosity and that $\bar{b}_{j0}(1) = 1/2nk_bTb_{j0}(1)$. The system of equations shown in Eq. (17) can be recast in terms of $\bar{b}_{j0}(1)$ as

$$\sum_{j=1}^{NS} H_{ij} \bar{b}_{j0}(1) = x_i, \quad i = 1, 2, \dots, NS \quad (20)$$

where

$$H_{ij} = \frac{32}{15} x_i \frac{m_i}{m_j} \sum_{k=1}^{NS} \frac{x_k m_k}{(m_i + m_k)^2} \times \left[5m_j (\delta_{ij} - \delta_{jk}) \frac{\Omega_{ik}^{(1,1)}}{k_b T} + \frac{3}{2} m_k (\delta_{ij} + \delta_{jk}) \frac{\Omega_{ik}^{(2,2)}}{k_b T} \right] \quad (21)$$

The collision integrals in Eq. (21) are general collision integrals. As already noted, general collision integrals are often expressed as the collision integral for the rigid-spheremodel multiplied by a reduced collision integral, $\Omega^{(l,s)*}$. When this convention is used, the equation for the H_{ij} terms becomes

$$H_{ij} = B \frac{x_i}{\sqrt{T}} \sum_{k=1}^{NS} \frac{x_k \sqrt{\mu_{ik}}}{(m_i + m_k)} \times \left[\frac{5}{3} (\delta_{ij} - \delta_{jk}) \sigma^2 \Omega_{ik}^{(1,1)*} + \frac{m_k}{m_j} (\delta_{ij} + \delta_{jk}) \sigma^2 \Omega_{ik}^{(2,2)*} \right] \quad (22)$$

All terms in Eq. (22) are expressed in cgs units. The constant B is given by the following relation:

$$B = (32/15)(3/2)2.0e-16\sqrt{\pi N_A/2k_b} = 52979 \quad (23)$$

See Ref. 20 for a discussion of the physical significance of the diagonal and off-diagonal elements of H . For a gas containing a single species, the equation for H_{ij} reduces to the following:

$$H_{ii} = 37462(\sigma^2 \Omega_{ii}^{(2,2)*} / \sqrt{M_i T}) \quad (24)$$

When Eq. (24) is incorporated into Eqs. (19) and (20), the standard expression for the viscosity of a pure species [Eq. (7)] is recovered. Equation (22) is sometimes expressed in terms of a reduced collision integral ratio,

$$H_{ij} = B \frac{x_i}{\sqrt{T}} \sum_{k=1}^{NS} \frac{x_k \sqrt{\mu_{ik}}}{(m_i + m_k)} \sigma^2 \Omega_{ik}^{(2,2)*} \times \left[\frac{5}{3} \frac{1}{A_{ik}^*} (\delta_{ij} - \delta_{jk}) + \frac{m_k}{m_j} (\delta_{ij} + \delta_{jk}) \right] \quad (25)$$

The reduced collision integral ratio A^* is the ratio of $\Omega^{(2,2)*}$ to $\Omega^{(1,1)*}$ for a given species pair. Equations (22) and (25) contain the general form for the H_{ij} coefficients. The general expression can be simplified for both diagonal and off-diagonal terms. For off-diagonal terms, $i \neq j$, the Kronecker delta terms $\delta_{ij} - \delta_{jk}$ and $\delta_{ij} + \delta_{jk}$ will only have nonzero values when $k = j$. This condition removes the summation from the equation leaving the terms

$$H_{ij} = B \frac{x_i x_j}{(m_i + m_j)} \sqrt{\frac{\mu_{ij}}{T}} \sigma^2 \Omega_{ij}^{(2,2)*} \left[-\frac{5}{3} \frac{1}{A_{ij}^*} + 1 \right] \quad (26)$$

Some approximate mixture viscosity formulas assume that $A^* = 5/3$, in which case the off-diagonal terms reduce to zero. The expression for the diagonal terms can be slightly simplified to

$$H_{ij} = B \frac{x_i}{\sqrt{T}} \sum_{k=1}^{NS} \frac{x_k \sqrt{\mu_{ik}}}{(m_i + m_k)} \sigma^2 \Omega_{ik}^{(2,2)*} \times \left[\frac{5}{3} \frac{1}{A_{ik}^*} (1 - \delta_{ik}) + \frac{m_k}{m_i} (1 + \delta_{ik}) \right] \quad (27)$$

The system of equations represented by Eq. (20) can be solved for the $\bar{b}_{j0}(1)$ terms using a standard pivoted Gaussian elimination routine. Another commonly used technique to solve the system of equations is by using Cramer's rule (see Ref. 8). The mixture viscosity is then found by the ratio of the determinant of an augmented H matrix over the determinant of the H matrix, where the augmented matrix includes an extra row and column containing the species mole fractions. Cramer's rule is the most commonly cited technique to solve for multicomponent viscosity. However, Cramer's rule is less stable and more prone to numerical error than pivoted Gaussian elimination (see Ref. 21). As will be shown, in the "results," Cramer's rule also requires more CPU time.

Solution of the system of NS equations given by Eq. (20) yields the exact first-order approximation of the multicomponent mixture viscosity. However, due to the complexity of this system of equations, they are seldom used in practice for the computation of viscosity in a CFD code. Instead, an approximate mixing rule is typically employed to produce reasonable results at a much lower computational cost. In the next section, several of the mixing rules most commonly applied to hypersonic airflows are introduced, and the relative merits of each scheme are discussed.

Wilke Mixing Rule³

Wilke's mixing rule³ was developed in 1950 through application of kinetic theory to the full first-order Chapman-Enskog relation. In addition to the already defined A^* ratio, the assumptions of Wilke can be explained succinctly with the following collision integral ratio definitions:

$$B_{ik} = \Omega_{ik}^{(2,2)*} / \Omega_{kk}^{(2,2)*}, \quad F_{ik} = \Omega_{ik}^{(2,2)*} / \Omega_{ii}^{(2,2)*} \quad (28)$$

First, Wilke assumed that the collision integral ratio $A^* = 5/3$ for all interactions, which makes all off-diagonal terms in the H matrix equal to zero. In addition, Wilke assumed that B_{ik} and F_{ik} are equal to 1 for all interactions, which is analogous to assuming that all binary interactions have the same (hard sphere) cross section. With these assumptions, the mixture viscosity can be expressed as an appropriately weighted sum of the individual species viscosities and is given by

$$\eta = \sum_{j=1}^{NS} \frac{x_j \eta_j}{\phi_j} \quad (29)$$

The scale factor in Eq. (29) is given by the following expression:

$$\phi_i = \sum_{k=1}^{NS} \left[1 + \sqrt{\frac{n_i}{\eta_k}} \left(\frac{M_k}{M_i} \right)^{\frac{1}{2}} \right]^2 / \sqrt{8 \left(1 + \frac{M_i}{M_k} \right)} \quad (30)$$

Wilke's mixing rule can be expected to yield reasonable results for nonpolar and nonionized gas mixtures, for which the off-diagonal terms of H can be shown to be much smaller than the diagonal elements and for which all binary interactions have the same general form. However, for polar or ionized gases, Wilke's mixing rule has been shown to give poor results (see Ref. 22). It is commonly assumed that Wilke's mixing rule³ is the fastest of the mixture viscosity formulations and as such is the most frequently used. However, this assumption will be shown to be incorrect in the "Results."

Armaly-Sutton Mixing Rule²

Armaly and Sutton developed an approximate mixture viscosity formulation² that significantly improves the accuracy of the computed mixture viscosity for ionized gases with only a small increase in complexity. They started with the multicomponent expression (25) and neglected the off-diagonal terms without assuming $A^* = 5/3$. Armaly and Sutton used an approximate formula for the binary collision diameter:

$$\sigma_{ij}^2 = (\sigma_i + \sigma_j)^2 / 4 = (2.6693e-5\sqrt{T}) / 4 \times \left[m_i^{\frac{1}{2}} / \sqrt{\eta_i \Omega_{ii}^{(2,2)*}} + m_j^{\frac{1}{2}} / \sqrt{\eta_j \Omega_{jj}^{(2,2)*}} \right]^2 \quad (31)$$

Inserting Eq. (31) into Eq. (25) for a diagonal term leads to

$$\eta = \sum_{i=1}^{NS} \frac{x_i^2}{H_{ii}} \quad (32)$$

The H_{ii} term in Eq. (32) is given by

$$H_{ii} = x_i \sum_{k=1}^{NS} \frac{2x_k \mu_{ik}}{\eta_{ik}(m_i + m_k)} \left[\frac{5}{3} \frac{(1 - \delta_{ik})}{A_{ik}^*} + \frac{m_k}{m_i} (1 + \delta_{ik}) \right] \quad (33)$$

The binary viscosity η_{ik} is defined by

$$\eta_{ik} = \frac{\sqrt{32\mu_{ik}}}{\left[(m_i^{\frac{1}{2}}/\sqrt{\eta_i})F_{ik} + (m_k^{\frac{1}{2}}/\sqrt{\eta_k})B_{ik} \right]^2} \quad (34)$$

The B_{ik} and F_{ik} parameters are defined by Eq. (28).

Rather than assuming constant values for the A^* , B , and F parameters as was done by Wilke,³ Armaly and Sutton² evaluated them using available cross-section data for air and hydrogen-helium mixtures. The numbers assigned to these parameters by Armaly and Sutton are as follows. The quantity A^* has the value 1.25 for all interactions except those of an atom with its own ion. In that situation, the recommended value was 1.1. However, for air species this value does not properly account for the resonant charge exchange process, which dominates the momentum transfer cross section. A more reasonable number for air species, based on quantum mechanical calculations for the N–N⁺ and O–O⁺ interactions,²³ is 0.21.

The F_{ik} parameter was assumed equal to 1 for all interactions, and B_{ik} was determined by solution of Eq. (32). The resulting values for B_{ik} were then grouped according to interaction type and a best-fit value was selected. According to Armaly and Sutton,² B_{ik} is given a value of 0.78 for neutral-neutral interactions, 0.15 for neutral-ion interactions, 0.2 for neutral-electron interactions, and 1.0 for ion-ion, ion-electron, and electron-electron interactions. Finally, it is assumed that $B_{ik} = F_{ki}$. This situation presents a rather curious inconsistency in the Armaly-Sutton formulation. Even though mathematically $B_{ik} = F_{ki}$, the value given to F_{ki} is always 1 where the value given to B_{ik} varies by interaction type. However, in practice this inconsistency is not important because the values of B_{ik} and F_{ik} are determined simply as best-fit parameters.

The Armaly-Sutton mixing rule² is typically expressed in a form similar to that used by Wilke's mixing rule,³ where the mixture viscosity is given by Eq. (29). In this form, the scaling parameter ϕ_i is given by

$$\phi_i = x_i + \sum_{k \neq i} x_k \left[\frac{5}{3} \frac{1}{A_{ik}^*} + \frac{M_k}{M_i} \right] / \left[1 + \frac{M_k}{M_i} \right] \times \left[F_{ik} + B_{ik} \sqrt{\frac{n_i}{\eta_k}} \left(\frac{M_k}{M_i} \right)^{\frac{1}{2}} \right]^2 / \sqrt{8 \left(1 + \frac{M_i}{M_k} \right)} \quad (35)$$

The Armaly-Sutton mixing rule has shown² to yield significantly better results than Wilke's mixing rule³ for ionized gases, at essentially no additional computational cost.

Gupta et al.–Yos Mixing Rule

Yos²⁴ and later Gupta et al.¹ introduced the following mixture viscosity correlation:

$$\eta = \sum_{i=1}^{NS} \left(x_i / \sum_{k=1}^{NS} \frac{x_k}{M_i} \Delta_{ik}^{(2)} \right) = \sum_{i=1}^{NS} \left(x_i / \sum_{k=1}^{NS} \frac{x_k}{M_i} \frac{16}{5} \pi \sigma^2 \Omega_{ik}^{(2,2)*} \sqrt{\frac{2\mu_{ik}}{\pi k_b T}} \right) \quad (36)$$

This mixture viscosity relation ignores all off-diagonal elements of H and makes further simplifications to the diagonal elements.

When expressed using the H_{ii} terms, the Gupta et al.–Yos mixture viscosity relation becomes

$$\eta = \sum_{i=1}^{NS} \frac{x_i^2}{H_{ii}} \quad (37)$$

The H terms are defined according to the following expression:

$$H_{ii} = \sum_{k=1}^{NS} \frac{x_i x_k m_k}{m_i + m_k} B \frac{\sigma^2 \Omega_{ik}^{(2,2)*}}{\sqrt{\mu_{ik} T}} = B \frac{x_i}{m_i \sqrt{T}} \sum_{k=1}^{NS} x_k \sigma^2 \Omega_{ik}^{(2,2)*} \sqrt{\mu_{ik}} \quad (38)$$

The B constant is defined by Eq. (23). The Gupta et al.–Yos formulation is, thus, more exact than Wilke's mixing rule³ because the true nature of the viscosity collision integrals is taken into account. However, the simplifications employed will cause poor agreement between Gupta et al.–Yos and the multicomponent formulation for significantly ionized flows. This was noted by Gupta et al.,¹ and this mixing rule was only designed for weakly or nonionized flows. Despite this, the Gupta et al.–Yos formulation as presented here remains the most commonly used method for computing mixture viscosity in hypersonic CFD codes.

Note that Yos²⁵ later proposed a modified formulation that approximately accounts for the effects of the off-diagonal terms by summing and adding them to the diagonal (also see Ref. 1). This formulation was shown²⁵ to give results in good agreement with the multicomponent formulation. However, because the cost of implementation is comparable to that of the full multicomponent formulation,¹ the method was not examined in this paper.

Results

Two standard benchmarks for evaluating mixing rules are accuracy and cost. The first aspect investigated was the computational cost (efficiency) of the mixture relations. A viscosity test bed code (written in C) was created containing functions for each of the earlier described mixture viscosity methods. For the Wilke³ and Armaly-Sutton² formulations, the species viscosities were calculated directly from Eq. (7) for neutrals and Eq. (10) for ions. However, similar results would be obtained (both in terms of efficiency and accuracy), if the neutral species viscosities were computed using a Blottner et al. style expression.²⁶

To create an apples-to-apples comparison of the results generated by each mixture viscosity method, the same set of collision integral data was used in each method. The data presented by Murphy and Arundell¹⁴ were chosen both because the collision integral data are of high quality and are readily available in the literature. These data have been used by other authors^{5,27} to validate transport property computations. The only binary interaction for which Murphy's data were not used was the N₂–N₂ interaction, where the coefficients suggested by Murphy did not match low-temperature experimental viscosity data.⁸ Therefore, data from Stallcop et al.,²⁹ which agree well with the experimental data, were used instead. Equation (13) was used to compute the collision integrals for the ion-ion, ion-electron, and electron-electron interactions.

To evaluate the computational efficiency of each mixture viscosity method, the clock() routine was invoked before and after each viscosity method call. The difference in the return value between the two clock() method calls is the time required to execute the viscosity method. Inside each viscosity method, the viscosity calculations were repeated 200,000 times to isolate the viscosity calculations themselves from any one-time operations such as temporary variable definitions and array memory allocations.

Two sets of runs were completed. One set used a 5-species air model and the other an 11-species air model. The results for these computations are shown in Table 3. The results were normalized with respect to the time required for Wilke's mixing rule³ to compute the viscosity of that mixture. There is a consistency in the results (as one would expect) between the 5- and 11-species air models. The cost of each method is roughly proportional to the square of the

[‡] Data available online at <http://WebBook.nist.gov> [cited July 2001].

Table 3 Relative computational cost of the methods used to compute mixture viscosity

Method	5-species air	11-species air	11 vs 5 species
Wilke ³	1.0	1.0	4.554
Armaly-Sutton ²	1.054	1.065	4.603
Gupta et al. ¹ -Yos ²⁴	0.891	0.919	4.697
Multicomponent (Gaussian)	1.927	2.098	4.958
Multicomponent (Cramer's rule)	1.979	2.250	5.177

number of species (25 vs 121). The 11-species air model requires about five times the computer time of the 5-species model, as one would anticipate.

Note from Table 3 that Wilke's mixing rule³ is not the most efficient method. The Gupta et al.¹-Yos²⁴ method uses less CPU time than Wilke³ for both the 5- and 11-species air models. This result is obvious if one looks at the higher-order mathematic function calls associated with each method. The Gupta et al.-Yos mixture expression requires fewer calls to the power (exponentiation) and square root functions and, thus, is slightly faster.

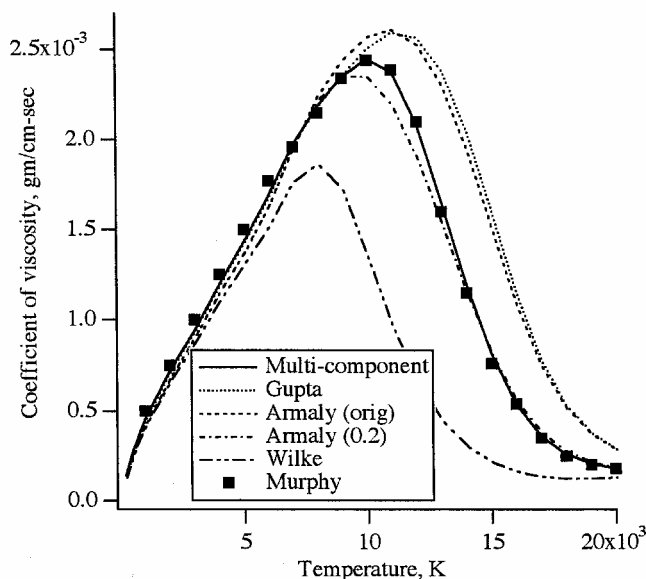
Because of the need to solve a system of equations, the multicomponent viscosity methods require about twice the computer time as the other methods. In addition, it appears that the multicomponent viscosity methods become comparatively more expensive as the number of species increases, although the increased cost ratio from 5- to 11-species is not large (about 10%). Using Gaussian elimination to solve the system of equations is slightly faster than using Cramer's rule. Because Gaussian elimination is also more stable and reliable method to solve a system of equations than Cramer's rule (see Ref. 21), it should be the method of choice when used in conjunction with multicomponent viscosity.

Computational efficiency is only one consideration when choosing a mixture viscosity methodology. A more important consideration is the accuracy of a given method. The multicomponent, the Gupta et al.¹-Yos,²⁴ Armaly-Sutton,² and Wilke³ methods were tested under equilibrium conditions for an 11-species air model over temperatures ranging from 200 to 20,000 K at reference pressures of 100 and 10 kPa.

To ensure that the methods were properly implemented, the results were compared against those of Murphy and Arundell¹⁴ and Murphy,¹⁵ who computed the viscosity of air using a detailed Chapman-Enskog method. The results of Murphy and Arundell¹⁴ and Murphy¹⁵ were, thus, chosen both because the collision integral data that they collected are of high quality and because they are readily available in the literature. These data have been used by other authors^{5,27} to validate transport property computations. As was already stated, to make a meaningful comparison with their results, it was necessary to use the Murphy and Arundell¹⁴ and Murphy¹⁵ collision integral data in the present study for all binary interactions. Note that as long as a consistent set of collision integral data are used for all computations, it is not necessary to evaluate the accuracy of the collision integral data to judge the relative merits of the mixing rules (although the choice of A^* for resonant charge exchange interactions in the Armaly-Sutton² rule complicates things somewhat). In all cases the multicomponent Chapman-Enskog method is the benchmark against which the various mixing rules are compared.

The results for the various methodologies are shown in Fig. 1. The multicomponent results and Murphy and Arundell¹⁴ and Murphy¹⁵ data match very closely along the entire temperature range indicating that the multicomponent mixture viscosity function was properly implemented in the viscosity test bed code. The curve shows a rising tendency until about 10,000 K, where the mixture viscosity value begins to decrease. This is because, although each individual binary viscosity coefficient increases with increasing temperature, ionized species viscosity is an order of magnitude or more less than neutral species viscosity. Above 10,000 K, the ionized species interactions begin to dominate the gas mixture, and the mixture viscosity begins to decrease.

The Gupta et al.¹-Yos²⁴ mixing rule matches the multicomponent value quite closely at low temperatures (weakly ionized gas

**Fig. 1** Mixture viscosity for equilibrium 11-species air at 100 kPa.

mixture). Above 9000 K when ionized species become significant, the Gupta et al.-Yos method overpredicts the mixture viscosity. This overprediction is in part because the off-diagonal terms of H , which account for collisional transfer of momentum between species, have been neglected in this formulation. At temperatures above 14,000 K, the Gupta et al.-Yos value is about twice the multicomponent value.

The value obtained by the Armaly-Sutton² mixing rule depends on the values assigned to the A^* , B , and F parameters. When the A^* value recommended in the original paper ($A^* = 1.1$) for atom-ion interactions with their own ion is used, the Armaly-Sutton results are very close to those obtained using the Gupta et al.¹-Yos²⁴ rule. Using a more representative value of 0.21 for the resonant atom-ion interactions produces a curve much closer to the multicomponent value. The different Armaly-Sutton² curves shown in Fig. 1 suggest that the Armaly-Sutton method can be tuned for different gas mixtures, assuming collision integral data are available. This was suggested by Armaly and Sutton in their original paper.² The Armaly-Sutton results are somewhat less accurate than those of Gupta et al.-Yos at low temperatures (about 4% lower at 500 K), but in general provide quite good results over the entire temperature range, with an accuracy comparable to the full multicomponent method and a cost comparable to results using the Gupta et al.-Yos mixing rule.

Not surprisingly, the least accurate mixture viscosity result is obtained using Wilke's mixing rule.³ At 500 K, the Wilke value is 7% lower than the multicomponent value. Wilke's mixing rule is very inaccurate at temperatures above 7500 K (when the flow becomes ionized) predicting a mixture viscosity value that is up to four times less than the multicomponent value.

Another set of mixture viscosity calculations were performed at a reference pressure of 10 kPa. This corresponds roughly to the postshock pressure of a Mach 20 normal shock wave at 60-km altitude. The results are shown in Fig. 2. The main physical difference between the two sets of computations is that dissociation and ionization occur at a lower temperature at a pressure of 10 kPa than they would at 100 kPa. Also because the pressure is lower, the electron number density at a given temperature will be lower at 10 kPa than it will be at 100 kPa.

The general nature of the curves is the same at 10 kPa as it was at 100 kPa with one exception. The Armaly-Sutton² method result with $A^* = 0.21$ for atom-ion interactions does not compare as closely to the multicomponent result. The separation between the two curves above 9000 K is larger for $p = 10$ kPa than it was for $p = 100$ kPa. This implies that a single set of Armaly-Sutton coefficients may not be generally applicable to any thermodynamic condition.

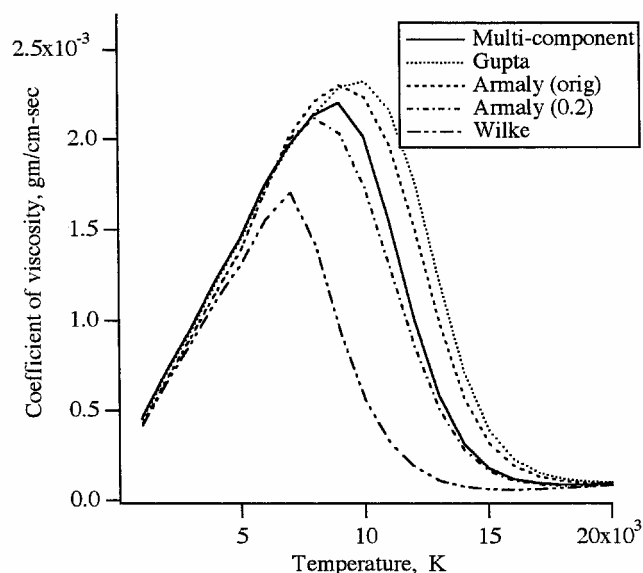


Fig. 2 Mixture viscosity for equilibrium 11-species air at 10 kPa.

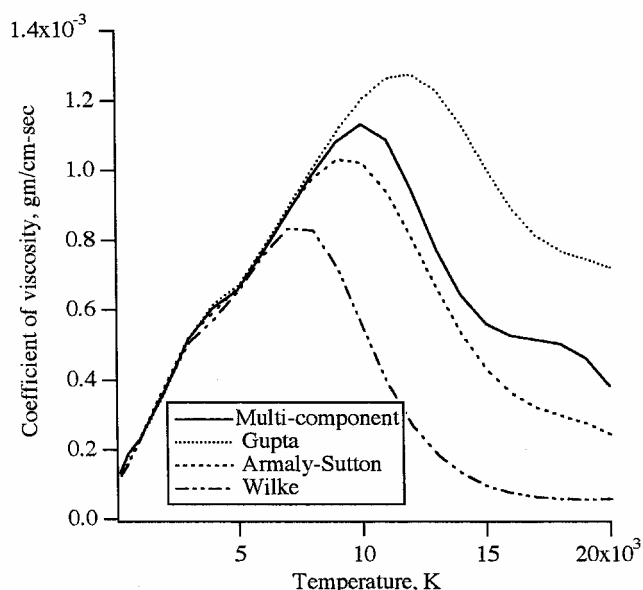


Fig. 3 Mixture viscosity for an equilibrium hydrogen-helium gas mixture at 100 kPa.

To examine the behavior of the mixture viscosity methodologies when applied to a different gas mixture, viscosity coefficients were computed for a six species, H_2 , H , He , H^+ , He^+ , and e , hydrogen-helium gas mixture at a reference pressure of 100 kPa for temperatures ranging from 200 to 20,000 K. Collision integrals for the relevant binary interactions were taken from Biolsi.³⁰ The initial, that is, low-temperature, mole fractions of H_2 and He were 0.864 and 0.136, respectively. This approximates the composition of the Jovian atmosphere. The Armaly-Sutton² coefficients used were the same as with air with the exceptions that the value of A^* for the $H-H^+$ interaction was set to be 0.18 and the value for the $He-He^+$ interaction was 0.025. These numbers follow the recommendations given in Ref. 2, which were also based on Biolsi's collision integral data.³⁰

The results of these calculations are shown in Fig. 3. At lower temperatures where the gas mixture consists mostly of neutral species, the four methods all compute approximately the same viscosity value. Above 7000 K, the results from using Wilke's mixing rule³ begin to deviate significantly from the other methods. Above 10,000 K when significant ionization begins to occur, the Gupta et al.¹-Yos²⁴ method tends to overpredict the mixture viscos-

ity. The Armaly-Sutton² results are closer to the multicomponent values than the Gupta et al.-Yos data; however, the correlation between the Armaly-Sutton² and multicomponent results is not as good for the hydrogen-helium gas mixture as it was for 11-species air. This again suggests that the Armaly-Sutton coefficients may have to be tailored to the specific gas mixture under consideration.

Conclusions

A review of the basic equations for computing the viscosity of neutral and ionized species was presented. The viscosity of neutral species is a function of temperature only, and that of ionized species viscosity is a function of both temperature and electron number density. Four commonly used methods for determining mixture viscosity were discussed. The performance and accuracy of these methods were tested for 11-species air and hydrogen-helium gas mixtures at temperatures ranging from 200 to 20,000 K, and recommendations for use in various situations are summarized next.

Solving the full multicomponent viscosity equations yields the most accurate result, but also requires at least twice the computer time of the other methods. If the multicomponent method is used, the system of equations should be solved using Gaussian elimination rather than with Cramer's rule. If computer time is not an issue and if adequate collision integral data exist for the gas mixture, the multicomponent viscosity method should be used for high-temperature applications.

Use of the Gupta et al.¹-Yos²⁴ mixing rule gives accurate results until significant ionization occurs in the gas mixture. At low temperatures, it is the approximate method that most closely matches the multicomponent results. This method requires the least computer time, even less than that used by Wilke's mixing rule.³ One disadvantage of the Gupta et al.-Yos method is that it requires reasonably accurate collision integral data for each species pair in the gas mixture. The Gupta et al.-Yos method appears applicable for low-to-moderate temperature applications where CPU time is an issue and where adequate collision integral data exists.

If the A^* , B , and F parameters are properly set, the Armaly-Sutton² mixing rule produces fairly accurate results over a wide temperature range and requires direct knowledge of only pure species collision integrals. The correlation with the multicomponent results continues even at temperatures where ionized species dominate the gas mixture. The Armaly-Sutton² method requires about half the CPU time of solving the full multicomponent equations and about 15% more time than the Gupta et al.¹-Yos²⁴ method. The Armaly-Sutton method appears applicable for high-temperature ionized gas flows where CPU time is an issue or for gas mixtures where adequate collision integral data does not exist for all binary interactions. The Armaly-Sutton method can be tuned through the A^* , B , and F parameters. A single set of parameters may not be applicable to every possible thermodynamic state.

Wilke's mixing rule³ is the least accurate method and requires about 10% more CPU time than does the Gupta et al.¹-Yos²⁴ method. The Wilke mixing rule should only be used for low-to-moderate temperature applications where either adequate collision integral data do not exist or where the Armaly-Sutton² parameters are unknown. Wilke's mixing rule³ should be the method of last resort.

Acknowledgments

The work performed in this paper was supported by the prime Contract NAS2-99092 to Elore Corporation. The authors thank Anthony Murphy, Commonwealth Scientific and Industrial Research Organization, Australia for providing us with his raw collision integral data for the 11-species air mixture, which allowed us to validate our computations against his work.

References

- Gupta, R. N., Yos, J. M., Thompson, R. A., and Lee, K.-P., "A Review of Reaction Rates and Thermodynamic and Transport Properties for an 11-Species Air Model for Chemical and Thermal Nonequilibrium Calculations to 30000 K," NASA RP-1232, Aug. 1990.
- Armaly, B. F., and Sutton, L., "Viscosity of Multicomponent Partially Ionized Gas Mixtures," AIAA Paper 80-1495, July 1980.

- ³Wilke, C. R., "A Viscosity Equation for Gas Mixtures," *Journal of Chemical Physics*, Vol. 18, No. 4, 1950, pp. 517–519.
- ⁴Copeland, D. A., "New Approximate Formulas for the Viscosity and Thermal Conductivity of Gas Mixtures," AIAA Paper 2002-0914, Jan. 2002.
- ⁵Selle, S., and Riedel, U., "Transport Coefficients of Reacting Air at High Temperatures," AIAA Paper 2000-0211, Jan. 2000.
- ⁶Sokolova, I. A., and Tirskiy, G. A., "Transport Properties of Gases and Plasma Mixtures for Gasdynamic Simulation," AIAA Paper 97-2584, June 1997.
- ⁷Riabov, V. V., "Approximate Calculation of Transport Coefficients of Earth and Mars Atmospheric Dissociating Gases," *Journal of Thermophysics and Heat Transfer*, Vol. 10, No. 2, 1996, pp. 209–216.
- ⁸Hirschfelder, J. O., Curtiss, C. F., and Bird, R. B., *Molecular Theory of Gases and Liquids*, Wiley, New York, 1954, pp. 481–528.
- ⁹Vincenti, W. G., and Kruger, C. H., *Introduction to Physical Gas Dynamics*, Wiley, New York, 1965, pp. 396–404.
- ¹⁰Svehla, R., "Estimated Viscosities and Thermal Conductivities of Gases at High Temperatures," NASA TR R-132, 1962.
- ¹¹Biolsi, L., and Biolsi, D., "Transport Properties for the Nitrogen System: N₂, N, N⁺, and E," AIAA Paper 83-1474, June 1983.
- ¹²Biolsi, L., "Transport Properties for the Oxygen System: O₂, O, O⁺, and E," AIAA Paper 88-2657, June 1988.
- ¹³Capitelli, M., Gorse, C., Longo, S., and Giordano, D., "Transport Properties of High Temperature Air Species," AIAA Paper 98-2936, June 1998.
- ¹⁴Murphy, A. B., and Arundell, C. J., "Transport Coefficients of Argon, Nitrogen, Oxygen, Argon–Nitrogen, and Argon–Oxygen Plasmas," *Plasma Chemistry and Plasma Processing*, Vol. 14, No. 4, 1994, pp. 451–490.
- ¹⁵Murphy, A. B., "Transport Coefficients of Air, Argon–Air, Nitrogen–Air, and Oxygen–Air Plasmas," *Plasma Chemistry and Plasma Processing*, Vol. 15, No. 2, 1995, pp. 279–307.
- ¹⁶Stallcop, J., Partridge, H., and Levin, E., "Collision Integrals for the Interaction of the Ions of Nitrogen and Oxygen in a Plasma at High Temperatures and Pressures," *Physics of Fluids B*, Vol. 4, No. 2, 1992, pp. 386–391.
- ¹⁷Mason, E. A., Munn, R. J., and Smith, F. J., "Transport Coefficients of Ionized Gases," *Physics of Fluids*, Vol. 10, No. 8, 1967, pp. 1827–1832.
- ¹⁸Spitzer, L., *Physics of Fully Ionized Gases*, Interscience, New York, 1962, pp. 127, 146.
- ¹⁹Mason, E. A., and McDaniel, E. W., *Transport Properties of Ions in Gases*, Wiley, New York, 1988.
- ²⁰Cowling, T. G., Gray, P., and Wright, P. G., "The Physical Significance of Formulae for the Thermal Conductivity and Viscosity of Gas Mixtures," *Proceedings of the Royal Society of London, Series A: Mathematical and Physical Sciences*, Vol. A276, 1963, pp. 69–82.
- ²¹Hadley, G., *Linear Algebra*, Addison Wesley Longman, Reading, MA, 1961, pp. 121–129.
- ²²Blake, L. H., "Approximate Transport Calculations for High-Temperature Air," *AIAA Journal*, Vol. 8, No. 10, 1970, p. 1968.
- ²³Stallcop, J. R., Partridge, H., and Levin, E., "Resonance Charge Transfer, Transport Cross Sections, and Collision Integrals for N⁺–N and O⁺–O Interactions," *Journal of Chemical Physics*, Vol. 95, No. 9, 1991, pp. 6429–6439.
- ²⁴Yos, J. M., "Transport Properties of Nitrogen, Hydrogen, Oxygen, and Air to 30000 K," Avco Corp., TR AD-TM-63-7, March 1963.
- ²⁵Yos, J. M., "Approximate Equations for the Viscosity and Translational Thermal Conductivity of Gas Mixtures," Avco Missiles, Space and Electronics Group, AVSSD-0112-67-RM, April 1967.
- ²⁶Blottner, F. G., Johnson, M., and Ellis, M., "Chemically Reacting Viscous Flow Program for Multi-Component Gas Mixtures," Sandia Labs., Rept. SC-RR-70-754, Albuquerque, NM, Dec. 1971.
- ²⁷Capitelli, M., Celiberto, R., Gorse, C., and Giordano, D., "Transport Properties of High Temperature Air Components: A Review," *Plasma Chemistry and Plasma Processing*, Vol. 16, No. 1, 1996, pp. 267s–302s.
- ²⁸Chapman, S., and Cowling, T. G., *The Mathematical Theory of Non-Uniform Gases*, Cambridge Univ. Press, Cambridge, England, UK, 1939.
- ²⁹Stallcop, J. R., Partridge, H., and Levin, E., "Effective Potential Energies and Transport Cross Sections for Interactions of Hydrogen and Nitrogen," *Physical Review A*, Vol. 62, No. 6, 2000, pp. 1168–1183.
- ³⁰Biolsi, L., "Transport Properties in the Atmosphere of Jupiter," NASA CR-158094, Dec. 1978.

Collision Integrals for Ion–Neutral Interactions of Nitrogen and Oxygen

Eugene Levin* and Michael J. Wright†
 ELORET Corporation, Sunnyvale, California 94087

Diffusion and viscosity collision integrals are computed for all ion–neutral binary interactions that occur in high-temperature partially ionized air, using a Tang–Toennies interaction potential. Resonant charge transfer effects are included as appropriate. Results are compared to more accurate computations where available. The computed collision integrals are estimated to be accurate to within $\pm 25\%$ over a temperature range from room temperature to 12,000 K. The data are presented in tabular form, making them immediately useful for engineering computations such as computational-fluid-dynamics simulations of reentry vehicles.

Nomenclature

B^*	=	ratio of collision integrals
C^*	=	ratio of collision integrals
C_{2n}	=	dispersion coefficients, \AA^{2n} eV
E	=	collision energy, eV
Q_i	=	transport cross section, \AA^2
r	=	separation distance, \AA
r_m	=	location of potential minimum, \AA
T	=	temperature, K
V	=	interaction potential energy, eV
V_0	=	short-range Tang–Toennies potential constant, eV
α_n, α_i	=	dipole polarizability of neutral(n), ion(i), \AA^3
β	=	short range Tang–Toennies potential constant, \AA
ϵ	=	depth of potential well, eV
κ	=	Boltzmann constant, 8.61755×10^{-5} eV/K
$\Omega_{i,j}$	=	collision integral, \AA^2

Introduction

DURING reentry of space vehicles into planetary atmospheres, the postshock gases will be under severe nonequilibrium conditions, resulting in partial dissociation of the molecules as well as ionization of some of the atoms and molecules. To calculate the transport properties of the resulting mixture for Earth entries, data are needed as a function of temperature for all possible binary interactions of the nitrogen and oxygen species present, including those between atomic or molecular positive ions and the neutral atoms and molecules. For the flow conditions encountered by typical Earth-entry vehicles, multiply ionized species and negative ions can be neglected, and the relevant species are N_2 , O_2 , NO , N , O , N_2^+ , O_2^+ , NO^+ , N^+ , O^+ , and e .

From Chapman–Enskog theory^{1,2} first-order expressions for the coefficients of viscosity, thermal conductivity, and ordinary diffusion in a gas mixture can be computed using just three binary interaction parameters: the diffusion collision integral $\Omega_{1,1}$, the viscosity

collision integral $\Omega_{2,2}$, and the ratio B^* , given by

$$B^* = \frac{5\Omega_{1,2} - 4\Omega_{1,3}}{\Omega_{1,1}} \quad (1)$$

One additional collision integral ratio $C^* = \Omega_{1,2}/\Omega_{1,1}$ is necessary if second-order expressions are desired.

Accurate experimental and theoretical results for these quantities are available for most of the neutral–neutral interactions in air.^{3–7} The ion–ion and ion–electron interactions are dominated by Coulomb forces, which can be adequately described using a shielded Coulomb potential over the range of conditions encountered during reentry.⁸ Some data on interactions between electrons and neutral atoms or molecules are available from experimental sources.⁹ The results for atomic ions interacting with neutral atoms in air are accurately known^{10,11}; however, most of the remaining ion–neutral interactions are not well known because experimental results (particularly at high temperatures) are sparse and accurate theoretical calculations are difficult to perform. Such detailed calculations must account for the degeneracies of the various electronic states of the atom, and for collisions involving molecules the cross sections must be determined by averaging over the possible orientations of the collision. Furthermore, for ion–neutral interactions of like species resonant charge exchange must be taken into account when calculating the momentum-transfer cross section and the resulting diffusion collision integral.

Of necessity, various compilations of transport properties for all binary interactions of the atoms, molecules, and ions in air have been prepared for engineering purposes.^{12–17} These compilations generally use high-fidelity data where available and fill in the “missing” interactions with approximations. For example, based on the work of Yos,¹⁶ the collision integrals for many of the ion–neutral interactions were simply taken to be the same as those computed for the N–O^+ interaction.¹⁸ These collision integrals were later borrowed by Gupta et al.¹⁵ in their compilation. Other approximations, such as the polarization (Langevin) potential used for many interactions in the reviews of Fertig et al.,¹² Capitelli et al.,¹³ and Murphy,¹⁴ provide reasonable accuracy for certain interactions, but do not reflect the underlying physics of the interaction, particularly at high energies. Still other approximations attempt to represent the interaction with separate piecewise models for the long- and short-range forces, often resulting in discontinuities in the potential or its first or second derivative. The intermolecular potential is often described using simple models for which collision integrals have been tabulated in the literature in order to avoid the integration of a more realistic potential function. Furthermore, there has often been minimal justification for the values of the parameters used in these models.

It would be desirable to develop a methodology by which ion–neutral interactions can be approximated by a uniform, continuous, physically plausible potential model with a small number of parameters that are either readily available in the literature or

Received 19 May 2003; revision received 22 August 2003; accepted for publication 22 August 2003. Copyright © 2003 by the American Institute of Aeronautics and Astronautics, Inc. The U.S. Government has a royalty-free license to exercise all rights under the copyright claimed herein for Governmental purposes. All other rights are reserved by the copyright owner. Copies of this paper may be made for personal or internal use, on condition that the copier pay the \$10.00 per-copy fee to the Copyright Clearance Center, Inc., 222 Rosewood Drive, Danvers, MA 01923; include the code 0887-8722/04 \$10.00 in correspondence with the CCC.

*Senior Research Scientist, Reacting Flow Environments Branch, NASA Ames Research Center, Mail Stop 230-3, Moffett Field, CA 94035.

†Senior Research Scientist, Reacting Flow Environments Branch, NASA Ames Research Center, Mail Stop 230-2, Moffett Field, CA 94035. Senior Member AIAA.

computable from such parameters. Although such a model could not capture all of the detailed physics of the interaction (including the statistical weighting of multiple potential energy surfaces¹¹ or the three-dimensional nature of atom–molecule and molecule–molecule interactions⁷), it might nevertheless be sufficiently accurate as an interim method for the computation of ion–neutral collision integrals until more accurate results become available.

In this paper, we present the results obtained by using an effective potential based on a one-dimensional Tang–Toennies model¹⁹ to represent the ion–neutral interactions over the entire range of separation distances. This form for the potential was originally developed for neutral atom–atom van der Waals interactions but was subsequently generalized and found to work well for other interactions that are primarily repulsive with a shallow well.^{6,20–22} Extension of this potential model to ion–neutral interactions should be reasonable because the model includes the relevant long-range polarization and dispersion terms as well as the short-range repulsion forces.

The collision integrals are computed by numerical computational methods,^{10,11} and the predictions for the diffusion and viscosity collision integrals $\Omega_{1,1}$ and $\Omega_{2,2}$ are compared to accurate theoretical calculations for $\text{N}^+ - \text{O}^+$ and $\text{N}^+ - \text{O}$. The predicted viscosity collision integrals $\Omega_{2,2}$ are also compared to accurate calculations for $\text{N} - \text{N}^+$ and $\text{O} - \text{O}^+$. The $\Omega_{1,1}$ and $\Omega_{2,2}$ results for 25 ion–neutral interactions are presented over a range of temperatures between 300 and 12,000 K in a tabular format that should facilitate their incorporation into existing engineering codes.

Method

The Tang–Toennies form for the effective potential is physically plausible. It is a continuous function dominated by an exponential repulsion term at short separation distances between the interacting species and by the damped dispersion and polarization terms at long range:

$$V = V_0 e^{-r/\beta} - \sum_{n=2}^{\infty} \left[1 - e^{-r/\beta} \sum_{k=0}^{2n} \frac{(r/\beta)^k}{k!} \right] \frac{C_{2n}}{r^{2n}} \quad (2)$$

The dispersion parameters C_6 , C_8 , and C_{10} of each binary interaction can be determined from the combining relations of Koutselos and Mason²³ using known C_6 and dipole, quadrupole, and octopole polarizabilities of the individual species involved. In a recent paper Selle and Riedel²⁴ have compiled from carefully selected sources

the values for the dispersion coefficient C_6 and the dipole polarizability α for all neutral and ionic components of air as well as the quadrupole polarizability α_q of the neutral species. These data are used for all species in this paper. Quadrupole polarizabilities of the ions as well as octopole polarizabilities of all species are estimated from the data of Koutselos and Mason.²³ Polarization forces are then used to determine C_4 and make corrections to the values of C_6 , C_8 , and C_{10} as described in Ref. 24. The C_{2n} coefficients for $2n > 10$ are estimated from the recursion relations^{7,25}

$$C_{2n+4} = C_{2n-2} (C_{2n+2}/C_{2n})^3 \quad (3)$$

We found only minor changes in the results arising from terms of the series after C_{12} , and therefore truncated our calculations after C_{16} .

The short-range repulsion constants V_0 and β of the Tang–Toennies potential are calculated from the location r_m and depth ϵ of the potential well minimum by requiring that $V(r_m) = -\epsilon$ and $V'(r_m) = 0$. The well parameters are found from the relations^{26,27}

$$r_m = \frac{K_1 (\alpha_n^{1/3} + \alpha_i^{1/3})}{[\alpha_n \alpha_i (1 + 1/\rho)]^{0.95}} \quad (4)$$

$$\epsilon = \frac{K_2 \alpha_n (1 + \rho)}{r_m^4} \quad (5)$$

where the parameter ρ is given by

$$\rho = \frac{K_3 \alpha_i / \sqrt{\alpha_n}}{1 + (2\alpha_i / \alpha_n)^{2/3}} \quad (6)$$

Equation (6) represents the ratio of the dispersion and induction forces and was introduced by Cappelletti et al.²⁶ for ion–neutral interactions as a correction to the neutral–neutral formulas. In Eq. (6), assuming that the polarizabilities are in units of \AA^3 (m^{-30}), $K_3 = 1 \text{\AA}^{(-1.5)}$; ρ is therefore a dimensionless quantity. The empirical constant $K_1 = 1.767$ was determined from neutral–neutral calibrations.²⁸ The constant $K_2 = 5.2$ was fixed²⁶ using $\text{Li}^+ - \text{He}$ and $\text{Li}^+ - \text{Ne}$ as reference systems. Use of these constants in Eqs. (4) and (5) return r_m and ϵ in units of \AA and eV, respectively. The computed well parameters ϵ and r_m together with the resulting Tang–Toennies potential parameters for all 25 interactions are reported in Table 1.

Table 1 Potential well characteristics and parameters of the Tang–Toennies potential function for selected ion–neutral interactions

Interaction	ϵ , eV	r_m , \AA	V_0 , KeV	β , \AA	C_4 , $\text{\AA}^4 \text{eV}$	C_6 , $\text{\AA}^6 \text{eV}$	C_8 , $\text{\AA}^8 \text{eV}$	C_{10} , $\text{\AA}^{10} \text{eV}$
$\text{NO}^+ - \text{N}_2$	0.1091	3.262	24.86	0.2542	125.28	547.48	2,450.0	6,869
$\text{NO}^+ - \text{O}_2$	0.1023	3.239	24.09	0.2517	113.83	492.49	2,185.8	6,155
$\text{NO}^+ - \text{NO}$	0.1075	3.257	42.26	0.2420	122.40	483.63	2,208.4	5,863
$\text{NO}^+ - \text{N}$	0.0800	3.157	131.32	0.2097	79.20	248.74	1,086.8	2,747
$\text{NO}^+ - \text{O}$	0.0637	3.094	45.20	0.2194	57.74	201.05	836.4	2,221
$\text{N}_2^+ - \text{N}_2$	0.0893	3.574	450.09	0.2209	125.28	698.76	4,302.0	17,156
$\text{N}_2^+ - \text{O}_2$	0.0833	3.554	421.24	0.2196	113.83	629.93	3,851.7	15,279
$\text{N}_2^+ - \text{NO}$	0.0879	3.569	1,163.31	0.2069	122.40	631.42	3,869.6	14,332
$\text{N}_2^+ - \text{N}$	0.0629	3.486	7,891.48	0.1769	79.20	344.35	1,974.8	6,357
$\text{N}_2^+ - \text{O}$	0.0484	3.436	1,121.13	0.1924	57.74	270.43	1,527.6	5,106
$\text{O}_2^+ - \text{N}_2$	0.1554	2.845	4.89	0.2656	125.28	344.11	928.7	1,173
$\text{O}_2^+ - \text{O}_2$	0.1472	2.819	4.90	0.2615	113.83	304.64	811.1	1,061
$\text{O}_2^+ - \text{NO}$	0.1535	2.839	7.37	0.2534	122.40	283.70	853.8	1,033
$\text{O}_2^+ - \text{N}$	0.1189	2.724	17.21	0.2186	79.20	123.41	400.9	527
$\text{O}_2^+ - \text{O}$	0.0980	2.648	10.29	0.2191	57.74	100.62	280.1	430
$\text{N}^+ - \text{N}_2$	0.1260	3.074	14.14	0.2540	125.28	409.76	1,439.1	3,188
$\text{N}^+ - \text{O}_2$	0.1186	3.050	14.32	0.2503	113.83	364.89	1,270.4	2,864
$\text{N}^+ - \text{NO}$	0.1241	3.068	23.87	0.2412	122.40	348.09	1,302.6	2,754
$\text{N}^+ - \text{N}$	0.0942	2.961	77.77	0.2063	79.20	164.24	623.3	1,339
$\text{N}^+ - \text{O}$	0.0762	2.891	37.63	0.2101	57.74	132.13	459.1	1,080
$\text{O}^+ - \text{N}_2$	0.1418	2.940	6.96	0.2625	125.28	370.57	1,115.0	1,832
$\text{O}^+ - \text{O}_2$	0.1339	2.914	7.00	0.2586	113.83	329.02	979.0	1,652
$\text{O}^+ - \text{NO}$	0.1396	2.934	10.84	0.2502	122.40	309.69	1,017.6	1,601
$\text{O}^+ - \text{N}$	0.1075	2.821	28.27	0.2152	79.20	139.78	481.3	801
$\text{O}^+ - \text{O}$	0.0879	2.748	15.75	0.2170	57.74	113.53	345.4	651

Table 2 Diffusion collision integrals $\Omega_{1,1}$ (\AA^2) as a function of temperature (K) for selected ion–neutral interactions

Temperature, K	300	500	1,000	2,000	3,000	4,000	5,000	6,000	8,000	10,000	12,000
$\text{NO}^+ \rightarrow \text{N}_2$	33.9	24.2	14.6	9.68	8.13	7.35	6.87	6.54	6.10	5.79	5.59
$\text{NO}^+ \rightarrow \text{O}_2$	32.2	22.5	13.7	9.25	7.82	7.11	6.66	6.36	5.93	5.64	5.44
$\text{NO}^+ \rightarrow \text{NO}^{\text{a}}$	49.2	41.6	35.0	31.1	29.4	28.2	27.3	26.6	25.7	25.1	24.7
$\text{NO}^+ \rightarrow \text{N}$	25.0	17.5	11.3	8.21	7.20	6.68	6.34	6.10	5.76	5.52	5.36
$\text{NO}^+ \rightarrow \text{O}$	21.4	14.8	9.64	7.20	6.38	5.94	5.65	5.43	5.13	4.91	4.76
$\text{N}_2^+ \rightarrow \text{N}_2^{\text{b}}$	49.1	43.7	37.0	32.2	30.1	28.9	28.1	27.5	26.6	26.0	25.6
$\text{N}_2^+ \rightarrow \text{O}_2$	31.6	23.3	15.2	10.9	9.53	8.85	8.41	8.11	7.69	7.39	7.17
$\text{N}_2^+ \rightarrow \text{NO}$	32.2	23.1	15.2	11.2	9.85	9.18	8.74	8.44	8.02	7.73	7.51
$\text{N}_2^+ \rightarrow \text{N}$	24.9	18.1	12.6	9.94	9.03	8.54	8.21	7.98	7.65	7.41	7.23
$\text{N}_2^+ \rightarrow \text{O}$	21.3	15.6	11.0	8.87	8.10	7.68	7.38	7.17	6.86	6.63	6.46
$\text{O}_2^+ \rightarrow \text{N}_2$	32.9	23.2	13.9	8.55	6.78	5.92	5.40	5.05	4.60	4.30	4.10
$\text{O}_2^+ \rightarrow \text{O}_2^{\text{a}}$	48.5	40.9	34.2	30.6	28.7	27.5	26.1	25.3	24.2	23.6	23.2
$\text{O}_2^+ \rightarrow \text{NO}$	30.7	22.2	13.6	8.47	6.77	5.94	5.44	5.10	4.66	4.37	4.17
$\text{O}_2^+ \rightarrow \text{N}$	23.2	16.7	10.4	6.87	5.72	5.14	4.79	4.54	4.21	3.99	3.84
$\text{O}_2^+ \rightarrow \text{O}$	19.5	13.9	8.63	5.88	4.98	4.52	4.23	4.02	3.74	3.54	3.40
$\text{N}^+ \rightarrow \text{NO}$	31.3	22.4	13.8	9.02	7.48	6.71	6.24	5.92	5.50	5.21	5.01
$\text{N}^+ \rightarrow \text{N}_2$	30.6	22.1	13.7	8.99	7.43	6.65	6.17	5.85	5.41	5.11	4.91
$\text{N}^+ \rightarrow \text{O}_2$	30.5	21.7	13.2	8.63	7.17	6.44	5.98	5.68	5.26	4.98	4.79
$\text{N}^+ \rightarrow \text{N}^{\text{c}}$	43.3	38.2	34.3	31.4	30.0	29.0	28.3	27.7	26.9	26.2	25.6
$\text{N}^+ \rightarrow \text{O}^{\text{d}}$	21.6	15.1	10.9	8.33	7.07	6.21	5.56	5.06	4.33	3.82	3.44
$\text{O}^+ \rightarrow \text{NO}$	31.4	22.4	13.6	8.64	7.01	6.21	5.73	5.40	4.97	4.68	4.48
$\text{O}^+ \rightarrow \text{N}_2$	31.7	22.8	13.8	8.68	7.01	6.18	5.68	5.34	4.90	4.60	4.40
$\text{O}^+ \rightarrow \text{O}_2$	33.7	23.4	13.7	8.45	6.80	6.00	5.51	5.19	4.76	4.47	4.28
$\text{O}^+ \rightarrow \text{N}^{\text{d}}$	23.3	16.3	11.8	9.23	8.09	7.36	6.80	6.34	5.60	5.02	4.56
$\text{O}^+ \rightarrow \text{O}^{\text{c}}$	33.6	29.6	27.0	24.9	23.8	23.1	22.6	22.2	21.6	21.1	20.8

^aFrom Ref. 33 combined with Tang–Tonnie’s results in Eq. (8). ^bRef. 34. ^cRef. 10. ^dRef. 11.

Once the interaction potential has been defined, the details of calculating the transport collision integrals have been described in our prior publications,^{4,10,29} and only a brief outline follows here. The scattering phase shifts resulting from collisions of the particles can be calculated from the interaction potentials either semi-classically^{10,30} or quantum mechanically.³¹ For the reduced masses and temperature range considered in this work, quantum mechanical effects are very small, and the semiclassical approach is sufficient. The transport cross sections $Q_i(E)$ for a range of collision energies E are obtained from weighted summations of the computed phase shifts and, in accordance with Chapman–Enskog theory,^{1,2} the collision integrals as a function of temperature are then determined by numerical integration of an average of the cross sections over a Boltzmann distribution,

$$\Omega_{n,s}(T) = \frac{2(n+1)}{\pi(s+1)! [2n+1 - (-1)^n] (\kappa T)^{s+2}} \times \int_0^\infty e^{-E/\kappa T} E^{s+1} Q_n(E) dE \quad (7)$$

The scaling factor that accounts for the normalization to scattering of hard spheres has been set to unity in Eq. (7).

For interactions between an atom or molecule and its ion, resonant charge transfer can significantly increase the size of the momentum-transfer cross section Q_1 , which directly affects the diffusion collision integrals $\Omega_{1,s}$. The viscosity cross section Q_2 and the resulting collision integral are unaffected by charge transfer, because of symmetry considerations.³² At high temperature the resulting momentum-transfer cross section is approximately equal to two times the resonant charge-exchange value.³² However, at lower temperatures both the charge exchange and isotropic cross sections must be accounted for when computing the momentum transfer cross section.³² Following the work of Murphy,¹⁴ we combine the charge-exchange and Tang–Tonnie’s contributions to the diffusion collision integral for all interactions between an atom or molecule and its ion using the empirical mixing rule

$$\Omega_{1,s} = \sqrt{[\Omega_{1,s}^{\text{ex}}]^2 + [\Omega_{1,s}^{\text{TT}}]^2} \quad (8)$$

where $\Omega_{1,s}^{\text{ex}}$ is the collision integral computed by integrating twice the resonant charge-exchange cross section as discussed above and

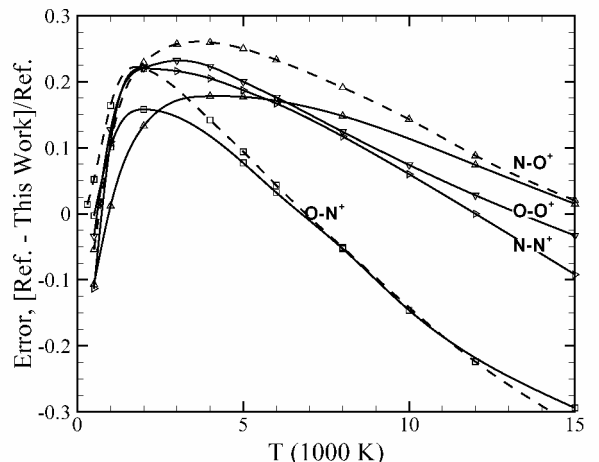


Fig. 1 Relative error of the collision integrals $\Omega_{1,1}$ (--- curves) and $\Omega_{2,2}$ (— curves) computed in this work compared with more accurate ab initio determinations: N-O^+ and O-N^+ from Ref. 11 and N-N^+ and O-O^+ ($\Omega_{2,2}$ only) from Ref. 10.

$\Omega_{1,s}^{\text{TT}}$ is the collision integral computed from the Tang–Tonnie’s potential.

Results and Discussion

Tables 2 and 3 show the computed diffusion and viscosity collision integrals for 25 ion–neutral interactions of nitrogen and oxygen. With the exception of the entries with footnotes, all reported values were obtained by integration of the Tang–Tonnie’s potential as already described. In Fig. 1 we compare the results obtained from the present Tang–Tonnie’s formulation with “reference” values previously determined from ab initio computations of the four atom–atomic-ion interactions.^{10,11} Only $\Omega_{2,2}$ is shown for the $\text{N}^+ \rightarrow \text{N}$ and $\text{O}^+ \rightarrow \text{O}$ interactions, because $\Omega_{1,1}$ would be affected by resonant charge transfer for these cases. These comparisons all show that the predicted viscosity and diffusion collision integrals agree with the benchmark results to within $\pm 25\%$ over the range from room temperature to 12,000 K. Above 12,000 K the population of molecules

Table 3 Viscosity collision integrals $\Omega_{2,2}$ (\AA^2) as a function of temperature (K) for selected ion–neutral interactions

Temperature, K	300	500	1,000	2,000	3,000	4,000	5,000	6,000	8,000	10,000	12,000
$\text{NO}^+ \rightarrow \text{N}_2$	33.7	25.1	15.8	10.6	8.97	8.16	7.69	7.36	6.90	6.67	6.36
$\text{NO}^+ \rightarrow \text{O}_2$	31.8	23.5	14.9	10.2	8.66	7.91	7.47	7.16	6.72	6.50	6.20
$\text{NO}^+ \rightarrow \text{NO}$	32.7	24.4	15.6	10.6	8.99	8.20	7.74	7.42	6.97	6.76	6.45
$\text{NO}^+ \rightarrow \text{N}$	25.4	18.8	12.3	8.97	7.91	7.37	7.04	6.81	6.46	6.27	6.04
$\text{NO}^+ \rightarrow \text{O}$	22.0	15.8	10.4	7.89	7.07	6.62	6.34	6.13	5.82	5.66	5.41
$\text{N}_2^+ \rightarrow \text{N}_2$	33.7	25.3	16.8	12.1	10.7	9.93	9.50	9.19	8.74	8.41	8.20
$\text{N}_2^+ \rightarrow \text{O}_2$	32.7	24.6	16.1	11.7	10.4	9.67	9.26	8.97	8.54	8.22	8.02
$\text{N}_2^+ \rightarrow \text{NO}$	32.7	24.6	16.5	12.1	10.7	10.0	9.59	9.30	8.86	8.54	8.35
$\text{N}_2^+ \rightarrow \text{N}$	26.1	19.5	13.6	10.7	9.78	9.26	8.96	8.74	8.40	8.14	7.98
$\text{N}_2^+ \rightarrow \text{O}$	22.2	16.5	11.8	9.60	8.85	8.42	8.15	7.95	7.62	7.37	7.21
$\text{O}_2^+ \rightarrow \text{N}_2$	31.4	24.1	15.4	9.56	7.59	6.64	6.10	5.74	5.26	4.96	4.73
$\text{O}_2^+ \rightarrow \text{O}_2$	31.0	23.6	14.7	9.09	7.27	6.38	5.88	5.55	5.10	4.81	4.59
$\text{O}_2^+ \rightarrow \text{NO}$	30.2	23.4	15.1	9.47	7.57	6.65	6.12	5.77	5.31	5.01	4.79
$\text{O}_2^+ \rightarrow \text{N}$	23.8	18.2	11.6	7.64	6.37	5.74	5.37	5.13	4.78	4.55	4.38
$\text{O}_2^+ \rightarrow \text{O}$	20.8	15.4	9.66	6.54	5.57	5.07	4.78	4.57	4.28	4.08	3.92
$\text{N}^+ \rightarrow \text{NO}$	31.2	23.7	15.2	9.97	8.28	7.45	6.98	6.66	6.21	5.92	5.70
$\text{N}^+ \rightarrow \text{N}_2$	31.9	23.8	15.3	10.0	8.27	7.42	6.93	6.60	6.14	5.84	5.62
$\text{N}^+ \rightarrow \text{O}_2$	30.4	22.9	14.6	9.55	7.96	7.18	6.72	6.41	5.98	5.69	5.47
$\text{N}^+ \rightarrow \text{N}^a$	20.4	16.4	13.3	10.5	9.15	8.33	7.74	7.26	6.48	5.84	5.31
$\text{N}^+ \rightarrow \text{O}^b$	21.8	15.4	11.1	8.61	7.52	6.75	6.13	5.64	4.90	4.37	3.98
$\text{O}^+ \rightarrow \text{NO}$	30.5	23.5	15.1	9.61	7.81	6.93	6.43	6.10	5.64	5.35	5.13
$\text{O}^+ \rightarrow \text{N}_2$	31.2	23.9	15.3	9.68	7.83	6.92	6.40	6.06	5.59	5.28	5.06
$\text{O}^+ \rightarrow \text{O}_2$	31.8	23.6	14.7	9.26	7.52	6.68	6.19	5.87	5.43	5.14	4.92
$\text{O}^+ \rightarrow \text{N}^b$	23.6	16.6	11.8	9.07	7.99	7.37	6.94	6.60	6.02	5.53	5.11
$\text{O}^+ \rightarrow \text{O}^a$	20.5	14.8	11.1	8.72	7.64	6.94	6.39	5.95	5.26	4.75	4.36

^aRef. 10. ^bRef. 11.

is very low, and any remaining ion–neutral interactions are primarily between atoms and atomic ions, where accurate ab initio results are known.

Additional analysis was required for molecular interactions involving resonant charge exchange. The diffusion collision integral for $\text{N}_2^+ \rightarrow \text{N}_2$ was evaluated by direct numerical integration of the momentum transfer cross sections tabulated by Phelps.³⁴ For the interactions $\text{NO}^+ \rightarrow \text{NO}$ and $\text{O}_2^+ \rightarrow \text{O}_2$, charge-exchange cross sections were taken from Moran et al.,³³ and the final diffusion collision integrals were computed by combining the charge-transfer and Tang–Toennies results using the mixing rule, Eq. (8), discussed in the preceding section. As an indication of the accuracy of this approach, Eq. (8) was also used to calculate $\Omega_{1,1}$ for the $\text{N}_2^+ \rightarrow \text{N}_2$ interactions and compared with the Phelps³⁴ data as a reference. The difference was found to be less than 15% over the range from 2000–12,000 K. There were insufficient data on the low-energy charge-exchange cross sections to extend the comparison to lower temperatures.

The number of significant figures presented in Tables 2 and 3 is one greater than justified by the error sources just discussed; however, there is a strong correlation of errors in $Q_i(E)$ for nearby values of the interaction energy E and similarly for the collision integrals $\Omega_{i,j}(T)$ for nearby values of T . Hence, the data as tabulated are useful for applications involving local interpolation or fitting.

The already defined collision integral ratios B^* and C^* were also computed in this work, but the results are not shown in the tables. To the accuracy warranted by the data, B^* was found to be nearly constant, $B^* = 1.1$, for temperatures above approximately 1000 K and varied between 1.3 and 1.2 at lower temperatures for all ion–neutral pairs. This is consistent with predictions based on polarizability, which would lead to a value of $B^* = 1.25$ at the low temperature limit. C^* was found to range from approximately 0.75 at low temperature (less than 1000 K) to a high temperature limit of 0.95 for all ion–neutral pairs.

Finally, it is interesting to compare the collision integrals computed using the current methodology with those obtained by using a pure Langevin (polarization) potential. The comparison for the case of $\text{N}-\text{O}^+$ is shown in Fig. 2, which shows the relative errors of the current (Tang–Toennies) formulation and a pure polarization potential as compared to the ab initio data in Ref. 11. Collision integrals for the polarization potential are computed using the formulas presented in Ref. 13. It can be observed that for this case the

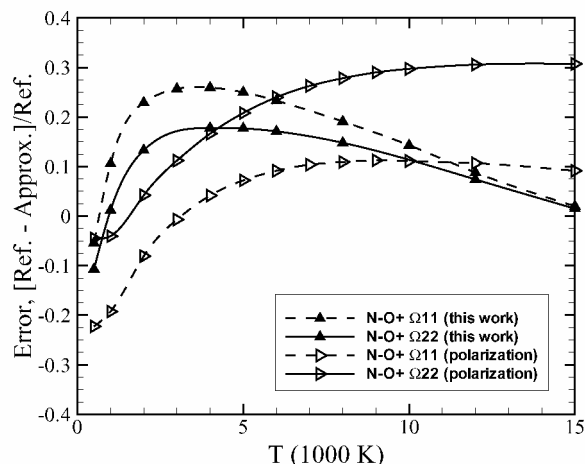


Fig. 2 Relative error of the collision integrals computed in this work and those computed using a polarization potential compared with more accurate ab initio determinations¹¹ for $\text{N}-\text{O}^+$.

simple Langevin potential model gives reasonable results even at the higher temperatures, although the Tang–Toennies results appear to be slightly more accurate, particularly for the viscosity collision integrals. This result is surprising, particularly because the form of the polarization potential differs markedly from an exponential at short separation distances and this region is the dominant contributor to the high-temperature results. The comparison is similar for the $\text{O}-\text{N}^+$ interaction (not shown).

The results in Fig. 2 indicate that use of the polarization potential might be a reasonable assumption when no other data are available. However, we believe that the Tang–Toennies potential method presented here is an improvement for several reasons. First, unlike the polarization model the Tang–Toennies model has the correct theoretical form at short range. This would permit flexibility in the computation of the short-range parameters (V_0 and β) that govern the high-temperature collision integrals. For example, experimental or ab initio short-range data could readily be incorporated into the methodology when available, significantly improving the fidelity of the results. Also, because the Tang–Toennies model accounts for

dispersion forces and higher-order polarizability effects the treatment of long-range forces should also be superior to that of the polarization potential. This would be particularly true for highly polarizable ions, such as N_2^+ . Finally, the agreement shown in Fig. 2 between the polarizability and ab initio results might not be achievable for other neutral-ion systems. In fact, Capitelli³⁵ has shown that using the polarizability potential can result in a significant overprediction of collision integrals in many neutral-ion systems.

Conclusions

A Tang–Toennies-based model is presented for the computation of ion–neutral collision integrals in reacting air. The use of a Tang–Toennies effective potential provides a physically reasonable model for ion–neutral interactions and avoids the use of simplistic or piecewise potentials. The calibration comparisons with more accurate data indicates that the results obtained are within $\pm 25\%$ over the critical range from 300–12,000 K. The methodology presented requires only a few physical parameters that are readily available in the literature for many species. Therefore this methodology can be extended to other ion–neutral interactions for which accurate potentials are not available.

Tables are presented for 25 ion–neutral interactions between oxygen and nitrogen species. These tables can be regarded as interim results pending better determinations. In addition to experiments and ab initio theoretical calculations, we suggest that the predictions might be improved by a better determination of the potential well and/or the repulsive wall. The short range parameters V_0 and β of the Tang–Toennies model are sensitive to the well constants, and the representations used in Eqs. (4) and (6) were based on empirical fits that might not be best for all ion–neutral interactions.

Acknowledgments

Support was provided by Contract NAS2-99092 from NASA to the ELORET Corporation. The advice of James Stallcop (NASA Ames Research Center) regarding the effective potential as well as techniques for calculating the long-range dispersion coefficients is acknowledged and appreciated.

References

- ¹Chapman, S., and Cowling, T. G., *The Mathematical Theory of Non-Uniform Gases*, 2nd ed., Cambridge Univ. Press, New York, 1952, Chap. 9.
- ²Maitland, G. G., Rigby, M., Smith, E. B., and Wakeham, W. A., *Intermolecular Forces, Their Origin and Determination*, Oxford Univ. Press, Oxford, 1981, Chap. 5.
- ³Cubley, S. J., and Mason, E. A., "Atom–Molecule and Molecule–Molecule Potentials and Transport Collision Integrals for High Temperature Air Species," *Physics of Fluids*, Vol. 18, No. 9, 1975, pp. 1109–1111.
- ⁴Levin, E., Partridge, H., and Stallcop, J. R., "Collision Integrals and High Temperature Transport Properties for N–N, O–O, and N–O," *Journal of Thermophysics and Heat Transfer*, Vol. 4, No. 4, 1990, pp. 469–477.
- ⁵Bzowski, J., Kestin, J., Mason, E. A., and Uribe, F. J., "Equilibrium and Transport Properties of Gases Mixtures at Low Density: Eleven Polyatomic Gases and Five Noble Gases," *Journal of Physical and Chemical Reference Data*, Vol. 19, No. 5, 1990, pp. 1179–1231.
- ⁶Stallcop, J. R., Partridge, H., and Levin, E., "Effective Potential Energies and Transport Cross Sections for Interactions of Hydrogen and Nitrogen," *Physical Review A*, Vol. 62, No. 6, 2000, pp. 062709(1–15).
- ⁷Stallcop, J. R., Partridge, H., and Levin, E., "Effective Potential Energies and Transport Cross Sections for Atom Molecule Interactions of Nitrogen and Oxygen," *Physical Review A*, Vol. 64, No. 4, 2001, pp. 0427221(1–12).
- ⁸Stallcop, J. R., Partridge, H., and Levin, E., "Collision Integrals for the Interaction of the Ions of Nitrogen and Oxygen in a Plasma at High Temperatures and Pressures," *Physics of Fluids B*, Vol. 4, No. 2, 1992, pp. 386–391.
- ⁹Park, C., Jaffe, R. L., and Partridge, H., "Chemical Kinetic Parameters of Hyperbolic Earth Entry," *Journal of Thermophysics and Heat Transfer*, Vol. 15, No. 1, 2001, pp. 76–90.
- ¹⁰Stallcop, J. R., Partridge, H., and Levin, E., "Resonance Charge Transfer, Transport Cross Sections, and Collision Integrals for $N^+(^3P)–N(^4S^0)$ and $O^+(^4S^0)–O(^3P)$ Interactions," *Journal of Chemical Physics*, Vol. 95, No. 9, 1991, pp. 6429–6439.
- ¹¹Partridge, H., Stallcop, J. R., and Levin, E., "Transport Cross Sections and Collision Integrals for $N(^4S^0)–O(^4S^0)$ and $N(^3P)–O(^3P)$

- Interactions," *Chemical Physics Letters*, Vol. 184, No. 5, 1991, pp. 505–512.
- ¹²Fertig, M., Dohr, A., and Fruhauf, H.-H., "Transport Coefficients for High-Temperature Nonequilibrium Air Flows," *Journal of Thermophysics and Heat Transfer*, Vol. 15, No. 2, 2001, pp. 148–156.
- ¹³Capitelli, M., Gorse, C., Longo, S., and Giordano, D., "Collision Integrals of High-Temperature Air Species," *Journal of Thermophysics and Heat Transfer*, Vol. 14, No. 2, 2000, pp. 259–268.
- ¹⁴Murphy, A. B., "Transport Coefficients of Air, Argon–Air, Nitrogen–Air, and Oxygen–Air Plasmas," *Plasma Chemistry and Plasma Processing*, Vol. 15, No. 2, 1995, pp. 279–307.
- ¹⁵Gupta, R. N., Yos, J. M., Thompson, R. A., and Lee, K. P., "A Review of Reaction Rates and Thermodynamic and Transport Properties for an 11-Species Air Model for Chemical and Thermal Nonequilibrium Calculations to 30,000 K," NASA RP-1232, Aug. 1990.
- ¹⁶Yos, J. M., "Transport Properties of Nitrogen, Hydrogen, Oxygen, and Air to 30,000 K," AVCO TM RAD-TM-63-7, Wilmington, MA, March 1963.
- ¹⁷Yun, K. S., and Mason, E. A., "Collision Integrals for the Transport Properties of Dissociating Air at High Temperature," *Physics of Fluids*, Vol. 5, No. 4, 1962, pp. 380–386.
- ¹⁸Bade, W. L., and Yos, J. M., "The NATA Code—User's Manual, Volume II," NASA CR-141743, April 1976.
- ¹⁹Tang, T. K., and Toennies, J. P., "An Improved Simple Model for the van der Waals Potential Based on Universal Damping Functions for the Dispersion Coefficients," *Journal of Chemical Physics*, Vol. 80, No. 8, 1984, pp. 3726–3741.
- ²⁰Stallcop, J. R., and Partridge, H., "The $N_2–N_2$ Potential Energy Surface," *Chemical Physics Letters*, Vol. 281, No. 1–3, 1997, pp. 212–220.
- ²¹Stallcop, J. R., Partridge, H., and Levin, E., "H– H_2 Collision Integrals and Transport Coefficients," *Chemical Physics Letters*, Vol. 254, No. 1, 2, 1996 pp. 25–31.
- ²²Stallcop, J. R., Bauschlicher, C. W., Partridge, H., Langhoff, S. R., and Levin, E., "Theoretical Study of Hydrogen and Nitrogen Interactions: N–H Transport Cross Sections and Collision Integrals," *Journal of Chemical Physics*, Vol. 97, No. 8, 1992, pp. 5578–5585.
- ²³Koutselos, A. D., and Mason, E. A., "Correlation and Prediction of Dispersion Coefficients for Isoelectronic Systems," *Journal of Chemical Physics*, Vol. 15, No. 4, 1986, pp. 2154–2160.
- ²⁴Selle, S., and Riedel, U., "Transport Coefficients of Reacting Air at High Temperatures," AIAA Paper 2000-0211, Jan. 2000.
- ²⁵Thakkar, A. J., "Higher Dispersion Coefficients: Accurate Values for Hydrogen Atoms and Simple Estimates for Other Systems," *Journal of Chemical Physics*, Vol. 89, No. 4, 1988, pp. 2092–2098.
- ²⁶Cappelletti, D., Liuti, G., and Pirani, F., "Generalization to Ion-Neutral Systems of the Polarizability Correlations for Interaction Potential Parameters," *Chemical Physics Letters*, Vol. 183, No. 3, 4, 1991, pp. 297–303.
- ²⁷Aquilanti, V., Cappelletti, D., and Pirani, F., "Range and Strength of Interatomic Forces: Dispersion and Induction Contributions to the Bonds of Dications and of Ionic Molecules," *Chemical Physics*, Vol. 209, No. 2, 3, 1996, pp. 299–311.
- ²⁸Liuti, G., and Pirani, F., "Regularities in van der Waals Forces—Correlation Between the Potential Parameters and Polarizability," *Chemical Physics Letters*, Vol. 122, No. 3, 1985, pp. 245–250.
- ²⁹Stallcop, J. R., Partridge, H., and Levin, E., "Potential Energies and Collision Integrals for the Interactions of Air Components. II. Scattering Calculations and Interactions Involving Ions," *Molecular Physics and Hypersonic Flows*, edited by M. Capitelli, Kluwer Academic, Norwell, MA., 1996, pp. 339–349.
- ³⁰Stallcop, J. R., "Semiclassical Elastic Scattering Cross Sections for a Central Field Potential," NASA SP-3052, 1969.
- ³¹Levin, E., Schwenke, D. W., Stallcop, J. R., and Partridge, H., "Comparison of Semi-Classical and Quantum Mechanical Methods for the Determination of Transport Cross Sections," *Chemical Physics Letters*, Vol. 227, No. 6, 1994, pp. 669–675.
- ³²Heiche, G., and Mason, E. A., "Ion Mobilities with Charge Exchange," *Journal of Chemical Physics*, Vol. 53, No. 12, 1970, pp. 4687–4696.
- ³³Moran, T. F., Flannery, M. R., and Cosby, P. C., "Molecular Charge Transfer II: Experimental and Theoretical Investigation of the Role of Incident-Ion Vibrational States in $O_2^+–O_2$ and $NO^+–NO$ Collisions," *Journal of Chemical Physics*, Vol. 61, No. 4, 1974, pp. 1261–1272.
- ³⁴Phelps, A. V., "Cross Sections and Swarm Coefficients for Nitrogen Ions and Neutrals in N_2 and Argon Ions and Neutrals in Ar for Energies from 0.1 eV to 10 keV," *Journal of Physical and Chemical Reference Data*, Vol. 20, No. 3, 1991, pp. 557–573.
- ³⁵Capitelli, M., "Transport Properties of Partially Ionized Gases," *Journal de Physique*, Vol. 38, No. 8, 1977, pp. C3/227–237.

Analysis of Afterbody Heating Rates on the Apollo Command Modules, Part 1: AS-202

Michael J. Wright*

NASA Ames Research Center
Moffett Field, CA 94035

Dinesh K. Prabhu†

ELORET Corporation
Sunnyvale, CA, 94087

Edward R. Martinez‡

NASA Ames Research Center

Abstract

Computational fluid dynamics simulations are performed to simulate the wake flow and afterbody heating environment of the Apollo AS-202 Command Module reentry. Fifteen three-dimensional simulations are computed which cover the majority of the high heating portion of the flight. Computed surface oil flow plots demonstrate that the flow remained attached on the windward side of the afterbody throughout the entry. The computed heat transfer generally agrees well with the flight data and is within the assumed $\pm 20\%$ uncertainty for 15 of the 19 functional calorimeters on the conical afterbody over most of the entry. Heat transfer is generally overpredicted in the attached flow region during the low Reynolds number portion of the trajectory, possibly due to non-continuum effects. Predicted heating at two calorimeters located near the separation line clearly shows jumps where the flow separates and reattaches as a function of time. This behavior is also seen in the flight data, indicating that the computational results are accurately predicting not only heating levels but separated flow extent as well. The worst agreement between the computations and the flight data occurs near the rear apex of the Command Module. The reason for this disagreement is not known at this time, but may be partially due to geometric differences between the apex as modeled in this work and the flight vehicle. The effects of sideslip are explored and found to be minor at all but four calorimeter locations.

I. Introduction

An improved understanding of the aerothermal environment on the afterbody of planetary entry vehicles is important for future missions. Current design practice typically requires a large uncertainty on computed afterbody heating rates. This large uncertainty can have significant impact on the afterbody Thermal Protection System (TPS), affecting the material selected for a given mission as well as the final system mass. Unnecessary conservatism in the afterbody heat shield design will also shift the center of gravity of the vehicle backward, reducing stability and possibly necessitating ballast in the nose. The main reason for this uncertainty is a lack of data for code validation. Ground test data are typically complicated by sting interference effects, and flight data are extremely limited. Therefore it is critical to understand and make use of the limited flight data that are available to improve the next generation of Earth and planetary entry vehicles and to assess the need for additional flight testing and computational fluid dynamics (CFD) model development.

* Senior Research Scientist, Reacting Flow Environments Branch, MS 230-2, Senior Member AIAA

† Senior Research Scientist, Reacting Flow Environments Branch, MS 230-2, Associate Fellow AIAA

‡ Senior Research Engineer, Thermo-Physics Facilities Branch

The Apollo program spent considerable resources on testing to quantify the aerothermal environment around the reentering Command Module. Ground-based tests were conducted in low enthalpy wind tunnels, shock tunnels and free-flight facilities,¹⁻⁶ the data from which were used to build engineering-level predictions of the expected flight heating rates. Two flight tests (Fire-I and Fire-II)⁷⁻⁸ were conducted primarily to measure radiative heating. Once the Apollo entry vehicle design was determined, two flight tests of the actual Command Module (AS-201 & AS-202) were conducted at orbital velocities,⁹ and two flights (Apollo 4 & 6) were conducted at super-orbital velocities.¹⁰ Although AS-201 did not carry an onboard inertial measurement unit (IMU), one was carried during the other three flights, which enabled an accurate reconstruction of the flight trajectory and vehicle orientation as a function of time. The range of entry velocities and angles of attack during these flights was sufficient to span multiple flow regimes, from laminar to fully turbulent flow, as well as a regime with minimal material response to one with strong pyrolysis gas injection and char formation. **Table 1**, reproduced from **Ref. 11**, lists the relevant entry conditions for each of the four Apollo test flights. In **Table 1** V is the entry velocity at atmospheric interface, α is nominal the angle of attack and γ is the flight path angle. The maximum theoretical heating rate in **Table 1** was determined by engineering correlations for a spherical stagnation point.

In a previous paper,¹² we compared CFD predictions of afterbody heating to flight data for the Fire-II flight experiment. The computations generally agreed with flight data to within the experimental uncertainty, and areas of disagreement were explainable by unmodeled TPS material response. Those results demonstrated the ability of modern computational methods to accurately compute the afterbody heating environment of a laminar axisymmetric flow without significant material response. The next steps are to examine flight data for vehicles at angle of attack, with the addition of significant material response and turbulent transition. A prime data source for this purpose is the four Apollo flight tests. Many previous researchers have studied forebody convective and radiative heating results from these flights,¹³⁻¹⁴ but to our knowledge the afterbody heating data have not been previously examined using modern CFD.

In this paper we take the first step at simulating the afterbody heating environment for the Apollo Command Module, concentrating on the orbital AS-202 mission. The AS-202 flight was chosen as the starting point for such an analysis for several reasons. First, as discussed previously this flight was the first with an onboard IMU, which permits an accurate trajectory reconstruction. Also, the AS-202 mission had the lowest afterbody heat fluxes of the four flights, and the recovered capsule indicated that the afterbody suffered little charring during entry. Therefore analysis of this mission can be used to first establish the ability to predict afterbody heating levels of a lifting vehicle in the absence of ablation before attempting to simulate the more complex flows.

II. Command Module Geometry

Figure 1 is a schematic drawing of the Apollo Command Module outer mold line (OML) as modeled in this work. The capsule was designed to enter the atmosphere at an angle of attack of approximately 25° via an offset center of gravity, thereby achieving a lift to drag ratio of about 0.3. Note that in the Apollo-era literature the spherical-section aeroshell, which points into the oncoming flow, is labeled the aft section due to the position of the astronauts. However, in this paper we will use the modern (flow-oriented) nomenclature and will refer to the spherical section as the forebody, and the conical section as the afterbody. The Command Module forebody consists of a spherical section with a radius of curvature of 4.694 m. The shoulder radius is 0.196 m or 10% of the radius of the body. The afterbody consists of a 33° conical section, blunted to a 0.231 m radius at the aft end. The maximum diameter of the capsule is 3.912 m and the axial length, including the TPS material, is 3.431 m.

It should be noted that in the early days of the Apollo program the OML of the Command Module underwent frequent design changes, and there is considerable discrepancy in the literature among values for the radii of the shoulder and the blunted rear of the capsule. The values used in this paper are consistent with the instrument locations and geometry description in **Ref. 9**. The OML as modeled in this work is a simplification of the actual geometry, neglecting the umbilical housing, scimitar antennae, viewing windows, and reaction control system (RCS) thrusters on the leeside. The scimitar antennae and umbilical housing in particular are sizable protrusions (see next section and dimensions in **Ref. 15**) that will certainly alter the flowfield in their vicinity. Also, due to the variable thickness of the TPS material applied to the aeroshell (see below), the effective shoulder radius varied from the windward to the leeward side of the vehicle. Hillje¹⁵ gives these radii to be 0.19 m on the windward centerline and 0.18 m on the leeward centerline, respectively for the Command Module flown during the AS-202 mission (CM-011). The shoulder radius variation was not modeled in this work.

The outermost layer of the TPS on the entire aeroshell consisted of Avcoat 5026/39G, an ablator developed for the Apollo program. The Avcoat material was injected into a phenolic honeycomb matrix which was bonded to a

Table 1 Entry conditions for the Apollo Command Module flight tests.

Flight Designation	V (km/s)	α (deg)	γ (deg)	Max Decel (g's)	Theoretical Max Heating (W/cm ²)
AS-201	7.67	20	-8.6	14.3	186
AS-202	8.29	18	-3.5	2.4	91
Apollo 4	10.73	25	-5.9	4.6	237
Apollo 6	9.60	25	-6.9	7.3	488

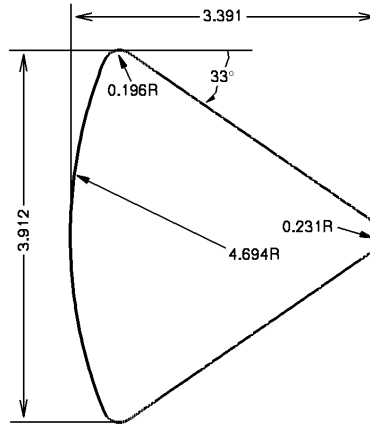


Figure 1. Schematic drawing of the outer mold line of AS-202 capsule as modeled in this work.

stainless-steel substructure.¹⁶ Avcoat 5026/39G was an epoxy resin reinforced with quartz fibers and lightened with phenolic microballoons to obtain a final density of 244.6 kg/m³.¹⁷ The final ablator thickness was variable according to the predicted aerothermal environment, and ranged from 6.86 cm on the windward side of the spherical forebody, to 1.79 cm near the rear apex of the conical afterbody.¹⁶ The afterbody of the capsule was painted with a titanium-oxide (white) paint for cosmetic reasons, and also to act as a moisture barrier during pre-launch storage.

III. Flight Instrumentation

A total of 12 pressure transducers and 12 calorimeters were placed on the forebody of the aeroshell. Usable pressure data were obtained from ten of the twelve pressure transducers, however none of the forebody slug calorimeters, which were designed specifically for the Apollo program, produced usable data during either the AS-201 or AS-202 flights.⁹ These calorimeters were redesigned before the Apollo 4 & 6 flights.¹⁰

Twenty-three calorimeters were placed on the afterbody. Of these, 19 functioned properly during the AS-202 mission. Figure 2 shows the locations of the surface-mounted calorimeters on the afterbody aeroshell for both the AS-201 and AS-202 test flights, and Table 2 gives the location of each calorimeter in terms of the coordinate system defined in Fig. 2. In this coordinate system, x is measured from the nose of the vehicle to the apex and θ is the circumferential angle. $\theta = 90^\circ$ lies along the positive z -axis and corresponds to the windward centerline assuming no sideslip, and $\theta = 270^\circ$ corresponds to the leeward centerline. It is important to note that the calorimeter locations given in Ref. 9 assumed that $x = 0$ was at the vehicle nose before the application of the ablative TPS material. Therefore all x -coordinates given in Table 2 were adjusted from those in Ref. 9 by the 5.23 cm ablator thickness at the nose.¹⁶ Those calorimeters that provided usable data during the entry are labeled in Table 2 with a letter code that matches that used in Fig. 17 of Ref. 9.

The afterbody calorimeters were designed to measure heating rates of less than 58 W/cm². A schematic diagram is given in Ref. 9. These calorimeters are essentially Gardon gages,¹⁸ which are in common use for measurement of steady state radiation and convective heat flux. The gage is explicitly designed to work in convective stagnation flows and is calibrated assuming that the peak temperature is at the center of the 0.66 cm diameter constantan foil disk. A potentially significant source of error is introduced when the gage is used in a shear flow moving parallel to the foil surface, causing the peak foil temperature to deviate from its center. One way to alleviate this error source is

Table 2 Afterbody calorimeter locations for AS-202.

ID ^a	X ^b (cm)	θ^b (deg)	Range (W/cm ²)	ID ^a	X ^b (cm)	θ^b (deg)	Range (W/cm ²)
-	72.6	93.7	0-114	l	228.8	182.9	0-28
a	120.8	85.3	0-57	m	106.8	215.3	0-11.4
b	169.8	92.0	0-57	n	69.5	225.5	0-11.4
c	205.6	115.0	0-57	-	205.6	191.3	0-28
d	294.8	83.4	0-57	o	136.6	229.8	0-11.4
e	343.1	Apex	0-28	p	152.6	234.0	0-28
f	69.5	138.0	0-57	q	184.3	276.4	0-28
g	161.5	142.8	0-28	r	205.6	267.8	0-28
h	54.5	178.5	0-28	s	294.8	265.0	0-28
i	54.5	270.0	0-11.4	-	74.1	253.0	0-28
j	94.1	178.6	0-28	-	88.0	253.0	0-57
k	157.6	177.5	0-28				

^a corresponds to Fig. 17 in Ref. 9. Those without letters were non-functional during AS-202.
^b refer to Fig. 1 for coordinate system definition.

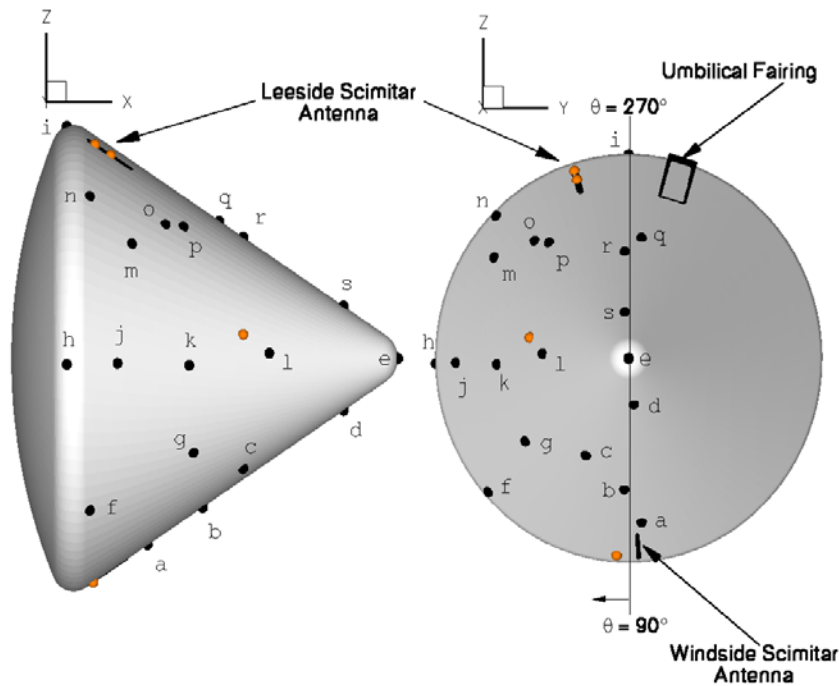


Figure 2. Locations of calorimeters on AS-202 conical afterbody. Orange symbols indicate inoperative instruments. Letters correspond to the ID in Table 2.

to use a larger diameter foil than required for the heating rate. In shear flow applications the standard guidance¹⁹ is to use a gage that has a maximum measurable heating rate of about 20 times the expected value. Comparing the ranges for each gage as listed in Table 2 with the observed flight heating levels in Figs 8(a-s), we note that this guidance was followed for all gages except “h” and “i”. The gage under laboratory conditions can produce a minimum uncertainty of $\pm 3\%$, but under flight conditions in shear flow an uncertainty of approximately $\pm 20\%$ is reasonable.²⁰ Since measurement uncertainties on the flight data were not given in the literature, a value of $\pm 20\%$ will be assumed in this work.

Twenty-four pressure transducers were also used on the afterbody of the spacecraft. However, none of the 22 pressure transducers on the conical afterbody and only one of the two on the shoulder detected a measurable pressure rise until just prior to parachute deployment. Therefore no meaningful comparisons to flight pressure data can be made.

Also shown in Fig. 2 is the approximate position of the two scimitar antennae and the umbilical fairing, which are not modeled in the current work. The antennae had a semicircular profile with a width of less than 2 cm and a maximum height of about 20 cm.¹⁵ The leeward antenna survived intact, but the antenna on the wind side was destroyed during the entry. Due to their small profile it is likely that their effect on the flowfield would be local, and therefore eliminating them from the OML used in this work should not have a major impact on the results. The one exception to this may be the heating data from calorimeter “a”, which is located immediately downstream of the windward antenna. The fidelity of the data from calorimeter “a” will be explored in the comparison to experimental data below. The umbilical housing had a larger profile, but was on the side of the afterbody opposite the majority of the calorimeters, and therefore should not have a major influence on the results presented here.

Finally, it should be noted that although afterbody radiometers were not used on AS-202, two radiometers were placed on the conical afterbody during the Apollo 4 & 6 flights. Although both were determined to be functional, neither measured any signal during the heating pulse, indicating that radiative heating to the conical section was negligible.¹¹ Since the reentry environment for the AS-202 flight was much less severe than that for Apollo 4 & 6, we can surmise that there was zero radiative heating to the afterbody for these flights.

IV. Aerodynamics and Trajectory Reconstruction

Flight aerodynamics were reported by Hillje,¹⁵ as reconstructed from the onboard IMU. The Command Module entered the atmosphere at 8.3 km/s at 4390 seconds after launch on a shallow flight path angle of -3.53 deg. and a nominal angle of attack of 18 deg. AS-202 was the first Apollo mission with an active guidance system, thus one of the primary flight objectives was to test the guidance and RCS. Therefore a roll reversal was planned between 4410 and 4480 seconds to orient the capsule in a lift-up position and enable a “skip” phase during the entry. Figure 3 shows the reconstructed altitude and velocity as a function of time.¹⁵ As seen in Fig. 3, a local minimum in altitude was achieved at about 4520 seconds, followed by the skip phase, which lasted until a local maximum in altitude was achieved at approximately 4690 seconds. After a second roll reversal, the capsule continued its descent. This skipping trajectory resulted in two distinct heating pulses during the entry, as seen in Fig 8. The angle of attack remained within ± 0.5 deg. of nominal during most of the entry, but began to increase at about 4900 seconds, reaching a value of about 20 deg. by 5000 seconds after launch. Although the vehicle was not intended to have any sideslip during the entry, the flight aerodynamics data indicate that a nearly constant sideslip angle of about 2.5 ± 0.5 deg. was present.¹⁵ This paper will examine the impact of sideslip on the afterbody heat transfer distribution.

Atmospheric conditions along the entry trajectory were obtained via sounding rockets to an altitude of 55 km. The sounding rocket data were then extrapolated vertically to entry interface using standard hydrostatic relations.²¹ Atmospheric density and temperature as a function of time for AS-202 are given in Ref. 9.

V. Methodology

The flowfield computations are performed using the CFD code DPLR.^{12,22} DPLR is a parallel multiblock finite-volume code that solves the reacting Navier-Stokes equations including finite-rate chemistry and the effects of thermal nonequilibrium. The Euler fluxes are computed using a modified (low-dissipation) form of Steger-Warming flux vector splitting,²³ with third-order spatial accuracy obtained via MUSCL extrapolation.²⁴ Viscous fluxes are computed to second-order accuracy using a central difference approach. DPLR has been used previously on several other planetary entry simulations.^{12,25-26} At the entry velocities considered in this work the level of flowfield ionization will be small. Forebody calculations near the peak heating point indicated ionization levels of less than 0.3%. Therefore a 5-species (N_2 , O_2 , NO, N, O) 5-reaction finite-rate air chemistry model is used.²⁷⁻²⁸ The flow is assumed to be in thermal nonequilibrium, according to the two-temperature model of Park.²⁹ Vibrational relaxation is modeled using a Landau-Teller formulation, where relaxation times are obtained from Millikan and White,³⁰ assuming simple harmonic oscillators.

Viscous transport and thermal conductivity are modeled using the mixing rules presented by Gupta et al.³¹ which have been shown to be reasonable approximations of the more accurate Chapman-Enskog relations in this flow regime.³²⁻³³ The self-consistent effective binary diffusion (SCEBD) method is used to compute the species diffusion coefficients.³⁴ This method allows for the variations in species diffusion coefficients to be accurately modeled without sacrificing the requirement that the diffusion velocities sum identically to zero. Post-flight interpretation of the heating data indicated that the flowfield on the conical afterbody remained entirely laminar prior to the atmospheric skip maneuver ($t < 4800$ s).⁹ The windward side of the afterbody was assumed to have

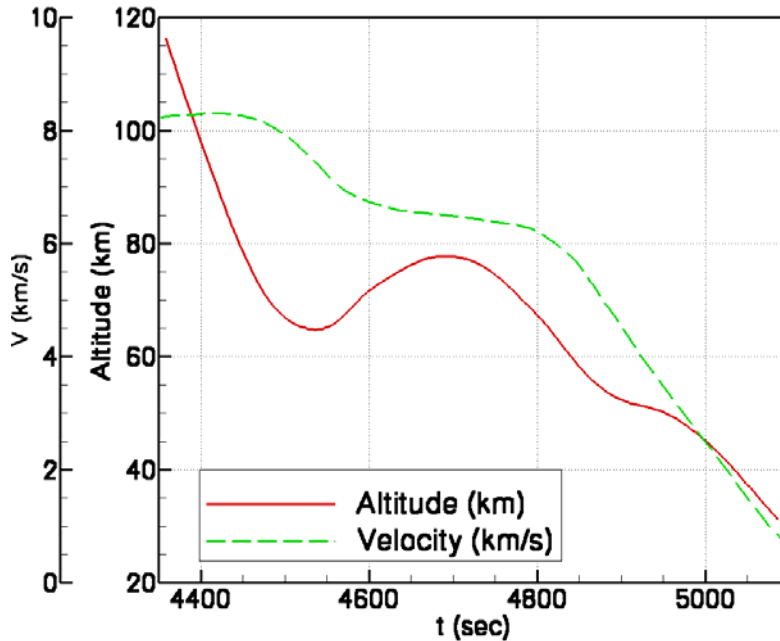


Figure 3. Altitude and velocity as a function of time from launch for AS-202.

transitioned to turbulence after the skip,⁹ however the leeward side apparently remained laminar. The majority of the results presented in this work assume laminar flow, however the possibility of turbulent transition, particularly after the skip maneuver, is explored. The impact of turbulence on heating levels for the attached flow region of the afterbody are examined using a compressible Baldwin-Lomax model³⁵ with a turbulent Schmidt number of 0.5.

Surface catalysis is modeled using a diffusion limited approach.²⁹ The surface is assumed to be fully catalytic to N_2 and O_2 recombination, which should be reasonable for the hydrocarbon resin based Avcoat material. At very high heat fluxes the quartz fibers in the material would begin to melt, which would reduce the effective surface catalycity, but this would not have occurred at the relatively low heat fluxes measured on the conical afterbody during this flight. The afterbody surface was initially coated with a titanium dioxide paint, which likely had a fairly low catalycity. However, this paint would have burned away early in the entry, exposing the highly catalytic Avcoat TPS to the flow. The asymptotic calorimeters on the aft shell were surface mounted, and thus exposed to the flow. Therefore it is possible that the calorimeters had a different catalycity than the underlying TPS, which could lead to catalytic heating jumps at the sensor location. However, in this case the calorimeter surface should be nearly fully catalytic, and thus should have blended well with the catalytic TPS. The surface was also assumed to be in radiative equilibrium with a constant emissivity of 0.85, a value typical of carbonaceous ablators. The foil disk of the calorimeter surface would possibly have a lower emissivity than the Avcoat, but since heat flux is a weak function of emissivity, this difference was not considered to be important. The effects of varying surface catalysis and emissivity on the computed heat transfer will be explored in the following section.

Shock-layer radiation is neglected, due to the low entry velocity and the fact that radiometers on the higher velocity Apollo 4 and 6 entries failed to detect any radiation signal on the afterbody.¹¹ Material ablation and thermal response are also neglected, as their effects on computed surface heating should be negligibly small for the low heat fluxes observed on the afterbody of the AS-202 flight.

Wake flows are sensitive to the details of the volume grid construction and it is important to generate a grid that is well aligned to anticipated flow features. In particular, it is extremely important that the grid have sufficient points in the shoulder region to capture the rapid expansion and accurately predict the flow separation point and the angle of the resulting shear layer.³⁶ There must also be sufficient points in the separated flow region to resolve the vortical structure and the wake compression, or neck. The baseline grid topology for this work (Fig. 4) consists of five grid blocks and is constructed to permit local refinement of the shoulder region and the wake core region while maintaining point matching at every block interface. The solution adaptive grid code SAGE³⁷ is used to tailor the outer boundary of the grid to the shock wave. A grid resolution study was performed to determine the final density requirements; the results are reported in the following section.

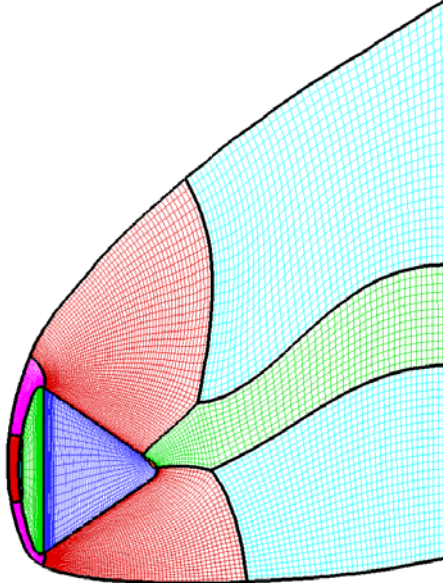


Figure 4. Grid topology used in this work. Every other point shown in each direction of the pitch plane and body surface.

Table 3 AS-202 Trajectory points and freestream conditions

Time ^a (s)	Alt. (km)	Re _D ^b	V (km/s)	M	ρ_{∞} (kg/m ³)	T_{∞} (K)	α (deg)	β (deg)
4455	76.8	7.5×10^4	8.24	28.6	$3.38e-5$	205	18.2	2.0
4475	71.3	1.8×10^5	8.15	27.6	$8.76e-5$	217	17.9	2.5
4500	70.0	3.0×10^5	7.92	26.2	$1.52e-4$	227	17.8	2.5
4510	66.0	3.2×10^5	7.80	25.6	$1.69e-4$	230	17.8	2.5
4530	64.9	3.4×10^5	7.53	24.5	$1.84e-4$	234	17.9	2.5
4560	66.0	2.7×10^5	7.07	23.2	$1.53e-4$	231	18.1	2.5
4600	71.6	1.3×10^5	6.74	22.9	$7.19e-5$	215	18.3	2.5
4650	76.2	5.7×10^4	6.56	22.8	$3.24e-5$	206	18.5	2.0
4700	77.2	4.3×10^4	6.49	22.7	$2.45e-5$	203	18.5	2.0
4750	74.5	7.6×10^4	6.39	22.0	$4.50e-5$	210	18.4	2.0
4800	67.3	2.1×10^5	6.21	20.5	$1.37e-4$	210	18.4	2.0
4825	62.9	3.5×10^5	5.97	19.2	$2.81e-4$	239	18.3	2.0
4850	58.2	5.3×10^5	5.62	17.6	$4.14e-4$	252	18.3	2.5
4875	54.6	6.9×10^5	5.07	15.6	$6.16e-4$	262	18.4	2.5
4900	52.4	7.6×10^5	4.53	13.2	$8.00e-4$	268	18.6	2.5

^aSeconds after launch. ^bFreestream Reynolds number based on body diameter.

VI. Results

Full three-dimensional CFD solutions were obtained for fifteen points along the trajectory, with freestream conditions listed in Table 3. The solutions range from 4455 to 4900 seconds after launch, with nine of the points concentrated in the first heat pulse ($t = 4455$ to $t = 4700$ s). The second heat pulse ($t = 4750$ to $t = 5100$ s) was explored in less detail primarily because of the number of RCS events during this time period, which make the data from many of the calorimeters more difficult to interpret, and the fact that the separated flow becomes unsteady late in the flight. Although the wake structure becomes more complex with increasing Reynolds number, the computations indicate that the flow remains steady until about $t = 4850$ s ($Re_D = 5.3 \times 10^5$), at which point the vortices begin to oscillate, leading to unsteady wake flow. The flowfield in the attached portion of the afterbody

remains steady throughout the entry. Most of the cases were run assuming bilateral symmetry; the effects of the small sideslip angle were neglected. This approximation should be reasonable for most of the calorimeter locations, but it may have a significant influence in certain areas. In order to quantify the impact of neglecting the sideslip angle, a single computation at $t = 4500$ s was performed which included yaw. The results are discussed below.

A. Grid Resolution

Grid resolution was confirmed by independently varying the point density in each of the three grid directions (axial, normal, and circumferential). Based on previous work^{12,36} the most critical area to resolve is the shoulder region, where the flow separates and the shear layer forms, therefore most of the axial refinement was confined to this area. Solutions were obtained on multiple volume grids to ensure that the final baseline grid density was sufficient to ensure grid independence. As expected, axial distribution at the shoulder was by far the most important metric to ensure a grid-resolved solution. The final grids consisted of 10,000 surface points, with clustering in the shoulder region, and 1.5 million volume points on a 180° circumferential distribution. This grid density was determined to provide a grid-converged answer at $t = 4510$ s. A separate resolution study was not performed at all trajectory points; it was assumed this grid density would be sufficient for the remaining fourteen (lower Reynolds number) solutions. All cases had the same surface grid, but outer boundaries were tailored for each case to ensure that the grid was well aligned to the bow shock and flow features.

B. Wake Structure and Surface Features

Examination of the wake structure for this type of flow is necessary to understand the resultant surface heating. An instructive first step is to examine flow structures in the pitch plane. Figure 5 shows the pitch plane streamlines colored by the local translational temperature for five selected trajectory points – $t = 4510, 4600, 4700, 4800,$ and 4900 s. The solutions in Fig. 5 span more than an order of magnitude in freestream Reynolds number, ranging from $-Re_D = 4.3 \times 10^4$ at $t = 4700$ s to $Re_D = 7.6 \times 10^5$ at $t = 4900$ s. In all cases the flow remains attached on the windward side of the conical afterbody, in contrast to pre-flight expectations.⁹ Separation occurs near the maximum diameter point on the shoulder on the lee side.

For all five cases, a critical point³⁸ (shown as a red dot) is apparent in the near wake on the lee side. Figure 5(f) shows the locations of the critical point for the five cases. The location of this critical point depends on the freestream Mach and Reynolds numbers, and the angle of attack. For the present set of computations, the angle of attack does not vary more than $\pm 0.4^\circ$ about an average value of 18.2° , and the thus dependence of the critical point location on the angle of attack is expected to be weak. It is evident from Fig. 5f that the critical point moves away from the surface with decreasing Reynolds number. However, the axial (x) location seems to be constant between $t = 4510$ s and $t = 4800$ s where the Mach number ranges from 25.6 to 20.5. This suggests that the Mach number has a weaker influence on the axial location of the critical point. However, at $t = 4900$ s, where the Reynolds number is the highest, and the Mach number the lowest in selected set of points, the critical point moves further upstream on the leeward side. This movement is a combined influence of both the freestream Mach and Reynolds numbers, which is complicated by the fact that neither is monotonic in time due to the skip maneuver.

The computed oil flow patterns (surface streamlines) on the afterbody are shown in Fig. 6 for the same trajectory points as in Fig. 5. The oil flow patterns represent the direction of the surface shear stress, which is computed from

$$\vec{\tau}_w = \mu_w \frac{\partial \vec{u}_t}{\partial n} = \mu_w \frac{\partial}{\partial n} [\vec{u} - (\vec{u} \cdot \vec{n}_w) \vec{n}_w]$$

where $\vec{\tau}_w$ is the surface shear stress and μ_w is the value of the coefficient of viscosity at the wall. Note that the velocity gradient in the wall-normal direction is computed using the tangential velocity, \vec{u}_t (easily obtained from the actual velocity, \vec{u} , and the unit outward normal, \vec{n}_w , to the body surface). As is typical for separated laminar flows, the size of the separation region increases with Reynolds number (see Fig. 6, which shows similar structures/patterns). At the highest Reynolds number ($t = 4900$ s), the surface oil flow pattern is very different from the others. However for this case the computed flowfield is unsteady and the present computations, which are not time accurate, cannot adequately capture the unsteadiness. The oil flow patterns in Fig. 6 are superimposed over the radiative equilibrium ($\varepsilon=0.85$) surface temperature contours (shown on a local scale of 200-1200 K relevant to the afterbody). The location of the critical points, such as nodes, foci, saddle points, on the surface are indicated as blue dots on the port side of the vehicle. The richness and complexity in the oil flow patterns is evident from the figures. Further, the separation lines and change in surface temperature across them are clearly seen. The areas of locally

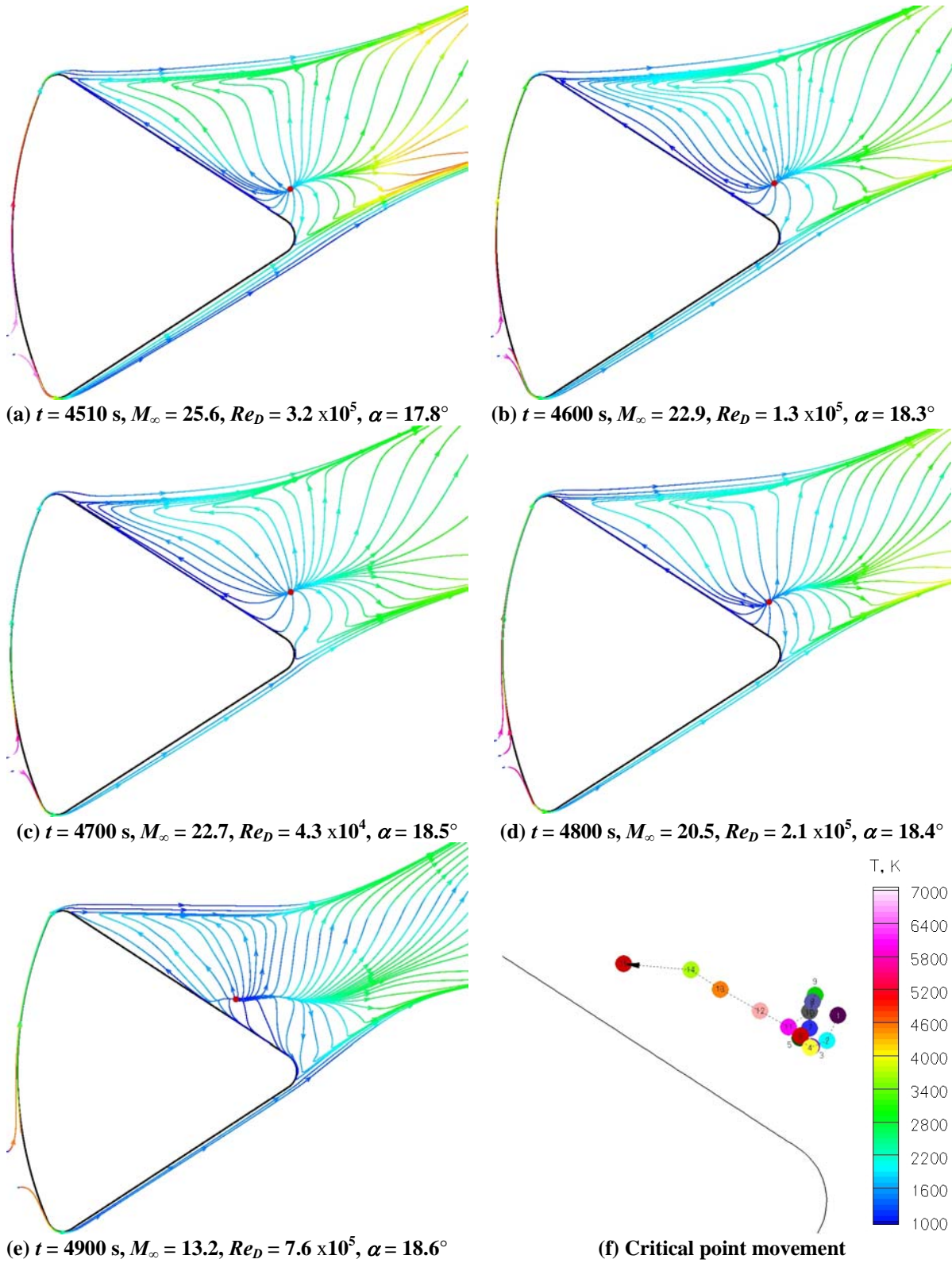


Figure 5. Streamlines colored by translational temperature in the pitch plane for five trajectory points between $t=4510$ and $t=4900$ s, and critical point location for all fifteen solutions.

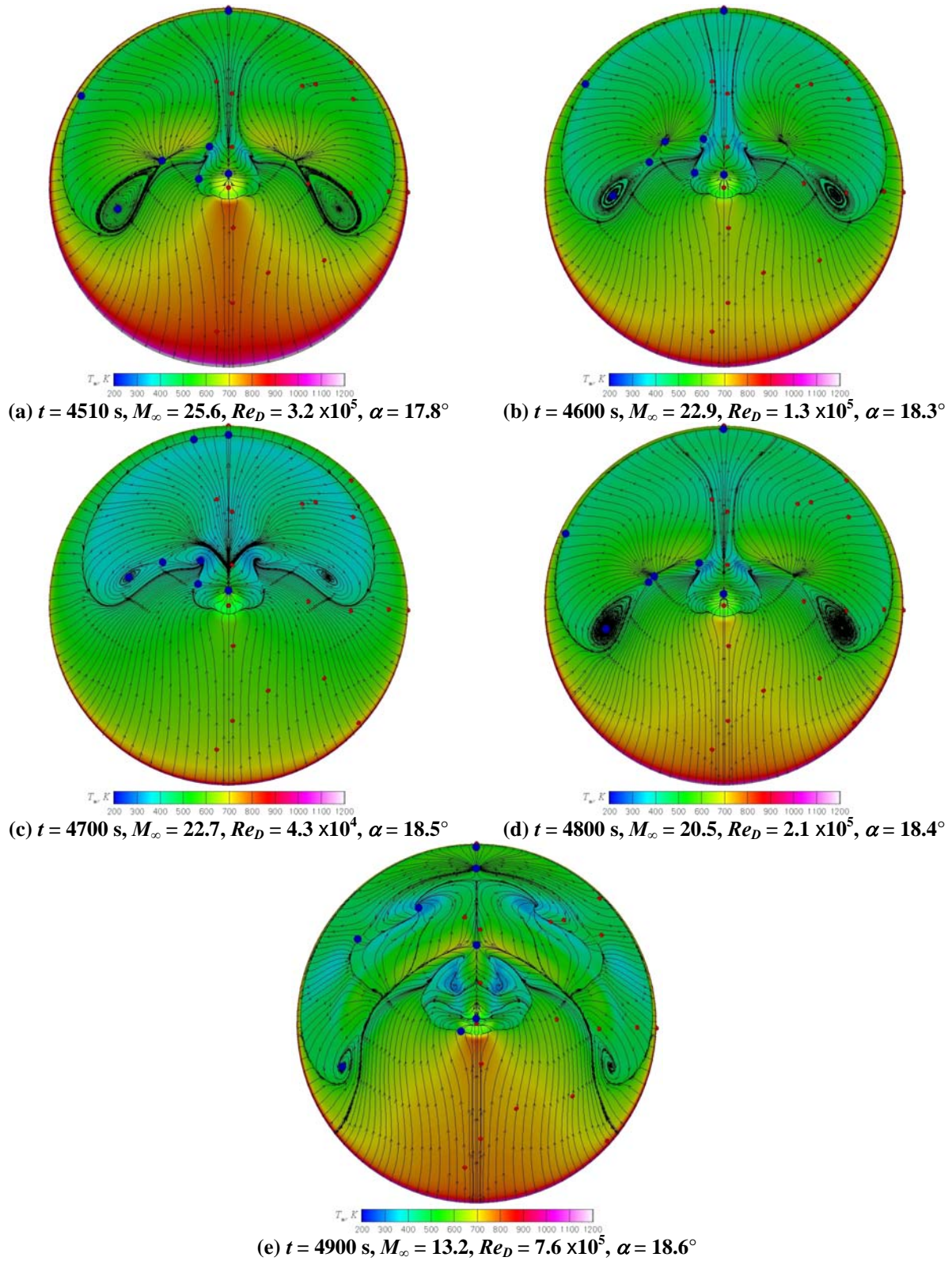


Figure 6. Oil flow patterns on the afterbody for five trajectory points between $t=4510$ and $t=4900$ s. Surface colored by radiative equilibrium temperature ($\varepsilon = 0.85$). The calorimeter locations are indicated by red dots, and the critical points are indicated by blue dots.

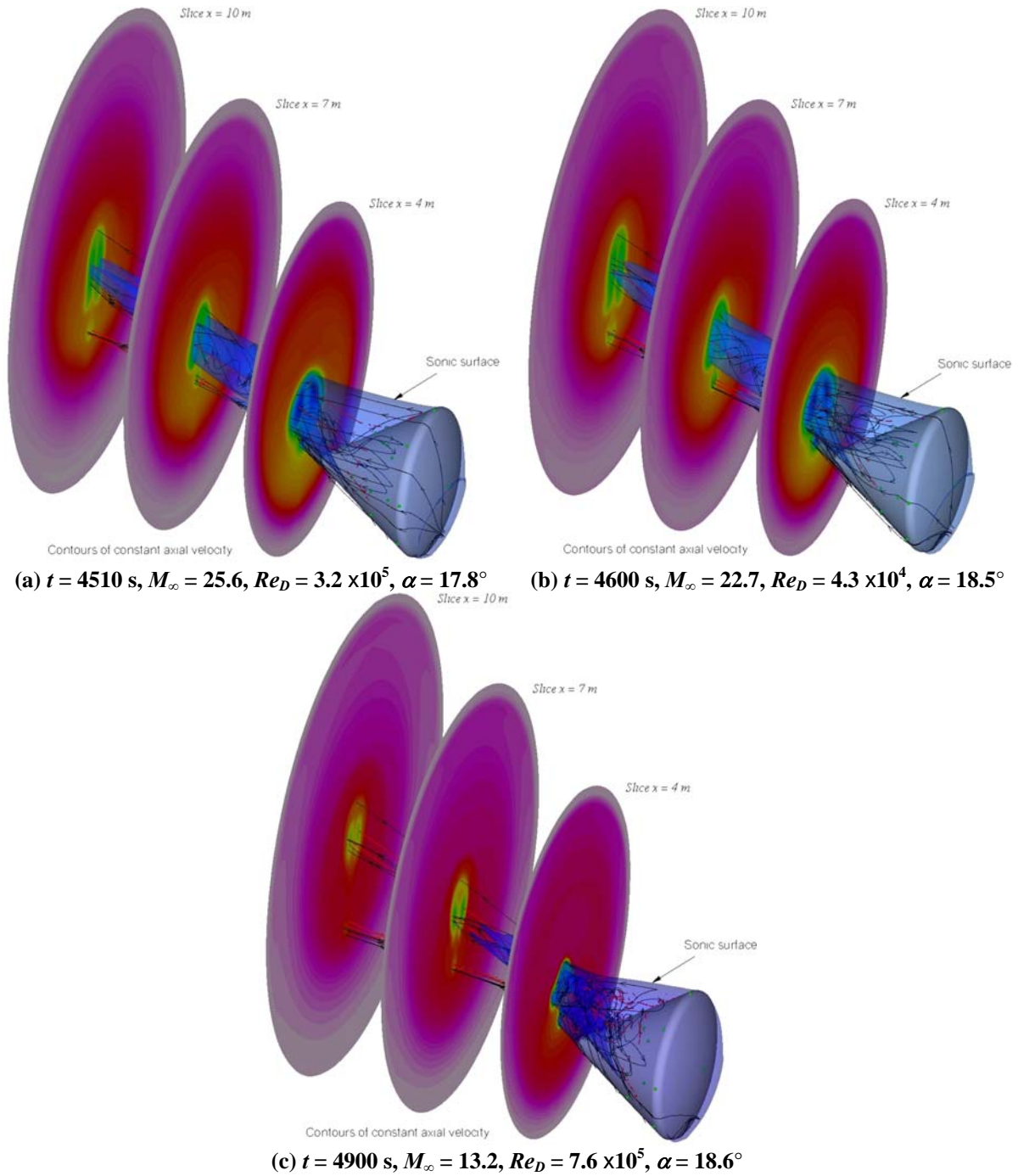


Figure 7. Three-dimensional wake flow structure from computations at three trajectory points. The translucent envelope around the vehicle is the sonic surface. The three planes aft of the vehicle are slices through the volume taken at $x = 4, 7,$ and 10 m . The slices are painted with contours of axial velocity (Cartesian component u). The solid red lines represent the vortex cores extracted using Tecplot[®] from the volume solutions.

increased temperature are seen at the nodes/foci. These local hot spots correspond to vortex impingement on the surface. Local maxima in surface temperature also occur at the rear apex for all cases.

Having examined the flow structures in the pitch plane and the vehicle surface, one can also examine the three-dimensional flow behind the vehicle. While the interactive use of flow visualization software provides much more information than static images, an attempt at presenting the nature of the wake flow is made in Fig. 7 for three trajectory points – $t = 4510, 4600,$ and 4900 s. Each figure shows the sonic surface envelope around the vehicle, along with vortex cores and volume streamtraces in the wake. Also shown are contours of axial velocity (Cartesian component u) on three slices through the volume at $x = 4, 7,$ and 10 m. The decrease in the extent of the sonic surface with decreasing Mach number is evident from the figure. The usual practice of examining the sonic region in the pitch plane to determine wake closure could be very misleading. Due to the crossflow induced by the angle of attack, the sonic surface develops two lobes corresponding to the off-axis trailing vortices, and this twin-lobed sonic surface extends much further aft in regions away from the pitch plane as these vortices separate in the wake. The characteristic rotational structure of the afterbody flow is clearly brought out through the volume streamtraces contained in the subsonic volume in the afterbody region. The vortex cores, extracted using Tecplot[®], are indicated as solid red lines in the figures. There are two large counter-rotating vortices on the leeside, and two more below these past the rear apex. The footprints of the four-vortex system are clearly seen in the axial slices through the volume. The separation between the upper and lower vortex system increases with decreasing Mach number.

C. Comparisons to Experimental Data

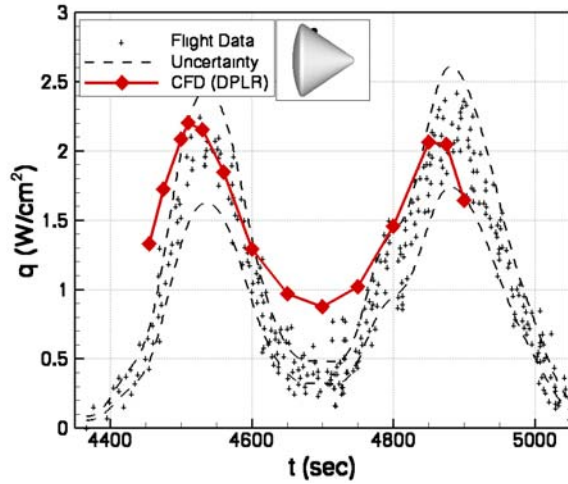
Figure 8 shows the comparison between the computed afterbody heat transfer and the experimental data for each of the 19 functional calorimeters on the AS-202 Command Module. The agreement between the computations and the data is generally within the assumed experimental uncertainty for 15 of the 19 calorimeters. The calorimeters will be discussed in four separate groups: those on the shoulder in attached flow (“ h ” and “ i ”) those on the windward (attached) side of the afterbody (“ $a-d$ ”, “ f ”, and “ g ”), those in the separated flow region (“ e ”, “ m ”, and “ $o-s$ ”) and those near the separation line (“ j ”, “ k ”, “ l ”, and “ n ”).

On each plot in Fig. 8 the flight data, which were scanned from Ref. 9, are shown as crosses. At some locations, particularly during the second heat pulse, there were multiple signal spikes at some locations. For example, notice the sharp heating spikes in the flight data on Fig. 8(l) at around $t = 4460$ and $t = 4900$ s. These spikes were determined by Lee⁹ to correspond to the times of RCS firings, and thus are considered to be spurious. The data points that were estimated by the present authors to be spurious are shown on the plots as open circles. The best fit to the data for each case was then obtained using a Fourier-function based least-squares fitting procedure neglecting the spurious data points. Dashed lines indicate the assumed $\pm 20\%$ uncertainty in the data, as discussed in the “Flight Instrumentation” section. For the purposes of this work the uncertainty was assumed to remain constant throughout the entry. Examination of Fig. 8 indicates that the assumed uncertainty encompasses the majority of the data scatter, with the exception of some of the calorimeters in the separated flow region, which have more scatter during the skip maneuver ($t = 4600$ to 4800 s). Finally, the CFD results at the fifteen trajectory points are shown as red diamonds.

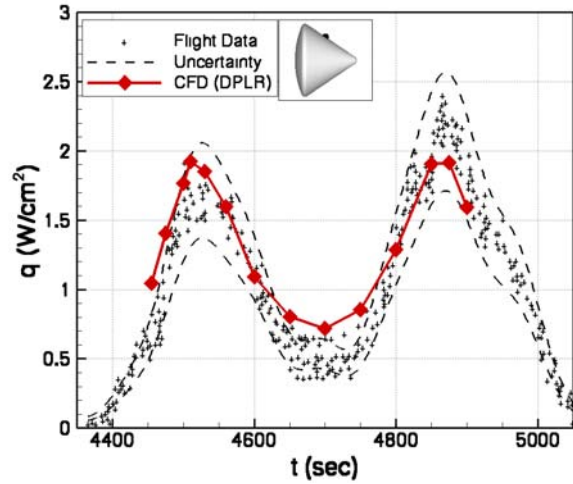
1. Shoulder Region

Two calorimeters were placed on the shoulder just before the maximum diameter point. Calorimeter “ h ” was placed midway between the windward and leeward centerline ($\theta = 178.5^\circ$), and “ i ” was placed on the leeward centerline ($\theta = 270^\circ$). Figure 8(h) shows the comparison between the computed heating levels and the flight data for calorimeter “ h ”. The agreement between the CFD and flight data is good. The peak heat flux predicted by the CFD is about 10 W/cm^2 at $t = 4510$ s, or about 6% higher than the flight data (9.4 W/cm^2). The agreement is generally within 20% over the entire trajectory, with the largest discrepancy occurring near the minimum between the two heat pulses ($t \sim 4700$ s).

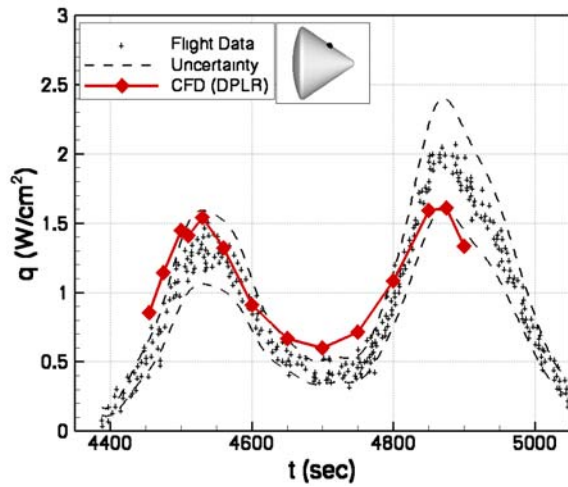
The comparison for calorimeter “ i ” on the lee centerline is shown in Fig. 8(i). Once again the agreement is within the assumed $\pm 20\%$ uncertainty throughout most of the flight. Note that calorimeter “ i ” apparently saturated above 3.7 W/cm^2 , and thus no data were obtained during the peak of the first heat pulse. However, the trends predicted by the CFD before and after this loss of signal are in good agreement with the flight data, although the sparsity of flight data between 4560 and 4700 seconds make comparison difficult. The good agreement between the flight data and the CFD for these shoulder-mounted calorimeters is somewhat surprising, given the size of the lateral gradient in heat flux at this location.



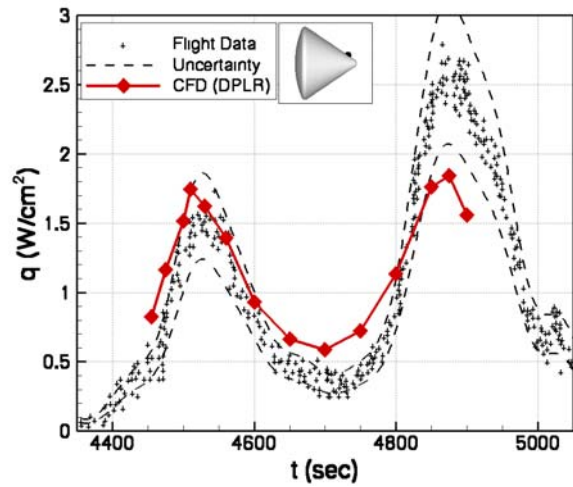
a) calorimeter "a"



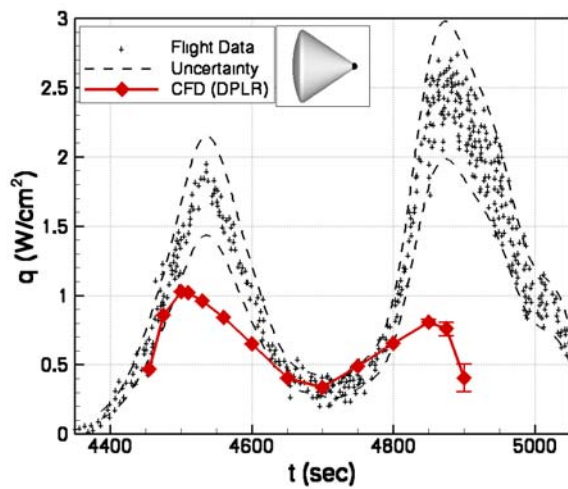
b) calorimeter "b"



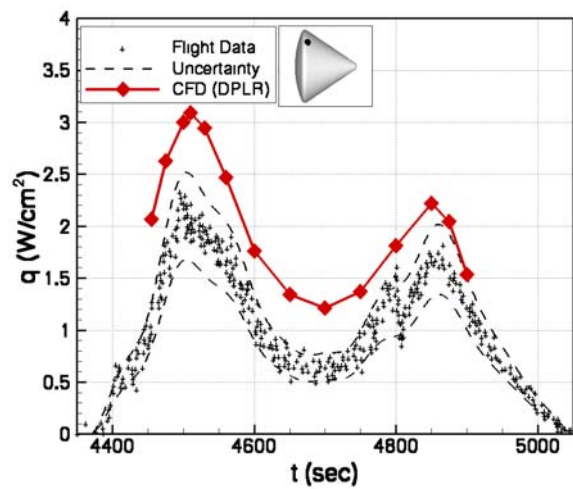
c) calorimeter "c"



d) calorimeter "d"

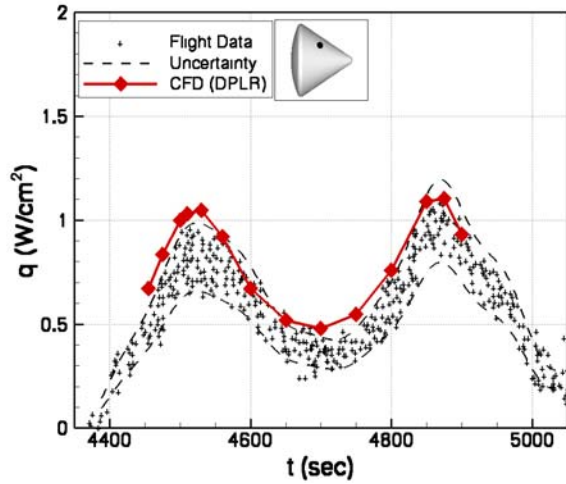


e) calorimeter "e"

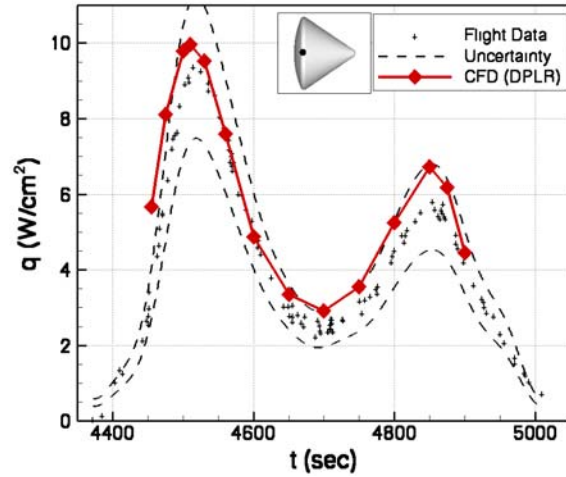


f) calorimeter "f"

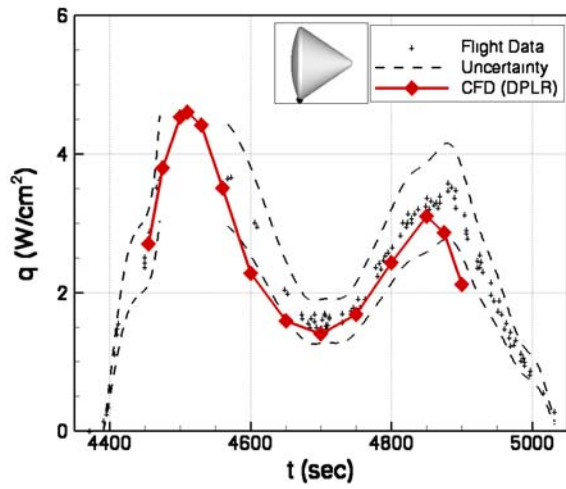
Figure 8. Comparison of computed and experimental heat transfer for AS-202. Letters indicate calorimeter ID in Table 2.



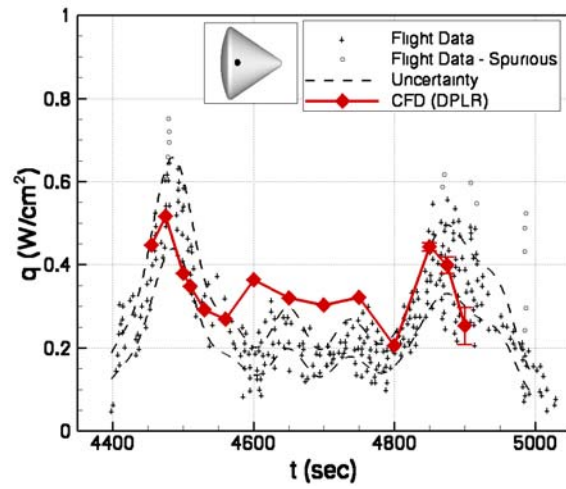
g) calorimeter "g"



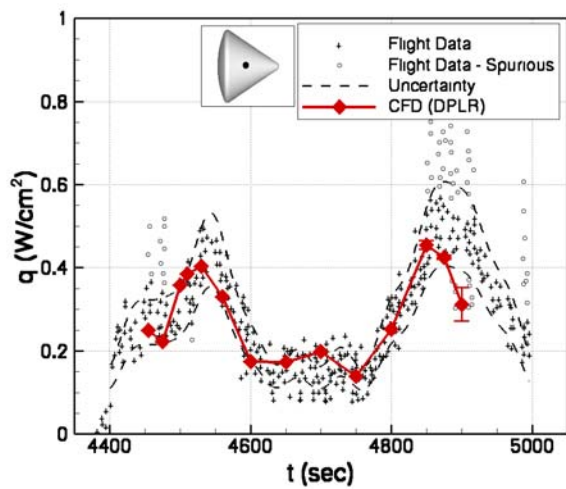
h) calorimeter "h"



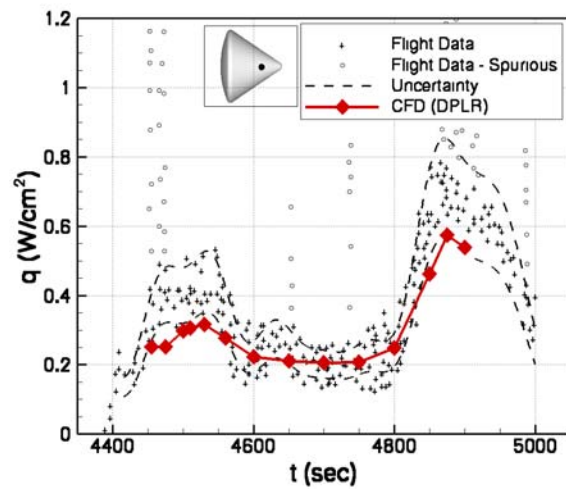
i) calorimeter "i"



j) calorimeter "j"

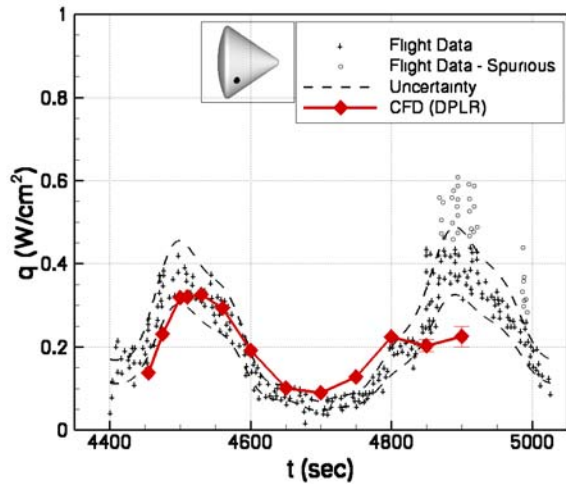


k) calorimeter "k"

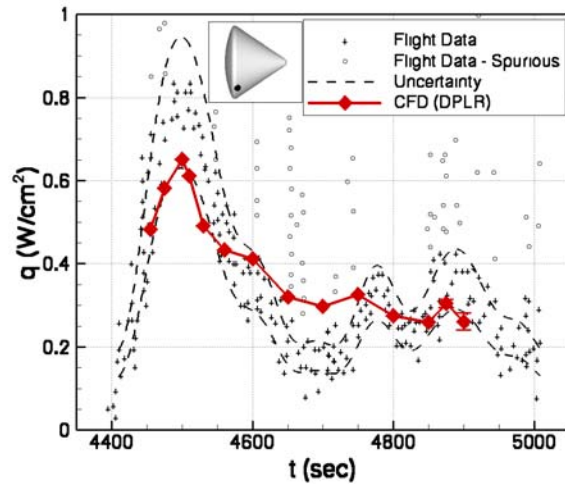


l) calorimeter "l"

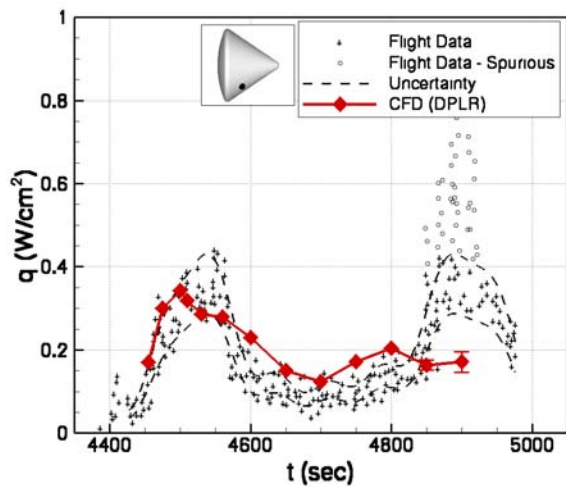
Figure 8. Comparison of computed and experimental heat transfer for AS-202, continued.



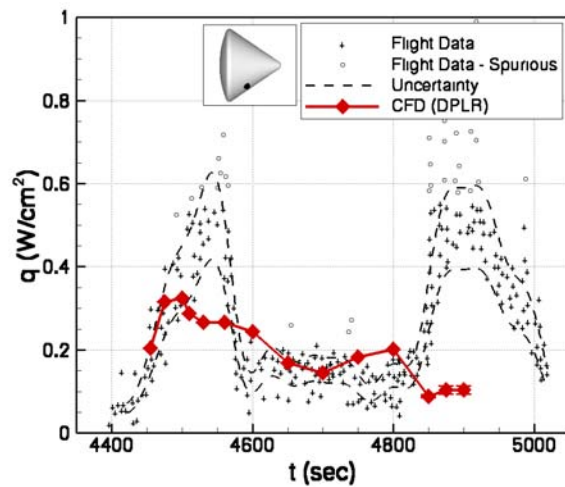
m) calorimeter "m"



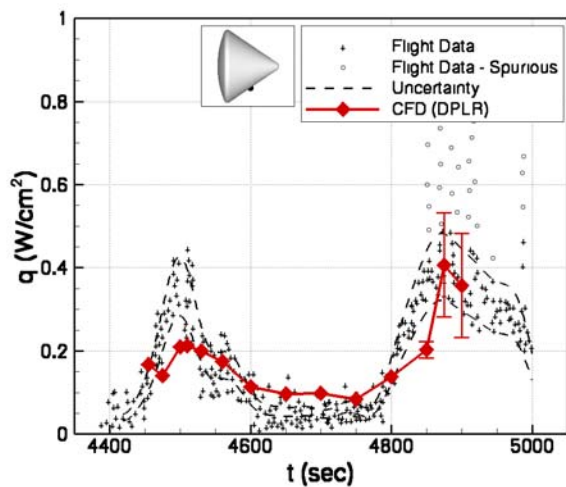
n) calorimeter "n"



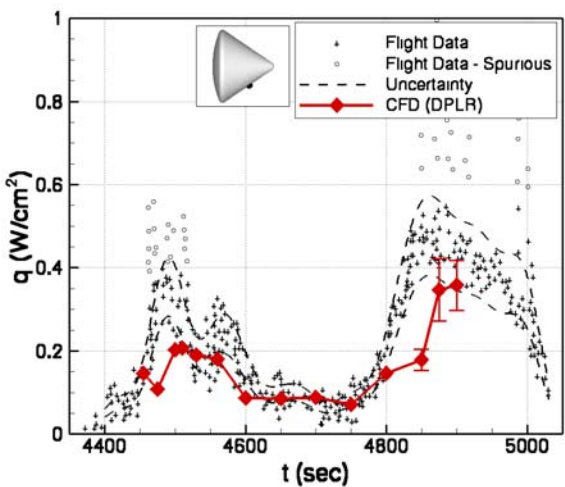
o) calorimeter "o"



p) calorimeter "p"



q) calorimeter "q"



r) calorimeter "r"

Figure 8. Comparison of computed and experimental heat transfer for AS-202, continued.

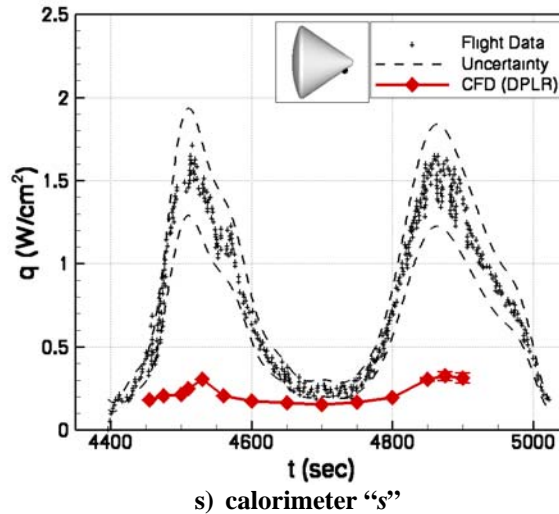


Figure 8. Comparison of computed and experimental heat transfer for AS-202, concluded.

2. Attached Flow Region

Six calorimeters were placed on the conical afterbody on the windward side in a region where the flow remained attached throughout the entry. Calorimeters "a" through "d" were placed on or near the windward centerline, as shown in Fig. 3. Calorimeter "g" was placed approximately midway between the shoulder and rear apex, at $\theta = 143^\circ$. The comparisons between the computed and experimental heat flux for these calorimeters are shown in Figs. 8(a)-8(d) and 8(g). From the figures we see that the agreement is generally good during the first heat pulse. The heating levels near the peak heating point ($t = 4510$ s) are predicted to within 10% at all locations. Computed heating levels during the early portion of the second heat pulse also agree well with flight data, although the CFD results for calorimeters "c" and "d" at the final two trajectory points ($t = 4850$ and $t = 4900$ s) are lower than the flight data. The difference between the computation and flight data appears to increase with distance from the shoulder (the CFD results for calorimeter "c" are about 23% below the flight data at $t = 4900$ s, while those for calorimeter "d" underpredict flight data by 30%). This may indicate that the flowfield is transitioning to turbulence on the attached afterbody during the second heat pulse. This possibility will be examined in a later section.

The computed heating at these calorimeters overpredicts the flight heating near the trough between the heat pulses, with the amount of overprediction near $t = 4700$ s ranging from over 100% at calorimeter "a" to about 26% at calorimeter "g". There are several possible reasons for the CFD to predict higher heating than was measured during flight during this time period. As discussed earlier, during the period between about 4600 and 4800 seconds the spacecraft was undergoing a skip maneuver that resulted in a local maximum in altitude at about 4700 seconds. During this skip phase local areas of non-continuum flow may have been present on the afterbody, which could result in an overprediction in heating. This possibility will be examined later in the paper. Another possibility arises from examination of the flight aerodynamic data in Hillje.¹⁵ During the high altitude skip phase of the entry, the uncertainty in vehicle orientation was much larger than average. In fact, between 4650 and 4750 seconds the uncertainty in angle of attack was approximately ± 2 deg., as opposed to ± 0.5 deg. during the remainder of the entry. It is possible that the low dynamic pressure during this portion of the trajectory could have prevented the vehicle from maintaining its trim orientation, resulting in a slightly smaller than expected angle of attack. If the angle of attack were small enough the flow could separate on the lee side of the afterbody, significantly reducing the predicted heating. In order to test this theory, a single run was made at $t = 4700$ s with an angle of attack of 16.5 deg. (2 deg. less than nominal). The wind side afterbody flow remained attached for this case, and the resulting heat transfer at calorimeters "a" through "d" was about 15% lower. While the trend is certainly in the right direction, these results indicate that angle of attack alone cannot account for the differences in this portion of the trajectory.

Calorimeter "f" (Fig. 8(f)) was placed near the rear of the shoulder at $\theta = 138^\circ$. For this calorimeter, the CFD predictions are uniformly 33-50% higher than the data. Given the level of agreement seen for the other five calorimeters in this region, as well as that seen for the two calorimeters on the shoulder, the reasons for this disagreement are not clear.

Finally, it should be noted that calorimeter “a” was at a location downstream of the windward scimitar antenna (see Fig. 3), which is not modeled in the current simulations. However, given the level of agreement between the computations and the flight data for this calorimeter, it seems reasonable to assume that the effect of this antenna on heating levels in this area was small.

3. Separated Flow Region

Seven calorimeters were placed in a region for which the flow remained separated during the entire heating portion of the entry. Computational results for five of these, calorimeters “m” and “o-r” are in generally good agreement with the flight data (see Figs. 8(m) and 8(o)-8(r)). At each of these locations the peak heat flux during each pulse was between 0.2 – 0.4 W/cm². Agreement between the simulation and flight data was generally within 15% during the first heat pulse and the trough between the pulses. In contrast, the CFD prediction was generally lower than the flight data during the second heat pulse, which could be a consequence of turbulent transition. Note that the computed flow in the separation region became unsteady after $t = 4850$ s. Therefore the computational results for 4850, 4875, and 4900 seconds include “error” bars, which attempt to bound the unsteadiness of the computed heat transfer.

The results for calorimeter “p” require further discussion. This calorimeter is located in close proximity to “o” (see Fig. 3), and the computational results predict very similar heat fluxes for each. In contrast the flight data indicate that the peak heating levels at calorimeter “p” were significantly higher than those at “o”. As a result the CFD underpredicts the heating at calorimeter “p” by about 45% at $t = 4530$ s, while the prediction at calorimeter “o” is well within the data scatter. This apparent discrepancy can be explained by examination of the afterbody layout in Ref. 9. While calorimeter “o” is mounted on a smooth area of the heatshield, calorimeter “p” was placed immediately in front of one of the rendezvous windows. Given this, it seems likely that the window created a local flow disturbance that affected the heat flux measured by calorimeter “p”.

Calorimeter “e” was placed at the rear apex of the aeroshell. As seen in Fig. 8(e), the computations agree well with the flight data early in the first heat pulse and during the trough, but the computations significantly underpredict the peak heating levels. At $t = 4530$ seconds the CFD result is about 45% lower than the flight data indicate. The disagreement during the second heat pulse can possibly be due to turbulent transition, but the differences in the first pulse are more difficult to understand. One possibility is that the local geometry of the apex is not accurately modeled in the current simulations. This will be explored in future work.

By far the poorest agreement between the flight data and the CFD occurs at calorimeter “s” (Fig. 8(s)), which is near the rear apex on the leeward side near the centerline. At this location the flight data indicates heating levels nearly as high as those at the apex (calorimeter “e”), and slightly higher than those observed at calorimeter “d”, which was at the same x-location but near the windward centerline. The computations predict very low heating levels at this location, consistent with those in the rest of the separated flow region. The reasons for this disagreement are not clear. Physically, the apex should create a separated flow region immediately behind it that would result in significantly lower heat transfer at calorimeter “s” than either “e” or “d”, unless a local vortex structure were generated that is not predicted in the CFD solutions. One possible explanation is that the non-zero sideslip angle significantly altered the flow patterns in this region; this effect will be explored in the following section. Unfortunately, calorimeter “s” was not functional on flight AS-201⁹ and a different instrumentation layout was used during Apollo 4 and 6,¹⁰ so it is not possible to use data from those flights to help determine whether the readings from AS-202 are spurious or indicative of a shortcoming in the current simulations.

4. Separation Line Region

Four calorimeters were placed in locations that were very near the separation line. Because the separation point is a function of Reynolds number, these calorimeters were in attached flow during a portion of the trajectory, and separated flow during the remainder. The agreement between the computations and the flight data for these calorimeters was also generally good throughout the entry, as seen in Figs. 8(j)-8(l) and 8(n). The clearest evidence of transition from attached to separated flow can be seen at calorimeter “j”, where the CFD shows sudden jumps in computed heating between $t = 4560$ and 4600 s and again between $t = 4750$ and 4800 s as the flow at this location attaches and then separates again. Similar jumps can be seen in the raw flight data at this location around $t = 4600$ and 4750 s (see Fig. 8(j)), although the levels are 20-30% lower than that predicted by the CFD. The computation also shows a jump in heating at calorimeter “k” at $t = 4700$ s that corresponds to a transition from separated to attached flow. However in this case the scatter makes it impossible to determine whether a corresponding event was seen during the flight. Transition from a separated to an attached flow state is not readily visible in the surface

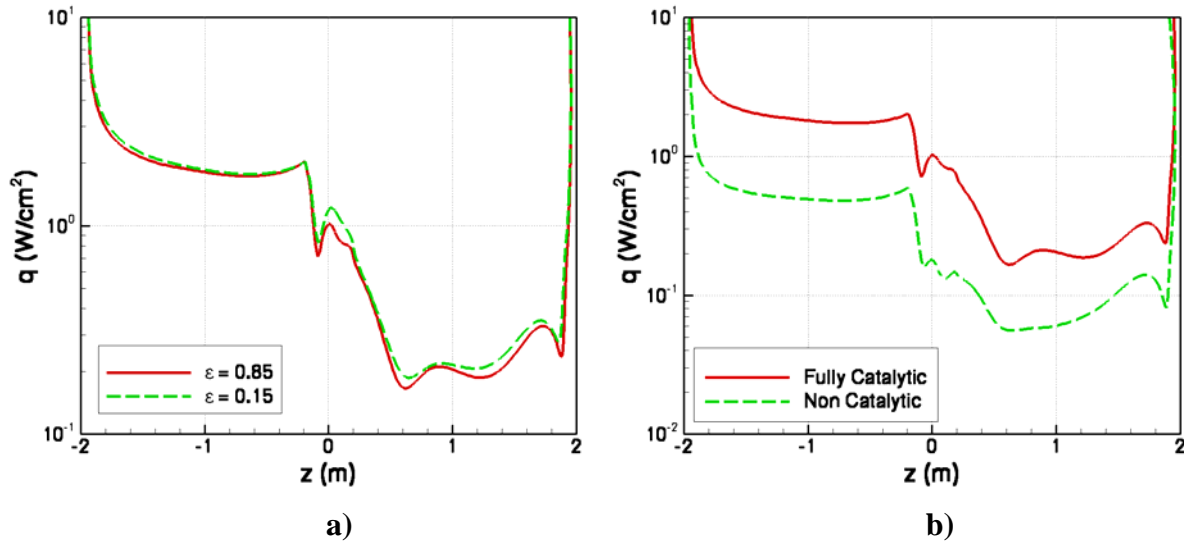


Figure 9. Impact of a) surface emissivity and b) surface catalycity on computed afterbody heat transfer along the vehicle centerline at $t=4510$ s.

heating at the other two calorimeter locations, however the general good agreement between the computations and the flight data indicates that the extent of separation is accurately predicted in the current simulations.

D. Surface Boundary Conditions

As discussed in the “Flight Instrumentation” section, the calorimeter surface may have a lower emissivity than the Avcoat TPS material. In order to quantify the impact of this emissivity difference on the results, a solution was run at $t = 4510$ s with a surface emissivity of 0.15 rather than the value of 0.85 assumed for the TPS. Figure 9(a) shows the comparison of computed centerline heating on the afterbody for these two cases. From the figure we see that, as expected, surface emissivity has only a small impact on the computed heat transfer. The largest effect occurs on the leeward side of the apex, where the lower emissivity increases the heat transfer by about 15%. The predicted heat transfer was within 10% over the rest of the surface. Similar results are expected at the other trajectory points.

In contrast, the computed heat transfer is very sensitive to the wall catalysis model employed. As stated earlier, the carbonaceous Avcoat TPS material should have a high catalycity. However, to bound the influence of catalytic heating on the total heat flux, a solution was run at $t = 4510$ s assuming a non-catalytic surface. As shown in Fig. 9(b), the assumption of a non-catalytic surface reduces the predicted heating rate by a factor of 3 to 4 over the entire afterbody. Given the level of agreement between the flight data and the fully catalytic results, it is clear that a fully catalytic surface assumption is indeed warranted for the Avcoat material.

E. Sideslip Effects

All computations presented thus far assumed zero sideslip (yaw). However, the flight data indicated that a small sideslip angle was indeed present during the majority of the entry (see Table 3).¹⁵ In order to assess the impact of yaw on the computed heating, a single case was run at $t = 4500$ s which included the measured sideslip angle ($\beta = 2.5$ deg.). The grid for this case was constructed by mirroring the baseline grid to generate a full 360° revolution, and then tailoring the outer boundary to the correct (asymmetric) shock location using SAGe. The resulting grid had approximately 3 million points. Figure 10 shows computed heating on the afterbody at $t = 4500$ s with and without yaw included in the simulation. The two images look qualitatively similar except for the expected “tilt” in the heating distribution for the case with sideslip. The most noticeable differences are in the relative magnitude of heating at the two vortex impingement points and the location of the cool streak down the leeward centerline. Based on Fig. 10 it would seem that the impact of sideslip on computed heating at most calorimeter locations would not be large, and this is in fact the case. A positive 2.5 deg. sideslip angle changed the predicted surface heating by more than 10% for only four of the 19 functional calorimeters. The most notable differences in the attached flow region occurred at calorimeters “ f ” and “ h ”, where a positive yaw caused a decrease in heating of about 14%, bringing the

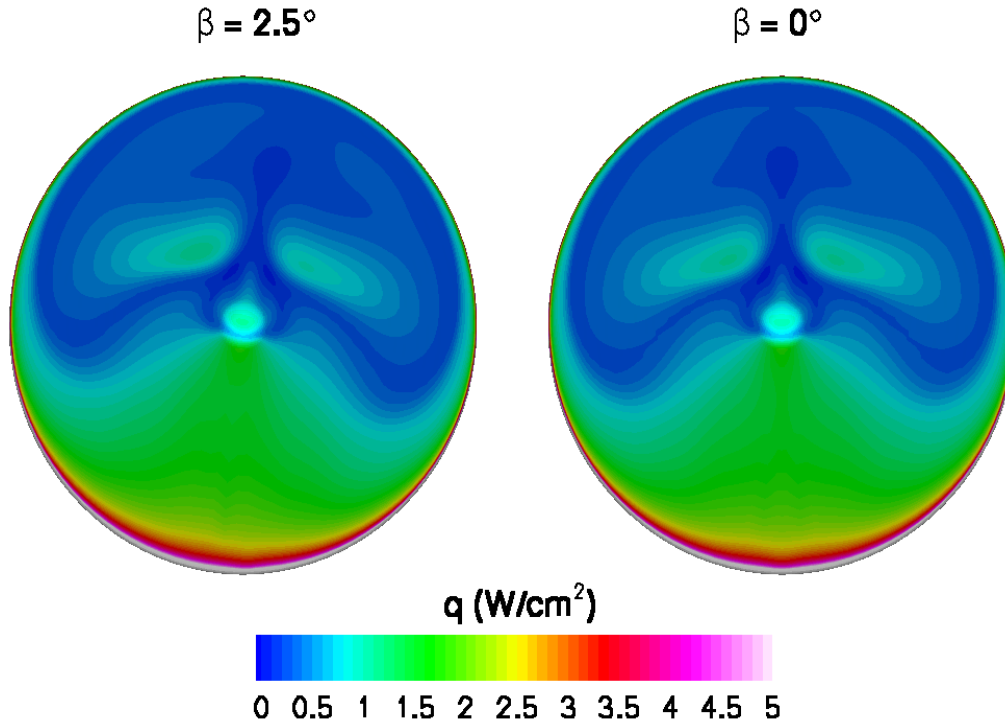


Figure 10. Impact of 2.5° sideslip angle on computed afterbody surface heat transfer at $t = 4500$ s.

computations at both locations in better agreement with flight data. In the separated flow region the positive yaw angle resulted in a 20% increase in predicted heating at calorimeters “ q ” and “ r ”, again resulting in better agreement with flight data. Interestingly the sideslip angle had essentially no effect on the predicted heating at calorimeters “ e ” and “ s ”, indicating that this could not have been the cause of the disagreement between the computations and flight data at these locations.

F. Transition to Turbulence

All of the calculations shown previously have assumed that the entire flowfield was laminar. Given the low freestream Reynolds numbers (see Table 3), particularly during the first heat pulse, this assumption should be reasonable; nevertheless the possibility of turbulent transition will be considered separately for the attached portion of the afterbody flow and the separated flow region.

Post-flight data analysis, based on the assumption that the flow was separated on the entire afterbody, seemed to indicate a transition to turbulence soon after the skip maneuver was complete ($t > 4800$ s).⁹ However, the current results show that the flow remains attached on the wind side, and that a laminar flow assumption accurately predicts windward heating levels during most of the second heat pulse. In order to evaluate the likelihood of transition in the attached afterbody flow we use the standard correlation $Re_\theta/M_{edge} > \text{const}$,³⁹ where Re_θ is the momentum thickness Reynolds number, and M_{edge} is the (supersonic) edge Mach number. The constant can vary between approximately 150 and 350 depending on the roughness characteristics of the surface. This quantity was computed on the surface for all trajectory points; the results for the case with the highest freestream Reynolds number ($t = 4900$ s) are shown in Fig. 11. The black lines in the figure denote the separation and attachments lines of the complex wake (see Fig. 6). From Fig. 11 we see that Re_θ never exceeds 150 in the attached flow portion on the wind side of the afterbody, indicating that the majority of the attached flow will remain laminar. Note that the high values of Re_θ/M_{edge} in and near the separated flow region are not necessarily indicative of turbulence since this criterion relies on accurate detection of the boundary layer edge, something that is difficult to do in a wake flow. This conclusion is consistent with the current analysis, although there is some evidence in the heating data of transition near $t = 4900$ s at calorimeters “ c ” and “ d ”. In order to evaluate the possibility of turbulent flow on the afterbody a fully turbulent solution was computed at $t = 4900$ s. The computed turbulent heating levels were 3.2 W/cm^2 at both calorimeters “ c ” and “ d ”, as compared to the laminar computed values of 1.3 and 1.6 W/cm^2 and the flight data of 1.8 and 2.4

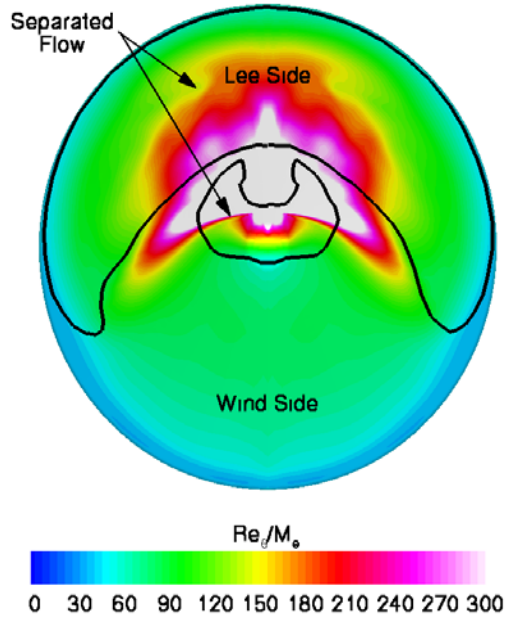


Figure 11. Computed transition parameter Re_{θ}/M_{∞} on the conical afterbody for $t = 4900$ s.

W/cm^2 , respectively. This suggests that while it is possible that the flow was transitional on this part of the body, a fully developed turbulent boundary layer was not established until later in the flight.

In order to estimate the likelihood of transition in the separated flow region we use the blunt-body separation shear layer correlation given by Lees.⁴⁰ This correlation is given by $Re_{ir} = \rho_e U_e L / \mu_e$, where ρ_e , U_e , and μ_e are the density, velocity, and viscosity respectively at the outer edge of the separation shear layer, and L is the laminar running length. According to Lees,⁴⁰ the local transition Reynolds number ranges from about 3×10^4 to 2×10^5 for edge Mach numbers between 2 and 4. This quantity was evaluated for several trajectory points and it was determined that the separated flow region would likely remain laminar until $t = 4900$ s, at which point the lee side shear layer reached a local Reynolds number within a factor of two of the critical value. Based on these results it appears that the assumption of laminar flow is valid in the separation region for the majority of the time period examined in this work. However, it should be noted that the correlation of Lees is for axisymmetric flows. It is possible that three-dimensional (crossflow) effects could hasten transition to turbulence for this case.

G. Non-Continuum Flow Effects

All solutions in this work were obtained assuming a continuum flow. However, at these Reynolds numbers, non-continuum effects may be present in the base region. In order to assess the importance of non-continuum effects on the computed heat transfer, the density gradient length local Knudsen number, Kn_{GLL} (see Ref. 41) was computed for all cases. Following the work of Boyd et al.,⁴¹ we assume that continuum breakdown will begin when $Kn_{GLL} > 0.05$. Figure 12 shows the resulting contours of Kn_{GLL} in the symmetry plane for $t = 4530$ and 4700 s. In the near wall region these computations indicate that at $t = 4530$ s the entire afterbody with the exception of the wind side of the rear apex should be in continuum flow. At $t = 4700$ s, $Kn_{GLL} > 0.05$ on the entire windside of the afterbody, and becomes quite large near the rear apex and the shoulder region, indicating that non-continuum effects are likely present. Interestingly, the near-wall continuum breakdown parameter is larger on the windward (attached) side of the frustum than in the separated flow region, due to the larger density gradients in the attached flow boundary layer. While Boyd et al.,⁴¹ did not explicitly quantify the relationship between Kn_{GLL} and the computed heat transfer, in general a Navier-Stokes solution will slightly overpredict heat transfer in the base region of a non-continuum flow.⁴² Given that Fig. 12 demonstrates a potential continuum breakdown near $t = 4700$ s, and that this effect should be more pronounced in the attached afterbody flow, non-continuum flow effects may partially explain the overprediction in heating observed for calorimeters “a-d” and “g” around this time.

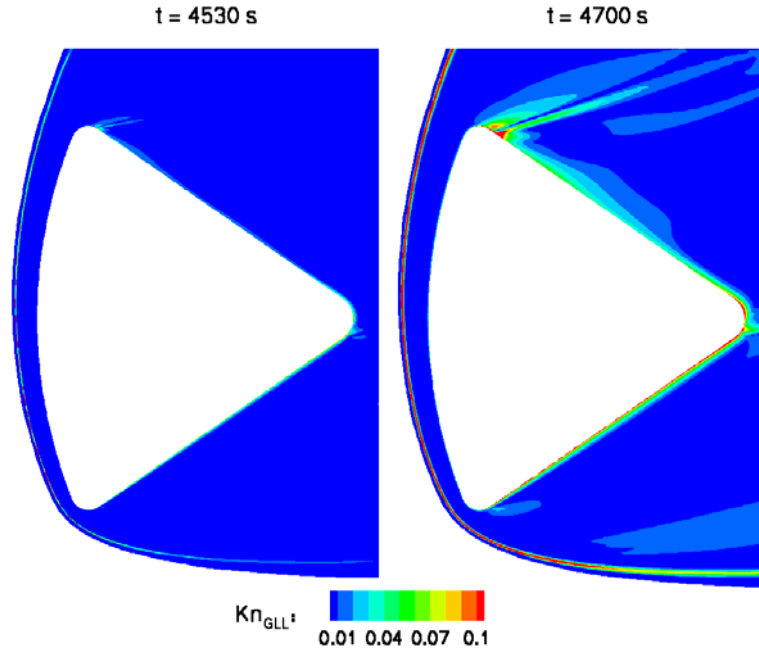


Figure 12. Contours of the continuum breakdown parameter Kn_{GLL} in the symmetry plane for $t = 4530$ and $t = 4700$ s.

VII. Conclusions

CFD simulations were performed to simulate the wake flow and afterbody heating environment of the Apollo AS-202 Command Module. The AS-202 mission entered the Earth's atmosphere at orbital velocities on a shallow flight path angle that led to low afterbody heating levels, making data reduction straightforward and providing a good set of validation data for laminar flow on a lifting entry capsule. Fifteen three-dimensional simulations were performed which covered the majority of the heating portion of the flight. The surface was assumed to be fully catalytic and in radiative equilibrium, which are appropriate assumptions for the Avcoat TPS material. The wake structure was examined, and surface oil flow plots demonstrated that the flow remained attached on the windward side of the afterbody throughout the entry. The computed heat transfer was well within the assumed $\pm 20\%$ uncertainty in the flight data for 15 of the 19 functional calorimeters on the conical afterbody over most of the flight. Heating was generally overpredicted on the windward side during the trough between the two heat pulses, possibly due to non-continuum effects, and underpredicted on the windward side late in the second heat pulse, possibly due to transition to turbulence on the flight vehicle that was not modeled in the current simulations. Predicted heating at two calorimeters located near the separation line clearly show jumps where the flow separates and reattaches as a function of time. This behavior was also seen in the flight data. The worst agreement between the computations and the flight data occurred near the rear apex of the Command Module. The reasons for this disagreement are not known at this time, but may be partially due to geometric differences between the apex as modeled in this work and the flight vehicle. The effects of sideslip were explored and found to be minor at all but four calorimeter locations.

The results presented in this work indicate that modern CFD methods are fully capable of predicting afterbody heating levels on a lifting Earth entry capsule in laminar flow, and form a solid basis from which our ability to predict aeroheating in the presence of turbulence and ablation can be explored. Furthermore, although more work needs to be done to fully validate afterbody aeroheating predictions, the current results suggest that the large design uncertainties ($\sim 200\%$) commonly applied to such simulations are needlessly conservative.

VIII. Acknowledgements

This work was funded by the In-Space Propulsion program under task agreement M-ISP-03-18 to NASA Ames. The work performed by the second author was supported by the prime contract NAS2-99092 to ELORET Corporation. The authors would like to thank Dr. David Saunders (ELORET) for his help converting the raw experimental data into usable form, Ryan McDaniel (NASA Ames) for his ideas on grid generation, Dr. Bernard

Laub (Ames) for discussions on the properties of the Avcoat TPS material, and Dr. Gary Allen (ELORET) for his guidance in interpreting the aerodynamic and OML data.

IX. References

- ¹ Jones, R., "Experimental Investigation of the Overall Pressure Distribution, Flow Field, and Afterbody Heat Transfer Distribution of an Apollo Reentry Configuration at a Mach Number of 8," NASA TM X-813, Jun. 1963.
- ² Bertin, J., "Wind Tunnel Heating Rates for the Apollo Spacecraft," NASA TM X-1033, Jan. 1965.
- ³ Marvin J. and Kussoy, M., "Experimental Investigation of the Flow Field and Heat Transfer over the Apollo Capsule Afterbody at a Mach Number of 20," NASA TM X-1032, Feb. 1965.
- ⁴ Yee, L., "Free-Flight Measurements of Heat Transferred to the Apollo Afterbody with and Without Heat Shield Ablation," NASA TM X-1096, Apr. 1965.
- ⁵ Lee, G. and Sundell, R., "Apollo Afterbody Heat Transfer and Pressure with and Without Ablation at M_∞ of 5.8 to 8.3," NASA TN D-6792, Apr. 1972.
- ⁶ Fox, G. and Marvin J., "An Investigation of the Apollo Afterbody Pressure and Heat Transfer at High Enthalpy," NASA TM X-11973, Mar. 1966.
- ⁷ Cauchon, D.L., "Project Fire Flight 1 Radiative Heating Experiment," NASA TM X-1222, 1966.
- ⁸ Cauchon, D.L., "Radiative Heating Results from the Fire II Flight Experiment at a Reentry Velocity of 11.4 Kilometers per Second," NASA TM X-1402, Jul. 1967.
- ⁹ Lee, D.B., Bertin, J.J., and Goodrich, W.D., "Heat Transfer Rate and Pressure Measurements Obtained During Apollo Orbital Entries," NASA TN D-6028, Oct. 1970.
- ¹⁰ Lee, D.B. and Goodrich, W.D., "The Aerothermodynamic Environment of the Apollo Command Module During Superorbital Entry," NASA TN D-6792, Apr. 1972.
- ¹¹ Lee, D.B., "Apollo Experience Report: Aerothermodynamics Evaluation," NASA TN D-6843, Jun. 1972.
- ¹² Wright, M., Loomis, M., and Papadopoulos, P., "Aerothermal Analysis of the Project Fire II Afterbody Flow," *Journal of Thermophysics and Heat Transfer*, Vol. 17, No. 2, 2003, pp. 240-249.
- ¹³ Henline, W., Chen, Y.-K., Palmer, G., and Stewart, D., "Trajectory-Based, 3-Dimensional Heating and Ablation Calculations for the Apollo Lunar/Earth Return Capsule," AIAA Paper No. 93-2788, Jul. 1993.
- ¹⁴ Park, C., "Stagnation Point Radiation for Apollo 4," AIAA Paper No. 2001-3070, Jun. 2001.
- ¹⁵ Hillje, E., "Entry Flight Aerodynamics from Apollo Mission AS-202," NASA TN D-4185, Oct. 1967.
- ¹⁶ Pavlosky, J.E. and St. Leger, L.G., "Apollo Experience Report: Thermal Protection Subsystem," NASA TN D-7564, Jan. 1974.
- ¹⁷ Crouch, R.K. and Walberg, G.D., "An Investigation of Ablation Behavior of Avcoat 5026/39M Over a Wide Range of Thermal Environments," NASA TM X-1778, Apr. 1969.
- ¹⁸ Gardon, R., "A Transducer for the Measurement of Heat Flow Rate," *Journal of Heat Transfer*, Nov. 1960.
- ¹⁹ ASTM E511-01, "Standard Test Method for Measuring Heat Flux Using a Copper-Constantan Circular Foil, Heat-Flux Transducer," 2001.
- ²⁰ Murthy, A.V., "Radiative Calibration of Heat-Flux Sensors at NIST: Facilities and Techniques," *Journal of Research of the National Institute of Standards and Technology*, Vol. 105, No. 2, 2000, pp. 229-300.
- ²¹ Pitts, D. and Carter, P., "High Altitude Atmospheric Measurements for the Reentries of Gemini 6 and 7," NASA TM X-58003, 1966.
- ²² Wright, M., Candler, G., and Bose, D., "Data-Parallel Line Relaxation Method for the Navier-Stokes Equations," *AIAA Journal*, Vol. 36, No. 9, 1998, pp. 1603-1609.
- ²³ MacCormack, R. and Candler, G., "The Solution of the Navier-Stokes Equations Using Gauss-Seidel Line Relaxation," *Computers and Fluids*, Vol. 17, No. 1, 1989, pp. 135-150.
- ²⁴ Yee, H., "A Class of High-Resolution Explicit and Implicit Shock Capturing Methods," NASA TM 101088, Feb. 1989.
- ²⁵ Wercinski, P., Chen, Y.-K., Loomis, M., Tauber, M., McDaniel, R., Wright, M., Papadopoulos, P., Allen, G., and Yang, L., "Neptune Aerocapture Entry Vehicle Preliminary Design," AIAA Paper No. 2002-4812, Aug. 2002.
- ²⁶ Wright, M., Bose, D., and Olejniczak, J., "The Impact of Flowfield Radiation Coupling on Aeroheating for Titan Aerocapture," AIAA Paper No. 2004-0484, Jan 2004.
- ²⁷ Park, C., "Review of Chemical-Kinetic Problems of Future NASA Missions, I: Earth Entries," *Journal of Thermophysics and Heat Transfer*, Vol. 7, No. 3, 1993, pp. 385-398.
- ²⁸ Bose D. and Candler, G., "Thermal Rate Constants of the $N_2 + O \rightarrow NO + N$ Reaction Using *ab initio* 3A" and 3A' Potential Energy Surfaces," *Journal of Chemical Physics*, Vol. 104, No. 8, 1996, pp. 2825-2833.

- ²⁹ Park, C., *Nonequilibrium Hypersonic Aerothermodynamics*, Wiley, New York, 1990.
- ³⁰ Millikan, R. and White, D., "Systematics of Vibrational Relaxation," *Journal of Chemical Physics*, Vol. 39, No. 12, 1963, pp. 3209-3213.
- ³¹ Gupta, R., Yos, J., Thompson, R., and Lee, K., "A Review of Reaction Rates and Thermodynamic and Transport Properties for an 11-Species Air Model for Chemical and Thermal Nonequilibrium Calculations to 30000 K," NASA RP-1232, Aug. 1990.
- ³² Palmer, G.E. and Wright, M.J., "A Comparison of Methods to Compute High Temperature Gas Viscosity," *Journal of Thermophysics and Heat Transfer*, Vol. 17, No. 2, 2003, pp. 232-239.
- ³³ Palmer, G.E. and Wright, M.J., "A Comparison of Methods to Compute High Temperature Gas Thermal Conductivity," AIAA Paper No. 2003-3913, Jun. 2003.
- ³⁴ Ramshaw, J.D., "Self-Consistent Effective Binary Diffusion in Multicomponent Gas Mixtures," *Journal of Non-Equilibrium Thermodynamics*, Vol. 15, No. 3, 1990, pp. 295-300.
- ³⁵ Brown, J.L., "Turbulence Model Validation for Hypersonic Flows," AIAA Paper No. 2002-3308, Jun. 2002.
- ³⁶ Gnoffo, P., Price, J., and Braun, R., "Computation of Near Wake Aerobrake Flowfields," *Journal of Spacecraft and Rockets*, Vol. 29, No. 2, 1992, pp. 182-189.
- ³⁷ Davies, C. and Venkatapathy, E., "The Self Adaptive Grid Code SAGE, Version 3," NASA TM 208792, Aug. 1999.
- ³⁸ Tobak, M. and Peake, D.J., "Topology of Three-Dimensional Separated Flows," *Annual Review of Fluid Mechanics*, Vol. 14, 1982, pp. 61-85.
- ³⁹ Tauber, M.E., "A Review of High-Speed Convective Heat-Transfer Computation Methods," NASA TP-2914, Jul. 1989.
- ⁴⁰ Lees, L., "Hypersonic Wakes and Trails," *AIAA Journal*, Vol. 2, No. 3, 1964, pp. 417-428.
- ⁴¹ Boyd, I.D., Chen, G., and Candler, G.V., "Predicting Failure of the Continuum Fluid Equations in Transitional Hypersonic Flows," *Physics of Fluids*, Vol. 7, No. 1, 1995, pp. 210-219.
- ⁴² Dogra, V.K., Moss, J.N., Wilmoth, R.G., Taylor J.C., and Hassan, H.A., "Effects of Chemistry on Blunt Body Wake Structure," *AIAA Journal*, Vol. 33, No. 3, 1995, pp. 463-469.

N_2 - CH_4 -Ar Chemical Kinetic Model for Simulations of Atmospheric Entry to Titan

Tahir Gökçen†

ELORET Corporation, NASA Ames Research Center, MS 230-2, Moffett Field, CA 94035

A detailed chemical kinetic model for N_2 - CH_4 -Ar mixtures is developed for nonequilibrium simulation of shock layers formed in front of probes entering Titan's atmosphere. The detailed kinetic model uses up-to-date chemical reaction mechanisms and reaction rates, and it is validated against existing shock tube experiments. A reduced kinetic model is also developed through sensitivity analysis of chemical reactions in the detailed model and reproduces the chemical kinetics of major species within the parameter space that may be encountered during Titan atmospheric entry. The reduced model, having fewer species and reactions than the detailed model, is better suited to coupled reacting CFD flowfield calculations.

I. Introduction

Shock layers formed in front of planetary probes entering the atmosphere of the Saturn moon Titan are expected to be in thermochemical nonequilibrium. Two examples of these probes are the Cassini-Huygens probe scheduled to enter the Titan atmosphere in December 2004, and a Titan probe under consideration by the In-Space Propulsion program at NASA for future aerocapture missions. Titan's atmosphere is known to be composed primarily of molecular nitrogen, methane, and argon. The relative mole fractions of species are uncertain at this time but believed to be N_2 (80-98%), CH_4 (2-10%), Ar (0-10%). Methane dissociates behind a strong shock wave at typical hypersonic entry conditions (e.g., speeds of 6-6.5 km/s, nonequilibrium temperatures of 5000-15,000 K, and pressures of 0.01-0.05 atm), and cyano radical (CN) is formed as a result of the nonequilibrium chemistry. Since CN is known to be a strong radiator, the probes are expected to experience significant radiative heating as a result of the nonequilibrium radiation emission from the shock layer. Implications of shock layer nonequilibrium in Titan atmospheric entry were apparently first pointed out and analyzed by Park,¹ and later by others, e.g., Nelson et al.,² Park and Bershader,³ and Park.⁴ Several aerothermal analyses carried out relatively recently in Refs. 5-11 also indicate that the radiative heating due to CN radiation will be a significant or even the dominant portion of the total heating. The radiative heat flux at the stagnation point was predicted to be as much as 0.5-7 times the convective heat flux. There are many reasons for such large variation in the predictions: freestream conditions, the vehicle nose radius (or shock stand-off distance), the uncertainty of the CH_4 mole fraction, radiation-flowfield coupling, and the models used for chemistry and radiation. Clearly, a chemical kinetic model plays a pivotal role in the flowfield simulation of a nonequilibrium shock layer and prediction of its radiation.

The chemical kinetic model most commonly used in aerothermal analyses so far was originally proposed by Nelson et al.² (Nelson-91 model). However, it is found that this model has several inconsistencies with respect to the current literature: it does not include important species and reactions for methane decomposition and CN formation; and the reaction rates used are significantly different from the current literature values. Therefore, there is a need to update the Nelson-91 model or to develop a new chemical kinetic model for N_2 - CH_4 -Ar mixtures.

The present paper gives a short evaluation of the Nelson-91 model, and proposes a new chemical kinetic model consistent with the current literature for simulations of Titan atmospheric entry. For the development of a new chemical kinetic model, the following approach is taken. First, a detailed chemical kinetic model for N_2 - CH_4 -Ar mixtures is developed using up-to-date chemical reaction mechanisms and reaction rates. Second, the detailed model is validated against four sets of existing shock tube experiments.

† Senior Research Scientist

Table 1. Nelson-91 Chemical Kinetic Model and Reaction Rates.

	$k_f = A T^n e^{-T_a/T}$	A (cc/mol/s)	n	T_a (K)
Dissociation Reactions				
1.	$C_2 + M \rightleftharpoons C + C + M$	9.68×10^{22}	-2.00	71000
2.	$N_2 + M \rightleftharpoons N + N + M$	3.70×10^{21}	-1.60	113200
3.	$CH + M \rightleftharpoons C + H + M$	1.13×10^{19}	-1.00	40913
4.	$CN + M \rightleftharpoons C + N + M$	1.00×10^{23}	-2.00	90000
5.	$CH_4 + M \rightleftharpoons CH_3 + H + M$	2.25×10^{27}	-1.87	52900
6.	$CH_3 + M \rightleftharpoons CH_2 + H + M$	2.25×10^{27}	-1.87	54470
7.	$CH_2 + M \rightleftharpoons CH + H + M$	2.25×10^{27}	-1.87	50590
8.	$NH + M \rightleftharpoons N + H + M$	1.13×10^{19}	-1.00	41820
9.	$H_2 + M \rightleftharpoons H + H + M$	1.47×10^{19}	-1.23	51950
Exchange Reactions				
10.	$C + N_2 \rightleftharpoons CN + N$	1.11×10^{14}	-0.11	23000
11.	$CN + C \rightleftharpoons C_2 + N$	3.00×10^{14}	0.00	18120
12.	$C_2 + N_2 \rightleftharpoons CN + CN$	7.10×10^{13}	0.00	5330
13.	$H + N_2 \rightleftharpoons NH + N$	2.20×10^{14}	0.00	71370
14.	$H_2 + C \rightleftharpoons CH + H$	1.80×10^{14}	0.00	11490
15.	$CN^+ + N \rightleftharpoons CN + N^+$	9.80×10^{12}	0.00	40700
16.	$C^+ + N_2 \rightleftharpoons N_2^+ + C$	1.11×10^{14}	-0.11	50000
Ionization Reactions				
17.	$N + N \rightleftharpoons N_2^+ + e^-$	1.79×10^9	0.77	67500
18.	$C + N \rightleftharpoons CN^+ + e^-$	1.00×10^{15}	1.50	164400
19.	$N + e^- \rightleftharpoons N^+ + e^- + e^-$	2.50×10^{34}	-3.82	168600
20.	$C + e^- \rightleftharpoons C^+ + e^- + e^-$	3.90×10^{33}	-3.78	130000
21.	$H + e^- \rightleftharpoons H^+ + e^- + e^-$	5.90×10^{37}	-4.00	157800
22.	$Ar + e^- \rightleftharpoons Ar^+ + e^- + e^-$	2.50×10^{34}	-3.82	181700

Finally, the model is simplified through analysis of the chemical reactions within a parameter space relevant to Titan atmospheric entry. Note that the adjectives “detailed” and “simplified” are used here for kinetic models in the sense that a detailed model is not practical to use in CFD flowfield calculations while a simplified model is.

II. Evaluation of Nelson-91 Chemical Kinetic Model

A summary of chemical reactions and reaction rates used in the Nelson-91 model is given in Table 1. Note that this model was originally described within the framework of Park’s two-temperature model (T - translational-rotational, T_v - vibrational-electronic). Rates of the dissociation reactions are assumed to be governed by an average temperature $\bar{T} = \sqrt{T T_v}$, all exchange reaction rates by T , and all ionization reaction rates by T_v . Nelson et al. do not give details of how the reaction mechanism was obtained and do not give any references for the sources of the reaction rates. However, it appears that the reaction mechanism and some of the reaction rates used are the ones proposed by Park.¹

The Nelson-91 model was evaluated by answering the following two questions: (1) How different are the reaction rates used in the Nelson-91 model from those more recently available in the literature? (2) Does the model have all the important species and reactions to describe the chemistry adequately for CN radiation predictions (if one uses up-to-date reaction rates)?

In answer to the first question, a summary of observations on the reaction rate constants used in the Nelson-91 model is given below. These observations are made for the temperature range of 1000-10,000 K in comparison with the recent literature data to be listed later. N_2 dissociation rate (heavy-particle impact) is smaller by about a factor of two for molecules and an order of magnitude for atoms. Electron-impact dissociation reaction has not been included (or the same rate as heavy-particle was used). C_2 dissociation rate is somewhat smaller at higher temperatures (as much as an order of magnitude at 10,000 K). CH_4 , CH_3 , and CH_2 dissociation rates are unusually larger (4-5 orders of magnitude). Note that the low-pressure-limit rates from the literature are used for comparison. CN dissociation rate is smaller by as much as 1-2 orders of magnitude at lower temperatures, and the activation temperature, T_a , is different. NH dissociation rate is larger by as much as an order of magnitude at higher temperatures, and T_a is different. The rate constant of reaction 12 (a CN forming reaction) is much larger, by about two orders of magnitude or more, mostly caused by the difference in activation temperatures used. The rate constant of reaction 17 is smaller by about an order of magnitude. The rate constant of reaction 20 is smaller by as much as an order of magnitude, and the rate constant of reaction 21 is larger by as much as 2-3 orders of magnitude. Note that the electron-impact ionization reactions (reactions 19-22) were erroneously listed as heavy-particle reactions in Ref. 2. It should be mentioned here that some of the literature data have large uncertainties themselves since they are extrapolated from the combustion-literature values, usually valid up to 5000 K only.

It is more difficult to evaluate whether the Nelson-91 model has all the important species and reactions to describe the chemistry adequately for CN radiation predictions. However, it is found that the mechanism does not include several radical reactions of CH_3 , CH_2 , CH , and H in CH_4 decomposition (rates of many of these reactions are of the same order as the CH_4 dissociation rate), and does not also include HCN species and its reactions for CN formation.

It should be noted at this point, without doing any detailed sensitivity analysis of reactions, that the above differences of the Nelson-91 model would translate to significant uncertainties on computed flowfield quantities such as species number densities, temperature (input for CN radiation calculations). It should also be noted that some of the experimental data for reaction rates and reaction mechanisms were not available in the literature when the Nelson-91 was proposed. Therefore, development of a new chemical kinetic model is undertaken.

III. Detailed Chemical Kinetic Model

A detailed chemical kinetic model for N_2 - CH_4 -Ar mixtures is developed including the reactions and species possibly present in the parameter space of temperature and pressure relevant to Titan atmospheric entry. The present detailed model includes a total of 28 chemical species (N_2 , CH_4 , CH_3 , CH_2 , CH , C_2 , H_2 , CN , NH , HCN , N , C , H , Ar , N_2^+ , CN^+ , N^+ , C^+ , H^+ , Ar^+ , e^- , C_2H_6 , C_2H_5 , C_2H_4 , C_2H_3 , C_2H_2 , C_2H , and C_3) and 74 reactions.

A summary of chemical reactions and reaction rates used in the detailed model is given in Table 2. As shown in the table, the chemical reaction rates are compiled from various sources. Nitrogen chemistry and reaction rates at high temperatures have been studied by Park in detail.^{12,13} Therefore, nitrogen dissociation and ionization reactions and their rates are taken from recent reviews of Park et al. (01),¹⁴ Park et al. (94),¹⁵ and Park et al. (93).¹⁶ Hydrocarbon species reactions and their rates are taken from comprehensive reviews of Baulch et al. (94),¹⁷ Baulch et al. (92),¹⁸ Tsang (92),¹⁹ Tsang and Herron (91),²⁰ Tsang and Hampson (86),²¹ NIST Chemical Kinetics database,²² and journal articles.²³⁻³¹

A thermodynamic database for the reacting species is an integral part of the chemical kinetic model since reverse reaction rates are computed from the equilibrium constants using the thermodynamic properties. Thermodynamic data and polynomial curve fits for the species of the detailed kinetic model are obtained from the NASA computer program CEA (Chemical Equilibrium with Applications) and its

Table 2. Detailed Chemical Reaction Set for N₂-CH₄-Ar Mixtures

	$k_f = A T^n e^{-T_a/T}$	A (cc/mol/s)	n	T_a (K)	Source
Dissociation Reactions					
1.	$N_2 + M \rightleftharpoons N + N + M$	7.00×10^{21}	-1.60	113200	P(01) ¹⁴
	enhanced rate for $M = N, C, H$	3.00×10^{22}	-1.60	113200	P(01) ¹⁴
	enhanced rate for $M = e^-$	3.00×10^{24}	-1.60	113200	P(01) ¹⁴
2.	$CH_4 + M \rightleftharpoons CH_3 + H + M$	4.70×10^{47}	-8.20	59200	B(94) ¹⁷
3.	$CH_3 + M \rightleftharpoons CH_2 + H + M$	1.02×10^{16}	0.00	45600	B(94) ¹⁷
4.	$CH_3 + M \rightleftharpoons CH + H_2 + M$	5.00×10^{15}	0.00	42800	DH(92) ²³
5.	$CH_2 + M \rightleftharpoons CH + H + M$	4.00×10^{15}	0.00	41800	DH(92) ²³
6.	$CH_2 + M \rightleftharpoons C + H_2 + M$	1.30×10^{14}	0.00	29700	DH(92) ²³
7.	$CH + M \rightleftharpoons C + H + M$	1.90×10^{14}	0.00	33700	DH(92) ²³
8.	$C_2 + M \rightleftharpoons C + C + M$	1.50×10^{16}	0.00	71600	KR(97) ²⁷
9.	$H_2 + M \rightleftharpoons H + H + M$	2.23×10^{14}	0.00	48350	B(94), ¹⁷ B(92) ¹⁸
10.	$CN + M \rightleftharpoons C + N + M$	2.53×10^{14}	0.00	71000	P(94), ¹⁵ T(92) ¹⁹
11.	$NH + M \rightleftharpoons N + H + M$	1.80×10^{14}	0.00	37600	D(98)-NIST ²²
12.	$HCN + M \rightleftharpoons CN + H + M$	3.57×10^{26}	-2.60	62845	TH(91) ²⁰
13.	$C_2H_6 + M \rightleftharpoons CH_3 + CH_3 + M$	6.62×10^{48}	-8.24	47090	B(94) ¹⁷
14.	$C_2H_5 + M \rightleftharpoons C_2H_4 + H + M$	1.02×10^{18}	0.00	16800	B(94) ¹⁷
15.	$C_2H_4 + M \rightleftharpoons C_2H_3 + H + M$	2.59×10^{17}	0.00	48600	B(94) ¹⁷
16.	$C_2H_3 + M \rightleftharpoons C_2H_2 + H + M$	4.16×10^{41}	-7.50	22900	B(94) ¹⁷
17.	$C_2H_2 + M \rightleftharpoons C_2H + H + M$	6.96×10^{39}	-6.06	67130	KR(97) ²⁷
18.	$C_2H + M \rightleftharpoons C_2 + H + M$	1.74×10^{35}	-5.16	57400	KR(97) ²⁷
19.	$C_3 + M \rightleftharpoons C_2 + C + M$	4.00×10^{16}	0.00	75500	KR(97) ²⁷
Radical Reactions					
20.	$CH_3 + N \rightleftharpoons HCN + H + H$	7.00×10^{13}	0.00	0	D(90) ²⁵
21.	$CH_3 + H \rightleftharpoons CH_2 + H_2$	6.03×10^{13}	0.00	7600	B(92) ¹⁸
22.	$CH_3 + CH_4 \rightleftharpoons C_2H_5 + H_2$	1.00×10^{13}	0.00	11600	TB(79)-NIST ²²
23.	$CH_3 + CH_3 \rightleftharpoons C_2H_4 + H_2$	1.00×10^{14}	0.00	16100	H(90)-NIST ²²
24.	$CH_3 + CH_3 \rightleftharpoons C_2H_5 + H$	2.40×10^{13}	0.00	6480	D(95)-NIST ²²
25.	$CH_3 + CH_2 \rightleftharpoons C_2H_4 + H$	4.22×10^{13}	0.00	0	B(94)-NIST ²²
26.	$CH_3 + CH \rightleftharpoons C_2H_3 + H$	1.00×10^{14}	0.00	0	DH(92) ²³
27.	$CH_3 + C \rightleftharpoons C_2H_2 + H$	5.00×10^{13}	0.00	0	DH(92) ²³
28.	$CH_3 + C_2H_6 \rightleftharpoons CH_4 + C_2H_5$	1.50×10^{-7}	6.00	3040	B(94) ¹⁷
29.	$CH_3 + C_2H_5 \rightleftharpoons CH_4 + C_2H_4$	1.95×10^{13}	-0.50	0	TH(86) ²¹
30.	$CH_3 + C_2H_4 \rightleftharpoons CH_4 + C_2H_3$	4.16×10^{12}	0.00	5600	B(94) ¹⁷
31.	$CH_3 + C_2H_3 \rightleftharpoons CH_4 + C_2H_2$	3.92×10^{11}	0.00	0	TH(86) ²¹
32.	$CH_3 + C_2H_2 \rightleftharpoons CH_4 + C_2H$	1.81×10^{11}	0.00	8700	TH(86) ²¹

(Continued on next page)

Table 2. (Cont'd)

	$k_f = A T^n e^{-T_a/T}$	A (cc/mol/s)	n	T_a (K)	Source
Radical Reactions (Cont'd)					
33.	$\text{CH}_2 + \text{N}_2 \rightleftharpoons \text{HCN} + \text{NH}$	4.82×10^{12}	0.00	18000	S(87)-NIST ²²
34.	$\text{CH}_2 + \text{CH}_4 \rightleftharpoons \text{CH}_3 + \text{CH}_3$	4.30×10^{12}	0.00	5050	Bo(85)-NIST ²²
35.	$\text{CH}_2 + \text{N} \rightleftharpoons \text{HCN} + \text{H}$	5.00×10^{13}	0.00	0	D(90) ²⁵
36.	$\text{CH}_2 + \text{N} \rightleftharpoons \text{CH} + \text{NH}$	6.00×10^{11}	0.00	20400	M(67)-NIST ²²
37.	$\text{CH}_2 + \text{C} \rightleftharpoons \text{CH} + \text{CH}$	1.62×10^{12}	0.00	23600	M(67)-NIST ²²
38.	$\text{CH}_2 + \text{H} \rightleftharpoons \text{CH} + \text{H}_2$	6.03×10^{12}	0.00	-900	B(92)-NIST ²²
39.	$\text{CH}_2 + \text{CH}_2 \rightleftharpoons \text{C}_2\text{H}_3 + \text{H}$	2.00×10^{13}	0.00	0	FJ(84)-NIST ²²
40.	$\text{CH}_2 + \text{CH}_2 \rightleftharpoons \text{C}_2\text{H}_2 + \text{H} + \text{H}$	2.00×10^{14}	0.00	5530	Ba(95)-NIST ²²
41.	$\text{CH}_2 + \text{CH}_2 \rightleftharpoons \text{C}_2\text{H}_2 + \text{H}_2$	1.58×10^{15}	0.00	6010	Ba(95)-NIST ²²
42.	$\text{CH}_2 + \text{CH} \rightleftharpoons \text{C}_2\text{H}_2 + \text{H}$	4.00×10^{13}	0.00	0	DH(92) ²³
43.	$\text{CH}_2 + \text{C} \rightleftharpoons \text{C}_2\text{H} + \text{H}$	5.00×10^{13}	0.00	0	DH(92) ²³
44.	$\text{CH}_2 + \text{C}_2\text{H} \rightleftharpoons \text{CH} + \text{C}_2\text{H}_2$	1.81×10^{13}	0.00	0	TH(86) ²¹
45.	$\text{CH} + \text{N}_2 \rightleftharpoons \text{HCN} + \text{N}$	4.40×10^{12}	0.00	11060	D(90) ²⁵
46.	$\text{CH} + \text{C} \rightleftharpoons \text{C}_2 + \text{H}$	2.00×10^{14}	0.00	0	DH(92) ²³
47.	$\text{CH} + \text{CH}_4 \rightleftharpoons \text{C}_2\text{H}_4 + \text{H}$	6.00×10^{13}	0.00	0	DH(92) ²³
48.	$\text{CH} + \text{CH} \rightleftharpoons \text{C}_2\text{H} + \text{H}$	1.50×10^{14}	0.00	0	DH(92) ²³
49.	$\text{CH} + \text{C}_2 \rightleftharpoons \text{C}_2\text{H} + \text{H}$	1.00×10^{14}	0.00	0	DH(92) ²³
50.	$\text{CH} + \text{C}_2\text{H} \rightleftharpoons \text{C}_2\text{H}_2 + \text{C}$	1.00×10^{14}	0.00	0	DH(92) ²³
51.	$\text{C}_2 + \text{N}_2 \rightleftharpoons \text{CN} + \text{CN}$	1.50×10^{13}	0.00	21000	S(97) ²⁸
52.	$\text{C}_2 + \text{H}_2 \rightleftharpoons \text{C}_2\text{H} + \text{H}$	6.60×10^{13}	0.00	4030	KR(97) ²⁷
53.	$\text{C}_2 + \text{C}_2 \rightleftharpoons \text{C}_3 + \text{C}$	3.20×10^{14}	0.00	0	KR(97) ²⁷
54.	$\text{CN} + \text{H}_2 \rightleftharpoons \text{HCN} + \text{H}$	2.95×10^5	0.00	1130	W(96) ²⁹
55.	$\text{CN} + \text{C} \rightleftharpoons \text{C}_2 + \text{N}$	5.00×10^{13}	0.00	13000	P(01) ¹⁴
56.	$\text{N} + \text{H}_2 \rightleftharpoons \text{NH} + \text{H}$	1.60×10^{14}	0.00	12650	DaH(90) ²⁶
57.	$\text{C} + \text{N}_2 \rightleftharpoons \text{CN} + \text{N}$	5.24×10^{13}	0.00	22600	B(94) ¹⁷
58.	$\text{C} + \text{H}_2 \rightleftharpoons \text{CH} + \text{H}$	4.00×10^{14}	0.00	11700	D(91) ²⁴
59.	$\text{H} + \text{N}_2 \rightleftharpoons \text{NH} + \text{N}$	3.00×10^{12}	0.50	71400	R(78) ³⁰
60.	$\text{H} + \text{CH}_4 \rightleftharpoons \text{CH}_3 + \text{H}_2$	1.32×10^4	3.00	4045	B(94), ¹⁷ B(92) ¹⁸
61.	$\text{H} + \text{C}_2\text{H}_6 \rightleftharpoons \text{C}_2\text{H}_5 + \text{H}_2$	1.45×10^9	1.50	3730	B(94) ¹⁷
62.	$\text{H} + \text{C}_2\text{H}_5 \rightleftharpoons \text{C}_2\text{H}_4 + \text{H}_2$	1.81×10^{12}	0.00	0	TH(86)-NIST ²²
63.	$\text{H} + \text{C}_2\text{H}_4 \rightleftharpoons \text{C}_2\text{H}_3 + \text{H}_2$	5.42×10^{14}	0.00	7500	B(94) ¹⁷
64.	$\text{H} + \text{C}_2\text{H}_3 \rightleftharpoons \text{C}_2\text{H}_2 + \text{H}_2$	1.20×10^{12}	0.00	0	B(94) ¹⁷
65.	$\text{H} + \text{C}_2\text{H}_2 \rightleftharpoons \text{C}_2\text{H} + \text{H}_2$	6.62×10^{13}	0.00	14000	B(94) ¹⁷
66.	$\text{C}_2\text{H} + \text{C} \rightleftharpoons \text{C}_3 + \text{H}$	1.00×10^{14}	0.00	0	DH(92) ²³

(Continued on next page)

Table 2. (Cont'd)

	$k_f = A T^n e^{-T_a/T}$	A (cc/mol/s)	n	T_a (K)	Source
Ionization Reactions					
67.	$N + N \rightleftharpoons N_2^+ + e^-$	4.40×10^7	1.50	67500	P(01) ¹⁴
68.	$C + N \rightleftharpoons CN^+ + e^-$	1.00×10^{15}	1.50	164400	N(91) ²
69.	$N + e^- \rightleftharpoons N^+ + e^- + e^-$	2.50×10^{34}	-3.82	168600	P(01), ¹⁴ P(93) ¹⁶
70.	$C + e^- \rightleftharpoons C^+ + e^- + e^-$	3.70×10^{31}	-3.00	130720	P(01) ¹⁴
71.	$H + e^- \rightleftharpoons H^+ + e^- + e^-$	2.20×10^{30}	-2.80	157800	P(01) ¹⁴
72.	$Ar + e^- \rightleftharpoons Ar^+ + e^- + e^-$	2.50×10^{34}	-3.82	181700	N(91) ²
73.	$CN^+ + N \rightleftharpoons CN + N^+$	9.80×10^{12}	0.00	40700	N(91) ²
74.	$C^+ + N_2 \rightleftharpoons N_2^+ + C$	1.11×10^{14}	-0.11	50000	N(91) ²

website.^{32,33} However, for the hydrocarbon species CH_4 , CH_3 , CH_2 , HCN , C_2H_6 , C_2H_5 , C_2H_4 , C_2H_3 , C_2H_2 , and C_2H , the thermodynamic data and curve fits are available only up to 6000 K, and most of these curve fits do not produce physical results when extrapolated to higher temperatures. The range of curve fits is extended by increasing the specific heat from its value at 6000 K to an asymptotic value at 30,000 K linearly. The asymptotic value of the specific heat at 30,000 K for each species is determined by accounting for the number of atoms, type of molecule, and estimated internal excitations.

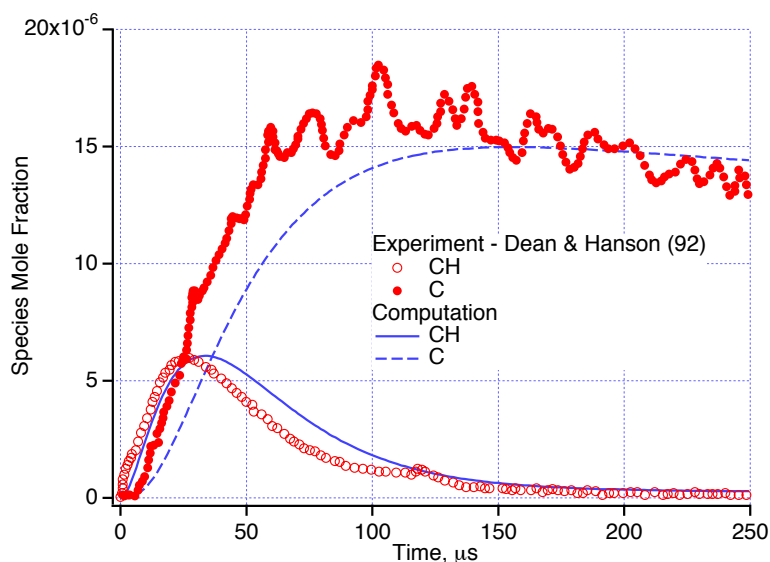
IV. Validation of Kinetic Model

Validation of the detailed model against a number of experiments is important to gain confidence in predictions of the model and determine the parameter space in which the model can be used. The detailed model has been validated against the following set of shock tube experiments: the experiments of Dean and Hanson (92),²³ Dean et al. (90),²⁵ Kruse and Roth (97),²⁷ and Mick and Roth (91).³¹ These experiments were chosen such that the measurements are sensitive to only a few reactions (or a small subset) of the kinetic model. Therefore, each of these experiments provides validation for certain reactions in the model. Computational simulations of the experiments were performed using the SENKIN and SHOCK programs in the CHEMKIN package.³⁴

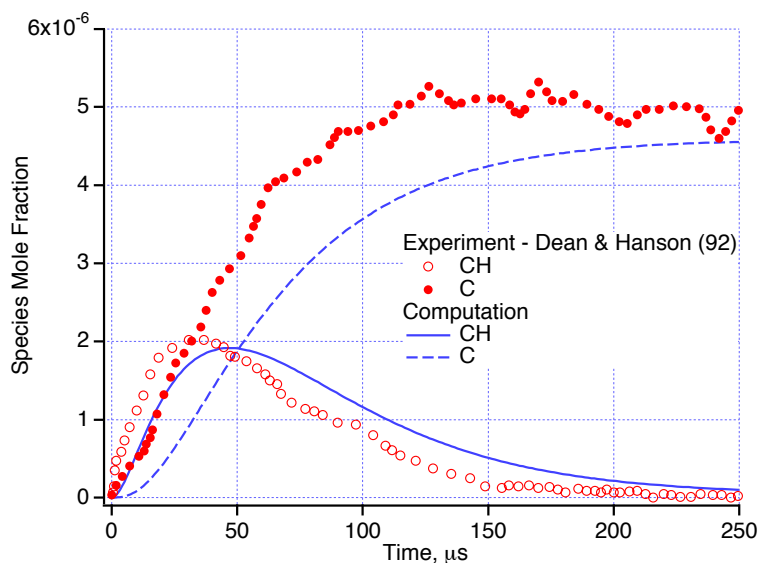
Shock tube experiments of Dean and Hanson (92)

In the experiments of Dean and Hanson (92),²³ CH and C concentration time histories were measured behind a reflected shock wave in dilute CH_4/Ar mixtures. The CH measurements were made using narrow-linewidth laser absorption, and the C-atom measurements were made using atomic resonance absorption spectroscopy (ARAS). These experiments are important for the model validation because dissociation rates of several hydrocarbon species in the literature were deduced from these measurements and used in the detailed model. It should be mentioned here that very similar CH concentration measurements in CH_4 dissociation were also obtained by Markus and Roth (92),³⁵ but their data did not include C concentration. Comparisons are made with the more comprehensive data of Dean and Hanson (92) only.

Comparisons of the detailed model simulation results and experimental data for two cases are presented in Fig. 1. It appears that the computed profiles are lagging the measured profiles by 15-20 μs . In the initial 15-20 μs period, the most important reactions for C and CH productions are the reactions 2-7. Dean and Hanson in Ref. 23 also presented a kinetic model to fit their experimental data. There are many differences between the present model and their model. The present methyl (CH_3) dissociation rate (reaction 3 in Table 2) is smaller by a factor of two than the one used in Ref. 23, which is the primary cause of the observed time lag. As will be shown later, the computed C and CH results are very



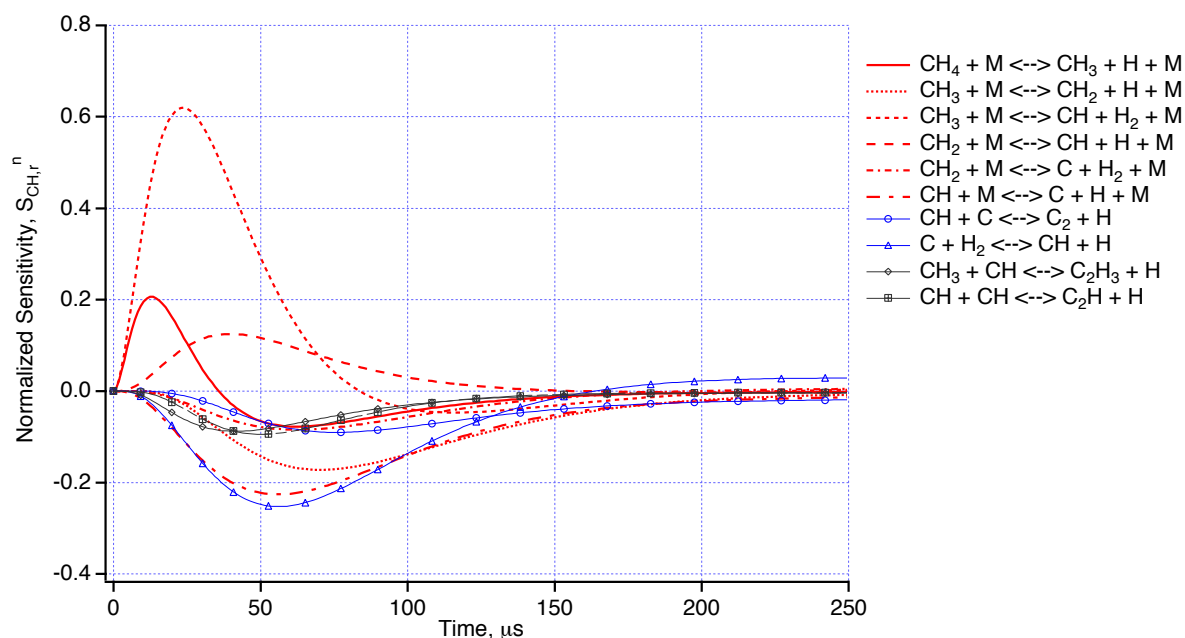
a) $p = 0.89$ atm, $T = 3100$ K, 30 ppm CH_4 in Ar.



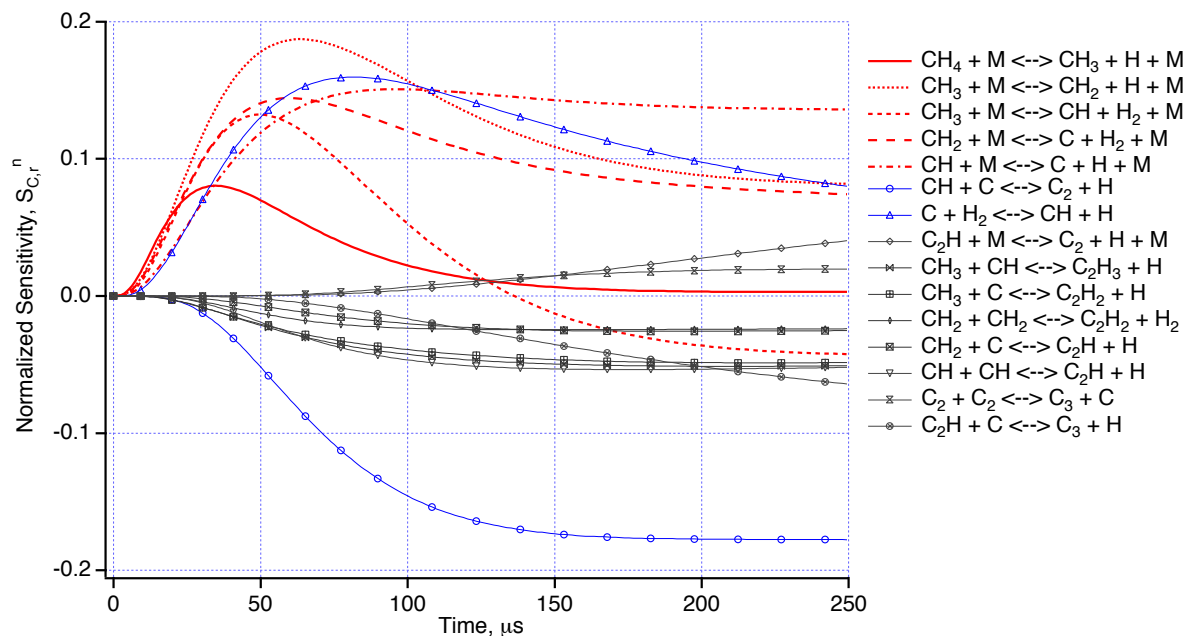
b) $p = 0.85$ atm, $T = 3127$ K, 6 ppm CH_4 in Ar.

Figure 1. Comparison of the detailed model simulation against the shock tube experiments of Dean and Hanson (92) for two cases: Time history of CH and C mole fractions.

sensitive to this reaction rate. However, this rate in the present model was not changed solely to match the experimental data better since no error bars were given on the measurements. In general, if there is a recommended rate available from a comprehensive review in the literature, e.g., Baulch et al. (94),¹⁷ then the recommended rate is used. Also, the present methane dissociation rate (reaction 2 in Table 2) is different from the one used in Ref. 23. In the present model, the low-pressure-limit rate constants are used for the pressure-dependent dissociation reactions. This assumption should be reasonably good at these pressures, based on the work of Kiefer and Kumaran (93).³⁶ The present CH_4 dissociation rate may also contribute to the discrepancy but to a smaller extent. Despite the observed time lag, the present model predicts experimental peak values of C and CH mole fractions and qualitative shapes of these curves over the entire time history reasonably well. Overall agreement between the computed and



a) CH sensitivity coefficients



b) C sensitivity coefficients

Figure 2. Sensitivities of the computed mole fractions to the reaction rates, $p = 0.89$ atm, $T = 3100$ K, 30 ppm CH_4 in Ar.

measured profiles is considered good, given that the computed mole fractions are sensitive to a number of reaction rates.

Linear sensitivity analysis has been widely used in the combustion literature for analysis of chemical reactions. In the present work, linear sensitivity analysis is also used, as implemented in the SENKIN program of the CHEMKIN package. Sensitivity coefficients are calculated to determine the rate-limiting

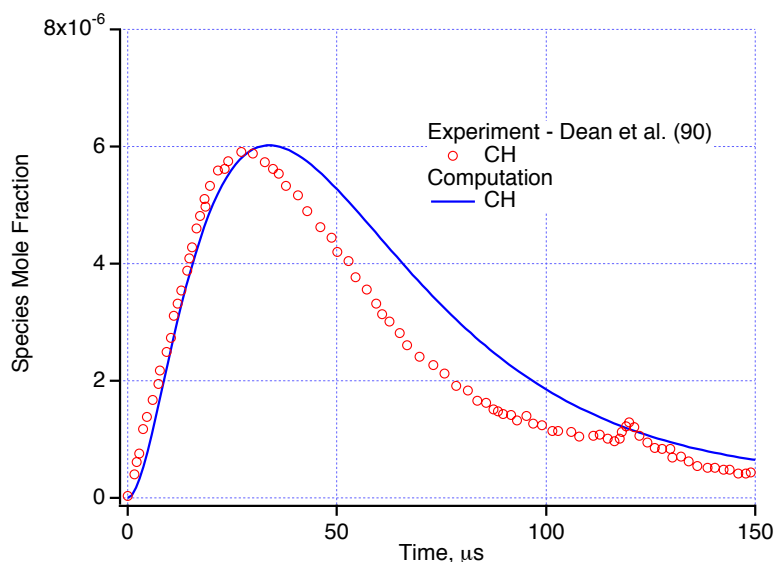
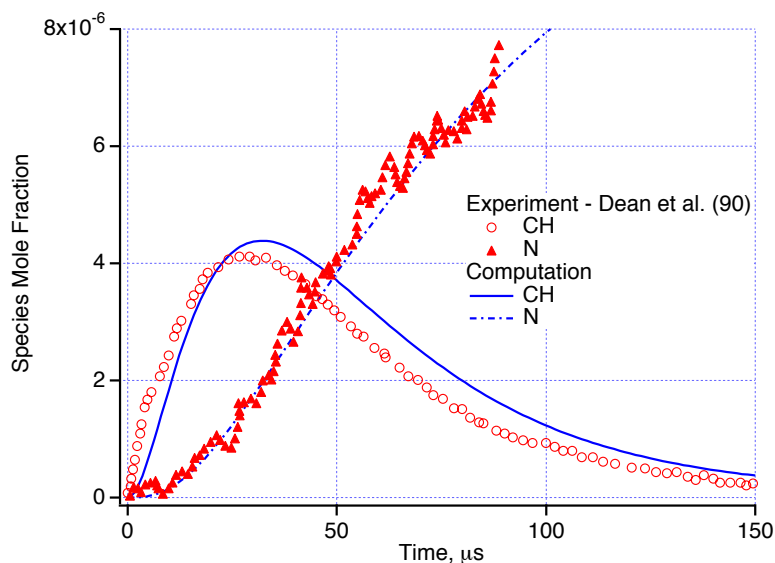
a) $p = 0.89$ atm, $T = 3096$ K, 30 ppm CH_4 in Ar.b) $p = 0.88$ atm, $T = 3065$ K, 30 ppm CH_4 and 5% N_2 in Ar.

Figure 3. Comparison of the detailed model simulation against the shock tube experiments of Dean et al. (90): Time history of CH and N mole fractions.

steps in the production and consumption of certain species. The sensitivity coefficients of computed CH and C mole fractions with respect to the kinetic model reactions are presented in Fig. 2. The following example is helpful for interpretation of sensitivity coefficients: the normalized sensitivity coefficient of parameter X with respect to reaction r (at time level n) is defined as

$$S_{X,r} = \frac{k_r}{X_o} \cdot \frac{\partial X}{\partial k_r};$$

and $S_{X,r}^n = 0.1$ means that if the rate constant for reaction r were doubled, the parameter X would increase by an amount approximately equal to 10% of X_o . The maximum value of X over the time history of the solution is used for the normalization parameter X_o . The computed CH and C results are

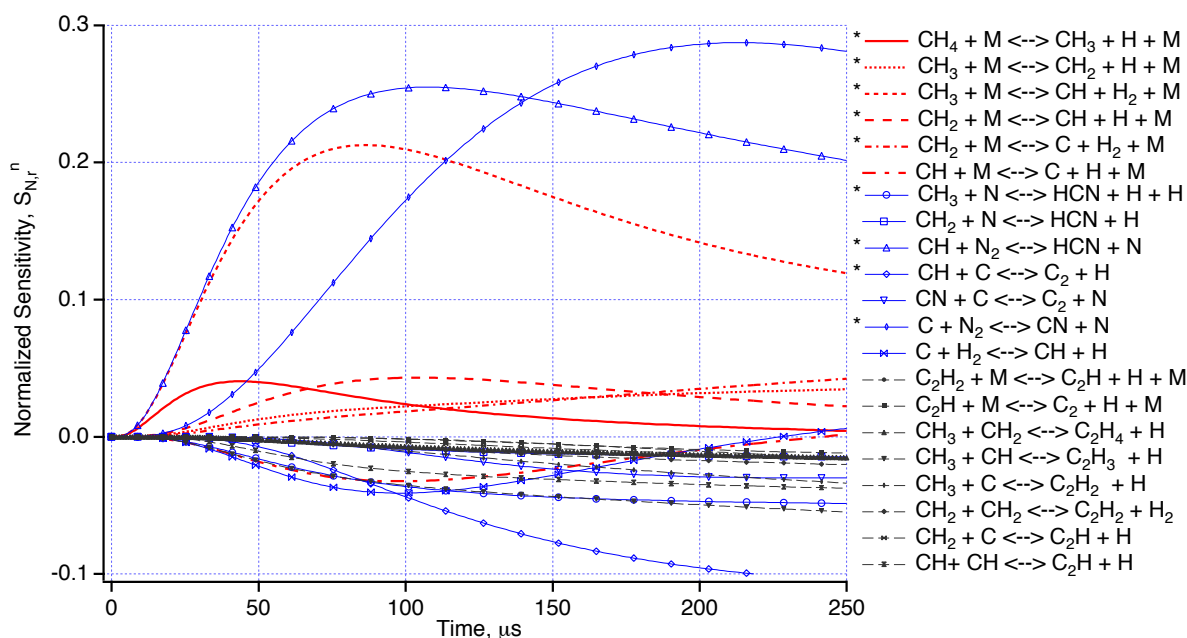


Figure 4. Sensitivity coefficients of the computed N mole fractions to the reaction rates, $p = 0.88$ atm, $T = 3065$ K, 30 ppm CH_4 and 5% N_2 in Ar.

sensitive to a number of chemical reactions in the detailed model, as shown in Fig. 2. Therefore, these comparisons provide validation for only those reactions affecting CH and C results (a subset of the model).

Shock tube experiments of Dean et al. (90)

In the experiments of Dean et al. (90),²⁵ N-atom and CH concentration time histories were measured behind a reflected shock wave in dilute CH_4/Ar and $\text{CH}_4/\text{N}_2\text{-Ar}$ mixtures. The CH measurements were made using narrow-linewidth laser absorption, and the N-atom measurements were made using ARAS. These experiments were chosen because they provide model validation for the reactions of CH and C atoms with N_2 . It appears that, almost in parallel, similar work was also carried out by Lindackers et al. (90).³⁷ Comparisons are made only with the data from Dean et al. (90).

Comparisons of the detailed model simulation results and experimental data for two cases are presented in Fig. 3. The first case is very similar to the one shown in Fig. 1a (the present experimental data was scanned from Ref. 25), for methane pyrolysis in Ar only. The second case includes 5% N_2 and effects of related nitrogen reactions. The measured effect of 5% N_2 on the CH mole fraction is shown in Fig. 3, and it is reproduced by the computations. Agreement between the computed and experimental N-atom profiles is very good within the scatter.

Sensitivity coefficients of the computed N mole fractions with respect to the kinetic model reactions are presented in Fig. 4. The computed results are sensitive to a number of reactions in the detailed model, and a few significant reactions are marked with * in the legend of Fig. 4. This case provides validation for those reactions.

Shock tube experiments of Kruse and Roth (97)

In the experiments of Kruse and Roth (97),²⁷ C_2 concentration time histories were measured behind a reflected shock wave using ring dye laser absorption spectroscopy in dilute $\text{C}_2\text{H}_2/\text{Ar}$ mixtures. C and C_3 were also measured using ARAS and emission spectroscopy, respectively. Although the experiments covered the temperature range of 2580-4650 K, as a validation case, C_2 concentration time history at a

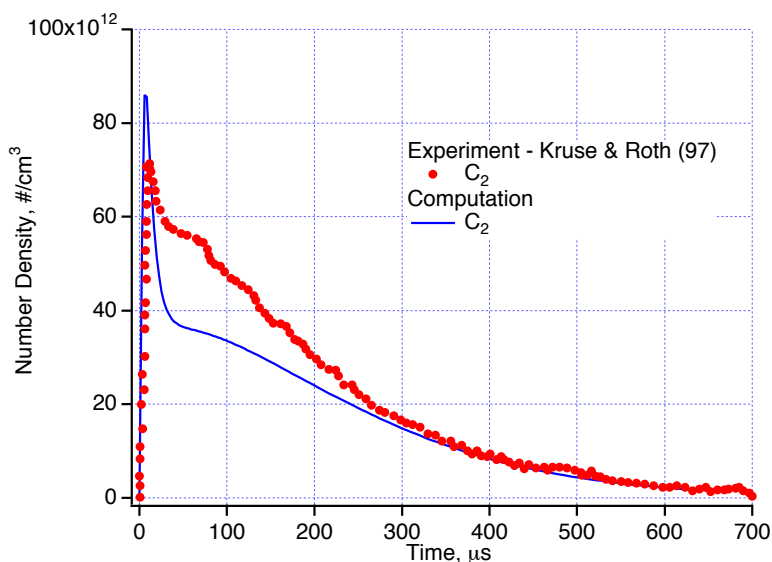


Figure 5. Comparison of the detailed model simulation against the shock tube experiments of Kruse and Roth (97): Time history of C_2 number density at $p = 1.82$ bar, $T = 4450$ K, 50 ppm C_2H_2 in Ar.

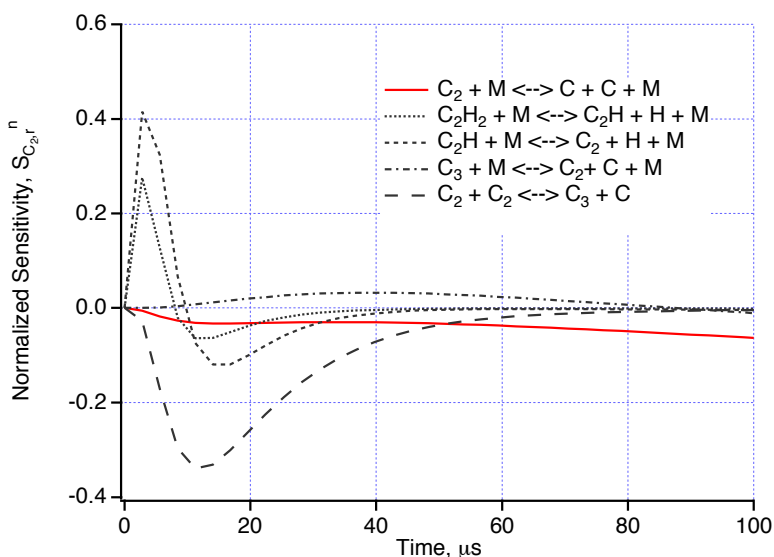


Figure 6. Sensitivity coefficients of the computed C_2 mole fractions to the reaction rates for the first 100 μs , $p = 1.82$ bar, $T = 4450$ K, 50 ppm C_2H_2 in Ar.

relatively high temperature of 4450 K was chosen. These experiments provide validation for the rates of several C_2 and C_2H reactions.

Comparison of the computed and experimental C_2 number densities is presented in Fig. 5. Although the detailed model underpredicts the amount of C_2 formed in the first 200 μs , overall agreement between the computed and experimental profiles is reasonably good. Kruse and Roth (97) using a different kinetic mechanism for C_2H_2 pyrolysis obtained a better fit for their measurements but only after modifying C_2 thermodynamic data. They also suggested that JANAF thermodynamic data for either C, C_2 , or C_3 be

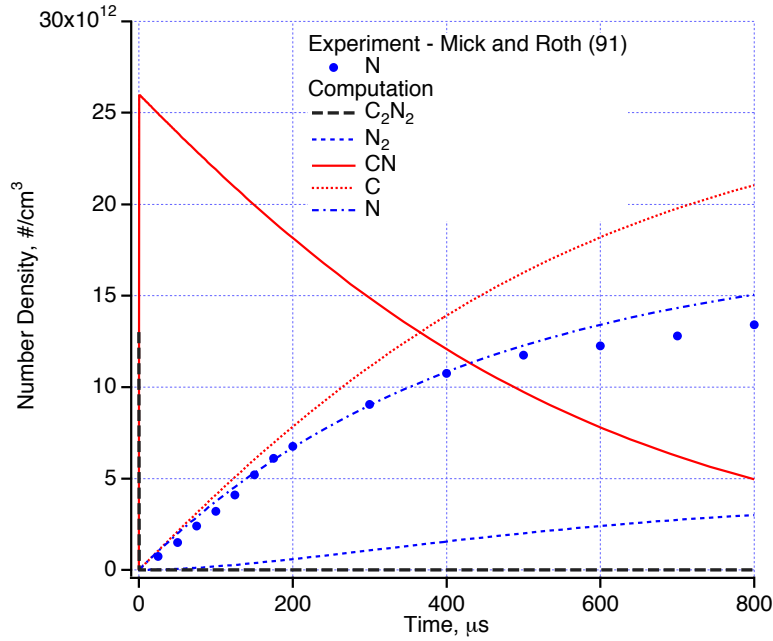


Figure 7. Comparison of the detailed model simulation against the shock tube experiments of Mick and Roth (91): Time history of N number density at $p = 1.9$ bar, $T = 5290$ K, 5 ppm C_2N_2 in Ar.

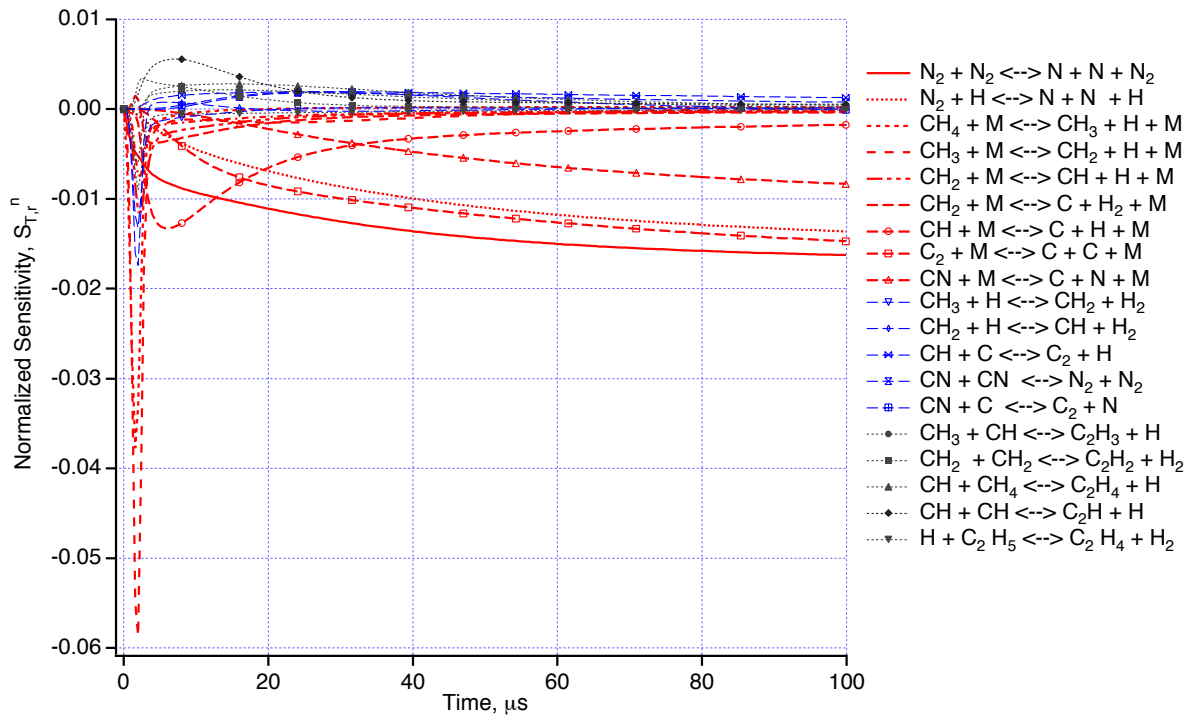
modified in order to explain their experimental data. In the present work, the thermodynamic database was not modified. For this case, the computed C_2 mole fractions are sensitive to only a few reactions, but C_2 sensitivity coefficients to these reactions are relatively large, especially in the first 40 μs . The sensitivity coefficients of computed C_2 mole fractions with respect to the kinetic model reactions are presented in Fig. 6. Since the reaction rates of all the reactions in Fig. 6 are obtained from Kruse and Roth (97), the differences observed in Fig. 5 are most likely due to the differences in the thermodynamic database used in both models.

Shock tube experiments of Mick and Roth (91)

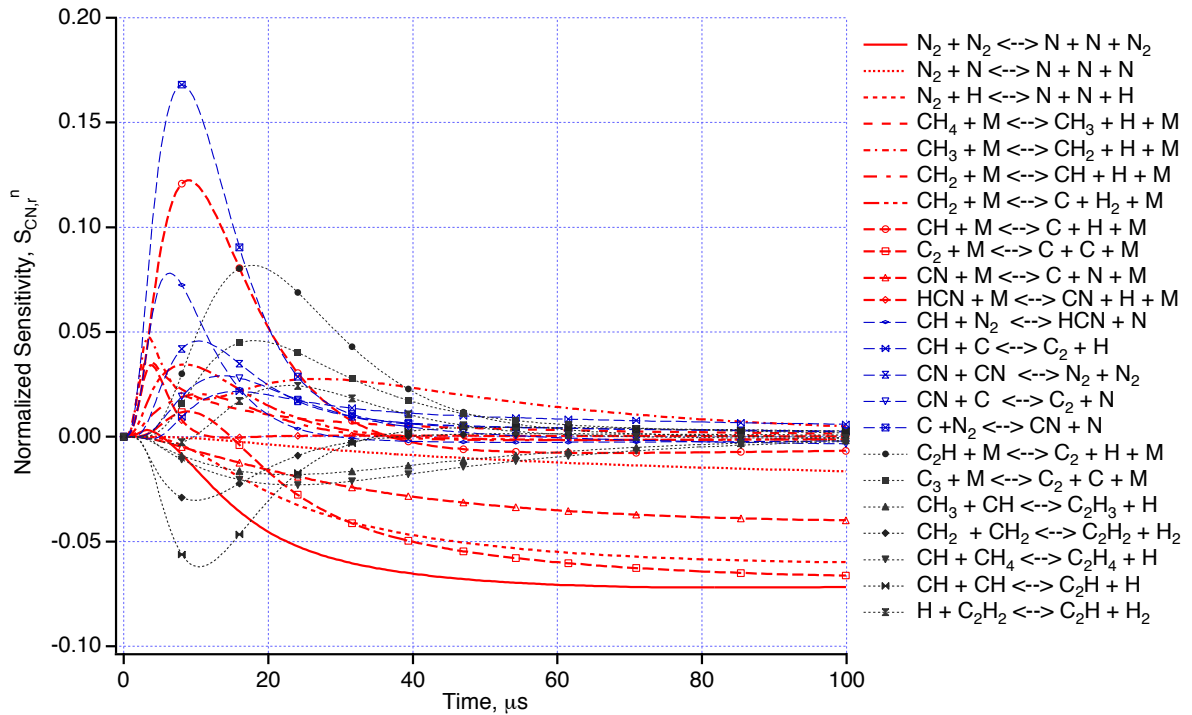
In the experiments of Mick and Roth (91),³¹ N concentration time histories were measured behind a reflected shock wave using ARAS in dilute C_2N_2/Ar mixtures. These experiments were chosen because they provide validation for the CN dissociation rate used in the model. For simulation of the experiments, the reaction $C_2N_2 + M \rightleftharpoons CN + CN + M$ is added to the kinetic model, with the forward rate constant $k_f = 1.07 \times 10^{34} T^{-4.32} e^{-65420/T} \text{ cm}^3/\text{mol.s}$ obtained from Ref. 31.

Comparisons of the detailed model simulation results and experimental data for one case are presented in Fig. 7. C_2N_2 decomposes rapidly and provides a well-characterized CN source, and N atoms are formed from CN dissociation. The computations predict the experimental N number density over the time history very well. Although sensitivity coefficients are not shown here, the computed N number density is primarily sensitive to the CN dissociation rate (reaction 10) and the reaction 57 in Table 2.

For all validation cases, comparisons between the measurements and detailed model predictions are reasonably good. However, it should be cautioned that all these experiments are at relatively low temperatures ($T \leq 5000$ K). For Titan atmospheric entry, the model will be extrapolated to much higher shock layer temperatures. Nevertheless, these validation cases provide a strong foundation for the N_2 - CH_4 -Ar model development. A comprehensive shock tube experiment program is currently under way at the NASA Ames EAST facility to measure the radiation from N_2 - CH_4 shock waves at velocities relevant to Titan atmospheric entry. The detailed model will be validated against the EAST facility experiments in the future.



a) T sensitivity coefficients



b) CN sensitivity coefficients

Figure 8. Sensitivity coefficients of temperature and CN mole fractions to the reaction rates at constant pressure, $p = 0.05$ atm. Initial conditions: $T_i = 10,000$ K, 5% CH_4 in N_2 .

V. Sensitivity Analysis and Simplification: Reduced Model

Even though the detailed model can easily be used for one-dimensional CFD analysis of shock tube flows, it is too complex and costly to implement in a 2-D or 3-D CFD flowfield code for aerothermal analysis. For this purpose, the detailed model is simplified (or reduced) through analysis of the chemical reactions.

For simplification of the model, the following approach is taken. A parameter space of temperature and pressure relevant to Titan entry is estimated. Through analysis of chemical reactions within this parameter space, certain reactions and species are eliminated from the detailed model. In general, all the species that do not exist in any significant amounts within the parameter space are eliminated. However, the following considerations are also taken into account: the species known to be strong radiators (e.g., CN, N_2^+ , NH, CH, C_2 , etc.) and their reactions are included whether these species exist in any significant amounts or not; and certain species (e.g., CH_3 , CH_2 , HCN, CN^+) which do not exist in any significant amounts but provide important reaction paths through their reactions for methane decomposition and CN formation are also included. Sensitivity analysis is an important tool to eliminate unimportant species and reactions. Sensitivity analysis of flowfield variables that influence CN radiation computations is performed to simplify the detailed model within the parameter space of interest.

For typical Titan entry trajectories (e.g., see Nelson et al. (91),² Takashima et al. (03),⁸ Olejniczak et al. (03)⁹), when shock layers formed in front of the probes at anticipated entry velocities and altitudes are considered, it is estimated that pressures at the stagnation point behind the shock wave range from 0.01 atm to 0.05 atm, and the shock layer temperatures range from 5000 to 15,000 K. Also, for a typical shock stand-off distance of 10 cm, at various entry speeds in the range of 3.0-6.5 km/s, examining chemistry of particles behind the shock wave over a time period of 100 μs is estimated to be sufficient (for radiative heating to the stagnation point).

Since our primary interest is to simulate nonequilibrium radiation emission from the shock layer due to CN, accurate simulation of the following variables is considered important for Titan entry: temperature, and the number densities of N, CN, H, and e^- . Although the choice of four species number densities seems somewhat arbitrary, it is believed that their sensitivities would provide sufficient redundancy to allow elimination of unimportant reactions for CN radiation emission calculations. Sensitivity coefficients of these variables are computed at constant pressures of 0.01, 0.025, 0.05, 0.1, and 0.5 atm, and initial temperatures of 5000, 8000, 10,000, and 15,000 K over a time period of 100 μs . The pressure range up to 0.5 atm is considered because some of the existing shock tube experiments for Titan entry were obtained at higher pressures.^{3,4,5,7} Note that the temperature and pressure ranges and the time period are chosen for shock layer simulations of Titan atmospheric entry only. From the sensitivity calculations performed, all the reactions not affecting either temperature or the number densities of N, CN, H, and e^- within the parameter space are eliminated.

For one representative case, computed sensitivity coefficients of T and CN mole fractions with respect to the kinetic model reactions are shown in Fig. 8. These calculations are carried out at constant pressure of 0.05 atm, and initial conditions are 5% CH_4 in N_2 at temperature of 10,000 K. As expected, the computed temperature is mostly sensitive to the dissociation reactions of molecules and a few radical reactions. The CN sensitivities shown in Fig. 8b indicate that CN mole fractions are sensitive to a number of radical reactions (in addition to the dissociation reactions). It is interesting to note that some of the C-2 hydrocarbon chemistry reactions are also affecting the CN mole fractions, especially in the first 20 μs . Obviously, these sensitivities strongly depend on the prescribed pressure and initial conditions. At higher pressures, the methane dissociation is completed much faster, and its effect on CN formation is limited to a shorter time period. At lower pressures, the methane dissociation proceeds at a slower rate and its effects on CN formation is spread over a longer time period.

From the analysis of chemical reactions, it is found that the detailed model can be simplified (or reduced) to a model consisting of 21 species (N_2 , CH_4 , CH_3 , CH_2 , CH, C_2 , H_2 , CN, NH, HCN, N, C, H, Ar, N_2^+ , CN^+ , N^+ , C^+ , H^+ , Ar^+ , and e^-) and 35 reactions for shock layer analysis of Titan entry. In other words, the simplified chemical reaction set would be sufficient for flowfield simulations of temperature and number densities of N, CN, H, and e^- . A summary of chemical reactions and reaction

Table 3. Simplified Chemical Reaction Set for N₂-CH₄-Ar Mixtures

	$k_f = A T^n e^{-T_a/T}$	A (cc/mol/s)	n	T _a (K)	Source/Uncert. Est.
Dissociation Reactions					
1.	$N_2 + M \rightleftharpoons N + N + M$	7.00x10 ²¹	-1.60	113200	P(01) ¹⁴ /F=3.0
	enhanced rate for M = N, C, H	3.00x10 ²²	-1.60	113200	P(01) ¹⁴ /F=3.0-5.0
	enhanced rate for M = e ⁻	3.00x10 ²⁴	-1.60	113200	P(01) ¹⁴ /F=5.0
2.	$CH_4 + M \rightleftharpoons CH_3 + H + M$	4.70x10 ⁴⁷	-8.20	59200	B(94) ¹⁷ /F=2.0
3.	$CH_3 + M \rightleftharpoons CH_2 + H + M$	1.02x10 ¹⁶	0.00	45600	B(94) ¹⁷ /F=1.26-3.2
4.	$CH_3 + M \rightleftharpoons CH + H_2 + M$	5.00x10 ¹⁵	0.00	42800	DH(92) ²³ /F=1.26-2.0
5.	$CH_2 + M \rightleftharpoons CH + H + M$	4.00x10 ¹⁵	0.00	41800	DH(92) ²³ /F=1.26-2.0
6.	$CH_2 + M \rightleftharpoons C + H_2 + M$	1.30x10 ¹⁴	0.00	29700	DH(92) ²³ /F=1.26-2.0
7.	$CH + M \rightleftharpoons C + H + M$	1.90x10 ¹⁴	0.00	33700	DH(92) ²³ /F=1.26-2.0
8.	$C_2 + M \rightleftharpoons C + C + M$	1.50x10 ¹⁶	0.00	71600	KR(97) ²⁷ /F=1.26-2.0
9.	$H_2 + M \rightleftharpoons H + H + M$	2.23x10 ¹⁴	0.00	48350	B(94), ¹⁷ B(92) ¹⁸ /F=1.26-2.0
10.	$CN + M \rightleftharpoons C + N + M$	2.53x10 ¹⁴	0.00	71000	P(94), ¹⁵ T(92) ¹⁹ /F=1.5-2.0
11.	$NH + M \rightleftharpoons N + H + M$	1.80x10 ¹⁴	0.00	37600	D(98)-NIST ²² /F=1.26-2.0
12.	$HCN + M \rightleftharpoons CN + H + M$	3.57x10 ²⁶	-2.60	62845	TH(91) ²⁰ /F=1.5-2.0
Radical Reactions					
13.	$CH_3 + N \rightleftharpoons HCN + H + H$	7.00x10 ¹³	0.00	0	D(90) ²⁵ /F=10.0
14.	$CH_3 + H \rightleftharpoons CH_2 + H_2$	6.03x10 ¹³	0.00	7600	B(92) ¹⁸ /F=10.0
15.	$CH_2 + N_2 \rightleftharpoons HCN + NH$	4.82x10 ¹²	0.00	18000	S(87)-NIST ²² /F=10.0
16.	$CH_2 + N \rightleftharpoons HCN + H$	5.00x10 ¹³	0.00	0	D(90) ²⁵ /F=10.0
17.	$CH_2 + H \rightleftharpoons CH + H_2$	6.03x10 ¹²	0.00	-900	B(92)-NIST ²² /F=5.0-10.0
18.	$CH + N_2 \rightleftharpoons HCN + N$	4.40x10 ¹²	0.00	11060	D(90) ²⁵ /F=1.5-3.2
19.	$CH + C \rightleftharpoons C_2 + H$	2.00x10 ¹⁴	0.00	0	DH(92) ²³ /F=10.0
20.	$C_2 + N_2 \rightleftharpoons CN + CN$	1.50x10 ¹³	0.00	21000	S(97) ²⁸ /F=1.26-2.0
21.	$CN + H_2 \rightleftharpoons HCN + H$	2.95x10 ⁵	0.00	1130	W(96) ²⁹ /F=3.2-5.0
22.	$CN + C \rightleftharpoons C_2 + N$	5.00x10 ¹³	0.00	13000	P(01) ¹⁴ /F=2.0-5.0
23.	$N + H_2 \rightleftharpoons NH + H$	1.60x10 ¹⁴	0.00	12650	DaH(90) ²⁶ /F=1.26-2.0
24.	$C + N_2 \rightleftharpoons CN + N$	5.24x10 ¹³	0.00	22600	B(94) ¹⁷ /F=1.6-2.0
25.	$C + H_2 \rightleftharpoons CH + H$	4.00x10 ¹⁴	0.00	11700	D(91)/F=1.6-2.0
26.	$H + N_2 \rightleftharpoons NH + N$	3.00x10 ¹²	0.50	71400	R(78) ³⁰ /F=2.0-3.2
27.	$H + CH_4 \rightleftharpoons CH_3 + H_2$	1.32x10 ⁴	3.00	4045	B(94), ¹⁷ B(92) ¹⁸ /F=1.6-2.0
Ionization Reactions					
28.	$N + N \rightleftharpoons N_2^+ + e^-$	4.40x10 ⁷	1.50	67500	P(01) ¹⁴ /F=10.0
29.	$C + N \rightleftharpoons CN^+ + e^-$	1.00x10 ¹⁵	1.50	164400	N(91) ² /F≥10.0
30.	$N + e^- \rightleftharpoons N^+ + e^- + e^-$	2.50x10 ³⁴	-3.82	168600	P(01), ¹⁴ P(93)/F=10.0
31.	$C + e^- \rightleftharpoons C^+ + e^- + e^-$	3.70x10 ³¹	-3.00	130720	P(01) ¹⁴ /F=10.0

(Continued on next page)

Table 3. (Cont'd)

	$k_f = A T^n e^{-T_a/T}$	A (cc/mol/s)	n	T_a (K)	Source/Uncert. Est.
32.	$H + e^- \rightleftharpoons H^+ + e^- + e^-$	2.20×10^{30}	-2.80	157800	P(01) ¹⁴ /F \geq 10.0
33.	$Ar + e^- \rightleftharpoons Ar^+ + e^- + e^-$	2.50×10^{34}	-3.82	181700	N(91) ² /F \geq 10.0
34.	$CN^+ + N \rightleftharpoons CN + N^+$	9.80×10^{12}	0.00	40700	N(91) ² /F \geq 10.0
35.	$C^+ + N_2 \rightleftharpoons N_2^+ + C$	1.11×10^{14}	-0.11	50000	N(91) ² /F \geq 10.0

rates used in the simplified model is given in Table 3. Further simplification of the model is possible by eliminating some of the radical-radical reactions (e.g., reactions 13, 15, 16, 17, 35), but they are retained here because of their uncertainties.

In Table 3, the uncertainty factors (F) for each reaction rate in the reduced model (as well as the source) are also listed. Following the notation of Baulch et al.¹⁷, F is defined such that the range of values of k_f is bounded by multiplication and division of k_f by a factor F. It is difficult to put uncertainty factors on these reaction rates because shock layer temperatures for Titan entry are much higher than the temperature range over which these rates are reviewed and measured. Therefore, these F factors should be considered a lower limit on the uncertainty. Some of these uncertainty factors are obtained from the review articles cited, and some are purely based on subjective judgement of the author (based on literature surveys and the uncertainties on similar reaction rates). Even though it is subjective, it is still useful to have some estimate of the reaction rate uncertainties. These uncertainty factors are used in a companion paper by Bose et al. (04)³⁸ for uncertainty analysis of the thermochemical modeling for Titan atmospheric entry.

VI. Sample Case: Shock Tube Flow at $u_1 = 6.3$ km/s

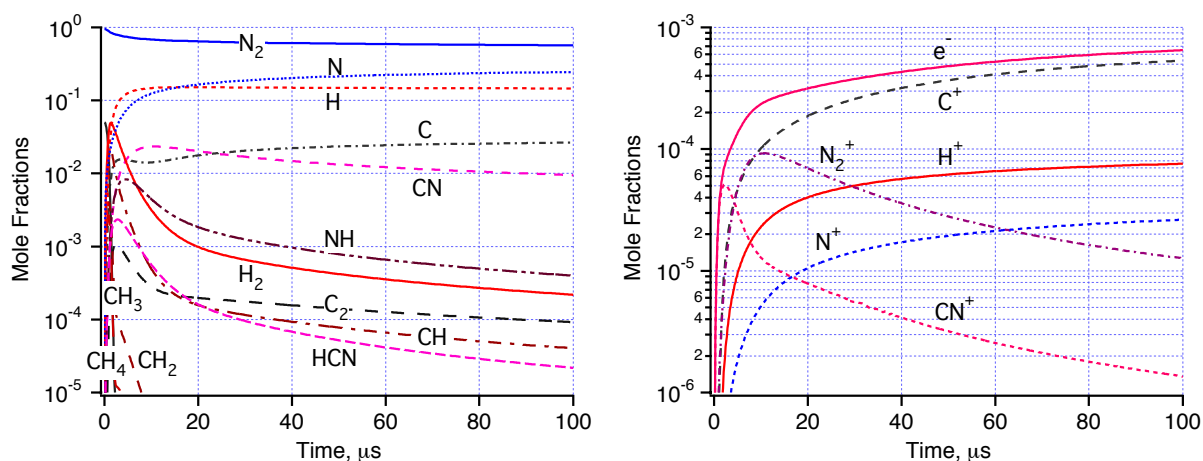
A sample case of shock tube flow, duplicating typical shock layer conditions in Titan atmospheric entry, is chosen to present simulations using the different kinetic models. Figure 9 shows the computed species mole fractions as functions of time using the detailed, reduced and Nelson-91 models.

As shown in Fig. 9, the detailed model predicts that at these conditions methane decomposition is completed within 10 μ s. Afterwards, the major species remaining are N_2 , N, H, C, CN, NH, H_2 , C_2 , CH, and HCN. Although this case does not involve significant ionization, CN^+ associative ionization reaction provides an initial ionization path. C^+ , N_2^+ , and H^+ represent the most significant ionized species.

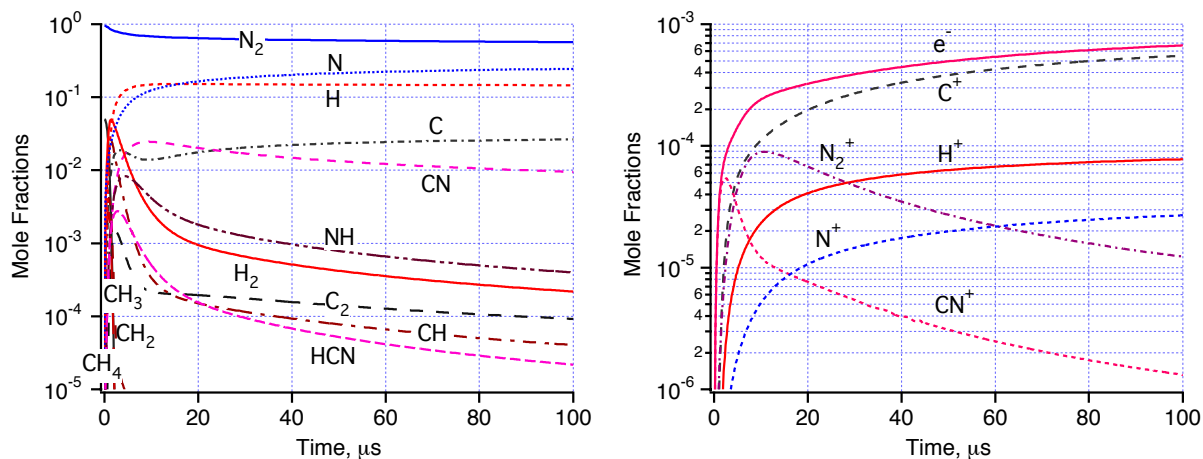
The reduced model results in comparison with the detailed model results show minor differences in terms of major species, which is not coincidental of course because the reduced model was developed based upon those criteria. The main differences are within the first 10-20 μ s, and even in that range, the maximum differences between the detailed and reduced model predictions of N_2 , N, CN, and H mole fractions are less than 0.006, 0.001, 0.0025, and 0.003, respectively.

In Fig. 9c, the Nelson-91 model results for species mole fractions are presented. In comparison with the detailed model results, there are significant differences (as expected from the evaluation of the Nelson-91 model). The Nelson-91 model predicts that at these conditions methane decomposition is almost instantaneous, due to the much larger methane dissociation rates used. The major species remaining afterwards are N_2 , N, H, C, CN, NH, C_2 , H_2 , and CH. In comparison with the detailed model values, computed CN levels are higher and N levels are lower. The Nelson-91 model also predicts much higher ionization levels than the detailed model. Electron-impact ionization of H is the dominant ionization reaction (reaction 21 in Table 1), and H^+ , C^+ , and N^+ represent the most significant ionized species. Note that if these calculations were carried out using a two-temperature model, the computed ionization levels would be smaller.

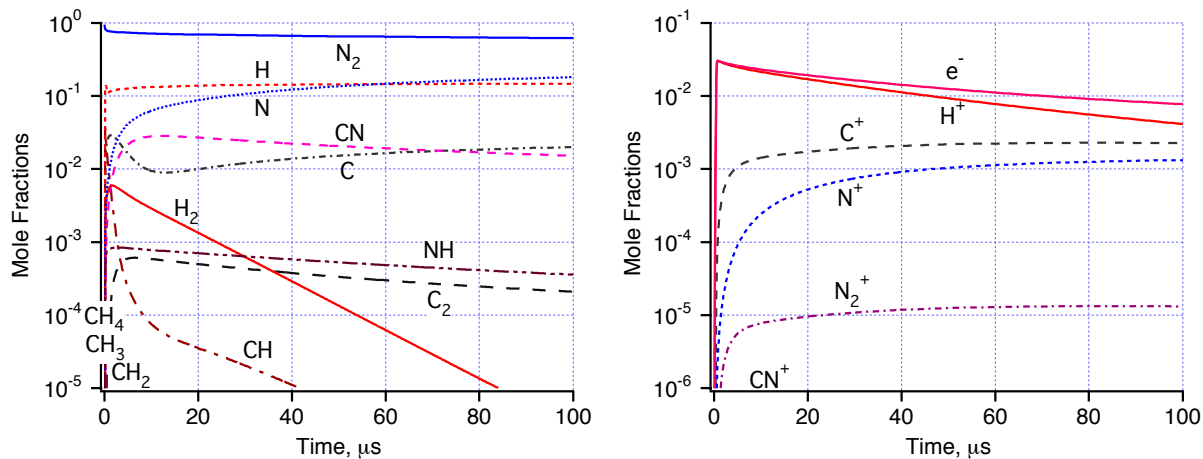
Finally, comparisons of CN number densities and temperatures using different models are presented in Fig. 10. CN number density and temperature are the most important flowfield parameters affecting



a) The detailed model



b) The reduced model



c) The Nelson-91 model

Figure 9. The time histories of computed mole fractions using different kinetic models: shock tube flow, $p_1 = 0.1$ Torr, $T_1 = 300$ K, $u_1 = 6.3$ km/s, 5% CH_4 in N_2 . Neutral and charged species are shown separately.

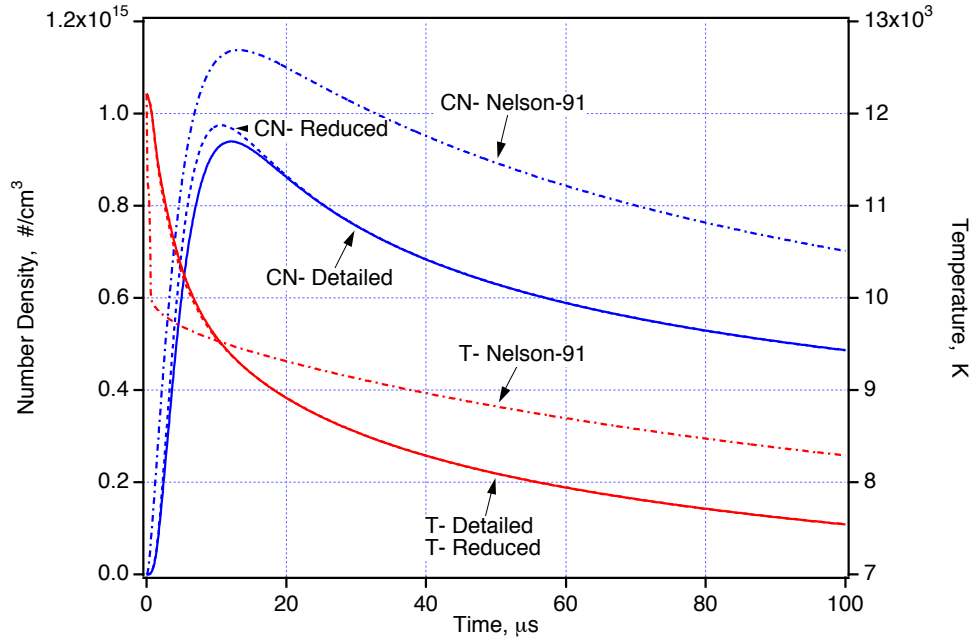


Figure 10. Comparisons of the computed CN number densities and temperatures using different models: shock tube flow, $p_1 = 0.1$ Torr, $T_1 = 300$ K, $u_1 = 6.3$ km/s, 5% CH_4 in N_2 .

computations of shock layer radiation due to CN. The present model predicts lower CN number densities and lower temperatures behind the shock in comparison with the Nelson-91 model. Although computation of radiative heating to Titan probes is outside the scope of this paper, it is expected that the radiative heating computed with the present model would be much smaller than that of the Nelson-91 model.

VII. Concluding Remarks

A detailed chemical kinetic model for N_2 - CH_4 -Ar mixtures is developed for nonequilibrium flowfield simulation of shock layers formed in front of probes entering Titan's atmosphere. The detailed kinetic model uses up-to-date chemical reaction mechanisms and reaction rates consistent with the literature, and it is validated against existing shock tube experiments. For all the validation cases presented, comparisons between the measurements and detailed model predictions are reasonably good, and these cases provide a strong foundation for the present kinetic model. It should be cautioned that all these experiments are at relatively low temperatures ($T \leq 5000$ K); and for Titan atmospheric entry applications, the reaction rates used in the model will be extrapolated to much higher shock layer temperatures. Further validation studies are needed to reduce uncertainties and increase the confidence level of predictions. A comprehensive shock-tube experiment program is currently under way at the NASA Ames EAST facility to measure the radiation from N_2 - CH_4 shock waves at velocities relevant to Titan atmospheric entry (6-6.5 km/s). The detailed model will be validated against the EAST experiments in the future.

A reduced kinetic model having fewer species and reactions than the detailed model is also developed for coupled reacting CFD flowfield calculations. There are important differences between the present kinetic model and the Nelson-91 model in terms of species and reaction mechanisms for methane decomposition and CN formation, and the reaction rates used. As mentioned, a chemical kinetic model is only one of the building blocks used in shock layer radiation analysis. A complete radiative heating analysis of Titan probes is outside the scope of the present paper. However, the developed model should be suited to such analyses in the future.

Acknowledgments

This work was funded by the In-Space Propulsion program under task agreement M-ISP-03-18 to NASA Ames Research Center. The support from NASA Ames Space Technology Division through contract NAS2-99092 to ELORET Corporation is gratefully acknowledged.

References

- ¹ Park, C., "Radiation Enhancement by Nonequilibrium During Flight Through The Titan Atmosphere," AIAA Paper 82-0878, June 1982.
- ² Nelson, H. F., Park, C., and Whiting, E. E., "Titan Atmospheric Composition by Hypervelocity Shock-Layer Analysis," *Journal of Thermophysics and Heat Transfer*, Vol. 5, No. 2, 1991, pp. 157-165; also AIAA Paper 89-1770, June 1989.
- ³ Park, C. S. and Bershader, D., "Determination of The Radiative Emission of Hypersonic Flow Simulating The Cassini-Titan Atmospheric Entry Probe Environment," AIAA Paper 90-1558, June 1990.
- ⁴ Park, C. S., "Studies of Radiative Emission from the Simulated Shock Layer of the Huygens Probe," Ph. D Dissertation, Stanford University, Stanford, CA, 1991.
- ⁵ Bailion, M., and Taquin, G., "Radiative Heat Flux: Theoretical and Experimental Predictions for Titan Entry Probe," *Capsule Aerothermodynamics*, AGARD Report R-808, May 1997.
- ⁶ Bailion, M., Pallegoix, J. F., and Soler, J., "Huygens Probe Aerothermodynamics," AIAA Paper 97-2476, June 1997.
- ⁷ Koffi-Kpante, K., Zeitoun, D., and Labracherie, L., "Computation and Experimental Validation of N₂-CH₄-Ar Mixture Flows Behind Normal Shock Wave," *Shock Waves*, Vol. 7, No. 6, 1997, pp. 351-361.
- ⁸ Takashima, N., Hollis, B. R., Zoby, E. V., Sutton, K., Olejniczak, J., Wright, M. J., and Prabhu, D., "Preliminary Aerothermodynamics of Titan Aerocapture Aeroshell," *AIAA paper 2003-4952*, July 2003.
- ⁹ Olejniczak, J., Wright, M. J., Prabhu, D., Takashima, N., Hollis, B. R., Zoby, E. V., and Sutton, K., "An Analysis of the Radiative Heating Environment for Aerocapture at Titan," *AIAA paper 2003-4953*, July 2003.
- ¹⁰ Olejniczak, J., Prabhu, D., Bose, D., and Wright, M. J., "Aeroheating Analysis for the Afterbody of a Titan Probe," AIAA Paper 04-0486, Jan. 2004.
- ¹¹ Wright, M. J., Bose, D., and Olejniczak, J., "The Impact of Flowfield-Radiation Coupling on Aeroheating for Titan Aerocapture," AIAA Paper 04-0484, Jan. 2004.
- ¹² Park, C., "Assessment of a Two-Temperature Kinetic Model for Dissociating and Weakly Ionizing Nitrogen," *Journal of Thermophysics and Heat Transfer*, Vol. 2, No. 1, 1988, pp. 8-16.
- ¹³ Park, C., *Nonequilibrium Hypersonic Aerothermodynamics*, John Wiley & Sons, Inc., New York, 1990, Chap. 8.
- ¹⁴ Park, C., Jaffe, R. L., and Partridge, H., "Chemical-Kinetic Parameters of Hyperbolic Earth Entry," *Journal of Thermophysics and Heat Transfer*, Vol. 15, No. 1, 2001, pp. 76-90.
- ¹⁵ Park, C., Howe, J. T., Jaffe, R. L., and Candler, G. V., "Review of Chemical-Kinetic Problems of Future NASA Missions, II: Mars Entries," *Journal of Thermophysics and Heat Transfer*, Vol. 8, No. 1, 1994, pp. 9-23.
- ¹⁶ Park, C., "Review of Chemical-Kinetic Problems of Future NASA Missions, I: Earth Entries," *Journal of Thermophysics and Heat Transfer*, Vol. 7, No. 3, 1993, pp. 385-398.
- ¹⁷ Baulch, D. L., Cobos, C.J., Cox, R. A., Frank, P., Hayman, G., Just, Th., Kerr, J. A., Murrels, T., Pilling, M. J., Troe, J., Walker, R. W., and Warnatz, J., "Evaluated Kinetic Data for Combustion Modelling, Supplement I," *Journal of Physical Chemistry Reference Data*, Vol. 26, No. 6, 1994, pp. 847-1033.
- ¹⁸ Baulch, D.L., Cobos, C.J., Cox, R.A., Esser, C., Frank, P., Just, Th., Kerr, J.A., Pilling, M.J., Troe, J., Walker, R.W., and Warnatz, J., "Evaluated Kinetic Data for Combustion Modelling," *Journal of Physical Chemistry Reference Data*, Vol. 21, No. 3, 1992, pp. 411-429.

- 19 Tsang, W., "Chemical Kinetic Data Base for Propellant Combustion II: Reactions Involving CN, NCO, and HNCO," *Journal of Physical Chemistry Reference Data*, Vol. 21, No. 4, 1992, pp. 753-791.
- 20 Tsang, W., and Herron, J. T., "Chemical Kinetic Data Base for Propellant Combustion I. Reactions Involving NO, NO₂, HNO, HNO₂, HCN and N₂O," *Journal of Physical Chemistry Reference Data*, Vol. 20, No. 4, 1991, pp. 609-663.
- 21 Tsang, W., and Hampson, R. F., "Chemical Kinetic Data Base for Combustion Chemistry. Part I. Methane and Related Compounds," *Journal of Physical Chemistry Reference Data*, Vol. 15, No. 3, 1986, pp. 1087-1279.
- 22 NIST Chemical Kinetics Database, Version 7.0, 2003.
- 23 Dean, A. J., and Hanson, R. K., "CH and C-Atom Time Histories in Dilute Hydrocarbon Pyrolysis: Measurements and Kinetic Calculations," *International Journal of Chemical Kinetics*, Vol. 24, 1992, pp. 517-532.
- 24 Dean, A. J., Davidson, D. F., and Hanson, R. K., "A Shock Tube Study of Reactions of C Atoms with H₂ and O₂ Using Excimer Photolysis of C₃O₂ and C Atom Atomic Resonance Absorption Spectroscopy," *The Journal of Physical Chemistry*, Vol. 95, 1991, pp. 183-191.
- 25 Dean, A. J., Hanson, R. K., and Bowman, C. T., "High Temperature Shock Tube Study of Reactions of CH and C-Atoms with N₂," Twenty-Third Symposium (International) on Combustion/The Combustion Institute, 1990, pp. 259-265.
- 26 Davidson, D. F., and Hanson, R. K., "High Temperature Reaction Rate Coefficients Derived from N-Atom ARAS Measurements and Excimer Photolysis of NO," *International Journal of Chemical Kinetics*, Vol. 22, 1990, pp. 843-861.
- 27 Kruse, T., and Roth, P., "Kinetics of C₂ Reactions during High-Temperature Pyrolysis of Acetylene," *Journal of Physical Chemistry A*, Vol. 101, 1997, pp. 2138-2146.
- 28 Sommer, T., Kruse, T., and Roth, P., "Perturbation Study on the Reaction of C₂ with N₂ in High-Temperature C₆₀/Ar + N₂ Mixtures," *Journal of Physical Chemistry A*, Vol. 101, 1997, pp. 3720-3725.
- 29 Wooldridge, S. T., Hanson, R. K., and Bowman, C. T., "A Shock Tube Study of Reactions of CN with HCN, OH, and H₂ using CN and OH Laser Absorption," *International Journal of Chemical Kinetics*, Vol. 28, 1996, pp. 245-258.
- 30 Roose, T. R., Hanson, R.K., Kruger, C. H., "Decomposition of NO in the Presence of NH₃," *Proceedings of International Symposium on Shock Tubes and Waves*, Vol. 11, 1978, pp. 245-253.
- 31 Mick, H. J., and Roth, P., "High Temperature Thermal Decomposition of CO and CN" *Proceedings of the 18th International Symposium on Shock Waves*, 1991, pp. 805-812.
- 32 Gordon, S., and McBride, B.J., "Computer Program for Calculation of Complex Chemical Equilibrium Compositions, and Applications. Analysis Part I," NASA RP-1311, 1994.
- 33 The NASA computer program CEA (Chemical Equilibrium with Applications) website, 2003, (<http://www.grc.nasa.gov/WWW/CEAWeb>).
- 34 The CHEMKIN Collection, Release 3.6.1, Reaction Design, Inc., San Diego, CA.
- 35 Markus, M. W., and Roth, P., "On the Reaction of CH with CO Studied in High Temperature CH₄/Ar + CO Mixtures," *International Journal of Chemical Kinetics*, Vol. 24, 1992, pp. 433-445.
- 36 Kiefer, J. H., and Kumaran, S. S., "Rate of CH₄ Dissociation over 2800-4300 K: The Low-Pressure-Limit Rate Constant," *Journal of Physical Chemistry*, Vol. 97, 1993, pp. 414-420.
- 37 Lindackers, D., Burmeister, M., and Roth, P., "Perturbation Studies of High Temperature C and CH Reactions with N₂ and NO," Twenty-Third Symposium (International) on Combustion/The Combustion Institute, 1990, pp. 251-257.
- 38 Bose, D., Wright, M. J., and Gökçen, T., "Uncertainty and Sensitivity Analysis of Thermochemical Modeling for Titan Atmospheric Entry," AIAA Paper 04-2455, June 2004.

A Study of Possible Solar Sail Applications for Mars Missions

Thomas K. Percy*

Science Applications International Corporation, Huntsville, AL, 35806

and

Travis Taylor† and T. Conley Powell‡

BAE Systems, Huntsville, AL, 35806

A study was performed in conjunction with the In Space Technology Investment Area of NASA's Marshall Space Flight Center to investigate potential applications of solar sails to Mars missions. While solar sails have been proposed as possible candidates for several missions, including Geostorm and a Polar Observer mission, Mars has often been overlooked as a potential destination. It was found that solar sails may have potential in Mars observation missions with smaller payloads. Sail aerocapture maneuvers also show an improvement in payload delivery capability. This study has shown that solar sail spacecraft rival chemical interplanetary probes to Mars and may have applications in future Mars exploration.

Nomenclature

β	=	solar sail lightness parameter
μ	=	gravitational parameter
σ	=	sail film areal density

I. Introduction

A study was performed in conjunction with the In Space Technology Investment Area of NASA's Marshall Space Flight Center to investigate potential applications of solar sails to Mars missions. While solar sails have been proposed as possible candidates for several missions, including Geostorm and a Polar Observer mission, Mars has often been overlooked as a potential destination. Solar sailing has not been extensively considered for Mars in large part because industry is proficient at completing these missions with current chemical propulsion technologies. However, in an effort to investigate new and potentially superior propulsion options for Mars missions, solar sails were studied. Some of the preliminary results will be reviewed here.

Solar sailing presents many possible benefits in the arena of interplanetary exploration. By eliminating virtually all propellant requirements, solar sails present a significant weight reduction over traditional chemical systems. For inner planet missions, where there exists a fairly high level of solar photonic pressure, solar sails can provide maneuvering capabilities once on station around a planet. This orbital flexibility may offer the opportunity to investigate several different destinations at a planet. For example, by carrying a modest instrument suite, a solar sail spacecraft could potentially visit several moons of a single planet with no additional propellant requirement. All that is necessary to complete the maneuver is time.

Mission and systems analysis techniques and assumptions will be outlined in the following pages. Analysis of different trajectories for solar sail travel to Mars will be discussed. The subsystems involved in a solar sail spacecraft will also be outlined and assumptions about functionality and mass will be laid out. Finally a case study involving a small scientific mission to Mars' moon Phobos will be discussed to display one possible application of solar sailing to Mars exploration missions.

* Systems Engineer, System Technologies, SAIC, 675 Discovery Dr. Suite 300, Huntsville, AL 35806, Member.

† Senior Scientist, Advanced Projects, BAE Systems, 310 Voyager Way, Huntsville, Alabama 35806

‡ Senior Scientist, Advanced Projects, BAE Systems, 310 Voyager Way, Huntsville, Alabama 35806.

II. Analysis Overview

The analyses that comprised this study were broken down into two separate but related areas. The first involved mission analyses performed in the areas of trajectory and general mission architecture. A conceptual systems integration model facilitated the systems interaction analyses performed in the second area of the study. This model allowed analyses on subsystem interactions with emphasis on subsystem mass, a critical characteristic in solar sail design. By coupling these two analysis regimes, a fairly complete initial analysis was performed which allowed the tracking of mission architecture effects on system and subsystem performance.

Several assumptions were first laid out to simplify the analysis. Specific assumptions will be discussed in detail in the systems analysis segment of this report. One important universal assumption involves mass margins for the analysis. A margin of 30% was added to all subsystem component masses. This conservative estimate allows for growth from the current best estimates of subsystem masses that are available from industry. While a complete solar sail spacecraft design is highly dependent on the mass of the system, and thus may be penalized by overly conservative estimations, it was the consensus of the parties involved that current mass estimates were far too speculative to allow for smaller margins.

Figures of merit for the analysis included transfer time and launch vehicle requirements. Typical solar sail designs offer a reduction in launch mass that may lead to the use of smaller and less costly launch vehicles. While cost is not specifically addressed, launch vehicle selection was considered for this study to reflect this potential benefit. The main driver of the study was the investigation of overall payload delivery capability of the solar sail system, both in general and as specifically applied to the Phobos DRM.

III. Mission Analysis

A. Earth-Mars Trajectory Analysis

The mission analyses performed for this study involved trajectory analysis^{1,4,8}. Various mission designs for sending solar sail spacecraft to a closed Mars orbit from Earth orbit were presented. The mission trajectory types considered were simple ballistic trajectories with radial and asymptotic thrust vectors, Hohmann-A transfers, and the Sundiver transfer⁸. The results obtained suggest that the ballistic trajectory makes the most sense for an Earth-to-Mars solar sail mission. The Sundiver mission approach offers no advantage.

It was necessary to make a few approximations and assumptions for the trajectory analysis. The patched-conic approximation was used and it was assumed that the orbits of Earth and Mars are circular and coplanar. Also, other body influence such as the outer or inner planets were not modeled, as their influence should be minimal for this type of mission.

The approach taken in this analysis utilized modified orbital equations based on the effective gravitational constant, $(1 - \beta)\mu$, where β is the lightness parameter of the solar sail spacecraft and μ is the gravitational constant of the sun⁸. The angle α was defined as the angle between the asymptotic velocity vector and Earth's radius vector and allowed for the tracking of the solar sail's attitude with respect to the solar pressure. This angle was held constant for simplicity of analysis.

As seen in Figures 1 and 2, the trip time is significantly reduced by opting for a direct transfer as opposed to the Sundiver maneuver which is popular with the solar sailing community for outer planet missions. These charts assume an α of 90° and an Earth escape velocity of 3000 m/s.

From the derived trajectory data, Mars arrival conditions were determined and capture methods were investigated. The hyperbolic approach velocity at Mars was found to be on the order of 5 to 12 km/s. A maneuver which will be referred to as sail aerocapture was considered as the method of braking at Mars¹². Essentially, by passing through the outer levels of the appreciable Martian atmosphere, the large sail area would provide enough drag to reduce the velocity and capture into a highly elliptical orbit. Once this capture maneuver is completed, a small thruster would raise the periaapsis of the orbit out of the atmosphere and

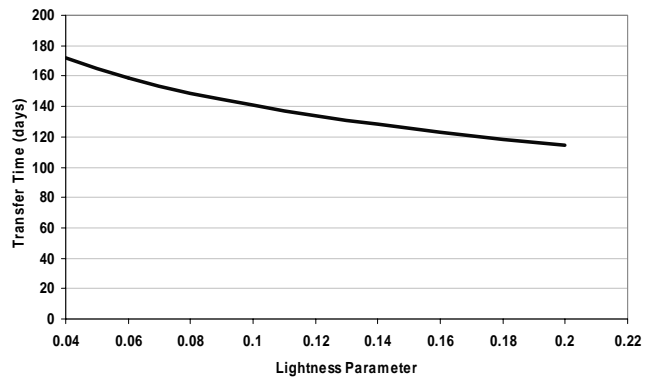


Figure 1: Trip Time versus Lightness Parameter; Earth Escape velocity equals 3000 m/s

solar pressure would be used by the sail craft to maneuver into the final orbit around Mars. This maneuver is currently under investigation, though initial indications are that it will be possible. More will be shown about the different capture techniques investigated in the systems analysis section.

B. Orbit Raising at Mars

Maneuvering in the Martian system to raise the orbit of the solar sail will take anywhere from 30 to 70 days based on preliminary models developed for this study. The maximum light-pressure acceleration obtainable from the solar sail is $\beta\mu_S/r_M^2$, where μ_S is the gravitational constant for the Sun and r_M is the radius of Mars' orbit. μ_S/r_M^2 is $2.5546 \times 10^{-3} \text{ m/s}^2$. Thus the maximum light-pressure acceleration for a vehicle with a lightness parameter of 0.2 is $5.1092 \times 10^{-4} \text{ m/s}^2$. The maximum change in orbital radius per revolution is given approximately by

$$\Delta r = 5.52 \beta \mu_S r^3 / \mu_M r_M^2 \quad (1)$$

from which the equation

$$\left(\frac{\mu_M}{r} \right) - \left(\frac{\mu_M}{r_0} \right) = \frac{1.38 \beta \mu_S t}{pr_M^2} \quad (2)$$

is obtained in which r_0 is the initial radius at time $t = 0$.

Figure 3 shows the results of orbit raising from a circular orbit at a height of 4,000 km to a final height of 10,000 km using a solar pressure propelled, spiral trajectory for orbit raising. The orbit height is given as a function of time. The reduced solar pressure is still sufficient for orbital flexibility with a solar sail spacecraft.

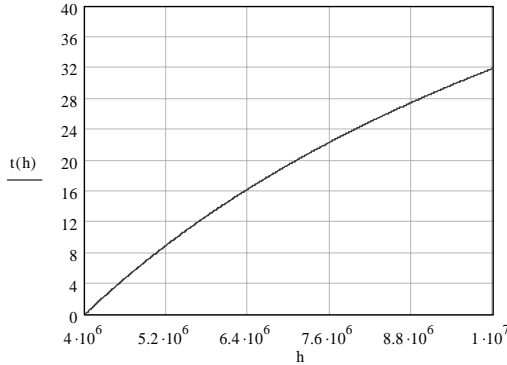


Figure 3: Time for Orbit Raising

This orbital flexibility allows for investigation of Martian satellites and the ability to modify Mars orbits for coverage of a wide range of Martian latitudes and longitudes.

IV. System Analysis

The system analysis approach taken in this study facilitated the assessment of subsystem masses and the effect of subsystem interactions on that mass. The systems unique to solar sail spacecraft were assessed based on industry estimations and projections of fabrication capabilities. Subsystems which are similar to those used in current interplanetary probes are scaled from existing systems. In many cases these subsystems were scaled from the Mars Odyssey spacecraft launched in 2001. A schematic of the solar sail system can be seen in figure 4.

A. Solar Sail Systems

Systems unique to solar sail spacecraft are focused mainly in propulsion, specifically the sail and sail structure and the attitude control system. Sail shape was restricted to a square configuration to follow with the current solar sail investigations taking place in the field. In addition, CP1 was selected as the baseline sail material. This material is currently under examination in several solar sail test cases^{7,9}. In addition to its use in solar sail scale modeling, the fabrication of large sheets of CP1 is also being investigated. This leads to the conclusion that a square sail comprised of sheets of CP1 is the most likely candidate for first generation solar sails. For this study, the system was assessed parametrically over a range of areal densities from 2 to 10 g/m^2 and a reflectivity of 85% was assumed to account for any degradation over the life of the system.

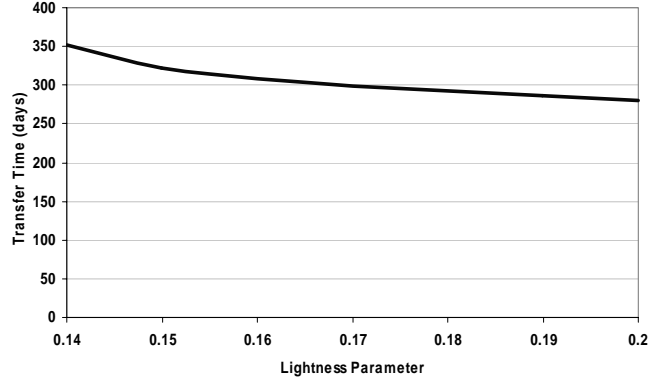


Figure 2: Trip Time versus Lightness Parameter; Earth Escape velocity equals 3000 m/s; Sundiver Maneuver

The sail structure was assumed to be a deployable boom system. There are two major designs for deployable boom structures currently being considered for solar sails^{7,10}. Both designs require little or no deployment mechanisms. The linear density of the boom structure for this study was assumed to be 50 g/m based on industry projections.

Attitude control of solar sail spacecraft can be achieved with several different types of systems⁸. For this model, a payload boom with a gimbal system was assumed for shifting the center of gravity of the system with respect to the center of pressure. This allows for directional control during the Earth-Mars portion of the solar sail trajectory and may also prove useful during the sail aerocapture maneuver at Mars. Small reflective structures known as sail vanes were also included at the tips of the sail booms for quick response attitude control during the orbit raising portion of the solar sail function. For mass estimation purposes the sail vanes are assumed to be 0.5% of the total sail area. Small reaction wheels were also included for spacecraft stabilization during the sail deployment operations.

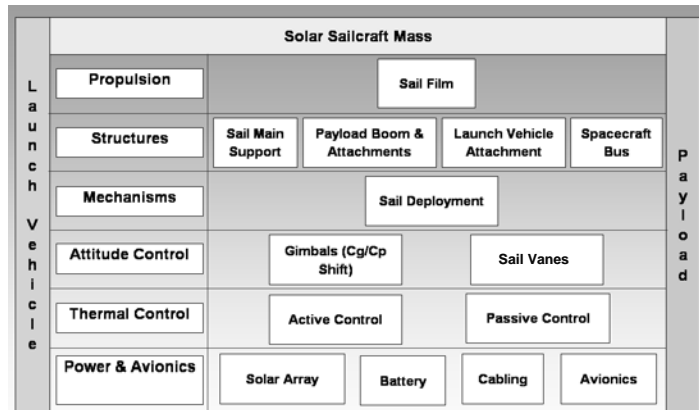


Figure 4: Solar sail spacecraft subsystem breakdown

B. Spacecraft Bus and Other Subsystems

The spacecraft bus was assumed to be a highly integrated system at the end of the payload boom, thus facilitating a traditional analysis approach to subsystems such as power, data handling, navigational instrumentation, thermal control and structural mass. The structure of the bus is based on historical data from other satellite programs and interplanetary probes. Given that the bus structure for the solar sail spacecraft is slightly smaller than typical interplanetary probes, the model was verified by cross referencing with micro-satellite structure masses. The launch vehicle adapter and attachments were assumed to be 55 kg and these structures were assumed to be jettisoned before transit and thus not included in the spacecraft mass for trajectory assessment¹¹.

The power supply for the spacecraft was sized based on 115 W/kg solar arrays. The power requirement for the spacecraft subsystems was assumed to be 1.5 kW EOL at 1 AU. Batteries with a mass of 10 kg were also included for power storage. The mass of the navigation and avionics systems was taken directly from the systems on Mars Odyssey.

C. Capture Method Analysis

A simple trade of capture technique was performed taking two procedures into consideration. The first was the previously mentioned sail aerocapture, which requires a very small chemical system for raising the periapsis of the initial orbit of the solar sail. This system was included at a mass of approximately 10 kg. The second option was the traditional chemical burn for orbital insertion. The results show that carrying the required chemical capture system limits the payload capability. This technique also increases the overall sail size necessary to complete the mission due to the increase in overall spacecraft mass. In some cases the mass was increased by as much as 225% over the sail aerocapture system. For example, results show that the sail size would be 20,705 m² with a chemical capture system compared to 10,870 m² in the aerocapture mode. Also, chemical capture may require the jettisoning of the sail system before the capture burn in order to reduce propellant requirements and allow the

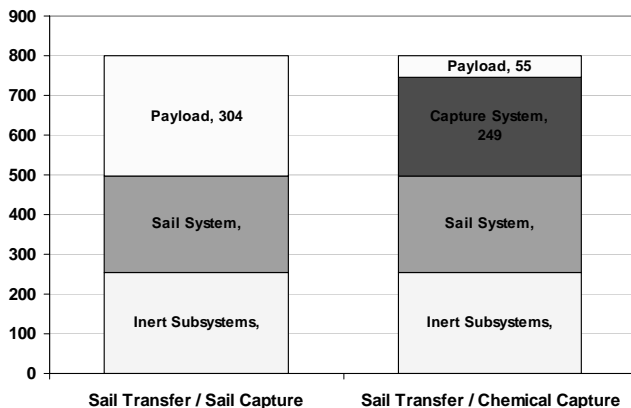


Figure 5: Stack Masses for Capture Mode Comparison

spacecraft to be launched on a Delta II as opposed to a Delta IV launch vehicle⁵. The analysis results indicate that choosing a chemical capture system puts a limit on potential scientific payload that is only slightly higher than the DRM payload where the selection of aerocapture allows significantly higher payload delivery (see Figure 5). Thus it can be seen that sail aerocapture has significant potential for increasing mission performance.

In a comparison of scientific payload delivery versus transfer time, it is shown that increasing the lightness number will reduce the trip time however it also reduces the mass delivery potential if the total spacecraft mass is held constant. Given a spacecraft mass, a trade must be made between sail mass (increased sail size reduces transfer time) and payload delivery mass capability. Figure 6 presents this finding as well as a comparison to the Mars Odyssey mission. Both the solar sail spacecraft and the Mars Odyssey have the same dry spacecraft mass if their respective propulsion system masses are ignored. Not only can the solar sail deliver more scientific payload mass than was delivered by Mars Odyssey, but it is also capable of doing so in a shorter amount of time.

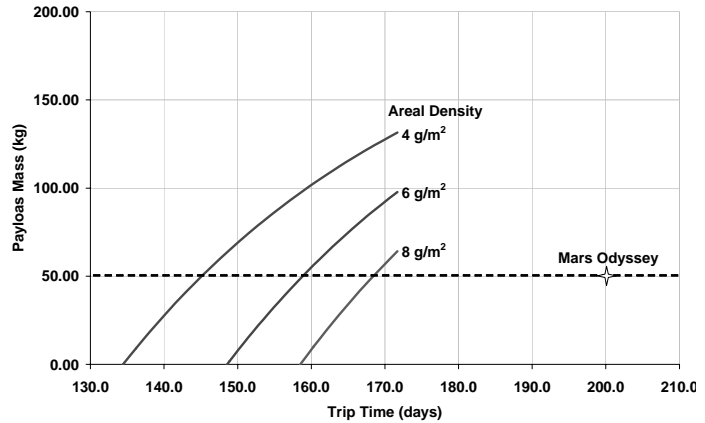


Figure 6: Sail payload delivery potential versus trip time

V. Case Study: Phobos Rendezvous

For this study, a specific reference mission was also investigated. The mission entailed delivering a 50 kg instrument suite to an orbit that matches the Martian moon Phobos for the purpose of scientific observation. The Mars Odyssey spacecraft’s scientific instrument suite, weighing approximately 50 kg, was chosen as a model for this mission.

The solar sail system was modeled parametrically over a range of sail film areal densities to investigate the effect of further development of sail materials. Taking into account the system analysis assumptions mentioned above, the analysis was run with the goal of delivering a scientific instrument suite of 50 kg. Figure 7 displays the payload delivery capability of a 500 kg solar sail spacecraft over a range of trip times. The figure shows that as trip time increases so too does the payload capability. This is due to the fact that increased trip time equates to a reduced sail area for a standard spacecraft mass. This reduction in sail area reduces the mass of the sail dependent systems (solar sail film, sail structure etc.) and provides more margin for payload mass. Figure 7 also displays the benefit of lower film areal densities.

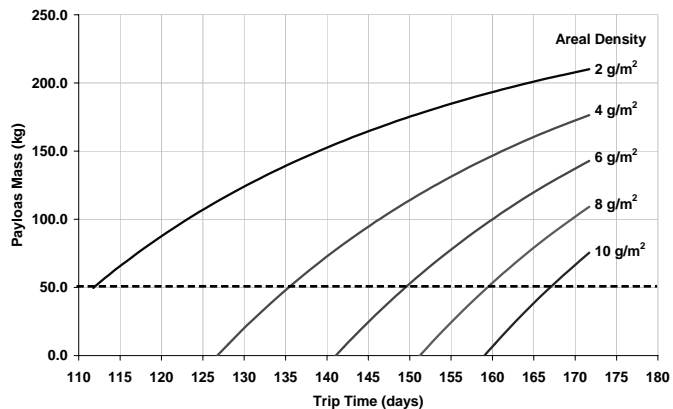


Figure 7: Sail payload delivery potential versus trip time over a range of film areal densities

Table 1: Subsystem Masses

Power System	62.2 kg
Sail Film	189.3 kg
Sail Structure	22.2 kg
S/C Bus	31.6 kg
Hardware & Attac	24.6 kg
TPS	28.6 kg
ACS	20.4 kg
Avionics	53.3 kg
Scientific Payload	50.2 kg
PR Propulsion	9.7 kg
Other	7.8 kg
	500.0

In one specific case, a 500 kg spacecraft system can deliver a 50 kg payload in 168 days with a sail area of 14,558 m², given a sail lightness parameter of 0.045 and a sail areal density of 10 g/m². The characteristic acceleration of this system is 0.226 mm/s². The mass of the subsystems of this solar sail spacecraft can be seen in Table 1. This system can be launched in a Delta II launch vehicle⁵.

VI. Conclusion

It can be seen from this study that solar sails have the potential for missions to Mars if the technology develops as projected. Their mass delivery potential rivals that of previous scientific observation missions. Transfer times calculated with systems employing solar photonic pressure are shorter than most Hohmann Type I trajectories currently used by conventional chemical systems. The trajectory models also indicated that a departure from conventional solar sail Sundiver maneuver is necessary to bring transfer times to competitive levels in Earth-to-Mars situations. There is a potential for orbital flexibility on station that could allow more than one mission to be performed by one orbiting platform. Also, the projected reductions in injected mass could reduce overall mission cost by allowing for the use of smaller launch vehicles.

Finally, the issue of capture technique at Mars was addressed. Study results indicate that sail aerocapture is an effective technology that, could impact a range of solar sail missions. Using a solar sail transfer vehicle and capturing with conventional chemical propulsion systems vastly reduces the effectiveness of the solar sail technology. However, by integrating aerocapture technology, the full potential of the solar sail spacecraft can be realized. While solar sails are effective for missions like Geostorm and Polar Observer, this study shows the potential for solar sail application to a much broader portfolio of missions.

Acknowledgments

The work described in this paper was performed by Science Application International Corporation (SAIC) and BAE Systems under contract with the NASA Marshall Space Flight Center (MSFC) in Huntsville, Alabama. Special thanks go to Les Johnson, manager of NASA MSFC In-Space Propulsion, and Sandy Montgomery, Solar Sail technology area manager, for providing encouragement and direction for this work. T.K. Percy would like to thank his wife, Erin, for her patience and support. T.K. Percy would like to give special recognition to SAIC management, especially Frank Curran, program manager of the In-Space Technology Assessment program, for support and encouragement of this work and to Mike Cupples for his guidance. T. C Powell would like to acknowledge the patience and support of his wife, Judy.

References

- ¹Bate, R. , Mueller, B. , White, J. *Fundamentals of Astrodynamics*. Dover Publications, Inc. New York, 1971.
- ²Frisbee, R. , Brophy, J. “Inflatable Solar Sails for Low-Cost Robotic Mars Missions”. AIAA 97-2762.
- ³Garner C. et al. “Developments and Activities in Solar Sail Propulsion”. AIAA 2001-3234.
- ⁴George, L.E. , Kos, L.D. “Interplanetary Mission Design Handbook: Earth to Mars Opportunities and Mars to Earth Opportunities, 2009-2024”. NASA/TM 1998-208533.
- ⁵Isakowitz, S.J. et al. *International Reference Guide to Space Launch Systems*. 3rd ed., AIAA, Reston, 1996.
- ⁶Leipold, M. et al. “Solar Sail Technology Development and Demonstration”. 2000.
- ⁷Lichodziejewski, D. et al. “Bringing an Effective Solar Sail Design Toward TRL 6”. AIAA 2003-4659.
- ⁸McInnes, C. *Solar Sailing: Technology, Dynamics and Mission Applications*. Springer Verlag 1998.
- ⁹Murphy, D. et al. “Progress And Plans For System Demonstration of a Scalable Square Sail System”. AIAA/ASME/SAE/ASEE Joint Propulsion Conference, 2003.
- ¹⁰Murphy, D. et al. “Scalable Solar Sail Subsystem Design Considerations”. AIAA 2002-1703.
- ¹¹Noca, M. et al. “Evaluating Advanced Propulsion Systems for the Titan Explorer Mission”. IEPC-01-175.
- ¹²Taylor, T. et al. “Solar Sail Application to Comet Nucleus Sample Return”. AIAA 2003-5275.

SOLAR SAIL APPLICATION TO COMET NUCLEUS SAMPLE RETURN

Dr. Travis S. Taylor, Tryshanda T. Moton*, Don Robinson, R. Charles Anding
Teledyne Brown Engineering, Inc.
300 Sparkman Drive
Cummings Research Park
Huntsville, AL 35805

Dr. Gregory L. Matloff
Bangs/Matloff Aerospace Consulting Co.
417 Greene Avenue
Brooklyn, NY 11216

Dr. Gregory Garbe, Edward Montgomery
Solar Sail Propulsion Project
MSFC, TD 20
Huntsville, AL 35812

Abstract

Many comets have perihelions at distances within 1.0 Astronomical Unit (AU) from the sun. These comets typically are inclined out of the ecliptic. We propose that a solar sail spacecraft could be used to increase the inclination of the orbit to match that of these 1.0 AU comets. The solar sail spacecraft would match the orbit velocity for a short period of time, which would be long enough for a container to be injected into the comet's nucleus. The container would be extended from a long durable tether so that the solar sail would not be required to enter into the potentially degrading environment of the comet's atmosphere. Once the container has been filled with sample material, the tether is retracted. The solar sail would then lower its inclination and fly back to Earth for the sample return. In this paper, we describe the selection of cometary targets, the mission design, and the solar sailcraft design suitable for sail-comet rendezvous as well as possible rendezvous scenarios.

Selection of Cometary Targets Suitable for Solar Sail Rendezvous

The concept of solar sail rendezvous missions has been studied for quite some time. During the 1970s, a design team at the Jet Propulsion Laboratory (JPL) discovered a trajectory that could allow a solar sail to rendezvous with Halley's Comet at its perihelion in the mid-1980s [1]. A rendezvous with Halley's Comet for that passage was looked at extensively by NASA scientists.

However a dedicated Comet Halley rendezvous mission was never flown by the United States.

Exploration of the mission-enabling properties of solar sailing to chase and rendezvous with comets continues as a small, although important focus of research interests. New comets approach the Sun from the outer regions of the solar system, beyond the orbit of Pluto. One of these comets shows up every few years. These comets are thought to

*AIAA Member, propulsion systems engineer

typically have made only a few passes by the Sun and many are making their first approach to the Sun. These comets are thought to have remained essentially unchanged from the early formation of the solar system. As a result, comets and the matter that compose them are of very high interest for scientific research interests [2].

It is very likely that a solar sail spacecraft could be used to rendezvous with many comets that have perihelions close to Earth's orbit. Table 1 shows

many short-period comets with perihelion less than or equal to 1.0 AU, which have been observed to have two or more apparitions [3]. The design effort for the Halley Rendezvous mission suggested a sail design that could operate at 0.25 AU or closer from the Sun for at least 1 year without appreciable damage to the solar sail spacecraft. Technology development efforts on materials indicate that sailcraft capable of sustained operation inside 0.2 AU might be possible in the near future [2].

<u>Comet</u>	<u>Orbital Period</u> (Years)	<u>Perihelion</u> (AU)	<u>Eccentricity</u> ----	<u>Inclination</u> ----	<u>Aphelion</u> (AU)
2P Encke	3.28	0.33	0.850	11.9	4.09
107P Wilson-Harrington	4.29	1.00	0.623	2.8	4.29
26P Grigg-Skjellerup	5.10	1.00	0.664	21.1	4.93
96P Machholz	5.24	0.13	0.958	60.1	5.91
45P Honda-Mrkos-Pajdusakeva	5.30	0.54	0.822	4.2	5.54
73P Schwassman-Wachmann 3	5.35	0.94	0.694	11.4	5.18
5D Brorsen	5.46	0.59	0.810	29.4	5.61
103P Hartley 2	6.26	0.95	0.719	9.3	5.84
3D Biela	6.62	0.86	0.756	12.5	6.19
72P Benning-Fujikawa	9.01	0.78	0.820	8.7	7.88
8P Tuttle	13.50	1.00	0.824	54.7	10.30
27P Crommelin	27.40	0.74	0.919	29.1	17.40
55P Tempel-Tuttle	32.90	0.98	0.904	162.7	19.60
23P Brorsen-Metcalf	70.50	0.48	0.972	19.3	33.70
121P Pons-Brooks	70.90	0.77	0.955	74.2	33.50
1P Halley	76.00	0.59	0.967	162.2	35.30
109P Swift-Tuttle	135.00	0.96	0.964	113.4	51.70
35P Herschel-Rigollet	155.00	0.75	0.974	64.2	56.90

Table 1. Comets with Perihelion Close to Earth's Orbit

Table 1 shows that there are at least 18 comets that approach Earth's orbit. Nine of them have aphelions of 4.09-6.19 AU

(these may have been influenced by Jupiter, although an analysis of this is beyond the scope of this paper). The

table also shows that 8 have inclinations 0—20 degrees, 4 have inclinations 21—60.1 degrees, 3 have inclinations 61-100 degrees, 3 have inclinations 101-180 degrees. The average inclination for the class is 47.3 degrees. The average perihelion for the class is 0.74 degrees. The average eccentricity for this comet class is 0.844.

Comet velocity at various points along its orbit and sailcraft velocity at various orbital locations can be determined according to G. R. Fowles [4]. From Eq. (6.49) of this reference, we easily obtain an equation relating comet velocity at perihelion V_o to circular-orbit velocity at perihelion V_c and eccentricity e as

$$V_o = V_c(e + 1)^{1/2} \quad (1)$$

Modifying Fowle's Eq. (6.51) to find perihelion velocity from perihelion solar separation R_o and aphelion solar separation R_1 yields

$$V_o / V_c = \{ [2R_1 / R_o] / [1 + (R_1 / R_o)] \}^{1/2} \quad (2)$$

Knowing the spacecraft velocity at perihelion and the perihelion distance, we can equate energy at perihelion to energy at any other solar distance R_{so} (assuming no orbital energy change) to calculate orbital velocity at R_{so} , which is

$$V_{so} = [V_o^2 - 2.65 \times 10^{20} / (R_{so} - R_o) / (R_{so} R_o)]^{1/2} \quad (3)$$

Comet and Sailcraft Orbits

As comets approach the Sun, they have close to the energy needed to escape from the solar system. They typically have substantial inclinations from the

ecliptic plane, which makes the comets difficult to reach in terms of energy requirements. Since some of these comets are discovered only a few months prior to their perihelion passage, it becomes essential to prepare a spacecraft for launch for this type of mission within a few months notice. However, high performance sailcrafts having characteristic accelerations (a_c) greater than 5mm/s^2 , can reach some of these comets on short notice if the inclination of the comet's orbit is not too high and if the comet approaches from an acceptable direction relative to the position of the Earth in its orbit. If such a high performance sailcraft were available when the new comet approaches, a ready-made instrument package could be placed on the ship. In an ideal scenario, this would be done in a high orbit, such as L4 or L5. However, this might be accomplished by a tether deployment from a station that has taken a few weeks to gain the necessary escape energy to place it in this high orbit [2].

Sample Mission Design for Solar Sail Rendezvous, Sample Return (SSRSR) to Comet 107P Wilson-Harrington

Rationale for Target Choice

This object is chosen for a number of reasons. One, its perihelion is at 1 AU, which requires less spacecraft orbit adjustment. Two, it orbits the Sun every 4.29 years, allowing ample mission opportunities. Three, its inclination is 2.8 degrees, which also results in less maneuver requirements (less inclination changing). Also called Minor Planet 4015, this comet's aphelion is 4.29 AU and its orbital eccentricity is 0.623 [3]. Interestingly, Comet 107P was an alternate target for Deep-Space 1. As an Earth-crosser, it belongs to the class of

objects, which sometimes strike the Earth. As a comet, its surface may contain biological progenitors (it is even speculated that primitive life may be found there). So a sample-return mission to this object may have large scientific and public support.

Spacecraft Design

Disc Sail: One possible architecture for the solar sail rendezvous-sample return (SSRSR) solar sailcraft is a disc sail. We assume a 50-kg payload, a disc sail radius of 50 m (which implies a sail area of 7,850 m²). The sail-film areal mass density is 0.006 kg/m², and the structural mass factor is 0.3. We assume a sail reflectivity (REF_{sail}) of 0.9. The spacecraft areal mass density ($\sigma_{s/c}$) is 0.012 kg /m².

First, we calculate sailcraft lightness factor, $\beta_{s/c}$ using Eq. (4.19) of Ref. 3

$$\beta_{s/c} = 0.000787[(1 + REF_{sail}) / (\sigma_{s/c})] = 0.12 \quad (4)$$

This means that the sail acceleration is $7.2 \times 10^{-5} \text{ g}$ or $7.3 \times 10^{-4} \text{ m /sec}^2$ if the sail is oriented normal to the sun.

Square Sail: A second architecture we considered is the typical square sail. The sail is assumed to be 100 m on a side. The sail areal density is the same as that of the disc. The support booms for the square sail have a linear density of 50 g/m. The total lightness parameter for the square sail is about 0.12 and therefore has similar sail acceleration as for the disc sail.

Either of the above architectures will suffice for the SSRSR mission provided that the lightness parameter is on the

order of 0.1. It is the lightness parameter that drives the capability to perform the SSRSR mission. It should also be noted here that all materials suggested for the spacecraft architecture are currently available although state-of-the-art.

The Launch Vehicle and Departure from Earth Space

A Delta-class expendable booster is the recommended launcher for the sailcraft. We suggest that the upper stage be powerful enough to supply an Earth-escape (hyperbolic excess) velocity of about 3 km/s. This is the same hyperbolic excess required to insert an Earth-launched spacecraft into a Mars-bound Hohmann-transfer ellipse [7]. A more capable upper stage supplying the 8 km/s hyperbolic excess required to insert the spacecraft on a Jupiter-bound trajectory is, as will be discussed below, another option.

Sail Maneuver 1: Inclination Change

Our first sail maneuver is inclination change, using a curve-fit to Fig. 4.23 of McInnes [5]

$$\Delta I / \Delta T = (\beta_{s/c} / 0.05) \exp[-1.323 \ln(R_{so}) - 2.3] \quad (5)$$

where $\Delta I / \Delta T$ is inclination change in degrees per week, and R_{co} is the constant

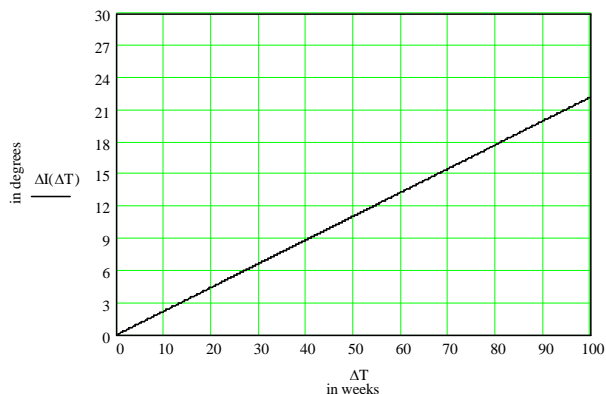


Figure 1. Inclination cranking versus time

cranking-orbit radius from the Sun during the inclination-change maneuver, in Astronomical Units (AU). To alter inclination by 2.8 degrees to match the comet's inclination takes 12.7 weeks or 89 days. This maneuver will actually take a bit longer (about 10%) since the s/c is moving at a higher velocity than Earth's circular velocity after it departs Earth-space.

It is worth noting here other possible target missions and mission durations required. Figure 1 shows the inclination cranking achieved as a function of weeks. After 100 weeks an inclination of about 22 degrees could be reached. From Table 1 this shows that possibly 8 target comet orbits could be matched in about two years or less.

Estimating Comet Perihelion Velocity

From Equation 1 where V_o is comet velocity at perihelion and V_c is circular velocity at comet's perihelion, substituting Earth's circular velocity as the circular velocity at comet perihelion, and using $e = 0.623$, we find that the comet's perihelion velocity relative to the Sun is 38 km/s, or about 8 km/s faster than the Earth at perihelion and 5 km/s faster than the spacecraft in its post-earth-escape solar orbit.

$$ACC_t = ACC_{s/c} \sin \theta \cos \theta, \quad (7)$$

where $ACC_{s/c}$ is the sailcraft acceleration if oriented normal to the Sun. In this case, an angle of 45 degrees between normal to the sail and the Sun results in a tangential acceleration of $3.25 \times 10^4 \text{ m/s}^2$, which is more than enough.

Forward suggests that we might obtain a mirror-like sail coating by embossing the sail reflective layer with images of

Comet Rendezvous Alternative 1: A Holographic Sail

This rendezvous alternative assumes a tangential component of sailcraft acceleration after the inclination-cranking maneuver. Elementary kinematics reveals that the spacecraft can match the comet's perihelion velocity in 0.5 years if it has a tangential acceleration of $3.17 \times 10^{-4} \text{ m/s}^2$, less than 1/2 of its solar-radiation-pressure acceleration at 1 AU if it is oriented normal to the Sun.

From Forward's "grey solar sail" paper [6], tangential acceleration can be written as

$$ACC_t = [(REF_{sail} + \alpha + R_b - R_s) \sin \theta \cos \theta] / (c \sigma_{s/c}), \quad (6)$$

where α = sail absorptance, R_b is sail back (mirror-like) reflectance, R_s is sail specular reflectance, θ is the sail-Sun aspect angle (0 degrees for sail normal to Sun), S is the solar flux in watts per square meter, and c is the speed of light. For a specular sail, the tangential acceleration component will be very low.

But if the sail is back-reflective, we can apply Forward's Eq. (50) from ref. 6 to obtain

corner-cube reflectors [8]. This might be done holographically [9].

Comet Rendezvous Alternative 2: High-Energy Upper Stage

This alternative replaces the tangential acceleration by sail near perihelion with an upper stage capable of leaving Earth-space at a hyperbolic-excess velocity of 8 km/s [4]. The sail is only used during the pre-rendezvous phase of the mission for inclination cranking. Interestingly,

this approach has been used before—for the launches of Pioneer 10 and 11 and Voyager 1 and 2 in the 1970’s. If this option is selected, more time must be devoted for the inclination-cranking maneuver.

Comet Rendezvous Alternative 3: Optimized Sailing Application

This approach applies results of an optimized-sail trajectory analysis reported on pp 139-140 of McInnes [1]. In the results of this computer simulation, a sail with $\beta_{s/c} = 0.05$ departs a Sun-centered circular orbit at 1 AU to a high-eccentricity solar elliptical orbit. The spacecraft requires 3 orbits of the Sun to increase its semi-major axis to 3 AU, which we require for comet rendezvous. Since acceleration scales with increasing $\beta_{s/c}$, we can do it with our sailcraft configuration in 1.5 orbits or about 5 years.

Sample Collection

Previous missions describe comet sample collection by placing solar sail probes into orbits where they pass as close to the surface of the comet nucleus as the thermal capacity of the probe will allow. The system proposed here utilizes a similar concept of releasing a sample capturing device such as a capsule roughly the size of a 12-ounce soda can attached to the sailcraft by a tether (possibly Spectra 1000™). Once the sailcraft is within the orbit of the comet, a tether system will be spring launched toward the comet to pick up a sample of matter from the comets nucleus. The sailcraft will be capable of releasing the tethered capsule and then altering its trajectory to avoid incineration or any other impact from the comet’s matter that may potentially damage the solar

sail. The capsule will then be closed and retracted and a sample of the comet’s nucleus matter is returned to scientists for examination back on Earth.

Considering the reference mission design discussed thus far, the sample return spacecraft will match velocities with the 107P/Wilson-Harrington comet. Matching velocities reduces the risk of particle impacts since it is likely to only incur very minor damage and slight course alterations from low velocity gas and particle collisions. If the relative velocity of spacecraft to dust is high, problems could occur similar to the European Space Agency (ESA) Giotto mission which intercepted Halley’s comet in March of 1986 [10]. Giotto received significant course alteration and damage. Fourteen seconds before closest approach Giotto was hit by a ‘large’ dust particle which caused the spacecraft angular momentum vector to shift 0.9 degrees. The primary concern for SSRSR is likely to be the possibility of gas jets erupting from the comet with course altering force. However, some of the comets we are considering are somewhat inactive, including 107P/Wilson-Harrington according to the work and assessment by Marsden [11], “the observations suggest that the object is a largely inactive comet that undergoes occasional outburst.”

The spacecraft will utilize cameras and built in digital signal processing techniques to analyze the surface for an optimal landing location. The mission may last weeks, which will allow the Comet Mission Earth Team to make the final decision of the landing site. If any of the potential landing sites show gas jet activity, landing will be attempted in some other area. The soda can sized

lander will separate with the gentle release of a spring-loaded mechanism and will begin to move away from the main body of the sailcraft very slowly. A tether reel on the sailcraft will maintain approximately zero tension as the tether reels out at a speed matching the lander's speed. The tether will also have a fiber optic cable wound around it that will enable direct optical communication between the sailcraft and the lander's main computer. The main computer on the sailcraft will use data from the lander's proximity detector to control very small cold gas thrusters for a proper comet relative velocity touchdown at a selected comet landing site. The current assumption is that the comet velocity matching will not leave a significant comet rotational component relative to the sailcraft and subsequently the lander.

The soda can lander will adhere to the comet by implementing synthetic Gecko skin coated landing pads. Geckos are small reptiles whose feet have hundreds of thousands of hair-like "setae" with hundreds of submicroscopic pads ("spatulae") at each seta tip, which appear to cling by van der Waals forces to almost any surface even while under conditions of vacuum and particulate contamination. Experiments and analyses have been conducted that suggest the skin can be synthesized and may deliver adhesion forces of as much as 10 N per 100 mm² [12]. The lander will simply bump into the comet nucleus and the pads will adhere to the surface.

The comet nucleus is sampled via a "sampling tool" which is a counter-rotating drill-like system. The sampling tool will rotate slowly and be pulled deeper into the comet nucleus as it

rotates. The counter-rotation will produce almost zero net torque to help minimize the probability that the comet nucleus section being drilled will break away in an uncontrolled manner. The comet nucleus material is collected in a comet nucleus material bag. When the desired size of the comet material sample has been obtained the drilling portion of the sampling tool will be ejected as a volume exchange and the material bag is sealed. The sampling tool ejection mechanism will also provide an external seal where it was previously housed and provides additional protection for the material bag.

In order to obtain separation of the lander from the comet the lander will release the Gecko skin landing pads and leave them on the comet in much the same way the Lunar Excursion Modules left the landing gear behind. The initial separation from the comet is powered by stored energy in a spring mechanism. The lander computer will send a signal to sailcraft indicating a successful separation and the sailcraft will then reel in the tether. The maximum tension expected on the tether will be due to the force necessary to accelerate the approximately 10 kg lander and full sample material bag to the sailcraft velocity. Development of a sample storage system for the flight back to Earth must be considered if ice particles are to be maintained. A detailed analysis of the environmental requirements necessary to maintain the sample should be conducted, but is beyond the scope of this paper.

Earth Return

The sailcraft will fly the sample back to Earth by undoing the orbit and inclination changes discussed previously. Once the sailcraft approaches Earthspace it is possible that it can survive an aerobraking encounter with the Earth whereas its sail is used as the aerobrake ballute. Therefore only inclination-cranking and minor maneuvers may be required on the Earthbound leg. The aerobraking maneuver could leave the sail in an elliptical orbit around Earth with its periapsis at a low enough orbit that the Shuttle could capture the sample and return it to Earth. It is also possible that if the periapsis is too high for Shuttle capture that the soda can lander could be launched toward Earth using a stored energy spring or cold gas thruster. The tether would be reeled out in order for the Shuttle to capture it. This should be investigated further.

Conclusion

We have shown here a concept mission architecture for a comet nucleus sample return using a solar sail rendezvous. A small tethered soda can spacecraft could then be used to capture a sample of the comet's nucleus and return it to Earth. The sailcraft would return the sample to Earthspace whereas the sail is used for an aerobrake. The sample could then be returned to Earth via the Space Shuttle. The analysis presented here suggests that a solar sail spacecraft is ideal for the comet nucleus sample return. More detailed studies for the mission concept should be conducted.

References

1. C. R. McInnes, *Solar Sailing*, Springer-Praxis, Chichester, UK (1999), pp.4-11; pp 139-140.
2. Wright, J. L., *Space Sailing*, Gordon and Breach Science Publishers, PA, (1992), pp.42-45.
3. R. P. Binzer, M. S. Hanner, and D. I. Steel, "Solar System Small Bodies," A. N. Cox ed., *Allen's Astrophysical Quantities*, 4th. ed., Springer-Verlag, NY (2000)
4. G. R. Fowles, *Analytical Mechanics*, Holt, Rinehart, and Winston, NY (1962).
5. N. C. Wickramasinghe, F. Hoyle, S. Al-Mufti, and D. h. Wallis, "Infrared Signatures of Prebiology—or Biology," in *Astronomical and Biochemical Origins and the Search for Life in the Universe*, ed. C. B. Cosmovici, S. Bowyer, and D. Werthimer, Editrice Compositori, Bologna, Italy (1997), pp 61-76.
6. G. L. Matloff, *Deep-Space Probes*, Springer-Praxis, Chichester, UK (2000).
7. R. R. Bate, D. D. Mueller, and J. E. White, *Fundamentals of Astrodynamics*, Dover, NY (1971), pp. 362-365.
8. R. L. Forward, "Grey Solar Sails," *J. Astronaut. Sci.*, 38, 161-185 (1990); also published as AIAA 89-2343.
9. G. L. Matloff, G. Vulpetti, C. Bangs, and R. Haggerty, "The Interstellar Probe (ISP) : Pre-Perihelion Trajectories and Application of Holography," NASA / CR- 2002-211730, NASA/MSFC, Huntsville Alabama (2002).

10. D.R. Williams,
<http://nssdc.gsfc.nasa.gov/planetary/giotto.html>, 2003.
11. B. G. Marsden,
<http://cometography.com/pcomets/107p.html>, 2003.
12. Autumn, K., *et al.* (2000).
Adhesive force of a single gecko
foot-hair.” *Nature*, 405, pp. 681-
685.

Bringing an Effective Solar Sail Design Toward TRL 6

David Lichodziejewski, Billy Derbès
L'Garde, Inc.

John West
Jet Propulsion Laboratory
California Institute of Technology

Rich Reinert
Ball Aerospace

Dr. Keith Belvin, Richard Pappa
NASA Langley Research Center

Abstract

Solar sails reflect photons streaming from the sun and convert some of the energy into thrust. This thrust, though small, is continuous and acts for the life of the mission without the need for propellant⁽¹⁾. Recent advances in sail materials and ultra-low mass structures have enabled a host of useful missions utilizing solar sail propulsion. The team of L'Garde, Jet Propulsion Laboratories, Ball Aerospace, and Langley Research Center, under the direction of NASA, has been developing a solar sail configuration to address NASA's future space propulsion needs. Utilizing inflatable deployed and Sub Tg rigidized boom components, this 10,000 m² sailcraft achieves an areal density of 14.1 g/m² and a characteristic acceleration of 0.58 mm/s². The entire configuration released by the upper stage has a mass of 232.9 kg and requires just 1.7 m³ of volume in the booster. After deployment, 92.2 kg of non-flight required equipment is jettisoned resulting in a sailcraft mass, including payload and control system, of 140.7 kg.

This document outlines the accomplishments of a Phase 1 effort to advance the technology readiness level (TRL) of the concept from 3 toward a TRL of 6. The Phase 1 effort, the first of three proposed phases, addressed the design of the solar sail, its application to several missions currently under review at NASA, and developed a ground test plan to bring the technology toward a TRL of 6.

Introduction

Early in the program, with the support of NASA, solar sail missions under consideration were researched and a mission set of interest was

developed. Relevant mission parameters and environs were identified and defined. These requirements were used to refine a solar sail design meeting and exceeding these requirements. This design includes all elements required for power generation, communications, and navigation. An equipment list was generated, components selected, and mass properties developed. To enhance the flight performance of the concept, a carrier concept was developed to jettison all non-essential deployment-related components before the mission.

An important aspect of the Phase 1 effort was to generate a test plan to raise the TRL from 3 toward 6. A list of test articles was developed to validate section properties such as boom modulus, torsional stiffness, and deployability. Sail sections and quadrants will also be fabricated for testing and validation. A 10 m subscale system test article will be fabricated for ground testing at L'Garde and will then undergo a vacuum deployment and structural test in Langley Research Center's (LaRC) 16 m vacuum chamber. Finally, a 20 m square test article will be built and tested at NASA's Plum Brook 30 m thermal/vacuum test facility. This test, which will

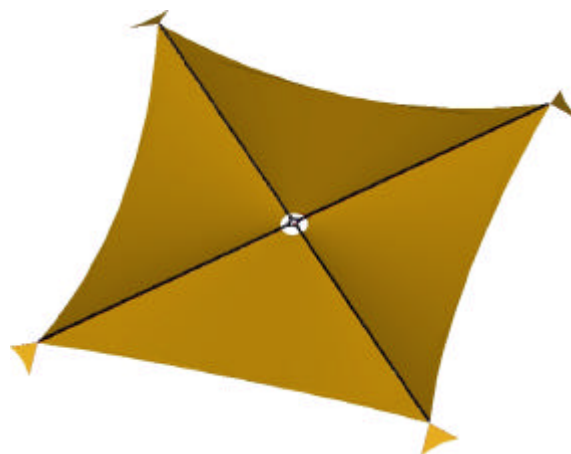


Figure 1. Baseline Solar Sail Design

Copyright 2003 by L'Garde Inc. Published by the
American Institute of Aeronautics and Astronautics,
Inc. with permission

validate the sail system at space thermal and vacuum conditions, will bring the sail system toward TRL 6. Achieving a TRL level of 6 requires testing in a “relevant environment”. Our tests will simulate space thermal and vacuum conditions but will still be conducted in 1 g. Many issues related to the 1 g environment will remain after testing of this large and gossamer structure. As a result, achieving a full TRL of 6 on the ground will not be possible, however, we will come as close as possible in a ground testing environment.

Design Overview

The baseline design is shown in figure 1. This 100m square configuration was designed around the solar sentinel or sub L1 sun observation mission. This solar sail mission utilizes thrust from the sun to descend below the L1 Lagrange point providing a stable vantage point closer to the sun yet remaining in the same orbital period as the Earth. This same configuration can be used for a host of other missions with no or minimal modification other than scaling.

Baseline Mission

As future phases of this program will require test articles of a specific configuration, a baseline mission was selected around which to optimize the

design. The Solar Sentinel or Geostorm ⁽²⁾ mission was selected as a likely candidate for future missions. This scenario takes advantage of the constant thrust available from the solar sail to place a payload in a solar orbit inside of the L1 point, yet remain in the same period as the Earth’s. This position provides an excellent vantage point for solar observation and warning of adverse solar activity. Satellites can station keep at the L1 Lagrange point without the need for additional propulsion, see figure 2. This point is about 230 Earth radii (Re) from the Earth toward the sun along the Earth-sun line. Using the constant thrust from the sail it is possible to descend to a closer orbit to the sun yet remain in the same period as the Earth, and remain on the Earth-sun line. An orbital analysis shows that the baseline sail design can descend an additional 520 Re closer to the sun. This location can provide information of solar activity with a lead-time 3 times greater than current solar observing missions.

Solar sails provide thrust normal to the sail, by changing the angle of the sail normal with respect to the sun-sail line (β), thrust vectors can be developed with components normal to the sun sail line. With a thrust component normal to the plane of the ecliptic, the sailcraft can orbit the sun above the plane of the ecliptic in a non-Keplarian orbit as shown. The line

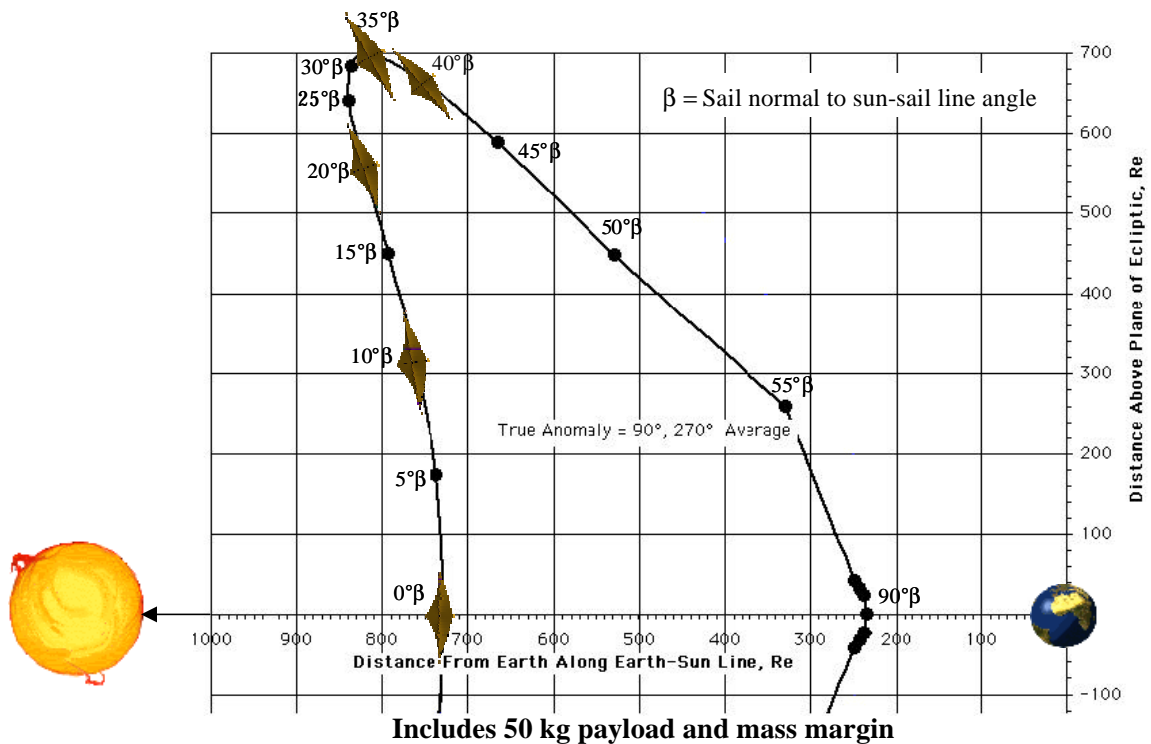


Figure 2. Baseline Mission

shown represents a family of solar orbits depending on the β angle of the sail. The baseline design can maintain a position relative to the earth-sun line at a point 700 Re above the plane of the ecliptic, and 800 Re closer to the sun. Additionally, the sailcraft can maintain this distance from the Earth-sun line while orbiting in a halo orbit. Thus several sailcraft can provide multiple simultaneous observation points of the solar wind. By combining the data gathered by these instruments, a 3-D map of incoming solar anomalies can be developed.

Control System

Control vanes resembling one scaled quadrant of the solar sail have been integrated into the structure to provide full 3-axis control. By modulating a small amount of reflective area near the boom tips, forces are generated large enough to control the sail orientation. Actuators mounted at the tips of the boom provide the torque required to rotate the vane.

Support Structure

During earlier solar design work at L'Garde, it was discovered that the sail suspension technique can have a large impact on system mass and scalability. Several attachment techniques were reviewed (figure 3) and the stripe architecture was selected as the most efficient⁽⁵⁾.

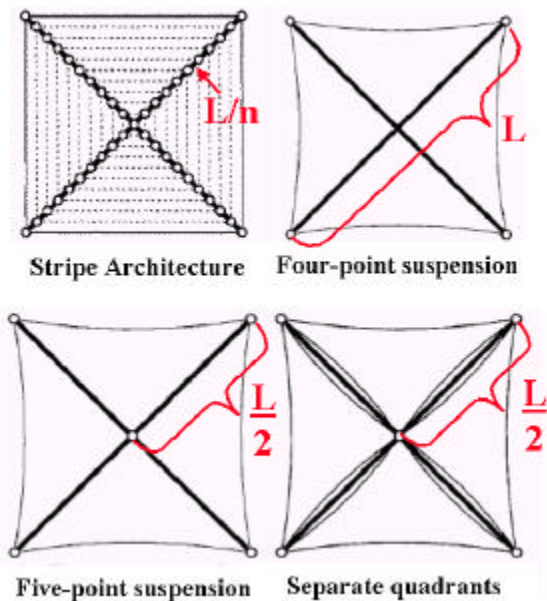


Figure 3. Sail Attachment Techniques

Stripe architecture is highly scalable. For larger sails/booms additional attachment point along the booms can be added to keep the load length L to a minimum. The other methods require large increases in L, which require significant increases to

the strength and mass of the booms to defeat the Euler buckling.

Spreader System

The booms are not sized to withstand the bending generated by the solar flux alone. A tensioned truss or spreader system is used to increase the moment of inertia of the boom to absorb the bending, see figure 4. The spreader system consists of lightweight rigid spreader bars mounted to rigid rings integrated into the boom

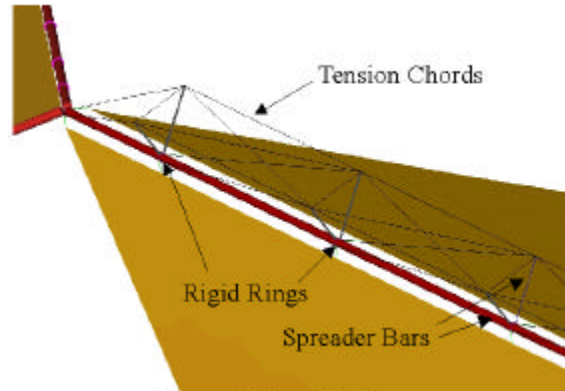


Figure 4. Spreader System

Iso-Grid Boom Design

The booms are designed in an iso-grid configuration. High modulus fibers are oriented as shown in a boom built for Team Encounter (figures 5,6). The fibers are impregnated with a Sub Tg resin to rigidize the structure after deployment (this is described in the Sub Tg section). Longitudinal uni-directional fibers are oriented to absorb the compressive loads in the booms, while the lateral fibers absorb the inflation loads and stabilize the longitudinal fibers and the cross section. These lateral fibers provide the burst margin required for deployment contingencies.

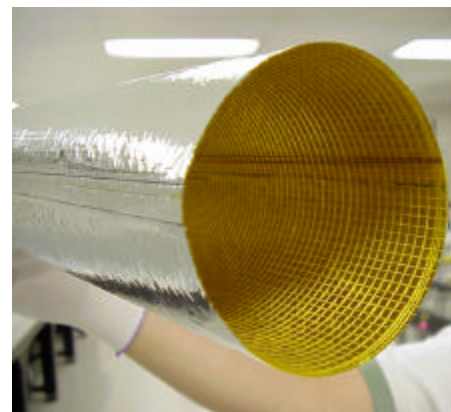


Figure 5. Boom Design

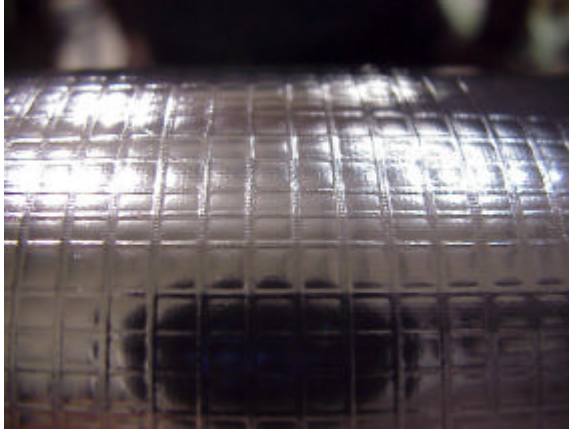


Figure 6. Boom Material Close-up

Conical Deployment

Figure 7 shows the conical boom packaging and deployment scheme developed for deployment control of the inflatable rigidizable support booms⁽³⁾. The technique uses a unique concentric packaging arrangement about the boom axis and provides a high degree of deployment control (patent pending). To deploy the conical boom, inflation gas is introduced at the base. The resulting deployment is smooth and predictable. As the tube is under pressure during deployment, it is able to withstand loads during deployment.

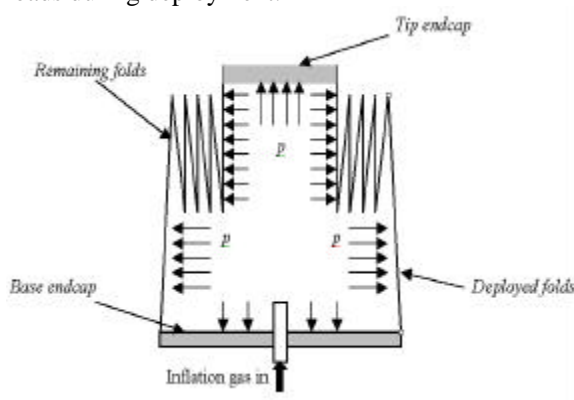


Figure 7. Conical Inflation Schematic

A deployment sequence of a Team Encounter sail conical boom is shown in figure 8. This deployment took place while the boom was floating in a water trough to simulate a 0 g deployment condition in one plane. The deployment proceeded smoothly and in a linear, consistent, and predictable manner.



Figure 8. Solar Sail Boom Conical Deployment in Water Trough to Simulate Space Deployment

Sub Tg Rigidization

Sub Tg or cold rigidization takes advantage of the increase in modulus of certain materials below their glass transition temperature (Tg)^(3,4). Sub Tg structures can be constructed for a variety of missions, from low Earth orbit (LEO) to deep space applications and this technique was selected to form the support structure for the sail.

A solar sail boom undergoing cold rigidization testing for Team Encounter is shown in figure 9. The boom is housed in a foam test chamber. While not visible through the chamber walls, the position is indicated as shown. The arrows depict the positions and loading orientation of cables used to apply compressive loads to the boom. The cables simulate the static loading of the striped sail architecture after deployment and exposure to the solar flux. This strength is achieved by using the Sub Tg resin at the expected space equilibrium temperatures

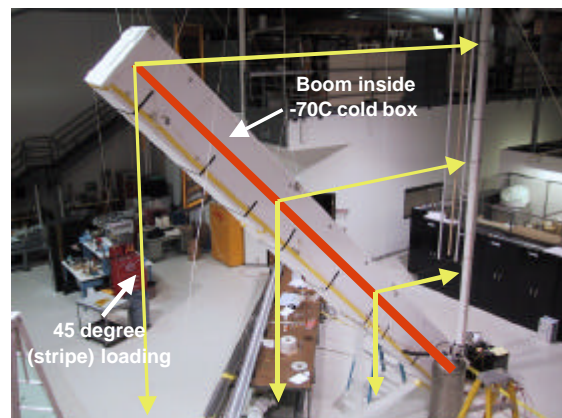


Figure 9. 7m Sub Tg Solar Sail Boom Test

Sub Tg rigidizable structures are simple and reliable. They are completely passive and in general require no heaters or vents. However, since their rigidization depends on temperatures below their Tg,

a thorough understanding of the thermal environment is required. If the deployed structure must endure large thermal excursions, it will be tailored to have a higher transition temperature and heaters may be required to “soften” the structure for deployment. Multi-layer insulation (MLI) is required to mitigate the effects of on-orbit thermal gradients and to retain the initial softening thermal energy during the deployment sequence.

Sail Material

Mylar⁽⁶⁾ has been selected for utilization as the sail membranes. This material, used in the electronics industry, is low cost and readily available. An example of a sail fabricated with Mylar is shown in figure 10. This sail was fabricated and tested for the Team Encounter program. The sail was deployed in the orientation to gravity shown demonstrating the feasibility of successful deployment of these thin films. The tension load in the sail due to gravity is roughly 600 times greater than the tension load generated by the solar flux, deployment in gravity is highly conservative and gives good confidence for deployment in 0 g.



Figure 10. Mylar Sail During Deployment Test

Test and analysis have been conducted to ensure Mylar is compatible with the space environment for the intended mission duration. Special coatings are

utilized to maximize heat rejection to space, keeping the Mylar below its melting point in orbits as close as 0.25 AU from the sun. These coatings are concurrently optimized to shield the Mylar from the degrading effects of ultra-violet (UV) radiation. Tests and analysis have been conducted showing that even after exposure to the maximum expected particle radiation doses, the mechanical properties are ample to withstand the expected sail loading conditions. These specialized coatings, coupled with the low stress concentrations afforded by the striped sail architecture, and the low cost and high availability, make Mylar an excellent choice for use as a solar sail membrane.

Space Segment

The Space Segment consists of all items released from the upper stage. This includes the sailcraft, shown on the top of figure 11, and the carrier shown toward the bottom. After deployment of the sail, the carrier is jettisoned to free the sailcraft from all non-flight required components and mass. The 50.0 kg payload envelope is visible toward the center of the sailcraft portion, and all of the spacecraft specific elements are shown toward the top of the configuration. The stowed solar arrays and communication antennas are visible toward the top.

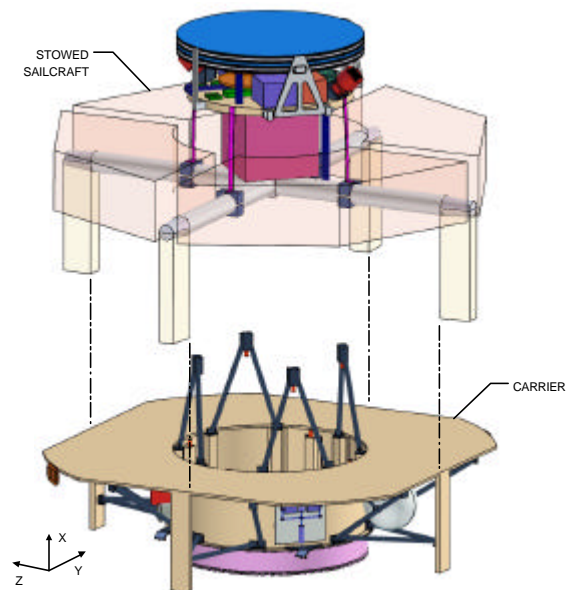


Figure 11. Space Segment (Shown Separated)

The space segment fits well inside of the Delta payload fairing as shown in figure 12. With a sufficient payload interface fixture, it may be possible to fit two space segments on a single launch.

Deployment

Once the Space Segment has successfully separated from the upper stage deployment can be initiated. Vane deployment is initiated by rotating the vane booms from their stowed position into proper position for deployment. The vane booms are deployed which pull the vane membranes into their deployed configuration, figure 13, (a). Next, the spreader system, which has been pulled together for stowage, is released in preparation for deployment. The main boom deployment is initiated by introducing inflation pressure into the stowed booms. The booms simultaneously deploy the sails and the spreader system drawing the tension cables into position by deploying the rigid rings in a sequence, figure 13, (b). An inflation control system carefully monitors the deployment length of each boom and modulates the amount of inflation gas introduced to each boom to ensure the deployment progresses symmetrically, figure 13, (c). Once equilibrium temperature is achieved and the structure is fully rigidized, the carrier is released. (d). The sailcraft is now in its final configuration and providing thrust.

Scalability

Many missions require large sails in order to carry more payload or to achieve higher specific accelerations. A scaling analysis was undertaken using L’Garde analysis tools and the results shown in figure 14. The X-axis depicts the size of the sails in square meters, while the Y-axis shows the areal density of the sailcraft. All configurations shown on the chart assume a 50.0 kg payload, and 43.3 kg of spacecraft elements for power generation, communications, and guidance and control. In reality these requirements will likely change with the given mission scenarios, however, in the interests of this scaling analysis, these parameters were fixed.

The striped sail architecture and excellent mechanical synergism with the conically stowed boom allows scalability without high mass penalties. As shown in figure 14, the baseline design, with

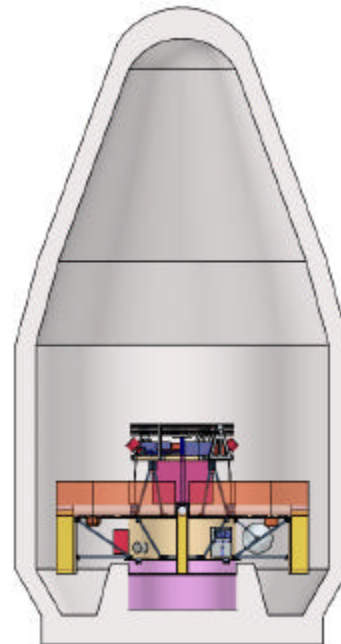
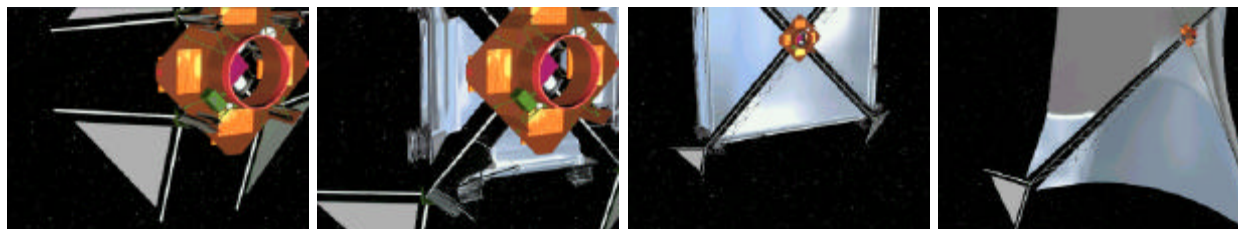


Figure 12. Space Segment in Delta II minor modification and scaling, is capable of all of the NASA “high-pull” missions shown.

Phase 2 and 3 Test Plan

To raise the TRL level to 6 a solar sail system must be tested in a “relevant environment”. To this end a series of test articles is planned that will raise the TRL to ~6. We intend to simulate the vacuum and thermal environs of space during our tests but we are limited to testing terrestrially at 1 g. With a structure as large and gossamer as a solar sail, this 1 g limitation will always be a factor. Suspension techniques will be used to mitigate the effects of 1 g but issues will remain. An important aspect of the effort will be to carefully utilize the test results at 1 g to validate a series of analytic finite element analysis (FEA) models. With these techniques, validated predictions of the structural performance of the solar sail configurations at 0 g will be generated. In this way we will raise the TRL as close to 6 as is possible on the ground, but we will not



(a) (b) (c) (d)
Figure 13. Sail Deployment Sequence (Courtesy Thomas Dynamics Modeling)

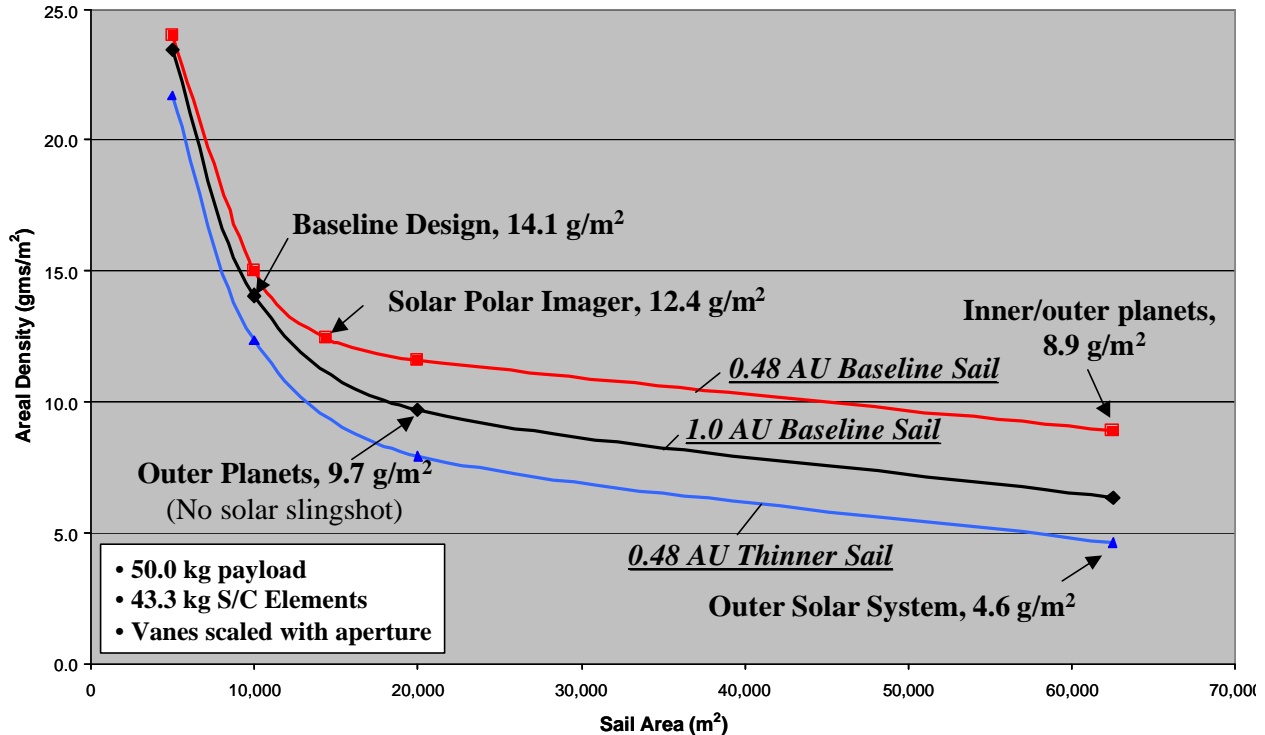


Figure 14, System Scalability

achieve all requirements for TRL 6, hence the TRL ~6 designation.

Component Tests

Initially material and component test will be conducted. The sail and Sub Tg laminate will be subjected to UV and particle radiation to validate and expand on tests already conducted. Component tests of sail and boom sections will be used to validate the mechanical characteristics. This data will be used to validate the structural models.

Subsystem Tests

A 10m sail quadrant will be deployment tested in ambient conditions as will a full-scale vane quadrant. Additionally a boom with spreader system will be deployed both in ambient and vacuum condition in LaRC's 16 m vacuum chamber. Finally a sail quadrant with two full booms and spreaders will be deployed and tested in the LaRC chamber, as will the full-scale vane and representative actuator. Structural data will be obtained, as will photogrammetry and laser vibrometry. All data will be used to validate structural assumption and the structural FEA models.

10m Test Article

The component and subsystem tests will lead to a 10m sector test of a full solar sail configuration. As

scaling of the various materials of the concept is not feasible, a 10 m on a side sector of the full-scale configuration will be fabricated and tested. While the LaRC chamber is not equipped with cryogenic capabilities, cold plates will be used locally to rigidize the boom components and allow structural testing. Again, photogrammetry and laser vibrometry will be conducted and all data will be used to validate structural assumption and FEA models.

20m Test Article (Phase 3)

In a planned follow-on contract, a larger 20 m sector of the solar sail configuration will be thermal vacuum tested in NASA's Plum Brook 30 m chamber. This ambitious test will bring all of this work and analysis together. A successful conclusion will see the solar sail system TRL level raised as close to 6 as is possible under ground test conditions paving the way for a flight experiment.

Summary

The team of L'Garde, Ball Aerospace, JPL, and LaRC has developed a highly scalable solar sail configuration to meet and exceed the requirements of many of NASA's future missions. This configuration was enabled by utilizing inflatable deployed and sub Tg rigidized booms. Striped sail architecture, coupled with L'Garde's conical boom deployment technique allows scalability without high

mass penalties. A comprehensive test plan was developed to raise the TRL level of this technology toward 6 by 2005. This focused program will pave the way for a flight experiment of this highly efficient space propulsion technology.

Acknowledgments

Much appreciation is extended to Greg Garbe and Sandy Montgomery of NASA Marshall Space Flight Center, for their vision, advocacy, and technical expertise in development of the solar sail. Many thanks to Team Encounter for access to their design and hardware, their work forms the foundation for much of the solar sail design shown. The team would like to acknowledge the support of Jeff Bladt of Ball Aerospace, and Dr. Guru Singh for their control system expertise. L'Garde would also like to thank Dr. Gyula Greschik for his assistance in the solar sail design and structural analysis. Thanks also to TDM for the deployment animations. Part of this research was carried out at the Jet Propulsion Laboratories, California Institute of Technology, under a contract with NASA.

References

- 1) McInnes, C.R., Solar Sailing Technology, Dynamics and Mission Applications, Springer-Praxis, London, UK, 1st Ed.
- 2) West, John, and Derbès, Billy, "Solar Sail Vehicle System Design for the Geostorm Warning Mission". AIAA-2000-5326, September 21, 2000.
- 3) D. Lichodziejewski, R. Cravey, G. Hopkins, "Inflatably Deployed Membrane Waveguide Array Antenna for Space" AIAA 2003-1649, 4th Gossamer Spacecraft Forum, April 7-10, 2003, Norfolk, VA
- 4) K. Guidanean, D. Lichodziejewski, "An Inflatable Rigidizable Truss Structure Based on New Sub-Tg Polyurethane Composites", AIAA-2002-1593, 3rd Gossamer Spacecraft Forum, Apr. 25, 2002, Denver, CO
- 5) Greschik, G. and Mikulas, M.M., "Design Study of a Square Solar Sail Architecture", Center for Aerospace Structures, University of Colorado, Boulder, CO.
- 6) DuPont, Inc., "Mylar Product Information," no. 222367D, December 1997, available at www.dupontteijinfilms.com

Development of Solar Sail Propulsion for Inner Solar System NASA Science Missions

Edward E. Montgomery IV* and Les Johnson†
NASA Marshall Space Flight Center, Huntsville, Alabama 35812

This paper examines recent assessments of the technology challenges facing solar sails, identifies the systems and technologies needing development, and the approach employed by NASA's In-Space Propulsion program in NASA to achieve near-term products that move this important technology from low technology readiness level toward the goal of application to science missions in near-Earth space and beyond.

I. Background

Solar sails are a near-term, low-thrust, propellantless propulsion technology suitable for orbital maneuvering, station keeping, and attitude control applications for small payloads. Furthermore, these functions can be highly integrated, reducing mass, cost, and complexity. The solar sail concept is based on momentum exchange with solar flux reflected from a large, deployed thin membrane. Thrust performance increases as the square of the distance to the Sun. In comparison to conventional chemical systems, there are missions where solar sails are vastly more and less economical. The less attractive applications involve large payloads, outer solar system transfers, and short trip times. However, for inclination changes and station keeping at locations requiring constant thrust, the solar sail is the only economical option for missions of more than a few weeks duration.

Solar sails were identified in a study process performed under the auspices of the In-Space Propulsion (ISP) Technologies program and funded by NASA's Office of Space Flight. It is the purpose of the ISP program to advance midlevel maturity propulsion technologies to a level needed to be selected and used in NASA robotic science missions. Figure 1 illustrates the regime of investments made in the ISP program.

II. Mission Need for Solar Sails

NASA's Sun-Earth Connection program under the Office of Space Sciences has published an evolutionary vision for utilizing solar sails to advance their science goals.¹ Shown in Fig. 2, this mission need roadmap starts with a modest-sized, near-term technology demonstration mission and ends with a very large, very gossamer interstellar probe.

Geostorm, a space weather-related mission, is of less interest now than when the report was written. In the interim, the National Oceanic and Atmospheric Administration has decided to press forward with more conventional propulsion options. The nearest term project pulling the sail technology is the Solar Polar Imager (SPI), followed by the L1 Diamond and the Particle Acceleration Solar Orbiter (PASO). Each of these is addressed below. The new human exploration mission initiative announced by President Bush recently has a component of in-space technology development, but the decision has been made to keep ISP focused toward the development of primary propulsion for robotic science missions rather than delivering humans or cargo to the Moon and Mars.

A. Solar Polar Imager

Missions that have to make an inclination change are known to be challenging for chemical rockets. In equation (1), V is the starting orbital velocity and θ is the plane change angle.² Equation (1) gives the standard relationship for calculating the effect of a velocity change on an orbit.

$$\Delta V = 2V \sin \frac{\theta}{2} \quad ..1$$

* Manager, Solar Sail Propulsion Project, TD05

† Manager, In-Space Propulsion Technology Projects Office, TD05

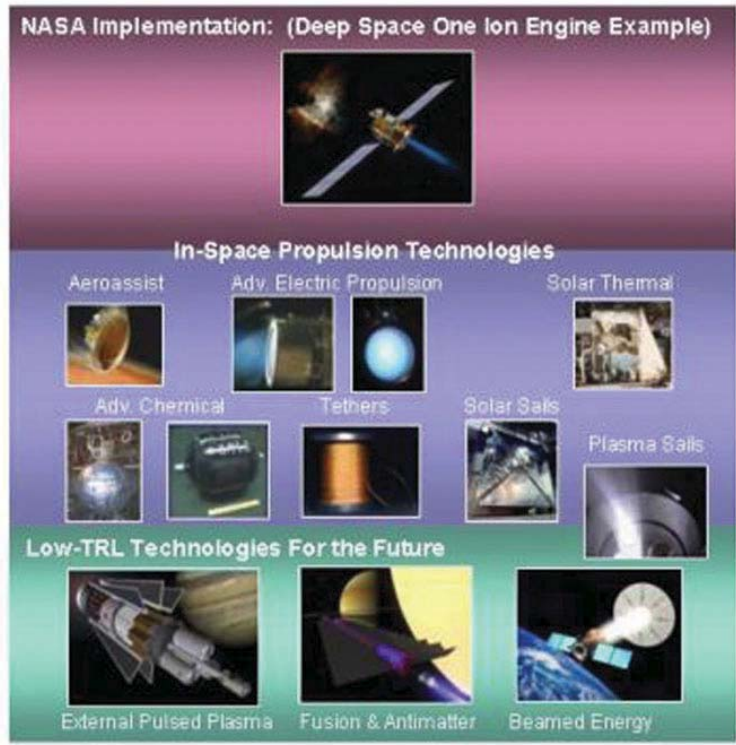
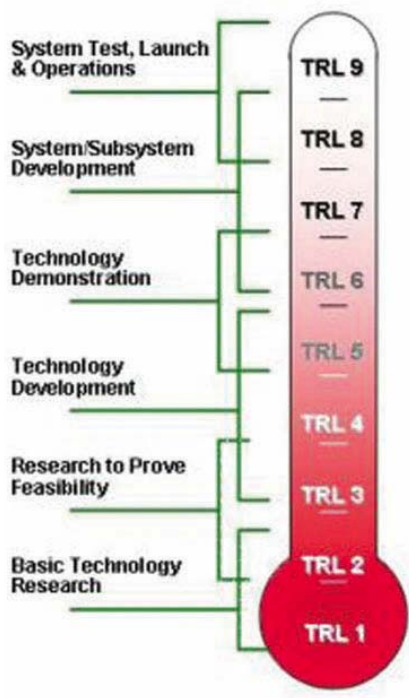


Figure 1: ISP program will advance mid-TRL technologies to support NASA mission applications.

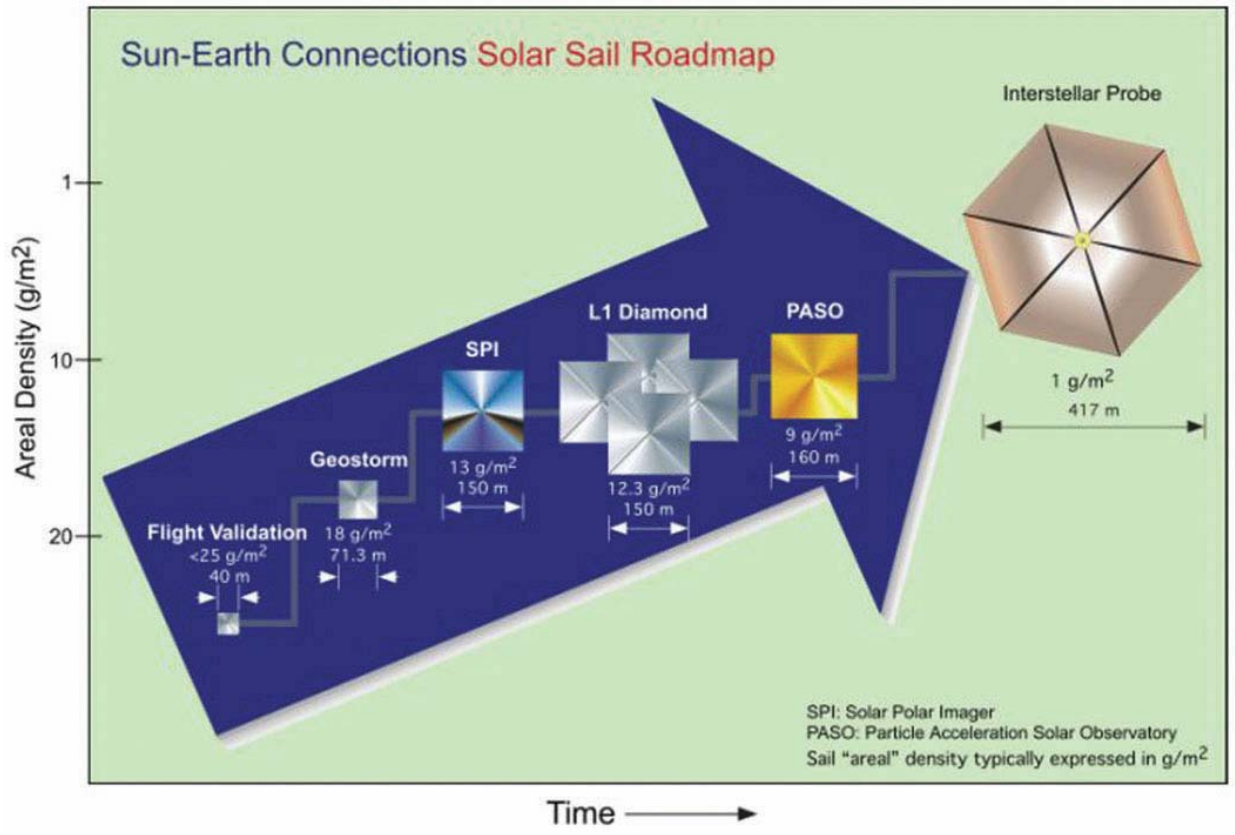


Figure 2: Primary mission pull.

This assumes the thrust is directed along the angular momentum vector of the orbit. For chemical systems, the small penalty resulting from the instantaneous change in the direction of the angular momentum vector can generally be ignored. For solar sails, the changing orientation between the angular momentum vector and the solar vector would have to be factored in to the maneuver. The mass penalty for carrying propellant to do these type maneuvers impulsively is high and is one of the strong justifications behind the assessment that solar sails are an enabling technology for the SPI. The science objectives of this mission include measurement of the Sun's polar irradiance and magnetic field, imaging the full effect of coronal mass ejections (CMEs) and evolution on the full three-dimensional corona, and linking of variations in the high-latitude heliosphere to surface conditions. The mission profile calls for travel in the ecliptic, then taking up a 0.48 AU heliocentric circular orbit inclined 60°. Mission designers have estimated a sail ~150 m across will be needed.

A study by Harris³ established the initial mission concept. Later, studies by Neugebauer⁴ and Ayon et al.⁵ refined the science objectives and the mission and system design. Figure 3 represents the most current flight system concept. The SPI mission concept was recently selected (Liewer⁶) for further refinement under the Vision Mission NASA Research Announcement (NRA).

B. L1 Diamond

The L1 Diamond mission will make use of a solar sail's unique propellantless thrust nature to hover in space sunward of the Earth-Sun L1 libration point. Conventional spacecraft can be parked in a relatively small region of space that will require only occasional station-keeping thruster firings. The always-on thrust of a sail can be used to park a science experiment in a much larger volume of space. The vantage points available to science are only a function of sail size and lightness and a relatively large range of locations is reachable within the near-term state of the art. L1 Diamond is a constellation of four spacecraft cooperatively and concurrently gathering data to validate models of processes in situ through a three-dimensional sample region of space. See Fig. 4.

L1 science objectives are to measure the properties of solar wind turbulence (as seen in density, velocity vector, and magnetic field) as a function of separation in space and time, ranging from the dissipation scales of hundreds of kilometers to the outer scale of millions of kilometers. Direct measurements of the possible spatial symmetries of the turbulence is also desired along with measurements of the spatial variation in propagating waves, shocks, and other disturbances in the solar wind. Another objective is the discovery of associations of the turbulence with

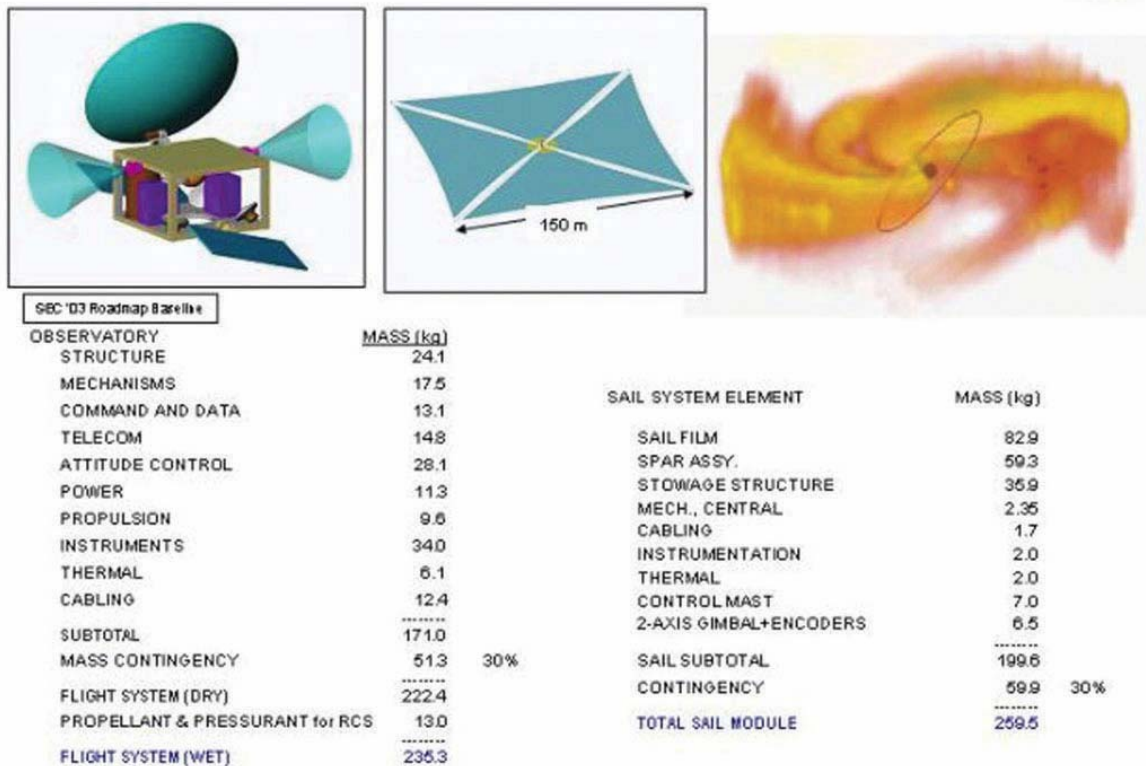


Figure 3: SPI mass summary example flight system summary.

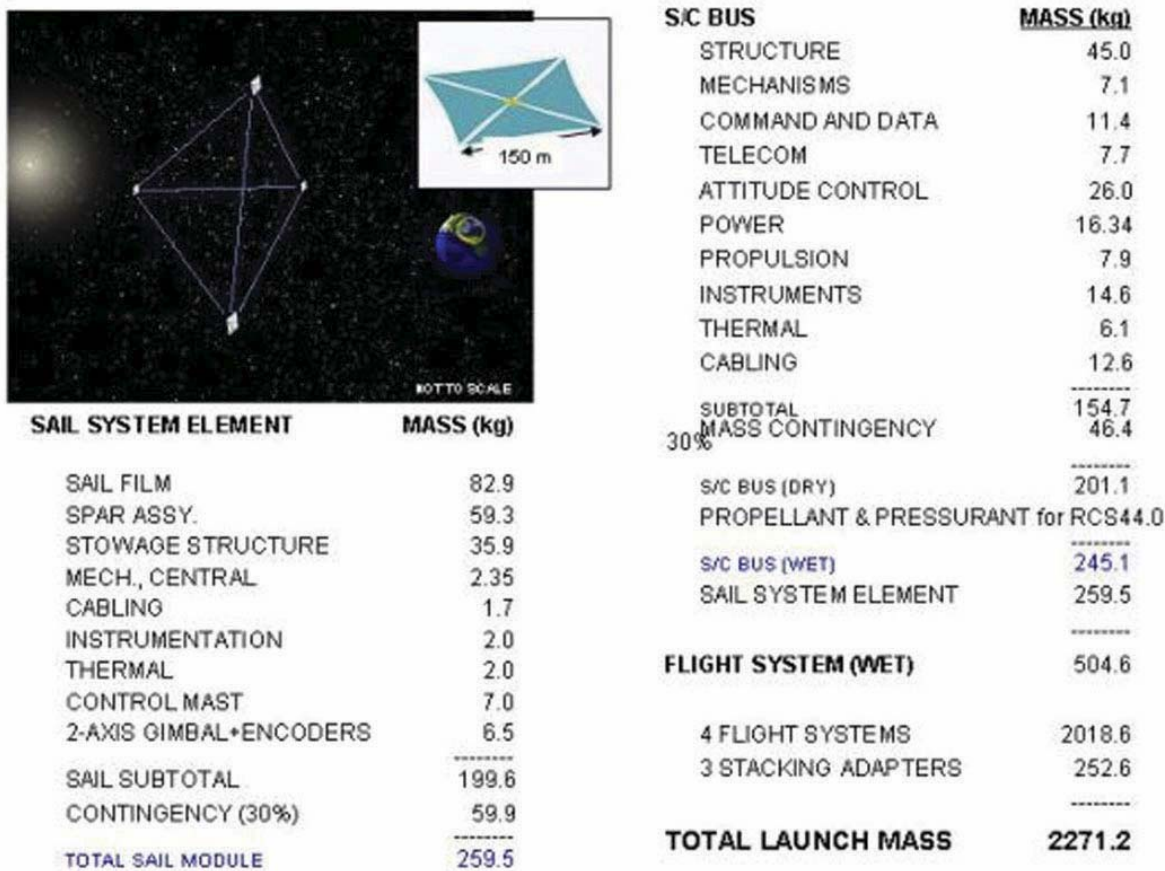


Figure 4: L1 Diamond mass summary example flight system summary.

suprathermal and energetic particles. The Delta IV launch vehicle has been suggested to put the spacecraft into a ballistic transfer from Earth to an Earth-Sun L1 halo orbit that would take ~90 days. The solar sail would accomplish the transition from the initial libration point to the various constellation stations. Three spacecraft will be in a triangle formation whose centroid is 280 to 500 Earth radii sunward of Earth on the Sun-Earth line. A fourth spacecraft is located above the ecliptic plane. Continuous solar viewing for at least 3 yr is needed.

C. Particle Acceleration Solar Orbiter

Finally, PASO will drive the next development of the next class of solar sails to transfer a science instrument payload to a very close solar orbit (0.169 AU). See Fig. 5. The PASO measurement strategy is to capture high-resolution images of high-energy solar flares, allowing the detection of composition. The mission will also employ a neutron spectrometer and a gamma-ray spectrometer. Solar wind and magnetic field instruments will also be included. The science objectives are to understand particle acceleration mechanisms, distinguish between flare and shock accelerated particles, and study the active region evolution. The mission concept begins with a Delta launch and then transfer from 1 AU to a 0.169 AU circular solar equatorial orbit with a period of 25.4 days. The transition to the final lower solar orbit will take 3 yr during which active CME source regions will be in continuous view. Mission science operations will continue another 4–5 yr in the final orbit.

D. Other Missions for Solar Sails

Since the thrust of a solar sail is small, it does not suit missions involving massive payloads or short trip times. However, if a very high ultimate velocity is needed, such as fast flyby missions to the outer planets or extra-solar system destinations, solar sails can be the only feasible alternative. Although solar pressure has greatly attenuated at those distances, the long trip time out at constant thrust integrates to a considerable total velocity increase. A study by Price and others showing how the flight times for solar sails to the heliopause is less than half of the most efficient reaction jet rockets.⁷ See Fig. 6.

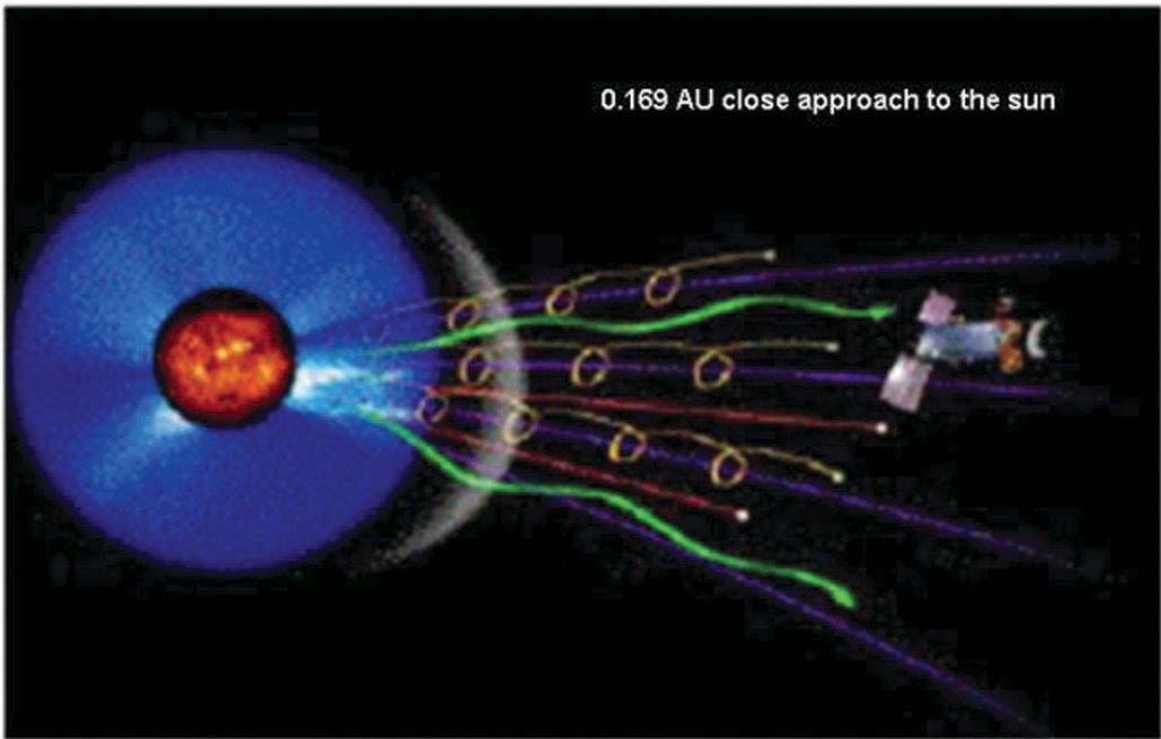


Figure 5: PASO mission concept.¹

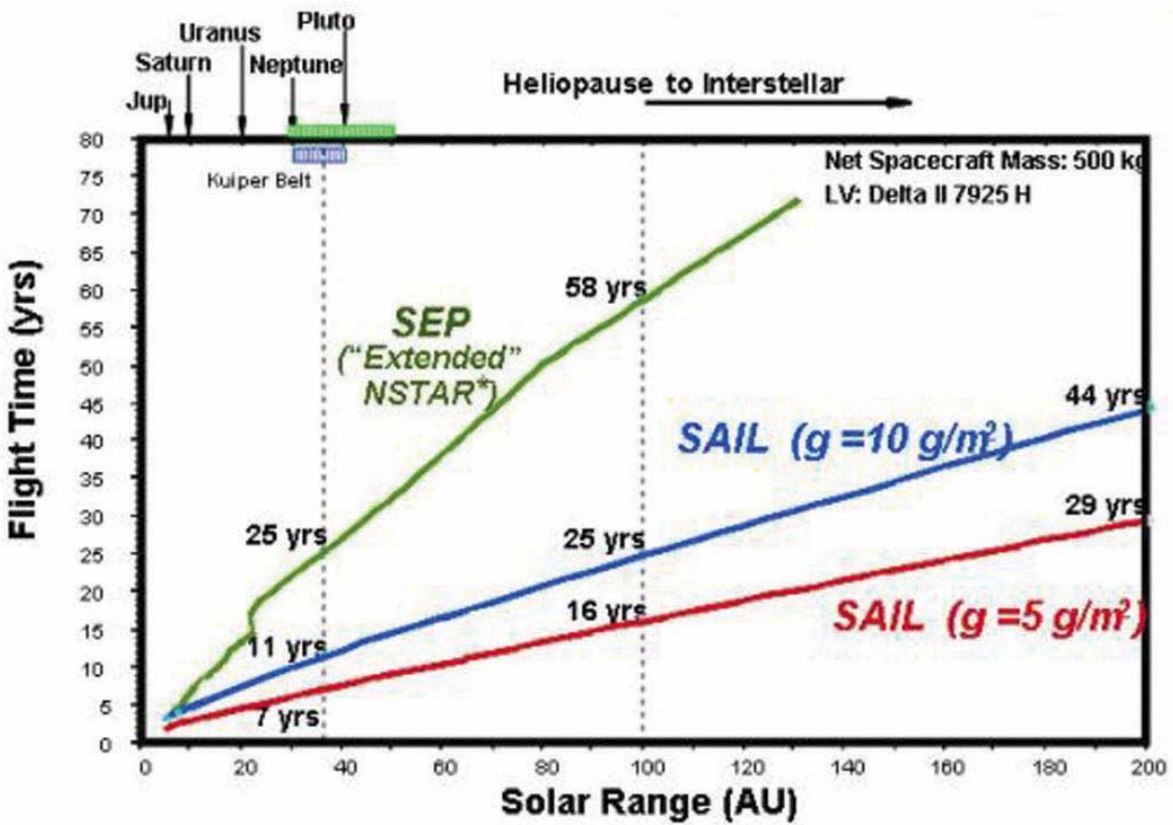


Figure 6: SEP/solar sail performance comparison.

Recent research by Taylor and Matloff suggests that the outer planetary stopover missions for small robotic science packages may also be a possibility utilizing a bimodal sail. The concept is an unconventional, high-altitude pass, low-dynamic-pressure aerobraking maneuver. Gossamer mass properties could enable trajectory shaping with relatively nonstressing (small thermal or pressure shocks) aerobrake maneuvers. Sail and boom loads for a Titan aerocapture might only be a fraction of what the same sail would encounter from solar pressure in Earth orbit.⁸

The Interstellar Probe Mission will measure, in situ, the properties and composition of interstellar plasma and neutrals, low-energy cosmic rays, and interstellar dust. The technology challenges are great. Mission designers believe at least a 200-m highly reflective sail will be needed with an areal density of $<1 \text{ g/m}^2$ —beyond any known technology. ISP has classified this as an emerging technology.

III. Technology Challenges

In January 2002, the results of a panel of experts from industry, academia, and the Government was formed to assess the state-of-the-art solar sail technology and provide guiding inputs for the ISP program to use in formulating a plan to bring the maturity of solar sails to technology readiness level (TRL) 6.⁹ This level is defined as a full system, validated in a relevant environment. The delineation between it and the next level is used in a space mission. The result of the panel is summarized in Fig. 7.

A similar activity was conducted in March 2004.¹⁰ The results largely validated the previous assessments and indicated that the state of the art had been improved dramatically, was maturing in the proscribed directions, and was addressing the priority needs in a developmental approach; i.e., roadmap, consistent with the recommendations of the technical community. Members of the Technology Assessment Group (TAG) included Government, industry, and academia. Export control regulations precluded foreign participation.

IV. Formulation of a Technology Development Program

The Solar Sail Propulsion (SSP) technology area was formed within ISP to accomplish the program objectives for solar sails utilizing the TAG's input. Organizing the topic area began with identifying that four different solar sail types existed, each having specific characteristics (listed in Fig. 8) that identified a common class of missions and peculiar technology requirements. The first class is indicative of some validation flight concepts and can be said to have some TRL 7 flight heritage through the Russian Znamiya program and the NASA Inflatable

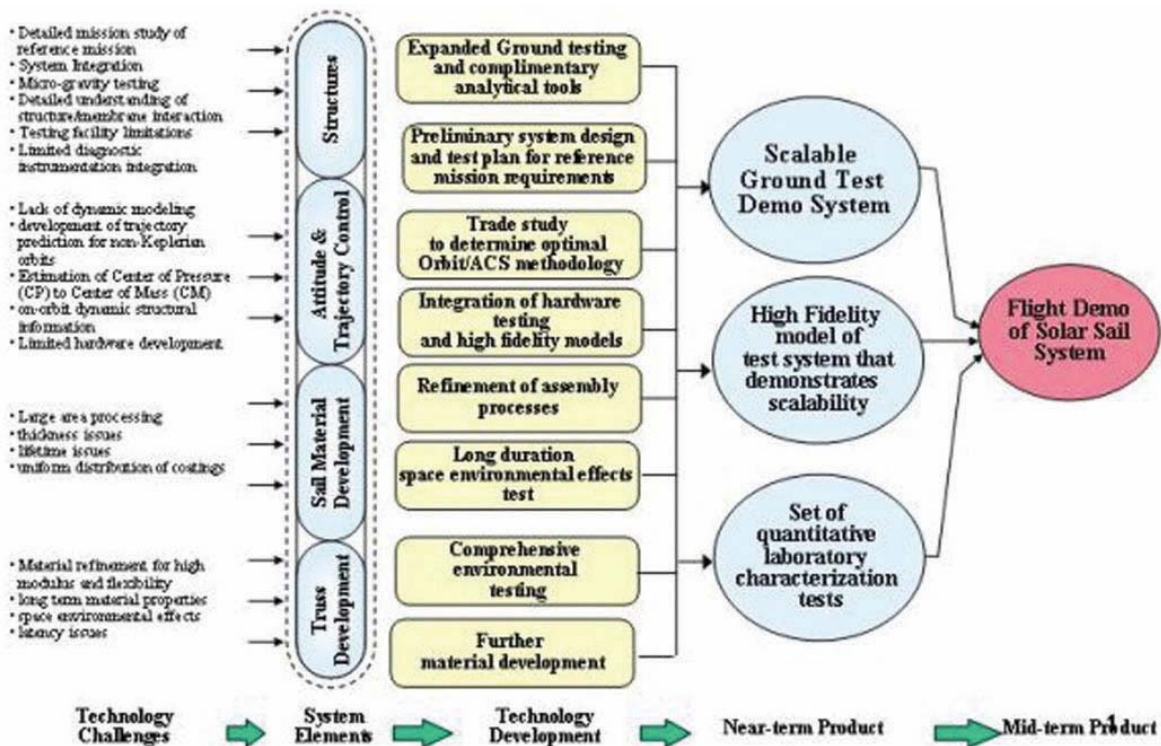


Figure 7: Solar sail technology assessment group roadmap.

Mission Class	Timeline	SOA	Technology Challenges	NASA Mission Application
GEO/GTO Short Life	Past/Now	Encounter(?), Cosmos, ST-7, Znamya, Inflatable Antenna Exp	AO, radiation belts effects, high GG torques	None
1 Au	Near Term	ISP Ground Demo, ST-5 Geostorm	Validation in a space environment, Infusion into mission applications	L1 Diamond Solar Polar Imager (SPI)
<0.25 Au	Mid-Term	Mission analysis, Future ISP work	Materials environments, Thrust vector range, Lightweight system, 100s m system scale size	Particle Acceleration Solar Observatory (PASO) Titan Explorer Saturn Ring Observer
Extra Solar	Far-Term	Mission concept analysis, Gossamer, Encounter(?)	Ultra-lightweight system Integrated system architecture Sub to kilometer system scale size	Interstellar Probe (ISP) Geospace System Response Imagers (GSRI) Outer Heliosphere Radio Imager (OHRI)



Figure 8: Sail technology classes.

Antenna Experiment. The last mission type is one requiring extremely lightweight systems for which there are no TRL 3 candidates. The other two applications are the focus of the ISP program. In defining a roadmap for those, it logically fit a serial effort to develop first the 1 AU sail, and then extend the technology to the harsher environments at <0.25 AU from the Sun.

Budget limitations drove the need to focus technology development on the most near-term classes. A convenient discriminator between the classes is the region of space in which they are intended to support missions. This logic led to the establishment of the following mission statement: (1) Raise solar sail technology as a primary propulsion system for inner solar system NASA missions to TRL, (2) solar sail propulsion technology shall be scalable to inner solar system NASA missions, and (3) attain closest approach to TRL 6 possible on the ground by the end of FY06.

An investment strategy was derived utilizing the guideline that at least 75% of the program investment would go to competitively selected efforts. The implications drove the procurement of the 1 AU sail in three annual NRA cycles. The next inner solar system sail class would then follow in three additional cycles. Figure 9 illustrates the SSP roadmap.

Looking across the roadmap at the mission concepts, a survey of the two key sail design parameters—areal density and root area—indicates the level of material science and fabrication knowledge needed. Revealed in the evolutionary path for the structural solution are evolution steps at plateaus around 15, 70, and 150 m.

V. Future Plans

NASA plans a vigorous program to bring solar sails to prepare solar sail technology for validation and flight implementation in the missions shown.

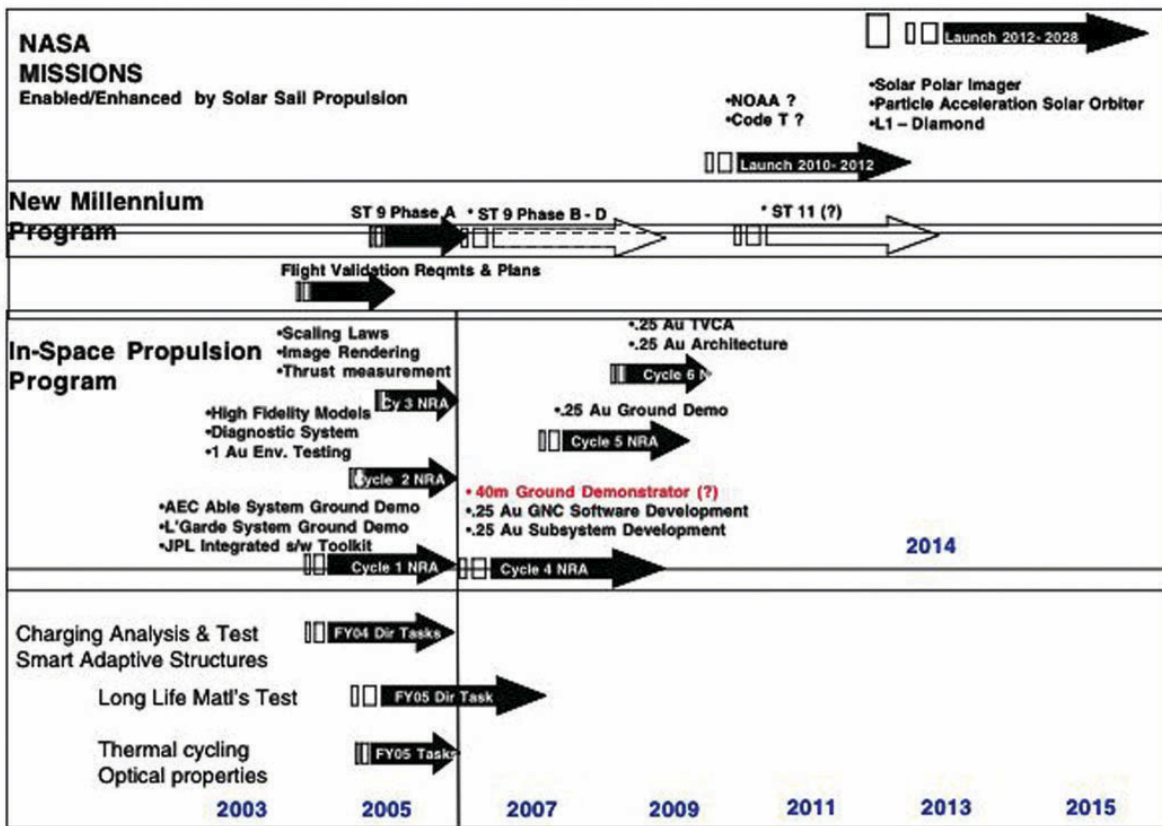


Figure 9: SSP roadmap.

VI. Summary

The objective of the SSP technology area investment is to develop solar sail technology to the level of validating a system in a relevant environment. High value science missions have been identified that require solar sails. Experts have met and defined the development needs and products, and a time-phased program has been laid out to prepare NASA to go places only sails can go.

References

- ¹"Sun-Earth Connection Roadmap 2003–2028," National Aeronautics and Space Administration, September 2002.
- ²McCuskey, S.W., *Introduction to Celestial Mechanics*, Addison-Wesley Publishing Co., Reading, MA, pp. 112–113, 1963.
- ³Harris, H. M., "Coronal Transients and Space Weather Prediction Mission," Jet Propulsion Laboratory Report, JPL D–12611, 1995.
- ⁴Neugebauer, M., et al., "A Solar Polar Sail Mission—Report of a Study to Put a Scientific Spacecraft in a Circular Polar Orbit About the Sun," Jet Propulsion Laboratory/Caltech, February 1998.
- ⁵Ayon, J., et al., "Sun-Earth Connection Roadmap 2003–2028," NP–2002–8–500–GSFC, January 2003.
- ⁶Liewer, P., "Solar Polar Imager: Observing Solar Activity From a New Perspective," Proposal to the ROSS 2003 Visions Mission NASA Research Announcement, September 2003.
- ⁷Price, H., "Solar Sail Technology Development Final Report to In-Space Propulsion for FY'01 Tasks at JPL," Jet Propulsion Laboratory, August 28, 2002.
- ⁸Taylor, T., and Matloff, G., "Bi-Modal Solar Sail Concept," Teledyne Brown Engineering, Final Report, Contract H–35191D, September 2003.
- ⁹Garbe, G., "Solar Sails Technology Assessment Group Final Report," NASA Marshall Space Flight Center, AL, January 29, 2002.
- ¹⁰Adams, C., et al., "Solar Sail Propulsion, 2004 Technology Assessment Group, Final Report," NASA Marshall Space Flight Center, AL, April 2004.



Oops, someone has a bad link to us...

The item you have requested was not found. It is possible it has been moved, renamed, or replaced with newer material. For your convenience a search panel and links to the major sections of Marshall Space Flight Center's Web Sites are provided below.

...but we will help you find it!

Search Marshall Space Flight Center's Web Sites

- Enter keywords, phrases, or a sentence:

[MSFC Home](#)

[Space Transportation](#) | [Science](#) | [Space Projects](#) | [Educational Services](#) | [Instructional Materials](#) |
[What We Do for You](#) | [NASA News](#) | [Cool Sites](#)

If you continue to have problems, please contact the Owner or Curator of the web page, or if no one is listed, email the [System Administrator](#) for assistance. Please provide the **Address** or **URL** of the web page when reporting a problem.

Advanced Space Storable Propellants for Outer Planet Exploration

Daniel P. Thunnissen*

User Technology Associates, Inc., Pasadena, California, 91101

and

Carl S. Guernsey†, Raymond S. Baker‡, and Robert N. Miyake§

Jet Propulsion Laboratory, California Institute of Technology, Pasadena, California, 91109

An evaluation of the feasibility and mission performance benefits of using advanced space storable propellants for outer planet exploration was performed. For the purpose of this study, space storable propellants are defined to be propellants which can be passively stored without the need for active cooling. A secondary purpose of this study was to provide guidance as to the limits, benefits, and possible methods of passively storing such mild cryogenic propellants for deep space missions. The study was composed of four distinct efforts. First, candidate propellants were defined and their relevant properties determined. Second, a propellant combination analysis using the Two Dimensional Kinetics 1997 (TDK97) program was conducted. Third, a thermal storage design was analyzed. Lastly, a mission and systems analysis was performed for three outer planetary missions. The missions are representative in complexity, duration, and requirements for a variegated set of outer planet exploration missions currently being considered by NASA. Nonetheless, the analysis conducted and outlined in this paper determined that outer planet exploration using advanced storable propellants was feasible and offered a significant benefit in delivered payload compared to previous design studies.

Nomenclature

A	area
A_0, a, B_0, b, c_0	Beattie-Bridgeman constants
b	mass flow rate
C_F	thrust coefficient
c_1, c_2	propulsion constants
d	diameter
F	thrust
FOM	figure of merit
M	molecular mass (molecular weight)
MR	mixture (oxidizer-to-fuel) ratio
m	mass
n	number of stages
p	pressure
I	impulse
T	temperature
t	time
V	volume

*Systems Engineer; Senior Member AIAA

†Principal Engineer, Thermal and Propulsion Engineering Section; Senior Member AIAA

‡Staff Engineer, Propulsion Flight Systems Group

§Principal Engineer, Thermal and Propulsion Engineering Section

β	$1 + c_2/\rho_{ave}$
ΔV	change in velocity
v	molar specific volume
ρ	density
g_c	conversion factor (9.80665 m-lbm/lbf-sec ² in the Imperial system of units, 1 in SI system of units)
\mathcal{R}	universal gas constant, 8314.51 J/kmol-K

subscripts:

<i>ave</i>	average
<i>bo_stg</i>	relevant stage at burn out
<i>c</i>	combustion chamber
<i>CPU</i>	central processing unit
<i>e</i>	nozzle exit
<i>f</i>	final
<i>f_stg1</i>	stage 1 final
<i>fuel_tank_loaded</i>	fuel tank fully loaded with fuel
<i>GR</i>	Guernsey-Rapp
<i>hold-up</i>	hold-up/residual propellant
<i>i</i>	initial
<i>i_stg2</i>	stage 2 initial
<i>inj</i>	injected
<i>lim_ΔV</i>	limiting change in velocity
<i>max</i>	maximum
<i>ox</i>	oxidizer
<i>ox_tank</i>	oxidizer tank
<i>ox_tank_loaded</i>	oxidizer tank fully loaded with oxidizer
<i>pres</i>	pressurant gas
<i>pres_tank</i>	pressurant tank
<i>pres_tank_fuel</i>	pressurant tank for the fuel
<i>pres_tank_fuel_loaded</i>	pressurant tank for the fuel fully loaded with pressurant
<i>pres_tank_ox</i>	pressurant tank for the oxidizer
<i>pres_tank_ox_loaded</i>	pressurant tank for the oxidizer fully loaded with pressurant
<i>prop</i>	propellant
<i>prop_loaded</i>	total propellant loaded
<i>prop_tank</i>	propellant tank
<i>prop_dry</i>	dry propulsion system
<i>prop_stg1</i>	stage 1 propellant
<i>prop_wet</i>	wet propulsion system
<i>sp</i>	specific
<i>struc</i>	stage structure
<i>t</i>	total
<i>thermal</i>	thermal control
<i>total_stg</i>	relevant stage total
<i>ρ_{sp}</i>	density specific

superscripts:

<i>j</i>	stage number
<i>pres_tank_i</i>	in the pressurant tank at launch
<i>pres_tank_f</i>	in the pressurant tank at end of stage burn
<i>prop_tank_i</i>	in the propellant tank at launch
<i>prop_tank_f</i>	in the propellant tank at end of stage burn

I. Introduction

Chemical propulsion for planetary exploration missions has for decades depended on the use of propellants that can be passively stored at Earth-ambient conditions. By contrast, launch vehicle propulsion systems routinely use cryogenic propellants (such as liquid hydrogen) that offer higher specific impulse than is available from Earth-storable propellants. Unfortunately, the application of such propellants to long-duration space missions is complicated by the need to limit or eliminate boil off of the cryogenic propellants. The development of zero-G vent systems and/or cryocooler technologies for such purposes is just now in its infancy and will make considerable demands on spacecraft resources such as mass and power.

It has long been recognized that there is a middle ground between the extremes of using Earth storable propellants and “hard” cryogenics such as liquid hydrogen: space storable propellants.¹ In this context, a “space storable” propellant is one that can be stored in interplanetary space without the need for either venting or cryogenic cooling. Conventional Earth-storable propellants fit into this category, as do a number of mildly cryogenic propellant candidates. The use of such propellants has the potential to significantly increase the performance of chemical propulsion systems for missions of planetary exploration without requiring the technology investment or impacts on spacecraft resources that would be entailed in adopting the use of deeply cryogenic propellants.

A. Purpose of Study

A great deal of work was done during the 1970’s to identify the benefits of space storable propulsion for planetary exploration.^{2,3,4,5,6,7,8,9} However, much of the underlying documentation of this work has been lost over the years and many of the studies suffer from one or both of two weaknesses: they were performed by staunch advocates of the technology and/or they did not provide an “apples-to-apples” comparison of potential space storable propulsion systems to the system-level performance of other space storable concepts or conventional propulsion systems.

This study attempts to take a fresh and unbiased look at the potential for space storable propulsion by addressing the following questions:

- What are the attractive candidates for space storable propulsion systems, and what are their performance characteristics under a uniform set of assumptions?
- What propellant storage temperatures are truly obtainable by passive means without resorting to exotic or unproven technologies?
- What are the system-level performances of attractive space storable propellant combinations under a uniform set of assumptions?

In addressing the last of these questions, a further question arose:

- To what extent does advanced chemical propulsion have a role to play as the use of solar electric propulsion becomes more routine, and how might its utility be affected by the emergence of new technologies such as aerocapture?

The overall motivation behind this study is to provide guidance as to the limits, benefits, and possible methods of passively storing mild cryogenic propellants for deep space missions. In particular, this guidance is to be given in the context of the last question posed above.

B. Approach

The first step was to define candidate propellants and determine relevant properties that are required for evaluation of their performance in a propulsion system. This was accomplished primarily through brainstorming and literature searches. The intent was to cast a wide net and try to make sure that at least all major classes of propellant were addressed, although it was clearly not possible to address every possible propellant. This was followed by a down-select based on propellants which were clearly not space storable or had properties (such as easy detonability) which made their use in spacecraft propulsion extremely doubtful.

Once a set of candidate fuels and oxidizers were selected, propellant performance calculations were performed for all possible combinations of these fuels and oxidizers using the Two Dimensional Kinetics 1997 (TDK97) computer code which is described later in this report. Assumptions used in these calculations were held constant for all propellant combinations in an attempt to get a true “apples to apples” comparison. Once these results were obtained, the candidate propellant combinations were ranked using four different figures-of-merit (FOMs) which relate to expected system-level performance. One of these figures-of-merit, the “limiting ΔV FOM”, was judged to be the most likely to reflect actual system-level performance and that ranking was used in a final down-select for the system studies. Rather than simply selecting the n highest-ranked combinations, combinations were selected starting from the top of the list but taking account of unique storability issues and/or development histories.

In parallel with the first two efforts, a thermal storage analysis was conducted to provide guidance on feasible temperatures for passive space storage of propellants. This was done as a point design for propellant tanks of a fixed size and mass. Scaling relations were then developed to allow this model to be applied in the system performance assessments. A system-level performance analysis was then applied to the three outer planet missions described above. This assessment relied on a common set of assumptions for all propellant combinations except for the propellant performance, propellant properties (density and temperature) and thermal control requirements.

This paper is an abbreviated version of a final report that was produced.¹⁰

II. Candidate Propellants & their Relevant Properties

This section begins with a discussion of the candidate propellants initially chosen for this study. A brief overview of the qualitative reasoning for eliminating certain oxidizers and fuels from consideration follows. The section ends with a discussion of propellant properties.

A. Candidate Propellants

A list of 37 propellants was generated for preliminary consideration. Table 1 lists the candidate oxidizers for this study. Four oxidizers listed in Table 1 can also serve as monopropellants: H₂O₂, HAN/Glycine, HAN/MEO, and HAN/TEAN. Table 2 lists the candidate fuels for this study. Hydrazine is the only fuel listed in Table 2 that can also serve as a monopropellant. The oxidizers and fuels listed in Table 1 and Table 2, respectively, do not constitute a complete list of possible propellants. The oxidizers and fuels listed were initially chosen qualitatively from dozens to hundreds of potential propellants based on their heritage, use in previous design studies, or current development. The focus of this activity was liquid bipropellants. Solids, gels, and tripropellants were not considered.

B. Initial Propellant Down Select

Five oxidizers and five fuels were eliminated from consideration prior to any propellant performance predictions. This section provides a brief description on why each of the propellants was eliminated.

1. Oxidizers Eliminated

HNO₃, MON-10, MON-30, and RFNA were eliminated from consideration because they have similar or inferior properties to oxidizers that were kept in the pool for additional analysis. Both HNO₃ and RFNA are “represented” by

Table 1: Candidate Oxidizers

Name	Symbol or Abbreviation
Anhydrous Nitric Acid	HNO ₃
Bromine Pentafluoride	BrF ₅
Chlorine Pentafluoride	ClF ₅
Chlorine Trifluoride	ClF ₃
FLOX	82%F ₂ , 18%O ₂
Fluorine	F ₂
Hydrogen Peroxide	H ₂ O ₂
Hydroxylammonium Nitrate/Glycine	HAN/Glycine
Hydroxylammonium Nitrate /Methanol	HAN/MEO
Hydroxylammonium Nitrate /Triethanol Ammonium Nitrate	HAN/TEAN
Inhibited Red Fuming Nitric Acid	IRFNA
Mixed Oxides of Nitrogen 10	MON-10
Mixed Oxides of Nitrogen 25	MON-25
Mixed Oxides of Nitrogen 30	MON-30
Nitrogen Tetroxide (MON-3)	NTO or N ₂ O ₄
Oxygen	LOX or O ₂
Oxygen Difluoride	OF ₂
Perchloryl Fluoride	ClO ₃ F
Red Fuming Nitric Acid	RFNA
Tetrafluorohydrazine	N ₂ F ₄

Table 2: Candidate Fuels

Name	Symbol or Abbreviation
Acetylene (Ethyne)	C ₂ H ₂
Aerozine-50 (50% N ₂ H ₄ /50% UDMH)	A50
Alumizine	n/a
Benzene	C ₆ H ₆
Ethanol	C ₂ H ₅ OH
Ethylene	C ₂ H ₄
Hydrazine	N ₂ H ₄
Hydrogen	LH ₂
Hydyne (UDMH 60%/DETA ^a 40%)	MAF-4 or U-DETA
Kerosene	RP-1 or CH _{1.97}
Lithium (liquid)	LLi
Methane	CH ₄
Methanol	CH ₃ OH
Monomethyl Hydrazine	MMH
Pentaborane	B ₅ H ₉
Propane	C ₃ H ₈
Unsymmetric Dimethylhydrazine	UDMH

^aDETA = diethylenetriamine H(C₂H₄NH)₂NH₂

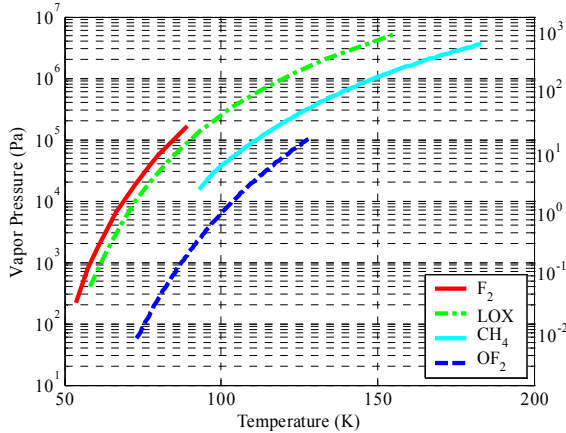


Figure 1: Vapor Pressures for Cryogenics & Near-Cryogen Propellants.

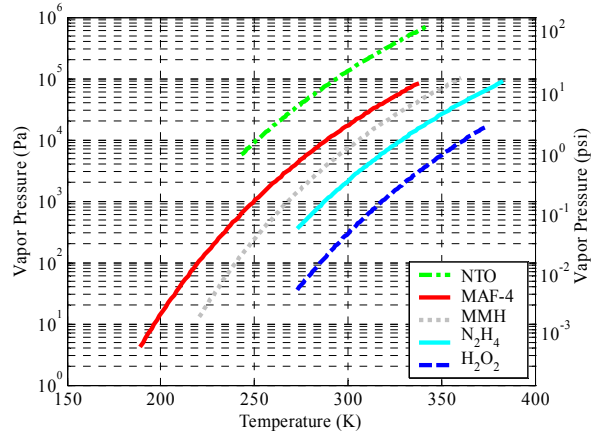


Figure 2: Vapor Pressures for Earth-Storable Propellants.

IRFNA, which was kept for additional investigation. Both MON-10 and MON-30 are “represented” by MON-25, which was also kept for additional investigation. For propellant combinations where either IRFNA or MON-25 proves to be a promising oxidizer, the eliminated oxidizers HNO_3 , MON-10, MON-30, and RFNA could be revisited. Finally, HAN/TEAN was ruled out because its development program has been terminated. It had poor performance (compared to the other two HAN based monopropellants listed in Table 1) and several unresolved issues.**

2. Fuels Eliminated

The reasons for eliminating the five fuels C_2H_2 , A50, alumizine, LH_2 , and LLi from further consideration are more varied. C_2H_2 is highly flammable, highly explosive fuel that is difficult to store in liquid phase and hence, not a credible propellant. A50 has similar properties to N_2H_4 and MMH, which were both kept for additional analysis. Alumizine contains 43% Al powder in a N_2H_4 gelling agent. The challenges of developing a set of leak-tight valves suitable for a long-life propulsion system when this much solid material is contained in the propellant was felt to make this fuel undesirable for such applications. Furthermore, performance predictions using the Two Dimensional Kinetic (TDK) software would not account for losses due to two-phase flow and hence would not be comparable to the other propellants. LH_2 was ruled out since it is not space storable by any passive means. Finally, LLi was eliminated from consideration since it is not space storable as a liquid due to its very high melting point.

C. Propellant Properties

Based on the qualitative elimination process previously described, 13 oxidizers and 12 fuels advanced to a full propellant combination analysis that is presented in the following section. Detailed properties such as density, heat of formation, melting point, boiling point, toxicity, and storability of these 25 propellants are provided in Ref. 10. Also listed in Ref. 10 are limited properties for the five oxidizers and five fuels that were not considered for further analysis.

An additional property of interest to this study is the vapor pressure of these propellants. Figure 1 plots the vapor pressure for several cryogenics and near-cryogen propellants as a function of temperature.^{11,12} Figure 2 plots the vapor pressure for Earth-storable propellants as a function of temperature.^{11,12,13} Neither tabular data nor an equation was available for determining the vapor pressure of ClF_5 . However, the vapor pressure of

Table 3: Vapor Pressure, Critical Temperature, and Critical Pressure for Several Propellants

Propellant	Vapor Pressure (kPa)	Critical Temperature (K)	Critical Pressure (MPa)
CH ₄	6.5 ^a	455.65	4.640
	190.7 ^b		
ClF ₅	339.9 ^c	416.15	5.516
F ₂	174.6 ^a	143.95	5.573
	1335.6 ^b		
H ₂ O ₂	0.2 ^c	732.15	21.684
LOX (O ₂)	98.7 ^a	154.35	5.036
	1013.2 ^b		
MAF-4 (U-DETA)	15.8 ^c	558.15	5.401
MMH	105.6 ^c	585	8.237
N ₂ H ₄	1.4 ^c	653	14.692
NTO (N ₂ O ₄)	96.2 ^c	431	9.928
OF ₂	2.0 ^a	213.45	5.016
	52.5 ^b		

^a90 K; ^b120 K; ^c293.15 K

**Reed, B., NASA Glenn Research Center, Cleveland, OH, e-mail correspondence (June – July 2003).

ClF_5 at 293 K (20 °C) is estimated to be 3.4 bar (49.3 psi).¹⁴ Table 3 provides the vapor pressure at temperatures of interest, the critical temperature, and critical pressure for several propellants.^{11-14,15} Vapor pressures are exploited in the mission and systems analysis that is discussed in the Mission & System Analysis section.

III. Propellant Combination Analysis

This section discusses the propellant combination analysis that was performed with Two Dimensional Kinetic 97 (TDK97) computer analysis program. The section begins with an explanation of the TDK analysis including assumptions, the method used, and a summary of results. A discussion of the various figures of merit that were used to compare the different propellant combinations follows. Based on these figures of merit, the various propellant combinations are ranked and down selected for further systems analysis.

A. Two Dimension Kinetics (TDK) Analysis

This section begins with a brief explanation of the Two Dimensional Kinetic (TDK) program. A detailed explanation of the assumptions used in the TDK analysis follows. A summary of results is then introduced. Reference 10 provides detailed tabular results and discusses the performance analysis performed on the HAN-based monopropellants that were considered.

1. Explanation of TDK

The Two Dimensional Kinetic (TDK) computer program is a primary tool in applying the JANNAF liquid rocket thrust chamber performance prediction method. Originally developed in the late 1960s, the code has undergone improvements and modifications in the decades since. For example, a Mass Addition Boundary Layer (MABL) module, which allows secondary exhaust products to be injected tangential to the primary flow, was added to the code in the 1990s.

As the name suggests, the TDK97 code represents the (February) 1997 release of the computer program.¹⁶ TDK97 estimates performance parameters such as specific impulse, thrust, mass flow rate, and thrust coefficient. In TDK, the theoretical specific impulse is calculated using the One-Dimensional Equilibrium (ODE) module which was adapted from the Chemical Equilibrium and Applications/Chemical Equilibrium and Transport (CEA/CET) codes.¹⁷ The ODE module is used to calculate the theoretical performance of the propellants at a given chamber pressure, mixture ratio and propellant energy content. A kinetic reaction file of the combustion products is not needed when using ODE. In fact, only limited thermodynamic data are needed for the propellants themselves, as they are treated as a source of enthalpy and atoms only.

The full JANNAF performance prediction method begins with an ODE calculation discussed. It then estimates the magnitude and interactions of various loss mechanisms that occur in a liquid rocket engine. Divergence, boundary layer, finite rate kinetics, mixture ratio maldistribution, and energy release are all losses that can be estimated by the TDK code. To estimate the kinetic losses, one of the major sources of performance loss, kinetic reaction files are needed for all of the constituents of the combustion products. If these reaction files are not available, only an ODE calculation is possible. TDK97 is discussed in detail in Ref. 16.

2. TDK Assumptions

TDK97 requires an input file to execute. A typical input file with a brief explanation of each input parameter is presented in Ref. 10. A more detailed explanation of all input parameters can be found in Ref. 16.

For all propellant combination cases, a reference nozzle throat radius of 8.81 mm (0.347 inches) and a parabolic wall profile were assumed. All combinations assumed a combustion chamber pressure of 1.03 MPa (150 psia) and a nozzle area ratio of 100:1. No effort was made to optimize the nozzle design for each propellant combination. These assumptions yielded a total thrust level of approximately 450 N (~100 lbf) for all combinations. The major differences among input files for the vast majority of various propellant combinations investigated occurs in the REACTANTS/REACTIONS section of the input file where the propellants are listed, the mixture ratio of oxidizer to fuel is specified, and the appropriate reaction set is included.

The appropriate kinetic reaction set for each propellant combination is based on the combustion elements. The TDK97 software package provides 12 of these reaction sets. For example, if the combustion elements include hydrogen (H), nitrogen (N), and oxygen (O), as in the propellant combination nitrogen tetroxide/hydrazine (NTO/ N_2H_4) the system10.dat reaction set is used. Several propellant combinations of interest used reaction sets that were not among these 12 provided with TDK97. However, each of these reaction sets was created (simplified) from the most general reaction set (system12.dat). In total, five new reaction set files were created. These five newly created reaction sets are provided in their entirety in Ref. 10.

B. TDK Propellant Combination Results

Since 13 oxidizers and 12 fuels were down selected for performance analysis, a total of 156 propellant combinations are possible. Each propellant combination was analyzed by varying the mixture (oxidizer-to-fuel) ratio to find the optimal (maximal) specific impulse. In some cases, only a few TDK runs were required to hone in on this optimal mixture ratio. In other cases, a dozen or more TDK runs were required. Each TDK run lasts from a few seconds to a few minutes. All runs were performed on a 1 GHz Toshiba Satellite Pro Pentium III computer with 512 Mbytes of RAM. A summary of these specific impulse results (to the nearest mixture ratio tenth or twentieth) is provided in Table 4.

Reference 10 also provides a summary of the combustion chamber temperature results (to the nearest tenth of a Rankine). Several propellant combinations yield combustion chamber temperatures greater than the melting point of typical combustion chamber materials. For example, FLOX/MMH reaches over 3900 K (~7500 °R) in the combustion chamber. State-of-the art (rhenium/iridium) materials for combustion chambers cannot exceed approximately 2400 K (4300 °R). However, rocket engines are routinely built from materials which can not withstand the full adiabatic flame temperature and cooled by radiation, fuel film cooling, or regenerative cooling. An assessment of engine cooling was considered beyond the scope of the present study.

Sixteen propellant combinations involving carbon, fluorine, and hydrogen gave the TDK computer program problems. These propellant combinations are underlined in Table 4. When analyzing these propellant combinations, the TDK program terminated prematurely during the ODE calculations before results were obtained, usually giving a SINGULAR MATRIX warning. This problem was avoided by using the full thermodynamic properties set (THERMO = 'THERMO.DAT') instead of an abbreviated set that the TDK program typically uses for convenience and to reduce run times. Using the full thermodynamic properties set often increased the time of each TDK run (particularly for propellant combinations with high mixture ratios) but did not impact the results significantly. This was verified by comparing the TDK results of propellant combinations that were able to run with both the abbreviated and full thermodynamic properties set.

TDK runs with propellant combinations involving either bromine pentafluoride (BrF₅) as the oxidizer or pentaborane (B₅H₉) as the fuel were scaled from the ODE result. Table 4 bolds these propellant combinations.

Table 4: Summary Matrix of TDK Results for Specific Impulse

	MAF-											
	C ₆ H ₆	C ₂ H ₅ OH	C ₂ H ₄	N ₂ H ₄	4	CH ₄	CH ₃ OH	MMH	B ₅ H ₉	C ₃ H ₈	CH _{1.97}	UDMH
BrF ₅	243.6	249.7	265.1	282.4	263.3	259.3	250.1	271.5	255.2	257.7	253.8	267.3
	@2.5	@4.2	@3.5	@1.9	@3.7	@7.6	@4.0	@2.1	@2.7	@5.7	@4.4	@2.6
ClF ₅	287.8	254.6	313.9	333.6	286.7	315.6	308.9	314.8	318.3	311.5	305.8	299.4
	@1.8	@1.0	@2.85	@2.8	@1.9	@5.3	@2.9	@2.5	@5.9	@4.0	@3.2	@2.3
ClF ₃	271.8	239.8	298.5	313.6	264.4	297.6	286.0	293.2	296.8	294.1	288.6	277.1
	@1.9	@1.0	@2.9	@2.4	@1.9	@5.5	@3.0	@2.6	@6.7	@4.1	@3.3	@2.4
FLOX	206.8	359.0	307.3	370.8	366.4	371.6	350.4	376.1	371.8	335.4	290.6	372.0
	@6.9	@2.6	@6.3	@1.5	@2.4	@4.3	@2.1	@2.4	@3.8	@6.0	@6.4	@2.4
F ₂	316.6	303.0	347.4	384.3	341.3	356.4	360.9	365.2	366.0	348.7	340.6	351.7
	@1.3	@0.8	@2.0	@1.9	@1.5	@3.1	@2.05	@1.8	@4.0	@2.7	@2.2	@1.8
H ₂ O ₂	312.7	310.1	323.5	326.3	319.6	320.7	306.6	323.7	346.6	318.8	316.3	322.4
	@5.2	@3.8	@5.55	@1.8	@3.8	@7.1	@2.8	@2.95	@2.9	@6.3	@5.9	@3.6
IRFNA	290.5	290.3	305.1	315.5	302.8	301.8	287.8	309.3	325.9	299.2	295.6	306.5
	@3.8	@2.9	@4.1	@1.3	@2.8	@5.4	@2.1	@2.25	@2.9	@4.75	@4.5	@2.7
MON-25	304.7	305.7	321.5	330.5	318.9	320.5	302.7	325.2	333.6	316.4	311.8	322.6
	@3.25	@2.5	@3.5	@1.2	@2.45	@4.65	@1.9	@1.95	@3.0	@4.1	@3.8	@2.35
NTO	300.6	301.7	317.8	327.6	315.2	316.4	298.7	321.9	331.2	312.4	307.7	319.1
	@3.2	@2.4	@3.4	@1.2	@2.4	@4.5	@1.8	@1.9	@2.9	@3.95	@3.65	@2.3
O ₂	324.1	324.9	346.5	349.1	340.5	347.9	319.6	346.6	356.8	341.4	334.7	344.7
	@2.1	@1.6	@2.25	@0.8	@1.6	@3.0	@1.25	@1.3	@1.9	@2.6	@2.4	@1.5
OF ₂	303.9	355.8	364.9	370.1	370.6	378.0	348.7	371.9	379.3	375.4	356.8	373.0
	@4.2	@2.45	@3.9	@1.3	@2.5	@4.5	@1.85	@2.05	@3.5	@3.9	@3.9	@2.4
ClO ₃ F	312.9	299.0	295.1	325.8	311.5	312.8	297.3	318.7	324.2	308.2	303.2	315.3
	@3.65	@2.6	@3.35	@1.2	@2.5	@4.8	@1.9	@2.0	@3.3	@4.2	@3.9	@2.4
N ₂ F ₄	303.5	318.7	190.8	356.8	321.1	325.2	335.2	339.8	342.0	262.6	165.8	328.1
	@1.8	@2.7	@3.7	@2.7	@2.4	@4.7	@2.9	@2.5	@6.0	@3.5	@3.7	@2.5

The ODE result was used since a full TDK analysis was not possible due to unavailable kinetic reaction sets. An ODE run using the TDK97 software entailed setting the input variables ODK, TDK, MABL, and IMABL to 0 and the input variable MABLK to F. The other difference between an ODE input file and a typical TDK input file would be the lack of kinetic reaction set data with only the four lines REACTIONS, LAST REAX, THIRD BODY REAX RATE RATIOS, and LAST CARD remaining. Although the ODE run provides a good indicator of the location of the mixture ratio for optimal specific impulse, the ODE prediction is not identical to that of a full TDK run. For example, an ODE run for LOX/MMH indicates the optimal mixture ratio (for specific impulse) is 1.1 while a full TDK run concludes the optimal mixture ratio is 1.3. Hence, the “optimal” mixture ratio of an ODE analysis is not guaranteed to coincide with what TDK would have predicted but analyses completed indicate ODE is typically within 20% of the “optimal” mixture ratio. The performance and optimal mixture ratio is also expected to vary with chamber pressure. As was mentioned earlier, this study held the chamber pressure constant at 1.03 MPa (150 psia).

Scaling the actual ODE result to provide a full “TDK like” result entailed:

- 1) Finding the frozen specific impulse (where chemical reactions are assumed to halt at the nozzle throat) from the TDK output of all propellant combinations other than those involving BrF₅ or B₅H₉.
- 2) Calculating the ratio of this frozen specific impulse to the full TDK specific impulse (this ratio ranged from ~0.962 to ~1.021).
- 3) Taking the average of this ratio across all fuels for each oxidizer (for B₅H₉) and all oxidizers for each fuel (for BrF₅) (this ratio ranged from ~0.971 to ~1.003).
- 4) Dividing the frozen specific impulse from the ODE output for the relevant propellant combination by the average ratio determined in step 3.

For example, the frozen specific impulse of MON-25 with all twelve fuels is summarized in Table 5 along with the full TDK specific impulse and the corresponding ratio of the two.

The average of the final column is ~0.9803. Hence, the scaled specific impulse for MON-25/B₅H₉ is 327.0 lbf-s/lbm divided by 0.9803 or 333.6 lbf-s/lbm. This is the best estimate of the full TDK performance of MON-25/B₅H₉ from the frozen ODE result and existing performance data of MON-25 with other fuels. Other propellant combinations (including those with BrF₅) were scaled in a similar manner.

It is apparent from Table 4 that BrF₅ is a very poor oxidizer. Combined with the fact that only ODE results were available, BrF₅ was eliminated from further consideration. B₅H₉, however, appears to be a very promising fuel although very high combustion chamber temperatures (~5000 to ~8000 °R) raise questions about the feasibility of using this fuel. Due to these temperature concerns and the fact the performance of propellant combinations using B₅H₉ could not be verified, it also was eliminated from further consideration. Furthermore, propellant combinations including B₅H₉ produce two-phase reaction products, complicating performance assessments. The development of kinetic reaction rate sets for both BrF₅ and B₅H₉ are recommended to verify the accuracy of the scaled results presented in this report. If the performance can be verified, B₅H₉ should be investigated with various oxidizers in a full mission and systems analysis.

The theoretical performance (including kinetic, two-dimensional, and boundary layer losses) of all results was reduced 2% to account for an assumed 98% combustion efficiency (i.e., vaporization and mixing efficiency). There may be practical limitations imposed by chamber cooling and/or two-phase flow effects that might prevent the performances computed from actually being attained in a practical rocket since no effort was made to optimize the nozzle design.

C. Figures of merit to compare results

The following section describes five figures of merit that were used to compare the results of the TDK runs summarized in Table 4. These figures of merits were used to select a subset of propellants most likely to yield the highest usable payload in the system studies for more detailed analysis. Reference 10 provides detailed tabular

Table 5: MON-25 Frozen and Full Specific Impulses

Fuel	Frozen Specific Impulse at the Nozzle Throat (lbf-s/lbm)	Full TDK Specific Impulse (lbf-s/lbm)	Ratio of Frozen Specific Impulse to Full TDK Specific Impulse (-)
C ₆ H ₆	297.3	304.7	0.975608
C ₂ H ₅ OH	300.4	305.7	0.982532
C ₂ H ₄	313.5	321.5	0.975236
N ₂ H ₄	326.6	330.5	0.988160
MAF-4	312.4	318.9	0.979750
CH ₄	314.3	320.5	0.980658
CH ₃ OH	298.5	302.7	0.986115
MMH	319.2	325.2	0.981452
B ₅ H ₉	327.0	n/a	n/a
C ₃ H ₈	309.4	316.4	0.977861
CH _{1,97}	304.4	311.8	0.976398
UDMH	316.0	322.6	0.979524

results of all the figure of merits discussed.

1. Specific impulse

Historically, specific impulse has been the primary figure of merit to compare propellant combinations. Specific impulse has two complementary definitions: the change in total impulse per unit mass and the thrust per mass flow rate.

$$I_{sp} = \frac{I_t}{m_{prop} \cdot g_c} = \frac{F}{b \cdot g_c} \quad (1)$$

Specific impulse is typically quoted in lbf-s/lbm (often abbreviated as simply seconds). From the rocket equation it is apparent that the higher the specific impulse the better since a higher change in velocity can be achieved (or less propellant is required for an equivalent change in velocity):

$$\Delta V = g_c \cdot I_{sp} \cdot \ln \frac{m_i}{m_f} \quad (2)$$

The primary benefits of using the specific impulse as a figure of merit are its theoretical simplicity and ubiquity in aerospace education. The most significant drawback of using the specific impulse as a figure of merit are the fact that it is not a reliable parameter for ranking the performance of propulsion systems using different propellants. The specific impulse of a propellant combination tells nothing of the density, handling, thermal limitations, or toxicity of the propellants being used. In designing and building actual propulsion flight systems and integrating them into a spacecraft, these issues are often as important if not more important than the specific impulse. Figure 3 compares the top ten propellant combinations based on (de-rated) specific impulse.

2. Average density

The average density figure of merit is defined as the average density of the propellant combination at the mixture ratio of interest:

$$\rho_{ave} = \frac{(1 + MR) \cdot \rho_{ox} \cdot \rho_{fuel}}{(\rho_{ox} + MR \cdot \rho_{fuel})} \quad (3)$$

The average propellant density is significant in that propellants having lower density will require larger, heavier tanks and pressurization systems. Therefore, it is possible for a propellant combination that delivers high specific impulse to have poor overall system performance if it has low average density (pressure-fed liquid oxygen and hydrogen is the consummate example). The primary benefits of using the average density as a figure of merit are its simplicity and practicality. The primary drawback of using the average density as a figure of merit is the fact that it tells nothing of the performance of the propellant combination of interest besides incorporating the mixture ratio. On

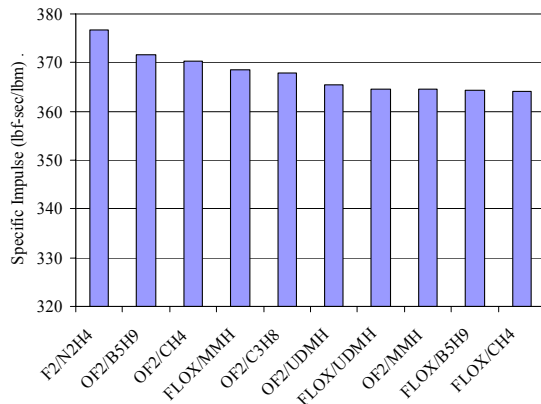


Figure 3: Top Ten Propellant Combinations Based on Specific Impulse.

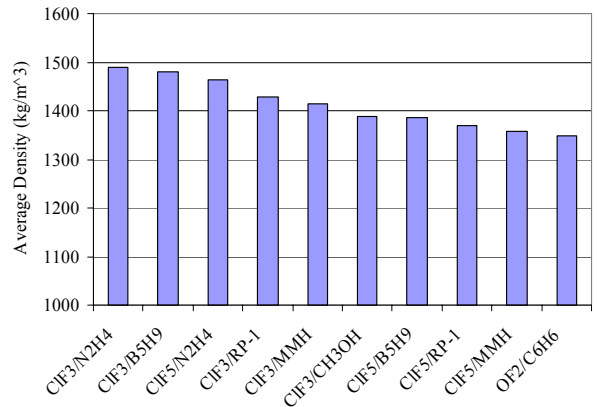


Figure 4: Top Ten Propellant Combinations Based on Average Density.

its own it is not a credible figure of merit but when combined with the specific impulse provides a more comprehensive figure of merit (see the sections that follow). Figure 4 compares the top ten propellant combinations based on average density.

3. Guernsey-Rapp Figure of Merit

In 1988 C. Guernsey and D. Rapp of the Jet Propulsion Laboratory (JPL) proposed a new propulsive figure of merit.¹⁸ This figure of merit was intended to introduce propellant density and produce a “specific impulse-like” figure of merit. This figure of merit, hereafter referred to as the Guernsey-Rapp FOM, is defined as the derivative of propulsion system total impulse with respect to propulsion system mass:

$$FOM_{GR} = \frac{dI_t}{dm_{prop_wet}} \quad (4)$$

The Guernsey-Rapp FOM assumes that the propulsion system dry mass is linearly related to the propellant volume:

$$m_{prop_dry} = c_1 + c_2 \cdot V_{prop} \quad (5)$$

The propulsion system wet mass is therefore:

$$\begin{aligned} m_{prop_wet} &= m_{prop_dry} + m_{prop} \\ &= (c_1 + c_2 \cdot V_{prop}) + m_{prop} \\ &= \left(c_1 + c_2 \cdot \frac{m_{prop}}{\rho_{ave}} \right) + m_{prop} \\ m_{prop_wet} &= c_1 + m_{prop} \left(1 + \frac{c_2}{\rho_{ave}} \right) \end{aligned} \quad (6)$$

The Propulsion System Design Tool (PSDT, see the section entitled “Mission & System Analysis”) was used to estimate the values of c_1 and c_2 for two typical Earth storable bipropellant systems using two different propellant tank technologies. The PSDT was used to generate curves of propulsion system wet mass as a function of propellant mass. The analysis was performed on both an NTO/MMH and an NTO/N₂H₄ system. Figure 5 shows the propulsion system wet mass as a function of propellant mass for both titanium and composite overwrapped pressure vessel (COPV) tank technologies.

Equation (6) can be rewritten as

$$m_{prop_wet} = c_1 + m_{prop} \cdot \beta \quad (7)$$

The constants c_1 and β can then be derived from the data generated by the PSDT, shown in Fig. 5. c_1 is then calculated from β by using the following equation:

$$c_2 = \rho_{ave} \cdot (\beta - 1) \quad (8)$$

Table 6 summarizes the results for the two systems studied. The PSDT predicts a linear relationship between propulsion system wet mass and propellant mass, as expected. For a given tank technology, there is only about a 3% difference in c_2 between the two propellant combinations.

The values of c_2 were then averaged for each tank technology resulting in a c_2 of 103.3 kg/m³ for titanium propellant tanks and 63.4 kg/m³ for COPV propellant tanks. These values were used to calculate the

Table 6: Derived Constants of the Guernsey-Rapp FOM for Four Propulsion System Types

System	Tank Type	c_1 (kg)	c_2 (kg/m ³)
NTO/MMH	Ti	35.0	101.6
NTO/N ₂ H ₄	Ti	34.7	104.9
NTO/MMH	COPV	32.4	62.4
NTO/N ₂ H ₄	COPV	32.5	64.4

Guernsey-Rapp FOM for all propellant combinations studied. In reality, the general application of these values of c_2 to all propellants is not accurate. For example, spacecraft using cryogenic propellants must use significant thermal hardware to isolate the tanks. The mass of this hardware depends on both the tank volume and propellant mass (see the section entitled “Thermal Storage Analysis”). Therefore, these systems will tend to have a higher c_2 and a lower Guernsey-Rapp FOM than Earth storable systems with comparable specific impulses. However, the intent here is to broadly sort the propellant combinations to select a subset for more detailed analysis. The results of a more rigorous analysis are compared in the section entitled “Mission & System Analysis” to this broad application of c_2 in the Guernsey-Rapp FOM.

Returning to equation (6) which can be solved for the propellant mass:

$$m_{prop} = \left(\frac{1}{1 + c_2 / \rho_{ave}} \right) (m_{prop_wet} - c_1) \quad (9)$$

Expressing the total impulse as a function of the propellant mass:

$$I_t = m_{prop} \cdot I_{sp} \quad (10)$$

Hence, the Guernsey-Rapp FOM is:

$$\begin{aligned} FOM_{GR} &= \frac{dI_t}{dm_{prop}} \frac{dm_{prop}}{dm_{prop_wet}} \\ &= I_{sp} \cdot \left(\frac{1}{1 + c_2 / \rho_{ave}} \right) \\ FOM_{GR} &= \frac{I_{sp}}{1 + c_2 / \rho_{ave}} \end{aligned} \quad (11)$$

The primary benefit of the Guernsey-Rapp FOM is that it accounts for both specific impulse and average propellant density in a nonarbitrary manner. The primary drawback of the Guernsey-Rapp FOM is that the meaning of figure of merit is not entirely clear: how does overall system performance correlate with the derivative of impulse with respect to wet mass? Figure 6 compares the top ten propellant combinations based on the Guernsey-Rapp FOM for both titanium and composite overwrapped pressure vessel (COPV) propellant tanks. COPVs are assumed for the pressurant tanks in all cases.

It is worth noting the rankings of propellants according to the Guernsey-Rapp FOM are rather insensitive to the coefficient c_2 . That is to say, although the absolute value of the FOM is different for titanium and COPV propellant tanks as shown in Fig. 6, the relative rankings of the various propellant combinations are essentially the same.

4. Limiting ΔV Figure of Merit

In an attempt to overcome some of the limitations of the figures of merit previously discussed, a new figure of merit was developed to represent the maximum ΔV that could be obtained using a given propellant combination. The assumption was made that the propulsion system dry mass is linearly dependent on propellant volume as given by equation (5) introduced earlier. Substituting equation (6) into the rocket equation for a purely propulsive system (neglecting payload) yields:

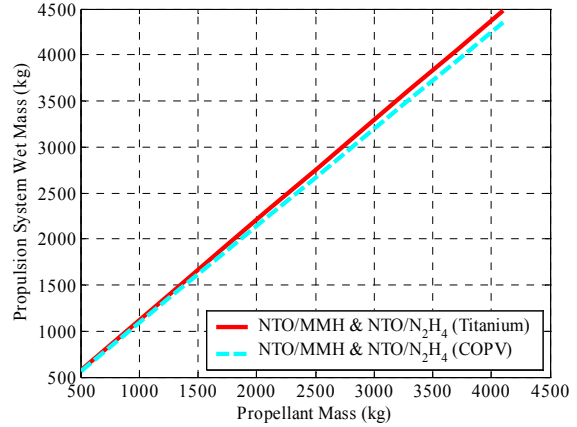


Figure 5: Propulsion System Wet Mass as a Function of Propellant Mass for Typical Bipropellant Systems.

$$\begin{aligned}
\Delta V &= g_c \cdot I_{sp} \cdot \ln \frac{m_i}{m_f} \\
&= g_c \cdot I_{sp} \cdot \ln \frac{m_{prop_wet}}{m_{prop_dry}} \\
\Delta V &= g_c \cdot I_{sp} \cdot \ln \frac{c_1 + m_{prop} \left(1 + \frac{c_2}{\rho_{ave}} \right)}{c_1 + c_2 \cdot \frac{m_{prop}}{\rho_{ave}}}
\end{aligned} \tag{12}$$

Taking the limit as the propellant mass goes to infinity yields:

$$\begin{aligned}
\Delta V_{max} &= \lim_{m_{prop} \rightarrow \infty} g_c \cdot I_{sp} \cdot \ln \frac{c_1 + m_{prop} \left(1 + \frac{c_2}{\rho_{ave}} \right)}{c_1 + c_2 \cdot \frac{m_{prop}}{\rho_{ave}}} \\
\Delta V_{max} &= g_c \cdot I_{sp} \cdot \ln \left(1 + \frac{\rho_{ave}}{c_2} \right)
\end{aligned} \tag{13}$$

Normalizing this value by the constant g_c yields the limiting ΔV FOM:

$$\begin{aligned}
FOM_{lim_AV} &= \frac{\Delta V_{max}}{g_c} \\
FOM_{lim_AV} &= I_{sp} \cdot \ln \left(1 + \frac{\rho_{ave}}{c_2} \right)
\end{aligned} \tag{14}$$

The benefit of this FOM is that its interpretation is unambiguous. Under the assumption given in equation (6) it represents the maximum ΔV that can be obtained with a single-stage propulsion system as propellant mass goes to infinity. It is to be expected that the ability of propellant combinations to deliver a usable payload with a finite quantity of propellant would follow a similar ranking. The major drawback of this figure-of-merit is that it does not introduce “real world” effects such as the impact of propellant storage temperature on pressurization system mass. However, it was judged adequate to assist in rationally selecting propellant combinations for study at the system level where these effects could be accounted for.

Figure 7 compares the top ten propellant combinations based on the limiting ΔV FOM for both titanium and COPV propellant tanks. The same values for c_2 were applied to limiting ΔV FOM as in the Guernsey-Rapp FOM.

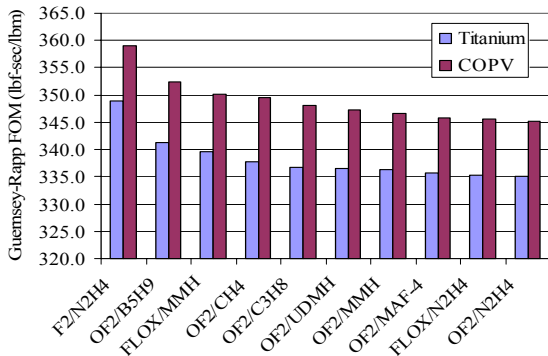


Figure 6: Top Ten Propellant Combinations Based on the Guernsey-Rapp FOM.

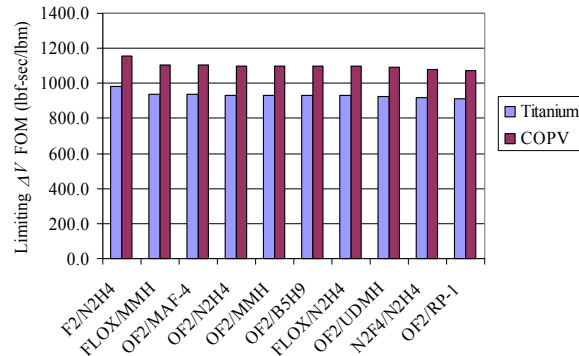


Figure 7: Top Ten Propellant Combinations Based on the Limiting ΔV FOM.

Consequently, this general application of a single value of c_2 to all propellant combinations is also inaccurate. However, it is only applied here to select a subset of promising propellant combinations for more detailed analysis (see the section entitled “Mission & System Analysis”).

5. Density specific impulse

The density specific impulse is defined as the product of the average density and specific impulse (which were defined earlier):

$$I_{\rho_sp} = \rho_{ave} \cdot I_{sp} \quad (15)$$

The primary benefit of using the density specific impulse as a figure of merit is its accounting of both the specific impulse and average density of a propellant combination (arguably the two most important parameters). The density specific impulse is also widely used in industry. The primary drawback of using the density specific impulse as a figure of merit is the arbitrariness of simply multiplying these two parameters. The relative importance of these two parameters is simply assumed to be equal, which the preceding discussions illustrate is not necessarily the case. Figure 8 compares the top ten propellant combinations based on density specific impulse.

D. Rankings and Down Select

The rankings summarized in Fig. 3 through Fig. 8 indicate several propellant combinations that are worthy of further analysis. A total of ten were selected for a full mission and systems analysis. Three propellant combinations, F_2/N_2H_4 , $OF_2/MAF-4$, and OF_2/N_2H_4 , have high rankings in most of the figures of merit presented. Three propellant combinations ClF_5/N_2H_4 , H_2O_2/N_2H_4 , and LOX/MMH , have high potential and interesting characteristics. Four propellant combinations, LOX/N_2H_4 , NTO/MMH , NTO/N_2H_4 , and LOX/CH_4 , represent current state-of-the-art, have existing development programs, or have been the topic of possible development programs. The rankings of these ten propellant combinations by the various figures of merit discussed are presented in Table 7 below.

Noticeably absent from Table 7 are the oxidizers IRFNA, MON-25, and ClO_3F and the fuels C_2H_5OH and C_2H_4 . Propellant combinations using these propellants provided poor performance in virtually all rankings. Each of the ten propellant combinations that were selected for a full mission and systems analysis is described briefly below:

1. F_2/N_2H_4

This combination was actively studied until the early 1980s. It provides extremely high specific impulse combined with high density yielding the highest ranking in four of the five figures of merit. Unfortunately, it suffers from significant safety concerns related to the extreme reactivity of the fluorine oxidizer. However, there exists a very significant body of work addressing material compatibility issues and ground safety issues from the NASA technology programs in the 1970s and early 1980s and from Air Force work conducted during the 1980s.²⁻⁹ Storing LF_2 passively at 120 K requires a pressure in excess of 1.3 MPa (188 psi).

2. $OF_2/MAF-4$

This propellant combination shares many of the positive and negative characteristics of F_2/N_2H_4 but offers better storability for both the oxidizer and fuel. However, OF_2 is not established oxidizer and $MAF-4$ has not been used significantly since the early space program in the 1960s. It is worth noting that OF_2 can be stored at 120 K at a pressure under 100 kPa (15 psi) to quantify the advantage over LF_2 .

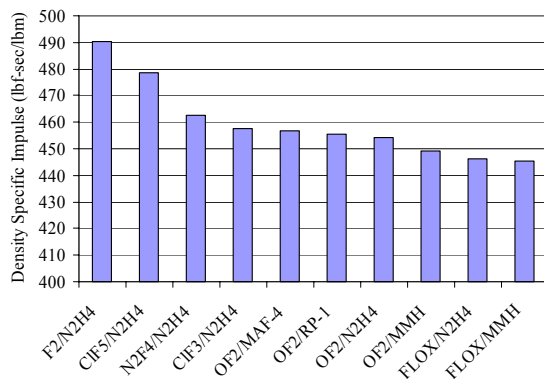


Figure 8: Top Ten Propellant Combinations Based on Density Specific Impulse.

Table 7: Summary of Propellant Combination Rankings

Propellant Combination	I_{sp}	ρ_{ave}	FOM_{GR}	$FOM_{lim \Delta V}$	I_{ρ_sp}
F_2/N_2H_4	1	21	1	1	1
$OF_2/MAF-4$	12	32	8	3	5
OF_2/N_2H_4	13	36	11	5	7
ClF_5/N_2H_4	45	3	41	22	2
H_2O_2/N_2H_4	51	40	51	40	37
LOX/MMH	32	135	32	44	110
LOX/N_2H_4	27	124	28	32	84
NTO/MMH	63	77	61	60	69
NTO/N_2H_4	50	59	50	41	48
LOX/CH_4	30	144	39	100	138

3. OF_2/N_2H_4

This propellant combination is very similar to the $OF_2/MAF-4$ propellant combination previously discussed. This combination is attractive from a systems perspective since it does provide for the possibility of a N_2H_4 monopropellant system, albeit at the cost of a much higher fuel freezing temperature (~ 275 vs. ~ 189 K).

4. ClF_3/N_2H_4

This propellant combination is readily storable in flight and on the ground. It offers both higher specific impulse and higher density than conventional storable propellants. The oxidizer can be passively stored at Earth ambient conditions, eliminating the need for ground cooling provisions required by the mild cryogenics such as F_2 . This propellant combination was considered for Strategic Defense Initiative (SDI) systems in the 1980s and there is some technology base on which to build. However, it does suffer from the high freezing point of hydrazine. Furthermore, there is no current U.S. source of production for the oxidizer.

5. H_2O_2/N_2H_4

This propellant combination offered a surprisingly high FOM. Furthermore, it has the advantage of being able to use either propellant as a monopropellant for reaction control of the spacecraft. The long-term storage of H_2O_2 without decomposition is a significant challenge. Propellant calculations in this document refer to 100% H_2O_2 , while typically the highest commercial purity is on the order of 70%.

6. LOX/MMH

This propellant combination provided the highest limiting ΔV FOM for a propellant combination that uses LOX as the oxidizer. Both these propellants are very well established and understood.

7. LOX/N_2H_4

This combination was considered because there has been recent work at two rocket engine companies to develop engines using these propellants. In particular, the TRW Space & Technology division in Redondo Beach, CA (now part of Northrop Grumman) achieved a specific impulse in excess of 353 lbf-s/lbm at a mixture ratio of ~ 0.8 for a 900 N (200 lbf) class engine.¹⁹ As with previous combinations mentioned, it is somewhat penalized by the relatively high (~ 275 K) freezing point of the hydrazine.

8. NTO/MMH

This combination represents state-of-the-art for chemical propulsion. The conventional storable propellant combination of NTO and MMH has flown hundreds of times in space since its development early in the space program. Engines built by several vendors exist at various thrust levels for this propellant combination. The performance achieved by an actual NTO/MMH 445 N main engine is ~ 324 lbf-s/lbm at a mixture ratio of 1.65.²⁰ This specific impulse is higher than the de-rated TDK result obtained in this study (315.5 lbf-s/lbm at 1.9). Nonetheless, the TDK result was used in the subsequent mission and systems analysis to be consistent with the remainder of the propellant combinations investigated.

9. NTO/N_2H_4

This combination also represents state-of-the-art chemical propulsion. Although a more recent propellant combination development than NTO/MMH, this combination is now well established from its successful use in the Lockheed-Martin A2100 line of spacecraft and several well publicized deep-space missions (Mars Global Surveyor, NEAR, Mars Odyssey, etc.). Several engines exist in the 445 N class for this propellant combinations. The performance achieved by an actual NTO/ N_2H_4 445 N main engine is greater than 324 lbf-s/lbm at a mixture ratio of ~ 0.85 .²¹ This specific impulse is higher than the de-rated TDK result obtained in this study (321.0 lbf-s/lbm at 1.2). Nonetheless, the TDK result was used in the subsequent mission and systems analysis to be consistent with the remainder of the propellant combinations investigated.

10. LOX/CH_4

This propellant is often discussed in literature.^{22,23,24} Liquid oxygen and methane are logical propellant choices for in-situ propellant production missions to Mars based on the Sabatier/Electrolysis (S/E) process, since both propellants can be produced from the Martian atmosphere provided hydrogen is available.²⁵ This propellant combination suffers from a very low limiting ΔV FOM that needs to be examined in detail.

IV. Thermal Storage Analysis

The following section describes the assumptions and analysis method for thermal control of advanced space storable propellants.

A. History of Space Storable Propellant

Since space flight began in the late 1950's, propellant storage on spacecraft for attitude control and ΔV requirements has been an issue. Earth storable propellants, though storable at temperature levels around room

temperature, have relatively stringent temperature level and stability requirements. The driving requirement for the most common propellants in use today is maintaining a minimum temperature above the propellant's freezing point. Propellants are in general not allowed to freeze in order to allow maneuvers and reaction control throughout the mission and to prevent bursting of propellant lines or components due to uncontrolled thawing. As an example, the flight allowable temperature level for hydrazine (N_2H_4) is between ~ 276 to ~ 318 K ($+3$ to $+45$ °C). To preclude propellant freeze, most thermal control designs set the lower temperature at 10 K (10 °C) above the freeze temperature, at 286 K ($+13$ °C). Other propellants such as monomethyl hydrazine (MMH) and nitrogen tetroxide (NTO) have an allowable temperature ranges that go below 273 K (0 °C). Upper allowable temperature ranges are often determined by the limitations of the test facilities in which the hardware is qualified, although there can be real limitations introduced by thermal stability of rocket engines or the chemical stability of the propellants themselves. Typical upper allowable flight temperature ranges for storable propellants range from 318 to 333 K (45 to 60 °C). These are rarely driving requirements for the thermal control of the propellants. Thermal control of these propellants is accomplished using a combination of tank heaters and multilayer insulation (MLI). In some cases waste heat from spacecraft electronics or power systems can be used to minimize the electrical power required to avoid propellant freezing.

B. Future Space Storable Thermal Design/Hardware

Future missions may benefit from the use of advanced propellants, which provide increased specific impulse and/or density when compared to conventional storable propellants. Advanced low-temperature storage will be required for many of these propellants. An initial evaluation has been done which concludes that a passive system can be developed to store propellants at about 120 K (-153 °C) using existing technology.

Passive storage of propellant at 120 K (-153 °C) for long periods is feasible, but unproven and non-trivial. This goal presents many challenges in thermal isolation and control that will require substantial development. One example is the mechanical support structure and mechanisms required for large tanks and isolation required for the lines. The requirement to support the tank and lines for launch loads, both acceleration and vibration requires sufficient structure, which in general implies relatively large mechanical support systems with potentially large conducted thermal loads.

The following is a baseline for propellant system evaluation. Figure 9 shows a schematic representation of the basic tank thermal control concept. The baseline was used to size the thermal subsystem for the propulsion module, which was then scaled based on tank size, mass, and area. The baseline assumed for this evaluation is a one-meter diameter propellant tank. This tank is supported at the top and bottom with a large boss, through which are fill and drain lines. The support structure is assumed to be tube struts. For stability, it is assumed that the supports are one bi-pod mount and one tripod mount. The struts are made of titanium and have a length on the order of 75 cm, are about 5 cm in diameter, and have a wall thickness of 0.075 cm. This tank is assumed to be mounted in a dedicated propulsion module, with clearances for tank installation and radiant heat transfer around the tanks. This assumption is used to determine the surface area of the propulsion module so that the environmental heating and thermal losses can be calculated. For a bipropellant module there will be two propellant tanks, and two pressurant tanks. For the 1 m tanks assumed in the reference design, this leads to a propulsion module about 2.5 meters in diameter and a height of about 1.5 meters.

The storage of most cryogenic propellants at or below their normal boiling point would require the development of systems that provide storage temperatures below 100 K (-173 °C). As an example, a liquid oxygen (LOX) storage

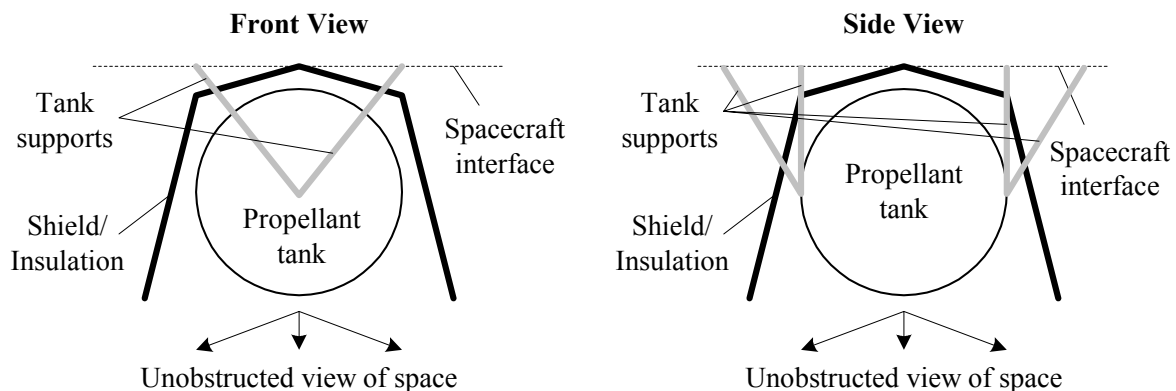


Figure 9: Propellant Tank Thermal Control Concept Sketch.

tank will have to be held at a temperature level of ~80 K unless the LOX is stored at an elevated pressure. While current Dewar technology holds its working fluid at temperatures less than 20 K, all these systems provide limited operational times. An example is the Space Infrared Telescope Facility (SIRTF), which has a large cryogenic Dewar, but has a total mission life of 30 months. Cruise times for outer planet missions are on the order of many years. An example is the current Cassini mission and the future Jupiter Icy Moons Orbiter (JIMO) mission, which have transit times on the order of 5 or more years. While it may be possible, with improvements in technology, to lower the threshold for passive storage below 120 K, it is clear that long-term storage with zero boil-off at temperatures as low as 20 K (-253 °C) will require the use of active cooling systems.

However, as previously stated, the evaluation of technology extension utilizing current knowledge of materials and design, the lowest temperature practical for a passive thermal control system is on the order of 120 K (-153 °C). In order to bridge this gap between the normal boiling point of attractive propellants and the minimum storage temperature, the vapor pressure of each propellant was investigated as a function of temperature. It was previously shown in the section entitled “Candidate Propellants & their Relevant Properties” that the vapor pressures of all of the down-selected propellants are manageable at 120 K (-153 °C). There is no intrinsic reason that propellants need to be stored below their normal boiling point. For example, nitrogen tetroxide has a normal boiling point of 294 K (21 °C), but is commonly stored at temperatures up to 323 K (50 °C). What is necessary is to maintain the pressure in the feed system above the propellant vapor pressure all the way to the combustion chamber to prevent two-phase flow. When injector stability concerns are considered, this means that the propellant tank operating pressure will need to be maintained at or above about twice the vapor pressure of the propellant at its storage temperature.

The thermal control concept incorporates several key features: The spacecraft bus temperature was assumed to be 293 K (20 °C). The primary thermal design assumptions for the baseline thermal tank design are summarized below:

- Tank is designed to radiate and is shielded from the Sun, spacecraft, and other thermal sources as shown in Fig. 9.
- Surface area where energy is radiated is one half of the spherical area (1.57 m²) of the tank.
- A shield with the effectiveness of a 20-layer MLI blanket shields the tank from the sun and spacecraft bus.
- The opening in the shield is 1.4 m in diameter.
- The tank has a (20 layer) MLI blanket around the spacecraft side (emissivity = 0.01).
- The tank is painted black with an emissivity of 0.90.
- Five titanium struts for structural support whose length, diameter, and thickness are 0.75 m, 2.5 cm, and 1 mm, respectively. The struts have thermal isolators where they attach to the tank.
- Two propellant lines: a fill line and a supply line (1.27 cm internal diameter 310 stainless steel with a length of 30 cm and a wall thickness of 0.75 mm). Note that the requirement that the propellant tank be protected from solar exposure so that it can radiate to deep space puts a significant operational constraint on the spacecraft

C. Analysis

The evaluation method used developed a mass estimate for thermal control systems for passive space storable propellant systems. This basic method uses the thermal balance calculations with various ranges from the Sun. This provides the external environmental input, which in general drives the thermal design of propulsion modules as well as thermal requirements for bus mounted propulsion systems.

The evaluation in general is for flight systems that have a solar range of 0.7 AU to Pluto range (which is about 40 AU, which essentially is an interstellar mission). For systems that have flight ranges that go closer to the Sun than 0.7 AU, specific thermal control systems, as well as operational constraints may be necessary. Behind an effective thermal sunshade, the effects on the temperature of passively cooled hardware can be quite independent of solar distance. This is illustrated by the flight temperature data shown in Fig. 10.

These are temperatures measured in the telescope barrel section of the Near-infrared IMaging

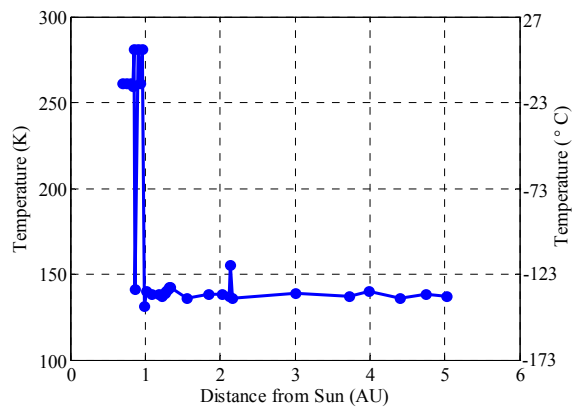


Figure 10: Flight Temperature Variations as a Function of Solar Distance.

Spectrometer (NIMS) on the Galileo spacecraft. A cover and heaters protected this instrument from contamination until the spacecraft returned to 1 AU for the final time. After the cover was jettisoned and the heaters were turned off, the temperature at this point in the telescope quickly dropped to approximately 138 K (-135 °C) and showed little variation with further increases in the distance from the sun. The focal plane of this instrument was passively cooled to an operating temperature of about 80 K.

For 120 K (-153 °C) systems, a passive thermal rejection system is required along with flight restrictions. The size and mass of such a thermal rejection system has been estimated for a 1 meter diameter 120 K propellant tank. Further, the 120 K propellant tank also requires a 120 K pressurant tank. The mass of the thermal shield has been estimated. The effect of operational limitations must be evaluated for each mission and its scientific requirements.

D. Results

For nominal room temperature propellants, current thermal control techniques provide the control required, but if lower temperatures or wider flight ranges especially for flights closer than 0.7 AU, extended thermal control techniques and designs are required.

In general the mass requirements are based on surface area, and the mass is scalable using the size of the tanks and pressure tanks. The mass required for lines, and engine assemblies is included, and assumes that the lines and thrusters are mounted on the propulsion module. The heat loads resulting from the aforementioned assumptions are summarized in Table 8. Negative numbers in Table 8 indicate a net heat absorption and temperature rise. Initial results shows that with current technology propellants can be space stored to a lower level of 120 K (-153 °C).

Table 9 shows the results for the baseline case. The baseline assumes that the propellant tanks are spheres having diameters of 1 m. The pressure tanks are spheres having diameters of 0.5 m. For the case where both tanks operate at 120 K, combining the two low-temperature tanks requires more surface area for separation and field of view, thus the total area sensitive mass requires a 2.5 multiplication factor over a single tank. This assumes that the two propellant tanks are the same size (1 meter diameter each) and the pressure tanks are the same size (0.5 meter diameter each). This MLI is slightly less than for the Option 2 120 K tank because the shields provide a slightly

Table 8: Hemispherical Tank Energy Transfer

Hemispherical Tank Temperature (K)	Tank Heat Rejection Capability (W)	Heat Transfer to the Tank from the ...			Total (W)	Net (W)
		Spacecraft (W)	Fill and Supply Lines (W)	Support Struts (W)		
60	1.04	6.55	6.98	0.93	14.46	-13.42
80	3.80	6.52	6.38	0.85	13.75	-9.95
100	8.00	6.47	5.78	0.77	13.02	-5.02
120	16.60	6.38	5.18	0.69	12.25	4.35

Table 9: Results for Thermal Sizing of Baseline System^a

Option	Option 1:	Option 2:		Option 3:
	Both Tanks Stored at 300 K	300 K Tank	120 K Tank	Both Tanks Stored at 120K
Surface Area Dependent Thermal Mass				
Primary Shield	n/a	n/a	2.08 kg	1.65 kg
Secondary Shield	n/a	n/a	1.5 kg	3.75 kg
Propellant Tank MLI/Surface Coat	3.2 kg	3.2 kg	1.53 kg	1.44 kg
Propellant Tank Heater	0.25 kg	0.25 kg	n/a	n/a
Pressurant Tank MLI/ surface Coat	0.8 kg	0.8 kg	0.42 kg	0.4 kg
Pressurant Tank Heaters	0.1 kg	0.1 kg	n/a	n/a
Structure MLI	21.5 kg	24 kg	n/a	26.5 kg
Tank Mass Dependent Thermal Mass				
Propellant Tank Thermal Isolator	2.2 kg	2.2 kg	3.5 kg	3.5 kg
Pressurant Tank Thermal Isolator	0.5 kg	0.5 kg	0.9 kg	0.9 kg
Fixed Mass				
Valve Plate Thermal	0.9 kg	0.9 kg	0.75 kg	0.75 kg

^apropellant tank diameters = 1 m each; propellant tank wet mass = 300 kg each; pressurant tank diameters = 0.5 m each; pressurant tank wet mass = 10 kg each

better isolation since both of the propellant and pressure tanks in the propulsion module are at 120 K. Consequently, the structure will be cooler (since there is no 300 K tank). The “structure MLI” is specifically for insulation for the structure that supports the two propellant tanks, two pressure tanks, and the rocket engine mechanical support structure. The structure may be a little larger to support the larger shields and there may be more spacing between the tanks. The estimates in Table 9 were then used to scale the thermal system mass based on tank diameters and masses. The final formulation is as follows:

For Option 1:

$$m_{thermal} = 13.01 \cdot (d_{ox_tank}^2 + d_{fuel_tank}^2) + 13.16 \cdot (d_{pres_tank_ox}^2 + d_{pres_tank_fuel}^2) + 0.0073 \cdot (m_{ox_tank_loaded} + m_{fuel_tank_loaded}) + 0.05 \cdot (m_{pres_tank_ox_loaded} + m_{pres_tank_fuel_loaded}) \quad (16)$$

For Option 2:

$$m_{thermal} = 15.06 \cdot d_{ox_tank}^2 + 14.12 \cdot d_{fuel_tank}^2 + 15.2 \cdot d_{pres_tank_ox}^2 + 14.27 \cdot d_{pres_tank_fuel}^2 + 0.0117 \cdot m_{ox_tank_loaded} + 0.0073 \cdot m_{fuel_tank_loaded} + 0.09 \cdot m_{pres_tank_ox_loaded} + 0.05 \cdot m_{pres_tank_fuel_loaded} + 1.65 \quad (17)$$

For Option 3:

$$m_{thermal} = 17.23 \cdot (d_{ox_tank}^2 + d_{fuel_tank}^2) + 17.38 \cdot (d_{pres_tank_ox}^2 + d_{pres_tank_fuel}^2) + 0.0117 \cdot (m_{ox_tank_loaded} + m_{fuel_tank_loaded}) + 0.09 \cdot (m_{pres_tank_ox_loaded} + m_{pres_tank_fuel_loaded}) + 1.5 \quad (18)$$

V. Mission & Systems Analysis

The goal of the mission and systems analysis was to determine the benefit of the selected propellant combinations to relevant mission scenarios. This analysis considered not only the performance of the propellant, but also its impact on the thermal and propulsion system design. This section describes the mission scenarios, the system study approach, and the results of the system study.

A. Mission Scenarios

Three mission scenarios were selected from a recent paper for this study to cover a range of ΔV requirements and injected mass assumptions.²⁶ Table 10 summarizes the mission scenarios that were studied. All scenarios assumed launch on a Delta-IV heavy vehicle. Note that the payload masses are as calculated from Ref. 26. The results of the current study are based on different assumptions.

The term “payload” refers to the spacecraft system delivered to the final orbit, not including the propulsion stage or stages and its associated structural, cabling, and thermal hardware. The mission trajectories chosen from Ref. 26 are not necessarily optimized for the use of chemical propulsion. For example, the very high ΔV required for the Neptune mission is in part a result of the use of solar electric propulsion in the inner solar system to inject the probe on a relatively fast trip to Neptune. There are trades that could be done between trip time and orbit insertion ΔV that are not within the scope of this study. Therefore, the actual injected masses for these missions given in this study should not be considered as absolutes, but in relative terms.

1. Neptune Orbit Insertion

The Neptune Orbit Insertion mission was selected for its difficulty. This mission requires the highest ΔV and injected mass combination that might still be tractable with advanced space storable propellants. The destination is a

Table 10: Mission Scenarios Studied from Ref. 26

Mission	ΔV Required (km/s)	Injected Mass (kg)	Payload for Specific Impulse of 325 lbf-s/lbm (kg)	Payload for Specific Impulse of 370 lbf-s/lbm (kg)	Payload for Aerocapture (kg)
Neptune Orbit Insertion	6.1	3423.8	-78.4	80.5	1680.2
Jupiter Orbit Insertion	1.4	2335.3	1339.4	1438.5	729.3
Saturn Post-Aerocapture Periapsis Raise	3.3	1656.4	374.8	NA	NA

Table 11: Comparison of Assumptions between Ref. 26 and this Study

Assumption	Reference 26	This Study
Number of stages	1	1 or 2
State-of-the-art storable specific impulse	325 s	As calculated from TDK analysis with a 2% derating factor (321.0 s for NTO/N ₂ H ₄)
Future advanced storable chemical propellant specific impulse	370 s	As calculated from TDK analysis with a 2% derating factor (376.6 s for F ₂ /N ₂ H ₄)
Chemical propulsion module dry mass/ propellant mass	0.2	Tabulated using propulsion equipment list for specific propellant combo, structural coefficient, and thermal equipment scaling
Stack support structural mass/ propulsion module mass	0.05	Stage structural mass/supported wet mass = 0.05 (see Ref. 25)
Thermal mass	Included in chemical propulsion module dry mass	Scaled based on thermal equipment list and propellant storage requirements (see section entitled “Thermal Storage Analysis”)

4,000 km x 430,000 km elliptical orbit with an apoapsis just beyond the moon Triton. This mission requires an Earth departure hyperbolic excess velocity (C3) of 23.7 km²/s². It then uses a Solar Electric Propulsion (SEP) stage to provide 6.8 km/s of ΔV over the 10.5 year cruise to Neptune. The trajectory includes both a Jupiter and Venus flyby/gravity assist. Delivered payloads for this scenario from Ref. 26 show very meager results for chemical systems, especially when compared to a system using aerocapture.

2. Jupiter Orbit Insertion

The Jupiter Orbit Insertion mission resides at the opposite end of the spectrum with a relatively low ΔV and moderate injected mass. The destination for this mission is a 1,000 km x 1,880,000 km orbit with its apoapsis at Callisto. The mission requires a C3 of 85 km²/s². This scenario represents a class of missions in which systems using chemical propulsion deliver more payload than systems using aerocapture, based on the results in Ref. 26.

3. Saturn Post-Aerocapture Periapsis Raise

The Saturn mission is unique in that it requires both aerocapture and a large amount of propulsive ΔV for a periapsis raise maneuver. The results summarized in Ref. 26 suggest that this mission is not possible without aerocapture technologies. This mission begins with an Earth departure C3 of 23.5 km²/s². A SEP stage provides 6.1 km/s of ΔV over the 6.7 year cruise. The spacecraft captures into an orbit around Saturn using aerocapture. It then uses a chemical system to perform a periapsis raise maneuver to reach its destination orbit of 120,000 km circular for ring observations in the Cassini gap. This scenario represents a class of missions where there may be synergy between aerocapture and advanced space storable propellants.

B. Major Assumptions and Summary of Results

Table 11 compares the assumptions made in Ref. 26 to those made in this study. In general, this study attempts to make a more realistic accounting of system impacts of using advanced space storable propellants. Staging was also considered for each of the maneuvers studied in order to maximize delivered payload.

For each mission scenario, the state-of-the-art space storable system, NTO/N₂H₄, was analyzed using both 1 and 2 stages. For two-stage systems, the ΔV was split evenly. The remaining propellant combinations were then analyzed using the number of stages that yielded the highest delivered payload for the NTO/N₂H₄ system. Table 12 shows the results of the stage trade study for each mission scenario.

A comparison of the results show a lower predicted delivered mass than that reported in Ref. 26. This is a result of a lower specific impulse and a more conservative estimate of propulsion stage dry mass. The remainder of this section details the assumptions and analysis procedure that went into generating Table 12.

Table 12: Comparison of Delivered Payload for 1 and 2 Stage systems using NTO/N₂H₄

Mission Scenario	Delivered Payload for a Single Stage System (kg)	Delivered Payload for a Two Stage System (kg)
Neptune Orbit Insertion	-125	159
Jupiter Orbit Insertion	1217	1155
Saturn Post-Aerocapture Periapsis Raise	301	334

C. Systems Analysis Approach and Other Assumptions

The systems analysis was performed using the JPL Team X Propulsion System Design Tool (PSDT). Team X is an integrated concurrent engineering design team using Microsoft Excel based design tools that are integrated to provide a real-time rapid design environment.²⁷ The PSDT has been used in hundreds of spacecraft mission design studies in Team X. For this study, the PSDT has been used independent of the Team X environment to design and size the propulsion subsystem.

The PSDT takes many inputs including stage ΔV , initial mass, specific impulse, mixture ratio, propellant tank pressure and temperature, pressurant tank pressure and temperature, and many others to compute propulsion system design characteristics. The outputs from the PSDT include propulsion system dry mass, propellant mass, pressurant mass, tank size, and residual propellant mass. The PSDT is capable of designing a system with up to three stages or a single stage with up to three different types of systems.

1. Propulsion Schematic & Equipment List

The first major input into the PSDT is an equipment list based on a propulsion system schematic. For this study, the Europa Orbiter system schematic was used as a baseline. Europa Orbiter assumes a monopropellant hydrazine system for attitude control, which was not considered in this study of primary propulsion stages. Figure 11 shows the schematic for this study.

It was assumed that this schematic was appropriate for all propellant combinations in use. The propulsion stages designed in this study provide ΔV only. A reaction control system (RCS) is assumed to be part of the delivered payload. One advantage of using hydrazine fuel is that a small portion of the fuel could be used for attitude control using monopropellant hydrazine thrusters, if having a separate RCS as part of the payload were undesirable.

Baseline components were assumed based on this schematic and a total system thrust of 450 N. Table 13 shows the mass-equipment list for this schematic. The total fixed mass of this system is 24.9 kg.

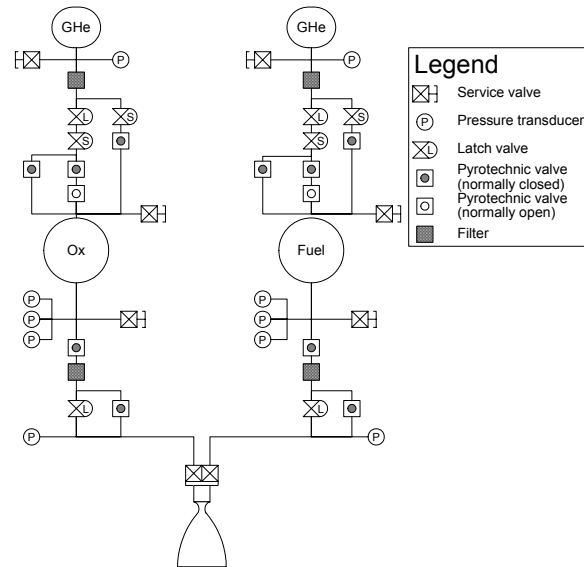


Figure 11: Baseline Propulsion System Schematic.

Table 13: Fixed Propulsion Mass Equipment List^a

Component	Qty.	Unit Mass (kg)	Total Mass (kg)	Cont. (%)	Total Mass with Cont. (kg)
Gas service valve	4	0.01	0.04	30	0.05
HP latch valve	2	0.35	0.70	30	0.91
Solenoid valve	4	0.35	1.40	30	1.82
HP transducer	2	0.06	0.12	30	0.16
Gas filter	2	0.15	0.30	30	0.39
NC pyro. valve	10	0.12	1.20	30	1.56
NO pyro. valve	2	0.12	0.24	30	0.31
Liquid service valve	4	0.28	1.12	30	1.46
Test service valve	4	0.01	0.04	0	0.04
LP transducer	8	0.06	0.48	30	0.62
Liquid filter	2	0.72	1.44	30	1.87
Mass flow control	2	0.03	0.06	30	0.08
Temp. sensor	17	0.03	0.51	30	0.67
Lines, fittings, misc.	1	5.00	5.00	50	7.50
Biprop main engine	1	5.76	5.76	30	7.49
TOTAL					24.93

^aHP = high pressure; LP = low pressure; NO = normally open; NC = normally closed

2. Governing System Equations

Next, mission ΔV and injected mass are input. Propellant is calculated using the classical rocket equation, rearranged for propellant mass:

$$m_{prop} = m_i \cdot \left[1 - \exp\left(-\frac{\Delta V}{g_c \cdot I_{sp}}\right) \right] \quad (19)$$

The propellant is then split into fuel and oxidizer using the mixture ratio:

$$m_{ox} = m_{prop} \cdot \left(\frac{MR}{1 + MR} \right) \quad (20)$$

and

$$m_{fuel} = m_{prop} - m_{ox} \quad (21)$$

The initial mass for the second stage of two stage systems was calculated by subtracting the stage 1 propellant and an estimated stage 1 burnout mass from the injected mass. The stage 1 burnout mass is iterated in the final steps of the process to converge the design.

$$m_{i_stg2} = m_{inj} - m_{prop_stg1} - m_{f_stg1} \quad (22)$$

3. Propellant Tanks

Once the propellant mass was calculated, the tanks were sized using the PSDT. The PSDT takes many inputs to size the propellant and pressurant tanks. Table 14 lists the assumptions for propellant tank sizing.

All propellant tanks used these assumptions, with the following exceptions:

- 1) F_2 tanks were sized for an MEOP of 2.8 MPa (400 psi) due to fluorine's high vapor pressure at 120 K.
- 2) OF_2 and LOX tanks are aluminum due to the incompatibility of these propellants with titanium.

Table 14: Propellant Tank Inputs to PSDT

Characteristic	Value
Number of tanks	1
Ullage at launch	10%
Volume contingency	10%
Burst factor of safety	1.5
Maximum expected operating pressure (MEOP)	2.1 MPa (300 psi)
Hold-up/Residual plus margin	2.7%
Tank shape	sphere
Expulsion device type	std. surface tension
Liquid outlet tube diameter	9.525 mm
Gas inlet tube diameter	6.35 mm
Boss radius	50.8 mm
Mount style	boss
Boss outlet orientation	radial
Boss type	double
Tank material	titanium
Min. fabrication thickness	0.508 mm
Machining tolerance	0.0762 mm

With these assumptions, the PSDT generates tank masses based on required tank volume as shown in Fig. 12. Note that tank mass is linear with volume, given the assumptions in Table 14. In addition to this, 2 kg was added to each cryogenic propellant tank to account for internal cooling loops that would be necessary during pre-launch operations.

4. Pressurant Tanks

The pressurant tank and pressurant gas supply were then sized based on propellant tank volume and the assumptions in Table 15 and Table 16. As shown in the schematic in Fig. 11, an independent pressurant tank pressurizes each propellant tank. Sizing of the pressurant gas supply assumed that the pressurant expansion was isothermal at the propellant storage temperature throughout the burn.

Given the pressure and temperature of the gas, the molar specific volume can be calculated using the Beattie-Bridgeman equation of state for a real gas:

$$p = \frac{\mathfrak{R} \cdot T}{v^2} \left(1 - \frac{c_0}{v \cdot T^3} \right) \left(v + B_0 - \frac{B_0 \cdot b}{v} \right) - \frac{v \cdot A_0 - A_0 \cdot a}{v^3} \quad (23)$$

The constants A_0 , a , B_0 , b , and c_0 for helium are 2188.62 kg-m⁵/kmol²-sec², 0.05984 m³/kmol, 0.014 m³/kmol, 0 m³/kmol, and 40 m³-K³/kmol, respectively.²⁸ Helium was the only pressurant gas considered. Coefficients for other

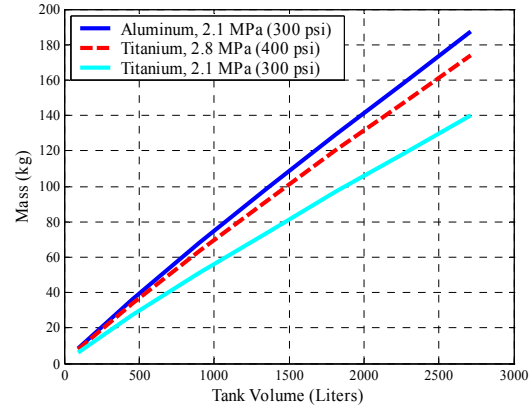


Figure 12: PSDT Propellant Tank Mass Trends. Note that these trends are based on assumptions listed in Table 14.

Table 15: Pressurant Tank Inputs to PSDT

Characteristic	Value
Number of tanks	1
Burst factor of safety	1.5
MEOP	27.6 MPa (4000 psi)
Volume contingency	10%
Pressurant gas	helium
Pressurant in the pressurant tank	
Pressure of pressurant @ launch	27.6 MPa (4000 psi)
Pressure of pressurant @ end of burn	3.4 MPa (500 psi)
Tank shape	near sphere
Diameter to length ratio	1
Head height/radius	0.66
Liquid outlet tube diameter	6.35 mm
Gas inlet tube diameter	6.35 mm
Boss radius	25.4 mm
Mount style	boss
Boss outlet orientation	axial
Boss type	single
Liner shell material	titanium
Liner thickness	0.381 mm
Adhesive thickness	0.127 mm
Composite material	p-phenylene-benzobisoxazole (PBO)
Derating factor for fiber strength	0.85
Minimum fiber thickness	0.0508 mm

Table 16: Propellant Storage Temperatures, Vapor Pressures, and Partial Pressures of Helium

	Storage Temp. (K)	Vapor Pressure at Storage Temperature		Partial Pressure of Helium in Propellant Tank	
		(kPa)	(psi)	(kPa)	(psi)
F ₂	120	1335.5	193.7	1422.4	206.3
OF ₂	120	52.4	7.6	2016.0	292.4
ClF ₃	318	339.9	49.3	1728.5	250.7
LOX	120	1013.5	147	1054.9	153
H ₂ O ₂	318	0.2	0.03	2068.2	299.97
NTO	318	96.5	14	1971.9	286
N ₂ H ₄	318	1.4	0.2	2067.0 ^a	299.8 ^a
MAF-4	318	15.9	2.3	2052.6	297.7
MMH	318	105.5	15.3	1962.9	284.7
CH ₄	120	191.0	27.7	1877.4	272.3

^a2756.6 kPa (399.8 psi) when used with F₂

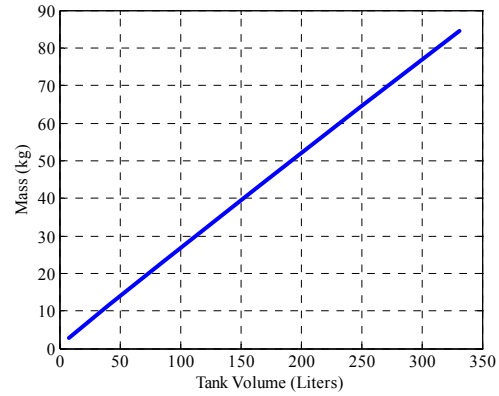


Figure 13: PSDT Pressurant Tank Mass as a Function of Volume.

gases are found in Ref. 28. For a given pressure and temperature, equation (23) yields four roots: two imaginary numbers, a negative real number, and a positive real number. The molecular mass of helium is 4.003 kg/kmol and v^* is the positive real root of equation (23) (the only root that makes physical sense). With the correct molar specific volume known, the density of the pressurant gas is found via:

$$\rho_{pres} = \frac{M}{v^*} \quad (24)$$

Now, based on these assumptions, the density of the gas is known both at launch and at the end of the burn for both the pressurant in the propellant and the pressurant tank. Using the conservation of mass, the volume of the pressurant tank is:

$$V_{pres_tank} = \frac{\rho_{pres}^{prop_tank_f} \cdot V_{prop_tank} - \rho_{pres}^{prop_tank_i} \cdot V_{ullage}}{\rho_{pres}^{pres_tank_i} - \rho_{pres}^{pres_tank_f}} \quad (25)$$

The PSDT is then used to size the pressurant tank based on volume and maximum expected operating pressure. Figure 13 shows the pressurant tank mass trend as a function of pressurant tank volume, based on the assumptions in Table 16. Given this set of assumptions, the trend is linear.

With the pressurant gas density and volumes known, the relevant pressurant masses are easily found via:

$$m_{pres} = \rho_{pres} \cdot V_{pres} \quad (26)$$

5. Miscellaneous Governing Equations

Once the tanks have been sized, it is possible to tabulate the mass of each propulsion stage and determine the delivered payload. Propulsion system mass is determined using the PSDT as described above. The mass of the stage structure is estimated as 5% of the carried mass, or the mass of the wet spacecraft including the stage and everything that it carries. This assumption is based on a similar analysis for a Mars Sample Return orbiter and ascent vehicle where the actual structural mass was estimated.²⁵

$$m_{struc} = 0.05 \cdot m_{total_stg} \quad (27)$$

The thermal control mass is calculated based on a scaling approach described in the section “Thermal Storage Analysis”. The hold-up and residual, or unusable propellant plus required reserves to account for performance

uncertainty, is estimated as 2.7% of the total loaded propellant which is the standard assumption for systems of this size in Team X studies.

$$m_{hold-up} = 0.027 \cdot m_{prop_loaded} \quad (28)$$

The stage burnout mass is the sum of propulsion system dry mass, structural mass, thermal mass, propellant residual and holdup, and pressurant mass.

$$m_{bo_stg} = m_{prop_dry} + m_{struc} + m_{thermal} + m_{hold-up} + m_{pres} \quad (29)$$

For two-stage systems, the burnout mass of stage 1 must be iterated in order to get the system to converge. Delivered payload is then calculated by subtracting the wet mass of all stages from the injected mass.

$$m_{payload} = m_{inj} - \sum_{j=1}^n (m_{bo_stg}^j + m_{prop}^j) \quad (30)$$

D. Summary of System Analysis Results

The approach described above was applied to the three mission scenarios for all ten propellant combinations selected in “Propellant Combination Analysis”. The delivered payload for each propellant combination is shown in Table 17. The results are summarized in Fig. 14, Fig. 15, and Fig. 16 in terms of delivered payload relative to the state-of-the-art propellant combination NTO/N₂H₄. The ranking of propellants in terms of delivered payload is the same for all mission scenarios studied.

Propellant combinations using halogenated oxidizers consistently deliver the highest amount of payload for the selected missions with F₂/N₂H₄ performing the best in all cases. LOX/CH₄ performs the worst in all cases, delivering significantly less payload than either state-of-the-art propellant combination NTO/N₂H₄ or NTO/MMH. Combinations of LOX with N₂H₄ and MMH as well as

Table 17: Delivered Payload Mass

Propellant combination	Neptune (kg)	Jupiter (kg)	Saturn (kg)
F ₂ /N ₂ H ₄	260	1318	409
OF ₂ /N ₂ H ₄	230	1292	389
OF ₂ /MAF-4	228	1291	388
ClF ₅ /N ₂ H ₄	195	1251	361
LOX/N ₂ H ₄	179	1243	351
LOX/MMH	166	1232	342
H ₂ O ₂ /N ₂ H ₄	160	1217	335
NTO/N ₂ H ₄	159	1217	334
NTO/MMH	145	1202	324
LOX/CH ₄	121	1192	309

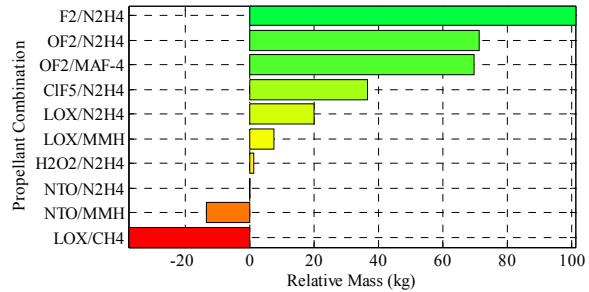


Figure 14: Delivered Payloads for Neptune Mission Scenario Relative to State-of-the-art NTO/N₂H₄.

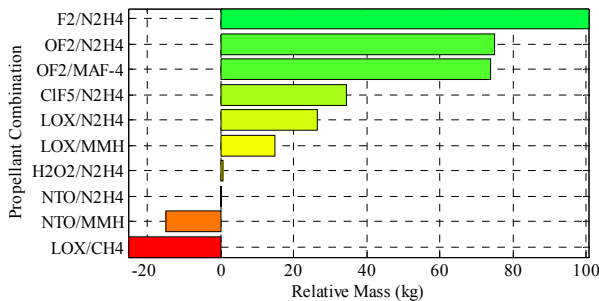


Figure 15: Delivered Payloads for Jupiter Mission Scenario Relative to State-of-the-art NTO/N₂H₄.

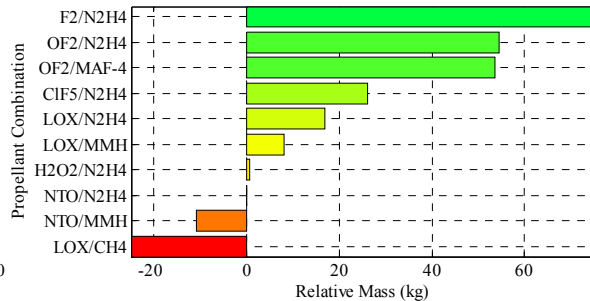


Figure 16: Delivered Payloads for Saturn Mission Scenario Relative to State-of-the-art NTO/N₂H₄.

ClF₅ with N₂H₄ exhibit modest improvements over the state-of-the-art.

Figure 17 compares the percentage increase in delivered payload over the state-of-the-art propellant combination NTO/N₂H₄ for the three mission scenarios. Higher percentage improvements correspond to the higher ΔV mission scenarios.

1. Neptune Mission

Figure 18 shows the total mass breakdown for the Neptune mission scenario. The total mass for each system is the same and equal to the arrival mass from Ref. 26. The trend in the stage 1 wet mass matches the trend in delivered payload. The system delivering the highest payload is the system with the lowest stage 1 wet mass. On the other hand, stage 1 burnout mass does not follow the same trend. Figure 19 compares the components of stage 1 burnout mass.

Here, the several competing characteristics of the system are evident:

- propellant performance (tank, thermal control mass)
- propellant density (tank, thermal control mass)
- propellant storage temperature (thermal control mass, propulsion, and pressurant mass)

This observation is most dramatic with the LOX/CH₄ system. Despite the fact that this propellant combination offers a moderately high specific impulse of 340.9 lbf-s/lbm, the low average density and low storage temperature result in large tanks and heavy thermal hardware making it the worst system performer of the group. In contrast, LOX/MMH has a slightly lower specific impulse but takes advantage of significantly higher fuel density and storage temperature to achieve a lower stage 1 wet mass and higher delivered payload.

Delivered payload mass is significantly higher (about 200 kg) in this study for each propellant combination than the results shown in Ref. 26. The primary reason for this is staging the large Neptune insertion maneuver. However, according to Ref. 26, aerocapture delivers 1420 kg more payload than the best performing chemical system, F₂/N₂H₄. This is due to the very high ΔV of this mission and the fact that the chemical system grows exponentially with ΔV , while the aerocapture systems grow more linearly with a gradual slope.²⁶

2. Jupiter Mission

Figure 20 and Fig. 21 show the same mass breakdown for the Jupiter single stage mission scenario. The trends are identical to the Neptune mission, although the relative increase in performance for the best propellant combinations is smaller due to the smaller ΔV required by this mission. The delivered payload for this mission is lower than that shown in Ref. 26 for comparative systems. In this case, a single stage system was assumed. Also, the approach more explicitly accounts for propulsion stage mass, resulting in lower overall delivered payloads.

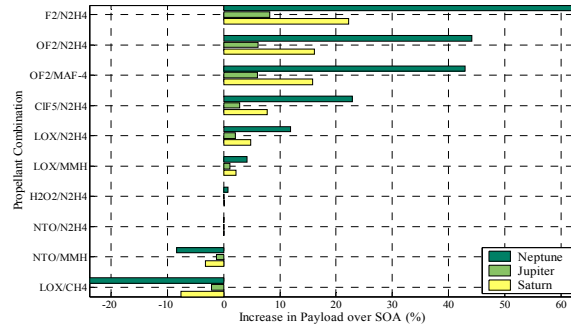


Figure 17: Percentage Increase in Delivered Payload Over State-of-the-art, NTO/N₂H₄.

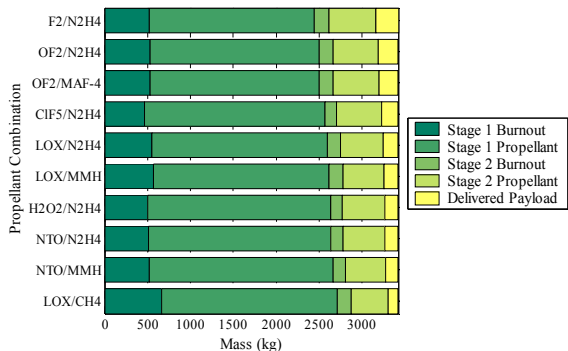


Figure 18: Mass Breakdown for the Neptune Mission Scenario.

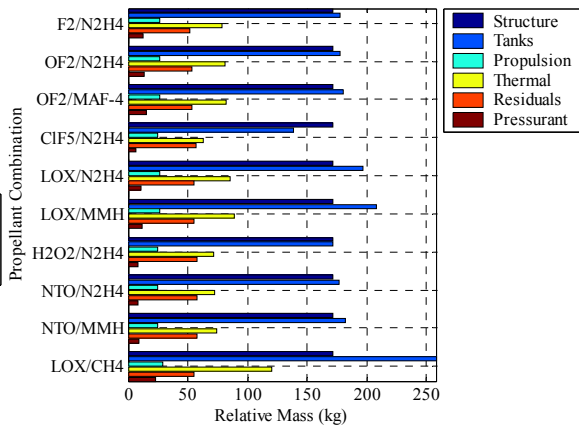


Figure 19: Stage 1 Mass Breakdown for the Neptune Mission Scenario.

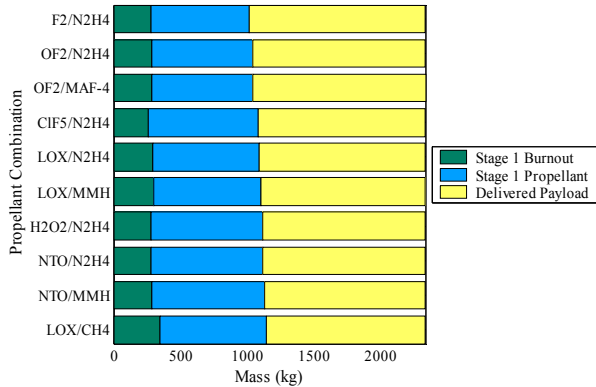


Figure 20: Mass Breakdown for the Jupiter Mission Scenario.

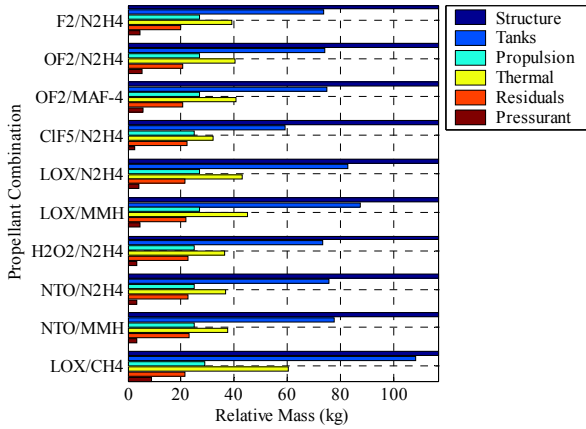


Figure 21: Stage 1 Mass Breakdown for the Jupiter Mission Scenario.

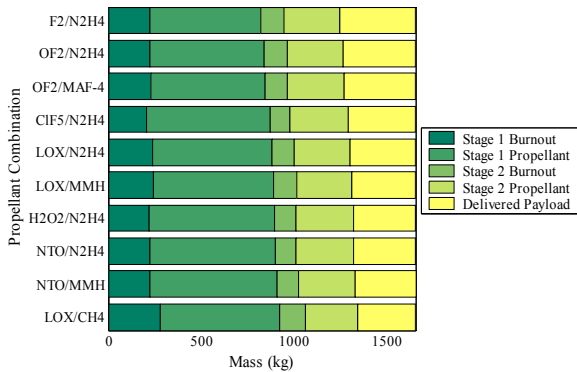


Figure 22: Mass Breakdown for the Saturn Mission Scenario.

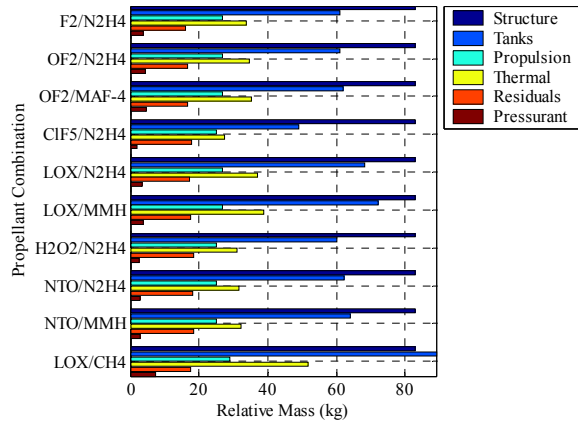


Figure 23: Stage 1 Mass Breakdown for the Saturn Mission Scenario.

3. Saturn Mission

Figure 22 and Fig. 23 show the mass breakdowns for the Saturn mission scenario. Once again, the trends are consistent with the trends in the other mission scenarios. The delivered payload for this mission scenario is slightly lower for the reference case, NTO/N₂H₄, than that shown in Ref. 26. This is again due to the fact that stage mass has been more explicitly defined resulting in a heavier stage mass and lower payload mass than that calculated in Ref. 26.

4. Comparison to Figures of Merit

In the section “Propellant Combination Analysis”, several figures of merit were described for use in preliminary assessment of propellant combinations and propulsion systems using them. Table 18 compares the ranking based on the Guernsey-Rapp FOM, limiting ΔV FOM, density specific impulse, and the actual system study discussed in this section.

The limiting ΔV FOM appears to match the system study results the closest of the three figures of merit, despite the inaccurate application of c_2 in its calculation (see “Propellant Combination Analysis”). The differences between the limiting ΔV FOM and the system study rankings are limited to switching of consecutive propellant combinations. Those combinations that are affected tended to yield

Table 18: Ranking of the Ten Propellant Combinations Considered in System Study by Various Figures of Merit

Propellant Combination	FOM_{GR}	$FOM_{lim \Delta V}$	$I_{p,sp}$	Sys. Study
F ₂ /N ₂ H ₄	1	1	1	1
OF ₂ /N ₂ H ₄	3	3	4	2
OF ₂ /MAF-4	2	2	3	3
ClF ₅ /N ₂ H ₄	7	4	2	4
LOX/N ₂ H ₄	4	5	8	5
LOX/MMH	5	8	9	6
H ₂ O ₂ /N ₂ H ₄	9	6	5	7
NTO/N ₂ H ₄	8	7	6	8
NTO/MMH	10	9	7	9
LOX/CH ₄	6	10	10	10

payloads of approximately the same size. Therefore, the limiting ΔV FOM is shown to be reasonably accurate at predicting relative system level performance between two propellant combinations.

The other FOMs do not appear to predict relative performance as accurately, although there are some interesting trends. All rankings show F_2/N_2H_4 to be the best performer. OF_2/N_2H_4 and $OF_2/MAF-4$ rank in the top four in all four FOMs used. LOX/N_2H_4 ranks in the top five in three of the four methods. LOX/CH_4 ranks last in the group in three of the four methods used. A more comprehensive summary of data generated in this system study can be found in Ref. 10.

VI. Conclusions & Recommendations

The major conclusions drawn from the results presented in the rest of this paper are:

- 1) *Propellant combinations using fluorinated oxidizers provided by far the largest improvement in system performance (defined in terms of delivered useful payload mass) of any of the combinations studied.* In particular, the combination of liquid fluorine oxidizer with hydrazine fuel provided the best performance, although other halogenated oxidizer and fuel combinations (such as $OF_2/MAF-4$) could provide substantial performance improvements and have superior storability characteristics.
- 2) *Passive storage of propellants at temperatures as low as 120 K is feasible using the existing state-of-the-art in spacecraft thermal control.* Sunshades are required for this passive storage and will impose pointing constraints on the spacecraft. The attainable storage temperature is a very weak function of distance from the sun. Passive storage at temperatures as low as 80 K may be possible, but it likely to depend on exotic and unproven technologies.
- 3) *Space storable chemical propulsion may offer significant system benefits for missions using solar electric propulsion and/or aerocapture technologies.*
 - A *Neptune Orbiter* mission was studied which used solar electric propulsion in the inner solar system to provide a relatively fast transit time to Neptune, but relied on chemical propulsion for a very large (6.5 km/s) orbit insertion burn. The use of a space storable fluorine/hydrazine system could result in a *64% increase in useful payload* delivered compared to a state-of-the-art chemical propulsion system. It must be noted that aerocapture technologies promise to offer even larger increases in delivered mass for this mission, but their feasibility and actual delivered performance are still undetermined.
 - A *Saturn Orbiter* mission that uses solar electric propulsion to provide for a fast transit was studied which had previously been shown to be enabled by the use of aerocapture for orbit insertion.²⁶ However, a fairly large (3.3 km/sec) maneuver is required to raise the periapse to the desired orbit. The only propulsion technology available for this purpose is chemical propulsion. For this mission, it was found that the use of a fluorine/hydrazine system could result in a *22% increase in useful payload* when compared to the state-of-the-art.
 - We also examined a *Jupiter Orbiter* mission which had relatively modest (1.4 km/s) orbit insertion ΔV and which previous studies had shown little benefit to be obtained from the use of solar electric propulsion or aerocapture.²⁶ For this mission, it was found that an *8% increase in useful payload* could be obtained through use of a space storable fluorine/hydrazine propulsion system compared to the state-of-the-art.

In general, it was found that the potential mission benefit of space storable propulsion is highly dependent on the specific mission design. Mission designs which require higher ΔV from the chemical propulsion system show larger percentage increases in performance, but at the price of delivered payloads which may or may not be adequate to meet the science objectives of the mission. Further, it was noted that the mission designs which were adopted from Ref. 26 may not be representative of the mission designs that would in fact be selected for a mission based on the use of chemical propulsion in the outer solar system. For example, the highest delivered mass reported for the Saturn Orbiter mission in Ref. 26 was less than 500 kg, while the Cassini spacecraft is expected to deliver a useful payload of over 1500 kg when it enters Saturn orbit in 2004. Mission designs and trajectories providing similar performance might be found which could satisfy the science objectives of the Saturn mission studied here. Unfortunately, such mission design studies are well beyond the scope of the present effort.

The feasibility of developing space storable propulsion systems using halogenated oxidizers needs further study that could not be completed within the scope of this task. Although numerous previous studies have concluded that these oxidizers can be handled safely, there has also been much skepticism expressed about this conclusion.²⁹ Indeed, when it was mandated that all US planetary missions would be launched on the Space Shuttle, the National Research Council issued its 1981 report entitled "Liquid Rocket Propulsion Technology: An Evaluation of NASA's Program", which recommended against use of fluorinated oxidizers in the Space Shuttle, deeming it a "national asset". This soon led to the termination of work on fluorinated propellants within NASA. However, based on

NASA's current plan to launch robotic missions using expendable launch vehicles, this conclusion is no longer relevant.

Fortunately, many of these safety and ground handling issues have been addressed in the literature.^{2,3,4} Unfortunately, many of the personnel with first-hand experience are no longer available and few have recent experience.

In addition to safety issues, there are fundamental reliability questions related to the fact that soft seal materials are not available for use with fluorinated oxidizers. Development of reliable metal-to-metal seals capable of large numbers of cycles without leakage is a challenge that will require substantial expenditures. Fortunately, there has been substantial work done on basic material compatibility with fluorinated oxidizers.⁵ Considerable component- and subsystem-level design work has also been performed.^{1,6,7}

During this limited study, it was not possible to perform a complete literature search and evaluation of these issues, much less to bring together those remaining engineers with experience in halogenated oxidizers to assist in assessing the issues. This forms the basis of our first recommendation.

A. Recommendations

As a follow-on task, we recommend that a thorough literature search of the properties, handling practices, and safety of halogenated oxidizers be performed. In addition, one or more workshops should be held to bring together people with relevant experience in working with halogenated oxidizers. The objectives of this study would be a comprehensive assessment of the safety, technical, and cost issues associated with developing a space storable propulsion system.

The conclusion of the present study that passive storage below 120 K is a significant challenge is less optimistic than previous studies which concluded that storage temperatures as low as 80 K were attainable with existing technology.^{8,9} We recommend that further work be performed to understand this discrepancy and see if lower storage temperatures might indeed be attainable.

We also recommend:

- The study of the potential for using hard cryogenic propellants with active cooling for deep space missions. Such a study is currently planned by the In-Space Propulsion Program.
- A more thorough study of a spacecraft configuration and mission operational concept using SEP and passive cryogenic chemical stages to determine if the pointing constraints and thermal control assumptions in this report are feasible.
- That a TDK kinetic reaction set for B₅H₉ be obtained from the literature so that the potential of this fuel can be more accurately assessed.

Acknowledgments

The authors thank Brian Reed (NASA Glenn Research Center) for lengthy discussions and information regarding nontoxic propellants, in particular HAN-Glycine and HAN-Methanol; Joe Lewis and Andre Yavorian (JPL) regarding propellant compatibility and the HEPS program; and Jeff Hall, Muriel Noca, and Robert Bailey (JPL) regarding their AIAA paper that is referenced many times in this paper and is the foundation upon which the mission section is based.

The work described in this paper was performed at the Jet Propulsion Laboratory, California Institute of Technology, under a contract to the National Aeronautics and Space Administration. This work was funded in whole by the In-Space Propulsion Technologies Program, which is managed by NASA's Office of Space Science in Washington, DC, and implemented by the In-Space Propulsion Technology Projects Office at Marshall Space Flight Center in Huntsville, AL. The program objective is to develop in-space propulsion technologies that can enable or benefit near and mid-term NASA space science missions by significantly reducing cost, mass and travel times.

References

¹Bond, D., "Technology Status of a Fluorine-Hydrazine Propulsion System for Planetary Exploration," AIAA Paper 79-0907, May 1979.

²_____, *Prelaunch Operations for a Space Storable Propellant Module, Final Report*, General Dynamics, Convair Division, GDC-BNZ 69-013-8, San Diego, CA, May 1970.

³_____, *Study of Safety Implications for Shuttle Launched Spacecraft Using Fluorinated Oxidizers, Final Report, Volume I*, TRW Systems Group, NAS 7-100, Redondo Beach, CA, November 1975.

⁴Schmidt, H., *Handling and Use of a Fluorine and Fluorine-Oxygen Mixtures in Rocket Systems*, NASA Lewis Research Center, NASA-SP-3037, Cleveland, OH, 1967.

- ⁵Toth, L., Moran, C., and Lewis, J., *Materials Compatibility with Fluorine*, Chemical Propulsion Information Agency (CPIA), CPIA Publication 296, Columbia, MD, March 1979.
- ⁶Appel, M., *Progress on the Development of Liquid Fluorine-Hydrazine Rocket Engine*, Chemical Propulsion Information Agency (CPIA), CPIA Publication 296, Columbia, MD, March 1979.
- ⁷Weiner, R., Solis, C., and Hagler, R., *Control Component Development for a Fluorine-Hydrazine Propulsion System*, Chemical Propulsion Information Agency (CPIA), CPIA Publication 296, Columbia, MD, March 1979.
- ⁸Stultz, J., "Thermal Analysis of a High Energy Propulsion System for a Rover Class Mars Orbiter", AIAA Paper 78-888, May 1978.
- ⁹Stultz, J., and Grippi, R., *A Summary and Update of the Configuration and Temperature Control Studies for a Fluorine-Hydrazine Propulsion Systems*, Chemical Propulsion Information Agency (CPIA), CPIA Publication 296, Columbia, MD, March 1979.
- ¹⁰Guernsey, C., Baker, R., Miyake, R., and Thunnissen, D., *Space Storable Propulsion: Advanced Chemical Propulsion Final Report*, Jet Propulsion Laboratory, JPL D-27810, Pasadena, CA, February 2004.
- ¹¹Kit, B. and Evered, D., *Rocket Propellant Handbook*, Macmillan Co., New York, NY, 1960.
- ¹²Sarner, S., *Propellant Chemistry*, Reinhold Publishing Corporation, New York, NY, 1966.
- ¹³Marsh, W. and Knox, B., *USAF Propellant Handbooks Hydrazine Fuels, Volume I*, Bell Aerospace Company, AFRPL-TR-69-149, Buffalo, NY, March 1970.
- ¹⁴_____, "MSDS Nr: 023_AL - Chlorine pentafluoride", *Air Liquide Safety Data Sheet* [online database], URL: http://www.airliquide.com/safety/msds/en/023_AL_EN.pdf [cited 16 November 2003].
- ¹⁵_____, *Rocket Engines and Propulsion Systems*, Kaiser Marquardt, MP 7014, Van Nuys, CA, February 1995.
- ¹⁶Dunn, S., Coats, D., and Nickerson, G., *TDK97, Two-Dimensional Kinetics (TDK) Nozzle Performance Computer Program, User's Manual*, Software & Engineering Associates, Inc., NAS8-39048, Carson City, NV, January 1998.
- ¹⁷Gordon, S. and McBride, B., *Computer Program for Calculation of Complex Chemical Equilibrium Compositions and Applications. Part I: Analysis*, NASA Center for AeroSpace Information, NASA-RP-1311, Hanover, MD, 1994.
- ¹⁸Guernsey, C. and Rapp, D., *Propulsion: Its Role in JPL Projects, the Status of Technology, and What We Need to Do in the Future*, Jet Propulsion Laboratory, D-5617, Pasadena, CA, 8 August 1988.
- ¹⁹Chazen, M. and Mueller, T., "A Summary of the Space Storable Rocket Technology Program," AIAA Paper 95-2940, July 1995.
- ²⁰Wu, P., Woll, P., Stechman, C., McLemore, B., Neiderman, J., and Crone, C., "Qualification Testing of a 2nd Generation High Performance Apogee Thruster," AIAA Paper 2001-3253, July 2001, p. 1.
- ²¹Rattenni, L., "Design and Performance of the Orbital Star-2 Propulsion Subsystem" AIAA Paper 2001-3394, July 2001, p. 12.
- ²²Crocker, A. and Peery, S., "System Sensitivity Studies of a LOX/Methane Expander Cycle Rocket Engine," AIAA Paper 98-3674, July 1998.
- ²³Zubrin, R., Frankie, B., Muscatello, T., and Kito-Borsa, T., "Progress in the Development of Mars In-Situ Propellant Production Systems," AIAA Paper 99-0855, January 1999.
- ²⁴Pempie, P., Froehlich, T., and Vernin, H., "LOX/Methane and LOX/Kerosene High Thrust Engine Trade-off," AIAA Paper 2001-3542, July 2001.
- ²⁵Thunnissen, D., Rapp, D., Voorhees, C., Dawson, S., and Guernsey, C., "A 2007 Mars Sample Return Mission Utilizing In-Situ Propellant Production," AIAA Paper 99-0851, January 1999.
- ²⁶Hall, J., Noca, M., and Bailey, R., "Cost-Benefit Analysis of the Aerocapture Mission Set," AIAA Paper 2003-4658, July 2003.
- ²⁷Mark, G., "Extreme Collaboration," *Communications of the ACM*, Vol. 45, Issue 6, June 2002.
- ²⁸Dodge, B., "Beattie-Bridgeman Equation," *Chemical Engineering Thermodynamics*, McGraw-Hill Company, New York, NY, 1944, pp. 183-186.
- ²⁹Yankura, G., and Appel, M., *Proceedings of the Fluorine Handling Workshop*, Jet Propulsion Laboratory (JPL), JPL D-567, Pasadena, CA, March 1983.

Advanced Chemical Propulsion Study

Gordon Woodcock* and Dave Byers†

*Gray Research, 655 Discovery Drive, Suite 300, Huntsville, AL 35806 USA, grw33@comcast.net

† SAIC, , 4465 Pacific Coast Hwy, Torrance, CA 90505 USA, byersdc@aol.com

Leslie A. Alexander

Code TD-05, Marshall Space Flight Center, NASA, Huntsville AL 35812

and

Al Krebsbach

Code TD-05, Marshall Space Flight Center, NASA, Huntsville AL 35812

A study was performed of advanced chemical propulsion technology application to space science (Code S) missions. The purpose was to begin the process of selecting chemical propulsion technology advancement activities that would provide greatest benefits to Code S missions. Several missions were selected from Code S planning data, and a range of advanced chemical propulsion options was analyzed to assess capabilities and benefits re these missions. Selected beneficial applications were found for higher-performing bipropellants, gelled propellants, and cryogenic propellants. Technology advancement recommendations included cryocoolers and small turbopump engines for cryogenic propellants; space storable propellants such as LOX-hydrazine; and advanced monopropellants. It was noted that fluorine-bearing oxidizers offer performance gains over more benign oxidizers. Potential benefits were observed for gelled propellants that could be allowed to freeze, then thawed for use.

I. Introduction

Chemical propulsion has been the mainstay of space exploration propulsion since the beginning of space missions. It is still the only technology applicable to launch from Earth to orbit, but a number of alternatives are emerging for in-space propulsion. In-space chemical propulsion has relied almost exclusively on two technologies since the beginning: Earth storable propellants, used as (1) bipropellants, and (2) monopropellants. Hydrazine has been the dominant and almost exclusive choice for monopropellant, and oxides of nitrogen, usually N_2O_4 , with hydrazine compounds, have been the dominant and almost exclusive choice for bipropellants. Propellant delivery has been almost exclusively pressure-fed using helium pressurization of propellant tanks (a few small pump-fed systems have flown). Ignition systems are not needed; the bipropellant combinations are hypergolic and hydrazine as a monopropellant is reliably decomposed by a catalyst.

These systems are reliable; much experience and proven hardware designs exist; performance is reasonable, and operations experience has been good.

On the other hand, better-performing propellant combinations are known; the current propellants are toxic; and pressure-fed propellant delivery systems are comparatively high in inert mass due to the high pressures.

Space science missions are becoming more demanding on propulsion, thus needing better performance. One option is to introduce new technology such as electric propulsion or aerocapture. An alternative option is to improve the performance of current technology. The study reported here investigated this alternative option.

II. Objectives of the Study

1. Develop a workable description of "advanced chemical" propulsion technology and a suite of technology options applicable to Code S missions
2. Develop a preliminary assessment of the benefits of advanced chemical propulsion, relative to competing technologies, by technology option and versus mission characteristics or category

3. Provide guidance for future more detailed systems analyses, and recommend technology advancement directions for future directed and competed technology advancement tasks.
4. Identify specific high-priority systems analysis areas of investigation.

III. Mission Selection

A small set of missions was selected as appropriate to achieving the objectives. The selected missions, and their reasons for selection, are as follows:

Mission	Reason for Inclusion
Neptune Orbiter, (capture, SEP/chem.)	High delta V, test benefits of cryogenics
Venus Aeronomy	Modest delta V, small, test alternatives to conventional storable propellants
Titan Explorer	Aerocapture baseline case for which state-of-the-art chemical propulsion almost works
Titan Sample Return	Difficult mission, test cryogenics capability to do return with aerocapture, also all-propulsive option
Telemachus	Test ability of advanced chemical propulsion to replace multiple inner solar system gravity assists
Solar Probe	Benefits of advanced chemical propulsion to replace STAR-48 as "C3 topper"

The C3 topper is a smaller upper stage added to a launch vehicle to obtain higher launch energy than possible with the launch vehicle standard configuration. C3 is a measure of launch energy, the square of the so-called hyperbolic excess velocity.

Figures appended to this paper provide summary descriptions of these missions, taken from NASA Code S mission planning data. They do not represent approved missions, but were used as representative examples of potential future mission needs for purposes of analyzing benefits of advances in chemical propulsion technology.

IV. Advanced Chemical Propulsion Options

The study was structured to issues dealing with advantages and disadvantages of advanced chemical propulsion technology, both generically and for the specific missions in the mission set. In this paper we cover the most significant of these issues.

The study considered relatively few propellants among the hundreds of propellant combinations and variations that could be considered. The reference was $N_2O_4 - MMH$. We also considered gelled $N_2O_4 - MMH$. LOX-hydrazine was used as representative of a space storable propellant with greater Isp. LOX-LH₂ represented high-performance deep cryogenics.

Exotic propellants are exceptionally noxious substances that yield exceptional performance, especially high Isp with relatively dense propellants. We considered fluorine-bearing oxidizers as typical of this class. A review of fluorine-bearing oxidizers indicated that those with higher performance potential are mild cryogenics. The storable oxidizer CLF₅ offers little Isp advantage. It is, however, very dense. We selected OF₂-MMH as representative of the class.

Hybrids were represented by a paraffin-like fuel loaded with a metallic hydride, using LOX as the oxidizer. Isp approaching 350 seconds is projected by the advocates.

Advanced monopropellants use hydrazine or amine-related compounds such as HAN, soluble in water or ionic liquids, together with fuel compounds, to produce a monopropellant that gets its energy from a combustion reaction rather than decomposition. Isp projections range from 225 to about 300. We used 275.

V. Study Approach

The study developed performance predictions for the propellants considered, and developed an initial version of a spread-sheet-based spacecraft propulsion system performance and mass model. The model was used for parametric as well as point-design calculations of systems performance. The parametric performance data were used to develop generic conclusions regarding advantages and disadvantages, and the point-design data were used to assess performance of the various propulsion systems on specific missions.

The model developed inert mass data, calculated propellant load requirements, and estimated payload and/or initial mass, parametrically and for specific mission cases. Heat leak for cryogenics with varying thickness of multi-layer insulation (MLI), and performance and mass of cryocoolers, were included. Cryocoolers were assumed in all cryogenic cases.

VI. Propellants Performance

The TDK performance prediction code was used to estimate performance for N_2O_4 – MMH, LOX-hydrazine, LOX-LH₂, and OF₂-MMH. Calculations were made for chamber pressures 0.7, 1.4, and 3.5 MPa (100, 200 and 500 psia), area ratios 100 and 200, and a range of mixture ratios. Axisymmetric inviscid calculation results were discounted 2% Isp for combustion inefficiency and 2% for viscous and divergence effects. Some modern spacecraft engines use area ratios approaching 400. Most of our comparisons were based on area ratio 100 and chamber pressure 0.7 MPa. The increase in Isp at 400 area ratio is typically 10 seconds. Results of calculations are presented in Figures 1 - 6. For LOX-LH₂ we used Isp 420 for pressure-fed systems and 445 for small pump-fed systems.

Uncertainties associated with small LOX-LH₂ systems are significant. Chamber pressure for pressure-fed systems will be quite low because of the mass penalties for pressurizing hydrogen, and the performance of pump-fed systems will depend on small pump performance and operating characteristics. The Isp estimates we used are believed to be somewhat conservative.

In comparing LOX-hydrazine to N_2O_4 – MMH, we noted that N_2O_4 – hydrazine is also an option yielding about 5 seconds more Isp than the reference.

State of the art for gelled propellants is as tactical missile propellants. IRFNA and UDMH or MMH have been successfully tested in prototype missile systems. Gellants reduce Isp but additives such as aluminum increase it, recovering the loss due to the gellants. Solid propellant gas generators (SPGGs) provide efficient, lightweight pressurization. We assumed the Isp loss by gallants would be compensated by other additives such as metals.

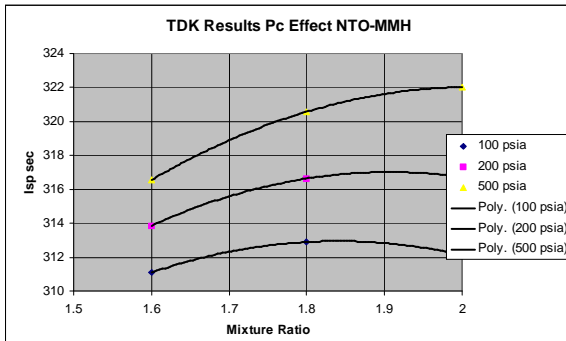


Figure 1 Isp for NTO-MMH

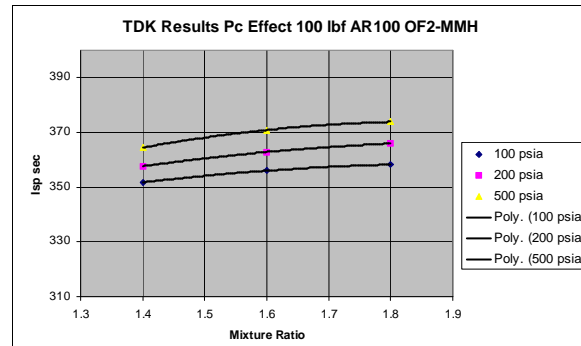


Figure 3 Isp for OF2-MMH

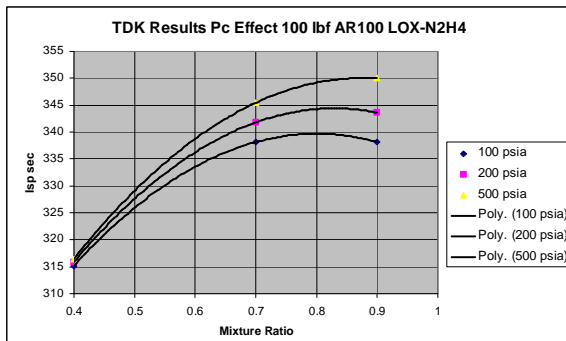


Figure 2 Isp for LOX-Hydrazine

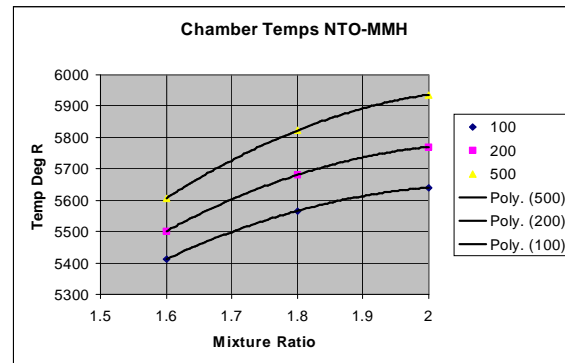


Figure 4 Chamber Temperatures NTO-MMH

VII. Main Results

Overall Stack-Up:

Performance of the propulsion options is affected by space vehicle mass and other considerations discussed below. An overview of general performance trends is presented in Fig. 7. LOX-LH₂ performance also varies significantly with system assumptions as described below; as shown here, a simple pressure-fed LOX-LH₂ system with cryocoolers is not competitive.

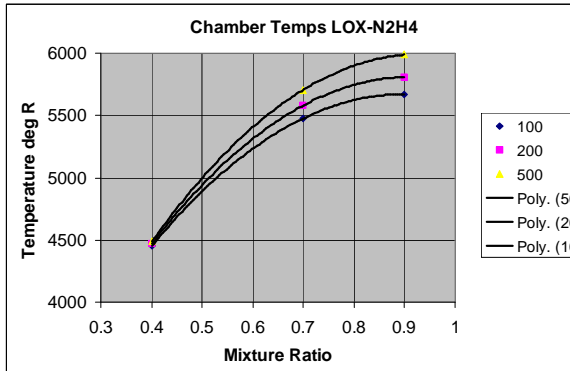


Figure 5 Chamber Temperatures LOX-Hydrazine

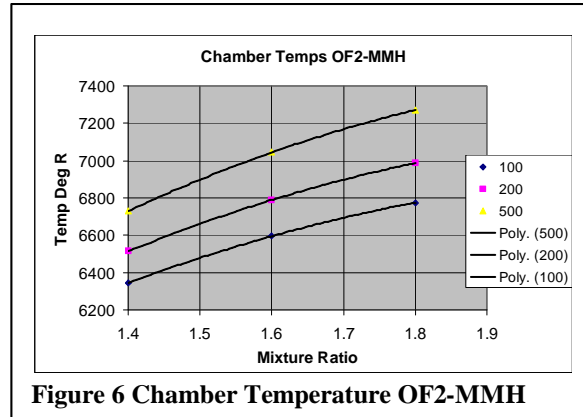


Figure 6 Chamber Temperature OF2-MMH

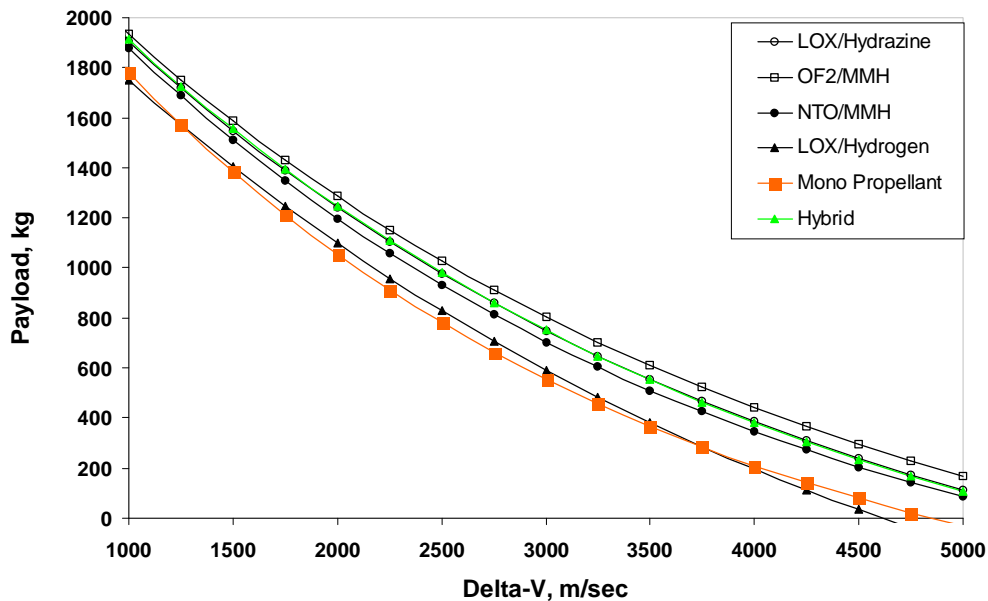


Figure 7 General Performance Trends for Advanced Chemical Propulsion

OF₂-MMH is the highest-performing system. LOX-hydrazine and the advanced hybrid have essentially equal performance. The baseline is next, and monopropellants and LOX-LH₂ have the poorest performance.

The performance differences depicted here are not dramatic. At higher delta Vs, the best systems typically offer payload 20% - 50% greater than the baseline. At lower delta Vs there is little motivation to adopt a new system, unless one were to select a monopropellant because of its relative simplicity. However, for a mature technology like chemical propulsion, even modest improvements can exhibit high leverage, especially for commercial users.

Fig. 8 shows inert mass trending for the propellants mainly considered in this study, above with full cryocooler mass penalty and below with no cryocooler mass penalty. The LOX-hydrogen system is low pressure pressure-fed in both cases; pump-fed systems exhibit somewhat less inert mass due to savings in pressurization and tank masses.

LOX-hydrazine – This combination suffers penalties relative to the baseline that tend to offset its higher Isp: (1) Overall lower density, slightly increasing tank and pressurization mass; (2) low temperature for LOX, requiring insulation, a greater mass of pressurization gas, and in most cases a cryocooler. Our analysis showed a modest net performance advantage. Fig. 9 presents a typical inert mass comparison with the baseline storables.

Cryocoolers – A space vehicle carrying a cryogenic propellant for more than a few months requires a cryocooler (refrigeration machine) to maintain the cryogen in a liquid state and prevent boiloff. The cryocooler represents an

inert mass penalty and requires power, which represents an additional mass penalty. For this study, we used cryocooler state-of-the-art from the literature, extrapolated as necessary to cover the range of power required. Fig. 10 shows curve-fit mass trending for cryocoolers.

The mass shown is the cryocooler machine only. Mass estimates in the study included power and control electronics, the power source (usually solar), and cooler thermal rejection. Heat leak into the cryogenic tank was calculated by an approximate formula for MLI, corrected for actual/theoretical heat leak ratio $f =$ about 2. Estimates for plumbing penetrations and tank supports were added. Subsequent research of references indicates the actual/theoretical ratio should be about 1.3 – 1.5. Optimization of MLI for a typical hydrogen tank is shown in Fig. 11. Typical power requirements and distribution of mass are shown in Fig. 12. Future studies should estimate and evaluate anticipated improvements in cryocooler technology. Mass reduction and efficiency improvement are both very beneficial.

$$Q = f\sigma\epsilon(T_o^4 - T_i^4)/N_{layers}$$

Cryogenic Propulsion – While missions up to some months’ duration may be possible without cryocoolers, and mild cryogenics such as liquid oxygen may be usable in a passively-cooled mode, for this study we assumed cryocoolers were needed for all missions involving cryogenic propellants, except the C3 topper. The significant mass penalty of cryocoolers reduces the performance potential for LOX-hydrogen systems.

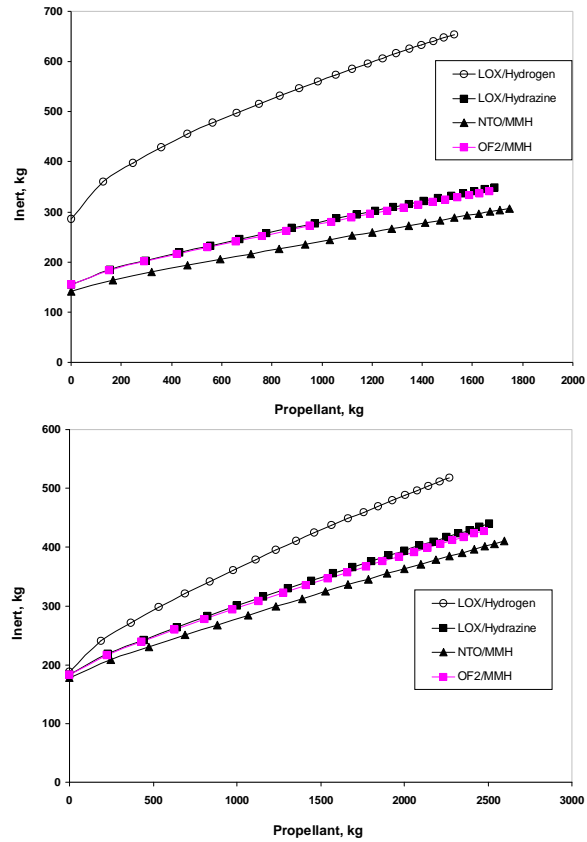


Figure 8 Propulsion System Inert Mass Trends

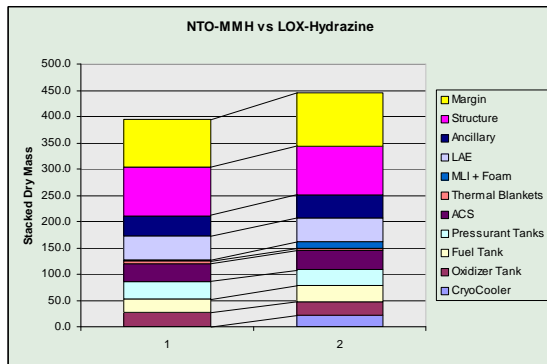


Figure 9 Inert Mass Comparison, Storables vs LOX-Hydrazine

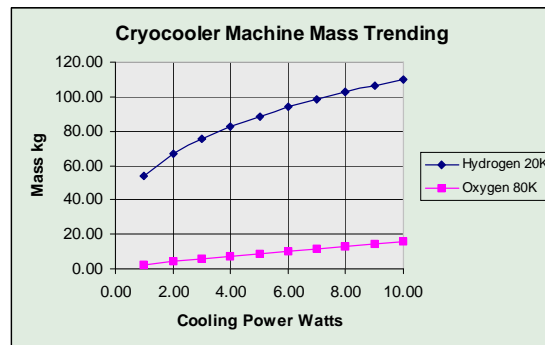


Figure 10 Cryocooler Mass Trending

Over 90% of the penalty is associated with the hydrogen cryocooler. The effects of the mass penalty on payload are reduced if the cryocooler and its support equipment can be jettisoned before the propellant is used. This may be feasible for some of the more challenging missions that benefit from cryogenic propulsion because these missions involve one major propulsion maneuver, such as planetary capture, perhaps followed in a few hours or days by further maneuvers, after which the propulsion system is not used.

Accordingly, there are 5 cases of interest for LOX-hydrogen, in ascending order of technology:

1. Pressure-fed, full cryocooler mass penalty
2. Pressure-fed, jettison cryocooler power and thermal systems (may be easier than jettisoning the cryocooler itself, since the latter must make intimate thermal contact with the well-insulated propellant tanks)
3. Pressure-fed, jettison entire cryocooler system
4. Pump-fed, jettison entire cryocooler system
5. Pump-fed, no cryocooler (short duration mission)

Figure 13 shows the effect of these variations, relative to the baseline, for a median-size system with start mass (including payload) 3000 kg. The cryogenic system varies from worst to best performer, depending on the technology level.

There is also a significant size effect, as illustrated in Figure 14. Here, the median technology level (3, pressure-fed, jettison entire cryocooler) is compared for start masses of 1000 and 5000 kg. Again, the cryogenic system varies from worst to best performer. The change is mainly due to reducing dominance of thermal insulation mass as the propellant load and tank size increase.

Figure 15 presents an inert mass comparison between a pressure-fed cryogenic system and the storable baseline. For the pump-fed cryogenic system the propellant and pressurant tank penalties are much less, but the other differences change very little.

Literature review indicates (1) such a pump can be built, but will be exploring new ground; (2) the best approach is a conventional turbopump.

Exotic propellants offer moderate performance increases, and merit further evaluation. Their typically high combustion temperature raises doubts as to realization of high Isp potential, and this in particular needs assessment. LOX-hydrazine comes within 20 sec of OF₂-MMH at chamber temperatures 660 C less. We note that the contemporary iridium-coated rhenium combustion chamber technology was originally developed for use with fluorine. Further examination of fluorine-hydrazine is recommended, since better performance at acceptable combustion temperatures may be achieved. The boiling point of fluorine is about 85K versus 125K for OF₂. In most applications this won't make much difference.

Advanced Monopropellants - In smaller systems with moderate delta V requirements, they (advanced monopropellants) perform about as well as other propellants/systems evaluated. The simplicity of only one propellant is attractive. Note in the Telemachus perihelion performance discussed below, monopropellant performs about as well as the other options.

These systems need a catalyst bed or ignition system. Once ignited, they probably do not need a catalyst to continue combustion. For single-burn missions they may be particularly attractive. They may not be as suitable for attitude control propellants (low thrust, small impulse bit). Thus they may not be so attractive where an NTO-hydrazine system can fulfill both functions.

Gelled Propellants - Propulsion system geometry for the tactical missile application is cylindrical (Fig. 16), ideal for a missile but problematical for some spacecraft propulsion systems. (It is, however, well suited to Mars ascent propulsion system geometry.) It would be useful to investigate feasibility of near-spherical tank geometries, especially efficient expulsion of gelled propellant. Brief discussions with investigators familiar with gelled

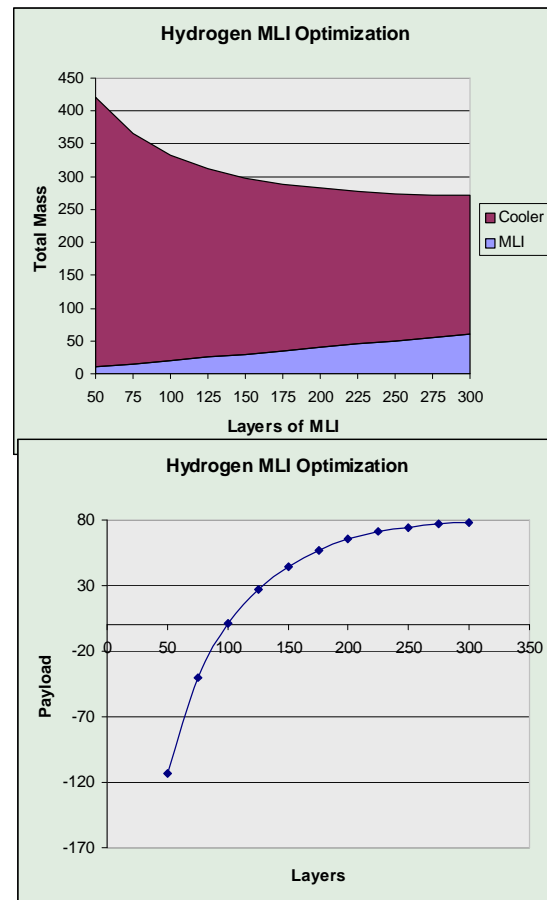


Figure 11 Hydrogen MLI Optimization

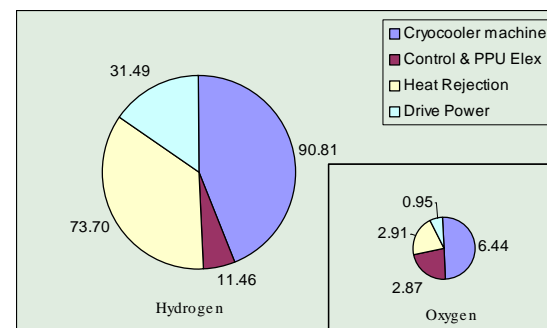


Figure 12 Power and Mass Distributions

propellant state of the art indicated that a conventional positive expulsion device such as a bladder would work well for near-spherical tank geometry.

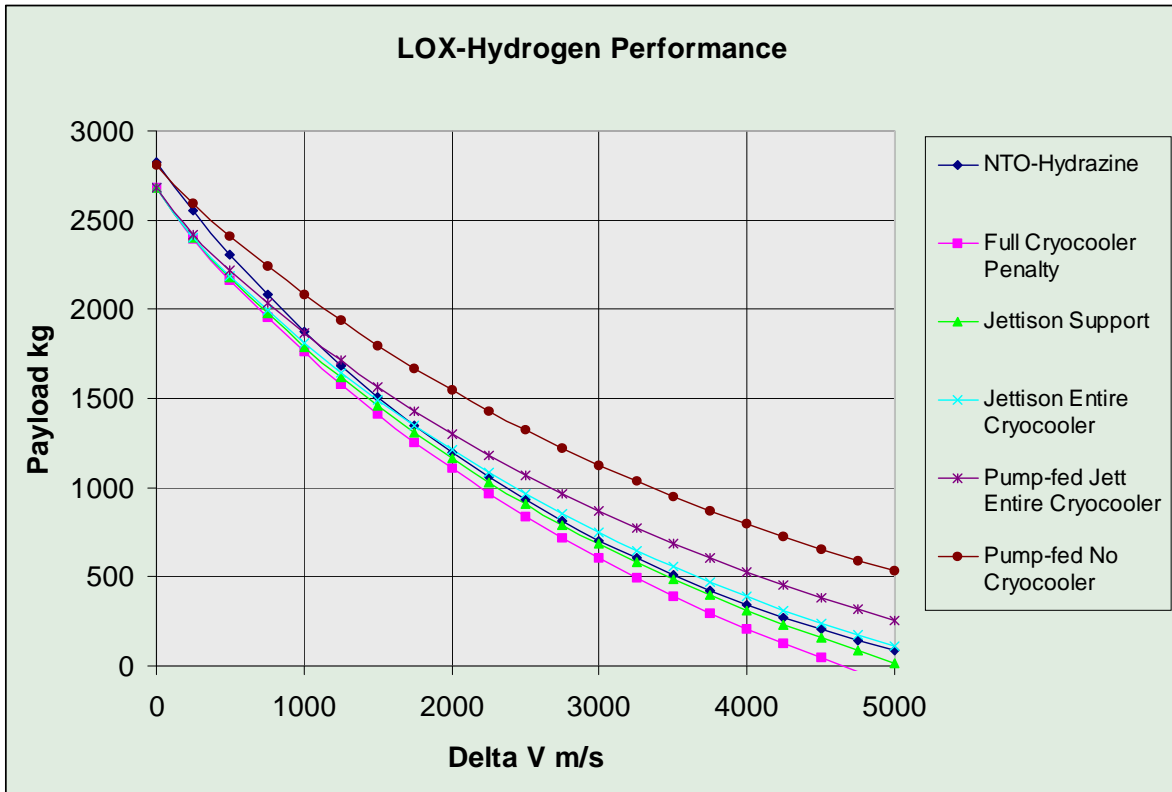


Figure 13 Cryogenic Performance Trending as a Function of Technology

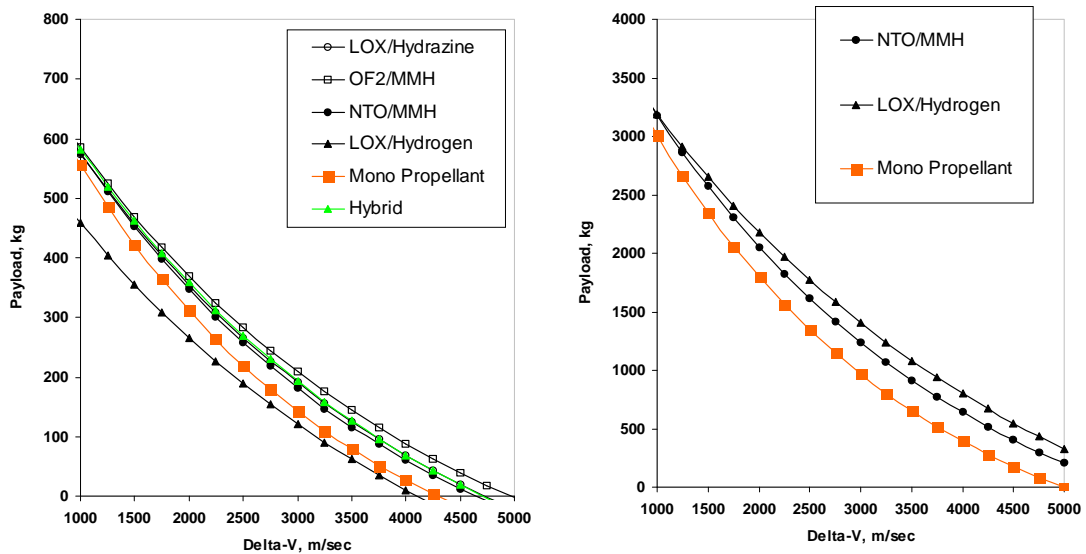


Figure 14 Cryogenic Performance Trends for 1000 & 5000 kg Start Mass

SPGG pressurization is nominally only suited for one burn. (More than one SPGG could be used.)

Our evaluation is that gelled propellants are suited for planetary ascent propulsion and should be evaluated for that application, but may offer few advantages for in-space application. Cases where the gelled propellant can be allowed to freeze and then be thawed for use may show a system-level benefit. Current research is directed to capability to freeze and thaw gelled propellants; this would be a significant advantage for a Mars ascent system.

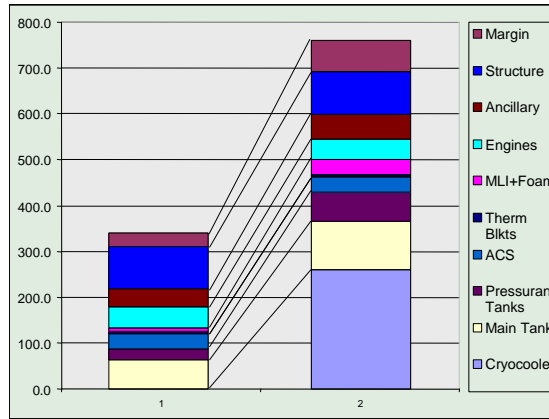


Figure 15 Inert Mass Comparison, Storable vs Cryogenic Propellants

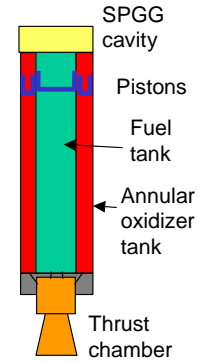


Figure 16 Gelled Propellant Geometry

Specific Mission Applications – Propulsion comparisons are further illuminated by some of the specific applications analyzed during the study.

The C3 Topper burns immediately after launch vehicle separation to maximize benefit of Earth’s gravity field. A cryocooler is not required for a cryogenic stage since duration is quite short. Starting total mass will be on the order of 5 to 10 t. Thrust required is 15 to 25 kN (3 to 5 klbf). The higher Isp of a cryo stage offers significant performance advantage over a solid rocket motor as illustrated in Figure 17.

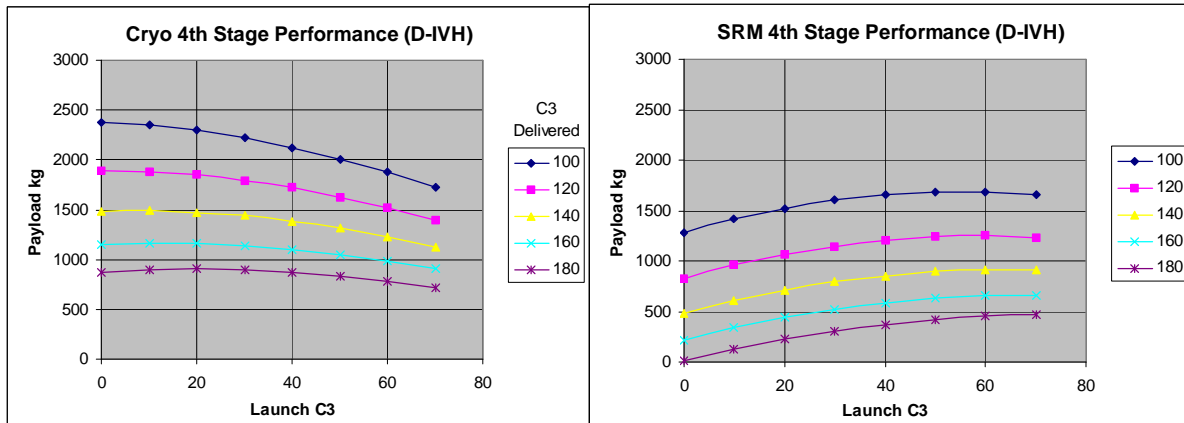


Figure 17 Comparison of Cryogenic C3 Topper to Solid Propellant Rocket Motor

The Telemachus mission has two major propulsion needs. A C3 Topper or an electric propulsion system eliminates the inner planet gravity assists of the baseline mission by enabling transfer direct to Jupiter, and saving several years of transfer time. Once arriving at perihelion, a further burn is required. Figure 18 shows a mass comparison of advanced chemical propulsion technologies for this maneuver. The monopropellant is the most logical alternative to the baseline bipropellant in view of its simplicity. Higher performing systems offer little performance advantage. We expect a similar result for Venus Aeronomy.

Several alternative mission profiles were evaluated for Neptune Orbiter. The baseline reference in this case is SEP-aerocapture, which can deliver about 1200 kg payload to the highly elliptic Neptune orbit. None of the advanced chemical options reach that performance capability. The best of the options evaluated could deliver about 600 kg, assuming SEP/VGA delivery to Neptune transfer (eliminating need for aerocapture), as shown in Figure 19.

We found a non-nuclear option for Titan Sample Return, using two EELV heavy launches. The first delivers an aerocaptured spacecraft to Titan orbit, carrying the descent/ascent system. The second delivers another aerocaptured spacecraft to Titan orbit, carrying the return system. After the sample is acquired, the ascent system makes rendezvous with the return system and transfers the sample. The return system uses advanced chemical propulsion to depart Titan for return to Earth. The sample carrier performs Earth entry and landing similarly to current Mars

sample return mission concepts. A cryogenic stage was preferred for this application, but a storable propellant stage could do the return with a longer trip time.

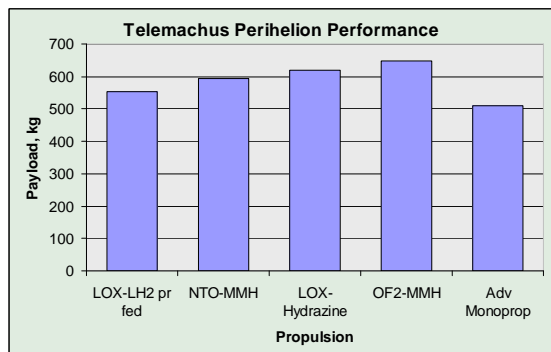


Figure 18 Propulsion Performance Comparison for Telemachus Perihelion Burn

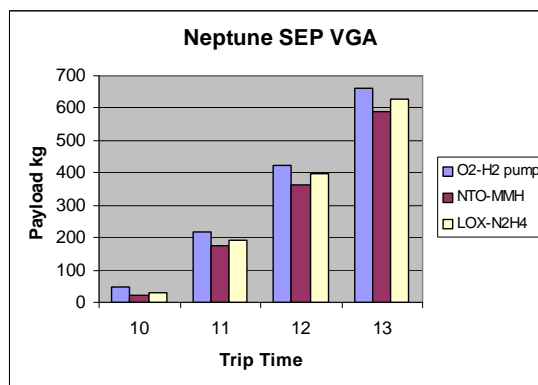


Figure 19 Propulsion Performance Comparison for Neptune Capture (Trip times in years)

VIII. Indications and Conclusions

Many of our conclusions were preliminary, or regarded as indicative only, since this was a brief study intended to point the way for more detailed work. In general, chemical propulsion is a mature technology and the improvements identified, while significant, are not dramatic.

The most promising applications for advanced chemical propulsion appeared to be those where high performance is needed, and in those cases the highest-performing propulsion options appeared to offer the greatest benefit. LOX-hydrogen offers best performance, if (1) cryocooler mass penalty can be ameliorated, and (2) a pumped engine is developed, to reduce mass penalties associated with hydrogen pressurization and increase Isp. The simplest application for LOX-hydrogen is a small upper stage for launch vehicles (the “C3 Topper”). This extends the C3 capability of current EELVs to about 200, albeit with less and less payload as C3 is increased. The benefits are appreciable beginning at C3 about 40. Without a C3 topper, EELV payload goes to zero at C3 less than 100. The cryogenic C3 topper offers payload increase over a solid rocket about 50% to 60%.

Significant technology needs, beyond small turbopumps, for hydrogen use are development of thick MLI, and improvements in cryocooler mass and efficiency. Performance advantages for LOX-hydrogen depend on these technology advances; without them, its performance was less than current technology.

After LOX-hydrogen, the best performers were OF₂-MMH and LOX-hydrazine in that order. If LOX-hydrogen technology is not developed, or experiences delays or difficulties, fluorine-bearing oxidizers should be given serious consideration. Fluorine-hydrazine may prove a better option than OF₂-MMH. LOX-hydrazine offers modest performance advantages, and may be of particular interest for short-duration missions for which cryocoolers are not needed, or if a passive cooling method can be developed.

We spent relatively little effort on hybrids. Hybrids with metal hydride additives may offer Isp ~ 350. If so, they may be competitive. This class of hybrids should be regarded as high risk, high payoff. Modest-scale testing to confirm performance potential might prove relatively inexpensive, and would go a long way towards assessing the payoff potential.

Advanced monopropellants appeared promising for modest performance applications. At Isp >= 275, performance about equals state-of-art biprops, and systems are simpler. Whether they would be more reliable needs to be assessed. Catalysts and/or ignition remain a technology issue.

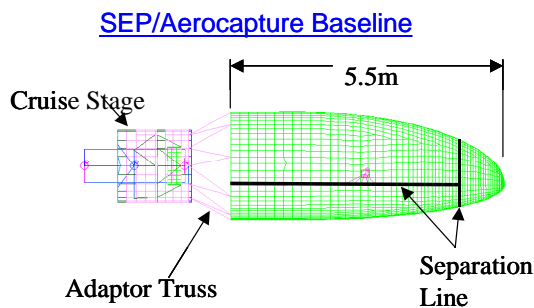
Gelled propellants appear mainly of interest to planetary ascent. However, if gels can increase the propellant storage temperature, they could be of interest for missions nearer the Sun. Also, if gels can permit long-period freezing of propellants on trajectories to the outer planets, they may simplify spacecraft/propulsion thermal design for these missions.

IX. References

1. Falk, A. Y., Clapp, S. K., and Nagal, C. K., Space Storable Propellant Performance Study, NASA CR-722487, Nov. 1968.

2. Schneider, S. J., On-Board Propulsion System Analysis of High Density Propellants, AIAA Paper No. 98-3670, 34th AIAA/ASME/SAE/ASE Joint Propulsion Conference and Exhibit, July 13-15, 1998, Cleveland, OH.
3. Schmidt, H. W., Handling and Use of Flourine and Fluorine-Oxygen Mixtures in Rocket Systems, NASA SP-3037, 1967.
4. Bond, D. L., Appel, M. A., and Kruger, G. W., Fluorine-Hydrazine Propulsion Technology Update, The 1980 JANNAF Propulsion Meeting, Vol. 5, pp. 147-164.
5. Personal Communication, B. Reed, NASA Glenn Research Center, August, 2003.
6. Stultz, J. W., Thermal Analysis of High-Energy Propulsion System for a Rover Class Mars Orbiter, AIAA Paper No. 78-888, 2nd AIAA/ASME Thermophysics and Heat Transfer Conference, Palo Alto, CA, May, 1978
7. Dunn, S., Coates, D., and Nickerson, G. (1999), TDK99 Two Dimensional Kinetics (TDK) Nozzle Performance Computer Program User's Manual, SEA Inc.
8. Reed, B. R. and Schneider, S. J., Hydrogen/Oxygen Auxiliary Propulsion Technology, AIAA Paper No. 91-3440, Conference on Advanced Space Exploration Initiative Technologies, Sept. 4-6, 1991, Cleveland, OH (also NASA TM 105249).
9. Honda, L., Calvignac, J., and Matuszak, L., Storable Thruster Technology Program-Mission Study, JANNAF 2002.
10. Plachta, D. and Kittel, P. An Updated Zero Boil-off Propellant Storage Analysis Applied to Upper Stages or Depots in a LEO Environment, AIAA 2002-3589, 36th AIAA/ASME/SAE/ASEE Joint Propulsion Conference and Exhibit, July 7-10, 2002, Indianapolis, IN.
11. ter Brake, H. J. M. and Wiegerinck, G. G. M., Low-power Cryocooler Survey, Cryogenics, 42 (2002), pp. 705-718.

Neptune Orbiter



• SSE Long-Term Mission (after 2013)

• Mission Objectives

- Orbit Neptune, visit all major parts of Neptune system
- Cassini-like science investigation of the Neptune system
 - Neptune atmosphere, interior, fields
 - Many Triton flybys/gravity assists
 - Nereid flyby upon approach
 - Small inner satellites
 - Rings
 - Significant orbit evolution over mission lifetime: "Tour"

• Mission Requirements

- Sciencecraft requirements
 - Payload: mass, power, (data volume?)
 - Driving observation accommodations
 - NAC pointing & stability during ~500 km Triton flybys
 - Telecom; Cooled IR focal plane
- ~2 years in Neptune orbit
- Cruise "not much more than 10 years"

Neptune Orbit: 4000 x 400,000 (alt's) 157.3 deg incl.

Mission Payload 500 kg Orbiter + 75 kg monopropellant [for periapse raise if aerocapture; otherwise est. 40 kg]

Target Launch Date 2010

Mission architectures/transportation

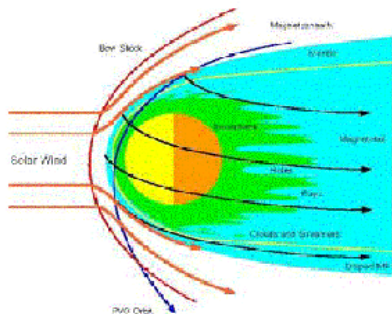
challenges

- Multiple gravity assists incl Jupiter to Neptune
 - Cruise time for most trajec. over 10 years
- SEP to fast Neptune transfer; arrival V_i ? 15 km/s; Capture ? $V > 5$ km/s

• Options

- SEP/Aerocapture
- SEP/Advanced Chem
- [NEP]
- MXER Tether/Adv. Chem
- Solar Sail/Aerocapture

Venus Aeronomy Probe



SEC Mission

Science Objectives

- Determine Mechanisms for Energy Transfer From Solar Wind to Ionosphere and Upper Atmosphere
- Measure Charged Particles Responsible for Auroral-Type Emissions and Infer their Acceleration Mechanisms
- Determine Formation Processes for Ionospheric Magnetic Flux Ropes, Ionospheric "Holes" on the Nightside and the Loss of Ionospheric Plasma in the Form of Streamers, Rays and Clouds

Mission Description

- Example Mission Design
 - Small Delta II
 - 1-Year Flight Time, 1 year OPS
 - High Inclination Elliptical Orbit
- 150 km x 12,000 km
- Flight System Concept
 - Spin-Stabilized Platform
 - Floating Potential Neutralization
 - Solar array power
 - Mass Unk. probably tens of kg science payload

Target Launch Date Unknown

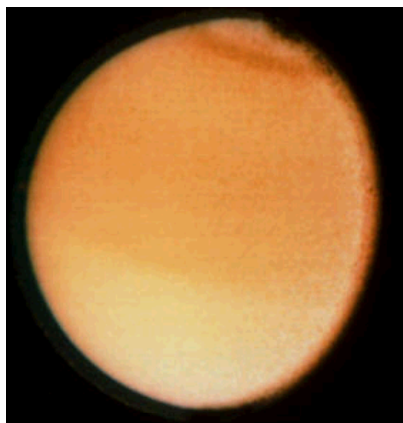
Mission architectures/ Transportation challenges

- Launch direct to Venus; propulsive capture into elliptical orbit

Options

- Aerocapture
- Advanced Chem; good example of small advanced chem system
- MXER Tether/Adv. Chem

Titan Explorer



- SSE mid-term mission (Project start after 2005)
- Mission Objectives
 - Orbiter and *in situ* element at Titan
 - Detailed investigation of Titan and its organic environment
 - Global high-resolution IR & SAR mapping
 - Global measurements of gross surface morphology, composition, chemistry
 - Atmospheric composition, structure, dynamics
 - Composition & distribution of organics, organic chemical processes, context, & energy sources
 - Pre- & proto-biological chemistry

Mission Requirements

- Sciencecraft requirements
 - Payload: mass, power, (data volume?)
 - Driving observation accommodations
 - Telecom
 - Cooled IR focal plane
 - SAR
- ?2 years in Titan orbit
- One year *in situ* element lifetime
- Cruise time?

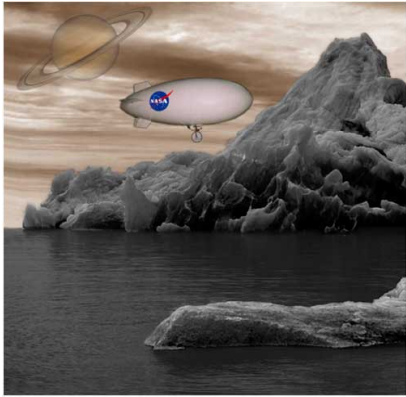
Mission architectures / Transportation challenges

- Inner SS / Jupiter gravity assists to Titan
 - Cruise time for most trajectories 8 years or less
- SEP transfer to Saturn; arrival V_{∞} ? ? km/s
 - Aerobraking V_{rel} 6 - 10 km/s, ? $V > 4 - 8$ km/s
- JGA tends to yield higher encounter velocity at Titan

Transportation options

- Gravity assist or SEP to Saturn system
- Rigid aeroshell or ballute aerocapture
- Propulsive capture

Titan Sample Return



Long-Term SSE Mission

Science Objectives

- Obtain selected surface samples, including "pre-biotic" material if it exists on Titan
- Each sample in its own container and identified as to location and situation where sampled
- Maintain Titan surface temperature throughout return mission

Mission Requirements

Titan orbit 1800 – 2000 km

Short surface stay time?

RTG required on lander, or can we get by with batteries?

Titan orbit rendezvous with sample container transfer

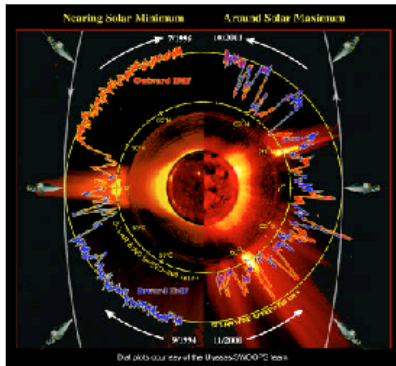
Propulsive return to TEI; spacecraft supports Earth lander (power, GN&C)

Direct entry landing at Earth, passive lander

Transportation Challenges

- Achieving trip time (high delta Vs)
- Ascent from Titan through deep atmosphere
- High approach velocity
- Outer solar system lack of energy source (for propulsion)
- In-space baseline is NEP

Solar Probe



SEC mission

Mission Description

• Mission Design

- Launch opportunity every 13 months (baseline is May 2010 launch)
- Two solar passes (polar, 4 RS) within 7.1 yr; three within 11.1 yr
- Atlas 551/Star-48B launch; 713 kg @ C3 128 km² /s²
- JGA traj., post-perihelion DV for successive passes
- 3.1-yr cruise; 0.02 x 5 AU final orbit with period 4 yr

• Flight System Concept

- 15° half-angle carbon-carbon heat shield
- 3-axis stabilized with 0.2° pointing control and 0.05° knowledge
- RTG power source (3 Multi-Mission RTGs supply 330 W BOL)
- Ka-band downlink, X-band uplink, 34-m DSN dishes
- Data rate: up to 40 kbps real-time with 200 kbps additional stored data
- Payload: 50 kg, 47 W

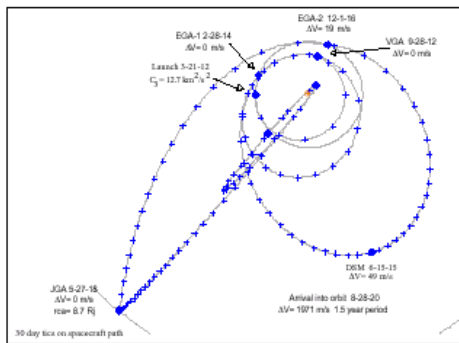
Transportation Options:

Advanced Chem or SEP to replace Star-48B
Alternatives to JGA do not appear reasonable

Science Objectives

- Determine acceleration processes and find source regions of fast/slow solar wind at min/max solar activity
- Locate the source and trace the flow of energy that heats the corona
- Construct 3-D coronal density configuration from pole to pole; determine subsurface flow pattern and structure of polar magnetic field and its relationship with the overlying corona
- Identify acceleration mechanisms & locate source regions of energetic particles; determine the role of plasma waves and turbulence in the production of solar wind and energetic particles

Telemachus



Science Objectives

- Understanding our changing Sun and its effects throughout the Solar System (Space Science Enterprise Strategic Plan, November 2000)
- Reveal through helioseismology how convection and rotation couple & magnetic flux accumulates in the polar regions (solar dynamo)
- Uncover the mechanism(s) in the polar regions of the Sun that accelerate the solar wind & energetic particles and expel plasma and magnetic fields (CMEs)
- Exploit polar viewpoint to examine distribution of radio and x-ray emission simultaneously from all solar longitudes
- Determine the physics of the strongest stream/ stream plasma interactions and transient shocks where they are first formed in the heliosphere

Mission Description

- Example Mission Design
- Delta III Launch, 1765 kg @ $C_3 = 17 \text{ km}^2/\text{s}^2$ (12.7 min)
- VEEJGA Trajectory with Perihelion DV
- 8.4 yr cruise, 3 yr science ops
- 0.2×2.5 AU Final Orbit, Period: 1.5 years - 90° Heliographic Inclination
- 1st 4.5 years ecliptic (VEEJGA); 3 years In Final Orbit (polar)
- Flight System Concept
- 3-Axis and Spin-Stabilized Platform
- Solar Arrays (Ultraflex, High Efficiency Silicon, High Temp Cells)
- Payload: 33 kg, 42 W, 8 kbps
- 2239 m/s DV
- 30 arcsec (control), 10 arcsec (knowledge)

Transportation Options

- SEP or Adv Chem to obtain Jupiter trajectory directly without Earth or Venus gravity assist; also, advanced chem may benefit perihelion DV; note severe thermal environment
- Probably no reasonable alternative to JGA; could evaluate solar sail

Modeling of Spacecraft Advanced Chemical Propulsion Systems

Michael P.J. Benfield* and Jeremy A. Belcher†

Science Applications International Corporation, Huntsville, Alabama, 35806

This paper outlines the development of the Advanced Chemical Propulsion System (ACPS) model for Earth and Space Storable propellants. This model was developed by the Systems Technology Operation of SAIC-Huntsville for the NASA MSFC In-Space Propulsion Project Office. Each subsystem of the model is described. Selected model results will also be shown to demonstrate the model's ability to evaluate technology changes in chemical propulsion systems.

Nomenclature

ACS	= attitude control system
C_{MLI}	= constant from the literature, kg/m ² -layer
D_{TP}	= propellant tank diameter, m
D_{TPF}	= fuel tank diameter, m
D_{TPMAX}	= larger of fuel or oxidizer tank diameter, m
D_{TPOX}	= oxidizer tank diameter, m
F_{REG}	= ratio of regulator inlet to outlet pressure at DOP, >1.0 (baseline value of 1.5)
g_0	= universal gravitational constant, 9.80665, m/sec ²
I_{sp}	= propellant combination specific impulse, sec
M_{ACS}	= total mass of monopropellant ACS, kg
M_{BT}	= total blanket mass of system, kg
M_{CAB}	= cable harness mass, kg
M_{CE}	= mass of cryocooler control electronics, kg
M_{CRR}	= mass of cryocooler radiator, kg
M_{CRY}	= mass of cryocooler, kg
M_{DIST}	= distribution element (in propellant/pressurant feed system) mass, kg
M_F	= fuel mass, kg
M_{GC}	= ground cooling mass penalty for cryogenic propellant, kg
M_{HDOP}	= mass of gaseous helium in propellant and pressure tanks at DOP, kg
M_{HPDOP}	= mass of gaseous helium in propellant tank at DOP
MLI	= multi-layer insulation
M_O	= launch mass, kg
M_P	= total propellant mass, kg
M_{PACS}	= mass of monopropellant for ACS, kg
M_{POW}	= mass of power system required for cryocooling, kg
MR	= mixture ratio, mass of oxidizer/mass of fuel
M_{TCRS}	= mass of soft cryogenic propellant cryocooling subsystem, kg
M_{TPC}	= mass of composite propellant tank, kg
N_{LEGS}	= number of distribution lines in propellant/pressurant feed system
N_{MLIT}	= number of layers of MLI assumed to cover entire propulsion system
P_{TP}	= propellant tank pressure, psia
R_{HE}	= helium gas constant, 2077.25 J/kg-K
T_C	= cold head temperature, K
T_E	= environmental temperature for specific mission/system, K

* Systems Engineer, Systems Technology Operation, 675 Discovery Drive, Huntsville, AL 35806, AIAA Member.

† Junior Engineer, Systems Technology Operation, 675 Discovery Drive, Huntsville, AL 35806, AIAA Member.

- T_{THDOP} = temperature of helium tank at DOP, K
- ΔV = velocity required for maneuver, m/sec
- V_{TPHDOP} = volume of expelled propellant, m³
- W_C = cooling power, W
- W_{IN} = power into cryocooler, W
- Wt = rejected heat, W
- Z = compressibility factor representing departures from ideal gas performance
- α_{POW} = specific mass of the power system, kg/W
- ρ_F = fuel density, kg/m³
- ρ_{HBOM} = helium density, kg/m³
- ρ_{OX} = oxidizer density, kg/m³

I. Introduction

The ACPS was developed by the Systems Technology Operation of SAIC-Huntsville for the NASA MSFC In-Space Propulsion Project Office. It was created to give a means to evaluate advanced Earth and space storable chemical propulsion systems for missions of interest. The model is intended to provide for rapid and accurate estimates of the key characteristics and performances of advanced chemical propulsion systems as functions of propulsion technology options and specific mission requirements. Overall ACPS architectures were based on recent studies and the successful AXAF-I and Cassini propulsion subsystems. Components were parametrically modeled using a combination of experience-based and State-of-the-Art (SOA) physics-based models. At the present, the model can evaluate a broad range of technology options and mission combinations. A model modification is planned that will add a hard cryogen propellant (LH₂) capability.

Figure 1 shows a diagram of the overall ACPS model. Initial inputs to the model include the mission profile (masses, delta-v's and spacecraft thermal environment) and selected subsystem options (propellant residuals, feed system pressure changes, etc.). There are 10 subsystems in the model as shown in Figure 1. The ACPS output represents a spacecraft for a given mission.

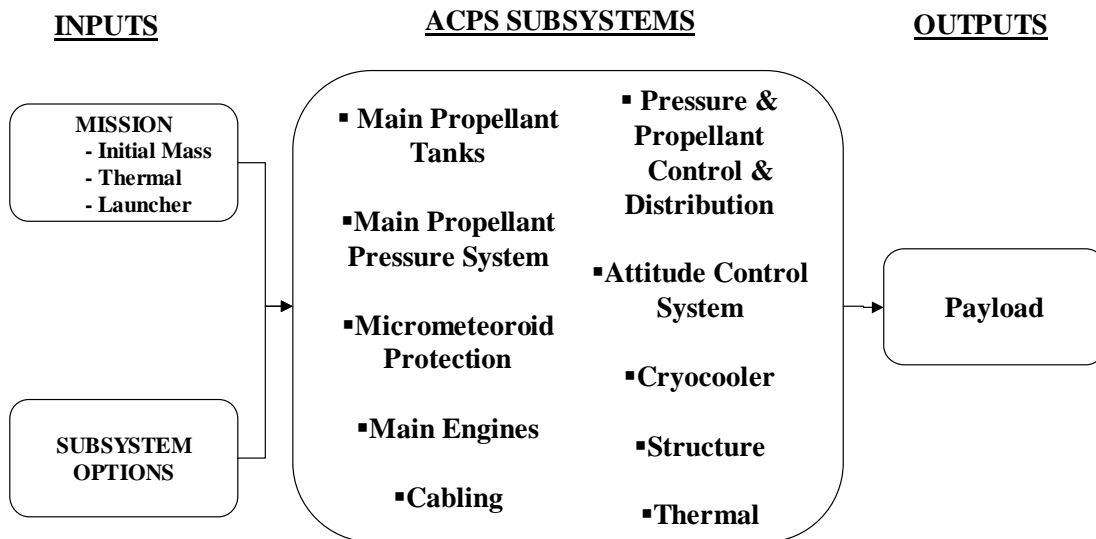


Figure 1: The ACPS Model Flow.

II. Architectures

The ACPS architecture is based on the AXAF (Chandra) (Reference 1 and 2) and Cassini (Reference 3 and 4) propulsion systems, a recent study of planetary stages that included both soft cryogenic and Earth-storable propellant combinations (Reference 5), and a review of planetary spacecraft by the Lockheed Martin Corporation (Reference 6). Both Earth-storable and soft cryogen propellant systems were assumed to be relevant to the model. Options include a monopropellant as well as bi-propellant main engine system. Spherical tanks that were longitudinally located to one another were assumed for this model for comparison purposes. Pressurant tanks were also assumed to be nested with the propellant tanks.

III. Propellant Load

The propellant load for the mission is calculated by the Eq. (1).

$$M_p = M_o \left(1 - e^{\frac{-\Delta V}{g_o I_{sp}}} \right) \quad (1)$$

Depending on the mission, several ΔV burns and mass additions (sample return) or mass deletions (lander separation) can be added in the appropriate sequence to determine the amount of propellant needed for a given mission profile. Once the amount of propellant has been determined for the mission, residuals and margins are then added. Knowing the mixture ratio of the propellants, the amount of oxidizer and fuel can then be determined for the main propellant tanks.

IV. Main Propellant Tanks

Once the propellant load of the oxidizer and fuel is known, the volume and mass of the main propellant tanks can be calculated. Figure 2 depicts the overall method for calculating the main propellant tank mass.

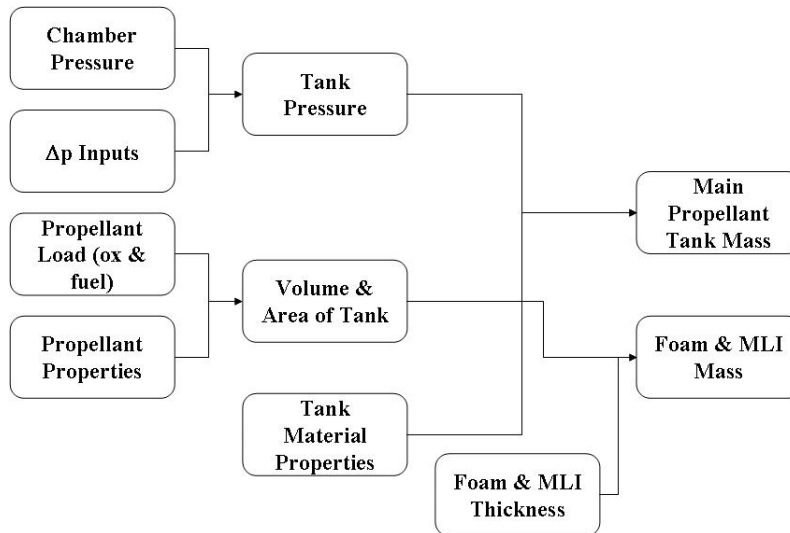


Figure 2: Main Propellant Tank Subsystem Flow.

The propellant tank pressure is a driver on tank mass and is derived from the main engine chamber pressure assumed. The feed system from the tank to the engine is assumed to have pressure drops associated with the engine injector, a venturi value, and lines. Those pressure drops are inputs to the system and can be changed to accommodate specific design approaches. Either a composite overwrap or titanium tank may be selected for evaluation.

For composite propellant tanks, the model is scaled from the AXAF-I propellant tanks with the mass of each composite tank calculated by an equation located in the ITAR version of the paper available to U.S. citizens and restricted from export or public disclosure.

For Titanium tanks, the model is scaled from values for commercially available tanks obtained from Reference 7. Tank masses for various burst and operating pressures were selected. These masses included the propellant management devices (PMD). The tank masses were all linearly normalized to an operating pressure of 300 psia for this model. Having this data, a linear regression equation was created for tank mass as a function of tank diameter. Figure 3 shows the relationship between the titanium tank mass and the tank diameter.

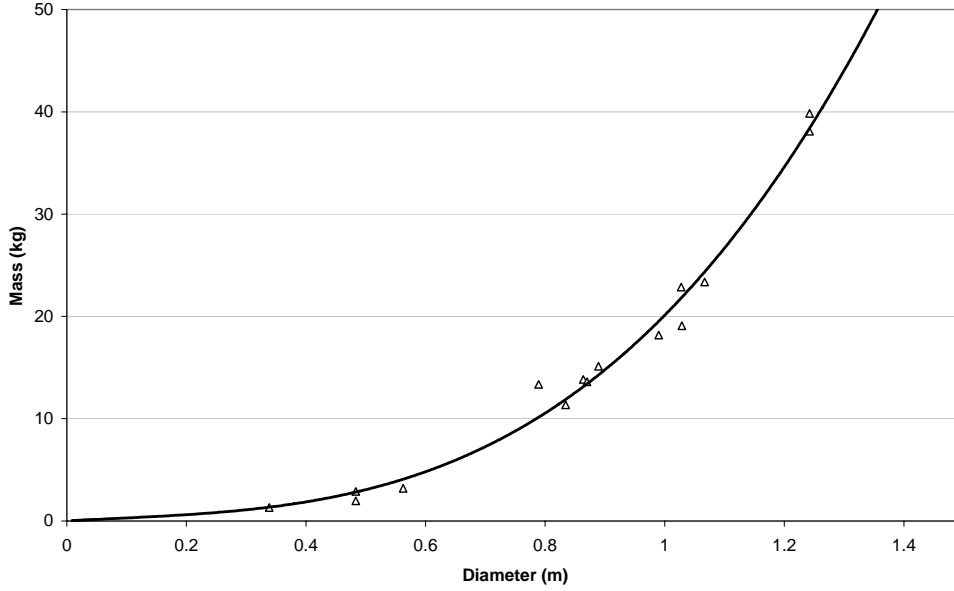


Figure 3: Titanium Shell Mass as a Function of Tank Diameter.

From this figure, Eq. 2 can calculate taking the linear regression curve generated and knowing that the tanks were normalized to an operating pressure of 300 psia, the titanium tank mass.

$$M_{TPT} = \left(\frac{P_{TP}}{300} \right) \left[22.34(D_{TP})^3 - 5.50(D_{TP})^2 + 3.28(D_{TP}) \right] \quad (2)$$

V. Propellant Pressurization

The method used for determining the amount of helium required to pressurize the system is taken from Reference 8. Because nested tanks are envisioned for these spacecraft, it is assumed that the helium temperature will always equal the propellant temperature. Using this assumption and the information from Reference 8, Eq. (3) was developed to calculate the required helium amount.

$$M_{HDOP} = M_{HPDOP} \left(1 + \frac{F_{REG} P_{TP}}{ZR_{HE} T_{THDOP} \rho_{HBOM} - F_{REG} P_{TP}} \right) \quad (3)$$

$$M_{HPDOP} = \frac{P_{TP} V_{TPHDOP}}{ZR_{HE} T_{THDOP}} \quad (4)$$

VI. Main Engines

The main engine model was scaled from data from References 9. This was slightly modified to account for the heavier rhenium engines (Reference 10 and Reference 11) assumed herein. Rhenium engines were selected, as they are the highest performing engines available at the thrust levels of interest. Figure 4 shows the relationship between the main engine mass between 0-10 kg and main engine thrust levels between 100-1000 N.

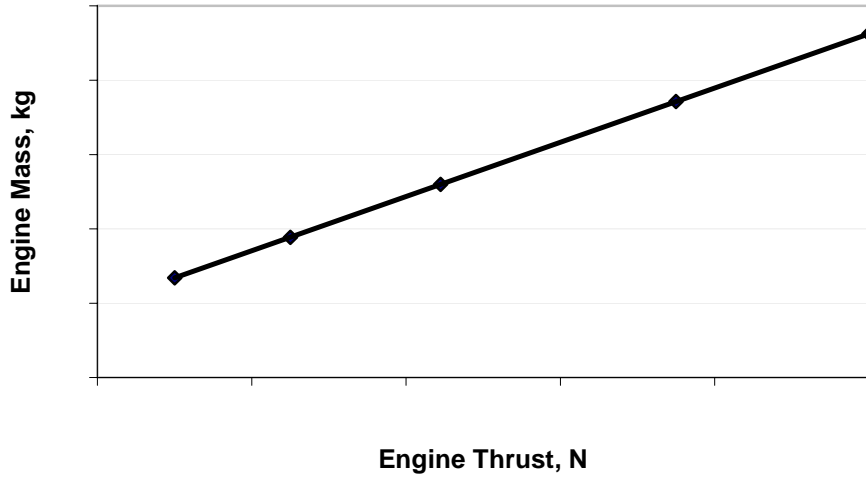


Figure 4: Engine Mass as a Function of Engine Thrust.

Accounting for the engine mounts and heat shields results in an equation, located in the in the ITAR version of the paper available to U.S. citizens and restricted from export or public disclosure, which calculates the mass of the main engines and the associated mounts and heat shields.

VII. Pressure and Propellant Control/Distribution

The propellant and pressurant control and distribution components were separately considered. The control components consisted of valves, regulators, and other components that influence the values of pressure and flow rate. The control components were assumed to be like those used on Cassini as they were representative of a highly reliable spacecraft. Minor modifications were made because of the separation of the pressurant tanks for the oxidizer and fuel assumed herein. The types and number of Earth and space-storable pressurant and propellant control elements were from the Cassini spacecraft (Reference 3). The masses of the Earth and space-storable pressurant and propellant control elements were from Reference 12. Table 1 shows the data for the propellant and pressurant components. The distribution elements consisted of lines, tie downs, heaters, and MLI, etc. associated with the distribution of the pressurant and propellant systems and the AXAF propulsion system was used as a reference for those elements.

Number of Engines	Monopropellant		Bipropellant	
	Earth-storable	Cryogenic	Earth-storable	Cryogenic
1	12.61 kg	-	23.66 kg	43.99 kg
2	14.17 kg	-	25.22 kg	47.08 kg

Table 1. Masses of Pressurant and Propellant Control Components.

Equation (5) calculates the mass of the distribution elements of the chemical system.

$$M_{DIST} \approx 2.37(N_{LEGS}) \left\{ (M_F)^{1/3} \left[\frac{(MR)\rho_F + \rho_{OX}}{\rho_F \rho_{OX}} \right]^{1/3} \right\} \quad (5)$$

VIII. Attitude Control System (ACS)

The attitude control system (ACS) was based on Cassini and was assumed to use hydrazine monopropellant system that utilized 12 fully redundant thrusters for three-axis stabilization (References 3 and 4). The required hydrazine propellant mass is extremely mission dependent, but was set as the same fraction of initial spacecraft mass as used for Cassini (Reference 4):

$$M_{PACS} = 0.0237(M_0) \quad (6)$$

Masses of the spherical propellant tanks were set as a fraction of the ACS propellant mass derived from a straight-line plot of the values on AXAF-I (Reference 1) and Cassini (Reference 4). The mass of the distribution elements was taken from AXAF-I data modified to account for the different number of thrusters on Cassini. Incorporating all of the scaling performed, the final mass of the ACS is found by Eq. (7).

$$M_{ACS} = 0.025 M_0 + 18.7 \quad (7)$$

IX. Zero Boiloff (ZBO)

The cryocooler model is designed for zero-boiloff (ZBO). Historical cryocooler data were obtained from reference 5 and 6 as a basis for scaling the mass of a cryocooler for soft cryogenes (LOX, F2, Methane, etc.). The total mass of the ZBO subsystem can be assumed to be the sum of cryocooler, control electronics, radiator, required power and a small cooling loop for ground operations as shown in Eq. (8).

$$M_{TCRS} \approx [M_{CRY} + M_{CE} + M_{CRR} + M_{POW} + M_{GC}] \quad (8)$$

The mass of the cryocooler itself is given by Eq. (9) (Reference 13).

$$M_{CRY} \approx 157 \text{ EXP}(-0.0533T_c) (W_c)^{(0.009T_c + 0.1275)} \quad (9)$$

The controller electronics mass was obtained from the lowest values of power processor specific mass in Reference 14. The controller electronics mass is given by Eq. (10).

$$M_{CE} \approx 0.02 W_{IN} \quad (10)$$

The radiator mass was scaled from data taken from Reference 15. The model assumed a beryllium radiator, a view factor of 1 and was maintained at a temperature 30 degrees above the environmental temperature of the spacecraft. The mass of the radiator associated with the cryocooler system is given by Eq. (11).

$$M_{CRR} \approx (W_c + W_{IN}) f(W_t) \left[\frac{378}{T_E + 30} \right]^4 \left(\frac{1.5}{1.0} \right) (0.78) \quad (11)$$

The mass of the power system is given in Eq. (12) and M_{GC} was assumed to be a constant small mass.

$$M_{POW} \approx \alpha_{POW} W_{IN} \quad (12)$$

X. Thermal

The MLI and foam for the propellant tanks and the thermal control for the propellant distribution systems were accounted for in the model of those subsystems. Reference 16 provides for 13 layers of MLI over the entire structure of the propulsion system. For modeling purposes the area that requires these layers will be assumed to be a cylinder with a diameter that is 1.1 times larger than the larger of the fuel or oxidizer tank and a length that is 1.1 times the addition of the fuel and oxidizer tanks. Because of the tandem cylindrical tank approach for this architecture, this was assumed to model the entire propulsion system. Equation 13 calculates the mass of the thermal blankets assumed to cover the entire chemical propulsion system.

$$M_{BT} = C_{MLI} N_{MLIT} \left\{ 2\pi [1.1(D_{TPMAX})] [1.1(D_{TPF} + D_{TPOX})] + [2\pi [1.1(D_{TPMAX})]^2] \right\} \quad (13)$$

XI. Structure

The structural model for the ACPS has two components: primary (load bearing) structure and secondary structure (tank supports). Data was obtained from a spacecraft manufacturer of several spacecraft of their primary and secondary structures as a function of their initial system mass and their propellant load (Reference 5). Linear

regression curves were applied to each set of data. Figure 5 shows the primary structure as a function of initial system mass. Figure 6 depicts the relationship between secondary structure and propellant load.

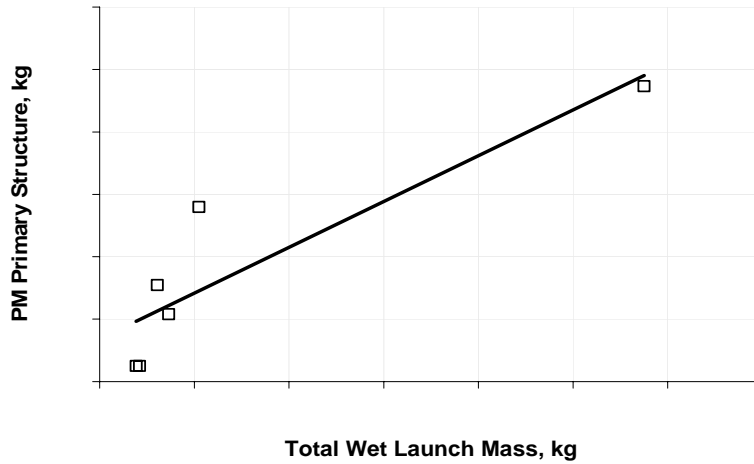


Figure 5: Propulsion Module Primary Structure vs. Total Launch Mass.

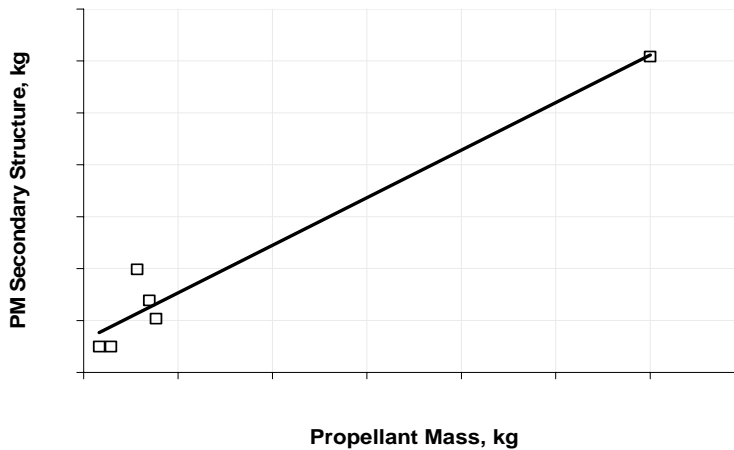


Figure 6: Relationship between Secondary Structure and Propellant Mass.

From these curve fits, equations are derived that are located in the in the ITAR version of the paper available to U.S. citizens and restricted from export or public disclosure, to predict the mass of the structural subsystem for the ACPS.

XII. Cabling

The cable harness for the ACPS is assumed to also vary with the linear dimension of the total propellant volume. Hence, the mass of the cable harness is given by Eq. (14).

$$M_{CAB} = 17.72(M_p)^{1/3} \left[\frac{(MR)\rho_F + \rho_{OX}}{\rho_F \rho_{OX}} \right]^{1/3} \quad (14)$$

XIII. Selected Outputs

The ACPS has the capability to assess different propulsion technologies and mission requirements to determine their impact at the system level either in payload, system wet mass, or initial mass of the system. Small detailed effects such as the effect of the delta-pressure change from the cavitating venturi in the feed system can be shown at the system level. Figures are provided below that outline some of the capabilities of the model.

Figure 7 shows the detailed mass breakdown of the wet mass of several propellant combinations for a given Mo of 3000 kg and a ΔV of 2500 m/sec. By comparing several different propulsion combinations at once and giving the detailed mass breakouts, one can see where the advantages of a system are at the system level.

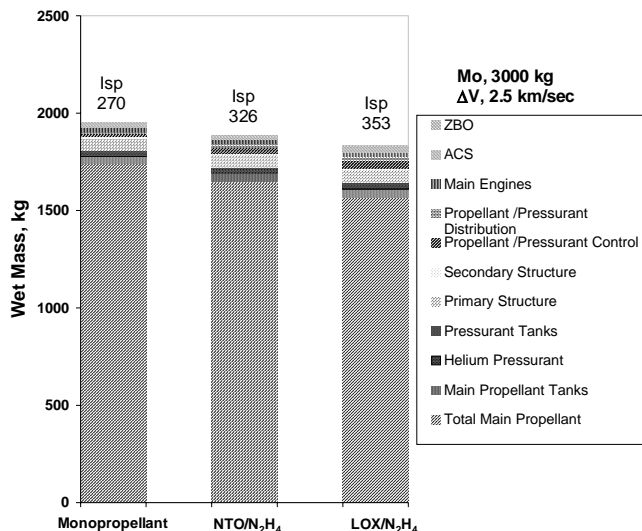


Figure 7: Wet Mass of Selected Propellant Combinations.

Figure 8 depicts the effect of both raising the combustion chamber temperature of a NTO/N₂H₄ engine (either by raising the chamber pressure or the mixture ratio) and advancing the state-of-the-art in tank technologies. Given a mission requirement of a Mo of 2000 kg and a ΔV of 2000 m/sec, the results indicate in Figure 8 that either changing the mixture ratio or advancing tank technologies will increase payload. Increasing chamber pressure alone does not have the desired effect.

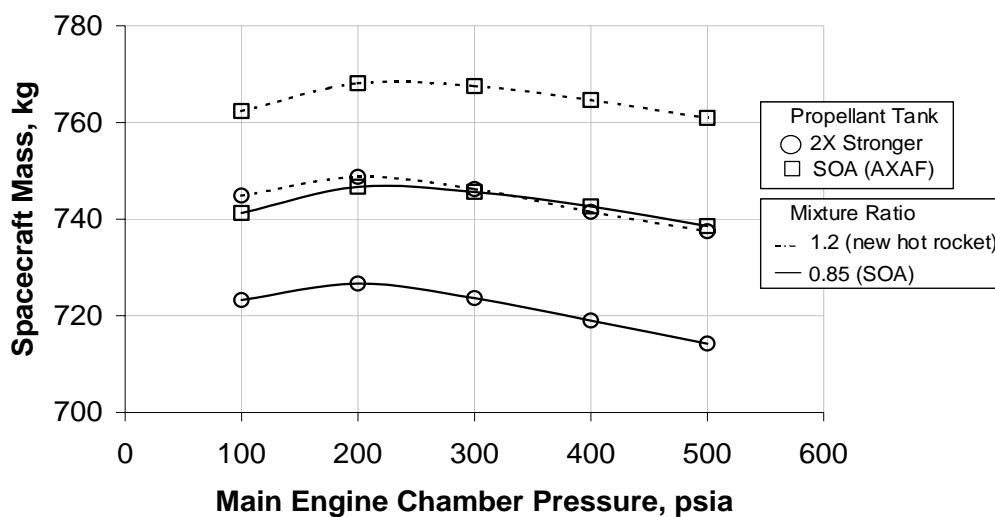


Figure 8: ACPS Payload for MR, Chamber Pressure, and Tank Technology Increases.

XIV. Conclusion

The Advanced Chemical Propulsion System (ACPS) model has been created using both engineering-based models and experience-based models to allow a user to assess the impact of advanced propulsion technologies on selected missions. Parametric descriptions of a wide range of propulsion systems were used to develop certain subsystems of the model. Selected examples have shown the capability of the model to determine changes in propulsion technologies at the system level.

XV. Acknowledgements

The work described in this paper was performed by Science Applications International Corporation (SAIC) under contract with the NASA Marshall Space Flight Center (MSFC) in Huntsville, Alabama. Special thanks go to Les Johnson, manager of NASA MSFC In-Space Propulsion, and Les Alexander, program manager of NASA MSFC Advanced Chemical Propulsion program, for providing encouragement and direction for this work. Further thanks go to Dave Byers of SAIC and Gordon Woodcock of Grey Research for their guidance in the creation of this model. Our many thanks to SAIC management, especially Frank Curran, program manager of the In-Space Technology Assessment program, for support and encouragement of this work.

References

1. Mayer, N. L., Advanced X-ray Astrophysics Facility-Imaging (AXAF-I) Propulsion Subsystem, AIAA 96-2869, 32nd AIAA/ASME/SAE/ASEE Joint Propulsion Conference & Exhibit, Lake Buena Vista, FL., 1996.
2. NASA DPD692 SE09, Advanced X-ray Astrophysics Facility Mass Properties Report, March, 1999.
3. Barber, T. J. and Cowley, R. T., Initial Cassini Propulsion System In-flight Characterization, AIAA 2002-4152, 38th AIAA/ASME/SAE/ASEE Joint Propulsion Conference & Exhibit, Indianapolis, IN., 2002.
4. Leeds, M. W., Eberhardt, R. N., and Berry, R. L., Development of the Cassini Spacecraft Propulsion Subsystem, AIAA 96-2864, 32nd AIAA/ASME/SAE/ASEE Joint Propulsion Conference & Exhibit, Lake Buena Vista, FL., 1996.
5. Personal Communication, Gamber, T., Lockheed Martin Corporation, January, 2004.
6. Honda, L., Calvignac, J., and Matuszak, L., Storable Thruster Technology Program-Mission Study, The 2002 JANNAF Propulsion Meeting, 2002.
7. http://www.psi-pci.com/Data_Sheet_Index_PMD-VOL.htm, Pressure Systems Inc., March, 2004.
8. *NASA Pressurization Systems Design Guide, Volume 1 – System Analysis and Selection*, NASA-CR-80317.
9. Personal Communication, G. Woodcock, April, 2003.
10. Wu, P.-K., et al., Qualification Testing of a 2nd Generation High Performance Apogee Thruster, AIAA 2001-3253, 37th AIAA/ASME/SAE/ASEE Joint Propulsion Conference & Exhibit Salt Lake City, UT, 2001.
11. Krismer, D., et al., Qualification Testing of a High Performance Bipropellant Rocket Engine Using MON-3 and Hydrazine, AIAA 2003-4775, 39th AIAA/ASME/SAE/ASEE Joint Propulsion Conference & Exhibit, Huntsville, AL, 2003.
12. Schneider, S. J., On-Board Propulsion System Analysis of High Density Propellants, AIAA 98-3670, 34th AIAA/SAME/SAE/ASEE Joint Propulsion Conference & Exhibit, Cleveland, OH, 1998.
13. ter Brake, H. J. M. and Wiegerinck, G. G. M., Low-power Cryocooler Survey, *Cryogenics*, 42, 705-718, 2002.

14. Glaister, D. S., Donabedian, M., Curran, D. G. T., and Davis, T., An Assessment of the State of Cryocooler Technology for Space Applications, The Aerospace Corporation, Report No. TOR-98 (1057)-3, 1998.
15. Juhasz, A. J., Tew, R. C., and Thieme, L. G., Parametric Study of Radiator Concepts for a Stirling Radioisotope Power System Applicable to Deep Space Missions, NASA/TP-2000-209676, 2000.
16. Honda, L., Calvignac, J., and Matuszak, L., Storable Thruster Technology Program-Mission Study, The 2002 JANNAF Propulsion Meeting, 2002.

Results Of An Advanced Development Zero Boil-Off Cryogenic Propellant Storage Test

David Plachta**

NASA Glenn Research Center Cleveland, OH 44135

I. Abstract

A zero boil-off (ZBO) cryogenic propellant storage concept was recently tested in a thermally relevant low-earth orbit environment, an important development in the effort to apply this concept to flight projects. Previous efforts documented the benefits of ZBO cryogenic storage applied to launch vehicle upper stages in a low-earth orbit (LEO) destinations. Central to that analysis is a ZBO Cryogenic Analysis Tool that estimates the performance of each component and the ZBO system. The developments in this test are essential to the validation of that tool. This test was the first on a flight representative configuration in a thermally representative environment. The test article was comprised of a spherical 1.4 m diameter insulated propellant tank, with a submerged mixer, a cryogenic heat pipe, flight design cryocooler, and a radiator. All were enclosed in a thermal shroud and inserted into and tested in a vacuum chamber that simulatee a LEO thermal environment. Thermal and pressure control tests were performed at sub-critical LN₂ temperatures and approximately 2 atmospheres pressure. The cold side of the ZBO system performed well. In particular, the heat pipe performed better than expected, which suggests that the cryocooler could be located further from the tanks than anticipated, ie. on a spacecraft bus, while maintaining the desired efficiency. Also, the mixer added less heat than expected. The tank heating rate through the insulation was higher than expected (9.4 watts); also the temperatures on the cryocooler hot side were higher than planned. This precluded the cryocooler from eliminating the boil-off. The results show the cryocooler was successful at removing 6.8 watts of heat at approximately 75K and 150 watts of input power, with a heat rejection temperature of 311 K. The data generated on the ZBO components is essential for the upgrade of the ZBO Cryogenic Analysis Tool to more accurately apply the concept to future missions.

II. Introduction

The purpose of ZBO is to control tank pressure without the need to vent propellant, by a synergistic application of active refrigeration (via a cryocooler) and multi-layer insulation. In this case, the heat enters the tank walls, primarily through radiation, and is removed by a submerged fin heat exchanger coupled to the cryocooler. The cryocooler rejects the heat to the cryoshroud (which simulates the LEO temperature) through a radiator.

Predecessors to this development test were two successful ZBO tests,^{1,2} both of which provided important stepwise developments of this concept and added needed definition. The test reported here is an important evolution of the concept because it is more representative of flight, mainly because of the use of a flight-like cryocooler.

This testing was part of a roadmap effort to advance the ZBO concept toward future flight applications of cryogenic upper stages of launch vehicles. Recent analysis shows substantial benefit³ of ZBO when compared to passive cryogenic propellant storage for low earth orbit (LEO). Accordingly, this development test was performed in a simulated LEO environment, under vacuum and with an environmental temperature of 230K. Note that no tank

* Aerospace Engineer, Propellant Systems Technology Branch, 21000 Brookpark Rd., MS 86-2, Cleveland, OH 44135

shading nor any radiation model was created to determine the actual environment temperatures of the configuration. Flight representative components were used, where possible, including a joint Air Force/ NASA developmental high efficiency flight-type cryocooler along with a one-of-a-kind cryogenic heat pipe. The test hardware configuration used is shown in **figure 1**.

The principal development reported here is the integration of the flight cryocooler, including a flexible coupling, a cryogenic heat pipe, and a submerged mixer to a cryogenic storage tank. This provides important information to validate analytical models on the overall system efficiency, system control, forced convection requirements (coupling of the mixer to the heat exchanger), and the effects of heat rejection.³

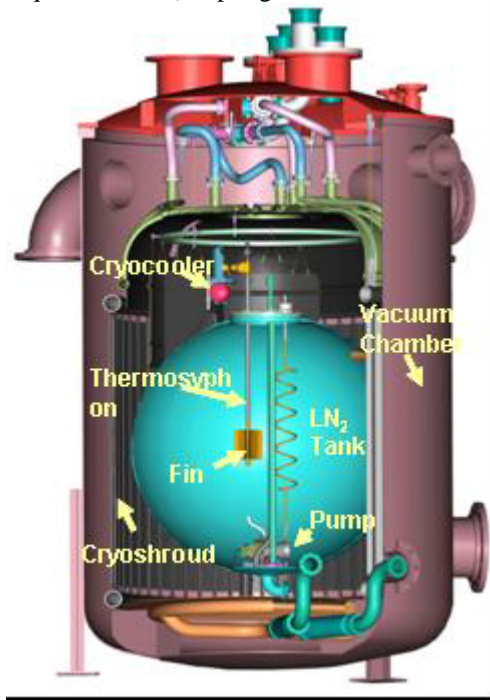


Figure 1: Test Configuration. This cutaway model shows the arrangement of the key components within the propellant tank and the cryocooler.

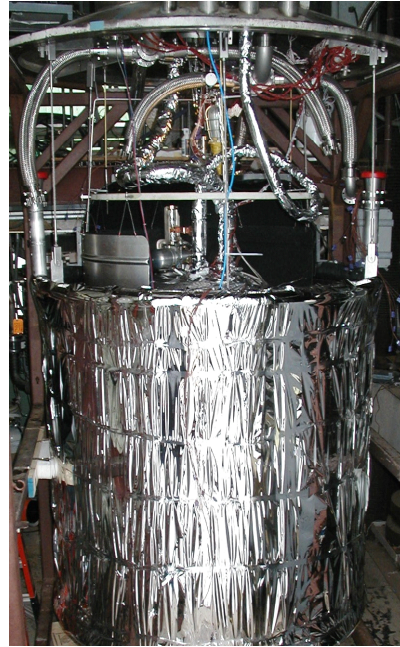


Figure 2: Test Hardware. The full assembly is supported from the vacuum chamber lid. The cryocooler and radiator are visible above the cylindrical shroud. The top cryoshroud is not present in this photo.

III. Experimentation

A. Facility

NASA Glenn Research Center's Small Multi-Purpose Research Facility (SMiRF), is a test bed used to evaluate the performance of thermal management systems. The vacuum chamber, 1.8 m diameter by 3 m long, produces a vacuum of 1.8×10^{-5} torr. The cylindrical cold GN₂ shroud, used to provide a controlled thermal environment to the test article, was augmented with a top and bottom section of similar design to provide a completely enclosed thermal shroud. The shroud was controlled to 230 K (227 to 233 K). In addition, the shroud sections are covered with a mylar sheet, to even out their temperature and reduce the thermal load. **Figure 2** shows this assembly, minus the top shroud, being lowered into the vacuum chamber.

B. Test Article

Tank: The tank is spherical with a diameter of 1.4 m. It is a thin-walled, flight-weight tank made of 2219 aluminum. The tank is hung from the vacuum chamber lid with six stainless steel cables, 0.6 cm thick. For tests, the tank is filled with LN₂ at 138 kPa (20 psia).

Insulation: The insulation on the test tank consists of two multi-layer insulation (MLI) blankets. Each blanket is comprised of 17 double aluminized mylar (DAM) radiation shields alternatively spaced with double silk net spacers. Two blankets are used, for a total of 34 layers of MLI. The blankets are held together with Nylon fasteners and reinforced Mylar cover sheets. Nylon button-pin studs, epoxied to the tank wall, support the blankets. Approximately 2/3rds of the tank is covered with this insulation, which was originally fabricated and tested in 1977 was used again in 1998¹. The other third of the insulation was replaced using similar materials and construction. The outside layer of older insulation had evidence of oxidation and the blankets did not assemble to the tank as neatly as they had in 1998. However, it was not replaced.

Fitted MLI blankets, comprised of approximately 10 layers of mylar, are assembled to insulate the tank supply, vent, and drain lines as well as the cryocooler flexible link and cryogenic heat pipe. Velcro and aluminized mylar tape are used to attach this insulation. The insulated tank, as assembled to the vacuum tank lid, is shown in **figure 3**. The estimated tank heating rate with this insulation is 6.8 watts.



Figure 3. 1.4 m dia spherical tank shown with insulation assembled.

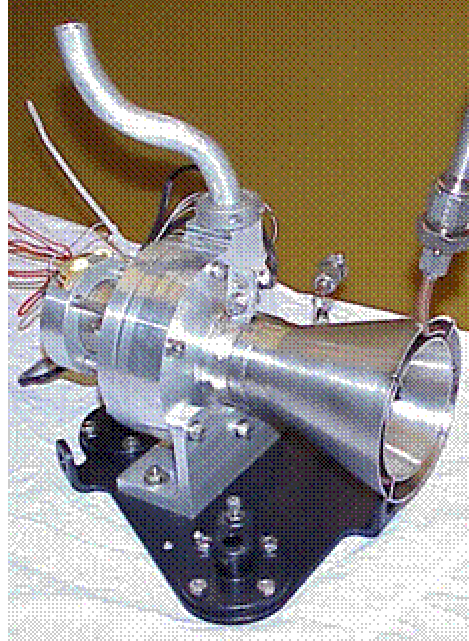


Figure 4. Pump used to destratify LN₂. Pump was mounted inside the tank, on the bottom baffle plate. Its outflow was directed to the fin on the thermosyphon.

Heat Removal System: A pump is mounted off the bottom baffle plate inside the test tank. With a design flow rate of 33 liters per minute and a differential head of 1.5 m at 10 watts input power, this pump can easily break up the top stratified layer of the tank liquid when the tank is filled. The pump is shown in **figure 4**.

The pump outlet is directed at the fin of the heat exchanger, which is located equal distance from the top and bottom of the tank. The pump moved the heat that entered the sidewalls and circulated it to the fin; natural convection also moved heat to the fin. The fin is soldered to the heat pipe, or thermosyphon. The thermosyphon is an original design. It is sized so that the evaporator area is 3 times bigger than the condenser, which helps maintain a relatively constant thermal resistance over a broad range of temperatures. A design fill level of 15% was used to keep the maximum pressure in the pipe to a reasonable level. The thermosyphon is charged with high purity GN₂ gas at 225 psi.

The selected design's calculated thermal resistance is 0.335 K/W, with a heat flow of 8W. It is interesting to note that a solid copper rod of the same dimensions would have a thermal resistance of 12.5 K/W at 77K. The thermosyphon design and its performance is described in more detail in reference 4.

The fin end of the thermosyphon is the evaporator. In it, heat causes evaporation which then moves to the condenser. The condenser is mated through a flexible link to the cryocooler. The exterior of the thermosyphon is vacuum jacketed to prevent removal of heat that migrates to the top of the tank, to better represent a low-gravity

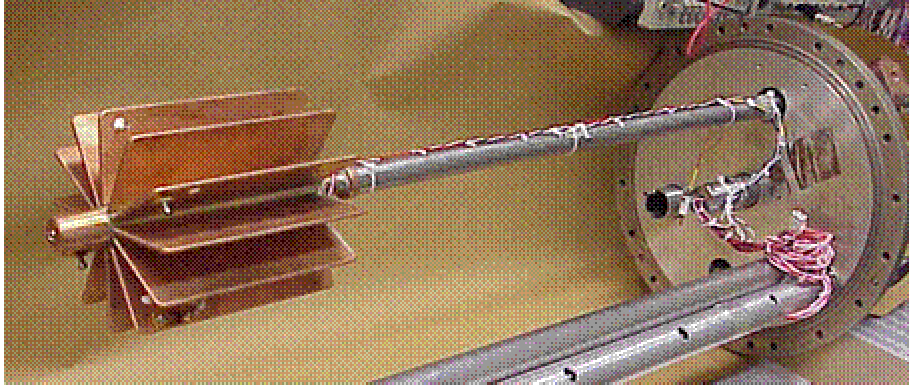


Figure 5: Thermosyphon. Cryogenic heat pipe or thermosyphon shown assembled to tank lid. Copper fin is soldered to the evaporator.

application. The vacuum jacket on the thermosyphon is welded to a flange that is mated to the tank. The thermosyphon and fin are shown in **figure 5**.

The cryocooler is a High Efficiency Cryocooler (HEC) was designed and fabricated by Northrop Grumman under funding from NASA and the Air Force Research Laboratory.. It was designed for an actual flight application, but has not yet been qualified for

flight. It has a capacity of 10 W of heat removal capacity at 95K (300K rejection temperature). Performance curves developed at the Air Force Research Laboratory indicate that it could remove 7 W of heat at an input power of 140 watts under our expected conditions (75K), which appears to be enough to achieve ZBO at LEO. The cooler weighs just 4 kg. It is shown mounted on the radiator in **figure 6**.

Heat is rejected through the radiator, also depicted in figure 6. The radiator is a solid aluminum structure and serves to support the cryocooler while rejecting its heat along with that entering the test tank. The majority of heat is rejected to the cryoshroud, although a portion is intercepted by the tank itself. The radiator interior, which is where the cryocooler is mated is painted black. The exterior was left unpainted. The radiator is supported by stainless steel wires from a low conductivity micarta ring, which is hung via Kevlar cables from the vacuum chamber lid. The radiator did not come into contact with the cryogenic tank walls, although at its perimeter it is very close to the outside layer of tank insulation.

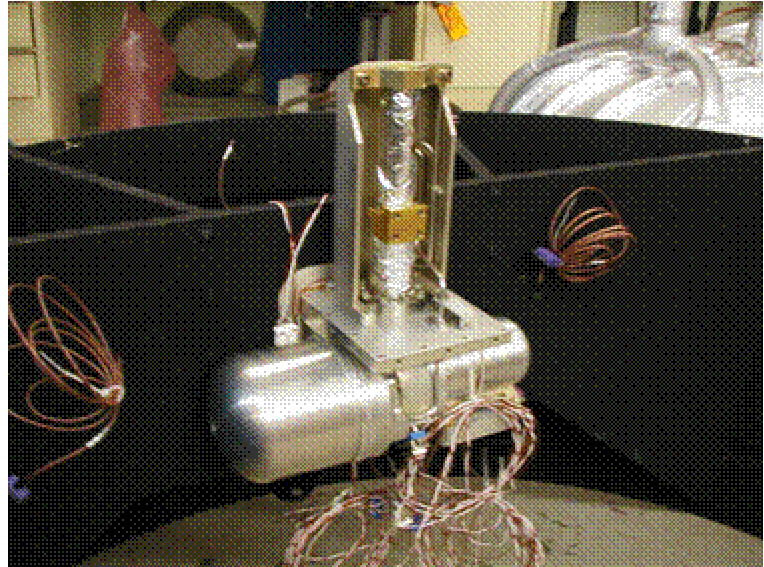


Figure 6: Cryocooler. HEC Cryocooler shown mounted on radiator. It was designed to remove 10 watts at 95K.

During assembly, pneumatically actuated pins hold the radiator/cryocooler assembly to the test tank lid to prevent substantial movement of this structure that hangs from the vacuum chamber lid. Those pins are retracted prior to installation into vacuum chamber.

In an actual flight configuration, the cryocooler and radiator assembly would likely be mounted on the spacecraft bus and the propellant tank would be shielded from the hot radiator.

The test tank temperature sensors are used primarily for fill level information and liquid temperature. The instrumentation on the thermosyphon is used to determine its performance and the flexible link temperature data is used to find the heat going in the cryocooler. It was calibrated at temperature prior to the test. The pump speed is used to determine its outflow and its heat addition to the tank. Temperature data on the plumbing and support cables is used to determine the heat entering the tank from those sources. The temperature sensors on the outside of the insulation are used to determine if the insulation temperatures are steady.

Cryocooler power is only locally available at the power source, which includes two true power meters. These meters are also used to calibrate the pump power. Videotape is used to verify and time stamp these measurements.

Facility instrumentation includes an ion gauge for the vacuum level, a gas analyzer, and 30 thermocouples on the cryoshroud.

Test Sequence: The vacuum chamber is pumped down for several days to remove as much vapor as possible. The insulation was purged with GN2. The cryoshroud system is brought down to the desired temperature. When the vacuum chamber gas analyzer indicates that the vapor is gone, the test tank was filled with LN2 to 99% full. During this process, the tank is vented to prevent overpressure. When the vent rate and the exterior insulation are steady over several hours, the cryocooler is turned on to eliminate boil-off. The tank mixer is turned on periodically to destratify and move the heat to the fin.

IV. Results

The first test determined that the baseline heating rate was be 9.4 watts. This was significantly higher than expected. This same tank and insulation was tested in 1998² with liquid hydrogen, where it was found to have a heating rate of 14.5 watts, which when adjusted for LN2 and the different environmental temperature used for these tests, is equivalent to 6.8 watts. That heating rate was less than that of the same insulation that was fabricated in the late 1970's (reference 4). Obviously, substantial degradation of the thermal properties has occurred.

The tank strut heating was 0.7 watts. The heating rate from the cryocooler, when off, was 0.9 watts. The heat soak back from the radiator on the MLI was 0.2 watts.

A. Cold Side Performance

Table 1 charts the temperatures between the cryocooler and the liquid nitrogen in the tank. The temperature difference is a substantial system inefficiency, despite our efforts to minimize this delta T. The actual and design temperatures are both shown. The most significant difference between and design and actual temperatures is the difference in the fin and saddle temperatures. This is where the thermosyphon was located and it proved to have half the thermal resistance predicted based on other heat pipes. Note that few have been made of this size and temperature, and there is little design data. The condenser and evaporator sizes were well matched, which contributed to its outstanding performance. See **figure 7** and reference 4.

This design is somewhat relevant to the micro-g environment, which would use a heat pipe with wicking. Wicking affects start-up and not the performance of condenser or evaporator. The thermosyphon's entrainment along the walls could aide response and might serve to reduce ΔT . That would not occur in a heat pipe with wicking. While the flow characteristics and heat pipe start up would be different and potentially more difficult, this development means that heat pipe length should have minimal effect, within reason, permitting more flexibility in cryocooler configuration, potentially sharing heat loads, compressors, and controllers.

	Predicted K	Actual K
Liquid	82.4	82.4
Fin (evaporator)	82.1	82.3
Condensor	79	81.3
Flex Link hot	78.1	79.2
Flex link cold	74	75.6
Cryocooler	73.8	75.5
Total Drop	8.6	6.9

Table 1: Temperatures of the cold side heat removal system of the ZBO test set-up.

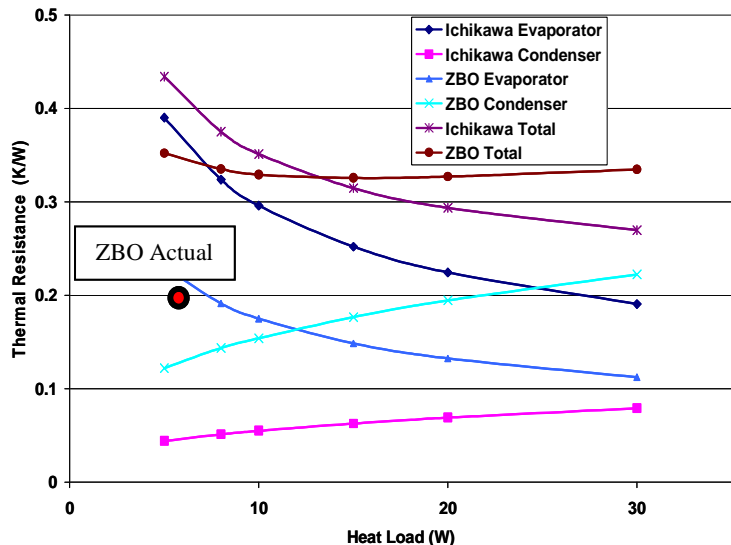


Figure 7. The thermosyphon performed much better than expected. The close matching of the evaporator and condenser was responsible.

B. Mixer Performance

The mixer was very effective in destratifying the propellant. It took only 30 seconds to do so, at a mixer power of 3.5 watts. With our pump duty cycle of once per 90 minutes, this equals 0.058 watts of average power (which is heat that the cryocooler must remove). Furthermore, if the pump is sized for an in-space application, then it would only need to overcome cryogen surface tension forces, further reducing the pump power requirement to 0.0007 watts for LO₂; 0.0014 for LH₂ (reference 3).

The mixer was not needed for heat removal. The heat removal rate did not increase when the pump was on. This was not anticipated. For these ground tests, free convection was sufficient to move the heat from the tank walls to the fin, which was in the center of the tank (see **figure 1**). This is because of the low viscosity of the cryogen, which contributes to a high Grashoff number (a high Grashoff number results in high free convection rates). It is also proportional to gravity, so in the microgravity environment of space, free convection rates will be substantially reduced.

C. Radiator Performance

The heat from the test tank (9.4 watts) and the heat from the cryocooler compressor (150 watts) went to the radiator. The radiator's purpose was to minimize the cryocooler hot-side temperature by moving this heat out to the cryoshroud. The temperatures on the radiator were 311 K, which was 21 K warmer than anticipated. Because the cryocooler cold-side temperature is dependent on this temperature, this caused the cryocooler cold-side to be warmer for the same input power, which is additional system inefficiency. Post-test radiator analysis explored many radiator concepts, to determine the potential improvement in its performance and the best design for an in-space application of this size. A different radiator that included a capillary heat pipe and additional struts, would have reduced the cryocooler interface temperature to 273 K, or 43 K above the shroud temperature. This would have improved the heat removal capacity to 7.8 watts, which still would not have been enough to achieve ZBO.

D. Tank Pressure Control

Tank pressure versus time is shown in **figure 8**. While the cryocooler reduced the pressure rise rate, it was not sufficient to remove the heat that entered the tank. Steady state pressure control has not yet been achieved.

Figure 9 shows that pump speed and duration did not have an effect on the tank pressure control.

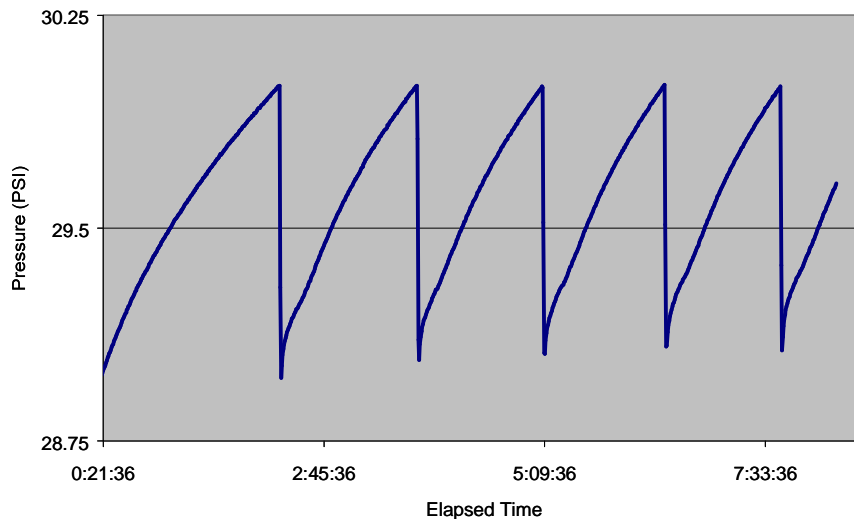


Figure 8. Tank pressure data with tank filled with LN₂. Q= 6.6 watts, 98% full tank, 227 K Cryoshroud. Pressure (psi) on the Y-axis. Steady state was never reached.

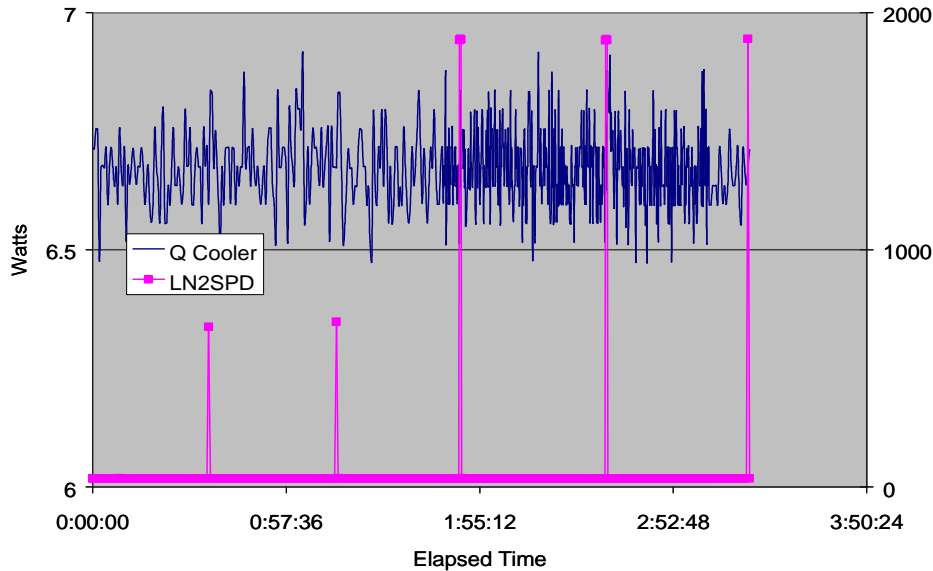


Figure 9. Changes in pump speed or on time had no affect on heat removal rate.

V. Future Work

Analysis has begun on an actual spacecraft configuration with a cryogenic propulsion stage in a zero boil-off configuration. The spacecraft thermal model will determine if the low-Earth orbit temperature of 230 K used in this test is too conservative. Preliminary results indicate that sunshades and spacecraft bus shielding can dramatically reduce this temperature and substantially reduce the cooling requirements. That thermal model combined with the test data obtained here will be the basis for follow on testing or future modeling.

VI. Conclusion

The baseline tank heating rate was too high to achieve zero boil-off with the cryocooler and radiator used. The primary source of the problem was poor insulation, which had degraded through years of storage. From the data obtained on the cryogenic heat pipe, it appears that cryocoolers can be located on the spacecraft bus instead of close coupling with the propellant tank – a much-improved situation. This is due to the low temperature gradient of the thermosyphon and its relative insensitivity to length. Also, the average power required for the mixer was less than anticipated. The developments on the heat pipe, mixer, and the radiator will be incorporated in the ZBO Cryogenic Analysis Tool and adds important definition and data that will be applied to future ground tests and to in-space mission concepts.

References

1. D. Plachta, "Hybrid Thermal Control Testing of a Cryogenic Propellant Tank," NASA Technical Memorandum 1999-209389, Adv. Cryo. Eng., Vol. 45 (Kluwer, New York, 2000) 465.
2. A. Heyayat, L. Hastings, C. Bryant, D. Plachta, "Large Scale Demonstration of Liquid Hydrogen Storage With Zero-Boil-Off," Adv. in Cryo. Eng., 47, (AIP, New York, 2002), 1276
3. D. Plachta, P. Kittel, "An Updated Zero Boil-Off Cryogenic Propellant Storage Analysis Applied to Upper Stages or Depots in an LEO Environment, NASA TM-2003-211691, presented at the 2002 AIAA Joint Propulsion Conference, Indianapolis, Indiana, July 8, 2002.
4. R. Christie, D. Plachta, "Design and Operating Characteristics of a Cryogenic Nitrogen Thermosyphon," to be published, presented at the Cryogenic Engineering Conference, Anchorage, Alaska, September 23-25, 2003.

**Momentum eXchange
Electrodynamic Reboost
(MXER) Tether
Technology Assessment Group
Final Report**

July 24, 2003

Prepared by:

**Mr. Kirk Sorensen
In-Space Propulsion Technologies Program
NASA Marshall Space Flight Center
Huntsville, Alabama 35812**

Table of Contents

1.0	Introduction to the In-Space Propulsion Technologies Program.....	3
2.0	MXER Tether Concept of Operations.....	3
2.1	MXER Tether Configuration.....	3
2.2	MXER Tether Momentum Exchange.....	4
2.3	MXER Tether Electrodynamic Reboost.....	8
2.4	MXER Tether Orbital Selection.....	11
2.5	MXER Tether Launch Options.....	12
2.6	MXER Tether Technology Challenges.....	13
3.0	Pre-meeting Objectives.....	14
4.0	Approach.....	15
5.0	Worksheets and Discussion.....	16
5.1	MXER Subsystem – High Tensile Strength Tether.....	16
5.2	MXER Subsystem – Code Development.....	18
5.3	MXER Subsystem – Electrodynamic Tether System.....	19
5.4	MXER Subsystem – Tether/Payload Catch Mechanism.....	20
5.5	MXER Subsystem – Power and Energy Storage Systems.....	21
5.6	MXER Subsystem – Plasma Contactors.....	23
6.0	MXER TAG Summary and Conclusions.....	25
7.0	Research Opportunities.....	26
8.0	Appendices.....	27
8.1	Appendix A: MXER TAG Agenda.....	28
8.2	Appendix B: TRL and R&D ³ Definitions.....	29
8.3	Appendix C: MXER TAG Participants.....	31
8.4	Appendix D: Derivation of the mass of a tether segment.....	33
8.5	Appendix E: Derivation of Electrodynamic Reboost Parameters.....	35
9.0	Attachments (Appendices continued).....	40
9.1	Appendix F: In-Space Propulsion Overview (Attachment 1).....	N/A
9.2	Appendix G: MXER TAG Technology Reprioritization Planning Status (Attachment 2).....	N/A
9.3	Appendix H: MXER Programmatic Presentation (Attachment 3).....	N/A
9.4	Appendix I: MXER Technical Presentation (Attachment 4).....	N/A

1.0 Introduction to the In-Space Propulsion Technologies Program

NASA's In-Space Propulsion Technology (ISPT) Projects Office manages the research that is at the forefront of NASA's efforts to provide propulsion technologies that will enable a new era of scientific discovery in space. A portfolio of reliable, advanced propulsion technologies will enable science at new destinations, significantly reduce mission trip time and cost, increase the scientific payload mass fraction, and allow for longer on-station operations. Consequently, the Technology Assessment Group (TAG) plays an integral role in identifying NASA's future challenges and required activities for ISPT. Typical products of a TAG can be, but are not limited to, activities such as technology roadmap development, technology readiness level assessment, and recommendation of technology maturation strategies.

A large number of the missions proposed by NASA's Office of Space Science (OSS) require orbits that escape the Earth's gravity, whether to continue on to other planets, such as Mars Odyssey or Cassini, or to place scientific instruments in more useful orbits, such as Space Infrared Telescope Facility (SIRTF) and Microwave Anisotropy Probe (MAP). Currently, these missions rely on the chemically-propelled upper stages of their launch vehicles to send them into these hyperbolic escape orbits. A typical example of this would be the solid-propellant Star 48 motor used as the third stage of the Delta 7925. The low specific impulse of these upper stages directly limits the amount of payload that a given launch vehicle can send on one of these hyperbolic orbits.

The Momentum-eXchange/Electrodynamic Reboost (MXER) tether would directly benefit this class of interplanetary missions by providing a significant fraction of the orbital energy needed to escape the Earth's gravity well. In so doing, it would significantly reduce the amount of mass required to be launched into low Earth orbit to accomplish these missions. A typical interplanetary mission utilizing a MXER tether boost would require only 40-60% of its standard mass. This reduction in launch mass would lead to the use of smaller and less expensive launch vehicles, and an overall launch savings to the missions that utilize a MXER tether facility without the disadvantage of prolonged spiral trajectories through the radiation belts.

Due to the multiuse and long-life characteristics of the MXER tether, its required technology represents a significant advance over the state-of-the-art in tether technology. In order to realize its vision of lower cost access to space, advancements, but not dramatic breakthroughs, are required in many of the technologies that make it viable.

2.0 MXER Tether Concept of Operations

2.1 MXER Tether Configuration

As currently envisioned, the MXER tether facility would consist of a rotating, 100-120 km long tether with a number of masses and mechanisms distributed along its length. At the tether "tip" would be a mechanism to enable a rapid rendezvous between the tether and a suitably prepared payload. Roughly on the other end would be a ballast mass, which would probably consist of the spent stage of the launch vehicle that inserted the MXER facility into orbit. The tether itself would be composed of a material with a high specific tensile strength (tensile strength/material density), coated or treated in some fashion to protect it against atomic oxygen and ultraviolet radiation flux. Additionally, the tether would be configured in a multi-strand, cross-linking configuration that would provide redundant load paths in the event that portions were severed by micrometeoroids or orbital debris.

A portion of the high-strength tether, probably 40-80 km, would be integrated with a conductive material, such as aluminum, that would enable this portion of the tether to conduct significant electrical current. Interspersed at regular intervals along this electrodynamic region of the tether would be tether “control” stations; smaller spacecraft-like units that would collect solar power and store the energy for use in driving electrical current through the tether during electrodynamic rebost operations. The MXER tether facility may then accurately be considered a type of “distributed” spacecraft.

2.2 MXER Tether Momentum Exchange

The MXER tether would normally operate in an elliptical orbit around the Earth. The perigee of the orbit would be in the low-Earth orbit (LEO) altitude range of 300-500 km, and the apogee of the orbit would vary from about 5000-8000 km, depending on the specific requirements of the mission scenario. The specific energy of any orbiting object (energy per unit mass) is proportional to the distance between the perigee and apogee of the object’s orbit (the line of apsides or 2x the semi-major axis). Therefore, each kilogram of mass in a MXER tether facility in a 400 km x 8000 km orbit has significantly more orbital energy than each kilogram in a payload in a low, 400 km circular Earth orbit.

This energy differential is the heart of the exchange of momentum and orbital energy that takes place between the tether and the payload. As the tether passes through the perigee region of its orbit, because of its greater orbital energy, it is moving significantly faster than a spacecraft that is in a circular orbit at those altitudes. A typical example would be a tether moving at 8.9 km/s at perigee versus another spacecraft moving at 7.7 km/s in its low circular orbit. Obviously, rendezvous between the center-of-mass of the tether and the payload would be impossible with this magnitude of relative velocity. But rendezvous is possible with the tip of the tether, if the tether is configured properly.

In order for the tip of the tether and the payload to rendezvous, the tether must be rotating at such an angular rate that the velocity of the tip of the tether is exactly the difference between the center-of-mass velocity of the tether and the payload’s velocity.

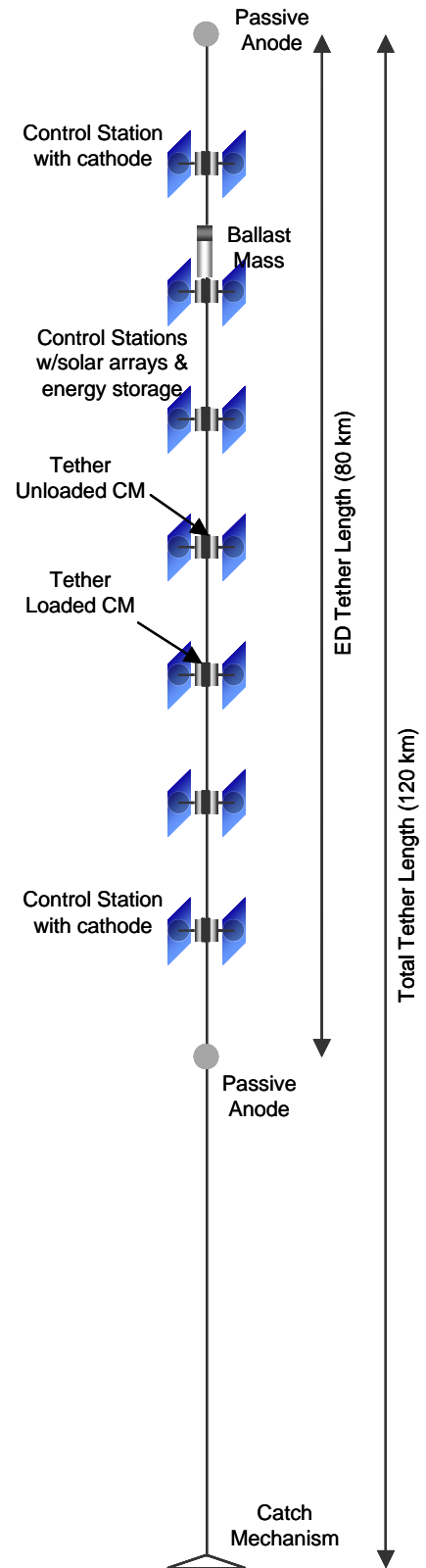


Figure 1: Overall tether configuration (conceptual).

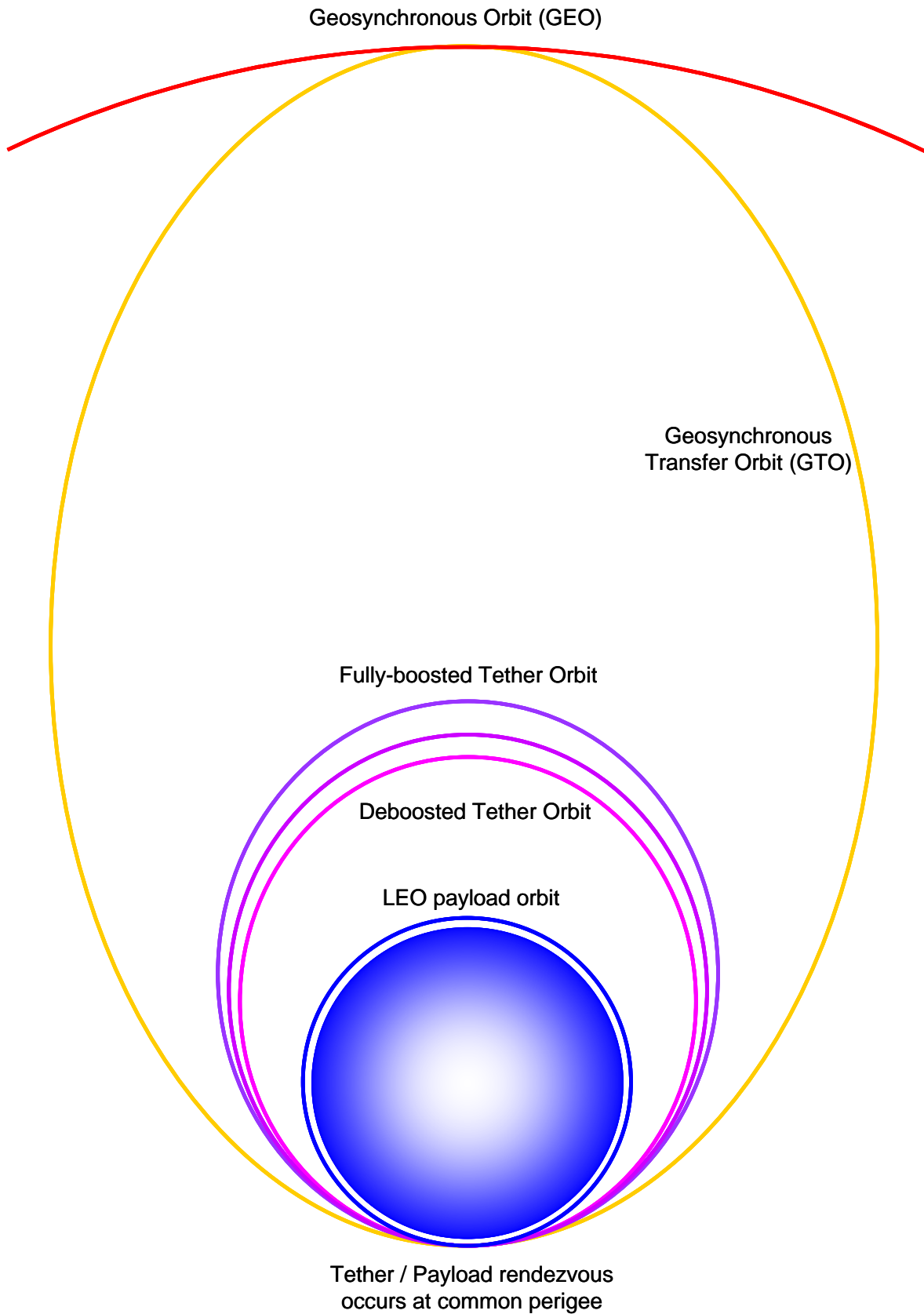


Figure 2: Orbital geometry of a payload transfer to geosynchronous orbit via MXER tether.

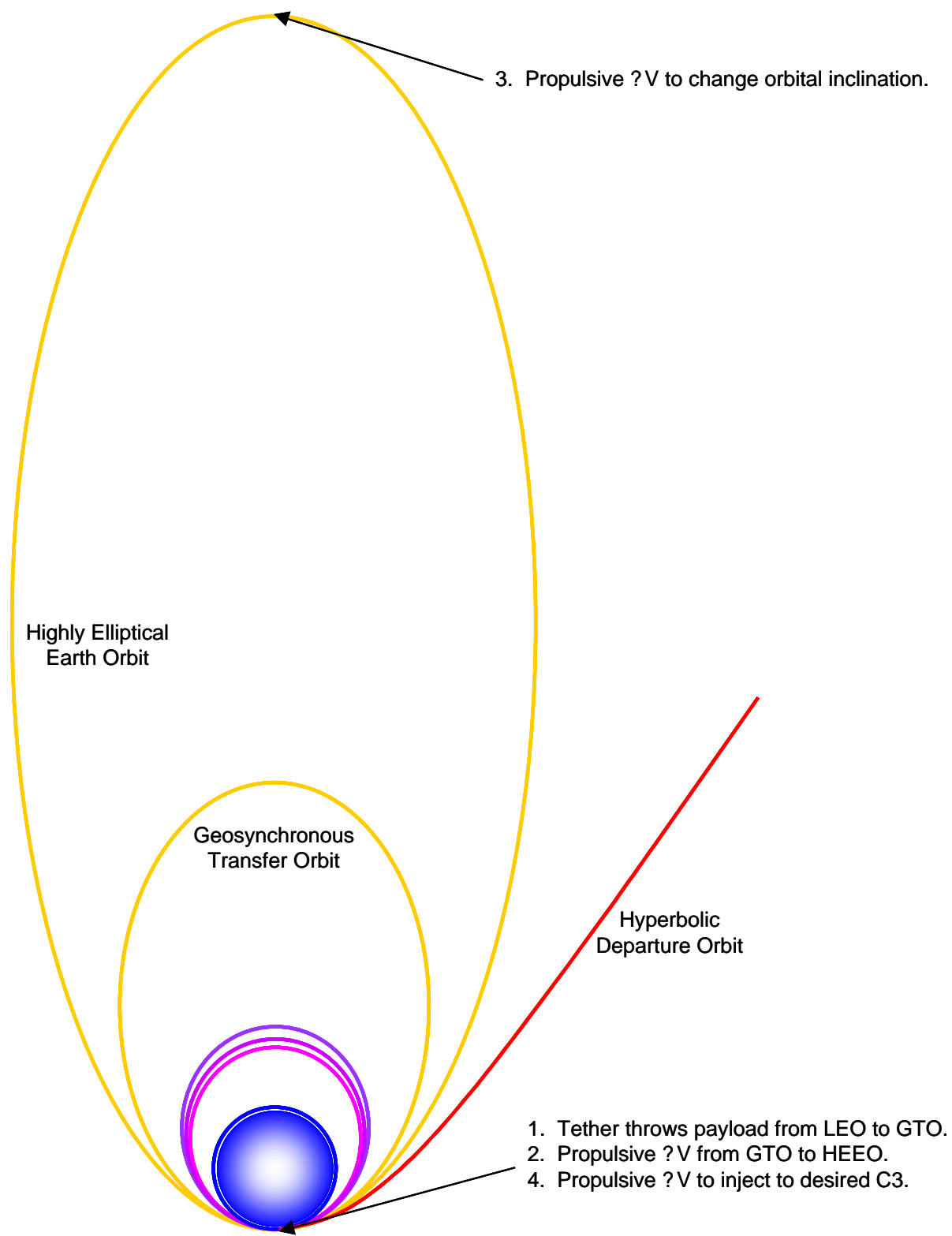


Figure 3: Orbital geometry of a hyperbolic interplanetary injection using a MXER tether assist.

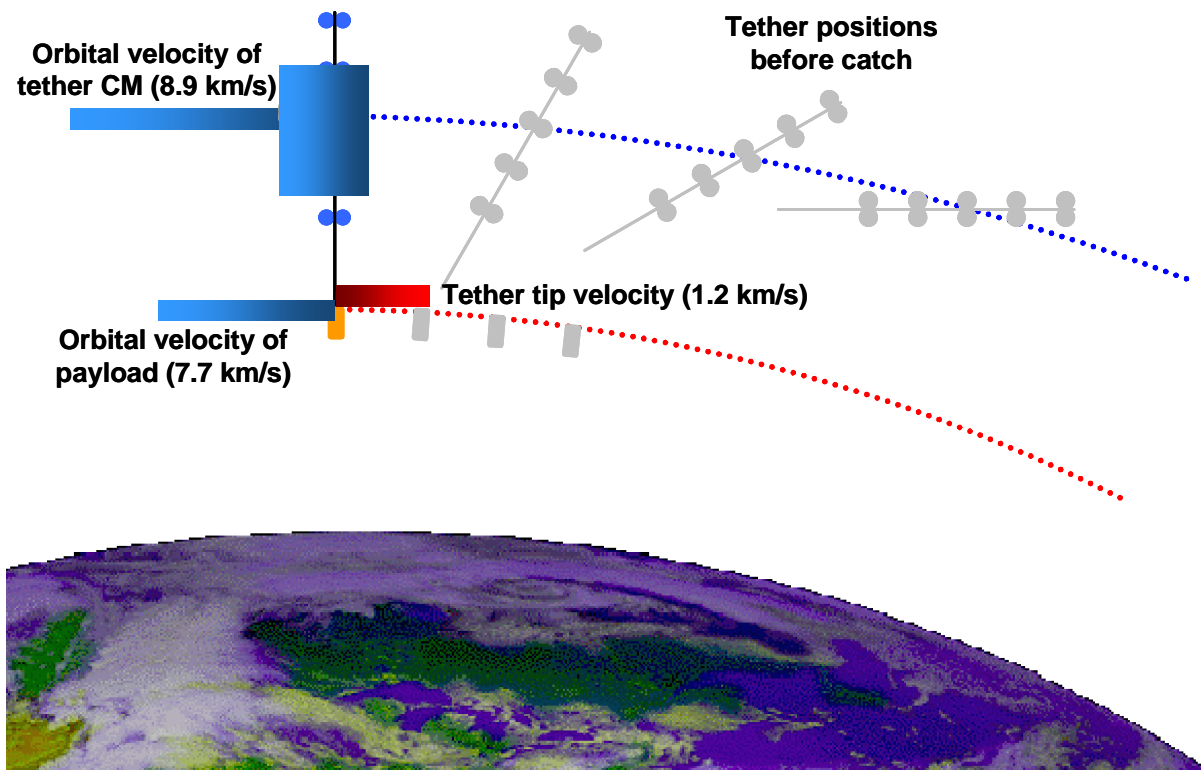


Figure 4: Tether tip approaching payload before rendezvous.

In the example just described, this would lead to a tip velocity of 1.2 km/s, which would be the difference in velocity between the 8.9 km/s tether and the 7.7 km/s payload. If the tether is rotating in the same plane of its orbit in the same direction (counterclockwise), then the center-of-mass of the tether will be at a higher altitude than the payload, and it will conduct an “underhanded” catch. If the tether is rotating in the same plane as its orbit but in an antiparallel direction (clockwise) then the center-of-mass of the tether will pass beneath the payload at a lower altitude and conduct an “overhanded” catch.

The final moments of tether/payload rendezvous happen rapidly as the tether tip approaches the payload in a nearly radial fashion (from the perspective of the payload), all the while decelerating rapidly. Ideally, the relative velocity of the tether tip and payload should go to zero even as the relative position between the two approaches zero. At this moment, the tether tip and payload will have matched position and velocity perfectly and some type of physical contact can be made between the two in order to begin the momentum exchange. Although they have matched position and velocity, they do not match acceleration, since the tip of the tether is under constant centrifugal acceleration due to its rotation, and the payload is in “freefall”.

The ideal, zero-relative error case is probably impossible in practice, so a “catch” mechanism is required at the tip of the tether that is tolerant of some level of positional and velocity error. Concepts for this catch mechanism include a design where a hook on the end of a boom on the payload snares a net-like structure on the end of the tether, causing it to collapse as the payload begins to be accelerated by the tether’s rotation.

After the payload makes contact with the catch mechanism on the end of the tether, it ceases its freefall motion around the Earth and begins to be accelerated centripetally by the tension of the

tether. From an astrodynamics perspective, the now joined tether/payload combination have assumed a new, lower-energy orbit than the one the tether previously had—however, for the payload, its new orbit is significantly more energetic than the one it had previously.

As the tether continues to rotate, the payload continues to be accelerated centripetally and to gain more and more orbital energy and momentum. For an ideal momentum exchange, the tether would carry the payload for a complete elliptical orbit and then release it at its next perigee when the payload is half a rotation from its original catch geometry. In other words, if the payload was caught underhanded, it would be thrown overhanded, and vice versa.

However, to carry the payload for another three-hour orbital period would involve many rotations of the tether, and so another attractive scenario would be to release the payload from the tip of the tether only half a rotation after it is caught. Although the payload would not be released exactly at orbital perigee, it would be only 10-15° off perigee.

When the payload is released, the velocity of the tether's tip is now ADDED to the velocity of the center-of-mass (CM) of the tether, leading to another significant increment of velocity. Continuing with the previous example, the payload would release from the tether with a velocity of 10.1 km/s, 1.2 km/s faster than the center-of-mass, and 2.4 km/s faster than it was originally traveling in its original low Earth orbit. Thus, a MXER tether can increase the orbital velocity of a payload by twice its tip velocity. Also interesting to note is the fact that the payload receives this energy almost as an instantaneous impulse...even faster than a conventional chemical upper stage.

2.3 MXER Tether Electrodynamic Reboost

The tether itself, after the payload is thrown, assumes an orbit even lower than it had before, having lost orbital energy and momentum by its interaction with the payload. Without reboost, it would soon not be possible to use the tether facility again. Thus it is clear that the momentum exchange process is not “something-for-nothing”, but rather an exchange of momentum and energy that clearly obeys the principles of orbital mechanics.

Hence, the problem of tether reboost must be considered if the tether is to achieve its potential as a reusable system for orbital transfer. A number of options are possible for the reboost of the tether, but each must follow the simple astrodynamics principle that in order to change apogee, there must be thrust at perigee, and vice versa. By conducting the catch and release maneuvers near perigee, the tether's orbital apogee was reduced, and in order to reboost apogee, reboost thrust must be applied near perigee. This means that during most of a tether's orbit, propulsion of any fashion will not be effective—only in the arc centered about perigee. Furthermore, solar energy collected during most of the tether's orbit should be stored so that it can be used at perigee to drive electric propulsion or electrodynamic reboost.

Chemical rocket propulsion could be used to reboost the tether's orbit relatively quickly over a few orbits, but the amount of energy added would simply be the same as the orbital energy the payload received, and the momentum-exchange tether would have little purpose. Any tether concept considering chemical reboost would be better served by using that chemical propulsion to boost the payload to a higher orbit in the first place, and save the time and expense of the tether.

Electric propulsion is another option. The reboost propulsion could come from ion or Hall thrusters driven by solar power and stored energy collected during most of the tether's orbit. The electric propulsion option would have several advantages over electric propulsion "tugs" that have been considered to carry spacecraft from low orbits to higher ones. The orbital energy imparted to the tether by the electric propulsion system would be entirely stored in the tether's orbit, and then delivered quickly to a payload during a catch/throw maneuver. This would save the payload from having to spiral slowly at low thrust through the Van Allen radiation belts. There would also be no need to "spiral down" after payload delivery, thus saving time and propellant. However, any tether using electric propulsion for reboost would still be limited by propellant as to how many times it could reboost before exhausting its propellant supply. Additionally, it would be no small matter to resupply a series of control stations along the tether with the propellant needed for continuing operations, especially since each one would be in an elliptical, non-Keplerian orbit!

Electrodynamic propulsion is a very attractive option for reboost of the tether because it takes advantages of the orbital environment to provide a "propellantless" solution. It is known from electromagnetic theory (EM) that if a conductive wire passes through a magnetic field, a potential difference (voltage) is set up across that wire. That induced voltage is literally a force on the free electrons within the wire, pushing them to move a particular direction. Charge in motion is electrical current, and EM theory also tell us that each section of a wire with current flowing through it will feel a body force applied to that section of wire (if the wire is in a loop, the sum of all these forces will be zero). The direction of that force will be perpendicular to both the direction of the magnetic field and the direction of current flow (or the orientation of the wire).

If the tether has conductive elements within it, such as aluminum, copper, or silver fibers, as it passes through the Earth's magnetic field, a voltage will be set up along the tether. However, that voltage will not cause current to flow through the tether if there are not sources of electrons on one end of the tether and a method to expel electrons from the other end. Without this ability to collect and emit electrons, the conductive tether will simply have a voltage difference, no current, and no force on the tether. One might think of it as an electrical circuit with a battery in series with a switch. If the switch is open, a potential difference (voltage) exists, but the electrons have no way to get from one side of the battery to the other (the circuit is not closed).

Fortunately, there is a way to "close the switch" for a tether in orbit around the Earth. Sunlight striking the upper layers of the Earth's atmosphere tends to ionize some of the atoms present, creating a plasma of positive ions and negative electrons. This region of space around the Earth is called the **ionosphere**, and it broadly ranges from 150 km to 1000 km. The MXER tether passes through the ionosphere during each elliptical orbit, and it is possible to collect electrons from the ionosphere, let them flow through the conductive tether, and emit them back to the ionosphere. The devices that make possible this emission and collection of electrons are called **plasma contactors**, and they are specifically called anodes if they collect electrons, and cathodes if they emit electrons.

With an anode at one end of a conductive tether and a cathode at the other, ionospheric electrons can be collected and emitted from an electrodynamic (ED) tether, and current will flow along the tether. The natural passage of the tether through the Earth's magnetic field will set up a voltage direction that will cause electrons to want to flow downward (i.e. from higher altitudes to lower altitudes) along the tether. This direction of current flow will cause a force whose direction will roughly oppose the direction of the tether's motion around the Earth. This force will reduce the energy of the tether's orbit and cause it to orbit at lower and lower altitudes and eventually deorbit.

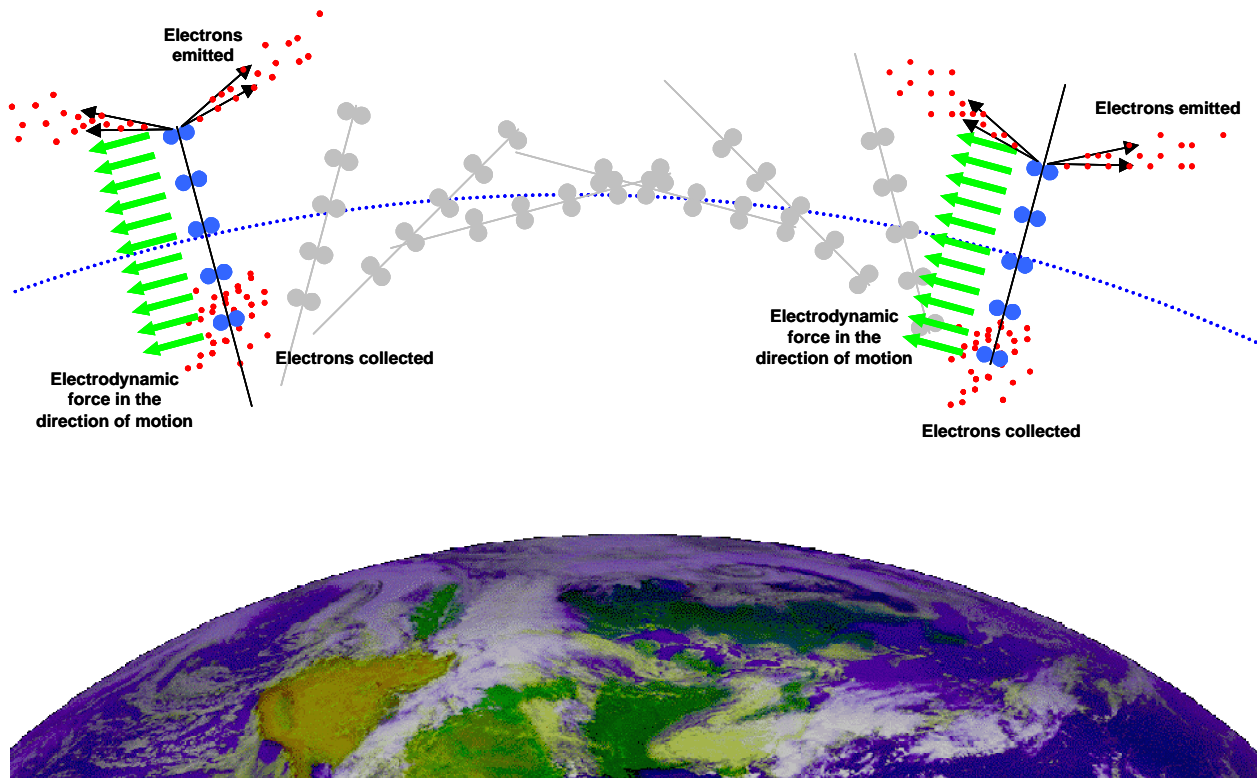


Figure 5: Electrodynamic reboost is accomplished by driving electrical current through the tether.

Obviously, if the tether is allowed to move passively through the magnetic field and flow current, an undesirable deorbiting force will be created. However, if onboard power is used to overcome this induced voltage, it is possible to force electrons to flow in the opposite direction from the deorbit case. In this scenario, a voltage produced by power systems on the tether would cause electrons to be collected at lower levels of the ionosphere, flow upward through the conductive tether, and be emitted at higher altitudes through the cathode. This direction of current flow would produce a force that would be roughly in the same direction as the tether's motion, and would add orbital energy to the tether. This addition of orbital energy would come about because work is done on the electrons as they are moved from lower to higher potential within the magnetic field, and the resulting work is manifested as an increase in the orbital energy of the tether. A mechanical analog to this scenario would be pumping water up a vertical pipe rather than allowing it to flow downward.

Electrodynamic tether reboost is very attractive because it does not consume any propellant and is only possible when the tether passes through the ionosphere, which would be the sections of its orbit before and after perigee. This is precisely when the tether must be reboosted anyway in order to increase its apogee. Rockets push against their own propellant for momentum exchange, and electric propulsion allows them to push harder, but in each case the propellant is the reaction mass. ED tether reboost uses power to drive electrical current, which allows the tether to "push" against the Earth's magnetic field, using the planet itself as the reaction mass. This technique increases the angular momentum of the tether's orbit at the expense of the Earth's rotational angular momentum. ED tether reboost then should not be viewed as "something for nothing", but energy from the Sun used to extract momentum from the Earth.

2.4 MXER Tether Orbital Selection

Due to the oblateness of the Earth, the orbits of all satellites are constantly modified by the Earth's central gravitational "bulge". This oblateness causes orbits to rotate about the polar axis of the Earth (nodal regression), as well as to rotate about their own angular momentum vectors (apsidal regression). These continuous orbital changes have been utilized for many years to accomplish orbital rendezvous or to put satellites in "Sun-synchronous" orbits. In the past, all orbital rendezvous between spacecraft have been accomplished by the matching of position, velocity, and acceleration between the two spacecraft. Since both spacecraft in such a rendezvous scenario are in identical orbits, the Earth's gravity modifies their orbits in an identical fashion, and no relative disturbances affect their operations.

The MXER tether and its payload, however, are able to exchange momentum between each other precisely because they are in different orbits. The payload, in a low Earth orbit, has significantly less orbital energy than the tether, which operates in an elliptical Earth orbit. The rotation of the tether allows the tip of the tether and the payload to meet at an instantaneous moment of common position and velocity (but not acceleration) during which a "catch" takes place. Due to the momentary nature of the catch maneuver, it is considered prudent to place the tether and payload in an orbital arrangement that allows the possibility of multiple catch attempts should the first one be aborted.

Consideration of a proper orbit for the tether and payload that allows multiple opportunities inherently suggests an arrangement where the payload's orbit and the tether's orbit remain coplanar, even under the modifying effects of Earth's non-uniform gravity field. The effects of apsidal regression can be accommodated through proper angular phasing of the tether and payload. But nodal regression will nearly always cause two orbits to become non-planar. There are only two viable options: either drive nodal regression to zero or cause nodal regression to be coplanar with apsidal regression. The first solution leads to a strictly polar orbit (where nodal regression goes to zero) and the second leads to a strictly equatorial orbit, where nodal and apsidal regressions become coplanar because the polar axis of the Earth and the angular momentum vector of the orbits are collinear.

A polar orbital arrangement would have the benefit of enabling access to the tether from any launch site on the surface of the Earth, but would severely degrade electrodynamic reboost since the tether's motion would be roughly parallel to the field lines of the Earth's magnetic field. Payloads being launched to geosynchronous orbit would suffer severe penalties from plane-change maneuvers and apsidal retargeting. Additionally, a polar orbit would make interplanetary injection difficult because of the necessity to retarget the line of nodes of the released payload's orbit.

The equatorial orbit, on the other hand, has excellent electrodynamic reboost possibilities due to the fact that the Earth's magnetic field lines and the tether's velocity vector are roughly perpendicular. Additionally, payloads bound for a geosynchronous orbit would particularly benefit from an equatorial orbit since that is their ultimate orbital inclination. Interplanetary spacecraft bound for deep space destinations would require plane-change maneuvers ranging from small to moderate before interplanetary injection. However, launch into an equatorial orbit is only practical from a launch site on the equator itself, and thus an equatorial geometry would present far fewer options for launch vehicle and launch site selection.

2.5 MXER Tether Launch Options

Due to the more favorable aspects of the equatorial orbital geometry, this configuration has been the subject of most MXER tether research. The limitations on launch vehicle selection are rather severe; currently there are only two launch options for a purely equatorial orbit. One is launch on an Orbital Sciences' Pegasus booster staged from Kwajalein Atoll in the Pacific, the other is launch on a Ukrainian Zenit rocket launched from Boeing's SeaLaunch Odyssey platform in the Pacific.



Figure 6: SeaLaunch Odyssey platform on the equator.

Due to the large payload capability of the Zenit-2 (16 metric tonnes) and the small payload capability of the Pegasus (400 kg), the sea-launched Zenit option is preferred. Additionally, the Zenit-2 has a large second stage (9 metric tonnes) that may be retained as a ballast mass for the MXER tether facility. Although a larger air launch approach or other launch scenarios are possible and might be attractive options, the SeaLaunch scheme is the present baseline illustration.

In the case of the Zenit launch scenario, the MXER tether facility, consisting of a series of control stations, the Zenit second stage, and a catch mechanism, would be launched from the SeaLaunch platform into an equatorial low Earth orbit. Then the tether would be deployed, section-by-section, until it reached its full length. Collected solar power would be used to drive current through the electrodynamic portion of the tether to first spin it up about its center-of-mass, and then to boost it from its low Earth orbit to its operational elliptical orbit. Simulation scenarios indicate that the boost from LEO to its operational orbit would take from 9 to 12 months.

After arriving at its operational orbit, the MXER tether would be ready to catch and throw payloads launched to an equatorial orbit. For a tether designed to throw payloads from LEO to a geosynchronous transfer orbit (apogee altitude of 36,000 km), the tip velocity of the tether would be approximately 1200 m/s. This in turn would lead to a payload capability of the 25-metric tonne (MT) tether facility of 2-3 MT.

A launch capability of 2-3 MT to equatorial LEO would be desired. Again, the Pegasus launch vehicle would not have sufficient payload (400 kg) and the Zenit-2 would have far too much (16 MT). In order to utilize the Odyssey launch platform, a rocket that employed the same propellants as the Zenit would be very important. There are only two rockets today that use LOX/kerosene propulsion exclusively, the Zenit (Ukraine—Yuzhnoye) and the Soyuz/Molniya (Russia—Korolev). Additionally, there are three more launch vehicles in design that plan to use

LOX/kerosene propellants on both stages, the Angara (Russia—Chelomei), the K-1 (US—Kistler) and the Falcon (US—SpaceX).

Of these, the Kistler K1 has the closest payload capability (5000 kg) to the payloads of interest. Therefore, it is envisioned that a K1 rocket would launch from the Odyssey launch platform and deliver a payload to LEO that would be caught and thrown by the tether. If this payload was bound for an interplanetary destination, it would then boost to a highly-elliptical Earth orbit (LEO x 200,000 km), conduct a plane-change burn at apogee to target hyperbolic declination, and then conduct a hyperbolic injection burn at perigee. If the payload was bound for geosynchronous orbit, it would conduct a burn at apogee that would nearly circularize its orbit, and then phase orbits until it reached its proper orbital longitude, where it would finally circularize its orbit with a short burn.

This single-launch strategy is considered attractive for most interplanetary missions of interest, but the size of most GEO satellites (average launch mass of 4500 kg) could mean that a MXER tether facility with only 2000-3000 kg of payload capability might not be attractive to large portions of the commercial market. Therefore, a two-launch MXER facility is being actively considered. This facility would be launched by a pair of Zenit-2 rockets and would have a total mass of 50 MT and a payload capability of 4000-6000 kg. Such economic tradeoffs are still a matter of active evaluation and discussion.



Figure 7: Zenit launch from the SeaLaunch Odyssey platform.

2.6 MXER Tether Technology Challenges

The technology challenges that await the development of a MXER tether facility are thus seen clearly following the physics of its operation:

- The tether requires highly accurate orbital propagation of its dynamic structure so that payload and tether tip can meet at a location of common position and velocity.
- The tip of the tether must be equipped with a catch mechanism that can tolerate some level of positional and velocity error so as to make physical contact with the payload, then must be able to release it easily a short time later.
- The tether itself must be composed of a light, strong material that sustain the tremendous tension forces within the tether while resisting the degrading effects of the space environment over its operational lifetime.

- The tether must also incorporate significant amounts of conductive material so as to provide a conductive path for electrical current with a minimal level of resistance.
- The tether facility must have the capability to collect solar power and store energy so that electrical current can be rapidly driven across the induced voltage gradient during passage through the ionosphere.
- Electrons must be collected from and emitted to the ionosphere so that current can flow through the tether and provide a force to reboost the tether.
- The tether facility and its payloads must be able to be launched to the proper orbits on economic, practical launch vehicles.
- The overall tether configuration chosen must be conducive to development, construction, packaging, launch, deployment, and utilization in a practical and economic manner.
- Finally, the tether facility must have a sufficient payload capacity and provide a sufficient performance improvement to be attractive to potential customers.

3.0 Pre-meeting Objectives

The objective of the 2003 MXER TAG was to update the existing technology roadmap, technology readiness level (TRL) levels, research and development degree-of-difficulty (RD³), state-of-the-art (SOA), gaps, and gap fillers. The MSFC MXER team recognizes that several key technologies must be advanced before a MXER technology demonstration can be developed. These key technologies include, but may not be limited to, the following: development of a high-strength, survivable tether; highly-accurate orbital propagation of a dynamic structure; catch mechanisms to allow the payload and tether to positively contact one another; power and energy storage systems; development of large current plasma contactors; and other technologies to enable electrodynamic reboost of the tether facility in a reasonable time. Currently, a mission that will provide some key data for long-duration tether missions is being developed by Tethers Unlimited and Stanford University under a Phase I Small Business Technology Transfer Research (STTR) contract from NASA/MSFC. This Multi-Application Space Tether (MAST) experiment will deploy three 10-centimeter sized satellites along a 1-kilometer long tether and use these picosatellites to study the dynamics and survivability of a prototype tether material and configuration in orbit.

The July 2003 TAG meeting for MXER tether systems was intended to create an open forum in which to exchange information, express ideas, and offer any technical advice and recommendations to the In-Space Propulsion Technology Projects Office pertaining to the development of a technology roadmap. These inputs should attempt to address all challenges and issues for each MXER tether subsystem that must be overcome in order to meet the required performance, schedule, and system goals for a proposed MXER design.

Anticipated accomplishments of the TAG session are updating the existing technology roadmap and providing a consensus technology level assessment and technology maturation assessment.

4.0 Approach

The Momentum-eXchange/Electrodynamic Reboost (MXER) Tether Technical Assessment Group (TAG) convened on July 24, 2003 at Gray Research, Inc. in Huntsville, Alabama. The In-Space Propulsion Technology Projects Office began the TAG with a programmatic presentation by Rae Ann Meyer followed by an overview of the reprioritization process given by Gwen Artis. Dr. Joseph Bonometti, Emerging Propulsion Technologies (EPT) Project Manager, followed with a programmatic overview of MXER tethers and other EPT projects. Kirk Sorensen finished the presentations with a technical overview and state-of-the-art technology levels applicable to MXER. These presentations were then followed by a general discussion of MXER development by the TAG participants and moderated by the TAG chair. Following the discussions, the TAG participants formed three sessions of two discussion groups throughout the afternoon. The discussion groups were as follows:

1. Dynamic Modeling and Conductive Tether Material
2. Catch Mechanism and Power/Energy Storage Systems
3. Plasma System Contactors and Strength Tether Material

Each group had thorough discussions about their respective MXER sub-systems, and as part of the process, completed the TAG worksheets that are included in Section 5.0. Following the afternoon break, the TAG reconvened as an entire group and came to a consensus agreement for each worksheet's content. The definitions of TRL and RD³ are found in Appendix B.

5.0 Subsystem Worksheets and Discussion

5.1 High Tensile Strength Tether

The high-strength tether is the backbone of the tether facility, carrying all other elements in tension and providing the path wherewith the tension forces are conveyed to the payload. Unlike the short (10-20 km), gravity-gradient-stabilized tethers that have been flown to this point, a MXER tether will be long (100-120 km) and rotate at a significant angular rate. The tension loads to which the tether will be subjected are orders of magnitude more than current tether missions. The rotation of the tether will cause the tension loads to be minimum at the tip of the tether and maximum at the loaded center-of-mass (assuming the design payload is attached to the tip).

The critical figure-of-merit for the strength tether is the characteristic velocity of the material, which is simply an alternative expression of tensile strength of the material divided by its density. The characteristic velocity is employed because of its utility within Moravec's tether/payload mass ratio equation, as shown in Appendix D. Characteristic velocities of high-strength materials of interest are given in the table below.

Material	Tensile Strength (GPa)	Material Density (kg/m ³)	Characteristic velocity (m/s)	
			safety factor = 2	safety factor = 3
UHMWPE (Spectra 2000)	3.5	970	1900	1550
PBO (Zylon)	5.8	1540	1940	1580
current PIPD (M5)	5.3	1700	1770	1440
anticipated PIPD (M5)	9.5	1700	2360	1930
Kevlar	2.76	1440	1380	1130

As important as characteristic velocity is as a figure-of-merit, it is critical that the material itself survive the environment of space. The tether is threatened by damage from micrometeoroid / orbital debris (M/OD) as well as atomic oxygen, ultraviolet light and other forms of radiation.

The only credible form of protection from M/OD is to provide multiple load paths through the tether so that if one is severed, the tensile load can be shunted around the damage to the remaining, undamaged portions of the tether. If these load paths are physically separated from one another, then only a piece of debris on the same scale as their physical distance can sever them all simultaneously.

Atomic oxygen (AO) is generated by photo-dissociation of the upper layers of the atmosphere. As the tether passes through the lower parts of its orbit, the AO can degrade the tether through oxidation of the material. Protection from AO can be provided by an already-oxidized layer on the surface of the tether material. Some candidates being investigated today include a nickel- or silsesquioxane-coated polymer.

Ultraviolet protection may be provided to the tether by coating it with a photoactive pigment that promotes electrons to higher levels and prevents ionization.

Two contracts were awarded under the ISP Cycle II NRA to Lockheed Martin Astronautics and Tethers Unlimited for development and testing of high-strength, multi-strand, survivable tethers.

5.1 – High Tensile Strength Tether

Element	SOA	TRL	RD ³	Gap	Gap Filler
Tether Material	PE (Spectra 2000) PBO (Zylon) PIPD (M5)	3	III	Advanced materials, design optimization, comprehensive tether survivability model, break mitigation	Trade study, Robust design, material research, integration of tethers, model refinement, develop health monitor, laboratory experiments
Structure	Multi-load path tether Flat tape tether	4	III	2-D versus 3-D designs	MOD Testing
Coatings	Nickel Silsesquioxane Suntan oil (UV)	2	III	Compatibility of UV/AO resistant coatings together	Tether pigmentation
Deployer	Tethered Satellite System (TSS) Small Expendable Deployer System (SEDS)	3+	III	Mass optimization, retrieval capability, compatible with multiple tether materials and cross-sections, libration damping	Trade study, deployer development, ground testing
Sensors	Laser Ranging RF sensing Formation Flying technology	4	II	Accurate position sensing, integration of sensor(s) with the tether	Sensor system deployment, ground testing

5.2 Code Development

Accurate orbital propagation has been a challenge since the dawn of the space age. If the Earth's gravity could be modeled as a central acceleration and there were no external forces, the problem would be fairly simple. But the Earth's gravitational field departs significantly from a spherical model due to the equatorial bulge, and there are additional gravitational forces from the Moon and the Sun. There are also disturbances from atmospheric drag, electrodynamic interactions, and solar radiation pressure.

In addition to these external perturbations there are the complications of modeling the internal dynamics of the tether system. Many of these dynamic effects are on a large enough scale (~100 km) that they cannot be separated from the external interactive forces such as gravity. Various models of tether dynamics of differing fidelity have been proposed and used, such as bead-spring, finite-difference, and finite-element. All operate on the principle of discretizing the tether's distributed mass and solving for the dynamics of the system.

External force models for the tether are at a rather advanced state of development, since they have been developed and used for many other spacecraft programs. The TAG did not anticipate significant future work going towards improved gravitational, magnetic, and ionospheric models. The internal dynamic modeling of the tether has not received nearly so much attention, and so significant resources have been recommended to improving the state-of-the-art in tether modeling. The MXER tether with its tapering, high-strength, rotating configuration represents a significant departure from the gravity-gradient, low-tension tether modeling that has been done in the past.

Two contracts were awarded under the ISP Cycle II NRA to Tethers Unlimited and Smithsonian Astrophysical Observatory for improved modeling of MXER-type tethers, with particular emphasis on assessing the feasibility of the tether/payload "catch" maneuver.

5.2 – Code Development					
Element	SOA	TRL	RD ³	Gap	Gap Filler
Internal Modeling of Tether Dynamics	Implicit Finite-Element Model	3	III	Propagation speed Code validation	Cross-validation Ground-test Flight test
Control	ED tether libration control (Hoyt)	2	III	Level of Control	Continued modeling
External Force and Environment Models					
Gravitational	EGM360 (1997) Grace (2003)	9	N/A		
Magnetospheric	IGRF2000	9	N/A		
Ionospheric	IRI	9	N/A	Variability Solar flare	
Albedo Model	Average value by month	?	?	Rapid change	

5.3 Electrodynamic Tether System

The conductive, electrodynamic tether can be thought of as the “engine” of the MXER tether system. As electrical current flows through the ED tether in the Earth’s magnetic field, a propulsive force is generated which is used to reboost the tether and restore the orbital energy and angular momentum transferred to the payload.

The exact configuration of the ED tether and its association with the strength tether have not been determined at this point. It is possible that the ED tether might be integrated within the strength tether in some fashion, or it might be wrapped over the surface of the strength tether. Another possibility is to “string” the ED tether alongside the strength tether and then link them together periodically. Each configuration has its advantages and disadvantages.

The main components of the electrodynamic tether system are the conductive tether itself, plasma contactors to collect and emit electrons, solar arrays for power collection, and energy storage systems. In order to minimize reboost duration, it is desirable to maximize reboost acceleration. A derivation is included in Appendix E that has simple expressions for ideal force/power ratio and force/mass (acceleration).

5.3 – Electrodynamic Tether System					
Element	SOA	TRL	RD ³	Gap	Gap Filler
Electric Insulation	Individually coated wires	6	III	Withstand high positive bias in M/OD environment	Impact tests under vacuum in plasma New materials
Thermal Control	ProSEDS coatings Non-conducting/ conducting	6/3	II/III	Adequate Lifetime (if conduction)	New, longer life materials
Conducting interior Physical geometry	Separate conducting & strength member	8	I	Higher current	
Thrust transfer from ED to spacecraft/strength tether	Coil loop & no stress on current member	3	II	How to use conductor as part of load carrier Differential thermal expansion	Integrated/impregnated materials Short lengths nest in coatings on strength member
Electric propulsion Mainly used for ion engines & propellant versus ED tether system	Ion/Hall engines Requires ~20 kW each (~100 kW total)	4	I	Trajectory controls System effectiveness	Do system analysis
Strength-to-weight (overall)					
Triple junction program					
Survabiitiy (AO/UV)					

5.4 Tether/Payload Catch Mechanism

The development of a lightweight, error-tolerant catch mechanism is crucial for ensuring successful rendezvous between the tether tip and the payload. The tether/payload rendezvous problem differs from both a traditional orbital rendezvous and an orbital intercept. In an intercept problem, such as between a ballistic missile and an anti-missile system, two objects seek to match position in space at a specified moment, but make no attempt to match velocity or acceleration, and these intercepts typically result in destruction of both objects. A traditional orbital rendezvous, on the other hand, involves two objects matching position, velocity, and acceleration with each other by assuming identical orbits. They can then approach at an exceedingly low relative velocity and gently connect.

The tether/payload rendezvous problem is bounded by these extremes. The tip of the tether, due to its rotation, is able to match position and velocity, but not acceleration, with the payload. Although the tether tip is under centrifugal acceleration, the payload is in “freefall” while in orbit around the Earth. They then can meet at an instantaneous moment of zero relative position and velocity error. The physics are somewhat analogous to a point on the rim of a rolling wheel. That point will make contact with a corresponding point on the ground at zero relative velocity during each rotation of the wheel, however, the point itself is under constant acceleration due to that rotation. Another useful analogy to the physics of the situation is a person standing on a roof or elevated platform. If someone were to throw a tool to them, it would rise and be constantly decelerated by gravity until its velocity reached zero. If done correctly, the person on the platform could reach out and grab the tool when it reached zero velocity and before it started to fall back down again.

Due to these unique constraints, the catch mechanism needs to be tolerant of as much position and velocity error as is practical. This desire is countered by the need for the catch mechanism mass to be as low as possible, since the catch mechanism and the payload are both considered the “tip mass” in Moravec’s tether equation (Appendix D). Hence, catch mechanism mass trades directly for payload mass and should be minimized as much as possible.

A clear figure-of-merit for a catch mechanism design then is the volume wherein a catch could take place divided by the mass of the catch mechanism—a type of specific volume. Other important considerations are packaging and deployment, survivability in the orbital environment, any consumables needed by the catch mechanism, and ease of release after the payload has been captured.

Two contracts were awarded under the ISP Cycle II NRA to Lockheed Martin Astronautics and Tennessee Technological University for further catch mechanism development.

5.4 – Tether/Payload Catch Mechanism					
Element	SOA	TRL	RD ³	Gap	Gap Filler
Catch Mechanism	Design concepts	3	III	<ul style="list-style-type: none"> Analysis and validation Spacecraft interface 	<ul style="list-style-type: none"> Defining metrics Defining modeling interfaces

5.5 Power and Energy Storage Systems

In order to provide the electromotive force (voltage) to drive electric current through the conductive tether, a source of power is required. For reasons of cost, programmatic risk, and the need for distributed power, a central nuclear power source is not being considered. Solar power systems, whether based on photovoltaic or concentrated dynamic power, are the baseline for the tether design.

Assuming an equatorial orbit for the tether, and tether rotation within its orbital plane, the solar arrays would clearly have to pivot about an axis aligned with the tether's angular momentum vector in order to constantly track the Sun. This approach would yield full illumination when the solar declination is 0° (i.e. at the equinoxes of March 22 and September 22). Solar declination will range between -23.5° and $+23.5^\circ$ throughout the year, and tracking both for tether rotation (on a period of 6-8 minutes) and for solar declination (on a period of 12 months) would, in theory, require a two-axis tracking system. For photovoltaics, the power loss incurred by not tracking for declination ($1 - \cos(23.5^\circ) = 8.3\%$) may not be a concern, but for a concentrating solar array or a solar-dynamic system, such accuracy in pointing might be necessary.

The tether's rotation will also cause significant centrifugal acceleration to any solar array design, depending upon its position along the tether. There will also be much higher radiation loads on the arrays because of their passage in and out of the Van Allen radiation belts. These radiation concerns may lead to a consideration of alternative photovoltaic materials, such as indium phosphide or gallium-indium-nitride. They may even lead to an inherently radiation-hard solution such as solar thermal power, even though its pointing requirements are more stringent. Rotation about axes raises concerns about power transfer across rotating slip rings. Further issues for the solar arrays concern packaging, deployment, and lifetime of rotating components.

A variety of different solar array configurations have been hypothesized:

- No-axis tracking (a one- or two-sided solar array deployed along the axis of the tether).
- A "venetian blinds" approach deployed along the tether axis with single-axis tracking.
- "Stacked squares" that would be deployed along the tether axis and supported at their corners by some type of multi-strand tether structure.
- Circular disk solar arrays deployed outward from the tether with two-axis tracking via a universal joint.

During most of its orbit, the tether facility will be at too high an altitude to drive electrical current. Sizing a power system only for the period when power is required (an arc centered around perigee) could lead to a disproportionately large power system. Therefore, energy storage is required to store up this solar power and release it when it is required.

The energy storage requirements for the tether system are significantly larger than previous spacecraft designs and could drive new technologies. Early analyses have shown that standard battery technologies, such as nickel-cadmium and nickel-hydrogen, will probably have too low a specific energy and round-trip efficiency to lead to attractive MXER tether systems. Energy storage techniques such as lithium-ion batteries or mechanical energy storage systems such as flywheels show much more promise.

Flywheels may solve another problem for tether energy storage—the rapid rate of discharge of the energy storage system. An energy storage system charging and discharging during each orbital period (~3 hours) would have ~3000 cycles per year. The discharge of a chemical

battery system can lead to large heat loads. The discharge of a flywheel system may be an improvement over the battery, both in heat generated and in depth-of-discharge. Batteries will discharge low-voltage direct current (DC) power, which must be converted to alternating current (AC), transformed to high voltage, and rectified back to DC power. The flywheel will likely be able to deliver its energy as high-voltage AC power, which can then be rectified to the high-voltage DC power needed to drive electrodynamic tether current. The flywheel system may thus serve to simplify the power management and distribution system.

The power management and distribution (PMAD) system is an important component of the system, converting power from the low voltages produced by the solar arrays to the high voltages required by the energy storage system and/or the electrodynamic tether. It would be very desirable if the PMAD system could be integrated to some degree with a flywheel charge/discharge system, leading to a reduction in system mass.

Comparatively little effort thus far has been spent in the examination of the detailed power generation / energy storage issues related to a MXER tether system, but this could be an active area of solicitation in future research announcements.

5.5 – Power and Energy Storage Systems					
Element	SOA	TRL	RD ³	Gap	Gap Filler
Photovoltaic solar panels	Dual-junction GaAs/Ge	5	I	High radiation doses shorten lifetime	<ul style="list-style-type: none"> concentrating arrays cover glass thin-film CuInSe² indium phosphide gallium/indium nitride
Solar panel orientation	Mechanical slip rings Bearings	7	I	Panels must track the Sun during tether orbit and tether rotation and account for solar declination	<ul style="list-style-type: none"> Stacked array design (Global Aerospace) Rotating universal joint (Tennessee Tech)
Solar panel structure	AEC-Able UltraFlex circular solar array	7	I	Demonstrating large panels in high power	<ul style="list-style-type: none"> UltraFlex panels are being developed for Solar Electric Propulsion (SEP) missions Good compatibility with rotating universal joint
Chemical energy storage (batteries)	NiCd NiH ₂ Li-Ion	4	III	Duty cycle and high-voltage requirement of tether operation	<ul style="list-style-type: none"> Continue to monitor battery technology advancements
Mechanical energy storage (flywheels)	Glenn Research Center (GRC) Flywheel Program	3	III	Magnetic bearings	<ul style="list-style-type: none"> Materials research / development
Power management and distribution (PMAD)	GRC technology	7	I	High-voltage operations and power system integration	<ul style="list-style-type: none"> Possible integration with flywheel charge/discharge system

5.6 Plasma Contactors

The plasma contactors serve to collect electrons from the ionosphere and emit them back. They essentially “close the circuit” in the electrodynamic tether. Without plasma contactors, it would be impossible to flow current unidirectionally through the tether and obtain force.

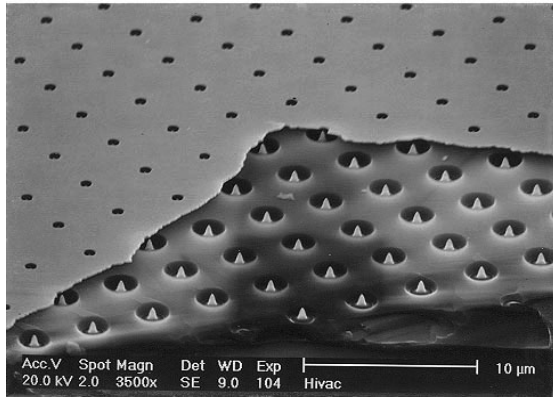
The anode is the plasma contactor that is designed to collect electrons. As such, it is positively biased to be attractive to ambient electrons. The solid, spherical end mass of the TSS missions was positively biased and used as an anode for current collection (on the order of 0.5 A), although its massive design would not be amenable to large-scale current collection. On the TSS-1R mission in 1996, it was discovered that the spherical anode had collected roughly 3x the current that had been anticipated before the mission.

The concept of using the tether itself as an anode was put forward by Professor Juan Sanmartin in 1994. This bare-wire anode offered the possibility of improved current collection since it had much more surface area per unit mass, and changes in the bias voltage had a more pronounced effect on current collection levels. Interest in assessing the performance of the bare-wire anode was one of the primary reasons why the ProSEDS tether mission was pursued. There have been concerns expressed about self-shielding of the bare-wire anode at high current levels (>10 A) due to the formation of a magnetic field around the wire. This may have an impact on its applicability for tethers that flow large currents like MXER.

Further investigation of TSS flight data and the bare-wire anode led Dr. Nobie Stone, former project scientist of TSS, to pursue an innovative concept called the grid-sphere anode. The grid-sphere concept seeks to incorporate the best features of the spherical collector and the bare-wire anode into a single structure. The grid-sphere anode would consist of an inflated pressurized sphere with a conductive mesh embedded within the inflatable material. The material would be photolyzable and would be designed to degrade under the ultraviolet exposure it would receive in orbit, leaving only the conductive mesh material behind. The sphere would be positively biased and the electric field created would attract electrons, but allow neutral particles to pass through, significantly reducing atmospheric drag. Dr. Stone was awarded a Phase I Small Business Innovative Research (SBIR) in January 2003 to further work on the grid-sphere, and was awarded a Phase II SBIR in October 2003. At the conclusion of Phase II he plans to develop and test a 5-meter version of the grid-sphere anode.

Plasma contactors that emit electrons are referred to as cathodes, and by and large, their technology levels are significantly higher than those for anodes. Much of this is because cathode technology has been advanced for years by electric propulsion systems for spacecraft as well as charge-control on large space structures such as the International Space Station (ISS). The state-of-the-art in cathodes is represented by the hollow cathode, which uses a heated element and a gas supply to create a conductive “cloud” that allows electrons to transfer to the ionosphere. Hollow cathodes have been used with ion engines for years as neutralizers and are currently used on the ISS for charge control. Although they are at a high state of readiness, there are concerns about lifetime, expellant gas consumption, and power consumption associated with their use. However, early analyses show that the MXER tether could carry enough gas consumable to accomplish its mission without significant mass penalty.

Another cathode technology that is actively being pursued are field-emission array cathodes (FEAC). FEAC technology offers the possibility of truly propellantless electrodynamic tether propulsion since it has no gas consumable like the hollow cathode. The most well-known FEAC configuration is called a Spindt-type cathode, and consists of an array of microscopic tips



beneath a charged grid. The electric field set up between the tip and the grid can approach exponential levels, and electrons can quantum-mechanically “tunnel” out of the tip and be injected into the ambient ionospheric plasma. In addition to an elimination of consumables, FEACs also promise low power consumption ($< 1 \text{ W/A}$) and a small mass and volume ($> 10 \text{ A/cm}^2$).

Current FEAC materials have proven susceptible to atomic oxygen, which “blunts” the tips of the FEAC and severely degrades emission performance. A small effort in FY04 is being funded at JPL under

Dr. Colleen Marrese in the testing of FEAC samples (NbC, IrO₂, MgPt, NbNi) that show promise against AO degradation. Additionally, FEAC concepts have been proposed (notably by Dr. Vlad Hruby of Busek, Inc.) that utilize carbon nanotubes in place of Spindt-type cathodes in the FEAC. These nanotubes show promise to “stay sharp” even under prolonged AO exposure and are a topic of future research.

5.6 – Plasma Contactors					
Element	SOA	TRL	RD ³	Gap	Gap Filler
Bare-wire anode	ProSEDS tether	5	II	<ul style="list-style-type: none"> Operation at high current levels Environmental interaction and damage 	<ul style="list-style-type: none"> Multiple wire structures Surface coatings
Grid-sphere anode	SRS SBIR research / Goodyear inflatable circa 1967	3/5	II	<ul style="list-style-type: none"> Numerical current collection model Grid-design to withstand tether-induced accelerations 	<ul style="list-style-type: none"> Extending linearized model to include physics Validate numerical model in lab experiments Adapt thin-film manufacturing Fabricate 5m sphere
Hollow cathodes	ISS / ProSEDS	8	I	<ul style="list-style-type: none"> Startup / heating power Xenon consumption rate 	<ul style="list-style-type: none"> Improved current emission / reduced gas consumption
Field-emission array cathodes	Spindt-type cathode array	3	III	<ul style="list-style-type: none"> Lifetime in orbital environment Tip blunting 	<ul style="list-style-type: none"> Materials research to address environment
Solid expellant cathode	Fabricated test samples	3	III	<ul style="list-style-type: none"> Material consumption rate 	<ul style="list-style-type: none"> Further research

6.0 MXER TAG Summary and Conclusions

Discussion during the TAG was centered on what the state-of-the-art currently is for MXER subsystems. The TAG discussed the various and most critical items needing advancement in the TRL scale and how MXER technology can be matured within the In-Space Propulsion (ISP) Program guidelines. The primary item of consensus of the TAG participants was the need to advance material survivability technology for the MXER tether and supporting subsystems. The rationale for MXER is lower cost and faster transit from LEO to GTO. Traversing this region will enhance not only commercial GEO satellites, but also, almost all NASA's deep space missions. However, the promise is only realized if the MXER tether station is reused many times to amortize its initial costs. Thus the attractiveness to MXER is directly proportional to the orbital operational lifetime achievable with the materials and technology developed in the next few years. No dramatic breakthroughs are required and all applicable physics is well understood.

Funding support was noted as presently insufficient to advance the technology at a rate compensatory with its enormous potential benefits. No major program is in place to move the technology into its prototype flight stage. Many MXER technologies can be matured on the ground, but the most important are only validated in space (tip propagation/tracking, spin-up, electrodynamic reboost, etc.). Even the actual debris damage probability is not well established for a MXER type operation in the space environment. Flight experiments will be crucial to MXER development.

The TAG members generally were optimistic about the future of tethers in space. Although the MXER tether system was generally received as a viable concept, the majority of attendees had not worked on any specific MXER research or development program. Much of the scientific and technical knowledge represented was on pure ED tethers for deboost or past scientific flight missions such as TSS1. This was seen as an excellent foundation to start from, but MXER would have to begin establishing an industrial and academic base familiar with the details and nuances of its architecture. One clear conclusion was that an educational outreach effort is vital, not only to the general public, but to the engineers, scientists and managers in the aerospace community.

With the diverse expertise at the TAG, a number of other space tether applications were surfaced that related to the MXER roadmap. The ISS electrodynamic reboost tether was one of the most prominent tether applications. Such a system would allow the space station to remain in orbit indefinitely without constant propellant resupply. It could also be a tremendous technology application for a MXER type control station. Other uses are for satellite and space debris de-orbit, radiation belt remediation, Earth-Moon roundtrip transportation, formation flying, atmospheric sampling, and other unique propulsion/science applications.

Generally, the MXER concept was well received and the participants embraced the "Panama Canal" analogy that was presented as an excellent means to convey the use and genre of MXER as a gateway to space. Perhaps it will be the first in-space transportation infrastructure that significantly reduce costs and spurs the imagination to a future abundance of space

journeys. As a major funding source for space tether development and research, NASA's ISPT Projects Office efforts are seen as significant to all space tether stakeholders.

7.0 Research Opportunities

The In-Space Propulsion Technology Projects Office (ISPT) of NASA's Office of Space Science (OSS) is currently soliciting proposals in a number of areas for basic supporting research and technology investigations. A few are associated with advanced in-space propulsion and MXER tethers. All the solicitations can be found at:

<http://research.hq.nasa.gov/research.cfm>

This includes SBIR and STTR Phase I and II solicitations and material research under Code U. Future funding is anticipated through a Cycle III NASA Research Announcement (NRA), which is expected to be released in the Spring of 2004. Details on this and other solicitations can also be found at the above web address. The EPT project area will make every effort to contact TAG participants and other MXER tether stakeholders on these and other funding/teaming opportunities as they become available.

8.0 Appendices

- 8.1 Appendix A: MXER TAG Agenda**
- 8.2 Appendix B: TRL and RD³ Definitions**
- 8.3 Appendix C: MXER TAG Participants**
- 8.4 Appendix D: Derivation of the Mass of a Tether Segment**
- 8.5 Appendix E: Derivation of Electrodynamic Reboost Parameters**

8.1 Appendix A: MXER TAG Agenda

**MXER Technology Assessment Group
Preliminary Agenda
Gray Research, Inc.
Huntsville, AL**

24 Jul 03

8:15	Administrative/Introductions	Gray
8:30	In-Space Propulsion Program Overview	Meyer
9:00	Technology Reprioritization	Artis
9:20	Break	
9:30	MXER Programmatic Overview	Bonometti
10:30	MXER Technology Overview	Sorensen
11:00	Breakout Sessions	
	<ul style="list-style-type: none">▪ Key Technologies / System Architecture▪ Technology Approaches▪ TRL Assessment▪ TRL Advancement	
12:00	Lunch	
1:00	Breakout Sessions, continued	
4:00	Break	
4:10	Subgroup Feedback	Sorensen
5:00–5:15	Wrap-up	Bonometti

8.2 Appendix B: TRL Definitions

TECHNOLOGY READINESS LEVEL (TRL) DEFINITIONS

System / Subsystem Development (6-8)	System Test, Launch & Operations (8-9)	TRL 9	Actual system 'flight proven' through successful mission operations
		TRL 8	Actual system completed and 'flight qualified' through test and demonstration (Ground or Flight)
Technology Development (3-5)	Technology Demonstration (5-6)	TRL 7	System prototype demonstration in a space environment
		TRL 6	System / subsystem model or prototype demonstration in a relevant environment (Ground or Space)
	Research to Prove Feasibility (2-3)	TRL 5	Component and / or breadboard validation in relevant environment
		TRL 4	Component and / or breadboard validation in laboratory environment
Basic Technology Research (1-2)	Research to Prove Feasibility (2-3)	TRL 3	Analytical and experimental critical function and / or characteristic proof-of-concept
		TRL 2	Technology concept and / or application formulated
	(1-2)	TRL 1	Basic principles observed and reported

8.2 Appendix B: R&D³ Definitions

ASSESSING NEW TECHNOLOGIES/CONCEPTS R&D “DEGREE OF DIFFICULTY” (R&D³ also referred to as AD²) (courtesy of John Mankins, NASA HQ)

<u>R&D³</u>	<u>DESCRIPTION</u>
I	Very low degree of difficulty anticipated in achieving research and development objectives for this technology; only a single, short-duration technological approach needed to be assured of a high probability of success in achieving technical objectives in later systems applications.
II	Moderate degree of difficulty anticipated in achieving R&D objectives for this technology; a single technological approach needed; conducted early to allow an alternate approach to be pursued to be assured of a high probability of success in achieving technical objectives in later systems applications.
III	High degree of difficulty anticipated in achieving R&D objectives for this technology; two technological approaches needed; conducted early to allow an alternate subsystem approach to be pursued to be assured of a high probability of success in achieving technical objectives in later systems applications.
IV	Very high degree of difficulty anticipated in achieving R&D objectives for this technology; multiple technological approaches needed; conducted early to allow an alternate system concept to be pursued to be assured of a high probability of success in achieving technical objectives in later systems applications.
V	The degree of difficulty anticipated in achieving R&D objectives for this technology is so high that a fundamental breakthrough in physics/chemistry/etc. is needed; basic research in key areas needed before feasible system concepts can be refined.

8.3 Appendix C: MXER TAG Participants

Mr. Douglas Bentley

Cortland Cable Company

Dr. Sven Bilén

Pennsylvania State University

Dr. Joseph Bonometti

NASA/MSFC

Dr. Roy Broughton

Auburn University

Dr. Stephen Canfield

Tennessee Technological University

Dr. Mario Cosmo

Smithsonian Astrophysical Observatory

Mr. Benjamin Donahue

Boeing

Mr. Dave Edwards

NASA/MSFC

Dr. Brian Gilchrist

University of Michigan

Dr. John Glaese

bd Systems Inc.

Ms. Melody Herrmann

NASA/MSFC

Dr. Robert Hoyt

Tethers Unlimited, Inc.

Dr. Enrico Lorenzini

Smithsonian Astrophysical Observatory

Mr. Leland Marshall

Lockheed Martin Astronautics Operations

Dr. Manuel Martinez-Sanchez

Massachusetts Institute of Technology

Ms. Rae Ann Meyer

NASA/MSFC

Ms. Mary Nehls

NASA/MSFC

Dr. John Peddieson

Tennessee Tech. University

Ms. Tara Polsgrove

NASA/MSFC

Dr. Raymond Sedwick

Massachusetts Institute of Technology

Ms. Gweneth Smithers

NASA/MSFC

Mr. Kirk Sorensen

NASA/MSFC

Mr. Jeffrey Staines

Tennessee Technological University

Dr. Nobie Stone

SRS Technologies

Mr. Mark Vaccarro

NASA/MSFC

Mr. John Westerhoff

University of Illinois

Dr. Paul Wilbur

Colorado State University

Dr. Ken Wright

NASA/MSFC

8.4 Appendix D: Derivation of the mass of a tether segment

The cross-sectional area of the tether at its tip will simply be the force of the payload (its mass divided by centrifugal acceleration) divided by the tensile strength of the tether material (derated by some safety factor). If t is the tensile strength of the tether material (in pascals), f is the safety factor, m is the mass of the design payload (kg), v_{tip} is the tip velocity (m/s), and l is the distance from the loaded center-of-mass to the tip (m), then the cross-section is given by:

$$A_{tip} = \frac{m_{tip} v_{tip}^2 f}{\ell t}$$

Scanning from the tip to the center of rotation, each additional section increases the tension to the tether, which depends on its cross-sectional area and its distance from the center of rotation. An analytical expression for the cross-section is:

$$A(r) = A_{tip} \exp\left(\frac{f r v_{tip}^2}{t} \left(1 - \frac{r^2}{\ell^2}\right)\right) = A_{tip} \exp\left(VR^2 \left(1 - \frac{r^2}{\ell^2}\right)\right)$$

In this expression, r is the distance along the tether from the center of rotation and ρ is the tether's material density. VR is the velocity ratio, a useful quantity that will be defined shortly.

The total mass of the tether would be obtained if this equation was integrated from the tip to the center of rotation. If this equation included gravitational effects, a closed-form integration would not be possible, but this simpler form can be integrated and results in the following expression:

$$m_{tether} = \rho \int_0^\ell A(r) dr = m_{tip} \sqrt{\rho} \frac{f r v_{tip}^2}{t} e^{\left(\frac{f r v_{tip}^2}{t}\right)} \operatorname{erf}\left(\sqrt{\frac{f r v_{tip}^2}{t}}\right)$$

This complicated expression can be simplified tremendously if several new quantities are defined. First, it is expressed as a ratio between the tether's mass and the mass at its tip. Second, the characteristic velocity is defined, which represents the specific tensile strength of the tether material (tensile strength / material density).

$$v_c = \sqrt{\frac{2T}{fd}} \quad \longrightarrow \quad \frac{m_{tether}}{m_{tip}} = \sqrt{\rho} \frac{v_{tip}^2}{v_c^2} e^{\left(\frac{v_{tip}}{v_c}\right)^2} \operatorname{erf}\left(\sqrt{\frac{v_{tip}^2}{v_c^2}}\right)$$

Finally, the velocity ratio (VR) is defined, which is the velocity of the tether's tip divided by the characteristic velocity. With its substitution, the tether/payload mass ratio assumes a particularly simple form:

$$VR = \frac{v_{tip}}{v_c} \quad \longrightarrow \quad \boxed{MR = \frac{m_{tether}}{m_{tip}} = \sqrt{\rho} (VR) \operatorname{erf}(VR) e^{VR^2}}$$

From the complications of its original expression, we can see that the tether/payload mass ratio is wholly dependent on the velocity ratio, which is in turn dependent on the tip velocity and the material selection.

It is interesting to note that the mass of the tether is only a function of the tether's tip velocity, the material chosen, and the mass on the tip. It is not a function of tether length, surprisingly. Additionally, note that the mass ratio is not only exponentially dependent on the velocity ratio, but on the **square** of the velocity ratio. Therefore, it is absolutely important to obtain the highest characteristic velocity possible in the tether material.

For instance, the characteristic velocity calculation for PBO (tensile strength = 5.8 GPa, density 1540 kg/m³) at a safety factor of 3 would be:

$$v_c = \sqrt{\frac{2T}{fd}} = \sqrt{\frac{2(5.8 \times 10^9 \text{ Pa})}{3 \left(1540 \frac{\text{kg}}{\text{m}^3} \right)}} = \sqrt{\frac{11.6 \times 10^9 \frac{\text{kg}}{\text{m} \cdot \text{s}^2}}{4620 \frac{\text{kg}}{\text{m}^3}}} = \sqrt{2.51 \times 10^6 \frac{\text{m}^2}{\text{s}^2}} = 1584 \frac{\text{m}}{\text{s}}$$

Thus we see the critical importance of having a material with as high a characteristic velocity as possible.

8.5 Appendix E: Derivation of Electrodynamic Reboost Parameters

It is desired to obtain a relationship for the power/force ratio on an electrodynamic tether.

Starting with the relationship for force on an electrodynamic tether:

$$\vec{F} = \vec{J} \times \vec{B} \quad \text{or} \quad \vec{F} = (I\vec{L} \times \vec{B})$$

In this expression, F is force in newtons, J is the electrical current vector (the scalar value of current multiplied by the length vector L), and B is the magnetic field vector in tesla. In order to simplify the math and more clearly elucidate the problem, assume that J and B are orthogonal to one another. In that case, the expression for force becomes:

$$F = ILB$$

The expression for power consumed, assuming there no resistive losses in the tether, is:

$$P = IV$$

where I is the electrical current in amperes and V is electrical potential in volts.

The induced voltage along the tether, due to passage through the magnetic field, is:

$$V = (\vec{W} \times \vec{B}) \cdot \vec{L}$$

where W represents the velocity of the tether across magnetic field lines, and B and L represent the magnetic field and length vectors, respectively. Again, assuming velocity and magnetic field are orthogonal, and that the length vector of the tether is collinear with the cross product, this simplifies to:

$$V = WBL$$

Substituting the voltage expression into the power expression, and dividing power by force yields:

$$\frac{P}{F} = \frac{IWBL}{ILB} \quad \text{which simplifies to} \quad \frac{P}{F} = W$$

This result shows that in the absence of electrical resistance, the power required to generate force depends only on the velocity across the field lines. It is interesting to note that electrical current, tether length, and magnetic field strength do not factor into the result. For instance, doubling tether current doubles force, but also doubles power consumption; similarly, doubling tether length or magnetic field strength doubles force, but also doubles the induced voltage to overcome.

A tether in low Earth orbit has a velocity of ~7700 m/s, so in an ideal case, it would require 7700 W of power to produce 1 N of force. The MXER tether has a perigee velocity of ~9000 m/s, so it would require no less than 9000 W of power to produce 1 N of force. So, much to the dismay of

a designer looking for an optimum, these simple results indicate that no change in current or tether length will improve the power/force ratio.

The result that the power/force ratio depends only on velocity is another manifestation of the concept of “back EMF” so familiar to electric motor designers. The electrodynamic tether itself is an example of an electric motor.

Next, reconsider the derivation with electrical resistivity along the tether considered. In that case, the power equation becomes:

$$P = IV + I^2R$$

where R represents electrical resistance in ohms. Total resistance can be calculated from the material resistivity (r) in ohm-meters multiplied by length (L) in meters divided by cross-sectional area (A) in meters squared.

$$R = \frac{rL}{A}$$

Representative resistivity values are 26.2 nO-m for high-purity aluminum (2710 kg/m³) and 16.7 nO-m for copper (8940 kg/m³). Length multiplied by cross-section gives volume, which can be multiplied by material density for a mass estimation of the conductive tether. Substituting induced voltage as before, the equation for power becomes

$$P = IWBL + \frac{I^2 rL}{A} \quad \text{or} \quad P = IL \left(WB + \frac{Ir}{A} \right)$$

Then the P/F ratio becomes

$$\frac{P}{F} = \frac{IL \left(WB + \frac{Ir}{A} \right)}{ILB} \quad \text{which simplifies to} \quad \frac{P}{F} = W + \frac{Ir}{AB}$$

The first term is the induced voltage (or back EMF) from the tether’s movement through the magnetic field and the second term represents the effect of electrical resistance. Minimizing the power/force ratio would be accomplished by reducing electrical current or material resistivity, or increasing cross-sectional area of the conductive material. Increasing the Earth’s magnetic field strength is obviously not an option!

Increasing the cross-sectional area of the conductive tether would drive electrical resistance lower and lower, and bring the power/force ratio closer to its minimum value (velocity). But increasing cross-section will lead to increased mass, which will reduce acceleration. What is clearly needed now is an expression for force/mass (acceleration). There is every reason to believe that an expression for acceleration will have a minimum since on one end (small cross-sections) resistance will drive up the mass of the power supply and on the other end (large cross-section) the mass of the conductive tether will dominate.

Recognizing that the power generation system obviously has a substantial mass, an obvious extension to this derivation would be to try to solve for an optimum force/mass ratio, or

acceleration. For simplicity, we will only consider the ED conductive tether mass and the power supply system mass. This ignores the mass of the ballast and the high-strength tether, but it will serve to illuminate some trends.

Again, we begin with the relationship for force on an electrodynamic tether:

$$\vec{F} = \vec{J} \times \vec{B} \quad \text{or} \quad \vec{F} = (\vec{I}L \times \vec{B}) \quad \text{simplifying to} \quad F = ILB$$

The expression for mass should include the masses of the electrodynamic tether components. The mass of the power supply will be represented by a specific power value, often used in electric propulsion analyses, called “alpha”. α is given in kilograms of power supply per watt of useable power generated. The mass of the electrodynamic tether is simply the density of the conductive material multiplied by its volume (length multiplied by cross-section).

$$M = \alpha P + DLA$$

Substitute the relationship for power derived previously into the mass relationship.

$$P = IV + I^2R$$

$$M = \alpha IV + \alpha I^2R + DLA$$

Furthermore, substitute the relationship for induced voltage and resistance into the mass relationship.

$$M = \alpha IWB L + \alpha I^2 \frac{rL}{A} + DLA$$

$$M = L \left(\alpha IWB + \alpha I^2 \frac{r}{A} + DA \right)$$

Dividing the force expression by the mass expression yields:

$$\frac{F}{M} = \frac{IBL}{L \left(\alpha IWB + \alpha I^2 \frac{r}{A} + DA \right)} = \frac{IB}{\alpha IWB + \alpha I^2 \frac{r}{A} + DA}$$

For simplicity, invert the expression and simplify:

$$\frac{M}{F} = \alpha W + \frac{\alpha r}{AB} + \frac{DA}{IB}$$

The term I/A represents the current density (A/m^2) and is replaced by J .

$$\frac{M}{F} = \alpha W + \frac{\alpha r J}{B} + \frac{D}{JB}$$

This expression represents the inverse of the acceleration term and ideally should be minimized if maximum acceleration is desired. Terms such as alpha or resistivity appear in the numerator

of the expression, and so obviously, to minimize the expression, the minimum values of alpha and resistivity are desired. But current density appears both in the numerator and the denominator of the components of the expression, therefore in order to calculate the minimum value of the expression (with respect to current density) we must take the derivative of the expression and set it to zero. The derivative with respect to current density is:

$$\frac{d\left(\frac{M}{F}\right)}{dJ} = \frac{\mathbf{ar}}{B} - \frac{D}{J^2 B}$$

Setting it to zero and solving for current density yields:

$$\frac{\mathbf{ar}}{B} - \frac{D}{J^2 B} = 0$$

$$\mathbf{ar} = \frac{D}{J^2}$$

$$J = \sqrt{\frac{D}{\mathbf{ar}}}$$

If we then substitute this value of current density back into the original expression, we obtain:

$$\frac{M}{F}_{\min} = \mathbf{a}W + \frac{\mathbf{ar} \sqrt{\frac{D}{\mathbf{ar}}}}{B} + \frac{D}{\sqrt{\frac{D}{\mathbf{ar}}} B} = \mathbf{a}W + \frac{\sqrt{D\mathbf{ar}}}{B} + \frac{\sqrt{D\mathbf{ar}}}{B} = \mathbf{a}W + \frac{2\sqrt{D\mathbf{ar}}}{B}$$

Inverting the result gives us the maximum value of acceleration for a given set of conditions.

$$\frac{F}{M}_{\max} = \mathit{acceleration}_{\max} = \frac{B}{\mathbf{a}WB + 2\sqrt{D\mathbf{ar}}}$$

Now we will examine how these results might be used. Let us assume we have made a selection of a conductive material for the tether—aluminum, for example. Let us also assume that the technologies chosen for the power supply give us a value for alpha—50 kg/kWe was representative for the Deep Space 1 mission. Substituting these values into the expression for ideal current density would yield:

$$J = \sqrt{\frac{D}{\mathbf{ar}}} = \sqrt{\frac{2710 \frac{\text{kg}}{\text{m}^3}}{\left(0.05 \frac{\text{kg}}{\text{W}}\right) (26.2 \times 10^{-9} \Omega \cdot \text{m})}} = \sqrt{\frac{2710 \frac{\text{kg}}{\text{m}^3}}{1.31 \times 10^{-9} \frac{\text{kg}}{\text{m} \cdot \text{A}^2}}} = \sqrt{2.06 \times 10^{12} \frac{\text{A}^2}{\text{m}^4}} = 1.44 \times 10^6 \frac{\text{A}}{\text{m}^2}$$

Thus, for an aluminum conductor and this value of alpha, the maximum acceleration should be expected when 144 amps flow through each square centimeter of conductive tether. This value

of current density can then be used to ascertain the ideal cross-section of the conductive tether. For instance, if the tether, on average, flows 20 A of current, then an aluminum ED tether should have about 14 mm² of cross-sectional area. For an 80-km ED tether, the conductive tether mass would then come to about $(80000 \text{ m})(0.000014 \text{ m}^2)(2710 \text{ kg/m}^3) = 3040 \text{ kg}$.

9.0 Attachments (Appendices Continued)

- 9.1 Appendix F: In-Space Propulsion Overview (Attachment 1)**
- 9.2 Appendix G: MXER TAG Technology Reprioritization Planning Status (Attachment 3)**
- 9.3 Appendix H: MXER Programmatic Presentation (Attachment 2)**
- 9.4 Appendix I: MXER Technical Presentation (Attachment 3)**

Results of Evaluation of Solar Thermal Propulsion Gordon Woodcock ... Consultant to Gray Research, Inc. Dave Byers ... Consultant to SAIC

ABSTRACT

The solar thermal propulsion evaluation reported here relied on prior research for all information on solar thermal propulsion technology and performance. Sources included personal contacts with experts in the field in addition to published reports and papers. Mission performance models were created based on this information in order to estimate performance and mass characteristics of solar thermal propulsion systems. Mission analysis was performed for a set of reference missions to assess the capabilities and benefits of solar thermal propulsion in comparison with alternative in-space propulsion systems such as chemical and electric propulsion. Mission analysis included estimation of delta V requirements as well as payload capabilities for a range of missions. Launch requirements and costs, and integration into launch vehicles, were also considered.

The mission set included representative robotic scientific missions, and potential future NASA human missions beyond low Earth orbit. Commercial communications satellite delivery missions were also included, because if STP technology were selected for that application, frequent use is implied and this would help amortize costs for technology advancement and systems development. A "C3 Topper" mission was defined, calling for a relatively small STP. The application is to augment the launch energy (C3) available from launch vehicles with their built-in upper stages

Payload masses were obtained from references where available. The communications satellite masses represent the range of payload capabilities for the Delta IV Medium and/or Atlas launch vehicle family.

Results indicated that STP could improve payload capability over current systems, but that this advantage cannot be realized except in a few cases because of payload fairing volume limitations on current launch vehicles. It was also found that acquiring a more capable (existing) launch vehicle, rather than adding an STP stage, is the most economical in most cases.

PURPOSE

The purpose of the evaluation was to assess suitability of solar thermal propulsion for in-space propulsion applications, by examining performance and probable cost to customers on a range of representative missions, compared to current systems.

BACKGROUND

The study was requested by NASA Headquarters, Code S, to evaluate solar thermal propulsion for the In-Space Propulsion Technology program administered by the Marshall Space Flight Center (MSFC). The study was assigned to SAIC under the ISTA contract, which supports In-Space Propulsion at Marshall. The study was administered by Les Alexander and Bonnie James of the MSFC In-Space propulsion organization. The study was initiated in late July 2002, with a completion date of September, 2002.

Solar thermal propulsion has been under technology development for about 30 years. The fact that hydrogen gas, heated to 2500 – 3000K and expanded through a nozzle, could deliver specific impulse (Isp) in excess of 800 seconds, was well-known through demonstrations in the nuclear rocket program. Solar furnaces are known to reach this temperature range. It was seen as likely that a solar thermal propulsion system could reach much higher efficiency in converting energy of sunlight to thrust than is possible with solar electric propulsion. The reason is that concentration of sunlight onto a thruster, thereby heating hydrogen, might have much higher efficiency than converting sunlight to electricity by solar arrays and powering an electric thruster with the electricity. This higher efficiency, it is argued, would compensate for the lower Isp, making solar thermal propulsion potentially competitive with solar electric propulsion and capable of much shorter trip times.

MISSIONS AND REQUIREMENTS

Missions were selected to suit the objectives of the assessment. A list of missions with reasons for selection is given in Table 1. Estimates of performance requirements are given in Table 2.

The current In-Space Propulsion (ISP) technology program is sponsored by Code S; therefore the study focused on representative Code S missions. Commercial communications satellite delivery missions were included because if STP technology were selected for that application, frequent use is implied and this would help amortize costs for technology advancement and systems development. The "C3 Topper" mission is a case where the STP is relatively small. It does not present a problem for payload fairing volume, and its competition is probably solid propellant, with Isp less than 300 seconds. The HEDS gateway was selected

because it is a mission application for which new in-space propulsion development is needed regardless of the technology selected, and STP is not at a non-recurring cost disadvantage relative to other systems. The “no-hydrogen” application to an RLV upper stage is a different competitive environment than ELV launchers because the STP does not compete with developed cryogenic upper stages. In this case the STP cannot use hydrogen but is competing with other systems that also cannot. The STP would probably use ammonia as propellant; methane is possible but it is cryogenic and much more flammable than ammonia.

The payload masses were obtained from references where available. The communications satellite masses represent the range of payload capabilities for the Delta IV Medium launch vehicle family. The payloads cited in Table 2 are, in all cases, the mission payload and do not include apogee propulsion. Communications satellite payloads are often cited in terms of geosynchronous transfer orbit (GTO) but the figures here are payload to the mission orbit, geosynchronous equatorial orbit (GEO).

Table 1: Tabulation of Missions Evaluated for STP Application

<ul style="list-style-type: none"> • NGST • Space Interferometry Mission • Terrestrial Planet Finder • Medium GEO Comsat • Large GEO Comsat • C3 Topper for outer planets missions • HEDS L1 Gateway • RLV Upper Stage 	<ul style="list-style-type: none"> • Representative small science payload (to ESL2) • Representative medium science payload (to ETSO) • Representative large science payload (to ETSO) • High-demand commercial payload • High-demand commercial payload (larger) • Smaller STP leads to less volume concern • Large payload for EML1 which requires in-space propulsion development • If “no hydrogen” safety constraint applied, STP with ammonia may be competitive
--	--

Table 2: Top-Level Requirements for Selected Missions

Description	Destination	Payload Mass (kg)	Remarks
NGST	Earth-Sun L2	1400	From ISP Requirements Matrix
Space Interferometry Mission	Earth Trailing Solar Orbit (ETSO)	3900	From ISP Requirements Matrix
Terrestrial Planet Finder	Earth-Sun L2	4800	From ISP Requirements Matrix
Medium GEO Comsat	GEO	1900	L/V capability less apogee motor
Large GEO Comsat	GEO	3000	L/V capability less apogee motor
C3 Topper	Outer Planets	300 – 1500 kg	Generic capability
HEDS L1 Gateway	Earth-Moon L1	24,000	JSC HEDS DRM briefing
RLV Upper Stage (Non-Hydrogen)	GEO or C3=0	5000 kg or more (NEP)	Rationale is safety

An existing ISP requirements matrix was interrogated to obtain destination and payload mass data for the Code S payloads. The GEO comsat masses represent the smallest and largest Delta IV Medium options. Except for fairing volume considerations, STP upper stages would deliver more payload on the same launch vehicle, but these masses were considered representative. The C3 Topper was examined generically. Scientific payloads for outer planet missions, from the ISP requirements matrix, range from about 300 kg for small, simple payloads such as planetary flyby payloads, up to 1500 kg for a Titan orbiter/lander. Even larger payloads may be of interest at a later time. Examples of greater payload requirements, presently not very quantified, are a large Europa lander intended to penetrate Europa’s ice to search for the putative ocean below, and a Titan sample return mission. The HEDS L1 Gateway mission payload was obtained from a JSC planning presentation. The Gateway is a small habitable space station. The RLV upper stage mission presumes that these payloads will utilize the launch capability of an RLV. Smaller payloads may also be of interest. One such case is launch of an experimental nuclear electric propulsion (NEP) stage to LEO with an STP stage designed to transfer the NEP stage to C3=0 so that the nuclear propulsion system is not started in Earth orbit. This case requires an estimated payload mass to C3=0 of 5800 kg.

MISSION PERFORMANCE AND COST ANALYSIS

Payload Performance

A performance baseline was created for application to the GEO and Earth escape missions. These missions are similar in that both require expanding an initially circular orbit to a highly elliptic orbit, for GEO with apoapse at 42,164 km and for escape or Earth-Moon L₁ (EML1), essentially at infinity, i.e. C₃ = 0. For EML1 the C₃ is actually about -2 km²/sec² but this is essentially the same from a delta V viewpoint. For the GEO missions, an apoapse delta V about 1800 m/s is required; for Earth escape no apoapse maneuver is needed, and for insertion at L₁ the maneuver is about 650 m/s. High thrust systems can get to L₁ or L₂ via a powered lunar gravity assist for apoapse maneuvers (2 required) totaling about 250 m/s but STP does not have high enough thrust-to-mass ratio to perform the gravity assist thrusting maneuver.

The simplest way to fly from LEO to these destinations with STP is continuous thrusting. The result is a spiral path away from Earth with substantial G losses. STP does not have high enough Isp to accept these losses; its payload performance would be less than that for conventional chemical propulsion and

there would be no benefit to using STP. Glenn Research Center provided an example continuous-thrust trajectory. Their mission profile assumptions were as follows:

- Three Phase LEO to GEO Transfer
- Spiral out from 500km altitude to approximate GEO radius
- Circularize using a maximum-eccentricity rate change steering law
- Plane change to zero inclination using a discontinuous-thrust inclination-change control law
- Decreasing the aggressiveness of the inclination change reduces propellant mass at the expense of trip-time (see Figure 1).

While this isn't an optimal transfer, it will not be far from an optimal result.

5% margins were added to trip time and propellant expenditure to account for small deviations in the final semi-major axis ($\pm 100\text{km}$) and inclination ($\pm 1^\circ$).

The results, illustrated in Figure 1, show delta V about 6.2 km/s versus about 4.2 for a high-thrust system.

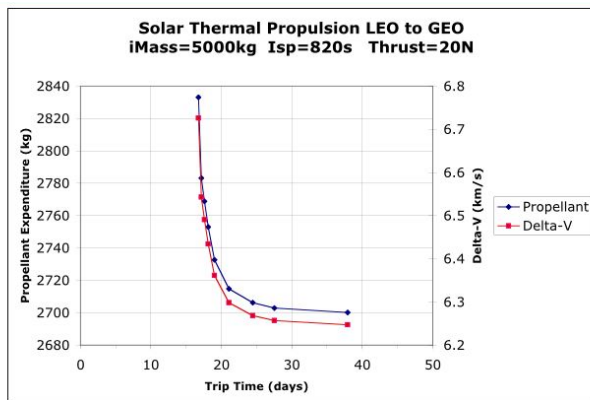


Figure 1: STP Spiral Delta Vs Provided By NASA Glenn Research Center

If the STP operates with intermittent burns near periapse, gravity losses are minimized and the STP can approach the delta V of a high-thrust system. The price for this is increased trip time. The question, clearly, is how much of a trip time increase must be incurred. This, in fact, was the motivation for the energy storage STP concept: one could collect solar energy all around the orbit and deliver it quickly near periapse. Also, if solar energy collection is discontinued during thrusting, simultaneous pointing to the Sun and of the thrust vector is not required, and the STP overall configuration is simplified. However, the very poor demonstrated efficiency of the storage concept (due to heat leak out of the storage system) in early tests led us to doubt its viability.

In the time available for the assessment study, rigorous optimization of intermittent thrusting was not possible. Such an optimization would constrain trip time and minimize delta V within that constraint. We approximated this by adopting a thrusting program that is arguably near-optimal, and evaluating the trip time. The thrusting program uses pitch angle modulation to hold periapsis constant during apoapse raising and to hold apoapsis constant during periapse raising. This relies on the thrusting effects shown in Figure 2. If pitch modulation is not used, the periapsis thrust intervals will raise periapse, resulting in g losses. As thrusting periods are increased, the g losses become greater. The upper limit is continuous thrust as described above. The lower limit is very short periapsis thrust periods and very long trip times. A true optimum is expected to let the apsides increase slightly, reducing pitch angle losses. The pitch modulation decreases thrust effectiveness; for this study an integrated thrust effectiveness of 90% for periapse maneuvers and 95% for apoapse maneuvers was selected. This does not yield optimal time-constrained transfers but was selected for expediency and ability to approximate optimal performance. Integration results for transfer to GEO are shown in Figure 3. Note that this result has a different thrust than assumed for Figure 1; this should be taken into account when comparing trip times. Each plot point in Figure 3 represents one thrusting period.

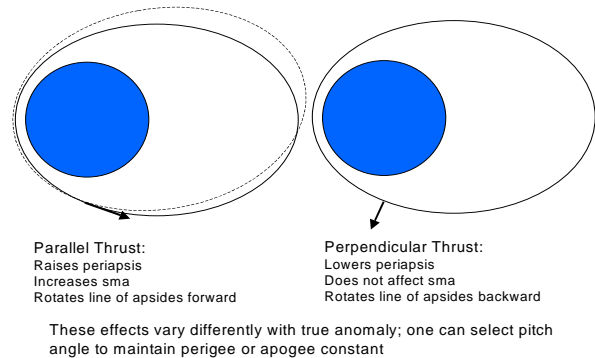
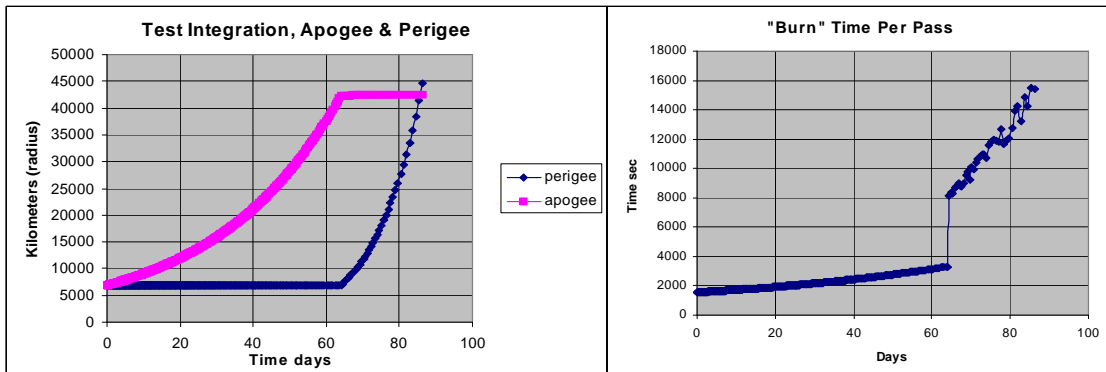


Figure 2: Pitch modulation thrust effects

For escape and libration point missions we assumed the same net effectiveness to obtain delta V for periapse maneuvers, and assumed no gravity losses for maneuvers at the destination.

These delta Vs were used with an STP mass estimating model to develop STP performance capabilities for the missions. Specific impulse for STP thrusters was estimated at 811 seconds, assuming (a) 2800K radiation temperature in the absorber cavity (this presumes collection of the concentrated solar energy in a cavity absorber, and radiative transfer from the absorber to the thruster), (b) 2700K thruster wall



Start mass 5000 kg; Thrust 12 N; Isp 811
 Effectiveness criterion set 90% perigee, 95% apogee
 Delta V 4350 m/s; does not include plane change; with
 plane change ~ 4600 m/s
Bottom Line: Trip time and delta V are OK but longer than
 desirable

Figure 3: Results of integration for LEO-GEO transfer

temperature, (c) 2600K hydrogen temperature, (d) nozzle area ratio 20, (e) 10% energy loss to viscous dissipation in the nozzle, and (f) a 10 degree average flow divergence angle exiting the nozzle.

High energy missions to the outer planets have generally used multiple gravity assists to attain the trajectory energy needed to reach these destinations in reasonable time. The Pioneer and Voyager spacecraft were launched directly to Jupiter and used Jupiter and other gravity assists to continue on to the outer solar system. More recent missions (Galileo, Cassini) have used multiple inner planet gravity assists to get to Jupiter. It is possible to launch directly to the desired high energy, and this has been discussed as one option for a Pluto flyby. It is also possible to use electric propulsion, probably with a single Venus gravity assist, to perform these missions without requiring the launch vehicle to attain very high launch energy.

A major reason for interest in direct, rather than gravity assisted, trajectories is that Jupiter is not always in a position suitable for gravity assist to the planets of the outer solar system. Jupiter is available for a launch to Pluto in 2004, and offers a slight assist in 2006. It is then out of position for about 10 years.

Existing launch vehicles are tailored for the GTO market. They perform launches to LEO well, and can achieve C3 up to 20 – 40 km²/sec² fairly well. Above this energy range their payload capability declines rapidly and goes to zero before C3 100. The reason is the relatively high inert mass of the upper stage, which starts before orbital velocity is reached.

For high energy, the usual solution is a solid rocket motor (SRM) upper stage as a “C3 topper”.

Existing-design spacecraft SRMs are suitable. This assessment asked whether STP could fit this application.

Since the total payload in the shroud is much less than the design value, STP’s low density is almost certainly not a problem. Its high Isp is a benefit. Unfortunately, STP is at a disadvantage because of its low thrust. The SRM C3 topper delivers its delta V deep in Earth’s gravity well and STP cannot, because its burn time is at least many days, while the time to essentially exit Earth’s gravity well is less than a day at C3 30 to 40.

Since the gravity well advantage is a function of current and target C3, a high Isp system may have an overall advantage even if it cannot take advantage of the gravity well. This is partially illustrated in Figure 4. The Figure shows the differential advantage as the increment in “hyperbolic excess velocity” per unit delta V. The ratio is one for delta V outside the gravity well. Note that C3 is just the square of the hyperbolic excess velocity. At C3 30 to 40, the gravity well advantage factor is about 2. One may expect that a system with Isp 800 operating outside the gravity well could have an advantage over one with Isp 300 operating in the gravity well.

A spread-sheet analysis was constructed to examine parametrically the performance of an STP C3 topper compared to a solid propellant motor C3 topper. The STP was assumed to operate entirely outside the gravity well and the solid rocket entirely in it, at an altitude of 500 km. Performance was evaluated for a range of launch C3s from 0 to 70 and a range of target

C3 from 100 to 180. (A 14-year Pluto trajectory requires C3 about 160.) Results are shown in Figure 5.

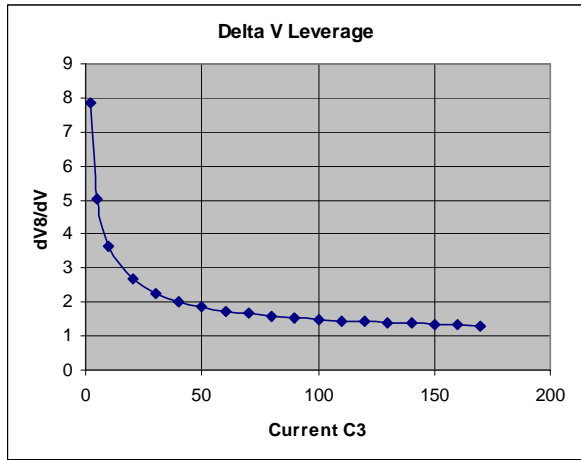


Figure 4: Gravity Well Differential Advantage

An STP propulsion system offers better performance to high C3 than the usual solid rocket. STP is compared here to a solid rocket stage, both as kick stages on a Delta IVM+ 5,4. For either system a launch C3 near 40 is preferred. This is a small STP and it operates only in deep space, so there is little concern about environmental degradation of the concentrator ... (a) the burn is continuous so the time of exposure is less; (b) the severe radiation environment of the van Allen belts is not applicable, nor is concern about atomic oxygen. Payloads are typically 500 – 1500 kg (reference IISTP). Neither system reaches the desired payload at typically desired C3s. For example, the payload for a direct launch to Pluto flyby is quoted as 450 kg and requires a C3 of about 160. A Titan Explorer is quoted at about 1400 kg with C3 for direct launch about 110. A larger launch vehicle such as a Delta IV Heavy would probably enable the desired performance.

A further consideration is that the Next Generation Ion technology program is presently conducting technology advancement for an electric propulsion system that can do these missions with adequate payload margin. The mission profile for both would employ a single Venus gravity assist. This profile is available every year. Venus gravity assist might also improve the performance of the STP option; this was beyond the scope of the assessment study. It does not improve the performance of the solid rocket option.

The C3 topper may be a useful application for STP but must be evaluated in light of the expected performance capability of solar electric propulsion systems.

Launch Vehicle Compatibility

The issue of low-density hydrogen was mentioned above. This problem arises because the current stable of launch vehicles was not designed for upper stages that operate on only hydrogen, and liquid hydrogen is far less dense than other propellants. The problem is exacerbated because the STP upper stage option gives best performance if launched to LEO, while the design case for these launchers is launch to GTO. Thus in the case of STP, we want not only to reduce the average density of the payload fairing contents but also to increase the mass.

The situation is presented graphically in Figure 6. On the left is a typical planned mission application, as depicted for the Delta IVM+ 5,4. The numerical designation means a five-meter fairing and four strap-on solid propellant boosters. The payload capability to GTO is approximately 6000 kg, which divides roughly evenly as 3000 kg GEO payload and 3000 kg apogee insertion propulsion. The apogee propulsion system for such missions is normally integrated into the spacecraft, but is shown schematically as separate to indicate its relatively high density.

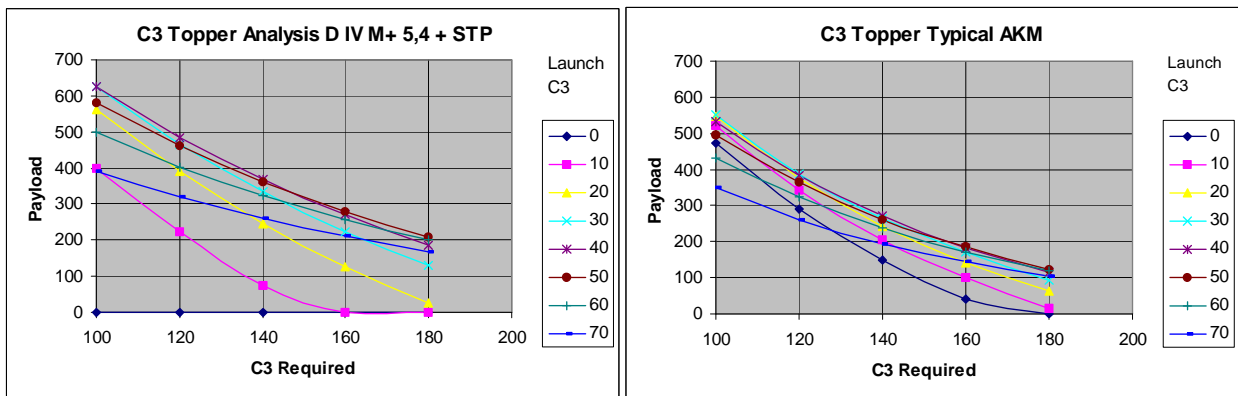


Figure 5: C3 Topper Analysis, STP Versus Solid Propellant Rocket

In terms of payload mass performance capability, the STP would allow stepping down to the Delta IVM+ 5,2 which has only two solid propellant boosters instead of four. Its payload to LEO is about 9000 kg, and this is the mass to be placed in the fairing. Of this, about 2/3 is the STP stage. The same size fairing is used. We replace a high-density 3000 kg apogee insertion stage with a low-density STP of twice the mass that performs both perigee and apogee maneuvers. Quite simply, it doesn't fit because it leaves little or no room for the mission payload.

Cost Factors

We presume that launch customers are not concerned with the technical features of launch systems and care only about price, timely service and risk of failure. A customer views selection of a launch vehicle and upper stage as a single integrated choice and will choose the system that best suits his/her needs. For this analysis we neglected the payload fairing volume issue and considered only payload mass delivery performance and cost to customers. We considered the geosynchronous orbit delivery mission as representative.

A few years ago, the gaps between launch vehicles were large. For smaller payloads, the Delta II family offered configurations with varying numbers of strap-on solids. For median payloads the Atlas II

family offered a couple of configurations, as did Ariane IV. Heavy payloads had only the Titan IV-Centaur as a choice. A higher-performance upper stage might offer an opportunity to save large sums in launch cost. Today, assuming all or most of the EELV options in development reach the marketplace, many more options are available. Table 3 summarizes performance of the Delta and Atlas families. In addition, Sea Launch, Ariane IV and V, the Japanese H2A, and various Russian and Chinese vehicles are available. Performance figures for LEO in the table include a column with 10% margin taken out; this is to indicate possible needs for airborne flight equipment to support an STP stage.

A launch customer has a choice of purchasing a launch vehicle which, with an STP upper stage, can meet his/her delivery requirements, or purchasing a larger vehicle that can do so without an STP upper stage. As mentioned before, all the launch vehicles in Table 3 can perform a GEO delivery mission without an STP, by delivering the payload to a geosynchronous transfer orbit (GTO). The payload needs an apogee insertion propulsion system, usually either an apogee kick motor (solid propellant) or a storable propulsion system integrated with the payload. The launch vehicle configuration and cost do not change whether or not an STP is used. Therefore the trade is whether the added performance of an STP stage outweighs its cost when

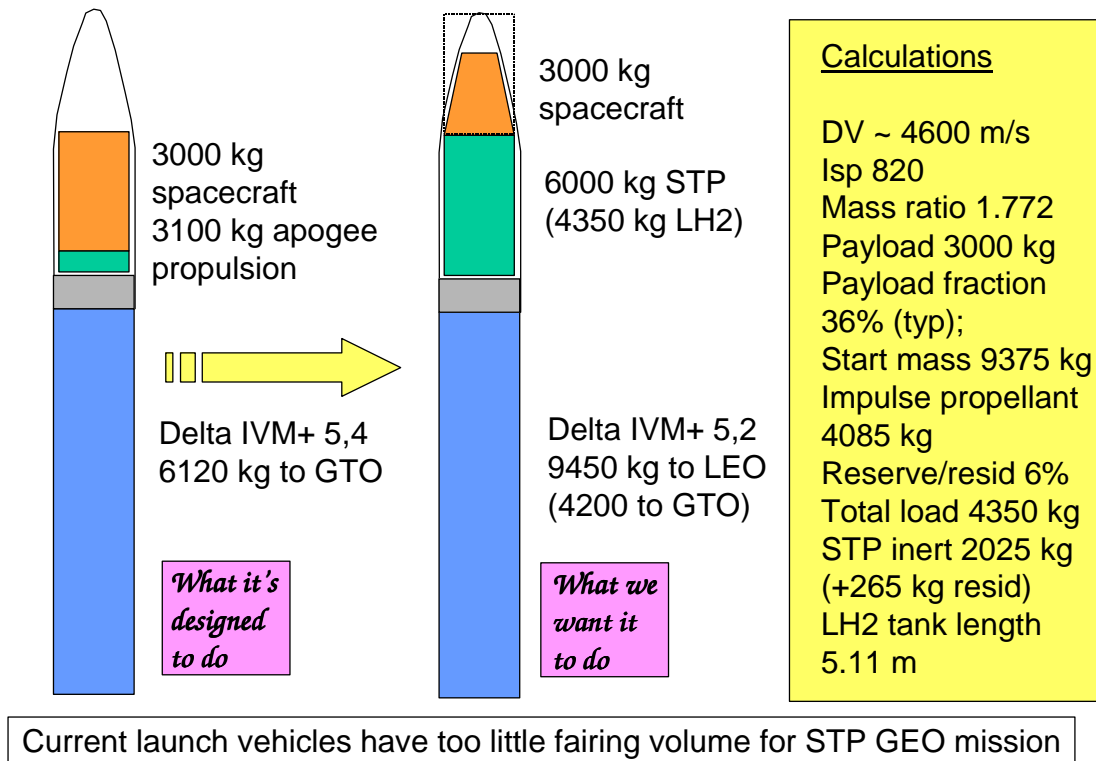


Figure 6: Graphical Illustration of Payload Fairing Volume Problem

considering the alternative of a larger launch vehicle that does not need the STP, and needs only an inexpensive apogee insertion system.

STP costs were estimated as comparable to the costs for a cryogenic upper stage with similar capability.

Table 3: Summary of Launch Vehicle Payload Performance

	LEO	Less 10% for adapters	GTO
Atlas IIA	7316	6584.4	3066
Delta IVM	8500	7650	3900
Atlas IIAS	8618	7756.2	3719
Atlas IIIA	8640	7776	4037
Delta IV M+ 5,2	10500	9450	4200
Atlas IIIB	10718	9646.2	4477
Delta IV M+ 4,2	12000	10800	5200
Atlas V 402	12500	11250	5000
Delta IV M+ 5,4	13700	12330	6120
Atlas V 552	20050	18045	8200
Delta IVH	24500	22050	10500

Figure 7 shows the customer-choice cost comparison developed for this assessment.

For each launch vehicle, the performance and cost are plotted with and without the STP upper stage. The launch vehicle without STP is plotted as a dark blue diamond, and with STP a magenta square. (Launch vehicle costs were obtained from Isakowitz *Space Launch Systems* Vol. III.) A connecting dotted arrow is shown for a few example cases. For example, at the lower left, the Delta II can deliver about 1000 kg

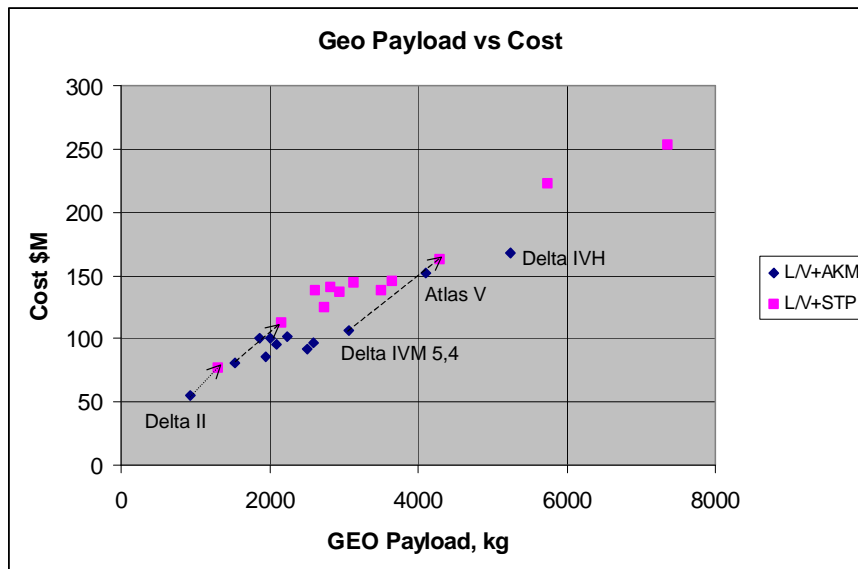
to GEO at a cost of about \$55 million. If one adds an STP upper stage, the payload capability increases to about 1400 kg and the cost increases by about \$25 million. The alternative is to purchase an Atlas IIA, which can deliver about 1700 kg at a cost about \$85 million.

In almost every case, the logical customer choice is clearly to choose the larger launch vehicle. That choice involves less risk and in most cases less cost. The Delta IVM 5,4 with STP shows a slight advantage over the Atlas V but probably not enough to outweigh the risk difference. If a customer were to have a large payload that exceeds the Delta IV Heavy payload mass capability, choosing an STP might be preferred over a two-part delivery with assembly.

It is also important to recognize that a customer who can afford the delivery delay of low-thrust propulsion (a few months), can elect to use payload onboard electric propulsion to complete the GEO delivery. This increases payload performance by about half the gap between conventional and STP-aided performance at very little cost except for the delay.

The conclusion of this part of the assessment is that, even aside from payload fairing volume issues, few customers will choose an STP upper stage instead of a larger launch vehicle.

A caveat on this conclusion is important: If a launch vehicle were designed expressly to use an STP upper stage, and configured to eliminate the cryogenic upper stage, the unit cost/performance tradeoff would



- In general, less costly for customer to upgrade launch vehicle than buy STP
- Delta II is an exception but shroud size is too small
- Delta IVM 5,4 may be an exception, but expect severe volume problems

Figure 7: Launch Customer Cost Trade Summary

probably favor this configuration over a conventional launch system. If this makes business sense (including the non-recurring cost of new development) one could expect one or more commercial launch companies to request that NASA advance STP technology to TRL 6 to reduce the business risk of such a development.

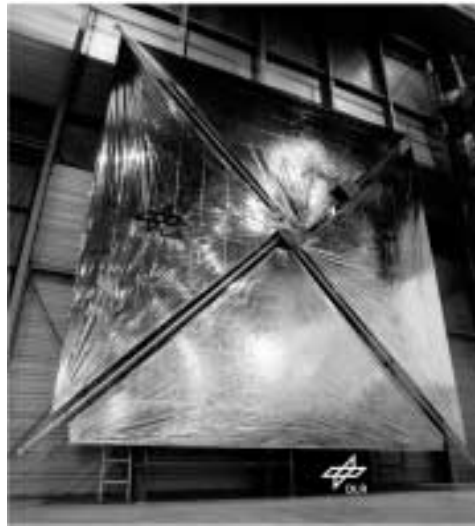
CONCLUSIONS AND RECOMMENDATIONS

- a) Solar Thermal Propulsion (STP) offers no unique mission capabilities not available through alternate propulsion technologies. State of the art chemical propulsion can perform all the missions for which STP is a candidate, albeit at a performance disadvantage in many cases. STP could provide better payload mass performance than alternate propulsion technologies in many cases, but as noted next, STPs with this performance don't fit in the fairings.
- b) The volume required for STP hydrogen propellant makes most STP missions impractical with current launch vehicles. These launch vehicles are designed to efficiently deliver payloads to a geosynchronous transfer orbit (GTO), using an integral cryogenic upper stage. The cryogenic upper stage is also required for launches to low Earth orbit (LEO). Therefore, if an STP is used as an upper stage, it and its payload must fit in a fairing volume nominally designed for a payload plus dense apogee insertion stage. The STP payload is larger; STP offers a performance improvement; otherwise would not be of interest for this mission. The STP itself is about twice the mass of the apogee insertion stage and has far less density. Thus a severe fairing volume problem is to be expected and in fact exists.
- c) Current launch vehicles, as noted, are designed to be efficient for GEO and near-Earth space missions. If the launch vehicle options currently in development all enter the market, several upgrade increments will exist in the payload range of interest. It usually will be cheaper to buy a bigger launcher than to buy an STP upper stage.
- d) We found a few applications that could benefit appreciably from STP. In particular, a "C3 topper" mission was found for which STP offers a performance advantage and the payload fairing volume is not a problem. STP was competitive, but not necessarily superior, for a mission of delivery of a "Gateway" payload to the Earth-Moon L1 libration point, and for application as a shuttle upper stage. The shuttle upper stage application did not permit the use of hydrogen, so an STP using ammonia propellant and a conventional bipropellant chemical stage were compared; performance was about equal.



Advanced Space Transportation Program

Solar Sails



**DLR
20 m Sail**

General Description:

Propellantless Propulsion system that utilizes solar photon pressure to obtain thrust. Sail film is compactly stowed for launch and deployed and supported by deployable booms

Mission Applications:

Can enable or enhance outer planets missions and other important science missions

Status:

- Sail materials of 4.5g/m^2 ; System 19g/m^2
- Commercial venture (Encounter 2001) scheduled to launch in 1Q 04
- Selection pending NMP decision for ST-7

Future Plans / Challenges:

- Technology development towards flight validation
 - 10g/m^2
 - GN&C
 - Deployment
- Further advances in materials and lightweight structures
- Ground validation & testing of quarter-scale model

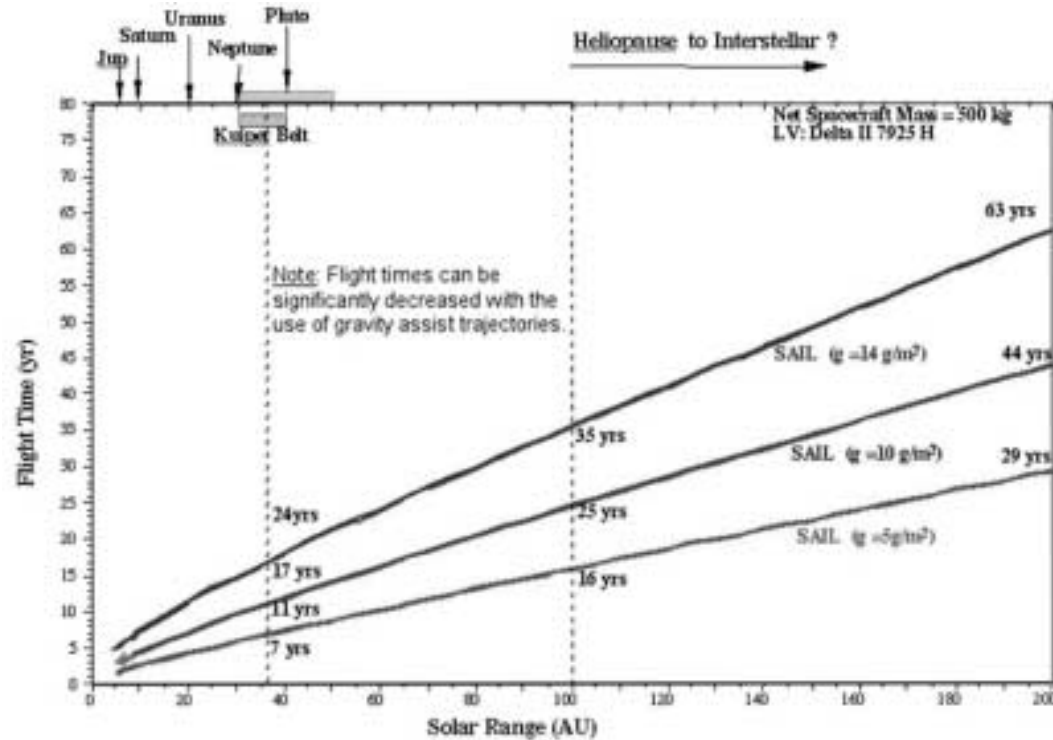
AEC-Able Coilable Boom (TRL 8, 3g/m^2)





Solar Sails: Flight Times and Destinations

Solar Sails enable rapid outer planetary missions, high solar inclination and non-Keplerian orbits



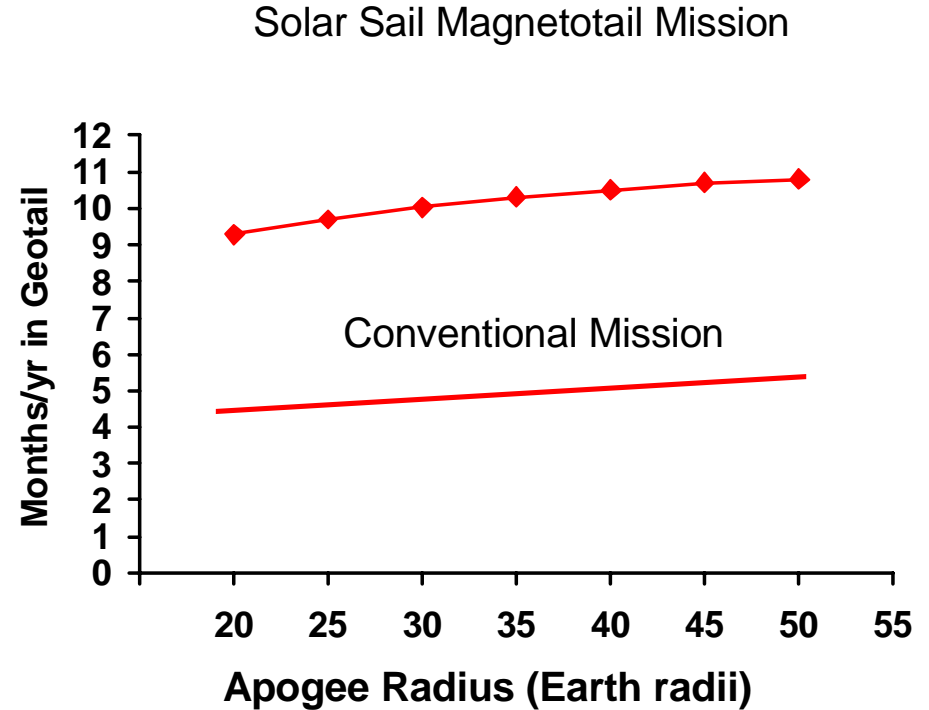
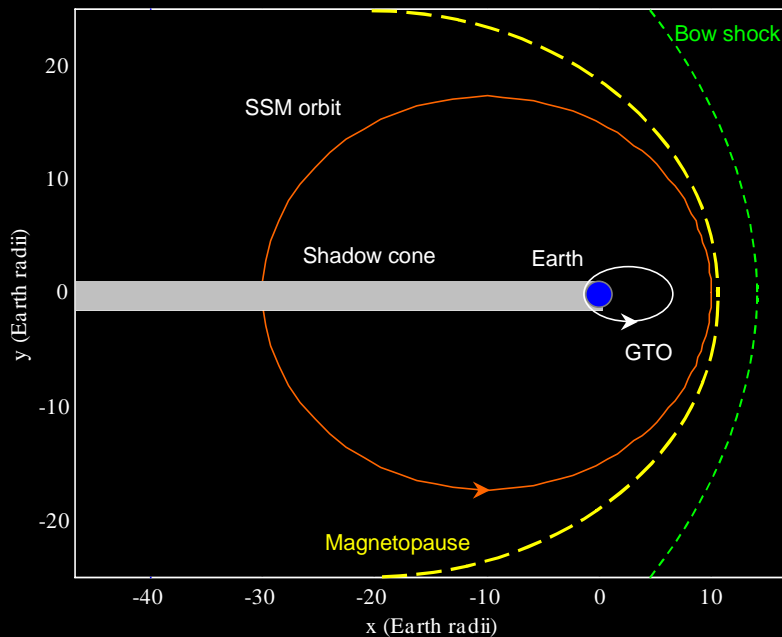
Flyby Capabilities: Minimum Flight Time vs. Solar Range

Benefits:

- No propellants required
- As technology advances (lighter sail material) performance enhances (more ΔV)
- Very straightforward design (challenge is scaling to large area and low density)
- No environmental issues
- Ideal for station keeping applications

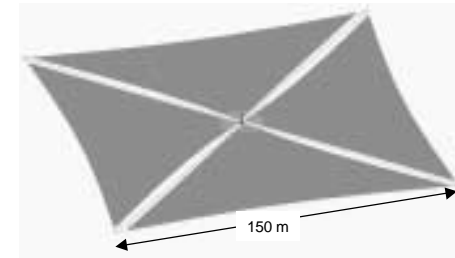
Solar Sail Magnetotail (SSM) Mission

- Precess orbit apse line to stay permanently in Magnetotail

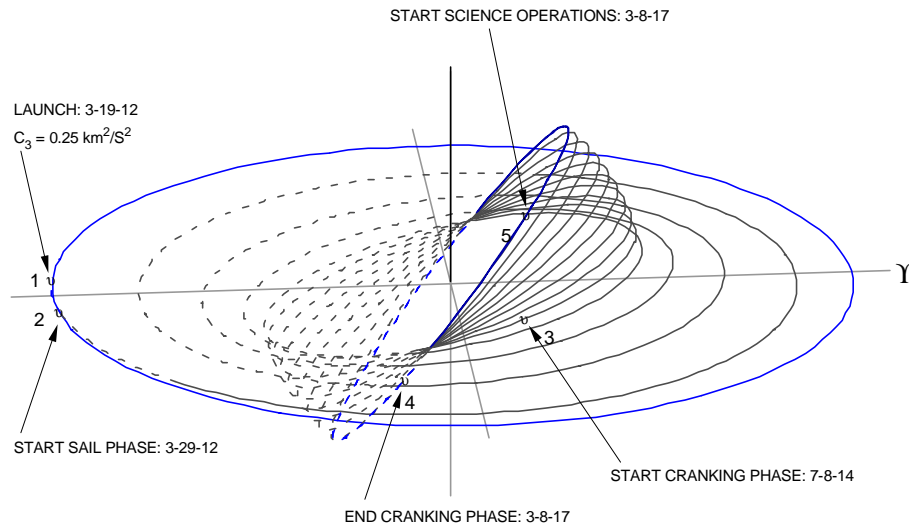
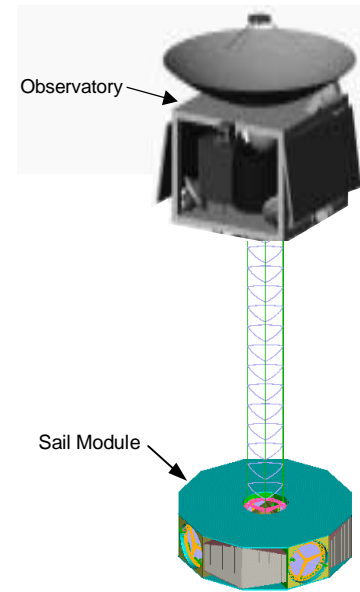


Solar Polar Imager (SPI)

- Solar Sail propulsion enables the Solar Polar Imager (SPI) mission
 - Sail provides constant thrust to crank the solar orbit to a high inclination
 - Sail enables a low period orbit with many solar polar science encounters



SPI Configuration



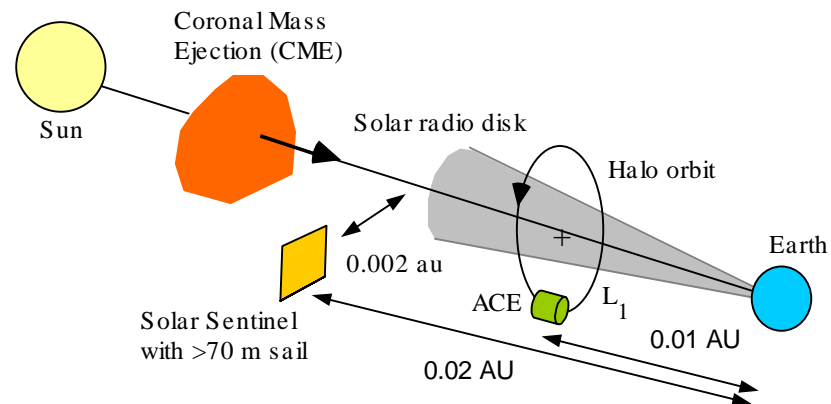
SPI Trajectory

	NMP ST7	Solar Polar Imager (SPI)
Edge Width	40 m	150 m
Area	1,500 m ²	20,000 m ²
Sail Subsystem Mass	29 kg	257 kg
Payload Mass (non-sail)	151 kg	215 kg
Flight System Mass	180 kg	472 kg
Sail Subsystem Area Density	19.1 g/m ²	12.9 g/m ²
Total Area Density	120.0 g/m ²	23.6 g/m ²
Characteristic Acceleration	0.07 mm/s ²	0.34 mm/s ²

Sailcraft Parameters

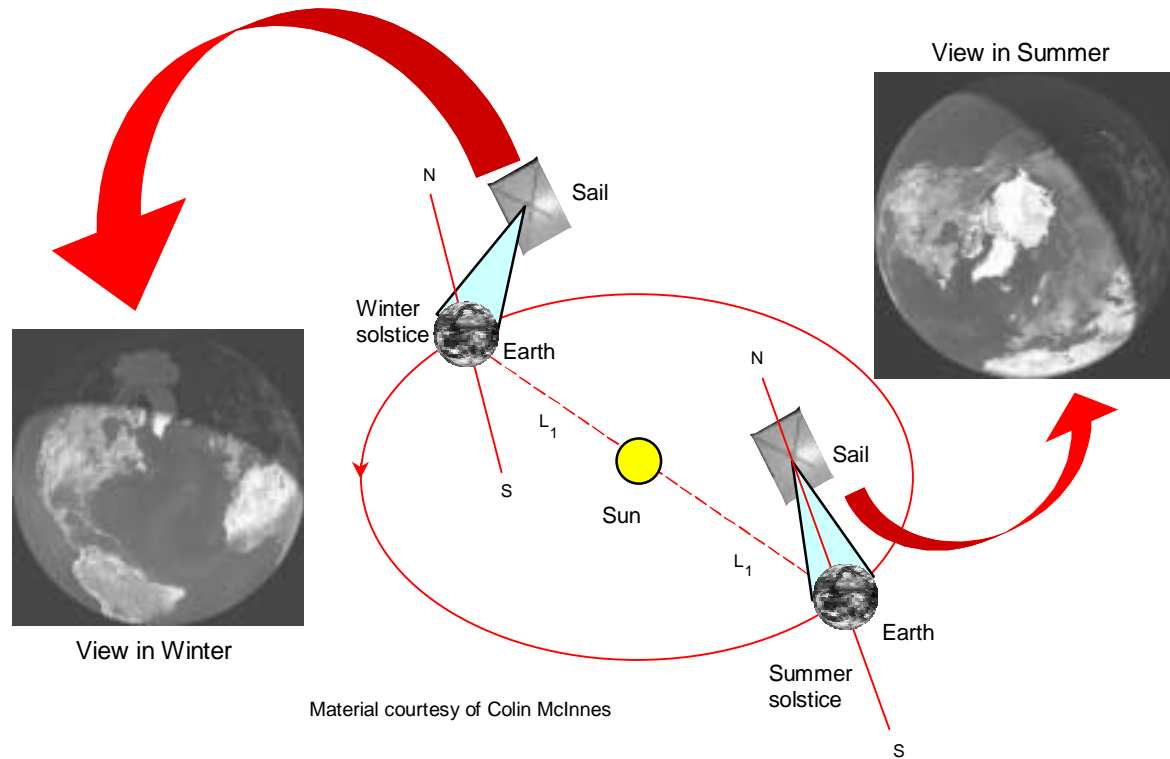
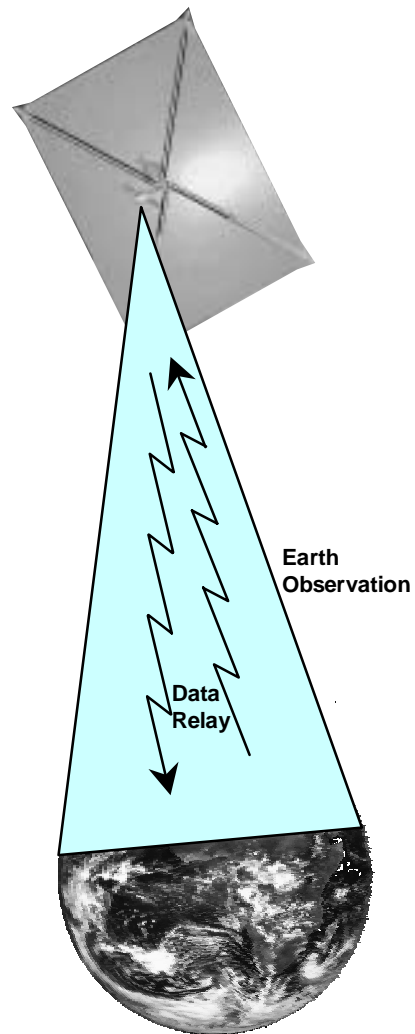
Solar Sentinel Mission Class

- Use solar sail to achieve non-Keplerian orbit near the sun-earth line, at least twice as far from the earth as the current warning system (ACE at the L_1)
 - Assumed payload 250 kg
 - The better the sail the closer to the Sun one can fly
 - Sail Size in range at 250 m or less
 - Sail is used for life of mission (> 5 yrs)
 - Fly a halo orbit to maintain communications



Pole Sitter Mission

- Continual coverage of the polar regions with no propellant usage!
- Altitudes ranging from 0.75 million km to 3.5 million km, depending on sail performance and inclination chosen





TECH ISP IN-SPACE PROPULSION TECHNOLOGIES



Aeroassist *Potential Mission Applications*

Potential Aeroassist Mars Mission

Previous Mars missions -- Global Surveyor, Pathfinder and the Viking Landers -- have laid the groundwork for the use of aeroassist technologies for Outer Planets missions in many significant ways, including identifying challenges inherent to those missions that could make use of these technologies.



Mars Exploration Rover Entry



Mars Exploration Rover Decent

For example, in the area of thermal protection system design, recent vehicles for Mars missions have had a uniform thickness on the fore body -- a heat shield that protects the front of the spacecraft -- while the spacecraft required a

- **POTENTIAL MISSION APPLICATIONS**
- **FUNDAMENTAL PHYSICS**
- **TECHNICAL PUBLICATIONS**
- **LINKS**
- **ISP MAIN**
- **TECH MAIN**

CURRENT TECHNOLOGIES**Aeroassist**

*Aerocapture -
Aerobraking -*

Solar Electric Propulsion

*Next Generation
Electric Propulsion -
SEP Hall -*

Solar Sails**Advanced Chemical****Tethers**

*Momentum Exchange -
Electrodynamic -*

Solar Thermal

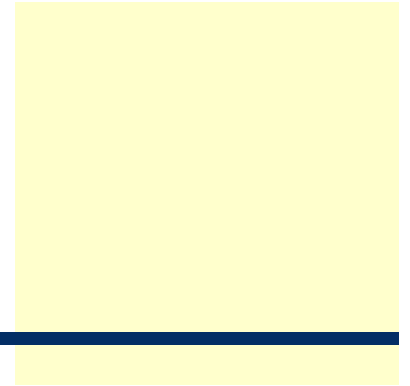
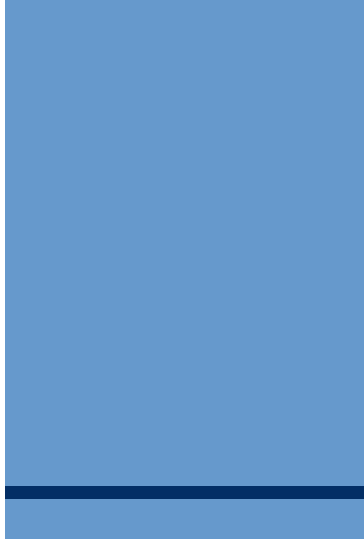
EMERGING TECHNOLOGIES

Aerogravity Assist -

heavier than optimum back shell -- the heat shield that protects the back of the craft. This was an acceptable choice for relatively low atmospheric heating conditions experienced during the Mars missions; smaller entry shells and payload mass requirements were within permissible range. Similarly, as a result of relatively lower heating, recession -- the burning away of the heat shield -- and turbulence did not affect the aerodynamic performance of the spacecraft's design during these missions. This will not be the case, however, for the majority of the Outer Planets, aerocapture missions. The Galileo Probe experienced significant recession and the lessons learned from limited analysis of the mission were very useful in grasping the importance of understanding the interaction between atmospheric turbulence and the craft's thermal protection system, material response and resulting changes in aerodynamic performance.

Aeroassist could be a critical part of the answer to NASA's search for cost-efficient propulsion technologies to explore the space frontier. With the International Space Station now undergoing assembly in space with humans living onboard, NASA is seeking to develop the next logical exploration strategy for robotic missions and the next destination for humans.

Aeroassist, as a whole, should be viewed as an integrated system with a variety of maneuvers interacting to propel a spacecraft into deep space and to achieve the necessary goals of a specific mission. The benefits of this propulsion technology are many -- reduced spacecraft propellant requirements, launch weight, vehicle expense and trip times. Used in combination with each other or alone, the aeroassist family could offer advancement of today's propulsion technologies for safe, affordable exploration of the space frontier.





TECH ISP

IN-SPACE PROPULSION TECHNOLOGIES



Tethers

Potential Mission Applications

Robotic Exploration Benefits of MXER Tether Technology

MXER tether technology also has clear benefits for robotic exploration missions to the Moon, Mars, asteroids, and other destinations. Most of these missions must be launched on high-energy, Earth escape trajectories in order to reach their destinations. In a similar fashion to the LEO-GTO transfer discussed earlier, the robotic missions use the upper stage of their launch vehicles to provide this boost. Most of the propulsive capability of the upper stage of the launch vehicle is expended simply to escape the gravity field of the Earth. For instance, to boost from LEO to a trans-Mars injection (TMI) trajectory with a vis-viva energy of $10 \text{ km}^2/\text{s}^2$ requires a DV of 3650 m/s. Of this 3650 m/s, 3200 m/s is simply the energy required to escape the Earth's gravity!

- POTENTIAL MISSION APPLICATIONS
- FUNDAMENTAL PHYSICS
- TECHNICAL PUBLICATIONS
- LINKS

- ISP MAIN
- TECH MAIN

CURRENT TECHNOLOGIES**Aeroassist**

Aerocapture -
Aerobraking -

Solar Electric Propulsion

Next Generation
Electric Propulsion -
SEP Hall -

Solar Sails**Advanced Chemical****Tethers**

Momentum Exchange -
Electrodynamic -

Solar Thermal

EMERGING TECHNOLOGIES

Aerogravity Assist -



2001 Mars Odyssey spacecraft.
At ~550 kg and an injection C3 of 10 km²/s²,
this spacecraft would have made an excellent
payload for an MXER tether facility.

If a robotic Mars mission were to use a MXER tether catch and throw it into a highly-elliptical Earth orbit, this would provide it 3000 m/s of this 3650 m/s needed for its TMI trajectory. Then the mission would only require a much smaller 650 m/s burn to attain its trajectory. By providing most of the energy needed for escape, the MXER tether would allow a much smaller upper stage to be used, and consequently a much smaller and less expensive launch vehicle to be employed. For instance, the Mars Global Surveyor had a mass of ~1000 kg and launched on a Delta 7925 launch vehicle (cost: \$90 million). If it had used an MXER tether to give it most of the energy needed for TMI, it could have been launched on a Taurus-class launch vehicle (cost: \$12 million) and used an

augmented onboard propulsion system to give it the final kick to Mars. Hence, in this scenario, the MXER tether could have saved nearly \$80 million in launch costs.

For robotic missions, the MXER tether could serve as a fully reusable, permanent "upper stage" in orbit to boost spacecraft from LEO to high-energy, pre-escape trajectories. In so doing, it would dramatically reduce the launch costs of these missions, and allow many more scientific missions to be conducted within the same budgetary constraints.

Commercial Benefits of MXER Tether Technology

The MXER tether has clear benefits for commercial payloads. The majority of communications satellites are launched to a geosynchronous Earth orbit (GEO)--an orbit where the satellite can appear to "hang" over one position on the equator. In order to launch a satellite from low Earth orbit (LEO) to GEO, two large orbital maneuvers must be made:

- Boost satellite from LEO (300 km x 300 km) to a geosynchronous transfer orbit (GTO, 300 km x 36000 km) with a DV (delta-V, or change in velocity) of 2400 m/s.
- Circularize orbit from GTO to GEO (36000 km x 36000 km) with a DV of 1400 m/s.

In most cases, the launch vehicle (such as an Atlas or Delta) provides the maneuver from LEO to GTO, and the satellite uses its onboard propulsion systems to provide the second maneuver from GTO to GEO. The rocket equation requires that the mass of the rocket's upper stage to provide this first maneuver must be approximately equal to that of the payload. That means that a given rocket can put roughly twice as much payload into LEO than into GTO. For instance, the Zenit 3SL (Sea Launch) rocket can put approximately 5 MT into a GTO orbit, but it can put nearly 12 MT into LEO.

The MXER tether could be used to replace the upper stage on a transfer from LEO to GEO. For instance, if the Zenit 3SL was not required to put its payload into GTO but into LEO instead, it could launch two 5 MT satellites instead of one. Then the MXER tether could catch the satellites and throw them into GTO. The onboard propulsion systems of the satellites would finish the task and put themselves into GEO. Hence, using an MXER tether for the LEO-GTO transfer would allow us to launch twice as many payloads on the same launch vehicles, effectively reducing the price by 50%!

Human Lunar Exploration Benefits of MXER Tether Technology

For future human missions to the Moon, MXER

tether technology could not only send payloads to the Moon for much less cost than current systems, but it could also potentially enable large amounts of lunar material (tens of tonnes) to be returned to Earth for study. Additionally, a future two-tether architecture (one tether in Earth orbit, the other in lunar orbit) might eliminate 95% of the propulsive DV required to travel between LEO and the surface of the Moon!

The key to this dramatic capability is the fact that the tether is a giant energy storage mechanism. By virtue of its orbit around the Earth, the tether is storing a vast amount of orbital energy. When it catches and throws a payload, it exchanges momentum with that payload, and consequently loses some of that orbital energy. The MXER tether design discussed previously pushes against the Earth's magnetic field to restore that orbital energy, but another form of reboost is possible when it catches payloads returning from the Moon on a high-energy trajectory, and then throws them down to a low-energy LEO. That way, the tether would exchange momentum with the payload in reverse: it would take the payload from a high-energy state to a lower-energy state, and it would be reboosted in return.

The merit of this is especially obvious when examining a trajectory from LEO to the surface of the Moon. Starting from LEO, the payload must execute a propulsive DV of 3200 m/s to get on a trans-lunar injection (TLI) trajectory;

then four days later, it must execute another 900 m/s DV for lunar orbit insertion (LOI) and then another 2200 m/s for descent to the surface.

Then from the lunar surface, the whole situation proceeds in reverse: 2100 m/s DV for ascent to lunar orbit, 900 m/s DV for trans-Earth injection (TEI), and finally another 3200 m/s to capture into LEO. The irony of the trajectory is apparent: speed up, slow down, speed up, slow down ... each time using large amounts of propellant to reduce the orbital energy that previously took so much propellant to create!

Isn't there a better way? Wouldn't it be useful to have a system that takes the energy lost during lunar descent and then gives that same energy back to the payload during lunar ascent? What about a system that recovers the energy used to send the payload to the Moon by slowing down the same payload on the return trip?

With a conventional rocket, this is impossible. Momentum exchange in a rocket takes place when the rocket's payload goes one way, and the combusted propellant goes the opposite way and disperses into space, never to be recovered again. But a tether system exchanges momentum between two solid objects, the payload and tether station, instead of between a solid payload and gaseous propellant, as in the case of a rocket. Hence, the tether, as a solid object in an orbit with a

given orbital energy, can act as an orbital energy "bank", accepting deposits and paying out returns.

When a payload in LEO is caught and thrown by a tether into a TLI trajectory, it has taken energy from the tether for itself. When it arrives at the Moon, it can be caught by a tether and dropped down to the surface. Thus, it takes the energy it received from the Earth orbit tether and transfers it to the lunar orbit tether. Consequently, the lunar tether attains a more energetic orbit.

When the payload is ready to return to Earth, it is caught by the lunar orbit tether and thrown back on a TEI trajectory. The lunar orbit tether loses energy in the transfer, and drops back into its previous orbit. As the payload approaches Earth, it is caught by the Earth orbit tether and "thrown" into a low energy, low Earth orbit. Thus the Earth orbit tether recovers the energy it used to send the payload to the Moon in the first place.

The story gets very interesting when we examine what happens when we want to send cargo to the surface of the Moon. Suppose a cargo vehicle uses the Earth and lunar tethers to send 20 MT of cargo to the lunar surface. Then, in order to balance the energy of the tether system, it must load up 20 MT of lunar regolith (surface material) or water to take back to LEO. Hence, for every metric tonne of cargo

we send to the lunar surface from LEO, we can bring back a metric tonne of lunar material.

This capability could be a fantastic boon for human utilization of space. Large quantities of lunar material could be used on Earth to test mining and extraction processes for the lunar surface; the physical, chemical, and geologic history of the material could be examined; even the novelty of having a "moon rock" could be made available for anyone who wanted one!

Additionally, the availability of lunar regolith and water in LEO could spur the development of new industries. Ultra-pure manufacturing of pharmaceuticals, metals, and spacecraft could be enabled. Lunar material could be the lifeblood of industrial activity in low Earth orbit ... all of it made possible by the unique orbital transfer capabilities of tethers.



TECH ISP

IN-SPACE PROPULSION TECHNOLOGIES



Tethers

Fundamental Physics

Momentum-exchange / electrodynamic reboost (MXER) tether systems show great promise for use in propellantless orbital transfer. In 1998, MSFC and Boeing conducted a simple, preliminary examination of the system requirements of a tether facility to boost payloads from LEO to GTO. Work conducted at MSFC and TUI over the last two years has updated and refined these results, and led to alternate configurations and concepts that show greater promise for successful utilization. Two appendices are included that detail analysis techniques and mathematical derivations that can be used in tether facility design.

Diagrams and equations are better displayed in .pdf format. Click [HERE](#) to view the Tether Fundamental Physics .pdf document.

- **POTENTIAL MISSION APPLICATIONS**
- **FUNDAMENTAL PHYSICS**
- **TECHNICAL PUBLICATIONS**
- **LINKS**

- **ISP MAIN**

- **TECH MAIN**

**CURRENT
TECHNOLOGIES**

Aeroassist

*Aerocapture -
Aerobraking -*

**Solar Electric
Propulsion**

*Next Generation
Electric Propulsion -
SEP Hall -*

Solar Sails

**Advanced
Chemical**

Tethers

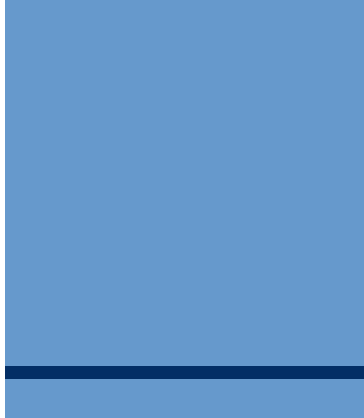
*Momentum Exchange -
Electrodynamic -*

Solar Thermal

**EMERGING
TECHNOLOGIES**

Aerogravity Assist -







TECH ISP

IN-SPACE PROPULSION TECHNOLOGIES



Next Generation Electric Propulsion *Fundamental Physics*

In an ion bombardment thruster, electrons are emitted from a hollow cathode, pass through a gaseous propellant, most commonly Xenon, and are collected at the anode of the discharge chamber. As the electrons pass through the gas, they collide with or bombard the neutral Xenon and, if there is sufficient energy transfer, knock an electron free from the Xenon atom leaving a positive charged ion. To increase the cross-section of the collision, a magnetic field is imposed on the discharge chamber. This makes it more difficult for the electrons to reach the anode, increasing the time spend in the Xenon gas, and increasing the probability of an ionizing collision.

Once the ion is generated it is accelerated through an electric field of several kV/mm across a set of grids to exhaust velocities on order 30 km/sec. The grids are designed to focus the ions into beamlets as parallel to the thruster axis. The grid at the exit plane of the discharge chamber, called the screen grid is biased, along with the discharge chamber to a high positive potential of 1 to 3kV. The downstream grid, called the accelerator grid, is biased to a negative potential of several hundred volts. The function of this grid is to prevent electrons outside the thruster from being accelerated back into the discharge chamber. The potential downstream of the thruster

- **POTENTIAL MISSION APPLICATIONS**
- **FUNDAMENTAL PHYSICS**
- **TECHNICAL PUBLICATIONS**
- **LINKS**
- **ISP MAIN**
- **TECH MAIN**

CURRENT TECHNOLOGIES

Aeroassist

Aerocapture -
Aerobraking -

Solar Electric Propulsion

Next Generation
Electric Propulsion -
SEP Hall -

Solar Sails

Advanced Chemical

Tethers

Momentum Exchange -
Electrodynamic -

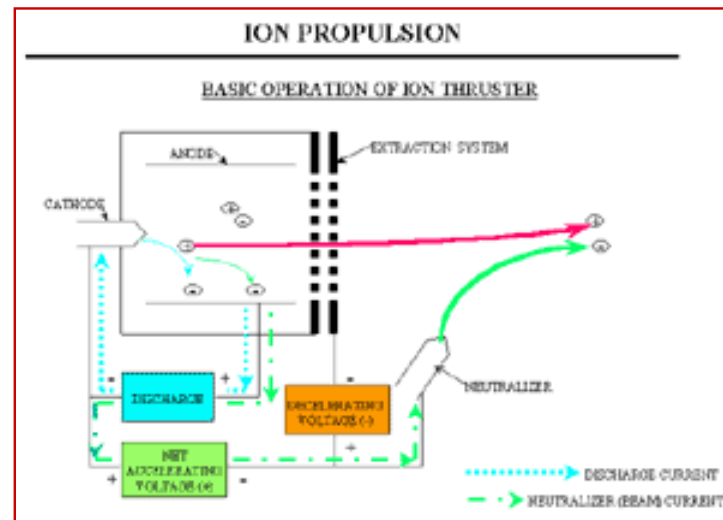
Solar Thermal

EMERGING TECHNOLOGIES

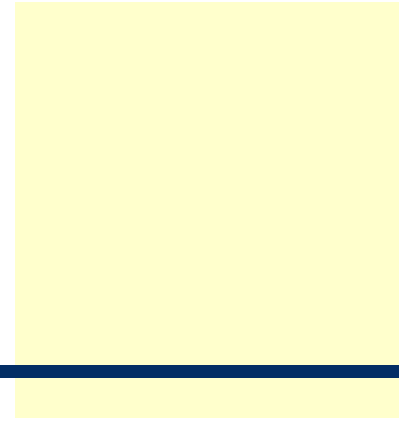
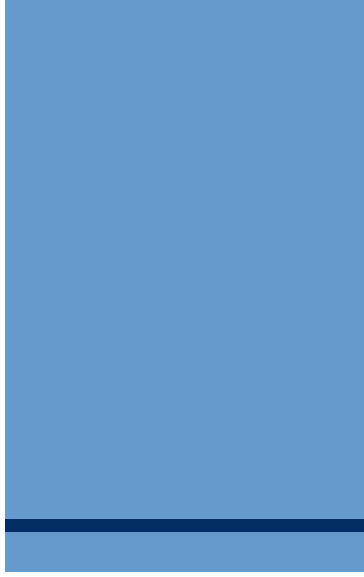
Aerogravity Assist -

is zero volts. As the ion is accelerated through the grids, it reaches its maximum velocity at the plane of the negative accelerator grid. It is decelerated slightly as it leaves the thruster and reaches the zero potential of space. The final energy imparted to the ion of $\frac{1}{2} mv^2$, where m is mass and v is velocity, is equal to the charge of the ion times the net electric field, which is approximately equal to the screen grid potential.

The final step is to neutralize the ion beam by injecting the electrons that were removed in the ionization process back into the beam. If this were not done, space charge of positive ions would build up resulting in ions turning around and returning to the spacecraft or other surfaces in an attempt to find an electron.



click to enlarge image



News Release

National Aeronautics and
Space Administration

Marshall Space Flight Center
Huntsville, Alabama 35812



Nancy Lovato (818) 354-9382
Jet Propulsion Laboratory, Pasadena, Calif.

July 30, 2003

Dom Amatore (256) 544-0034
Marshall Space Flight Center, Huntsville, Ala.

RELEASE: 03-131

NASA'S ION ENGINE RECORDS NO TUNE-UPS, NO PROBLEMS

The future is here for spacecraft propulsion and the trouble-free engine performance that every vehicle operator would like to see, achieved by an ion engine running for a record 30,352 hours at NASA's Jet Propulsion Laboratory, Pasadena, Calif.

The engine is a spare of the Deep Space 1 ion engine used during a successful technology demonstration mission that featured a bonus visit to comet Borrelly. It had a design life of 8,000 hours, but researchers kept it running for almost 5 years -- from Oct. 5, 1998, to June 26, 2003 -- in a rare opportunity to fully observe its performance and wear at different power levels throughout the test. This information is vital to future missions that will use ion propulsion, as well as to current research efforts to develop improved ion thrusters.

"Finding new means to explore our solar system -- rapidly, safely and with the highest possible return on investment -- is a key NASA mission," said Colleen Hartman, head of Solar System Exploration at NASA Headquarters, Washington, D.C. "Robust in-space flight technologies such as ion propulsion are critical to this effort and will pioneer a new generation of discovery among our neighboring worlds."

While the engine had not yet reached the end of its life, the decision was made to terminate the test because near-term NASA missions using ion propulsion needed analysis data that required inspection of the different engine components. In particular, the inspection of the thruster's discharge chamber, where xenon gas is ionized, is critical for mission designers of the upcoming Dawn mission. Dawn, part of NASA's Discovery Program, will be launched in 2006 to orbit Vesta and Ceres, two of the largest asteroids in the solar system.

"The chamber was in good condition," said John Brophy, JPL's project element manager for the Dawn ion propulsion system. "Most of the components showed wear, but nothing that would have caused near-term failure."

-more-

Marc Rayman, former Deep Space 1 project manager, said, "There are many exciting missions into the solar system that would be unaffordable or truly impossible without ion propulsion. This remarkable test shows that the thrusters have the staying power for long duration missions."

Ion engines use xenon, the same gas used in photo flash tubes, plasma televisions and some automobile headlights. Deep Space 1 featured the first use of an ion engine as the primary method of propulsion on a NASA spacecraft. That engine was operated for 16,265 hours, the record for operating any propulsion system in space. Ion propulsion systems can be very lightweight, because they can run on just a few grams of xenon gas a day. While the thrust exerted by the engine is quite gentle, its fuel efficiency can reduce trip times and lower launch vehicle costs. This makes it an attractive propulsion system choice for future deep space missions.

"The engine remained under vacuum for the entire test, setting a new record in ion engine endurance testing, a true testament to the tremendous effort and skill of the entire team," said Anita Sengupta, staff engineer in JPL's Advanced Propulsion Technology Group. "This unique scientific opportunity benefits current and potential programs."

"The dedicated work of NASA's Solar Electric Technology Application Readiness test team, led by JPL, continues to exemplify a commitment to engineering excellence," said Les Johnson, who leads the In-Space Propulsion Program at NASA's Marshall Space Flight Center, Huntsville, Ala. "This work, along with significant contributions from NASA's Glenn Research Center in Cleveland, will take NASA's space exploration to the next level."

NASA's next-generation ion propulsion efforts are led by the In-Space Propulsion Program, managed by the Office of Space Science at NASA Headquarters and implemented by the Marshall Center. The program seeks to develop advanced propulsion technologies that will help near and mid-term NASA science missions by significantly reducing cost, mass or travel times.

The Jet Propulsion Laboratory is managed for NASA by the California Institute of Technology, Pasadena, Calif.

For more information on NASA and its programs, visit:

<http://www.nasa.gov>
<http://www.jpl.nasa.gov>
<http://www.msfc.nasa.gov>

-end-



TECH ISP

IN-SPACE PROPULSION TECHNOLOGIES



Solar Thermal *Fundamental Physics*

Missions:

Low Earth Orbit to Geosynchronous Orbit Transfers as well as all inner solar system exploration (Sun to Mars).

Fundamental Principles:

Solar thermal propulsion (STP) conceived in 1956 by Krafft Ehricke. STP effectively bridges the performance gap between chemical and electric propulsion by potentially offering higher Isp's (800 - 1000 secs) than chemical options (300 - 500 secs) and higher thrust-to-weight ratios than electric systems. STP requires only one propellant and combines medium thrust with moderate propellant efficiency to enable relatively short 30-day trips from low Earth orbit to geostationary Earth orbit. Typically hydrogen is used as the propellant due to its low molecular weight corresponding to a high Isp.

The propulsion system of a solar thermal-powered spacecraft consists of three basic elements: a Concentrator which focuses and directs incident solar radiation, a thruster/absorber which receives solar energy, heats and expands

- **POTENTIAL MISSION APPLICATIONS**
- **FUNDAMENTAL PHYSICS**
- **TECHNICAL PUBLICATIONS**
- **LINKS**

- **ISP MAIN**
- **TECH MAIN**

CURRENT TECHNOLOGIES

Aeroassist

Aerocapture -
Aerobraking -

Solar Electric Propulsion

Next Generation
Electric Propulsion -
SEP Hall -

Solar Sails

Advanced Chemical

Tethers

Momentum Exchange -
Electrodynamic -

Solar Thermal

EMERGING TECHNOLOGIES

Aerogravity Assist -

propellant (hydrogen) to produce thrust, and a propellant system which stores cryogenic propellant for extended periods and passively feeds it to the thruster/absorber. Figure X shows the typical components of a STP thruster..

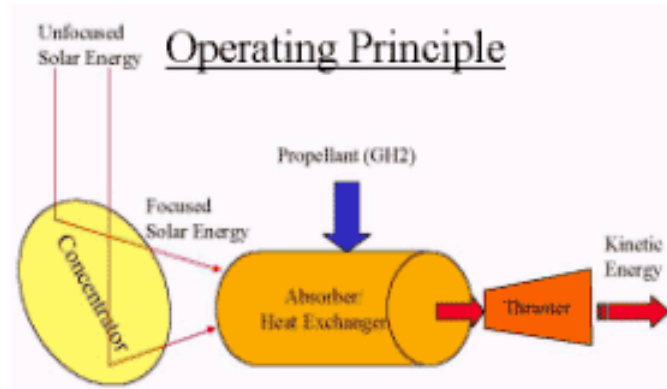


Figure X: Solar Thermal Propulsion Thruster

Two concentrator designs, rigid or inflatable, were originally being evaluated under two different contracts. However, these two different programs have since been merged, with the inflatable concentrator design taking lead as the primary technology.

An inflatable solar concentrator offers significant advantages in comparison to state-of-the-art rigid panel concentrators, including low weight, low stowage volume, and simple gas deployment. Figure Y shows a concentrator made of CP-1, a NASA-developed, flight-qualified polyimide material, which was designed and fabricated by SRS Technologies as part of a Glenn Small Business Innovation Research Phase II contract. The concentrator has a front clear canopy film and a rear aluminum-coated reflector film. The two films are seamed at the edges and are held to the support ring using a network of catenaries. For the EMRCE test, a rigid aluminum ring was

used to decouple the effects of the inflatable concentrator with that of the usual inflatable, thin-film torus support structure. The concentrator is elliptical to account for the diverging beam from the solar simulator.



Figure Y. Inflatable solar concentrator, rigidized struts, and hexapod pointing and focus control system setup inside Glenn's Tank 6 Solar Thermal Vacuum Facility.

<http://www.grc.nasa.gov/WWW/RT2001/5000/5490wong2.html>

Two system level approaches for STP are currently being explored. The first approach provides propulsion for orbit transfer and is typically an expendable upper stage. The solar energy is collected by inflated concentrators and used directly

(direct gain) in the absorbers to heat hydrogen to high temperatures (as high as 2780 K or 5000 R). The sun must be acquired during each propulsive burn. The absorber configuration is a windowless heat exchanger having a delivered specific impulse potential of 800 to 960 sec. Volumetric absorber concepts can potentially provide performance levels approaches 1100 sec. Solar absorber/thruster, and inflated concentrator technology development have continued to be advanced under Air Force Research Laboratory (AFRL) sponsorship over the last 20 years.

The second design approach (thermal storage) involves the incorporation of a thermal energy storage medium in which solar energy is acquired and stored during the coast period of the orbit and when a propulsive burn is required, propellant flows through the thermal storage medium to provide thrust. The storage of solar energy enables a higher thrust than the direct gain concept with smaller concentrators. For efficient operation, the burns of this engine concept should be performed in the eclipse portion of the orbit. This greatly simplifies the sun tracking and thrust orientation compared with the direct gain concept since the system does not have to be "on sun" during the burn. In the current design concept, which uses rhenium coated graphite as the thermal storage medium, a delivered specific impulse of 700 to 900 sec is predicted dependent on the thermal storage temperature. Once the vehicle is in orbit, the concept can also provide on orbit power using the concentrators and thermionic elements to generate electricity. To achieve the desired long life for the power system, the concept typically incorporates a rigid concentrator.

Figure Z shows an artists concept of a spacecraft propelled by an STP system. STP is limited by the ability to focus enough solar radiation to heat the heat exchanger, so that its

applications are typically missions within the inner solar system.

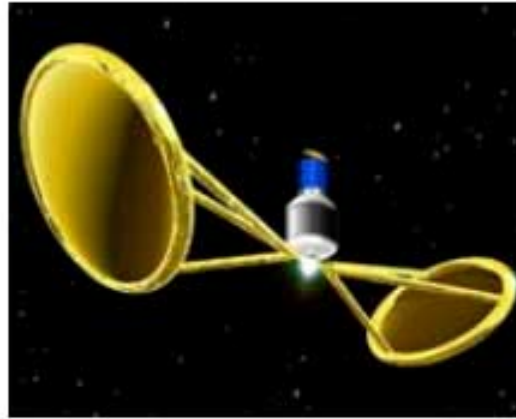


Figure Z: Solar Thermal Propulsion Concept Vehicle



TECH ISP

IN-SPACE PROPULSION TECHNOLOGIES



Solar Thermal *Potential Mission Applications*

Low Earth Orbit to Geosynchronous Orbit Transfers as well as all inner solar system exploration (Sun to Mars).

- **POTENTIAL MISSION APPLICATIONS**
- **FUNDAMENTAL PHYSICS**
- **TECHNICAL PUBLICATIONS**
- **LINKS**

- **ISP MAIN**
- **TECH MAIN**

**CURRENT
TECHNOLOGIES**

Aeroassist

*Aerocapture -
Aerobraking -*

**Solar Electric
Propulsion**

*Next Generation
Electric Propulsion -
SEP Hall -*

Solar Sails

**Advanced
Chemical**

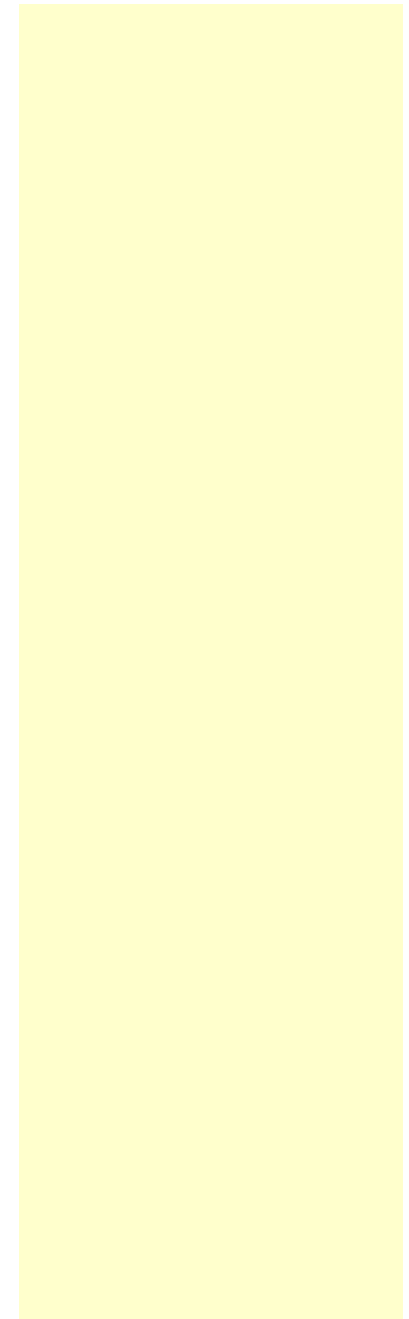
Tethers

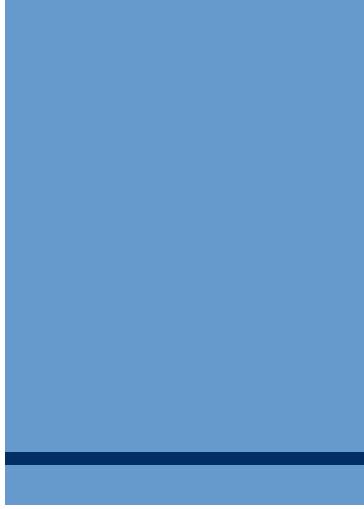
*Momentum Exchange -
Electrodynamic -*

Solar Thermal

**EMERGING
TECHNOLOGIES**

Aerogravity Assist -







TECH ISP

IN-SPACE PROPULSION TECHNOLOGIES



Hall Thruster *Fundamental Physics*

Hall thrusters use an axial electric field to accelerate ions, similar to ion thrusters. Combining a radial magnetic field with this generates an azimuthal Hall current. This current interacts with the radial magnetic field producing a volumetric ($j \times B$) accelerating force on the plasma. As with ion thrusters, Hall thrusters can be categorized according to their respective power sources (i.e. solar or nuclear).

- POTENTIAL MISSION APPLICATIONS
- FUNDAMENTAL PHYSICS
- TECHNICAL PUBLICATIONS
- LINKS

- ISP MAIN
- TECH MAIN

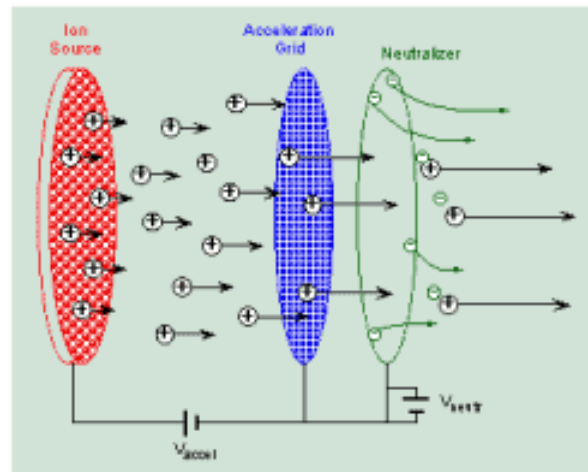


Figure XXX - Schematic of Operation Mechanism for a Hall Thruster

CURRENT TECHNOLOGIES**Aeroassist**

*Aerocapture -
Aerobraking -*

Solar Electric Propulsion

*Next Generation
Electric Propulsion -
SEP Hall -*

Solar Sails**Advanced Chemical****Tethers**

*Momentum Exchange -
Electrodynamic -*

Solar Thermal

EMERGING TECHNOLOGIES

Aerogravity Assist -

The Hall thruster nominally operates in the 1500s specific impulse regime. It provides greater thrust to power than the conventional gridded ion engines, thus reducing trip times and requiring lower operational lifetimes when compared to that technology in Earth Orbit applications. The technology in the far term, by adding a second acceleration stage, has shown promise of providing over 4000s Isp, the regime of the gridded ion and necessary for deep space applications.

The Hall thruster system consists of three parts, the thruster, the power processor, and the propellant system. A simplified schematic diagram of a Hall thruster is presented in Figure YYY. The typical propellant for a Hall thruster is a high molecular weight inert gas such as xenon. A power processor is used to generate an electrical discharge between a cathode and an annular anode through which the majority of propellant is injected. A critical element of the device is the incorporation of a radial magnetic field, which serves to impart a spin to the electrons coming from the cathode and to retard their flow to the anode. The spinning electrons collide with the neutral xenon, ionizing it. The xenon ions are then accelerated from the discharge chamber by the electric potential maintained across the electrodes by the power processor. The velocity of the exiting ions, and hence the specific impulse, is governed by the voltage applied by the discharge power supply and is typically 15,000-16,000 m/s at 300 V. Figure ZZZ shows a test firing of a Hall Thruster.

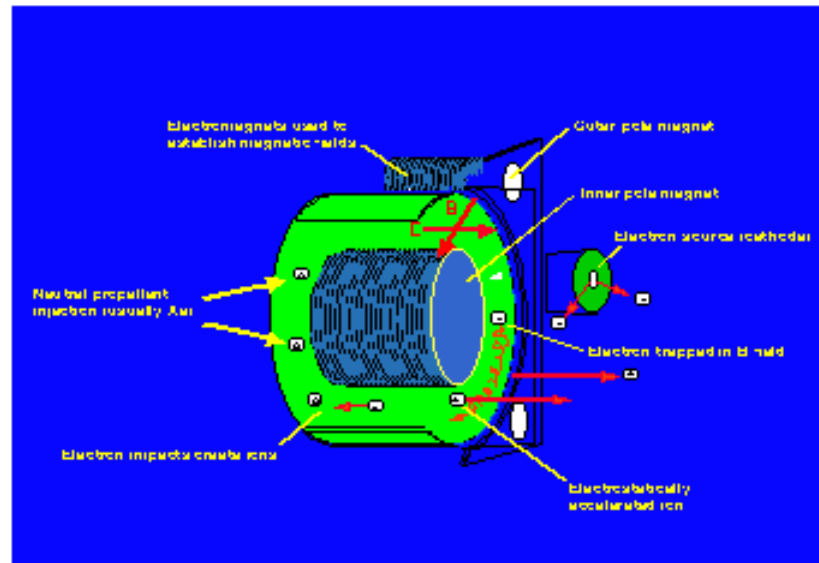


Figure YYY. Simplified Hall Thruster Schematic

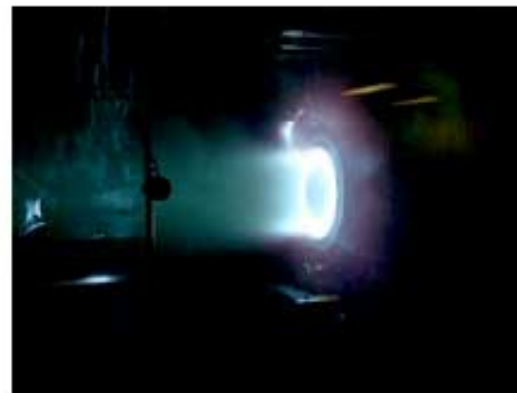
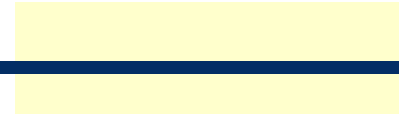


Figure ZZZ. Hall Thruster Test





TECH ISP

IN-SPACE PROPULSION TECHNOLOGIES



Hall Thruster

Potential Mission Applications

Current: The Hall thruster is an electric propulsion device used for orbit raising, on-orbit maneuvers, and deorbit functions which are currently performed by hydrazine monopropellant or hydrazine derivative/nitrogen tetroxide bi-propellant thrusters.

Future: The technology in the far term, by adding a second acceleration stage, has shown promise of providing over 4000s Isp, the regime of the gridded.

- **POTENTIAL MISSION APPLICATIONS**
- **FUNDAMENTAL PHYSICS**
- **TECHNICAL PUBLICATIONS**
- **LINKS**

- **ISP MAIN**
- **TECH MAIN**

**CURRENT
TECHNOLOGIES**

Aeroassist

*Aerocapture -
Aerobraking -*

**Solar Electric
Propulsion**

*Next Generation
Electric Propulsion -
SEP Hall -*

Solar Sails

**Advanced
Chemical**

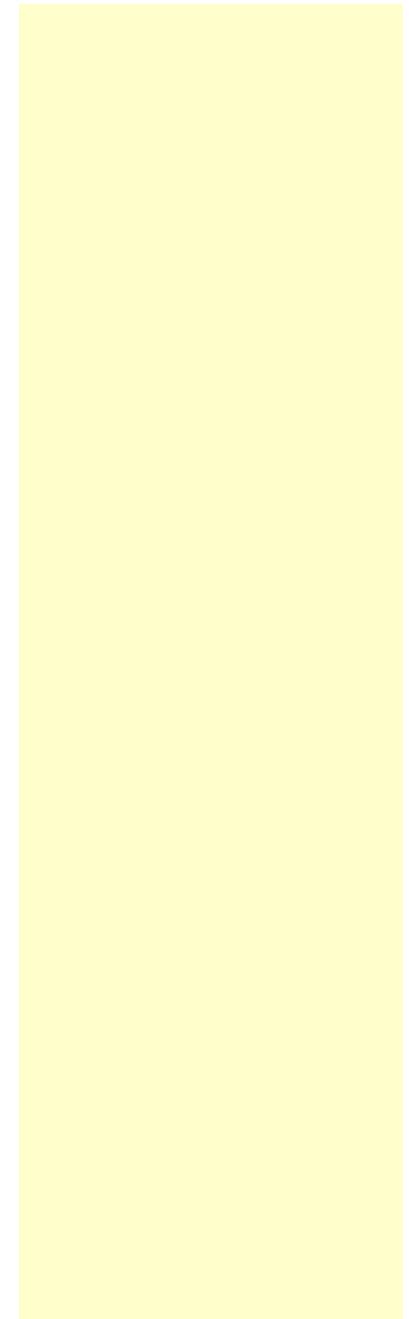
Tethers

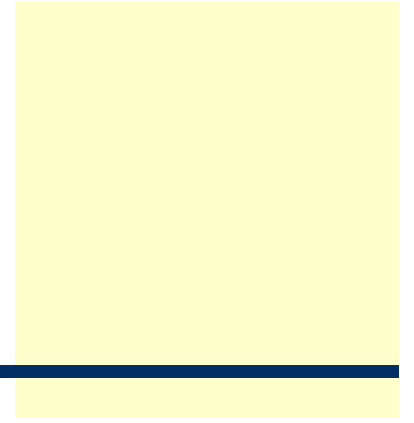
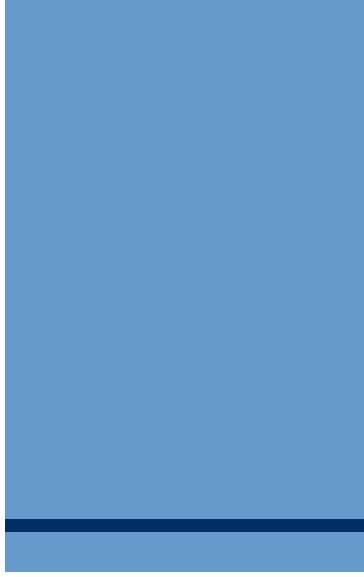
*Momentum Exchange -
Electrodynamic -*

Solar Thermal

**EMERGING
TECHNOLOGIES**

Aerogravity Assist -







TECH ISP

IN-SPACE PROPULSION TECHNOLOGIES



Solar Electric Propulsion *Potential Mission Applications*

Click [HERE](#) for .pdf version. Some equations and diagrams may display better in the .pdf version.

Space missions are characterized by a term "Delta Velocity" (or Delta V), which is a convenient measure of propulsion requirements. Mission Delta V's increase as propulsion requirements become more demanding, as, for example, when mission durations or target distances from the Earth increase. The fundamental performance expectation of a space mission, regardless of propulsion type, is specified by the "Rocket Equation", which relates the ratio of final to initial masses to the ratio of the Delta V to the specific impulse, which is proportional to the propellant velocity. The final mass contains the payload and additional masses required to operate the propulsion system and it is **generally** desirable to achieve as high a final mass as practical. The Rocket Equation is shown in Figure 1 and illustrates the fact that as Delta V increases, it is necessary to increase the specific impulse in order to maintain a given mass ratio. The Rocket Equation, see Figure 1 below,

- POTENTIAL MISSION APPLICATIONS
- FUNDAMENTAL PHYSICS
- TECHNICAL PUBLICATIONS
- LINKS

- ISP MAIN
- TECH MAIN

CURRENT TECHNOLOGIES

Aeroassist

Aerocapture -
Aerobraking -

Solar Electric Propulsion

Next Generation
Electric Propulsion -
SEP Hall -

Solar Sails

Advanced Chemical

Tethers

Momentum Exchange -
Electrodynamic -

Solar Thermal

EMERGING TECHNOLOGIES

Aerogravity Assist -

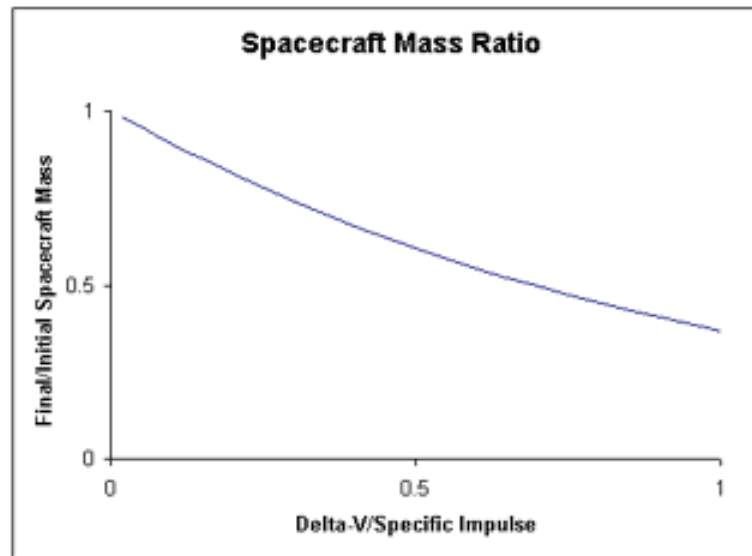


Figure 1

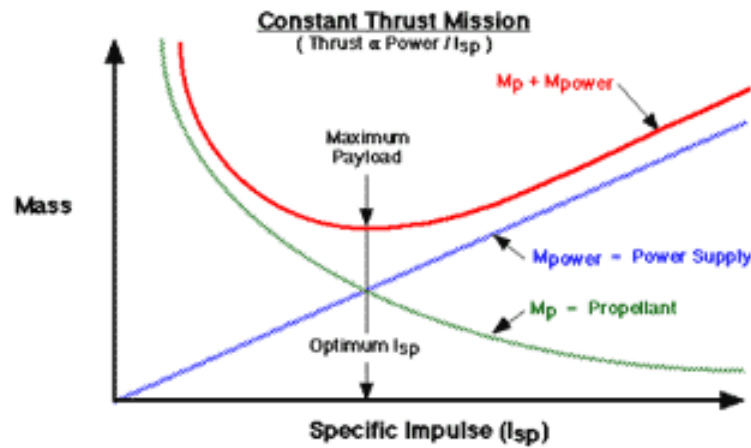


Figure 2

suggests that the optimum mission performance would always occur at the highest possible specific impulse. The practical

situation is more complex, however, and is illustrated in Figure 2 above, which shows, for a mission with a given Delta V, the trends, as a function of specific impulse, of the masses of propellant and power subsystems associated with an electric propulsion system. The propellant mass drops monotonically with increasing specific impulse, as predicted from the Rocket Equation. However, the power, and associated mass, required to achieve desired thrust, hence acceleration, levels increases directly with the specific impulse. This basically occurs because the thrust and power increase, respectively, directly and as the square of the specific impulse. The trends shown on Figure 2 then imply that for a given mission there is a specific impulse that minimizes the total mass of the electric propulsion system (which is closely approximated by the sum of the power and propellant masses). At that minimum, the mission payload is maximized and electric propulsion concepts are typically chosen that operate at or near the optimum specific impulses for a given mission. It is important to note that the optimum specific impulse tends to increase both with increasing mission Delta V (as suggested by Figure 1) and with decreasing specific mass (the ratio of total mass to power level) of the spacecraft. This helps explain the increasing interest in electric propulsion as more difficult missions are of interest and as the mass of spacecraft subsystems, such as power, structure and thermal control, have continued to decrease.

Electric propulsion offers specific impulses far greater than theoretically achievable with chemical propulsion but cannot practically achieve the thrust, or acceleration, levels associated with chemical propulsion. These characteristics imply that electric propulsion offers significant benefits for difficult space applications that do not require high accelerations (which are

necessary in multiple situations including Earth launch, planetary ascent propulsion, and rapid deceleration maneuvers). The payload benefits of electric propulsion have been quantified for many mission types. Figure 3, below, compares the performance of chemical and electric propulsion (when operated near the optimum specific impulse described above) for typical Earth orbit transfer, outer-planetary, and interstellar missions. It is seen that electric propulsion benefits range from major increases to outright enablement of payload masses, with the payload benefit increasing with mission difficulty. The comparative trip times required for chemical and electric propulsion are extremely mission-specific. It is typical, however, that as the mission Delta Vs increase electric propulsion trip times vary from longer to shorter than those for chemical propulsion.

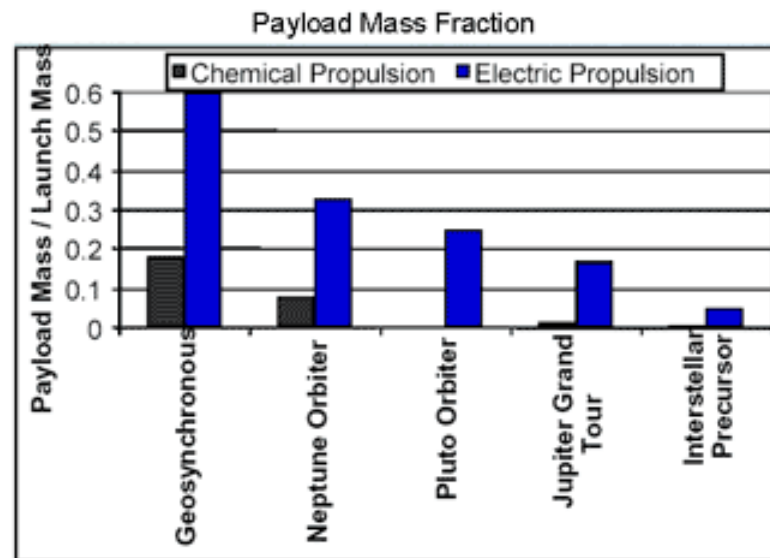


Figure 3

Courtesy of NASA GRC

The functional elements of all electric propulsion systems are similar and are shown below on Figure 4. Power is made available from some source. At present electric propulsion systems derive power from photovoltaic arrays but plans are underway to also use fission nuclear power sources for outer planetary mission where the available solar power is too low. In the further future, alternate power options such as beamed energy and fusion power may become available for use with electric propulsion. This flexibility with respect to power source makes electric propulsion a candidate for a great range of mission applications and the significant and on-going improvements in the specific mass of power subsystems has been a major factor in the acceptance of electric propulsion. Propellant is also stored on-board the spacecraft. At present, most electric propulsion systems use xenon as a propellant, but other options are being considered as the application space increases. The power is used to ionize and accelerate the propellant, via a variety of methods (see the Fundamental Physics section) to produce the desired thrust.

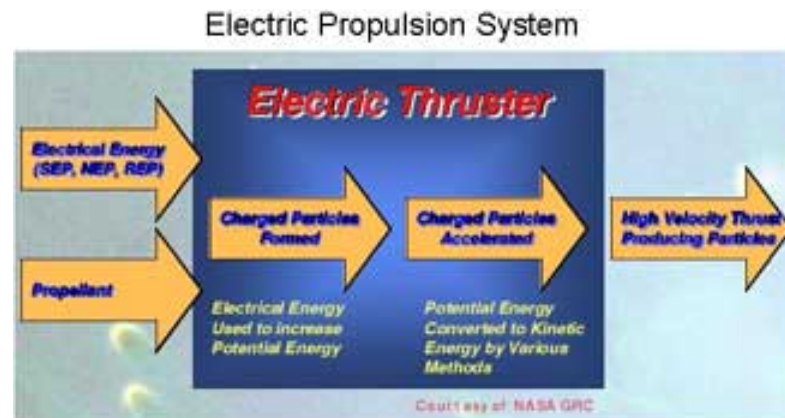
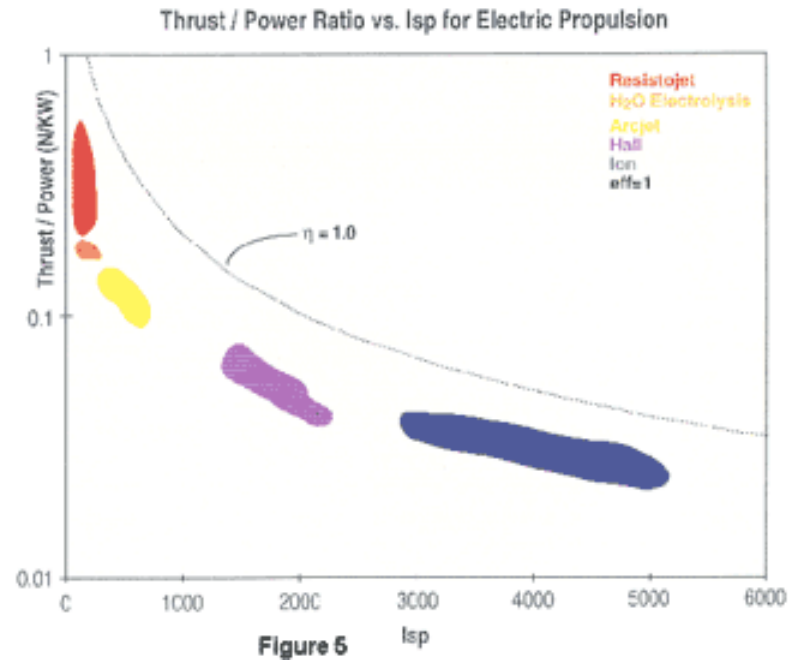


Figure 4

Ion and Hall Effect Thruster (HET) subsystems are now being routinely used for stationkeeping of geosynchronous orbit (GEO) spacecraft of many countries. Application of low power (~ 3 kW) ion propulsion for primary (prime mover) functions has begun with the successful DS-1 mission and insertion of spacecraft into GEO. Ion and HET concepts offer different operating regimes, as illustrated on Figure 5 below, which shows the ratio of thrust to power for several electric propulsion concepts over their range of specific impulse; they have been extensively demonstrated. It is seen that HET's operate from about 1500 to 2500 seconds and ion thrusters tend to operate at specific impulses greater than 3000 seconds. These different operating regimes are due to the quite different physics of the ion and HET subsystems and while attempts are underway to expand the operating range of both concepts, the relative relationship of the operating ranges is expected to remain as shown in Figure 5. For that reason, HET subsystems will tend to be optimum for missions with lower Delta Vs than those most strongly benefited by ion propulsion. (It is important to note that the final choice of a propulsion subsystem may depend on considerations other than payload, but only mission performance is considered herein). As a practical matter, HETs tend to have specific impulses that provide a highly desirable combination of increased payload and trip times for Earth-orbit transfer missions, which have Delta Vs of order 6000 meters/second for a transfer from Low Earth Orbit (LEO) to GEO. On the other hand, planetary missions tend to have significantly (>2X) higher Delta Vs than Earth orbit transfer applications and, therefore, ion propulsion is generally the concept of choice for those uses. Based on the extremely successful applications of ion and HET propulsion, it is anticipated that both concepts will find extensive and

increasing use for high-energy scientific and other space missions.





TECH ISP

IN-SPACE PROPULSION TECHNOLOGIES



Solar Electric Propulsion *Fundamental Physics*

Click [HERE](#) for .pdf version. Some equations may display better in the .pdf version.

The purpose of any propulsion device, whether chemical or electric, is to provide the impulse required by the particular mission to the vehicle. This impulse is simply the product of the thrust and the time the thrust is applied:

$$I_{tot} = T \times t \quad (1)$$

One figure of merit of a thruster is how much impulse can be gained from one pound of propellant; something of a fuel efficiency. This is referred to as the specific impulse, defined as

$$I_{sp} = (T \times t) / (M_o \times g) \quad (2)$$

Where M_o is the initial mass of the propellant and g is the gravitational constant.
Since the thrust is mass times the acceleration of the jet exhaust,

- POTENTIAL MISSION APPLICATIONS
- FUNDAMENTAL PHYSICS
- TECHNICAL PUBLICATIONS
- LINKS

- ISP MAIN

- TECH MAIN

CURRENT TECHNOLOGIES

Aeroassist
Aerocapture -
Aerobraking -

Solar Electric Propulsion
Next Generation
Electric Propulsion -
SEP Hall -

Solar Sails

Advanced Chemical

Tethers
Momentum Exchange -
Electrodynamic -

Solar Thermal

EMERGING TECHNOLOGIES

Aerogravity Assist -

$$I_{sp} = (M_o \times a \times t) / (M_o \times g) = vJ / g \quad (3)$$

Thus, the higher the exhaust jet velocity, the more efficient the thruster.

The exhaust jet velocity is a function of the potential energy converted to kinetic energy by the thruster system. For a chemical rocket, the total energy available is stored in the internal energy of the propellant. This energy is then converted to the kinetic energy of the exhaust jet by a chemical reaction involving the propellant and an oxidizer. For an electric system, the energy comes from a source external to the thruster and propellant, is converted and conditioned to the proper form of electrical energy, and then used to accelerate the propellant.

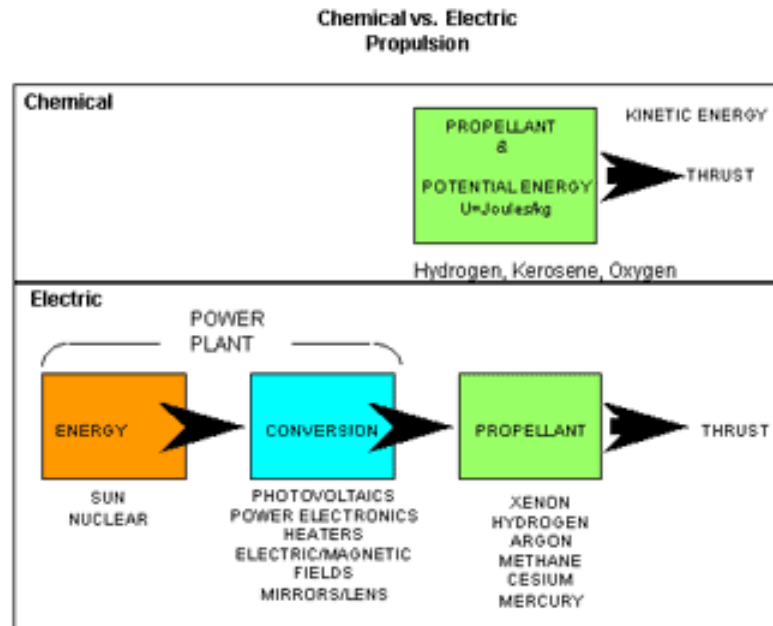


[Figure 1]

If U is the stored internal energy density of the chemical propellants, the total energy available is

$U \times M_0 = \frac{1}{2} M_0 v_J^2$ and v_J is a function of U only.

Clearly the only way to add energy to a chemical system is to add propellant which does not improve the I_{sp} since it does not increase the exhaust velocity.

Electric systems do not have this limitation. For example, an electric system, which accelerates ions through an electric field, called an electrostatic thruster, has energy available of

$$eV = \frac{1}{2} m v_J^2$$

where e is the charge of the ion (usually the electronic charge), and m is the mass of the ion. Therefore for the electrostatic system v_J is a function of the square root of the charge to mass ratio of the accelerated ion. This value is generally on order of 103. As a result, the electrostatic thruster inherently has an I_{sp} of thousands of seconds whereas a chemical system is inherently limited to several hundreds of seconds. Comparison of the state of the art Electrostatic Thruster System and a Centaur Upper Stage System is shown in Table I shown below.

There are some trade offs however for the higher I_{sp} of electric systems. Even though the weight of the propellant can be reduced, some of this savings is offset by the weight of the electric power conversion and conditioning subsystems. If these subsystems are not very efficient, they can quickly eliminate any weight savings at the system level. The basic equation for efficiency of any thrust system is

$$\text{Eff} = \frac{T^2}{2 \times \dot{m} \times P} = \frac{T}{2P} \times (T \times t) / M_o \quad (4)$$

where \dot{m} is the total propellant flow rate and P is the electrical power used by the system. Combining equations (3) and (4) shows that

$$\text{Eff} \times 2/g = T/P \times \text{Isp} \quad (5)$$

Therefore, for a given amount of electrical power, thrust must be given up to increase the Isp and reduce propellant mass. This in turn requires a longer thrust time to deliver the total impulse capability of the system. This can be seen in the comparison in Table 1. Electric propulsion can be used only for missions, which provide enough flight time to allow the total impulse to be delivered. This is why electric propulsion is of great interest for interplanetary missions, non-time critical orbit raising missions, and on-orbit station keeping. The savings in propellant weight also make electric propulsion attractive for missions, which require thrust maneuvers at the destination. Essentially, any mission which would utilize a large impulsive burn of a chemical rocket followed by very long coast times would be a candidate for an electric propulsion system.

Equation (5) can also be rearranged to show

$$(I_{\text{tot}})^2 / (2 \times \text{Eff}) = P \times t \times M_o = E \times M_o \quad (6)$$

For a chemical thruster, this reduces to $(U \times M_o) \times M_o$
 While for an electric system it becomes $P \times t \times (M_o + M_{\text{power plant}})$.

For the electric propulsion system, since the energy is not a "consumable", it is possible to reduce weight by increasing the thrust time if not constrained by mission time.

COMPARISON OF CENTAUR & SEPS TOTAL IMPULSE = 6×10^7 Nsec	
<u>CENTAUR</u>	<u>SOLAR ELECTRIC STAGE</u>
• $V_j = 4300$ m/sec	• $V_j = 29400$ m/sec
• $I_{sp} = 440$ sec	• $I_{sp} = 3000$ sec
• $T = 66000$ N	• $T = 1$ N (Stage)
• Burn Time = 880 sec	• Burn Time = 5×10^7 sec
• Propellant Wt = 13600 kg	• Propellant Wt = 2000 kg

Table 1



TECH ISP

IN-SPACE PROPULSION TECHNOLOGIES



Advanced Fuels

[.pdf version](#) - some equations may be easier to view as .pdf

General Description:

Many compounds are currently being analyzed and tested as advanced chemical propellants. The number of compounds used in a propellant is often used to categorize the propellant. As such, future propellants being analyzed are typically called monopropellants, bipropellants, tripropellants. High energy density matter (HEDM) is also being analyzed to increase the Isp of current propellants.

Monopropellants

The most common monopropellant in use is hydrazine. It is passed through a catalyst bed, where it decomposes into nitrogen and ammonia and delivers a specific impulse of about 230 lbf-s/lbm. Propulsion systems of this sort are well suited to pulsed operations of short duration, such as small spacecraft attitude control. (Adams, 1994)

NASA is also developing new monopropellant systems to replace the current hydrazine monopropellant systems. The monopropellants under consideration are environmentally friendly, have a higher density, and have better thermal characteristics than hydrazine. The near-term goal is to

- **POTENTIAL MISSION APPLICATIONS**
- **FUNDAMENTAL PHYSICS**
- **TECHNICAL PUBLICATIONS**
- **LINKS**
- **ISP MAIN**
- **TECH MAIN**

CURRENT TECHNOLOGIES

Aeroassist

Aerocapture -
Aerobraking -

Solar Electric Propulsion

Next Generation
Electric Propulsion -
SEP Hall -

Solar Sails

Advanced Chemical

Tethers

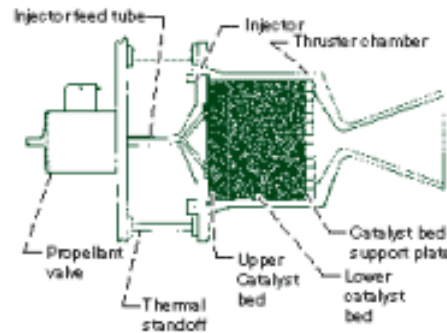
Momentum Exchange -
Electrodynamic -

Solar Thermal

EMERGING TECHNOLOGIES

Aerogravity Assist -

improve mission performance and greatly reduce ground operations costs. For the far-term, a very high performance (high specific impulse) system is being sought. The key to this goal is the development of a high-temperature catalyst; research in this area is underway. (Schneider, 1997) .



The bipropellant that is most often used in interplanetary spacecraft with relatively small engines is nitrogen tetroxide/monomethyl-hydrazine, commonly referred to as NTO/MMH. This combination yields an Isp of 317 lbf-s/lbm. NASA seeks to improve performance to 326 lbf-s/lbm by using of a rhenium-alloyed thrust chamber, which will allow both higher operating temperatures and pressures. (Frisbee, 2000a)

NASA has also been working to improve the efficiency of LH2/LOX systems. Large pump-fed engines, like those found in the Space Shuttle main engines (SSMEs) can achieve an Isp of 450 lbf-s/lbm, while smaller pressure-fed engines can reach an Isp of 423 lbf-s/lbm. The problem has been that the high Isp may be offset by higher structural weight, because refrigeration systems are required to store the cryogenic fuels.

The following table summarizes other bipropellant systems

that have been investigated. The "type" column describes the how the propellant may be stored. "Space storable" refers to combinations that may be stored for extended periods in the space environment.

Propellant	Type	I_{sp} (s)
NTO/MMH	Earth Storable	317
O ₂ /CH ₄	Space Storable	365
O ₂ /H ₂	Refrigerated	423
ClF ₅ /N ₂ H ₄	Space Storable	350
OF ₂ /C ₂ H ₄	Space Storable	415
N ₂ F ₄ /N ₂ H ₄	Space Storable	395
F ₂ /N ₂ H ₄	Space Storable	415
OF ₂ /C ₂ H ₆	Space Storable	410
OF ₂ /B ₂ H ₆	Space Storable	420

Tripropellants

There are many chemical reactions that result in a higher specific impulse than the 423 seconds that is provided by the LH₂/LOX workhorse. However, many of these are unacceptable as rocket propellants because the exhaust is not a gas. Tripropellant technologies are an attempt to use these reactions by adding a third component (usually hydrogen) to the fuel and oxidizer. So far, lithium-fluorine-hydrogen and beryllium-oxygen-hydrogen mixes show the most promise for a tripropellant application. (Frisbee, 2000 I)

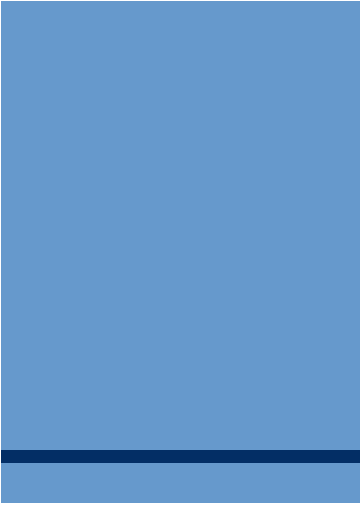
The beryllium-oxygen-hydrogen system could generate an Isp of 705 s and is being investigated by the U.S. Air Force. A lithium-fluorine-hydrogen system has the potential for generating an Isp of 705 s. Early testing shows that while it has a higher combustion efficiency than the beryllium-oxygen-hydrogen system, it only allows a slight advantage over a fluorine-hydrogen bipropellant system.

High Energy Density Matter (HEDM)

In addition to the normal tripropellant approach, researchers have been looking at chemical additives that will increase the specific impulse generated by conventional bipropellant systems. These increases are achieved by adding high-energy chemicals in order to increase Isp, thrust, and safety. This is not unlike adding chemicals to your car's fuel tank in order to achieve greater mileage. At the current time, HEDM is still in the basic research phase. (Frisbee, 2000d)

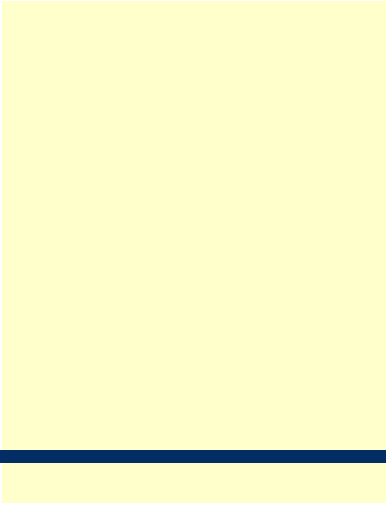
According to preliminary analyses that have been done at NASA's Lewis Research Center (now known as the Glenn Research Center), solid particles in a cryogenic carrier fluid (such as LH2) can carry HEDM additives to conventional combustion chambers. Adding these high-energy chemicals can increase the specific impulse by 19-49 s (figured from the LH2/LOX baseline figure of 423 s). The table below summarizes the increases. (Palaszewski, 1998)

Carbon atoms	+ 49 s
Boron atoms	+ 31 s
Aluminum atoms	+ 27 s
Hydrogen atoms	+ 19 s



In addition to the increase to specific impulse, HEDM additives have the potential to increase propellant and vehicle density, allowing for more compact vehicles. These improvements would allow a higher percentage of deliverable payload weight to vehicle weight in future launch vehicles.

All of the chemical technologies discussed in this section will improve our ability to achieve orbit from the Earth's surface, but will have limited utility in traveling to other planets.





TECH ISP IN-SPACE PROPULSION TECHNOLOGIES



Aerocapture *Potential Mission Applications*

Mars Sample Return

The Mars Sample Return mission is part of NASA's continued exploration of the Red Planet. Launching early in the next decade (2011), the spacecraft will fly to Mars, land, and return with soil, rock, and atmospheric samples. Robotics will be utilized to the maximum extent possible to allow samples to be collected from various locations around the landing sight. This mission could serve as a precursor to a manned flight to Mars, which may take place later in the decade.

Titan Explorer

Launching at the end of this decade (2010-2011), the Titan explorer mission is designed for orbital and surface analysis of Saturn's largest moon. After almost a 10-year flight, the spacecraft will make multiple orbits of Titan before deploying a mini chemistry lab to the surface. This advanced robotic lander will have the capability to move locations via ground and/or flight to collect and analyze surface samples at various locations on the moon. A variety of measurements and analysis will be performed in orbit and on the surface with the results sent back to earth via an advanced communications

- **POTENTIAL MISSION APPLICATIONS**
- **FUNDAMENTAL PHYSICS**
- **TECHNICAL PUBLICATIONS**
- **LINKS**
- **ISP MAIN**
- **TECH MAIN**

**CURRENT
TECHNOLOGIES****Aeroassist**

*Aerocapture -
Aerobraking -*

**Solar Electric
Propulsion**

*Next Generation
Electric Propulsion -
SEP Hall -*

Solar Sails**Advanced
Chemical****Tethers**

*Momentum Exchange -
Electrodynamic -*

Solar Thermal

**EMERGING
TECHNOLOGIES**

Aerogravity Assist -

suite.

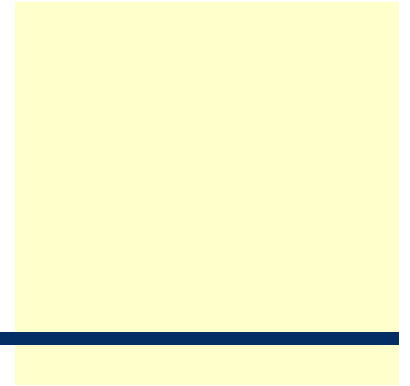
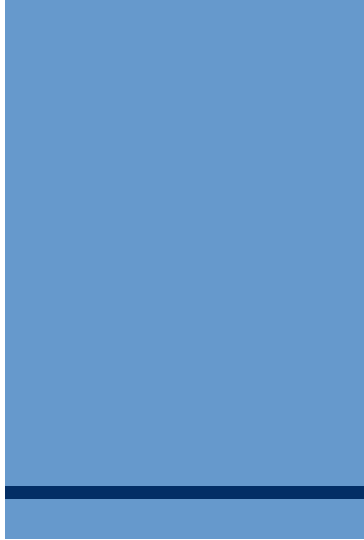
Neptune Orbiter

Launching in the latter half of this decade (2006-2007), the Neptune orbiter mission is designed to provide valuable insight into the eighth planet in our solar system and its largest moon Triton. After a 10-year flight, the Neptune Orbiter will circle 2 to 4 years on station while utilizing advanced communication techniques to relay valuable information about Neptune's atmospheric and magnetospheric properties. The orbiter will also perform multiple flybys of Triton providing physical and atmospheric information on this satellite. Since Triton is thought to be a Kuiper Belt object, captured by Neptune, insight into the origins of our solar system and its continued development are a primary mission goal.

Venus Surface Sample Return

TBD







Aerocapture *Fundamental Physics*

The principles behind aerocapture are simple. The density of the atmosphere surrounding a celestial body creates friction, slowing the spacecraft and places it into an elliptical orbit around the body. Unfortunately, friction creates heat, so the aerocapture mechanism must be able to survive extreme temperatures while protecting the craft from the heat generated by the maneuver. Any lift of the craft must also be taken into consideration, and the lift /drag coefficient (L/D) for the spacecraft must be known along with atmospheric density characteristics.

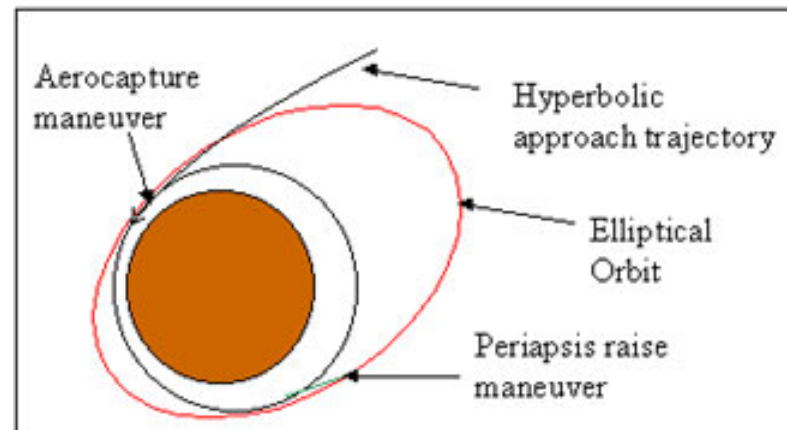


figure 1

- **POTENTIAL MISSION APPLICATIONS**
- **FUNDAMENTAL PHYSICS**
- **TECHNICAL PUBLICATIONS**
- **LINKS**
- **ISP MAIN**
- **TECH MAIN**

**CURRENT
TECHNOLOGIES****Aeroassist**

*Aerocapture -
Aerobraking -*

**Solar Electric
Propulsion**

*Next Generation
Electric Propulsion -
SEP Hall -*

Solar Sails**Advanced
Chemical****Tethers**

*Momentum Exchange -
Electrodynamic -*

Solar Thermal

**EMERGING
TECHNOLOGIES**

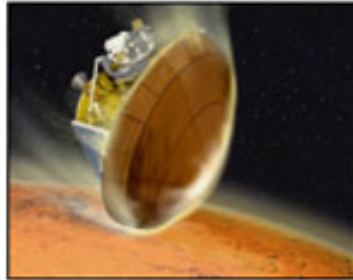
Aerogravity Assist -

The aerocapture maneuver starts with a hyperbolic approach trajectory into the atmosphere of the body. Once the spacecraft velocity has been reduced enough to achieve orbit, a periapsis maneuver using thrusters is necessary to raise the craft out of the atmosphere. Figure 1 shows the maneuver. If a circular orbit is desired, aerobraking can be employed to change the orbit shape.

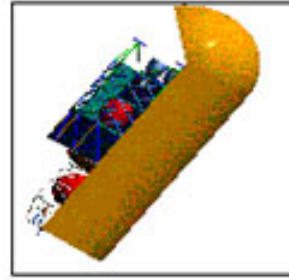
Aerocapture mechanisms can be realized in two ways. The spacecraft itself can be designed as an aerocapture device with heat shielding applied to the external surfaces where appropriate (Aeroshell.) The spacecraft may deploy an aerocapture device, such as an inflatable ballute or shield that can then be discarded when the aerocapture maneuver is complete (Aeroshell). For examples of these aerocapture concepts see Figure 2. Many people will remember the movie 2010 where a ballute was used to slow the spacecraft once it reached Jupiter. The aerocapture devices and/or shielding must weigh/cost less than propellant based orbital capture systems. Analysis has shown that a 30-40% weight savings can be realized using aerocapture over other propulsion techniques.

Figure Y: Aerocapture Concepts

Low-L/D aeroshell



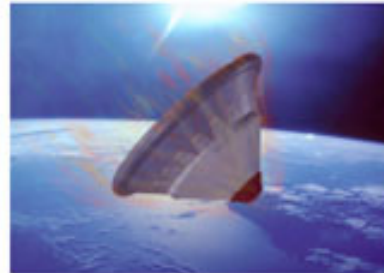
Mid-L/D aeroshell



Ballutes



Inflatable Aeroshells





TECH ISP

IN-SPACE PROPULSION TECHNOLOGIES

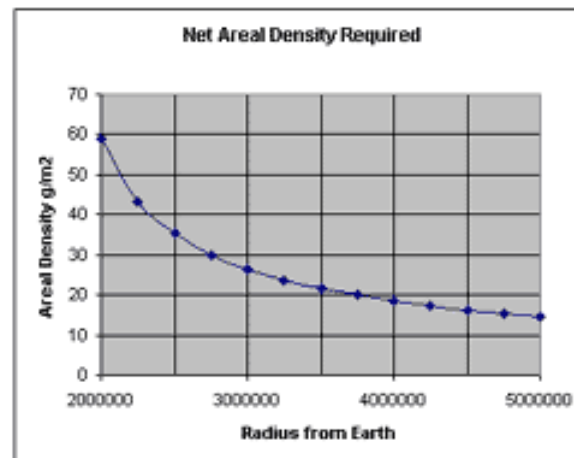


Solar Sails

Potential Mission Applications

Solar sail missions are of two types: those for which sails offer unique performance advantages, and those for which a reasonable alternative propulsion technology exists and could be selected. The first category includes such as (1) the Earth pole-sitter mission, (2) the Solar Sentinel mission, and (3) the Solar Polar Imager mission. The first two of these require continuous thrust for the duration of the mission. Also, these two missions can be scaled so that any reasonable sail performance enables a mission to be performed. Competing systems such as electric propulsion will eventually run out of propellant, while the sail continues to deliver thrust with no, or very small, expenditure of mass. The solar polar mission requires a large delta V (~ 40 km/s) to be delivered at less than 1 au from the sun. While alternative systems can perform this mission, the large delta V tends to favor the sail.

For the pole-sitter and Solar Sentinel mission, mission performance improves with sail performance. There is no



- POTENTIAL MISSION APPLICATIONS
- FUNDAMENTAL PHYSICS
- TECHNICAL PUBLICATIONS
- LINKS

- ISP MAIN
- TECH MAIN

CURRENT TECHNOLOGIES

Aeroassist

Aerocapture -
Aerobraking -

Solar Electric Propulsion

Next Generation
Electric Propulsion -
SEP Hall -

Solar Sails

Advanced Chemical

Tethers

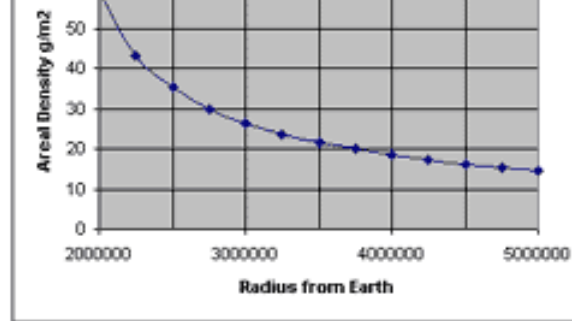
Momentum Exchange -
Electrodynamic -

Solar Thermal

EMERGING TECHNOLOGIES

Aerogravity Assist -

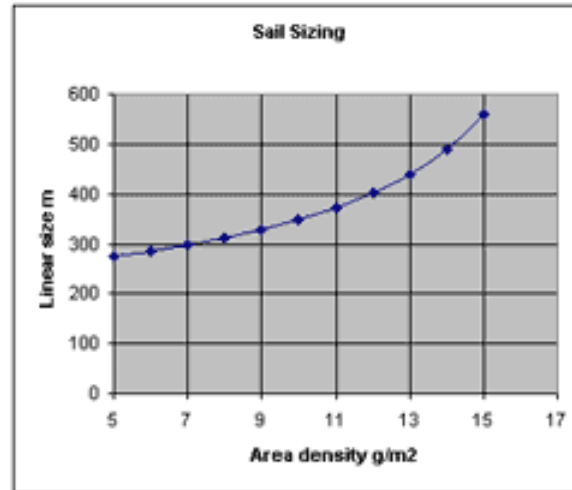
"floor" of sail performance below which the mission cannot be done. The



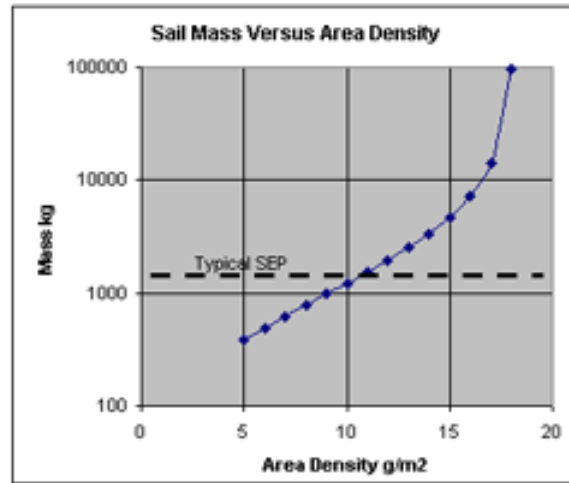
Sentinel is to operate between the Earth and the Sun, closer to the Sun than the L1 point. At L1, a spacecraft can perform a sentinel mission with only station-keeping propellant. The continuous thrust of a sail allows the spacecraft to move closer to the Sun, with sail thrust offsetting the gravitational imbalance arising from moving toward the Sun from the L1 point. The better the sail, the closer to the Sun one can fly. Sails about 15 g/m² are feasible with today's state of the art. Foreseeable improvements are forecast to reduce the mass to as low as 5 g/m². Figure 1 illustrates needed sail performance as a function of distance from Earth. For reference, the L1 point is about one million km from Earth. The figure shows net area density. For sail mass equal payload mass, for example, the sail alone needs to be at half the density shown. A "reasonable" sail can get to about three times the distance from the Earth as the L1 point.

The second mission category usually compares a solar sail to a solar electric propulsion system. For planetary science missions, a typical science spacecraft, payload for the solar sail or SEP, is 1000 kg. A typical SEP for such a mission would have 25 kilowatts electric power at Earth's distance from the Sun, an efficiency of conversion of electric power to thrust power of 65%, a specific impulse of 4000 seconds, and a mass-to-power ratio about 50 kg per kilowatt (electric). Given these parameters, one can estimate the size of solar sail needed to provide the same initial acceleration. Since both systems have thrust proportional to the square of distance from the Sun, the performance comparison tends to remain valid.

Assuming a square-rigged sail, the chart to the right shows sail size versus sail areal density. A sail about 20 g/m² cannot match the acceleration of the SEP even with no payload, so the curve begins to diverge as one



approaches this value. Sail mass is proportional to sail area multiplied by area density, so as the sail becomes larger, the mass increases rapidly. As shown in the second chart below on the left, sail performance is better than the representative SEP below about 10 g/m² and degrades rapidly above 10 g/m². (Note that this graph is a logarithmic scale.) Therefore, we can consider a density of 10 g/m² a goal to be reached in order to make solar sails performance-competitive with solar



electric propulsion.

Click [HERE](#) for .pdf charts on Potential Sail Mission Applications.



Solar Sails

Fundamental Physics

[.pdf version](#) - some equations may be easier to view as .pdf

A photon sail is a spacecraft accelerated by the momentum of the electromagnetic photons that are reflected from it. Types of photon sailcraft are laser sails (which are pushed by laser beams), maser sails (which are pushed by collimated microwave beams) and solar sails. The solar sail is accelerated by momentum transfer from photons emitted by the Sun that strike the sail. If the sail is fully opaque (non transmissive), the radiation pressure of the solar photons impinging against a sail oriented with its reflective surface normal to the sunlight can be written:

$$\text{Rad. Pres.} = (1 + \text{Ref sail}) \text{ SF} / c \text{ Newton} / \text{m}^2, (1)$$

where Ref sail is sail reflectivity, SF is the solar flux striking the sail (1,368 watts / m^2 at the Earth's distance from the Sun - the Solar Constant S.C.), and c is the speed of light (3×10^8 m/sec). The solar flux striking the sail surface varies with the square of the inverse of the distance to the Sun's center.

Sail Kinematics

- POTENTIAL MISSION APPLICATIONS
- FUNDAMENTAL PHYSICS
- TECHNICAL PUBLICATIONS
- LINKS

- ISP MAIN
- TECH MAIN

CURRENT TECHNOLOGIES

Aeroassist

Aerocapture -
Aerobraking -

Solar Electric Propulsion

Next Generation
Electric Propulsion -
SEP Hall -

Solar Sails

Advanced Chemical

Tethers

Momentum Exchange -
Electrodynamic -

Solar Thermal

EMERGING TECHNOLOGIES

Aerogravity Assist -

If one multiplies Eq. (1) by the sail area normal to the Sun, A_{sail} in square meters, the resulting equation yields the force of the sunlight on the sail surface. Applying Newton's Second Law and dividing this result by spacecraft mass M_s/c kilograms, the sailcraft's acceleration due to solar radiation pressure is obtained :

$$ACCs/c = (1 + Ref\ sail) SF A_{sail} / (M_s/c c) = (1 + Ref\ sail) SF / (ss/c c) \text{ m/s}^2, (2)$$

where ss/c is the sailcraft's areal mass thickness in kilograms per square meter.

A convenient Figure of Merit for sail designers is the sailcraft Lightness Factor, LFs/c , which is the ratio of solar radiation pressure acceleration to solar gravitational acceleration on the sailcraft. From Newton's equation for Universal Gravitation,

$$LFs/c = (1 + Ref\ sail) SF R_{sun}^2 / (G M_{sun} ss/c c), (3)$$

where G is the Gravitational Constant $6.67 \times 10^{-11} \text{ N m}^2 \text{ kg}^{-2}$, R_{sun} is the distance of the sailcraft from the sun's center ($1.5 \times 10^{11} \text{ m}$ at the solar orbit of the Earth-1 Astronomical Unit or 1 AU) and M_{sun} is the Sun's mass ($1.99 \times 10^{30} \text{ kg}$). Substituting in Eq. (3), we obtain the simplified result :

$$LFs/c = 0.000773 (1 + Ref\ sail) / ss/c . (4)$$

At the Earth's distance from the Sun, a fully unfurled sail with a Lightness Factor of 1 is accelerated by solar radiation pressure at $5.92 \times 10^{-3} \text{ m/s}^2$ or about 6×10^{-4} Earth surface gravities. The areal mass thickness of such a sailcraft will be 0.00146 kg / m^2 .

Solar sails must therefore be very light and very reflective. If the sailcraft described in the previous paragraph has a mass

of 500 kg, the sail area normal to the Sun must be about 3.42×10^5 square meters. This sail will be considerably larger than a football field!

What if the Sail is Not Normal to the Sun?

Let's call the angle between incident sunlight and the normal to the sail "q". If the sail is normal to the sunlight, $q = 0$ degrees.

If the sail is not normal to the Sun, the normal value of solar irradiance (in watts / m²) striking the sail is multiplied by $\cos q$, according to Lambert's Law. Since the cross-sectional sail area normal to the incident sunlight is also reduced by $\cos q$, the sailcraft acceleration at Sun-sail angle q ($ACCs/c, q$), is related to the sailcraft acceleration for the case of perpendicular sunlight ($ACCs/c, q=0$) by the equation:

$$ACCs/c, q = ACCs/c, q=0 \cos^2 q . \quad (5)$$

When the sail is not normal to the Sun, there will be two components to the sailcraft's solar-radiation-pressure acceleration vector. These are $ACCs/c, rad$, the component of spacecraft acceleration radial to the Sun and $ACCs/c, tan$, the acceleration component tangential to the spacecraft's orbit around the Sun. Mathematically,

$$ACCs/c, rad = ACCs/c, q \cos q , \quad (6a)$$

and

$$ACCs/c, tan = ACCs/c, q \sin q . \quad (6b)$$

In the 2-sail solar photon thruster discussed below, Lambert's

Law does not apply because the main, collector sail is always normal to incident sunlight and all sunlight striking the main collector is directed against the thruster, regardless of thruster angular orientation. For such a sailcraft, the $\cos^2\theta$ term in Eq. (5) is replaced by $\cos \theta$.

Sail Thermal Effects

As well as being low in mass and highly reflective, the sail must be constructed of heat-tolerant material. This is because all of the solar energy absorbed by the sail must be radiated from the sail as infrared electromagnetic radiation.

The radiant power absorbed by an opaque sail oriented normal to the Sun is written:

$$P_{\text{abs}} = (1 - R_{\text{fsail}}) SF A_{\text{sail}} \text{ watt} , (7)$$

Since absorbed electromagnetic radiation can be reemitted as infrared from both sides of the sail, the sail's radiant emittance can be expressed as :

$$W_{\text{sail}} = (1 - R_{\text{fsail}}) SF / 2 \text{ watt} / \text{m}^2 . (8)$$

The Stefan-Boltzmann Law for greybodies can be used to relate sail radiant emittance to sail absolute radiation temperature T_{sail} :

$$W_{\text{sail}} = s e T_{\text{sail}}^4 \text{ watt} / \text{m}^2 , (9)$$

where s is the Stefan-Boltzmann Constant ($5.67 \times 10^{-8} \text{ W m}^{-2} \text{ K}^{-4}$) and e is the sail material's emissivity. (For a blackbody, $e = 1$). Equating Eqs. (8) and (9) and substituting $SF = 1,368 \text{ watt} / \text{m}^2$ at 1 AU, the Earth's average distance from the Sun,

$$T_{\text{sail}} = 331 \left[\frac{1 - \text{Re}_{\text{sail}}}{\epsilon} \right]^{1/4} \text{ degrees Kelvin. (10)}$$

The maximum sail radiation temperature must never exceed the melting point of the sail material. For most materials, the maximum allowable radiation temperature is a few hundred degrees Kelvin less than the sail-material melting point.

Some Sail Configurations

Figure 1 shows six proposed sail configurations. A disc sail consists of a circular sail film supported and stabilized by a series of spars as shown. The payload is often at the center of the spar structure.

Square sails are square or rectangular (when viewed from top or bottom). The spars and payload are often arranged in a manner similar to disc sail designs.

Parachute sails physically separate payload from sail. These are attached by a series of cables, as shown.

The parabolic sail or solar-photon thruster is a multi-sail configuration. A main collector normal to the Sun focuses sunlight upon a smaller thruster. The thruster can be steered allowing the spacecraft to alter the direction of reflected sunlight and thus be more maneuverable than other sail configurations.

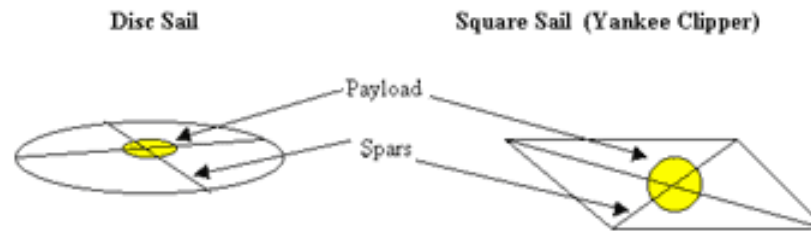
Although many sail designs rotate so that centripetal force can aid in sail unfurlment, the heliogyro spins like a gyroscope, although more slowly. In some designs, sail film rolls out from canisters near the center along spars within the sail blades.

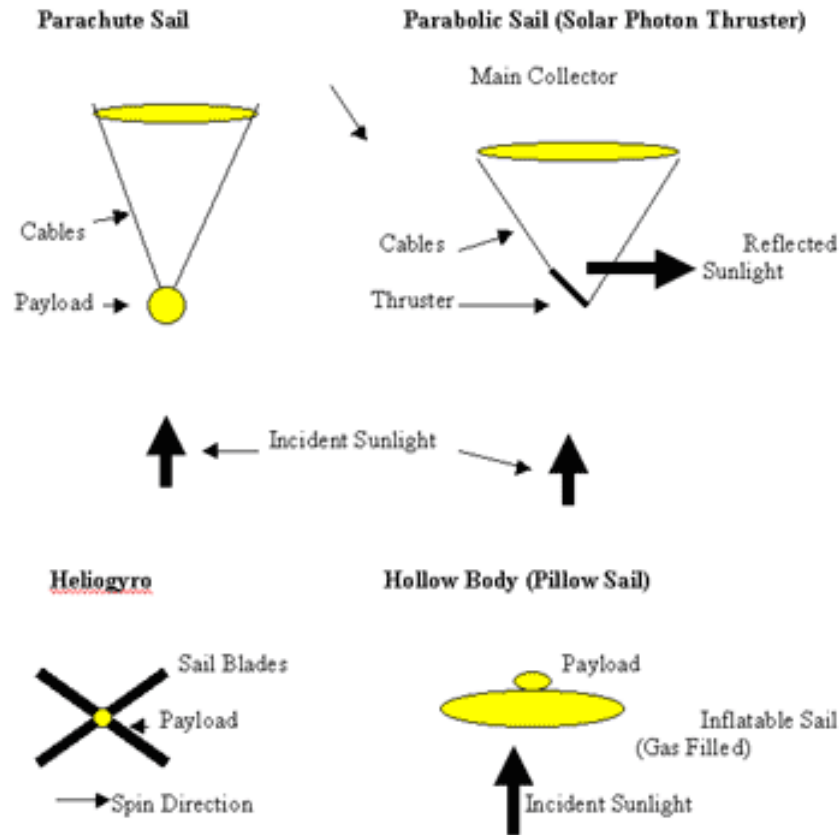
Hollow body or pillow sails are inflatable devices with the surface facing the Sun coated with a reflective layer. Although these may be easier to unfurl than other sail concepts, they have the disadvantage of being more massive.

Solar-Sail Limitations and How to Overcome Them

One major limitation to solar-sail application in the outer solar system and beyond is the inverse-square-law of solar irradiation. As the sail doubles its distance from the Sun, the solar flux and radiation-pressure acceleration fall by a factor of 4X.

Figure 1. Some Solar Sail Configurations



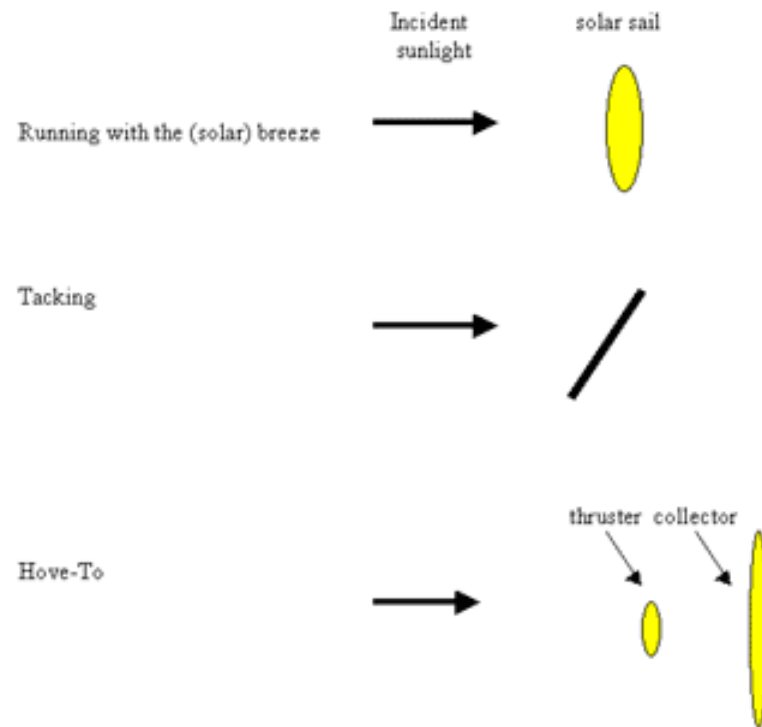


In concept, this effect can be compensated for by replacing sunlight in the outer system and beyond by collimated radiation. Studies have indicated that solar-powered visible and infrared lasers or collimated microwave masers in the inner solar system can project beams against sails very far from the Sun. Such sailcraft should properly be called "light sails" rather than solar sails.

Solar Sail Maneuvers and Orientations

Solar sail maneuvers can be classified using analogues with maneuvers performed by conventional oceanic sailing craft. As shown in Fig. 2, a sailcraft can be oriented with its sail normal to the incident sunlight. In such an orientation, reflected solar photons produce maximum thrust on the sail surface. The craft "runs with the (solar) breeze".

Figure 2. Some Solar-Sail Maneuvers and Orientations



If the sail is oriented at an angle to the incident sunlight, the sailcraft's thrust will be at an angle to incident sunlight. In this orientation, the spacecraft "tacks".

In a two-sail solar photon thruster, thrust can be greatly reduced by reflecting sunlight from the thruster back towards the main collector sail. This orientation is analogous to the "hove-to" maneuver performed by an oceanic sailcraft to slow the craft under high-wind conditions.

Solar-Sail Materials

A number of choices exist for solar sail materials. Many of these are reviewed in the references.

For an Earth-launched near-term sailcraft, one approach is to create the sail

using a sandwich of three materials. A metallic, highly-reflective (front) layer faces the Sun, followed by a layer of flexible, temperature-resistant plastic. The back layer is composed of a highly emissive material such as chromium. The function of the layer facing the Sun is to reflect as much of the sunlight as possible (up to about 90%). The plastic layer's function is to improve sail flexibility during the sail unfurlment process. Sunlight absorbed by the front layer is reemitted as infrared electromagnetic radiation from the back emissive layer. Some current three-layer sail designs have areal mass thicknesses less than about 10 grams per square meter and are capable of operating within 0.1 AU from the Sun. The sail thickness is typically of the order of a few microns.

Additional sail strength can be achieved by including strips of metallic ribbing within the sail structure. These might minimize the effects of micrometeoroid impacts.

Some researchers have examined the possibility of using plastics that would rapidly degrade when exposed to solar ultraviolet radiation. In a sail constructed of this material, the "sandwich" layers would be reflective, emissive, and finally

UV-sensitive plastic. This approach could greatly reduce sail areal mass thickness.

The thinnest Earth-launched sails might consist of a stack of strong, temperature-resistant composite fibers. Perhaps coated with a reflective layer, the areal mass thickness of such a sail could be less than 1 gram per square meter. A sailcraft constructed using this material could operate well within 0.1 AU. Sail unfurlment may be an issue for very thin Earth-launched solar sails.

Ultimate solar-sail performance requires a space-manufacturing infrastructure. Using vapor-phase deposition, large-metallic sheets 20-30 nanometers thick could be produced in space. Areal mass thickness of 0.05 grams per square meter might be possible. Some metallic hyperthin sails could (theoretically) approach the Sun within the 0.05 AU of the Sun's center.

Nanotechnology might, in the farther future, allow for the creation of perforated or mesh solar sails. If the perforations are substantially smaller than the wavelength of incident light, low mass and high reflectance might combine to greatly increase sail performance.

Solar-Sail Missions

The solar sail is unique among currently-feasible advanced propulsion schemes because it requires no propellant and can accelerate endlessly without thrusting under the influence of sunlight or some other source of electromagnetic radiation. Once unfurled, a solar-sail constructed of material that does not readily degrade in the space environment, should have a very long operational life. Many space missions are possible

using solar sails that are more difficult or impossible using other in-space propulsion modes.

In general (unless power-beaming is applied), these are either inner solar-system missions or missions in which spacecraft acceleration is accomplished within the inner solar system.

The solar sail could accelerate to velocities of 100 km/sec or higher after unfurlment during a close solar flyby. But (since the solar flux will be reduced from its near-Earth value by a factor of 25X at the 5-AU solar distance of Jupiter) the solar-sail will be ineffective for stopping at outer-solar-system destinations.

In low-Earth orbit, atmospheric drag is also an issue for the high-area, low-mass solar sail. Even solar-photon thrusters may be drag limited to unfurlment orbits in excess of 500 km above Earth's surface.

Near-term scientific missions

In the near-term, solar-sails in the 6-10 grams per square meter range, with areas of about 104 square meters are under consideration for inner-solar-system solar observer missions. Stationed for years between the Earth and Sun, such craft could give early warning of solar flares approaching the Earth.

If they are constructed of material capable of withstanding radiation produced by repeated passes through Earth's Van Allen radiation belts, sail configurations such as the solar-photon thruster could maintain constellations of satellites at various locations within Earth's magnetosphere. The payloads of these craft could monitor the near-Earth plasma environment for examine space-magnetic interactions with the terrestrial environment.

The solar-photon-thruster sail configuration could enable the "pole sitter," a spacecraft situated at lunar distances over or

nearly over one of Earth's poles. Pole sitters have application to high-latitude communication, climate studies and Earth viewing.

Sails could be considered for payload delivery or round-trip visits to inner-solar system planets as far out from the Sun as Mars or for launching probes to the outer solar system. Fast flybys of outer-solar-system objects such as Kuiper Belt comets (30-50 AU from the Sun) are possible.

Perhaps the most exciting near-term possibility is a sailcraft equipped with a sail that is unfurled within the orbit of Venus or perhaps Mercury and then accelerated out of the solar system on a trajectory capable of reaching the heliopause (the limit of the Sun's influence--at 250 AU from the Sun) within a few decades. Such an interstellar probe could monitor in situ the interaction between the Sun and the galaxy.

Space-commercialization and Earth-protection missions

As humanity's space infrastructure matures, Earth-launched or space-manufactured solar-sails will offer opportunities to those seeking to develop the space-environment or to protect the Earth from cosmic collisions. Near-Earth asteroids and comets could be explored and mined using solar sails. If advanced terrestrial and space telescopes can provide decades-long warnings of collisions between Earth and near-Earth objects (NEOs), solar sails-could be unfurled around or near the offending asteroids or cometary nuclei. Radiation pressure on sails attached to NEOs could alter collision trajectories to near-miss trajectories. Alternatively, sails could be used as concentrators to heat NEO surfaces enough for trajectory-altering jets of material to be ejected.

To the Oort Belt and the stars!

As 0.1 gram / square-meter sails capable of withstanding very close perihelion passes are developed in the farther future, solar-system exit velocities in excess of 300 km/sec will become possible. Then, space-mission planners could design robotic missions to nearer Oort Belt comets within a few thousand Astronomical Units of the Sun with flight times of a few decades.

Ultimate space-manufactured solar sails will allow the possibility of Earth-Mars roundtrips with durations measured in months rather than years. The same technology may allow visits to the nearer stars at solar-system exit velocities higher than 1,000

km /sec. The one-way travel time to the Sun's nearest interstellar neighbors (proxima and Alpha Centauri) will be about 1,000 years for such spacecraft. Advances in laser and maser power-beaming technologies may eventually substantially reduce interstellar-voyage durations.

Conceptual Design and Analysis of an MXER Tether Boost Station

Kirk F. Sorensen
Propulsion Research Center / TD40
NASA Marshall Space Flight Center, AL 35812
kirk.sorensen@msfc.nasa.gov

Momentum-exchange / electrodynamic reboost (MXER) tether systems show great promise for use in propellantless orbital transfer. In 1998, MSFC and Boeing conducted a simple, preliminary examination of the system requirements of a tether facility to boost payloads from LEO to GTO. Work conducted at MSFC and TUI over the last two years has updated and refined these results, and led to alternate configurations and concepts that show greater promise for successful utilization. Two appendices are included that detail analysis techniques and mathematical derivations that can be used in tether facility design.

Introduction

The development of tether technology has opened up an exciting new possibility for spacecraft—propellantless propulsion. Rockets push against their own exhaust, but an electrodynamic tether pushes against the Earth's magnetic field, and in essence, the Earth itself, to enable payloads to acquire higher-energy orbits.

A pure momentum-exchange (MX) tether does not create orbital energy; it only exchanges it. If it catches and throws a payload, its orbital energy will be reduced, and it will assume a lower orbit. Without reboost, it will soon lose too much orbital energy and enter the atmosphere and burn up.

Any type of propulsion system, in theory, could be used to reboost an MX tether. Chemical, nuclear, and electric are all options, but if any *rocket* reboost technologies are chosen, the MX tether will have a payload fraction that is governed by the specific impulse of the propulsion system, according to the rocket equation.

On the other hand, a pure electrodynamic (ED) tether is limited to the regions above the Earth where the ionosphere and magnetic field are relatively strong (<1000 km). It collects electrons from the ionosphere to flow current through its conductive tether¹. That tether acts like a wire moving through the field lines of the Earth's magnetic field; consequently a $\mathbf{J} \times \mathbf{B}$ force is exerted on the system. The ED tether can passively generate power (at the expense of orbital energy) or use a power supply to drive current through the tether and generate motive force (increasing orbital energy).

In theory, an ED tether could dock with a payload and slowly spiral up to a higher orbit, then release it and spiral back down. However, again the ED tether is limited to altitudes less than 1000 km, and achieves performance similar to other low-thrust, high-power propulsion systems that have very low thrust-to-weight ratios.

The MX and ED tethers, by themselves, do not achieve exceptional improvements in performance over existing technologies, but a hybrid of the two, the momentum-exchange/electrodynamic reboost (MXER) tether, may have capabilities far beyond either technology separately.

In principle, a rotating MXER tether in an elliptical orbit could catch a payload in a low Earth orbit, carry it for a single orbit, and then throw it into a higher energy orbit, all in a short period of time. It can then employ electrodynamic reboost over a period of weeks to restore the orbital energy it gave to the payload. Hence, the tether system can give a payload all of the performance and efficiency of a "high-thrust", impulsive orbit transfer, but slowly reboost itself using only electricity.

1998 Tether Transportation System (TTS) Study

In March 1998, a NASA study² was commissioned to assess the viability of a tether facility to boost payloads from low Earth orbit (LEO) to geosynchronous transfer orbit (GTO). The study also included participation from Boeing and the Smithsonian Astrophysical Observatory.

This material is declared a work of the US Government and is not subject to copyright protection in the United States.

The study considered both single-tether and multiple-tether designs to conduct the boost from LEO to GTO. Ultimately, it concluded that a two-tether design, with one tether in a 400 x 2019 km orbit and the other in a 434 x 25048 km, offered the lowest mass solution. The study also baselined high-Isp electric propulsion for orbital reboost, and thus necessitated refueling operations to replenish the exhausted propellant.

The astrodynamics in the study made the simplifying assumption of a spherical Earth, and thus did not assess the impact of the oblateness of the Earth, and the consequent nodal and apsidal regression of the tether orbits. This effect has dramatic consequences for tether design.

Progress since the TTS Study

Since the TTS study was conducted significant progress has been made at MSFC, Tethers Unlimited³, and Boeing in the design and analysis of MX tethers.

*Astrodynamic*s

More advanced astrodynamic analyses have been conducted on the MX tether concept. It was quickly seen that the assumption of a spherical Earth had inadvertently led to a nonviable tether design.

The oblate shape of the Earth causes changes in position of the line of nodes and line of apsides of an orbit.⁴ Specifically, the line of nodes (the line formed by the intersection of the orbital and equatorial planes) will rotate about the planetary rotational axis; the line of apsides (the line drawn between the apoapsis and periapsis of an orbit) will rotate about the angular momentum vector of the orbit.

Because nodal and apsidal regression are functions of orbital energy, eccentricity, and inclination, two spacecraft that have the same inclination but different eccentricities will soon become non-planar due to differential nodal regression, as illustrated in Figure 1. Hence, a tether system and a payload in a non-equatorial orbit will soon be out-of-plane with each other.

However, when an object is in an equatorial orbit around a planet, the planetary rotational axis and the angular momentum vector of the orbit will be collinear, and nodal and apsidal rotation will become coplanar. Hence, sustained nodal regression will not change the coplanarity of the tether and payload orbits if they are both equatorial.

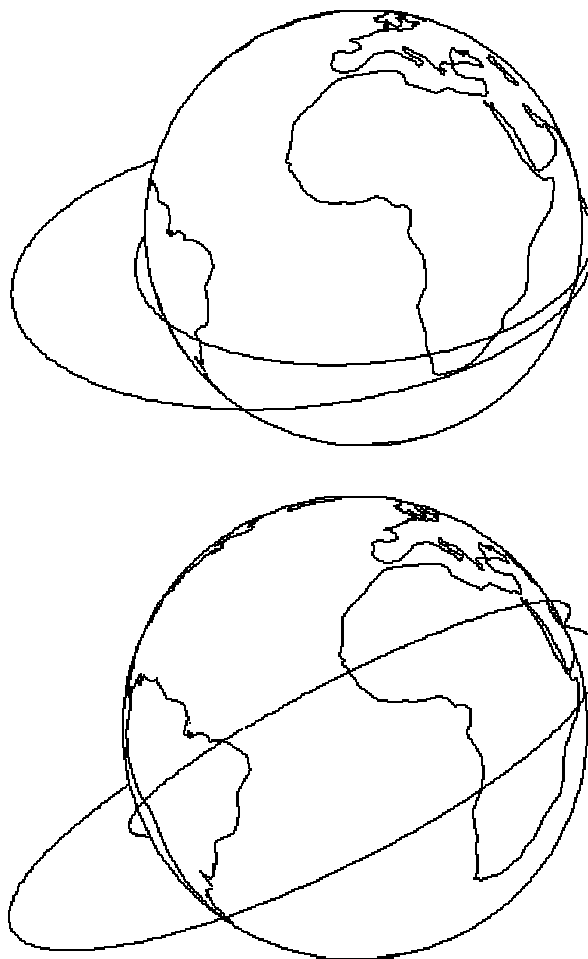


Figure 1: Two non-equatorial orbits, initially coplanar, will evolve differently due to differential nodal regression; 15 days later, they are decidedly non-planar.

While the equatorial orbit cures the problem of differential nodal regression, the differential rates of apsidal regression will soon doom a two-tether system like the one baselined in the TTS study. In that study, the orbital periods of the first and second tethers were configured so that they were integer multiples of each other; hence, if the payload was released by the first tether and missed being caught by the second tether, it would have another opportunity several orbits later. However, when the effect of apsidal regression is factored into the problem, it becomes clear that even for two tethers with resonant periods, two collinear lines-of-apsides will be an exceedingly rare occurrence.

The solution to this problem is to abandon the two-tether system. Although it has mass benefits relative to a single-tether system, **the reality is that it is astrodynamically nonviable.**

Multiple rendezvous opportunities exist for a single-tether system if the payload's orbit is further constrained to be a circular one. That way, the location of tether tip/payload contact can move in angular position around the payload's orbit as the line of apsides of the tether's orbit rotates.

Hence, astrodynamic reality drives the design from a two-tether system in an arbitrary inclination to a single tether in an elliptical equatorial orbit and a payload in a circular equatorial orbit. An extended derivation of the orbital requirements necessary to achieve repeated rendezvous attempts in these orbits is given in Appendix A.

Orbital Reboost

Another important advancement of tether design since the TTS study has been the pursuit of electrodynamic reboost of the tether station as opposed to propulsive reboost.

The TTS study baselined the use of high-Isp ion engines as the propulsive means of restoring orbital energy and angular momentum to the tether station that is lost during catch and throw operations. Use of propulsive reboost limits the performance of the tether station to the mass fractions governed by the rocket equation; although that the tether can deliver these impulses quickly and at an astrodynamically efficient location.

Concomitant with the use of propulsive reboost is the requirement to resupply the tether station with propellant at given intervals. This leads to rendezvous and docking requirements with the tether station that drive the design in directions that may not be ideal from an astrodynamic standpoint. For example, the TTS study settled on a tether configuration that located most of the tether mass at the CM of the tether facility, rather than utilizing that additional mass as endmass. Also, rendezvous and docking with a spinning tether in an elliptical orbit would definitely be beyond the capabilities of the space shuttle, and may require a dedicated transfer vehicle and automated rendezvous and docking capability.

As has been noted in the introduction, electrodynamic reboost, while less mature than propulsive reboost, offers a way to conceivably break the bands of the rocket equation altogether, and offer purely propellantless propulsion. It would involve weaving a length of conductive metallic tether into the structure of the strength tether. The electrodynamic tether would be designed so that its integrated force vector would be directed through the tether's CM.

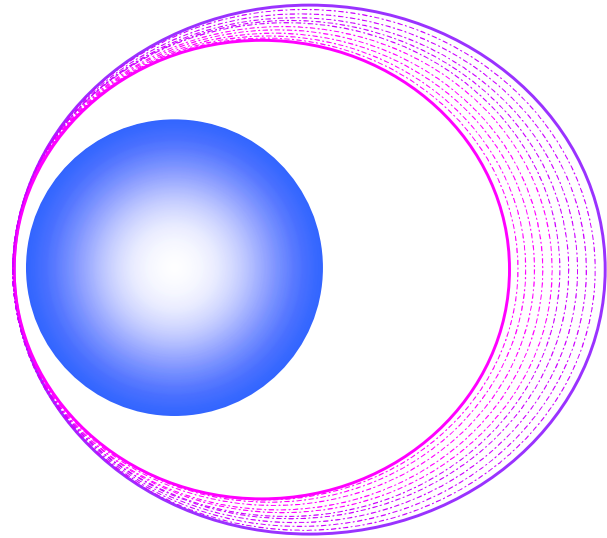


Figure 2: Electrodynamic reboost centered on an arc about perigee can be used to boost apogee and restore orbital energy.

By using solar power to drive electrical current through the electrodynamic tether on an arc centered about perigee, the apogee of the tether station could be reboosted slowly over a period of weeks, as shown in Figure 2. The orbital energy and angular momentum that had been transferred to the payload would be restored to the tether station. Effectively, the electrodynamic tether would move through the Earth's magnetic field in the same way that an armature moves through an magnetic field in an electric motor, and it would "push" against the magnetic field, transferring some of the Earth's rotational angular momentum to the tether station.

For those who might be squeamish about "slowing down the Earth", it should be noted that the amount of the Earth's rotational angular momentum transferred to the tether is *many, many orders of magnitude less* than the amount that is currently being transferred to the Moon's orbit through tidal action!

Electrodynamic tether propulsion is being pursued actively now at MSFC through the ProSEDS mission, which is scheduled to fly in late 2001. ProSEDS will demonstrate passive current flow through the tether that will slow down the orbit of the spacecraft and cause an accelerated reentry. ProSEDS and its follow-on missions will be our first steps in demonstrating that electrodynamic tether propulsion can be used to change orbits.

Tether/Payload Rendezvous

From the outset, it has been recognized that rendezvous between the tip of the tether and the payload *is the most significant problem in momentum-exchange tethers*. Perhaps a bit of perspective may enlighten the difficulty.

When orbital rendezvous takes place today between two spacecraft, they strive to match orbits with one another. In the simplest sense, it could be said that they strive to make their position, velocity, and acceleration vectors equal so that they can dock to one another. If one has ever watched the docking operations of the shuttle and space station, it is quickly seen that these docking operations, as they near their conclusion, take place exceedingly slowly and with extremely high precision, often with millimeters of positional error and millimeters per second of velocity error.

Tether/payload rendezvous is a completely different operation. If the tether and payload were to match orbits by matching position, velocity, and acceleration, there would be no momentum to exchange between them!

Therefore, tether/payload rendezvous is based around the concept of matching the position and velocity of the tether tip and the payload at one point in time and space. Acceleration is NOT matched. This is accomplished by setting the angular rotation rate of the tether such that the tether tip velocity is the difference between the orbital velocity of tether CM and the payload. A simpler way to express this concept is to imagine the tether like a wheel, rolling around the orbit of the payload, and the tip of the tether like a point on the wheel, making contact with the payload for an instant of time.

Another way to imagine tether/payload rendezvous is to imagine working on the roof of a house on a hot Saturday. You call down to someone to throw you up a drink. They do so, and the drink rises quickly while decelerating, and comes to a stop right before your eyes for a moment. It has the same position and velocity as you, but different acceleration. You reach out and grab the drink at that instant or else it will fall back down to the ground. Similarly, from the perspective of the payload, the tether tip descends rapidly from above, comes to a stop, and then ascends rapidly. During that moment of zero relative velocity, contact must be made between the tether tip and payload.

So while conventional orbital rendezvous takes place over a long period of time at very low relative velocity, tether/payload rendezvous must happen nearly

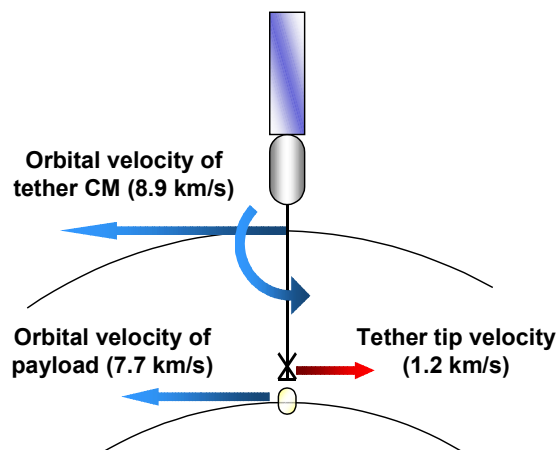


Figure 3: The tip velocity of the tether is configured to be equal to the difference in orbital velocity between the tether and payload, enabling them to match position and velocity instantaneously.

instantaneously, and must be tolerant of significant position and velocity errors. An excellent animation of tether/payload rendezvous is available on the Tethers Unlimited website at:

<http://www.tethers.com/LEO2GTO.mov>

Therefore, using conventional rendezvous techniques for tether rendezvous is of limited utility. They don't work fast enough, with enough error tolerance, to be useful. But it should also be remembered that the requirements for tether/payload are different than for shuttle/station rendezvous. There is no need for a hard docking; they just need to hold on to each other long enough for the tether to transfer significant momentum to the payload before it is released.

The payload capture mechanisms that have been developed at MSFC over the past year are based around this concept. They are tolerant of several meters of positional error and nearly a meter per second of velocity error. They are designed to work very quickly, be very lightweight, and to collapse to a structurally efficient configuration upon payload capture. They are designed to be essentially passive and require no propellant replenishment, power, or active control. They may also have the added benefit of reducing the intensity of the payload capture maneuver on the tension of the tether.

Currently, Tennessee Tech University, under contract to MSFC, is researching the mechanical properties of these payload capture mechanisms and will be conducting preliminary ground testing in the summer of 2001.

Tether Station Configuration

Advancements in the configuration and design of tether boost stations have been made since the TTS study. During the summer of 2000, research into advanced lunar and Mars missions led to an effort to design a tether facility that could accommodate those mission requirements. Several configuration innovations were identified during that design cycle that were later applied to the design of a smaller tether facility for boosting communications satellites from LEO to GTO.

For the lunar/Mars boost station, the following were technology drivers:

- Due to the large initial mass of the station (200 MT), the design had to be modular and capable of increased capacity over its design life.
- All elements were designed to fit within the mass and volume constraints of a hypothetical second-generation launch vehicle. (15m long, 5m diameter cylinder, 20 MT to a 400 x 400 km orbit)
- The station had to be capable of truly propellantless electrodynamic reboost. (i.e. no consumables)
- Due to the relatively short orbital arc through which electrodynamic reboost was feasible, the station needed substantial energy storage capability.
- Access between the payload/tether tip and the central station was highly desirable.

Based on these requirements, an innovative configuration was developed, shown in Figure 4. It consisted of a central, “backbone” ballast tank, that could be filled with water as the station grew in mass. The tank could be launched in a single launch and would serve as the structural hub of the tether station. Its integrated truss structure would accept flywheels (for energy storage) and tether reels, each sized for the capacity of the launch vehicle.

The facility would be designed to be assembled on orbit and have a gross mass of 200 MT at completion, most of which would be the mass of the tether still wound on their spools. Of the eight tether spools, only two would be deployed initially, giving the tether facility an initial payload capacity of 20 MT. This payload capacity would be sufficient to support early human missions to the lunar surface. The remainder of the tether spools would remain undeployed and serve as ballast mass.

It was envisioned that as round-trip traffic between the lunar surface and LEO grew, returning lunar spacecraft would exchange their payloads on the lunar surface for ballast mass, most likely water. This water would be acquired at the tip of the tether and then transported by

means of the tether climber. At the central station, this water would be used to fill the ballast tank.

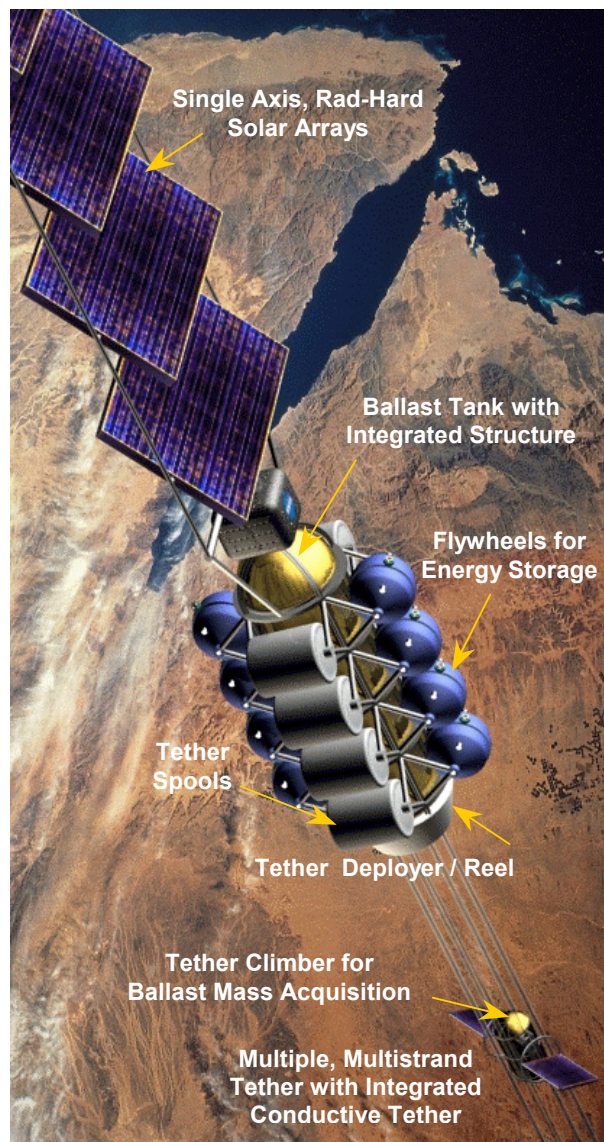


Figure 4: Conceptual configuration of a modular tether station demonstrating power collection, energy storage, staged tether deployment, and allocation for ballast mass collection.

After a number of missions, the ballast tank would reach its full capacity of 200 MT, and the remainder of the tether would be deployed (with the assistance of the tether climber). At this stage, the total mass of the tether facility would reach 600 MT and the station would reach its final payload capacity of 80 MT. This payload capacity would be sufficient to support significant human Mars mission efforts, as well as larger scale lunar exploration.

Conclusion

Significant progress on the astrodynamics, orbital reboost, payload/tether rendezvous, and configuration have been achieved since the MSFC/Boeing Tether Transportation System study of 1998. Significant changes to the baseline design since the TTS study include:

- Single tether facility in an equatorial, elliptical orbit instead of two tether facilities
- Propellantless electrodynamic reboost instead of high specific-impulse electric propulsion
- Design and development of payload catch mechanisms with significant margin for position and velocity error
- A modular, upgradable tether facility configuration that concentrates mass at the endmass rather than the center of mass of the tether system

Acknowledgements

Dr. Robert Hoyt and Dr. Robert Forward of Tethers Unlimited have done tremendous work improving the state of the art in tether design; collaborations with them have been very valuable. Leroy Allen of Media Fusion was an integral part of the design of the tether configuration presented herein and generated all the visualizations. I would like to especially thank Les Johnson, Jonathan Jones, and Charles Schafer of MSFC for support, new ideas, and lots of patience. And thanks to my wife, Quincy Sorensen, for inadvertently inventing the payload catch mechanism.

References

1. Johnson, C., et al., *Electrodynamic Tethers for Spacecraft Propulsion*. AIAA 98-0983.
2. Bangham, M.E., Lorenzini, E., Vestal, L., *Tether Transportation System Study*. NASA TP-1998-206959, 1998, pp. 7-2, 7-3.
3. Hoyt, R., and Uphoff, C., *Cislunar Tether Transportation System*. AIAA 99-2690.
4. Vallado, D. *Fundamentals of Astrodynamics and Applications*, McGraw Hill, 1997.
5. Bate, R., Mueller, D., White, J. *Fundamentals of Astrodynamics*, Dover Publications, 1971.
6. Bogar, Thomas, et al., *Hypersonic Airplane Space Tether Orbital Launch (HASTOL) System: Interim Study Results*. AIAA 99-4802.
7. Moravec, Hans. "A Non-Synchronous Orbital Skyhook," *Journal of the Astronautical Sciences*, Vol. 25, No. 4, pp 307-322, October-December 1977.
8. Moravec, Hans. "Non-Synchronous Orbital Skyhook for the Moon and Mars with Conventional Materials," unpublished paper, 1978. (available at <http://www.frc.ri.cmu.edu/users/hpm/>)

Appendix A

Basic Tether Orbital Design Principles

This appendix will detail the basic astrodynamics principles used in the design of a MXER tether facility; it will defer detailed analysis of the electrodynamic reboost to a future paper.

Basic, intermediate, and “advanced” levels of analysis will be presented, as well as a technique for achieving a resonant orbit (multiple catch opportunities) between the payload and the tether while still accounting for the secular effects of Earth’s gravitational zonal harmonics (J2, J4, J6). It is hoped that these principles, or variations on them, will be of use to those attempting to design momentum-exchange tether facilities.

Basic Orbital Analysis

Several assumptions are useful when beginning the analysis of an MXER tether. The first assumption is that the tether station has an infinitely massive endmass and a negligible tether mass. This means that the center of mass of the tether/payload system will not shift when payloads are caught and released. This in turn will mean that the rotational moment arm of the tether will not change in length. It will be seen that the movement of the center of mass of the payload/tether system is what governs the momentum exchange inherent in tether orbital transfer.

Another useful assumption is that the tether is always in the proper phase. In other words, when the tether is catching payloads, one can assume it is on the downswing (hanging down relative to the local horizontal), and when the tether is throwing payloads, it is on the upswing (hanging up relative to the local horizontal). Additionally, it is assumed that all these operations take place at the perigee of the tether station’s orbit.

As the model becomes more refined, it is possible to remove certain simplifying assumptions (infinite mass) and assure others (proper phasing).

The payload begins in a circular orbit; assume 400 km altitude, for instance. Then assume that the tether is 100 km long. Because of the assumption of infinite endmass, this means that the rotational moment arm on the tether is also 100 km long.

The circular orbital velocity of the payload can be calculated⁵ from the following equation (which for 400 km leads to an orbital velocity of 7.67 km/s):

$$v_{circ} = \sqrt{\frac{\mu}{r}}$$

Next, the ΔV required to achieve the desired orbit must be known. Three logical destinations for payloads thrown by a tether would be geosynchronous transfer orbit (GTO) for communications satellites, a 48-hr, pre-escape orbit for planetary spacecraft using high-thrust propulsion, or a trans-lunar injection (TLI) for lunar missions and planetary spacecraft using low-thrust propulsion.

LEO (400x400) to GTO (400x36000 km)	2400 m/s
LEO (400x400) to 48hr (400x120700 km)	2900 m/s
LEO (400x400) to TLI (400x384400 km)	3100 m/s

The desired tether tip velocity will roughly be $\frac{1}{2}$ of the ΔV to be imparted to the payload. For a throw into a trans-lunar trajectory, assume a total ΔV of 3 km/s. Divided into two phases (catch and throw) gives a tether tip velocity of 1.5 km/s.

Since the tether’s tip will have to be at the same position and velocity of the payload, it can be assumed that the center of mass (CM) of the tether should be moving 1.5 km/s faster than the payload. Hence, the tether’s CM is at an altitude of 500 km (400 km + 100 km) and a velocity of 9.2 km/s (7.7 km/s + 1.5 km/s). These values will yield a preliminary apogee for the tether CM. Note that these values are obviously incorrect, but they are good approximations.

Using the following equations⁵:

$$\mathcal{E}_{MXER} = \frac{v^2}{2} - \frac{\mu}{r}$$

yields a specific mechanical energy of $-16.0 \text{ km}^2/\text{s}^2$. Semi-major axis and apogee can then be calculated, and the apogee comes out as 11,620 km altitude.

This apogee value can then serve as an input to the spreadsheet tether model. Experience has shown that it is better to set up the spreadsheet using the following independent variables:

- Circular orbital altitude of the payload
- Tether length
- Apogee of the tether CM

By constraining the perigee of the MXER tether according to the tether length and the payload’s orbit, and then varying the apogee so as to target the DV

requirement, the system is more easily optimized for other, more subtle constraints.

Acceleration on the payload is a function of the tether tip velocity and the tether length. If the tip acceleration exceeds an acceptable value, the tether length can be increased. This will reduce tip acceleration while maintaining tether tip velocity. Conversely, if tip acceleration is low, the tether length can be reduced in order to reduce the susceptibility of the tether to damage or debris. As will be shown, tether mass is *not* a function of tether length, but of tether tip velocity.

Intermediate Orbital Analysis of Momentum Exchange

In the basic stage of analysis, the tether station loses no altitude for each catch and throw because an infinite ballast mass has been assumed. This can be changed by entering mass values for the endmass and the tether. Now the moment arm of the tether will no longer be the tether length; it will instead be the distance from the CM of the tether station to the payload.

The location of the CM will be critical for further calculations of orbital mechanics, because as the tether catches and throws payloads, the CM moves up and down the length of the tether. The propagation of the position and velocity of the CM is what determines how much the tether orbit drops during catching and throwing maneuvers. This will become more clear as the analysis proceeds.

To begin with, guess a value for the endmass. Typical values are 5-8x the mass of the payload, although no answer is the “right” answer. In theory, tether stations could be defined with no endmass at all!

The next step is to calculate the mass of the tether itself. In an unpublished work, Hans Moravec^{7,8} derived the

mass of a spinning tether in free space. This equation gives the ratio of the mass of the payload and the mass of the tether as a function of tether tip velocity and tether material:

$$MR = \frac{m_{tether}}{m_{tip}} = \sqrt{\pi}(VR)\exp(VR^2)\operatorname{erf}(VR)$$

In this equation, VR is the velocity ratio and is defined as the tip velocity of the tether divided by the characteristic velocity V_c of the tether material, which is further defined by the following equation.

$$V_c = \sqrt{\frac{2T}{Fd}}$$

T is the tensile strength of the tether material; d is the material density, and F is a safety factor. A safety factor of 3 is assumed in all these calculations. Characteristic velocity can be thought of as a specific tensile strength. Erf is the Gaussian error function.

Further examination of the tether mass ratio equation shows that it is only a function of one variable: the velocity ratio. The exponential dependence of the tether mass on the *square* of the velocity ratio can result in a very large increase in tether mass for a given tip velocity. Hence, it is critical to choose a material with as high a characteristic velocity as possible.

The table below⁶ shows that Spectra 2000 has the best characteristic velocity of any material in existence. Spectra 2000 is a form of highly oriented polyethylene manufactured by AlliedSignal. It is currently mass-produced as fishing line, and sold under the brand name Spiderwire[®].

Assuming the use of Spectra 2000 as the tether material with a safety factor of 3, the mass ratios between the

material	Vc (km/s)	density	20 C	300 C	600 C	800 C	1000 C	1200 C
Spectra 2000	1.658	970	4.0					
Carbon	1.599	1800	6.9					
Zylon (PBO)	1.574	1560	5.8	3.7				
Textron beta-SiC	1.262	2930	7.0	6.6	6.0	5.6	5.2	4.5
Carbon/Ni-coated	1.222	2680	6.0					
S-glass	1.120	2500	4.7					
Quartz Glass (SiO ₂)	1.044	2200	3.6	3.6	3.6	3.6	3.6	
0.72 beta-SiC/Ti-coate	0.995	3370	5.0	4.8	4.3	4.0	3.7	3.2
Tyranno (SiTiCO)	0.957	2550	3.5	3.5	3.5	3.5	3.5	3.5
Nextel (alpha-Al ₂ O ₃)	0.753	3880	3.3					
Altex (Al ₂ O ₃ /SiO ₂)	0.696	3300	2.4	2.4	2.4	2.4	2.4	1.5
0.65 Nextel/Al-coated	0.560	3400	1.6	1.4				
Tungsten Wire	0.316	19350	2.9	2.9	2.9	2.9	2.9	2.9

tether and payload for the following tip velocities are:

1200 m/s tip velocity (LEO to GTO)	1.50
1500 m/s tip velocity (LEO to TLI)	2.86

Hence, a tether to throw a payload to trans-lunar injection must have nearly 3 times the mass of the payload it is throwing.

Using the center of mass of the tether, the endmass, and the payload, it is possible to calculate a CM for the system, both before and after catching the payload.

Another important realization is that the tether station's rotational rate remains constant during catching and throwing of payloads. This statement seems counterintuitive, but because the payload has the velocity appropriate for its position on the tether, the rotation rate remains unchanged. This can also be examined in the framework of angular momentum.

$$H = I\omega$$

Although the moment of inertia of the tether station increases when the payload is caught on the end, the total angular momentum of the station increases commensurately, and the angular rate remains constant.

After catching a payload, the CM of the tether station will move to a location much closer to the payload. Recall that the CM location is the only point on the tether that follows a Keplerian orbit. This means that right before catching, the new CM location was in a *non-Keplerian* orbit, with a position and velocity (relative to the center of the Earth) that is quite different than the original CM.

To understand what the tether station's new orbit will be, the new CM's position and velocity must be used to propagate a new orbit. This new orbit will have less orbital energy than the previous orbit. The tether station has lifted the payload from a lower energy state to a higher one, at the expense of its own orbital energy. A similar process takes place when the payload is thrown, and the tether station drops to an even lower orbital energy. This is the heart of the concept of momentum exchange.

Advanced Orbital Analysis of Momentum Exchange: Establishing a Resonant, Repeating Orbit

As has been mentioned, the iterative nature of MXER tether design lends itself well to implementation in a spreadsheet. A spreadsheet was developed in MS Excel to enable the orbital parameters of the tether station and

payload to be determined accurately and changed rapidly. The iterative capabilities of Excel enable equations that encompass circular references to be solved quickly and accurately. For instance, the mass of the tether is a function of the tether tip velocity, which is a function of the distance from the center of mass of the tether station, which is a function of the mass of the tether, and so forth.

An important consideration when considering a capture operation between a tether and its payload is the possibility it might fail. In such a case, the simplest way to recover from the failure is to configure the orbits so that they will meet again at a future time.

In a real-world mission scenario, many perturbative effects must be considered and modeled in order to accurately propagate an orbit:

- Non-ideal mass distribution of the Earth
- Lunar and solar perturbations
- Atmospheric drag effects
- Ionospheric and magnetic interactions with the spacecraft
- Solar radiation pressure

In this analysis, the only perturbative effect considered is the first gravitational harmonic of the Earth, often referred to as J_2 . J_2 models the oblateness of the Earth, and it induces both secular (constant) and sinusoidal changes in three of the orbital elements of a spacecraft.

For a spacecraft in an equatorial elliptical orbit, the secular rate of change⁴ in the longitude of the ascending node is given by the equation:

$$\dot{\Omega} = -\frac{3}{2}J_2 \frac{R_{\oplus}^2}{p^2} \bar{n}$$

Similarly, the secular rate of change of the argument of periapsis is given by:

$$\dot{\omega} = 3J_2 \frac{R_{\oplus}^2}{p^2} \bar{n}$$

The rate of the change of the initial value for mean anomaly is given by:

$$\dot{M}_o = -\frac{3}{2}J_2 \frac{R_{\oplus}^2}{p^2} n\sqrt{1-e^2}$$

Since the initial value of mean anomaly is being shifted on each orbit, an accessory definition to orbital period

and mean motion is necessary. For example, because of perturbations, one orbital period no longer defines the time that the spacecraft takes to go from periapsis to periapsis; instead it takes a little longer, as shown in Figure A-1.

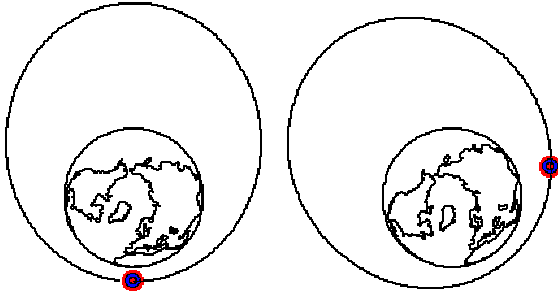


Figure A-1: The periapsis position is not reached after each orbital period due to perturbations. This shift must be accommodated for in calculations of the perturbed orbit.

The actual time between periapsis passages can be calculated from the following equation:

$$p' = \frac{2\pi}{\bar{n}}$$

While the difference between the orbital period of such a satellite and the time between periapsis passages may only amount to a few seconds, a few seconds for a tether travelling at 9 km/s will mean that the tether misses the payload by many tens of kilometers.

Mean motion is defined as the average angular distance (in radians) a spacecraft travels each second:

$$n = \sqrt{\frac{\mu}{a^3}}$$

The “mean” mean motion is defined as the mean motion minus the change in the initial value of mean anomaly:

$$\bar{n} = n - \dot{M}_0$$

This “mean” mean motion is used in calculating the rates of change in ascending node and apsidal location.

A resonant orbit can be defined between a tether in an elliptical equatorial orbit and a payload in a circular equatorial orbit by solving the following equality:

$$mp'_2(\dot{\Omega}_1 + \dot{\omega}_1 + \bar{n}_1) - \ell(2\pi) = mp'_2(\dot{\Omega}_2 + \dot{\omega}_2)$$

In this equality, m and ℓ represent the resonance ratio. For instance, if the payload completes 3 orbits for every 1 orbit of the tether station, m=3 and ℓ =1.

Although this is a highly implicit equation, every variable term within it can be boiled down to four numbers, the perigee and apogee of the payload and tether. Further analysis shows that if the payload is in a circular orbit, its perigee and apogee will be the same, and if the tether is designed to catch the payload, the perigee of its CM will simply be the payload’s perigee plus the tether arm length. This leaves only the tether’s apogee to be solved, and the iteration features of Excel solve it quickly.

A spreadsheet that incorporates all these features in it has been developed and is available upon request to those who wish to conduct their own analyses. Please contact the author at kirk.sorensen@msfc.nasa.gov.

Appendix B

Techniques for Tether Mass Property Evaluation

Characteristic velocity is:

$$v_c = \sqrt{\frac{2T}{fd}}$$

Dividing tip velocity by characteristic velocity yields a velocity ratio:

$$VR = \frac{v_{tip}}{v_c}$$

In Moravec's derivation⁷ of the mass of a tapering tether, he made several simplifying assumptions to enable the equation to be integrated.

- A uniform tether with uniform properties.
- A tether that connects two equal endmasses; hence, the center of mass of the system would be at the center of the tether.
- Centrifugal accelerations only (no gravitational interaction).

His equation for tether area as a function of radius (from the center of rotation of the system) is:

$$A(r) = \frac{m_{tip} v_{tip}^2 f}{\ell \tau} \exp\left(VR^2 \left(1 - \frac{r^2}{\ell^2}\right)\right)$$

The area of the tether at the center of rotation ($r = 0$) is:

$$A(r) = \frac{m_{tip} v_{tip}^2 f}{\ell \tau} \exp(VR^2)$$

Similarly, the area of the tether at the tip ($r = \ell$) is:

$$A(r) = \frac{m_{tip} v_{tip}^2 f}{\ell \tau}$$

This can be integrated in the form:

$$m_{tether} = \rho \int_0^{\ell} A(r) dr$$

The mass ratio is:

$$MR = \frac{m_{tether}}{m_{tip}} = \sqrt{\pi}(VR) \exp(VR^2) \operatorname{erf}(VR)$$

Since any terms containing reference to the length of the tether have dropped out of the expression, we can conclude that the mass of the tether is a function only of the mass at the tether tip, and the velocity ratio. Unfortunately, it is a function of the exponential of velocity ratio squared, which means that the tether mass will grow very quickly for increasing tip velocities.

In order to derive the center-of-mass of the tether segment, each differential mass element must be multiplied by its distance from the center of rotation. The result is then divided by the overall mass.

$$CM = \frac{\rho \int_0^{\ell} A(r) r dr}{\rho \int_0^{\ell} A(r) dr} = \frac{\rho \int_0^{\ell} A(r) r dr}{m_{tip} (MR)}$$

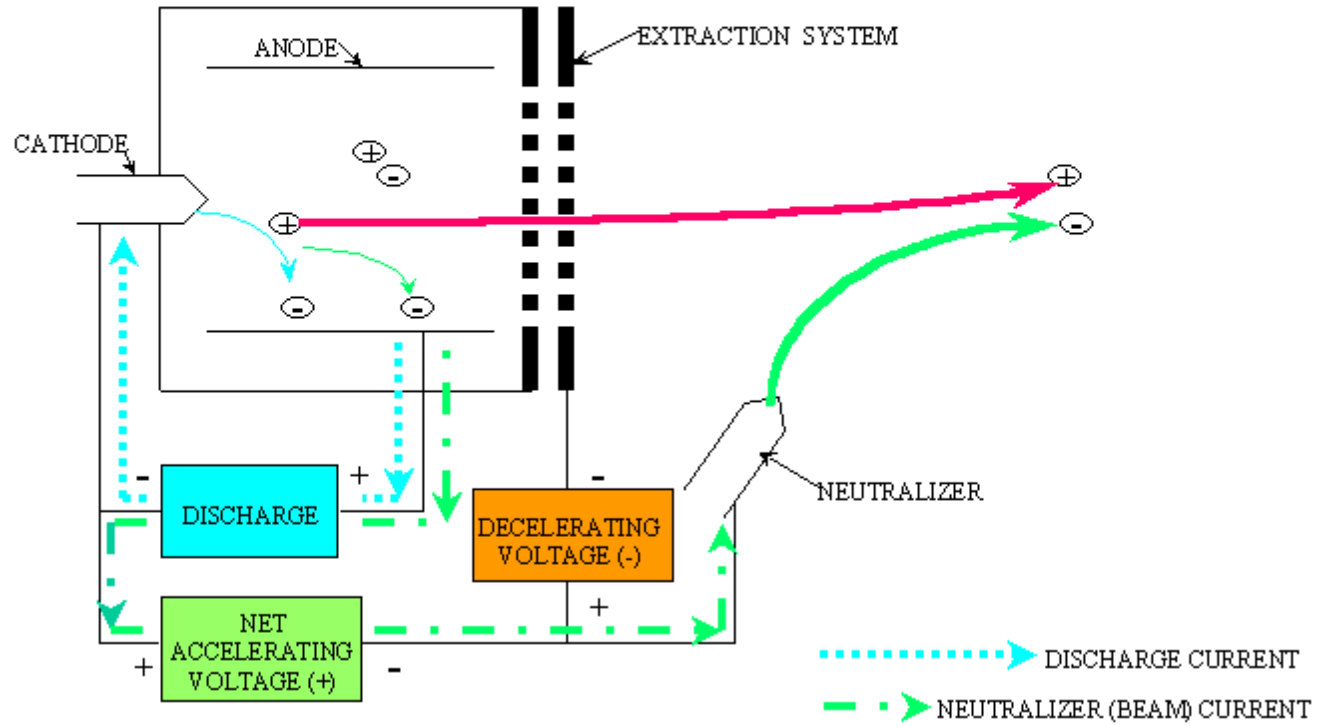
After integration and simplification, this yields:

$$CM = \frac{\ell}{MR} [\exp(VR^2) - 1]$$

Hence, it can be clearly seen that the location of the center-of-mass of the tether segment is essentially only a function of velocity ratio and segment length. This interesting result means that the properties of the tether are quite independent of tether geometry.

ION PROPULSION

BASIC OPERATION OF ION THRUSTER



Ion & Hall Effect Thruster Systems.

Potential Mission Applications

Space missions are characterized by a term “Delta Velocity” (or Delta V), which is a convenient measure of propulsion requirements. Mission Delta V’s increase as propulsion requirements become more demanding, as, for example, when mission durations or target distances from the Earth increase. The fundamental performance expectation of a space mission, regardless of propulsion type, is specified by the “Rocket Equation”, which relates the ratio of final to initial masses to the ratio of the Delta V to the specific impulse, which is proportional to the propellant velocity. The final mass contains the payload and additional masses required to operate the propulsion system and it is **generally** desirable to achieve as high a final mass as practical. The Rocket Equation is shown in Figure 1 and illustrates the fact that as Delta V increases, it is necessary to increase the specific impulse in order to maintain a given mass ratio. The Rocket Equation, see Figure 1 below,

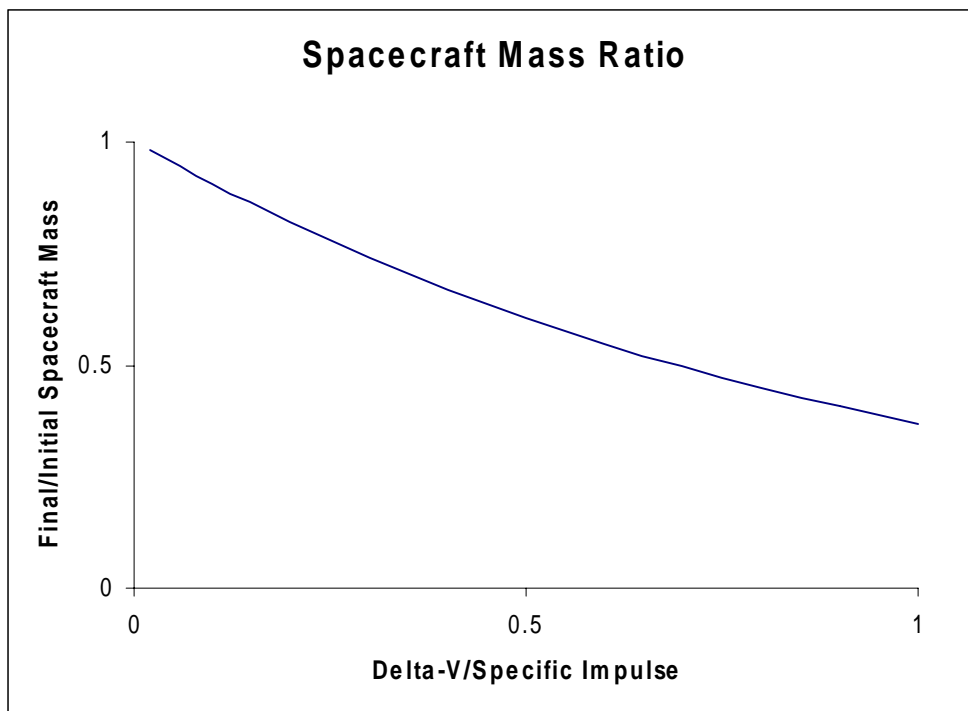


Figure 1

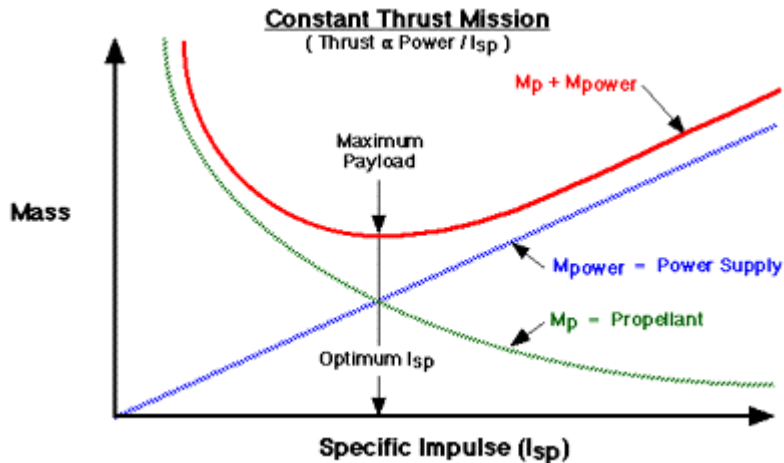


Figure 2

suggests that the optimum mission performance would always occur at the highest possible specific impulse. The practical situation is more complex, however, and is illustrated in Figure 2 above, which shows, for a mission with a given Delta V, the trends, as a function of specific impulse, of the masses of propellant and power subsystems associated with an electric propulsion system. The propellant mass drops monotonically with increasing specific impulse, as predicted from the Rocket Equation. However, the power, and associated mass, required to achieve desired thrust, hence acceleration, levels increases directly with the specific impulse. This basically occurs because the thrust and power increase, respectively, directly and as the square of the specific impulse. The trends shown on Figure 2 then imply that for a given mission there is a specific impulse that minimizes the total mass of the electric propulsion system (which is closely approximated by the sum of the power and propellant masses). At that minimum, the mission payload is maximized and electric propulsion concepts are typically chosen that operate at or near the optimum specific impulses for a given mission. It is important to note that the optimum specific impulse tends to increase both with increasing mission Delta V (as suggested by Figure 1) and with decreasing specific mass (the ratio of total mass to power level) of the spacecraft. This helps explain the increasing interest in electric propulsion as more difficult missions are of interest and as the mass of spacecraft subsystems, such as power, structure and thermal control, have continued to decrease.

Electric propulsion offers specific impulses far greater than theoretically achievable with chemical propulsion but cannot practically achieve the thrust, or acceleration, levels associated with chemical propulsion. These characteristics imply that electric propulsion offers significant benefits for difficult space applications that do not require high accelerations (which are necessary in multiple situations including Earth launch, planetary ascent propulsion, and rapid deceleration maneuvers). The payload benefits of electric propulsion have been quantified for many mission types. Figure 3, below, compares the performance of chemical and electric propulsion (when operated near the optimum specific impulse described above) for typical Earth orbit transfer, outer-planetary, and interstellar missions. It is seen that electric propulsion benefits range from major

increases to outright enablement of payload masses, with the payload benefit increasing with mission difficulty. The comparative trip times required for chemical and electric propulsion are extremely mission-specific. It is typical, however, that as the mission Delta Vs increase electric propulsion trip times vary from longer to shorter than those for chemical propulsion.

Payload Mass Fraction

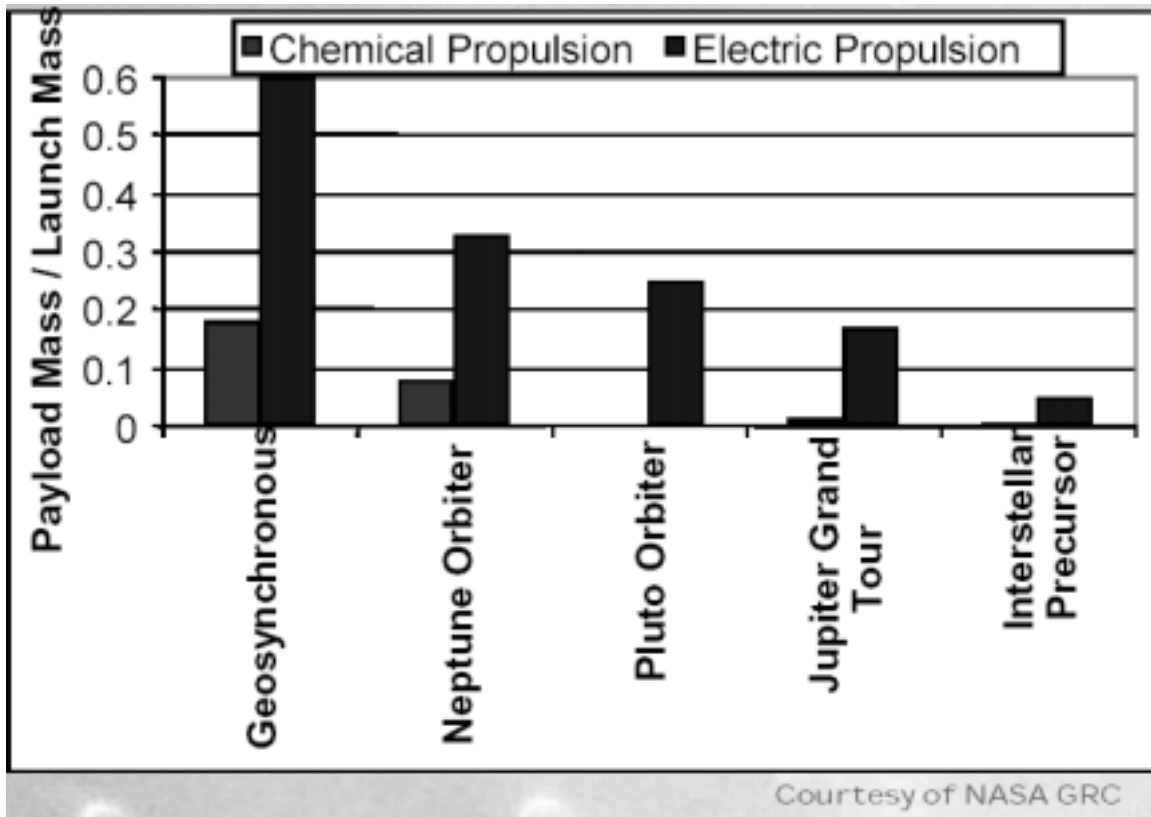


Figure 3

The functional elements of all electric propulsion systems are similar and are shown below on Figure 4. Power is made available from some source. At present electric propulsion systems derive power from photovoltaic arrays but plans are underway to also use fission nuclear power sources for outer planetary mission where the available solar power is too low. In the further future, alternate power options such as beamed energy and fusion power may become available for use with electric propulsion. This flexibility with respect to power source makes electric propulsion a candidate for a great range of mission applications and the significant and on-going improvements in the specific mass of power subsystems has been a major factor in the acceptance of electric propulsion.

Propellant is also stored on-board the spacecraft. At present, most electric propulsion systems use xenon as a propellant, but other options are being considered as the application space increases. The power is used to ionize and accelerate the propellant, via a variety of methods (see the Fundamental Physics section) to produce the desired thrust.

Electric Propulsion System

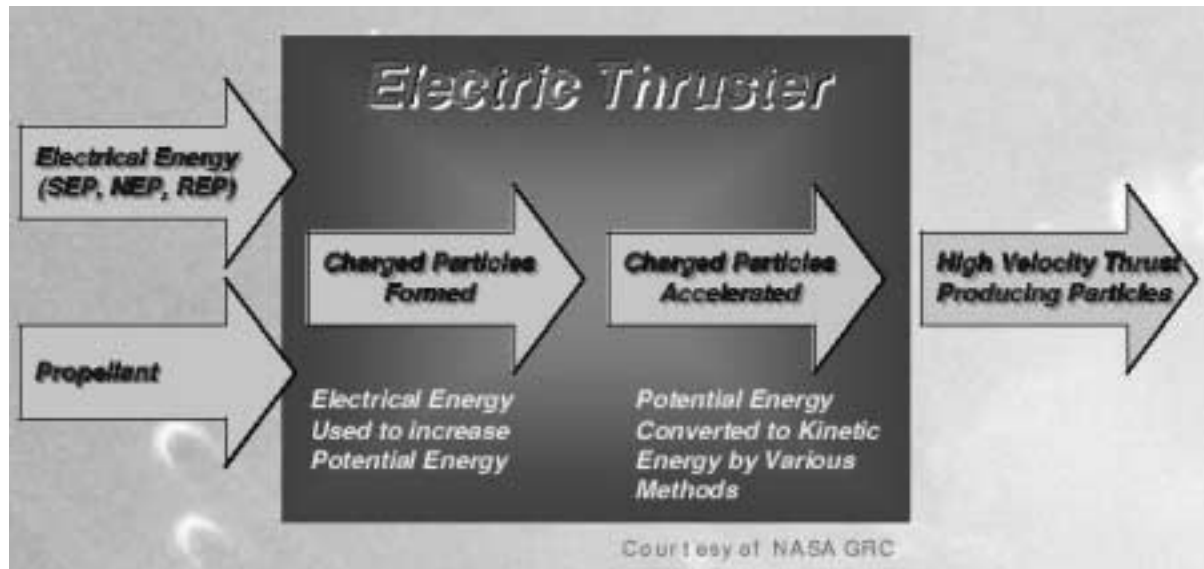


Figure 4

Ion and Hall Effect Thruster (HET) subsystems are now being routinely used for stationkeeping of geosynchronous orbit (GEO) spacecraft of many countries. Application of low power (~ 3 kW) ion propulsion for primary (prime mover) functions has begun with the successful DS-1 mission and insertion of spacecraft into GEO. Ion and HET concepts offer different operating regimes, as illustrated on Figure 5 below, which shows the ratio of thrust to power for several electric propulsion concepts over their range of specific impulse; they have been extensively demonstrated. It is seen that HET's operate from about 1500 to 2500 seconds and ion thrusters tend to operate at specific impulses greater than 3000 seconds. These different operating regimes are due to the quite different physics of the ion and HET subsystems and while attempts are underway to expand the operating range of both concepts, the relative relationship of the operating ranges is expected to remain as shown in Figure 5. For that reason, HET subsystems will tend to be optimum for missions with lower Delta Vs than those most strongly benefited by ion propulsion. (It is important to note that the final choice of a propulsion subsystem may depend on considerations other than payload, but only mission performance is considered herein). As a practical matter, HETs tend to have specific impulses that provide a highly desirable combination of increased payload and trip times for Earth-orbit transfer missions, which have Delta Vs of order 6000 meters/second for a transfer from Low Earth

Orbit (LEO) to GEO. On the other hand, planetary missions tend to have significantly (>2X) higher Delta Vs than Earth orbit transfer applications and, therefore, ion propulsion is generally the concept of choice for those uses. Based on the extremely successful applications of ion and HET propulsion, it is anticipated that both concepts will find extensive and increasing use for high-energy scientific and other space missions.

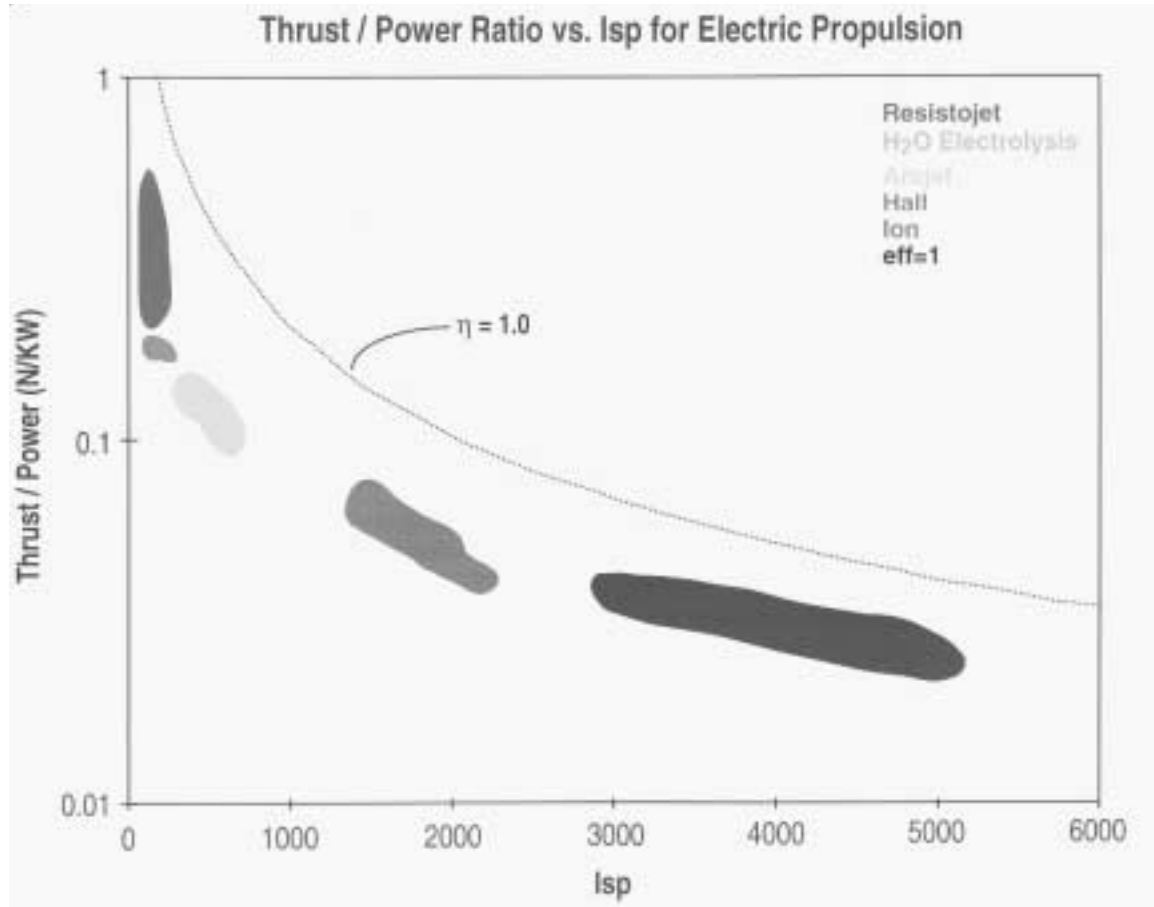


Figure 5

SEP Fundamental Physics

The purpose of any propulsion device, whether chemical or electric, is to provide the impulse required by the particular mission to the vehicle. This impulse is simply the product of the thrust and the time the thrust is applied:

$$I_{\text{tot}} = T \times t \quad (1)$$

One figure of merit of a thruster is how much impulse can be gained from one pound of propellant; something of a fuel efficiency. This is referred to as the specific impulse, defined as

$$I_{\text{sp}} = (T \times t) / (M_o \times g) \quad (2)$$

Where M_o is the initial mass of the propellant and g is the gravitational constant. Since the thrust is mass times the acceleration of the jet exhaust,

$$I_{\text{sp}} = (M_o \times a \times t) / (M_o \times g) = v_J / g \quad (3)$$

Thus, the higher the exhaust jet velocity, the more efficient the thruster.

The exhaust jet velocity is a function of the potential energy converted to kinetic energy by the thrust system. For a chemical rocket, the total energy available is stored in the internal energy of the propellant. This energy is then converted to the kinetic energy of the exhaust jet by a chemical reaction involving the propellant and an oxidizer. For an electric system, the energy comes from a source external to the thruster and propellant, is converted and conditioned to the proper form of electrical energy, and then used to accelerate the propellant.

[Insert Figure 1]

If U is the stored internal energy density of the chemical propellants, the total energy available is

$$U \times M_o = \frac{1}{2} M_o v_J^2 \text{ and } v_J \text{ is a function of } U \text{ only.}$$

Clearly the only way to add energy to a chemical system is to add propellant which does not improve the I_{sp} since it does not increase the exhaust velocity. Electric systems do not have this limitation. For example, an electric system, which accelerates ions through an electric field, called an electrostatic thruster, has energy available of

$$eV = \frac{1}{2} m v_J^2$$

where e is the charge of the ion (usually the electronic charge), and m is the mass of the ion. Therefore for the electrostatic system v_j is a function of the square root of the charge to mass ratio of the accelerated ion. This value is generally on order of 10^3 . As a result, the electrostatic thruster inherently has an I_{sp} of thousands of seconds whereas a chemical system is inherently limited to several hundreds of seconds. Comparison of the state of the art Electrostatic Thruster System and a Centaur Upper Stage System is shown in Table I shown below.

There are some trade offs however for the higher I_{sp} of electric systems. Even though the weight of the propellant can be reduced, some of this savings is offset by the weight of the electric power conversion and conditioning subsystems. If these subsystems are not very efficient, they can quickly eliminate any weight savings at the system level. The basic equation for efficiency of any thrust system is

$$\text{Eff} = T^2 / (2 \times \dot{m} \times P) = T / (2P) \times (T \times t) / M_o \quad (4)$$

where \dot{m} is the total propellant flow rate and P is the electrical power used by the system. Combining equations (3) and (4) shows that

$$\text{Eff} \times 2/g = T/P \times I_{sp} \quad (5)$$

Therefore, for a given amount of electrical power, thrust must be given up to increase the I_{sp} and reduce propellant mass. This in turn requires a longer thrust time to deliver the total impulse capability of the system. This can be seen in the comparison in Table 1. Electric propulsion can be used only for missions, which provide enough flight time to allow the total impulse to be delivered. This is why electric propulsion is of great interest for interplanetary missions, non-time critical orbit raising missions, and on-orbit station keeping. The savings in propellant weight also make electric propulsion attractive for missions, which require thrust maneuvers at the destination. Essentially, any mission which would utilize a large impulsive burn of a chemical rocket followed by very long coast times would be a candidate for an electric propulsion system.

Equation (5) can also be rearranged to show

$$(I_{tot})^2 / (2 \times \text{Eff}) = P \times t \times M_o = E \times M_o \quad (6)$$

For a chemical thruster, this reduces to $(U \times M_o) \times M_o$
While for an electric system it becomes $P \times t \times (M_o + M_{\text{power plant}})$.

For the electric propulsion system, since the energy is not a “consumable”, it is possible to reduce weight by increasing the thrust time if not constrained by mission time.

COMPARISON OF CENTAUR & SEPS
TOTAL IMPULSE = 6×10^7 Nsec

<u>CENTAUR</u>	<u>SOLAR ELECTRIC STAGE</u>
• $V_j = 4300$ m/sec	• $V_j = 29400$ m/sec
• $I_{sp} = 440$ sec	• $I_{sp} = 3000$ sec
• $T = 66000$ N	• $T = 1$ N (Stage)
• Burn Time = 880 sec	• Burn Time = 5×10^7 sec
• Propellant Wt = 13600 kg	• Propellant Wt = 2000 kg

Table 1

Chemical vs. Electric Propulsion

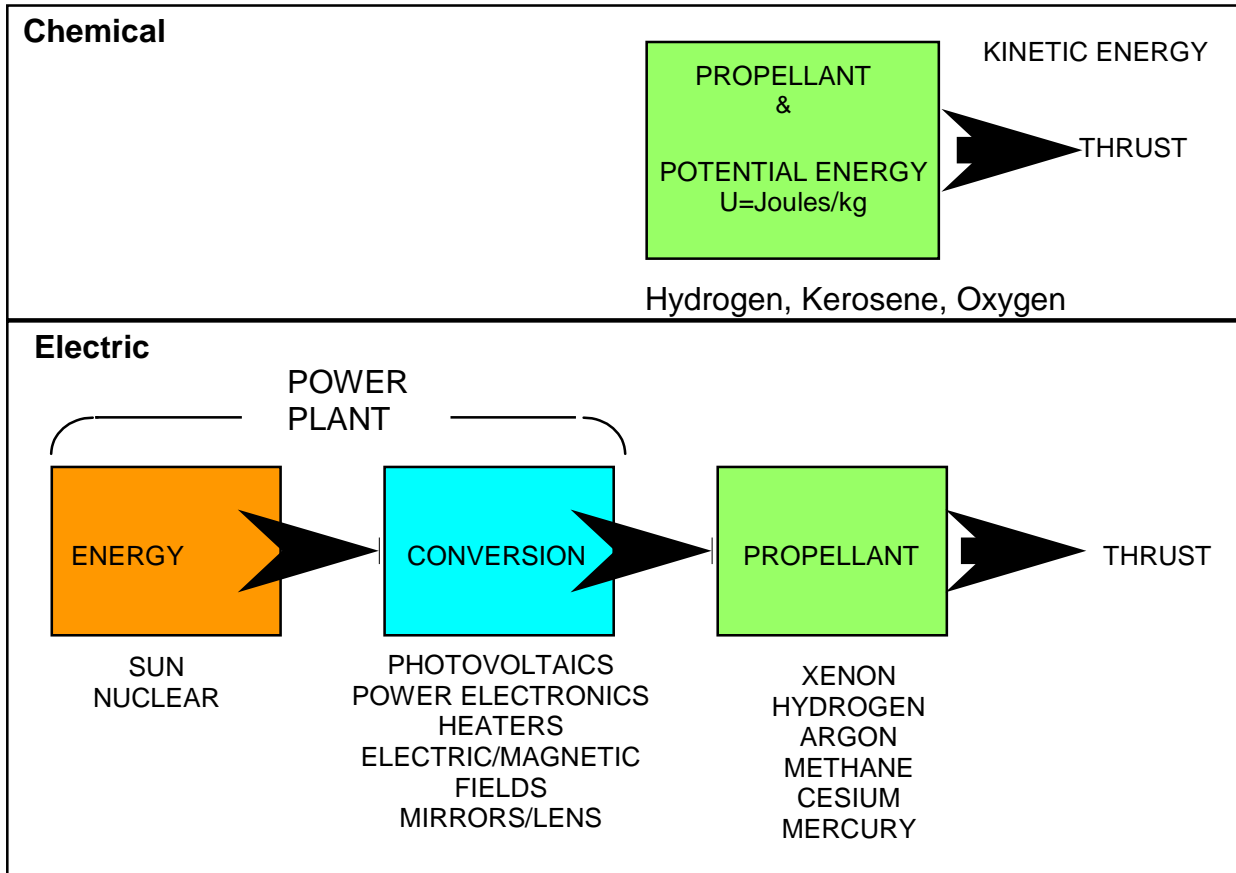


[Figure 1]

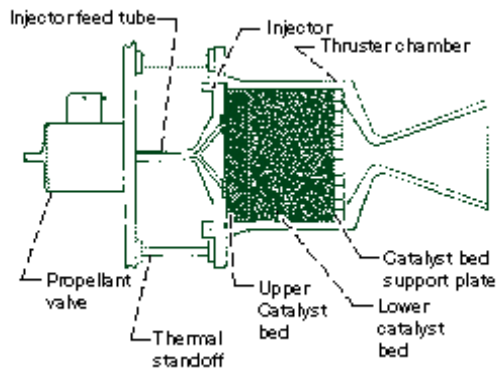
Advanced Fuels

Many compounds are currently being analyzed and tested as advanced chemical propellants. The number of compounds used in a propellant is often used to categorize the propellant. As such, future propellants being analyzed are typically called monopropellants, bipropellants, tripropellants. High energy density matter (HEDM) is also being analyzed to increase the I_{sp} of current propellants.

Monopropellants

The most common monopropellant in use is hydrazine. It is passed through a catalyst bed, where it decomposes into nitrogen and ammonia and delivers a specific impulse of about 230 $lb_f\text{-s}/lb_m$. Propulsion systems of this sort are well suited to pulsed operations of short duration, such as small spacecraft attitude control. ([Adams, 1994](#))

NASA is also developing new monopropellant systems to replace the current hydrazine monopropellant systems. The monopropellants under consideration are environmentally friendly, have a higher density, and have better thermal characteristics than hydrazine. The near-term goal is to improve mission performance and greatly reduce ground operations costs. For the far-term, a very high performance (high specific impulse) system is being sought. The key to this goal is the development of a high-temperature catalyst; research in this area is underway. ([Schneider, 1997](#))



Bipropellants

The bipropellant that is most often used in interplanetary spacecraft with relatively small engines is nitrogen tetroxide/monomethyl-hydrazine, commonly referred to as NTO/MMH. This combination yields an I_{sp} of 317 $lb_f\text{-s}/lb_m$. NASA seeks to improve performance to 326 $lb_f\text{-s}/lb_m$ by using a rhenium-alloyed thrust chamber, which will allow both higher operating temperatures and pressures. ([Frisbee, 2000a](#))

NASA has also been working to improve the efficiency of LH₂/LOX systems. Large pump-fed engines, like those found in the Space Shuttle main engines (SSMEs) can achieve an I_{sp} of 450 $lb_f\text{-s}/lb_m$, while smaller pressure-fed engines can reach an I_{sp} of 423 $lb_f\text{-s}/lb_m$. The problem has been that the high I_{sp} may be offset by higher structural weight, because refrigeration systems are required to store the cryogenic fuels.

The following table summarizes other bipropellant systems that have been investigated. The "type" column describes the how the propellant may be stored. "Space storable" refers to combinations that may be stored for extended periods in the space environment.

Propellant	Type	I_{sp} (s)
NTO/MMH	Earth Storable	317
O ₂ /CH ₄	Space Storable	365
O ₂ /H ₂	Refrigerated	423
ClF ₅ /N ₂ H ₄	Space Storable	350
OF ₂ /C ₂ H ₄	Space Storable	415
N ₂ F ₄ /N ₂ H ₄	Space Storable	395
F ₂ /N ₂ H ₄	Space Storable	415
OF ₂ /C ₂ H ₆	Space Storable	410
OF ₂ /B ₂ H ₆	Space Storable	420

Tripopellants

There are many chemical reactions that result in a higher specific impulse than the 423 seconds that is provided by the LH₂/LOX workhorse. However, many of these are unacceptable as rocket propellants because the exhaust is not a gas. Tripopellant technologies are an attempt to use these reactions by adding a third component (usually hydrogen) to the fuel and oxidizer. So far, lithium-fluorine-hydrogen and beryllium-oxygen-hydrogen mixes show the most promise for a tripopellant application. ([Frisbee, 2000 I](#))

The beryllium-oxygen-hydrogen system could generate an I_{sp} of 705 s and is being investigated by the U.S. Air Force. A lithium-fluorine-hydrogen system has the potential for generating an I_{sp} of 705 s. Early testing shows that while it has a higher combustion efficiency than the beryllium-oxygen-hydrogen system, it only allows a slight advantage over a fluorine-hydrogen bipropellant system.

High Energy Density Matter (HEDM)

In addition to the normal tripopellant approach, researchers have been looking at chemical additives that will increase the specific impulse generated by conventional bipropellant systems. These increases are achieved by adding high-energy chemicals in order to increase I_{sp} , thrust, and safety. This is not unlike adding chemicals to your car's fuel tank in order to achieve greater mileage. At the current time, HEDM is still in the basic research phase. ([Frisbee, 2000d](#))

According to preliminary analyses that have been done at NASA's Lewis Research Center (now known as the Glenn Research Center), solid particles in a cryogenic carrier fluid (such as LH₂) can carry HEDM additives to conventional combustion chambers. Adding these high-energy chemicals can increase the specific impulse by 19-49 s (figured from the LH₂/LOX baseline figure of 423 s). The table below summarizes the increases. ([Palaszewski, 1998](#))

Carbon atoms	+ 49 s
Boron atoms	+ 31 s
Aluminum atoms	+ 27 s

Hydrogen atoms	+ 19 s
----------------	--------

In addition to the increase to specific impulse, HEDM additives have the potential to increase propellant and vehicle density, allowing for more compact vehicles. These improvements would allow a higher percentage of deliverable payload weight to vehicle weight in future launch vehicles.

All of the chemical technologies discussed in this section will improve our ability to achieve orbit from the Earth's surface, but will have limited utility in traveling to other planets.
<http://siliconsky.com/sao/fit/advanced.htm>



TECH ISP

IN-SPACE PROPULSION TECHNOLOGIES



Currently Under Study

Contents of this area will be updated at the conclusion of the relevant FY03 Study.

- **LINKS**
- **TECHNICAL PUBLICATIONS**
- **WORKING WITH NASA**

- **ISP MAIN**

**CURRENT
TECHNOLOGIES**

Aeroassist

*Aerocapture -
Aerobraking -*

**Solar Electric
Propulsion**

*Next Generation
Electric Propulsion -
SEP Hall -*

Solar Sails

**Advanced
Chemical**

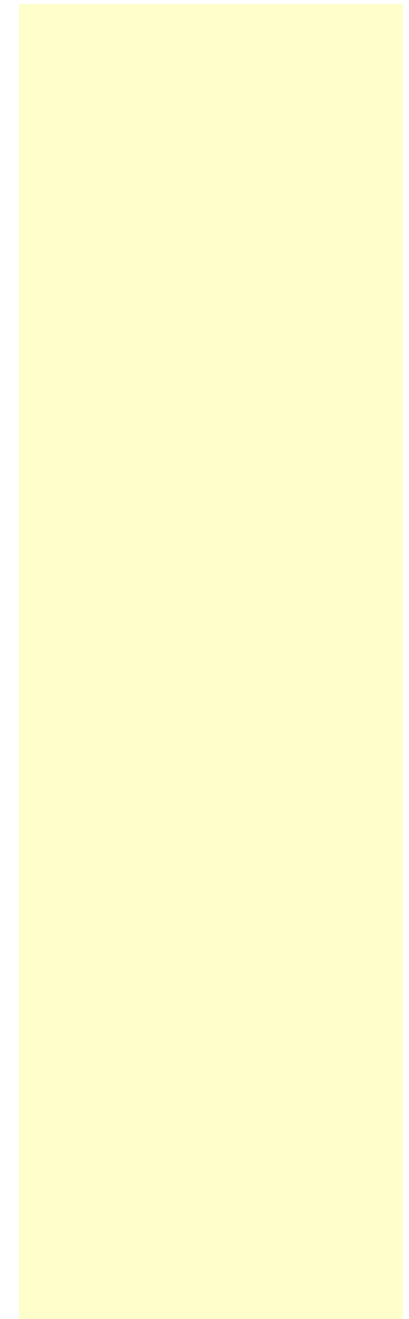
Tethers

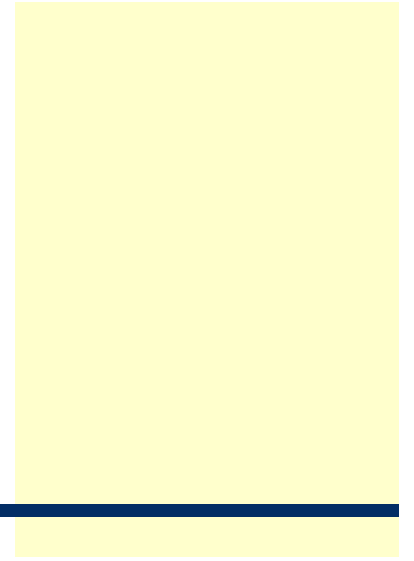
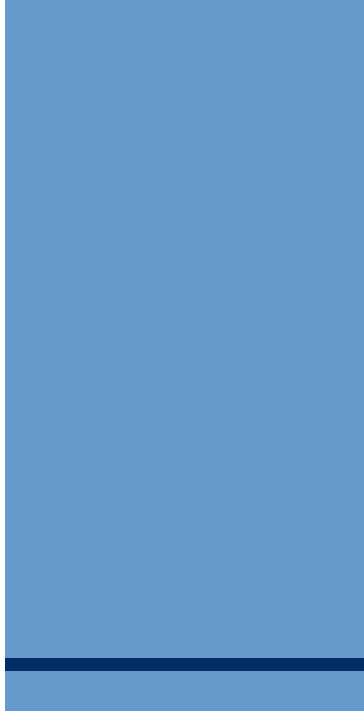
*Momentum Exchange -
Electrodynamic -*

Solar Thermal

**EMERGING
TECHNOLOGIES**

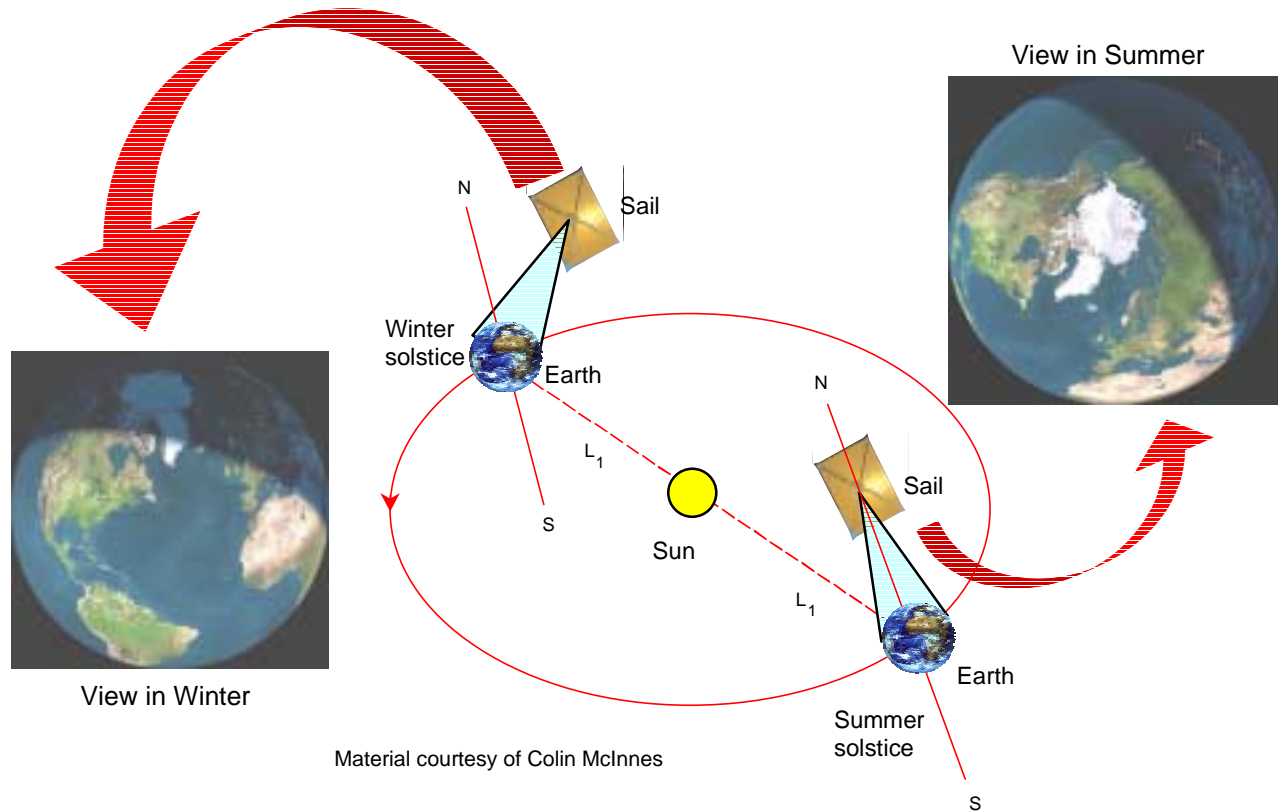
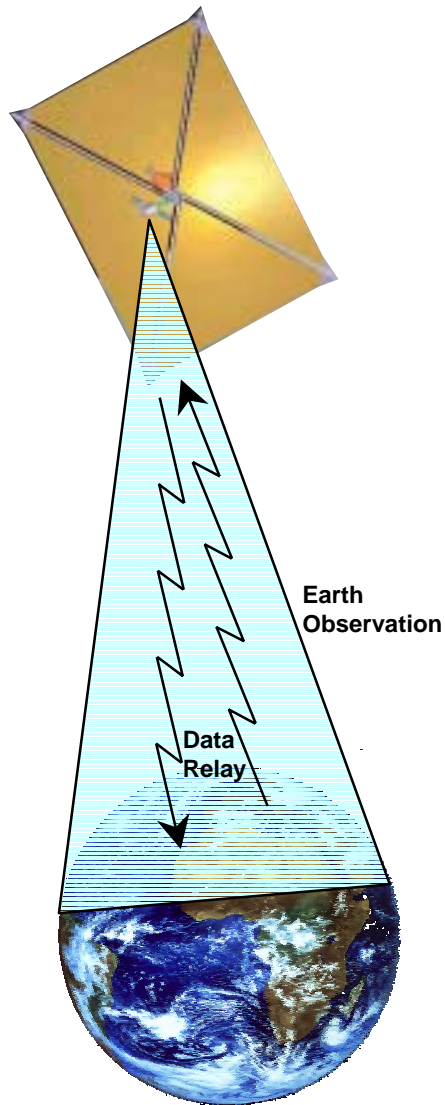
Aerogravity Assist -





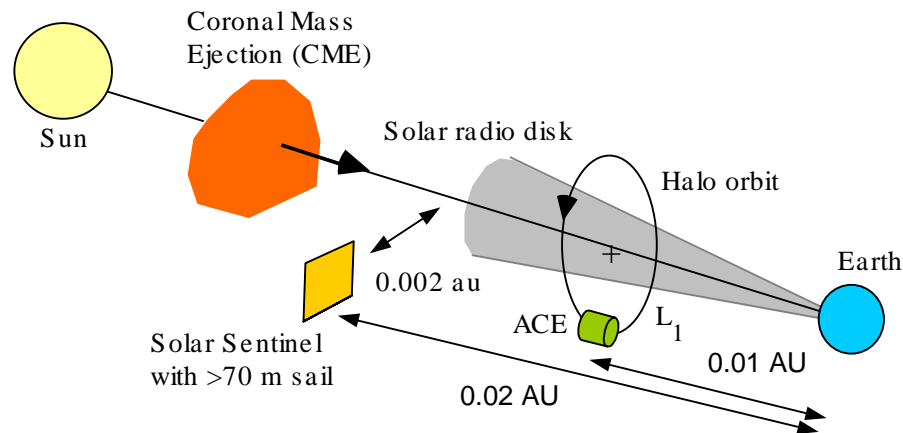
Pole Sitter Mission

- Continual coverage of the polar regions with no propellant usage!
- Altitudes ranging from 0.75 million km to 3.5 million km, depending on sail performance and inclination chosen



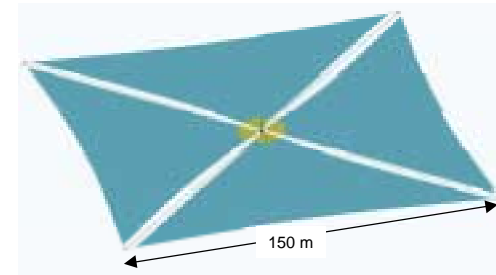
Solar Sentinel Mission Class

- Use solar sail to achieve non-Keplerian orbit near the sun-earth line, at least twice as far from the earth as the current warning system (ACE at the L_1)
 - Assumed payload 250 kg
 - The better the sail the closer to the Sun one can fly
 - Sail Size in range at 250 m or less
 - Sail is used for life of mission (> 5 yrs)
 - Fly a halo orbit to maintain communications

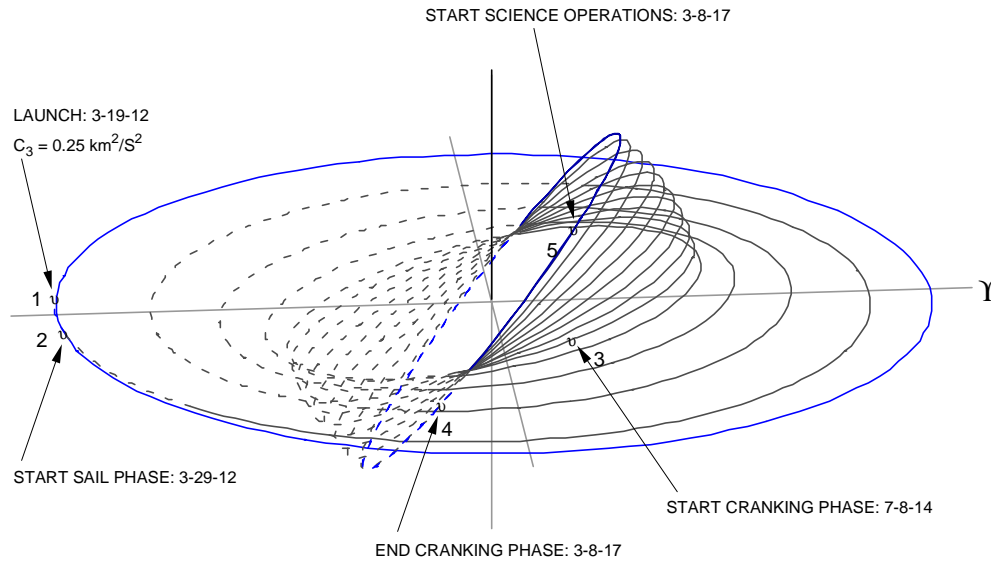
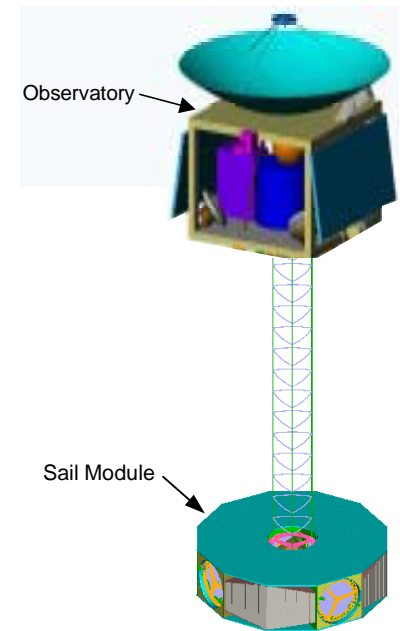


Solar Polar Imager (SPI)

- Solar Sail propulsion enables the Solar Polar Imager (SPI) mission
 - Sail provides constant thrust to crank the solar orbit to a high inclination
 - Sail enables a low period orbit with many solar polar science encounters



SPI Configuration



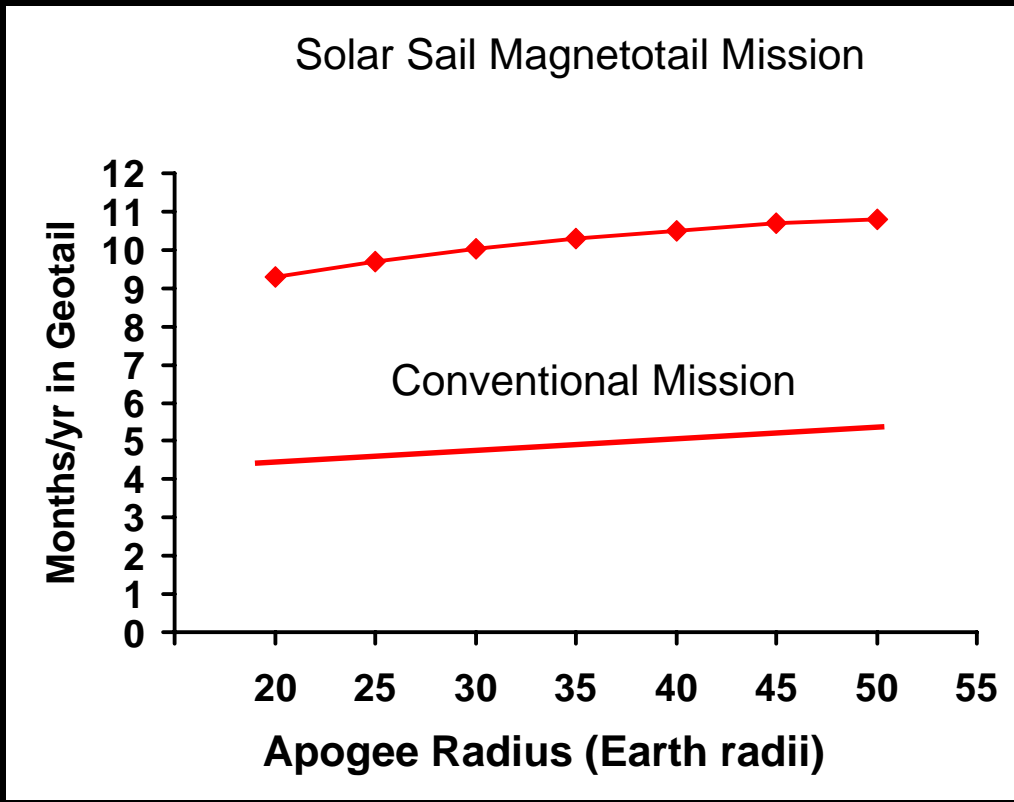
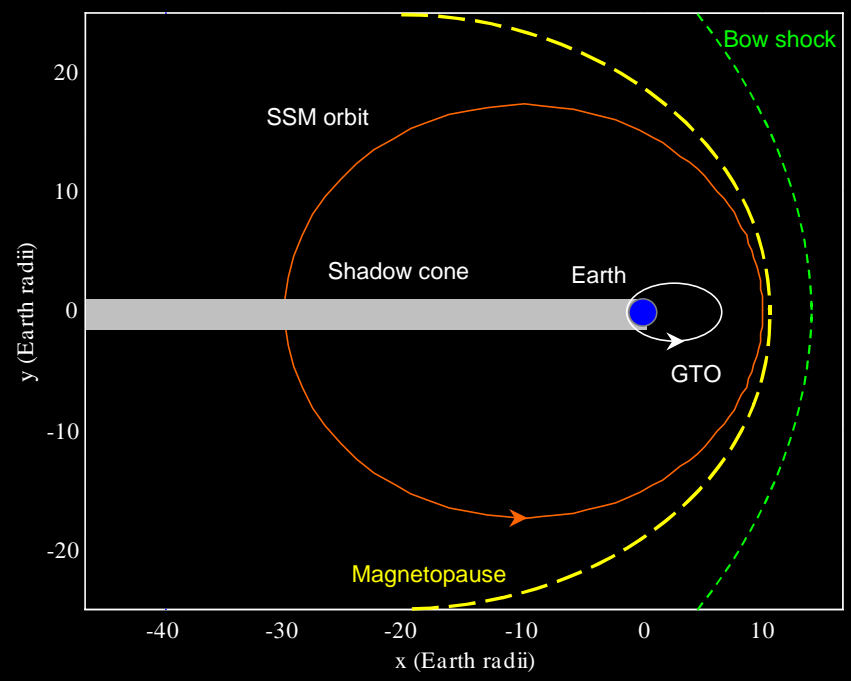
SPI Trajectory

	NMP ST7	Solar Polar Imager (SPI)
Edge Width	40 m	150 m
Area	1,500 m ²	20,000 m ²
Sail Subsystem Mass	29 kg	257 kg
Payload Mass (non-sail)	151 kg	215 kg
Flight System Mass	180 kg	472 kg
Sail Subsystem Areal Density	19.1 g/m ²	12.9 g/m ²
Total Areal Density	120.0 g/m ²	23.6 g/m ²
Characteristic Acceleration	0.07 mm/s ²	0.34 mm/s ²

Sailcraft Parameters

Solar Sail Magnetotail (SSM) Mission

- Precess orbit apse line to stay permanently in Magnetotail



A photon sail is a spacecraft accelerated by the momentum of the electromagnetic photons that are reflected from it. Types of photon sailcraft are laser sails (which are pushed by laser beams), maser sails (which are pushed by collimated microwave beams) and solar sails. The solar sail is accelerated by momentum transfer from photons emitted by the Sun that strike the sail. If the sail is fully opaque (non transmissive), the radiation pressure of the solar photons impinging against a sail oriented with its reflective surface normal to the sunlight can be written:

$$\text{Rad. Pres.} = (1 + \text{Ref}_{\text{sail}}) \text{SF} / c \text{ Newton} / \text{m}^2, \quad (1)$$

where Ref_{sail} is sail reflectivity, SF is the solar flux striking the sail (1,368 watts / m^2 at the Earth's distance from the Sun—the Solar Constant S.C.), and c is the speed of light (3×10^8 m/sec). The solar flux striking the sail surface varies with the square of the inverse of the distance to the Sun's center.

Sail Kinematics

If one multiplies Eq. (1) by the sail area normal to the Sun, A_{sail} in square meters, the resulting equation yields the force of the sunlight on the sail surface. Applying Newton's Second Law and dividing this result by spacecraft mass $M_{\text{s/c}}$ kilograms, the sailcraft's acceleration due to solar radiation pressure is obtained :

$$\text{ACC}_{\text{s/c}} = (1 + \text{Ref}_{\text{sail}}) \text{SF} A_{\text{sail}} / (M_{\text{s/c}} c) = (1 + \text{Ref}_{\text{sail}}) \text{SF} / (\sigma_{\text{s/c}} c) \text{ m/s}^2, \quad (2)$$

where $\sigma_{\text{s/c}}$ is the sailcraft's areal mass thickness in kilograms per square meter.

A convenient Figure of Merit for sail designers is the sailcraft Lightness Factor, $\text{LF}_{\text{s/c}}$, which is the ratio of solar radiation pressure acceleration to solar gravitational acceleration on the sailcraft. From Newton's equation for Universal Gravitation,

$$\text{LF}_{\text{s/c}} = (1 + \text{Ref}_{\text{sail}}) \text{SF} R_{\text{sun}}^2 / (G M_{\text{sun}} \sigma_{\text{s/c}} c), \quad (3)$$

where G is the Gravitational Constant $6.67 \times 10^{-11} \text{ N m}^2 \text{ kg}^{-2}$, R_{sun} is the distance of the sailcraft from the sun's center (1.5×10^{11} m at the solar orbit of the Earth—1 Astronomical Unit or 1 AU) and M_{sun} is the Sun's mass (1.99×10^{30} kg). Substituting in Eq. (3), we obtain the simplified result :

$$\text{LF}_{\text{s/c}} = 0.000773 (1 + \text{Ref}_{\text{sail}}) / \sigma_{\text{s/c}}. \quad (4)$$

At the Earth's distance from the Sun, a fully unfurled sail with a Lightness Factor of 1 is accelerated by solar radiation pressure at $5.92 \times 10^{-3} \text{ m/s}^2$ or about 6×10^{-4} Earth surface gravities. The areal mass thickness of such a sailcraft will be $0.00146 \text{ kg} / \text{m}^2$.

Solar sails must therefore be very light and very reflective. If the sailcraft described in the previous paragraph has a mass of 500 kg, the sail area normal to the Sun must be about 3.42×10^5 square meters. This sail will be considerably larger than a football field!

What if the Sail is Not Normal to the Sun?

Let's call the angle between incident sunlight and the normal to the sail "θ". If the sail is normal to the sunlight, θ = 0 degrees.

If the sail is not normal to the Sun, the normal value of solar irradiance (in watts / m²) striking the sail is multiplied by cos θ, according to Lambert's Law. Since the cross-sectional sail area normal to the incident sunlight is also reduced by cos θ, the sailcraft acceleration at Sun-sail angle θ (ACC_{s/c,θ}), is related to the sailcraft acceleration for the case of perpendicular sunlight (ACC_{s/c,θ=0}) by the equation:

$$ACC_{s/c,\theta} = ACC_{s/c,\theta=0} \cos^2 \theta . \quad (5)$$

When the sail is not normal to the Sun, there will be two components to the sailcraft's solar-radiation-pressure acceleration vector. These are ACC_{s/c, rad}, the component of spacecraft acceleration radial to the Sun and ACC_{s/c, tan}, the acceleration component tangential to the spacecraft's orbit around the Sun. Mathematically,

$$ACC_{s/c, \text{rad}} = ACC_{s/c,\theta} \cos \theta , \quad (6a)$$

and

$$ACC_{s/c, \text{tan}} = ACC_{s/c,\theta} \sin \theta . \quad (6b)$$

In the 2-sail solar photon thruster discussed below, Lambert's Law does not apply because the main, collector sail is always normal to incident sunlight and all sunlight striking the main collector is directed against the thruster, regardless of thruster angular orientation. For such a sailcraft, the cos²θ term in Eq. (5) is replaced by cos θ.

Sail Thermal Effects

As well as being low in mass and highly reflective, the sail must be constructed of heat-tolerant material. This is because all of the solar energy absorbed by the sail must be radiated from the sail as infrared electromagnetic radiation.

The radiant power absorbed by an opaque sail oriented normal to the Sun is written:

$$P_{\text{abs}} = (1-\text{Ref}_{\text{sail}}) SF A_{\text{sail}} \quad \text{watt} , \quad (7)$$

Since absorbed electromagnetic radiation can be reemitted as infrared from both sides of the sail, the sail's radiant emittance can be expressed as :

$$W_{\text{sail}} = (1-\text{Ref}_{\text{sail}}) SF / 2 \quad \text{watt} / \text{m}^2 . \quad (8)$$

The Stefan-Boltzmann Law for greybodies can be used to relate sail radiant emittance to sail absolute radiation temperature T_{sail} :

$$W_{\text{sail}} = \sigma \epsilon T_{\text{sail}}^4 \quad \text{watt} / \text{m}^2, \quad (9)$$

where σ is the Stefan-Boltzmann Constant ($5.67 \times 10^{-8} \text{ W m}^{-2} \text{ K}^{-4}$) and ϵ is the sail material's emissivity. (For a blackbody, $\epsilon = 1$). Equating Eqs. (8) and (9) and substituting $SF = 1,368 \text{ watt} / \text{m}^2$ at 1 AU, the Earth's average distance from the Sun,

$$T_{\text{sail}} = 331 [(1 - \text{Ref}_{\text{sail}}) / \epsilon]^{1/4} \quad \text{degrees Kelvin.} \quad (10)$$

The maximum sail radiation temperature must never exceed the melting point of the sail material. For most materials, the maximum allowable radiation temperature is a few hundred degrees Kelvin less than the sail-material melting point.

Some Sail Configurations

Figure 1 shows six proposed sail configurations. A disc sail consists of a circular sail film supported and stabilized by a series of spars as shown. The payload is often at the center of the spar structure.

Square sails are square or rectangular (when viewed from top or bottom). The spars and payload are often arranged in a manner similar to disc sail designs.

Parachute sails physically separate payload from sail. These are attached by a series of cables, as shown.

The parabolic sail or solar-photon thruster is a multi-sail configuration. A main collector normal to the Sun focuses sunlight upon a smaller thruster. The thruster can be steered allowing the spacecraft to alter the direction of reflected sunlight and thus be more maneuverable than other sail configurations.

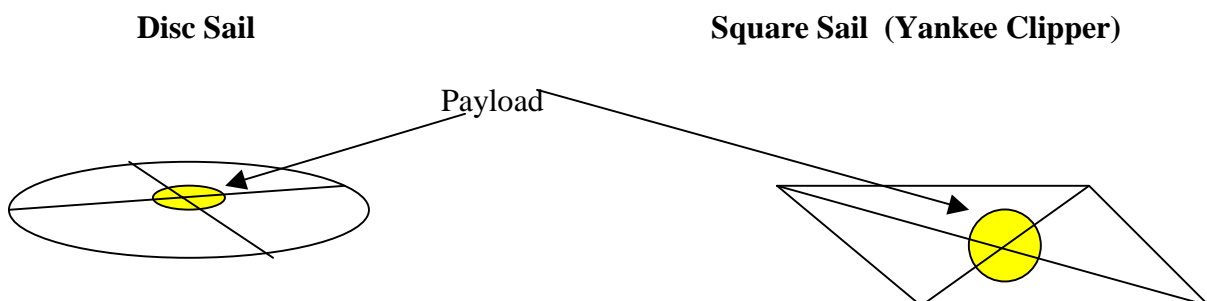
Although many sail designs rotate so that centripetal force can aid in sail unfurlment, the heliogyro spins like a gyroscope, although more slowly. In some designs, sail film rolls out from canisters near the center along spars within the sail blades.

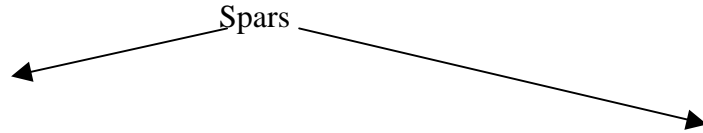
Hollow body or pillow sails are inflatable devices with the surface facing the Sun coated with a reflective layer. Although these may be easier to unfurl than other sail concepts, they have the disadvantage of being more massive.

Solar-Sail Limitations and How to Overcome Them

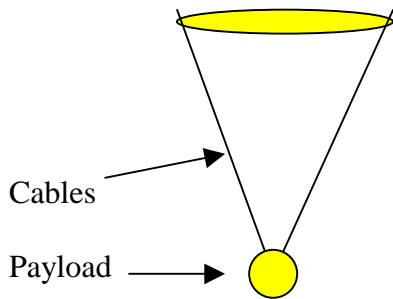
One major limitation to solar-sail application in the outer solar system and beyond is the inverse-square-law of solar irradiation. As the sail doubles its distance from the Sun, the solar flux and radiation-pressure acceleration fall by a factor of 4X.

Figure 1. Some Solar Sail Configurations

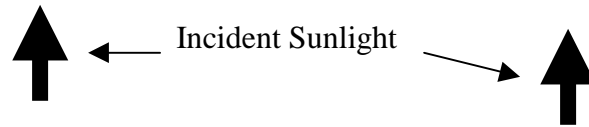
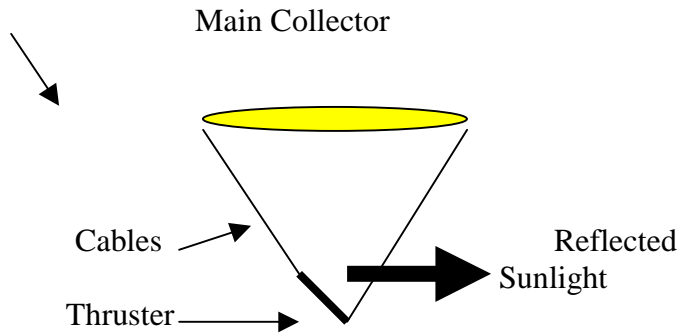




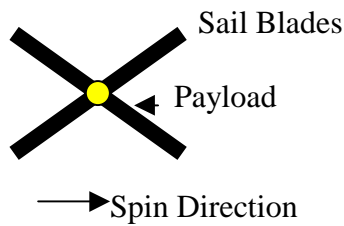
Parachute Sail



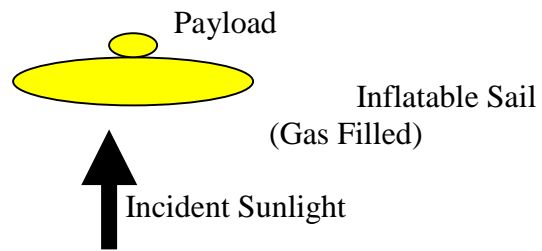
Parabolic Sail (Solar Photon Thruster)



Heliogyro



Hollow Body (Pillow Sail)

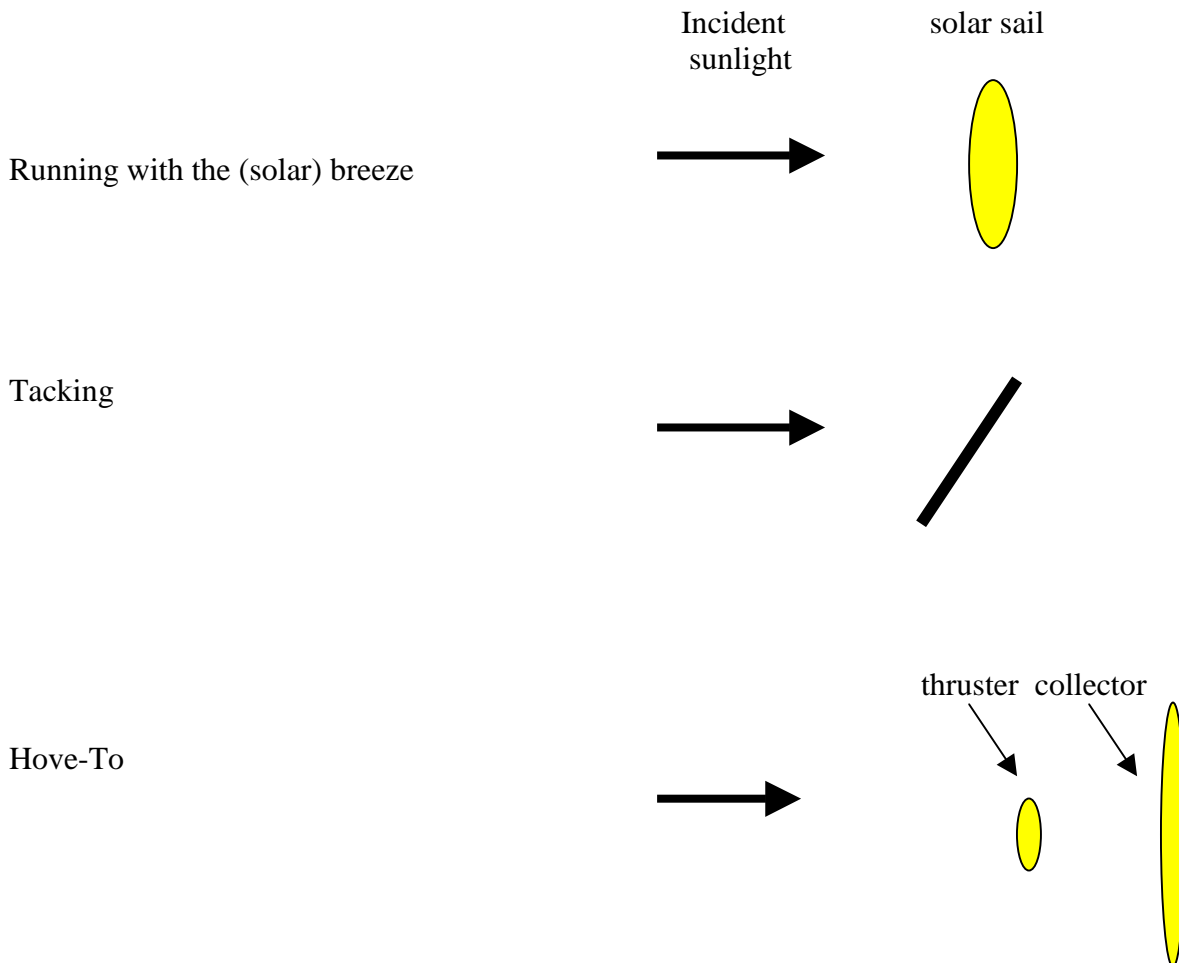


In concept, this effect can be compensated for by replacing sunlight in the outer system and beyond by collimated radiation. Studies have indicated that solar-powered visible and infrared lasers or collimated microwave masers in the inner solar system can project beams against sails very far from the Sun. Such sailcraft should properly be called “light sails” rather than solar sails.

Solar Sail Maneuvers and Orientations

Solar sail maneuvers can be classified using analogues with maneuvers performed by conventional oceanic sailing craft. As shown in Fig. 2, a sailcraft can be oriented with its sail normal to the incident sunlight. In such an orientation, reflected solar photons produce maximum thrust on the sail surface. The craft “runs with the (solar) breeze”.

Figure 2. Some Solar-Sail Maneuvers and Orientations



If the sail is oriented at an angle to the incident sunlight, the sailcraft’s thrust will be at an angle to incident sunlight. In this orientation, the spacecraft “tacks”.

In a two-sail solar photon thruster, thrust can be greatly reduced by reflecting sunlight from the thruster back towards the main collector sail. This orientation is analogous to the “hove-to” maneuver performed by an oceanic sailcraft to slow the craft under high-wind conditions.

Solar-Sail Materials

A number of choices exist for solar sail materials. Many of these are reviewed in the references.

For an Earth-launched near-term sailcraft, one approach is to create the sail using a sandwich of three materials. A metallic, highly-reflective (front) layer faces the Sun, followed by a layer of flexible, temperature-resistant plastic. The back layer is composed of a highly emissive material such as chromium. The function of the layer facing the Sun is to reflect as much of the sunlight as possible (up to about 90%). The plastic layer's function is to improve sail flexibility during the sail unfurlment process. Sunlight absorbed by the front layer is reemitted as infrared electromagnetic radiation from the back emissive layer. Some current three-layer sail designs have areal mass thicknesses less than about 10 grams per square meter and are capable of operating within 0.1 AU from the Sun. The sail thickness is typically of the order of a few microns.

Additional sail strength can be achieved by including strips of metallic ribbing within the sail structure. These might minimize the effects of micrometeoroid impacts.

Some researchers have examined the possibility of using plastics that would rapidly degrade when exposed to solar ultraviolet radiation. In a sail constructed of this material, the "sandwich" layers would be reflective, emissive, and finally UV-sensitive plastic. This approach could greatly reduce sail areal mass thickness.

The thinnest Earth-launched sails might consist of a stack of strong, temperature-resistant composite fibers. Perhaps coated with a reflective layer, the areal mass thickness of such a sail could be less than 1 gram per square meter. A sailcraft constructed using this material could operate well within 0.1 AU. Sail unfurlment may be an issue for very thin Earth-launched solar sails.

Ultimate solar-sail performance requires a space-manufacturing infrastructure. Using vapor-phase deposition, large-metallic sheets 20-30 nanometers thick could be produced in space. Areal mass thickness of 0.05 grams per square meter might be possible. Some metallic hyperthin sails could (theoretically) approach the Sun within the 0.05 AU of the Sun's center.

Nanotechnology might, in the farther future, allow for the creation of perforated or mesh solar sails. If the perforations are substantially smaller than the wavelength of incident light, low mass and high reflectance might combine to greatly increase sail performance.

Solar-Sail Missions

The solar sail is unique among currently-feasible advanced propulsion schemes because it requires no propellant and can accelerate endlessly without thrusting under the influence of sunlight or some other source of electromagnetic radiation. Once unfurled, a solar-sail constructed of material that does not readily degrade in the space environment, should have a very long operational life. Many space missions are possible using solar sails that are more difficult or impossible using other in-space propulsion modes.

In general (unless power-beaming is applied), these are either inner solar-system missions or missions in which spacecraft acceleration is accomplished within the inner solar system. The solar sail could accelerate to velocities of 100 km/sec or higher after

unfurlment during a close solar flyby. But (since the solar flux will be reduced from its near-Earth value by a factor of 25X at the 5-AU solar distance of Jupiter) the solar-sail will be ineffective for stopping at outer-solar-system destinations.

In low-Earth orbit, atmospheric drag is also an issue for the high-area, low-mass solar sail. Even solar-photon thrusters may be drag limited to unfurlment orbits in excess of 500 km above Earth's surface.

Near-term scientific missions

In the near-term, solar-sails in the 6-10 grams per square meter range, with areas of about 10^4 square meters are under consideration for inner-solar-system solar observer missions. Stationed for years between the Earth and Sun, such craft could give early warning of solar flares approaching the Earth.

If they are constructed of material capable of withstanding radiation produced by repeated passes through Earth's Van Allen radiation belts, sail configurations such as the solar-photon thruster could maintain constellations of satellites at various locations within Earth's magnetosphere. The payloads of these craft could monitor the near-Earth plasma environment for examine space-magnetic interactions with the terrestrial environment.

The solar-photon-thruster sail configuration could enable the "pole sitter," a spacecraft situated at lunar distances over or nearly over one of Earth's poles. Pole sitters have application to high-latitude communication, climate studies and Earth viewing.

Sails could be considered for payload delivery or round-trip visits to inner-solar system planets as far out from the Sun as Mars or for launching probes to the outer solar system. Fast flybys of outer-solar-system objects such as Kuiper Belt comets (30-50 AU from the Sun) are possible.

Perhaps the most exciting near-term possibility is a sailcraft equipped with a sail that is unfurled within the orbit of Venus or perhaps Mercury and then accelerated out of the solar system on a trajectory capable of reaching the heliopause (the limit of the Sun's influence--at 250 AU from the Sun) within a few decades. Such an interstellar probe could monitor *in situ* the interaction between the Sun and the galaxy.

Space-commercialization and Earth-protection missions

As humanity's space infrastructure matures, Earth-launched or space-manufactured solar-sails will offer opportunities to those seeking to develop the space-environment or to protect the Earth from cosmic collisions. Near-Earth asteroids and comets could be explored and mined using solar sails.

If advanced terrestrial and space telescopes can provide decades-long warnings of collisions between Earth and near-Earth objects (NEOs), solar sails--could be unfurled around or near the offending asteroids or cometary nuclei. Radiation pressure on sails attached to NEOs could alter collision trajectories to near-miss trajectories. Alternatively, sails could be used as concentrators to heat NEO surfaces enough for trajectory-altering jets of material to be ejected.

To the Oort Belt and the stars!

As 0.1 gram / square-meter sails capable of withstanding very close perihelion passes are developed in the farther future, solar-system exit velocities in excess of 300 km/sec will become possible. Then, space-mission planners could design robotic missions to nearer Oort Belt comets within a few thousand Astronomical Units of the Sun with flight times of a few decades.

Ultimate space-manufactured solar sails will allow the possibility of Earth-Mars roundtrips with durations measured in months rather than years. The same technology may allow visits to the nearer stars at solar-system exit velocities higher than 1,000 km /sec. The one-way travel time to the Sun's nearest interstellar neighbors (proxima and Alpha Centauri) will be about 1,000 years for such spacecraft. Advances in laser and maser power-beaming technologies may eventually substantially reduce interstellar-voyage durations.



science@nasa
The Science Mission Directorate



- + Visit NASA.gov
- + Visit science@nasa
- + Contact NASA

Science Missions

[Home](#) | [Earth-Sun System](#) |
[Solar System](#) | [Universe](#)

Site Search:

Science Missions

[Earth-Sun System](#) | [Solar System](#) | [Universe](#) | [A-Z](#) | [Phase](#)

The Science Mission Directorate manages quite a few missions, some well-known and others not so well known. Many involve cooperation with international partners or other U.S. agencies. For full names and brief descriptions of these missions, see:

- [Earth-Sun System](#)
- [Solar System](#)
- [Universe](#)

At a Glance...

- Today our robotic explorers have traveled throughout the Earth and Solar System, and seen the birth of the earliest galaxies.
- Questions about the very nature of the universe can be pursued not only with philosophical speculation but also with scientific observation.

Related Links...

- [Mission Highlights on the NASA](#)

Under Study	Development	Operating	
Aquarius	AIM	ACE	Polar
Const. X	CALIPSO	ACRIMSAT	QuikSCAT
EUSO	CINDI	Aqua	RHESSI
GEC	CloudSat	ASPERA-3	Rosetta
Geospace	Dawn	Aura	RXTE
Glory	DSCOVR	Cassini	SAGE III
GOES-R	GLAST	Chandra	SAMPEX
GPM	Herschel	CHIPS	SOHO
Hydros	Kepler	Cluster	SORCE
IBEX	New Horizons	Deep Impact	Spitzer
Juno	NPP	EO-1	Stardust
JWST	OCO	ERBS	Suzaku
LDCM	Planck	FAST	SWAS
LISA	POES N,N'	FUSE	Swift
LRO	SOFIA	GALEX	Terra
MagCon	Solar-B	Geotail	TIMED
MMS	ST-5	GOES N,O,P	TOMS-EP
Moonrise	ST-6	GP-B	TOPEX/Poseidon
MSL	ST-7	GRACE	TRACE
NuSTAR	STEREO	HETE-2	TRMM
OSTM	THEMIS	HST	UARS
Phoenix	TWINS	IceSAT	Ulysses

Portal [+ more]

- 40+ Years of Earth Science:
 - 1958-1967
 - 1968-1977
 - 1978-1987
 - 1988-1997
- NASA Space Science History [+ more]

SDO		IMAGE	Voyager
Sentinels		INTEGRAL	Wind
SIM		Jason	WIRE Testbed
Solar Probe		Landsat 7	WMAP
ST-8		MER	XMM-Newton
ST-9		MESSENGER	
TPF		MGS	
WISE		MRO	
		Odyssey	

Past				
ASCA	DXS	IMP-8	MPL	Surveyor
Astro-1	Equator-S	IRTS	NEAR	SRTM
Astro-2	EUVE	ISO	ORFEUS	Starshine
BBXRT	Galileo	IUE	Pioneer 10/11	TERRIERS
Clementine	Genesis	KAO	Pioneer Venus	TSS-1
CGRO	GOES L	Leonid MAC	POES L	TSS-1R
COBE	GOES M	Lunar Pros.	POES M	Viking
CONTOUR	HALCA	Magellan	Ranger	Voyager
CRRES	VLBI	Mariner	ROSAT	WIRE
DE-1	Hipparcos	MCO	SAC-B	Yohkoh
DS 1	IEH-3	Mars Obs.	SNOE	
DS 2	ISEE-3/ICE	Mars Path.	Spartan	

NASA > [science@nasa](#) > [Missions](#)



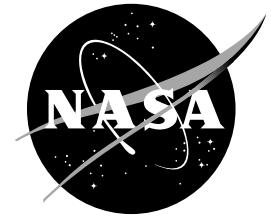
+ [NASA Privacy Statement, Disclaimer,
and Accessibility Certification](#)
+ [Use of NASA Images](#)



NASA Official: [Sharron Sample](#)
Last Updated: August 19, 2005
+ [Contact NASA](#)

NASA Facts

National Aeronautics and
Space Administration



Marshall Space Flight Center
Huntsville, Alabama 35812

FS-2004-10-131-MSFC

October 2004

Solar Sail Propulsion

Traditionally, solar exploration missions have been limited by the performance margins of state-of-the-art chemical rocket engines and by the amount of fuel a spacecraft must carry to travel in space -- up to 25 percent of the launch weight of typical planetary-exploration spacecraft. Now, NASA researchers are developing a key in-space propulsion technology (fig. 1) that -- for some applications -- could replace conventional chemical fuels with an inexhaustible natural resource: sunlight.

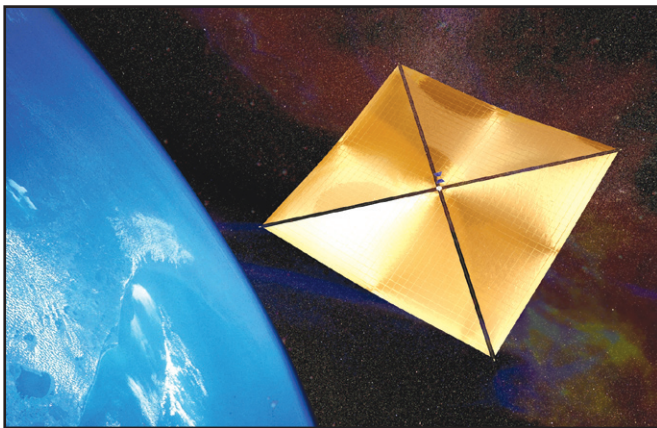


Figure 1: Solar Sail Propulsion concept in Earth Orbit.

Solar sail propulsion is now being developed by NASA scientists and their partners in industry and academia, led by NASA's In-Space Propulsion Technology Office at Marshall Space Flight Center in Huntsville, Ala. The Center implements the In-Space Propulsion Technologies Program on behalf of NASA's Science Mission Directorate in Washington.

Using the Sun's energy as a way to travel through space could give spacecraft more mobility and versatility during flight -- thus opening up new regions of the Solar System for exploration and science.

Solar Sail History

The idea of "sailing" through space has been around for years. NASA considered the use of solar sails in the 1970s as a potential propulsion system for performing a rendezvous with Comet Halley during its 1986 flyby of Earth. Lightweight technologies such as "sails" were not mature enough at that time and the mission was deemed unfeasible. However, as more and more advances in design and construction of the large solar sails and their hardware systems were made in the 1980s and 1990s, the viability of the technology increased.

Solar sail propulsion uses sunlight to propel vehicles through space, much the way wind pushes sailboats across water. The technology uses solar photons -- sunlight -- which are reflected off giant, mirror-like sails made of lightweight, reflective material 40 to 100 times thinner than a piece of writing paper. The continuous photonic pressure provides enough thrust to perform maneuvers, such as hovering at a fixed point in space and rotating the space vehicle's plane of orbit, which would require too much propellant for conventional rocket systems. Because the Sun supplies the necessary propulsive energy, solar sails also require no onboard propellant, thus reducing payload mass.

Solar Sail Design

The sail itself would vary in size from tens of meters up to 1000 meters in diameter, depending on its mission destination, and typically would be shaped like a square. It would be compactly stored -- to about the size of a suitcase -- and stowed for launch. Once deployed, the sails would be supported by ultra-lightweight trusses.

Solar sails are composed of flat, smooth material covered with a reflective coating and supported by lightweight structures attached to a central hub. Near-term sails likely will use aluminized Mylar -- a strong, thin polyester film -- or CP-1, a space-rated insulating material. Both are proven materials previously flown in space. More robust sails might use a meshwork of interlocking carbon fibers.

There are three basic types of near-term solar sail designs: three-axis stabilized square sails, heliogyro sails and spinning disc sails. Heliogyro and spinning disc sails are similar in that both spin as they travel in space; however, their structural designs differ.

Heliogyro sails (fig. 2) are composed of several vanes, extending directly from a central hub, that “roll out” because of the spinning motion of the craft. Circular in shape, spinning disc sails (fig. 3) are connected to a structure composed of interlocking masts and booms which surround and connect to a craft.

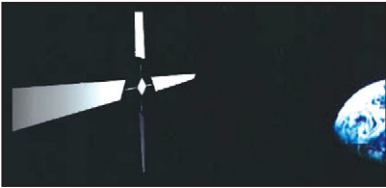


Figure 2: Concept design of heliogyro solar sail system.

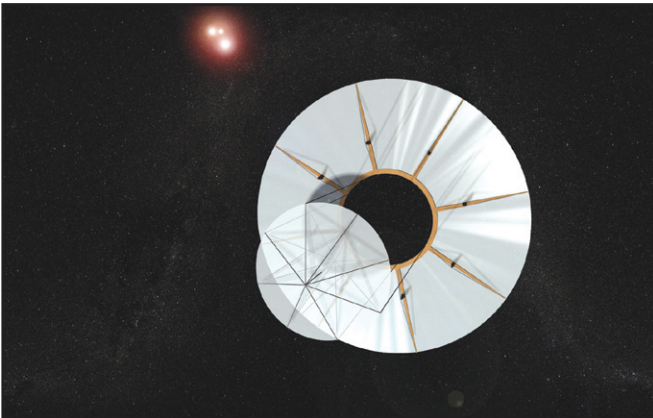


Figure 3: Concept design of spinning disc solar sail system.

NASA is concentrating its development effort on the three-axis stabilized, square sail (fig.4). This sail looks much like a kite and uses a rigid structure to extend and suspend the sail material in space to catch sunlight. Four booms extend from a central hub that houses the four sail quadrants during launch.

These booms are made of fiber-reinforced composite shell, much like an inflatable tube, or graphite rods assembled in a truss -- a structural frame that provides support -- which are lightweight yet stiff and weigh less than an ounce per foot. The sail orientation and resulting thrust vector -- the direction in which the force is applied -- is controlled by imposing a torque, a twisting motion or rotation, on the sail. This is done either by using control vanes -- miniature sails -- or by offsetting the center of the structure's mass from the center of solar pressure -- much like the effect of pushing on a revolving door.

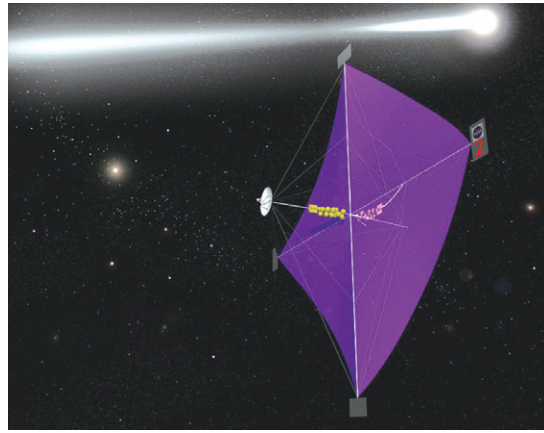


Figure 4: Concept design of 3-axis stabilized square solar sail system.

Two teams have been selected by NASA to lead hardware development activities that will culminate in ground demonstrations of key solar sail technology systems. L'Garde Inc., of Tustin, Calif., is developing a solar sail system that employs inflatable booms that are flexible at ambient temperatures but “rigidize” at temperatures below minus 35 degrees Celsius. Able Engineering Company, of Goleta, Calif., is developing a system based on the company's “CoilABLE Booms,” which uncoil in space, much the way a screw is rotated to remove it from an object. This boom system has flown on several missions, including the Mars Pathfinder, launched in December 1996, and the Mars Polar Lander, which launched in January 1999.

Both hardware development activities produced 10-meter subscale solar sails that were tested under thermal vacuum conditions in 2004. The demonstration of a 20-meter subscale solar sail system at NASA's Glenn Research Center's Plum Brook facility near Sandusky, Ohio, will follow in early 2005.

Solar Sail Missions

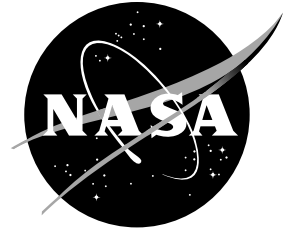
Solar sail propulsion is a leading candidate for missions that require a space vehicle to complete a large variety of maneuvers, such as changing orbital elements or orientation, hovering at a fixed point, or for missions that require constant vehicle thrust to achieve science objectives. These propulsion technology systems eventually could lead to missions to study the Sun and its heliosphere -- the magnetized bubble of plasma around the Sun -- that are impossible using today's technology.

Solar sail research is part of NASA's In-Space Propulsion Technologies Program, which is managed by the Science Mission Directorate in Washington and implemented by the Marshall Space Flight Center in Huntsville. The program's objective is to develop in-space propulsion technologies that can benefit near and mid-term NASA space science missions by significantly reducing cost, mass and travel times.

For more information about solar sail research, visit:
<http://www.inspacepropulsion.com>

National Aeronautics and
Space Administration

Marshall Space Flight Center
Huntsville, Alabama 35812



Opening the Space Frontier In-Space Propulsion Technologies Discovering our Solar System

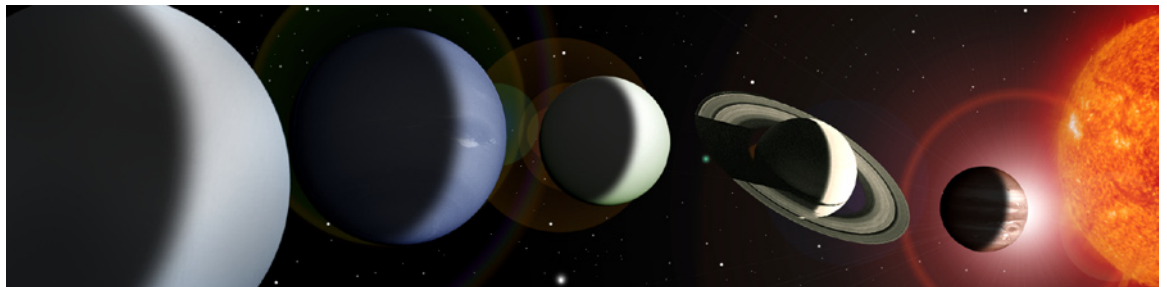
A key challenge facing NASA propulsion researchers is finding a faster and more efficient way of traveling in space. Current propulsion technologies often take years to accomplish deep-space missions—more than six years for NASA's Galileo probe, which launched in October 1989, to reach Jupiter to study the planet and its moons, and 12 years for Voyager 2, which launched in August 1977, to complete its fly by of Jupiter, Saturn, Uranus and Neptune. Today, however, NASA technologists are seeking new means to overcome these obstacles and improve scientific discovery at the destination.

The In-Space Propulsion Technology Program—managed by NASA's Science Mission Directorate in Washington and implemented by the In-Space Propulsion Technology Office at NASA's Marshall Space Flight Center in Huntsville, Ala.—currently is developing alternative propulsion technologies that one day will be used to carry scientific missions to any point in the Solar System—faster than ever before and with greater return on investment. NASA fuels discoveries that make the world smarter, healthier and safer.

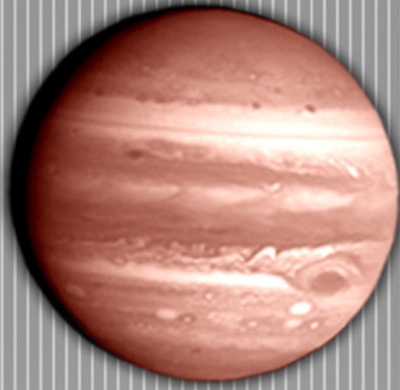
Partnering with researchers in academia, industry and government across America, the project office at the Marshall Center serves as a focal point for technology development and integration. The office is responsible for investigating and developing in-space propulsion technologies that can enable or benefit near-term and mid-term NASA science missions by significantly reducing cost and travel times, and increasing the amount of available capacity for payload.

Center partners include Ames Research Center in Moffett Field, Calif.; Glenn Research Center in Cleveland, Ohio; Jet Propulsion Laboratory in Pasadena, Calif.; Langley Research Center near Hampton, Va.; and White Sands Test Facility in Las Cruces, N.M.

The In-Space Propulsion Technology Program concentrates its efforts in five technology areas: aerocapture technology, next generation electric propulsion, solar sail propulsion, advanced chemical and solar thermal propulsion, and emerging propulsion technologies.



"I had the ambition to not only go farther than man had gone before, but to go as far as it was possible to go."
—Captain Cook (on his voyage to the Pacific in Endeavor.)



Jupiter

Distance from Earth

390.6 million miles
(628.7 million kilometers)

Temperature

Interior temps may reach 35,000 degrees Fahrenheit
(19,400 degrees Celsius)

Atmosphere

90 percent normal and liquid metallic hydrogen, 10 percent helium, with traces of methane, water and ammonia

Geology

Gaseous materials density to an inner core 10-15 times the size of Earth

Moons

16 confirmed, 12 unconfirmed

Rings

A single, faint ring similar to Saturn's in composition

Aerocapture Technology

Aerocapture is part of a family of “aeroassist” technologies under consideration to place spacecraft in long-duration, scientific orbits reducing the need for heavy onboard fuel loads, which historically have inhibited vehicle performance and available capacity for payloads.



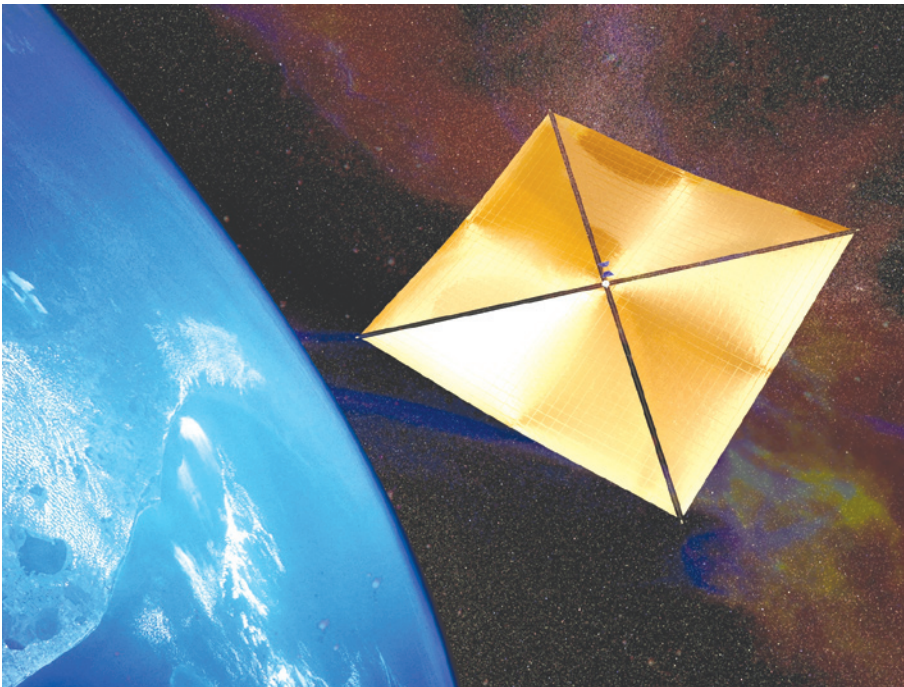
Aerocapture vehicle at Earth orbit

Aerocapture uses a planet's or moon's atmosphere to assist in decelerating an incoming spacecraft in order to accomplish a quick, near-propellantless orbital “capture,” or placement of a space vehicle in its proper orbit. The atmosphere's density creates friction, acting as a natural brake to slow down a spacecraft and allowing the craft to enter an elliptical, or oval-shaped, orbit. Small onboard thrusters are then used to raise the craft into its final circular orbit.

This nearly fuel-free method of decelerating a space vehicle could reduce the typical mass of an interplanetary spacecraft by more than half, allowing for a smaller and less expensive launch vehicle, and enabling greater scientific return. The technology also could shorten trip times to outer planets in the Solar System, allow for long-duration orbits and support precise vehicle landings on planets millions of miles from Earth.

Solar Sail Propulsion

Solar sail propulsion uses an inexhaustible natural resource—the Sun—to propel a craft through space. Photons—sunlight—are reflected off giant, reflective sails made of thin, lightweight material. The sails harness the pressure exerted by the photons to provide thrust. This simple, innovative technology is a low-cost, propellantless alternative to conventional chemical rocket propulsion for some types of space missions.



Solar Sail Propulsion at Earth orbit

Because the spacecraft directly uses the Sun's energy to travel through space, there is no engine and no need to carry primary propulsion fuel, thereby reducing payload mass while providing continuous thrust indefinitely. The technology also has no environmental impact on Earth because it obtains its propulsive power from the Sun after leaving the planet.

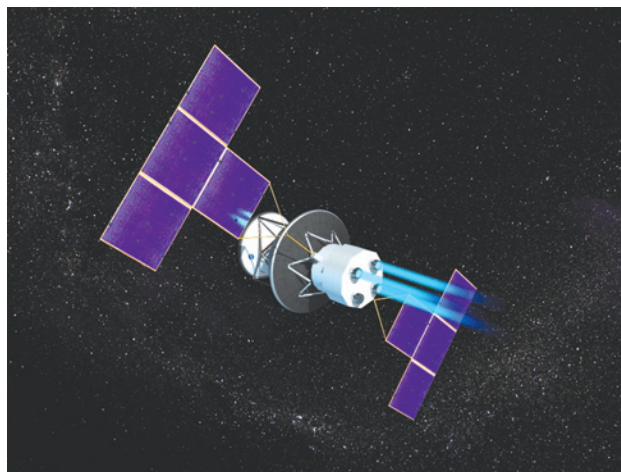
This propellantless propulsion technology could open up new regions of the Solar System for exploration and science. The technology could also extend the duration of some space missions.

Next Generation Electric Propulsion

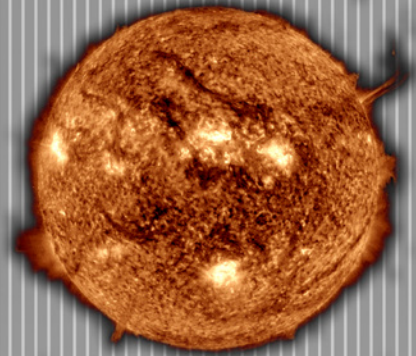
NASA's Next Generation Electric Propulsion technology area develops key propulsion elements for solar electric propulsion systems.

The solar electric propulsion systems under development use electrical energy from the Sun to ionize and electrostatically accelerate a propellant to produce thrust. A lightweight alternative to state-of-the-art

chemical propulsion, a solar electric spacecraft generates low, sustained thrust for a longer period of time. One such technology NASA has proven in flight is ion propulsion, in which an ion thruster uses electrostatic energy. Ion propulsion powered the



Artist's concept of spacecraft propelled by solar electric propulsion using next generation ion thrusters.



Sun

Distance from Earth

93 million miles
(149.7 million kilometers)

Temperature

Core temperatures reach up to 27 million degrees Fahrenheit
(15 million degrees Celsius)

Atmosphere

75 percent hydrogen, 25 percent helium, with 0.1 percent metals made from hydrogen via nuclear fusion; produces huge amounts of energy

Geology

Huge ball of hot gas and nuclear reactions; center of Solar System, where planets, moons, asteroids, comets, meteoroids, and other rock and gas orbit

Moons

61

Rings

None



Saturn

Distance from Earth

795.2 million miles
(1.27 billion kilometers)

Temperature

Interior temps reach 21,000 degrees Fahrenheit (11,600 degrees Celsius)

Atmosphere

Approximately 75 percent hydrogen and 25 percent helium, with traces of water, methane and ammonia

Geology

Gaseous surface above liquid-metallic hydrogen layers, molecular hydrogen layers and a rocky core

Moons

18 confirmed, 12 unconfirmed

Rings

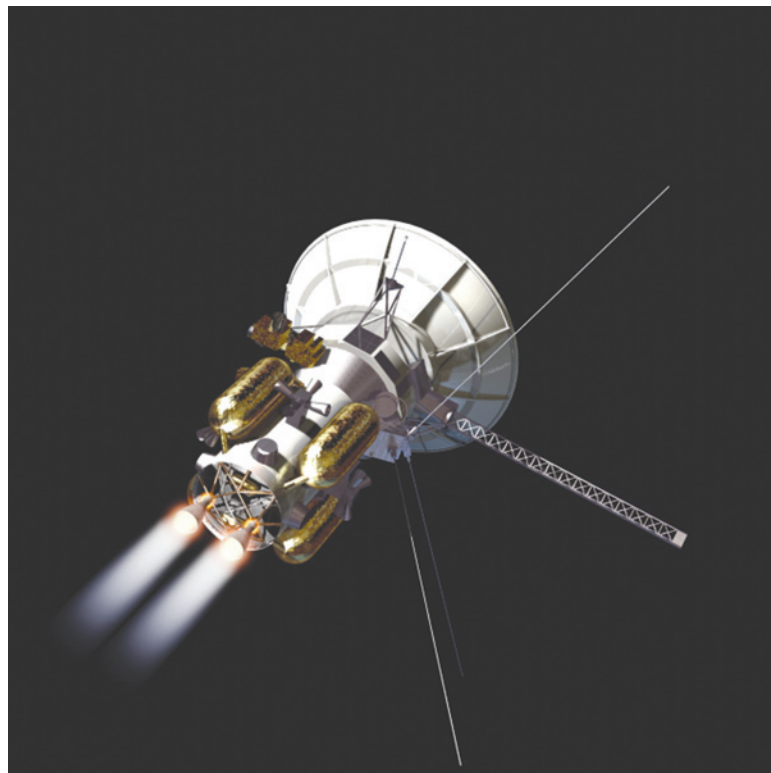
Trademark rings are composed of water, ice, and icy rock particles

Deep Space 1 technology demonstrator, which flew by Comet Borrelly in September 2001. The mission was completed in December 2001.

Solar electric-powered spacecraft—less hampered by the mass limitations of conventional chemical systems—can travel faster, carry heavier payloads and accomplish broader mission objectives than traditional deep-space probes. Shorter trip times plus reduced spacecraft mass could mean lower operational costs and a less expensive launch vehicle.

Advanced Chemical & Solar Thermal Propulsion

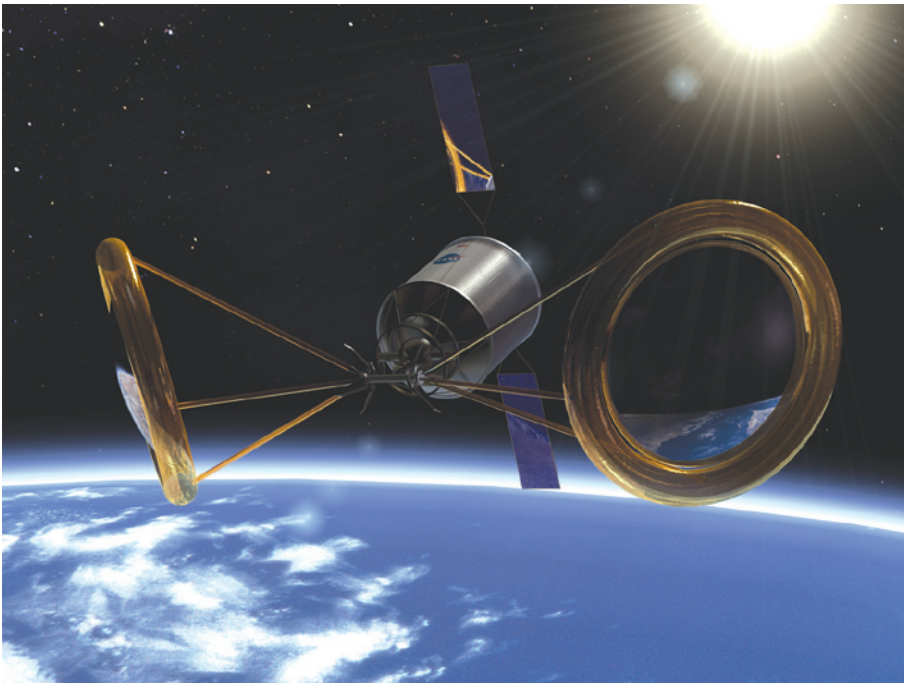
Advanced chemical propulsion technologies offer solutions for improving rocket propulsion for in-space applications. NASA researchers are investigating advanced reformulations of conventional chemical fuels and studying the combustion properties of new propellants to decrease propulsion system mass and increase payload mass.



Artist concept of spacecraft powered by advanced chemical propulsion

Advanced chemical propulsion technologies can provide near-term, cost-effective ways for future spacecraft to explore the space frontier. Advanced chemical systems could make use of new technology developments such as cryogenic propellant—extremely low-temperature propellant—for extended missions. They also could make use of lightweight storage components and deliver higher specific impulse, or total thrust achieved per amount of fuel burned, and ease the demands placed on aerobraking.

Advanced chemical propulsion is an attractive technology option for improved transportation of payloads in space because the systems generate a tremendous amount of thrust, necessary to overcome the gravitational effects of a planet or other satellite.



Solar thermal propulsion at Earth orbit

Solar thermal propulsion provides a fuel-efficient, low-cost alternative to conventional chemical propulsion systems for some mission applications.

A solar thermal-powered spacecraft captures solar energy with inflatable concentrator mirrors that focus sunlight inside a high-temperature engine cavity to heat propellant. Because solar thermal propulsion requires only one propellant gas in combination with sunlight to boost a payload from a low orbit to a high one, the system increases payload space previously allocated to fuel storage.

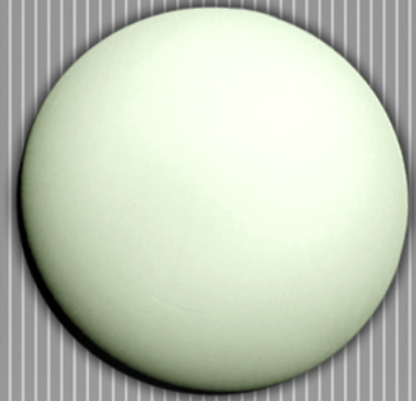
Solar Thermal Propulsion systems are candidates for interplanetary travel—inner Solar System missions from the Sun to Mars—and automated exploration.

Emerging Propulsion Technologies

The In-Space Propulsion Technology Program actively identifies and evaluates innovative candidate technologies for development. These innovative concepts under research are the responsibility of the Emerging Propulsion Technologies project area. Ultra-light solar sails and pulsed plasma thrusters are some of the many possible concepts that fall into this technology area. One technology presently being investigated utilizes a very long cable, or tether, in space.

Tether technology promises to be a propellantless propulsion system that could dramatically reduce the cost of raising and maintaining the orbits of spacecrafts, including those destined for deep space.

The Momentum-eXchange/Electrodynamic Reboost tether or MXER tether may be a viable alternative to conventional chemical propulsion (upper stages). MXER could provide a reusable in-space infrastructure for high-thrust and high-efficiency spacecraft propulsion.



Uranus

Distance from Earth

1.69 billion miles
(2.72 billion kilometers)

Temperature

-350 degrees Fahrenheit
(-212 degrees Celsius)

Atmosphere

83 percent hydrogen, 15 percent helium, 2 percent methane

Geology

Primarily rock and ice; helium/hydrogen core

Moons

21

Rings

11 faint rings



Neptune

Distance from Earth

2.71 billion miles
(4.35 billion kilometers)

Temperature

-350 degrees Fahrenheit
(-212 degrees Celsius)

Atmosphere

Hydrogen, helium and methane levels similar to Uranus; fastest atmospheric winds in the solar system, exceeding 1,500 mph (2,414 kilometers per hour)

Geology

Gaseous outer surface; core of rock, ice and liquid hydrogen

Moons

8

Rings

Four faint, dark rings



Proposed tether technology at Earth orbit

A MXER tether system is an innovative combination of technologies designed to help propel satellites from Low Earth orbit to higher energy orbits, such as to the Moon, Mars and beyond. The system consists of a long, strong cable -- approximately 100 to 150 kilometers long (62 to 93 miles) -- rotating in an elliptical orbit around Earth. Like a catapult, one end of the tether catches payloads in low Earth orbit. As it rotates, the tether accelerates the payloads to higher velocities and then throws them into higher-energy orbits.

Once the payload is released, the momentum given to it from the tether is restored using electrodynamic forces to push against the Earth's magnetic field. By using solar power to drive ionospheric current through the tether and create thrust, the tether can reboost itself, or increase its energy and raise its orbit, without using propellant.

More about In-Space Propulsion

"There is nothing so far removed from us to be beyond our reach, or so far hidden that we cannot discover it." — Rene Descartes

The mission of NASA's In-Space Propulsion Technology Program and the technologies being researched and developed under its charter is threefold: to enable science at new destinations; to significantly reduce the time and cost required for spacecraft to reach their destinations; and to allow mission planners to shift their focus from the difficulty of the journey to the science challenges at the destination.

All these technologies play a part in the efforts of the In-Space Program to develop advanced propulsion systems that will revolutionize NASA's interplanetary science mission goals.

Research in these technology areas is being done by the In-Space Propulsion Technology Program, which is managed by NASA's Science Mission Directorate in Washington and implemented by the In-Space Propulsion Technology Office at the Marshall Space Flight Center in Huntsville, Ala. The program's objective is to develop in-space propulsion technologies that can enable or benefit near and mid-term NASA space science missions by significantly reducing cost, mass and travel times.

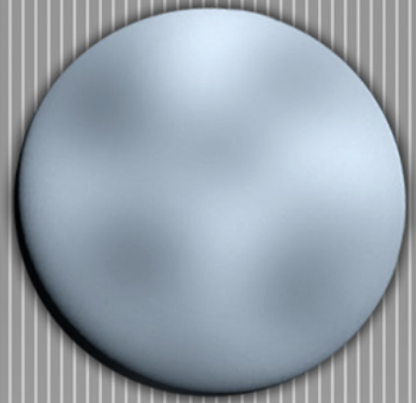
To find out more about the planned missions of NASA's Science Mission Directorate and the Marshall Center's In-Space Propulsion Technology Office, visit:

<http://www.nasa.gov>

<http://www.inspacepropulsion.com>

Marshall Space Flight Center Media Relations Department

<http://www.msfc.nasa.gov/news>



Pluto

Distance from Earth

3.58 billion miles

Temperature

-373 degrees Fahrenheit

Atmosphere

Indications of heavy nitrogen, with some carbon monoxide and methane; entire atmosphere may freeze solid except when closest to Sun

Geology

Studies suggest 70 percent rock, 30 percent water ice containing nitrogen, methane, ethane, and carbon monoxide

Moons

1 (Charon)

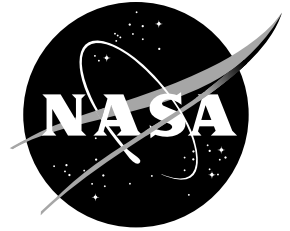
Rings

Note: For 20 years out of every 240, Pluto's orbit brings it closer to the Sun than Neptune. This phenomenon last occurred between February 1979 and February 1999. It will start again in 2219.

Explore. Discover. Understand.

National Aeronautics and
Space Administration

Marshall Space Flight Center
Huntsville, Alabama 35812



Ultra-Light Tank Technology for In-Space Applications

NASA solar system exploration missions are undergoing a transition from fly-by observers to missions that orbit, land on and return samples from planetary bodies. These new missions are often more demanding of propulsion capabilities, increasing the need for more efficient propellant management to accomplish mission objectives. To meet this challenge, NASA scientists are looking at new and improved systems that not only will maintain propellants long-term, but also reduce overall propulsion system mass.

Research is underway to advance material and manufacturing technologies and related design methodology for lighter-weight in-space propulsion system tanks. Sponsored by the In-Space Propulsion Technology Project, NASA's Jet Propulsion



An ultra lightweight composite overwrapped tank, designed and fabricated by Carleton Pressure Technology Division of Westminster, Md., and NASA's Jet Propulsion Laboratory in Pasadena, Calif., during the development phase of the Mars Exploration Rover Program. Research of lightweight in-space propulsion system tank technologies is sponsored by the In-Space Propulsion Technology Project at the Marshall Space Flight Center in Huntsville, Ala.

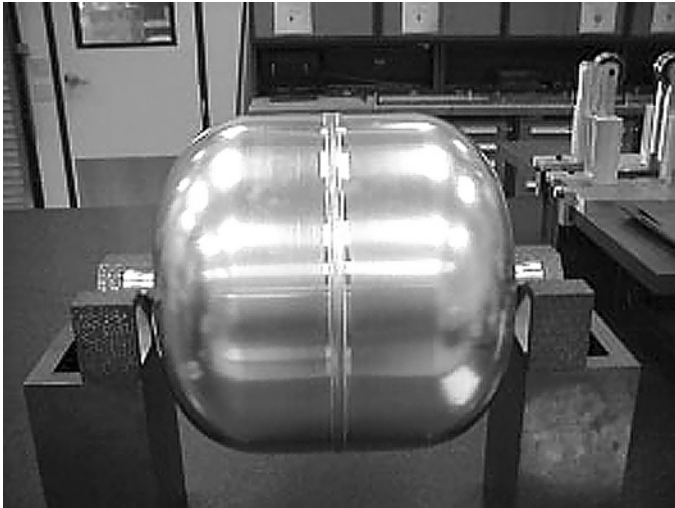
Laboratory in Pasadena, Calif., and its industry partners are maturing composite, over-wrapped tanks to greatly reduce their weight. A composite over-wrap provides added strength to the tank, which is an essential element that stores spacecraft propellant and pressurant in a propulsion system.

Improvements in the area of composite over-wrapped propellant and pressurant tanks could result in a reduction of overall spacecraft propulsion system weight. This weight reduction could allow additional payload and scientific instrumentation to be flown—potentially resulting in greater scientific return.

Typically, propellant tanks are the largest component of in-space chemical propulsion systems. A state-of-the-art propellant tank is usually made from titanium alloy—a high strength, low weight metal alloy that is 40 percent lighter than steel and has high resistance to corrosive environments, such as salt air. New, ultra-light tank technology (ULTT) could offer not only the same level of strength and corrosion resistance, but also reduce propellant tank mass by as much as 50 percent as compared to an all-titanium tank.

Propellant tanks normally are made with a thick metal liner and a composite fiber over-wrap. ULTT utilizes an ultra-thin (0.005 to 0.010 inch) chemically etched metallic liner over-wrapped with a new ultra-high-strength, ultra-thin, low-density composite fiber, T1000. The liner provides hermetic sealing—to prevent the escape of propellant or entry of air—and propellant compatibility, while stresses due to pressure and external loads are efficiently carried by the T1000 graphite composite. This tank

technology could significantly reduce the mass of pressurant tanks. Overall, ultra-light tank technology could result in mass savings ranging from about 10 kilograms to 40 kilograms for most missions.



An aluminum liner for ultra-lightweight tank technologies, designed and fabricated by Carleton Pressure Technology Division of Westminster, Md., and NASA's Jet Propulsion Laboratory in Pasadena, Calif., during the development phase of the Mars Exploration Rover Program. Research of lightweight in-space propulsion system tank technologies is sponsored by the In-Space Propulsion Technology Project at the Marshall Space Flight Center in Huntsville, Ala.

Current tasks in ultra-light tank technology include acceptance and margin testing of state-of-the-art propellant tanks and stress rupture life testing to expand the database on fiber over-wrap material properties. This will establish lower allowable design margins and ensure long-term performance with minimum fiber mass—enabling ultra-lightweight propellant tanks.

The Advanced Chemical Propulsion Technology Area in the In-Space Propulsion Technology Office at the Marshall Center is partnering with NASA's Jet Propulsion Laboratory in Pasadena to advance ultra-light tank technology for in-space application.

Research in advanced chemical propulsion is being conducted by the In-Space Propulsion Technology Program, which is managed by NASA's Science Mission Directorate in Washington and implemented by the In-Space Propulsion Technology Office at the Marshall Space Flight Center in Huntsville, Ala. The program's objective is to develop in-space propulsion technologies that can enable or benefit near and mid-term NASA space science missions by significantly reducing cost, mass and travel times.

NASA fuels discoveries that make the world smarter, healthier and safer.

For more information, visit:

<http://www.inspacepropulsion.com>

<http://www.nasa.gov>

Explore. Discover. Understand.



07-Sep-2005

[Research Home](#)

[Opportunity Definitions](#)

[Search](#)

[Proposal Site](#)

- [Subscribe for email notification](#)
- [Submit Notice of Intent to Propose](#)
- [Submit Proposal Information](#)

[NASA Links](#)

- [HQ's CBD](#)

[Notices](#)

[Helpful References](#)

[Research Task Books](#)

[Help](#)

National Aeronautics & Space Administration

Open Solicitations (Office of Space Science)

Program Title of Solicitation	Announcement Number	Solicitation Release Date	NOI Due Date	Proposals Due Date
----------------------------------	---------------------	------------------------------	-----------------	--------------------

There are no data matching your search criteria.

NOTICE: Unless otherwise indicated in the solicitation itself, instructions for the format, content, and submission of proposals for all NASA Research Announcements (NRA's) is given in the document entitled "[Office of Space Science \(OSS\) Guidebook for Proposers Responding to a NASA Research Announcements \(NRA\)](#)".



Curator: [NASA Peer Review Services](#)

Responsible NASA Official: [Greg](#)

[Lindsay](#)

[Disclaimer](#)



NATIONAL AERONAUTICS
AND SPACE ADMINISTRATION

- + Visit NASA.gov
- + Contact NASA

Site Search:



NASA'S SCIENCE RESOURCES HELP AGENCIES RESPOND TO KATRINA

NASA science instruments and Earth-orbiting satellites are providing detailed insight about the environmental impact caused by Hurricane Katrina. Images and data are helping characterize the extent of flooding; damage to homes, businesses and infrastructure; and potential hazards caused by the storm and its aftermath.

NASA, along with academic institutions and partner agencies, is working to ensure the Department of Homeland Security and the Federal Emergency Management Agency (FEMA) have the best available information to aid in responding to this catastrophic event.

- + Current News Stories
- + NASA Press Releases
- + Sign up for Email Updates
- + Media Contacts

[Click here for more information...](#)



Science + Advisory Committees
Strategy + Strategic Planning
+ Science Roadmaps



Missions + Earth-Sun System
+ Solar System
+ Universe
+ All Missions

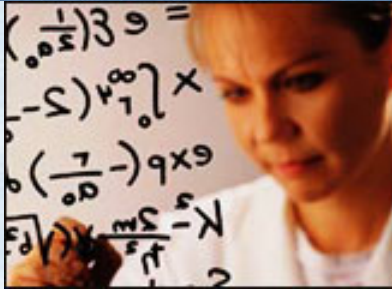
sciencespectrum



Images of the Day

Multimedia *Images, Animations,
Videos, and Interactivity
Produced from NASA's
Science Programs.*

sciencecommunities



**Scientists/
Engineers** + Research Opportunities
+ Amateur Astronomy
+ E/PO Opportunities



Educators + Education Products



**Kids & Young
Adults** *Activities, Games and
Puzzles Designed for
Fun and Learning.*



+ NASA Privacy Statement, Disclaimer,
and Accessibility Certification
+ Use of NASA Images



NASA Official: Sharron Sample
Last Updated: July 5, 2005
+ Contact NASA



Office of Space Science
NASA Announcements Opportunity

[*NRA Home*](#)

[*OSS
Home*](#)

[*NASA
Home*](#)

[Table of Contents](#)

OMB Approval No. 2700-0087

**RESEARCH OPPORTUNITIES IN SPACE SCIENCE - 2002
(ROSS-2002)**

**NASA Research Announcement
Soliciting Basic Research Proposals**

NRA 02-OSS-01

Issued: January 28, 2002

Proposals Due

**Starting March 21, 2002,
through February 14, 2003**

**Office of Space Science
National Aeronautics and Space Administration
Washington, DC 20546-0001**

**RESEARCH OPPORTUNITIES IN SPACE SCIENCE - 2002
(ROSS-2002)**

Table of Contents

SUMMARY OF SOLICITATION

1. INTRODUCTION AND GENERAL POLICIES
2. INSTRUCTIONS FOR PREPARATION AND SUBMISSION OF PROPOSALS
3. OSS EDUCATION AND PUBLIC OUTREACH PROGRAM
4. ITEMS OF SPECIAL IMPORTANCE
5. SUMMARY INFORMATION APPLICABLE TO THIS SOLICITATION

TABLE 1: SOLICITED SCIENCE PROGRAM ELEMENTS (IN ORDER OF PROPOSAL DEADLINES)

TABLE 2: SOLICITED SCIENCE PROGRAM ELEMENTS (IN ORDER OF APPENDIX A)

APPENDIX A: DESCRIPTION OF PROGRAM ELEMENTS

A.1 ASTRONOMY AND PHYSICS DIVISION

A.1.1 Overview

A.1.2 Astrophysics Data Analysis

A.1.3 Long-Term Space Astrophysics

A.1.4 Astrophysics Theory

A.1.5 Space Astrophysics Research and Analysis

A.1.6 High Energy Astrophysics

A.2 SOLAR SYSTEM EXPLORATION DIVISION

- A.2.1 Overview
- A.2.2 Cosmochemistry
- A.2.3 Planetary Geology and Geophysics
- A.2.4 Origins of Solar Systems
- A.2.5 Mars Data Analysis
- A.2.6 Sample Return Laboratory Instruments and Data Analysis
- A.2.7 Planetary Astronomy
- A.2.8 Near Earth Object Observations
- A.2.9 Planetary Atmospheres
- A.2.10 Exobiology
- A.2.11 Planetary Instrument Definition and Development
- A.2.12 Planetary Major Equipment
- A.2.13 Astrobiology Science and Technology Instrument Development
- A.2.14 Mars Fundamental Research
- A.2.15 Mars Instrument Development Project

A.3 SUN-EARTH CONNECTION DIVISION

- A.3.1 Overview
- A.3.2 Solar and Heliospheric Physics
- A.3.3 Geospace Sciences
- A.3.4 Sun-Earth Connection Theory
- A.3.5 Sun-Earth Connection Guest Investigator
- A.3.6 Sun-Earth Connection Instrument Development
- A.3.7 Living With a Star Targeted Research And Technology
- A.3.8 Living With a Star Geospace Instrument Development

A.4 INTERDISCIPLINARY PROGRAM ELEMENTS

A.4.1 Overview

A.4.2 In-Space Propulsion Technologies

RESEARCH OPPORTUNITIES IN SPACE SCIENCE - 2002 (ROSS-2002)

SUMMARY OF SOLICITATION

1. INTRODUCTION AND GENERAL POLICIES

The stated mission of the Space Science Enterprise of the National Aeronautics and Space Administration (NASA) is to solve the mysteries of the universe, to explore the solar system, to discover planets around other stars, and to search for life beyond Earth. To carry out this mission, NASA's Office of Space Science (OSS) sponsors a broad range of research programs relevant to its four Science Themes, defined as:

- *Astronomical Search for Origins and Planetary Systems (ASO)* that addresses the origins of galaxies, stars, proto-planetary and extra-solar planetary systems, Earth-like planets, and the origin of life;
- *Solar System Exploration* (abbreviated as ESS) that seeks to understand all aspects of our Solar System, including the planets, satellites, small bodies, and solar system materials, and the search for possible habitats of life beyond Earth;
- *Structure and Evolution of the Universe (SEU)* that involves the study of cosmology, the large scale structure of the universe, the evolution of stars and galaxies, including the Milky Way and objects with extreme physical conditions, and an examination of the ultimate limits of gravity and energy in the Universe; and
- *The Sun-Earth Connection (SEC)* that concerns the Sun as a typical star and as the controlling agent of the space environment of the Solar System, especially the Earth.

From a humanistic point of view, these four themes seek to answer four fundamental questions:

"How did the Universe begin and evolve?"

"Where did we come from?"

"Where are we going?" and

"Are we alone?"

Further information about these themes, as well as access to the most recent Strategic Plans (as of late 2001) for both NASA and OSS, may be found through the OSS homepage on the World Wide Web at <http://spacescience.nasa.gov> .

OSS pursues these science themes using a wide variety of both space flight programs and investigations in basic science and technology. This current NASA Research Announcement (NRA) ROSS-2002 solicits proposals for Supporting Research and Technology (SR&T) investigations that seek to understand naturally occurring space phenomena and space science-related technologies. Proposals in response to this NRA should be submitted to the most relevant science Program Elements given in Appendix A (see also the Table of Contents that prefaces this Summary of Solicitation). [Table 1](#) at the end of this Summary lists these Program Elements in the order of their deadlines for the submission of proposals, while [Table 2](#) lists them in the order in which they are organized in Appendix A. [Tables 1](#) and [2](#) also cross reference these Program Elements to the four OSS Science Themes noted above. Appendix A contains detailed descriptions of each Program Element, and questions about each may be directed to their respective Discipline Scientist(s) identified in the "Programmatic Information" section that concludes each one.

The ROSS NRA's issued in 2000 (NRA 00-OSS-01) and 2001 (NRA 01-OSS-01) organized the Program Elements into nine "clusters" based on their scientific objectives and/or research techniques. However, in mid-2001, the Office of Space Science was reorganized into three scientific Divisions,

- Astronomy and Physics Division,
- Solar System Exploration Division, and
- The Sun-Earth Connection Division.

Therefore, starting with this ROSS-2002 NRA, the Program Elements are now organized into four main Sections in Appendix A, of which the first three are managed respectively by these three new OSS science Divisions, while the

fourth one contains Interdisciplinary Program Elements. Each of these four main sections of Appendix A is prefaced with an "Overview" subsection that provides a broad introduction to its program content and objectives that all interested applicants to this NRA are urged to read before preparing their proposals.

Recommendations for funding for the proposals submitted to this NRA will be based on the peer evaluation of each proposal's intrinsic merit, its relevance to NASA's objectives, and its cost. For the purposes of this NRA

- (i) by intrinsic merit is meant the proposal's science and technical merits, the capabilities of the proposing institution, the qualifications of the proposing personnel, and the overall standing of the proposal among similar proposals and/or evaluation against the state-of-the-art;
- (ii) by relevance to NASA's objectives is meant the proposal's relevance to the objectives of the OSS science Program Element in this NRA to which the proposal is submitted as well as to the achievement of the OSS and NASA goals as given respectively in their most recent Strategic Plans; and
- (iii) by cost is meant the reasonableness and realism of the proposal's requested budget in addition to its size with respect to the available funds.

Finally, it should be noted that, regardless of the merits of the submitted proposals, the Government's obligation to make awards is contingent upon the availability of appropriated funds through the Federal budget process from which payment can be made and the receipt of proposals in response to this NRA that NASA determines are acceptable for award.

Participation in this program is open to all categories of U.S. and non-U.S. organizations, including educational institutions, industry, nonprofit institutions, NASA Centers, and other Government agencies. Historically Black Colleges and Universities (HBCU's), other minority educational institutions, and small businesses and organizations owned and controlled by socially and economically disadvantaged individuals or women are particularly encouraged to apply. Participation by non-U.S. organizations in this program is

encouraged subject to NASA's policy of no-exchange-of-funds (see further information in the [*NASA Guidebook for Proposers*](#) discussed below).

Finally, all prospective proposers are advised that safety is a top priority in all NASA's programs. Safety is the freedom from those conditions that can cause death, injury occupational illness, damage to or loss of equipment or property, or damage to the environment. NASA's safety priority is to protect: (1) the public, (2) astronauts and pilots, (3) the NASA workforce (including employees working under NASA instruments), and (4) high-value equipment and property. All proposals submitted in response to this solicitation are expected to comply with this policy.

2. INSTRUCTIONS FOR PREPARATION AND SUBMISSION OF PROPOSALS

Starting with last year's ROSS-2001 NRA, the policies and procedures for the preparation and submission of proposals, as well as those for NASA's review and selection of proposals for funding, are now presented in a separate document entitled *Guidebook for Proposers Responding to NASA Research Announcements* (abbreviated as *NASA Guidebook for Proposers*) that is accessible by opening the single Web site portal for the submission of proposals to any of the NASA program offices at the World Wide Web URL <http://research.hq.nasa.gov>, and linking through the menu item "Helpful References," or may be directly accessed at URL <http://www.hq.nasa.gov/office/procurement/nraguidebook/> .

By reference, this [*NASA Guidebook for Proposers, Edition: 2001 \(May 4, 2001\)*](#) is hereby incorporated into this ROSS2002 NRA, and proposers to this NRA are responsible for understanding and complying with its procedures before preparing and submitting their proposals. Proposals that do not conform to its standards may be declared noncompliant and returned without review. The required proposal *Budget Summary* form is now both available from and must be submitted through the same Web site as that for the *Cover Page/ Proposal Summary* (see Summary Information below; note: this online submission of the *Budget Summary* is a new procedure that starts with this OSS solicitation). After the requested data are entered, both of these forms are printed for submission with the required hard copies of the proposal.

The other chapters and appendices of this [*NASA Guidebook for Proposers*](#) provide supplemental information about the entire NRA process, including NASA policies for the solicitation of proposals, guidelines for writing complete and effective proposals, the NASA policies and procedures for the review and selection of proposals, as well as for issuing and managing the awards to the institutions that submitted selected proposals, and Frequently Asked Questions (FAQ's) about a variety of the NASA proposal and award processes and procedures. Note that the NASA policy for proposals involving non-U.S. participants is given in Section (I) of Appendix B of this [*NASA Guidebook*](#). Comments and suggestions of any nature about this *Guidebook* are encouraged and welcomed and may be directed at any time to Dr. David Bohlin, Code SS, Office of Space Science, NASA Headquarters, Washington, DC 20546-0001; telephone: 202-358-0880; E-mail: david.bohlin@hq.nasa.gov (if submitted by E-mail, use "Proposer's Guidebook" as the Subject of the message).

The World Wide Web site for submitting both a Notice of Intent (NOI) to propose (which is encouraged but not required) and a proposal's *Cover Page/ Proposal Summary* and *Budget Summary* is given in Section 5, Summary Information, below (also Chapters 2 and 3 of the [*Guidebook for Proposers*](#) contain detailed information about these two items). Although a point of contact for assistance in accessing and/or using this Web site is given in the Summary Information below, interested applicants to this NRA are urged to access this site well in advance of the various due dates for materials to familiarize themselves with its structure.

3. OSS EDUCATION AND PUBLIC OUTREACH PROGRAM

The Office of Space Science is committed to fostering the broad involvement of the space science community in Education and Public Outreach (E/PO) with the goal of enhancing the Nation's formal education system and contributing to the broad public understanding of science, mathematics, and technology. Progress towards achieving this goal has become an important part of the broad justification for the public support of space science.

As a consequence of the plans and policies that have been established and implemented over the past several years, a significant national E/PO space science program is now underway as described by the OSS E/PO *Newsletters*

and the *Annual Reports* that may be accessed by opening the "Education" link on the OSS homepage at <http://spacescience.nasa.gov>. This site also provides access to the two key documents that establish the basic policies and guidance for all OSS E/PO activities: A strategic plan entitled *Partners in Education: A Strategy for Integrating Education and Public Outreach Into NASA's Space Science Programs* (March 1995), and an *implementation plan entitled Implementing the Office of Space Science Education/Public Outreach Strategy* (October 1996). Both of these documents may also be obtained in hard copy from Dr. Jeffrey D. Rosendhal, Office of Space Science, Code S, NASA Headquarters, Washington DC 20546; E-mail: jeffrey.rosendhal@hq.nasa.gov.

In response to the many constructive comments received from members of the space science community on how to improve, simplify, and streamline OSS's efforts to involve scientists in E/PO activities, substantial changes in procedures for incorporating E/PO into research grants were made starting in 2001 that are continued into 2002. These changes are intended to decrease the overall workload on the space science community, increase the likelihood that more E/PO proposals of merit will be funded, and more effectively encourage successful science proposers to add an E/PO component to their "parent" research effort. In addition, OSS has worked to open up new avenues for E/PO participation for space scientists and to develop a variety of approaches that allows such contributions to be recognized and acknowledged (details may be accessed through the "Education" Web site indicated above).

A summary of the key elements of the current OSS E/PO program that apply to this NRA are as follows:

- E/PO proposals are solicited only from those proposers whose research proposals have been selected for a research award under this NRA;
- The cost cap on E/PO proposals by individual investigators is now \$15K/year;
- Selected Principal Investigators have two windows of opportunity to submit an E/PO proposal, either: (i) no later than 45 days after the date of their letter of selection for a new research award (with the anticipation of starting the E/PO activity within the first half of the first year of the parent research award); or (ii) no later than 75 days in advance of the yearly anniversary date of their award (with the anticipation of starting the E/PO activity in conjunction with the next year's funding supplement

for the award);

- Anyone holding an existing multiple year research award funded through any previous OSS NRA may propose an E/PO supplement to be funded through their "parent" research award or to participate in E/PO in some other appropriate fashion (see the indicated Education Web site);
- The "Institutional Proposal" option has been reintroduced that allows several OSS-funded researchers located at the same institution to collectively carry out a more ambitious, expansive E/PO program (a cost cap of \$50K/year but no more than \$125K over the nominal three-year lifetimes of the parent awards); and
- Consistent with past E/PO policies and to ease the burden of NASA's administration of such small supplemental awards, the total period of performance for any E/PO award is restricted to not exceed that of its parent research award.

For further details and specific guidance and information on preparing and submitting a proposal for E/PO funding under this or any previous OSS NRA, reference the Web site at <http://spacescience.nasa.gov/education/scientists/guidelines/index.html>. Questions and/or comments and suggestions about the OSS E/PO program are sincerely welcomed and may be directed to either Dr. Philip Sakimoto (telephone: 202-358-0949; E-mail: phil.sakimoto@hq.nasa.gov) or Ms. Rosalyn Pertzborn (telephone: 202-358-1953; E-mail: rpertzbo@hq.nasa.gov).

4. ITEMS OF SPECIAL IMPORTANCE

- (i) Because this ROSS-2002 NRA is released far in advance of most of the deadlines given in Tables 1 or 2, additional programmatic information for any Program Element may develop before its proposals are due. If so, such information will be added as Amendments to this NRA as posted at its Web site no later than 30 days before the proposal deadline. Although NASA OSS will also send an electronic notification of any such amendments to all subscribers of its electronic notification system (see item (iii) below), it is the responsibility of prospective proposers to check this NRA's Web site for updates concerning the Program Element(s) of interest.
- (ii) OSS now requires the electronic submission of certain key elements of proposals through the World Wide Web (see below in [Section 5](#), Summary Information). While every effort is made to ensure the reliability and accessibility of this Web site, and to maintain a Help Desk via E-mail, difficulty may arise at any point on the Internet including the user's own equipment. Therefore, prospective proposers are urged to familiarize themselves with this site and to submit the required proposal materials well in advance of the deadline(s) of the Program Element(s) of interest.
- (iii) OSS maintains an electronic notification system to alert interested subscribers of the impending release of its research program announcements. Subscription to this service is accomplished through the menu item "To subscribe to the OSS electronic notification system" found on the menu of the OSS research page at http://research.hq.nasa.gov/code_s/code_s.cfm. Owing to the increasingly multidisciplinary nature of OSS programs, this electronic service will notify subscribers of all NASA OSS program announcements regardless of the type and science objectives (about 10 to 15 per year). Regardless of whether or not this service is subscribed to, all OSS research announcements may be accessed from the menu listing *Current (Open) Solicitations* at the Web site given above as soon as they are posted (typically by 8:30 a.m.

Eastern Time on their date of release).

- (iv) For more information about the types of research supported by the program elements in previous editions in this series of ROSS NRA's, abstracts for currently funded investigations are available through the menu listing *Past/Archive Solicitations & Selections* at http://research.hq.nasa.gov/code_s/code_s.cfm.

5. SUMMARY INFORMATION APPLICABLE TO THIS NRA

+ICI- Program Alpha-Numeric Identifier	NRA 02-OSS-01
+ICI- Date of NRA Release	January 28, 2002
+ICI- Access to text	Link through the menu listings <i>Research Solicitations +IZI-Current (Open) Solicitations</i> starting from the OSS home page at http://spacescience.nasa.gov .
+ICI- Guidance for preparation and submission of proposals (including default page limits)	" NASA Guidebook for Proposers Responding to a NASA Research Announcement (NRA) " at URL http://www.hq.nasa.gov/office/procurement/nraguidebook/
+ICI- <i>Notice of Intent (NOI) to Propose</i> (encouraged but not required): - Desired due date - Web site for electronic submission - Late submission (up to	- See Tables 1 or 2 below for Program Element of interest - Open appropriate menu listing at http://research.hq.nasa.gov (available for submissions for +AH4-30 days starting +AH4-90 days prior to Proposal Deadline (Help Desk E-mail: r-help@nasaprs.com) - Submit information specified in Section 3.1

15 days prior to Proposal Deadline)	of NASA Guidebook for Proposers by E-mail to deb.tripp@hq.nasa.gov
+ICI- <i>Cover Page/ Proposal Summary and Budget Summary</i> : - Deadline - Web site for electronic submission	- Same as for proposals (see Tables 1 or 2 for Program Element of interest); print completed items from Web site http://research.hq.nasa.gov - Same as above (open for submissions starting +AH4- 45 days prior to Proposal Deadline (Help Desk: E-mail: r-help@nasaprs.com)
+ICI- Proposal page limits	Default values given in Section 2.3 of NASA Guidebook for Proposers (unless otherwise specified in Program Element in Appendix A).
+ICI- Submission of proposal (including printed <i>Cover Page/Proposal Summary and Budget Summary</i>): - Required Number - Deadline - Address for submission by U.S. Postal Service, commercial delivery, or private courier	- Signed original proposal plus 15 copies (unless otherwise specified in Program Element in Appendix A). - 4:30 p.m. ET on date in Tables 1 or 2 for Program Element of application. <u>Name of Program Element</u> ROSS-2002 NRA Office of Space Science NASA Peer Review Services 500 E Street, SW, Suite 200 Washington, DC 20024 Telephone: 202-479-9030
+ICI- Selecting Official	Cognizant Division Director for Program Element of application (unless otherwise noted), NASA Office of Space Science

+ICI- Announcement of selections	Goal: 150 days after Proposal Deadline
+ICI- Initiation of funding for new awards	Goal: 46 days after proposal selections <u>or</u> passage of NASA Fiscal Year 2003 budget, which ever occurs <u>last</u> .
+ICI- Further information: - For a specific Program Element - For <u>general</u> NRA policies and procedures	- See cognizant Discipline Scientist(s) identified at end of each Program Element in Appendix A. - Dr. J. David Bohlin Code SSO Office of Space Science NASA Headquarters Washington, DC 20546-0001 E-mail: david.bohlin@hq.nasa.gov

Your interest and cooperation in responding to this ROSS-2002 NRA are welcome. Comments about the inclusive nature and/or structure of this NRA for the OSS supporting research and analysis programs are also sincerely solicited and may be directed to either the Discipline Scientists identified for the Program Elements in Appendix A or to the point of contact for "general NRA policies and procedures" identified in the table of Summary Information above.

Dr. Colleen N. Hartman
Director
Solar System Exploration
Division

Dr. Anne L. Kinney
Director
Astronomy and Physics
Division

Dr. George L. Withbroe
Director
The Sun-Earth Connection
Division

TABLE 1

**SCIENCE PROGRAM ELEMENTS SOLICITED IN THE ROSS-2002
NRA
(in order of the proposal due dates)**

NRA Appendix	Science Program Element (see Appendix A)	NOI Due Date [M/D/Y]	Proposal Due Date [M/D/Y]	Relevant OSS Science Themes [1]			
				ASO	SEU	ESS	SEC
A.2.14	Mars Fundamental Research	2/25/02	3/21/02			X	
A.4.2	In-Space Propulsion Technologies	3/04/02	4/03/02	X	X	X	X
A .1.6	High Energy Astrophysics [2]	2/22/02	4/05/02		X		
A.3.8	Living With a Star Geospace Instrument Development	3/01/02	4/12/02			X	X
A.3.6	Sun-Earth Connection Instrument Development	3/01/02	4/12/02			X	X
A.2.15	Mars Instrument Development	2/28/02	5/01/02			X	
A.2.3	Planetary Geology and Geophysics [3]	3/08/02	5/03/02			X	
A.1.5	Space Astrophysics Research and Analysis	3/13/02	5/10/02	X	X		

A.3.5	Sun-Earth Connection Guest Investigator	3/15/02	5/17/02				X
A.2.2	Cosmochemistry [3] X	3/29/02	5/24/02	X		X	
A.2.9	Planetary Atmospheres [3]	4/05/02	6/07/02			X	
A.2.6	Sample Return Laboratory Instruments & Data Analysis	4/08/02	6/07/02	X		X	
A.2.4	Origins of Solar Systems	3/15/02	6/14/02	X		X	
A.2.8	Near Earth Object Observations	4/26/02	6/28/02	X		X	
A.2.7	Planetary Astronomy [3]	4/26/02	6/28/02	X		X	
A.1.2	Astrophysics Data Analysis	5/15/02	7/10/02	X	X		
A.1.3	Long-Term Space Astrophysics	5/15/02	7/10/02	X	X		
A.3.3	Geospace Sciences	5/24/02	7/26/02			X	X
A.2.11	Planetary Instrument Definition and Development	6/07/02	8/07/02			X	
A.2.10	Exobiology [3]	6/07/02	8/09/02	X		X	
A.2.5	Mars Data Analysis	6/14/02	8/16/02			X	
A.1.4	Astrophysics Theory	6/27/02	8/30/02	X	X		

A.3.7	Living With a Star Targeted Research & Technology	7/19/02	9/20/02				X
A.2.13	Astrobiology Science and Technology Instrument Development	9/06/02	11/06/02	X		X	
A.3.2	Solar and Heliospheric Physics	12/13/02	2/14/03				X
A.2.12	Planetary Major Equipment [3]	See ESS Program Element of interest. [3]		X		X	
A.3.4	Sun-Earth Connection Theory	Not solicited in this NRA					X

Please also see [Amendments](#)

Notes:

- [1] ASO: Astronomical Search for Origins; SEU: Structure and Evolution of the Universe; ESS: Solar System Exploration; SEC: The Sun-Earth Connection.
- [2] The *High Energy Astrophysics* Program Element now combines those separately identified in the ROSS-2001 NRA as *X-ray and Gamma-ray Astrophysics* and as *Cosmic Ray Astrophysics*.
- [3] The proposals for *Planetary Major Equipment* Program Element A.2.12 may be submitted in conjunction with Program Elements A.2.2: *Cosmochemistry*; A.2.3: *Planetary Geology and Geophysics*; A.2.7: *Planetary Astronomy*; A.2.9: *Planetary Atmospheres*; and A.2.10 *Exobiology*.

TABLE 2

**SCIENCE PROGRAM ELEMENTS SOLICITED IN THE ROSS-2002
NRA
(in order of listing in Appendix A)**

NRA Appendix	Science Program Element (see Appendix A)	NOI Due Date [M/D/Y]	Proposal Due Date [M/D/Y]	Relevant OSS Science Themes [1]			
				ASO	SEU	ESS	SEC
A.1.2	Astrophysics Data Analysis	5/15/02	7/10/02	X	X		
A.1.3	Long-Term Space Astrophysics	5/15/02	7/10/02	X	X		
A.1.4	Astrophysics Theory	6/27/02	8/30/02	X	X		
A.1.5	Space Astrophysics Research and Analysis	3/13/02	5/10/02	X	X		
A.1.6	High Energy Astrophysics [2]	2/22/02	4/05/02		X		
A.2.2	Cosmochemistry [3]	3/29/02	5/24/02	X		X	
A.2.3	Planetary Geology and Geophysics [3]	3/08/02	5/03/02			X	
A.2.4	Origins of Solar Systems	3/15/02	6/14/02	X		X	
A.2.5	Mars Data Analysis	6/14/02	8/16/02			X	
A.2.6	Sample Return Laboratory Instruments & Data Analysis	4/08/02	6/07/02	X		X	

A.2.7	Planetary Astronomy [3]	4/26/02	6/28/02	X		X		
A.2.8	Near Earth Object Observations	4/26/02	6/28/02	X		X		
A.2.9	Planetary Atmospheres [3]	4/05/02	6/07/02			X		
A.2.10	Exobiology [3]	6/07/02	8/09/02	X		X		
A.2.11	Planetary Instrument Definition and Development	6/07/02	8/07/02			X		
A.2.12	Planetary Major Equipment [3]	See ESS Program Element of interest. [3]		X		X		
A.2.13	Astrobiology Science and Technology Instrument Development	9/06/02	11/06/02	X		X		
A.2.14	Mars Fundamental Research	2/25/02	3/21/02			X		
A.2.15	Mars Instrument Development	2/28/02	5/01/02			X		
A.3.2	Solar and Heliospheric Physics	12/13/02	2/14/03				X	
A.3.3	Geospace Sciences	5/24/02	7/26/02			X	X	
A.3.4	Sun-Earth Connection Theory	Not solicited in this NRA.					X	

A.3.5	Sun-Earth Connection Guest Investigator	3/15/02	5/17/02				X
A.3.6	Sun-Earth Connection Instrument Development	3/01/02	4/12/02			X	X
A.3.7	Living With a Star Targeted Research & Technology	7/19/02	9/20/02				X
A.3.8	Living With a Star Geospace Instrument Development	3/01/02	4/12/02			X	X
A.4.2	In-Space Propulsion Technologies	3/04/02	4/03/02	X	X	X	X

Please also see [Amendments](#)

Notes:

- [1] ASO: Astronomical Search for Origins; SEU: Structure and Evolution of the Universe; ESS: Solar System Exploration; SEC: The Sun-Earth Connection.
- [2] The *High Energy Astrophysics* Program Element now combines those separately identified in the ROSS-2001 NRA as *X-ray and Gamma-ray Astrophysics* and as *Cosmic Ray Astrophysics*.
- [3] The proposals for *Planetary Major Equipment* Program Element A.2.12 may be submitted in conjunction with Program Elements A.2.2: *Cosmochemistry*; A.2.3: *Planetary Geology and Geophysics*; A.2.7: *Planetary Astronomy*; A.2.9: *Planetary Atmospheres*; and A.2.10 *Exobiology*.

[Back to Top](#)

[Go to the Table of Contents](#)

[Go to the Cover of NRA 02-OSS-01](#)

[NRA Home](#)

[OSS Home](#)

[NASA Home](#)

Curator: [NASA Peer Review Services](#)

Program Scientist:

Last updated: January, 2002



Office of Space Science
NASA Announcements Opportunity

[NRA Home](#)

[OSS
Home](#)

[NASA
Home](#)

A.4 INTERDISCIPLINARY PROGRAM ELEMENTS

A.4.1 OVERVIEW

Occasionally the Office of Space Science (OSS) sponsors program elements that apply across all, or nearly all four of its science themes as defined in Section 1 of the Summary of Solicitation of this NRA, for example, the Applied Information Systems Research (AISR) program that was previously solicited from 1998 through 2001. However, at the time of publication new proposals are not being solicited for this AISR program although it may be added later as an amendment during the life of this ROSS-2002 NRA; if so, it will be released at least 90 days in advance of its Proposal Due Date. There is a new interdisciplinary program for which proposals are solicited under this NRA, namely the In-Space Propulsion Technologies, [Appendix A.4.2](#).

A.4.2 IN-SPACE PROPULSION TECHNOLOGIES

1. Scope of Program

The goal of the In-Space Propulsion (ISP) program of the NASA Office of Space Science is to develop advanced propulsion technologies for use beyond Earth orbit that reduce trip times, mass, and/or cost associated with NASA science missions to the outer planets, satellites, small bodies, and other solar system destinations. This offering of the In-Space Propulsion Technologies (ISPT) program is the second in what is anticipated to be a series of solicitations to support the ISP program (Note: the first such solicitation, for the next Generation Ion Engine Technology, was issued as an amendment to

the ROSS-2001 NRA 01-OSS-01, which may be accessed by linking through "Amendments" at URL http://research.hq.nasa.gov/code_s/nra/current/NRA-01-OSS-01/index.html).

This ISPT program specifically solicits proposals for the development of the following four advanced in-space propulsion technologies that are expected to enable or enhance a wide variety of NASA's science missions:

- Aerocapture;
- High Power Electric Propulsion for Near-Term Nuclear Systems;
- Power Conversion Technologies for Nuclear Electric Propulsion (NEP); and/or
- Solar Sails.

Expanded definitions of the technologies identified above are further provided in the ISP Program Proposal Information Package (PIP) that may be accessed on line at URL http://www.spacetransportation.com/code_s/inspaceannounce.html.

Note that the intent of this ISP Technologies program is not to provide flight hardware that may be used by any specific missions but to develop technologies that may enable missions to be planned that might otherwise be considered untenable. Each submitted proposal may address only one of these technologies, although there is no restriction on the number of proposals that may be submitted by a given organization either by itself or as the lead of a team of organizations.

Teaming arrangements of all kinds is encouraged by all types of proposing organizations, including nonprofit and for-profit, private and governmental. If a non-NASA organization wishes to team with a NASA Center, such negotiations must be accomplished prior to submission of the proposal and all associated costs must be included in the cost section of the proposal. Note that no preference will be given to proposals that seek to team with a NASA Center, nor for proposals that come from a NASA Center. However, for those wishing to consider teaming with a NASA Center the points of contact are:

- NASA Ames Research Center: Mr. Dan Rasky (phone: 650-604-1098, E-mail: drasky@mail.arc.nasa.gov)
- NASA Glenn Research Center: Mr. William Taylor (phone: 216-433-6568, E-mail: william.j.taylor@grc.nasa.gov)
- NASA Johnson Space Flight Center: Mr. Tri Nguyen (Phone: 281-483-0468, E-mail: tri.x.nguyen1@jsc.nasa.gov)
- NASA Langley Research Center: Mr. Jerry Kegelman (phone: 757-864-8022, E-mail: j.t.kegelman@larc.nasa.gov).
- NASA Marshall Space Flight Center: Mr. James Wyckoff (phone: 256-544-7922, E-mail: james.wyckoff@msfc.nasa.gov)
- Jet Propulsion Laboratory: Mr. Dave Vaughn (phone: 818-393-6338, E-mail: david.a.vaughn@jpl.nasa.gov)

2. Programmatic Information

2.1 General Provisions

The technology areas included in this solicitation are only those four given in Section 1 above.

All activities selected through this Program Element will be funded solely through multiyear contracts having a base period of performance of one year or less. Proposals for efforts greater than one year must be structured with a one year initial period with options for extension in time increments not to exceed one year each. The total proposed period of performance may not exceed three years.

Proposals must define clearly measurable milestones (a minimum of two per year) to be achieved in order to justify continuation of funding. Funding approval for the subsequent year(s) will be based on achievements toward milestones for the first year and the continued program need and funds thereafter. Exercise of contract options will be based on performance and there is no guarantee that any options will be funded for the remaining performance timeframe.

The following budget information is tentative and is provided for

planning purposes only and is subject to the availability of funds. In general it is expected that the first year funding will be modest and then grow substantially in the second and third years.

- Aerocapture

The anticipated budget for this technology area for the initial selections is \$2.25M for no more than four awards. Total funding available for Fiscal Years (FY's) 2003 and 2004 is anticipated but not guaranteed to be in the range of \$4M to \$7M per year.

- High Power Electric Propulsion for Near-Term Nuclear Systems

The anticipated budget for this technology area for the initial selections is approximately \$575K for no more than three awards. Total funding available for FY's 2003 and 2004 in this area is anticipated to be approximately \$3M per year.

- Nuclear Electric Propulsion (NEP) Power Conversion Technologies

The anticipated budget for this technology area for the initial selections is approximately \$1M. It is anticipated that only a few (perhaps just one) initial awards will be made. Total funding available for FY's 2003 and 2004 in this area is anticipated to be approximately \$3M per year.

- Solar Sails

The anticipated budget for this technology area for the initial selections is approximately \$400K for no more than one award. Total

funding available for FY's 2003 and 2004 is anticipated to be approximately \$4M per year.

2.2 OSS Education And Public Outreach (E/PO) Program

Consistent with Section 3 of the Summary of Solicitation of this NRA, OSS policy strongly encourages participation by the space science community in education and public outreach activities with the goal of enhancing the Nation's formal education system and contributing to the broad public understanding of science, mathematics, and technology. The baseline policy given in this Summary of Solicitation of this NRA is that proposals for E/PO activities are voluntary on the part of the selected investigators, and this policy is applicable to this ISP program since there may be unusual opportunities associated with its engineering and technology development efforts that may be of special interest to the public and educational community. However, in order to allow for E/PO activities that are appropriately scaled to the much larger awards contemplated for this ISP program element, the policy for E/PO activities is hereby amended to allow budgets of up to 5% of the proposed research activity rather than being capped at \$15K per year as specified in the Summary of Solicitation.

2.3 Proposal Preparation and Submission Information

IMPORTANT INFORMATION

As discussed in the *Summary of Solicitation* of this NRA, the Office of Space Science (OSS) is now using a single, unified set of instructions for the submission of proposals. This material is contained in the document entitled NASA Guidebook for Proposers Responding to NASA Research Announcement – 2001 (or NASA Guidebook for Proposers for short) that is accessible by opening URL <http://research.hq.nasa.gov>, and linking through the menu item "Helpful References," or may be directly accessed online at URL <http://www.hq.nasa.gov/office/procurement/nraguidebook/>. This NRA's Summary of Solicitation also contains the schedule and instructions for the

electronic submission of a Notice of Intent (NOI) to propose and a proposal's Cover Page/Proposal Summary, which now also includes the required Budget Summary, and the mailing address for the submission of a proposal.

Note: In addition to the page limitations stated in Section 2 of the NASA Guidebook for Proposers for the various sections of a proposal, ISP proposals must also contain a Statement of Work (SOW) to be performed, not to exceed three pages in length, which is to be inserted directly after the "References" section of the proposal.

Because the awards to be made through this Program Element will be contracts with options to continue on a yearly basis, they have additional programmatic requirements including reporting, data base entries, and reviews. To support these requirements, NASA will provide a total of four days of training for all selected participants at the NASA Marshall Space Flight Center (MSFC) in the areas of Risk Management (for awards in excess of \$750K) and the Space Transportation Information Network (STIN). Therefore, proposals to this ISPT program must include an appropriate budget for this activity. The MSFC Advanced Space Transportation Program (ASTP) Office will have responsibility for implementation of awards under this amendment. Those who receive an award under program shall provide initial task inputs to ASTP's on-line, password protected, STIN database and submit monthly updates pertaining to: the technology task overview such as technology readiness levels, technical performance measures, risk management, resources, schedule (format compatible with Microsoft Project 2000), and milestones. In addition, a monthly electronic status submittal of accomplishments, issues, and upcoming events will be required. Note that the STIN database requires only a browser to access the system; no special plug-ins are required, and the system was designed, developed, and tested for full functionality on Mac, PC, and Unix platforms.

Other reporting requirements include a Final Report in a format suitable for publication as a Contractor Report. Descriptions of this type of report can be found at http://nodis3.gsfc.nasa.gov/library/displayDir.cfm?Internal_ID=N_PG_2200_002A_&page_name=main.

Finally, all selected participants in this program will be required to develop and present a technical paper at a suitable technical conference and/or publish their results in an appropriate technical journal.

Reviews will be held in conjunction with project level or task milestones, with a minimum of a kick-off and final reviews. These reviews will document the progress against Technical Performance Measures (TPM's) and other performance metrics such as, deliverables, completion of design drawings, test results, cost vs. budget statistics, and adherence to planned schedules.

Questions concerning this Program Element may be directed to the ISP Program Executive:

Ms. Carol W. Carroll
Solar System Exploration Division
Code SE
Office of Space Science
NASA Headquarters
Washington, DC, 20546-0001

Phone: 202-358-1574

Facsimile: 202-385-3097

E-mail: carol.carroll@hq.nasa.gov

[Back to Top](#)

[Go to the Table of Contents](#)

[Go to the Cover of NRA 02-OSS-01](#)

NRA Home

OSS Home

NASA Home

Curator: [NASA Peer Review Services](#)

Program Scientist:

Last updated: January, 2002

EMERGING PROPULSION TECHNOLOGY (EPT) CONCEPTS FOR HIGH PAYOFF DEVELOPMENT.

Archived Synopsis: EMERGING PROPULSION TECHNOLOGY (EPT) CONCEPTS FOR HIGH PAYOFF DEVELOPMENT.

The synopsis NNM04AA02L has been archived.



Owner: Ron Crider | [Technical Support](#) | [Section 508 Compliant](#)

Last revised: February 08, 2005 by DLE

NAIS

Business
Opportunities

Reference
Library

Procurement
Sites

Email
Notification

Feedback

Search All NASA's On-Line
Synopsis

Search Using Your Most Recent
Preferences

Feedback

ADVANCEMENTS IN CHEMICAL PROPULSION TECHNOLOGIES FOR IN-SPACE APPLICATIONS

Archived Synopsis: ADVANCEMENTS IN CHEMICAL PROPULSION TECHNOLOGIES FOR IN-SPACE APPLICATIONS

The synopsis NNM04AA01L has been archived.



Owner: Ron Crider | [Technical Support](#) | [Section 508
Compliant](#)

Last revised: February 08, 2005 by DLE



Office of Space Science
NASA Announcements Opportunity

[NRA Home](#)

[OSS
Home](#)

[NASA
Home](#)

**RESEARCH
OPPORTUNITIES
IN
SPACE SCIENCE - 2004
(ROSS-2004)**

**NASA Announcements of
Opportunity
Soliciting Basic Research
Proposals**

NNH04ZSS001N

Issued: January 30, 2004

**Proposals Due: See below and
Tables 3 and 4 in
the Summary of Solicitation**

- **NOTICE:** All individuals interested in applying to this solicitation are urged to read the [NRA Summary of Solicitation](#) for critically important information about necessary Web and mailing addresses.

- [Amendments](#)

- [Download Files](#)

- Complete alphabetical index to all programs, including any new ones added as amendments after initial release, follows below on this page. (Note that amendments appear in **red**.)

- The Web site for electronic submission of Notices of Intent (NOI's) and for the Cover Page/Proposal Summary for all program elements in this NRA: <http://proposals.hq.nasa.gov/>

ROSS 2004

Program Title of Solicitation	Announcement Number	Solicitation Release Date	NOI Due Date	Proposals Due Date
ASTRO -E2 Guest Observer - Cycle 1	NNH04ZSS001N-ASTROE2	1/30/2004	6/16/2004	8/18/2004
Astrophysics Data	NNH04ZSS001N-ADP	1/30/2004	4/30/2004	6/25/2004
Astrobiology: Exobiology and Evolutionary Biology	NNH04ZSS001N-EXB	1/30/2004	6/04/2004	8/06/2004
Astrobiology Science and Technology for Exploring Planets	NNH04ZSS001N-ASTEP	1/30/2004	3/16/2004	7/30/2004
Astrobiology Science and Technology Instrument Development and Mission Concept Studies	NNH04ZSS001N-ASTID	1/30/2004	9/03/2004	1/27/2005
Astrophysics Theory	NNH04ZSS001N-ATP	1/30/2004	6/25/2004	8/27/2004
Astronomy & Physics Research and Analysis	NNH04ZSS001N-APRA	1/30/2004	2/27/2004	6/18/2004
Beyond Einstein Foundation Science	NNH04ZSS001N-BEFS	1/30/2004	6/25/2004	8/27/2004
Cosmochemistry	NNH04ZSS001N-COS	1/30/2004	3/26/2004	5/21/2004
Critical Issues in Electric Propulsion	NNH04ZSS001N-CIEP	1/30/2004	3/05/2004	4/30/2004

Discovery Data Analysis	NNH04ZSS001N-DDAP	1/30/2004	2/20/2004	3/26/2004
FUSE Guest Investigator - Cycle 6	NNH04ZSS001N-FUSE	1/30/2004	8/06/2004	9/17/2004
GALEX Guest Investigator - Cycle 1	NNH04ZSS001N-GALEX	1/30/2004	3/12/2004	4/16/2004
Geospace Sciences	NNH04ZSS001N-GEO	1/30/2004	5/28/2004	7/23/2004
HYABUSA Participating Scientist	NNH04ZSS001N-HYA	10/18/2004	11/19/2004	1/21/2005
In-Space Propulsion Program - Cycle 3	NNH04ZSS001N-ISP	11/03/2004	12/03/2004	2/04/2005
INTEGRAL Archival and Theoretical Research Program	NNH04ZSS001N-INTEG	11/15/2004	12/15/2005	2/15/2005
Long-Term Space Astrophysics (LTSA)	NNH04ZSS001N-LTSA	1/30/2004	4/30/2004	6/25/2004
Living With A Star Targeted Research & Technology	NNH04ZSS001N-LWS	1/30/2004	7/09/2004	9/10/2004
Mars Data Analysis	NNH04ZSS001N-MDAP	1/30/2004	6/11/2004	8/13/2004
Mars Fundamental Research	NNH04ZSS001N-MFRP	1/30/2004	2/25/2004	4/09/2004
Mars Instrument Development Project	NNH04ZSS001N-MIDP	Not solicited this year.		

Near Earth Object Observations	NNH04ZSS001N-NEOO	1/30/2004	4/09/2004	6/04/2004
Origins of Solar Systems	NNH04ZSS001N-SSO	1/30/2004	4/02/2004	5/28/2004
Origins Science Mission Concept Studies	NNH04ZSS001N-SMCS	2/18/2004	3/17/2004	4/28/2004
Outer Planets Research	NNH04ZSS001N-OPR	1/30/2004	3/05/2004	4/30/2004
Planetary Astronomy	NNH04ZSS001N-PAST	1/30/2004	4/16/2004	6/11/2004
Planetary Atmospheres	NNH04ZSS001N-PATM	1/30/2004	3/05/2004	5/21/2004
Planetary Geology and Geophysics	NNH04ZSS001N-PGG	1/30/2004	3/10/2004	5/07/2004
Planetary Instrument Definition and Development	NNH04ZSS001N-PID	1/30/2004	6/04/2004	8/06/2004
Planetary Major Equipment	NNH04ZSS001N-PME	See ESS Program Element of Interest		
Planetary Protection	NNH04ZSS001N-PPP	1/30/2004	6/04/2004	8/06/2004
RXTE Guest Investigator - Cycle 10	NNH04ZSS001N-RXTE	1/30/2004	7/09/2004	9/20/2004
Sample Return Laboratory Instruments and Data Analysis	NNH04ZSS001N-SRL	1/30/2004	4/09/2004	6/04/2004

Solar and Heliospheric Physics	NNH04ZSS001N-SHP	1/30/2004	12/10/2004	2/22/2005
STARDUST Participating Scientists Program	NNH04ZSS001N-SPS	10/04/2004	11/03/2004	01/07/2005
Sun-Earth Connection Instrument Development	NNH04ZSS001N-SECID	Not solicited this year.		
Sun-Earth Connection Guest Investigator	NNH04ZSS001N-SECGI	1/30/2004	3/19/2004	5/14/2004
Sun-Earth Connection Theory	NNH04ZSS001N-SECT	1/30/2004	3/05/2004	4/28/2004
Swift Guest Investigator - Cycle 2	NNH04ZSS001N-SWIFT	CANCELLED		
Terrestrial Planet Finder/Foundation Science	NNH04ZSS001N-TPF	1/30/2004	4/02/2004	5/28/2004
Venus Express Mission U.S. Participating Scientists Program	NNH04ZSS001N-VeXPSP	12/30/2004	1/28/2005	3/30/2005

NRA Home	OSS Home	NASA Home
--------------------------	--------------------------	---------------------------

Curator: [NASA Peer Review Services](#)



07-Sep-2005

[Research Home](#)

[Opportunity Definitions](#)

[Search](#)

[Proposal Site](#)

- [Subscribe for email notification](#)
- [Submit Notice of Intent to Propose](#)
- [Submit Proposal Information](#)

[NASA Links](#)

- [HQ's CBD Notices](#)

[Helpful References](#)

[Research Task Books](#)

[Help](#)

National Aeronautics & Space Administration

Definition of Notice of Intent (NOI) to Propose

(Currently Office of Earth Science, Office of Human Resources & Education, Office of Biological and Physical Research, Office of Aerospace Technology, Office of Equal Opportunity Programs and Office of Space Flight only)

NASA strongly encourages all prospective principle investigators to submit a Notice of Intent (NOI) to Propose in response to research announcements. Submission of an NOI is not binding and the information will be used for planning purposes only. The Notice of Intent to Propose may be submitted electronically through the Internet by completing the form available at [Proposal Online](#). You are urged to use these electronic notice of intent forms unless you do not have access to the Internet. In that case, NASA will accept a FAX copy sent to 202-479-0511 with the following information:

- Principal Investigator and Co-Investigator names and addresses, (including Zip + 4)
- Research Opportunity Identifier
- Title of proposal
- Telephone number
- Fax number
- Email address
- A brief summary of your proposal (Please limit this summary to no more than 3000 characters.)

NOI electronic submission can be accessed by individual code pages.



Curator: [NASA Peer Review Services](#)

Responsible NASA Official: [Greg](#)

[Lindsay](#)

[Disclaimer](#)



NRA Proposers Guidebook - Final

***NEW* - The 2005
NRA Proposers
Guidebook is now
on line:**

The MS Word version is
available at:

[http://www.hq.nasa.gov/
office/procurement/
nraguidebook/
proposer2005.doc](http://www.hq.nasa.gov/office/procurement/nraguidebook/proposer2005.doc)

**Proposers to ROSES-
2005 program
elements with NOI due
dates after July 15,
2005, should refer to
the 2005 NRA**

**Proposers Guidebook.
Proposers to ROSES-
2005 elements with
NOI due dates prior to
July 15, 2005, should
read and follow the
directions provided in
the notice on this page
titled "Notice to
proposers responding
to NNH05DA001N,
"Research
Opportunities in Space
and Earth Sciences
2005" (ROSES-2005)."**

**Previous Notices
and Versions:**

**Notice to
proposers
responding to
NNH05DA001N,
Research
Opportunities in
Space and Earth
Sciences
2005" (ROSES-
2005).**

Section IV(a) of ROSES-2005 incorporates by reference the 2005 edition of the "Guidebook for Proposers responding to a NASA Research Announcement" (hereafter referred to as the 2005 Guidebook). ROSES-2005 makes several references to requirements that are given in the 2005 Guidebook. At this time (May 2005), the 2005 Guidebook is not available for proposers to ROSES-2005 program elements.

Proposers to ROSES-2005 program elements with NOI due dates prior to July 15, 2005, should refer to the 2004 edition of the "Guidebook for Proposers responding to a NASA Research Announcement" (2004 Guidebook, <http://www.hq.nasa.gov/office/procurement/nraguidebook/>) for requirements subject to the following comments:

Starting in January of 2005, NASA began using its updated proposal and evaluation automated management system known as NSPIRES (<http://nspires.nasaprs.com/>). NSPIRES is designed to be capable of receiving full

electronic proposals directly (or through Grants.gov for those NRA solicitations that will not be exclusively awarding contracts). It is expected, however, that a phased implementation of NSPIRES capabilities will occur. Please examine each solicitation (or element thereof for any omnibus solicitation) to verify the extent to which NSPIRES capabilities will be employed. NSPIRES will provide extensive assistance for offerors, including on-line assistance and an available help desk.

Carryover funds will no longer be included as part of the budget proposal. NASA reserves the right to use unexpended funds from prior grant awards, but the availability of such funds will not be an element of proposal submission. This is a change to Section 2.3.11(a) of the 2004 Guidebook.

It is no longer permitted to append to the proposal reprints from and/or preprints for peer-reviewed publications; this is a change to Section 2.3.13 of the 2004 Guidebook.

NEW NOTICE REGARDING THE 2005 NRA PROPOSERS

Release of the 2005 NRA Proposers Guide has been delayed. The Guidebook is still in preparation. We now anticipate the 2005 NRA Proposers Guide will be available no later than the first week of March, 2005. We regret any inconvenience this may cause.

As noted previously, the new 2005 Guidebook will provide updates on NASA requirements for responding to NASA Research Announcements, including discussion of proposal elements and structure for use with the NSPIRES web-based integrated proposal and peer review management system. In the interim, general information about NASA's NRA processes can be found by referring to the 2004 NRA Proposers Guidebook, but users are cautioned that the proposal format for NASA's 2005 NRAs has been revised to allow integration with Grants.Gov in the near future.

****** NOTICE FOR
2005 NRA
PROPOSERS ******

The 2005 NRA Proposers Guide will be released soon. We anticipate the 2005 NRA Proposers Guide will be available no later than February 11, 2005. The new 2005 Guidebook will provide updates on NASA requirements for responding to NASA Research Announcements, including discussion of proposal elements and structure for use with the NSPIRES web-based integrated proposal and peer review management system. In the interim, general information about NASA's NRA processes can be found by referring to the 2004 NRA Proposers Guidebook, but users are cautioned that the proposal format for NASA's 2005 NRAs has been revised to allow integration with Grants.Gov in the near future.

**There are now
three versions of
the NRA
Proposers
Guidebook. Each
NRA specifies
which version to
follow. Check the
NRA carefully.**

**The 2004 NRA
Proposers
Guidebook is now
on line:**

The PDF version is available
at:

[http://www.hq.nasa.gov/
office/procurement/
nraguidebook/
proposer2004.pdf](http://www.hq.nasa.gov/office/procurement/nraguidebook/proposer2004.pdf)

The MS Word version is
available at:

[http://www.hq.nasa.gov/
office/procurement/
nraguidebook/](http://www.hq.nasa.gov/office/procurement/nraguidebook/)

[proposer2004.doc](#)

The 2003 NRA Proposers Guidebook:

The PDF version is available
at:

[http://www.hq.nasa.gov/
office/procurement/
nraguidebook/
proposer2003.pdf](http://www.hq.nasa.gov/office/procurement/nraguidebook/proposer2003.pdf) (includes
the errata sheet dated 1/31/03)

The MS Word version is
available at:

[http://www.hq.nasa.gov/
office/procurement/
nraguidebook/
proposer2003.doc](http://www.hq.nasa.gov/office/procurement/nraguidebook/proposer2003.doc) (includes
the errata sheet dated 1/31/03)

The 2001 NRA Proposers Guidebook:

The PDF version is available
at:

[http://www.hq.nasa.gov/
office/procurement/
nraguidebook/propgdbk.
pdf](http://www.hq.nasa.gov/office/procurement/nraguidebook/propgdbk.pdf)

The HTML version is available
at:

[http://www.hq.nasa.gov/
office/procurement/
nraguidebook/gdbkcvr.
html](http://www.hq.nasa.gov/office/procurement/nraguidebook/gdbkcvr.html)

NASA Procurement Library
Sites:

[Home](#) | [Index](#) | [Laws, Regs](#) | [Pre-Solicit. Planning](#) | [Solicit. to Award](#) | [VPO](#) | [Contract Management](#) | [Pricing](#) | [Metrics](#) | [Resources](#)

Owner: *Monique Sullivan*,
monique.sullivan-1@nasa.gov

Curator: *Susie Marucci*, susie.marucci@nasa.gov

Updated August 2005

[NASA Privacy Statement](#)



Products and Technologies Technical Topics

Developers Home > Products & Technologies > Java Technology > J2SE > Desktop Java >

Join Sun Developer Network
Login | Register | Why Register?

Desktop Java

Java Plug-in Technology

Downloads

Reference

- Documentation
- FAQs
- Code Samples & Apps
- Technical Articles & Tips

Community

- Forums
- Bug Database

Learning

- New to Java Center
- Tutorials & Code Camps
- Training
- Certification
- J2SE Learning Path
- Quizzes

Regional Sites

Java Plug-in technology, included as part of the Java 2 Runtime Environment, Standard Edition (JRE), establishes a connection between popular browsers and the Java platform. This connection enables applets on Web sites to be run within a browser on the desktop.

Note - For information on differences in behavior between newer and older versions of Java Plug-in, see [Encountering OBJECT, EMBED, and APPLET Tags With Different Plug-in Versions and Browsers](#).

Where Do You Get Java Plug-in?

Java Plug-in technology is part of the current version of the Java 2 Runtime Environment, Standard Edition (JRE). [Download the JRE](#).

Java Plug-in Demonstration Applets

We have demonstration pages that test J2SE release-specific applets -- see [Code Samples and Apps](#).

Deploying JavaBeans Components

The [JavaBeans Bridge for ActiveX](#) technology is part of Java Plug-in technology and bundled with the JRE. It provides developers of legacy OLE/COM/ActiveX containers such as Word or Visual Basic

Related Links

Popular Downloads

- J2SE 5.0
- J2SE 1.4.2
- Java Web Services Developer Pack 1.3

Technical Topics

- Desktop
- Security
- Performance
- Mobility
- Web Services

Products & Technologies

- Sun Java Desktop System
- J2SE 5.0
- Core Java
- Sun Java Studio Enterprise
- StarOffice SDK

Sun Resources

- Professional Certification

with the ability to embed and use portable JavaBeans components in the same way they would previously embed and use platform-specific OLE/COM/ActiveX components.

Java Upgrade Program

Now is the time to upgrade to Sun's official JRE. Help yourself and your customers and realize immediate benefits through the richer, broader applications, and applets you develop.

What's new

March 2005

Online Chat, April 12, on Java Plug-In Technology Got a question about Java Plug-In technology? Get answers in this chat with three key members of the Java Plug-In technology team at Sun: Dennis Gu, Calvin Cheung, and Danielle Pham.

October 2003

Java Upgrade Guide: Migrating From the MSJVM to the Sun JRE Use our practical guide to help you transition from the MSJVM to Sun's official JRE.

October 2003

Upgrade to the Official Sun Java Platform Read about the benefits of upgrading the MSJVM to the official Sun JRE in this article, and visit the Upgrade Program Site where you'll find resources, including a detailed technical guide, a forum, and more.

Community

Events

2005 JavaOne Conference.

San Francisco, CA

Once again the Java developer community takes over San Francisco, CA for the annual Java development event, JavaOne. This years event is June 27 - 30, 2005. » [Read More](#)

Feedback

Send general comments about Java Plug-in to:

- Professional Training
- JavaOne Online
- New to Java Center
- Developer Tech Support
- Java Upgrade Program
- Java Community Process

Sun JavaDesktop projects on java.net

- JDIC
- JDNC
- JavaHelp
- Java3D
- Project Looking Glass

<http://java.sun.com/docs/forms/plugin-sendusmail.html>

Though we value your input, before you send feedback, please review our pages of [Frequently Asked Questions \(FAQ\)](#). Please note that due to the volume of messages we receive, we typically do not respond to individual messages.



[About Sun](#) | [About This Site](#) | [Newsletters](#) | [Contact Us](#) | [Employment](#)
[How to Buy](#) | [Licensing](#) | [Terms of Use](#) | [Privacy](#) | [Trademarks](#)

Copyright 1994-2005 Sun Microsystems, Inc.

A Sun Developer Network Site

Unless otherwise licensed, code in all technical manuals herein (including articles, FAQs, samples) is provided under this [License](#).

[XML](#) [Content Feeds](#)

Java Frequently Asked Questions

Welcome to the Mac OS X Java Frequently Asked Questions (FAQ) for developers. This page is intended to provide answers to frequently asked questions about the direction and current features of Java on Mac OS X, as well as common development questions and problems. Due to the high volume of email we receive, we cannot respond to every question or suggestion, but we are interested in what you have to say. If after reading the Java Developer FAQ, you still have a question, please [contact us](#).

Please note that the “Common Development Questions” and “Known Issues” sections pertain to J2SE 1.4 unless otherwise noted. For 1.3.1 development issues, please see our [Java Documentation](#) section for Technical Notes and Q&As regarding J2SE 1.3.1 on Mac OS X.

Java on Mac OS X

1. [What version of Java is included on Mac OS X?](#)
2. [Does Mac OS X support multiple J2SE versions on a single OS installation?](#)
3. [Can I remove a Java update after I have installed it?](#)
4. [What J2SE version do Java Applets run under inside a browser?](#)
5. [Is there a J2SE release for Mac OS 9 and earlier?](#)
6. [Do the Mac OS X System Updates contain Java updates?](#)

FAQ Categories

- [Java on Mac OS X](#)
- [Additional APIs and products](#)
- [Java2 Enterprise Edition](#)
- [Common Development Questions](#)
- [Known Issues](#)
- [Additional Information](#)

1: What version of Java is included on Mac OS X?

J2SE 5.0 Release 1 for Mac OS X Tiger is now available via manual download, based on J2SE 5.0 Update 2 (JDK version 1.5.0_02). Mac OS X Tiger also includes JDK versions 1.4.2_07 and 1.3.1_15. For information on earlier releases of Java on Mac OS X, please see the Java Version Strings section of [Technical Note 2110](#).

There are no plans to release J2SE 5.0 for earlier releases of Mac OS X.

[Back to Top](#) ▲

2: Does Mac OS X support multiple J2SE versions on a single OS installation?

Mac OS X Tiger supports the existence of up to three major JDK versions (1.3.x, 1.4.x, 1.5.x). Previous releases of Mac OS X allowed 1.3 and (where available) 1.4 to coexist as well. The standard command-line commands such as java and javac use 1.4 on any system which has a 1.4 JDK installed, including systems which also have JDK 1.5. Apple developer tools such as Jar Bundler and Xcode both allow you to specify a Java version for double-clickable apps to use. Please see the [Java 1.4 Info.plist Dictionary Keys](#) documentation for details on how this is done. Please note that applications requiring J2SE 5.0 / JDK 1.5 must explicitly request version 1.5.

[Back to Top](#) ▲

3: Can I remove a Java update after I have installed it?

It is important to note that the current release system only allows for the **most recent release** of each supported major version — 1.3 and 1.4 on Panther; 1.3, 1.4, and 5.0 on Tiger — to be present at the same time on a single system. In other words, you can not roll a Mac OS X Panther system back to Java 1.4.1 after installing 1.4.2 — the only way of doing so is to reinstall the entire system. The same applies for any other Java-related Software Updates or Developer Previews. For this reason, **it is strongly recommended that**

Developer Previews of Java on Mac OS X be installed on non-critical systems.

[Back to Top](#) ▲

4: What J2SE version do Java applets run under inside a browser?

Apple's Safari browser can be configured to run Java applets in either J2SE 1.4 or 5.0 on Tiger systems using the Java Preferences application in `/Applications/Utilities/Java/J2SE 5.0/`. Safari only supports J2SE 1.4 on Mac OS X 10.2 and 10.3. Other browsers developed to specifically use 1.3.1 will need to be updated to use a newer Java runtime. If you would like to see your favorite browser use J2SE 1.4 or 5.0 on Mac OS X, please contact the vendor and ask them to work with Apple to adopt a newer J2SE version.

[Back to Top](#) ▲

5: Is there a J2SE release for Mac OS 9 and earlier?

The latest Mac OS Runtime for Java on Mac OS 9 provided a 1.1.8 Java VM. There are no plans to bring any versions of J2SE to Mac OS 9. If you are looking to make use of certain extension APIs on Mac OS 9, such as Swing, JavaHelp, or the newer Collections API, keep in mind that you can download 1.1.x versions of these libraries from <http://java.sun.com>.

[Back to Top](#) ▲

6: Do the Mac OS X System Updates contain Java updates?

Unless specifically mentioned in the summaries or release notes, system updates typically do not contain updates to any J2SE installations on Mac OS X.

[Back to Top](#) ▲

Get information on [Apple](#) products.
Visit the Apple Store [online](#) or at [retail](#) locations.
1-800-MY-APPLE

Copyright © 2005 Apple Computer, Inc.
[All rights reserved.](#) | [Terms of use](#) | [Privacy Notice](#)



[Skip Navigation \(press 2\)](#)

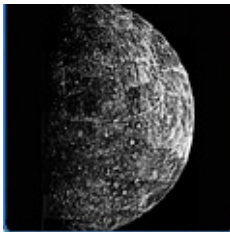
- + [Visit the NASA Portal](#)
- + [NSSDC Home](#)

- [Planetary Home](#)
- [About Planetary](#)
- [Fact Sheets](#)
- [Frequently Asked Questions](#)
- [Search](#)
- [Contact Us](#)

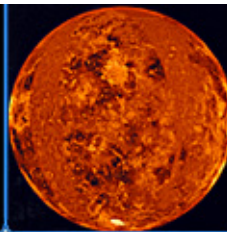


Find it@NSSDC

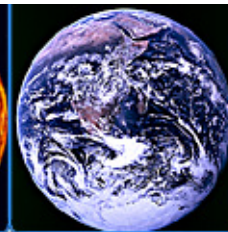
[Mercury](#)



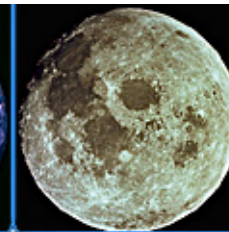
[Venus](#)



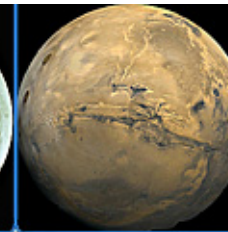
[Earth](#)



[Moon](#)



[Mars](#)



[Asteroids](#)



[Jupiter](#)



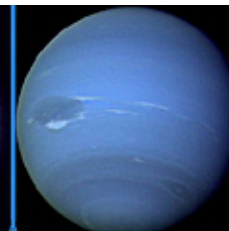
[Saturn](#)



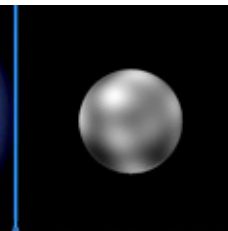
[Uranus](#)



[Neptune](#)



[Pluto](#)



[Comets](#)



Data Services

- [Deep Impact Images](#)
- [Image Resources](#)
- [Multimedia Catalog](#)
- [Catalog of Spaceborne Imaging](#)

Flight Mission Information

- [Information by Project](#)
- [Chronology of Lunar and Planetary Exploration](#)

- [Selected Planetary Mission information from the NSSDC Master Catalog](#)

Related Information Services

- [NSSDC Master Catalog](#): Detailed information about data held at NSSDC
- [Planetary and Lunar Reference Books](#)

Education Resources

- [The Schoolyard Solar System](#)
- [Moon Trees](#)
- [Radio Jove](#)

Other Data Archive/Service Centers

- [Planetary Data System](#)
- [Regional Planetary Image Facilities](#)
- [NASA Educator Resource Centers](#)

Other Resources

- [NASA and other publications available online](#)
- [NASA Field Centers](#)
- [NASA History Office](#)
- [NASA's Discovery Program](#)
- [NASA Newsroom](#)
- [More Resources](#)

[This Day in Planetary and Lunar Exploration History](#)

September 07

1958

Launch of Black Knight 1 to ~500 km, Great Britain's first rocket to reach space.

What's New in Lunar & Planetary Science

The [Mars Reconnaissance Orbiter](#) launched successfully on Friday, August 12 at 1143 UT (7:43 a.m. EDT). The spacecraft will reach Mars in March 2006 and later begin science operations from a low (255 x 320 km) orbit. For more information on the launch, see the [NASA press release](#).

The [MESSENGER](#) spacecraft flew by Earth on Tuesday, 2 August on its way to Venus and eventually Mercury. Closest approach of 2347 km over central Asia occurred at 19:13 UT (3:13 p.m. EDT).

Preliminary results from the July 4 Deep Impact [Deep Impact](#) encounter with comet Tempel 1 have been released. For more information see the [NASA Press Release](#) from 8 July. [Deep Impact images of the comet and impact](#) are available.

[Upcoming Planetary Events and Missions](#)

Search for Mission Information

To search for information on any mission, enter the spacecraft name in the box below.

Spacecraft Name:

- [NASA Home](#)
- [GSFC Home](#)
- [SED Home](#)
- [SSED Home](#)
- [SSEDSO Home](#)
- [NSSDC Home](#)



- + [NSSDC Security and Privacy Statement](#)



- NASA Official: [Dr. Ed Grayzeck](#)
- Curator: [Dr. David R. Williams](#)
- Version 2.1
- Last updated: 04 July 2005



NATIONAL AERONAUTICS
AND SPACE ADMINISTRATION

- + NASA Homepage
- + NASA en Español
- + Marte en Español

SEARCH MARS



NASA's Mars Exploration Program

OVERVIEW

SCIENCE

TECHNOLOGY

MISSIONS

PEOPLE

FEATURES

EVENTS

MULTIMEDIA

ALL ABOUT MARS

Mars for Kids



Mars for Students



Mars for Educators



Mars for Press



+ Mars Home

Features

+ LIST OF ALL FEATURES

"Porkchop" is the First Menu Item on a Trip to Mars

Ancient cultures looked to the patterns of tea leaves or animal entrails to divine the course of the future. At JPL, the course of a future Mars mission can be found in a porkchop.

Porkchop plot, that is. In the sometimes peculiar vocabulary of JPL mission designers, that nickname describes the porkchop-shaped, computer-generated, contour plots that display the launch date and arrival date characteristics of an interplanetary flight path for a given launch opportunity to Mars or any other planet.

Developing a porkchop plot is the first thing on the menu when mission designers are scoping out an interplanetary voyage. This is the sort of task accomplished by engineers in JPL's Navigation and Mission Design Section, whose unique, high-caliber expertise is signified by its recognition as NASA Center of Excellence.

Sending a spacecraft to another planet has been compared to throwing a dart at a moving target -- only the thrower is also on a moving platform, the Earth. It is further

complicated by the fact that the Sun's gravity curves the trajectory of the dart. At launch, the spacecraft is aimed to arrive at the point the planet will be months from now.

Getting to the planet Mars, rather than just to its orbit, requires that the spacecraft be inserted into its interplanetary trajectory at the correct time so it will arrive at the Martian orbit when Mars will be there. This task might be compared to throwing a dart at a moving target. You have to lead the aim point by just the right amount to hit the target. The opportunity to launch a spacecraft on a transfer orbit to Mars occurs about every 26 months.

To be captured into a Martian orbit, the spacecraft must then decelerate relative to Mars using a retrograde rocket burn or some other means. To land on Mars, the spacecraft must decelerate even further using a retrograde burn to the extent that the lowest point of its Martian orbit will intercept the surface of Mars. Since Mars has an atmosphere, final deceleration may also be performed by aerodynamic braking direct from the interplanetary trajectory, and/or a parachute, and/or further retrograde burns. From "The Basics of Spaceflight" <http://www.jpl.nasa.gov/basics/bsf4-1.html>

[The Revolving Door to Mars >>](#)

[Full Text](#)

Porkchop Plot

"Porkchop" is the First Menu Item on a Trip to Mars

[The Revolving Door to Mars](#)

[Roller Coaster to Mars](#)

[Save Your Baggage Allowance for Science](#)

[Extreme Parallel Parking](#)

CREDITS

FEEDBACK

RELATED LINKS

SITEMAP



- + Freedom of Information Act
- + The President's Management Agenda
- + FY 2002 Agency Performance and accountability report
- + NASA Privacy Statement, Disclaimer, and Accessibility Certification
- + Freedom to Manage



Last Updated: NaN undefined
NaN
NaN:NaN:NaN UTC
+ Comments and Questions



DAWN

A Journey to the Beginning of the Solar System

[mission](#) [science](#) [spacecraft](#) [operations](#) [outreach](#) [background](#) [news](#) [images](#) [home](#)

Welcome to the Dawn website.

Dawn's goal is to characterize the conditions and processes of the solar system's earliest epoch by investigating in detail two of the largest protoplanets remaining intact since their formations. Ceres and Vesta reside in the extensive zone between Mars and Jupiter together with many other smaller bodies, called the asteroid belt. Each has followed a very different evolutionary path constrained by the diversity of processes that operated during the first few million years of solar system evolution.

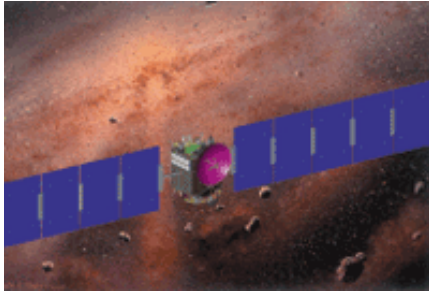
Those who are interested in following the developments of the mission may wish to subscribe to one of the mission's newsletters, [the Education and Public Outreach Newsletter](#) or [the Science team newsletter, Dawn's Early Light](#). Information on subscriptions can be obtained by clicking on the respective links. In addition to the website that is maintained by the science team there is a [more extensive website](#) under development by the Education and Public Outreach team. On this website we concentrate on the history and rationale for the mission. Material on the mission, its science, the spacecraft, operations, outreach, background, news, and images can be accessed by clicking on the appropriate heading at the top of this page.

Dawn has much to offer the general public. It brings images of varied landscapes on previously unseen worlds to the public including mountains, canyons, craters, lava flows, polar caps and, possibly ancient lakebeds, streambeds and gullies. Students can follow the mission over an entire K-12 experience as the mission is built, cruises to Vesta and Ceres and returns data. The public will be able to participate through the Solar System Ambassadors and through participation on the web.

The top level question that the mission addresses is the role of size and water in determining the evolution of the planets. Ceres and Vesta are the right two bodies with which to address this question, as they are the most massive of the protoplanets, baby planets whose growth was interrupted by the formation of Jupiter. Ceres is very primitive and wet while Vesta is evolved and dry. The instrumentation to be flown is complete, flight-

proven and similar to that used for Mercury, Mars, the Moon, Eros and comets. The science team consists of leading experts in the investigation of the rocky and icy planets using proven measurement and analysis techniques.

Dawn has the potential for making many paradigm-



Dawn Spacecraft

shifting discoveries. Ceres may have active hydrological processes leading to seasonal polar caps of water frost, altering our understanding of the interior of these bodies. Ceres may have a thin, permanent atmosphere distinguishing it from the other minor planets.

The three principal scientific drivers for the mission are first that it captures the earliest moments in the origin of the solar system enabling us to understand the conditions under which these objects formed. Second,

Dawn determines the nature of the building blocks from which the terrestrial planets formed, improving our understanding of this formation. Finally, it contrasts the formation and evolution of two small planets that followed very different evolutionary paths so that we understand what controls that evolution.

This mission is very timely. Its journey in time to understand the conditions at the formation of the solar system provides context for the understanding of the observation of extra solar-planetary systems. It provides data on the role of size and water in planetary evolution and forms a bridge between the exploration of the rocky inner solar system and the icy outer solar system. Finally, it completes the first order exploration of the inner solar system, addresses NASA's goal of understanding the origin and evolution of the solar system and complements ongoing investigations of Mercury, Earth and Mars.

For the full Dawn press package, [click here](#).

To view the paper on the Dawn mission presented at the 2002 Asteroids, Comets and Meteors conference, [click here](#).(pdf file)

Dawn title art background is from a painting by William K. Hartmann titled "A cocoon nebula, perhaps the primordial solar nebula."

[Mission](#) | [Science](#) | [Spacecraft](#) | [Operations](#) | [Outreach](#) | [Background](#) | [News](#) | [Images](#) | [Home](#) | [EPO Website](#)

For more information contact C. T. Russell, ctrussell@igpp.ucla.edu.

Last updated March 4, 2005.

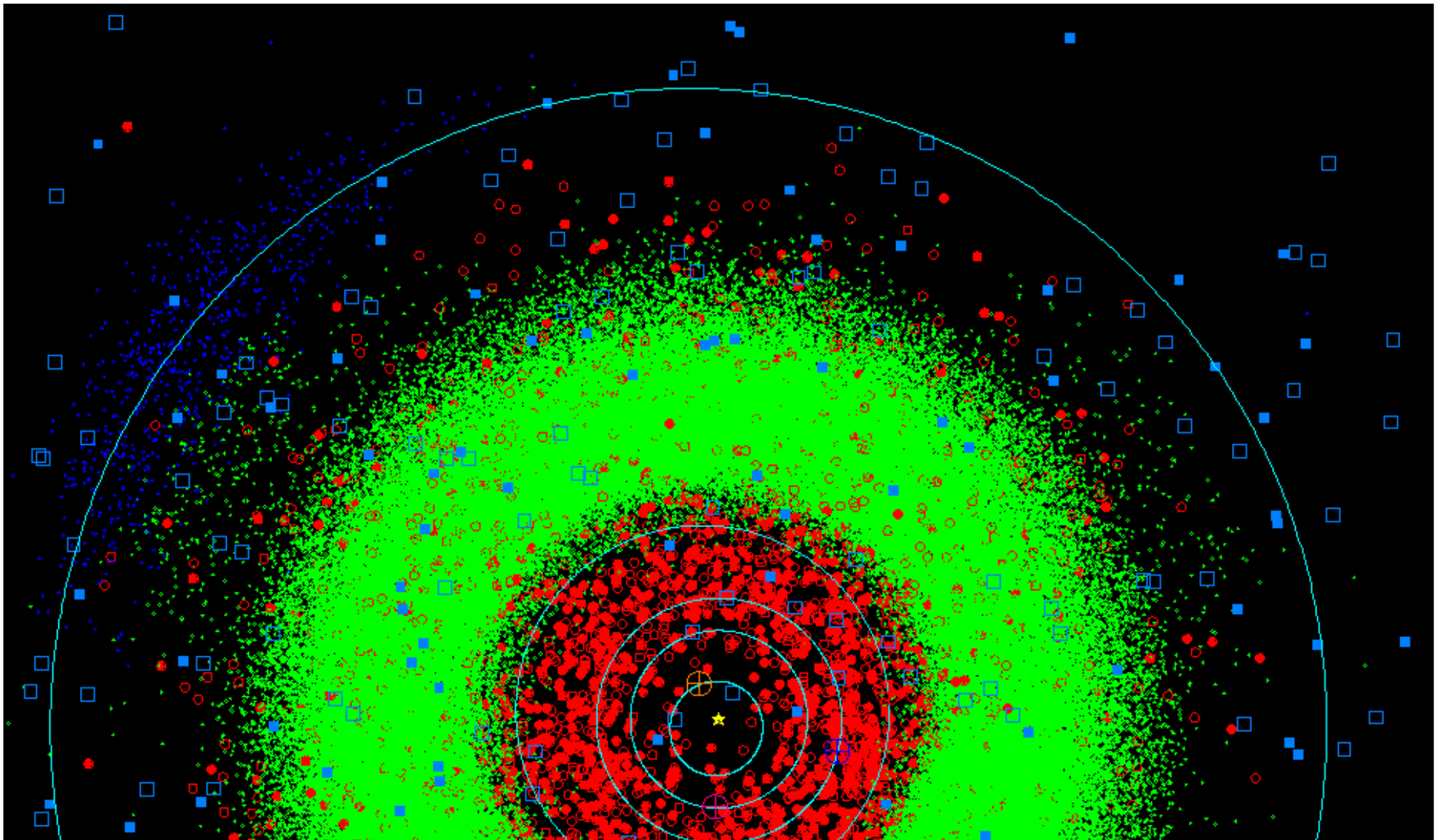
Plot of the Inner Solar System

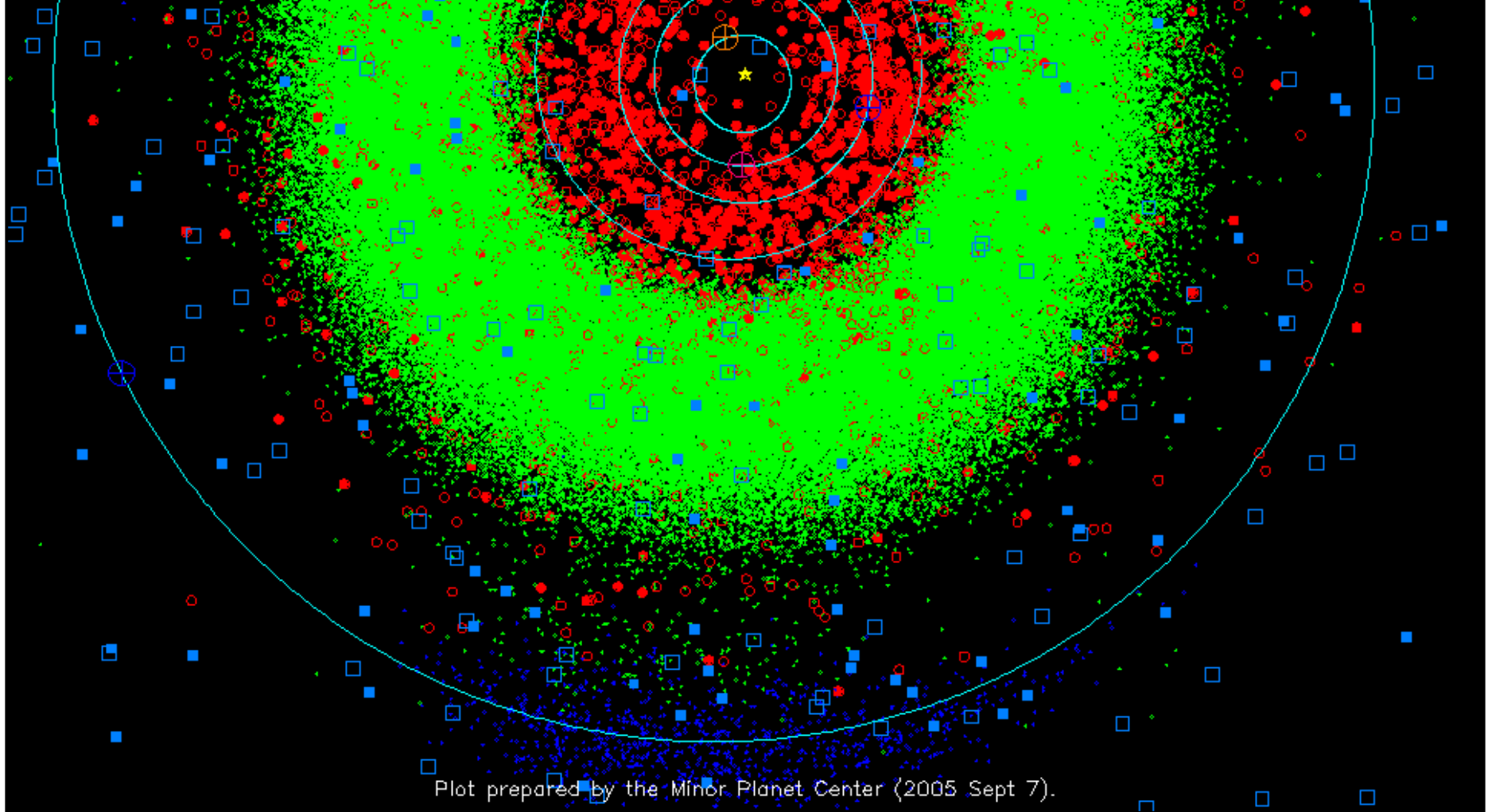
The plot below shows the current location of the major planets (Mercury through Jupiter) and the minor planets that are in the inner region of the solar system.

Also available is a [view of the innermost region of the solar system](#). The plot is of the same form as the plot on this page.

An [animated version of this plot is available](#) from our Animations page.

This plot must not be reproduced without the [express written consent of the Minor Planet Center](#).





The orbits of the major planets are shown in light blue: the current location of the major planets is indicated by large colored dots. The locations of the minor planets, including numbered and multiple-apparition/long-arc unnumbered objects, are indicated by green circles. Objects with perihelia within 1.3 AU are shown by red circles. Objects observed at more than one opposition are indicated by filled circles, objects seen at only one opposition are indicated by outline circles. The two "clouds" of objects 60° ahead and behind Jupiter (and at or near Jupiter's distance from the sun) are the [Jupiter Trojans](#), here colored deep blue. Numbered periodic comets are shown as filled light-blue squares. Other comets are shown as unfilled light-blue squares.

In this view, objects in direct orbits (most of the objects in this plot) move counterclockwise and the vernal equinox is towards the right. (The equinox directions are the direction of the sun as seen from the earth.) The plot is correct for the date given at the bottom of the plot.

Back to [minor planet lists](#) and [comet lists](#). [Credits](#).



MPC



CBAT

- [Kuiper Belt Page](#)
- [Quaoar Crystalline Ice](#) **NEW**
- [The 1000 km Scale KBOs](#)
- [Planet X](#)
- [Sedna](#)
- [HISS](#)
- [Is Phoebe a KBO?](#)
- [Damocloids Strike Back](#)
- [Images and Movies](#)
- [Classical KBOs](#)
- [Scattered KBOs](#)
- [The Plutinos](#)
- [Planetary Migration](#) **NEW**
- [Edge of the Classical Belt](#)
- NEW**
- [Binaries](#)
- [Plan View](#)
- [IAU KBO Table](#)
- [IAU Centaur & SKBO Table](#)
- [KBO Ephemerides](#)
- [General Ephemerides](#)
- [Dates Last Seen](#)
- [Predicted Occultations](#)
- [Surfaces of Kuiper Belt Objects](#)
- [Kuiper Belt To Comet](#) **NEW**
- [Bibliography ADS Version](#)
- [John Davies' Book](#)
- [Pluto and New Horizons](#)
- [Why is it called that? History](#)
- [TAOS Project](#)
- [Distant EKOs](#)
- [Comet Home Page](#)

KUIPER BELT

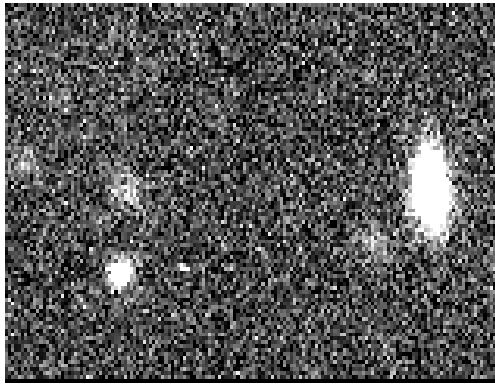


Starting in 1992, astronomers have become aware of a vast population of small bodies orbiting the sun beyond Neptune. There are at least 70,000 "trans-Neptunians" with diameters larger than 100 km in the radial zone extending outwards from the orbit of Neptune (at 30 AU) to 50 AU. Observations show that the trans-Neptunians are mostly confined within a thick band around the ecliptic, leading to the realization that they occupy a ring or belt surrounding the sun. This ring is generally referred to as the Kuiper Belt.

The Kuiper Belt holds significance for the study of the planetary system on at least two levels. First, it is likely that the Kuiper Belt objects are extremely primitive remnants from the early accretional phases of the solar system. The inner, dense parts of the pre-planetary disk condensed into the major planets, probably within a few millions to tens of millions of years. The outer parts were less dense, and accretion progressed slowly. Evidently, a great many small objects were formed. Second, it is widely believed that the Kuiper Belt is the source of the [short-period comets](#). It acts as a reservoir for these bodies in the same way that the [Oort Cloud](#) acts as a reservoir for the long-period comets.

The study of the trans-Neptunians is a rapidly evolving field, with major observational and theoretical advances in the last few years. A partial list of relevant papers is included on this Web page. You can also find a Table of the known trans-Neptunians, the discovery images for 1992 QB1, and a blink sequence which shows how these objects are identified.

David Jewitt



[Comet Jewitt](#)

Visitor number

535121

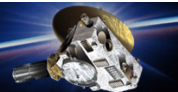
since 96/Aug/22

Last Updated 2005 Aug

[© Copyright Reserved](#)

NEW HORIZONS

NASA's Pluto-Kuiper Belt Mission



[+ HOME](#) [+ OVERVIEW](#) [+ SCIENCE](#) [+ MISSION](#) [+ SPACECRAFT](#) [+ EDUCATION](#) [+ NEWS CENTER](#) [+ GALLERY](#) [+ LINKS](#)

Pluto

TIMELINE

- JANUARY 11, 2006**
LAUNCH WINDOW OPENS
- FEBRUARY 2007**
JUPITER GRAVITY ASSIST
- MARCH 2007-JUNE 2015**
INTERPLANETARY CRUISE
- JULY 2015**
PLUTO-CHARON ENCOUNTER
- 2016-2020**
KUIPER BELT OBJECT ENCOUNTERS

COUNTDOWN

DAYS	HRS	MINS	SECS
00	00	00	00

Opening of primary launch window

FEATURED IMAGE



[view more images >](#)

+ LATEST NEWS



September 1, 2005
September Comes, Complete With Sister Worlds

As New Horizons was wrapping up a successful space-environment testing campaign, news emerged that scientists had discovered two Kuiper Belt Objects almost as large as Pluto. Even more exciting was the discovery of an object larger than Pluto - and three times as distant - deep into the classical Kuiper Belt. New Horizons Principal Investigator Alan Stern touches on these historic engineering and science events in this month's PI Perspective column. [+ Read more](#)



Happy Anniversary Pluto!

Pluto still fascinates us. 75 years after American astronomer Clyde Tombaugh spotted the tiny world in a series of telescope images. Click here to read more about Pluto's remarkable discovery.



[Subscribe to New Horizons E-News](#)

+ TO PLUTO AND BEYOND

New Horizons is the first mission to the last planet - the initial reconnaissance of Pluto-Charon and the Kuiper Belt - sent out to explore the mysterious worlds at the edge of our solar system.

+ SEND YOUR NAME TO PLUTO

Time is running out to send your name to Pluto! Click here before **Sept. 15, 2005**, to save your "place" on New Horizons.

+ P-K BITS

Pluto was discovered in 1930 by American astronomer Clyde Tombaugh

[view all >](#)

+ DOWNLOAD SCREENSAVER



Put New Horizons on your computer! [Download this mission screensaver.](#)

+ LAUNCH APPROVAL

NASA's environmental and launch risk analysis for the proposed New Horizons mission continues. The Final Environmental Impact Statement for the mission was released in July 2005. Following completion of the National Environmental Policy Act (NEPA) public comment and review process, NASA will decide whether to proceed with launch preparation. NASA expects to issue the NEPA record of decision for New Horizons in September 2005. If NASA decides to proceed with launch preparation, it will then request Presidential launch approval for the mission. [+ Read more](#)



Editor: JHU/APL Webmaster
JHU/APL Official: Kerri Besser
Last Updated:NaNNaNNaN
[+ Contact JHU/APL](#)

Frequently Asked Questions About Quaoar

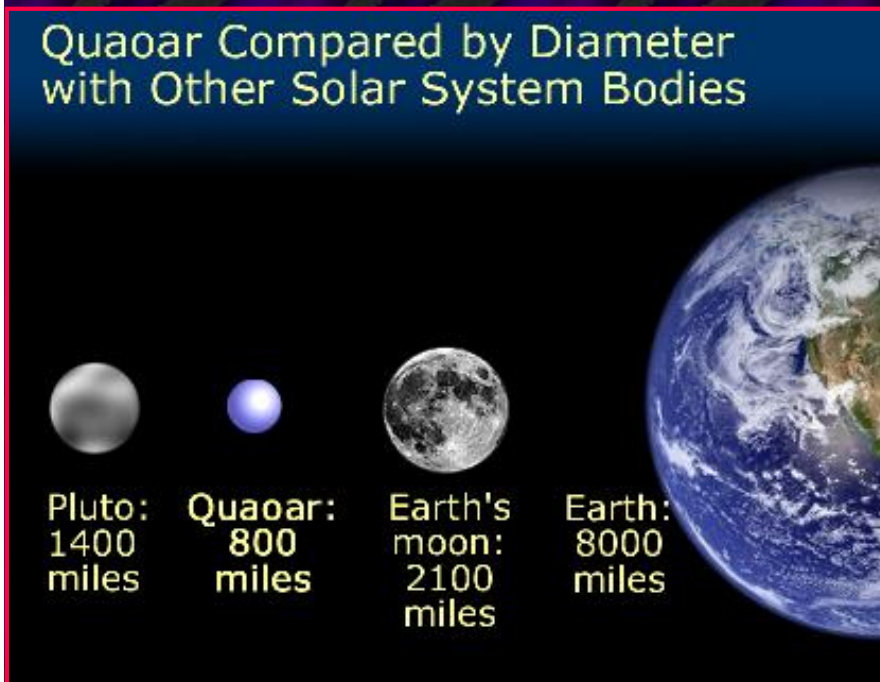
What is Quaoar?

Quaoar is a newly discovered Kuiper Belt object, found in June 2002 by [Chad Trujillo](#) and [Mike Brown](#) at Caltech in Pasadena. It's the largest Kuiper Belt object currently known, half the diameter of Pluto (about 1/8 the volume), and 1.6 billion kilometers (1 billion miles) further away than Pluto.

How big is Quaoar?

Quaoar is about 1250 km in diameter, roughly the size of Pluto's moon Charon. Nothing larger has been found in our solar system since Pluto was discovered in 1930 (and Pluto's moon Charon in 1978). It's huge, in fact, if you took the 50,000 numbered asteroids and put them together, it would be about the same volume as Quaoar.

Here's a picture of Quaoar compared to some other Solar System objects.



(NASA and A. Feild (STSci))

Is Quaoar a Planet?

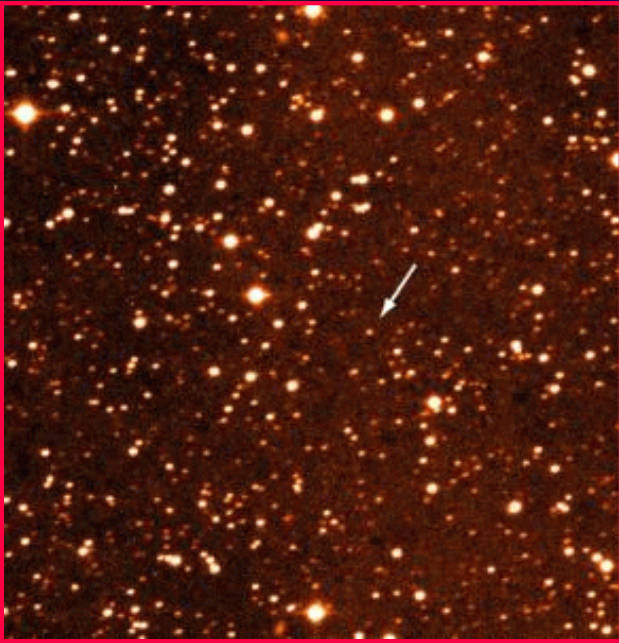
We don't think so. It's about half the size of Pluto and further away, but there are other big objects out there, too. Varuna (900 km in diameter) and 2002 AW197 (also 900 km in diameter) are two of the biggest Kuiper Belt Objects, and they are not considered "planets" either. There are about 600 known Kuiper Belt Objects, most of which are only about 100 km in diameter, and all of which were discovered since 1992 by different scientists who have been looking for them. It's similar to the asteroid belt, but beyond Neptune and contains maybe 100 times more material. You can read more about the Kuiper Belt at [the Kuiper Belt Homepage](#). Note that the

Kuiper Belt is also called the Edgeworth-Kuiper Belt and the trans-Neptunian Belt. We think we should be able to find 5 - 10 more of these really big Kuiper Belt Objects over the next couple of years, including perhaps a couple "super-Plutos".

How was Quaoar found?

First of all, we are looking for objects like Quaoar because we think there may be a lot of objects like it that are undiscovered, and maybe even objects bigger than Pluto. We spent about 7 months looking for it with a semi-automated telescope, the [Oschin Telescope](#) at Palomar, California. It has a mirror diameter of 48 inches (1.2 meters), which is large compared to amateur telescopes (typically ranging from 0.1 - 0.3 meters in diameter), but small compared to most professional telescopes (1 - 10 meters in diameter). Although the mirror isn't very big, the Oschin Telescope has a huge field of view for its size, about 3 square degrees. That's about the same amount of sky area as 12 moons in each picture.

Here's the discovery images. We took three pictures of the same patch of sky with 90 minutes between them. These pictures are about 150th of the entire field we get with the telescope. In a single night, we cover about 1700 times the area you see below. [Click for enlargement:](#)



You can download the raw data [here](#).

What is that other, faint object in the image?

There's lots of little specks in the images, most of them are "static" caused by cosmic rays --- similar to the static on your t.v. Sometimes they line up and look a lot like a moving object. So basically, we ignore anything that is only one or two pixels in size --- it really has to look a lot like a star, being several pixels across and "round" looking. Also, it has to move in a straight line and be present on all the images. You can probably find a lot of these things in the discovery images that it don't fit all the criteria of a real object.

Also, it's true that we may miss some very faint objects. But we are interested in finding the brightest ones, so in the interest in saving time, because there are only a couple of us working on this project and there is a lot of data,

some of the faintest objects may be real, and we may not recognize them in the images. But we consider that "acceptable loss" because we are looking for the biggest, brightest things anyway. People in the future will find the smaller, fainter things.

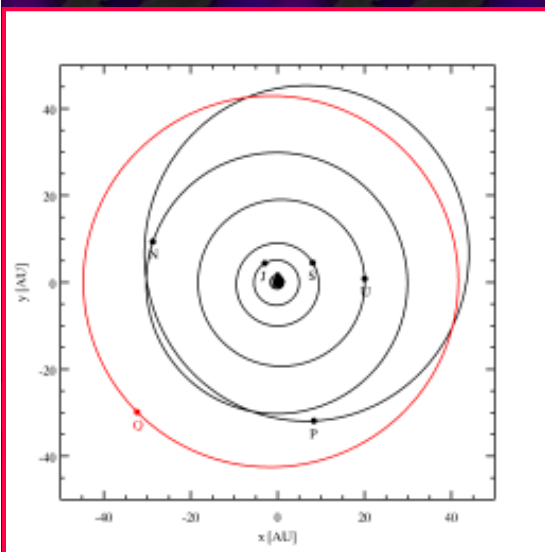
How far away is Quaoar?

Quaoar is at about 42 AU away from us, more distant than Pluto and Neptune, which are both at about 30 AU. 1 AU is an "Astronomical Unit" and is equal to the distance between the Earth and the Sun, about 150 million kilometers. So Quaoar is about 6 billion kilometers from us. At walking speed, it would take you about 100,000 years to get there. Going at the speed the Space Shuttle orbits the earth, it would take 25 years to get there. It takes light 5 hours to get there from the sun.

Quaoar is in a nearly circular orbit. Its eccentricity (a measure of the ellipticity of a circle) is less than 0.04, meaning that its distance from the sun only changes by about 8% over the course of a Quaoar year (which is 285 Earth years). This is very different from Pluto, which has an eccentricity about 6 times larger. You can see its orbit below. Because this object is so bright, within a month of discovery we were able to trace Quaoar's position back two decades in survey data. Quaoar's orbit is also inclined to the ecliptic (the plane of the solar system), by about 8 degrees.

This process is often called "[precovery](#)". Click on that link, it's cool.

Quaoar's orbit (red) compared to the planets (black). The Gas Giant planets (Jupiter, Saturn, Uranus and Neptune) and Pluto are labeled with the first letter of their name. Click for a bigger mpeg version.



Are Quaoar and Pluto going to crash into each other?

No, it kind of looks like it from the picture above of the orbits, but they don't collide, Quaoar's orbit is tilted with respect to the other planets by about 8 degrees. Pluto is tilted by about 20 degrees, so although it looks like they might hit each other from the "top view", a "side view" would show that their orbits don't intersect.

How do we know how big Quaoar is?

We measured the size of Quaoar in two ways:

(1) Optical measurements using the Hubble Space Telescope. Using a normal ground based telescope, you can't see Quaoar's size directly. You can tell it's there, but it's just a pinpoint of light just like any other star. But, the Hubble Space Telescope (HST) has much better "angular resolution" (it can see details a lot better) than a normal telescope because it is outside the Earth's atmosphere. By very carefully measuring Quaoar's size about 10 times over the course of an hour and comparing them to a nearby star, we can see directly that Quaoar is 1250 km in diameter.

You can see the HST images [here](#). Note that the vertical elongation is due to object motion during the exposure ("blurring"), and not the size of the object. Also, there is a paper about this technique [here](#).

(2) Thermal measurements. Using the [IRAM telescope in Spain](#), we measured the heat coming from Quaoar. Optical wavelength light (i.e. what your eye sees and what a "normal" telescope measures) only tells you about the amount of sunlight that is reflected from Quaoar back to Earth. So, a small white object could reflect the same amount of light as a large dark object. However, a dark object absorbs much more light than a white object, so it will be hotter. By measuring the heat (1.2 millimeter wavelength "light") coming from Quaoar and comparing it with the optical reflected light, we know that Quaoar has a diameter of 1250 km.

Where did the name come from?

The Tongva people (sometimes called the San Gabrielino Native Americans) inhabited the Los Angeles area before the arrival of the Spanish and other European people. The name "Quaoar" (pronounced kwah-o-wahr) comes from their creation mythology. In the words of Mark Acuña, Tongva scholar, dancer and tribal elder:

"'Quaoar' the great force of creation sings and dances the high ones (Deities) into existence. While Quaoar has no form or gender he is usually referred to with the male pronoun. He dances and sings first 'Weywot' who becomes Sky Father; they sing and dance 'Chehooit' Earth Mother into existence. The trio sing 'Tमित' Grandfather Sun to life. As each divine one joins the singing and dancing, the song becomes more complex and the dance more complicated. In turn 'Moar', Grandmother Moon (a very complex deity), 'Pमित' the Goddess of the sea, 'Manit', the Lord of dreams and visions, 'Manisar' the bringer of food and harvests, 'Tukupar Itar' Sky Coyote (who is also our major hero), 'Tolmalok', the Goddess of Shishongna (the underworld) join in the singing, dancing and creating. And finally the great seven giants who hold up the worlds are created. The High Ones in turn are aided by 'Eagle, Duck, Bear, and Frog' in a grand earth diving story. Frog brings up soil out of the deep dark sea, and the four animals dance it flat and wide. The 'Gods and Goddesses' then furnish the world 'Tovangar' with hills, mountains, trees, rivers, etc. 'Tobohar' (first man) and 'Pahavit' (first woman) are also part of this great 'Creation song and dance cycle'."

You can find out more about the Tongva at the [Tongva website](#).

The IAU has voted and approved the name Quaoar, which is now its official name.

What is Quaoar made of?

We don't know exactly. We suspect that most Kuiper Belt Objects are made of equal portions of rock and ices. There are many chemicals which are normally liquids or gas on Earth that would be different types of ice on Quaoar, including water, methane ice (natural gas ice), methanol ice (alcohol ice), carbon dioxide ice (dry ice), carbon monoxide ice (very gross) and others. We know that there is water ice on Quaoar from measurements made at the Keck Telescope.

Are there more big Kuiper Belt Object like Quaoar that we haven't seen?

It is very likely that there are more big Kuiper Belt Objects like Quaoar. We looked at only 5% of the entire sky before finding Quaoar. So there could be 20 Quaoars out there and we wouldn't have seen them yet. It is also likely that a few Plutos are out there waiting to be discovered. We have so far looked mostly in the plane of the solar system, where objects are most likely to be. It's likely that our discovery rates will go down as we get further and further from the solar system plane (the ecliptic) but we still expect to find maybe 10 more objects, given current models of the Kuiper Belt thickness.

Where is it?

Here's the ephemeris, in J2000 coords. Times are in UT, right ascension in hours, declination in degrees. It has a red magnitude of 18.6 or so right now. Or get it from [HORIZONS](#), which will give you the position of any solar system body for any time you want.

```
2003-Mar-12 08:00 16 47 53.48 -15 14 22.5
2003-Mar-19 08:00 16 47 52.25 -15 13 04.1
2003-Mar-26 08:00 16 47 46.40 -15 11 39.4
2003-Apr-02 08:00 16 47 36.06 -15 10 09.4
2003-Apr-09 08:00 16 47 21.45 -15 08 35.6
2003-Apr-16 08:00 16 47 02.92 -15 06 59.6
2003-Apr-23 08:00 16 46 40.83 -15 05 22.7
2003-Apr-30 08:00 16 46 15.57 -15 03 46.4
2003-May-07 08:00 16 45 47.61 -15 02 12.2
2003-May-14 08:00 16 45 17.49 -15 00 41.5
2003-May-21 08:00 16 44 45.73 -14 59 15.8
2003-May-28 08:00 16 44 12.89 -14 57 56.2
2003-Jun-04 08:00 16 43 39.53 -14 56 44.0
2003-Jun-11 08:00 16 43 06.27 -14 55 40.5
2003-Jun-18 08:00 16 42 33.69 -14 54 46.6
2003-Jun-25 08:00 16 42 02.30 -14 54 03.1
2003-Jul-02 08:00 16 41 32.66 -14 53 30.7
2003-Jul-09 08:00 16 41 05.30 -14 53 10.2
2003-Jul-16 08:00 16 40 40.69 -14 53 01.8
2003-Jul-23 08:00 16 40 19.23 -14 53 05.6
2003-Jul-30 08:00 16 40 01.31 -14 53 21.8
2003-Aug-06 08:00 16 39 47.27 -14 53 50.3
```

Orbital Elements

Here's the orbital elements, as computed by the method of Bernstein & Khushalani (2000):

```
# Barycentric osculating elements in ICRS at epoch 2445471.8:
a 43.373493 +/- 0.009720 AU
e 0.037457 +/- 0.000055
i 7.992 +/- 0.000 deg
Node 188.923 +/- 0.001 deg
Arg of Peri 156.292 +/- 0.242 deg
Time of Peri 2478635.182 +/- 76.022 JD
```

What was the time, date and place of discovery?

The first discovery image was taken at 2002 June 04 05:41:40 (Universal Time = Greenwich, England) from the Palomar Observatory 48-inch Oschin telescope. I identified Quaoar in the image at 2002 Jun 05 10:48:08 (Pacific Daylight Time).

News Articles

[Google News Search](#)



Chad Trujillo

chad@gps.caltech.edu



SIZE AND ALBEDO OF KUIPER BELT OBJECT (20000) VARUNA

David Jewitt and Herve Aousel

Institute for Astronomy, University of Hawaii

and Aaron Evans

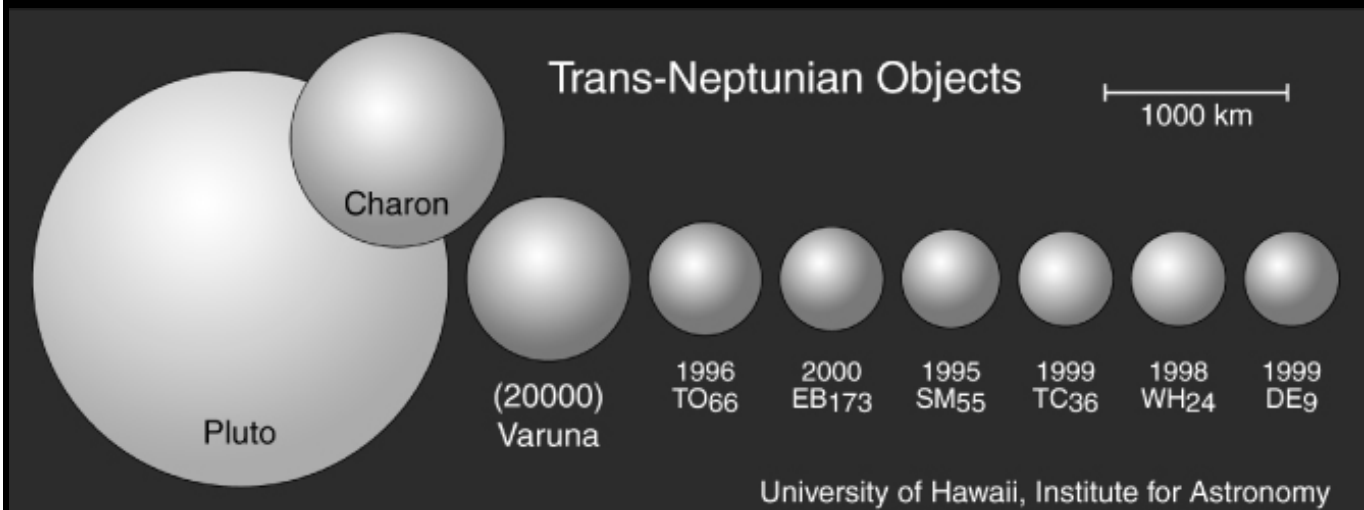
Dept. Physics and Astronomy, State University of New York at Stony Brook

NATURE, 2001, 411, 446-447 (May 24 issue)

Abstract

Observations within the last decade have revealed the existence of a large number of bodies in orbit about the sun beyond Neptune. These bodies, commonly known as Kuiper Belt Objects (KBOs), are products of agglomeration in the rarefied outer regions of the protoplanetary disk of the sun. Scientific interest focuses on the primitive nature of the KBOs and on their role as the likely source of short-period comets. Unfortunately, the KBOs are difficult astronomical targets, so that even such basic physical properties as the sizes and albedos remain unknown. Here we report the first simultaneous thermal and optical measurements of a bright KBO and use them to solve separately for the albedo and size. (20000) Varuna has equivalent circular diameter $D = 900(+125/-145)$ km and red geometric albedo $p = 0.070(+0.030/-0.017)$. The surface is darker than Pluto, suggesting a composition largely devoid of fresh ice, but higher than the canonical albedo of 0.04 previously assumed for these bodies.

[PS Figure](#) [PDF Figure](#) [TIFF Figure](#)



[Blink Pair](#) showing the motion of (20000) Varuna. The interval is 1 day. R-band, 250-sec integrations from the UH - 2.2 meter telescope.

The individual pictures from [Day 1](#) (2001 Apr 24) and [Day 2](#) (2001 Apr 25). Images by Scott Sheppard.

The [PS version](#) of the paper and the [PDF version](#), too..

The [editorial](#) by Tegler and Romanishin and the [Trout](#) piece.

Additional Figures from the paper:

[PS Figure 1](#), [PDF Figure 1](#) and [PS Figure 2](#), [PDF Figure 2](#).

After we measured the size, we went back to measure the rotation period and shape of Varuna. To our surprise, we were able to estimate the density of the object. The low value (1000 kg per m**3) is due to internal porosity. The resulting paper is here as a [PDF](#).

Last updated May 2002



[David Jewitt Home Page](#)



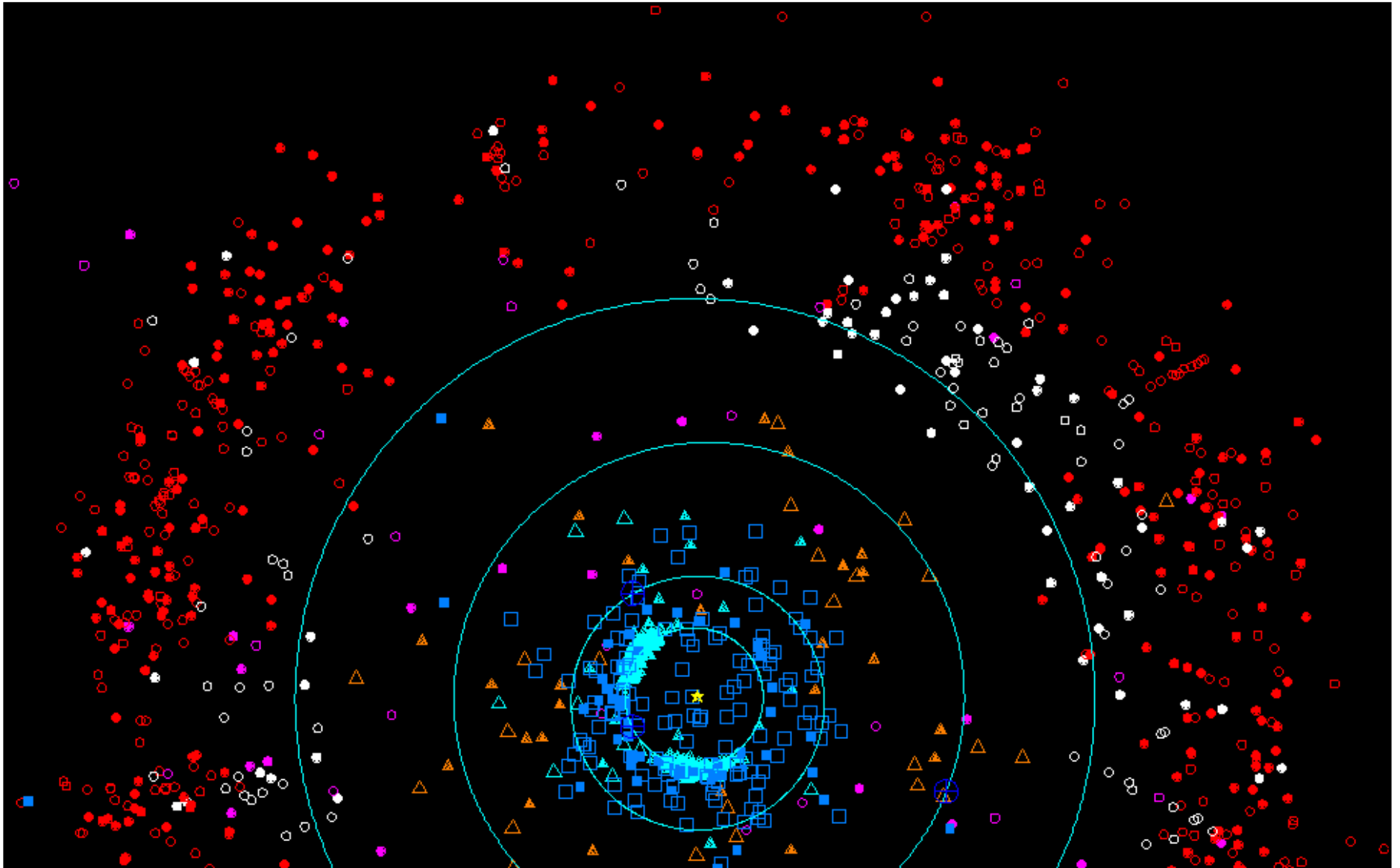
[Kuiper Belt Home Page](#)

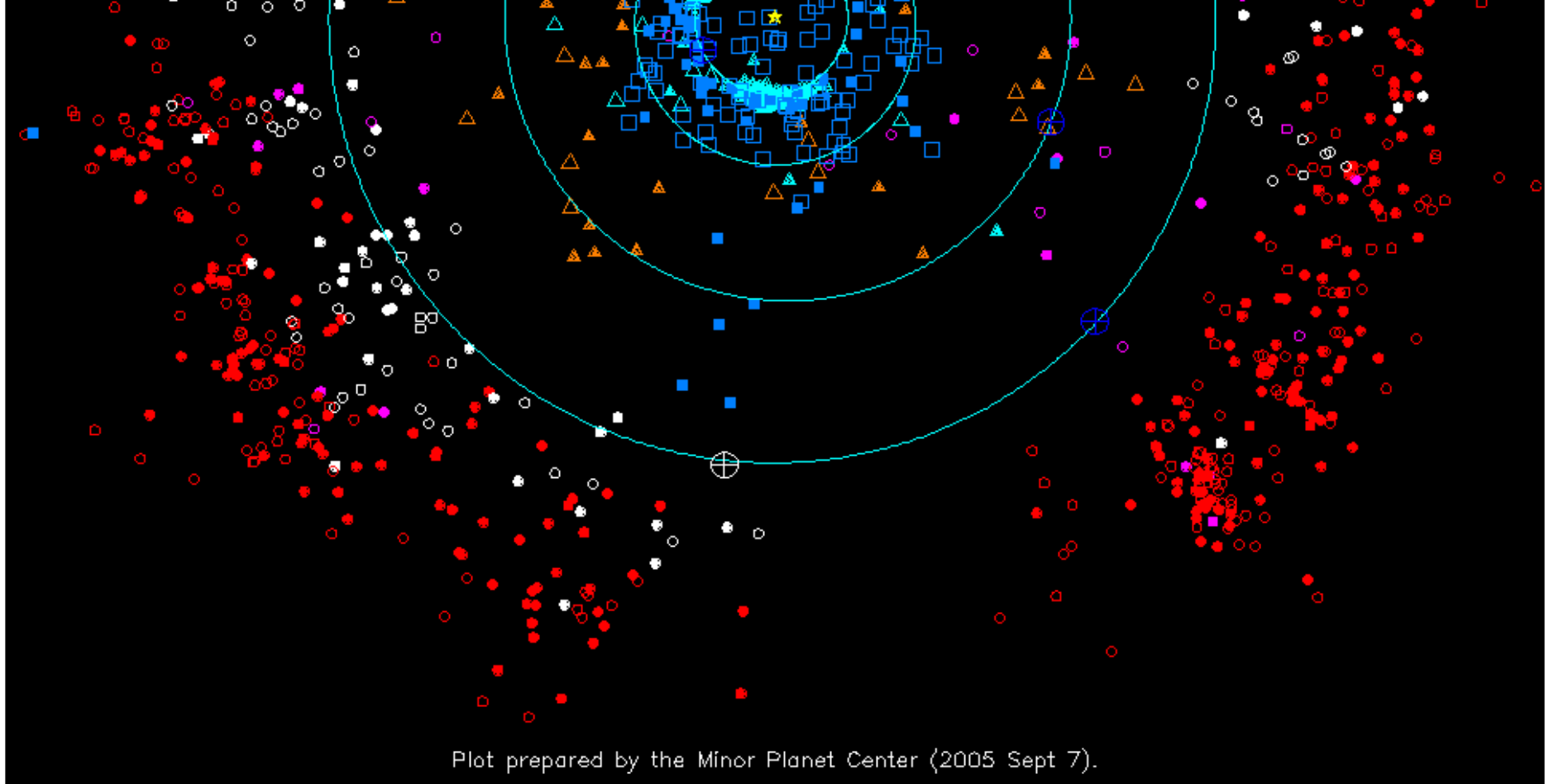
Plot of the Outer Solar System

The plot below shows the current locations and orbits of the Jovian planets (Jupiter through Neptune) and the current locations of various distant minor bodies.

An [animated version of this plot, showing the motion of the objects over a 100-year time period](#), is available from our Animations page.

This plot must not be reproduced without the [express written consent of the Minor Planet Center](#).





The orbits of the planets are shown in light blue and the current location of each object is marked by large dark-blue symbols. The current location of the minor bodies of the outer solar system are shown in different colors to denote different classes of object. Unusual high-e objects are shown as cyan triangles, [Centaur objects](#) as orange triangles, Plutinos (objects in 2:3 resonance with Neptune) as white circles (Pluto itself is the large white symbol), scattered-disk objects as magenta circles and "classical" or "main-belt" objects as red circles. Objects observed at only one opposition are denoted by open symbols, objects with multiple-opposition orbits are denoted by filled symbols. Numbered periodic comets are shown as filled light-blue squares. Other comets are shown as unfilled light-blue squares. Dual-status objects are shown as minor planets.

In this view, objects in direct orbits (most of the objects in this plot) move counterclockwise and the vernal equinox is towards the right. (The equinox directions are the direction of the sun as seen from the earth.) Details of the designations are given in the [lists of unusual minor planets](#). The plot is correct for the date given in the diagram caption.

Back to [minor planet lists](#) and [comet lists](#). [Credits](#).

MPC

MPC

CBAT

CBAT



Near Earth Object Program

NEO BASICS	SEARCH PROGRAMS	DISCOVERY STATISTICS	SPACE MISSIONS	NEWS	FAQ
ORBIT DIAGRAMS	ORBIT ELEMENTS	CLOSE APPROACHES	IMPACT RISK	IMAGES	RELATED LINKS

NEO GROUPS

In terms of orbital elements, NEOs are asteroids and comets with perihelion distance q less than 1.3 AU. Near-Earth Comets (NECs) are further restricted to include only short-period comets (i.e orbital period P less than 200 years). The vast majority of NEOs are asteroids, referred to as Near-Earth Asteroids (NEAs). NEAs are divided into groups (Aten, Apollo, Amor) according to their perihelion distance (q), aphelion distance (Q) and their semi-major axes (a).

Group	Description	Definition
NECs	Near-Earth Comets	$q < 1.3$ AU, $P < 200$ years
NEAs	Near-Earth Asteroids	$q < 1.3$ AU
Atens	Earth-crossing NEAs with semi-major axes smaller than Earth's (named after asteroid 2062 Aten).	$a < 1.0$ AU, $Q > 0.983$ AU

Apollos	Earth-crossing NEAs with semi-major axes larger than Earth's (named after asteroid 1862 Apollo).	$a > 1.0 \text{ AU}$, $q < 1.017 \text{ AU}$
Amors	Earth-approaching NEAs with orbits exterior to Earth's but interior to Mars' (named after asteroid 1221 Amor).	$a > 1.0 \text{ AU}$, $1.017 < q < 1.3 \text{ AU}$
PHAs	Potentially Hazardous Asteroids: NEAs whose Minimum Orbit Intersection Distance (MOID) with the Earth is 0.05 AU or less and whose absolute magnitude (H) is 22.0 or brighter.	$MOID \leq 0.05 \text{ AU}$, $H \leq 22.0$

WHAT IS A PHA?

Potentially Hazardous Asteroids (PHAs) are currently defined based on parameters that measure the asteroid's potential to make threatening close approaches to the Earth. Specifically, all asteroids with an Earth **Minimum Orbit Intersection Distance (MOID)** of 0.05 AU or less and an **absolute magnitude (H)** of 22.0 or less are considered PHAs. In other words, asteroids that *can't* get any closer to the Earth (*i.e.* MOID) than 0.05 AU (roughly 7,480,000 km or 4,650,000 mi) or are smaller than about 150 m (500 ft) in diameter (*i.e.* $H = 22.0$ with assumed albedo of 13%) are *not* considered PHAs.

There are currently 720 known PHAs.

This "potential" to make close Earth approaches does **not** mean a PHA **will** impact the Earth. It only means there is a possibility for such a threat. By monitoring these PHAs and updating their orbits as new observations become available, we can better predict the close-approach statistics and thus their Earth-impact threat.

[Near-Earth Objects](#) | [NEO Groups](#) | [NEOs and Life on Earth](#) | [Target Earth](#) |
[NEOs As Future Resources](#)

[SITE MAP](#)

[FEEDBACK](#)

[CREDITS](#)

[PRIVACY](#)

[MAILING LIST](#)



Site Manager: Don Yeomans

Webmaster: Ron Baalke

Last Updated: NaN undefined NaN



NEO BASICS	SEARCH PROGRAMS	DISCOVERY STATISTICS	SPACE MISSIONS	NEWS	FAQ
ORBIT DIAGRAMS	ORBIT ELEMENTS	CLOSE APPROACHES	IMPACT RISK	IMAGES	RELATED LINKS

The following table lists potential future Earth impact events that the JPL Sentry System has detected based on currently available observations. Click on the object designation to go to a page with full details on that object.

Sentry is a highly automated collision monitoring system that continually scans the most current asteroid catalog for possibilities of future impact with Earth over the next 100 years. Whenever a potential impact is detected it will be analyzed and the results immediately published here, except in unusual cases where an [IAU Technical Review](#) is underway. For more information on impact monitoring and risk assessment see our [Impact Risk Introduction](#) and [Frequently Asked Impact Risk Questions](#).

It is normal that, as additional observations become available, objects will disappear from this table whenever there are no longer any potential impact detections. For this reason we maintain a [list of removed objects](#) with the date of removal.

[Where is 1950 DA?](#)

70 NEAs: Last Updated Sep 03, 2005
Sort by [Palermo Scale \(cum.\)](#) or by [Object Designation](#)

Object Designation	Year Range	Potential Impacts	Impact Prob. (cum.)	V _{infinity} (km/s)	H (mag)	Est. Diam. (km)	Palermo Scale (cum.)	Palermo Scale (max.)	Torino Scale (max.)
2004 VD17	2091-2104	5	1.1e-04	18.22	18.8	0.580	-1.06	-1.13	1
99942 2004 MN4	2036-2056	4	1.8e-04	5.87	19.2	0.320	-1.35	-1.35	1
1997 XR2	2101-2101	2	9.7e-05	7.17	20.8	0.230	-2.44	-2.71	1
1994 WR12	2054-2102	134	1.0e-04	9.84	22.4	0.110	-2.96	-3.75	0
1979 XB	2056-2101	3	3.3e-07	24.54	18.5	0.685	-3.07	-3.14	0
2000 SG344	2068-2101	68	1.8e-03	1.37	24.8	0.040	-3.08	-3.43	0
2000 QS7	2053-2053	2	1.3e-06	12.32	19.6	0.420	-3.27	-3.46	0
1998 HJ3	2100-2104	3	2.1e-07	24.09	18.4	0.694	-3.49	-3.69	0
2004 XK3	2029-2104	66	1.7e-04	6.55	24.5	0.040	-3.81	-4.06	0
1994 GK	2051-2071	7	6.1e-05	14.87	24.2	0.050	-3.83	-3.84	0
2000 SB45	2074-2101	83	1.5e-04	7.54	24.3	0.050	-3.86	-4.28	0
2001 CA21	2020-2073	4	1.7e-08	30.66	18.5	0.678	-3.89	-4.10	0
2005 QK76	2030-2092	15	4.6e-05	19.64	25.2	0.030	-4.01	-4.36	0
2005 ED224	2018-2064	6	2.8e-06	25.17	24.0	0.054	-4.27	-4.48	0
2002 TX55	2089-2096	3	1.8e-05	10.15	23.6	0.060	-4.38	-4.42	0
2005 EL70	2034-2058	2	1.8e-06	35.50	24.1	0.050	-4.48	-4.49	0

2005 BS1	2016-2041	5	8.2e-05	12.36	27.3	0.010	-4.51	-4.51	0
2001 BB16	2084-2100	4	5.4e-06	3.57	22.6	0.100	-4.57	-4.70	0
2002 VU17	2084-2099	5	1.9e-05	13.69	24.8	0.040	-4.80	-5.22	0
2000 TU28	2104-2104	1	2.3e-07	9.47	20.4	0.280	-4.81	-4.81	0
2001 AV43	2066-2097	6	1.7e-05	3.71	24.4	0.040	-4.82	-5.03	0
2002 RB182	2044-2086	13	1.5e-06	13.20	22.8	0.090	-4.89	-5.23	0
2002 MN	2070-2101	8	3.3e-06	10.40	23.3	0.070	-4.91	-5.30	0
2002 GJ8	2089-2089	1	1.2e-08	26.27	19.3	0.460	-5.02	-5.02	0
2001 FB90	2021-2091	3	7.7e-09	26.56	19.9	0.345	-5.02	-5.13	0
2004 VM24	2074-2098	18	2.9e-05	12.86	25.7	0.020	-5.03	-5.48	0
2004 PU42	2071-2103	18	7.7e-05	10.11	26.8	0.010	-5.23	-5.85	0
2005 NX55	2011-2102	85	3.1e-08	24.75	21.9	0.140	-5.26	-5.97	0
2001 GP2	2043-2099	32	1.0e-04	2.58	26.9	0.010	-5.26	-5.71	0
2004 HZ	2023-2023	1	9.1e-08	13.26	22.3	0.120	-5.27	-5.27	0
1996 TC1	2054-2075	4	9.4e-07	24.04	23.9	0.060	-5.28	-5.52	0
1995 CS	2042-2073	6	3.7e-06	24.91	25.5	0.030	-5.34	-5.70	0
2004 FU162	2006-2104	824	6.5e-05	9.80	29.0	0.006	-5.38	-6.37	0
1994 GV	2048-2086	23	9.2e-05	8.15	27.5	0.010	-5.40	-5.99	0
6344 P-L	2022-2052	2	2.8e-08	15.34	21.1	0.207	-5.43	-5.66	0

2000 LG6	2075-2101	20	8.6e-04	2.10	29.0	0.010	-5.49	-5.91	0
2004 ME6	2017-2099	43	1.1e-07	12.05	22.6	0.102	-5.64	-6.35	0
2005 AU3	2048-2105	15	9.1e-06	14.46	26.0	0.020	-5.70	-6.06	0
2001 BA16	2033-2051	4	5.3e-06	4.90	25.8	0.020	-5.77	-5.80	0
2003 LN6	2061-2099	3	1.6e-06	3.96	24.5	0.040	-5.85	-5.88	0
2002 UV36	2087-2087	1	1.5e-05	8.06	26.5	0.020	-5.90	-5.90	0
2001 SB170	2089-2095	2	6.5e-08	22.49	22.5	0.110	-5.92	-6.18	0
1999 RZ31	2056-2056	1	4.5e-07	8.20	23.8	0.060	-5.92	-5.92	0
2001 QJ96	2032-2032	1	9.0e-09	26.69	22.0	0.130	-5.94	-5.94	0
2004 VZ14	2076-2104	6	2.0e-06	15.20	25.3	0.030	-5.97	-6.45	0
1999 SF10	2080-2100	3	1.0e-06	4.76	24.0	0.050	-5.98	-6.23	0
2004 GE2	2100-2100	1	1.9e-08	20.57	21.4	0.180	-6.02	-6.02	0
1998 DK36	2025-2100	24	7.1e-07	6.19	25.0	0.030	-6.42	-6.54	0
2004 BN41	2086-2098	2	1.5e-06	7.56	25.8	0.020	-6.57	-6.69	0
2002 XV90	2101-2101	3	8.2e-07	7.63	25.2	0.030	-6.61	-6.69	0
2003 WT153	2044-2103	39	1.2e-05	4.33	28.1	0.010	-6.75	-7.41	0
1997 TC25	2090-2096	2	2.9e-07	9.92	24.9	0.040	-6.80	-6.81	0
2004 RU109	2038-2053	5	6.1e-07	12.93	26.5	0.020	-6.81	-7.21	0
2002 TY59	2074-2084	2	4.8e-07	8.22	25.4	0.030	-6.84	-6.84	0

2003 UQ25	2093-2093	1	5.2e-08	18.01	24.2	0.050	-6.96	-6.96	0
2003 DW10	2046-2054	3	4.1e-07	7.82	26.1	0.020	-6.98	-7.10	0
2002 CB19	2049-2049	1	5.7e-08	15.73	24.8	0.040	-6.99	-6.99	0
1997 UA11	2073-2073	1	1.5e-07	11.96	25.2	0.030	-7.06	-7.06	0
2001 UO	2020-2020	1	5.4e-09	16.28	24.1	0.050	-7.28	-7.28	0
2003 UM3	2022-2099	38	1.2e-06	14.38	28.1	0.010	-7.38	-7.97	0
2005 GQ33	2051-2103	8	7.2e-09	20.78	23.7	0.060	-7.41	-7.90	0
1991 BA	2014-2096	11	8.7e-07	18.03	28.7	0.010	-7.48	-7.97	0
2000 SZ162	2070-2096	3	5.3e-07	4.18	27.1	0.010	-7.67	-8.01	0
1998 BT13	2036-2036	1	6.0e-08	8.03	26.4	0.020	-7.79	-7.79	0
2001 YN2	2020-2020	1	3.2e-09	18.49	24.9	0.030	-7.85	-7.85	0
2004 XB45	2035-2054	2	2.0e-08	17.00	26.3	0.020	-7.99	-8.04	0
2004 XM29	2045-2045	1	4.0e-10	15.11	22.9	0.090	-8.19	-8.19	0
2003 YS70	2075-2103	2	8.9e-07	3.14	28.8	0.010	-8.30	-8.37	0
2004 XO63	2065-2065	1	4.5e-09	8.16	26.1	0.020	-9.06	-9.06	0
2002 TA58	2081-2081	1	3.0e-09	11.30	26.6	0.020	-9.50	-9.50	0

Table Legend

Object Designation

Temporary designation or permanent number for this object. Assigned by the [Minor Planet Center](#).

Year Range

Time span over which impacts have been detected. Typically, searches are conducted 100 years into the future.

Potential Impacts

The number of dynamically distinct potential impacts that have been detected by Sentry. There can be several qualitatively unique pathways to impact in a given year, e.g., some with an extra revolutions around the sun, others deflected to impact by an earlier planetary encounter.

Impact Prob. (cum.)

The sum of the impact probabilities from all detected potential impacts.

V_{∞}

The velocity of the asteroid relative to the Earth, assuming a massless Earth.

H

Absolute Magnitude is an intrinsic measure of brightness. It is the apparent magnitude of the object when it is 1 AU from both the sun and the observer, and at full phase for the observer.

Est. Diam.

The estimated diameter of the asteroid, assuming a visual albedo $p_V = 0.154$. The actual diameter could differ by as much as a factor of two.

Palermo Scale (cum.) & (max.)

The cumulative and maximum hazard ratings according to the [Palermo Technical Impact Hazard Scale](#).

Torino Scale (max.)

The maximum detected hazard rating using the [Torino Impact Hazard Scale](#). According to this ten-point scale, a rating of zero indicates the event has "no likely consequences." A Torino Scale rating of 1 indicates an event that "merits careful monitoring." Even higher ratings indicate that progressively more concern is warranted.

[SITE MAP](#)

[FEEDBACK](#)

[CREDITS](#)

[PRIVACY](#)

[MAILING LIST](#)



Site Manager: Don Yeomans

Webmaster: Ron Baalke

Last Updated: NaN undefined NaN

Home

Database Search

Database Cautions

Database Clues

Database Codes

Database Statistics

Bibliography

NStars Project

NStars Team

NStars Research

Data Displays

Tools & Utilities

Feedback

2001 AAS Conf.

The NASA NStars research project was originated in 1998 and is based at the Ames Research Center in California. Its mission is to be the most current, complete and accurate source of scientific data about all stellar objects within the current study radius of 25 parsecs. At present this includes approximately 2600 stars. The techniques, methods and know how being developed to accomplish this will form the basis to expand this knowledge base further out into our galaxy. NStars provides research grade internet capabilities to astronomers and other scientists, support for NASA deep space missions and basic star information to students and amateur sky observers.

Turnbull and Tarter SETI Target List [[PDF 1,137KB](#)] [[PS 1,960KB](#)]





Galaxies Galore, Games and More

Galaxies are
made of billions
of stars.

- About
Galaxies
- Computer
Needs
- Teaching
Tips
- Galaxy
Links
- Amazing
Space



Build Our
Milky Way

Galaxies
Galore

Galaxy
Games

Tried the activities? [Tell us what you think!](#)
If you are a teacher, please fill out the [teacher evaluation](#) !



SPACE
Meet the Men and Women of NASA



Liftoff to Learning: The Mathematics of Space-Rendezvous

- Home Page
- What is NASA Quest?

- Calendar of Events
- What is an Event?
- How Do I Participate?

- What NASA People Do
-Biographies/Journals

- Pics, Flicks and Facts
- Reruns - Archived Events
- Questions and Answers
- In the News

- Educators and Parents



Sitemap | Search |



Contact

Video Title: [The Mathematics of Space - Rendezvous](#)

Video Length: 17:00

Videos may be viewed using free

[RealPlayer](#)

Click on the highlighted title to see the video using RealPlayer

Mathematics Standards:

Mathematics as Problem Solving
Mathematics as Communication
Mathematics as Reasoning
Computation and Estimation
Algebra
Geometry

Measurement

Subjects: The mathematics of spacecraft orbital rendezvous.

Description: This program addresses the basic mathematical operations of spacecraft rendezvous in Earth orbit. Middle school students in a mathematics class work to solve some problems that permit the Space Shuttle to rendezvous and dock with the Russian Space Station Mir. The video has stopping points to permit viewers to work the problems as well.

Table of Contents

- [Equations Used in the Program](#)
- [Class Activities](#)
- [References](#)

Background

In a few years, the International Space Station (ISS) will be ready for full-time occupancy by crews of astronauts. From their vantage point in space, astronauts will study Earth's environment and conduct a variety of scientific and technological experiments that will ultimately help to improve life on Earth.

One of the critical tasks to the construction and use of a space station is the ability to rendezvous in space. Consequently, the first phase of the international Space Station program is a series of Space Shuttle mission rendezvous and docking activities with the Russian Space Station Mir. By bringing crew and equipment to Mir, Shuttle astronauts have gained valuable practice in the maneuvers they will need to work with the ISS. These maneuvers are complex and docking is a delicate operation. Each maneuver employs extensive use of mathematics to achieve the objective.

The objective of this video is to invite students to work out some of the fundamental equations Shuttle crews use for rendezvous. The equations presented in the video are listed in a following section of this guide.

Some students may become confused with some of the mathematical operations shown. The video is designed with stopping places for you to work the mathematics with your students.

One rendezvous concept presented in the video may need some additional explanation. By firing its rocket engines to increase velocity, the Space Shuttle actually slows down. Conversely, firing engines to slow down causes the vehicle to speed up. These paradoxical statements are easier to understand when you remember that movement in space is a three-dimensional problem. Changes in velocity leads to changes in altitude.

On Earth, rendezvous between two automobiles is a relatively simple operation. Both drive at specific speeds to arrive at a specific location. When the automobiles arrive at the right place, they stop. In space, the rendezvous location is over a specific place on Earth, but it is also at a specific altitude. When the two spacecraft arrive, they cannot stop. Doing so will cause them to fall back to Earth. Instead, their rendezvous is at a specific location and

altitude (three dimensions), and at a specific time. Time is important when you consider that the spacecraft will be traveling at 5 or more kilometers per second. A mere 5-second error will cause the spacecraft to miss each other by 25 kilometers.

The nature of space rendezvous is also complicated by some basic physical laws. Altitude and velocity of a spacecraft are related. Spacecraft in low orbits travel very fast because the gravitational pull is strong. In higher orbits, spacecraft travel slower because the force of gravity is less. The force of gravity between two objects (Earth and the Shuttle) is determined by the following mathematical relationship that was first formulated by Isaac Newton and later modified by Henry Cavendish.

$$f = G \frac{m_1 m_2}{r^2}$$

G in the equation is the gravitational constant. The r in the equation is the distance between the center of Earth and the center of the Shuttle (not the altitude of the Shuttle over Earth's surface). As you can see, r has an inverse square relationship in the equation. That means that the closer the centers of the two bodies are to each other, the greater the force of attraction. It also means that increasing the distance between the centers decreases the attraction by an inverse square.

The difference in gravitational attraction with change in distance (orbital altitude) is where the speed-up/slow-down paradox comes in. You must travel faster in a lower orbit than a higher one to stay in orbit. If you want to go to a higher orbit, you must fire your rocket engines to accelerate. The acceleration causes your spacecraft to climb higher above Earth. As you climb higher, your velocity diminishes until you are traveling at the right velocity for the higher orbit. It is a slower velocity than you were traveling before the firing of the engines. In other words, you sped up so that you could slow down in a higher orbit.

The reverse is true if you want to go to a lower orbit. To descend, you fire rocket engines in the opposite direction you are traveling. This causes your spacecraft to slow. Earth's gravity

pulls your spacecraft downward, and, as you fall, your speed increases until you are at the right speed for the new altitude. Your speed is greater in the lower orbit. Thus, you slowed down to speed up.

Although somewhat complicated, this paradox helps to accomplish rendezvous. For example, when the two spacecraft are on opposite sides of Earth from each other, having one spacecraft in a lower orbit will enable it to close the distance. In the lower orbit, the spacecraft will not only travel faster than the higher spacecraft, but the orbit has a smaller circumference as well. After closing the distance, the lower spacecraft can begin maneuvers to adjust to the right altitude for the rendezvous. How long to fire rocket engines, when to do it, and in what directions is determined with mathematics.

Equations Used In the Program

[contents](#)

Degrees longitude orbital ground track shifts eastward with each orbit.

$$\frac{x}{92 \text{ min}} = \frac{360^{\circ}}{24 \text{ hrs (60 min/hr)}} \quad x = 23^{\circ}$$

Number of orbits so that Mir flies over Moscow.

Mir - Moscow = Longitude Distance

$$\frac{105^{\circ} - 37^{\circ}}{68^{\circ}} = \frac{68^{\circ}}{23^{\circ}/\text{orbit}} = 2.9565 \text{ orbits}$$

or 3 orbits

Time for Mir's orbit to cross Moscow.

$$\frac{92 \text{ min/orbit} \times 3 \text{ orbits}}{276 \text{ min}} \quad \text{or} \quad \frac{276 \text{ min}}{60 \text{ min/hr}} = 4.6 \text{ hr}$$

Mir's orbital speed.

$$\frac{\text{Distance}}{\text{Time}} = \text{Speed}$$

Distance (circumference) Mir travels during one orbit. (The altitude is the distance from Earth's center to Mir.)

$$6,778 \text{ km} \times 2 \pi = C_{\text{Mir}}$$

$$42,587 \text{ km} = C_{\text{Mir}}$$

Mir's orbital speed.

$$\frac{42,587 \text{ km}}{92 \text{ min}} = \text{speed}$$

$$463 \text{ km/min} = \text{speed}$$

or

$$\frac{63 \text{ km/min} \times 60 \text{ min/hr}}{27,780 \text{ km/hr}}$$

Shuttle speed change needed to raise orbit 7 kilometers. (It is stated in the video that a change in velocity of 0.4 meters per second raises the Shuttle 1 kilometer.)

$$\begin{array}{r} \text{target altitude} \quad 305 \text{ km} \\ \text{present altitude} \quad - 298 \text{ km} \\ \hline 7 \text{ km} / 1 \text{ km} \end{array}$$

$$\frac{7 \text{ km}}{1 \text{ km}} \times 0.4 \text{ m/sec} = 2.8 \text{ m/sec}$$

Classroom Activities

[contents](#)

How High?

Materials:

Earth globe
Metric ruler

Objective: To learn why it is necessary to exaggerate altitudes when orbits are shown in model form.

Procedure:

Measure the diameter of the globe you are using for the model. Determine its scale. To do this, you will need to know the actual diameter of the Earth (12,756 km). Using the same scale, determine how high above the globe's surface the Space Shuttle and Mir would be (400 km).

Discussion:

Diagrams of planets and spacecraft orbiting them are difficult to portray accurately. The diagrams of Earth, the Space Shuttle, and Mir Space Station used in the video greatly exaggerate the distance the orbiting spacecraft are above Earth. Without doing this, the orbits would lie so closely to the surface of Earth that the lines would be indistinguishable.

Extension: Using the same scale, determine how far the Moon would be from Earth.

Sine Curve Orbits?

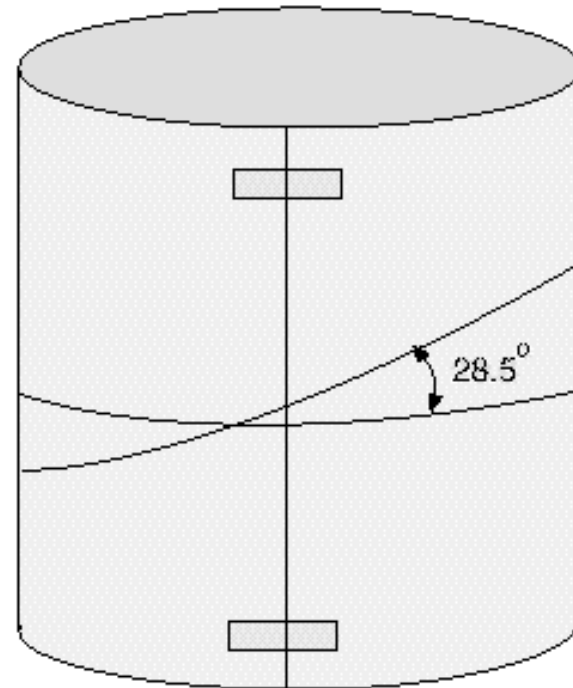
Materials:

Earth globe
Paper
Tape
Marker
Scissors

Objective: To show why a sine curve orbital plot is created when an orbit is portrayed on a flat map.

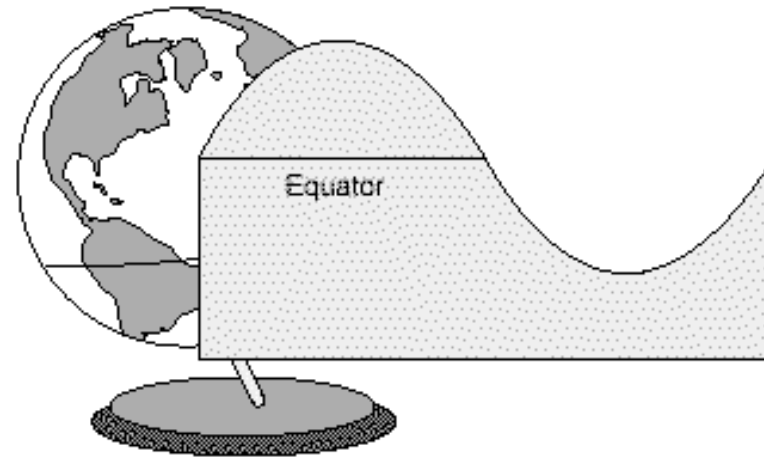
Procedure:

When shown on a flat map, Space Shuttle orbits resemble sine curves. To show why this happens, wrap and tape a cylinder of paper around an Earth globe. Use a marker pen to draw an orbit around the cylinder. Start with an orbit inclined 28 degrees. Draw the line around the cylinder so that it falls on a plane inclined to the globe's equator by 28 degrees. Remove the cylinder and cut the paper along the line you drew. If you drew the line carefully, the edge of the cut will fall on a plane. Unwrap the cylinder and look at the shape of the orbit.



Discussion:

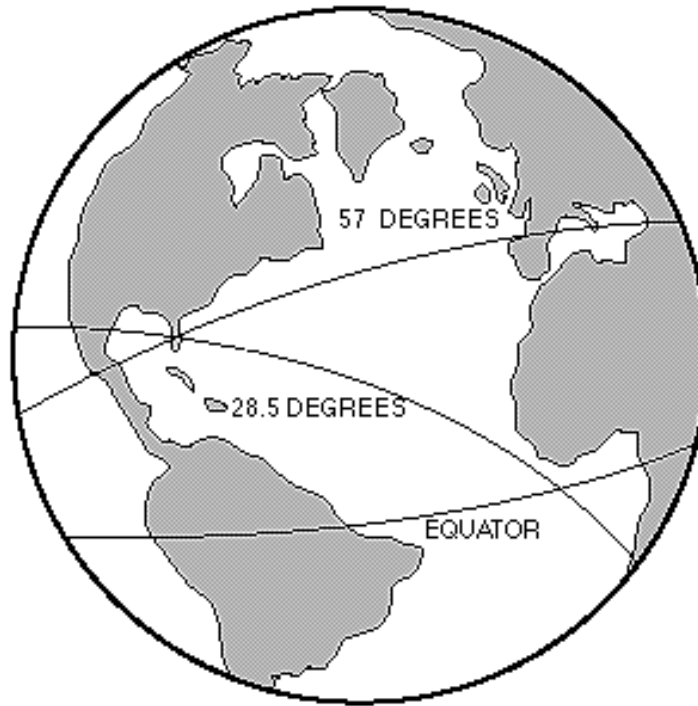
Orbital maps displayed in Mission Control at the NASA Johnson Space Center show three Space Shuttle orbits at a time. A small Space Shuttle orbiter is displayed on one of the orbits over the geographic position the actual orbiter is flying. The curve of the orbits resembles a sine curve. The steepness of the curve is determined by the angle in which the Space Shuttle was launched in respect to Earth's equator.



Many Shuttle orbits are inclined at 28.5 degrees. This is the geographic latitude of the Kennedy Space Center. When a Shuttle is launched due east, its orbit is inclined 28.5 degrees. This happens because an orbit must be concentric with the center of Earth. In geographic terms, the orbit must be a great circle.

Extension:

Create other cylinders for different orbits such as 35 degrees and 51.6 degrees (orbit of the International Space Station). Compare the steepness of the curves when the cylinders are flattened.



STS-84 Crew Biographies

[contents](#)

Commander: [Charles J. Precourt \(Col., USAF\)](#)

Pilot: [Eileen M. Collins \(Lt. Col., USAF\)](#)

Payload Commander, Mission Specialist: [Jean-Francois Clervoy](#) (Ingenieur en Chef de l'Armement, ESA Astronaut)

Mission Specialist: [Edward T. Lu \(Ph.D\)](#)

Mission Specialist: [Carlos I. Noriega \(Major, USMC\)](#)

Mission Specialist, NASA-Mir 4: [Jerry M. Linenger \(Capt., USN\)](#)

Mission Specialist: Elena V. Kondakova

Mission Specialist, NASA-Mir 5: [C. Michael Foale \(Ph.D.\)](#)

To obtain biographic information, click on highlighted names



SPACE



AEROSPACE



ASTROBIOLOGY



WOMEN OF NASA

.....
DONALD JAMES IS THE RESPONSIBLE NASA OFFICIAL FOR NASA QUEST.
MARK LEON IS THE RESPONSIBLE NASA OFFICIAL FOR THE LEARNING TECHNOLOGIES PROJECT.



NASA EDUCATION

- + Low Bandwidth
- + Non-Flash Version
- + Contact Us

FIND IT @ NASA :

+ GO

+ SEARCH EDUCATION

+ ABOUT US

+ EDUCATION CALENDAR

+ NASA EDUCATION OFFICES

+ NASA EDUCATION PROGRAMS

- + NASA Home
- + NASA Education Home

Central Operation of Resources for Educators

- CORE HOME

+ ABOUT CORE

+ SEARCH ONLINE CATALOG

+ REQUEST A CATALOG

+ HOW TO ORDER

+ EXPRESS MAILING LIST

+ CONTACT CORE



CORE is a worldwide distribution center for NASA's educational multimedia materials. Educators may purchase exciting materials for a minimal charge.

FEATURED PRODUCTS



Blast Back to School With Space Science Bulletin Board

Teachers get this great starter set for your classroom!

[+ Read More](#)



Blast Back to School Family Activity Kit

Parents and children will all have fun with this special activity packet.

[+ Read More](#)

EDUCATION HIGHLIGHTS

NASA ERCN

CORE partners with NASA's Educator Resource Center Network. Find out what the ERCN has for you.

[+ View site](#)



NASA Bulletin Board Collection

Earth Science, Space Science, Living and Working in Space and Return to Flight - these are just a few of the bulletin board sets available.

[+ Read More](#)



NASA CONNECT™

Good Stress: Building Better Muscles and Bones

Videotape

[+ Read More](#)



NASA Science Files™

The Case of the Great Space Exploration Videotape

[+ Read More](#)



Audio Descriptive Videos

Audio descriptive videotapes for the sight impaired audience now available!

[+ Read More](#)

NASA Educational Themes

NASA TV programming, online resources, and classroom materials, including CORE products, are highlighted each month.

[+ View site](#)

NASA Educational Materials

NASA online publications are a perfect compliment to CORE products.

[+ View site](#)



- + NASA Home Page
- + Inspector General Hotline
- + Equal Employment Opportunity Data Posted Pursuant to the No Fear Act
- + Budgets, Strategic Plans and Accountability Reports
- + Freedom of Information Act
- + The President's Management Agenda
- + NASA Privacy Statement, Disclaimer, and Accessibility Certification



Editor: Dr. Shelley Canright
NASA Official: Dr. Adena Williams
Loston
Last Updated: August 25, 2005



Articles for May 5, 2005

Previous Articles

National
Standards

Resources

Trivia

Calendar

Glossaries

Just For Fun

About Us

F.A.Q.

Feedback

Subscribe

Home



TO WORLDS BEYOND
The Vision for
Space Exploration



Need Help?

Weathering The Storms

From the NE archives: Guiding jets in and out of airports is no small task, and it's further complicated when rain, lightning and ice are added to the mix.

[the full story...](#)

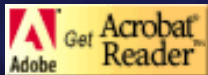
Article and Lessons
for: [\[K-4\]](#) [\[5-8\]](#) [\[9-12\]](#)



It's summer time!

We are taking a break from writing lesson plans, but that doesn't mean we have nothing to offer you. Search our site for archived lesson plans (we never throw anything away!), games, interesting articles, national standards, and more. Begin with the left navigation bar, and go from there!

Have a relaxing summer!



Contact Information

[NASA Education Home Page](#)

NASA Official—Jim Pruitt
Site Manager—Jeremy Raper

Contact us via our [Feedback](#) page, e-mail us at info@nasaexplores.com, or call NASAexplores at 256.544.0340.

Web Services Provided by UNITeS

[NASA Web Privacy Statement](#)

Chip Off the Old Rock



For 14 years, Marilyn Lindstrom has been keeping a watchful eye on a large group of meteorites. For all of her hard work, an asteroid and a mountain in Antarctica have been named after her. What do these have to do with meteorites? Read more to find out!

[the full story...](#)

Article and Lessons
for: [\[K-4\]](#) [\[5-8\]](#) [\[9-12\]](#)





NASA EDUCATION

- + NASA Home
- + Low Bandwidth
- + Non-Flash Version
- + Contact Us

+ ABOUT US

+ EDUCATION CALENDAR

+ NASA EDUCATION OFFICES

+ NASA EDUCATION PROGRAMS

FIND IT @ NASA :

+ GO

- + ADVANCED SEARCH
- + SEARCH EDUCATION



+ ELEMENTARY & SECONDARY EDUCATION



+ HIGHER EDUCATION



+ INFORMAL EDUCATION



NASA Explorer Schools Program

- + [Find out More](#)
- + [2005 Schools Announced](#)
- + [Delta Researchers Schools Announced](#)



NASA Science and Technology Scholarship Program (STSP)

- + [View](#)
- + [Cooperative Agreement Notice](#)



Minority University-SPace Interdisciplinary Network (MU-SPIN)

- + [View site](#)



NASA Explorer Institutes

- + [Learn more](#)
- + [2005 Funding Opportunity](#)
- + [2004 Explorer Institutes](#)



Welcome to StenniSphere

- + [Read More](#)



Educator Astronauts Join the Corps

[+ Read More](#)
[+ View Video](#)
[+ View Astronaut Training Journal](#)



A Broader Vision of Discovery

[+ Read More](#)



Reduced Gravity Flight Opportunities Program

[+ Find out More](#)



Students Team with NASA on Space Experiments

[+ Read More](#)

EDUCATION NEWS AND EVENT FEATURES

09.02.05 - NASA's Science Resources Help Agencies Respond to Katrina

NASA science instruments and Earth-orbiting satellites are providing detailed insight about the environmental impact caused by Hurricane Katrina.

[+ Read More](#)

09.01.05 - Space Grant Consortia

NASA's Office of Education has competitively selected seven consortia in the National Space Grant College and Fellowship Program. Their role is to assist NASA in inspiring students to pursue careers in science, technology, engineering and mathematics.

[+ Read More](#)

08.31.05 - NASA Invites Students to Conduct Real-World Science

NASA scientists are working to inspire the next generation of explorers by inviting high school students to participate in the 2005 Hyper-G Competition, a nationwide science contest beginning Sept. 1, 2005.

[+ Read More](#)

08.30.05 - NASA Awards State Education Grants

The NASA Explorer Schools Partnerships for Sustainability is designed to inspire students to pursue careers in science, technology, engineering and mathematics.

[+ Read More](#)

+ TECHNOLOGY & PRODUCTS OFFICE



Return to Flight Educator Resources

[+ Read More](#)



NASA Helps Kids Build Robots

[+ Read More](#)

+ EDUCATION FLIGHT PROJECTS OFFICE



Send Your Art to Space!

[+ Read More](#)



Science in Space Challenge

[+ Read More](#)

08.26.05 - Digital TV Service for Alaska and Hawaii

The satellite signal carrying NASA TV to viewers in Alaska and Hawaii will convert from analog to digital at 12:01 a.m. EDT, October 1.

[+ Read More](#)

08.22.05 - Station Crew Talks With Ohio Students

Cincinnati students will experience the excitement of exploration and discovery when they make a long-distance phone call to the ISS crew.

[+ Read More](#)

[+ View Archives](#)



- + NASA Home Page
- + Inspector General Hotline
- + Equal Employment Opportunity Data Posted Pursuant to the No Fear Act
- + Budgets, Strategic Plans and Accountability Reports
- + Freedom of Information Act
- + The President's Management Agenda
- + NASA Privacy Statement, Disclaimer, and Accessibility Certification



Editor: Dr. Shelley Canright
NASA Official: Dr. Adena Williams
Loston
Last Updated: September 7, 2005



NASA Spacelink has Moved

NASA Spacelink and other information providers across NASA are moving content into the NASA home page. The NASA home page is now the best place to find the type of content you have come to expect from Spacelink. The Spacelink team looks forward to serving you through NASA's premier Web site.

www.nasa.gov - This is your starting point to explore NASA on the Web, see showcased initiatives, and find breaking news.

For NASA Educational news and initiatives visit the following sections of the NASA home page:

For Educators

[K-4](#) | [5-8](#) | [9-12](#) | [Post Secondary](#) | [Informal](#)

For Students

[K-4](#) | [5-8](#) | [9-12](#) | [Post Secondary](#)

Also, visit the new [For Kids](#) section that is both informative and fun for kids of all ages.

Please contact us if you have questions or
comments:
education@nasa.gov



- + Inspector General Hotline
- + Equal Employment Opportunity Data Posted Pursuant to the No Fear Act
- + FY 2005 Budget Request
- + 2003 Strategic Plan
- + Freedom of Information Act
- + The President's Management Agenda
- + FY 2004 Agency Performance and Accountability Report
- + NASA Privacy Statement, Disclaimer, and Accessibility Certification



Editor: Jim Wilson
NASA Official: Brian Dunbar
Last Updated: December 14, 2004
+ Contact NASA

THE SPACE EDUCATORS' HANDBOOK

SPACE GAMES GALLERY HOME PAGE



Copyright, 1969, Edu-Cards

SPACE GAME ARTIFACTS

[The game of SPACE CHALLENGE](#)

[The game of SPACE RACE](#)

[The game of SPACE PUZZLES](#)

[Johnny Apollo Pinball Game](#)

[Mission to the Stars Pinball Game](#)

[RETURN TO SPACE MUSEUM HOME PAGE](#)

[SPACE EDUCATORS' HANDBOOK HOME PAGE](#)

[SCIENCE FICTION SPACE TECHNOLOGY HOME PAGE](#)

[SPACE MOVIES CINEMA HOME PAGE](#)

[SPACE COMICS](#)

[SPACE CALENDAR](#)

The page is 508 compliant

[Notices: What You Need to Know About NASA JSC Web Policies](#)

Last modified: Wednesday, 30-Nov-04 11:00:00 AM CDT

Author: Jerry Woodfill / NASA, Mail Code ER7, jared.woodfill1@jsc.nasa.gov

Curator: Cecilia Breigh, NASA JSC ER

Responsible Official: Andre Sylvester, NASA JSC ER7

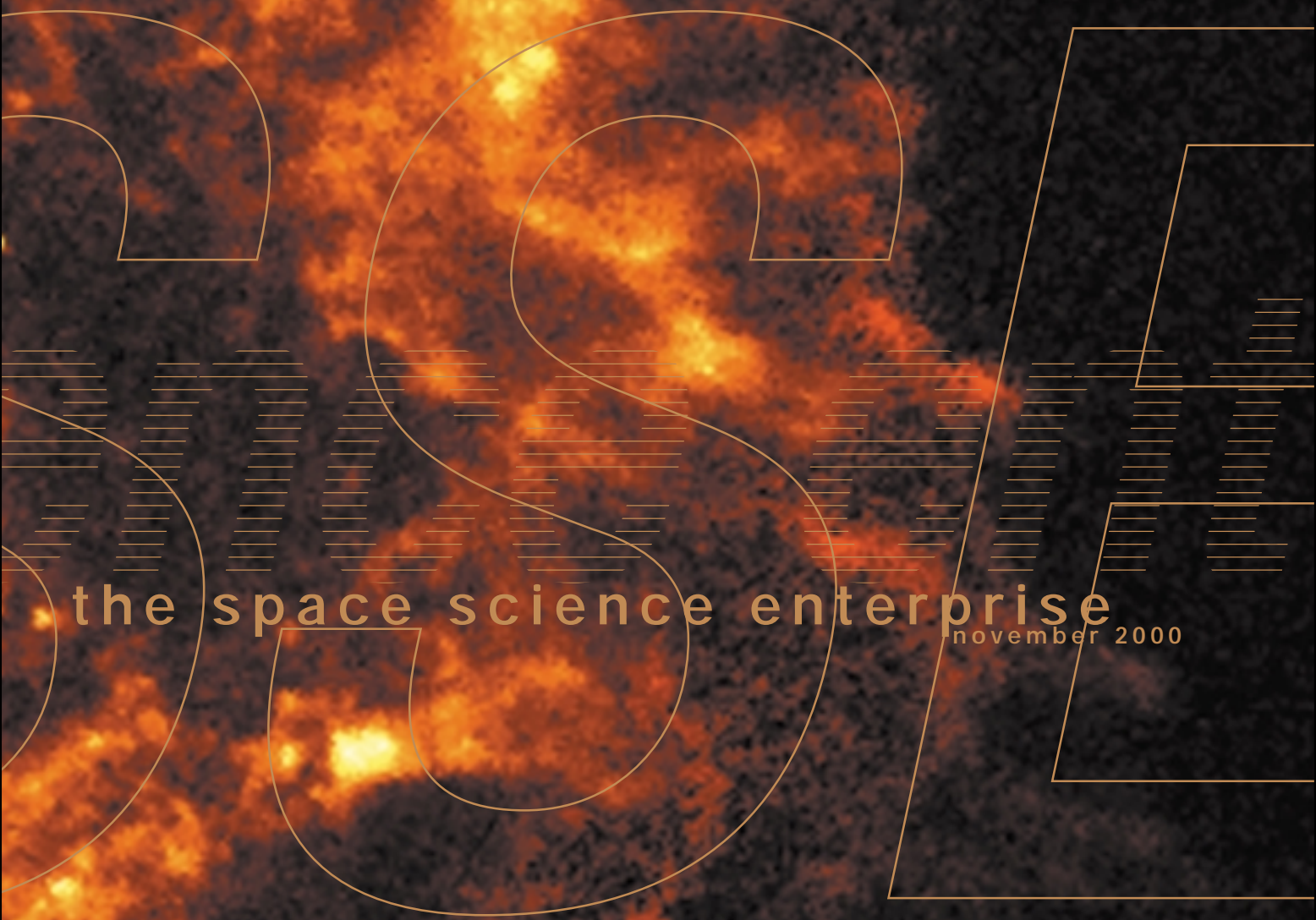
Automation, Robotics and Simulation Division, Walter W. Guy, Chief.





Space Science

Strategic Plan



the space science enterprise

november 2000

Dedicated to the memories of
Herbert Friedman and John A. Simpson
– Pioneers of Space Science –



Cassiopeia A: The 320-year-old remnant of a massive star that exploded. Located in the constellation Cassiopeia, it is 10 light years across and 10,000 light years from Earth. This X-ray image of Cassiopeia A is the official first light image of the Chandra X-ray Observatory. The 5,000-second image was made with the Advanced CCD Imaging Spectrometer (ACIS). Two shock waves are visible: a fast outer shock and a slower inner shock. The inner shock wave is believed to be due to the collision of the ejecta from the supernova explosion with a circumstellar shell of material, heating it to a temperature of ten million degrees. The outer shock wave is analogous to a tremendous sonic boom resulting from this collision. The bright object near the center may be the long sought neutron star or black hole that remained after the explosion that produced Cassiopeia A. (Credit: NASA/CXC/SAO)

the space science enterprise

strategic plan

november 2000



National Aeronautics and
Space Administration

NP-2000-08-258-HQ

November 2000

Dear Colleagues and Friends of Space Science,

It is a pleasure to present our new Space Science Strategic Plan. It represents contributions by hundreds of members of the space science community, including researchers, technologists, and educators, working with staff at NASA, over a period of nearly two years.

Our time is an exciting one for space science. Dramatic advances in cosmology, planetary research, and solar-terrestrial science form a backdrop for this ambitious plan. Our program boldly addresses the most fundamental questions that science can ask: how the universe began and is changing, what are the past and future of humanity, and whether we are alone. In taking up these questions, researchers and the general public—for we are all seekers in this quest—will draw upon all areas of science and the technical arts. Our Plan outlines how we will communicate our findings to interested young people and adults.

The program that you will read about in this Plan includes forefront research and technology development on the ground as well as development and operation of the most complex spacecraft conceived. The proposed flight program is a balanced portfolio of small missions and larger spacecraft. Our goal is to obtain the best science at the lowest cost, taking advantage of the most advanced technology that can meet our standards for expected mission success. In driving hard to achieve this goal, we experienced some very disappointing failures in 1999. But NASA, as an R&D agency, makes progress by learning also from mistakes, and we have learned from these.

Over the coming years, I invite you to watch as our plans come to fruition. This is your program, and we are managing it for you to answer the profoundest questions that we all share. I fully expect exciting surprises as our voyage of discovery continues to expand our knowledge about the history and future of our universe and of humankind within it.



Edward J. Weiler
Associate Administrator for Space Science

the space science enterprise seeks to



discover

- how the universe began and evolved
- how we got here
- where we are going
- and whether we are alone



table of contents

Letter from the Associate Administrator2

our goals

Section I-1: Introduction 8

Section I-2: Goals and Objectives12

Section I-3: The Role of Technology18

Section I-4: The Role of Education and Public Outreach22

our program

Section II-1: Recent Accomplishments and Current Program28

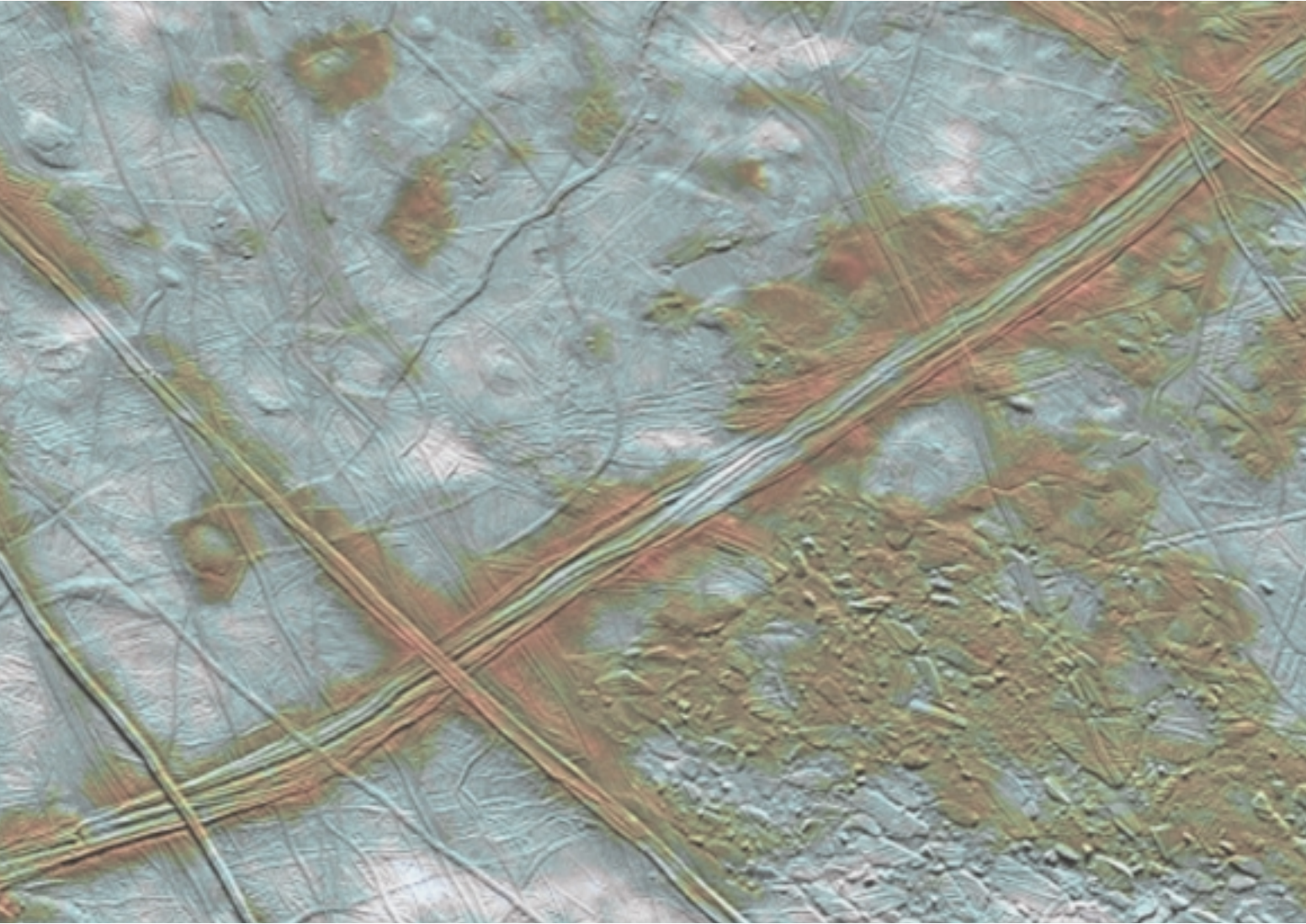
Section II-2: Principles and Processes 44

Section II-3: Flight Program: 2003 and Beyond50

Section II-4: Technology Program	76
Section II-5: Research and Data Analysis	86
Section II-6: Education and Public Outreach	94
Section II-7: Partnerships	98
Section II-8: A Vision of the Future	104

 appendices

Section A-1: Science Goals and Missions	110
Section A-2: Glossary of Missions	114
Section A-3: Enterprise Concurrence and Acknowledgments	122





the space science enterprise

our goals

introduction

Thousands of years ago, on a small rocky planet orbiting a modest star in an ordinary spiral galaxy, our remote ancestors looked up and wondered about their place between Earth and sky. On the threshold of the 21st century, we ask the same profound questions:

- How did the universe begin and evolve?
- How did we get here?
- Where are we going?
- Are we alone?

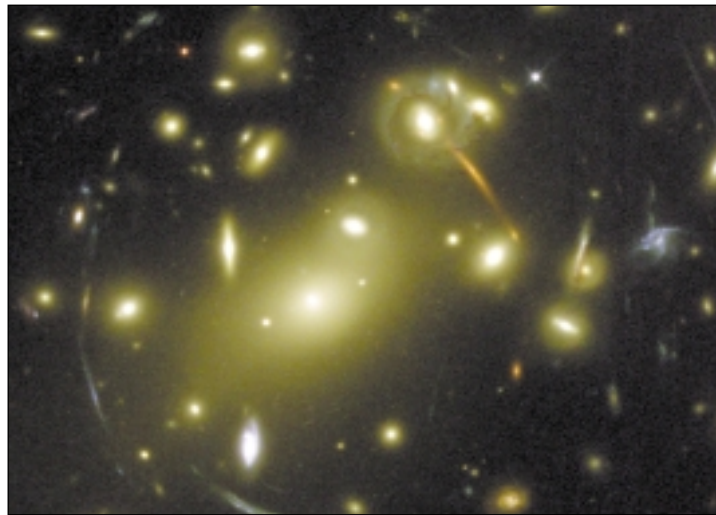
Today, after only the blink of an eye in cosmic time, we are beginning to answer these profound questions. Using tools of science that range from abstract mathematics and computer modeling to laboratories and observatories, humans are filling in the details of the amazing story of the universe. In the last 40 years, space probes and space observatories have played a central role in this fascinating process. Today, NASA addresses these four profound questions through its many space science activities.

How did the universe begin and evolve? We seek to explain the earliest moments of the universe, how stars and galaxies formed, and how matter and energy are entwined on the grandest scales. We study astrophysical objects, such as neutron stars and black holes, with extreme conditions that demonstrate fundamental laws of physics at work. We study the behavior of matter, radiation, and magnetic fields under

less severe conditions, in the giant laboratory of our Solar System. The understanding thus gained applies directly to the history and behavior of stars and galaxies.

How did we get here? We investigate how the chemical elements necessary for life have been built up and dispersed throughout the

cosmos. We look for evidence about how the Sun has behaved over time and what effect this has had on Earth and everything on it. We send probes to other planets to learn about their similarities and differences as keys to how they formed and evolved, and study the comets and asteroids in our Solar System for clues to their



Following the successful December 1999 servicing mission, the Hubble Space Telescope observed the gravitational bending and focusing of light from very distant objects by a massive foreground cluster of galaxies.

effects on the evolving Earth. We carry out ground-based research on the environmental limits of life to learn how it might have arisen and evolved on early Earth.

Where are we going? Our ultimate place in the cosmos is wrapped up in the fate of the universe. Nearer to home, the variability of our Sun and vulnerability of Earth to possible impacts by small Solar System bodies are being investigated. We are comparing the climate histories of Earth and its sibling planets. Humanity has taken its first steps off our home world, and we will

contribute to making it safe to travel throughout the Solar System and will ascertain what resources possible destinations could offer to human explorers.

Are we alone? Beyond astrophysics and cosmology, there lies the central human question: Are we on Earth an improbable accident of nature? Or is life, perhaps even intelligent life, scattered throughout the cosmos? We seek to explain how planets originated around our Sun and other stars—planets that might support life. We observe nearby stars for indirect

evidence of other planets, and look to the future when advanced observatories in space might be able to directly image such relatively small objects across the vast interstellar void. Beginning with life found in astonishing places on Earth, we conjecture about what kinds of environments could bear and support life, and how common habitable planets might be. Is there now, or has there ever been, life in our own Solar System other than on Earth?

Answers to these deep questions will not be extracted from narrow

Some Recent Space Science Discoveries

In recent years, space research has returned momentous results. Observations from the Hubble Space Telescope have yielded much better estimates of the age and size of the universe and the amount of matter within it, while x-ray observations from the Rossi X-ray Timing Explorer have led to the discovery of magnetars, a special type of neutron star that has the most powerful magnetic field known. By mapping the structure of leftover radiation from the Big Bang, NASA balloon-borne experiments have provided the first firm evidence to date for the “inflation” theory in cosmology. Exotic objects like black holes, for most of a century just a prediction of abstract mathematics, are now known to be commonplace. We are revealing secrets of the inconceivably luminous quasars and gamma ray bursters, now known to be in the remotest regions of the early universe. The Chandra X-ray Observatory has revealed a new class of medium mass black holes. Dozens of planet-like objects have been discovered around other stars, suggesting that our Solar System is not unique. Interest in the possibility of life elsewhere than on Earth has been galvanized by images of Mars from the Mars Global Surveyor and by evidence from the Galileo spacecraft that Jupiter’s moon, Europa, might have a liquid water ocean under an icy outer crust. The structure of our own star, the Sun, and its complex effects on Earth are becoming much better understood. U.S. instruments on the European Solar and Heliospheric Observatory and the Japanese Yohkoh mission have detected “rivers” of flowing gas beneath the Sun’s surface, as well as new predictors for the occurrence of solar activity that can affect Earth. We have learned much about causes of the solar wind, and even traced individual solar disturbances all the way from the Sun to Earth.

inquiries, but will be built up by combining innumerable individual clues over the years to come. The broad outlines of much of the puzzle are discernible now, but a clear picture of the whole awaits years of varied research that will undoubtedly produce many surprises along the way.

This Space Science Enterprise Strategic Plan tells about the science goals and objectives that will lead us toward answers to the fundamental questions. It lays out our near-term program of activities to pursue these goals and objectives. It tells how we will invent and demonstrate the new technologies that we need to pursue our ambitious vision, and how we will contribute to human space

flight. And it explains how we plan to share the excitement and understanding from our discoveries with teachers, schoolchildren, and the general public.

In Part I of the Plan, we describe our science goals and objectives, outline how progress in technology goes hand in hand with our ability to pursue them, and then present our approach to sharing our findings with the public on whose behalf we are conducting this important task of discovery.

In Part II we present in more detail our plans and hopes for the program. We describe some exciting recent accomplishments and projects currently under development, general principles that

guide us in structuring and carrying out the program, and our specific mission and research plans for new activities beginning in 2003. In subsequent sections we give more detail about the technology program that supports our bold vision, about our basic research programs, and about our public education and outreach programs. NASA cannot succeed without the active participation of scientists, technologists, and engineers all over the U.S. and collaboration with other nations as well. We therefore describe our many partnerships within the Federal Government, across the country, and around the world. The last section of Part II presents a vision of the future of the scientific exploration of the cosmos.

Astrobiology: Science of Synthesis

Answering our fundamental questions will call on all of modern science's tools of inquiry, ranging from astronomy, biology, and chemistry, through zoology. To gather these capabilities together and focus them on our fundamental questions, NASA is nurturing a new multidisciplinary science, Astrobiology. The place of life in the universe and its roots in the origin of the cosmos itself are the themes that run through this Strategic Plan to weave the Space Science Enterprise's many programs together into a unified voyage of discovery.

goals and objectives

The Space Act of 1958, which charters NASA as a Federal agency, defines a broad spectrum of goals and purposes for the Agency. The NASA Strategic Plan separates responsibility for its programs into Strategic Enterprises, which identify at the most fundamental level what we do and for whom. Each Strategic Enterprise has a unique set of goals, objectives, and strategies that address the requirements of its primary external customers.

Within NASA's Enterprise structure, the space sciences are gathered together into the Space Science Enterprise. These space sciences include space astronomy, planetary exploration, the physics of the Sun and the space between the Sun and planets, and fundamental physics experimentation carried out in space. This document is the enterprise-level Strategic Plan for the Space Science Enterprise.

The Agency Plan establishes a three-part Agency mission: advancing and communicating knowledge, human exploration of space, and developing new technology. Our Enterprise's programs contribute directly to these three Agency missions. Our role in technology development serves not only our Enterprise's and NASA's purposes, but also the broader purpose of strengthening our Nation's technology base.

The Space Science Enterprise works closely with the scientific community to articulate science goals that

NASA Mission

- To advance and communicate scientific knowledge and understanding of Earth, the Solar System, and the universe
- To advance human exploration, use, and development of space
- To research, develop, verify, and transfer advanced aeronautics and space technologies

The Space Science Enterprise's foremost role in support of the NASA mission is the discovery of new scientific knowledge about the universe. The Space Science Enterprise will:

Discover how the universe began and evolved, how we got here, where we are going, and whether we are alone.

directly support the Agency research mission. To address the other elements of the NASA mission, we also establish Enterprise goals for education and public outreach, support to human space flight, and technology. These four goals define the framework for formu-

lating and managing the space science program.

Within this context, all of our strategic planning and management, including selections for mission implementation and related research activities, are

Table I—Enterprise Goals and Objectives

NASA Mission	Enterprise Goals	Enterprise Objectives
<p>To advance and communicate scientific knowledge and understanding of Earth, the Solar System, and the universe</p>	<p>Chart the evolution of the universe, from origins to destiny, and understand its galaxies, stars, planets, and life</p>	<p style="text-align: center;"><u>Science Objectives</u></p> <ul style="list-style-type: none"> • Understand the structure of the universe, from its earliest beginnings to its ultimate fate • Explore the ultimate limits of gravity and energy in the universe • Learn how galaxies, stars, and planets form, interact, and evolve • Look for signs of life in other planetary systems • Understand the formation and evolution of the Solar System and Earth within it • Probe the origin and evolution of life on Earth and determine if life exists elsewhere in our Solar System • Understand our changing Sun and its effects throughout the Solar System • Chart our destiny in the Solar System
	<p>Share the excitement and knowledge generated by scientific discovery and improve science education</p>	<p style="text-align: center;"><u>Education and Public Outreach Objectives*</u></p> <ul style="list-style-type: none"> • Share the excitement of space science discoveries with the public • Enhance the quality of science, mathematics, and technology education, particularly at the pre-college level • Help create our 21st century scientific and technical workforce
<p>To advance human exploration, use, and development of space</p>	<p>Use robotic science missions as forerunners to human exploration beyond low-Earth orbit</p>	<p style="text-align: center;"><u>Human Space Flight Objectives</u></p> <ul style="list-style-type: none"> • Investigate the composition, evolution, and resources of Mars, the Moon, and small bodies • Develop the knowledge to improve space weather forecasting
<p>To research, develop, verify, and transfer advanced aeronautics and space technologies</p>	<p>Develop new technologies to enable innovative and less expensive research and flight missions</p>	<p style="text-align: center;"><u>Technology Objectives*</u></p> <ul style="list-style-type: none"> • Acquire new technical approaches and capabilities • Validate new technologies in space • Apply and transfer technology <p style="font-size: small; margin-top: 10px;">* Associated activities are discussed in Sections I-3 and I-4</p>

Table II—Science Objectives and Research Focus Areas

Science Objectives	Research Focus Areas
Understand the structure of the universe, from its earliest beginnings to its ultimate fate	<ul style="list-style-type: none"> • Identify dark matter and learn how it shapes galaxies and systems of galaxies • Determine the size, shape, age, and energy content of the universe
Explore the ultimate limits of gravity and energy in the universe	<ul style="list-style-type: none"> • Discover the sources of gamma ray bursts and high energy cosmic rays • Test the general theory of relativity near black holes and in the early universe, and search for new physical laws using the universe as a laboratory • Reveal the nature of cosmic jets and relativistic flows
Learn how galaxies, stars, and planets form, interact, and evolve	<ul style="list-style-type: none"> • Observe the formation of galaxies and determine the role of gravity in this process • Establish how the evolution of a galaxy and the life cycle of stars influence the chemical composition of material available for making stars, planets, and living organisms • Observe the formation of planetary systems and characterize their properties • Use the exotic space environments within our Solar System as natural science laboratories and cross the outer boundary of the Solar System to explore the nearby environment of our galaxy
Look for signs of life in other planetary systems	<ul style="list-style-type: none"> • Discover planetary systems of other stars and their physical characteristics • Search for worlds that could or do harbor life
Understand the formation and evolution of the Solar System and Earth within it	<ul style="list-style-type: none"> • Inventory and characterize the remnants of the original material from which the Solar System formed • Learn why the planets in our Solar System are so different from each other • Learn how the Solar System evolves
Probe the origin and evolution of life on Earth and determine if life exists elsewhere in our Solar System	<ul style="list-style-type: none"> • Investigate the origin and early evolution of life on Earth, and explore the limits of life in terrestrial environments that might provide analogues for conditions on other worlds • Determine the general principles governing the organization of matter into living systems and the conditions required for the emergence and maintenance of life • Chart the distribution of life-sustaining environments within our Solar System, and search for evidence of past and present life • Identify plausible signatures of life on other worlds
Understand our changing Sun and its effects throughout the Solar System	<ul style="list-style-type: none"> • Understand the origins of long- and short-term solar variability • Understand the effects of solar variability on the solar atmosphere and heliosphere • Understand the space environment of Earth and other planets
Chart our destiny in the Solar System	<ul style="list-style-type: none"> • Understand forces and processes, such as impacts, that affect habitability of Earth • Develop the capability to predict space weather • Find extraterrestrial resources and assess the suitability of Solar System locales for future human exploration

Another major function of the triennial review of our Enterprise Strategic Plan is to articulate nearer-term focus areas for research that provide more specific guidance over 5-10 year periods.

founded on our science goals and objectives (Table I). While these are formulated at a high enough level that we expect them to remain stable over many decades, we continue to refine their articulation. In doing so, we work with our research community to update our strategic plan, rephrasing our objectives periodically to reflect our growing knowledge.

Another major function of the triennial review of our Enterprise Strategic Plan is to articulate nearer-term focus areas for research that provide more specific guidance over

a 5-10 year period (Table II). These research focus areas are derived from our science objectives in consultation with our research communities, and are phrased to help mission and research decisionmaking and progress assessment.

The next two sections (I-3 and I-4) describe the roles of technology and education and public outreach in the space science program. Part II of the plan presents the program itself, beginning in section II-1 with our fundamental principles. Sections II-2 and II-3 of the plan describe our current program and

our proposed flight mission program for the future. To be as clear as possible about how these missions will advance us toward our long-range science aspirations, the presentation organizes the missions in these sections by the eight Enterprise science objectives laid out above. Appendix A maps the missions onto the more specific Enterprise research activity areas. The remainder of Part II presents our programs in technology, basic research, and education and public outreach, as well as our overall strategies for partnering with other entities to reach our goals.

the role of technology

The space science technology development program develops and makes available new space technologies needed to enable or enhance exploration, expand our knowledge of the universe, and ensure continued national scientific, technical, and economic leadership. It strives to improve reliability and mission safety, and to accelerate mission development. Since the early 1990's, the average space science mission development time has been reduced from over nine years to five years or less, partly by integration and early infusion of advanced technologies into missions. For missions planned in the years 2000 to 2004, we hope to further reduce development time to less than four years.

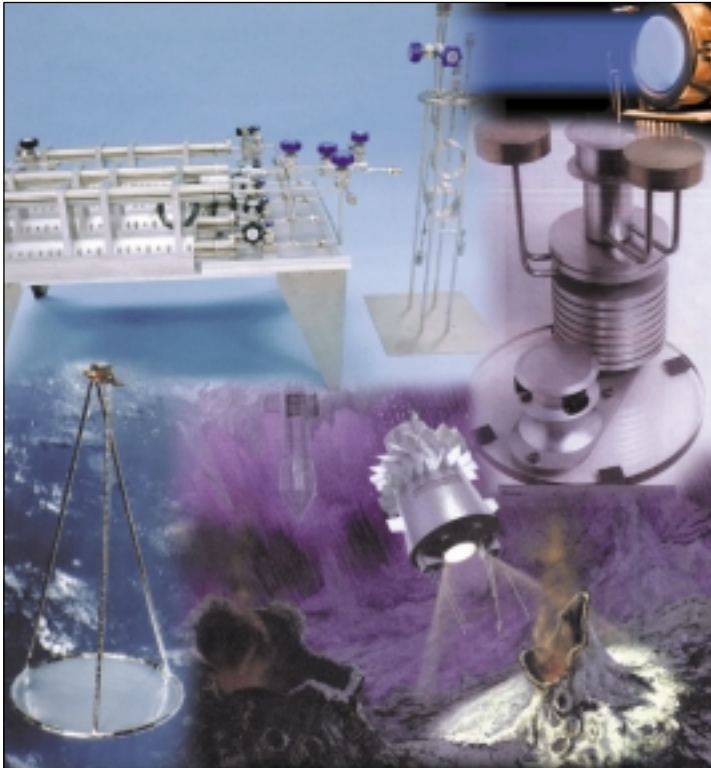
Our technology program encompasses three key objectives. First, we strive to develop new and better technical approaches and capabilities. Where necessary, we then validate these capabilities in

space so that they can be confidently applied to science flight projects. Finally, we use these improved and demonstrated capabilities in the science programs and ultimately transfer

them to U.S. industry for public use.

To achieve the technology goals for meeting future space science missions capability requirements for-

Enterprise Technology Objectives	Enterprise Technology Activities
Acquire new technical approaches and capabilities	<ul style="list-style-type: none"> • Focus technology development on a well-defined set of performance requirements covering the needs of near-term to mid-term strategic plan missions (“mission pull”) • Guide basic technology research to meet projected long-range needs (“vision pull”) • Promote partnerships with other agencies, industry, academia, and foreign collaborators to take advantage of capabilities developed elsewhere
Validate new technologies in space	<ul style="list-style-type: none"> • Identify technologies of high value to future Enterprise missions and fund their development to the point that they are ready for ground or space demonstration • Formulate, develop, and implement cost-effective space demonstrations of selected technologies on suitable carriers
Apply and transfer technology	<ul style="list-style-type: none"> • Use new technologies, in multiple missions where possible, to reduce costs and shorten mission development time across the program • Maximize benefits to the Nation by stimulating cooperation with industry, other Government agencies, and academia



The Space Science Enterprise provides requirements to, and in turn benefits from, a broad spectrum of Agencywide technology programs.

mulated in science roadmaps, the Enterprise technology strategy is to:

Focus technology development on science program requirements.

When near-term Enterprise mission concepts are defined sufficiently to begin detailed scoping of their instrumentation, systems, and infrastructure, performance requirements are derived. Technology development is focused on meeting

the identified requirements (“mission pull” technologies). Basic technology research is focused on perceived longer range technology needs (they are characterized with less precision than near-term requirements). These longer range needs are generated from advanced mission concepts developed by mission study groups working with science advisory groups. Identified needs are then

used to allocate support for maturation of more revolutionary technical approaches (“vision pull” technologies). The balance between “mission pull” and “vision pull” contributes to program agility and results in long-term continuing progress of the overall program notwithstanding short-term changes in circumstances.

Fund technologies of high value to future Enterprise missions to the point that they are ready for ground or space demonstration.

A large number of technology concepts are given the benefit of exploratory research in the expectation that a fraction of these will emerge as promising. It is critical that these promising candidates for use in missions are identified and funded to the point where they are tested in a relevant environment on the ground, adopted by a flight project for further maturation, or are proposed as a candidate for space flight validation.

Formulate and implement cost-effective space demonstrations of selected technologies on suitable carriers.

Project managers need assurance that adopted new technology will perform in the relevant space environment. In many cases this environment can be simulated on the ground in a satisfactory manner. Often this is not the

case, however. It is necessary to identify those technologies that require space flight demonstration and perform these demonstrations.

Use these technologies in multiple missions to reduce costs and shorten mission development time across the program. Since the early 1990's, the average science mission development time has been reduced from over nine years to five years. Although many factors can compress mission development time, infusion of validated new technology in the early mission phases can facilitate this. We compare requirements for future missions to look for common needs that can be met through a coordinated technology development effort. Where possible, we sequence missions so that later projects build on technology developed and successfully demonstrated for earlier ones.

Promote partnerships with other agencies, industry, and academia to take advantage of external capabilities. Technology infusion succeeds best through formal and informal interactions between mission developers, scientific principal investigators, and technology providers. In the early phases of development, detailed analyses and trade-off studies are conducted to determine technical feasibility and to establish technology priorities.

Technology
infusion succeeds
best through
formal and
informal
interactions
between mission
developers,
scientific principal
investigators,
and technology
providers.

Joint activities and partnerships with universities, industry, and other Government agencies can be particularly important in speeding identification and realization of the most attractive technology for specific needs. Technical capabilities can sometimes be efficiently acquired through cooperation with international partners. In conducting cooperative activities in technology, the Enterprise protects proprietary data and intellectual property.

Maintain excellence by engaging the outside community in technology development and evaluation. The Enterprise integrates industry, academia, and other Federal agencies' laboratories into the program. Industry, for example, develops valuable technology by using internal resources (IR&D and profit dollars), and through service to non-NASA customers. Similarly, the university community holds a vast and unique technological resource. University groups, receiving significant funding from other sources, are often leaders in essential technology areas. This approach—of using a mix of dedicated peer-reviewed efforts at NASA Centers, other Government agencies, industry, and universities—ensures that the “best and brightest” are tapped for the required developments. This approach dovetails with the practices of following parallel paths in early development followed by descopeing and down-selecting. Independent merit review will be used to assure excellence in both internal NASA and external technology development efforts. These reviews will consider whether work is “best-in-class,” contributes to specific, documented, and otherwise unaddressed Enterprise requirements, and is advancing significantly the state-of-the-art.

Space science missions have revealed the universe through new eyes and opened up new worlds to explore and understand. They have shown us that black holes really exist and have given us fundamental new information about the origin and evolution of planets, stars, galaxies, and the universe itself. They have opened up the tantalizing prospect of searching for life beyond Earth. By engaging the imaginations of teachers, students, and the general public, space science has demonstrated extraordinary potential for strengthening interest in science and improving the quality of science, mathematics, and technology education in America. By attracting bright individuals to advanced study in technical fields, space science also plays a significant role in ensuring a continuing cadre of trained scientists, engineers, and technologists to meet our society's needs in the 21st century.

d public outreach

To meet our goals and objectives, we integrate education and public outreach into all space science

missions and research programs. The resulting program is an important element of NASA's

overall education effort, and was designed in close collaboration with the NASA Office

Education and Public Outreach Objectives	Education and Public Outreach Activities
<p>Share the excitement of space science discoveries with the public</p> <p>Enhance the quality of science, mathematics, and technology education, particularly at the pre-college level</p> <p>Help create our 21st century scientific and technical workforce</p>	<ul style="list-style-type: none"> • Incorporate a substantial, funded education and outreach program into every space science flight mission and research program • Increase the fraction of the space science community that contributes to a broad public understanding of science and is directly involved in education at the pre-college level • Establish strong and lasting partnerships between the space science and education communities • Develop a national network to identify high-leverage education and outreach opportunities and to support long-term partnerships • Provide ready access to the products of space science education and outreach programs • Promote the participation of underserved and underutilized groups in the space science program by providing new opportunities for minorities and minority universities to compete for and participate in space science missions, research, and education programs • Develop tools for evaluating the quality and impact of space science education and outreach programs



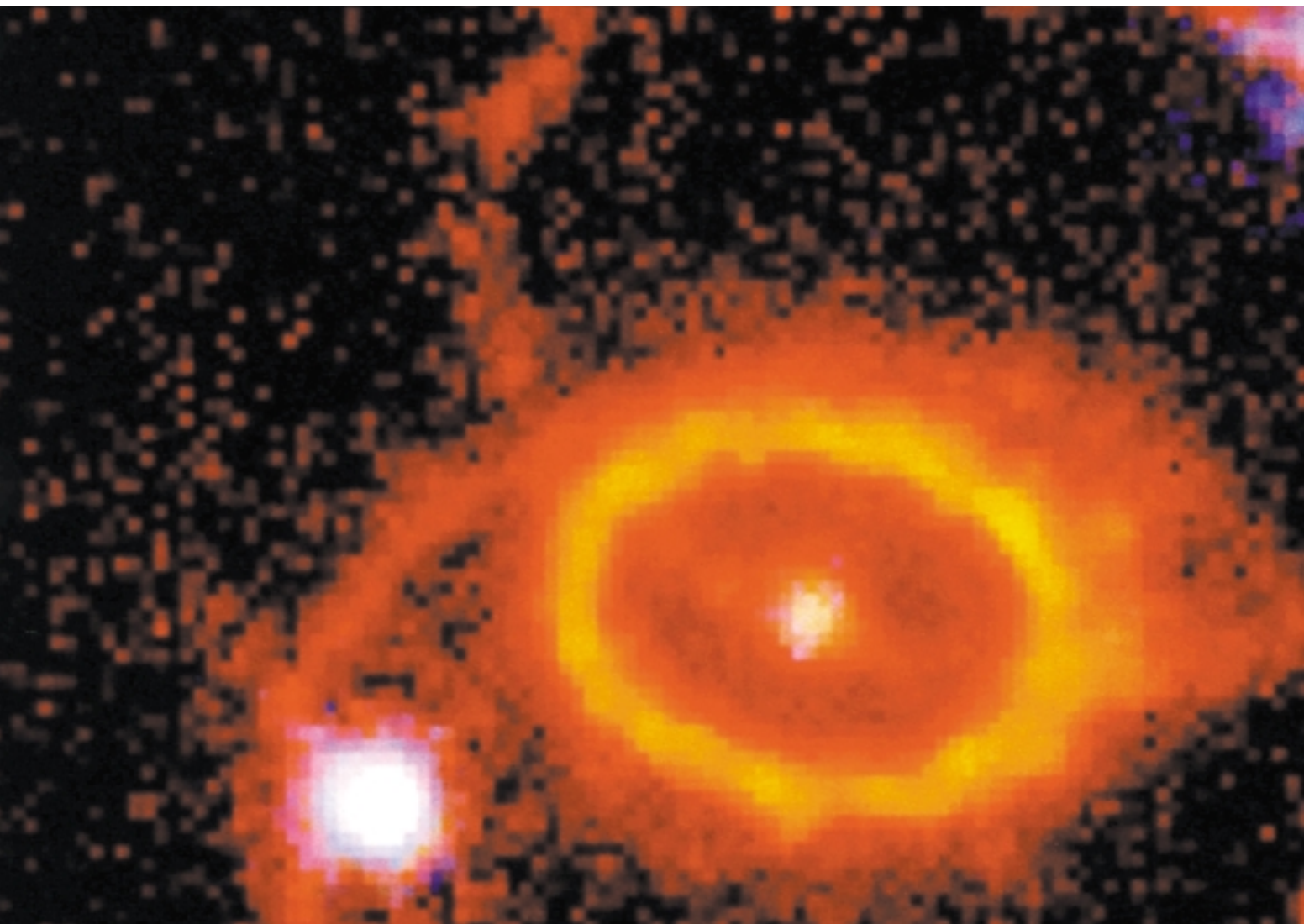
Children from the Daniel Boone Regional Library, Columbia, Missouri (a Space Place partner), displaying their own spacecraft—all made from recycled materials.

of Human Resources and Education and the Office of Equal Opportunity Programs. NASA mandates that the Agency “involve the education community in our endeavors to inspire America’s students, create learning opportunities, enlighten inquisitive minds,” and “communicate widely the content, relevance, and excitement of NASA’s missions and discoveries to inspire and to increase understand-

ing and the broad application of science and technology.”

It is our fundamental premise that all Americans should be able to participate in the adventure of exploring and understanding the universe. The Enterprise works closely with both the space science and education communities to identify education and outreach opportunities focused on the

needs of educators and the general public. Establishing productive, long-term partnerships between educators and space scientists helps maintain this focus. Our education and outreach information and materials are made readily available in a variety of formats useful to educators and suitable for bringing the accomplishments of the Space Science Enterprise to the general public.





the space science enterprise

our program

recent accomplishments

In section II-3 of this Strategic Plan, we will present missions under study for development over the 15-year period from 2003 through about 2018. To understand these plans and how they were derived, it helps to review the progress we have made since our last plan was released in late 1997. In *Recent Accomplishments* in this section, we highlight achievements since the last Plan. Then, in *Missions Currently Under Development*, we describe missions in an advanced study stage today that we will begin to implement before the end of 2002. Some of the missions described there will be launched after 2002 and most will be operating in 2003 and beyond. Missions are presented in **bold** when they are first introduced.

and current program

Recent Accomplishments

The Space Science Enterprise has made exciting advances in many goal areas during recent years. In this subsection, we briefly describe progress in astrophysics and cosmology, Solar System exploration, technology, and education and public outreach programs.

How did our universe, starting with what we have come to call the “Big Bang,” a featureless process that produced only the lightest elements, come to be the place that we know, rich in the rest of the chemical elements from which stars, planets, and life itself formed? The opportunity to put instruments in space that observe at many wavelengths has provided us with an explosion of evidence addressing these questions.

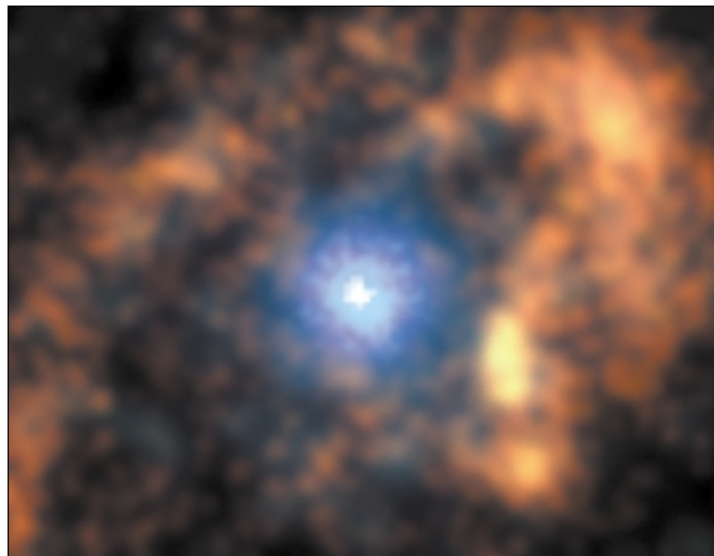
The Chandra x-ray image shows the complex region around Eta Carinae, a massive supergiant star that is 7,500 light-years from Earth. The outer horseshoe shaped ring is about two light-years in diameter and was probably caused by an outburst that occurred more than a thousand years ago.

In the late 1980’s, the **Cosmic Background Explorer (COBE)** satellite gave us a glimpse of the beginnings of structure very early in the history of the universe, a view sharpened by the subsequent **BOOMERANG** balloon-borne observations. The **Compton Gamma Ray Observatory (CGRO)** observed evidence for the synthesis of heavy elements in supernova explosions and their subsequent spread throughout the Milky Way. It observed large numbers of mysterious gamma ray bursts; believed now to originate in very distant sources, these brief gamma ray

“flashes” must represent enormous amounts of emitted energy. Vast amounts of energy in gamma rays are also seen to be coming from the jets in distant galaxies.

Two x-ray satellites, the **Rossi X-ray Timing Explorer (RXTE)** and the Japanese-U.S. **ASCA** mission, have helped us understand disks of accreting material in binary systems and provided evidence for spinning black holes in active galactic nuclei.

Recently, the newly launched **Chandra X-ray Observatory (CXO)** is showing us details of the



structure and composition of objects we could only begin to see a few years ago. For example, Cassiopeia-A is a supernova remnant already known to be a powerful emitter of radio waves. A CXO x-ray image of it (shown on the Plan cover) shows with remarkable clarity, not only the wispy structure characteristic of a supernova remnant, but also what appears to be a neutron star at the center, the remaining densely packed core of the original star. These exciting results are showcased through a nationally-distributed planetarium show “Journey to the Edge of Space and Time,” co-produced by the Boston Museum of Science, which takes hundreds of thousands of viewers per year on a spectacular voyage from the Milky Way to the farthest reaches of our universe.

New results on the elemental and isotopic composition of solar particles, galactic cosmic rays, and the solar wind are being achieved by the **Advanced Composition Explorer (ACE)**. The observations have shown that galactic cosmic rays are boosted to their enormous energies from the debris of supernovae, but long after the supernova explosions themselves. In a surprising and unrelated discovery, ACE found that the solar wind came to a virtual standstill for two days in May 1999. This event, believed to be related to a massive ejection of



Glowing like a multi-faceted jewel, the planetary nebula IC 418 lies about 2,000 light-years from Earth in the constellation Lepus. The Hubble Space Telescope reveals some remarkable textures weaving through the nebula. Their origin is still uncertain.

material from the Sun, strongly affected Earth’s magnetosphere.

Another recent mission, the **Submillimeter Wave Astronomy Satellite (SWAS)** studies the processes of star formation by observations of water, molecular oxygen, isotopic carbon monoxide, and atomic carbon. Results of observations of dark interstellar clouds, evolved stars, external

galaxies, and planetary nebulae confirm some of our ideas about interstellar chemistry, but have contradicted our expectations about the amount of oxygen and water in many cool molecular clouds.

NASA has made rapid advances in its goal toward tracing our cosmic roots through a better understanding of the formation of galaxies,



Astronauts replace gyroscopes inside the Hubble Space Telescope during the HST-3A mission.

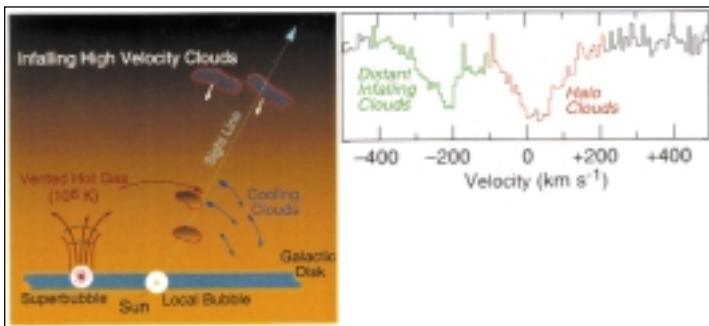
stars, heavy elements, and planetary systems. Discoveries by the **Hubble Space Telescope (HST)** have invigorated astronomy in many areas. Astronomers have observed details of the surfaces or outer layers of Mars, Saturn, Jupiter, Uranus, and Pluto through visible, ultraviolet, and infrared images taken by HST. The crisp resolution of HST has revealed various stages of the life cycle of stars in images of galactic nebulae. After a multi-year observing and analysis program, HST has enabled us to refine our estimate of the Hubble Constant, the rate at which the universe is expanding. This determines the age of the universe since the Big Bang to a precision of 10 percent, compared to the previous factor-of-two uncertainty. Thousands of

never before seen galaxies have been observed in the Hubble Deep Fields, doubling the number of far-flung galaxies available for deciphering the history of the universe. HST continues to hold the fascination of students, teachers, and the public, making the “New Views of the universe” traveling exhibit a highly popular destination for museum and science center visitors nationwide. Two versions of the exhibit, appropriate for large and small museums, are now traveling around the country, allowing visitors to experience Hubble’s discoveries and knowledge through interactive learning.

The **Far Ultraviolet Spectroscopic Explorer (FUSE)** is providing very high resolution ultraviolet spectra of the interstellar medium, giving information on the chemical content of material between stars and galaxies. The ultimate goal is to discover the conditions at the time of the Big Bang and how the universe has evolved since then.

Over the past few years, NASA-supported ground-based research has discovered dozens of sub-stellar companions orbiting nearby stars.

Turning to the Solar System, data from the Mars Orbiter Laser Altimeter (MOLA) instrument on the **Mars Global Surveyor** spacecraft show evidence for an



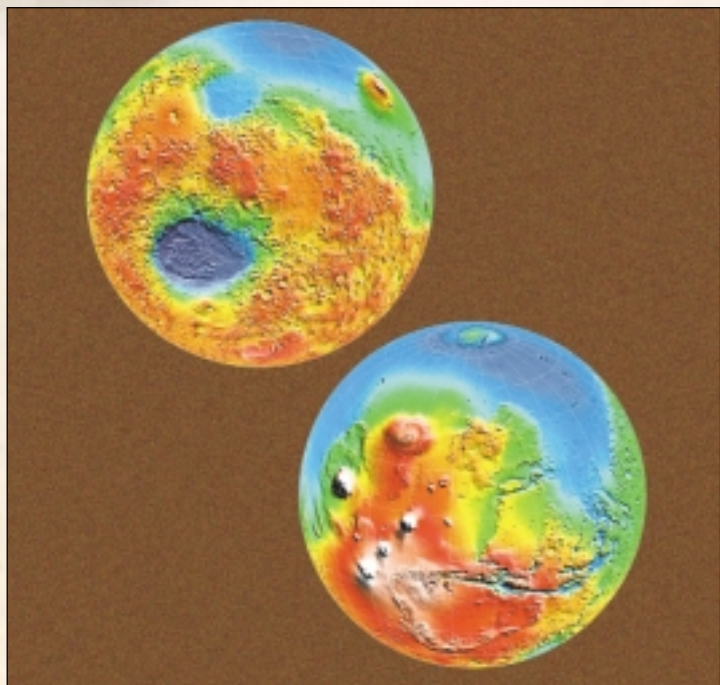
Galactic assembly and reconstruction: A typical high-latitude sight line through the Milky Way encounters interstellar clouds near the galactic plane and distant clouds in the outer regions of the galactic halo. Distant clouds fall in on the galaxy from the outside (assembly), while nearby gas is circulated and energized by supernovae (reconstruction). FUSE can diagnose these processes by examining the absorption of light passing through these clouds.

ancient ocean basin around the planet's north pole. These data, which comprise over 200 million high-precision measurements of the height of Mars' surface, indicate an ancient shoreline about 18,000 km long. The amount of water that would have been contained in the ocean is about what would be expected on the basis of other geological features such as the outflow channels that drain into the northern lowlands of the planet.

Since its continuation in 1998 as the **Galileo Europa Mission (GEM)**, Galileo has concentrated on intensive study of Jupiter's ice-covered satellite Europa. It has been known for nearly 30 years that Europa is covered with a crust of water ice; what is

not known is whether the ice extends all the way down to bedrock or floats on an ocean of liquid water. The possibility of a liquid ocean is extremely excit-

ing because of the implications for Europa as a possible habitat for life. GEM has yielded several lines of evidence that support the hypothesis of liquid water



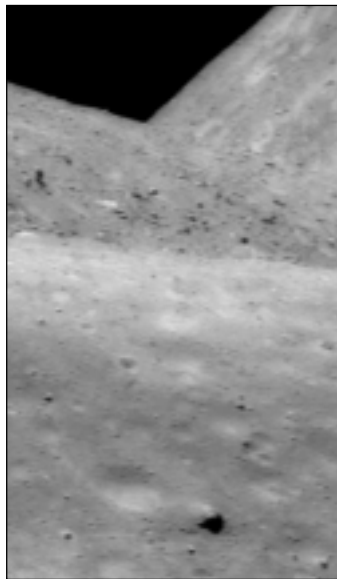
Top:
Global topographic map of Mars. The Mars Orbiter Laser Altimeter (MOLA) instrument on the Mars Global Surveyor spacecraft suggests what was once a vast ocean (blue indicates lower elevations).

Bottom:
Eruption in Tvashtar Catena, a chain of volcanic calderas (craters) on Jupiter's moon Io, as seen by NASA's Galileo spacecraft. The temperature of the lava is much higher than is typical for volcanic eruptions on present-day Earth.



beneath its icy crust. Galileo has also obtained dramatic images of other satellites of Jupiter, including vulcanism on the satellite Io.

The **Cassini** mission to Saturn, launched in 1998, has successfully completed three gravity assist maneuvers, two at Venus and one at Earth. A fourth and final gravity assist maneuver at Jupiter in December 2000 will put Cassini

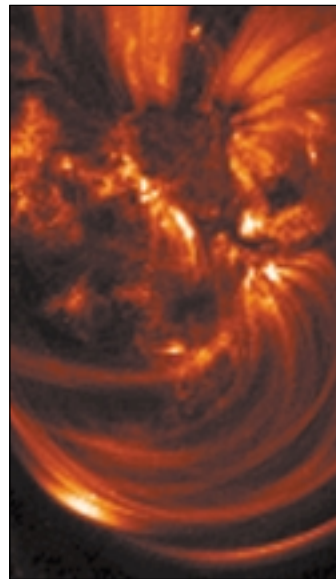


Left: This NEAR-Shoemaker image taken from an orbital altitude of 38 kilometers brings home the irregularity of the tiny world called Eros. Looking down the length of the asteroid, one sees near, middle, and far horizons. The whole scene is about one kilometer across.

Right: The million-degree solar plasma shown by TRACE shows a set of loops, possibly brought on by a large flare occurring a few hours earlier.

on a trajectory for arrival at Saturn in July 2004.

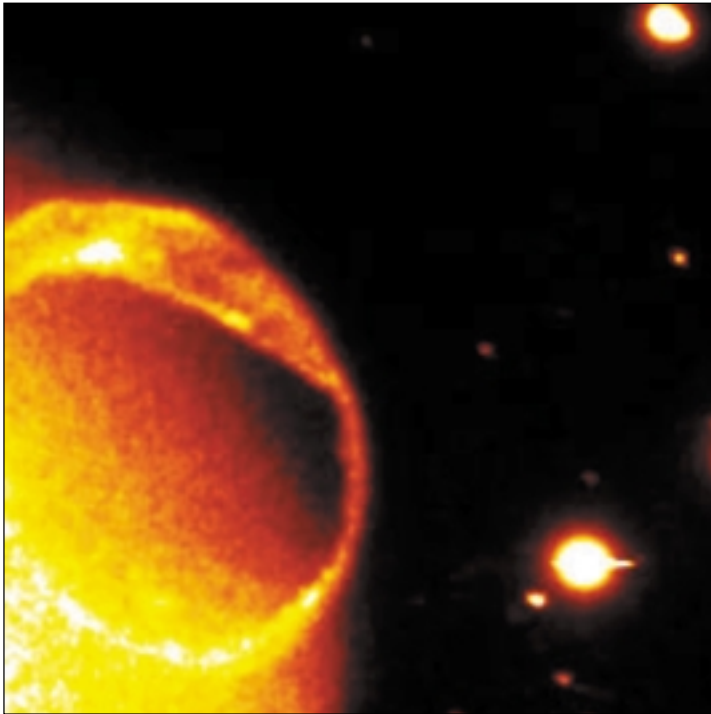
The first two **Discovery** missions were **Mars Pathfinder** and the **Near Earth Asteroid Rendezvous (NEAR)**. Pathfinder dramatically brought Mars exploration to television viewers and Internet users all over the world with its close-ups of the Mars surface. After missing its first rendezvous with asteroid 433 Eros in 1998,



NEAR has returned to be successfully placed into orbit around the asteroid and return high quality images, spectra, and altimetry.

Lunar Prospector, the third Discovery mission, successfully completed global spectroscopy and gravitational mapping of the Moon. The highlight of this mission was the discovery of evidence for trapped hydrogen, possibly in the form of water ice, in permanently shadowed craters near both lunar poles. Lunar Prospector epitomized the “faster, better, cheaper” goals of the Discovery program. It was developed, from project initiation to launch, in less than three years; it successfully completed all of its scientific goals; and it was by far the least expensive planetary exploration mission ever flown by NASA. **Stardust**, the fourth Discovery mission, was launched in January 1999. It will collect a sample of dust from the coma of comet Wild-2 in 2004 and return the sample to Earth for detailed analysis in 2006.

In 1998, the **Transition Region and Coronal Explorer (TRACE)** joined an international fleet of spacecraft, including the **International Solar Terrestrial Program (ISTP)** satellites **Wind** and **Polar**, **Yohkoh**, **Ulysses**, and **ACE**, for coordinated multi-



The IMAGE spacecraft observed highly dynamic auroral activity over the terrestrial pole during the major geomagnetic storm that occurred May 2000.

dimensional study of the Sun-Earth connection and the impacts of solar variability on Earth. At the very low cost of a Small Explorer mission, TRACE has provided dramatic, high resolution motion pictures of evolving structures in the solar atmosphere that clearly show the effects of magnetic activity. The Polar spacecraft obtained the first global images of Earth's space environment using fast

neutral atoms instead of light to "see" the plasma motions. The ESA **Solar and Heliospheric Observatory (SOHO)**, in which NASA is a major collaborator, has provided evidence for streams of hot plasma under the solar surface, as well as dramatic movies of massive blobs of ionized gas, a billion tons in size, being expelled from the Sun.

The **Fast Auroral Snapshot Explorer (FAST)** satellite, which

measures particles and fields in Earth's auroras with fast time resolution and high spatial resolution, has found the origin of long-wavelength radio emission from these regions. This process, which depends on the geometry of magnetic and electric fields, may explain previously mysterious particle acceleration in astrophysical plasmas in many settings outside the Solar System. The **Imager for Magnetospheric to Aurora Global Exploration (IMAGE)** is giving us a new perspective on the response of Earth's magnetosphere to the solar wind using a combination of neutral atom, ultraviolet, and radio imaging techniques.

These measurements are being complemented by data from U.S. instruments on ESA's **Cluster-II** mission, which consists of four identical spacecraft flying in formation between 25,000 and 125,000 km above Earth.

The popularity of total solar eclipses has provided unique, high-leverage opportunities to highlight solar and geospace research conducted by missions such as SOHO, TRACE, and IMAGE. Eclipse webcast events produced by the Live@The Exploratorium program from the path of totality offer participating space scientists the chance to discuss their research with thousands of visitors at museum sites around the country and through the Internet.

The New Millennium Program for flight technology validation was initiated with the **Deep Space 1 (DS-1)** mission. DS-1 successfully validated all twelve new technologies onboard for demonstration. Some of these technologies will enable future spacecraft to be built smaller and less expensively; others will increase spacecraft navigation autonomy, reducing operations costs.

Deriving the full benefit of the public investment in space science requires that its discoveries be shared with all Americans. Since

the publication of the 1997 Space Science Enterprise Strategic Plan, we have made major progress toward incorporating **Education and Public Outreach** into every facet of our programs. This section highlights a few examples of Education and Public Outreach programs connected with flight missions. In addition, an active public information program, including widely reported Space Science Update press events, has helped bring results of space science missions to public attention through print and electronic media. All flight missions are now

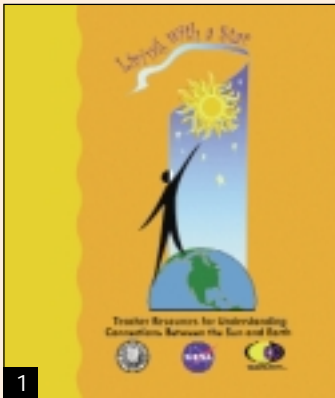
required to have substantive, funded education and public outreach programs as integral components. Participants in research grant programs are also strongly encouraged to include an education and outreach component as part of their research proposals. As a result, literally hundreds of education and public outreach activities of many different types are now underway in communities across the country. These activities have already benefited many students and educators and have reached a large segment of the public.

New Technologies Successfully Space-Validated by Deep Space 1

- Ion Drive for Primary Propulsion
- Solar Concentrator Arrays
- Autonomous Navigation
- Ion and Electron Spectrometer
- Small Deep Space Transponder
- Ka-Band Solid State Amplifier
- Beacon Monitor Operations
- Autonomous Remote Agent
- Low Power Electronics
- Power Actuation and Switching Module
- Multifunctional Structure
- Miniature Integrated Camera and Imaging Spectrometer

During a highly successful primary mission, DS-1 tested 12 advanced technologies in space.

Examples of Education and Public Outreach Activities Underway



1. A teacher resource directory provides access to space science education and outreach products for use by educators.
2. We have used workshops for teachers in communities across the country and national education conferences to test and distribute education products to tens of thousands of teachers.
3. Space science-centered exhibits are on display at a number of major science museums, and space science-based shows are playing at large and small planetariums across the country.
- 4,5. The internet is being routinely used as a tool for disseminating space science classroom materials and bringing major space science events to the public.



Missions Currently Under Development

Building on the exciting results of missions completed or still operating, many missions that were only proposals in our 1997 plan are graduating from their study phases into development and will be launched within the next few years.

The **Microwave Anisotropy Probe (MAP)** Explorer will measure fluctuations in the microwave background on angular scales much finer than COBE, fluctuations out of which the largest structures in the universe—the super-clusters of galaxies—eventually emerged. MAP should enable us to measure directly the size and contents of our universe at an age of only 300,000 years. Later, with even finer angular resolution and sensitivity, the European Space Agency (ESA)/NASA **Planck** mission will provide precision measurements of dark-matter, baryon, vacuum-energy densities, and the Hubble constant, and thus forecast the ultimate fate of the universe. Planck's polarization measurement capabilities will allow new and unique tests of cosmological inflation and perhaps measure its energy scale.

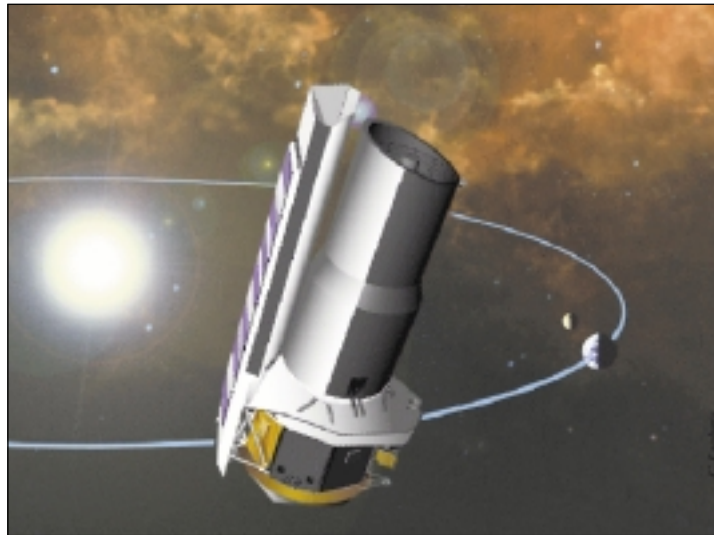
HST's new instruments are expected to continue the observato-

HST's new instruments are expected to continue the observatory's spectacular accomplishments.

ry's spectacular accomplishments. These upgrades include the instal-

lation of the Advanced Camera for Surveys, a new cooling system to reactivate the Near Infrared Camera and Multi Object Spectrometer, the Cosmic Origins Spectrograph, and the Wide Field Camera-3. The next major space observatory will be the **Space Infrared Telescope Facility (SIRTF)**. Once in operation, SIRTF will contribute extensively to the understanding of formation of stars and planets and will investigate the formation and early evolution of luminous galaxies.

While SIRTF will have unsurpassed sensitivity throughout the infrared wavelength regime, the



SIRTF is the final element in NASA's family of "Great Observatories," and consists of a cryogenic telescope and science instruments for infrared imaging and spectroscopy.

Stratospheric Observatory for Infrared Astronomy (SOFIA) will complement the space mission with much better spatial and spectral resolution for the detailed study of bright objects. A key scientific goal of SOFIA will be the investigation of conditions within the interstellar medium that enable the formation of stars and planets. As an aircraft, rather than a space observatory, SOFIA has several unique characteristics. It can continually upgrade its instrumentation and serve as a critical training ground for new generations of instrument builders.

The ESA-led **Far-Infrared and Submillimeter Telescope (FIRST)** will be able to observe very dusty galaxies with active star formation out to large distances, and therefore early in the universe. FIRST will also be able to study molecule formation in the dense molecular clouds in our own galaxy where stars and perhaps planets are forming.

The **Keck Interferometer**, a ground-based facility, will combine the infrared light collected by the world's two largest optical telescopes, the twin 10-meter Keck telescopes on Mauna Kea in Hawaii, to undertake a variety of astrophysical investigations.

The most violent events in the Universe emit bursts of gamma rays for



SOFIA will involve educators directly in its research programs by flying them on the observatory itself and centering its education and public outreach programs on these opportunities.

a few seconds. Observations with the Italian/Dutch Beppo-SAX satellite, complemented with results from the Compton Gamma Ray Observatory (CGRO), have shown that these mysterious events occur early in the history of galaxies and are clues to major events in their evolution. The Explorer mission **Swift**, and later the **Gamma Ray Large Area Space Telescope (GLAST)** will enable us to unlock the mysteries of these dramatic stellar explosions. Because of their great distances from us, spectral studies of these explosions will allow us to probe the intervening infrared background light, which absorbs the

higher energy gamma ray photons through electron-positron pair production. GLAST will also study the nature of cosmic jets and relativistic bipolar flows emanating from distant active galactic nuclei, and determine how much of the general all-sky diffuse gamma ray background is due to such sources, which were unresolved by instruments of the Compton Gamma Ray Observatory. In addition, GLAST will pursue the surprising discovery of the trickle of high energy gamma rays observed to continue to issue from some gamma ray bursters, sometimes for hours.

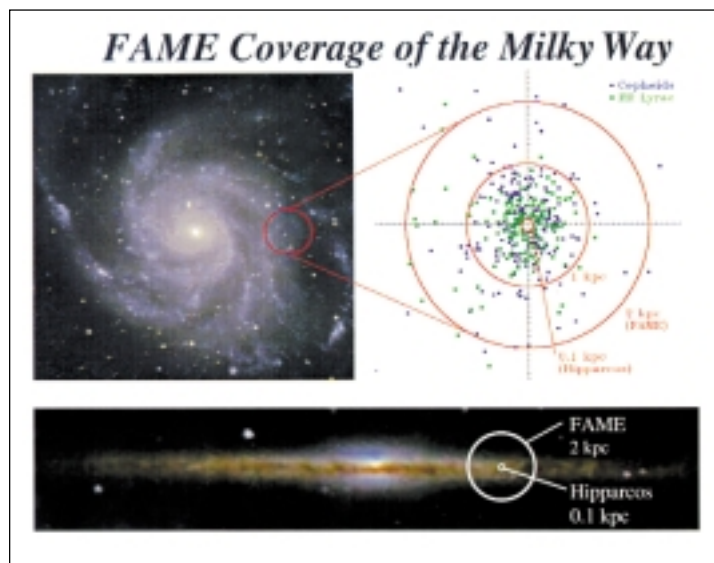
Explorer missions with targeted science objectives will complement major missions and in some cases provide key information that will help maximize the scientific return from them. The **Galaxy Evolution Explorer (GALEX)** will use high resolution ultraviolet spectroscopy and imaging to observe star formation over 80 percent of the lifetime of the universe, the period that spans the origins of most stars, elements, and galaxy disks and over which galaxies have evolved dramatically. The **Full-Sky Astrometric Explorer (FAME)** will be a space astrometry mission that offers the

unique opportunity to measure the positions, proper motions, parallaxes, and photometry of forty million stars to unprecedented accuracy. Through these data, the variability of 40,000 solar type stars will be characterized, the frequency of solar type stars orbited by brown dwarf and giant planet companions will be determined, and the distance scale of the universe will be improved. The **Cosmic Hot Interstellar Plasma Spectrometer (CHIPS)** will carry out spectroscopy of the diffuse background in the extreme ultraviolet

to determine the evolution of the million degree gas that lies outside the Solar System. This will lead to an understanding of key mechanisms responsible for recycling gas within the interstellar medium.

Planning and development continues for new missions in the **Mars Exploration Program (MEP)**. The losses of the Mars Climate Orbiter and Mars Polar Lander in 1999 were severe blows to the program, but scientific interest in Mars as a laboratory for comparative planetology and as a possible home for past or present life continues undiminished. Responding to reviews of these failures, we are planning a flight program firmly based on scientific objectives and will execute it at a pace consistent with technical readiness and available resources. Return of samples to Earth for analysis remains an important objective, but near-term missions will focus on orbital science, in situ analysis on the surface, and characterization of possible landing sites. The next mission will be an orbiter to be launched in 2001, and two enhanced rovers will follow in 2003.

The Galileo Europa Mission's intensive study of Europa has yielded evidence for a global liquid water ocean beneath the icy

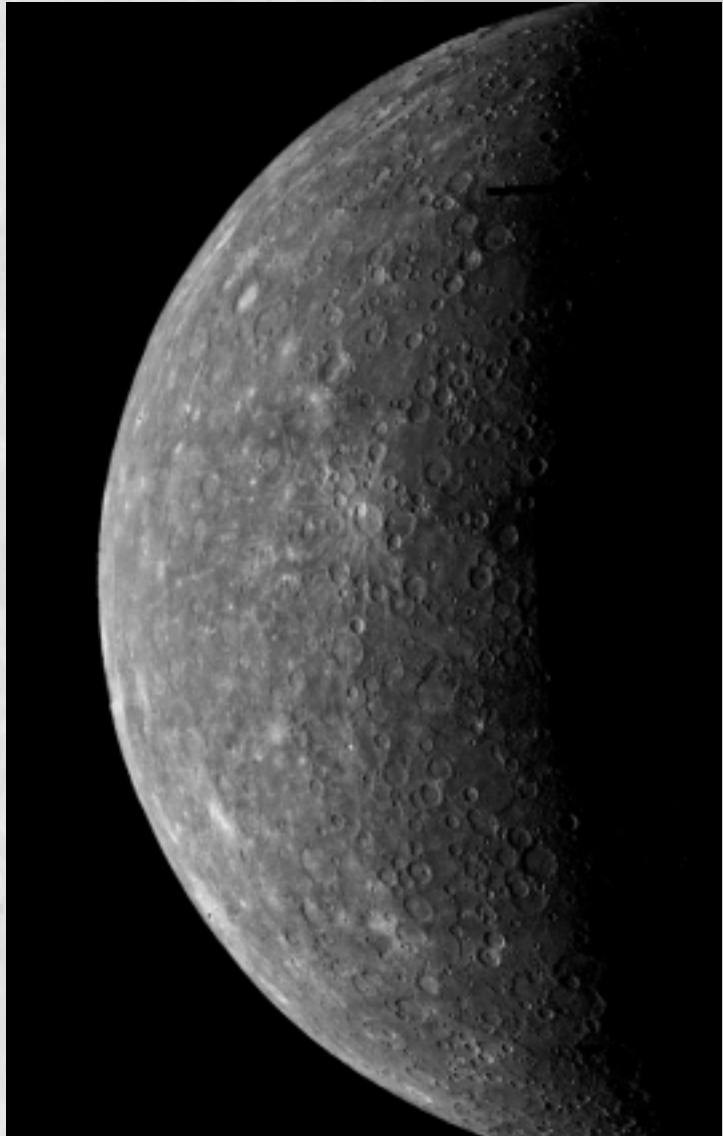


The innermost and outermost circles outline the volume covered by the Hipparcos and FAME missions, while the symbols mark the positions of two types of stars that can be used as cosmic yardsticks.

crust. Although this evidence is not conclusive, this would be such a momentous discovery that we are planning a **Europa Orbiter** mission system to obtain a definitive answer. Advanced technologies needed for this mission are being developed, and implementation of this follow-on mission could begin in the 2002-2003 timeframe.

A number of new **Discovery** missions that address related topics are in development. The **Comet Nucleus Tour (CONTOUR)** will fly by the nuclei of at least two comets at different evolutionary stages. CONTOUR will analyze the surface structure and composition of these nuclei to probe the diversity of comets. **Deep Impact** will excavate a crater in comet Temple-1 to study the structure of the cometary nucleus and to compare its interior composition with that of its surface. The objective of doing so is to gain a better understanding of the history of primordial material from the outer Solar System. As one component of the mission's public outreach program, the International Astronomical League will set up opportunities around the world to allow the public to observe the impact.

Another Discovery mission now under development, the **Mercury Surface, Space Environment,**



Mariner 10's first image of Mercury, acquired on March 24, 1974. Closer study of Mercury's high density, global magnetic field, and ancient surface will provide important clues for understanding the evolution of the inner Solar System.

Geochemistry and Ranging (MESSENGER) mission, will study how the inner Solar System formed by analyzing the physical properties and chemical composition of the closest planet to the Sun. The planet Mercury will be the focus of an ambitious education and public outreach program aligned with National Science Education Standards for teaching and learning under the auspices of the American Association for the Advancement of Science, the Challenger Center for Space Science Education, and several other national partners.

New insight into the material from which the Sun itself originally formed, still preserved in the outer atmosphere of the Sun, will be obtained by the **Genesis** mission when it collects and returns to Earth samples of the solar wind that streams out from the Sun.

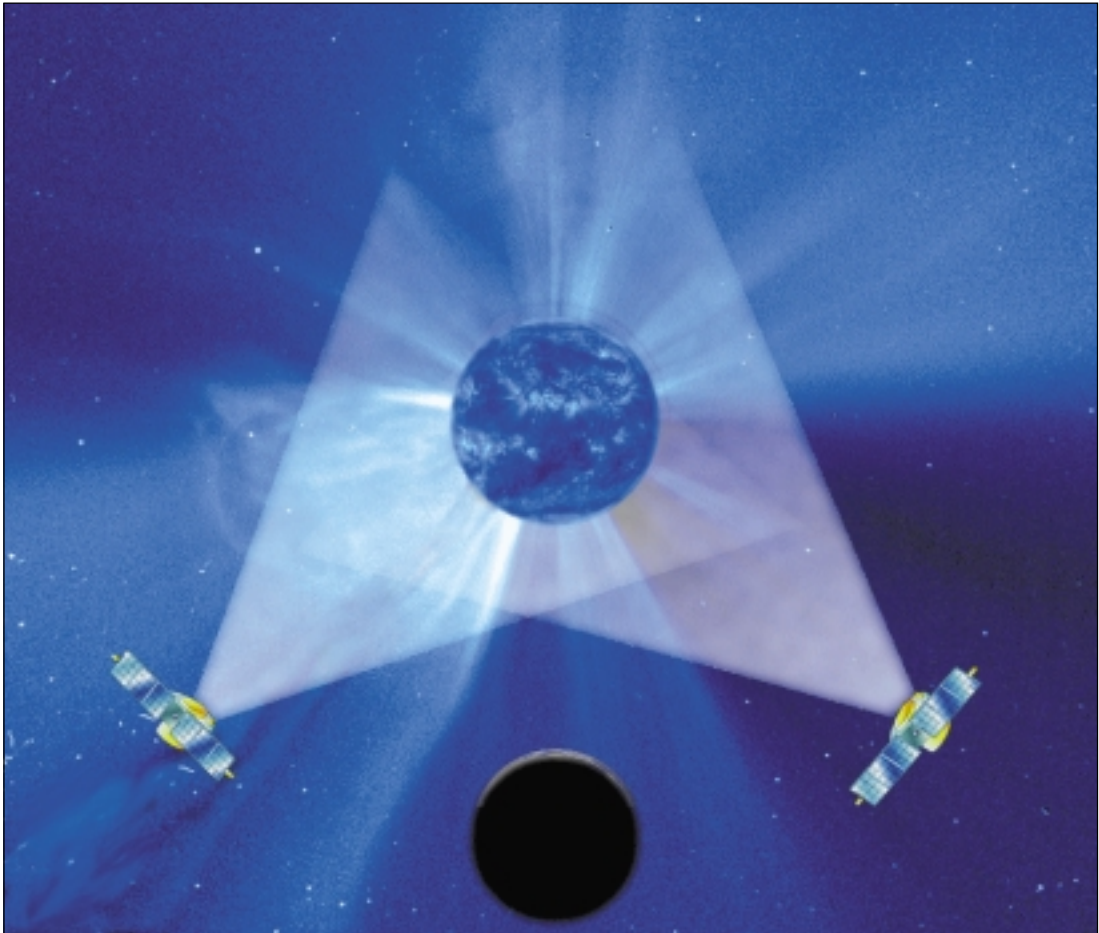
The Sun profoundly affects all the bodies in the Solar System, as well as the space between them. To explain these effects, we need to understand both the inherent characteristics of the Sun and how its emissions interact with the rest of the Solar System. Missions currently under development will advance our knowledge of the Sun's interior dynamics. Coordinated measurements of events that originate on

The Galileo
Europa Mission's
intensive study
of Europa has
yielded evidence
for a global
liquid water
ocean beneath
the icy crust.

the Sun, propagate through interplanetary space, and ultimately impact on Earth's magnetosphere and upper atmosphere are enabling us for the first time to determine cause and effect unambiguously. This research will be pursued within the new **Living with a Star** initiative, which will accelerate some currently planned missions and support new ones now being defined. For Living with a Star, the University of California-Berkeley Space Science Laboratory and the Lawrence Hall of Science are developing elementary and middle school activities highlighting the impact of the active Sun on Earth and society. These activities will be

part of the "Great Explorations in Math and Science" series, which is already used by thousands of school districts nationwide.

The **Solar Terrestrial Probe (STP)** program is a line of missions that study the Sun-Earth system. The STP program seeks to understand solar variability on time scales from a fraction of a second to many centuries. It will also correlate cause (solar variability) with effect over vast distances. The STP program will begin with the launch of the **Thermosphere-Ionosphere-Mesosphere Energetics and Dynamics (TIMED)** mission, which will provide a first global characterization of the region where the atmosphere tails off into space. TIMED will be followed by two missions that will address solar variability from different perspectives. NASA's contribution to **Solar-B** (a mission of the Japanese Institute of Space and Astronautical Science) will be the second STP mission. Solar-B will investigate the creation and destruction of the Sun's magnetic field and provide quantitative measurements of the photospheric field with greatly improved spatial resolution. The third STP mission is the **Solar Terrestrial Relations Observatory (STEREO)**, two identical spacecraft that will observe the Sun stereoscopically for the first time. STEREO will track the origin, propagation, and



STEREO will measure coronal mass ejections from the Sun in three dimensions for research to increase reliability of space weather alerts.

evolution of coronal mass ejections, powerful disturbances that travel from the Sun to Earth's orbit and beyond.

Explorer program missions now under development will supple-

ment the STP missions. The **High Energy Solar Spectrographic Imager (HESSI)** will explore the basic physics of particle acceleration and energy release in solar flares using simultaneous, high resolution imaging and spectroscopy

in x-rays and gamma rays with high time resolution. The **Two Wide-angle Imaging Neutral-atom Spectrometer (TWINS)** mission, in combination with IMAGE, will enable a three-dimensional visualization of Earth's

magnetosphere and resolution of large scale structures and dynamics within it by applying techniques similar to those of the IMAGE mission from two widely spaced high-altitude, high-inclination spacecraft.

The frequent access to space provided by smaller space missions has accelerated scientific and technical innovation in the space sciences. Balloon-borne payloads provide similar benefits at still lower cost. Observing from the top of the stratosphere, a new generation of **Ultra-Long Duration**

Balloons (ULDB's) that offer 100 days or more of observing time per flight is now under development. We expect this new capability to enable important and very cost-effective observations in such diverse areas as solar physics and infrared and hard x-ray astronomy.

All of the missions under development include substantial education and public outreach components that are well integrated with the activities of the science and technical teams. In support of these space science education and outreach efforts,

we have established a national network of 10 institutions across the country to serve as a bridge between the education, public outreach, and space science communities. The goals of this institutional infrastructure are to improve effectiveness of the space science community's participation in education and public outreach, to coordinate the diverse education and public outreach activities undertaken by space science researchers across the country, and to assure national availability of the resulting programs and products.

principles and processes

Our approach to accomplishing Enterprise science goals is founded on a set of fundamental principles that encompass the role of space science within NASA, program planning and structure, project management axioms, our relationship to our scientific stakeholders, the role of technology, our responsibilities to the public, and guidelines for international cooperation. This section presents these principles and then describes our strategic and tactical planning processes.

General Principles

Use scientific merit as the primary criterion for program planning and resource commitment.

The Space Science Enterprise is first and foremost a science program, among many activities conducted

by NASA. The scope of NASA's mission as provided in the Space Act of 1958 ranges from pure knowledge to advancing the state of practical know-how in many areas for the benefit of U.S. industry. In this context, NASA's space science programs also contribute to other

national purposes as secondary objectives. The primary means for establishing merit for Enterprise programs are open solicitation and competitive peer review.

Base the Enterprise Strategic Plan on science goals and objectives,

Peer Review

It is Enterprise policy that funding to support research and mission development be allocated by processes that use peer review to establish scientific merit. NASA uses the following uniform, Agencywide definition for peer review:

Peer review is a scientific evaluation by an independent in-house specialist, a specialist outside of NASA, or both, of proposals submitted in response to NASA research announcements, announcements of opportunity, and cooperative agreement notices. Peer review is also used to evaluate unsolicited proposals. Peer reviews evaluate relevance to NASA's objectives, intrinsic merit that includes scientific or technical merit of research methods, the researcher's capabilities and qualifications, and cost.

All selected science investigations must achieve a top rating for peer reviewed science merit. In making final selections, however, other factors besides science merit also have a role. These factors include alignment with Enterprise goals, national and Agency policy, program balance, available budgets, technological readiness, various types of risk, and contributions to education and public outreach.

For the special class of the New Millennium technology flight validation missions, technology considerations provide the primary selection criteria.

and structure its research and flight programs to implement these goals. These plans are developed every three years. Science objectives are set in partnership with the scientific community, and mission formulation is based on these science objectives within policy and budget constraints established by the Administrator, the President's Office of Management and Budget (OMB), and Congress. In planning, the first rule is to complete missions already started, except in the case of insuperable technical or cost obstacles. The Enterprise defines missions via its strategic planning process (generally larger missions) and incorporates missions formulated by the scientific community (e.g., Explorer and Discovery). While recognizing that not all scientific objectives can be

attained by small missions, the Enterprise emphasizes the “faster, better, cheaper” paradigm, where appropriate, to accelerate exploitation of new technological and scientific opportunities.

Aggregate consecutive missions that address related science objectives into “mission lines.” It is much easier to explain broad science objectives and a program of related missions to Agency stakeholders and the general public than it is to convey the significance of individual missions, which is often much more technical. Further, a stable funding profile for a series of related missions promotes continuity and flexibility in budget and technology planning. In structuring the flight program into mission lines, the first priority is to preserve and extend existing

lines. The second priority is to develop and establish new mission lines corresponding to new high priority science objectives. This is done by identifying and advocating compelling pathfinder missions for the new lines.

Preserve safety as NASA's number one priority; this includes mission success for robotic flight projects. Properly implemented, the “faster, better, cheaper” approach does not jeopardize this priority. Projects will not be approved for implementation until a clear technology path to successful implementation is demonstrated. Each Enterprise flight project will maintain reserves appropriate to its level of technical risk, and testing and reviews will be adequate to provide positive engineering assurance of sound imple-

Mission Formulation

Strategic, or NASA-formulated, missions are defined by NASA, with guidance from members of the space science community. Science payloads and investigations are then selected competitively by means of peer review in accordance with the principles set forth in NASA's Science Policy Guide. Examples of this category of missions are major space observatories, Mars Exploration Program missions, and Solar Terrestrial Probes.

Community-formulated missions, in contrast, are designed totally by science community-industry teams and selected by NASA through competitive peer review as complete packages. These missions add flexibility, rapid response to new opportunities, and frequent access to space. This category of missions includes the Explorer and Discovery lines.

All selected and implemented missions, whether NASA-formulated or community-formulated, address science goals and objectives in the Enterprise Strategic Plan.

mentation. In the event of project cost growth, reserves will be maintained by reallocation of resources within the project's science theme area, by schedule delays, or by descoping. If these measures are not sufficient, or if the necessary descoping diminishes expected scientific returns below the project's science requirements floor, the mission may be canceled. Resource shortfalls will not be relieved by deviating from proven space system engineering and test practices.

Ensure active participation of the research community outside NASA because it is critical to success. The outside community contributes vitally to strategic and programmatic planning, merit assurance via peer review, mission execution through participation in flight programs, and investigations supported by research grants programs. In addition, NASA science and technology programs conducted at the universities play an important role in maintaining the Nation's academic research infrastructure and in developing the next generation of science and engineering professionals, whether they pursue space research careers of their own or apply their technical skills elsewhere in the economy.

Maintain essential technical capabilities at the NASA Centers. NASA has significant scientific and technological capabilities at its

Centers. NASA Center scientists provide enabling support to the broader research community by serving as project scientists and operating unique Center facilities, and compete with external researchers for funding to conduct their own original research. Center staff maintain "corporate memory" for Enterprise programs and provide essential engineering support as well.

Apply new technology aggressively, within the constraints of prudent stewardship of public investment. Research in space science pushes the boundaries of our technical capabilities. The relationship between science and technology continues to be bi-directional: scientific goals define directions for future technology investment and development, while emerging technology expands the frontier of possibilities for scientific investigation (sections I-3 and II-4). To maintain the balance between risk and reward, new technologies are demonstrated wherever possible via validation in flight before incorporation into science missions. This policy is implemented through the New Millennium program, in which technology demonstration is the primary objective and science plays a secondary role.

Share the results and excitement of our programs through the formal education system and public engagement. A fundamental

consideration in planning and conducting all of our programs is the recognition that the national investment in space science is a public trust and the public has a right to benefit from our work. To discharge this commitment, we use not only print and electronic news media, but also museum and other exhibits and material for formal pre-college education. To ensure infusion of fresh results from our programs into these educational efforts, our policy is that each flight project must have an education and outreach component. The Enterprise has established a nationwide support infrastructure to coordinate the planning, development, and dissemination of educational material (sections I-4 and II-6).

Structure cooperation with international partners to maximize scientific return within the framework of Enterprise Strategic Plan priorities. The Space Act of 1958 provides that NASA shall cooperate in peaceful space activities with other nations. Today, most of the Enterprise's flight programs have international components (section II-7). In establishing these cooperative relationships, as indeed in all other aspects of our program, funding is allocated to U.S. participants in international programs through competitive peer review. Foreign participants in U.S. missions are likewise selected

on the basis of merit. In general, NASA seeks to lead where possible, and participate with our partners through collaborative roles in other deserving areas.

Strategic Planning

From its beginnings, NASA space science has based its planning on a foundation provided by the National Academy of Sciences. The Academy's Space Studies Board (formerly the Space Science Board) and its committees critically assess the status of various space science disciplines, identify the most promising directions for future research, outline the capabilities required, identify technologies needed to attain those capabilities, and examine the role of each mission in the context of the total space science program. Enterprise science goals, objectives, and missions can all be traced to Academy recommendations.

Synchronized with the triennial revision of the Agency Strategic Plan mandated by the Government Performance and Results Act of 1993 (GPRA), the Enterprise revises its own Strategic Plan at the same interval. In addition to general information about program and planning processes, the Enterprise Plan lays out science goals and science objectives and mission plans for the near- and mid-term. The near-term is a five-year period that starts

approximately two fiscal years from the date of issue of the Plan, while the mid-term extends about a decade beyond that. The Enterprise Plan describes near-term missions and how they address science goals and objectives in more detail than it does mid-term missions, which are presented briefly and schematically. Each release of the Plan also presents information about the Enterprise's technology needs and activities and a review of education and public outreach goals and programs.

The Enterprise works with the space science community to develop each Enterprise Strategic Plan. This work is done through NASA-formed advisory committees (the Space Science Advisory Committee and its subcommittees) with assistance from ad hoc planning groups, input from the general science community, and technical support from NASA's Centers. Development of the 2000 Plan illustrates the process.

Work on the 2000 plan began in late 1998, when the Enterprise's Science Board of Directors initiated the development of science and technology roadmaps for each Enterprise science theme (Astronomical Search for Origins, Structure and Evolution of the Universe, Solar System Exploration, and Sun-Earth Connection). These roadmaps—which were developed by roadmapping teams that included scientists, engi-

neers, technologists, educators, and communicators of science—address science goals, strategies for achieving these goals, missions to implement these strategies, technologies to enable these missions, and opportunities for communicating with the public. Each roadmapping team was either built from or overseen by its theme subcommittee of the Space Science Advisory Committee. The teams each held a series of meetings to obtain science priority views from community scientists, hear advocacy presentations for specific missions, examine technology readiness for alternative mission options, and discuss relative science priorities, balance, and optimum activity sequencing in light of this information. One technique used to foster convergence was taking straw polls among team members during successive meetings.

At the end of the roadmapping period, each of the four theme roadmapping activities submitted a summary document outlining science and mission recommendations to the Space Science Advisory Committee and to Enterprise Headquarters management. Enterprise management then combined the mission recommendations of the roadmapping teams into an integrated mission plan, guided by the current OMB five-year budget profile, realistic estimates of most likely future resource availability

beyond that, and additional Agency-level and Administration guidance. Likewise, science goals in the roadmaps were used to examine and restate those presented in the 1997 Enterprise Plan.

An integrated roadmap was presented and discussed at a planning workshop that expanded the membership of the Space Science Advisory Committee with other community members and representatives from the technology and education and public outreach communities. Attendees at the workshop also analyzed and revised the proposed updated science objectives, and derived a new set of shorter-term research activity areas. The resulting consensus mission plan and goals, objectives, and research activities serve as the nucleus for the current Strategic Plan.

A draft of this Plan was provided to the Space Studies Board and its

committees for review and feedback, and guidance received was used in finalizing the Plan. The findings and recommendations of the Academy's recently completed ten-year astronomy and astrophysics survey were consulted to assure consistency with the draft Plan. Finally, the Space Science Advisory Committee had an opportunity to review the revised Plan and suggest any final changes before the Plan went to press.

Tactical Planning and Budgeting

Congress appropriates funding to NASA for its programs on a yearly basis. While each Administration-submitted budget provides a five-year profile for the Agency's programs, only the first is implemented each year by Congress. Somewhat more than a year before the beginning of a fiscal year, the

Enterprise assembles a detailed budget proposal for submission to the Agency Administrator. Preparation of this budget, while based on the Enterprise Strategic Plan, is also guided by the previous year's budget estimate for the new year, policies and guidance provided by the Administrator and the OMB, and the current budget and technical status of missions in development or operating. Ongoing program balance and technology readiness are also considered. A GPRA performance plan for the same fiscal year is assembled in parallel with the new Enterprise budget request. Twelve months before the beginning of the new fiscal year, both the Agency budget and its GPRA performance plan are submitted to the OMB, and after a period of negotiations and adjustments, the President submits NASA's budget request with those of other Federal agencies to Congress for action.

Government Performance and Results Act of 1993 (GPRA)

This legislation requires each Federal agency to periodically develop and deliver to Congress three documents:

- A strategic plan that presents goals and objectives over a five year period; this plan must be revised at least every three years;
- A yearly performance plan that projects which measurable outcomes that support goals and objectives of the strategic plan will occur during the upcoming fiscal year; the performance plan is to be closely coordinated with the requested budget; and
- A yearly performance report, to be delivered six months after the end of the fiscal year in question, that summarizes the agency's achievements against projections in that fiscal year's performance plan.

flight program: 2003 and beyond

Here we present missions that we expect to graduate from the study and design phase and begin building in 2003 and beyond. We have grouped these projects to show how they address our science objectives. While the section mentions for context some of the missions that will already be under development or flying by 2003, those that will proceed from study and preliminary design to implementation (detailed design and fabrication) beginning in 2003 are named in **bold** when they are first mentioned under each objective. Note, however, that although many of our missions address more than one science objective, no effort has been made to mention every mission in every connection in which it can make a contribution.

d beyond

This section emphasizes missions that will begin implementation in the period 2003-2007. Planning for the period 2008 through the following decade is necessarily less certain. The end of each subsection also presents ideas for missions in this more remote timeframe based on reasonable extrapolations from our current scientific understanding and nearer-term mission plans. These future mission concepts are also introduced in **bold** in their part of each subsection.

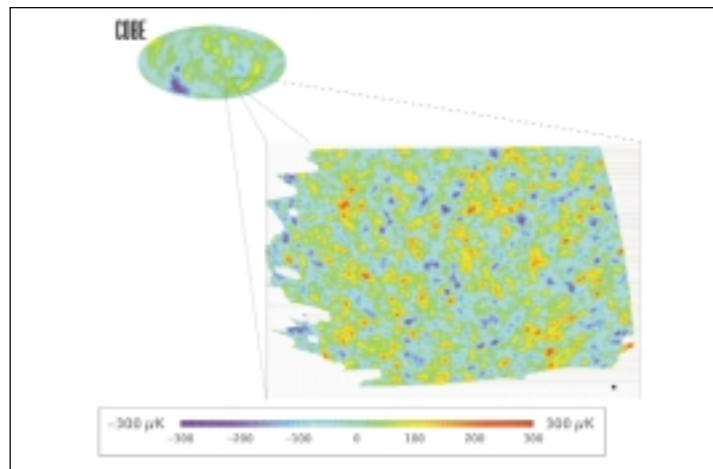
Detailed analysis of the cosmic microwave background can determine the geometry of the universe to high precision and shed light on the nature of the matter and energy that fill the universe. BOOMERANG observed this background over approximately 2.5 percent of the sky with angular resolution 35 times finer than COBE, and MAP and Planck will continue to extend and refine these measurements.

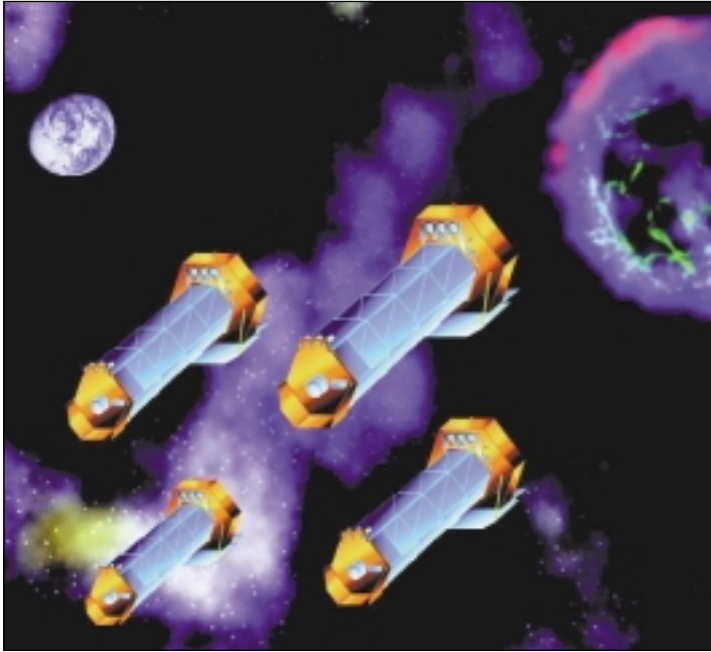
OBJECTIVE ONE: Understand the structure of the universe, from its earliest beginnings to its ultimate fate

The universe we see today is rich in structure, containing hundreds of billions of galaxies, each with hundreds of billions of stars. Clusters and super-clusters of galaxies are interspersed with vast, virtually empty voids, and the galaxies themselves can appear

totally isolated or in the process of merging with local companions. Yet observations to date of the very early universe show it to have been very smooth and almost featureless. How did the later structure, the basic extragalactic building blocks of the universe, come to be? What laws of physics worked to fill the gap between the primitive universe and the complexity we observe in the present?

With the Cosmic Background Explorer (COBE), we have cap-





The Constellation-X spacecraft will work in unison to simultaneously observe the same distant objects. By combining their data, these satellites become 100 times more powerful than any previous single x-ray telescope.

tured a glimmer of the earliest clumpings in the remnant primordial fireball through ripples in today's pervasive microwave background. Balloon-borne instruments such as BOOMERANG map a small portion of the cosmic microwave background radiation, the fossil remnant of the Big Bang. The Microwave Anisotropy Probe (MAP) Explorer and the ESA/NASA Planck mission will extend these measurements and permit precise determination of a

number of critical cosmological parameters that constrain models of the early universe.

But there is a missing link between the first condensations of matter after the Big Bang and the galaxies and clusters we see in the present. With the ability to identify the dark matter and learn how it shapes the galaxies and systems of galaxies, we will begin to determine the size, shape, and energy content of the universe. Ground-based surveys

such as the Two Micron All Sky Survey (2MASS), Sloan Digital Sky Survey (SDSS), and Explorer-class space missions will provide an inventory of low-mass objects in the neighborhood of the Sun. Mass in the gaseous state will be studied at a variety of wavelengths, corresponding to the temperature of the gas. These range from millimeter waves observed by ground-based interferometers to the x-rays from hot cluster gas seen by the Chandra X-ray Observatory (CXO).

An important advance will be to estimate the total mass in galaxies, clusters of galaxies, and even in non-luminous, dense regions by measuring the gravitational bending of light from background galaxies. Observing this "gravitational lensing" is among many motivations for the **Next Generation Space Telescope (NGST)**, along with investigating the birth of galaxies, the fundamental structures of the universe. These observations must be made at near-infrared wavelengths and require a telescope with a large aperture (for sensitivity to faint objects), excellent angular resolution, and the stable images of a space observatory.

The evolution of the universe will also be probed by **Constellation-X**, the x-ray equivalent of a very large optical telescope. It will improve significantly on the spectral information returned by the

current ESA X-ray Multi-Mirror Mission (XMM) and complement the high spatial resolution of CXO. Constellation-X will explore the epoch of formation of clusters of galaxies and how they evolve. The mission will trace black hole evolution with cosmic time and provide new insight into the contribution that the accretion of matter around black holes and other compact objects makes to the total energy output of the universe. Technological advances that will be needed for Constellation-X are under development: x-ray optics, x-ray calorimetry, reflection gratings, detectors for high-energy x-rays,

cryogenic coolers, and focusing optics for hard x-rays.

For Possible Implementation After 2007

The very highest energy cosmic rays are extremely rare, and a huge detector would be needed to observe any significant number of them. Earth's atmosphere, with millions of square kilometers of exposed area and an interaction target up to 10^{13} tons, can act as a giant detector for the extreme energy cosmic rays and neutrinos. We do not know where these particles come from or how they are acceler-

ated. It has been suggested that they might come from the annihilation of space-time defects formed at the beginning of the universe, so observing these mysterious particles with an **orbiting wide-angle light collector** could probe the Big Bang itself.

Beyond 2007, expected advances in detectors, interferometry, light-weight optics and cryogenics will allow a mission that can extend the Hubble Space Telescope-like (HST) resolution into the mid- and far-infrared to resolve the infrared background and to learn the history of energy generation and chemical element formation

Cosmic Journeys

The new Cosmic Journeys initiative is a series of major astrophysics observatories that will address aspects of three Enterprise science objectives:

- Understand the structure of the universe, from its earliest beginnings to its ultimate fate;
- Explore the ultimate limits of gravity and energy in the universe; and
- Learn how galaxies, stars, and planets form, interact, and evolve.

Beyond the fundamental scientific importance of these goals, can we discover new physics that we could use? For example, to send machines or people beyond our Solar System to even the nearest star at today's fastest speeds would take tens of thousands of years. As a result, we are particularly interested in the physics of these extreme phenomena:

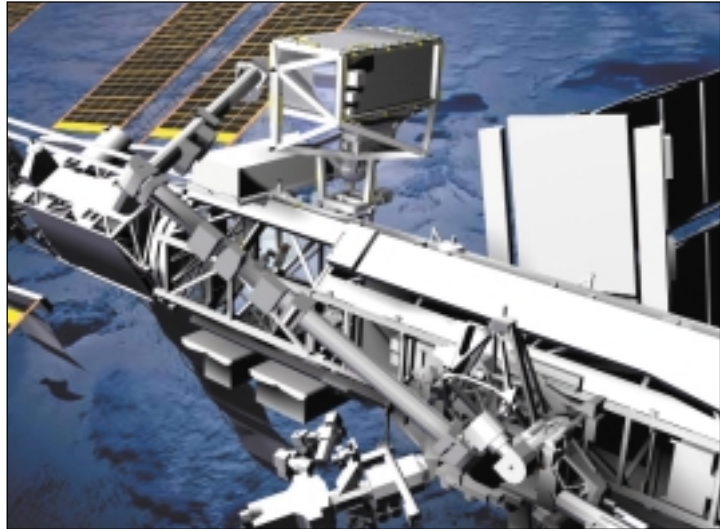
- The source of cosmic gamma ray bursts;
- The acceleration of ultra-high energy cosmic rays;
- Energetics of black holes; and
- Gravitational waves: whether they exist, and whether they travel at the speed of light.

in the universe. A pathfinder mission using one of two alternate technologies would provide much greater angular resolution than that of the Space Infrared Telescope Facility (SIRTF), as well as better sensitivity and signal-to-noise. This descendant of the HST, discussed further in connection with Objective Three, could be either a **space infrared interferometric telescope** or a **filled-aperture infrared telescope**. Technical requirements on the mirrors for such an instrument are challenging, but the necessary capabilities may evolve from earlier development for the NGST and the Terrestrial Planet Finder (Objective Four).

Measuring the **cosmic microwave background polarization** could provide an important test of the inflation theory, possibly detecting cosmological background gravitational waves produced when the universe was much less than a second old.

OBJECTIVE TWO: Explore the ultimate limits of gravity and energy in the universe

Cosmic rays, whose origin has long been a mystery, are important tracers of the dynamics and structure of our galaxy. The magnetic fields and shock structures with which

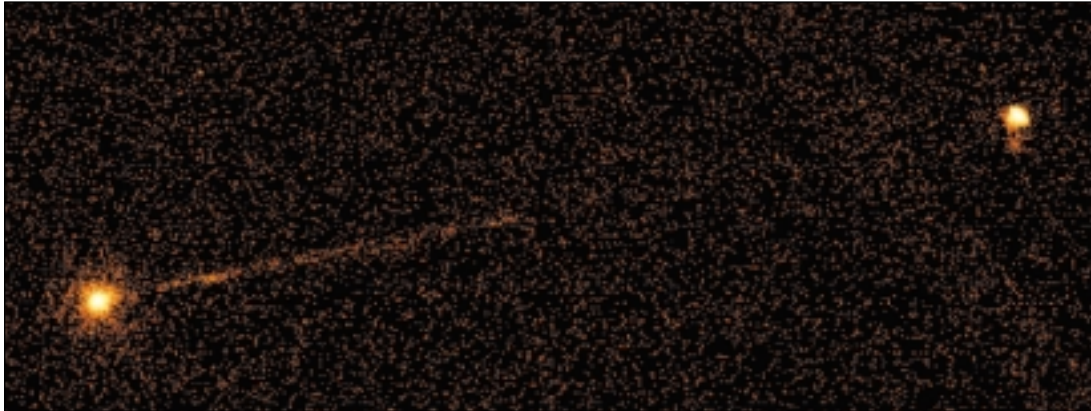


ACCESS instrument mounted on the International Space Station will explore the connection of cosmic rays with supernovae.

cosmic rays interact along their journey are not directly visible to us, so we must study these fields and structures by detailed measurement of the arriving particles themselves. We currently believe that most cosmic rays are accelerated by the shock fronts produced by supernovae. The **Advanced Cosmic Ray Composition Experiment for the Space Station (ACCESS)** is being designed to explore this connection of cosmic rays with supernovae. ACCESS will have the sensitivity needed to study cosmic rays up to the highest energies believed achievable by supernova shock acceleration, and will enable us to analyze their composition and thus address the origin, accel-

eration, and ultimate fate of the individual nuclei, from hydrogen to iron and heavier ions. ACCESS will require a number of technological advances. For the charged particle detectors and calorimeter, silicon pixel detectors with a large dynamic range readout and good spatial resolution will be needed. Advances are also needed in readout electronics for gas-filled detector tubes used in the transition radiation detectors.

Do gravitational waves exist, and what is the structure of space-time near black holes? Complementing the ground-based gravitational wave detectors that will become operational within the next few



The Chandra x-ray image of Pictor A shows a spectacular jet that emanates from the center of the galaxy (left), probably a black hole, and extends across 360 thousand light-years toward a brilliant hot spot (right). The hot spot is thought to be the advancing head of the jet, which brightens where it plows into the tenuous gas of intergalactic space. By observing dramatic phenomena like this spectroscopically, Constellation-X will enable us to unravel their underlying physical causes.

years, the **Laser Interferometer Space Antenna (LISA)** will be able to observe low-frequency gravitational waves not detectable from the ground. A joint NASA-ESA undertaking, LISA will search for gravitational waves from massive objects, ranging from the very early universe before light could propagate, to super-massive black holes in the centers of galaxies, as well as short-period compact binary stars in the Milky Way. Three key technologies are needed to make LISA a reality. First, the experiment will require inertial sensors whose proof masses can be isolated from all forces other than gravitation. Micro-thrusters must keep each of LISA's three independent spacecraft centered on its proof mass. Then, to measure the motions of the iso-

lated and widely separated proof masses, laser metrology to measure subpicometer changes between them is needed.

Constellation-X observations of broadened x-ray emission lines of iron in active galactic nuclei will measure black hole masses and spin, on the basis of relativistic effects that occur in the limit of very strong gravity fields.

[For Possible Implementation After 2007](#)

The key to understanding how condensed objects like quasars and pulsars work is to obtain more detailed observations of them. By using an orbiting telescope as part of a **space**

very long baseline interferometer (SVLBI), radio astronomy can achieve resolutions of about 25 microarcseconds. Such a mission could show us how matter is accreted onto black holes, how relativistic jets of matter are formed, and how gamma rays are produced near black holes. SVLBI can also investigate stellar evolution and the interstellar medium through observations of masers, pulsars, and close binary stellar systems. Among technical innovations in amplifiers and coolers, such a system would require very fast (gigabits per second) down-link communications to Earth.

Beyond this, the prize is to directly image a black hole, whose existence heretofore has been based on indirect evidence. This will require about

0.1 microarcsecond resolution, or almost ten million times better than CXO, which is itself about a factor of ten improvement over the earlier Einstein observatory. This is a technology leap that cannot be achieved in one step, so the plan is to focus on a mid-term mission as an intermediate step to this goal. The strawman configuration for a **microarcsecond x-ray imaging mission pathfinder** is a working interferometer with 100 microarcsecond resolution and about 100 cm² effective area. This would provide a substantial advance in scientific capability of its own, and allow us to detect and resolve an accretion disk around the massive black hole at the center of the Milky Way. It would also give us detailed images of jets, outflows, and broad-line regions in bright active galaxy nuclei, and to map the center of cooling flows in clusters of galaxies. The technology development for this investigation involves primarily matters of scale. The detectors would build upon both the Constellation-X micro-calorimeter and the CCD's designed for CXO, but with much larger arrays. Approaches to the technology for x-ray interferometry have been demonstrated in the laboratory.

A **high-resolution x-ray spectroscopy mission** (see Objective Three) would provide diagnostics of supernova mechanisms and a new view of accreting neutron stars

and black holes in our galaxy, as well as the local group of galaxies.

The only full-sky survey we have in high energy x-rays dates from 1979. Observations of these hard x-ray emissions are key to studying accreting neutron stars, galactic black holes, active galaxies, and creation of the chemical elements. The needed x-ray observations in the 10-500 KeV range could be acquired by a proposed **energetic x-ray imaging survey telescope**.

As described in the previous section, an **orbiting wide-angle light collector** would enable us to observe the very highest energy cosmic rays. Observing these mysterious particles would be an investigation of the highest energy processes in the universe and a probe of the Big Bang within the framework of Grand Unified Theories of fundamental physics.

OBJECTIVE THREE: Understand how galaxies, stars, and planets form, interact, and evolve

One of our fundamental science goals is to understand how structure first arose in the extremely dense but featureless early universe. Images that show that galaxies looked very different billions of



One possible concept for an NGST design, showing the telescope beneath a large Sun shade.

years ago from our familiar modern universe are clues to the link between the first condensations of matter after the Big Bang and the galaxies and clusters of galaxies we see today. The HST has shown that after galaxies form, they can be observed colliding with one another or being badly disrupted. SIRTf will expand on these investigations by studying the evolution of the most energetic galaxies. But these important observations will not fully answer the core question of how galaxies—the fundamental building blocks of the universe—originated.

The HST's aperture is too small to gather enough faint light from the remote past to detect galaxies in the process of formation. To do so, we will need observations at near-infrared wavelengths from a telescope with a larger aperture (to provide sensitivity to faint objects) and superb angular resolution (to observe structure in distant objects)—the **Next Generation**

Space Telescope (NGST). First of the Origins Observatories, NGST will have about ten times the light-collecting area of HST and will be most sensitive at the infrared wavelengths where galaxies being born are expected to be brightest. Also, although the HST and ground-based observatories have revealed much about the formation of stars

and their potential retinues of planets—and SIRTf and SOFIA will reveal much more—essential processes and events in the early lives of stars and planets are poorly known. Very young stars, as well as planets in the process of formation, will be important targets for NGST's powerful infrared instruments. When stars are first born,

they are cocooned in the dusty gas clouds from which they formed. This dust very effectively absorbs visible light but emits copious infrared radiation. NGST will be able to peer into the clouds in which the youngest stars and planets are found, and will reveal their location, mass, chemical composition, and dynamics. (As an example of scientific synergy, Cassini's observations of Saturn's rings will help us interpret observations of these clouds by providing a close-up view of the behavior of dust, ice, and magnetic fields in a relatively nearby setting.) To achieve NGST's demanding scientific goals, we are developing very lightweight optical structures, new generations of infrared detectors, energy-efficient cooling techniques, and precision deployable structures.



An image of the darkest portion of the sky reveals the structure of young galaxies at cosmological distances, as shown by the near infrared camera (NICMOS) on the Hubble Space Telescope. Some of the reddest and faintest objects may be over 12 billion light-years away.

NGST observations will be complemented by data from the ESA/NASA Far Infrared and Submillimeter Telescope (FIRST). Observing at longer wavelengths where many galaxies emit most of their radiation, FIRST will be well suited to finding high redshift galaxies and studying the most luminous galaxies, complementing NGST's searches in the near-infrared. The ESA-led INTEGRAL gamma ray mission will be supplying information on stellar formation via both high-energy spectroscopy and imaging.

The **Space Interferometry Mission (SIM)** will serve important objectives in both technology and science. For technology, it will demonstrate precision metrology and aperture synthesis imaging, both vital for future optical space interferometer missions. Its science contributions stem from its anticipated tiny positional error circle for observed objects, only four micro-arcseconds; this is about 100 times better than the Hipparcos astrometry mission. This precision will make SIM a powerful tool for studying the distances, dynamics, and evolution of star clusters in our galaxy, helping us understand how stars and our galaxy were formed and will evolve. It will extend our census of nearby planetary systems into the range of small, rocky planets for the first time. SIM will also improve the calibration of luminosities of standard stellar distance indicators to enable us to more accurately measure distances in the universe.

The **Terrestrial Planet Finder (TPF)** (see Objective Four) will build on these missions to extend our understanding of planetary systems.

With a hundred-fold increase in sensitivity for high resolution spectroscopy over previous obser-

vatories, **Constellation-X** will look across a broad range of redshifts to date the formation of clusters of galaxies. Matter predicted by Big Bang creation and subsequent stellar processing seems to be missing, and Constellation-X will search for it in the hot, metal-enriched intergalactic medium. Constellation-X will also be able to analyze the chemical composition of stellar coronae, supernova remnants, and the interstellar medium by observing x-ray spectral lines.

[For Possible Implementation After 2007](#)

An exciting new approach to studying the origin of the chemical elements (nucleosynthesis) is embodied in a concept for a **high-resolution x-ray spectroscopy mission**, which would enable sensitive spectroscopic and imaging observations of emitted radiation related to nucleosynthesis. Many of these spectral features lie in the hard x-ray range. Observations of the spectra of young supernova remnants, and studies of the time-evolution of prompt emissions from recent explosions, would provide diagnostics on the production and distribution of heavy elements, and on the explosion mechanism itself. Such a mission would also provide sensitive spectral studies of active

galaxies and measurements of magnetic field strengths in galaxy clusters. Technology development is needed for both the optics and the focal plane sensors. More complex multilayers will be needed to extend instrument response to the 200 KeV region. Germanium sensors will need the development of contact technologies and very large scale integration readout electronics operable at cryogenic temperatures.

An **x-ray interferometry pathfinder** system, such as the one described for Objective Two above, would add importantly to our knowledge of stellar structure, stellar plasma interactions, jets and outflows from active galactic nuclei, cooling flows in clusters of galaxies, as well as locate and resolve star formation regions.

Within our own galaxy, we are at the brink of understanding how planetary systems form. We have obtained spectacular images of stellar nurseries, and possibly of dust disks in the process of creating new planetary systems. We are beginning to peer more deeply into dusty clouds to identify the youngest members of new stellar clusters and probe the structure and basic physical properties of star forming regions. A **filled-aperture infrared telescope**,

which would also serve Objective One above, would determine how planetary system-forming disks evolve. With its keen infrared vision, it would probe deeper into protostellar disks and jets to investigate the physical processes that govern their formation, evolution, and dissipation, as well as those that determine their temperature, density, and compositional structure. As outlined above, a competing concept with the same science goals would be a **space infrared interferometric telescope**, whose high sensitivity, spectral, and angular resolution would allow the far infrared background to be resolved almost completely into individual sources. Major technology development for both is needed in the areas of ultra-lightweight

aperture technology, active sensing wavefront control, passive and active cooling, and enabling detector technologies. These technologies will build upon the ones developed for preceding missions such as NGST, SIRTF, and the Terrestrial Planet Finder.

Once the NGST has given us an understanding of the formation of the first galaxies in the early universe, we will be challenged to trace galaxy evolution back to the initial era of star formation, super-massive black holes, and metal element production in the present epoch. Capable of high resolution ultraviolet spectroscopy at a sensitivity a hundred times that of the HST, a follow-on **space ultraviolet optical telescope** would enable astronomers to follow the chem-

ical evolution of the universe and determine its fate. Tracing the distribution of visible matter would make it possible to quantify the birth rate of galaxies and the energetics of quasars. It might also shed light on the distribution of the underlying dark matter.

Ultimately, we would like to make in situ measurements of matter and magnetic fields outside the bubble of space filled by the Sun's solar wind. An **interstellar probe** mission would explore the structure of the heliosphere and go on to sample matter and magnetic fields in the interstellar medium directly, for the first time. To travel this distance in just two decades will require a new approach to propulsion, perhaps solar sails.

Origins Observatories

The Origins Observatories are a series of astronomical telescopes in which each successive mission builds on the technological and scientific capabilities of previous ones. The vision is to observe the birth of the earliest galaxies in the universe, to detect all planetary systems in the solar neighborhood, and to find those planets that are capable of supporting life. To achieve this vision, the Origins Observatories line includes these components:

- A series of spectroscopic, imaging, interferometric missions, observing at visual and infrared wavelengths to answer the vision's fundamental scientific questions.
- A systematic technology development program in which technology enabling one mission leads naturally into the technology needed for the next one.
- Basic research to understand new observations.
- A comprehensive education and public outreach effort.

OBJECTIVE FOUR: Look for signs of life in other planetary systems

Determining whether habitable or life-bearing planets exist around nearby stars is a fundamental Enterprise goal. In addition, learning about other nearby planetary systems will provide precious context for research on the origin and evolution of our own Solar System. By measuring the velocity variation of a star's motion caused by the gravitational effect of unseen companions, ground-based observations have revealed dozens of circumstellar objects in the solar neighborhood that are much less massive than stars, but still far heavier than Earth. It is not certain, however, that the objects so far discovered are "planets" as we usually think of them, and new generations of missions will be required to discover orbiting objects that are more like Earth.

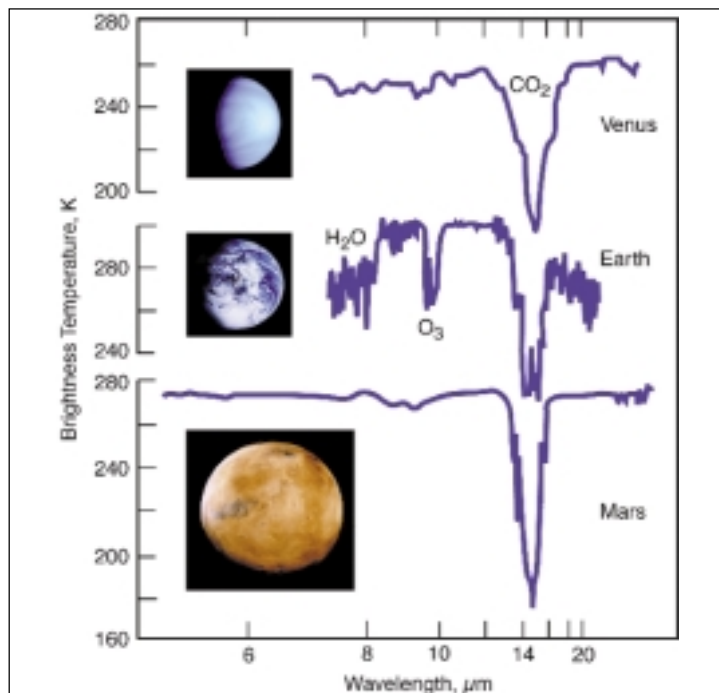
In 2003, several important projects that promise to detect planets substantially lower in mass than those known today will be nearing operation. These include the Keck Interferometer and the Full-sky Astrometric Mapping Explorer (FAME) mission.

While detecting the presence of Earth-mass planets is an impor-

tant objective, determining their key characteristics—above all, the possibility of life—is much more difficult. **Astrobiology** research is developing a working catalogue of possible atmospheric signatures that would be indicative of life on a planetary scale. For example, today's Earth is recognizable as living primarily because of its oxygenated atmosphere, but this was not always the case. Astrobiology is seeking to discover what Earth's biosignature would have looked

like at a time when free oxygen was negligible and other biogenic products would have been present in atmosphere.

Looking outside the Solar System, the discovery of numerous low-mass "non-stellar" bodies orbiting other stars is challenging our understanding of planet formation and implying that planetary systems may be commonplace. With our Solar System as a model for the propensity for



The atmospheric infrared spectra of Venus, Earth, and Mars all show a dominant carbon dioxide feature. In addition, Earth's spectrum exhibits water and ozone—the simultaneous presence of all three gases indicates a living planet.

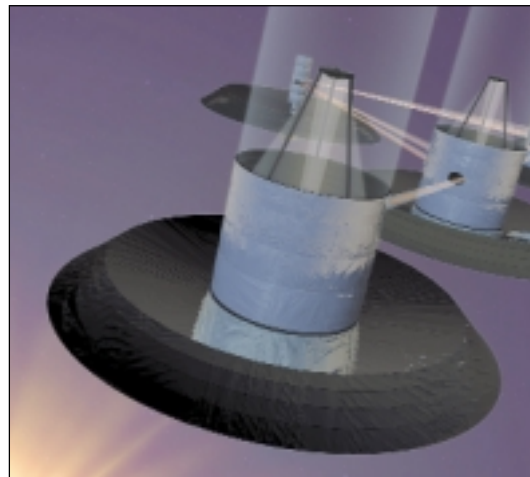
life, we can conjecture that there are other worlds in our galactic neighborhood capable of supporting life. Our exploration of the diversity of planetary systems around other stars will emphasize systems that may have characteristics necessary for life. In addition to contributing to our knowledge of the structure and dynamics of our galaxy, **SIM**, described under Objective Three, will be the first observatory capable of indirectly detecting planetary bodies with only a few times the mass of Earth in orbit around other stars.

Continuing the Origins Observatories line, the **Terrestrial Planet Finder (TPF)** will extend the search for signatures of life beyond our Solar System. TPF will be an interferometric telescope array that will separate the infrared light of a planet from that of the star that it orbits in order to measure the spectrum of the planet. It will be able to search about 200 nearby stars for planets that possess warm atmospheres containing significant amounts of water or oxygen, which would indicate the possible presence of biological activity of some kind. To do so, the design for TPF

will build upon large aperture, cryogenic optics, and infrared detector technologies also needed for the NGST, the beam control and nulling capabilities of the ground-based Keck Interferometer and SIM, and the precision free-flying demonstration of the **Space Technology-3 (ST-3)** mission.

For Possible Implementation
After 2007

The first decade of the new millennium should have yielded tantalizing clues about the nature of the planets in the solar neighbor-



Left: The Space Technology-3 (ST-3) mission will test new technologies by flying two spacecraft in formation and using laser beams to keep the spacecraft aligned in precise positions relative to each other.

Right: By combining the high sensitivity of space telescopes with the high resolution of an interferometer, TPF will be able to reduce the glare of parent stars by a factor of more than one hundred-thousand to see planetary systems as far away as 50 light-years. TPF's spectroscopy will allow atmospheric chemists and biologists to analyze the relative amounts of gases like carbon dioxide, water vapor, ozone, and methane to ascertain whether a planet might support life.

hood, and about the presence—or absence—of life there. However, the TPF will be only the first step toward a detailed understanding of planetary systems in our neighborhood. The modest collecting area of the elements of TPF will permit only the first reconnaissance of these systems. The next step in studying other planetary systems will be observatories with significantly larger apertures and wider wavelength coverage.

The sensitivity of astronomical observatories depends strongly on the size of the light-collecting aperture, so that much larger successors to TPF would be able to observe far more target systems and search for rarer chemical species in planetary atmospheres. This will allow a less ambiguous interpretation of planetary spectra and permit a much wider range of planetary types to be observed. Two concepts on the horizon are a spectroscopic mission, a “**life finder**,” and later, a complementary “**planet imager**.” The prize from this new generation of observatories would be a truly comprehensive picture of planetary systems, including their physical characteristics and more conclusive signatures of life outside our Solar System. These missions to follow TPF will depend on even more ambitious optical systems, in particular, mirrors tens of meters in diameter. Since current space telescope tech-

nologies appear limited to smaller collecting areas, large optical systems technology will continue to have high priority for the Space Science Enterprise. Astronaut-assisted deployment or positioning approaches might be of great value in assembling and operating these future observatories, and advanced remotely-supervised robotic systems may also be available in that time frame.

OBJECTIVE FIVE: Understand the formation and evolution of the Solar System and Earth within it

Earth and all of the other bodies in the Solar System formed at about the same time from the same reservoir of material—a disk of gas and dust encircling the early Sun. These bodies have similarities, but also exhibit striking differences. For example, Jupiter and Saturn both have massive hydrogen-helium atmospheres apparently surrounding ice and rock cores, while Uranus and Neptune are mostly large ice and rock cores with much less surrounding gas. All of these outer planets, in turn, differ dramatically from Earth and the other “rocky” bodies that inhabit the inner Solar System. What were the differences in formation and evolution that led to these and other

striking differences among the diverse bodies of the Solar System?

Looking more closely at the inner planets, we see that they are similar in size, but differ dramatically from one another in their atmospheres and surface properties. We believe that these rocky planets probably shared common origins but followed very different paths to the present. What evolutionary processes account for these differences? Are these processes still at work, and what do they imply about our future on Earth?

Superficially so different from Earth, Mars appears to have been much more Earthlike earlier in its history. One of the major objectives of the **Mars Exploration Program (MEP)** is to trace the evolutionary history of our neighbor planet. The Mars scientific community has adopted a “seek, in situ, sample” approach that employs surface and orbital reconnaissance to gain an understanding of the planet that will lead to multiple sample returns. To support this strategy, high-resolution orbital imaging will follow up on Mars Global Surveyor results that suggest the presence of near-surface water in recent times. Increasingly advanced landers will be interspersed with these orbital missions. One aspect of the program approach is to establish high bandwidth data return capabilities

to support the “seek, in situ, sample” approach.

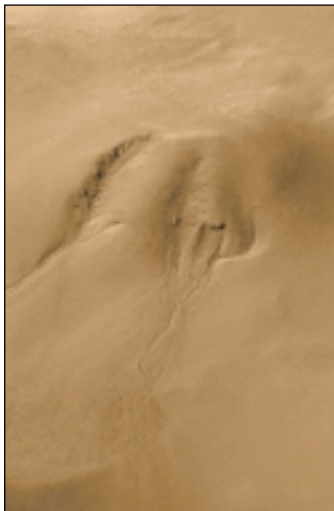
Key capabilities for near-term Mars missions include precision guidance and landing, surface hazard avoidance or tolerance, surface and atmospheric mobility, and aero-entry systems. Aerocapture would reduce propellant requirements. We need advances in systems for in situ analysis of materials that can help guide the selection of the small samples that we will be able to return. Sample return missions will also

require development of high-specific thrust, compact ascent propulsion systems. A variety of advanced information system and communications technologies, including autonomy, inter-spacecraft communication systems, and optical communications, will be applied to future missions.

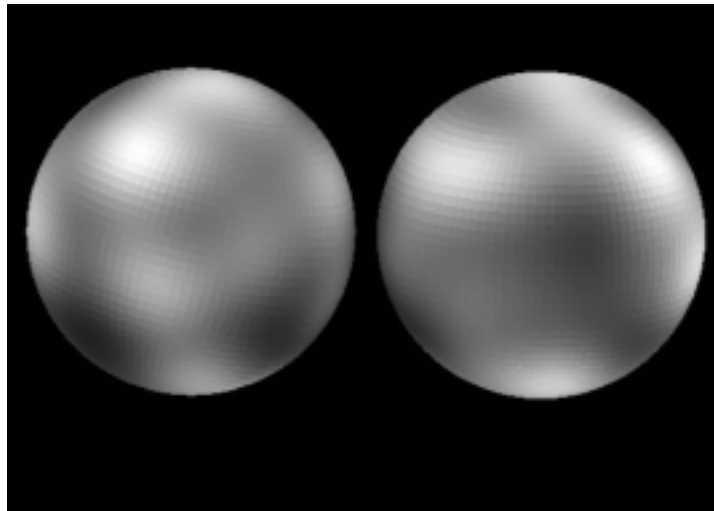
Valuable information about the early history of the Solar System resides at its boundaries. A **Pluto-Kuiper Express** mission would carry out the first reconnaissance of the last planet not visited by

spacecraft and scout the inner edge of the Kuiper Belt. Pluto and its large satellite Charon represent a poorly understood class of remote and icy dwarf planets. The Kuiper Belt is a flattened disk of icy debris, believed to be in a primitive state, remaining from the processes that formed the major planets in our Solar System.

Other candidate missions in the **Outer Planets Program** to follow the Europa Orbiter include the **Titan Explorer** and **Europa Lander**. These missions would



Left: High-resolution images from the Mars Global Surveyor (MGS) Mars Orbiter Camera (MOC) suggest that liquid water has seeped onto the surface in the geologically recent past.



Right: The surface of Pluto is resolved in these Hubble Space Telescope pictures. These images show that Pluto is an unusually complex object, with more large-scale contrast than any planet besides Earth. Variations across Pluto's surface may be caused by topographic features such as basins or fresh impact craters. However, most of the surface features, including the northern polar cap, are likely produced by a distribution of frosts and chemical byproducts.



Artist's concept: The Cassini spacecraft flies by with its high gain antenna pointed at ESA's Huygens probe as it reaches the surface of Titan. Saturn is dimly visible in the background through Titan's thick atmosphere of methane, ethane, and (mostly) nitrogen. Cassini is a joint mission of NASA, the European Space Agency, and the Italian Space Agency.

build on the results from preceding missions to conduct in-depth analyses of these icy, organic-rich environments to determine whether they hold the possibility of life. Mission sequence decisions will be based on continuing scientific discoveries and the progress of our technology programs. For example, exciting results from the Cassini-Huygens mission arriving in the Saturn system in 2004 might advance the

Titan Explorer ahead of other missions under study.

Highly capable, autonomous micro-avionics and very efficient on-board power subsystems are key to all future outer planetary missions. Multi-megarad radiation tolerance is a stringent requirement for all missions that operate in the Jovian environment. Avionics technologies projected for readiness in 2003 could support the Europa

missions, while further advances will be required for the Titan Explorer. The Titan mission will rely on advanced solar electric propulsion and aerocapture. Special requirements for Europa Lander readiness include progress in bioload reduction and advanced chemical propulsion for landing on this massive airless body.

The so-called primitive bodies, comets and asteroids, contain important clues to the early history of the Solar System. It is hypothesized that comets and asteroids were the fundamental "building blocks" of planet formation and that most of these bodies that we see today are the debris left over from this process. Impacts on Earth by comets may have delivered the materials needed for the origin of life here: water, atmospheric gases, and perhaps organic chemicals. The Deep Impact mission, which will advance the

Outer Planets Program

Exploration of the outer Solar System has revealed that the outer planets and their moons are rich in organic material, that subsurface liquid water may exist in some places, and that prebiotic chemical processes occur in some of these environments. The Galileo spacecraft has returned fascinating information about the moon Europa. The Cassini-Huygens mission, now en route to Saturn, will extend this exploration through intensive investigations of the organic-rich atmosphere and surface of Saturn's giant moon, Titan.

Continuing this exploration thrust, the Outer Planets program will focus on prebiotic chemistry in likely places in the outer Solar System. Mission sequence decisions will be based on ongoing scientific discoveries and technological progress. Destinations for missions in this line include returns to Europa and Titan, reconnaissance of the Kuiper Belt, and a more comprehensive study of the Neptune system, including its moon Triton.

study of the composition of primitive bodies pioneered by earlier missions to Halley's comet, will be launched in mid-decade. To take the next step, a **Comet Nucleus Sample Return** is a high priority new implementation start to complement ongoing Solar System exploration programs. The goal of this mission, which could initiate a new "To Build a Planet" mission line, is to return a pristine sample of material from a comet nucleus for detailed chemical analysis. The Comet Nucleus Sample Return will depend on micro-avionics, advanced computing, and spacecraft autonomy technologies that are currently being developed. Advances in solar electric propulsion that focus on increased lifetime and reliability are needed. Other key capabilities include an Earth-entry system that can survive very large entry speeds into our atmosphere.

For Possible Implementation After 2007

According to current planning, the Europa Orbiter, Pluto-Kuiper Express, Titan Explorer, and Europa Lander could be followed within the Outer Planets line by a **Neptune orbiter**. This mission is an important component of our investigation of the outer Solar System, including Neptune's moon, Triton, which may be an icy, organic-rich, captured Kuiper Belt object.



The composition and physical and chemical processes of comets are key to unlocking the secrets of the early Solar System. This dramatic pioneering image of the nucleus of Halley's Comet was obtained by the ESA Giotto spacecraft in March 1985.

A number of other exciting opportunities are being considered for implementation as follow-ons in the "To Build a Planet" line after 2007. For example: so Earth-like in some respects, but so alien in others, Venus presents a genuine puzzle. Why did a planet with strikingly Earth-like size, composition, and geological activity develop a radically different surface and atmospheric environment? Understanding this evolutionary divergence has important implications for the study of life-sustaining environments as well

as for our understanding of Earth's fragile, changing environment. A **Venus surface sample return** mission would help us to answer fundamental questions about the evolution of Earth-like planets.

Understanding the behavior of gas, dust, and radiation together is an important key to understanding the formation of the Solar System. In some ways, the rings of Saturn constitute a laboratory for the behavior of uncoalesced material in the primitive solar nebula. A **Saturn ring**

observer mission could perform detailed investigations of complex dynamic processes in Saturn's rings. In effect, we would be able to peer back in time to the epoch of planetary formation, when the material now contained in the planets was spread out in a disk encircling the Sun. It would also provide critical "ground truth" for a variety of observational and theoretical astrophysical studies. The Venus and Saturn ring missions would continue the "To Build a Planet" line.

The **Mars Exploration Program** will continue its search for evidence of water, the quintessential ingredient for life. A Mars synthetic aperture radar orbiter mission could detect buried water channels and help direct our search for ancient and modern water reservoirs. Advanced missions that could follow initial sample return missions could drill deeply (perhaps 10 to 100 meters) into the Martian

cryosphere and hydrosphere to follow up results from earlier sample return missions. Surface, subsurface, orbiting, and airborne elements would extend our ability to carry out wide-area exploration and sampling in three dimensions. Far-term missions will require many of the technology advances that will be developed for the nearer-term, as well as further progress in the areas of thermal control, inflatables, aerobraking, precision landing, autonomy, advanced electric propulsion, advanced power systems, optical guidance, and control.

Other mission candidates for later implementation include a Jupiter polar orbiter for long-term detailed investigations of Jupiter's interior, atmosphere, and magnetosphere; giant planet deep probes to measure bulk composition, chemical processes, and atmospheric dynamics of the giant planets; a lunar giant basin sample return to collect sam-

ples from a very old impact basin far from previously sampled sites on the Moon; and a multiple asteroid mission/protoplanet explorer to investigate the relationship of main-belt asteroids to planetary evolution. As technological progress continues, some of these missions come within the scope of the Discovery program.

OBJECTIVE SIX: Probe the origin and evolution of life on Earth and determine if life exists elsewhere in our Solar System

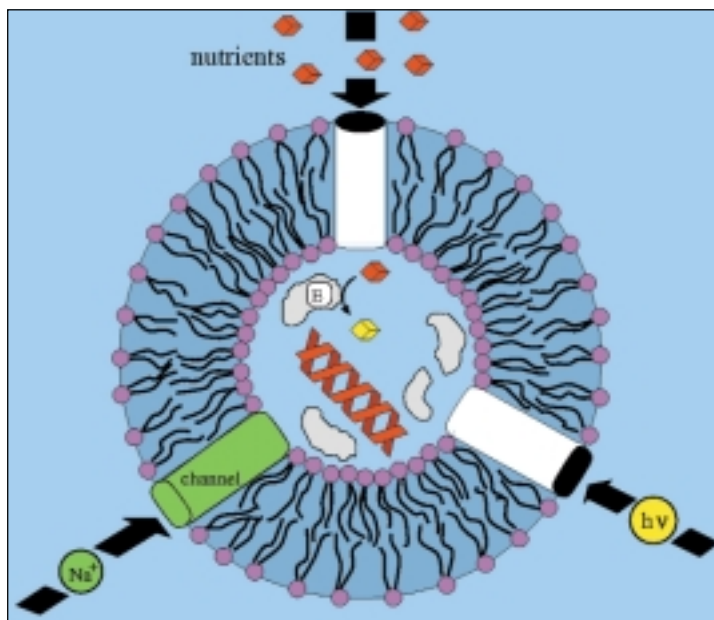
NASA research on the origin, evolution, and distribution of life in the universe is focused on tracing the pathways of the biologically critical elements from the origin of the universe through the major epochs in the evolution of living

To Build a Planet

An understanding of the formation and development of planets and their environments is a crucial missing link in our understanding of the Solar System and the development of life. At this juncture, we have learned enough to frame this subject in terms of three fundamental questions:

- What are the building blocks of which planets are made?
- What dynamic processes are involved in the initial formation of planets and planetary systems?
- What determines the diverse outcomes of planetary formation and evolution?

Answers to these questions are accessible to us in present-day Solar System objects: comets and asteroids, planetary rings, and the planets themselves.



A computer-generated dynamic model of a primitive cell used to test theories about the formation and behavior of Earth's earliest life.

systems. To understand the possibilities for life, we need to study the only known example, life here on Earth. NASA has made major contributions to discoveries in this area, such as the recognition that life began very early in Earth's history (3.85 billion years ago) and that our earliest microbial ancestor may have been a heat-loving, hydrogen-utilizing microbe. Major changes in the evolution of life have been tied to biological and geological processes (for example, the oxygenation of our atmosphere) and to extraterrestrial events such as an asteroid impact 65 million years ago that ended the age of the dinosaurs. Stellar evolution models suggesting that the Sun was much fainter at the time life was arising on Earth have called attention to the influence of solar vari-

The Astrobiology Institute

The new science of astrobiology synthesizes many scientific disciplines—astronomy to biology, geology to ecology, chemistry to informatics. Scientists from these disciplines, working toward the common goal of discovering the thread of life in the universe, have developed an Astrobiology Roadmap with three fundamental questions, ten goals, and 17 specific program objectives (<http://astrobiology.arc.nasa.gov>).

To pursue these goals and objectives, NASA has adopted an innovative approach to integrating efforts in these disparate disciplines by establishing the NASA Astrobiology Institute. The Institute advances our knowledge by forming interdisciplinary teams of researchers to attack major questions across a broad scientific front. It is a "virtual institute," in that it is a collaborative activity rather than a physical location. The members of these teams are geographically dispersed, but synthesize expertise in diverse fields by coordinating research goals, by frequent personnel exchanges, and by ongoing series of workshops, seminars, and courses, supported by the Institute's electronic networks.

ability on both the emergence and persistence of life on Earth.

A new space science research and analysis initiative, the **Astrobiology Initiative**, will study life in the Universe to determine how life began and evolves, whether there is life elsewhere than on Earth, and what the future of life is, on Earth and possibly beyond it. Understood broadly, the new field of astrobiology encompasses not only fundamental biology, but also cosmochemistry, exobiology, evolutionary biology,

gravitational biology, and even terrestrial environmental science and ecology. At NASA, some elements of this syncretic discipline fall into the purview of other enterprises. But the space science program addresses many of its most fundamental issues.

While not strictly a mission, the Astrobiology Initiative is comparable in scope and ambition to a major flight program. As a new research field, astrobiology intends to expand exobiology research and

encompass areas of evolutionary biology to further our understanding of how life may persist and evolve to exert a global environmental influence. One objective of astrobiology is to reconstruct the conditions on early Earth that were required for the origin of life and to determine the nature of processes that govern the evolution of life. Two approaches to learn about life on early Earth are to investigate the geological record and to use the genetic record, contained in contemporary microorganisms, to

Goals of Astrobiology

Question: How does life begin and develop?

- Goal 1: Understand how life arose on Earth.
- Goal 2: Determine the general principles governing the organization of matter into living systems.
- Goal 3: Explore how life evolves on the molecular, organism, and ecosystem levels.
- Goal 4: Determine how the terrestrial biosphere has co-evolved with Earth.

Question: Does life exist elsewhere in the universe?

- Goal 5: Establish limits for life in environments that provide analogues for conditions on other worlds.
- Goal 6: Determine what makes a planet habitable and how common these worlds are in the universe.
- Goal 7: Determine how to recognize the signature of life on other worlds.
- Goal 8: Determine whether there is (or once was) life elsewhere in our Solar System, particularly on Mars and Europa.

Question: What is life's future on Earth and beyond?

- Goal 9: Determine how ecosystems respond to environmental change on time-scales relevant to human life on Earth.
- Goal 10: Understand the response of terrestrial life to conditions in space or on other planets.

characterize traits of our microbial ancestors. From an experimental approach, researchers will develop and test pathways by which the components of life assemble into replicating systems that can evolve. Current research is expanding our understanding of the possibilities for the earliest life, utilizing simpler molecules and systems that could have been the precursors to the protein/RNA/DNA system used by all life today. It is only recently that we have been able to measure the scope of biological diversity. We have found that life thrives on Earth across the widest range of environments, inhabiting hydrothermal vents, extreme cold-deserts, environments at the limits of pH and salinity, and rocks kilometers beneath Earth's surface. This information will give us clues to how life may have evolved and where it could persist elsewhere.



Studies of hot springs on Earth will help guide the search for life on other planetary bodies by showing life at its limits and fossilization processes.

In order to develop a complete program, the Astrobiology Initiative is being complemented by new thrusts in advanced concepts and technology. Elements already identified are sample acquisition, preparation, processing, and quarantine; hyperspectral remote sensing and imaging; in situ detection of life and “smartlabs;” detection and analysis of non-equilibrium thermochemical states; extreme environment simulation chambers; biotechnology and bioinformatics; technologies to access planetary surfaces and subsurfaces; and next-generation planet imaging and analysis techniques. The intent is to identify specific areas in biotechnology, instrumentation, field studies, and missions where investment will significantly advance this new field.

Astrobiology is a major component of the **Research and Analysis**

Program (R&A, described at greater length in section II-5). The R&A program also supports the analysis of primitive meteorites—and will extend this work to returned samples from asteroids and comets—to learn about the early Solar System and the biologic potential of planetary bodies.

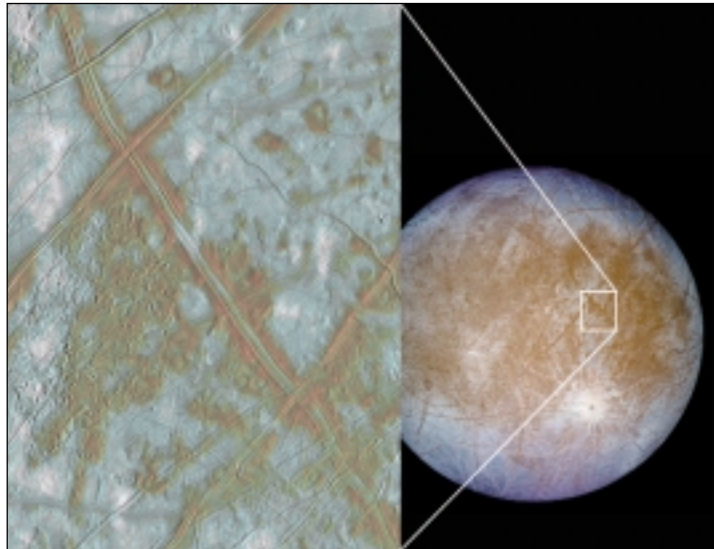
Flight missions will also contribute directly to the search for life or its antecedents in the Solar System. **Cassini**, en route since 1997, will arrive at Saturn in 2004. Its **Huygens** probe (provided by the European Space Agency) will explore the organic-rich atmosphere of Titan, Saturn's largest moon, to broaden our understanding of organic chemistry in our Solar System, perhaps discovering an organic sea or a record of the satellite's organic history.

A number of flight programs that will go into implementation after 2003 will also contribute vitally to the search for life and its origins. For example, it is ironic that the ancient surface on Mars may contain the best record in the Solar System of the processes that have led to life on Earth. The **Mars Exploration Program** will expand our understanding of volatiles on the planet, study its atmospheric history, and determine the elemental composition and global characteristics of Mars' surface. Future missions will explore the ancient

terrain and return samples, unveiling the Mars of over three billion years ago and, perhaps, also unveiling the precursors to life on ancient Earth. Part of the challenge will be to establish criteria to distinguish between materials of biological and non-biological origin both during sample selection and in subsequent detailed analysis of these samples on Earth. We will continue to search for and analyze Martian meteorites present on Earth to understand Mars and the exchange of materials between planets.

An understanding of Saturn's moon Titan could provide an important bridge between the study of life's chemical building blocks and the study of more evolved environments such as Mars and Earth. Follow-on to Huygens, **Titan Explorer** could investigate chemical conditions that might be similar to the early environment of Earth, and could offer a key to an ultimate understanding of the origin of life.

Images of Europa, an ice-covered moon of Jupiter, suggest existence of a sub-surface world of liquid water. We will pursue this suggestion of a second liquid water world in our Solar System with the Europa Orbiter, scheduled for launch in mid-decade. Actually, the presence of subsurface liquid water worlds

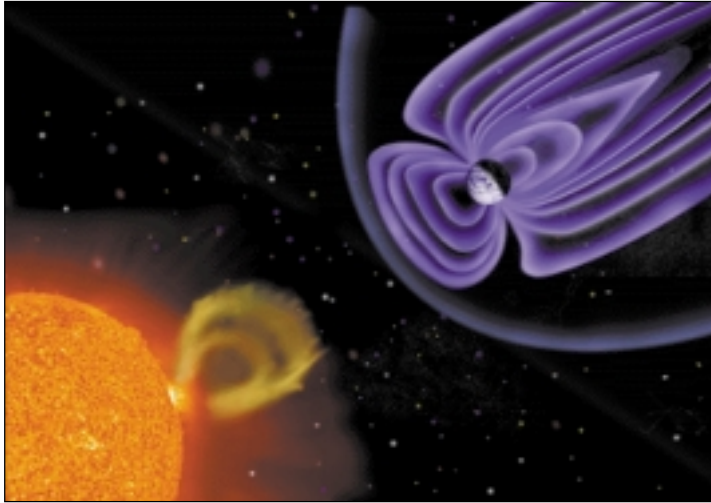


Images of Europa's surface indicate that water or slush may have oozed up through cracks in its icy crust. This suggests that a subsurface ocean has existed on this moon of Jupiter, and the discovery of a magnetic field around Europa indicates that a liquid ocean is still there beneath the ice.

now seems plausible in a number of satellites of the outer planets. These findings and our understanding of the early appearance and ubiquity of life on Earth reinforce the suspicion that life could exist elsewhere in the Solar System. By applying an understanding of the early evolution of life on Earth, as well as of its ability to thrive in extreme environments here, we can search for evidence of life elsewhere in our Solar System. A **Europa Lander** could be an important next step for this objective.

For Possible Implementation After 2007

If a Europa Lander returns evidence of a subsurface water ocean, we could consider how to carry out more technologically difficult penetration of the frozen crust to hunt for life below by a **Europa subsurface explorer**. As we learn more about the potential for life in the universe, astrobiology research will suggest new targets for missions. For instance, already being contemplated as other potential water habitats are Callisto and the deep subsurface



Solar activity interacts with Earth and its magnetosphere in complex ways.

of Mars, which could also be targets of very advanced spacecraft.

OBJECTIVE SEVEN: Understand our changing Sun and its effects throughout the Solar System

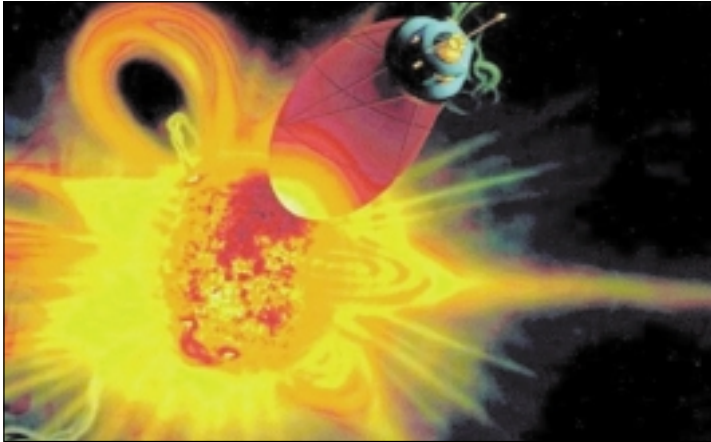
The Sun has profound effects throughout the Solar System, both on the bodies that orbit our own star and on the space between them. To explain these effects, we need to understand both the inherent characteristics of the Sun and how its emissions interact with the rest of the Solar System. These interactions at Earth are particularly important because of their practical near-term

effects (e.g., interference with satellite communications) and possible long-term implications (e.g., the effects of solar variability on climate). An understanding of the Sun and the consequences of its variation are also needed if we are to comprehend conditions at the dawn of life on Earth and predict our long-term future.

We are dramatically advancing our knowledge of how the Sun works through studies of solar interior dynamics. Using a growing fleet of spacecraft, we are making coordinated measurements of events that start at the Sun, propagate through interplanetary space, and ultimately impact Earth's magnetosphere and upper atmosphere. The next step is a first survey of the region

where the terrestrial atmosphere transitions to space, opening a new view of the response of Earth's magnetosphere to the solar wind. We are also gaining important insights into the workings of extra-terrestrial magnetospheres, exploring the most distant reaches of the Solar System, and completing the first exploration of the solar wind at the Sun's poles.

The **Solar Terrestrial Probe (STP)** program is a line of missions specifically designed to systematically study the Sun-Earth system. The STP program seeks an understanding of solar variability on time scales from a fraction of a second to many centuries. It will also determine cause (solar variability) and effect (planetary and heliospheric response) relations over vast spatial scales. Our first STP projects are the Thermosphere-Ionosphere-Mesosphere Energetics and Dynamics (TIMED) mission, NASA's contribution to the Japanese Solar-B mission, and the Solar Terrestrial Relations Observatory (STEREO); these will proceed into implementation before 2003. Planned follow-on STP missions focus on the responses of near-Earth space to solar input. **Magnetospheric Multiscale (MMS)** should help us quantitatively understand the fundamental plasma physics underlying the processes (including magnetic reconnection, plas-



Passing within three solar radii of the Sun, inside its outer atmosphere, Solar Probe will endure extreme conditions to provide unique data.

ma turbulence, and energetic particle acceleration) that control magnetospheric dynamics and thus clarify the impact of solar processes on the geospace system. The **Geospace Electrodynamic Connections (GEC)** mission will determine the spatial and temporal scales that govern the coupling between the magnetosphere and ionosphere, a major step toward understanding the connection between the solar wind, magnetosphere, and ionosphere. **Magnetotail Constellation (MagCon)** will employ a large number of very small satellites to map the structure of the magnetosphere. The availability of simultaneous multi-point measurements from missions such as MagCon will make it possible to construct the first high-fidelity “images” of the regional structure of the magnetosphere and to characterize in detail its response to variations in solar input.

Solar Probe will be our first voyage to a star, a mission to explore

the near-environment of our Sun. Solar Probe will make a close flyby of the Sun, making the first in situ measurements deep within its outer atmosphere. In addition to providing data essential for understanding the source of the solar wind, these observations will allow us to relate remote observations of solar phenomena to the actual physical processes that occur in the solar atmosphere.

The Gamma Ray Large Aperture Space Telescope’s (GLAST) greatly enhanced sensitivity relative to previous high energy gamma ray instruments will allow detailed studies of the physical mechanisms underlying the vast energy releases observed in solar flares.

Living with a Star (LWS), described under Objective Eight, is a special NASA initiative that directly addresses those aspects of the Sun-Earth system that affect life and society. Its program ele-

ments include a space weather research network; a theory, modeling, and data analysis program; and space environment test beds. The first LWS mission will be the **Solar Dynamics Observer**, which will focus on the solar interior with the goal of understanding the sub-surface roots of solar activity.

Community-formulated missions in the **Explorer Program** will take advantage of new scientific ideas and technologies to advance our knowledge of the Sun-Earth connection. In addition, missions undertaken within the **Discovery Program** will also contribute to our understanding of the terrestrial system. One example is information on Mercury’s magnetosphere to be returned by the MESSENGER Discovery mission.

[For Possible Implementation After 2007](#)

Atmospheric waves link the troposphere and upper atmosphere and redistribute energy within the ionosphere-thermosphere-mesosphere (ITM) system. Clusters of satellites using high-resolution visible and infrared sensors could provide **ITM wave imaging**, enabling us to understand generation and loss mechanisms of these waves, their interactions, and their role in energy transport within the region. Significant improvement

in infrared sensors will be required in order to enable this mission.

Understanding the heating and cooling of the solar corona by distinguishing between proposed heating mechanisms remains a challenge. Because much of the physics governing this activity occurs very rapidly and at very small spatial scales, this will require imaging and spectroscopic data able to resolve **microscale coronal features**. Implementation of such a mission will require significant developments in optics and detectors.

To fully understand the structure of the solar corona and to obtain a three-dimensional view of coronal mass ejections, we will need observations from above the Sun's poles to complement data obtained from the ecliptic plane. Viewing the Sun and inner heliosphere from a high-latitude perspective could be achieved by a **solar polar imager** in a Sun-centered orbit about one half the size of Earth's orbit, perpendicular to the ecliptic. Solar sail technology will be required to put a spacecraft in such an orbit in a reasonable time.

Future **LWS** missions will continue to contribute importantly to our scientific understanding of the underlying physical processes through which the Sun impacts Earth and society.

An **interstellar probe**, traveling more than 30 billion kilometers in 15 years or so, could directly study for the first time how a star, our Sun, interacts with the surrounding interstellar medium. On the way, it would investigate Solar System matter beyond Neptune, and then determine the structure and dynamics of the shock wave that separates our heliosphere from the space between the stars. Continuing on, it would explore the plasma, neutral atoms, dust, magnetic fields, and cosmic rays of the interstellar medium.

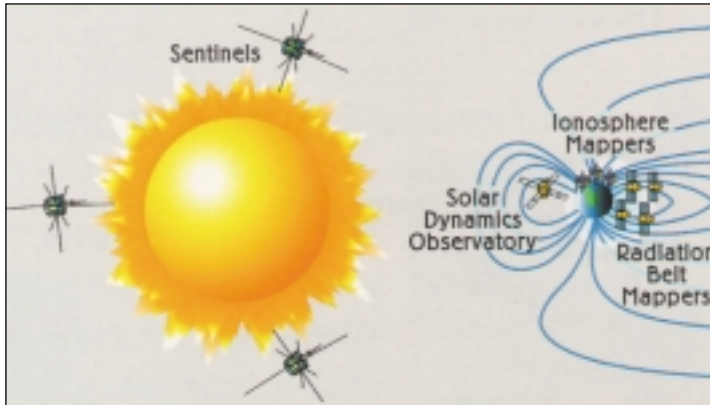
OBJECTIVE EIGHT: Chart our destiny in the Solar System

Evolutionary processes that have shaped Earth and other planets are

still at work in the Solar System today. For example, there is strong evidence that large impacts caused biological mass extinctions on Earth in the past, altering the course of biological evolution. The impact of Comet Shoemaker-Levy 9 on Jupiter in 1994 vividly demonstrated that major impacts still occur and could alter the future human habitability of Earth. The Space Science Enterprise supports the search for near Earth objects (**NEOs**). We believe there are between 700 and 1100 NEOs larger than 1 km whose orbits traverse Earth's, and we have discovered less than 450 of them to date. The motions of these objects are clearly of interest as potential hazards. Many of them are also the easiest objects for a spacecraft rendezvous, and may contain water or even rich mineral deposits.



Hubble Space Telescope image of Jupiter in July 1994. The dark spots are scars left by multiple impacts of the fragments of Comet Shoemaker-Levy 9. Jupiter's diameter is approximately eleven times that of Earth, which would fit into the Great Red Spot (at left in the image).



Living With a Star is a new initiative to understand space weather and the effects of the Sun on Earth. Various LWS spacecraft will provide information about Earth's upper atmosphere, the heliosphere, and the Sun itself.

We know that solar activity can strongly affect daily life in today's technological civilization by causing power-grid failures, temporary communications interruptions, and even outright failure of communications and defense satellites. Particle radiation from the active Sun can endanger astronauts in space. Solar variability is also one of the natural drivers of global climate that must be better understood for accurate evaluation of the impact of human activities on global climate. An understanding of the evolution of the Sun and the consequences of its variations are critical if we are to properly understand the conditions at the dawn of life and to predict our long-term future.

Future **Solar Terrestrial Probe** missions and Sun-Earth connec-

tion-related **Explorers** will continue to improve our understanding of solar variability and how a habitable environment is maintained on Earth in spite of it.

Living with a Star (LWS) is a NASA initiative that directly addresses those aspects of the Sun-Earth system that affect life and society. It includes a space weather research network; theory, modeling, and data analysis programs; and space environment test beds. The flight component of LWS is a network of spacecraft that will provide coordinated measurements from a variety of vantage points distributed around the Sun and Earth. Analyzed together, these measurements will allow us to better understand and predict the effects of space weather events. The first

planned LWS mission is the **Solar Dynamics Observatory (SDO)**, which will observe the Sun's outer layers to determine its interior dynamics and the activity of the solar corona, the source of sunspots and active regions, and origin of coronal mass ejections. A second LWS component is a constellation of **Sentinels** around the Sun to observe the movement and evolution of eruptions and flares from the dynamic Sun through the interplanetary medium to Earth's orbit. LWS geospace missions are the **Radiation Belt Mappers** and the **Ionospheric Mappers**. The Radiation Belt Mappers will characterize the origin and dynamics of terrestrial radiation belts and determine the evolution of penetrating radiation during magnetic storms. The LWS Ionospheric Mappers will gather knowledge of how Earth's ionosphere behaves as a system, linking incident solar energy with the top of Earth's atmosphere.

Beyond elucidating events and processes that might affect our destiny on Earth, missions to the Moon, Mars, and near-Earth asteroids will also contribute to our understanding of potential human destinations in the Solar System. Lunar Prospector returned evidence for hydrogen, possibly in the form of water ice, trapped in permanently shadowed regions near our Moon's north and south poles. Goals of the **Mars Exploration**

Program include investigating selected sites on that planet in detail and improving our understanding of how to ensure the safety and effectiveness of future human explorers, and perhaps eventually settlers. Future missions to Earth-approaching asteroids will assess the resource potential of these objects.

For Possible Implementation After 2007

Future elements of the **LWS Initiative** will provide coordinated measurements from an improved space weather research network, distributed around the Sun and Earth, to advance our ability to understand and predict space weather events and their effects. Future LWS components, such as a **solar-polar orbiter** and Earth **north and south “pole-sitters,”** are under study.

The **Mars Exploration Program** will continue and will build on the results of the nearer-term missions. From laboratory studies and space experimentation, astrobiology research may reveal whether life is limited to its planet of origin or can expand its evolutionary trajectory beyond. Outer Solar System missions to Europa and Titan would help clarify the larger context for life in our own family of planets and satellites.

Living With a Star

The Living With a Star Initiative is a set of missions and enhancements to our current program to augment our study of solar variability and its effects. Why do we care? The sphere of the human environment continues to expand above and beyond our planet. We have an increased dependence on space-based systems, a permanent presence of humans in Earth orbit, and eventually humans will voyage beyond Earth. Solar variability can affect space systems, human space flight, electric power grids, GPS signals, high frequency radio communications, long range radar, microelectronics and humans in high altitude aircraft, and Earth's climate. Prudence demands that we fully understand the space environment affecting these systems. In addition, given the enormous economic impact of even small changes in climate, we should fully understand both natural and anthropogenic causes of global climate change.

The Living With a Star Initiative includes:

- A space weather research network of spacecraft providing continuous observations of the Sun-Earth system for interlocking, dual use, scientific and applications research.
- A special data analysis and modeling program targeted at (1) improving knowledge of space environmental conditions and variations over the solar cycle, (2) developing techniques and models for predicting solar and geospace disturbances that affect human technology, and (3) assimilating data from networks of spacecraft.
- Space Environment Test beds for low cost validation of radiation-hardened and radiation-tolerant systems in high radiation orbits.
- Establishing and expanding partnerships for interdisciplinary science and applications with other NASA programs (Earth Science, Human Space Flight, Life Sciences), with other Federal agencies (e.g., via the interagency National Space Weather Program), with international collaborators, and with industry.

technology program

The next generation of spacecraft that will carry out our broad program of exploration must be more capable and more reliable while being more efficient in mass and power consumption. Some systems (telescopes, for example) will be much larger than today's; others (in situ probes for space physics, for example) will be much smaller. During the preparation of this Strategic Plan, the roadmap teams in the major Enterprise science areas that formulated science goals and collected and assessed mission concepts also analyzed the technical capabilities that would be needed to implement these concepts. These Enterprise technology needs were aggregated into ten *key capability* areas.

Key Capabilities

Advanced power and on-board propulsion are needed to support more capable instrumentation and telemetry, as well as to enable spacecraft to travel deeper and faster into space. Development in these areas will focus on power generation (solar and nuclear) and energy storage (battery technologies and flywheels); chemical, ion propulsion, and attitude control systems; solar sails; and micro-propulsion systems and components.

Sensor and instrument component technology progress is needed to provide new observational capabilities for astrophysics, space physics, and planetary science remote sensing, as well as vehicle health awareness. Areas for future work include miniaturized in situ and advanced remote sensing instruments, and new sensing techniques using distributed spacecraft and bio-sensors for astrobiology. Of particular importance to space science is

Of particular importance to space science is instrument capability to perform in harsh environments: vacuum, extreme temperatures, and intense radiation fields.

instrument capability to perform in harsh environments: vacuum, extreme temperatures, and intense radiation fields. New detector technologies will be based on fundamentally new measurement principles and techniques

using new materials and architectures, as well as expanded use of different spectral regions.

Many future mission concepts require constellations of platforms that act as a single mission spacecraft for coordinated observations or in situ measurements, or act as a single virtual instrument (for example, interferometry or distributed optical systems). Major areas for work in **distributed spacecraft control** are: advanced autonomous guidance, navigation, and control architectures; formation initialization and maintenance; fault detection and recovery; and inter-satellite communications.

High rate data delivery is essential to support virtual presence throughout the Solar System. We also want to minimize the mass and resource requirements of communications subsystems. Topics for advanced development in high rate data delivery include: information extraction and compression; low-

cost, low-mass systems; optical communications; in situ communications for surface exploration; improved components for deep space communications; and high rate distributed information systems.

Very advanced space systems will be self-reliant, self-commanding, and even inquisitive. These **intelligent space systems** must be able to: plan and conduct measurements based on current or historical observations or inputs; recognize phenomena of interest and concentrate activities accordingly; and monitor and maintain desired status or configuration over long periods of time without frequent communication with ground.

Many science objectives benefit from more populous spacecraft constellations or more frequent flight opportunities at a fixed cost. The former category includes constellations of measurement platforms in flight as well as networks of landed spacecraft for in situ measurements. These **micro-or nano-sciencecraft** would have: smaller, more lightweight, more capable and resource-efficient spacecraft “bus” and “payload” components; efficiently integrated bus-payload spacecraft designs; high performance data compression technology; low power, high performance electronics; and

Very advanced
space systems
will be self-reliant,
self-commanding,
and even inquisitive.

micro-electromechanical systems (MEMS) technology.

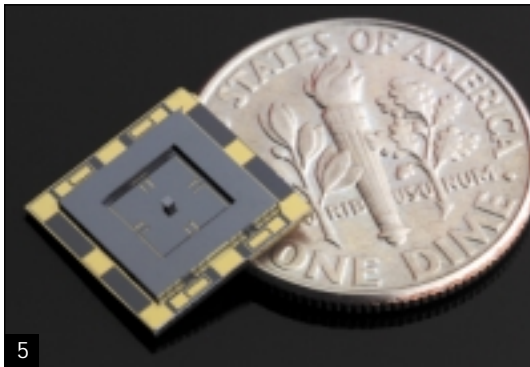
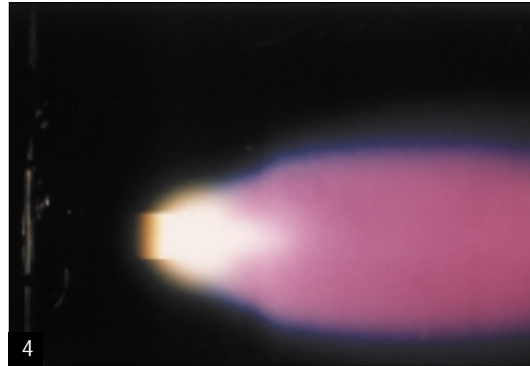
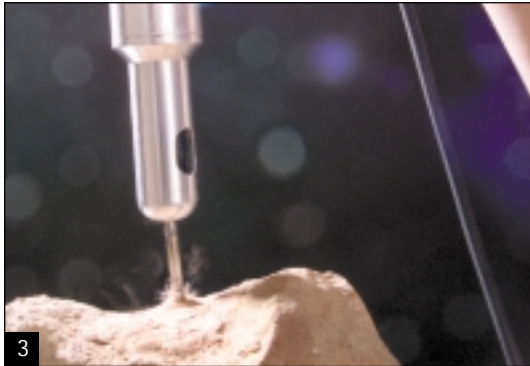
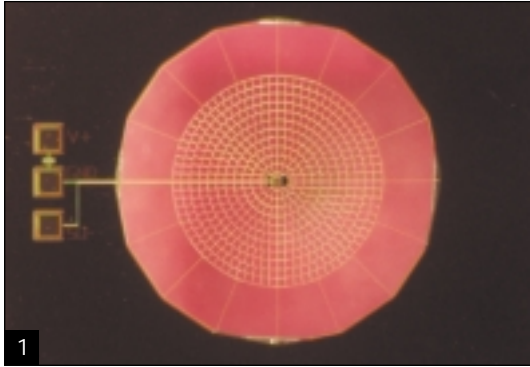
Advances in exploration of planetary surfaces will depend on **surface systems** technologies for safe, self-sufficient, and self-sustaining robotic and human presence independent from Earth for indefinite periods of time. Basic technology elements needed for surface and sub-surface sampling of planetary surfaces and small bodies will be teleoperated, along with autonomous robots and rovers with increased intelligence, speed, maneuverability, and dexterity. Specific capabilities would include drills, coring devices, and scoops, as well as sample handling, packaging, and return mechanisms.

Very large (km-scale) non-precision structures in space (e.g., sunshields, sails) and large (100m) precision structures (e.g., optical reflectors, antennas) levy

new requirements for **ultra-lightweight space structures and observatories**. Progress is needed in: materials; inflatable and deployable structures, including control for precision deployment and maintenance; lightweight optics and optical structures, and thin-film materials; and radiation shielding, survivable spacecraft materials, and telescope technology.

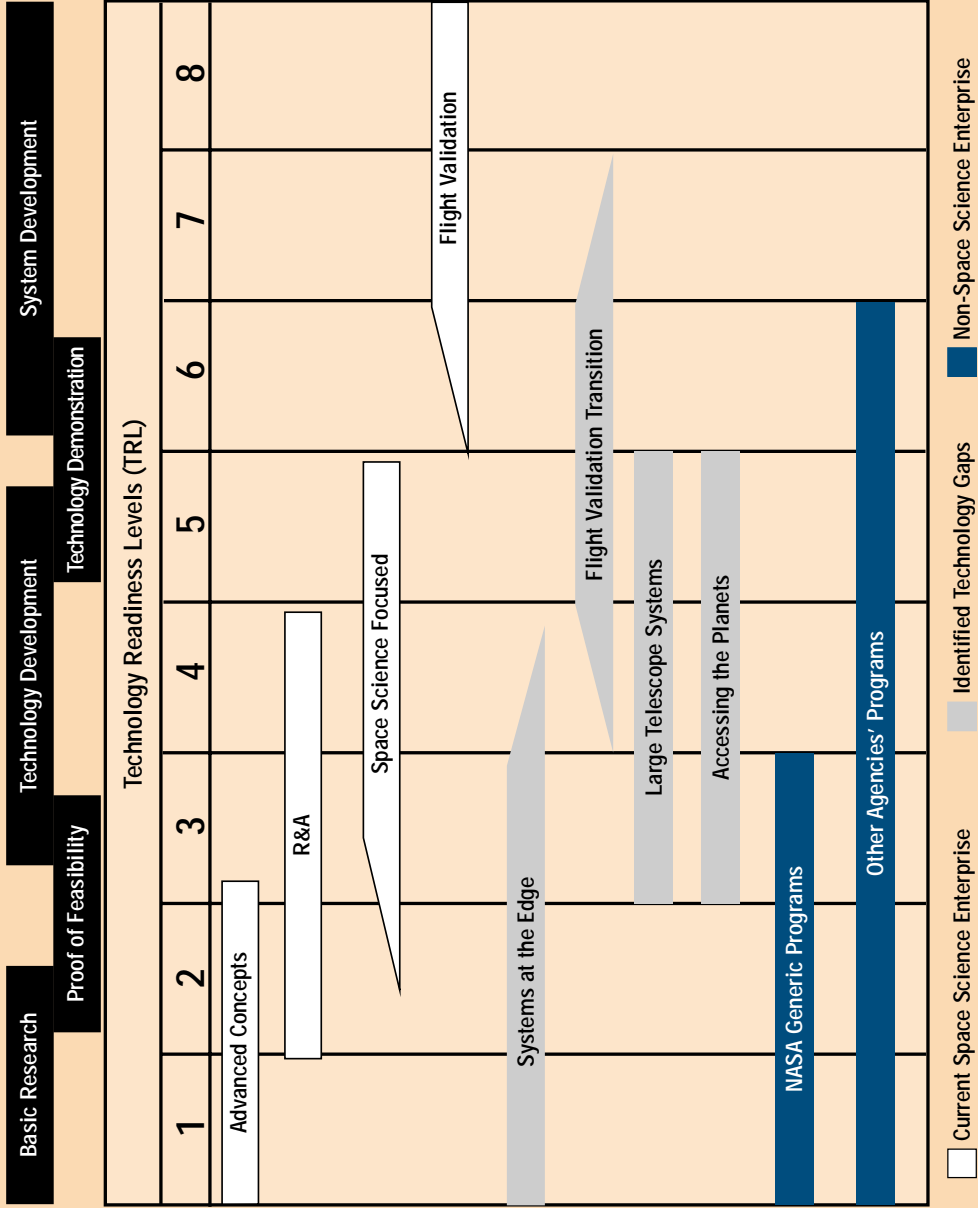
Improved reliability and agility are needed for in-space docking and flight in planetary atmospheres. **Atmospheric systems and in-space operations** development will focus on aeromaneuvering (ascent, entry, and descent systems, and aero-shell and hazard avoidance systems), aerial systems (balloons, airplanes, rotorcrafts, and gliders), and operations (rendezvous, docking, and sample transfer systems).

To bring all of these advanced flight capabilities together in innovative mission designs, we will need a **next generation infrastructure** on the ground. This will include high performance computing and networking, support for collaborative work, advanced design tools, and distributed networks of computer resources. Tools will be developed to increase efficiency and speed of technology maturation and infusion.



1. The Boomerang micromesh bolometer, reminiscent of a spider's web, uses a free-standing micromachined mesh of silicon nitride to absorb millimeter-wave radiation from the cosmic microwave background. Millimeter-wave radiation is absorbed and measured as a minute temperature rise in the mesh by a tiny Germanium thermistor, cooled to three tenths of a degree above absolute zero. 2. Aerogel, a low density material made from silicon dioxide, is protecting some crayons from the heat of the flame. Aerogels have primarily been used in scientific applications, most commonly as a particle detector in high energy physics. 3. An ultrasonic driller/corer developed at NASA Jet Propulsion Laboratory is shown drilling sandstone while being held from its power cord. Relatively small vertical force is used in this application—a factor that will be useful when the drill is used in future space missions to drill and core for samples during planetary and asteroid explorations. 4. A high power plasma thruster operates at a current level of 20,000 amperes and a peak power level of 10 megawatts. The technology may eventually be used to propel cargo or piloted vehicles to Mars and beyond. 5. This new microgyroscope is lighter, cheaper, higher-performing, and less complex than its conventional counterparts while uniquely designed for continuous space operation. Its dimensions are 4 by 4 millimeters, smaller than a dime, and its weight is less than one gram. 6. The Goldstone Deep Space Communications Complex, located in the Mojave Desert in California, provides radio communications for all of NASA's interplanetary spacecraft and is also utilized for radio astronomy and radar observations of the Solar System and the universe.

Space Science Technology Programs and Technology Readiness Levels



TRL 1 Basic principles observed and reported

TRL 2 Technology concept and/or application formulated

TRL 3 Analytical and experimental critical function and/or characteristic proof-of-concept

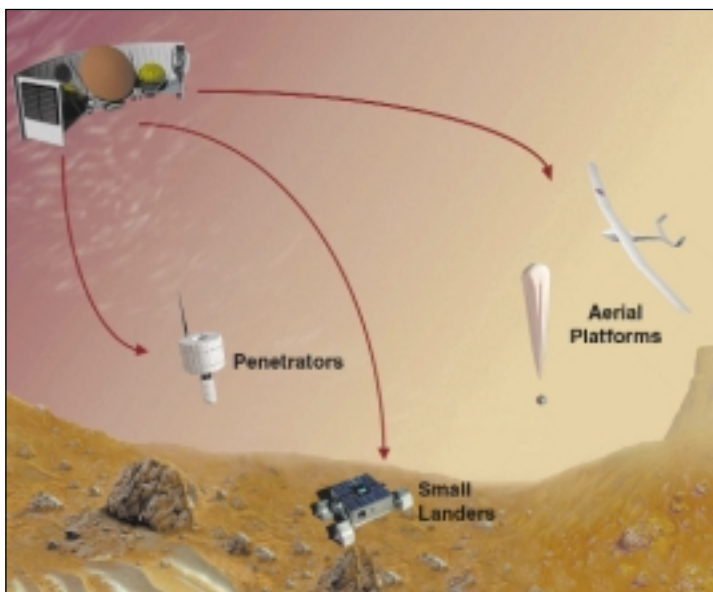
TRL 4 Component and/or bread-board validation in laboratory environment

TRL 5 Component and/or bread-board validation in relevant environment

TRL 6 System/subsystem model or prototype demonstration in a relevant environment (ground or space)

TRL 7 System prototype demonstration in a space environment

TRL 8 Actual system completed and "flight-qualified" through test and demonstration (ground or space)



A broad range of new technologies will be needed to carry out future space science missions. For planetary exploration, these include communications, instrumentation, descent systems, and intelligent mobile platforms.

The Technology Life Cycle

Taken with the Agency's Cross-Enterprise Technology Program that focuses on early stage technology research, Enterprise technology programs span the full spectrum of technology maturity, from fundamental seed ideas through flight validation. The concept of Technology Readiness Levels (TRLs) provides a systematic approach to technology management that supports maturity assessment and a consistent comparison of maturity

between different types of technology. Technology products typically progress through the development cycle through multiple programs. For instance, after an advanced proof-of-concept is demonstrated, it may be transitioned into either the Enterprise focused program or into the cross-Enterprise program for continued development, depending on the breadth of its applicability. This would be followed by system-level development and flight validation in the focused or flight validation programs.

Enterprise Technology Program Components

The Space Science Enterprise technology program to advance the state-of-the-art in the ten focus areas is organized into three major elements: an advanced concepts program, a focused technology program, and the New Millennium flight validation program.

The **Advanced Concepts Program** conducts studies for far-term technology (10-25 years in the future) by eliciting long-range science ideas, developing relevant far-term system concepts, and then deriving technology requirements and innovative approaches to support them.

The **Focused Technology Program** addresses high-priority technology requirements that directly support missions in the Enterprise Strategic Plan. While activities within this program are driven by the needs of space science, other Enterprises often benefit from them.

The **New Millennium Program** completes the technology development life cycle by validating new technologies in space. In addition to dedicated technology missions, other flight validation platforms, including the Space Shuttle and International Space Station, balloons, sounding rockets, and piggyback space-

craft or launch vehicle opportunities are also used to validate technologies in the space environment. Demonstrations flown as secondary payloads on expendable launch vehicles flown by NASA, or co-manifested on other U.S. Government or commercial concerns' launches, offer still other opportunities. The possibility of cooperation within international partnerships for technology demonstration is also being explored.

In addition to these major Enterprise technology programs, the Enterprise provides requirements to, and benefits from, **Agencywide technology programs**: Cross-Enterprise Technology Development Program (CETDP), High Performance Computing Capability (HPCC), and NASA Institute for Advanced Concepts (NIAC). These programs support technology requirements for all NASA space Enterprises, focusing on early stages of the technology life cycle for multiple Enterprise users. They emphasize basic research into physical principles, formulation of applications concepts, and component-level performance evaluation.

The program analyses performed in conjunction with the preparation of this Plan have revealed gaps in the capability to meet the technology needs of the Space Science Enterprise and its future

In addition to
these major
Enterprise
technology
programs,
the Enterprise
provides
requirements to,
and benefits from,
Agencywide
technology
programs.

expansion. We are therefore taking steps to fill these gaps by proposing a **new technology initiative** that encompasses several programs. These include Systems at the Edge (focusing on low TRL research), Accessing the Planets (for in situ planetary exploration), Flight Validation Transition (promoting transition of new technologies to space demonstration), and a Large Space Telescope Initiative (for far-term space observatories).

Technology Management

Management of the technology life cycle for **strategic, NASA-formulated missions** begins with the science theme roadmaps described in Section II-1. The Enterprise allocates resources in the Focused Technology Program and establishes priorities for the New Millennium Program and the Cross-Enterprise Program. The Research and Analysis program's yearly research solicitation also reflects the priorities established by the Science Board of Directors.

The technology programs are reviewed quarterly by Enterprise management. A Technology Steering Group, staffed by key program technologists at the NASA Centers, analyzes on a continuing basis the efficiency of resource allocations (gaps, overlaps, and redundancies) in the technology programs. The Steering Group reports periodically to Enterprise management. The Steering Group uses a variety of system analysis, risk analysis, and investment analysis tools and processes to determine the relative benefits and costs of alternative technologies, both those developed internally and those provided by university and industry partners.

Selected technology programs are periodically peer reviewed by

external expert technologists on behalf of Center and Headquarters management. On the basis of these reviews and reports, reallocation of resources is considered by the Enterprise every year during the budget development process or whenever appropriate in response to deviations from planned performance or budgets.

Technology infusion into the **community-formulated Explorer and Discovery programs** occurs by a different path, since these missions are proposed as integrated packages by the research

community and proceed directly to detailed definition without the benefit of a lead-in technology development program. For the Explorer program, an annual research solicitation offers a technology funding opportunity, primarily for instrument development. The Research and Analysis program offers a competitive program for funding of instrument development for planetary exploration. The selecting official has the option to allocate a small amount of funding for a proposal of unusual scientific merit that is not selectable

because it is considered technically immature. Up-to-date information on technologies considered ready to fly is provided to proposers in the Explorer and Discovery programs, as well as to the proposal reviewers to ensure that a consistent standard for technical readiness is applied during the review process. Finally, technology developments supported under the Focused Technology Program for the NASA-formulated missions also become available to community proposers in the Explorer and Discovery programs.

research and data analy

Underpinning the space science flight programs are two programs of space science activities called Research and Analysis (R&A) and Data Analysis (DA)—collectively called Research and Data Analysis (R&DA). Broadly put, research supported under R&DA programs develops the theoretical tools and laboratory data needed to analyze flight data, makes possible new and better instruments to fly on future missions, and analyzes the data returned so that we can answer specific questions posed and fit them into the overall picture. Although priorities within both programs are established in accordance with the Enterprise strategic goals, the program types differ in scope. While DA programs are tied to specific missions, which are focused on the achievement of specific strategic objectives, the scope of R&A programs is generally wider

because they must provide the new theories and instrumentation that enable the next generation of flight missions.

The alignment of R&A programs with Enterprise strategic goals is ensured through two mechanisms. First, NASA Research Announcements soliciting R&A proposals contain explicit prioritization criteria with respect to Enterprise objectives. Second, the entire R&A program is reviewed triennially to assess sci-

entific quality and productivity of the major components and to adjust plans to best support Enterprise goals.

Data Analysis (DA) programs have traditionally been performed by mission instrument teams and interdisciplinary scientists competitively selected for an individual mission for the lifetime of that mission. For some missions or mission groups, periodic open and competitive solicitations enable DA

participation by other investigators. As a matter of principle, the Enterprise has begun to add annual, open and competitive DA solicitations to all missions that can accommodate “guest investigations.”

Without a vigorous R&DA program it would not be possible to conduct a scientifically meaningful flight program. Examples of the contributions of the R&DA program abound across the whole frontier of space science.

Role of NASA’s Research and Data Analysis Programs

In a recent study (*Supporting Research and Data Analysis in NASA’s Science Programs: Engines for Innovation and Synthesis*, National Research Council, 1998), the Space Studies Board identified R&DA functions that are “integral elements of an effective research program strategy”:

- Theoretical investigations
- New instrument development
- Exploratory or supporting ground-based and suborbital research
- Interpretation of data from individual or multiple space missions
- Management of data
- Support of U.S. investigators who participate in international missions
- Education, outreach, and public information

Objectives of R&DA Programs

Theoretical, modeling, and laboratory work provide the tools to understand and integrate measurements made in space and on the ground, and can also directly impact future mission concepts. Numerical modeling of impacts and magnetohydrodynamics support both planning for future missions and understanding of data returned from past ones. Laboratory experiments, in turn, are used to validate these theoretical results. The R&A-supported laboratory work on meteorites underpins research on asteroids, as well as continuing analysis of fragments that are believed to have come to Earth from Mars. In a different vein, models for the atmosphere of Mars can be used to predict the performance of aerobraking systems for future spacecraft. The R&A Planetary Protection Program is developing methods to completely sterilize ice-penetrating probes so that we can one day confidently search for life on Europa without fear of a spurious detection due to contamination from Earth. And sample returns from Mars cannot be undertaken until the possibility of contamination of our own planet is fully understood and eliminated.

Exciting new revelations about the cosmos are not possible without the most **advanced detector and instrument systems** that can be built, most of which are developed through competitively-selected space science R&A programs. Many are given real-life testing in the sounding rocket and balloon programs before the decision is made to fly them on the much more expensive Earth-orbiting and deep space spacecraft. The new-generation detectors for the Hubble Space Telescope, the Chandra X-ray Observatory, Solar and Heliospheric Observatory, and

the upcoming Space Infrared Telescope Facility were largely developed within the R&A program. Similarly, future generations of instruments slated for possible use on our planetary missions are being designed and built within the R&A program. As illustrated in the table “Examples of Flight Hardware with R&A Heritage” (p.89), instrument concepts developed through the R&A program have been the basis for flight instrumentation for every class of NASA flight mission, from the smallest to the Great Observatories.



Time exposure of a hypervelocity oblique impact, from the right of the frame. Low-angle impacts cause the projectile to fragment, and significant pieces survive to disperse downrange without much change in velocity. (NASA Ames Vertical Gun Range)

After we have obtained them, we must **analyze and interpret data** returned by NASA's space science missions to fully exploit them for addressing our strategic science objectives. R&A and DA support the necessary advanced modeling and theory. For example, recent computational modeling of the

convective upwelling in Europa's ice shell has been used to interpret the "blisters" observed by the Galileo spacecraft to estimate the thickness of the shell and the depth of a possible liquid water ocean beneath it. Other Galileo data have been analyzed to reveal the physical state and major

dynamical processes within Jupiter's turbulent atmosphere and on the surfaces of the giant planet's diverse satellites. Our understanding of the effects on Earth of the nearest star, the Sun, is progressing as a result of interpretation of data from such missions as the Solar and

Examples of Flight Hardware with R&A Heritage

Chandra	Focal plane detectors
Cluster	Electron and ion analyzer predecessors
EUVE	Wedge and strip detectors
	Mirror
FAST	Wave-particle correlator
	Multiple-baseline electric field interferometer
FUSE	Holographic grating
	Delay-line detectors
	Mirror
Galileo	Ebert-Fastie spectrometer
Hubble Space Telescope	Multi-anode microchannel plate array detector
Lunar Prospector	Electron reflectometer
SNOE	X-ray photometer
SOHO	Ultraviolet spectrometer
	Delay-line detectors
	Multi-layer imaging
TIMED	Ultraviolet imager
TRACE	Normal incidence multilayer filters
Wind	Wave-particle correlator
	Electron and ion analyzer predecessors
Yohkoh	Glazing incidence x-ray optics

Heliospheric Observatory (SOHO) and the Transition Region and Coronal Explorer (TRACE). A very practical example is coronal mass ejections, which directly affect—in some cases permanently damage—Earth-orbiting communications satellites. A complete understanding of these ejections could have very significant benefits to our national security and to the space communications industry. In the more remote universe, R&DA supports investigations into one

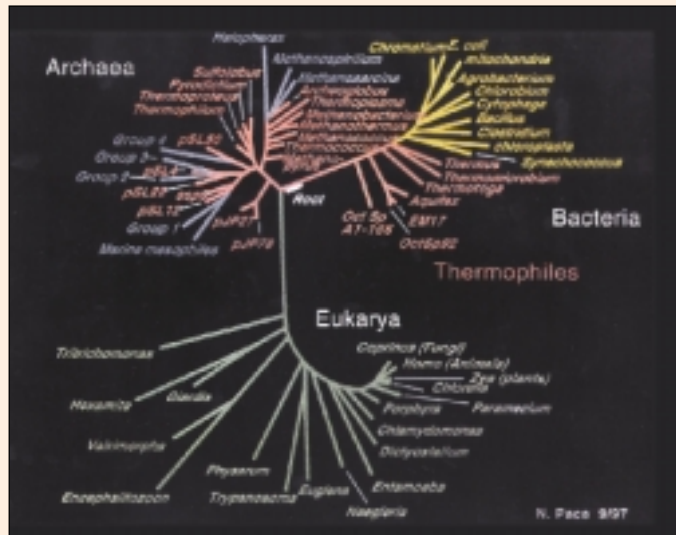
of the long-standing enigmas in astrophysics, the nature of gamma ray bursts. During brief flashes, these objects scattered over the sky are individually the brightest objects in the universe. A major advance was recently achieved when the visible counterpart to one of these bursters was observed simultaneously with its detection in gamma rays. Equally exciting, fine details of the fossil microwaves remaining from the Big Bang were revealed for the first time by one of a

series of balloon-borne experiments from the Antarctic.

Vast amounts of data are returned from space science missions. The volume, richness and complexity of the data, as well as the need to integrate and correlate data from multiple missions into a larger context for analysis and understanding, present growing opportunities. Exploration and discovery using widely distributed, multi-terabyte datasets will challenge all

Looking at the World in New Ways

R&A supported work that revealed the existence of a distinct and perhaps ancient type of microorganism, first christened *archaeobacteria*. Further studies supported this initially controversial theory. When the genomic sequence of *Methanococcus jannischii* was published, our perception of the taxonomy of life on Earth was sweepingly revised to today's three domains: bacteria, eukarya, and archaea. NASA-supported researchers thus discovered a previously unrecognized branch of life on Earth, an advance with profound implications for the search for life elsewhere in the universe.



aspects of **data management** and rely heavily on the most advanced analysis and visualization tools. The design and implementation of the next generation of information systems will depend on close collaboration between space science

and computer science and technology.

An example of such a collaboration is a National Virtual Observatory (NVO) initiative to collect most of the Nation's astronomical data, along with advanced visualization

and statistical analysis tools. This will support "observations" and discovery via remote access to digital representations of the sky in all wavelengths. The NVO will provide multi-wavelength data for millions of objects, allowing discovery of significant patterns from the

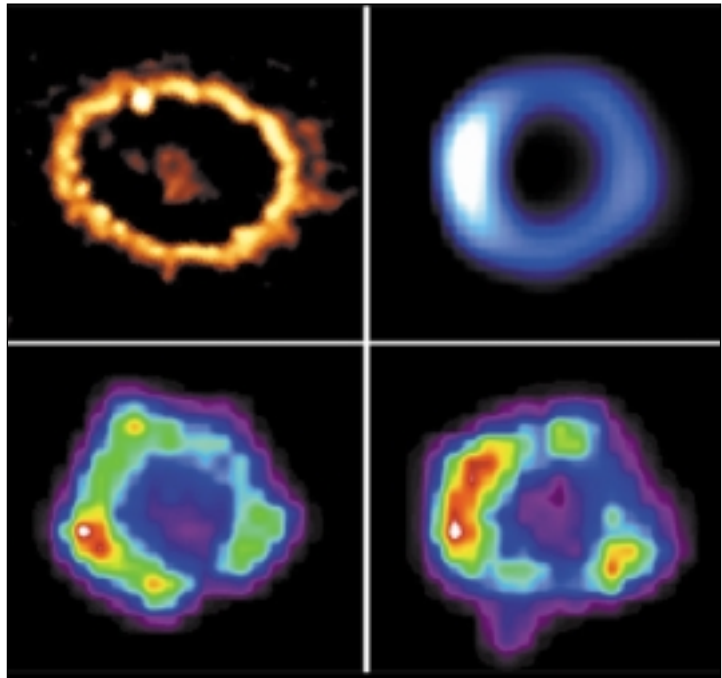
Accelerating Scientific Progress

BOOMERANG was designed to image the Cosmic Microwave Background (CMB). Work on BOOMERANG began shortly after the first detection of anisotropy by the COBE spacecraft. Though COBE detected anisotropy in the CMB, it was not able to resolve it. The challenge was to construct an experiment that could image the CMB with *40 times the angular resolution and 100 times the instantaneous sensitivity of COBE*. This was achieved by the BOOMERANG instrument, which was launched on a 10-day Antarctic voyage in late 1998, carrying a detector that had not existed just four years before. The results offer the first strong confirmation of the idea that the universe underwent a period of violent "inflation" during the first nanosecond after the Big Bang.



The BOOMERANG Telescope being readied for launch near Mt. Erebus in Antarctica. The 28 million cubic foot balloon carried the BOOMERANG telescope to an altitude of 120,000 feet, above 99 percent of the atmosphere.

exploration and mining of the statistically rich and unbiased databases. Another example is the data management and computing challenge posed by the Living With a Star (LWS) initiative. Special challenges posed by LWS include high performance computational methods for theoretical modeling and simulation, complex data analysis and visualization tools, correlative data analysis and visualization capabilities across widely varying spatial and temporal scales, and assimilation of observational data into theoretical models.



Images of the supernova SN1987A; combining information from several wavelengths helps unravel the mechanisms of astronomical phenomena. Clockwise from upper left: HST optical image; Australian Telescope Compact Array radio image; Chandra x-ray images from January 2000 and October 1999.

Setting the Stage for Future Missions

The Galileo mission has provided evidence that Europa has a liquid water ocean beneath its frozen crust, leading to speculation about possible sources of energy to support life in this ocean. Studies have indicated that without a ready supply of oxidized chemical species, the energy available for life would be minimal and any life on Europa would be very limited and difficult to detect. However, a recently developed alternative theory has revealed a novel pathway for chemical energy to be delivered to Europa. In this scenario, the intense radiation field surrounding Jupiter would produce oxidized and reduced carbon species that would be available to support life. This result is a vital consideration for the design of missions to search for life on Europa because it suggests searching the near-surface rather than penetrating kilometers of ice.

Responding to Unexpected Opportunities

On February 23, 1987, astronomers detected the first nearby supernova in 400 years. For the gamma ray measurements critical to understanding how new elements are formed in such a massive stellar explosion, NASA turned to its sub-orbital program as the only possible way to take advantage of this unprecedented but short-lived opportunity. A campaign of scientific balloon flights using gamma ray telescopes developed under the R&A program provided crucial evidence of how supernovae produce the heavy elements we see on Earth. Combined with observations from the ground and from space at other wavelengths, these gamma ray observations were key to developing a comprehensive picture of this stellar explosion.



[Supernova SN1987A](#)

Enabling a New Science

One of our most compelling questions is whether or not we are alone in the universe. If we are not, how does life emerge and evolve elsewhere in the universe? In fact, how did it appear on Earth? What is the future of life on Earth? These questions are the focus of the **astrobiology and exobiology** R&A program. Astrobiology has been at the forefront of an effort to break down discipline barriers to promote vigorous research at the boundaries between traditional scientific disciplines. Scientific debate on the potential for life on Europa, and even speculation on its possible nature, are recent examples of the resulting cross-disciplinary research that could motivate future missions.

To stimulate progress in astrobiology, the Space Science Enterprise recently created the Astrobiology Institute. The new Institute is an innovative virtual organization in which scientists throughout the country coordinate their research—and soon will be carrying out experiments—via high-speed computer links. It may be the most practical and efficient way to harness the highly diverse expertise of a geographically dispersed investigator population. The Astrobiology Institute will pioneer the technology that will enable teams of researchers and equipment scattered around the country, or even the world, to carry out front-line investigations.

education and public ou

Space Science Enterprise education and public outreach goals center on sharing the results of our missions and research programs with wide audiences and using space science discoveries as vehicles to improve teaching and learning at all levels. This is a deliberate expansion of the traditional role of the Enterprise in supporting graduate and postgraduate professional education, a central element of meeting our responsibility to help create the scientific workforce of the future. Our commitment to education now includes a special emphasis on pre-college education and on increasing the general public's understanding and appreciation of science, mathematics, and technology.

treach

Our policy for achieving our education and public outreach goals and objectives is to incorporate education and public outreach as an integral component of all of our activities, both flight missions and research programs. Contributing to education and outreach is the collective responsibility of all levels of Enterprise management and of all participants in the space science program. We focus on identifying

and meeting the needs of educators and on emphasizing the unique contribution space science can make to education and the public understanding of science. Our approach facilitates the effective participation of space scientists in education and outreach activities. Enterprise efforts are a significant element of NASA's overall education program and are aligned with the Agency's efforts to ensure that participation in

NASA missions and research programs is as broad as possible.

The two main elements of our education and public outreach program are support to education in the Nation's schools and informal education and public outreach that benefits both young people and adults.

With limited resources, high leverage is key to building a national pro-

Education and Outreach Implementation Approach

- Integrate education and outreach into Enterprise flight and research programs
- Encourage a wide variety of education and outreach activities
- Help space scientists participate in education and public outreach
- Optimize the use of limited resources by channeling individual efforts into highly leveraged opportunities
- Develop high quality education and outreach activities and materials having local, state, regional, and national impact
- Ensure that the results of our education programs and products are catalogued, archived, and widely disseminated
- Evaluate our activities for quality, effectiveness, and impact



Space science brings together inquiring minds of all ages.

gram that contributes both to improving teaching and learning at the pre-college level and to increasing the scientific literacy of the general public. The Enterprise achieves this leverage in **pre-college education** by building on existing programs, institutions, and infrastructure and by coordinating activities and encouraging partnerships with other ongoing education efforts. Such ongoing efforts include those inside NASA and within other Government agencies, and those being undertaken by non-governmental education organizations. We complement the very large investments in education being made by school districts, individual States, and other Federal

agencies, particularly by the National Science Foundation and the Department of Education. This entails establishing alliances with education-oriented professional societies, state departments of education, urban school systems, education departments at colleges and universities, and organizations that produce science materials intended for national distribution. Our efforts support local, state, and national efforts toward standards-based systemic reform of science, mathematics, and technology education. We use existing dissemination networks and modern information technology to make information and education programs and materials easily accessible.

The other main element of our program, enhancing the general public's understanding of science, develops new connections with **informal education and public outreach organizations** of many different types across the country. Alliances have been established with science museums and planetariums, as well as producers of public radio and television programs.

We will continue to explore new possibilities for partnerships and to experiment with new ways to bring the results of the space science program to teachers, students, and the public. For example, we will expand current partnerships and create new alliances with organizations such as the Boys and Girls Clubs of America, Girl Scouts of America, 4-H Clubs, professional societies for scientists and educators, public libraries, and rural museums.

We have made significant progress in these areas since the previous Enterprise Strategic Plan was released in 1997. We have embedded funded education and public outreach programs in all of our mission and research programs, established dozens of local, regional, and national partnerships, and established a national support network of education and outreach forums and brokers-facilitators (fully described in a separate Enterprise education and public outreach implementation plan).



The Space Weather Center exhibit introduces visitors to space weather and how it affects everyday life. An interactive exhibit, it incorporates near real-time data from NASA missions currently studying the Sun and near-Earth space. (The exhibit is a partnership of the Space Science Institute and NASA Goddard Space Flight Center.)

New education and public outreach efforts will build on these activities and accomplishments. For example, we will:

- Emphasize collaborations with science museums and planetariums. Collectively, these institutions attract more than 100 million visitors per year. They have enormous experience in developing and presenting public education programs. They also have the resources for creating such programs and are playing an increasingly important role in working with the formal education system. We plan to build on strong mutual interests between the Space Science Enterprise and the museum and planetarium community.
- Take advantage of the high technology nature of much of

the Space Science Enterprise's program to develop new materials and new programs in technology education. Many of the technologies being developed for our science program are also of great interest to the public, and we will explore ways to bring our technology as well as our science to the public.

- Develop, in collaboration with the NASA Office of Equal Opportunity Programs, new opportunities for underserved and underutilized groups to participate in space science missions, research, and education and outreach programs.
- Evaluate our education and outreach products and programs for quality and effectiveness. We must understand who our programs are reaching and what impact they are having, both on the formal education

system and on the general public's understanding of science. We will continue to improve our efforts based on regular feedback.

- Be alert for special events and particularly promising opportunities in our scientific program to bring space science to the public and to use space science to improve science, mathematics, and technology education at all levels. For example, our planned long-term program of Mars exploration provides an opportunity to literally "bring the American public along for the ride" and become genuine participants in the adventure of exploring another planet.

The full variety and scope of the Enterprise's current and planned education and outreach activities are described in our 1996 report "Implementing the Office of Space Science Education/Public Outreach Strategy." Our systemic approach, based on a long-term commitment to partnership with existing education and public outreach institutions, is making a significant and durable contribution to education and public understanding of science, mathematics, and technology.

partnerships

NASA's space science program exists within a much larger research and technology context that spans the globe. In some areas space science leads the pace of innovation, and in others it benefits from efforts and investments of others. Our pace of discovery is quickened by contributions from other U.S. Government agencies, U.S. universities and industry, and scientific collaborators around the world.

Other NASA Enterprises

Partnerships with other NASA Enterprises are essential to the Space Science Enterprise strategy. For example, the Space Science Enterprise works with the Human Exploration and Development of Space (HEDS) Enterprise to provide information essential to future human exploration and development of the Solar System. This includes scientific information about likely human destinations such as the Moon and Mars, surveys and characterization of space resources, and evaluation of space radiation hazards. The partnership with HEDS also involves using Enterprise missions to test technologies for human exploration of space and planetary environments.

HEDS, in turn, provides the Space Science Enterprise opportunities to accomplish investigations that would otherwise be impractical. For example, the Space Shuttle flies science pay-

loads such as telescopes to study the ultraviolet universe, sub-satellites to study the solar corona and the origin of solar wind, and cosmic dust collection experiments. The International Space Station

Partnerships with
other NASA
Enterprises are
essential to the
Space Science
Enterprise strategy.

will provide further opportunities for these and other types of investigations. Ultimately, some of the most important and complex science goals, such as understanding the possible origin and evolution of life on Mars, will be addressed by human explorers. Indeed,

answering questions of this magnitude may prove to be a significant part of the rationale for human exploration. Moreover, ambitious future space observatories may depend on human assistance in assembly, maintenance, and upgrading; the history of the Hubble Space Telescope provides brilliant examples of this synergy.

The Space Science, Earth Science, and new Biological and Physical Research Enterprises are jointly developing a program in Astrobiology, a new multidisciplinary research field that studies the origin and distribution of life in the universe, the role of gravity in living systems, and Earth's atmosphere and ecosystems.

Our studies of the Sun, the near-Earth space environment, Earth's middle and upper atmosphere, and other planets are also of interest to the Earth science community. For example, variations in solar radiation and particle emission cause variations in Earth's atmos-

phere. The study of other planets, particularly Venus and Mars, is another avenue to understanding why Earth is capable of sustaining life, and how global change processes might operate in other planetary settings.

The Aerospace Technology Enterprise also makes important contributions to the Space Science Enterprise. For example, aeronautics expertise at Ames Research Center supports the SOFIA airborne observatory program.

Our education and outreach programs are carried out in close collaboration with the Office of Human Resources and Education and the Office of Equal Opportunity Programs to ensure that space science initiatives complement existing activities and support NASA's overall programs in these areas.

Other U.S. Government Agencies

The National Science Foundation (NSF) has many programs that support or enhance NASA space science missions. NSF-supported ground-based research on the Sun, the planets, and the universe contribute to the intellectual foundations of many NASA space science flight missions. NASA and NSF jointly fund planet search

programs. NSF is also responsible for U.S. scientific activities in the Antarctic. NSF, the Smithsonian Institution, and NASA collaborate on the search for, collection, distribution, and curation of Antarctic meteorites. NASA and NSF have a joint program to use Antarctica as an analog for the space environment in developing long-range plans for Solar System exploration. NASA also uses Antarctica for a future generation of very long-duration balloon missions. There are close ties between NASA's astrobiology programs and NSF's Life in Extreme Environments (LEXEN) program.

The Department of Energy (DOE) similarly has a wide range of programs that support NASA space science activities. DOE has developed and supplied the radioisotope thermoelectric generators (RTGs) that have enabled a wide range of Solar System exploration missions—from Apollo to Viking to Voyager, as well as the Galileo and Cassini-Huygens missions to the outer planets. DOE has developed instruments and sensors for NASA's space science missions, particularly through its Los Alamos and Lawrence-Livermore Laboratories. DOE and NASA have jointly studied a mission to place high-energy particle detectors in space aboard

satellites and the International Space Station, and the agencies are working together on the Gamma Ray Large Area Space Telescope (GLAST). Data from DOE missions also support the International Solar Terrestrial Physics program.

For its part, the Department of Defense (DOD) has been a major developer of high sensitivity, large-area infrared detector arrays needed for many space science missions. These and technology for large-area deployable optical systems are important for future large telescopes in space. Through its Naval Research Laboratory (NRL), DOD has contributed instruments to space science missions such as the Compton Gamma Ray Observatory (CGRO) and the Solar and Heliospheric Observatory (SOHO). In another area, NASA and DOD cooperated on the Clementine mission, a DOD-led joint mission that surveyed the Moon. Space science, in turn, contributes to some DOD objectives. For example, research on solar flares, coronal mass ejections, solar energetic particles, and the terrestrial middle/upper atmosphere and magnetosphere is important for DOD command, control, and communications systems. DOD and NASA have established a partnership for expanded cooperation on the space environment.

In addition, NASA cooperates with the National Oceanic and Atmospheric Administration (NOAA) and DOD by providing data used for forecasting and understanding the space environment. This effort is part of an interagency (NASA, NSF, NOAA, DOD, DOE, Department of the Interior [DOI]) national space weather program. NASA also works closely with the U.S. Geological Survey of the Department of the Interior and the National Institute of Standards and Technology (NIST, Department of Commerce).

The formation of technology development partnerships is an important goal of the Space Science Enterprise. DOE, DOD, and other agencies such as NOAA share many needs and capabilities with NASA, and NASA works closely with them to identify opportunities for synergistic technology development.

In the education area, NASA works with NSF and the Department of Education to use space science missions and programs to contribute to science, mathematics, and technology education and to share the excitement of space science discoveries with the public. For example, we worked closely with the Department of Education's Gateway to Educational Materials Consortium to develop an online

From the
very beginning,
universities and
university scientists
have played a
central role in
the planning and
implementation
of space science.

resource directory for space science education products.

Universities

From NASA's very beginning, universities and university scientists have played a central role in the planning and implementation of space science. University scientists serve on NASA study teams and on key advisory committees that lay out long-range goals and objectives, strategies, and priorities for space science. University scientists develop new approaches for making critical measurements, serve as principal investigators for flight investigations, and carry out

the laboratory, theoretical, and computational studies required to interpret data returned from space science missions.

Universities exist to create new knowledge and to transmit it. The intellectual environment of universities encourages innovation. Thus, university scientists carry out basic space science research and other long-term research needed to investigate underlying principles that form the foundations of new technology. Universities have the principal responsibility for ensuring the steady stream of highly trained and motivated people needed to assure the future vitality of the Space Science Enterprise. Space science programs are also significant contributors to the ongoing development of scientists and engineers to meet larger national needs. Support from NASA flight projects and research grants programs is an important contributor to maintaining the infrastructure that permits this university participation.

The trend towards smaller, more frequent, and lower cost missions, together with the advent of advanced communications and information systems technologies, has allowed universities to take on greater responsibility for the design, development, and operation of entire missions rather than just the development of individual instru-

ments on larger NASA-developed missions. Easier electronic access to archived data and new policies that place science data in the public domain as soon as possible are helping scientists and students at a wide range of institutions, including colleges and smaller universities, to participate in the analysis of space science data.

For these reasons, the Space Science Enterprise is committed to a long-term partnership with our universities and their community of scientists and students.

Industry

Industry has made and will continue to make significant contributions to the planning, development and implementation of space science missions and research programs. Industry has played a critical role in the design, engineering, manufacture, construction, and testing of both large and small space missions; in the design, development, testing, and integration of advanced instruments; and in the development of advanced spacecraft, instrument, mission operations, and information system technologies. Many industry capabilities have been developed for commercial applications with DOD or NASA core technology support. The resulting extensive

The Space
Science Enterprise
is committed
to the long-term
support of
university research
and to continuing
to work closely
with university
scientists and
students.

space industry infrastructure is available for use for space science purposes. The establishment of partnerships with industry allows space science to benefit from the experience and capabilities of the industrial sector.

As noted earlier, universities are now partnering with industry to assume full responsibility for the design, development, and operation of entire missions. With the more frequent flight opportunities now being provided through the Explorer, Discovery, and

New Millennium programs, such partnerships are likely to play an even more important role in the Space Science Enterprise in the future. The reliance on the identification, development, and utilization of advanced technology to dramatically lower instrument, spacecraft, and mission operations costs requires strong partnerships between industry and the Enterprise. Strong partnerships are also important for facilitating the transfer of NASA-developed technology to industry and thereby realizing the commercial potential of these technologies and contributing to the long-term capability and competitiveness of American industry.

Other Nations

The quest for knowledge does not recognize national boundaries. Scientific expertise and capabilities are today more than ever distributed among many nations. Common interests and limited resources virtually dictate that nations cooperate in the pursuit of common goals. Further, the Space Act specifically mandates a leadership role for NASA in promoting international cooperation in space research. For all of these reasons, international cooperation is a fundamental aspect of virtually all Space Science Enterprise programs.

In some cases, other agencies and nations contribute to NASA-led missions. Foreign collaborators can join with U.S. teams to propose on NASA's competitive announcements, and foreign agencies can negotiate to stake out roles in U.S. strategic missions outlined in this and future plans. To support participation of U.S. investigators on foreign missions, the missions-of-opportunity option in Explorer and Discovery solicitations allows U.S. researchers to compete for funding to provide instrumentation or other contributions to missions developed by other countries or agencies.

International coordination of strategic planning poses a challenge, but one that merits continuing attention. Each agency, whether the European Space Agency or the numerous national agencies with which the Enterprise collaborates, has its own policies, planning cycles, funding processes, and scientific and technical priorities. The cooperative environment is characterized by a complex, but healthy, blend of competition and cooperation. But there is a general recognition, which NASA shares, that the opportunities for discovery outstrip the technical or financial resources of any individual player. As a result,



The Student-Tracked Atmospheric Research Satellite for Heuristic International Networking Experiment (STARSHINE) satellite leaves the cargo bay of the Space Shuttle *Discovery* near the completion of the STS-96 mission. The stowed Canadian-built remote manipulator system (RMS) arm is visible in the foreground.

we are continuing to work to better understand the goals and capabilities of our current and future partners, and we expect continuing

progress in maximizing all parties' returns on space science investment through cooperative approaches to space research.

a vision of the future

Sometime in the new century, humanity will know its place in the universe . . . and will begin the challenge of writing its future in the history of the cosmos. Our telescopes will have revealed in detail the most fundamental structures in nature: the galaxies and the stars. Life-bearing planets—if they exist—will have been at least tentatively identified. The next major step after detailed spectroscopy of planetary atmospheres must be imaging of their surfaces: even a dozen or so pixels in one direction across the face of an Earth-like planet orbiting a neighbor star would reveal continents and weather patterns, as well as seasonal variations. The optical designs for such an ambitious undertaking are not complicated, but pose enormous engineering challenges.

If there are new fundamental forces in nature that await discovery, we will have searched for them within the gravitational maelstrom of massive black holes and in the earliest moments after the Big Bang. Our most powerful x-ray interferometers will have revealed the detailed structure at the edges of black holes, and sub-millimeter interferometers will study the nature of gravity itself within the fossil remnant of the primordial fireball. The life story of our Milky Way galaxy, as its stars, planets, and life are built up from primordial atoms, will be much better understood.

Our most sophisticated robots will have traveled to the dark outer reaches of the Solar System and plunged beneath the icy surfaces of Europa and Titan, to seek out signs of organic activity, and perhaps, the struggles of life to maintain a foothold even in these forbidding environments. Closer to home, Mars will have been surveyed in detail, with sur-



The two Mars 2003 rovers will extend the surface exploration begun by Viking and Pathfinder. These new rovers will be able to travel 100 meters per day, and will carry scientific instruments to determine the geological context of rocks and soil and measure their chemical composition and fine scale structure—even scraping the surface off rocks to expose their unweathered interiors.

face samples returned to Earth for detailed study. Programs to survey the Red Planet for hidden resources of water will be well underway, as well as an extended geological and meteorological reconnaissance.

Our dynamic Sun and its surrounding planets will be understood as a system, including the effects of the Sun's life history on the origin and continuation of life in our Solar System. We will have gained the ability to predict and manage the effects of solar variability on Earth and on humans and machines in space. Our spacecraft will have ventured beyond the bubble of solar wind that surrounds the Solar System to take our first steps into interstellar space.

Thanks to technologies emerging today, Earthbound humanity will be able to participate actively in the great adventure of exploration. Our robotic emissaries to Mars and the other worlds in our Solar System will possess increasingly powerful capabilities for interaction with the home planet: virtual sight and sound, covering a broader spectrum of wavelengths and a far wider range of frequencies, will recreate on Earth the experience of exploring even the most forbidding environments in space. All our citizens will become space explorers.

At the same time, a new generation of technology may permit more



The Hubble Space Telescope (HST) was designed to be a serviceable spacecraft. An astronaut uses the Power Ratchet Tool on an HST bay door while replacing the observatory's flight computer.

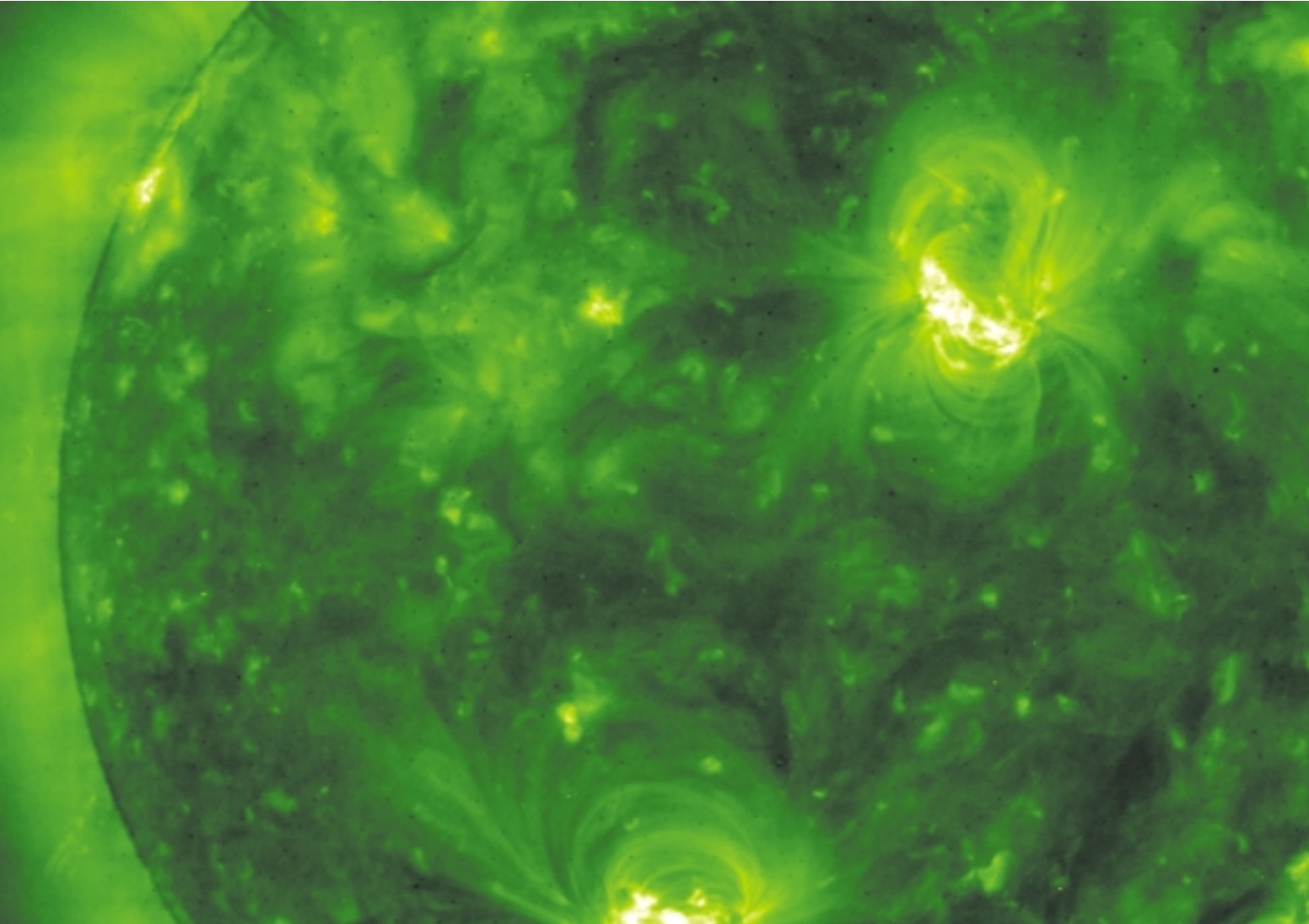
individuals, for a greater variety of reasons, to travel into space. It may be that future steps in understanding our place in the cosmos will be taken by a partnership between

humans and machines in space. Complex optical systems, satellite subsystems, and instruments may be better updated, replaced, or repaired by human partners than

by even very advanced remotely-operated robots. Trained geologists on Mars may one day amplify the capabilities of robotic collaborators used for large-area surveying and rapid reconnaissance by digging below the surface of dry riverbeds and along the shorelines of ancient oceans in search of the history of a biology—if any—beyond Earth.

One day, after our first planet-finding observatories have beamed back images of warm, wet worlds in orbit around neighboring stars, our descendants will begin to contemplate humanity's destiny of discovery beyond the Solar System.





The Solar and Heliospheric Observatory (SOHO) is a cooperative mission of ESA and NASA.



the space science enterprise

appendices

science goals and mission

Section A-1

Table A
Science Objectives, Research Focus Areas, and New Near-Term Missions*
(Implementation Begins 2003-2007)

		Mission Entering Implementation 2003-2007																				
Science Objective	Research Focus Area	NGST	Con-X	ACCESS	LISA	SIM	TPF	MEP	Europa Lander	Pluto-Kuiper	Titan Explorer	CNSR	Astro-biology	Solar Probe	MMS	GEC	MagCon	SDO	NEO			
Understand the structure of the universe, from its earliest beginnings to its ultimate fate	Identify dark matter and learn how it shapes galaxies and systems of galaxies	☐	☐																			
	Determine the size, shape, age, and energy content of the universe		☐																			
Explore the ultimate limits of gravity and energy in the universe	Discover the sources of gamma ray bursts and high energy cosmic rays			■																		
	Test the general theory of relativity near black holes and in the early universe, and search for new physical laws using the universe as a laboratory		☐		■																	
Learn how galaxies, stars, and planets form, interact, and evolve	Reveal the nature of cosmic jets and relativistic flows		☐																			
	Observe the formation of galaxies and determine the role of gravity in this process	■	☐																			
	Establish how the evolution of a galaxy and the life cycle of stars influence the chemical composition of material available for making stars, planets, and living organisms	☐	■																			
	Observe the formation of planetary systems and characterize their properties	☐				☐																
Look for signs of life in other planetary systems	Use the exotic space environments within our Solar System as natural science laboratories and cross the outer boundary of the Solar System to explore the nearby environment of our galaxy													☐								
	Discover planetary systems of other stars and their physical characteristics					■	☐															
Search for worlds that could or do harbor life						☐	■															

Table A (continued)

		Mission Entering Implementation 2003–2007																		
Science Objective	Research Focus Area	NGST	Con-X	ACCESS	LISA	SIM	TPF	MEP	Europa Lander	Piuto-Kuiper	Titan Explorer	CNSR	Astro-biology	Solar Probe	MMS	GEC	MagCon	SDO	NEO	
Understand the formation and evolution of the Solar System and Earth within it	Inventory and characterize the remnants of the original material from which the Solar System formed									■		■								
	Learn why the planets in our Solar System are so different from each other							□		□										
	Learn how the Solar System evolves							□	□	□	■	□								
Probe the origin and evolution of life on Earth and determine if life exists elsewhere in our Solar System	Investigate the origin and early evolution of life on Earth, and explore the limits of life in terrestrial environments that might provide analogues for conditions on other worlds												■							
	Determine the general principles governing the organization of matter into living systems and the conditions required for the emergence and maintenance of life												□							
	Chart the distribution of life-sustaining environments within our Solar System and search for evidence of past and present life								■		□		□							
	Identify plausible signatures of life on other worlds												□							
Understand our changing Sun and its effects throughout the Solar System	Understand the origins of long- and short-term solar variability													□				■		
	Understand the effects of solar variability on the solar atmosphere and heliosphere													■				□		
Chart our destiny in the Solar System	Understand the space environment of Earth and other planets																	■		
	Understand forces and processes, such as impacts, that affect habitability of Earth																		■	
	Develop the capability to predict space weather																		□	
	Find extraterrestrial resources and assess suitability of Solar System locales for future human exploration							□											□	

* ■=key (most important) research focus area addressed by a mission or program; □=other research focus areas addressed (a mission may have more than one). Projects in the Discovery and Explorer programs of community-formulated missions that will proceed to implementation in the 2003–2007 period have not been proposed or selected yet, but are expected to make focused contributions in numerous areas.

Table B
Science Objectives and Representative Mission Concepts
 (For Possible Implementation After 2007)

Representative Mission Concepts	Science Objectives							
	Understand the structure of the universe, from its earliest beginnings to its ultimate fate	Explore the limits of gravity and energy in the universe	Learn how galaxies, stars, and planets form, interact, and evolve	Look for signs of life in other planetary systems	Understand the formation and evolution of the Solar System and Earth within it	Probe the origin and evolution of life on Earth and determine if life exists elsewhere in the Solar System	Understand our changing Sun and its effects throughout the Solar System	Chart our destiny in the Solar System
Space infrared interferometric telescope	■		■					
Filled aperture infrared telescope	■		■					
Space VLBI		■	■					
X-ray interferometry pathfinder		■	■					
Orbiting wide-angle light collector	■	■						
Cosmic microwave background polarization	■							
Space ultraviolet optical telescope			■					
High resolution x-ray spectroscopy mission		■	■					
Energetic x-ray imaging survey telescope		■						
Interstellar probe			■				■	
Planet imager				■				
Life finder				■				
Future Mars Exploration					■			■
Neptune orbiter					■			
Venus surface sample return					■			
Saturn ring observer			■					
Europa subsurface explorer						■		
ITM wave imaging							■	
Solar polar imager							■	
Future Living With a Star							■	■

glossary of missions

Advanced Composition Explorer (ACE)—Measures energetic particles over a wide range of energy and mass, including the solar wind, solar particles, and the anomalous and galactic cosmic rays. The spacecraft measures the elemental and isotopic composition, from hydrogen to zinc, over the energy range of the cosmic rays from 100 eV to 500 MeV per nucleon for the charge range. ACE also provides realtime solar data from L1 for space weather applications.

Advanced Cosmic Ray Composition Experiment for the Space Station (ACCESS)—Attached payload for the International Space Station (ISS), it will measure the energy spectra from hydrogen to iron up to 10^{15} eV in order to test the supernova origin theory of cosmic rays.

Advanced Satellite for Cosmology and Astrophysics (ASCA)—Japanese x-ray imaging spectrometer mission. Launched in 1993, it served double its expected lifetime before suffering debilitating damage after an intense solar storm in July 2000.

Balloon Observations Of Millimetric Extragalactic Radiation and Geophysics (BOOMERANG)—Balloon-borne instrument that measured tiny variations in the cosmic microwave background radiation in order to detect the earliest ancestors of today's galaxies and to obtain indications that the geometry of the universe is flat, not curved. Jointly supported in the U.S. by NASA and NSF, BOOMERANG's science team included members from Canada, Italy, and the United Kingdom.

Cassini-Huygens—International mission involving NASA, the European Space Agency (ESA), the Italian Space Agency (ASI), and several separate European academic and industrial partners. The spacecraft carries a sophisticated complement of scientific sensors supporting 27 different investigations to probe the mysteries of the Saturn system. The mission consists of a NASA orbiter and ESA's Huygens Titan probe.

Chandra X-ray Observatory (CXO)—High resolution imaging and spectroscopy mission to observe high-energy cosmic events such as pulsars, supernova remnants, and black holes.

Cluster-2—ESA-led mission to study plasma structures, boundary layers, and energy transfer in three dimensions both within Earth's magnetosphere and in the solar wind. The mission consists of four identical spacecraft, each carrying a full complement of fields and particles instrumentation, flying in tetrahedral formation.

Comet Nucleus Tour (CONTOUR)—Will study the aging processes of comets by examining diverse comet nuclei. Using an innovative trajectory design, this spacecraft will conduct close-up observations of two short period comets, Encke and Schwassmann-Wachmann 3, known from ground-based telescopic observations to have different properties. An encounter with a third short period comet may be possible if sufficient resources remain for an extended mission. This is the sixth Discovery mission.

Compton Gamma Ray Observatory (CGRO)—Simultaneously obtained gamma ray measurements in an energy range spanning six orders of magnitude from 30 KeV to 30 GeV. The mission made many fundamental discoveries, including the discovery that gamma ray bursts are not galactic phenomena as previously believed, and that active nuclei of distant galaxies are dynamic and prolific emitters of enormous amounts of energy in high-energy gamma rays. CGRO was deorbited in June 2000.

Constellation X (Con-X)—Mission to measure x-ray spectral lines in hot plasmas in order to determine the elemental composition, temperature, and velocity of the emitting matter. Objectives are to determine the flow of gas in accretion disks around black holes in active galactic nuclei and in binary x-ray sources, measure the abundances of newly created elements in supernova remnants, and detect the influence of dark matter on the hot intergalactic medium in clusters of galaxies.

Cosmic Background Explorer (COBE)—Made precise measurements of the diffuse radiation with wavelengths between one micrometer and one centimeter over the entire celestial sphere, providing the first major step forward in space-based cosmology. COBE verified beyond all reasonable doubt that the cosmic microwave background has a cosmological origin with tiny primordial perturbations from which large-scale structure in the present-day universe grew.

Cosmic Journeys—Proposed initiative to probe the most profound aspects of nature by using the universe as a laboratory. Within the Cosmic Journeys initiative, the Journey to a Black Hole probes more and more closely to these extreme states of gravity. The Journey to Dark Matter seeks to unravel the mysterious nature of the universe's "missing mass," matter that we cannot see but know is present due to its gravitational effect on the visible universe. And the Journey to the Beginning of Time explores the basic physics revealed in the first few instants of the universe, observing as far back as the first 10^{-32} seconds of time.

Deep Impact—Will determine the composition of pristine material in a comet nucleus. The spacecraft will send a 500 kilogram projectile into the nucleus of comet Temple 1 to excavate a crater deep enough to penetrate beneath the chemically-altered crust of the nucleus. Experiments on the spacecraft will then examine the properties of the ejected material and observe the structure of the crater. The eighth Discovery mission.

Deep Space-1 (DS-1)—Technology validation mission that successfully validated solar electric propulsion and a suite of eleven other high priority spacecraft technologies.

Discovery Program—Level-of-effort program offering the scientific community regular opportunities to propose low-cost deep space missions. Proposals are selected through competitive peer review, and selected teams have responsibility for implementation of the entire mission with minimal management oversight by NASA. Teaming arrangements among university, industry, and/or Government laboratories are encouraged. Discovery is the deep space counterpart of the Explorer program.

Europa Orbiter—Will orbit this icy moon of Jupiter to determine if there is an underlying ocean, determine the thickness of the ice, and image the complex features on its icy surface. To determine if there is an ocean, the orbiter may use radar sounding, high-resolution laser altimeters, and free-falling probes equipped with seismometers. As a possible liquid water habitat in our Solar System, Europa is a critical target in the search for life beyond Earth.

Explorer Program—Level-of-effort program to provide frequent, low-cost access to space for physics and astronomy investigations with small to mid-sized spacecraft. Investigations selected for Explorer projects are usually of a survey nature, or have specific objectives not requiring the capabilities of a major observatory.

Extreme Ultraviolet Explorer (EUVE)—Explorer mission to survey the entire sky in the extreme ultraviolet, discover the brightest sources in the sky, and perform detailed spectroscopic investigations of the EUV radiation from stars, nebulae, and galaxies. EUV radiation provides unique information concerning the physical and chemical properties of hot gas and plasma, and this information contributes to our knowledge of the matter and energy interactions between stars and the interstellar medium.

Far Infrared and Submillimeter Telescope (FIRST)—ESA-led mission to study objects that radiate a substantial portion of their luminosity in this band. This includes detecting dusty galaxies at cosmological distances when the universe was less than one billion years old, regular spiral galaxies out to intermediate redshifts, and dense molecular clouds in our galaxy where stars are currently being formed. This will allow a study of the dynamical and chemical evolution of galaxies and stars.

Far Ultraviolet Spectroscopic Explorer (FUSE)—Explorer mission conducting high-resolution spectroscopy of faint objects at wavelengths from 905 to 1,195 angstroms. FUSE is probing the interstellar medium and galactic halo to measure the amount of cold, warm, and hot plasma in objects ranging from planets to quasars, including primordial gas created in the Big Bang.

Fast Auroral Snapshot Explorer (FAST)—Small Explorer mission investigating the plasma physics of various auroral phenomena at extremely high time and spatial resolution. In polar orbit around Earth, the spacecraft carries fields and particle instrumentation and features fast data sampling and a large burst memory.

Full-sky Astrometric Mapping Explorer (FAME)—Explorer to determine accurate positions, distances, and motions of 40 million stars within our galactic neighborhood. FAME will measure stellar positions to less than 50 microarcseconds.

Galaxy Evolution Explorer (GALEX)—Explorer space ultraviolet mission to map the global history and causes of star formation over the redshift range $0 < z < 2$, 80 percent of the life of the universe. GALEX will also explore the period over which galaxies have evolved dramatically, and the time that most stars, elements, and galaxy disks had their origins.

Galileo Europa Mission (GEM)—Conducted the first comprehensive investigation of Jupiter, its magnetosphere, and its planet-size moons. On its arrival at Jupiter in December 1995, Galileo dropped an entry probe into the planet's atmosphere that returned the first direct measurements of the physical properties and chemical composition of a gas giant planet. The orbiter discovered magnetic fields belonging to two of the satellites and has given us close-up views of their surfaces. The two-year Galileo Europa Mission, which focused primarily on the satellite Europa, followed the prime Galileo mission.

Gamma Ray Large Area Space Telescope (GLAST)—Mission to observe the gamma ray energy range from 20 MeV to 300 GeV. Fifty times more sensitive than the EGRET instrument on the Compton Gamma Ray Observatory, this instrument will observe thousands of active galactic nuclei (AGNs) and galactic sources, in addition to studying the more diffuse emissions from the Milky Way and other extended sources, including the diffuse all-sky background. A burst monitor will combine with the primary instrument to provide gamma ray burst observations over a wide energy range. Cooperative with the Department of Energy, Japan, and Europe.

Genesis—Mission to determine accurately the chemical composition of the Sun. The spacecraft will expose panels of ultra-pure materials to the solar wind for two years to collect samples of the material that continually streams off of the Sun. These samples will then be returned to Earth for detailed laboratory analysis. The fifth Discovery mission.

Geospace Electrodynamics Connections (GEC)—Near-term Solar Terrestrial Probe to help us understand how the interaction of Earth with the interplanetary medium is conditioned by the presence of Earth's atmosphere and its magnetic field. The mission will consist of four spacecraft following each other in the same orbit with variable spacing. The spacecraft generally fly in highly inclined elliptical parking orbits, but focused science campaigns will be conducted during satellite excursions down to 130 km or lower.

Geotail—ISAS-led mission to measure global energy flow and transformation in the magnetotail in order to increase our understanding of fundamental magnetospheric processes.

Global Geospace Science (GGS)—Consists of the Wind and Polar spacecraft and is part of the U.S. contribution to the International Solar Terrestrial Physics (ISTP) program. The objectives of GGS are to measure, model, and quantitatively assess geospace processes in the Sun-Earth interaction chain.

Gravity Probe B (GP-B)—Will test Einstein's general theory of relativity by measuring predicted dragging of space-time caused by the rotation of Earth. In order to make this measurement, GP-B will fly the world's most perfect sphere as a gyroscope. Also known as the Relativity Mission.

High Altitude Laboratory for Communications and Astrophysics (HALCA)—ISAS radio telescope in orbit that can be combined with large radio antennae on Earth to create a highly sensitive radio interferometric array. HALCA demonstrated the feasibility of space-Earth arrays and observation of fine structure in radio galaxies, jets from active galactic nuclei, and supernova remnants.

High Energy Solar Spectrographic Imager (HESSI)—Explorer mission to study the basic physics of the particle acceleration and explosive energy release in solar flares. HESSI will carry an x-ray and gamma ray imaging spectrometer with ultra-high temporal and spatial resolution in order to address the dynamic high-energy phenomena of the Sun.

High Energy Transient Explorer 2 (HETE 2)—Small mission to search for and detect the prompt x-ray and ultraviolet emission that may accompany gamma ray bursts, as well as measure their position and send the information to ground based optical telescopes fast enough to allow the prompt optical emission to be detected as well. Cooperative mission with Japan and France.

Hubble Space Telescope (HST)—Explores the universe in the visible, ultraviolet, and near-infrared regions of the electromagnetic spectrum. It is investigating the composition, physical characteristics, and dynamics of celestial bodies, examining the formation, structure, and evolution of stars and galaxies, studying the history and evolution of the universe, and providing a long-term space-based research facility for optical astronomy. Cooperative with ESA.

Imager for Magnetospheric to Aurora Global Exploration (IMAGE)—Explorer mission observing the response of Earth's magnetosphere to changes in the solar wind. The mission uses a combination of neutral atom, ultraviolet, and radio imaging techniques to provide global views of magnetospheric dynamics from a polar orbit.

Infrared Astronomical Satellite (IRAS)—Joint mission sponsored by the United Kingdom, the United States, and the Netherlands, that mapped the sky at infrared wavelengths. Mission ended in 1983.

Infrared Space Observatory (ISO)—ESA follow-on to IRAS, explored the "cool and hidden" universe through observations in the thermal infrared between 3 and 200 microns. Its objectives included studies of brown dwarfs in our galaxy, protoplanetary disks around nearby stars, and the evolution of galaxies.

International Gamma Ray Astrophysics Laboratory (INTEGRAL)—ESA-led gamma ray observatory dedicated to spectroscopy and imaging in the energy range 15 keV to 10 MeV. In addition to two gamma ray instruments it will have optical and x-ray monitors. This mission will study gamma ray lines from a range of astrophysical sources, giving us information on nucleosynthesis in supernovae, the supernova history of the Milky Way, active galactic nuclei, Seyfert galaxies, gamma ray bursts, and solar flare acceleration processes.

Keck Interferometer—Ground-based program to harness the twin 10-meter Keck telescopes together as a single instrument to search for planetary systems around other stars. This will complement and extend current ground-based planet detection capabilities and will serve as a prototype/test bed for future interferometers in space such as SIM and Terrestrial Planet Finder.

Laser Interferometer Space Antenna (LISA)—Joint NASA-ESA mission to detect and study in detail gravitational wave signals from massive black holes. This includes both transient signals from the terminal stages of binary coalescence, which we will call bursts, and binary signals that are continuous over the observation period.

Living With A Star (LWS)—Program to develop the scientific understanding of aspects of the connected Sun-Earth system that directly affect life and society, with specific emphasis on understanding the factors that affect human radiation exposure in space, the impacts of space weather on technical systems, and the effects of solar variability on the terrestrial climate. Program elements include the Solar Dynamics Observatory (SDO), Radiation Belt Mappers (RBM), Ionospheric Mappers (IM), and Sentinels missions; a program of space environmental test beds; and an associated theory, modeling, and data analysis program.

Lunar Prospector—Conducted the first global survey of minerals on the surface of the Moon. Of particular interest for future human exploration of the Moon, Lunar Prospector detected indications of water ice in the perpetually dark bottoms of craters near the north and south poles. The third Discovery mission.

Magnetospheric Multiscale (MMS)—Near-term Solar Terrestrial Probe to characterize the basic plasma processes that control the structure and dynamics of Earth's magnetosphere, with a special emphasis on meso- and micro-scale processes. The mission will consist of a constellation of five identical spacecraft, each carrying fields and particle instrumentation, flying in a variably spaced tetrahedron.

Magnetosphere Constellation (MagCon)—Solar Terrestrial Probe mission to understand the nonlinear dynamic responses and connections within Earth's magnetotail. It envisions placement of 50-100 autonomous micro-satellites, each carrying a minimum set of fields and particles instruments, into a variety of orbits.

Mars Exploration Program (MEP)—Program of successive Mars exploration missions to study: the solid planet, how it evolved, and what resources it provides for future exploration; the relationship to Earth's climate change process; and the potential for life there and elsewhere in the universe. The exploration series began with Mars Global Surveyor to orbit Mars and map the planet at infrared and visible wavelengths and observe selected areas at very high-resolution. MEP data will help us understand the geological and climatological history of the planet and lay the groundwork for choosing the sites for surface missions. The subsequent two missions, Mars Climate Orbiter (MCO) and Mars Polar Lander (MPL), were lost in 1999. Two geologic exploration rovers will be launched in 2003. Additional orbiter and lander missions to follow are under study.

Mars Pathfinder—Paved the way for future low-cost, robotic missions to Mars. The mission deployed a micro-rover named Sojourner on the Martian surface and acquired geological and meteorological data to characterize the surface composition, geology, morphology, and atmospheric structure and conditions in Ares Valles. The second Discovery mission.

Mercury Surface, Space Environment, Geochemistry, and Ranging (MESSENGER)—Will conduct a comprehensive global survey of Mercury's interior structure, surface composition, geological processes, tenuous atmosphere, and magnetic field. The spacecraft will operate in orbit around Mercury for approximately one Earth year. The seventh Discovery mission.

Microwave Anisotropy Probe (MAP)—Follow-on to the successful COBE mission, MAP is a medium-class Explorer to measure the fluctuations in the cosmic microwave background with sufficient sensitivity to infer whether the first large structures in the universe after the Big Bang were galaxies or large clusters of galaxies. MAP's observations will also be sensitive enough to determine the total amount of dark matter in the early universe.

MUSES-C—ISAS-led mission to return a sample from an Earth-approaching asteroid. NASA will contribute a micro-rover to explore the asteroid's surface.

Near Earth Asteroid Rendezvous (NEAR)—In orbit around Earth-approaching asteroid Eros, NEAR is conducting the first comprehensive investigation of the physical properties and mineral characteristics of one of these small bodies. The first Discovery mission.

New Millennium Program (NMP)—Flight program to demonstrate new technologies in space.

Next Generation Space Telescope (NGST)—Follow-on observatory to HST to study the formation of galaxies at near infrared wavelengths. It will combine a collecting area 10 times larger than HST with spectrometers optimized for near infrared radiation.

Planck—ESA-led third generation mission for exploring the fluctuations and anisotropies in the cosmic microwave background. Planck will improve previous measurements of the background by a factor of five.

Pluto/Kuiper Express—Miniaturized spacecraft to fly past the Pluto/Charon system and conduct a reconnaissance of the only planet that has not been visited heretofore by a spacecraft. Following the Pluto/Charon encounter, the spacecraft may be redirected to survey a diverse collection of icy Kuiper Belt objects beyond the orbit of Neptune.

Polar—Measures the entry of plasma into the polar magnetosphere, determines the ionosphere plasma outflow, obtains auroral images, and determines the energy deposited into the ionosphere and upper atmosphere. Polar is the second spacecraft in the Global Geospace Science program; it carries in situ fields and particles instrumentation and a remote sensing imager.

Roentgen Satellite (ROSAT)—International collaborative mission to observe and map x-ray emissions from galactic sources. ROSAT studied coronal x-ray emissions from stars of all spectral types, detecting and mapping x-ray emissions from galactic supernova remnants, evaluating the overall spatial and source count distributions for various x-ray sources. Additionally, ROSAT performed detailed studies of various populations of active galaxy sources, conducting morphological studies of the x-ray emitting clusters of galaxies, and performing detailed mapping of the local interstellar medium. Cooperative with Germany and the United Kingdom.

Rossi X-ray Timing Explorer (RXTE)—Explorer mission to detect fluctuations in the x-ray intensity of cosmic sources that occur as rapidly as one millisecond or less. RXTE also studies the x-ray emission over a broad spectral band and a wide range of time scales in x-ray sources of all kinds. These capabilities enable astronomers to study accretion onto black holes in sources as different as x-ray binaries in our galaxy and the cores of active galaxies and quasars millions of light-years away.

Solar and Heliospheric Observatory (SOHO)—ESA-led mission, component of the International Solar Terrestrial Physics program, to study the internal structure of the Sun, its outer atmosphere, and the origin of the solar wind. The spacecraft carries instruments devoted to helioseismology, remote sensing of the solar atmosphere, and in situ measurement of solar wind disturbances.

Solar Anomalous and Magnetospheric Particle Explorer (SAMPEX)—A small Explorer mission to investigate the origins and dynamics of solar energetic particles, heavy ions and electrons in the radiation belts, and anomalous cosmic rays. Its instruments observe the energy range from low energy solar particles to galactic cosmic rays.

Solar Dynamics Observer—First mission in the Living with a Star program, will observe the outer layers of the Sun to determine the Sun's interior dynamics and the origin of solar activity and coronal mass ejections.

Solar Probe—Will make the first measurements within the atmosphere of a star and will answer long-standing questions about how and where the corona is heated and how the solar wind is accelerated. The spacecraft, which will carry both imaging and in situ instrumentation, is targeted to pass within three solar radii of the Sun's surface.

Solar Terrestrial Probes (STP)—Program of successive missions to perform a systematic study of the Sun-Earth system. Its major goals are to provide an understanding of solar variability on time scales that range from a fraction of a second to many centuries and to determine planetary and heliospheric responses to this variability. The line begins with TIMED and is expected to continue near-term with Solar-B, STEREO, Magnetospheric Multiscale, Global Electrodynamical Connections, and Magnetospheric Constellation.

Solar Terrestrial Relations Observatory (STEREO)—Near-term Solar Terrestrial Probe to understand the origin and development of coronal mass ejections and trace the propagation and evolution of these disturbances from the Sun to Earth. The mission will consist of two identical spacecraft, one leading and the other lagging Earth in its orbit. Both spacecraft will carry instrumentation for solar imaging, for the tracking of solar ejection heading toward Earth, and for in situ sampling of the solar wind.

Solar-B—ISAS-led mission to reveal the mechanisms that give rise to solar variability and study the origins of space weather and global change. The spacecraft, which will be placed in polar Earth orbit, will make coordinated measurements at optical, EUV, and x-ray wavelengths, and will provide the first measurements of the full solar vector magnetic field on small scales.

Space Interferometry Mission (SIM)—First optical interferometer in space and a technological precursor to the Terrestrial Planet Finder. SIM will allow indirect detection of planets through observation of thousands of stars and investigate the structure of planetary disks with nulling imaging.

Stardust—Will fly through the coma of comet Temple-II, collect a sample of cometary dust, and return the sample to Earth for detailed laboratory analysis. A suite of remote-sensing instruments on the spacecraft will also investigate various physical and chemical properties of the comet. The fourth Discovery mission.

Stratospheric Observatory for Infrared Astronomy (SOFIA)—The next generation airborne observatory, SOFIA will provide astronomers routine access to the infrared and submillimeter part of the electromagnetic spectrum. It will observe a wide range of phenomena, from the formation of planets, stars, and galaxies, to the evolution of complex organic molecules in interstellar space. SOFIA will be ten times more sensitive than its predecessor, the Kuiper Airborne Observatory, enabling observations of fainter objects and measurements at higher spectral resolution. Cooperative with Germany.

Space Infrared Telescope Facility (SIRTF)—The fourth of NASA's Great Observatories and a follow-on to the Infrared Astronomical Satellite (IRAS). SIRTF will perform imaging and spectroscopy in the infrared of the formation of stars and planets and will investigate the evolution of luminous galaxies.

Submillimeter Wave Astronomy Explorer (SWAS)—Small Explorer mission to study water and other similar molecules throughout the galaxy. By measuring the density and distribution of these materials, the origin of ingredients necessary for life on Earth can be determined.

Swift Gamma Ray Burst Explorer—Explorer mission multiwavelength observatory for gamma ray burst astronomy. Swift has a complement of three co-aligned instruments. Two are an x-ray and a UV/optical focusing telescope that will produce arcsecond positions and multiwavelength light curves for gamma ray burst (GRB) afterglow. A third instrument is a wide field-of-view coded-aperture gamma ray imager that will produce arcminute GRB positions onboard within 10 seconds.

Terrestrial Planet Finder (TPF)—Currently envisioned as a long baseline infrared interferometer operating in the 7-20 micron wavelength range for direct detection of terrestrial planetary companions to other stars and of spectral signatures that might indicate a habitable planet.

Thermosphere-Ionosphere-Mesosphere Energetics and Dynamics (TIMED)—Solar Terrestrial Probe to understand the basic energetic and dynamics of the region where Earth's atmosphere transitions to space. The spacecraft, which will fly in a 600-km circular Earth orbit, carries remote sensing instrumentation that will be supplemented by significant collaborative investigations.

Titan Explorer—Mission to follow up on the scientific results at Titan expected from the Huygens probe and Cassini orbiter. Detailed study of the organic-rich environment of Titan may be of key importance to studies of pre-biotic chemistry.

Transition Region and Coronal Explorer (TRACE)—Small Explorer mission exploring the connection between fine-scale solar magnetic fields and the associated plasma structures. The spacecraft, which is in Sun-synchronous Earth orbit, carries a EUV/UV telescope for studies of fast-evolving dynamic phenomena on the Sun at one arc-second spatial resolution.

Two Wide-angle Imaging Neutral-atom Spectrometers (TWINS)—An Explorer program-supported Mission of Opportunity payload with the goal of assessing the geo-response to solar wind input. This will be accomplished through analysis of the first stereo views of Earth's magnetosphere, which will be provided by the flight of a pair of energetic neutral atom imagers on spacecraft with complementary orbits.

Ulysses—ESA-led mission to explore the high-latitude regions of the Sun and inner heliosphere. The spacecraft passes over the Sun's poles at a distance of about 2 AU and carries a variety of fields and particles instruments.

Voyager Interstellar Mission (VIM)—Combines the capabilities of the Voyager 1 and 2 spacecraft to explore the region where the Solar System merges with the interstellar medium and to sample the local interstellar medium itself. These spacecraft are now both beyond the orbit of Pluto and are speeding toward the edge of the Solar System.

Wind—Part of the Global Geospace Science Program. The goals of Wind are to determine the characteristics of the solar wind upstream of Earth and to investigate basic plasma processes occurring in the near-Earth solar wind. It also carries two modest-sized gamma ray burst instruments for measuring the spectra and count rate time-history of gamma ray bursts.

X-ray Multiple-mirror Mission (XMM)—ESA-led x-ray spectroscopy mission to determine the abundance and density of iron, silicon, oxygen, and other heavy elements in stars and x-ray binaries. An understanding of the cycling of these elements between stars and the interstellar medium is necessary for studying the formation of planets.

Yohkoh—ISAS-led mission to better understand the birth and evolution of various forms of solar activity, especially solar flares. Because x-rays outline the magnetic structure of the Sun's outer atmosphere, the spacecraft carries instrumentation that combines hard and soft x-ray imaging and spectroscopy.

Space Science Enterprise Concurrence

Edward J. Weiler, Associate Administrator
Earle K. Huckins, Deputy Associate Administrator
Jeffrey D. Rosendhal, Assistant Associate Administrator for Education and Public Outreach
Alan N. Bunner, Director for Structure and Evolution of the Universe
Scott Hubbard, Director for Mars Exploration
Anne L. Kinney, Director for Astronomical Search for Origins
Kenneth W. Ledbetter, Director for Flight Programs
Jay T. Bergstralh, Acting Director for Exploration of the Solar System
Guenter R. Riegler, Director of Research Program Management
Peter B. Ulrich, Director for Technology
George L. Withbroe, Director for Sun-Earth Connection

Enterprise Strategic Planning Working Group

Marc S. Allen (Lead), Assistant Associate Administrator for Strategic and International Planning
Ruth A. Netting (Coordinator), Senior Program/Policy Analyst
Jay T. Bergstralh, Planetary Science Discipline Scientist
Hashima Hasan, Origins Discipline Scientist
Donald Kniffen, High Energy Astrophysics Discipline Scientist
Mary M. Mellott, Geospace Discipline Scientist
Michael A. Meyer, Astrobiology Discipline Scientist
Jeffrey D. Rosendhal, Assistant Associate Administrator for Education and Public Outreach
Harley A. Thronson, Decade Planning Team Senior Science Manager
Giulio Varsi, Senior Technologist
Joel Vendette, Senior Graphic Designer
Hope Kang, Technical Writer/Editor

and acknowledgments

Acknowledgments

The NASA Office of Space Science would like to express appreciation for the work undertaken by the members of our science community to help formulate program options and prepare this Strategic Plan.

Galveston Strategic Planning Workshop Participants, November 2-4, 1999

David Akin, University of Maryland
Joseph Alexander, National Research Council
Louis Allamandola, NASA Ames Research Center
Marc Allen, NASA Headquarters
Christine Anderson, Air Force Research Lab
Charles Beichman, NASA Jet Propulsion Laboratory
Steven Benner, University of Florida
Jay Bergstralh, NASA Headquarters
Richard Binzel, Massachusetts Institute of Technology
David Black, Lunar and Planetary Institute
Baruch Blumberg, NASA Ames Research Center
Alan Boss, Carnegie Institution
Alan Bunner, NASA Headquarters
James Burch, Southwest Research Institute
Mike Calabrese, NASA Goddard Space Flight Center
Wendy Calvin, U.S. Geological Survey
Robert Carovillano, Boston College
Andrew Christensen, The Aerospace Corporation
Chris Chyba, SETI Institute
David DesMarais, NASA Ames Research Center
Michael Drake, University of Arizona
Charles Elachi, NASA Jet Propulsion Laboratory
Gordon Garmire, Pennsylvania State University
Paula Frankel, NASA Consultant
Robert Gehrz, University of Minnesota
Hashima Hasan, NASA Headquarters
Isabel Hawkins, University of California at Berkeley
John Hayes, Woods Hole Institute
Paul Hertz, Naval Research Laboratory
Robert Hoffman, NASA Goddard Space Flight Center
Steven Horowitz, NASA Goddard Space Flight Center
Richard Howard, NASA Headquarters
Scott Hubbard, NASA Ames Research Center

Galveston Strategic Planning Workshop Participants (continued)

Kenneth Johnston, U.S. Naval Observatory
Anne Kinney, NASA Headquarters
Donald Kniffen, NASA Headquarters
Edward (Rocky) Kolb, Fermi National Accelerator Laboratory
David Lavery, NASA Headquarters
Kenneth Ledbetter, NASA Headquarters
Tom Levenson, Levenson Productions
Molly Macauley, Resources for the Future
Bruce Margon, University of Washington
David McComas, Los Alamos National Laboratory
Ralph McNutt, Johns Hopkins University
Mary Mellott, NASA Headquarters
Richard Mewaldt, California Institute of Technology
Michael Meyer, NASA Headquarters
Daniel Mulville, NASA Headquarters
Firouz Naderi, NASA Jet Propulsion Laboratory
Ruth Netting, NASA Headquarters
Marian Norris, NASA Headquarters
Kathie Olsen, NASA Headquarters
James Papike, University of New Mexico
E. Sterl Phinney, California Institute of Technology
Carl Pilcher, NASA Headquarters
Thomas Prince, California Institute of Technology
Stephen Prusha, NASA Jet Propulsion Laboratory
Douglas Richstone, University of Michigan
Guenter Riegler, NASA Headquarters
Jeffrey Rosendhal, NASA Headquarters
Robert Semper, Exploratorium
William Smith, Association of Universities for Research in Astronomy
Larry Soderblom, U.S. Geological Survey
Carrie Sorrels, NASA Headquarters
Steven Squyres, Cornell University
Douglas Stetson, NASA Jet Propulsion Laboratory
Ellen Stofan, University of London and NASA Jet Propulsion Laboratory
Keith Strong, Lockheed Research Laboratory
Simon Swordy, University of Chicago
Harvey Tananbaum, Smithsonian Observatory
Harley Thronson, NASA Headquarters
James Trefil, George Mason University
Peter Ulrich, NASA Headquarters
Meg Urry, Space Science Telescope Institute
Samuel Venneri, NASA Headquarters
Richard Vondrak, NASA Goddard Space Flight Center
Edward Weiler, NASA Headquarters
George Withbroe, NASA Headquarters
Maria Zuber, Massachusetts Institute of Technology

Space Science Advisory Committee

Steven Squyres (Chair), Cornell University
David Black (former Acting Chair), Lunar and Planetary Institute
Christine Anderson, Air Force Research Laboratory
Roger Blandford, California Institute of Technology
Andrew Christensen, Aerospace Corporation
Alak Das, Air Force Research Laboratory
David DesMarais, NASA Ames Research Center
Michael Drake, University of Arizona
Alan Dressler, Carnegie Observatories
Jack Farmer, Arizona State University
Robert Gehrz, University of Minnesota
Daniel Hastings, U.S. Air Force
David Hathaway, NASA Marshall Space Flight Center
Isabel Hawkins, University of California
Klaus Keil, Hawaii Institute of Geophysics and Planetology
Edward Kolb, Fermi National Accelerator Laboratory
Molly Macauley, Resources for the Future
Bruce Margon, University of Washington
Daniel McCleese, NASA Jet Propulsion Laboratory
Richard Mewaldt, California Institute of Technology
James Papike, University of New Mexico
Douglas Richstone, University of Michigan
William Smith, Association of Universities for Research in Astronomy
C. Megan Urry, Space Telescope Science Institute
Richard Vondrak, NASA Goddard Space Flight Center
Maria Zuber, Massachusetts Institute of Technology

Sun-Earth Connection Advisory Subcommittee

Andrew Christensen (Chair), Aerospace Corporation
Cynthia Anne Cattell, University of Minnesota
Antoinette Broe Galvin, University of New Hampshire
George Gloeckler, University of Maryland
Joseph Bearak Gurman, NASA Goddard Space Flight Center
Robert Hoffman, NASA Goddard Space Flight Center
Mary Hudson, Dartmouth College
Stephen Kahler, Air Force Research Laboratory/VSFS
Paul Kintner, Cornell University
Martin Lee, University of New Hampshire
David McComas, Southwest Research Institute
Ralph McNutt, Applied Physics Laboratory
Jan Josef Sojka, Center for Atmospheric and Space Science
Theodore Tarbell, Lockheed Martin Advanced Technology Center
Michelle Thomsen, Los Alamos National Laboratory
Hunter Waite, Southwest Research Institute
Raymond Walker, University of California

Sun-Earth Connection Roadmap Team

Keith Strong (Chair), Lockheed-Martin Advanced Technology Center.
James Slavin (Co-Chair), NASA Goddard Space Flight Center
James Burch, Southwest Research Institute
Charles Carlson, University of California at Berkeley
Andrew Christensen, The Aerospace Corporation
Patrick Espy, Embry-Riddle University
Antoinette Galvin, University of New Hampshire
George Gloeckler, University of Maryland
Raymond Goldstein, NASA Jet Propulsion Laboratory
Leon Golub, Smithsonian Astrophysical Observatory
Michael Gruntman, University of Southern California
David Hathaway, NASA Marshall Space Flight Center
Isabel Hawkins, University of California at Berkeley
J. Todd Hoeksema, Stanford University
Lynn Kistler, University of New Hampshire
James Klimchuk, Naval Research Laboratory
Robert Lin, University of California at Berkeley
Barry Mauk, Applied Physics Laboratory
Ralph McNutt, Applied Physics Laboratory
Richard Mewaldt, California Institute of Technology
Thomas Moore, NASA Goddard Space Flight Center
Arthur Poland, NASA Goddard Space Flight Center
Karel Schrijver, Lockheed-Martin Advanced Technology Center
David Siskind, Naval Research Laboratory
Jan Sojka, Utah State University
Harlen Spence, Boston University
Jeffery Thayer, Stanford Research International
Richard Vondrak, NASA Goddard Space Flight Center

Astronomical Search for Origins and Planetary Systems Advisory Subcommittee (Origins)

Alan Dressler (Chair), Carnegie Observatory
David Black (former Chair), Lunar and Planetary Institute
Louis Allamandola, NASA Ames Research Center
Charles Beichman, NASA Jet Propulsion Laboratory
Omar Michael Blaes, University of California
Peter Bodenheimer, University of California, Lick Observatory
Adam Seth Burrows, University of Arizona
William Cochran, University of Texas at Austin
Heidi Hammel, Space Science Institute
Kenneth Johnston, U.S. Naval Observatory
Harold McAlister, Georgia State University
Susan Neff, NASA Goddard Space Flight Center
Robert Noyes, Smithsonian Astrophysical Observatory
Marcia Jean Rieke, University of Arizona
Steven Ruden, University of California at Irvine
Charles Steidel, California Institute of Technology
Hervey (Peter) Stockman, Space Telescope Science Institute

Structure and Evolution of the Universe Subcommittee

Bruce Margon (Chair), University of Washington
John Armstrong, NASA Jet Propulsion Laboratory
Arthur Davidsen, Johns Hopkins University
Gordon Garmire, Pennsylvania State University
Neil Gehrels, NASA Goddard Space Flight Center
Jacqueline N. Hewitt, Massachusetts Institute of Technology
Marc Kamionkowski, California Institute of Technology
Charles R. Lawrence, NASA Jet Propulsion Laboratory
Daniel Lester, University of Texas
Dan McCammon, University of Wisconsin
Peter Michelson, Stanford University
Bradley Peterson, Ohio State University
E. Sterl Phinney, California Institute of Technology
Simon Swordy, University of Chicago
Harvey Tananbaum, Center for Astrophysics
Daniel Weedman, Pennsylvania State University
Andrew Wilson, University of Maryland
Fiona Harrison (Executive Assistant to Chair), California Institute of Technology

Solar System Exploration Subcommittee (SSES)

Michael Drake (Chair), University of Arizona
Christopher Chyba (former Chair), SETI Institute
David Aikin, University of Maryland
Richard Binzel, Massachusetts Institute of Technology
Jeffrey Cuzzi, NASA Ames Research Center
Charles Elachi, NASA Jet Propulsion Laboratory
Jack Farmer, Arizona State University
Caitlin Griffith, Northern Arizona University
David Grinspoon, Southwest Research Institute
Bruce Jakosky, University of Colorado
Stamatios Krimigis, Johns Hopkins University
Laurie Ann Leshin, Arizona State University
William McKinnon, Washington University
Kenneth Nealson, NASA Jet Propulsion Laboratory
Carolyn Porco, University of Arizona
Sean Solomon, Carnegie Institution of Washington
David Stevenson, California Institute of Technology
Ellen Stofan, NASA Jet Propulsion Laboratory
Michael Zolensky, NASA Johnson Space Center



Jupiter as seen in October 2000 by the Cassini spacecraft as it speeds by on its way to Saturn. Jupiter's moon Europa, seen as the bright point at the right, casts its shadow on the planet.

Come join us on our voyage of discovery at
<http://spacescience.nasa.gov>



National Aeronautics
and Space Administration

Space Science Enterprise

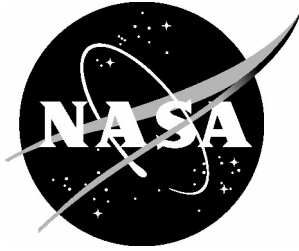
Code S

NASA Headquarters
Washington, DC 20546

<http://spacescience.nasa.gov>

NP-2000-08-258-HQ

NASA/TM-2004-213511



Optical Diagnostic System for Solar Sails: Phase 1 Final Report

Richard S. Pappa
Langley Research Center, Hampton, Virginia

Joseph R. Blandino
James Madison University, Harrisonburg, Virginia

Douglas W. Caldwell
Ecliptic Enterprises Corp., Pasadena, California

Joseph A. Carroll
Tether Applications, Inc., Chula Vista, California

Christopher H. M. Jenkins
South Dakota School of Mines and Technology, Rapid City, South Dakota

Thomas C. Pollock
Texas A&M University, College Station, Texas

December 2004

The NASA STI Program Office . . . in Profile

Since its founding, NASA has been dedicated to the advancement of aeronautics and space science. The NASA Scientific and Technical Information (STI) Program Office plays a key part in helping NASA maintain this important role.

The NASA STI Program Office is operated by Langley Research Center, the lead center for NASA's scientific and technical information. The NASA STI Program Office provides access to the NASA STI Database, the largest collection of aeronautical and space science STI in the world. The Program Office is also NASA's institutional mechanism for disseminating the results of its research and development activities. These results are published by NASA in the NASA STI Report Series, which includes the following report types:

- **TECHNICAL PUBLICATION.** Reports of completed research or a major significant phase of research that present the results of NASA programs and include extensive data or theoretical analysis. Includes compilations of significant scientific and technical data and information deemed to be of continuing reference value. NASA counterpart of peer-reviewed formal professional papers, but having less stringent limitations on manuscript length and extent of graphic presentations.
- **TECHNICAL MEMORANDUM.** Scientific and technical findings that are preliminary or of specialized interest, e.g., quick release reports, working papers, and bibliographies that contain minimal annotation. Does not contain extensive analysis.
- **CONTRACTOR REPORT.** Scientific and technical findings by NASA-sponsored contractors and grantees.

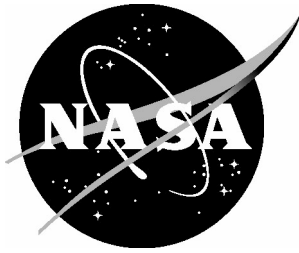
- **CONFERENCE PUBLICATION.** Collected papers from scientific and technical conferences, symposia, seminars, or other meetings sponsored or co-sponsored by NASA.
- **SPECIAL PUBLICATION.** Scientific, technical, or historical information from NASA programs, projects, and missions, often concerned with subjects having substantial public interest.
- **TECHNICAL TRANSLATION.** English-language translations of foreign scientific and technical material pertinent to NASA's mission.

Specialized services that complement the STI Program Office's diverse offerings include creating custom thesauri, building customized databases, organizing and publishing research results ... even providing videos.

For more information about the NASA STI Program Office, see the following:

- Access the NASA STI Program Home Page at <http://www.sti.nasa.gov>
- E-mail your question via the Internet to help@sti.nasa.gov
- Fax your question to the NASA STI Help Desk at (301) 621-0134
- Phone the NASA STI Help Desk at (301) 621-0390
- Write to:
NASA STI Help Desk
NASA Center for AeroSpace Information
7121 Standard Drive
Hanover, MD 21076-1320

NASA/TM-2004-213511



Optical Diagnostic System for Solar Sails: Phase 1 Final Report

Richard S. Pappa
Langley Research Center, Hampton, Virginia

Joseph R. Blandino
James Madison University, Harrisonburg, Virginia

Douglas W. Caldwell
Ecliptic Enterprises Corp., Pasadena, California

Joseph A. Carroll
Tether Applications, Inc., Chula Vista, California

Christopher H. M. Jenkins
South Dakota School of Mines and Technology, Rapid City, South Dakota

Thomas C. Pollock
Texas A&M University, College Station, Texas

National Aeronautics and
Space Administration

Langley Research Center
Hampton, Virginia 23681-2199

December 2004

The use of trademarks or names of manufacturers in the report is for accurate reporting and does not constitute an official endorsement, either expressed or implied, of such products or manufacturers by the National Aeronautics and Space Administration.

Available from:

NASA Center for AeroSpace Information (CASI)
7121 Standard Drive
Hanover, MD 21076-1320
(301) 621-0390

National Technical Information Service (NTIS)
5285 Port Royal Road
Springfield, VA 22161-2171
(703) 605-6000

Preface

NASA's new In-Space Propulsion (ISP) program recently selected teams led by AEC-ABLE Engineering, Inc. and L'Garde, Inc. to develop scale-model solar sail hardware over the next two years, and to demonstrate its functionality on the ground. Both are 4-quadrant, square sail designs with lightweight diagonal booms (<100 g/m) and ultra-thin membranes (<10 g/m²). To support this technology, the authors are engaged in a focused research effort to develop an integrated diagnostics instrumentation package capable of accurate monitoring of solar sail structures such as these during ground and near-term flight experiments. We refer to this activity as the "Optical Diagnostic System (ODS) for Solar Sails" project. Our design is mainly focused on the funded ISP Cycle 1 concepts being developed by AEC-ABLE and L'Garde, but the small size, low mass, low power, and modularity of the ODS design may also make it relevant to a wide range of other solar sails and other gossamer structures.

The approach taken focuses on lightweight optics and photogrammetric techniques to measure solar sail membrane and boom shape and dynamics, thermography to map temperature, and non-optical sensors including MEMS accelerometers and load cells. The diagnostics package must be light: <10 kg initially, evolvable to 2 kg for a 5000 m² mission sail. It must measure key sail structural characteristics including deployment dynamics, sail support tension, boom and sail deflection, boom and sail natural frequencies, sail temperature, and sail integrity. This report summarizes our work conducted in the initial 6-month Phase 1 period (conceptual design phase), and it complements the final presentation given in Huntsville, AL on January 14, 2004.

Acknowledgements

Many individuals supported the ODS Phase 1 study. We especially acknowledge significant supporting technical contributions from Scott Van Essen at Ecliptic Enterprises, Aaron Gough at South Dakota School of Mines and Technology, and Jon Miles at James Madison University. Additional technical contributors and reviewers include Tom Jones, Chris Sandridge, Eric Walker, Chris Meyer, Al Burner, and Tianshu Liu at NASA Langley; Diane Hurtado, Mike Jacox, and John Junkins at Texas A&M; Mike Fennell at Tether Applications; John Hoppe at Swales Aerospace; and John Rakoczy (our COTR) at NASA Marshall. The Principal

Investigators of the two ISP Cycle 1 sail development teams, Dave Murphy at AEC-ABLE Engineering and Leo Lichodziejewski at L'Garde, consulted with the team on several occasions during the study and provided helpful information related to integration of ODS with their sail systems. Their contributions are gratefully acknowledged. We also thank John Oldson for providing editorial assistance and co-investigator Joe Carroll for making major contributions to the writing of the final report.

Table of Contents

1. What is to be measured and why
2. ODS requirements derived to date
3. ODS baseline design concept
4. Lighting and target design
5. Camera configuration and design
6. Thermography
7. Distributed non-imaging sensors
8. Avionics system issues and design
9. Photogrammetry test of 10m sail quadrant
10. Known interface issues with each Cycle 1 sail design
11. Technology gaps and risks for bringing ODS to TRL 6

Section 1

What Is to Be Measured and Why

1.1 Introduction

A solar sail diagnostics system has a number of potential uses, including:

1. Determining whether the solar sail is configured and behaving as models predict
2. Answering questions that cannot be confidently answered without a flight test
3. Collecting data that can be used to identify failure mechanisms or other anomalies
4. On later missions, verifying that known problems have actually been solved.

Determining what is necessary and what is sufficient is difficult, given the extremely limited ground and flight test base for solar sails to date, the great difference between solar sails and most traditional (non-gossamer) spacecraft concepts, and the difficulty of providing a proper test environment on the ground (good vacuum, zero gravity or good gravity compensation, etc.). As a result, it is not yet clear exactly what kinds and quantities of data will be most useful, or what a minimum acceptable dataset will be. As discussed below, it is precisely this uncertainty that may be the strongest argument for an Optical Diagnostic System (ODS).

One of the useful things about imaging, and in particular video, is that it is the cheapest and most convenient way to collect huge amounts of data. The richness of the data allows it to be very useful when the system behaves unexpectedly, and it is not clear what is happening. On the other hand, if a solar sail is far from earth, that data needs high compression before downlink to be affordable. Compression is less of an issue for ground-based tests or tests in low earth orbit.

The combination of some form of imaging (even if not highly calibrated) *plus* other forms of data (strain gauge, acceleration, attitude, temperature, and maybe even electric fields) may be far more useful than any one form of data by itself. For example, structural vibration frequency may

give the best data on boom stiffness, and waveform analysis may indicate the presence of hysteresis, buckling, or other non-linearities. Such frequency data might be derived from video data or from a Fourier transform of strain gauge or other data. But unless there are other supplementary data, we may not be able to determine why the boom frequency is different from expectations. And if the data seem strange, imagery becomes invaluable, so one can see whether a boom is buckled or incompletely deployed, or whether the membrane has snagged or torn.

Another type of synergism is to use anomalies in data from non-optical sensors like strain gauges to trigger collection of additional higher-rate video imagery, or saving of recent image data that might otherwise be overwritten before download if everything appears normal.

1.2 ODS Objectives

The team has developed the following proposed primary and secondary objectives for ODS, which have been presented in the project reviews during Phase 1:

Primary: Gather data in a near-term solar sail flight experiment to validate structural analytical models for confident scaling to larger sizes.

Secondary: Observe/measure the unexpected, especially “known plausible” malfunctions

The focus of the ODS project is on development of a integrated diagnostic system suitable for an initial solar sail flight experiment, such as might be sponsored by NASA’s New Millennium Program. This diagnostic system may be judged to be unnecessary (or perhaps too massive unless miniaturized) for subsequent solar sail flights if everything behaves as predicted on the initial flight. Or perhaps a subset of the system used for health monitoring rather than validation of structural analytical models would be flown on subsequent development flights or even on early missions. The sailcraft in the initial flight experiment is assumed to be a square solar sail design at least 40 m in size (edge dimension) with four booms deploying from a central

hub that support individual quadrants of highly reflective membrane material. Candidate designs include the two concepts currently under development by AEC-ABLE Engineering Co. and L'Garde, Inc. for NASA's In-Space Propulsion Program.

1.3 What the life history of a solar sail suggests about ODS requirements

In deciding what needs to be measured and why, the team considered what problems might occur during the life history of a solar sail that could be detected by ODS. Our thoughts are summarized below.

1.3.1 Materials

The sail membrane and supporting structure must tolerate the sequence of configurations and environments the sail will see. Key environmental issues include energetic UV and ionizing radiation. The responses may vary with rate, temperature, the presence or absence of oxygen or other gases during or after exposure, and with the opacity of the metallization, especially after folding, unfolding, and other handling. Other issues include dryout in vacuum, blocking (sticking of adjacent film layers), extreme temperatures and gradients caused by shadowing or inadvertent focusing of light (especially during deployment), and modification of membrane properties by the surface metallization. Atomic oxygen may not be an issue, because drag would likely cause reentry before a membrane erodes much. As a minimum, ODS images need to be able to indicate the location and geometry of significant tears in the membrane. This may help us distinguish between many of the various failure modes discussed here.

1.3.2 Manufacturing

Different sail designs have different requirements on dimensional accuracy of membrane and structure. Critical dimensions may change with temperature, desiccation, and stress history, and they may not change uniformly. Solvent vapors may cause blocking or other problems.

Cleanliness may also have unexpected effects: an early prototype may be dusty enough to prevent blocking or depressurization damage, while a cleaner, flight sail may be vulnerable to one or both problems. It may be important for ODS to be able to see the results of serious manufacturing problems. Anything that imposes uni-axial tension can generate wrinkles. Such wrinkles may be more visible if a sail is in low orbit around earth because the varying position of the lit earth may allow better “wrinkle surveys” than can be done when the only significant light source is direct sunlight.

1.3.3 Storage

Storage temperature, duration, pressure cycling, and ambient atmosphere (dryness, solvents, etc.) could be issues. Bimetallic corrosion of the thin membrane coatings before launch could be an issue if both sides are coated with different materials. If a hydrated membrane can act as a polymer electrolyte, it may be necessary to store the sail in very dry air to prevent corrosion. This might best be detected by witness samples stored with the sail and removed before launch, but imagery taken after deployment may also be useful.

1.3.4 Launch

During launch, peak depressurization rates inside a fairing are of order 0.05 atm/sec. The sail design must either guarantee adequate venting of any trapped air volumes, or accept random local damage (including membrane bulging or bursting), and possible larger-scale damage due to piston effects of the stowed sail. Perforating the membrane may help if the stowage geometry does not allow too many holes to be sealed by adjacent folds. Imaging the folded sail during launch is infeasible, but we can image the results after deployment, especially with a telephoto inspection camera. Damage seems likely to be limited to exposed folds. The damage location and appearance may help narrow down the range of potential causes.

1.3.5 Deployment

Many if not most potential sail failure modes may first become evident during deployment. Booms may buckle; tensile elements may fail, jam, or snag; the membrane may snag or tear;

actuators can jam or otherwise fail; and electronics and/or software can malfunction. Imaging plus opportunistic sensing of other types may be particularly useful at diagnosing deployment-related failures and anomalies. Imaging systems require enough memory, processing power, and downlink bandwidth that also including other sensors (strain, acceleration, temperature, etc.) should not significantly increase system-level requirements.

1.3.6 Sail dynamics

Solar sails operate in an environment that provides negligible damping, so the sail design must itself provide adequate structural damping of any possible dynamics that could be induced in the system. Sail developers may need to build and exercise detailed and realistic sail FEA models, with damping parameters realistic for the sail environment, to understand this issue. Only after such models are built and exercised will we know how accurately we need to observe the dynamics in order to characterize damping. Damping by air during ground tests can be fairly high even in a reasonably good vacuum (e.g., 0.1 torr) due to the large surface area and ultra-low mass density of the membranes.

In addition, the perturbing effect of gravity will be unavoidably large in ground tests. Such tests may be far more useful for “stress-testing” our understanding of the sail’s dynamics in general, than for directly indicating the likely flight dynamics. The best ground test may involve multiple conditions, none of which simulates flight accurately, but which together exercise what are thought to be the key features of the design, operations, dynamics, and controls.

1.3.7 Long-term degradation

Long-term degradation includes the effects of micrometeoroid damage, cumulative radiation on the membrane or electronics, command or control malfunctions, thermal cycling, etc. One issue is whether the sail will retain enough control authority after impact damage, failure of individual control actuators, gross membrane tearing, or other problems. Another is whether the sail can recover from being flipped over onto its back. The sail’s effectiveness varies with its reflectivity and area, so any large degradation will be visible, though its cause may not be. Most of the ODS cameras will be monochromatic for highest measurement resolution, but the pan-tilt

inspection head might include one or more color cameras. (See Section 3 for a description of the ODS baseline design concept.) However, the value of color imagery may be limited by degradation of the color filters as they accumulate exposure to bright light. This may require use of special stable filter wheels with a monochromatic imager, rather than the conventional Bayer “mosaic” filter built into most small-format color imaging chips.

A related issue is gradual increases in sunlight intensity during missions that approach the sun. This increases sail temperature and temperature gradients (and hence thermal distortion), and may also affect sail degradation mechanisms.

1.3.8 Diagnostics during or after major system failures?

A solar sail may suffer a major structural or control failure. ODS need not remain operational after loss of power or downlink capability, but it may be feasible and worthwhile to retain imaging capability after lesser failures. For example, if a sail flips over, ODS will be on the unlit side (assuming the ODS baseline implementation). If the sail is not totally opaque, useful imaging may be possible until the batteries die. If the sail is opaque, tears and other flaws may be very visible. But such imaging should probably be regarded as an “opportunity” rather than a serious ODS design driver.

1.3.9 An early list of “known plausible” failure modes for ODS to handle

The list below was compiled by the ODS team for the kickoff meeting. It has not been reviewed and accepted by either the sail developers or the solar sail program office. We cannot currently guarantee that the baseline ODS design will be able to observe and distinguish between all of these failure modes, but thought it was worth including them for potential use during reviews later in the ODS development process.

Sail booms or ODS camera mast:

- Deployment jamming
- Buckling
- Thermally induced distortion

- Other unexpected bending or twisting
- Lower damping of boom/mast dynamics than expected
- Irregular deployment synchronization (if applicable)

Sail membrane:

- Damage from depressurization at launch (which may have varying effects)
- Damage from sticking or disorderly unfolding that creates stress concentrations
- Tearing due to any cause (grazing micrometeoroid impacts, thermal cycling, etc.)
- Degradation from local heating, UV, radiation, contamination, ODS targets, or ...?
- Lower damping of membrane dynamics than expected

Other:

- Getting maximum functionality in unexpected orbits (kick stage malfunction, etc.)
- Failure to separate completely and cleanly (this is apparently quite common)
- Control failures (e.g., controller upset or latch-up curable by cycling power)
- Control actuator malfunction (what sensors should ODS or the sail developer use?)
- Difficulties in recovering from unexpected attitudes (e.g., due to controller upset)

1.4 Importance of sail thermal gradients, construction errors, etc.

The low stresses planned for the sail membranes (<10 psi), in films with a Young's modulus in the 300-900 ksi range, means average membrane strains on the order of 1 to 30 parts per million. Any factors that can cause local length changes at least comparable to this can seriously alter the stress distribution in the membrane. If a small part of a membrane shrinks by more than this compared to the rest of the membrane, it may take all the loads. These concentrated loads may still be low, but they may be large enough to cause tearing, especially if "spiky" transient loads due to flapping, etc., are superimposed on them. Section 6 of the report shows how thermal gradients may cause length changes large enough to be an issue. Also, step-and-repeat membrane assembly techniques may induce cumulative size and shape errors that are hard to control and even harder to quantify. Changes in film tension, temperature, and humidity during assembly may also contribute errors that are only seen after deployment in orbit.

1.5 *How wrinkles and creases can affect sail dynamic behavior*

Due to their membrane nature, sails have unique features that affect sail behavior. Membranes have two distinct kinds of out-of-plane deformations: wrinkles and creases.

Wrinkle – an out-of-plane elastic deformation associated with the no-compression behavior of membranes. (This is the historical use of the term in membrane mechanics.) Wrinkles usually materialize as sinusoid-like waves. They may occur locally or be fully developed over the majority of the membrane surface. See Fig. 1-1.



Figure 1-1. Membrane wrinkling

Crease – an out-of-plane inelastic deformation associated with “yielding” of the membrane material. (There is some history to this use of the term, particularly in the paper and textile fields.) Creases usually materialize as sharp, cusp-like deformations, similar to balling up a sheet of paper and unfolding.

We have also recently seen a distinctive behavior when allowing small membrane samples with intersecting folds to unfold at very low tension. Complicated “puckers” can form at the intersections of folds. They can “cinch up” during unfolding, even if the initial folds were not creased. It takes modest (but not negligible) tension to remove them, even in 1.4-micron film.

Any parts of the membrane that see no significant tensile loads during or after deployment may retain creases or puckers. They may change local sail dimensions by $\gg 30$ ppm. This may actually be quite useful if it provides a self-regulating “slack management” feature to sail regions that might otherwise be slack. But creases and puckers can also potentially concentrate the sun’s energy by multiple reflections, possibly enough to cause local membrane overheating and damage, especially in missions close to the sun. The thin metal coatings on the sail membrane may also significantly affect the membrane response to creases and puckers, because the yield strain of the metal is far less than that of the film, and its Young’s modulus is far higher.

1.6 *Measurement Needs and Goals*

There are several important reasons for collecting data on solar sail behavior in space:

- Deployment is so complicated that reliable simulation may be simply infeasible
- Data are needed by theoretical/numerical models, including system-level damping
- Test theoretical/numerical modeling methods, to improve risk reduction analyses
- Characterizing membrane tear propagation in the actual space environment
- Unexpected phenomena are perhaps the most serious challenges to risk reduction

Model validation may be the most critical to solar sailing success. Experimental data must be considered in the context of high-fidelity computational models. The sails are membranes that will wrinkle if they are not kept in tension. Wrinkles and creases reduce the propulsive efficiency of a solar sail, may cause hot spots where membrane overheating can occur, and will likely cause significant departure from what is expected with a biaxially-tensioned membrane. Furthermore, slack directions and areas in the sail represent load-carrying indeterminacy that must be minimized to increase confidence in structural integrity under mission conditions.

There are several solar sail modeling methods that need to be evaluated in deriving ODS measurement requirements. Relevant field variables predicted by these methods include:

- Sail strain
- Lowest several sail natural frequencies and mode shapes
- Static boom shape
- Boom loading
- Lowest several boom natural frequencies and mode shapes
- Static sail shape
- Center of pressure

Other important solar sail measurement tasks include:

- Measure sail support tension
- Measure sail temperature
- Measure boom root loads

- Measure boom tip accelerations
- Observe deployment and report both qualitative and quantitative results
- Observe sails, booms, and other mission-critical components for structural health

We need to estimate the required accuracy of experimental solar sail measurements to avoid either under-designing or over-designing ODS. At a minimum, the experimental data must be at least as accurate as the models to be validated, although several times more accuracy is desirable for higher confidence. But how accurate will the model predictions be? A 7 kPa (1 psi) “skin” or membrane stress in a 21 MPa (300 ksi) elastic modulus sail causes ~3 micro-strain. Values this small are well within the capability of modern finite element (FE) codes. When compared to classical membrane solutions, FE computed frequencies and mode shapes have been shown to compare extremely well. Generally, computational model results will be considered successful if they are within 5% - 10% of experimental “truth.”

Center of Pressure (CP) is an important parameter in the design and control of solar sails, as is the Center of Mass (CM). CP is the position through which a force that is statically equivalent to the pressure load acts. The CP-CM offset and its uncertainty are fundamental to solar sail guidance and control [Ref. 1-1]. The CP in some ways is a metric for sail computation not unlike “rms figure error” is for antennas and optics. The CP depends on the global and local shape of the membrane, and hence sail shape is critical for solar sail model validation.

Table 1-1 lists the types of measurements needed for validating structural analytical models and modeling techniques for solar sails.

Table 1-1. Measurement goals for a 70 m solar sail flight experiment.

(Based partly on Ref. 1-2)

Parameter	Expected Range	Accuracy Target	Notes
Deployment Dynamics	<i>Qualitative:</i> Video of entire deploying sail <i>Quantitative:</i> Measure trajectories of booms & membranes	<i>Qualitative:</i> High-quality video at 10+ frames/sec <i>Quantitative:</i> 40mm	This is measured only once, so cameras for this purpose might be located off the sailcraft (e.g., on a carrier platform) or ejected later to reduce sail mass.
Shape	0-2 m (est.) out of plane	20 mm	20 mm is the mean accuracy for a uniformly distributed grid of targets.
Vibrations	<i>Natural Frequencies:</i> First 5-10 system modes <i>Damping:</i> 2% (est.) <i>Amplitudes:</i> 1 m (est.)	<i>Frequencies:</i> 1% <i>Damping:</i> 10% <i>Amplitude:</i> 20 mm	Image frame rate at least 2x the highest vibration frequency of interest.
Sail Tension	0 to 50 N	0.1 N	Will investigate in-situ measurement possibilities with L'Garde & ABLE.
Boom Stress	<i>Deploy:</i> 0 - 15 x 10 ⁶ Pa <i>Later:</i> 1 x 10 ⁶ Pa	<i>Deploy:</i> 10 ⁵ Pa <i>Later:</i> 10 ⁴ Pa	Highest stress levels occur during deployment, but difficult to measure then. Operational stresses much lower and also difficult to measure directly.
Film Stress	0 - 10 ⁶ Pa (Mostly under 10 ⁵ Pa)	10 ³ Pa	Very low operational stresses. Can be estimated using measured wrinkle patterns, sail shape, modes, and predictive structural model.
Temperature	Thermographic map	10° C	Not listed in the NRA, but important for some missions.
Sail Integrity	Identified by data trends versus time and/or optical observation	High-resolution imagery, perhaps one quadrant only	If not mass-prohibitive, high-resolution camera will include pan/tilt/zoom capability.

Also listed in Table 1-1 are estimated ranges of the measurement parameters and an accuracy target for each parameter assuming a sail size of 70 m. Accuracy targets for other sail sizes vary proportionately. This information is based in part on requirements listed for a proposed New Millennium Program ST7 solar sail flight experiment [Ref. 1-2].

Cables that collect loads from the sail membrane quadrants and carry them to the booms complicate the structural configuration of the sail. The cables and membranes carry tensile

loads, while the booms carry compressive loads and some bending. Boom loads are likely to be small (perhaps only a few Newtons), and the resulting deflections should be small, if the structure has enough damping. Sail loads are also likely to be small, but deflections may be considerably larger than those of the booms due to the relative differences in stiffness. The wide range of stiffness, coupled with potentially large sail displacements and nonlinear material behavior, makes it challenging to predict sail response. The dynamic response of membranes, due to their no-compression/wrinkling character, is extremely challenging to accurately predict. This implies that, even under the best situations, any sail diagnostics measurement package must be designed to work with considerable uncertainty with respect to structural model predictions.

1.7 *Optical diagnostics*

Photogrammetry is the science of measuring the location and size of three-dimensional (3D) objects with photographs [Ref. 1-3]. The image analysis procedures are related to those used in surveying. When dealing with time sequences of images, this technology is often called “videogrammetry” (or “videometrics”) instead of “photogrammetry,” although either term is acceptable [Ref. 1-4]. Modern close-range photogrammetry uses digital imaging sensors (either CCD or CMOS) and computer data analysis. It can measure hundreds or thousands of object points simultaneously. Measured sets of object points, also known as “point clouds,” can characterize static shape. Sequences of images can characterize structural dynamic properties (i.e., vibration) as well.

Digital photogrammetry records the object from at least two camera positions and calculates 3D coordinates of discrete points on the object’s surface by triangulation of light rays. These discrete points can be natural surface features, but when high accuracies are required, natural features can be inadequate. Solid-colored circular targets are usually installed on the object when highest measurement accuracies are required.

Rigorous statistical analysis is used in the numerical processing so a covariance matrix and other statistics indicating accuracy, precision, and reliability accompany the 3D coordinates. Such statistics are especially necessary when spatial deformation is indicated by the difference

between sets of coordinates obtained at different times. This enables decisions to be made at specific levels of confidence about what shape and position changes occurred in the object. The photogrammetric technique is extremely flexible, able to acquire measurements simultaneously over the surfaces of large objects. It has been proven by successful application to monitoring spatial deformation of a wide range of structures, including various gossamer research structures [Ref. 1-5].

The measurement accuracy achieved with photogrammetry depends on several inter-dependent factors including:

- Size and geometry of the test structure
- Number of cameras and their image resolution
- Camera synchronization (for dynamics measurements)
- Locations and pointing directions of cameras
- Illumination conditions
- Clarity and contrast of surface features (targets)
- Camera and lens characteristics
- Image compression procedures
- Camera stability
- Calibration and data analysis procedures

As will be shown in Section 3, we studied a variety of camera geometries during Phase 1. Those with the widest range of camera viewing directions (e.g., from the center and each corner of the sail) had the highest photogrammetric measurement precision. But they also had the highest expected integration cost, so the ODS baseline concept was restricted to cameras mounted only on a central camera mast. The baseline concept assumes that the camera mast is mounted on the sun side of the sail and views a grid of sunlit photogrammetry targets. An alternative implementation that is still being studied is mounting the camera mast on the back side of the sail instead (or in addition to a front-side mast) and using translucent photogrammetry targets that are visible from the back. In this report, we will assume the mast is on the front side.

1.8 Thermal imaging

Thermal gradients on the sail can cause relative size changes that are large compared to the average tensile strain of a few parts per million. This has led to an interest in thermal mapping of the sail as part of the ODS concept.

However, there is an important integration problem: the ODS cameras need to be mounted on the sunlit side of the sail (in the baseline concept), while thermal imagers should give much better data if they image the back of the sail, which has ~10X higher thermal emittance than the front. This implies using a separate back-side mast and imager installation. This will raise development and integration costs. In Phase 2 we will examine how accurately we can measure membrane thermal emissions using compact low-power passively cooled thermal imagers, for both sun-side and anti-sun-side imager locations.

A comparably critical issue that will be examined in Phase 2 is whether we may be able to ascribe any measured thermal imaging differences unambiguously to one or more of the following potential causes:

- illumination differences (direct or reflected)
- local solar absorptance differences, due to degradation or contamination
- local longwave emittance differences, or
- different reflected longwave radiation, if the sail is in low orbit around earth.

1.9 Non-imaging diagnostics

The mass, power, signal conditioning, memory, and downlink bandwidth needed for imaging swamps that of most other sensors, so it may be feasible to add various other sensors to ODS without significantly driving the ODS design. Such sensors can be particularly valuable if they can enable on-board (autonomous) selection of subsets of the image data as being of more than average interest (e.g., just before and after a sensed acceleration or strain transient). The main criteria are complementarity, synergism with the imaging data, and fairly easy integration.

1.10 Recommendations

Most of the recommendations relating to “what and why” are actually addressed in later sections of the report that focus in more detail on individual aspects of the ODS design. But two recommendations seem worth making here:

1.10.1 Developmental testing of ODS

ODS should use a wide variety of tests during development. Often the best tests are early and very informal ones. Sometimes poorly conceived early tests are the *most* instructive, if they occur early enough in development. Developmental imaging of prototype sails is also a key opportunity to assess what diagnostics may be useful in flight: what is unexpectedly useful or useless on the ground may also be so in flight. But one has to think through the implications of relevant differences in dynamics, environment, lighting, etc., between development and flight.

Perhaps even more important than testing ODS on prototype sails is testing single imagers with representative photogrammetry targets on small membrane samples that can be folded and then unfolded and hung at low tension. This gives the most representative membrane creases, wrinkles, and “optical noise.” One can also provide far better lighting and black baffling for such tests than is feasible for tests on larger prototypes. Such tests should help quantify glare and glint problems (see Section 4.1). This in turn will help optimize many aspects of the ODS design, including number of cameras and pixels, lens and lens shade design, and overall layout.

1.10.2 ODS architecture trades

We really don’t know yet how much data we can afford to collect, how easy it will be to do real-time compression and/or analysis on that data to minimize on-board storage and/or downlink needs, or how much ODS data an actual flight experiment will be able to send to earth, either in real time or after storage in some on-board archival memory. This should be addressed as flight experiment concepts become more specific. It appears worthwhile to keep more than one data handling architecture option open until more is known about the consequences, likely developmental problems, and possible flight opportunities.

1.11 References

- 1-1. Wie, B., “Dynamic Modeling and Attitude Control of Solar Sail Spacecraft,” Final Report, JPL Contract No. 1228156, January 2002.
- 1-2. Price, H., “Solar Sail Technology NMP ST7 Opportunity,” Website: http://nmp.jpl.nasa.gov/st7/ST7_TA_Solar_Sail.pdf, May 2001, p. 13.
- 1-3. Atkinson, K. B. (editor), *Close Range Photogrammetry and Machine Vision*, Whittles Publishing Company, 2001.
- 1-4. El-Hakim, S. F. (editor), *Videometrics and Optical Methods for 3D Shape Measurement*, SPIE Proceedings No. 4309, January 2001.
- 1-5. Pappa R. S. et al., “Photogrammetry Methodology Development for Gossamer Spacecraft Structures,” *Sound and Vibration*, Vol. 36, No. 8, August 2002, pp. 12-21.

Section 2

ODS Requirements Derived to Date

2.1 Status

The requirements in this section were presented by the ODS team to the project office at the Phase 1 final review on January 14, 2004, but they have not yet been officially endorsed. They are subject to change in Phase 2.

2.2 Keywords and Notation

The following keywords and notations have special significance herein.

[] The use of square brackets for requirements shall indicate values which are approximate or negotiable.

Shall. A keyword indicating a mandatory requirement that must be implemented.

Should. A keyword indicating flexibility of choice with a preferred alternative that shall be considered.

May. A keyword indicating a flexibility of choice with no implied preference. It can be interpreted as permission. Such statements are generally included for clarification; silence on a subject is equivalent to “may”.

Will. A keyword expressing a commitment by some party to provide something.

All sentences containing the keywords “shall” or “should” shall be interpreted by designers and implementers as instructions; they should be expected to be contractually or formally binding. Any sentence not containing one of these keywords may be interpreted as informational.

The following definitions are not used in this document, but will be used in later versions of the requirements:

Inspection (I) is the verification of compliance by the examination of documentation (the results of prior lower level verifications, drawings, vendor specifications, software version descriptions documents, etc.) or by direct examination of an attribute (dimensions, weight, physical characteristics, computer program code, etc.)

Analysis (A) is the verification by evaluation of data by generally accepted analytical techniques to determine that the item will meet specified requirements. Analytical techniques may include systems engineering analysis, statics, analog modeling, similarity, and computer simulation.

Test (T) is an empirical verification of operation of all or part of the subsystem under controlled conditions to determine that quantitative design or performance requirements have been met. It includes the collection and subsequent examination of quantitative data. Tests may rely on the use of instrumentation and special test equipment to measure the parameter(s) that characterize the requirement.

Demonstration (D) is an empirical verification of operation of all or part of the subsystem under controller conditions to determine that qualitative design or performance requires have been met. Demonstration relies on observation/recording of functional operation not requiring the use of elaborate instrumentation, special test equipment, or quantitative evaluation of data.

Sail size is defined as the outer edge dimension of a square sail.

Note: This sail size definition may need clarification for specific sail designs. For example, since the sail's outer edges are usually curved, we may want to use $\sqrt{\text{area}}$, or quadrant hypotenuse, or tip-to-tip distance of adjacent booms. This will be examined further in Phase 2.

2.3 Definition of Requirement Levels

1. **Level 1** requirements are between Customer and PI. They may be qualitative, “big picture,” or goals and thus require qualitative flowdown to clarify them. In the tables on following pages, all level 1 requirements are shown in bold on a gray background.
2. **Level 2** requirements are between primary project system elements. For this project, the system elements at this level are: ODS, Sail (the actual propulsive structure), Sailcraft, Modelers, Testers
3. **Level 3** requirements are between subsystem elements of a system. ODS is the only system that is decomposed at Level 3. The full complement of subsystems is TBD but includes: Cameras, Avionics, Photogrammetry Technique (maybe?), etc.

The requirement level is indicated in the following tables by the number of fields in its ID.

2.4 Functional Requirements (Level 1 reqts are bold on gray)

ID	Title	Requirement	Rationale
1	Sail Shape	ODS shall provide spatial measurements at sufficiently high frequency to determine sail shape, natural frequency, damping and modes and mode shapes	This is quantitative.
1.1	Sail Out-of-Plane	ODS shall measure out of plane sail displacements to an RMS precision of [0.025% of sail size (5 mm for 20 m sail)].	
1.2	Sail Motion	ODS shall measure out of plane displacements up to a frequency of [2] Hz.	Derived from models of first 10 mode frequencies.
1.3	Sail Modes	ODS shall provide measurements that support determination of the first [10] vibrational modes	
1.4	Sail Sampling Interval	ODS shall use a spatial sampling interval of [4 % of sail size] or better (less).	
1.5	Boom Measurement	ODS shall measure straightness and twist of the sail booms at [not less than 5] locations along their length to an RMS precision of [TBD].	
1.6	Boom Motion	ODS shall measure lateral displacements of the sail booms up to a frequency of [2] Hz.	
1.7	Measurement Method	ODS shall utilize photogrammetry as a primary sensing method.	This supports ability to find “deflated” shape.
1.8	Measurement Timing	ODS shall have the capability to take a set of measurements of the entire sail system within [0.02s] (Simultaneously with respect to 2 Hz time scales).	
2	Sail Stress	ODS shall provide adequate data to infer the stress state of the sail system	
2.1		ODS shall accommodate load and strain sensors.	
3	Deployment Monitoring	ODS shall observe and record sail system deployment, qualitatively monitoring sail system health and integrity	
3.1		ODS shall have the capability to image the entire sail system continuously.	
4	Post-Deploy Health Monitoring	ODS shall have the ability to qualitatively monitor sail system health and integrity after deployment	Needs definition of what health and integrity are.
4.1		ODS shall have an inspection capability that can resolve features of [0.1% of sail size].	
4.2		ODS shall have the ability to globally monitor sail health.	

2.5 Implementation Requirements (Level 1 reqts are bold on gray)

ID	Title	Requirement	Rationale
5	Mass	ODS shall weigh less than 10 kg, when used for 20 m sail vehicles. The ODS design should be evolvable to 2 kg on a 5000 m² sail or otherwise provide options for attaining this mass target.	
6	Power and Data	ODS shall operate within a power budget of 25 W. ODS shall require a daily data budget of <1 Gbyte/day.	
7	Flightworthi-ness	ODS shall use technology and architecture that are evolvable to a space flight system.	
7.1	Mission Assurance	ODS architecture and electronics shall be designed with consideration for acceptability according to a typical mission assurance plan.	
7.1.1	Radiation Environment	ODS shall be designed for a radiation environment consistent with high LEO (~1000 km).	
7.1.2	Design Life	ODS shall withstand its design environment for a minimum of [6 months] with a goal of [2 years].	
7.1.3	Redundancy	The ODS design shall provide for functional and/or block redundancy as appropriate to match ODS reliability with host reliability requirements.	

2.6 Programmatic Requirements (Level 1 reqts are bold on gray)

ID	Title	Requirement	Rationale
8	Validation	ODS shall be validated by comparison with more accurate instruments such as those already commonly used at LaRC	
9	EM Demonstration	ODS EM shall be demonstrated (fully integrated, with form, fit and function) during deployment of a 20 m sail.	
10	PB Operation	A prototype ODS shall be operational at Plum Brook for the 20-meter tests.	
10.0.1	Form, Fit & Function	Plum Brook ODS shall have functionality of a spaceflight ODS, and as much of the fit and function of a flight ODS as practical.	
10.0.2	GSE	All GSE required for ODS operation at Plum Brook shall be provided by the GSE team.	
11	No PB Interference	ODS shall not impose new requirements on Cycle 1 10- or 20-meter sail systems.	
11.1	Interference	ODS shall not interfere with Cycle 1 testing at Plum Brook.	
11.2	Interface	ODS shall not mechanically interface with the Cycle 1 testing hardware.	
11.3	No Targets Needed	ODS shall have some functionality without targets.	L'Garde sail will not have targets in 10m & 20m sails.
11.4	Environment	ODS shall operate in same environment as Cycle 1 Hardware at Plum Brook: down to [0.1] Torr, in the range [-10 to +50 °C]. ODS may provide heaters to mitigate low temperature but should account for such heaters in its power budget.	

2.7 Requirement for failure tolerance: sensor strings only, or full system?

The project office has requested that ODS have an additional Level 1 requirement to be one-failure tolerant. There are 2 major reasons for this. The first is the roadmap to a space flight system. A space flight system will have to be one-failure tolerant. The second reason is for in-vacuum testing of ODS on large prototype solar sails: it is not acceptable to break vacuum, repair ODS, and re-pump the chamber to repair ODS failures.

The Level 1 requirement may be worded something like this, "ODS shall provide the requisite data for validation of structural models while being tolerant to one failure per string."

Fault tolerance is easy to do on many aspects of the design, especially if it just requires redundant sensors and signal conditioning circuits. But it is not easy to do everything that way, such as with data compression, flight computers, and other avionics. We need to clarify whether ODS needs fault tolerance just at the single-sensor-string level, or higher up. For example, all sensors at a single boom tip will share common power and datalines to the hub, or common autonomous power and wireless links to the hub. Does each such boom-tip assembly require redundancy?

Additional sensors are particularly useful if they provide some additional value, but then losing them degrades the system. So paradoxically, adding a single sensor that provides more insight into system dynamics may degrade the system redundancy, compared to using a suite of 4 sensors, any 3 of which can provide the "required" data.

It appears best to answer this question on a case-by-case basis. For example, an extra MEMS type accelerometer and signal conditioning requires minimal extra mass, power, and data rates, and some geometries may allow complete solutions using "any 3 of 4." But in the case of cameras, the mass, power, cabling, and data rate implications are non-trivial, and redundancy requires complete image area overlap. So redundant accelerometers may make more sense than redundant cameras. Or we might arrange for the pan-tilt inspection head (Section 3 discusses the baseline ODS design concept) to include a camera that can substitute for any single failed fixed camera. Or other camera views of most of a quadrant may allow "good enough" analysis most of the time. So another question is whether and how much degradation is allowed after a single sensor failure, for each type of sensor.

The additional more serious question is what requirements for redundancy ODS should have inboard of the sensors, where redundancy can lead to far higher complexity and introduction of obscure failure modes. Here again, case-by-case study and decisions may be critical. A consistent requirement of fault tolerance may have far more serious implications than requiring tolerance of most but not all component failures.

Section 3

ODS Baseline Design Concept

3.1 Geometries considered for sail photogrammetry

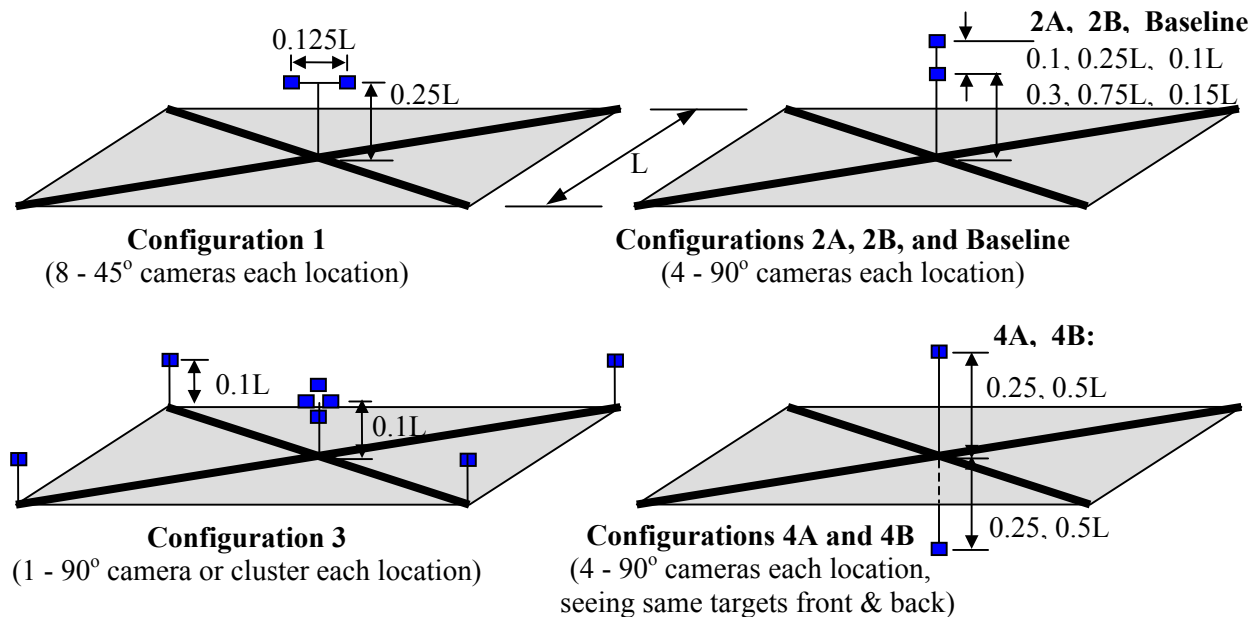


Figure 3-1. Four configurations and variations considered, including final baseline design

3.1.1 Strengths and weaknesses of each configuration

Photogrammetry infers 3D object positions from 2D imagery using multiple viewpoints for depth perception. The short baselines in Configurations #1 and #2 reduce depth perception. The main difference between these configurations is that #1 has the poorest depth perception near the left and right edges while #2 has poorest depth perception near the center. By contrast, #3 has good 3D precision everywhere because each quadrant is viewed from all 3 of its corners. It is also the most robust, especially if each boom-tip camera views the whole sail. A failed camera reduces precision but several complementary views are retained of each location on the sail. But #3 is also the hardest to integrate, with 5 camera masts and considerable high-bandwidth cabling. Configuration #4 is similar to #2, but has a much larger baseline. But it also requires some form of target (TBD) that is visible from both the front and the back of the sail.

3.1.2 Configuration downselect issues and process

At the kickoff meeting, the ODS team recommended configuration #3 as the baseline. But the integration complexity (5 camera masts and long cables), plus concerns about putting additional mass at the tips of the booms, led to immediate rejection of this design.

Configuration #4 led to 3 concerns about the aft boom. One was that any aft mass would tend to destabilize the sail, if it could move the overall vehicle CM aft of the sail plane. Another concern was an integration issue: it requires a way to mount camera masts on both the front and the aft side of the sail or its payload. This might conflict with payload design or interfaces to the booster. A third concern was constraints on sail membrane design imposed by the need for target visibility from both the front and the back side. Ensuring back side target visibility may require locally masking the sail during aluminization, or removing the metal later, or punching holes in the sail and patching them with translucent targets, or other similarly invasive approaches.

The above problems led us to focus on configurations #1 and #2. But front-mounted booms also have problems. One is that if their product of length and mass moves the vehicle CM too far forward, the sail can become excessively stable. Then the sail requires much more control authority to tilt to large angles to the sun, as is needed for high tangential thrust. For modest ODS masses, this should not be a problem, and may actually provide a benefit to the payload: the CM offset may allow the main sail payload to mount slightly aft of the sail plane to provide the desired near-neutral stability, rather than having to be packaged partly in front and partly aft of the center of the sail structure to ensure a suitable CM location.

In considering configurations #1 and #2, yet another boom concern surfaced. The L'Garde design minimizes sail weight by discarding a support package after deployment, and it does this by releasing it in front of the sail, after which the sunlit sail accelerates aft, away from the support package. Hence we seem to require a tilted and/or offset camera mast on the L'Garde sail. Configuration #1 might raise more concerns about support package re-contact after release. This plus a later differentiation of functions for the two camera locations led us to concentrate on configuration #2: a single central front-side camera mast, with sail-view cameras at two heights.

The ODS baseline design concept assumes that the front-side camera mast deploys and latches in place once, and then cannot change its length afterwards. Therefore, triangulation to determine sail shape requires two camera stations along the mast. This assumption was made because the team is not aware of any candidate inflatable mast technologies designed for in-space retraction. In any event, adding retracting motors or other devices to allow the camera mast to change length in space is expected to require a significant mass and cost penalty. But this possibility needs to be examined further. Perhaps a new mast technology will make it feasible to vary camera mast length. If that can be accomplished, the ODS team will reconsider using only a single platform of cameras, and doing photogrammetric triangulation by varying the camera mast length. Of course, this assumes the sail shape does not vary during the time required to acquire the two image sets.

3.2 Evolution of the baseline camera configuration

As noted in Section 3.1.1, the easy-to-integrate configuration #2 has poorer viewing geometry and hence depth perception than #3 or #4. But viewing geometry is not the only factor that affects photogrammetric precision: camera quality also is critical. One can compensate for smaller baselines by using higher-resolution imagers. The selection of a small-baseline configuration led us to focus on raising image quality to compensate. Some early concepts considered VGA-type imagers with 640 x 480 pixels; by the end of the study, our main focus was on SXGA imagers, with 1280 x 1024 pixels. Another change was even more important: using more cameras, each with a narrower view. This is discussed in more detail in Sections 4 and 5 of the report, but the 5 main arguments for using many cameras can be summarized here:

1. Using more cameras with narrower views reduces overall lens mass ***and*** improves resolution;
2. Having separate views of “near” and “far” regions allows more precision from fewer pixels;
3. Using more views limits the effects of sail glare to smaller fractions of the total sail area.
4. Using 4 cameras in a cluster to replace a single camera with a fisheye lens is more reliable if it is properly designed (only one-fourth of image area is lost by a camera failure).

5. Fisheye lenses have much more barrel distortion (correctable, but better to avoid altogether) than normal camera lenses.

But greatly increasing the number of cameras has diminishing returns. Most of the benefits really seem to come from having ~4 views per quadrant (the baseline concept uses 1 near-field view plus 3 narrower views of different “far” parts of the quadrant). Splitting the coverage this way also allows much of the quadrant to still remain visible even if strong reflected glare wipes out one or two camera views.

The other major change in the design concept was to specialize the functions of the two viewing locations. The lower platform is the primary cluster, with 4 cameras for each quadrant. The upper platform is mainly an inspection platform, with 3 cameras bore-sighted together on a pan-tilt head. Our initial concept for the inspection camera used a zoom lens, but we think the platform will be lighter, cheaper, more robust, and photogrammetrically more stable if we use multiple fixed-focal-length lenses bore-sighted together, with different fields of view. The wider views provide context for the narrower views. The widest-view camera may cover a full quadrant or more, while the next narrower view might be slightly narrower than the “far” view cameras on the lower platform, and can be used with them for good depth perception of ~10% of the sail area at a time. The narrowest-view camera allows high-resolution imagery of seams, tears, boom details, and other regions of interest anywhere on the sail.

3.2.1 Key consequences of this design evolution

One consequence of the specialization of the two viewing platforms is that we have very good full-time observing of the whole sail (other than small regions lost to glare), but full multi-view 3D photogrammetric solutions for only ~10% of the sail area at a time. This would seem to be a considerable loss, but there is another key factor here: the sail components have a variety of constraints on their size and shape. If the booms are not buckled, they are of known length, and the only uncertainty then is the extent of bending and/or twisting. We measure that with an additional set of 4 narrow-view cameras, one near the base of each boom, aimed radially outward along the boom. They view targets and natural features along the length of the boom. This

geometry provides the highest photogrammetric sensitivity for measuring boom bending and twist, which both occur parallel to the imager plane.

Similarly, the distance between targets on the sail is set during assembly, and will only change by significant amounts if the sail sticks together, tears, or becomes very slack. All these phenomena should be observable. Hence we do not need full 3D solutions all the time over the whole sail: just good imagery, plus an ability to infer the 3D shape from the images and known constraints, plus a way to test our inferences locally by using the inspection cameras plus the main array for full 3D photogrammetry. Deriving the process of estimating 3D sail shape (and sail dynamics) from image data from lower-platform cameras only plus known constraints will be a key effort for the ODS team starting in Phase 2 of the project.

Increasing the number of cameras and the number of pixels per camera greatly increases the amount of raw data to be handled. As discussed later in Section 8.1, we found that we could get good images and centroid estimates even with high compression (~24:1). This means that despite a large increase in raw data per image set, we have less data to download than the initially planned raw data volume. Selective download can reduce this further.

We have baselined all monochrome (“black and white”) cameras, except possibly for one camera on the pan-tilt platform. It may make sense for the narrowest-view camera to be either a color or multi-spectral camera, if it is determined that color features might provide indication of contamination, degradation, or other phenomena that would not be visible in monochrome views.

3.3 The final baseline ODS design

Our original configuration (proposed, but then rejected, at the kickoff meeting) had both cameras and other sensors at each corner of the sail. The corner-mounted cameras have gone away, but other distributed sensors have remained. The final baseline ODS configuration shown

in Fig. 3-2 shows those sensors, the boom-view cameras, the main observing camera cluster, and the inspection pan-tilt head.

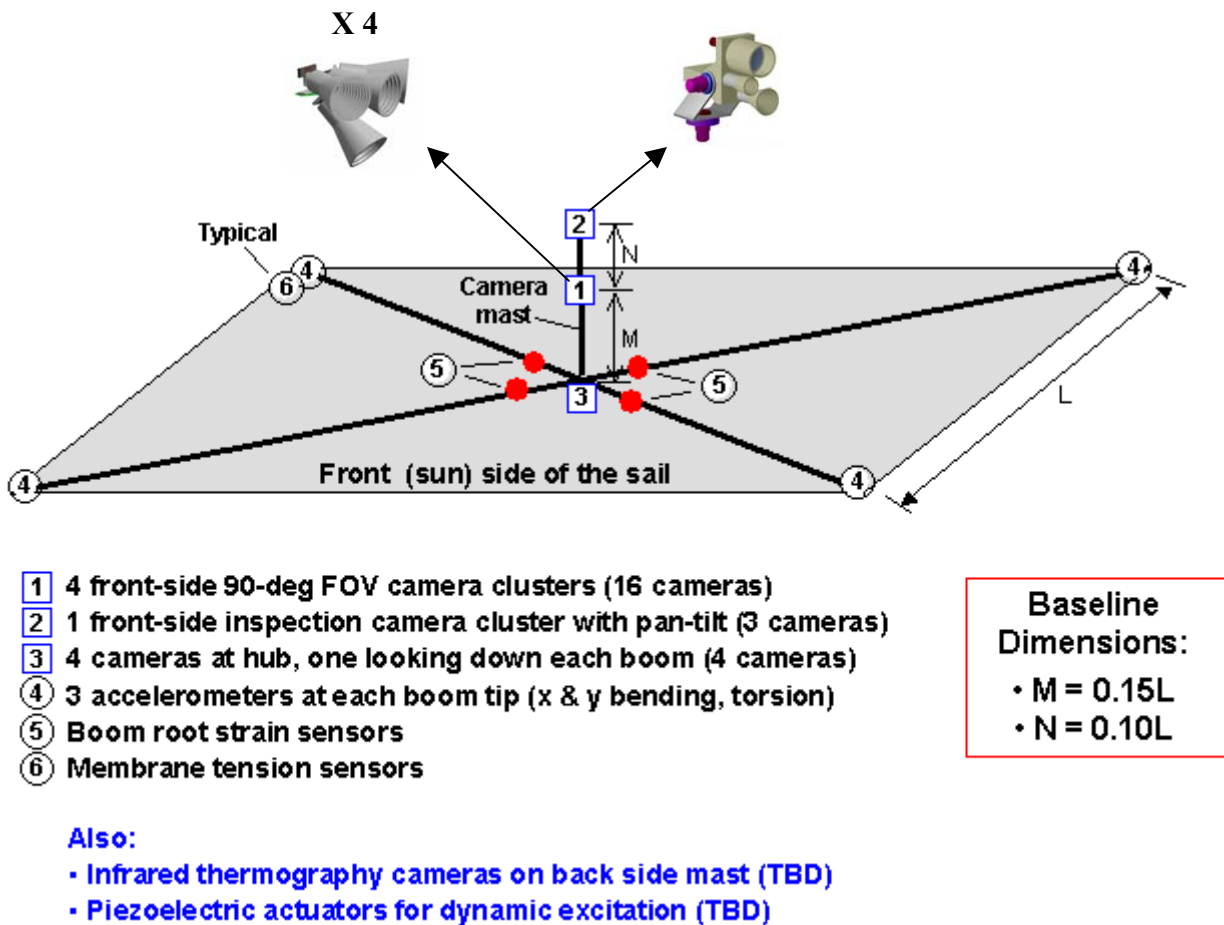


Figure 3-2. Baseline ODS design

3.4 Other solar sail optical diagnostic concepts considered

3.4.1 Imaging from dedicated inspectors: free-flying, tethered, or “virtually tethered”

Early in the project we considered dedicated inspectors, either free-flying or tethered. One problem with a free-flying inspector is keeping up with the sail during the mission because of the continuous light-induced sail acceleration. The inspector delta-V should not be a problem for brief periods only, especially during deployment (when sail acceleration is less). We considered

using L'Garde's support package as a host platform, but it stays attached until deployment is complete, so the most useful images would be missed.

An interest in keeping the inspector nearby for later viewing opportunities led to questions about tethering the inspector. The problem here is that sail acceleration is low enough that it will be hard to ensure tether deployment and also prevent rebound. The added component mass, complexity, and risks of a tethered inspector, which needs active attitude control, reliable damping of tethered oscillations, and its own power supply, seemed to greatly exceed those of the short central camera mast needed for configuration #2. Delivering power through the tether may make it stiff enough to be more like a poorly designed mast than a tether. Hence we focused on cameras mounted on a relatively rigid mast.

We also considered one other concept: a "virtual tether." If a solar sail is in a twilight sun-synchronous LEO orbit, it can counteract drag by canting to the sun and wobbling as it goes around its orbit, to keep the leading edge somewhat sunward. The sail is also displaced away from the normal orbit plane (by ~400m for a 20 g/m² test sailcraft) by solar pressure. It can actively maneuver to stay roughly that distance from a free-falling inspector. That "inspector" could even be an existing imaging spacecraft in a suitable orbit, whose mission is non-critical enough that risks from a test of this nature would be acceptable. Pursuing this was beyond the scope of the ODS study, but may merit study if early flight tests in twilight orbits are considered.

3.4.2 Imaging from the ground or other spacecraft?

There is an interesting question of what one can learn by imaging a 40m solar sail from the ground. The best imaging would be either from nearly any equipment at a really good site, or from tracking telescopes with adaptive optics. AMOS (the Air Force Maui Optical Site) has both a good site and good optics. There is an annual AMOS users conference in the September timeframe. A web link to the conference is: <http://www.maui.afmc.af.mil/conferences.html>

Since what we are observing is bright, we can use short exposure times and modest apertures. This allows an imager to "freeze" turbulence. This gives distortion rather than smearing. Multiple images taken at high data rates may allow deconvolution of the turbulence.

It may also be possible to get imaging by orbiting assets on a non-interference basis. But reflecting huge amounts of light toward them might cause problems with their sensors.

It is possible that the solar sail membranes will be quite wrinkled even a considerable time after deployment. High-speed images from a row of imagers on the ground (every few miles, for 50 miles or so) might be quite useful in determining the "light map" even if the imagers can't resolve any details of the sail.

3.4.3 Imaging of other solar sail tests

The Znamya-2 solar sail deployment test occurred in 1993. A 20-meter thin film structure was deployed from the Progress M-15 spacecraft using centrifugal force. Deployment was done after Progress left Mir, but while it was still nearby. Cosmonauts on Mir imaged the experiment using available equipment. Figure 3-3 shows two web images of the Znamya in space.

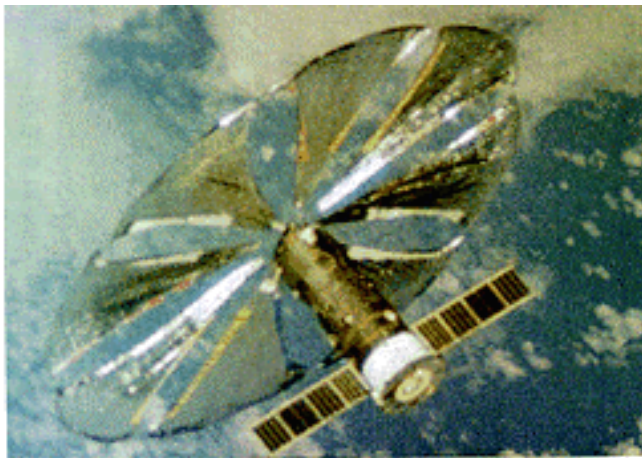


Figure 3-3. Images of 20-meter Znamya-2 sail after deployment, taken from Mir

The Planetary Society's Cosmos 1 solar sail flight experiment will have a small optical diagnostics system. The planned camera views are shown in Fig. 3-4.

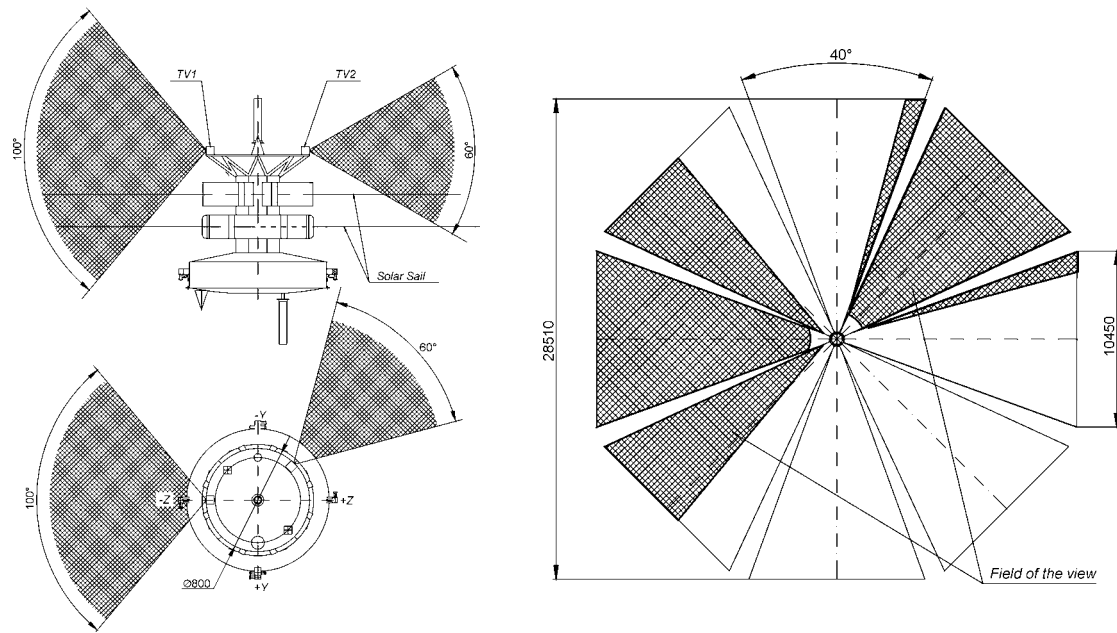


Figure 3-4. Planned camera views in Planetary Society's Cosmos 1 solar sail flight test

3.5 Some open issues on ODS design

3.5.1 Integrating sun and/or star-tracking cameras into ODS?

If there is a need to determine the sail thrust vector very accurately based on sail orientation data, we may need a sun and/or star camera co-mounted with the main ODS camera cluster. We cannot determine the orientation of the sail in inertial space without knowing the ODS cluster's inertial orientation. Mounting star trackers elsewhere limits ODS inertial accuracy to the accuracy of our estimate of bending between the cluster and the star tracker. The main drawback for this star tracker location is that a much better lens shade is needed: both the sun and the sail limit the star views. A final decision need not be made now, because we can use additional imagers of the same kind we plan to use, but with more suitable lenses, lens shades, and software.

3.5.2 Should the distributed non-optical sensors be a part of ODS?

The ODS team may possibly have a better grasp of what sensors are most useful to complement the imaging than the solar sail developers currently do. In addition, we may use anomalies detected by those sensors to trigger retention of imaging data that will otherwise be overwritten, and we may make more use of that data in combination with the imaging data (for model verification) than the sail developers do. So we have a vested interest in the nature and quality of that data. Furthermore, there is one ODS team and there are currently two sail contractors, so having the ODS team take responsibility for this is perhaps a more efficient use of limited funding.

But when it comes time to actually integrate a suite of sensors into a single flight sail design, it is more appropriate to have the ODS team play an advisory role, and give the sail contractor full responsibility to procure, integrate, and test distributed non-optical sensors and their signal conditioning, power supply, and data links. Integration seems likely to be both the costliest and the riskiest part of this effort, so it may be reasonable for the sail developer to take the lead. Both sail designs may have some other electronics and wiring out to the ends of the booms, so this effort would not be entirely unrelated to their current tasks. A final decision is not needed now, but it may be worth consideration as part of the overall program planning for solar sails.

Section 4

Lighting and Target Design

4.1 Lighting: Effects of lighting and glint on camera design & performance

A significant issue for ODS design is reflected glare and glint from the sail. In most cases, at least one imager will view an intense specular reflection of the sun. Over much of the rest of the sail, wrinkles and creases can cause local specular reflections to the imagers. The width of each glinting feature as seen by an imager will often be $\ll 1$ pixel, so the brightness recorded by the imager will be far less than that of the light source. But full glare from the sun can be $\sim 60,000X$ brighter than a target, while the diffuse reflection from a non-glinting sail is only $\sim 2\%$ as bright as a target. So even “micro-glint” can impede image analysis, either by generating false targets or by throwing off centroid position estimates of actual targets.

ODS bears some similarity to at least three other types of fairly common optical tasks: conventional photogrammetry, startracking, and finding an adversary approaching from the direction of the sun. But the overall task is quite different from any one of those three tasks.

The rest of this section discusses the problems resulting from the extremely wide range of potential “optical noise” or “stray light,” in order of decreasing light intensity, as follows:

- Potential permanent sensor damage from focused sunlight
- Partial or total loss of useful imaging when glare is too strong
- Difficulty finding & centroiding targets and other features where glint is highly variable
- Difficulty in evaluating long-term changes in diffuse reflectivity if glint is significant

And there is also one positive aspect of glint: glint variations may have diagnostic utility.

Figure 4-1 illustrates the basis of the glare problem. Clearly, when a highly reflective solar sail flies at an angle to the sun's rays, the ODS cameras on a sun-side mast will see bright specular reflections from somewhere on the side of the sail that is closer to the sun. At greater inclination angles, the bright spot migrates outboard but still occurs somewhere on the sail except at the steepest inclination angles. Less-intense light scattering towards the cameras also occurs from elsewhere on the sail, even when the sail is perpendicular to the incoming light. Of course, normal billowing (and local scalloping in the L'Garde sail design) of the membranes will affect this simplified behavior, causing the effects to shift spatially, but they will still occur.

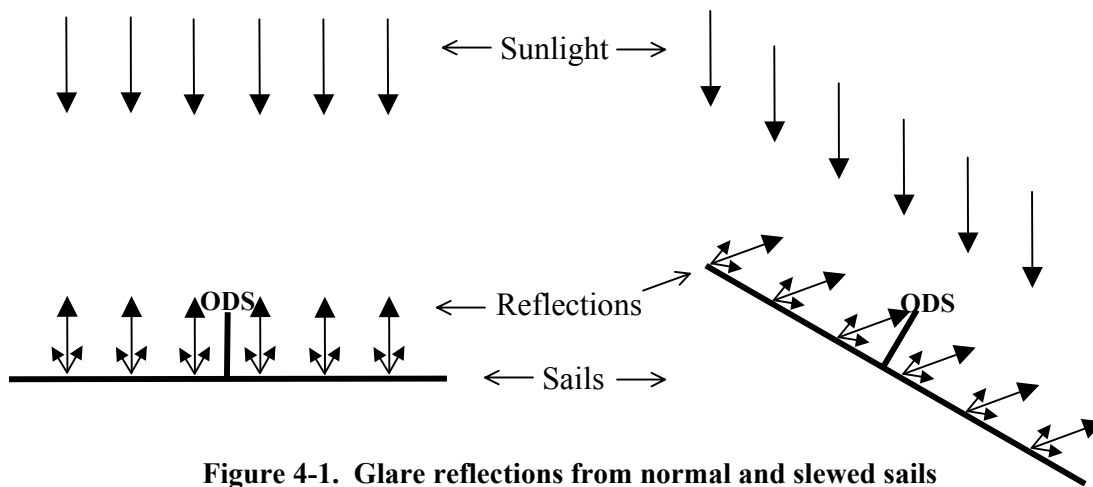


Figure 4-1. Glare reflections from normal and slewed sails

4.1.1 Damage from focused sunlight

The brightness of the specular reflection of the sun will be ~85% that of full sunlight, due to the imperfect specular reflectivity of the membrane. However, the sail will generally have some local curvature. If the membrane is concave in the region of the specular reflection, the “sunspot” focused onto the imager may be larger and may involve several times more energy than in a direct image of the sun through the same imager lens. The realistic worst-case ratio is not known, but is likely to be “at least several.”

One imager supplier (FillFactory) says that their STAR250 and STAR1000 imagers will not be damaged by focused sunlight except by direct overheating sufficient to cause local chip damage. Rough calculations suggest that this should not be a problem unless the local sail

curvature provides high concentration. If this is a concern, we can use smaller lens apertures. But beyond $f/4$ to $f/5.6$, lens resolution may be degraded too much.

Another option is an infrared (IR) cutoff filter. This eliminates half the energy, but less than half the signal. It also improves resolution, for several reasons. One is that IR photons have the longest wavelengths and hence are hardest to focus to a small spot. Perhaps more importantly, an IR cutoff filter will also eliminate most “wandering photoelectrons.” Most IR photons are absorbed deeper in the chip and can travel further before being captured by a pixel photodiode on the surface. Eliminating the IR-generated “wandering photoelectrons” can improve image resolution. It may also allow more of the overall desired level of smearing to be provided by the optics. This allows use of smaller and simpler lenses. A narrower-cut filter (perhaps green only) can improve the ratio of signal to heat input even more. It will also simplify lens color correction, further easing the requirements on the optics. Easing the requirements on the optics may in turn allow smaller lens shades to be used, reducing the size and mass of each ODS camera cluster.

4.1.2 Glare-induced degradation of image quality

When reflected sunlight falls on an imager, or even just on its lens, the images will have artifacts at various locations from multiple specular reflections off lens surfaces. There will also be a diffuse sheen from light that bounces off imperfectly black matte surfaces onto the image. Using 4 imagers per quadrant, each with its own lens and lens shade, will generally limit the resulting image degradation to only 1-3 images of 16 total. Fewer images will be affected on average if image coverage overlaps less. This conflicts with a preferred 10-20% image overlap for photogrammetry, and will require trades later as a part of detailed ODS design.

The high glare brightness vs. target and sail brightness make stray light suppression critical. Good lens shades will be essential. Also, narrow-pass filters (e.g. green only) allow anti-reflection lens coatings to perform better. Robert Breault (see www.breault.com) has described a basic strategy for stray light suppression in an elegant 4-step sequence:

1. List all surfaces that if lit can scatter light onto the detector.

2. List all surfaces that can be directly illuminated by undesired sources.
3. Eliminate any surfaces that are on both lists: that is the key issue.
4. After that is done, minimize the amount of light that can get between those lists.

Breault also says that looking for a “better black” is literally the last thing you should do in stray light control. A very poor black might be ~3% reflective, and a very good black ~0.6%. That means that having 3 bounces off bad coatings is better than 2 bounces off very good coatings. And very good coatings can introduce other problems. For example, Martin Black (now Equinox Interscience's Deep Space Black) is a very porous black anodize. The porosity helps provide multiple bounces locally, but it also attracts and snags dust and other contaminants. And it is not compatible with knife edges--because forming it rounds any edges and then forms a very open foam around those edges. So maybe a knife-edge design that is less black but smooth enough to keep clean will end up being better by the time it is launched and deployed. For more detail on stray light control and black surfaces, see Refs. 4-1 to 4-3.

In low earth orbit, reflections of clouds off a sail can cause problems, because they will often be roughly as bright as sunlit matte white targets. The earth view factor can exceed 30%, and much of that may be covered with clouds, so sail tests in low earth orbit may result in target-recognition problems more of the time than do solar sail missions beyond low orbit.

4.1.3 Glint issues with sails at low tension

“Glint” is here used to refer to specular reflection from creases, wrinkles or other regions smaller than a pixel in at least one direction. This can result in pixel brightnesses anywhere in the ~3:000:000:1 brightness range between the full intensity of a specular reflection and the ~2% diffuse reflectance of the sail. Glint should not be a serious problem if the film is under enough biaxial tension to remove stowage creases and avoid the wrinkles which occur with uniaxial tension. In “suitably tensioned” sails, seam and edge imperfections may be the major source of glint, and targets might be kept far enough away from such features to prevent problems.

But if the sail membrane tension remains low during and after deployment, creases from stowage may never fully straighten out. This may cause glint to be both high and variable across

the sail. It seems unlikely that ultra-thin membranes will form creases only at the intended folds when large quadrants are folded. Pleats will also form in random locations, especially when the folded sail is folded again at right angles to the initial folds. If some of these pleats pass close to targets, they may result in residual creases and glint that induce target centroiding errors.

In addition, simple tests on samples of aluminized 1.4 micron Mylar[®] film showed that unfolding it at very low biaxial tension created complicated puckers in small regions. Membrane tensions well above 1 psi seem necessary to remove the puckers. For films like aluminized Mylar[®] or CP1 (with specific gravities near 1.4), a tension of 1 psi occurs 0.5 m or 20” above the bottom of a hanging sample of film. Hence one cannot test samples much larger than this without applying tensions far higher than 1 psi. If the film is supported in “trampoline” mode, gravity self-loads scale with the radius of curvature. They are ~1 psi in each direction per meter of local radius of surface curvature. Hence on earth, only small film samples can be handled at low enough tensions to be representative of flight conditions.

Earth-based tests of far larger membranes necessarily apply far higher membrane tensions than the ~1 psi biaxial tension planned in orbit. Even static “trampoline” support of large membranes will apply far higher loads than expected in orbit. For example, if a quadrant 10 meters across the diagonal is supported at the corners under low enough tension to sag ~0.5 m in the middle, then the radius of curvature in the middle is ~30 m. The weight of the film will impose a tension of ~30 psi in each direction. One could provide operational tensions on this scale in flight sails, but that would increase the required boom strength and stiffness. And such tensions would assist tear propagation in the membrane. This would require the sail membranes to include some form of rip-stop network to prevent propagation of tears.

4.1.4 Effects of glint on optimum level of image defocus

The optimum level of image smearing for best centroiding is a function of the pixel-to-pixel noise level in the image. If noise is low, then the best centroiding should use significant, multi-pixel defocus (smearing). But if pixel-to-pixel noise level is high, as it may be, then centroiding errors will be lower if centroid calculations use fewer pixels (with shorter “moment arms”). The optimum amount of smearing may be much less than normally used in either photogrammetry or

startracking. This in turn has a bearing on lens design and filter selection. As noted earlier, an IR cutoff or narrow-band visible filter can reduce the number of wandering photoelectrons and the difficulty of providing a given image resolution. On the other hand, most suitable imager chips have significant variations in light sensitivity across each pixel. This results in centroiding artifacts if smearing is too low. With new small-format sensors having pixel pitches in the 3-8 micron range, and medium-speed lenses ($\sim f/4-5.6$), it may be harder to limit the smearing to the level desired over the whole image than to ensure that there is enough smearing.

4.2 Lighting trades for Plum Brook or other large-scale ODS tests

During Phase 1 we investigated the implications of lighting at the 30m Plum Brook vacuum chamber, where it was originally intended to test ODS on 20m prototype solar sails in 2005. Recently, we have learned that this ODS testing at Plum Brook **has been cancelled**. However, most of the results are relevant to other large-scale ODS/sail tests that may be done elsewhere. The issues and potential costs are significant if we want to obtain not just useful data on sail dynamics, but also realistic images. The main topics are brightness, flash vs continuous illumination, the spectrum, number, size, and positioning of the lights, and the value of black backdrops under and around the sail.

4.2.1 Brightness

We don't need and can't afford one-sun brightness ($\sim 100,000$ lux), but we want "adequate" lighting for ~ 5 Hz frame rate images. Assume the exposure time for each image is the full 0.2 second. In orbit, we can use $\sim f/4$ lenses and still have millisecond duration exposures. (Lenses much slower than $f/4$ would probably have worse resolution due to diffraction.) At Plum Brook, using faster lenses ($f/1.4$ to $f/2$) and 0.2-second exposures allows much dimmer lights. We also have the constraint that the lighting must be adequate for ground diagnostics using normal video cameras.

We don't need to fill the "pixel light buckets" but if we don't fill them some reasonable fraction of the way full, then shot noise starts to limit centroiding accuracy. With a PB-0300

CMOS sensor, 0.2-second exposure, and f/1.4 lenses, 100 lux lighting should fill the pixel buckets for normally lit bright white diffuse surfaces. On the other hand, "glare" surfaces can be far brighter than white. We would not be able to distinguish white targets from glare and glint if white surfaces filled the buckets. It might make sense for bright white to fill the buckets $<1/2$ full, so we can more easily distinguish glare from white targets. Then we might be able to get by with 50 lux lighting, or slower lenses than f/1.4.

4.2.2 Continuous vs flash illumination

Flash illumination looks considerably more cumbersome and expensive to realize, especially with multiple light sources (which we plan to have to see the effects of various lighting angles). The main value of flash is for synchronized exposure of all pixels on all imagers, despite the rolling focal plane shutters that are on most of them. This should not be an issue, because we think we can tolerate the small top-to-bottom delays (which can be a modest fraction of the exposure time). In addition, we can synchronize different imagers by periodically turning the light on and off. Flash lighting would also constrain the ground diagnostic imaging, which probably wants to be straight video. Both in orbit and on the ground, we can centroid based on single images. Then we can use this small dataset to compute a "simultaneous centroid" for each target, by adjusting the positions some small fraction of the time between exposures A and B, based on the row centroid (and hence exposure time offset) of each target.

4.2.3 Number of light source positions

It seems very expensive to try to collimate light before it hits a 20 m sail in large-scale ground tests. If we use a centered light source, the only part of the sail that will look like it would with the sail normal to the sun is the center. Outboard parts of the sail will look as they would look if tilted somewhat away from the sun, because of divergence of the light from the central source. We need to be able to switch to at least one off-axis light source, high up on the sidewall of the chamber. This would let us see what things look like on a sail quadrant that tips toward the sun. We may also want to put 2 lights against the wall halfway between two booms, perhaps 5 and 10m above the sail. Parts of the closest quadrant would then look as they would look at larger tilt angles to the sun. Such lighting would be strongly variable between the near side and

the far side. The near side would probably be of more interest since it would have more glare problems, which we need to evaluate to decide how much lens shading is needed. An alternative is a single movable light source, but position reproducibility might be a problem.

4.2.4 Light spectrum

We can use full-spectrum lighting of some type, or low-pressure sodium. Low-pressure sodium would eliminate chromatic smearing (this would be useful given the larger-aperture lenses we may need at Plum Brook). On the other hand, it seems poor in many other respects, including any color ground diagnostic imagers and any test documentation pictures we might want. So we will tentatively assume some form of full-spectrum lighting (incandescent, metal halide, or other).

4.2.5 Size and kind of each light source

The sun subtends $1/107$ radian at 1 AU. If the light is ~25m away, a sun-like source would be 23 cm in diameter. We do not think we need anything that small, but on the other hand, we think we do not want anything far larger than that if we can avoid it. Much larger sources would decrease the brightness of glint, and hence perhaps mislead us about how much we should be concerned about glare from wrinkles and creases. But if there are any electronics cables and/or support lines suspended over the sail, we would like the light source illuminating each spot on the sail to be much larger in diameter than the cable width, so these cables don't cast noticeable shadows. This is less of an issue if glint-related testing is done separately, on small samples.

This suggests that we may want one very bright and moderately compact light, rather than an array of 8-foot fluorescent tubes. And we want to focus as much of its output onto the square sail as possible, and as uniformly as possible. We would also like to absorb everything else before it reaches the sail and has a chance to scatter into the camera. One option that might work is a light source for a projector of some type: both the lamp and its cold mirror and condensers.

Another option is a single metal halide lamp with appropriate optics. Metal halide lamps have a good color balance, which may be useful for the diagnostic videos and documentation

photos. There are commercially available 1000W lamps that start out with 110,000 lumens. If we can deliver half of that to a 20x20m square sail area, the resulting light level is ~140 lux. Any other form of wide-spectrum lighting may generate far more waste heat for the same amount of light provided. For example, we would need about 5kW of incandescent lighting to equal 1kW of metal halide. The actual light source for metal halide is very small, so we could reflect and focus it efficiently (as we could with incandescent lighting) to cover the sail. But we don't know all the details, nor the complications that will come from putting such lamps in cooled pressurized boxes in vacuum. But for tests not done in vacuum, metal halide lamps may be very workable due to their high intensity, compact size, good color balance, and modest heat rejection requirements for any given light output.

Note that during setup, having multiple bright lights at different locations will be useful because the deep shadows from one source could be problematic. We might also put up the black backdrops fairly late in the installation process (after readying them early).

4.2.6 Black backdrops

There is one other important lighting-related item. We need black backdrops to obtain representative images: at least black polyethylene film, with a reflectance of ~3%, but preferably flocked black fabric, with ~0.6% reflectance. We want it on the chamber sidewalls, from the floor to at least ~15m up. It will make a large difference in the utility and representativeness of our images. It should also make any photos for distribution both more realistic and more dramatic. Black backdrops do reduce the lighting level by absorbing scattered light. But we need to minimize scattered light.

We also need the floor under the sail to be black. One reason is that it will get most of the light early in deployment, during boom deployment and the first part of sail deployment. Scatter off it will make the images of the boom less representative. The other thing is that a very black backdrop in the images (at least under the booms) will make images of the open-construction ABLE boom and L'Garde truss structure more representative. The boom itself is nearly black (graphite composite, except for any targets and non-black fittings). So to see what the boom would look like, given nearby glare from the sail, we need a background significantly blacker

than the graphite-fiber composite boom elements. Hence we may need strips of flocked black fabric at least under the booms, and black polyethylene film (or conductive-loaded black polyimide) elsewhere.

4.2.7 Conclusions

Tentative recommendations for illumination at Plum Brook are as follows:

Steady vs flash	Steady
Brightness:	>100 lux normal lighting on sail?
Spectrum	full color (metal halide?)
Light positions	center plus edge (as high as possible), plus 1-2 partway up wall
Light size	20-30 cm apparent source?
Black backdrops	Yes, on sidewalls & floor; black poly ok; flocked fabric better.

4.3 *Targets and Targetless Concepts and Issues*

Original ODS ground rules required that we be able to do some optical diagnostics without dedicated targets, and that we recommend target concepts to improve on this. The key issue affecting the visibility of targets in images is the uncertain “optical noise” of glare and glint from the sail, discussed in Section 4.1.

4.3.1 Targetless imaging

There are at least 3 “inherent optical targets” in the current sail designs:

1. The edges of the membrane
2. The boom structure
3. Construction seams

Unfortunately, these features are all linear rather than point targets. As a result, there is a reduced dimensionality to any shape solutions derived from them, except where visible structural

details (as there are in both the ABLE and L'Garde booms) indicate specific points along the line feature. Imperfections in the seams generate glinty scatter, but the glinting locations change with the lighting angle. Therefore it may not be feasible to use seam imagery for 2D location data.

There are at least 3 other forms of useful data in images of the sail itself. One is that any serious boom or membrane failures should be visible. Tears in the membrane that allow a view of the gap should be visible, because the sail's diffuse reflectivity (1-2%) is far brighter than the space background. Any large boom or membrane deviations from expected shape will generally involve buckling or other visible features. If such features are visible, the primary role of ODS will be helping us understand them and their cause; photogrammetric accuracy will be of secondary importance. If such features are not present, then we can reasonably assume the booms and sail are intact. We can use that assumption to constrain interpretations of all other visible features. In particular, we can infer that deviations from the expected target positions on intact tensioned sail quadrants viewed at an angle are due mostly to out-of-plane displacement. Once we estimate those displacements we can estimate their necessary in-plane effects (due to cosine effects) and iteratively refine the overall estimate of both in-plane and out-of-plane deformations of the sail.

A second form of useful data is that the sail's diffuse reflectivity may significantly deviate from Lambertian with near-normal illumination and near-grazing views. This needs testing with samples of representatively handled sail membrane. If this is the case, then we may be able to infer something about the radial component of membrane slope from brightness variations over the sail. But such variations can also be due to glint. Hence we may need to limit use of this technique to areas with low glint. (Glint can be estimated both from significant excess background brightness and also from spiky variations in brightness as the local slope changes.)

A third form of useful data is glint statistics themselves: higher glint at larger viewing angles suggests increased creasing and wrinkling. Wrinkling indicates current uniaxial tension, while creases can provide indications of both current tension and peak tension since deployment.

4.3.2 Target shape

For intentionally added targets, we can consider circles and ellipses, other solid-colored shapes, and more complicated “coded” targets. Coded targets allow automated unique identification of each target by software. But coded targets have to be quite large to cover enough pixels to allow identification. This may not be critical because we may be able to automate target identification from the overall pattern of targets, at least for fully deployed un-torn sails, especially if targets are laid out in a simple pattern. Automated identification may be hard during deployment or if a serious anomaly occurs, but such cases can be dealt with manually (at some cost and delay). Square targets or other shapes with sharp corners may impose local stress concentrations on the sail membrane, so circles or ellipses are preferable. Automated target recognition may be easier with circles than with ellipses, but the highly oblique view of distant targets requires properly oriented high-aspect-ratio elliptical targets to generate a circular image. And even then target images will be elliptical whenever the membrane deviates from the expected shape, or if the production technique does not easily lend itself to appropriately orienting each elliptical target. A more valuable clue for both recognizing and uniquely identifying individual targets may be the overall pattern they make.

One further target shape issue is whether the target should have uniform brightness or a Gaussian brightness distribution (or at least a feathered edge). Hard-edged targets that modify the membrane properties in any way are more likely to cause local glint at the edge if there is any buildup of slack there. (This was the case in the spray painted targets provided at the Phase 1 final review.) Glint at the edge of the target can cause an error in centroiding estimates. On the other hand, it may be easier to obtain a single uniform level of target brightness than to smoothly vary it as desired. We can probably deal with either hard- or soft-edged targets, but we should characterize their mechanical and optical properties before making a final decision.

4.3.3 Target brightness

White targets may be ~50X brighter than the diffuse background brightness of the sail membrane, but only ~1/60,000 as bright as a full specular reflection of sunlight off the sail. And there will nearly always be such an area on the sail. Around that region, there will be a region

with a wide range of average brightnesses due to glint covering some fraction of a pixel. The brightness of those pixels can be anywhere between $\sim 60,000X$ and 2% of the target brightness.

One can make targets “brighter than white” over a certain range of lighting and viewing directions by blazing them somewhat like a diffraction grating, but it may be hard to do that over the full range of lighting and viewing angles that are required while also keeping the brightness uniform (to minimize centroiding errors) and predictable (to ease distinguishing targets from glint). Other options are colored or fluorescent targets. But one cannot make the target bright enough in any wavelength region to outshine high glint or direct glare, and such targets are likely to run warmer than the rest of the sail. Overall, it seems both easier and more useful to try for uniform and stable matte white targets. SRS Technologies has demonstrated the capability to apply ultra-lightweight diffuse white targets to their CP1 membrane film during manufacture, and simple experiments during Phase 1 showed that ~ 2 micron thick spray painted targets can be applied to aluminized Mylar[®].

Matte white targets will be far brighter than the sail membrane over most of its area, and much dimmer over a very small area. In a halo around the glare spot (which is generally closer to the center of the sail than to the edge), one might even distinguish a target from a comparably bright region of sail by its brightness uniformity (if nearby glare doesn’t overwhelm the image).



Figure 4-2. Sample 1.25” dia. target disks



Figure 4-3. Target on sail

Figures 4-2 and 4-3 show prototype targets before and after installation on a preliminary CP1 sail. This particular membrane has been folded and relocated several times, which caused the dense permanent creasing visible in Fig. 4-3. Note that the sail glint in the photograph ranges from being significantly dimmer to being much brighter than the target itself. The target in Fig. 4-3 appears grayer than it actually is (it is, in fact, bright white) because the autoexposure electronics in the camera have incorrectly assumed an average gray scale for the picture of 18%.

4.3.4 Target size

Photogrammetric target centroiding accuracy is best if the target is at least several pixels high and wide (5-10 pixels is typically optimal) and is surrounded by a several pixel wide, uniformly bright annulus that is either much brighter or much darker than the target. We cannot ensure this with a solar sail. In the near field, the target can be several pixels across, but glare and glint may often be highly variable around the target. In the far field, the oblique view may greatly reduce glint and glint variability. We may be able to have targets several pixels wide, but $\sim 5:1$ foreshortening from the view angle may make it hard to justify targets $\gg 1$ pixel high. The billow will improve the view of far-corner targets, but any flapping could make them periodically considerably less visible.

But we may not need the farthest targets to subtend several pixels in height. Even the image of an ideal point target will usually spread over several pixels due to pixellation, lens limitations, and wandering photoelectrons. (In fact, limited smearing can aid centroiding.) The real far-field question is how many pixels high the target image must be to generate enough photoelectrons for the software to find the target and compute its centroid accurately enough. Even small sunlit targets should provide plenty of photons; the real issue is the background optical noise from sail glint.

There is a clear tradeoff between required target size and overall pixel count. If we use four times as many pixels to image a region of sail, then each target will cover as many pixels even if it has only half the linear dimensions and one-fourth the area. And the centroiding errors in pixels can be comparable, so having more pixels and smaller targets will reduce RMS centroiding errors by roughly half. Hence the final selection of target size and overall pixel

count (number per imager times number of imagers) should be made as a combined trade study to provide some desired accuracy at minimum total cost (i.e., marginal target cost vs marginal imaging system cost). One option is to use several different target sizes, with larger ones used either for the outboard strips or at least for the targets in the far corners of each quadrant.

One other size factor is that if the target brightness cannot be kept uniform, then smaller targets may reduce errors since brightness variations can themselves induce centroiding errors. But if these errors can be characterized in advance, they can be accounted for. And they should be fairly fixed, so errors will have more effect on estimates of sail static shape than on sail dynamics.

4.3.5 Target spacing and pattern

It may be worth varying the target spacing in some distinctive way that allows unique target identification from target spacing. But this makes intuitive shape estimation more difficult because the image “looks” noisier. Several intermediate options may be worth considering. One is uniform spacing plus an extra target at a different location on each row for an independent check on target identification. Another option is uniform spacing in one direction and non-uniform spacing in the other. It may be easier to fabricate and fold the targets and to visually interpret the image if the targets run down the middle of each strip (i.e., uniform spacing normal to the outer edge of the sail quadrant), but with non-uniform spacing along the strip length.

Another option is simply a uniform grid (which is easier to apply and to visually interpret) with a smart enough routine to identify the overall pattern, or to recognize that it cannot do so confidently. Or one could lay down a nominally regular pattern but make more effort to measure the actual target positions than to place them precisely. (This can be done with a high-end photogrammetry system.) This may introduce a pattern of random errors large enough to aid target verification, while not large enough to be visually misleading.

4.3.6 Number of targets

The more targets there are, the more modes of vibration we will be able to discriminate (if their vibration amplitude is large enough to be sensed). But one might also, by modeling and analysis, select a suite of target positions that allow robust separation of many modes using both spatial and temporal variations, without using large numbers of targets. This may be compatible with a philosophy of variable along-strip spacing and uniform cross-strip spacing. Also, the edges of each quadrant can serve as additional target features, though of reduced dimensionality. Because of this reduced dimensionality, we still need to have point-like (or possibly crossing-line) targets near the edge. But we can use the observed position of the edges of the quadrant to constrain the overall solution.

The number of targets may be driven mostly by a compromise between poor diagnostics with too few targets, and excessive hand labor and/or risk of damage during sail fabrication if there are too many targets. By comparison, it seems less likely that any analysis will be able to conclude that the first N modes *must* be discriminated but that all higher modes can be ignored.

Another factor that affects both the pattern and the overall number of targets is that the targets probably need to be away from the folds in the sail, and preferably far away from them. This may help keep targets from affecting the unfolding (if they affect film stiffness at all), as well as reducing local “glint gradients” around the targets that could bias centroid estimation

4.3.7 Optical targets for booms

The 4 boom-view cameras should see a boom-and-target view like that shown in Fig. 4-4, looking out through an ABLE boom. A similar pattern of boom elements and targets should be feasible on the L’Garde booms if the cameras look through the “V” truss structure (the spreader system) on the sunlit side of the booms. The targets can be either sunlit if they are tilted for a good combination of lighting and visibility, or they can be retroreflective if the boom-

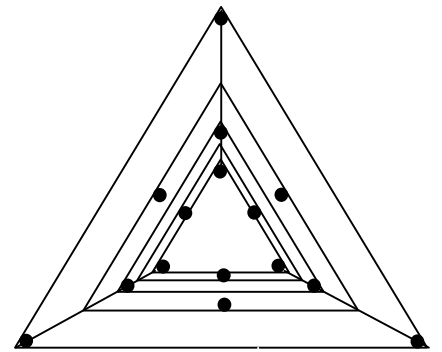


Figure 4-4. ABLE boom & targets

view cameras have LEDs or other light sources adjacent to their lenses.

4.4 Recommendations

4.4.1 Implications of glare and glint on design, and the need for membrane optical tests

When we choose an imaging chip for use in flight, one key factor is how sensitive to damage it is from focused sunlight, and whether it requires some sort of mechanical shutter and controls to keep it from seeing the sun. Adding shutters may drive ODS mass and risk of component failure, so such an option should not be considered lightly. Glare and glint also drive lens shade, lens, and camera housing design, and need early and adequate attention. They are also critical to target detection and centroiding. Section 11 discusses this topic in more detail and recommends near-term tests on suitably handled and lit membranes. These tests are best done on small folded and unfolded samples hanging under low tension. The tests can be done independently of the larger-scale ODS/sail tests and much earlier than those tests.

4.4.2 Target design recommendations

For both the AEC-ABLE and L'Garde sails, matte-white round or elliptical targets appear best. It is not yet clear how large they must be to ensure visibility and accurate centroiding. This should become clearer if the Phase 2 effort includes tests of sail glare and glint statistics as recommended in Section 4.4.1.

For the ABLE/SRS sail, in which the targets may be applied in a roll-to-roll process, it might be best to apply targets down the middle of each strip, or on every N^{th} strip. It may be costly to customize target elongation and orientation from target to target, or spacing from strip to strip, but it may be feasible to use several different target sizes and/or degrees of elliptical elongation for different subsets of the strips. In the case of the L'Garde sail, where the targets may be spray painted on during assembly of each quadrant, local variations in the target size, shape, orientation, and spacing may be more feasible simply by changing the spray paint mask.

Finally, it is not yet clear how many targets are needed, but 100-150 per quadrant currently appears to be acceptable to both the sail developers and to the ODS team. We also need to ensure that the positioning of targets allows the overlap regions between adjacent camera views to have enough common targets for good photogrammetric registration of the adjacent images.

4.5 *References*

- 4-1. Stray Radiation V, 18-20 August 1986, San Diego, CA; Robert P. Breault, chair/editor; SPIE Vol. 675. Breault's recommended stray light analysis procedure is on page 11. Also see SPIE volumes 511, 967, 1331, 1753, and 2260, all on the same subject, all with Breault as editor.
- 4-2. Equinox Interscience's Deep Sky Black coatings, at: www.eisci.com/deepsky.html
- 4-3. Optical Characterization of Black Appliques, K.A. Snail et al, Proc. SPIE, Vol. 2864, pp 465-474. The article is available online at: www.esli.com/downloads/SPIEArticle.pdf

Section 5

Camera Configuration and Design

A wide variety of issues contributed to our design decisions and/or recommendations on camera configuration and design. This chapter discusses these design issues and describes our recommended baseline camera configuration.

5.1 Factors that limit target centroiding accuracy

5.1.1 Summary

One of the main design drivers for ODS is good accuracy in estimating the position in images of photogrammetry targets and other features of interest. Another important factor is good angular and brightness resolution of visual details so we can better see the condition of the sail. Good visual resolution conflicts somewhat with best centroid estimation because optimum centroiding can involve intentional smearing of point features over several pixels (but this can also be done on the ground with software). The low angular resolution and poor grayscale in the images of Znamya shown in Section 3.4.3 should reinforce the value of sharp images. The lists below indicate key design factors for the images and imagers.

Image characteristics

- Size, brightness, and brightness uniformity of targets or other features being imaged
- Optical noise from the sail within a few pixels of the feature being analyzed
- Bright glare from other regions that can reach that part of the imaging by scattering

Imager characteristics

- Pixel field of view (pixel pitch/lens focal length)
- Lens point spread function
- Imager point spread function and sensitivity map across each pixel

- Any system electrical noise that degrades the stability of the camera grayscale

5.1.2 Determination of pixel centroiding errors on an early-model CMOS imager

We had a concern about centroiding errors that might come from using active pixel CMOS imagers, which are known to have large local variations of light sensitivity across each pixel. This led us to do a simple test. Rather than precisely moving the camera or a point light-source from one image to another, we used a single image of a black/white edge running across the image at a slight angle. The camera was a Photobit PB-0300 8-bit VGA imaging chip (640x480). Its photodiodes cover only 20% of each pixel's area, but the peak quantum efficiency is ~25%. This means that other parts of the pixel contribute some photoelectrons. The lens was an f/1.3, 8.5mm lens, stopped down to ~f/4 after focusing. (The lens did not have marked f/stops.)

Post-processing started by taking the difference between vertically adjacent pixels. We selected a reference row by finding the highest positive difference between adjacent rows in each column, and offsetting that by 1 if the value in RefRow+1 was higher than that in RefRow-1. Then an edge centroid was computed using only 4 pixels: RefRow-2, RefRow-1, RefRow, and RefRow+1, by calculating the center of gravity of differenced pixel values in those 4 rows. This gave a list of 640 centroids, one per column in the image.

The next step was to find a smoothed local average centered on each column but not including it. This average used 10 columns on either side, with triangular weights. The difference between the smoothed local average and individual column values was only 0.08 pixel RMS.

In a real ODS image, one would compute vertical centroids of each target using perhaps 3-5 adjacent columns of pixels (depending on the width of the target). This should reduce the error by of order $\sqrt{N_{Cols}}$. Including both row and column errors should increase the total centroid error by ~41%. Overall, ODS may do better or worse than this, depending on the actual imaging chip used, the lens quality and amount of defocus, the algorithm, etc. The point of this test was to see whether the intra-pixel sensitivity variations of active pixel CMOS imagers might severely

limit centroiding accuracy. It appears this will not be a problem, even with an extremely simple centroiding algorithm and an imaging chip that may be more susceptible to centroiding errors than many newer chips are.

5.2 *Why we may need ~20 cameras, and what views they should have*

5.2.1 Do we really need 4 cameras per quadrant?

The baseline ODS design concept used a cluster of 4 stationary miniature cameras as shown in Fig. 5-1 to image each sail quadrant from the lower camera platform. Four medium-view-angle cameras need not weigh more than 1 wider-view camera with comparable angular resolution, because a single camera will require a much larger imager, lens, and lens shade. And a single camera will not be able to provide comparable glare rejection, and it may not be able to equal the lens performance of a cluster of smaller cameras. This section discusses these issues in more detail.

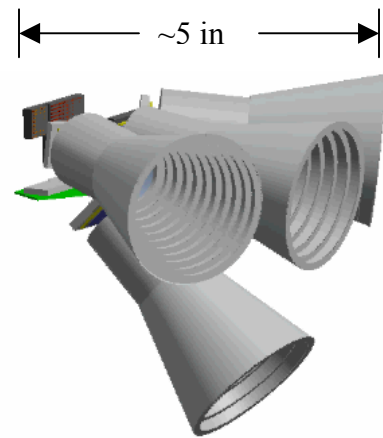


Figure 5-1. Cluster Concept

First, using many cameras allows us to have many lenses and lens shades. Then strong glare in one image need not blind the image of a whole quadrant, but just a fraction of the quadrant. Strong glare will generally occur in at least one quadrant, so going from 1 to 4 cameras per quadrant may reduce the typical “lost coverage” from ~25% to ~6% of the sail area. That also suggests that we may want to limit the overlap of adjacent images. Overlap means wider coverage, and hence wider “acceptance angles” for lens shades, and hence susceptibility to glare over a wider angle. On the other hand, modest overlap will allow viewing of more of a sail region whose main imager is blinded by glare, so this argument should not be overused.

Another argument for using several cameras per quadrant is that it lets us get by with fewer pixels overall, by using different lens focal lengths to compensate for different distances and view angle cosine effects. If we had only 1 wide or super-wide angle view per quadrant, most of the pixels would cover the nearfield, and we would need far more than 16 x 1.3MPixels (our current plan) for the same RMS error in estimated target positions. Centering the imager off the lens axis could also reduce variability of scale factor, but it requires far higher correction of off-axis lens errors. This would require much larger and heavier lenses and lens shades, and would not address the glare problem.

The arguments for multiple narrow-view cameras can also be used for a larger number of views than 4 per quadrant. But many of the benefits of many views come just from separating the views into near and far regions. Locating ODS on a central boom of modest height means that the near region covers most of the subtended solid angle of the sail, but only a small part of the total sail area. Glare will typically be far worse in some part of the near region than further away. This leads to the question of how many “far” views should be used per quadrant. The view of the far regions of a quadrant is a long, narrow, panoramic view, with a height of $\sim 15\text{-}30^\circ$ but a width of 90° (plus overlap). Most small-format imaging chips have 1:1, 4:5, or 3:4 aspect ratios, so we need at least 2 imagers to cover 90° of width while not wasting most of the image height, and 3 or 4 imagers to keep the average positional errors estimated from the far images comparable to those in near images. The final decision may hinge on the details of what views we should use, how many pixels we need overall, and on whether clusters of 4 rather than 5 cameras may simplify the structure of supporting electronics.

5.2.2 Degree of desired image overlap

The precision obtained from photogrammetry is due to the combination of rich image data and sophisticated processing. This can determine not just best-fit positions of different targets, but often also their relative locations, and sometimes even the lens distortions of the imagers used. Doing this requires viewing many of the same features from multiple angles. One of the desired photogrammetric processing procedures (known as relative orientation) requires at least 6, and preferably more, non-collinear targets to appear in adjacent images. Having triangular

overlap areas is best. Hence there may be reason for at least 10-20% overlap of adjacent images, and one tiling geometry may be better than another. The overall image tiling geometry sets the overlap geometry, but the amount of overlap can be adjusted as desired by varying the lens focal length and coverage for some or all of the views.

At the other extreme, a large overlap in ODS camera views will make glare a problem in more images. The best solution may be to provide enough overlap of adjacent images to allow good relative image registration, while trusting pre-flight data on lens distortion characteristics and the relative camera positions (but not orientations) of different imagers in a cluster or in the overall lower-platform ODS assembly of 16 cameras.

We want good geometric stability between imagers, and between each lens and its imaging chip. If handling, launch, and thermal cycling don't cause the imaging chip and lens elements to move (which we can check from common targets), then we can do long-term filtering of relative pointing estimates from targets in two adjacent views. If we want 1/10 pixel accuracy, and we have 5.2 micron pixels, we need to limit cumulative relative lens and imaging chip motion to <0.5 micron after ODS gets to orbit. Problems might occur for several reasons, including: ratcheting of clamped joints or failure of adhesive bonds after thermal cycling, potting compound dry out, or relaxation of a bulge in the imaging chip if air leaks out from the air gap in the sealed imaging chip package.

5.2.3 Camera view strategy: quadrant-centered, or boom-centered?

We have baselined a “quadrant-centered” cluster of 4 cameras per quadrant. But a boom-centered approach may also merit study. It aligns the diagonal of each wide-angle view with a boom, and covers the inner ~half of its length. For a given wide angle view angle, having the diagonals aligned with the booms covers the booms and sail further into deployment using only those 4 cameras than do geometries that don't align the far corners with the booms. This reduces the number of images needing to be captured and stored, or allows higher image capture data rates.

A boom-centered approach also better fits the "peaky" azimuthal distance variations to the far edge of the sail: it is >40% further away at the corners than in the middle of a quadrant. So ODS might use 15 mm lenses to view the corners, and a pair of 11 mm lenses to handle each far view region between corners. This gives higher magnification at the corner, whose targets are both further away and viewed more obliquely. This seems more efficient than using one wider-angle view centered on the quadrant, and two longer lenses, going from there out to the corner of each quadrant. If later analyses suggest that higher accuracy is desired in mid-quadrant, we may want to stay with a quadrant-centered cluster, but if equal accuracy is desired over the entire sail, or if higher accuracy is desired near the corners, boom-centered clusters may make more sense. This issue will be examined more in Phase 2.

5.3 *Camera lenses*

ODS requirements on lens design are not extreme if we use 4 or more cameras for each quadrant and do not require imaging of the sail using low levels of artificial light during eclipse. We have plenty of photons and slow dynamics, so medium-speed lenses ($\sim f/4-5.6$) may be adequate. Significantly slower lenses could provide enough photons, but the small-pixel imagers that enable a small ODS require medium-speed lenses for good resolution. The size of a lens shade for a given effectiveness may scale with the diameter of the front lens element, if it is easier to reduce external than internal scattering. Hence it may make sense to use a lens with a fairly small front element and larger elements closer to the imager.

We can tolerate significant image geometric distortion (which is typically barrel distortion) as long as it remains stable through launch vibrations and camera thermal cycling. We may possibly be able to correct for distortion and even camera thermal expansion well enough by predictive analysis, while using actual pre-flight imaging tests to calibrate each camera for focal length, lens/imager misalignment, point spread function, and relative position. If so, then we can use common-target image data in space just to generate accurate camera aim estimates.

5.3.1 Commercial, modified commercial, or custom lenses?

Many compact medium-speed lenses have been developed for non-zoom megapixel electronic cameras with various imager formats. Some of these lenses appear quite suitable optically for ODS. But the ODS environment also poses non-optical demands on the lens. It is not yet clear whether we should use stock lenses without modification. For example, many lenses use one or more very thin elements. We need to ensure that the lens barrel is vented well enough that the fairly quick depressurization during launch does not impose excessive loads. Also, many optical glasses discolor when exposed to proton radiation at the intensities found in the van Allen belts, solar wind, or solar flares. This affects the front element most, which in turn shields the other lens elements to some extent. Ceria-doped glasses are tolerant of radiation, so it may make sense to either make the front element out of a ceria-doped glass or add a flat ceria-doped filter in front of the lens. Extensive ultraviolet (UV) exposure may also darken cements used to form cemented doublets. Here again, a ceria-doped element or filter may be useful, because ceria-doped glasses also absorb UV. In addition, some lenses apparently use compliant spacers that are compressed externally during final lens testing to “tune” the lens. If such spacers or other materials outgas onto lens surfaces, optical clarity can be significantly reduced. Finally, we must ensure that our lenses have acceptable focus shift and other changes with temperature, and stable properties after many thermal cycles, especially if one or more early solar sail tests occur in non-twilight earth orbits.

For initial ground tests, it appears feasible to use stock lenses developed for CMOS imagers, as long as they can tolerate a fairly slow depressurization. For flight, more development will be required, but the required development effort is very familiar to team member Tom Pollock and the optics group he works with at Texas A&M. Some companies have indicated a willingness to adapt stock lenses (such as adding a color filter or ceria-doped front element) for a reasonable lot charge. This may conceivably allow use of “modified stock lenses” for flight.

5.3.2 Flatness of field requirements

For the image to come to a focus in a plane, the lens must meet the Petzval condition:

$$n_1 f_1 + n_2 f_2 = 0$$

This can be achieved with a combination of positive and negative lenses. For multiple elements, it is more accurate to use the reciprocals. Then displacement of an image point at height y_i from the paraxial image plane is (as shown on the web site www.wolfram.com):

$$\Delta x = \frac{y_i^2}{2} \sum_{j=1}^m \frac{1}{n_j f_j},$$

where the sum is over layers with indices of refraction n_j and focal lengths f_j .

Flat field correction is important to ODS because it affects the uniformity of defocus across the image. We can tolerate modest variations in smearing over the image, but we do not want large variations. The minimum lens solution might be an achromatic lens to reduce spectral smearing, plus a negative element (perhaps adjacent to or even bonded to the front of the imager package) for improved focal-plane flattening. Larger numbers of elements can better null out coma and other errors over a wider field, and need not greatly increase lens mass or cost, especially if we can use or adapt a stock lens design. We could end up using a lens similar to that shown below:

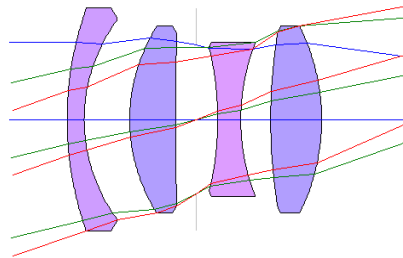


Figure 5-2. 4 Element Lens and Ray Tracing

5.3.3 Narrow-band filtering for improved resolution?

Since we have lots of photons in space, we can ease the lens requirements by filtering out everything except a modest spectral band, perhaps near 550 or 600 nm. This should ease chromatic and flat-field correction, and can eliminate most wandering photoelectrons (see below). Wavelengths near 550-600 nm are short enough to allow fairly good image resolution, but long enough for a strong signal (many photons and near-peak quantum efficiency). Long

wavelengths also have a lower rate of change of chromatic correction with wavelength than shorter wavelengths do.

5.3.4 Strawman lens specifications

- Stock C/CS-mount lenses will be specified if at all feasible.
- All lenses will have fixed aperture and fixed focal length.
- Telephoto on pan/tilt stage may require a focus motor; all other lenses are fixed focus.
- All structural components will be metal.
- Lubricants, if any, will be removed.
- All refractive elements will be glass.
- Front element or filter may be ceria-doped, if ODS environment requires it.
- Image plane may be tilted to achieve best focus at extreme edges of the sail.
- Cemented doublet elements are acceptable if optical epoxy resin is used in assembly.
- Spacing between elements at the element edge will be $\geq 0.5\text{mm}$ (unless cemented).
- Primary optical criterion is the Modulation Transfer Function, MTF; secondary criterion is spot size.

5.4 *Imaging chip options*

5.4.1 CCD vs CMOS imaging chips

There are two basic families of solid-state imagers to consider: CCDs and CMOS. Charge Coupled Devices (CCDs) are used in high-end imagers. They can have remarkably high quantum efficiency and remarkably low noise, but they degrade significantly when exposed to ionizing radiation. (In fact, they are often said to be the most “radiation soft” chips known.) An expected improvement in radiation hardness for space-capable imagers was the main reason for work on Complementary Metal-Oxide-Silicon (CMOS) imagers at JPL. This led to the formation of the Photobit company, which later became Micron Imaging. The commercial growth of CMOS imagers has been driven more by the higher degree of integration and lower mass-

production costs offered by CMOS chips, but the main feature of interest to us may be improved radiation hardness.

But CMOS imagers do have annoying idiosyncrasies. They have variable sensitivity across each pixel due to the row and column conductors and multiple active electrical elements in each pixel. But the tests described above in Section 5.1.2 with an early Photobit imager suggest that this variation need not seriously limit centroiding accuracy if we use a suitable amount of defocus (>1 pixel worth). CMOS imagers also have a higher noise floor than CCDs. That should not be an issue with ODS because we have so many photons that the major noise contribution for well-lit targets and other features will probably be shot noise, which is proportional to the square root of the number of photoelectrons in a pixel well. This is set by physics and can only be varied by using deeper wells. This requires larger pixels and hence larger imagers. CMOS also has a “wandering photoelectron” problem. Photoelectrons generated deep in the chip can wander 1-2 pixels away from where they are generated before they are captured by a photodiode. Longer wavelengths tend to be absorbed deeper in the chip, so this problem occurs mostly with photoelectrons generated by infrared photons.

CMOS imagers may have moderately worse resolution, photometry, and centroiding than CCDs. But frame-transfer CCDs have similar photometry problems unless they have good microlenses, and microlenses can degrade centroiding. A shortwave pass filter can minimize wandering photoelectrons, and they may not degrade centroiding as much as they degrade visual resolution. CCDs may have a moderate resolution advantage for equal pixel view angle, but CMOS imagers with moderately more pixels can counter it. This will result in a larger raw image size, but once it is compressed to the same usable resolution there may not be much difference. And if onboard target centroiding is done (TBD), the centroid downlink data volume should depend only on usable resolution, and not pixel count.

These cameras will probably run warm, especially in cases where reflected glare doubles the sunlight incident on the camera cluster. This will increase dark current. This tends to be more of an issue with CMOS than with CCDs. But our exposure times can be short, even with fairly slow lenses, so we may not have a problem here. And when there is “enough” light (i.e., when

pixel exposure exceeds $\sqrt{\text{RMSDarkNoiseInPhotoelectrons}}$, then dark noise is less of an issue than shot noise, which depends only on $\sqrt{\text{PhotoelectronsPerPixel}}$.

As CMOS imaging capabilities have improved, so have CCD chips: new chips take far less power, and offer pixels as small as 2 microns. They may be competitive for ODS if the radiation environment is modest. If the main focus of a flight experiment is deployment plus maneuvering in low earth orbit, CCDs may be fine. But if ODS must work well on missions lasting years without carrying heavy shielding to protect each of the ~24 imaging chips, CMOS is preferable.

5.4.2 Should we use frame-transfer or “rolling focal plane” imaging chips?

Both CCD and CMOS imagers are available in two types. One has a storage capacitor adjacent to each pixel, and a means of transferring charge between the pixel and the storage capacitor. This “frame transfer” topology allows simultaneous start and end of the exposure of all pixels on the imager. But it results in reduced quantum efficiency, larger chip area, and poorer centroid estimation. Only a small fraction of the available CCD and CMOS imagers operate this way, so it also greatly reduces the selection of potential imagers.

The other option involves different readout strategies for CCD and CMOS. In CCDs, the whole image slowly ratchets down, and at each step, the columns in a bottom read-out row are rapidly ratcheted into a readout cell. If the imager cannot be shuttered during readout, the smearing can be estimated and subtracted from the image. In CMOS imagers, the “charge buckets” stay in position, but one row at a time is read out. Hence reset of each row should occur a fixed time before readout, and hence also row-by-row. This results in a “rolling focal plane” exposure, with a typical ~30 millisecond time offset between the top and bottom of each frame.

Other things being close to equal, it appears preferable to use a frame-transfer imager. But the sail dynamics are slow enough that a ~30 millisecond variation in exposure time may not matter much in most cases, and other factors may be dominant. For example, the most suitable Micron frame-transfer chip has 12 micron pixels, while a comparable Micron rolling-focal-plane chip has 5.2 micron pixels. This makes a large difference in camera size (housing, lens, and lens-

shade), which becomes more important if ODS has ~24 cameras. In cases such as transients at the beginning and end of deployment, continuous imaging might allow reasonable interpolation to create synthetic “fixed time” images. Or computer simulation models can generate “synthetic focal plane views” that have a similar top-to-bottom variation in time.

5.4.3 Should we use color or monochrome imagers?

Many compact CCD and CMOS imaging chips are available in both monochrome and color versions. They are electrically identical and differ only in that the color version has a mosaic filter deposited on the image area. The usual mosaic is a Bayer pattern: a checkerboard that is half green-sensitive pixels, with the other half split between red and blue. Green is favored since human visual acuity is usually better with green than with red or blue.

Monochrome imagers seem preferable for most ODS cameras. One reason is that color imagers with mosaic filters result in poorer centroiding. Also, the mosaic filter materials may outgas, fade, or otherwise degrade in the persistent sunlight, even with good UV filtering. And we do not expect to see much in the way of color features in the sail anyway. Using monochrome imagers also allows narrow-band filtering for improved optical performance, as suggested in Section 5.3.3. Filtering with color imagers would simply make them low-performance monochrome imagers. However, it may make sense to use a color imager for one of the inspection cameras. This can use either a conventional mosaic filter or perhaps a multispectral filter wheel, which may be both more stable and more useful (but larger, more expensive, and less reliable).

5.4.4 Some candidate SXGA CMOS imaging chips

<u>Imager</u>	<u>Pixel pitch in microns</u>
Micron MT9M001	5.2
Omnivision OV9121	5.2
National Semi LM9638	6.0
Fill Factory IBIS5-1300	6.7

5.4.5 Why should ODS use ~20 megapixels to cover the sail?

The more pixels we use, the smaller the targets can be and still be found against background noise, and the better the centroiding will be. In particular, wherever noise is bad enough to compete with target brightness (and that will certainly occur in the region around the specular reflection point on the sail), the noise will be highly variable, and the target will not be. So if the minimum dimension of the target is several pixels in that region, then we can find the target because its pixels are the right brightness, not just “bright.” That suggests we want targets well over 1 pixel high close to the central boom, where glare and glint are likely to be most serious. That is easy to get, even with wider-angle lenses for the near field than for the far field. It also suggests that we may want to limit defocus or smearing to the minimum that gives acceptable centroiding, rather than the larger amounts that may give optimum centroiding.

5.4.6 Should the main photogrammetric cluster also include star tracking cameras?

The cameras in the main ODS cluster can have fairly stable relative geometry since they can mount near each other, and might even use a common housing. There may also be a reason to add one or more star trackers of comparable accuracy to that cluster. Then we can relate the observed sail dynamics to inertial space and not just to the cantilevered camera cluster itself. What we need is one or more of the same kind of imaging chip, but with faster lenses, much better lens shades, and suitable software. The best look angle will involve a trade between direct glare from the sun, and reflected glare, glint, and sheen from the sail membrane.

A more “natural” location for star trackers is on the anti-sun side of the sail, perhaps integrated into the main sail payload. This eases sunshield requirements, but it may complicate interpretation of ODS data if we cannot accurately relate ODS images to inertial space. Similarly, accurate steering of the sail may require relating a best-fit sail plane to inertial space. That can be done more accurately if the star tracker is closely coupled to the photogrammetric cluster viewing the sail. Another alternative is to add targets to the camera mast so we can

directly measure its distortion (static and dynamic) using the wide-angle views in the main camera cluster.

5.5 *Boom-view camera issues*

Besides the main photogrammetric cluster with its ~16 cameras, the ODS baseline concept includes 4 cameras nearly in the sail plane, one looking outward along each of the diagonal booms. They can use the same imaging chips, but with longer-focus, narrower-view lenses (~10°). This allows them to see boom bending and twisting very well, as should be easy to imagine if one considers the boom view sketched earlier in Fig. 4-4. But accurately estimating boom-camera look angles relative to each other and to the main camera cluster may be difficult. These cameras don't have overlapping views (by intent), and it is not clear whether their look angles relative to each other can be kept stable in both sail designs.

If the 4 boom-base cameras do not connect to each other structurally, but only to the boom base, their relative orientations may be perturbed by primary structure flexure. The question is whether we have any way to estimate the relative look angles of those 4 cameras with respect to each other and the main ODS cluster many meters away. We can measure flexing along the length of each diagonal boom very well, but our errors in estimation of the boom dynamics relative to each other may be >10X worse, both in steady-state error and also in dynamics, unless we can accurately relate the boom-view camera look angles to each other.

A related issue is that the longest camera baselines we have are between the boom views and the two other camera clusters (main and inspection). This can only provide 3D photogrammetric strength in views of a boom and adjacent sail features if we can relate the look angles of the cameras at each end of a baseline to each other. This might be done either by redundancy in the image data or by other data or constraints on mutual look angles or dynamics. The upper clusters can easily see the boom-view cameras, but we cannot easily add an upward-looking camera to a boom-view cluster because that camera would have to look nearly into the sun. So we may lose

our two longest baselines unless we have other means of establishing the relative look angles of both cameras compared to the baseline between them.

As noted in Section 5.4.6, we can put targets on the camera mast. If we put them at the base and halfway up to the main cluster, the 4 wide-angle cameras on the main cluster can view the targets. That should help us accurately measure most of the mast dynamics and any cluster tipping. But resolution of boom twist will be weak, and boom-view tipping cannot be viewed but must be inferred based on dynamic or other constraints.

Team member Tom Pollock has studied the dynamics of floppy 4-armed crosses. Three common modes are "Swastika" (rotation of the center in one direction, and the tips in another), a "scissors" mode, and one where 3 arms go in one direction and the 4th goes in the opposite direction with 3X larger amplitude. Adding our camera mast may give very interesting and poorly damped dynamics. If the dynamics may impede interpretation of our data, then we may need to measure them, to relate our long-baseline look angles to each other accurately.

5.6 *Inspection cameras and pan/tilt head*

We started off assuming the inspection camera would have a zoom lens, and realized that we might get better imaging, lower mass and cost, better reliability, and much better inspection-camera aiming data if we bore-sighted wide- and narrow-view cameras together on a pan/tilt head. Bore-sighting several small cameras also allows us to use one color imager on the pan/tilt head. (It seems prudent to include at least one multi-spectral imager out of ~24 cameras). Costs will probably be lowest if we use the same imager and support electronics that we use for the quadrant-view clusters and boom-view cameras, but with different lenses. The other imagers are all organized in clusters of 4 with shared support electronics, so the inspection platform can fairly painlessly use 4 imagers (with perhaps one of them being a star tracker if there is no better use for it).

One camera can have a quite narrow view (a few degrees). It may be able to see sail details smaller than the diameter of its own lens aperture. To see such small details over a range of distances, adjustable focus is needed, and hence a focus motor and control logic. Focus control need not be perfect. After some initial adjustments under ground control, it may be enough to adjust focus in an open-loop manner as a function of the commanded tilt angle (which approximately controls the distance to the sail region viewed).

The thermal imager discussed in Section 6 will have a narrow enough view that it will also need to mount on a pan/tilt head to see the whole sail. Thermal imaging signal/noise ratio is far worse on the front than on the back, but may be “good enough.” Mounting the thermal imager on the inspection pan/tilt head would simplify integration, and the wider-angle optical views can provide precise aiming data for the thermal imager for cases when that may not be reliably inferred from the content of the thermal image. (This may not be a problem if the optical targets are also brighter than the rest of the sail at long wavelengths.) Hence it is possible that the pan/tilt inspection platform will include a thermal imager if our work during Phase 2 shows that we can get good enough imaging from the front side of the sail to be diagnostically useful.

Figure 5-3 shows a candidate layout for the inspection platform, with multiple bore-sighted imagers mounted offset enough to look straight down without their view being obstructed by the camera mast they sit on. Figure 5-4 shows a design for a biaxial drive (that can be modified for ODS purposes) for a pan-tilt head from the company that built the robotic arms for the two Mars Exploration Rovers.

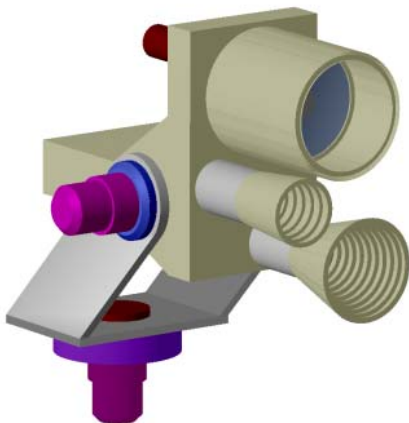


Figure 5-3. Inspection Platform Concept



Figure 5-4. Alliance Spacesystems Inc. Biaxial Drive

5.7 *What parameters drive system mass*

We have baselined ~24 cameras for ODS, which is a far larger number than we originally expected. Obviously a significant part of the overall system mass will scale with the number of cameras. Other things being equal, a 24-camera ODS will be heavier than a 12-camera ODS. But other things are not equal: using larger numbers of cameras may allow reductions in individual camera, lens, and lens shade mass enough to pay for much or all of the mass of a larger number of cameras. One early ODS camera design was <20 grams/camera for a VGA design. The lens, housing, lens shade, and imager plus support circuitry on a small circuit board each weighed ~5 grams. The actual design may weigh moderately more, especially if each camera has large amounts of flash memory to store raw data, but even here the camera mass may be <40 grams/camera. So even with 24 cameras and local image storage for each, the total camera mass may be less than half the allowable total ODS mass of 2 kg.

The rest of this section discusses some of the issues considered in selecting the types of cameras, which led to the expected mass being small enough that we can afford up to 24.

If one compares two cameras with the same number of pixels, field of view, and sunshade performance, and one has twice the pixel pitch of the other, then the camera housing, lens, and sunshade dimensions will also differ by a factor of 2. The smaller camera should be lighter by a factor of 4, if “minimum gauge” or radiation shielding are dominant, by a factor of 8 if they are not. So if other things are roughly equal, smaller is much better.

Now consider a different case, where larger pixels have the same pixel noise and quantum efficiency. The lens needs 2X the focal length, but only needs the same photon throughput, so it can use the same aperture diameter and hence 2X the lens f/number. The lens and lens shade should be the same size, but the lens might be slightly simpler and lighter. Diffraction-limited angular resolution should be the same (2X the f/number, 2X the pixel size). It is just the imager and housing (including lens barrel) that should be heavier, by a factor of 4 to 8. It seems likely that the real world may lie between these cases, so “much but not all” of the camera mass may

scale at a rate between the 2nd and 3rd power of the pixel pitch. Lenses may have a resolution that falls short of diffraction-limited by a factor of 2 or more, but if the performance shortfall does not itself change drastically with lens size, then the overall sensitivity of camera mass to pixel pitch should not change much.

Other factors that affect system mass include the number of cameras, the required thermal stability of the housing (aluminum vs invar), any imaging chip radiation shielding that may be needed, sunshade design and size, processing electronics including compression and memory, cabling, and structure to support the main camera clusters stably with respect to each other. If we use aluminum lens barrels and camera housings, the image size on the focal plane (in pixels) will increase with temperature because aluminum expands more than silicon does. The lens elements also respond to temperature, both with size changes and also with refractive index changes. (Thermal expansion of glass “should” decrease its refractive index, but polarization changes with temperature, and this can swamp density change effects.) With medium-speed lenses, focus shifts and distortion changes should be less of an issue than scale-factor changes due to the lens moving away from the imager proportionately more than the silicon imaging chip expands. Scale factor changes can be estimated and compensated for if we measure housing temperature and keep thermal gradients small enough to minimize any need for higher-order corrections.

5.8 Recommendations

Our tentative recommendations on the optical imagers are as follows:

Configuration	6 clusters of 4 cameras (pan/tilt, booms, 4 quadrants) w/shared electronics
Imager type	CMOS?, monochrome, no microlenses, 10-bit data, row-by-row exposure
Imager format	~1280x1024 pixel array, small pixels (~5u?), glass-sealed ceramic pack
Lenses	Modified stock, f/4-5.6, fixed focal length and focus (except inspection)
Filters	Ceria-doped; IR cutoff or narrow-pass visible (near 550 or 600nm?)
Lens shades	Fairly large, to reject strong glare from close to region being imaged

Housings Aluminum alloy, black coating on inside and white on outside
Fields of view TBD (some overlap, but perhaps less than usual in photogrammetry)

5.9 *References*

Micron Technology, Inc, CMOS image sensor page: <http://www.micron.com/products/imaging/>

Omnivision Products; 9000 series camera chip:

<http://www.micron.com/products/imaging/products/MT9M001.html>

Fill Factory, Ibis5-1300 and STAR (rad-hard) CMOS sensor pages:

<http://www.fillfactory.com/htm/products/htm/ibis5/ibis5.htm>

<http://www.fillfactory.com/htm/products/htm/star.htm>

National Semiconductor LM9638 product folder: <http://www.national.com/pf/LM/LM9638.html>

Janesick, J.R. *Scientific Charge-Coupled Devices*. SPIE Press, 906 p., 2001

Universe Kogaku America page on lenses for CCDs: <http://www.ukaoptics.com/ccd.html>

Section 6

Thermography

6.1 Motivation for investigating thermography for solar sails

Monitoring sail temperature during flight demonstrations can be important. Sail temperature is driven by front-side absorptance and rear-side emittance, and temperature changes indicate changes in one or both parameters. In addition, knowledge of the temperature field and associated thermal strain distribution is necessary to predict sail loads and dynamics. Average membrane tensions of 1-10 psi are planned, so mechanical strains will be only a few parts per million. Small temperature gradients across the surface could result in thermal strains exceeding mechanical strains. We are just beginning to study the effect of this on sail static shape and loads, and possible effects on sail dynamics. It might even affect sail control loop stability.

Team member Joe Blandino et al. demonstrated the effect of temperature variations on a spot-heated membrane [Ref. 6-1]. The center was heated 55°C warmer than the rest of the membrane. (Conduction in the plane of thin membranes is minimal.) The heated region expanded and became visibly slack.

6.2 Thermal modeling of solar sails

To better understand the temperature distribution that the sail may experience in space, a thermal model was developed. The sail was modeled using square elements. Figure 6-1 shows the radiation from the sun and interactions with space on one element. Radiation exchange between elements is neglected since the view factors are extremely small. In the front, the mean sail shape is concave but the self-view factor is modest, and the front-side emittance is very low due to the aluminum coating. On the back side, emittance is high, but billowing makes the sail quadrants convex, so only wrinkles and other small-scale features will allow the high-emittance back surface to “see itself” at all. And the view factor of such views will be small. One can

make an intuitive estimate of the importance of such views by imagining the best-fitting sphere to a locally concave region. The self-view-factor is roughly equal to the fraction of the full sphere's area that the local "dimple" covers. That will generally be only a few percent, except very close to a sharp crease that has not been straightened out. Conduction through the membrane is assumed perfect, and conduction in the plane of the membrane (mostly in the aluminum coating) is neglected because local radiative equilibrium dominates in-plane conduction over distances larger than a few millimeters. Average front and back side emittance values are assumed (i.e., the spectral nature of these values is neglected).

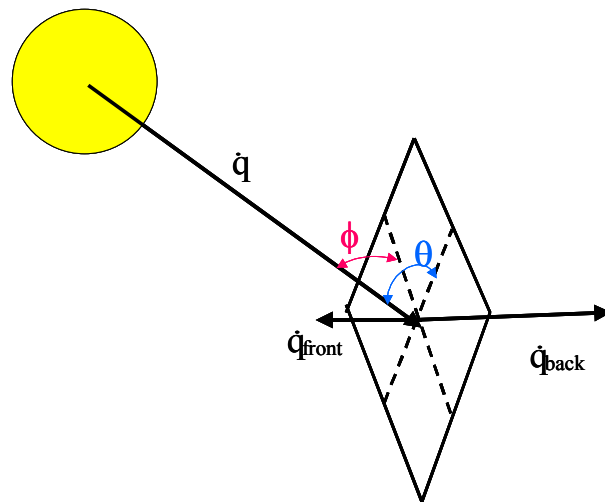


Figure 6-1. Radiation interactions for a sail element

An expression for the temperature at any point on the sail surface is obtained by performing an energy balance on the sail. The expression for temperature is

$$T_s = \sqrt[4]{\frac{\alpha_f \dot{q} \cos \phi \cos \theta}{\sigma(\epsilon_f + \epsilon_b)} + T_\infty^4} \quad (1)$$

where T_∞ is the background temperature, α_f is the front side absorptance, ϵ is the emittance (front and back), σ is the Stefan-Boltzmann constant, and \dot{q} is the normal solar flux. This is essentially the expression given by Salama et al. [Ref. 6-2]. The two angles are projections of the angle of incidence on planes normal to the sail and to each other. The solar intensity on the surface varies with overall sail orientation with respect to the sun, but it also varies with the billowed shape of

the sail. To approximate the billowed shape of the sail, photogrammetry was used to measure the gravity sag of one quadrant of a 2-m sail model. The general shape is shown in Fig. 6-2. The gravity sag is greater than the billow due to light pressure in space, but the data in Fig. 6-2 can be scaled in the x , y and z dimensions. Thus it can be used for any sail size and billow depth.

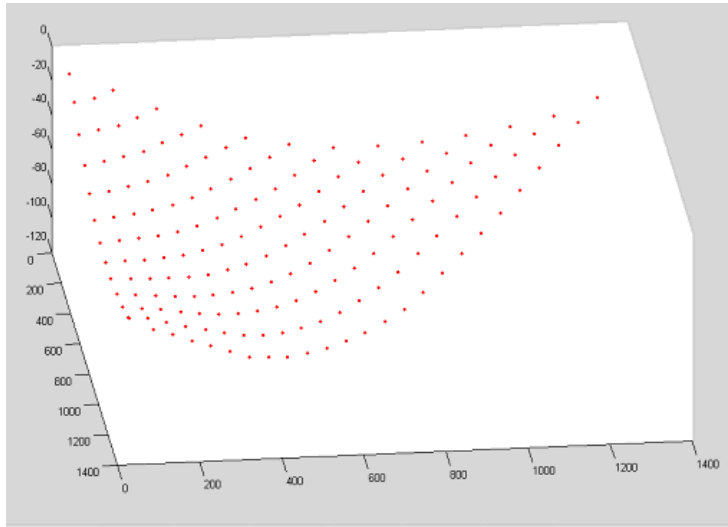


Figure 6-2. General sag shape used to estimate solar sail light pressure billow. Dimensions in mm.

We considered a 40 m square sail 1 A.U. from the sun. We estimated the temperature distribution for sail angles of 0° , 22.5° , and 45° away from normal to the sun, and billow depths of 0, 0.2 and 1 m. We assumed a Kapton[®] sail, aluminized on the front only, with $\alpha_f = 0.09$, $\epsilon_f = 0.04$, and $\epsilon_b = 0.50$. Table 6-1 presents the average sail temperature and temperature range, ΔT , for the 3 sail angles and billow depths.

Table 6-1. Sail temperatures for various sun angles and billow depths at 1 AU from sun

Billow Depth	Sun-sail angle = 0°		Sun-sail angle = 22.5°		Sun-sail angle = 45°	
	0.0 m	-21.9°C	0.0°C	-26.6°C	0.0°C	-42.7°C
0.2 m	-21.9°C	0.2°C	-26.8°C	0.5°C	-43.3°C	1.0°C
1.0 m	-21.9°C	0.3°C	-27.9°C	2.3°C	-45.7°C	5.2°C
	T_{avg}	ΔT	T_{avg}	ΔT	T_{avg}	ΔT

The temperature differences are modest, but they can result in dimension changes that exceed the mean strains caused by sail tension. Table 6-2 shows the coefficient of thermal expansion for 3 sail materials and the resulting thermal strain due to temperature differences.

Table 6-2. Sail thermal strain for three candidate materials

Material	Coef. of Thermal Exp.	ΔT	$\epsilon_{\text{Thermal}}$
Kapton[®]	$2.0 \times 10^{-5} / ^\circ\text{C}$	0.2 °C	4.0 $\mu\epsilon$
		0.5 °C	10.0 $\mu\epsilon$
		1.5 °C	30.0 $\mu\epsilon$
CP1 colorless polyimide	$3.7 \times 10^{-5} / ^\circ\text{C}$	0.2 °C	7.4 $\mu\epsilon$
		0.5 °C	18.5 $\mu\epsilon$
		1.5 °C	55.5 $\mu\epsilon$
Mylar[®]	$1.7 \times 10^{-5} / ^\circ\text{C}$	0.2 °C	3.4 $\mu\epsilon$
		0.5 °C	8.5 $\mu\epsilon$
		1.5 °C	25.5 $\mu\epsilon$

To compare the mechanical and thermal strains, Table 6-3 lists the 3 candidate materials and strains caused by a 68,940 Pa (10 psi) mechanical load, the upper limit of what has recently been discussed for solar sail membrane tensions. For Mylar[®] and Kapton[®], thermal expansion exceeds the mechanical strain if the temperature difference exceeds $\sim 1.2^\circ\text{C}$. For CP1, thermal expansion exceeds the mechanical strain even for temperature ranges under 0.5°C . If the sail membrane sees average tensile loads smaller than 68,940 Pa, which is likely, then the temperature gradients required for thermal effects to greatly redistribute loads will be proportionately smaller.

Table 6-3. Membrane mechanical strains for three materials under 68,940 Pa (10 psi) tension

Material	Tensile Modulus	$\epsilon_{\text{mechanical}}$
Kapton [®]	$2.96 \times 10^9 \text{ Pa}$	23.2 $\mu\epsilon$
CP1	$4.20 \times 10^9 \text{ Pa}$	16.4 $\mu\epsilon$
Mylar [®]	$3.79 \times 10^9 \text{ Pa}$	18.2 $\mu\epsilon$

Measurement of the sail membrane temperature hence seems quite valuable for understanding structural behavior in space. Temperature gradients across the sail surface can

develop due to variations in metallic coatings, sail orientation to the sun, and the billowed shape of the sail. The cases presented illustrate that only small temperature gradients, perhaps well under 1°C, are necessary for the thermal strain to become larger than the mechanical strain. Because the thermal strains will be significant, their effect on sail dynamics must be considered. This will be studied more in Phase 2.

6.3 *Optical properties of solar sails*

The approach described above assumes uniform solar absorptance and thermal emittance values over a typical membrane. Exercising the model shows that small perturbations in optical property values can generate significant changes in the temperatures and temperature differences predicted, and hence in thermal distortion and the resulting mechanical load distribution. Thus it is important to characterize and consider in a thermal model the wavelength dependent or spectral emittance and absorptance.

A sample of Kapton[®] polyimide film (Product 100HN) was acquired from Dunmore Corporation and later tested at Surface Optics Corporation (SOC) for spectral reflectance and transmittance. Dunmore first tested the film for quality conformance. Its properties were: film thickness: 0.001 inches; aluminum adhesion test results: 0.0%; emittance: 0.02; surface resistivity: 0.72 ohms/sq. SOC used the following test matrix to characterize the spectral reflectance of the samples: test coated and un-coated sides in similar fashion; acquire Hemispherical Directional Reflectance (HDR) (total reflectance), Diffuse Directional Reflectance (DDR), and Specular Directional Reflectance (SDR), where $SDR(\lambda) = HDR(\lambda) - DDR(\lambda)$. The tests included the 2 to 25 micron wavelength region, which covers a small part of the energy in the solar spectrum, and most of the long-wave emittance spectrum. The tests were run at 20 °C (room temperature), 60 °C, 100 °C, and 140 °C; with incident angles of 20°, 50°, and 70°; with average, perpendicular, and parallel polarization. The tests focused on temperatures warmer than shown in Table 6-1 because polyimide sails (of Kapton[®] or CP1, for example) seem most attractive in missions that go significantly closer to the sun than 1 AU. A brief synopsis of the results is provided below.

The spectral reflectance of the coated side of the membrane is relatively constant with both wavelength and polarization. It varies modestly with angle of incidence and temperature. Nearly all the reflected energy is specular, and the diffuse portion increases inversely with angle of incidence. An average value of reflectance, ρ , weighted with respect to temperature and angle of incidence offers a reasonable basis for thermal calculation. A representative depiction of spectral reflectance for coated Kapton[®] 100HN is provided in Fig. 6-3.

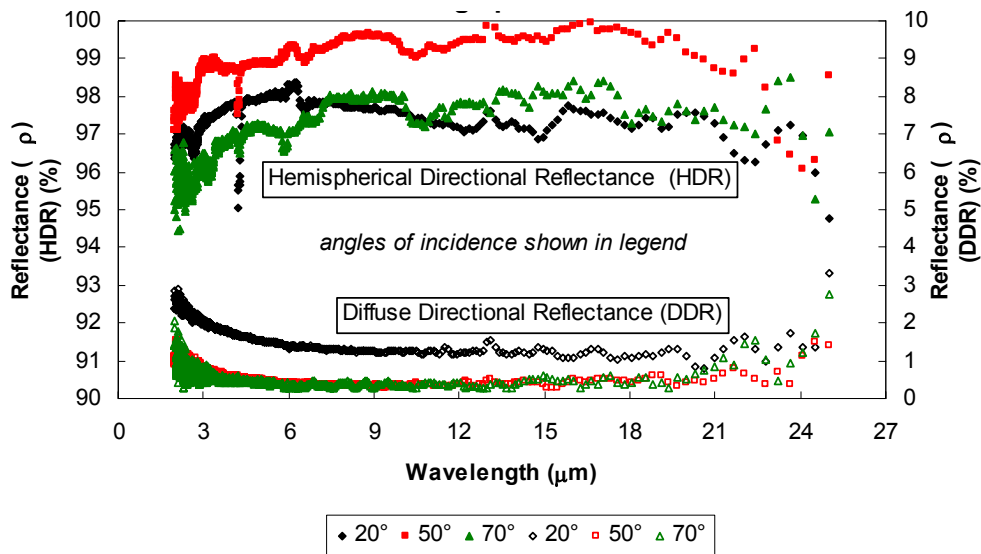


Figure 6-3. Spectral reflectance for coated Kapton[®] 100HN at 61.7 °C for average polarization

The spectral reflectance of the uncoated side of the membrane is highly variable with wavelength but mostly unaffected by polarization. Reflectance varies significantly with angle of incidence and insignificantly with temperature. The portions of reflected energy that are specular and diffuse vary significantly with wavelength and angle of incidence. An average value of reflectance, ρ , does not offer a reasonable basis for thermal calculation, so spectral analysis is needed. Representative spectral reflectance for coated Kapton[®] 100HN is shown in Fig. 6-4.

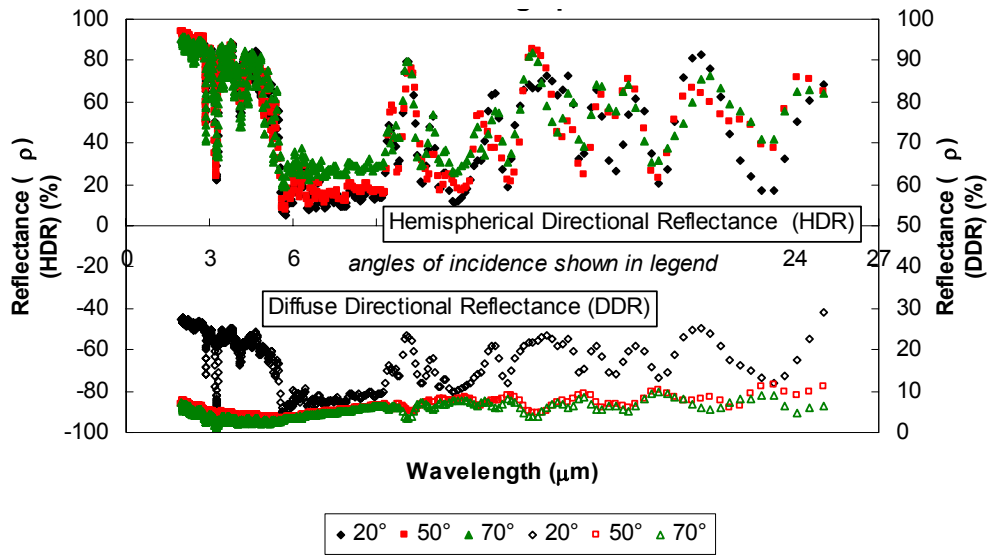


Figure 6-4. Spectral reflectance of uncoated Kapton® 100HN at 103.2 °C for average polarization

Spectral transmittance (see Fig. 6-5) should be evaluated and considered in any thermal analysis. A preliminary analysis suggests that 1-mil Kapton® transmittance can be an important factor in the infrared. A heating element placed behind a membrane sample may transmit energy through the membrane comparable to that emitted by the membrane. Transmission of direct sunlight may be less of an issue except directly looking at the sun, since very little of the sun’s radiation is in the long-wave thermal region used by the Indigo thermal imager.

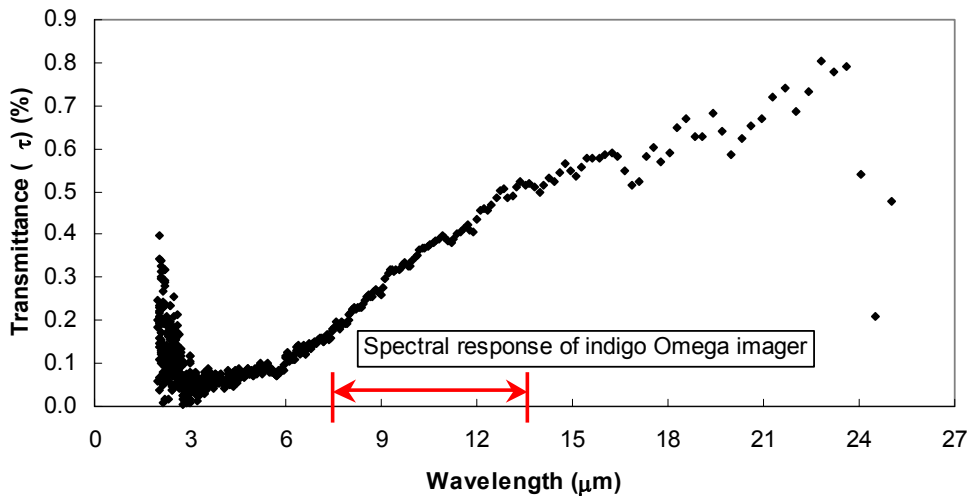


Figure 6-5. Hemispherical directional transmittance, one-side-coated Kapton® 100HN, normal

6.4 *COTS thermography equipment and testing*

We tested the indigo Omega (long-wave) miniature microbolometer-based imager [Ref. 6-3] to determine the feasibility of that approach for thermography. This new imager is very small, low mass (<120 grams), and has excellent image quality. It uses an uncooled 160×120 array of microbolometers based on vanadium oxide. It is sensitive to the 7.5-13.5 micron wavelength range. It acquires images at 30 Hz and features a noise equivalent temperature difference (Netd) of less than 85 mK. Its temperature detection range is –40 to 55 °C (extended).

We collected infrared image data from a 0.5m x 0.5m, 1-mil aluminized (on one side) Kapton[®] sample. We collected images using both an Omega and also 2 other high-quality thermal imagers that we had available: an Agema Thermovision 870 (mid-wave) infrared scanning system and a CMC Electronics Cincinnati TVS-8500 (mid-wave) infrared imaging system. These two systems are laboratory-grade instruments and the TVS-8500 represents the state of the art in Stirling-cooled, mid-wave focal plane array technology. The Thermovision system is old technology but robust and flexible in its operation. They both use shorter-wavelength ranges than the Omega.

We placed the three imagers behind a shield to minimize stray ambient reflections from the surroundings. We then placed the Omega and Agema side by side at the centerline of the membrane, positioned the CMC unit near the top of the membrane, and then heated the membrane with a circular resistive element centered behind the membrane. The images collected with the Omega and Agema units are shown in Figs. 6-6 and 6-7, first with no power applied and then with power applied at three different levels.

Specular reflections are apparent in all the images, but are more easily distinguished in the monochrome images produced by the indigo Omega system. At low power setting the warmed round region begins to be seen in the center of the membrane, and in the images for medium and high power setting (Fig. 6-7), the effects of natural convection become apparent.

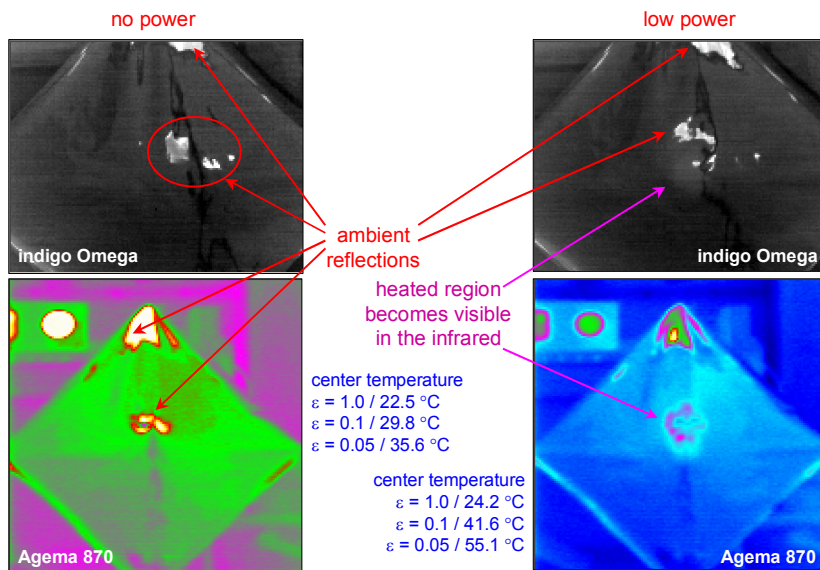


Figure 6-6. Infrared images of 0.5-m, 1-mil aluminized Kapton[®] sample, at ambient temperature (left) and with low heater power at center (right)

The Agema system calculates target temperature based upon a proprietary algorithm that considers three inputs from the user: T_{ambient} (temperature of the surrounding atmosphere), $T_{\text{reflected}}$ (a nominal average blackbody temperature of the objects surrounding the target), and ϵ (an estimated average target emittance). The temperature data listed in Figs. 6-6 and 6-7 show the sensitivity of a “true” temperature calculation to the average emittance assumed for the calculation.

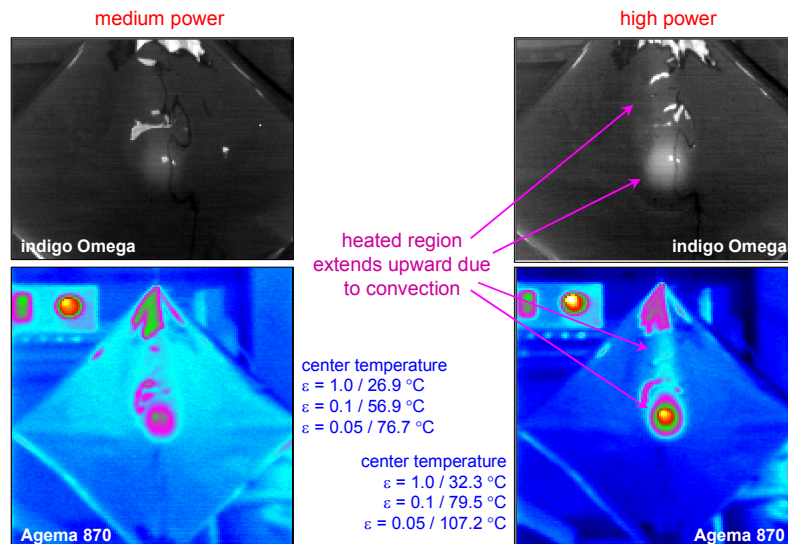


Figure 6-7. Infrared images of 0.5-m (on side), 1-mil aluminized Kapton[®] sample, with medium heater power at center (left) and high heater power at center (right)

6.5 *Trades between back side and front side thermography*

The main advantage of back side thermography is a far larger signal and somewhat lower noise, and hence a far better signal-to-noise ratio. The low front side membrane emittance reduces thermal radiation from the sail and efficiently reflects “noise” radiation from other objects. Particularly with sails in low earth orbit, the emitted signal may be swamped by a reflected longwave earth signal, which varies with cloud cover and height and is hence not easy to estimate and compensate for. On the back, the emittance is much higher, and reflected “noise” is weaker. But front-side thermography from the inspection platform should greatly ease integration, by eliminating any need for an aft mast and another pan-tilt head. The signal would be small, but it could be useful, especially if the front side longwave emittance can change due to sputtering, oxidation, contamination, etc. In Phase 2, we will explore more what might be learned from front-side thermography.

6.6 *Significance of optical property knowledge and nonuniformity*

According to equation (1) in Section 6.2, if the sunlight and effective longwave radiant ambient temperature are constant, the membrane temperature should scale with $(\alpha_f / (\epsilon_f + \epsilon_b))^{0.25}$. Hence changes in front-side solar absorptance or front or rear longwave emittance will affect the temperature. Since sail absorptance is low (~ 0.09), even modest changes due to contamination or other factors may make a significant difference in temperature and hence thermal distortion. Changes in emittance could also have an effect. But here things are more complicated. For example, if most of the thermal emittance is on the back, an increase in back emittance will drop the temperature but have little effect on the overall radiation emitted from the back: that will scale with $\alpha_f \epsilon_b / (\epsilon_f + \epsilon_b)$, or (since $\epsilon_f \ll \epsilon_b$) with $\sim \alpha_f$. Hence back side thermography may see front side absorptance changes much better than it sees back side emittance changes. Front side thermography should be sensitive to both absorptance changes and emittance changes, especially those on the front: the emitted energy scales with $\alpha_f \epsilon_f / (\epsilon_f + \epsilon_b)$. So paradoxically, front-side thermography, despite its weaker signal and stronger noise, may detect more membrane property

changes—but only if the signal-to-noise is “high enough.” (But it may not tell us what parameter changed.) All of these issues need further investigation.

6.7 Recommendations

The good sensitivity and low mass, power, and cost of thermal imagers like the new indigo Omega described in Section 6.4 may make such imagers an attractive part of ODS. The ODS baseline design currently assumes the thermal imager will be located on the back side of the sail because it faces deep space. But putting the imager on the inspection pan-tilt head on the front side of the sail may significantly ease ODS integration costs and constraints, and hence makes it easier to justify doing it. Doing thermography from the front results in much weaker signals and stronger noise, but the results may be sensitive to changes in more of the sail’s optical properties. For now, we will continue to assume that an additional support mast and pan-tilt unit is needed for a back side installation of the thermal imager until the suitability of moving it to the front can be unambiguously determined.

Many questions still need to be answered, including:

1. Can compact, low-power imagers like the indigo Omega be qualified for use in space?
2. Can front side thermography with microbolometer-based instruments like the Omega provide useful images of the sail?
3. What can such images tell us about sail properties, degradation, or other phenomena?

6.8 References

6-1. Blandino, J. R. et al., “The Effect of Asymmetric Mechanical and Thermal Loading on Membrane Wrinkling,” *AIAA Structures, Structural Dynamics, and Materials Conference*, AIAA paper 2002-1371, April 2002.

6-2. Salama, M., McInnes, C., and Mulligan, P., “Gossamer Sailcraft Technology,” Chapter 19 in Jenkins, C. H. (editor), *Gossamer Spacecraft: Membrane/Inflatable Structure Technology for Space Applications*, AIAA Progress in Astronautics and Aeronautics Series, vol. 191, 2001.

6-3. Webpage on Indigo Systems Omega thermal imager: www.indigosystems.com/product/omega.html.

Section 7

Distributed Non-Imaging Sensors

As noted in Section 3, we originally planned to have cameras not just in the center but also at each corner of the sail. This required distributed wiring that would also be able to handle various other distributed sensors, so such sensors were included in the study. To reduce expected ODS cost and mass, the solar sail program decided to limit the cameras to a central boom at the hub of the sail, which is located on the front side in the our baseline concept but potentially can be used on the back instead. Nevertheless, there remains a potential requirement (specifics are still TBD) for distributed sensors, and this is still within the scope of the ODS team's work. This section of the report lists the options and issues we see for the various distributed non-imaging sensors and their support hardware. This distributed subsystem must fit within the overall mass, power, cost, and "easy to integrate" constraints of the overall ODS.

7.1 Distributed sensor options and recommendations

The main focus in this area was sensors that complement the imaging sensors or provide data that could aid decisions about what imaging data to collect, retain, and/or download. Some of the categories below were included based on only a cursory assessment and need a more careful evaluation. The only categories discussed in detail are items 1-5 below.

7.1.1 Measurements considered

1. 3-axis acceleration at each boom tip (to measure boom bending and torsion)
2. Component temperatures (as convenient)
3. Strain at root of each boom (near hub), and perhaps along one or more booms
4. Membrane tension (at one or more support points of each quadrant.)
5. Laser-based systems (e.g., the LDRI)
6. Charging of local exposed non-grounded surfaces (to determine importance of grounding)
7. Diagnostic feedback from sail control actuators (motor currents, position, temperature, etc.)
8. Housekeeping data from distributed sensor support electronics (temperature, voltages, etc.)

7.1.2 Accelerometers

We considered conventional high-end accelerometers (Q-flex, etc.), lower-mass piezo-electric sensors, and some fairly new MEMS devices from Analog Devices and Silicon Designs. The option that now looks most attractive is the Silicon Designs SD1221 seismic-grade MEMS accelerometer chip. It has a ± 2 g full-scale range, 2000 g shock tolerance, an internal temperature sensor, and RMS noise of $\sim 2E-6$ g/Sqrt(Hz).

Figure 7-1 shows the SD1221. It weighs only 0.62 grams, is < 1 cm square, and requires ~ 10 mA at 5V. Signal output is a differential analog pair, with voltages each ranging from 0.5 to 4.5V. Taking full advantage of its accuracy and low noise requires a closely coupled analog-to-digital converter.

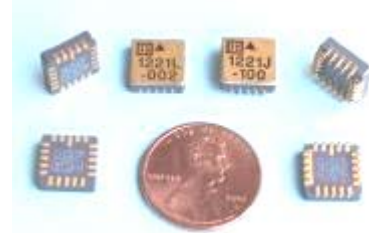


Figure 7-1. SD1221 accelerometers

7.1.3 Temperature sensors

We considered the temperature sensor options listed below:

1. DS1820 family (digital output; -55°C to $+125^{\circ}\text{C}$; “party line” can handle many sensors)
2. AD590 (current proportional to absolute temperature)
3. Thermistors (good over moderate temperature range)
4. Thermocouples, for wide temperature range (use any of the above as a reference temp)
5. Optical fiber temperature sensors (require a large central electronics element)

The Dallas/Maxim DS1820 family is an unusual digital-output sensor with “party line” wiring. It can only provide outputs in the -55°C to $+125^{\circ}\text{C}$ range but can survive a wider range. The “party line” wiring may simplify integration because 3 wires (and in some cases 2) are enough to provide power, commands, and data return from dozens of sensors. It is attractive in cases where many temperature sensors are needed and wiring must be minimized. It is available in various packages from TO-92 down to a $0.7 \times 1.4 \times 2$ mm chip-scale package. The DS1820 is one family of sensors and communication chips that use the Dallas “1-wire” protocol. That protocol may be a useful option for getting distributed sensor data to the central ODS package.

The AD590 has a nominal output current of 1uA/K over a 4-30V supply range. The current output reduces noise problems in most installations. Thermistors are generally used on devices exposed to only a modest temperature range because of their exponential variation of resistance with temperature. Thermocouples have a wide temperature range capability but also a low signal, so they are prone to noise problems unless wiring is short and/or well shielded. Optical fiber sensors are the lightest sensors, but their signal conditioning is (currently) the heaviest and most expensive.

7.1.4 Strain gauges and load cells

We considered the strain gauges and load cells listed below. The support electronics for optical fiber sensors are fairly substantial and may not be easy to miniaturize. And optical fibers respond to both stress and temperature, and hence would probably need thermal compensation. Furthermore, distributed (averaging) strain sensing does not uniquely indicate boom shape changes. But this technology is rapidly improving it so needs to be watched. Signal transmission distances of more than 100 meters are possible over fiber and the sensor weight is negligible. Currently, options 1 and 2 appear to have much lower risk.

1. Foil type uniaxial or rosette strain gages for boom root (from Measurements Group)
2. Sub-miniature load cell (Entran ELFM for ground tests; similar to flight hardware)
3. Optical fiber strain gages (single point)
4. Optical fibers for distributed strain sensing for boom shape determination.

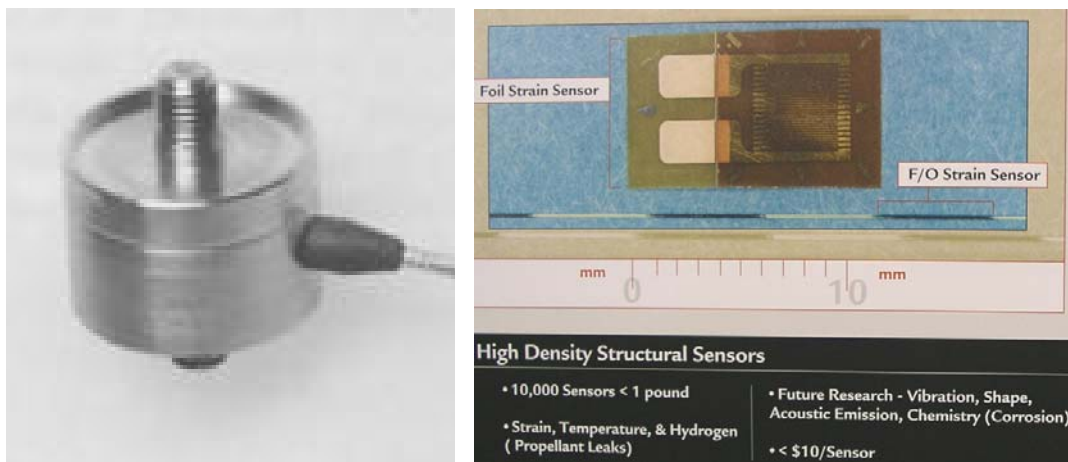


Figure 7-2. Precision Measurements miniature load cell and some strain sensor options

7.1.5 Laser Dynamic Range Imager

The Laser Dynamic Range Imager (LDRI) was developed by Sandia National Labs and NASA JSC and was used on Space Shuttle mission STS-97 in Dec. 2000. It is an interesting sensor for possible use for in-space shape/dynamics measurement of solar sails. It is an active, scannerless range imager that provides range information at each pixel of a video image. The illumination source is a diffused infrared laser beam. Although capable of measuring the shape of large diffuse objects at video rates, the low diffusivity of aluminized membranes makes it extremely difficult to receive adequate signal return for a full-field solar sail measurement. However, it could measure a field of attached diffuse targets. Technical contacts are Bob Nellums at Sandia, and George James and George Studor at JSC.

7.2 *Sensor support electronics, power, and data transmission*

In a large-scale gossamer structure, shielded analog wiring of any length will drive system noise, mass, and installation cost. The larger the structure, the more critical it is to digitize data locally, either at the sensor itself or in a nearby support module. Data transmission issues drive the support electronics design because wireless options require the support electronics package to provide its own power. Based on this understanding, we discuss data link options and issues first.

7.2.1 Wired vs wireless links: power and data options and issues

We considered the options listed below for connecting distributed sensor support electronic modules to the central ODS package located at the hub of the solar sail:

1. Concepts using wire for power and communications (RS422, RS485, LVDS, 1-wire)
2. Harms-Goubou (RF mostly trapped around a single conductor)
3. Short-range RF techniques (wireless modems, Bluetooth, etc.)
4. Short-range optical techniques (IrDA or laser in free space, fiber, or L'Garde boom)

Concepts using wires allow the ODS host platform to provide power to the remote electronics modules. But the larger the structure, the more the wiring weighs and costs to install. The “1-wire” approach uses a shared power/signal line plus a second wire as a ground. It may be the lightest and easiest to integrate, but it limits power and data rates. A 2-pair option may be significantly more capable: a power/ground pair, plus a differential signal pair.

Let us assume a 4-wire cable: either power + ground + signal pair, or a redundant “1-wire protocol” pair. We can use a design similar to the ProSEDS wire, namely 7 strands of 28AWG aluminum magnet wire twisted around an 8x400 Kevlar[®] core braid for strength. The twist is tight enough for the wires to clamp the core firmly and also to accommodate tensile load cycling without yielding the wire. Here we might twist 4 polyimide-insulated 30AWG wires around a 3x400 Kevlar[®] core. This design weighs 0.75 grams/meter, and the resistance of each conductor is 0.6 ohm/meter. The wire-twisting operation is compatible with occasional swapping of one pair to reduce cross coupling between the pairs. On a 70m sail, we would need ~200m of cabling. The mass is ~150 grams, <8% of the allowable ODS mass. If the cabling also delivers power and commands to boom-tip vane actuators, 150 grams may be very acceptable. A power-loop resistance of ~60 ohms may be acceptable if ultracaps in the module provide load leveling.

Wireless options require the remote support electronic packages to include solar cells. The low power needed places a premium on design simplicity, such as fixed body-mounted solar cells. High-end triple-junction solar cells reduce the required cell size and hence the module area that must face the sun. If it is desired to collect data during eclipse (including eclipse of the small solar array by other sail features, or shading caused by boom rotation during deployment), then the module also needs batteries, or at least ultracaps, plus suitable charge-control circuitry.

An additional issue with all 3 wireless data link options is possible obstruction of the signal path by sail features, either during deployment, normal operation, or anomalies. The best solution may conceivably vary with the sail design. For example, the inflated L’Garde booms may be able to act as RF waveguides, allowing use of Bluetooth or other protocols well beyond their normal range. If the inner surfaces are shiny enough, the booms might even act as optical

guides. (The L'Garde boom can bend enough for the ends to not have direct visual contact, so the inside surface treatment and its effect on RF and optical transmission may be critical.)

Our current baseline is wired connections. But we don't yet know whether the actual wiring can be anywhere near as light as the ProSEDS-derived concept suggested above (~0.75 grams/meter), or will be enough heavier that wireless concepts (and the resulting complexity of autonomous power supply, etc.) merit further study. If the wiring is exposed, it may need to be either shielded or redundant, either of which may significantly increase wiring mass.

7.2.2 Other design issues

Once the decision for wired vs wireless concepts is confirmed, the full sensor support electronics module can be designed. Functionally, this system is like an attached picosat. It needs power conditioning, sensors, signal conditioning, an FPGA or computer, and command, control, and communications. But rather than thinking of this in terms of satellite design approaches and costs, a more instructive perspective may lie in the work that DARPA and other organizations are doing on distributed sensor and communication networks.

A recent NIAC study of an ambitious global-monitoring concept (see Manobianco reference in Section 7.3) summarizes recent work on "Smart Dust" concepts and approaches (sensors and complete systems in the milligram class), and includes a 5-page bibliography reviewing work in this area. The Smart Dust work is far too developmental for ODS, but it is an indication of the direction in which distributed sensing systems are headed, and it seems very relevant to future gossamer spacecraft concepts. The discussions of issues like A/D conversion and local wireless data links at minimum power are clearly relevant to our needs.

Besides power and communications issues, other issues to be considered with the distributed sensor support modules include the following:

- Electronics radiation tolerance: latchup, functional interrupt, upset, and total dose
- Amount of local/distributed memory (esp. if data is desired before com-link is functional)
- Local vs central computational capability (FPGA vs 8-bit vs 16-bit vs 32 bit CPU)

- Amount of development required (commercial package vs custom-built)
- Degree of sophistication of software if it uses a CPU

7.2.3 Compatibility and synergism with sailcraft and other spacecraft needs

It is worth putting some care into the distributed-sensing aspect of ODS system design because it may be useful over a range of applications. For example, it may make sense for the L'Garde design to use a wireless link to command control surface actuation at the ends of their booms. It is also relevant to health monitoring and control of other gossamer structures. It is even relevant to large non-gossamer structures such as the International Space Station (ISS), where the complexity of the integration process may justify a wide range of autonomous distributed systems. For example, the floating-potential probe package developed by NASA Glenn and installed on ISS several years ago provided its own power and had a wireless link to ISS to reduce integration issues.

More immediately, we need to ensure that our thoughts and recommendations on sensors and support electronic concepts are at least compatible with, and preferably strongly synergistic with, any needs the sailcraft developers have for distributed power, control, and monitoring on their sail. Because of the issues of compatibility and potential synergism, and the fact that integration costs may dominate at least for wired options, we need to work closely with the sail developers during the next study phases to ensure that our work is relevant.

7.3 *References*

John Manobianco, Global Environmental MEMS Sensors (GEMS): A Revolutionary Observing System for the 21st Century. NIAC Phase I Final Report on USRA Grant Number 07600-093, December 2002. Includes 5 page bibliography, much of it covering recent work on “Smart Dust” and related concepts.

Silicon Designs accelerometer page: <http://www.silicondesigns.com/SelectChart.html>

Analog Devices AD 590 product page (also, many other useful product lines)
http://www.analog.com/Analog_Root/productPage/productHome/0,2121,AD590,00.html

“BASIC STAMP” microcontroller page, at Parallax Designs:

http://www.parallax.com/html_pages/products/basicstamps/basic_stamps_oem.asp

Mission Research Corporation, Santa Barbara: Advanced Instrument Controller
<http://www.mrcsb.com> (Note: Now part of ATK—AIC ref. not found)

Spectrolab (Boeing) solar cells: <http://www.spectrolab.com/prd/space/cell-main.asp>

Entran load cells: <http://www.entran.com/ltoc.htm>

Vishay Measurements Group: <http://www.vishay.com/company/brands/measurements-group/>

Maxim (Dallas Semiconductor) Single Wire Digital Output Temperature Sensor page:
http://www.maxim-ic.com/products/sensors/1_wire.cfm

Section 8

Avionics System Issues and Design

8.1 Evolution of thinking on data volume, compression, and operating mode

Our thinking in this area evolved considerably over the course of the Phase 1 study. The centroid testing described in Section 8.1.2 was a significant factor. We describe the evolution chronologically because it highlights the alternatives we considered and what led us to our baseline concept.

8.1.1 Early perspectives

We initially thought that image compression hardware would be so bulky and slow that it would make more sense to do compression as a post-processing operation on stored raw data rather than in real time or on stored data in each camera head. This led us to consider storing raw data. This in turn led us to consider using two different forms of compression: JPEG2000 or something else that provides visually useful information (especially low-rate images downloaded near real time), and another that does accurate target centroiding directly from the raw data to provide even lower bandwidth data that is very accurate. This reduces the bandwidth required for both visual and centroid downloads while retaining the raw data in case selective downloads are desired later.

This approach allowed the system to be decomposed into 4 pieces with fairly simple and well-defined interfaces: cameras to capture images, memory to store the raw image data, an image compression algorithm to operate on stored image data, and a separate centroiding algorithm. The simple interfaces and low throughput requirements (other than storing the raw image data) might simplify development. Note that with this philosophy, any questions raised by ground analysis of either the centroid or visual data might be answered by requesting download of the relevant raw data still in archival memory, or less-compressed forms of that data.

8.1.2 Centroiding tests on compressed images

We knew compressing images could reduce target centroiding accuracy, but we did not know by how much. We addressed this uncertainty by centroiding some high-quality target/sail images before and after compression. This allows us to quantify centroid shifts as a function of the compression algorithm and compression ratio. LaRC provided sample images to Ecliptic. Ecliptic used both JPEG and JPEG2000 methods to compress the images to various extents, and then LaRC used centroiding algorithms on both the raw and compressed images. We did not include MPEG compression because it relies on high similarity between consecutive frames, and we want to interleave images from many cameras on one compression device. MPEG may merit consideration if we want higher data rates and if hardware compact enough to use at each camera becomes available, or if we want to do compression on stored data.

The results for 8 targets are shown on the next page (X and Y centroid shifts in pixels) for several different compression ratios using both JPEG and JPEG2000. Overall, the errors associated with compression seem quite modest. The wavelet-based JPEG2000 method provided similar results (both visual and centroiding) typically at ~3X higher compression ratios than with the older JPEG algorithm, which uses discrete cosine transforms (DCT). But as might be expected, the newer JPEG2000 algorithm is computationally more intensive.

8.1.3 Baselining of real-time compression

These promising centroiding results suggested that we could compute centroids accurately enough from compressed image data that we might not ever need to download raw image data. This led us to consider again whether we could compress the image data in real time because then we could significantly reduce the amount of on-board memory required to store images until download. The onboard storage requirement was mainly driven by the deployment phase, which requires longer sustained imaging than is required later. Based on additional analyses, Ecliptic indicated that real-time compression by a single compressor should be feasible at the desired imaging rates, within the current specified ODS power and mass budget. The architecture compresses images from different cameras in sequence. That requires a buffer memory for each camera as shown later in Figure 8-4 (as part of the “camera electronics” module).

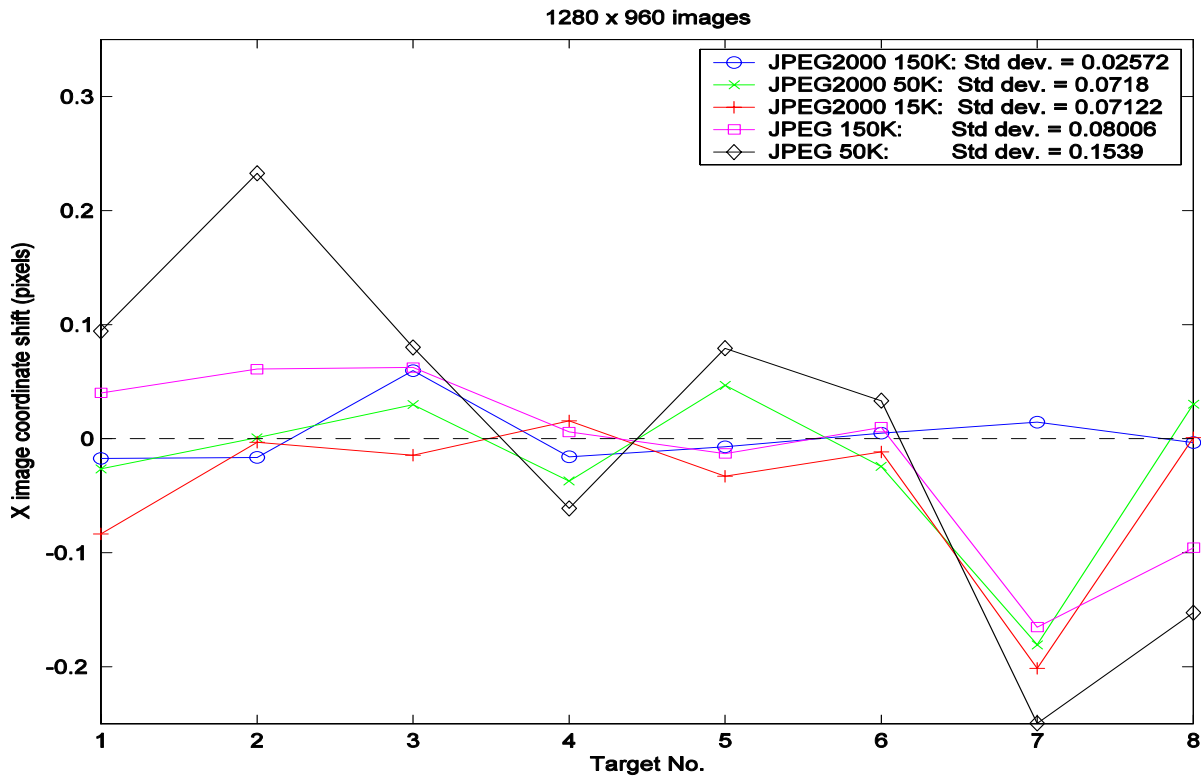


Figure 8-1. Compression Test: X Image Coordinate Shifts

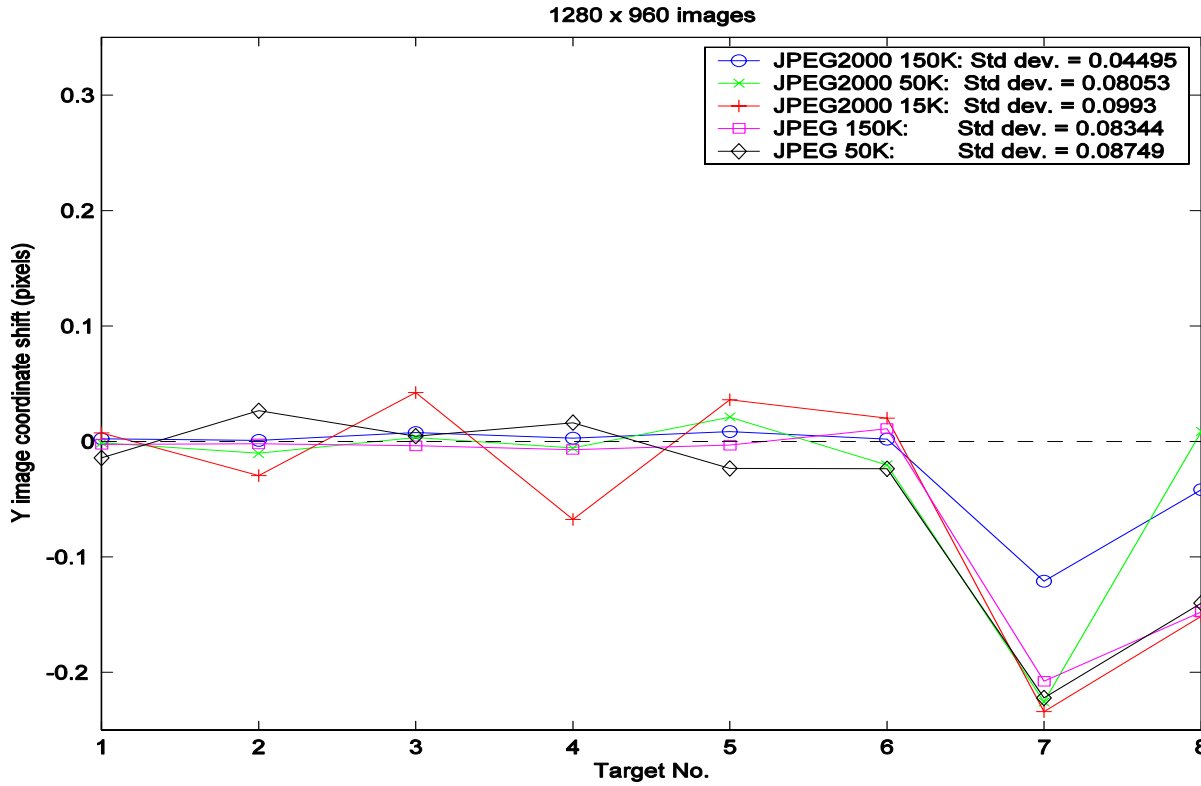


Figure 8-2. Compression Tests: Y Image Coordinate Shifts

8.1.4 Centroiding as an auxiliary form of image compression

In parallel with the above study of real-time compression, we also looked at real-time centroiding. The main value may be download of more useful data in real time. The effective compression ratio of centroid data may be of order $\sim 2000:1$. This compression ratio assumes that a set of twenty 10-bit SXGA images includes ~ 1600 usable bright spots (including multiply imaged targets and “false targets”), and that each bright-spot centroid requires ~ 80 bits to characterize its position, brightness, size, shape, and other features.

Centroiding should take far less computational power than JPEG2000. Preliminary analyses suggest that scanning the images to find bright spots may take more time than computing centroid position. One way around this is to use low-level logic to “snoop” on the two high-order bits of the image data during readout from the imager. Non-zero high-order bits can trigger capture of timer values. These timer values indicate the column and row of candidate bright spots. After the full image is downloaded and available for random-access readout, an algorithm can check each bright spot detected and decide whether to process it. It can use criteria such as nearby glare, contrast with surrounding pixels, brightness, size, shape, uniformity of target brightness, and other indicators that should preferentially select real targets over glint or glare.

This procedure is not incompatible with also doing conventional image compression using JPEG2000, MPEG, or other algorithms. It is an additional option that provides extremely compressed but directly useful data with a minimum of special hardware and computer power.

8.1.5 Estimated data budget (capture, compression, and download)

One can limit the amount of data to download by limiting how much is collected, or compressing it real time, or later, or by being selective about what to download or how far to send it. Limiting collection (i.e., reducing image resolution or image rate) is simplest but gives the least useful data. It is not yet entirely clear whether compressing it in real time will be more or less demanding (in power, mass, and developmental cost) than storing it and compressing it more slowly later. Other options include downloading only a subset of the captured images (e.g.,

every Nth image, plus those acquired during any interesting events such as accelerometer spikes). Then we would analyze those images and other data to decide what else to download. We might even overwrite some imagery before it is downloaded if deployment proceeds normally. Also, if the first mission occurs in LEO, or at least starts there, it may be feasible to collect and download large amounts of data without requiring high compression. It seems worth examining these options in more detail later as their implications and the likely mission details become clearer.

Table 8-1 shows a preliminary data budget. It assumes only 8-bit data for each pixel, and it assumes higher-rate imagery at the start and end of deployment than during the hour in between, with a peak of 80 frames/second to be compressed. Dynamic tests and triggered-event needs do not exceed those of deployment. The budget shows the contributions of the different types of activities and the importance of compression and centroiding in reducing download needs.

Table 8-1. Estimated ODS Imaging Data Volume Requirements

Parameter	Units	Sail Deployment Activities			Dynamical Surveys		Triggered Events	
		Release	Deploy	Lock	Imagery	Centroids	Imagery	Centroids
Mission Phase								
Duration	s	60	3600	60	300	300	120	120
Image Format, X		1280						
Image Format, Y		1024						
Pixels	Mpx	1.31						
Pixel Depth	bits	8						
Image Size	Mb	10.49						
Frame Rate	fps	4	0.5	4	4	4	4	4
Active Cameras		8	20	20	20	20	20	20
Raw Pixel Rate	Mpx/s	42	13	105	105	105	105	105
Raw Data Rate	Mb/s	336	105	839	839	839	839	839
Raw Data Volume	MB	2517	47186	6291	31457	31457	12583	12583
Compression Ratio	:1	25	80	25	80	2000	80	2000
Compressed Data Volume	MB	101	590	252	393	16	157	6
Compressed Data Rate	MB/s	1.7	0.2	4.2	1.3	0.1	1.3	0.1
Total Deployment Data Volume		----	942	----				
Downlink Data Rate	kbps		100		100	100	100	100
Downlink Efficiency			90%		90%	90%	90%	90%
Downlink Duration	hr		23		10	0.4	4	0.2

8.2 *Maturation of real-time JPEG2000 compression scheme*

The major issue here is whether flight-worthy JPEG2000 compression hardware and software will allow a sustained throughput of ~80 SXGA images/second (1280x1024 pixels each) with acceptable system mass, power, and cost. Better hardware is becoming available over time. The real questions are what throughput we will actually need, and whether suitable flight-worthy hardware will be available when the design must be frozen.

Our recommendation is to pursue development as funds become available, while periodically reviewing what image capture rates are really needed. If the desired imaging rates increase beyond what JPEG2000 compressors can handle, or if we run into other difficulties, MPEG options and/or a backup architecture described below may be worth attention.

8.2.1 A developmental backup to real-time compression: storing raw data in flash memory

It appears feasible to download raw image data into high-capacity, serial-access NAND flash memory chips. We need 10 memory chips per imager. Sequenced latching of pixel data allows 4 pixels of 10-bit image data to be buffered into 5 flash chips with a 48Mpixel/sec readout rate and 12MHz flash chip data rate. To capture even a single image, 2 banks of 5 chips are needed. One bank stores several lines of image data into a page buffer while the other goes off-line and programs the page into non-volatile memory. Those 10 memory chips can do sustained image capture at any desired rate up to the maximum for the imager (on the order of 30Hz). The highest-capacity chips now available are 1Gx8 Samsung chips. Ten such chips can store 6553 raw SXGA images. This allows 1 Hz imaging for over an hour, plus bursts up to 30Hz for much shorter periods that may be of particular dynamic interest such as the very beginning and end of deployment. Added images can be captured once earlier images have been post-processed or discarded. A single microcontroller might control 4 or more cameras, including image capture, real-time centroiding, and low-throughput software-based JPEG2000 compression.

The most risky aspect of this concept may be the high consumer demand and resulting delivery backlog for serial NAND flash chips due to their popularity in electronic cameras and other products. Cost, mass, power, and radiation tolerance should be less serious issues.

8.3 Baseline avionics architecture

Figure 8-3 shows the baseline ODS configuration. A central command and data handling (C&DH) computer provides overall instrument control and the single point interface with the host spacecraft. The 23 focal planes of the baseline configuration are divided into three groups by function and location. These are the boom view cameras (4 focal planes), the sail view assemblies (16 focal planes), and the inspection (pan/tilt) assembly (3 focal planes).

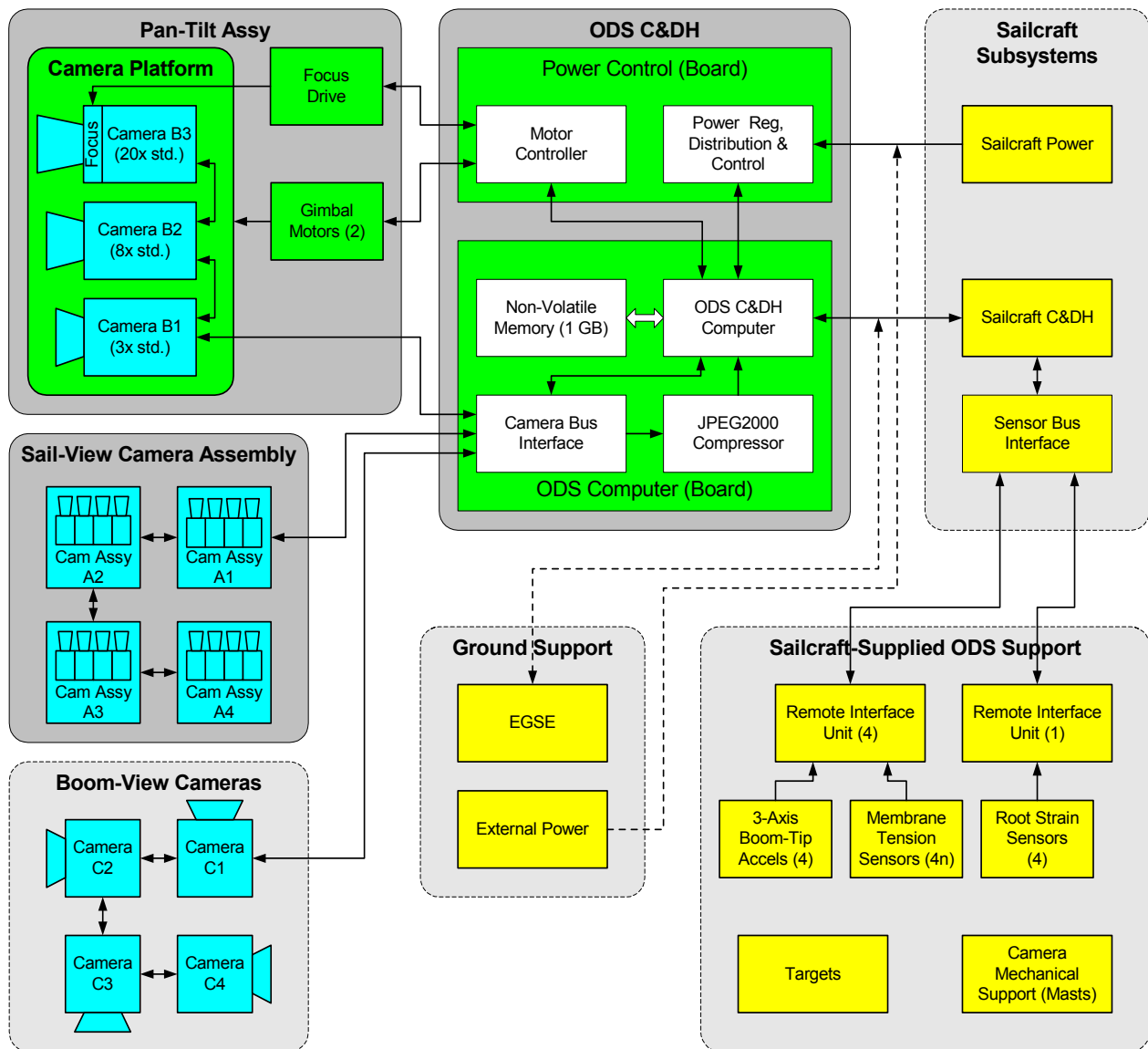


Figure 8-3. Avionics System Block Diagram

Imager control electronics will be distributed to each camera head, with a FPGA handling low level controls such as detector control, auto-exposure, and windowing (see Fig. 8-4), as well as buffer management, real-time centroiding, and communication with the C&DH system. Although each sail view assembly contains 4 Focal Plane Arrays, it is logically one camera and has one set of control logic (see Fig. 8-4). The other two camera groups (boom view and inspection assembly) use similar logic in different configurations. Each camera assembly communicates with the CPU over a bi-directional, synchronous serial LVDS link. Within each imager group, the individual imagers are daisy chained together. This shares bandwidth but reduces cabling requirements.

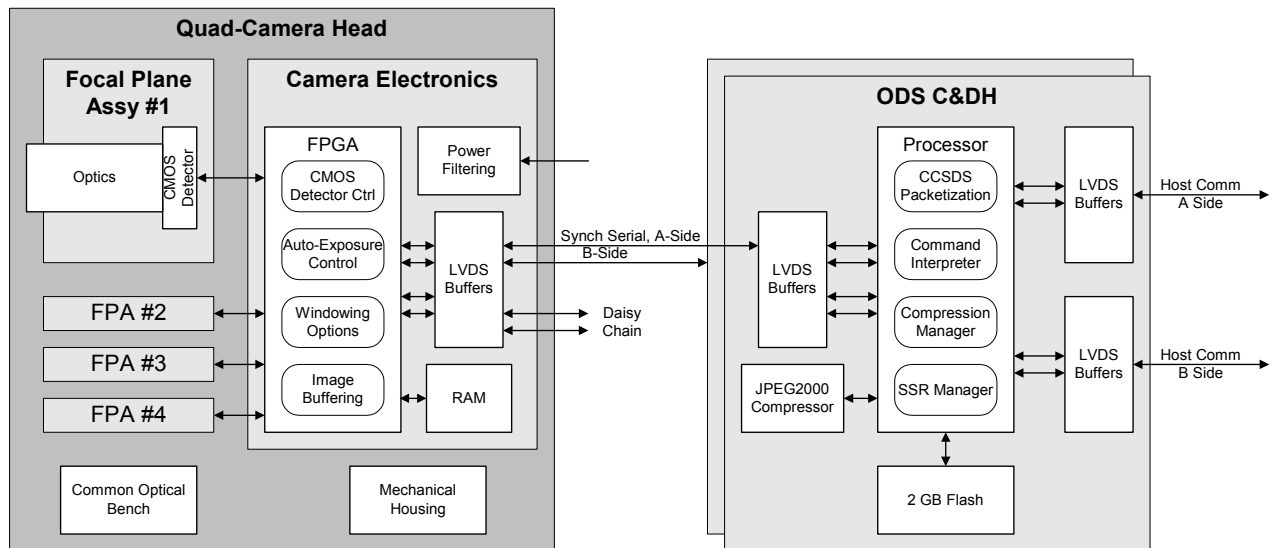


Figure 8-4. Data Flow Block Diagram

The primary requirements on the C&DH computer are for a large storage capacity, high throughput, and high-speed data compression. The general-purpose computation requirements (primarily C&DH housekeeping) are minor by comparison. The baseline configuration calls for a single board computer with four primary functional blocks: a moderate-performance general purpose CPU with high speed data throughput, a 1 gigabyte non-volatile (flash) memory, host communications (serial LVDS or RS-422), high-speed camera interface (serial LVDS), and a dedicated compression block running one or more JPEG2000 application-specific integrated circuits (ASICs). Collocated with the computer board is a power distribution board powering the C&DH and cameras, which includes motor controllers for the pan/tilt inspection assembly.

The system architecture allows for block redundancy in the C&DH system. Such redundancy is impractical in the camera assemblies within the allocated ODS mass and power budgets. But the imagers have high functional redundancy. Any single focal plane in the sail view assembly overlaps its neighbors, so that the loss of a single focal plane will result in only a small loss of coverage. And if a focal plane is lost, the inspection camera assembly provides a redundant capability to the sail view assembly.

8.4 *Impacts of space environment on avionics requirements and design*

8.4.1 Radiation effects

Spacecraft electronics need to be designed to tolerate single event effects including upset, latchup, and functional interrupt. They can disable a spacecraft at or near the start of its mission. By contrast, we can select hardware known to tolerate specific levels of total ionizing dose, for a given orbit and mission duration. Orbits that spend significant time in or near the heart of the van Allen belts (~1.3-2Re) will see far higher radiation dosages than other missions, but these doses will be accumulated gradually. If the sailcraft starts in LEO and spirals upward, the ODS job of characterizing deployment and operational dynamics may be complete before the electronics fail. But if the spacecraft starts in a GTO-like orbit, passing through the heart of the belts even at the beginning of the mission, total dose accumulates much faster, and careful attention may be necessary to verify that the ODS electronics will last long enough.

8.4.2 Other space-environment effects on avionics

Radiation may be the most serious issue for most of the avionics, but other issues should not be neglected. They include thermal cycling and extreme temperatures (which may particularly affect solder joints on surface-mount parts), venting during boost (which can cause structural overloads), outgassing (which can contaminate optics and change equilibrium component temperatures), and electrical discharges during passes through auroral zones. There does not seem to be a particular need to focus on these issues at this phase of ODS development, because the key issues are fairly generic and familiar to spacecraft avionics developers.

8.5 Recommendations on avionics TRL gaps that need to be filled

Most of the ODS avionics functions are routine spacecraft avionics functions, with technology readiness levels (TRLs) of 6-9. The exact TRL depends on whether ODS avionics uses hardware that has already flown. Routine functions include collecting non-imaging sensor data, switching devices on and off, formatting data for telemetry, validating commands and possibly code patches, and doing other supporting housekeeping and status checks.

Those aspects of the baseline avionics with low TRL are associated with high-throughput imaging: mostly controlling >20 SXGA imagers, capturing 80 frames/sec (total), and doing real-time JPEG2000 compression and centroiding. The two Mars Exploration Rovers have a similar numbers of cameras, mostly for self-inspection. But they do not have any high-rate capture or compression requirements, and they may not do centroiding at all.

The main key TRL gap is verifying that we can do JPEG2000 compression at a sustained rate of ~80 SXGA frames/second. JPEG2000 does not use frame-to-frame similarity, so a single frame test using a high-speed buffer may be adequate. We need to determine:

1. How fast we can download one stored SXGA image (using LVDS or another interface)
2. How long it takes to compress it (which may vary with the image and compression ratio)
3. How easily we can double-buffer, to download one image while compressing another.

Careful analysis of hardware specifications may eliminate most risk. But if JPEG2000 compression time varies with image content or compression ratio, we need tests on suitable images. And we do need good tests eventually (including radiation tests) to verify that there are no problems that may require our switching to raw-image capture plus later compression at lower rates, or switching to MPEG compressors if they allow higher throughput or compression.

Star trackers do bright-spot detection and centroiding. But the TRL is much lower for doing those tasks at ~80 SXGA frames/second on “noisy” solar sail images. We need to develop and test suitable algorithms, first on PCs and then on more flight-like hardware. It may be feasible to do the centroiding using mostly the same hardware used for conventional image compression.

Section 9

Photogrammetry Test of 10m Sail Quadrant

9.1 Scope and Challenges of the Test

A proof-of-concept photogrammetry test was conducted using the ODS baseline camera configuration (Section 3) with commercial, off-the-shelf digital cameras and diffuse-white circular targets distributed on a 10m solar sail quadrant. This test demonstrated the feasibility of measuring solar sail shape with cameras located at two elevations on a relatively short longitudinal boom (perpendicular to sail plane) extended from the hub of the spacecraft.

Note that although good results were obtained after considerable effort in the image analysis phase, the ODS baseline camera geometry (four overlapping cameras per quadrant at lower station and one camera on pan-tilt at upper station of the camera mast) is unusually challenging compared with typical geometries used in high-precision, close-range photogrammetry tests where additional camera locations--typically around the periphery of the object--are permitted. Initial studies in Phase 1 concluded that to minimize changes in the existing solar sail designs (a customer Level 1 requirement) that mounting ODS cameras along a central boom was the only logical choice, and that the job of the ODS team was to do the best it could from this location. Section 3.1 discusses several other camera configurations that were considered.

The ODS baseline geometry is technically challenging for photogrammetry for several reasons, including: 1) the camera stations are closely spaced along the camera support mast (10% of sail edge dimension) and there is no camera separation perpendicular to the support mast, 2) the cameras view the sail at a relatively shallow angle so there is considerable target foreshortening in the images, and 3) camera self-calibration, which requires roving camera positions and roll diversity, cannot be performed. Recently the images acquired in this test were reanalyzed using more-advanced software (*Australis* [Ref. 9-1] vs. *PhotoModeler* [Ref. 9-2]) in an attempt to improve the robustness of the solution with better analysis approaches and

algorithms. However, to date these efforts have been unsuccessful. The ODS team will continue to evaluate and improve the robustness of the baseline camera configuration and data analysis procedures during Phase 2. In Phase 2 we will also conduct photogrammetric parametric studies and optimizations using *Australis* and other simulation tools.

9.2 Test Configuration

The ODS proof-of-concept photogrammetry test used the 10m solar sail quadrant shown in Fig. 9-1. This seamed, 7-micron CP1 membrane was manufactured by SRS Technologies under a LaRC SBIR program and contains an early design of a shear compliant border to minimize membrane wrinkling. Dead weights on pulleys applied pre-tension loads of 5 lbs at each 45-deg corner. The test was conducted in air in the high-bay lab of Bldg. 1293 at NASA LaRC. Only static shape measurements were made; there was no attempt yet to measure structural dynamic characteristics (i.e., vibration properties). The room was darkened during the test except for a single illumination source, which was a 1000 W facility light (with built-in horizontal cylindrical reflector) located approximately 30 ft to the left and 30 ft above the center of the sail as viewed from the camera position of Fig. 9-1. The air handlers in the room were also turned off to avoid inadvertent movement of the membrane between photographs.

Note: The final ODS baseline camera configuration presented at the Phase 1 final review on January 14, 2004 specified camera platform heights of 15% (lower platform) and 25% (upper platform) of the edge sail dimension. The team selected these final values for the baseline shortly before the Phase 1 review, and there was not enough time to run another proof-of-concept test using these exact camera locations. The results presented in this section (and presented at the Phase 1 review) correspond to camera platform heights of 10% (lower platform) and 20% (upper platform) of the edge sail dimension. The platform separation distance is the correct baseline value of 10%, but both cameras are located 5% lower than in the baseline concept. Raising both camera platforms an additional 5% provides a slightly better viewing angle to the targets from the lower platform, which is particularly important with the L'Garde scalloped membrane design. Raising the upper platform still higher would improve both the stereo triangulation precision and our ability to inspect the sail particularly at distant locations. However, this option must be balanced with the associated increases in cost, integration complexity, and possible

dynamic interaction issues using a longer camera mast. We will re-examine these platform height selection decisions in Phase 2.

9.3 “Truth” Targets on Membrane Frame

Forty-seven retroreflective targets on precision machined tool pieces as detailed in Fig. 9-1 were distributed on the rigid aluminum frame surrounding the membrane to provide a set of “truth” 3D coordinates in the test. (Hubbs Machine and Manufacturing, Inc. [Ref. 9-3] produced these targets.) The 3D location of each retroreflective target was measured to a 1-sigma accuracy of approximately 0.004 inches in a prior test using a state-of-the-art Geodetic Services *V-STARs* industrial photogrammetry system [Ref. 9-4]. These coordinates can be compared with corresponding 3D coordinates calculated with the ODS images to determine absolute ODS measurement accuracy, which is estimated to be at least 10x less than *V-STARs* accuracy. Relative ODS measurement accuracy can also be determined by comparing known separation distances of various target pairs with corresponding truth values as detailed in Fig. 9-1. The *V-STARs* system currently can only measure retroreflective targets, so we were unable at this time to also measure “truth” coordinates for the diffuse-white ODS targets on the membrane with this top-end system. We will investigate ways to circumvent this limitation in Phase 2. Nevertheless, by comparing *V-STARs* and ODS-calculated coordinates at numerous locations on the membrane boundary frame, the accuracy expected for the interior ODS target points--if they are centroided as accurately as the retroreflective targets--can be inferred. Of course, the diffuse white targets on the sail will probably not be centroided as accurately as the retroreflective targets because their contrast ratio with the surrounding background is lower.

This test used the INCA1 model camera having a measurement accuracy of approximately 1 part in 100,000 (1:100,000) of the object size. We recently upgraded this camera to the latest version, an INCA3 model, having a measurement accuracy of approximately 1 part in 160,000 (1:160,000) of the object size. The INCA3 camera used with the *V-STARs* software is the most accurate digital photogrammetry system available on the market today. It will be used in Phase 2 testing for the ODS program.

9.4 ODS Targets and Camera Description

Figure 9-2 shows the grid of 52 targets placed on the membrane for these tests. The target spacing in the center region is approximately 1 m, and the spacing on the border is approximately 0.5 m. Targets were installed by hand and no attempt was made to precisely locate them. The target diameter was 1.25 inches. Figure 9-3 shows a close up of a typical target on the sail. The target material was standard bright-white Xerox paper, and the targets were attached using removable adhesive (3M remount spray adhesive) to allow easy removal if necessary.

Based on recent additional analyses, the recommended minimum number of targets per quadrant is now 100 (rather than 52). Therefore, the results provided in this section are conservative estimates of ODS measurement accuracy because adding additional targets to each quadrant should improve photogrammetric accuracy. The reason for this is that additional targets allow the software to make small adjustments more accurately in the calculated camera orientations (i.e., the 3D locations and pointing directions of the cameras). Errors in camera orientations, particularly the pointing directions, can significantly affect the photogrammetrically calculated 3D target coordinates.

A single off-the-shelf Olympus C-5050 digital camera, shown in Fig. 9-4, was used for all photography in this proof-of-concept test. It was pre-calibrated using the target grid and procedure supplied with the *PhotoModeler* software package, in which a grid of 100 targets is photographed from several viewing directions, the camera is rotated 90 degrees in some of the photographs, and then the images are analyzed simultaneously with a self-calibrating bundle adjustment algorithm. The consumer-grade Olympus C-5050 is a 5 megapixel (2560 x 1920) color CCD camera with an effective measurement resolution approximately equal to the ODS baseline scientific-grade 1.3 megapixel (1280 x 1024) monochrome CMOS camera. (Color cameras have significantly less resolution than monochrome units because of the color mask on the sensor and subsequent image interpolation, and consumer-grade cameras are manufactured to lower tolerances than scientific-grade cameras.) It has a built-in 3x motorized zoom lens that was used at two zoom settings (focal lengths of 7.1 and 11.3 mm) in the test.

For stability the camera was mounted on a tripod (adjustable to heights of 1m and 2m above the sail plane) and fired with a remote shutter release switch. The tripod was positioned 30 inches (0.8 m) behind the 90-deg corner of the aluminum boundary frame. All photography used an aperture setting of f/8 and an exposure time of 1.0 sec. The built-in flash was set to a low intensity that was sufficient to illuminate the retroreflective targets on the membrane boundary but did not wash out the diffuse white ODS targets on the membrane surface. The tripod was adjusted to two different heights, 1 m and then 2 m above the sail, and four images were shot at each height. The eight images were acquired in as short a period of time as possible (approx. 15 minutes) to maximize consistency of the data set. In Phase 2, we will use 8 synchronized scientific video cameras for additional ODS development tests of this type. With this new capability, all imagery will be acquired at exactly the same instant, just as it will be in space. These cameras will be capable of measuring both the static shape and the dynamics (i.e., vibration characteristics) of a sail quadrant system.

9.5 Imagery

Figure 9-5 shows the approximate viewing areas of each photograph taken at the upper camera elevation (20% of the sail edge dimension above the sail plane). Viewing areas from the lower camera elevation (10% of the sail edge dimension above the sail plane) are similar but include additional sail area closer to the camera because of the perspective foreshortening effect. At both elevations, Camera Views 1-3 used a focal length of 11.3 mm and Camera View 4 used a focal length of 7.1 mm. At 11.3 mm the horizontal field of view is 35 degrees, and at 7.1 mm it is 53 degrees. Note that ellipses are plotted in this graphic for simplicity. The projected viewings areas are in fact trapezoidal, which are wider near the back of the sail than near the front.

Figures 9-6 and 9-7 show the four images from each camera elevation. The cameras were oriented to include both the membrane and the boundary support frame. In space, slightly more membrane area would be imaged since there would be no rear support frame (along the hypotenuse of the quadrant). Also, in space the inner and outer cameras (Cameras 1 and 3 in Fig. 9-5) will probably be rolled slightly to better fill the image areas, allowing more of an adjacent quadrant to be imaged rather than deep space at the top of the membrane.

The two white lines on the membrane were not used in this ODS proof-of-concept test. In another investigation they provided discrete boundaries for photogrammetric line tracking methods (tracking the shape of the horizontal seam lines). These methods were briefly examined but have not been successfully implemented to date. The ODS baseline configuration does not require these white lines for photogrammetry measurements.

Figure 9-8 shows close-up views from both camera elevations of several targets on the membrane. Notable aspects of this imagery are:

- Target contrast from Camera 3, which looks away from the single illumination source located above and to the left of the sail, is considerably higher than the contrast from Camera 1.
- Membrane creasing (caused by folding and handling) causes significant glints near several targets in the images from Camera 1, which will reduce target centroiding accuracy.
- Some target images are slightly non-elliptical due to membrane unflatness.
- Greater target foreshortening occurs at the lower camera station as expected due to the perspective.

9.6 Data Analysis Procedure and Results

The eight images shown in Figs. 9-6 and 9-7 were analyzed as a single project using the commercial PhotoModeler photogrammetry software [Ref. 9-2]. Reference 9-5 details the data analysis procedure that was followed, and it will not be repeated here. In summary, the main steps are as follows:

- Mark the target locations in each image (known as “marking” or “centroiding”)
- Identify which points in the images refer to the same physical point (known as “referencing” or “correspondence”)
- Process, scale, and rotate the data
- Examine results and export for additional analyses

As mentioned earlier, the ODS geometry is technically challenging for photogrammetry for several reasons. A significant contributing factor is the relatively small angle between the two camera stations and the targets. For a vertical camera separation distance of 1 m (10% of sail edge dimension--the ODS baseline value), all targets further than 3.8 m from the cameras will have a relative viewing angle between the upper and lower camera stations of under 15 degs. Because the cameras are located 0.8 m behind the 90 deg corner, this region extends only 3.0 m into the sail quadrant. Fifteen degrees is the default minimum angle that PhotoModeler expects there to be between camera views to provide a robust, repeatable solution. Therefore, we needed to disable the default minimum value in the software and attempt a solution allowing smaller included angles for about half of the targets in the project. In order to have all angles above 15 degs requires a camera separation of at least 2.1 m (21% of sail edge dimension). Lengthening the camera mast for a flight experiment may unnecessarily complicate the design if acceptable solutions can be obtained at the shorter length. In Phase 2 we will measure the effects of greater camera separation distances using both experimental and simulated data sets.

The default PhotoModeler solution approach, which was followed here, uses a robust relative orientation calculation to estimate the camera 3D locations and orientation angles (known as the camera exterior parameters) prior to refining these values for each camera, in addition to computing the target 3D coordinates, in a free network (a.k.a. an inner constraints network) bundle adjustment. (Theoretically, a free network solution gives the minimum trace solution and is thus the most precise.) The relative orientation calculation makes no prior assumptions about the exterior parameters. In previous unrelated projects, it provided the correct solution the vast majority of the time. An alternative orientation approach is to resect each image individually using at least four control points per image. Resection is the technical term for calculating the 3D location and orientation angles (a.k.a. its pose) using control points. Control points are identifiable targets with known 3D coordinates. To obtain an accurate resection, the control points should be widely distributed in the image, preferably in three dimensions, and their coordinates must be known as accurately as possible. This is not always easy to achieve. In Phase 2 we will compare the effectiveness of using control points and camera resection against using a traditional relative orientation calculation.

PhotoModeler is best used in an iterative manner in most projects. That is, at the beginning of the data analysis only a few points and a few photographs are marked. Once perhaps 10 to 15 points are marked and referenced on three or four photographs, they are processed with the free-net bundle algorithm. Having confidence in that result, additional new markings and new photographs are added in stages, doing another bundle solution at each phase. This approach greatly minimizes the chances that errors will be made that are difficult to find or fix.

With the eight ODS images, this iterative analysis process often produced incorrect results in the early stages. Specifically, the computed camera locations and orientation angles were often poorly computed. If these values are not accurately calculated, subsequent bundle solutions will fail. Figure 9-9 shows an example of one of these intermediate and incorrect results. At this point, approximately 50 points have been marked and referenced and six of the eight images are included in the analysis. The computed camera locations are clearly incorrect, and the corresponding membrane shape is much more concave (curled up at the outer edges) than it should be.

However, after slowly adding additional points, and especially increasing the number of marked and referenced points that overlapping images had in common, PhotoModeler was eventually able to obtain an accurate solution, shown in Fig. 9-10. Visual examination showed all eight cameras to have the locations and orientations that were used in the test, and the sail membrane targets showed a uniformly concave shape with a maximum deflection at the center of the membrane as expected. On the periphery, the 3D coordinates of all 15 pairs of closely spaced retroreflective targets were also accurately computed.

Using these experiences and results as a starting point, in Phase 2 we will examine other data analysis approaches also, in particular those in *Australis*. We recently acquired and have begun successfully using the *Australis* photogrammetry package, written by Prof. Clive Fraser, who also wrote many principal parts of the *V-STARs* software when he was at Geodetic Services, Inc. several years ago. It has the same high computational accuracy and efficiency as *V-STARs*, but it also allows the import and analysis of TIFF images derived from arbitrary sources, something that *V-STARs* does not allow.

9.7 Measurement Accuracy

ODS measurement accuracy, that is, the photogrammetric accuracy achieved using the eight images shown in Figs. 9-6 and 9-7, is now evaluated by comparison of the calculated 3D coordinates of the retroreflective targets on the boundary of the membrane with the “true” coordinates measured with the *V-STARs* system. As mentioned previously (repeated for emphasis), the *V-STARs* system currently can only measure retroreflective targets, so we were unable at this time to also measure “truth” coordinates for the diffuse-white ODS targets on the membrane with this top-end system. Nevertheless, by comparing *V-STARs* and ODS-calculated coordinates at numerous locations on the membrane boundary frame, the accuracy expected for any interior ODS target points--if they are centroided as accurately as the retroreflective targets--can be inferred.

Figure 9-11 shows the relative accuracy achieved for the results shown in Fig. 9-10. The term “relative” is used because only the separation distance of pairs of targets is evaluated, not the absolute, individual 3D target coordinates relative to a fixed reference frame. Relative measurement accuracy is determined using the 15 sets of Hubbs precision-machined “double-vector” targets, the 3 invar scale bars, and the *V-STARs* autobar located on the periphery of the membrane, all having precisely known dimensions (length in one direction for the Hubbs targets and scale bars, and length in all three directions for the autobar). See Fig. 9-1 for more information. Note that all of the Hubbs targets are oriented vertically (i.e., in the out-of-plane direction) while the other objects are oriented horizontally. In Fig. 9-11 the results for the 15 Hubbs targets are underlined. All of these pairs of targets are manufactured with a precise separation distance of 1.000 inches to an accuracy (which was verified in a previous *V-STARs* project) of +/-0.001 inches.

Among these results, the largest relative errors in the calculated separation distances using the ODS images occurred, not surprisingly, in the two rear corners of the testbed, with a global maximum relative error in the vertical direction of 0.060 inches, or 6%. It can be inferred that the targets on the membrane, which are located closer to the camera than the rear-corner boundary targets, will all have less than 6% relative error in the vertical direction if centroided with equal precision. For targets on the membrane, this relative error indicates the maximum

measurement error that would be expected using the ODS baseline configuration for a 1-inch change in membrane shape in the out-of-plane direction (due to vibration or thermal effects, for example). All Hubbs target pairs (i.e., the values underlined in Fig. 9-11) other than those at the two rear corners have relative measurement accuracies in the vertical direction under 3% (i.e., their measured values are between 0.970 and 1.030 inches).

The other values in Fig. 9-11 that are close to 1.000 are for additional double-vector targets located at the ends of three precision Brunson invar scale bars. These are all oriented in the X direction. All six values are comparable to those obtained for the 15 Hubbs targets oriented in the Z direction. There are also two tables in Fig. 9-11. This information compares the true dimensions of the scale bars and autobar with those calculated using the ODS images. Once again, the relative accuracies in the X and Z directions are about 2%. For the autobar, a relative accuracy measurement was also obtained in the Y direction. From the position of the autobar, the Y direction is oriented approximately along the line of sight of the cameras. Because imagers can only detect object coordinate variations normal to their line of sight, this result shows the lowest accuracy, 12%, as would be expected.

Table 9-1 and Figs. 9-12 and 9-13 show the absolute accuracy achieved for the results shown in Fig. 9-10. The term “absolute” is used because the target coordinates calculated photogrammetrically from the ODS images are compared with the absolute, individual 3D target coordinates (i.e., their true locations) relative to a fixed reference frame.

Table 9-1. Accuracy of the ODS Photogrammetric Measurements

	Mean of 47 boundary targets, inches	Max. of 47 boundary targets, inches	Std. deviation (1 sigma) of 47 boundary targets, inches	Std. deviation / sail edge size
X direction:	-0.01	4.98	2.10	~ 1:200
Y direction:	-3.62	6.64	2.83	~ 1:150
Z direction: (out of plane)	0.004	0.24	0.10	~ 1:4000
Total vector:	3.98	8.25	3.10	~ 1:125

Table 9-1 summarizes the results. Of particular interest for application of the ODS baseline measurement configuration to other solar sail sizes is the last column in the table, which lists the measurement accuracy achieved relative to sail edge dimension. Similar accuracies should be expected with other sail sizes using the same camera equipment if all physical dimensions in the design are scaled by an equal amount. The absolute measurement accuracy achieved in the Z direction (out of plane) is by far the largest of the three directions and is approximately 1 part in 4000 of the sail edge dimension. *And it is the Z direction that we certainly have the most interest in.* Note: Among the 47 targets used in this calculation, 20 are located on the back frame of the sail quadrant (along its hypotenuse) and thus are further from the cameras than the ODS targets on the membrane. Because accuracy decreases at larger distances, the numbers presented in Table 1-1 are in fact biased somewhat toward higher values than we would expect to be achieved for targets located on the membrane itself. In this sense they are conservative estimates of ODS measurement accuracy.

Figures 9-12 and 9-13 show the spatial distribution of the absolute measurement errors (total vectors and Z vectors only, respectively). In these plots, the dots indicate the true target locations with the vectors extending from the true target locations to the ODS-measured target locations, with a vector magnification factor applied for better visualization (magnification is x5 in Fig. 9-12 and x200 in Fig. 9-13). For the total error vectors (Fig. 9-12), the measurement errors are clearly predominately in the radial direction relative to the location of the cameras located at the hub of the sail. This is exactly what would be expected because imagers cannot measure along their line of sight. The total error vectors also grow uniformly larger with increasing distance from the cameras. This is also expected because photogrammetric accuracy decreases with distance due to the effects of perspective. Note that the total vectors are rotated to a top view in Fig. 9-12, but when viewed from any other direction the data looks essentially the same (i.e., the out-of-plane total error vector components are extremely small).

Figure 9-13 shows the distribution of the Z (out of plane) error components using an amplitude plotting scale of x200 (rather than x5 as in Fig. 9-12). These results show a random distribution pattern, indicated a negligible bias error in the results. The maximum Z direction

error among the 47 boundary targets is 0.24 inches, and the standard deviation of the results is 0.10 inches, or 1:4000 as shown in Table 9-1.

9.8 References

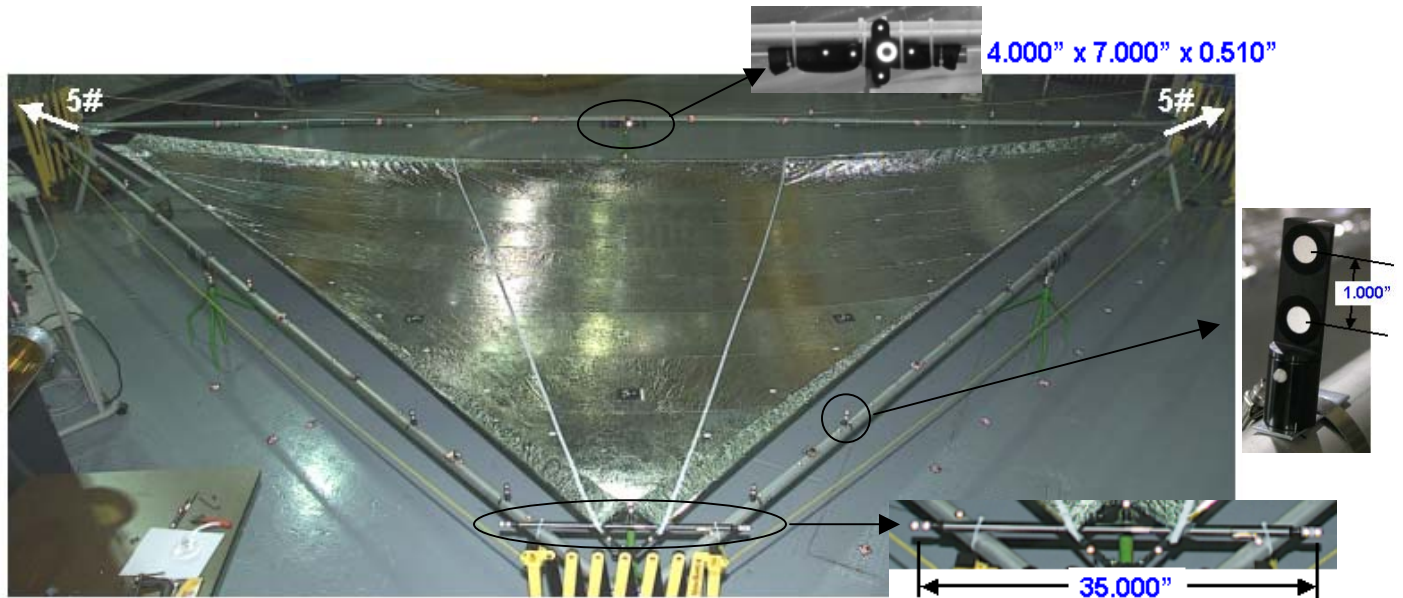
9-1. Australis photogrammetry software, Photometrix Pty Ltd., website: [http://
http://photometrix.com.au/](http://http://photometrix.com.au/).

9-2. PhotoModeler Pro photogrammetry software, Eos Systems, Inc., website: [http://
http://www.photomodeler.com/](http://http://www.photomodeler.com/).

9-3. Hubbs Machine and Machine and Manufacturing, Inc., optical targeting specialists, website: <http://www.hubbsmachine.com/>.

9-4. V-STARS industrial photogrammetry system, Geodetic Services, Inc., website: [http://
http://www.geodetic.com/](http://http://www.geodetic.com/).

9-5. Pappa, R. S., Jones, T. W., Black, J. T., Walford, A., Robson, S., and Shortis, M. R., "Photogrammetry Methodology Development for Gossamer Spacecraft Structures," *Proceedings of the 3rd AIAA Gossamer Spacecraft Forum*, AIAA Paper 2002-1375, April 2002 (also published as NASA TM-2002-211739, June 2002).



Four Methods Used for Checking Measurement Accuracy:

- 15 Hubbs precision tooling pieces (1.000 +/- 0.001 inches)
- 3 Scale bars (35.000 and 45.000 +/- 0.001 inches)
- 1 V-STARS autobar (4.000 x 7.000 x 0.510 +/- 0.001 inches)
- V-STARS photogrammetry survey (w/ GSI INCA camera)

Accuracy Checked

- Relative
- Relative
- Relative
- Absolute

No. Targets

- 30
- 12
- 5
- 47 TOTAL

Figure 9-1. SRS 10m sail quadrant used for ODS proof-of-concept photogrammetry test

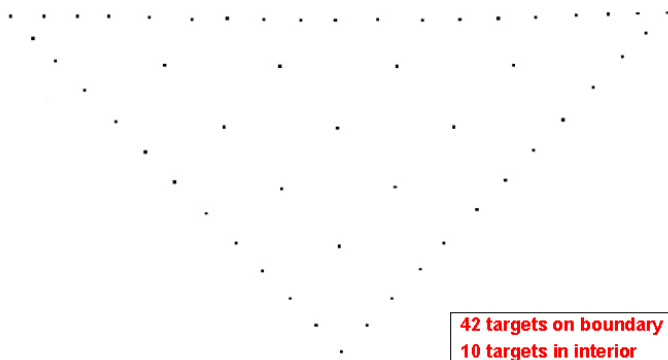


Figure 9-2. Targets locations on membrane



Figure 9-3. Typical target



Figure 9-4. Olympus 5-megapixel digital camera used in test

Four Images Acquired at Each Tripod Height

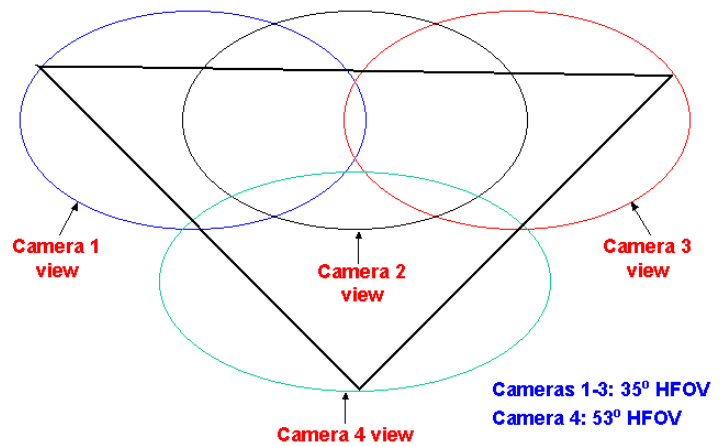
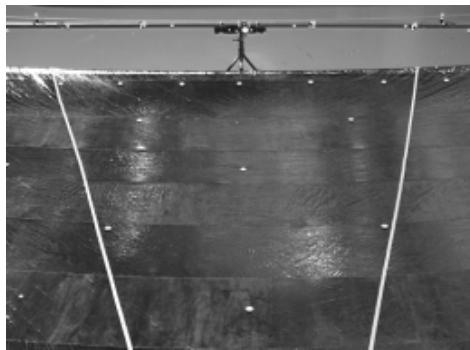
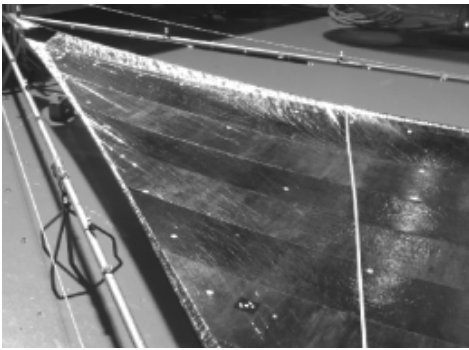


Figure 9-5. Approximate viewing regions



Views from upper camera platform

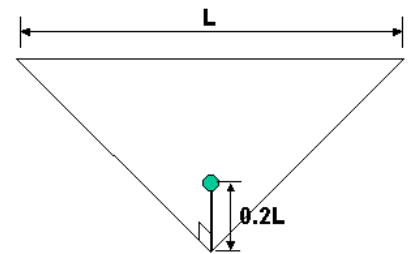
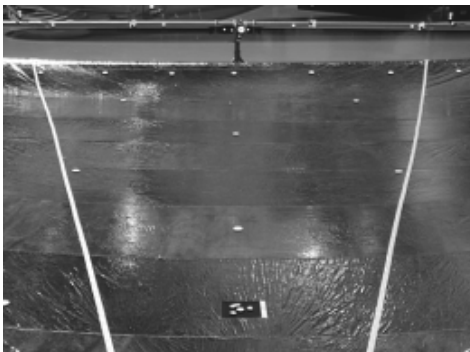
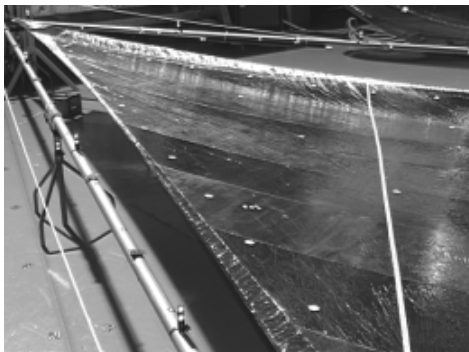


Figure 9-6. ODS camera views from 2 m above sail (20% of sail edge dimension)



Views from lower camera platform

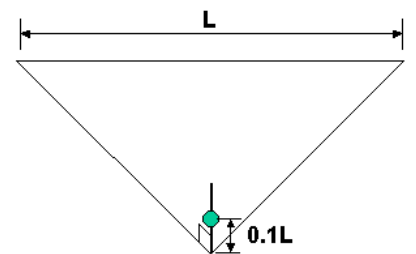
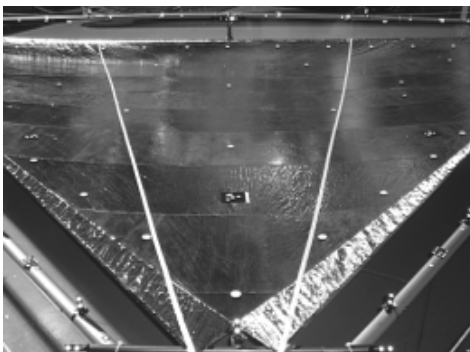
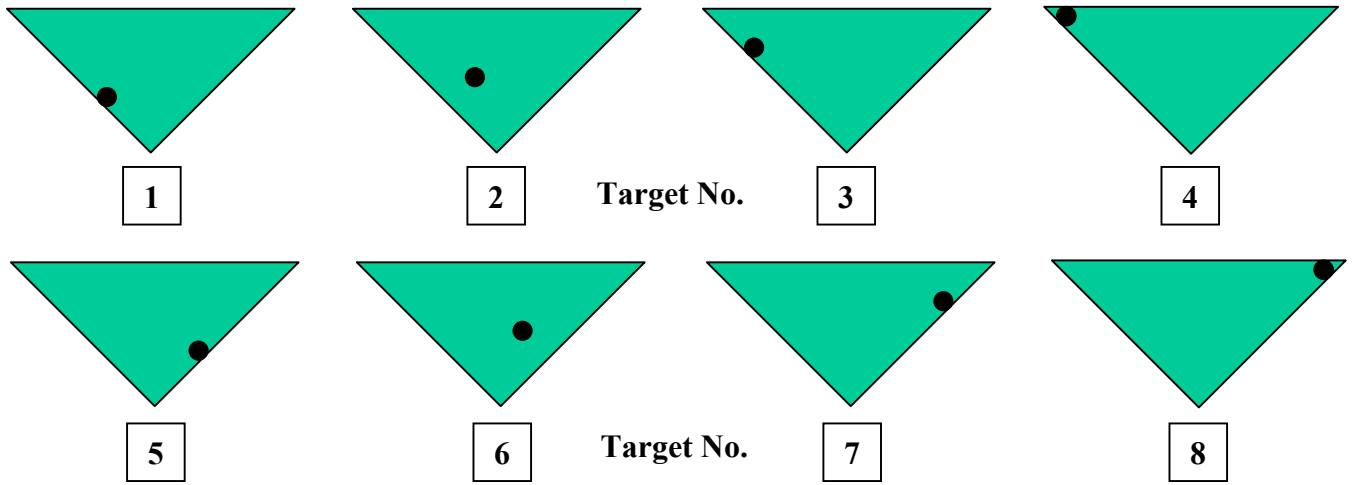


Figure 9-7. ODS camera views 1 m above sail (10% of sail edge dimension)



View from Camera Position 1
(per Fig. 9-5)

View from Camera Position 3
(per Fig. 9-5)

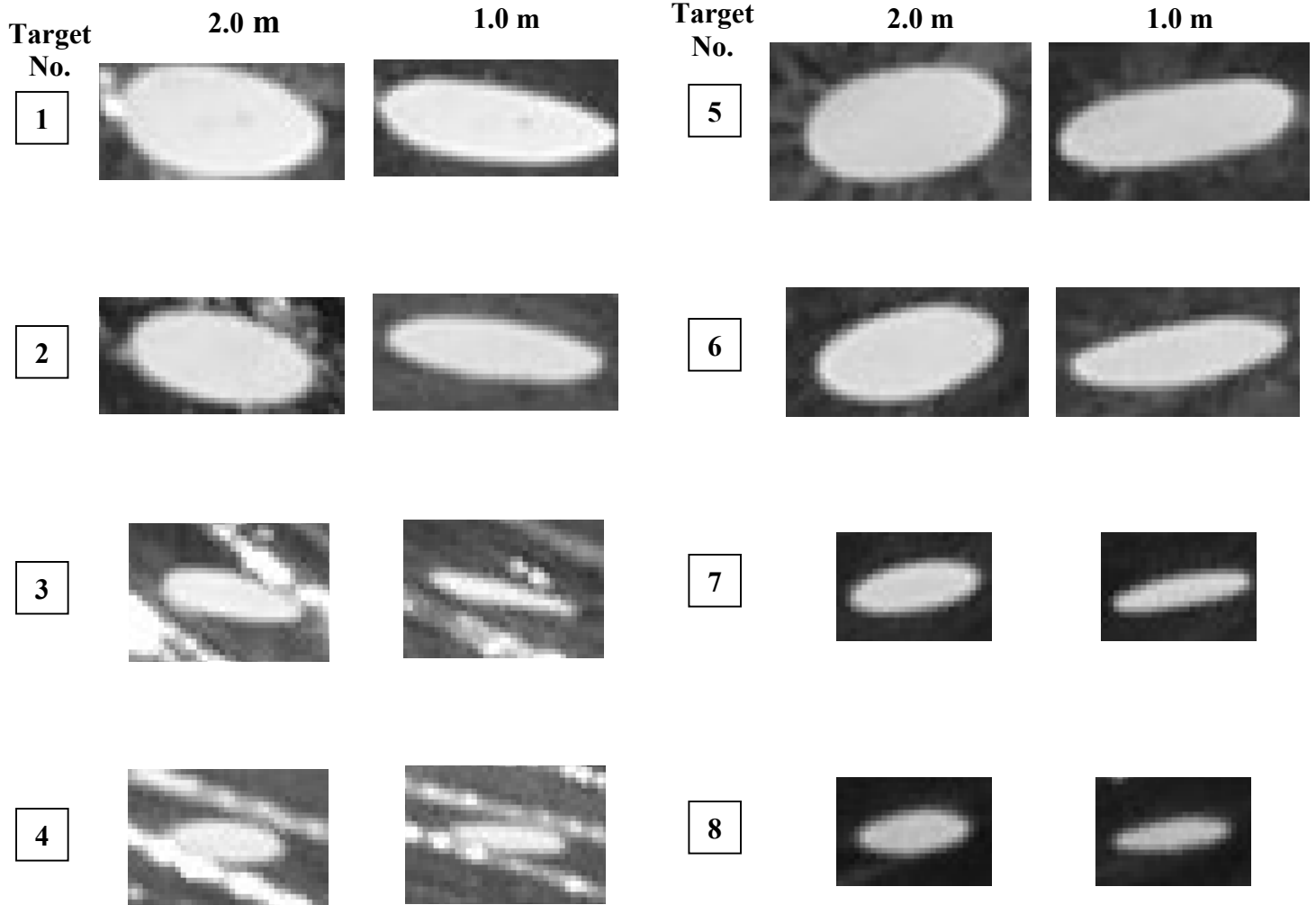


Figure 9-8. Close up views of select targets from Camera Positions 1 and 3

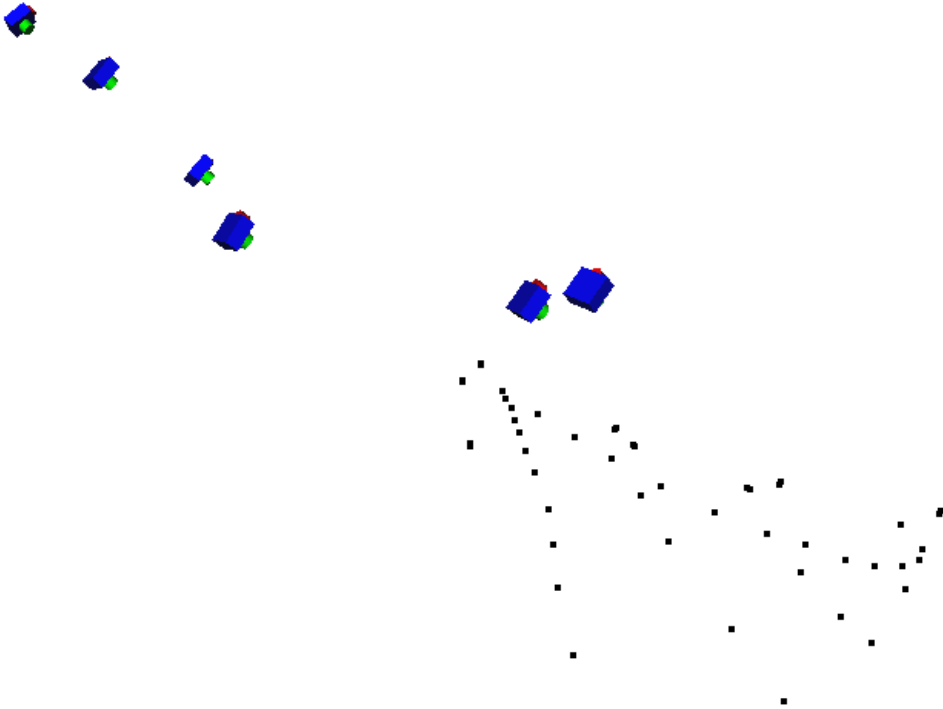


Figure 9-9. One of many bad camera orientation results encountered during image analysis



4 cameras at each location

These are the camera and target locations calculated directly from the 8 images using relative orientation and a free-network bundle solution (i.e., without control points or pre-measuring the camera locations and orientations)

Figure 9-10. Successful camera orientation and corresponding 3D point coordinates

Measurements of known distances (truth = 1.000 +/- 0.001 inches)

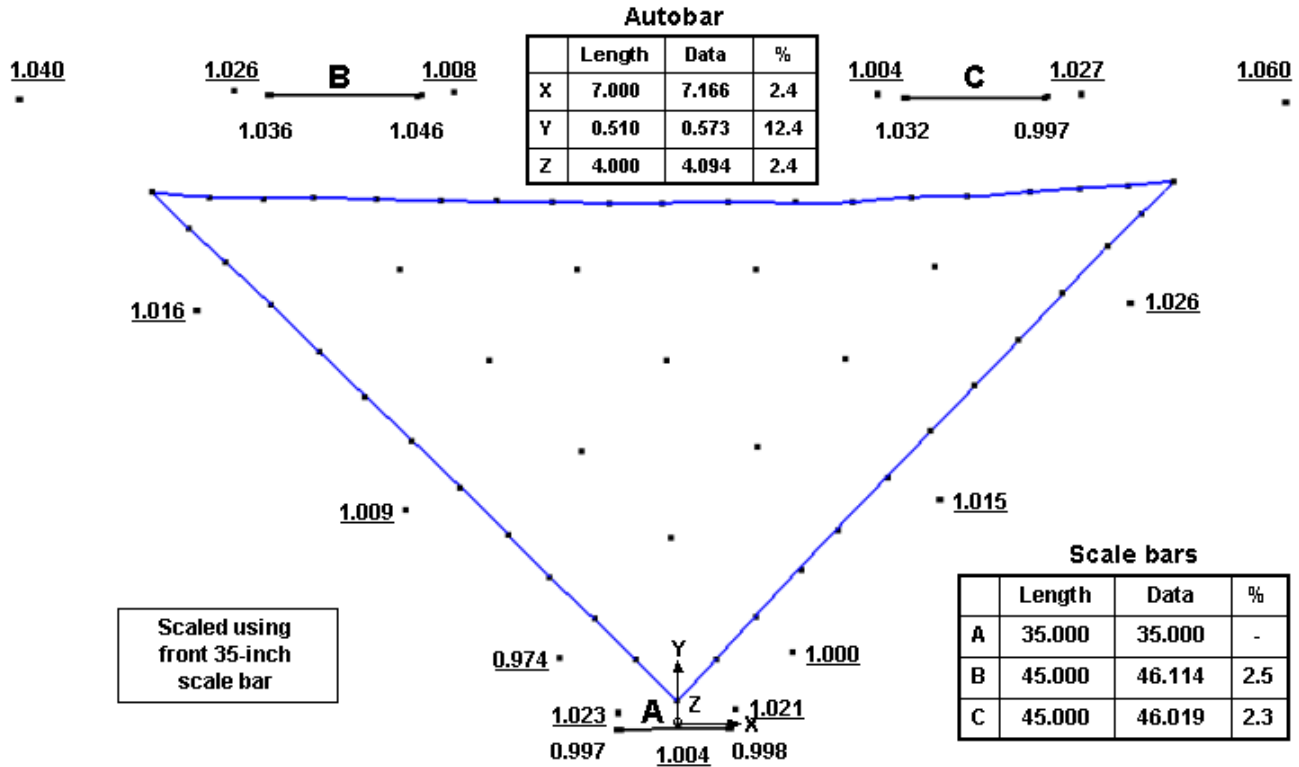


Figure 9-11. ODS *relative* measurement accuracy with cameras 1 m and 2 m above sail

Measured Location – True Location (Total vectors, amplified x5)

Measured Location – True Location (Z vectors only, amplified x200)

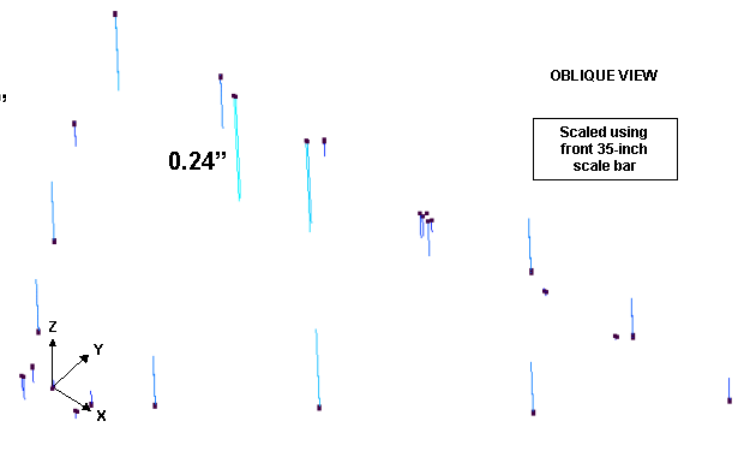
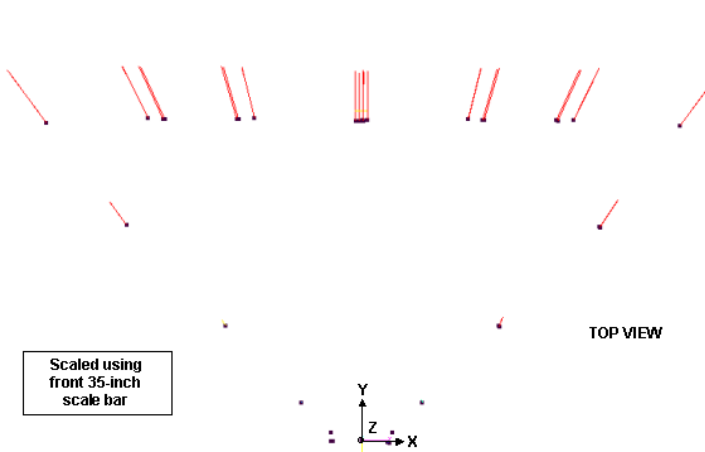


Figure 9-12 ODS *absolute* measurement accuracy (i.e., measured location minus true location)

Figure 9-13. ODS *absolute* measurement accuracy (i.e., measured location minus true location)

Total vectors shown. Dots indicate true 3D locations measured with V-STARS.

Z vectors shown. Dots indicate true 3D locations measured with V-STARS.

Section 10

Known Interface Issues with Each Cycle 1 Sail Design

10.1 *Common issues*

The issues listed below are common to both sail designs, but the answers may not be. Sections 10.2 and 10.3 show design-specific options for some of these common issues. The common issues identified to date include:

- Front vs back cameras and/or thermography: we need to study options overlooked in Phase 1
- Camera mast: design, ODS integration with mast, stability and knowledge of length
- Effects of ODS and camera mast on sail center of mass, static stability, and dynamics
- Stability and accuracy of knowledge of other sail dimensions ODS cannot estimate precisely
- Sail targets: number, pattern, design, attachment, location relative to folds, location accuracy
- Boom targets: same issues as sail targets, plus ensuring visibility over wide range of cases
- Visible and thermal appearance of membrane to ODS, and detectability of known anomalies
- Visible and thermal appearance of other interesting sail features, over a range of sun angles
- Sail slewing philosophy (affects glare: tilt same corner or quadrant towards sun, vs variable)
- Distributed wiring: protected or exposed, how attached, mass, possible need for redundancy
- Or tip/center wireless links: possible obstructions, need during deployment, redundancy
- Integration of distributed sensors with sail: accelerometers, load cells, strain, temperature, etc.
- Overall electrical integration of distributed ODS system with sail (power, data, grounding)
- Interfaces (if any) between ODS and sail during large-scale ground tests
- Possible schedule incompatibilities (we or they need decisions made before they are feasible)
- Implications of any required late design changes of sail or ODS on each other

10.2 Issues and options specific to ABLE sail design

A concept for mounting the main ODS camera clusters on an ABLE-type deployable mast is shown below. A possible boom-camera view of retroreflective targets is shown at right.

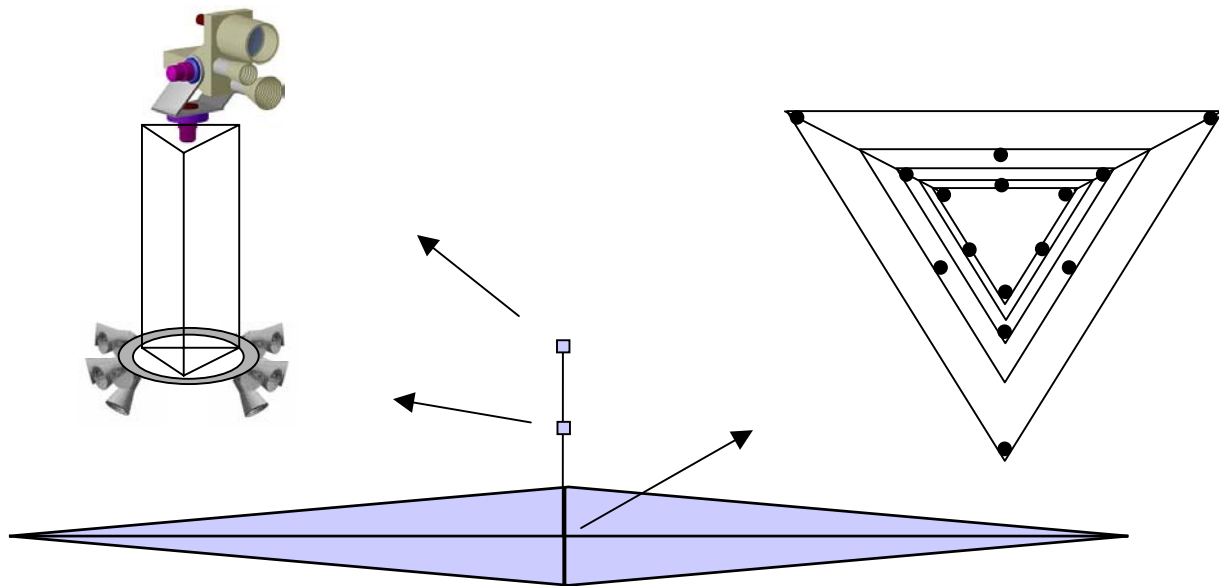


Figure 10-1. ODS mounting on ABLE camera mast, and possible boom target pattern

10.2.1 Relevant features of ABLE design

- The ABLE booms are deployed first, and then the sail.
- Deployment may be done while rotating edge-on to the sun, which might complicate imaging somewhat.
- The ABLE boom tips rotate as they deploy, and snap abruptly into place at full extension.
- Boom-view cameras must be offset from axis (a 1.3mm steel lanyard runs down the axis).
- A spreader bar on the mast tip rotates to effect roll. Moving ballast masses on the mast centerlines effect cant.

10.2.2 Boom-view cameras: position, coverage, and boom element visibility

Dave Murphy suggests we have targets at a maximum of 5 stations along the boom. On a 20m sail that puts the closest one at 2.84 m. To see a 0.4 m diameter boom at that distance requires a field of view of 8° . We need just 3/4 of the vertical height to see 3 targets at the corners of the bay, plus margin for misalignment and motion. How much margin is needed is TBD, but the other targets at each station will still stay in the view even after one leaves (or is occluded), and 2 of 3 should be enough for a good observation of boom bending and twist.

Putting the innermost targets at the middle of the battens allows a narrower camera field of view and hence more precision. There may be more in-plane bending than out-of-plane if peak bending is due to differences in support cable tension for adjacent quadrants. (This affects whether we use portrait or landscape image orientation.) We may want one extra target on the far end plate near the center (if we can do that without it being occluded by the central lanyard). This will help us know where the center of the boom tip is even if one or more of the other targets is occluded by boom cross-members inboard of that.

(Note: Additional studies may show that 3 accelerometers on each mast tip, plus targets on the sun-side face of the booms that are seen from the camera mast, is sufficient, and that we do not need cameras at the base of the booms and the targets described above. The cost/benefit ratio of doing so for a flight experiment may be too high.)

The lanyard is twisted by the action of the sail boom uncurling. From the camera viewpoint near the boom centerline, reflections off the lanyard are possible whether the camera is in front or behind the lanyard. The orientation that will cause glint is when a boom points towards the sun somewhat. When the sail deploys edge-on to the sun (while spinning), each camera may be pointed at the sun for a while. The potential for damage under these conditions must be checked.

The visibility of the boom elements themselves can be summarized as follows: the longeron is ~ 3 mm in diameter, the batten ~ 2 mm. They are both graphite epoxy with a satin black appearance. The diagonals may present some glint. They are 0.3 mm stranded stainless steel cabling. The boom fittings have a diffuse tan coating.

10.3 Issues and options specific to L'Garde sail

A concept for mounting the main ODS camera clusters on a L'Garde sail is shown below. The inflatable camera mast has a small offset at the base, so it can deploy around the carrier assembly, and is tilted for better clearance after deployment when the carrier is released and light pressure accelerates the sail backward away from the carrier. The cameras can mount offset to one side of the mast, so the mast can serve as a smooth bumper in case of carrier re-contact.

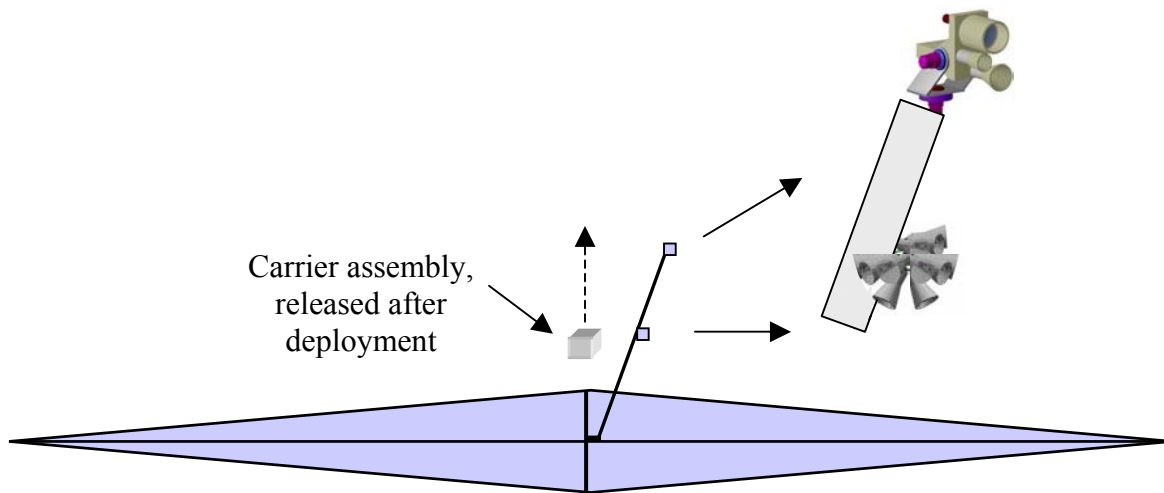


Figure 10-2. ODS mounting on tilted camera mast, plus support package fly-away

10.3.1 Relevant features of L'Garde design

- Membrane has a high-emittance thin iridescent black chrome coating on back.
- The booms have film over them so they can stay cooler, so their exact shape cannot be seen.
- Each boom has rings to support the sail, which can hold optical targets to image boom flex.
- The booms are aluminized internally and could act as a light pipe for data communication.
- Control assemblies at the tip may weigh ~200 grams and take $\ll 10W$ power (maybe $< 1W$).
- The sail's camber or depth/edge-length is likely to be in the 1%-5% range.
- L'Garde prefers that ODS not have wires running through the booms to the tip (heating, etc.).
- They want to minimize mass at boom tips (small compared to their ~200 gram tip vane assy).
- They do not want large moments from long camera masts at the boom tip.
- Their sail is light enough that ODS may affect axial CG location & hence sail stability.

10.3.2 Key mounting issues on L'Garde design

The carrier assembly needs to be on the sunward (front) side of the sail for the sail to fly away freely after it is deployed and released by the carrier. But the ODS camera platform needs to be there also. One option is to mount the camera boom slightly off center and tilted (10-15°), to leave a “fly-away” margin between the carrier and the camera boom. Other options currently appear more difficult: discard the ODS camera boom with the carrier or perhaps deploy a second ODS.

An offset camera mast will move the sail center-of-mass toward one corner of the sail. Since they need a CM offset for slewing, it may be simplest if the sail corner closest to ODS is also the one that tilts toward the sun when the sail slews. This moves the maximum glare region further from the center of the sail. (Having a corner rather than mid-quadrant facing the sun should further reduce the area affected by glare, although it means poor viewing of part of one boom.) Having a fixed sun azimuth should also simplify keeping the camera mast cool, despite direct and reflected sunlight.

Note that the camera mast could use supporting guy lines between the sail plane and just under the main platform, if such lines don't make fouling more likely during flyaway. But the shorter length and lower loads (especially in bending) suggest to us that we don't need that.

The boom-view cameras on the L'Garde sail can mount forward of the sail plane, possibly within the triangle defined by the tensile truss structure. Targets can mount at the base of the V, at the supporting rings along the boom, and also at the top of some of the compressive members that define the V.

10.4 ODS Team Questions for Solar Sail Vendors

10.4.1 ODS Primary-Equipment Accommodation

- What structure exists or can be provided to support ODS cameras (to achieve the desired views for photogrammetry)?
- What are limits to the size of extension booms, such that they will not adversely affect deployment, dynamics, or mass? (This answer will be very different for front-extension versus rear-extension masts.)
- Are there any special concerns regarding the accommodation of ODS support equipment (e.g., location, volume)?
- How are spacecraft support electronics to be accommodated? Is this yet definitive or is left as an exercise for a system contract (or proposal or study)?

10.4.2 Sail Targets

- What is the maximum target density (areal and mass) allowable? What other mechanical properties of targets must be specified (e.g., stiffness, thickness, etc.)?
- How will responsibility be allocated for the placement of ODS targets on the sail? Who is responsible for their specification? Who is responsible for their actual installation? Who is responsible financially for them and their installation?
- What can we say about accessibility to the sail, with or without targets, with respect to ODS activities, e.g., calibration?

10.4.3 Boom Targets

- What types of targets or retroreflectors can be attached to the masts?
- How will responsibility be allocated for the placement of ODS targets/reflectors on the masts? Who is responsible for their specification? Who is responsible for their actual installation? Who is responsible financially for them and their installation?
- What can we say about accessibility to the structure, with or without targets, with respect to ODS activities, e.g., calibration?

10.4.4 Mast-Tip Equipment

- Is any mast tip equipment besides accelerometers anticipated? What is the total allowable tip mass or total allowable additional tip mass beyond what is already contemplated?

- If “yes”, what is the power and data communications infrastructure anticipated? Can it be used as-is for accelerometer data? Can it be easily augmented?
- If “no”, will wired infrastructure be allowable (e.g., from a mast-deployment interference perspective)? What is an allowable linear mass density of such wiring? Stiffness? etc. What considerations are relevant with respect to mast deployment and interactions with wires (e.g., stowage, bending, etc.)? Is the mast structure useable as a power return?
- If wired infrastructure is not acceptable, what are the RF and optical properties of the booms and sails? What real estate can be made available at the mast tips for (solar) power generation?

10.4.5 Dynamics

- Is the sail structurally stable with respect to all sun angles? What is the maximum allowable off-normal sun angle?
- What reaction forces and torques are allowable for the PDS to impose on the ODS during deployment and operations?
- What are the intrinsic structural excitation sources and their magnitudes? Is there any need for artificial excitation to support dynamical (ODS) analysis? Can existing mechanisms provide such excitation?

10.4.6 Thermal

- What is the thermal conductivity of the sail material, both normal and transverse (in plane)?
- What are its expected α (front) and ε (thermal, both front and back)?

Section 11

Technology Gaps and Risks for Bringing ODS to TRL 6

Sections 11.1 and 11.2 below list recognized technology gaps and perceived risks in getting the Optical Diagnostic System for Solar Sails to a NASA technology readiness level (TRL) of 6. Sections 11.3 through 11.10 recommend near-term development efforts in each area, mostly in the same order the topics were discussed in the main body of the report.

11.1 Key technology gaps that need to be filled to get ODS up to TRL 6

Key technology gaps are listed below in estimated order of importance (critical items first):

1. Thermography: hardware selection, testing, and interpretation of imagery
2. Trade study: front side cameras (visible & IR) vs. back side cameras (visible & IR)
3. Cost/benefit study of cameras at hub for measuring bending/torsion of booms
4. Target requirements and test methods to validate them
5. Deriving sail shape and dynamics using cameras on lower platform only
6. Optimizing the height of both the upper and lower camera platforms
7. Photogrammetry and thermography instrument calibration techniques
8. Relevant ground tests of membrane optical properties
9. 80 Hz SXGA image compression at low power and mass w/space-qualifiable hardware
10. Design of both imagers and algorithms to handle high and variable noise in images
11. Efficient near-real-time SXGA image centroiding with minimum hardware and power

11.2 “Top Ten” known risks involved in getting ODS up to TRL 6

The list below is taken from the Phase 1 final presentation. It is included here as an independent ODS status check, somewhat orthogonal to the list of technology gaps in Section 11.1.

1. Validity of targeting approaches

- L’Garde targeting approach not yet demonstrated
- AEC-ABLE / SRS targets not yet validated
- Creases & wrinkles can significantly affect measurement accuracy

2. Uncertainty from ISP office about Level 1 requirements

- Affects complexity of components purchased or built
- Can affect schedule and cost

3. Camera design/placement affected by requirements of ground test program

- Much less light
- Vibration frequencies are much higher, so frame rates must go up ($f \sim 1/\text{Size}^2$)
- The structure has much more sag in gravity than in space
- We do not want the test program to drive the design

4. Procurement time

- ISP getting required \$\$ to LaRC in sync with expenditures
- Delays in subcontract award or component delivery

5. Compatibility of flight ODS with L’Garde carrier

- Carrier flies away on sun side (interference with ODS mast?)

6. Compatibility of breadboard and prototype ODS with L’Garde boom cooling

- L’Garde does not yet have a solution to this problem
- Could affect how cameras are mounted at LaRC and Plum Brook

7. Buckling deflection of L’Garde booms is low ($\sim <2$ cm for 10m sail)

- Can sufficient vibration be excited to measure, without structural damage

8. Cycle 1 10m tests get delayed or have problems unrelated to ODS

- Results in schedule slip to verification of Breadboard ODS

9. Method to place ODS system above sails in large-scale tests not yet well defined

- Potential interference with other supports
- Camera stability with pan-tilt movements

10. Transition to Phase 3 occurs just prior to start of new FY

- Additional funds needed in \sim Sept. 2004 for Phase 3

11.3 Sail dynamic analyses

11.3.1 How do thermal gradients, assembly errors, and creases affect membrane behavior?

During the study we realized that at least 3 different effects could swamp the intended uniform “few-ppm” tensile strain on solar sail membranes, and hence drastically change the planned uniform membrane tension. One effect is thermal gradients (see Section 6). Another is cumulative assembly errors. Large solar sails may necessarily involve step-and-repeat membrane assembly operations. This may lead to cumulative errors far larger than those found with sails small enough to assemble in deployed form on a flat surface. A third issue is the effect of creases, and intersecting creases that form puckers. The one saving grace about creases and puckers is that they straighten out at modest local membrane tension, and hence may provide passive slack management. This may help compensate for thermal gradients and assembly errors.

The task here is to understand the likely magnitude of these effects, and their combined effects on sail shape, dynamics, performance, and restrictions they may impose on sail operation. One potentially critical issue is to understand whether the effects of thermal gradients on sail shape could lead to positive feedback in the attitude control system, either due to the inherent geometry of the sail and its support structure, or due to plausible control-structure interactions: a possible control-induced flutter problem. Control interactions are a sail-developer responsibility, but developing sail dynamic models detailed and accurate enough to find inherent feedback mechanisms may be within the scope of ODS modeling, and could benefit later control stability studies by the sail developers.

11.3.2 What “natural” parameters summarize solar sail deviations from a plane?

The basic concepts in statistics (average, RMS error, and skewness) are amazing in their simplicity, completeness, and broad utility. Basic parameters of this sort might allow easy estimation of non-ideal sail performance due to billow, wrinkles, and creases. The question is what parameters might be most “natural.” For example, we can probably develop a precise definition for the “mean sail plane” of a billowed sail that is unambiguous, measurable, and useful for various analytical purposes.

Root mean square (RMS) surface slope compared to that mean sail plane should summarize cosine losses due to scattering of reflections away from the mean direction of the reflection. This parameter properly combines all the effects of surface slopes, on all relevant scales, without worrying what causes them--at least when the combination of sun angle and billow depth are not sufficient to shade part of the membrane. The value can be inferred from the ratio of sail area projected onto the mean plane, compared to total sail area. Hence if we can estimate the in-plane displacement of the edges of the sail (caused by out-of-plane deformations), then we can infer RMS slope, without knowing the details of the out-of-plane (OOP) displacements. The thrust loss due to scattered reflections should be $4r/(1+r)$ times the direct loss in area (which also affects thrust), where r is the sail reflectivity, assumed completely specular (which is a good approximation). A complementary parameter is the "average billow." This might be the difference between the mean OOP positions of the sail edge and the sail area. The CP shift due to billow may depend mainly on the product of this and the sail tilt angle to the sun, independent of details.

The effort here will be to look for a wider range of parameters like mean sail plane, RMS slope, and average billow, and use the models to estimate how well they can predict non-ideal sail behavior, and how readily their values can be derived from ODS and other flight data.

11.3.3 How can analytical models use ground and flight test data for verification?

ODS will generate large amounts of data: images, other sensor data, and (after processing on the ground) 3-D sail shape estimates. A key use of the data and shape estimates is structural model verification. Mission planners understandably like analytical models verified before using them to plan expensive missions. The question here is how to do that. Any model with a large enough number of input parameters can be made to fit any dataset, but that does not verify the model unless there is also reason for the specific inputs used. It is hard to describe this task in more detail than to say: it is everything that an intelligent modeler does between the time that he gets good-quality test or flight data, and the time he is ready to use his model to make predictions whose accuracy can be tested by later ground or flight experiments. Those predictions may span the range from thrust and thrust direction, to peak tensions at sail corner supports, to the

combined effects of sail control algorithms, sail structure, and thermal distortion. As ODS/sail tests are done, the data to drive this iterative loop become available, and progress can be made.

11.4 Image processing and display

11.4.1 Real-time scanning for targets

It appears that the most time-consuming part of looking for targets in images may be the initial brute-force, pixel-by-pixel scan of the whole image. But low-level logic can scan for the target as it is transferred and provide indications of where to look in the image for good target candidates. The main near-term task is to understand what circuitry is required for this, and whether it might easily fit into an FPGA used for control of multiple imagers and image capture.

11.4.2 Automated target recognition, identification, centroiding, and characterization

Most photogrammetry still depends on manual target identification unless coded targets are used. Coded targets for ODS would have to be quite large, and manual target identification could be extremely time-consuming because of the large number of targets and images. Automating target identification should be easier than in many photogrammetric projects because the sail has high regularity in space and time, with its slowly moving, nearly planar square grid pattern of targets, plus linear boom, sail-edge, and seam features in approximately known locations. A useful effort might include working on automating the following tasks:

1. Find candidate targets and judge tentatively whether they are targets based on local tests.
2. Find their centroids (and eventually, their size, shape, orientation, and total brightness).
3. Judge which targets they are in a grid (and eventually provide a confidence estimation).
4. Interpolate positions for missing targets and look again for them with adjusted criteria.

11.4.3 Automating generation of accurate 3D sail shape estimates from ODS imagery

As noted in Section 3.2 and elsewhere in the report, the specialization of the two main ODS camera platforms means that ODS cannot do traditional 3D multi-viewpoint photogrammetry of the whole sail at one time. On the other hand, we will have high-quality images of the whole sail and targets, and a variety of real-world constraints on the interpretation of those images that allows us to infer considerable depth information in generating a 3D model of the sail. There seems to be no question that this can be done; the key issue is how to do that in the most accurate and efficient way. What makes this effort complicated is actually the wide variety of tools that may be able to assist the process, and the wide variety of derivative products that different approaches may provide, and the uses and relative value of those derivative products.

For example, any technique that can iteratively project ODS imagery onto a 3D sail model and adapt the model to better fit the imagery could be not only powerful but also intuitively useful because it ends with a potentially very accurate 3D model of the billowed sail that is also photo-realistic. If this sail model is compatible with one or more popular standard CAD display programs that allow users to easily change perspective, it may become an extremely powerful, intuitively useful tool for a wide range of analysts, including sail developers, program and mission planners, and others interested in solar sail technology. Even difficulties in local fitting of the model can be made visible, for example using an overlay that shows where the model thinks the targets should be, or residual errors. This allows users to evaluate solution accuracy, and perhaps (by seeing error patterns on the sail), to understand the reason for the errors.

The near-term effort here might start by collecting data on a wider range of computer programs that may be useful in image processing and display. Then we would find and talk with current users about the relative strengths and weaknesses of the programs, and put together a more detailed plan for the remaining development. In parallel with this, we would investigate the most useful forms for ODS image data products, with a strong emphasis on making them easily usable with a variety of existing widely used programs. For example, we have found that next-generation Digistar digital planetarium projectors from Evans and Sutherland will accept 3D model data in Windows ActiveX/DirectX format. Putting models into that format may

ensure the models can be used in a wide range of applications, from PC-based to planetarium-based.

11.4.4 Consider goals, lighting, and other issues for large-scale ODS ground tests

This is an effort that requires input from both the ODS team and the sail program. Section 4.2 of the report discussed lighting trades for large-scale combined ODS/sail tests. If we do indeed want realistic images we need “representative” lighting: selectable bright lights in several positions to simulate sunlight approaching the sail from different directions, with each light small enough to look like a sun-like source. We also need black backdrops wherever feasible so the sail itself looks appropriately dark. But we cannot hope to get realistic sail glint because large-scale ground tests necessarily apply higher membrane tensions and hence straighten out creases and puckers. So the more serious issue is to carefully think through the purposes of the large-scale tests, and to find out what is actually worth doing in those tests, and what other tests are needed if the original goals of such tests are best met in other ways. Large-scale tests are useful for ODS since they allow us to test our image-processing techniques, and they should be useful for modelers, sail developers, and mission planners by providing data on sail dynamics in test environments. But large-scale ODS/sail tests cannot provide all the kinds of developmental test data that ODS needs, so additional smaller-scale tests are needed as described in Section 11.5.

11.5 Mechanical and Optical Tests of Membrane Crease and Pucker

11.5.1 The need for representative handling and lighting of representative membranes

The L’Garde flight sail will be metalized on both surfaces (aluminum on one side for reflectivity; a thinner chrome coating on the other side for emittance). The ABLE/SRS sail may be metalized on only one side. Despite the fact that the metal coatings are <5% as thick as the underlying plastic film, much of the memory of creases is due to the metals rather than the plastic because of their higher modulus and much lower yield strain compared to the plastic films, and the fact that the metals are on the surface, which maximizes strain in bending. Hence handling tests that seek to characterize crease or pucker formation and removal, and their effects

on sail glint and hence image quality, need to use films and coatings made of representative thicknesses of representative materials. And they must be handled in representative ways, at representative tensions. This cannot be done with large sail membranes in Earth gravity because gravity-induced tensions are far too high, whether the membrane is horizontal or vertical.

11.5.2 Handling tests to evaluate low-tension geometry of folded/unfolded membranes

The sail fold pattern will probably be z-folds in one direction followed by additional z-folds or rolling in the other direction. If the sail developers can provide data on how they expect the film to be secured against launch and depressurization (tightly clamped or not, etc.), it would be useful to have that data. When we deploy the film in ground tests, we need to take care to prevent tension spikes that would not occur in flight, and to provide “local unfolding” similar to that expected in flight with any pull-out tabs or other slack-management devices the sail is expected to use. On the other hand, if transient tension spikes are expected, for example at the end of deployment, it is important to try to mimic them in some way, or at least to do tests that bracket the range of expected peak tensions and their effects on creases, puckers, and other artifacts.

Once we have a way to mimic the expected handling of the sail membrane, at least insofar as it should affect crease and pucker formation and removal, then we can do realistic mechanical and optical tests on the membrane. Mechanical tests can look at the nonlinear stress-strain film response and see how that varies as a function of the peak tension in each direction since unfolding. A single exposure to “high enough” tension should take out most of the creases and puckers, much like shaking out a bed sheet after unfolding it. This should make the film behave much more like virgin film in both its mechanical and optical properties. We need to understand the extent of such changes. The sail developers may benefit because it may affect their thinking about imposing intentional transient peak tensions after deployment to straighten out creases and puckers before cumulative space exposure embrittles the membrane.

11.5.3 Optical testing of appropriately handled membranes

If mechanical tests show that traveling waves or other likely low-tension dynamics can “shake out” membrane creases and puckers without over-stressing the membrane or the boom structure, it is possible that glint will not be a problem. But if plausible handling can in some cases leave residual creases and possibly puckers, then careful glint testing seems necessary. The main purpose of these optical tests is to characterize glint intensity as a function of current tension, peak prior tension, and apparent local membrane tilt. The main emphasis should be on substantial local tilts because most of the sail is far from the “glare spot” and hence substantial local tilts are required to cause glint. Doing this test requires a small light source (not necessarily a point source) and good black baffling everywhere else. Then everything other than the light source that is viewed in specular reflections from the sail is far darker than the light source, and preferably fairly uniformly dark.

If the main ODS imaging cluster height is 15% of the sail edge dimension, then (neglecting billow) half of the sail area will be viewed at angles 69-78° from the normal, and $\frac{3}{4}$ of what is left will be viewed from 53-69°. And the sun may generally be either near normal or near 35° from normal to the mean sail plane. So over *most* of the sail area, generating glint viewable by the cameras will require fairly significant local membrane tilts (due to creases, puckers, or wrinkles caused by uniaxial tension). One slope-error survey technique that has been used with solar concentrators is to image the reflection of a fluorescent tube off the non-ideal surface. Moving the tube allows a 1-dimensional scan of one component of the local membrane slope. Repeating this in two orthogonal scan directions allows evaluation of the glint statistics for slope components in each direction. Results for the two directions may differ because the order of folding and unfolding may result in different crease patterns.

11.5.4 Collecting and interpreting glint statistics

The key output from two 1D glint surveys may be a graph of the frequency of various angular deviations from flatness and the characteristic sizes of those features, which should vary with membrane thickness. This requires imaging on a scale far finer than that of a single pixel in a flight-size sail, or estimating the glinting feature size from its “excess brightness.” This

assumes that the characteristic width of a reflecting region from a crease or pucker should be a function of the film thickness and tension far more than of the overall membrane size.

To limit the number of optical scans and post-processing runs required, it may be worth doing this test for two main cases, one with minimum peak tension after deployment, and one with much larger (but still plausible) peak tension, to see what difference that makes in glint statistics and potential noise in ODS imagery. Very informal manual tests may show several different types of behavior, each of which deserves characterization.

11.5.5 Diffuse membrane reflectivity

The same optical test setup used above can characterize “quasi-diffuse” membrane reflectivity after typical handling and with near-normal illumination and high-incidence viewing. In this case, it is very important that the main specular reflection from the membrane be trapped and absorbed fairly well so it doesn’t illuminate the baffle regions the camera sees reflected in its view of the membrane. We can also mask the direct illumination of the sail and subtract the “surrounding background” intensity from the intensity of the masked region to reduce the effect of stray light. The purpose of the test is to see whether and how the effective diffuse sail reflectivity changes with handling, view angle, tension, or anything else. As mentioned in the “targetless imaging” section of the report (Section 4.3.1), such changes might provide useful diagnostic information. It may be worth testing some membranes before and after exposure to plausible events that might change diffuse reflectivity to see whether such changes do occur.

11.5.6 Target optical tests

One more set of very useful optical tests is imaging “handled” membrane samples with targets on them. The imaging can be done with far higher resolution than would be present in flight. The resulting image can be smeared in digital post-processing to simulate lower-resolution target images with various degrees of smearing, intra-pixel sensitivity variations, and so forth. These tests could characterize the brightness uniformity of the targets and the presence of any glinting features associated with the targets that might affect accuracy. For example, the painted targets shown at the Phase 1 final review caused slight local expansion of the film, which

caused local slackness around the edge of the target. At certain lighting angles, that causes glint from one side of the target but not the other. The result is centroiding errors. (If this can occur with flight-design targets, then we should use smaller targets than would otherwise be optimum for photogrammetric accuracy.) Target-induced glint might be present at very low tensions but not higher tensions. We can then do image recognition and centroiding off-line with images degraded by digital smearing and noise. This allows a better understanding of target visibility, recognition, and centroiding errors as a function of target size in pixels and glint and glare level.

11.6 ODS camera development

Efforts are required here both on components (lenses, filters, lens shades and other stray-light-control features, imagers, and support circuitry) and system performance.

On the lenses, we should select and procure some “apparently suitable” stock lenses. We can take a few apart to see what may require changing for flight. Then we can contact the suppliers and determine their openness to making a small lot with any required changes, at a reasonable lot charge. Changes could include different spacers, better edge blackening, a smaller aperture, addition of a ceria-doped glass or colored glass front filter element, better venting, or tighter clearances to prevent relative shift in elements after shock or thermal cycling. If we can purchase modified lenses at a reasonable lot charge, then we can use stock lenses for most of the developmental testing. If nothing unpleasant is learned, then we would purchase custom lots. This should be done with enough lead-time that we can find a backup if necessary. If no suitable “modifiable” lens can be found, then an alternative path needs to be fleshed out--but the most nearly suitable stock lenses can still be used for most early development work.

For the imaging chips, we need to review the candidate datasheets more carefully and then choose at least two for testing. Many SXGA-class active pixel CMOS chips are available in “Evaluation/Development Kits (EDKs),” with PC-connected hardware and support software. This allows us to easily verify sensitivity and noise claims. We can also test an EDK for damage by focused sunlight. Nondestructive evaluation of the imaging chips is also useful. For example, for ~10 chips from the same batch, we can measure chip placement errors in the

ceramic package (offset, rotation, and tipping) and how much they vary. Another useful test for chips with glass covers is package bulge or breakage during fast depressurization in a vacuum chamber.

After these tests, we can substitute lenses selected above for the lens provided with the imager and do more useful ODS tests. Repeating the test described in Section 5.1.2 would be useful to quantify centroiding noise. We can also determine point spread function with a prototype lens, with and without color filters. Then, if the chips still look promising, it might be time for radiation testing of the imager and (in a proton environment) the lens to ensure it does not darken unacceptably, if we cannot find other radiation test data on those chips and optical glasses.

Then we can design and build prototype circuit boards and aluminum camera housings, assemble cameras, program any FPGAs as needed, and start testing for photogrammetric stability over temperature and shock. In parallel with this, we will be developing the rest of the avionics. When both are ready, we can test them together.

11.7 Thermography

As noted in Section 6.7, it seems worthwhile to focus near-term thermography efforts on answering the following questions:

1. Are compact low-power imagers like the Omega likely to be flight-qualifiable?
2. Can front-side thermography with those imagers provide useful images of the sail?
3. What can such images tell us about sail properties, degradation, or other phenomena?

The ODS team has already purchased an Omega, so testing it will be convenient. The more difficult task is providing suitable thermal imaging test subjects. The long-wave emittance of the front of the sail (~0.03-0.05) may actually be less than that of a few meters of room air with typical humidity. So we may want to do many of the tests in vacuum with good cold plates, etc.

But many of the tests aimed at characterizing the imager are independent of the exact details of the object that is imaged, so we can use “any convenient subject” for many images.

Well over half the thermography effort might really be focused on characterizing what we can learn from front-side or back-side thermal images of sail materials, both virgin and also after plausible types of mistreatment, including sputtering, radiation, contamination, etc. Many of these material property tests might best be done at Surface Optics Corp. because those tests are done in carefully controlled environments that make it easy to distinguish surface property changes from temperature changes.

By testing materials over a range of conditions, angles, and wavelengths, we can determine “what is there to be seen” and whether it may need multi-spectral filters to adequately distinguish different conditions. That can tell us whether we may need an infrared filter wheel on the thermal imager, for example to split the 7.5-13.5 micron region into several bands so we can distinguish temperature changes, contamination, or other effects.

11.8 Distributed non-imaging sensors, datalinks, and support electronics

The first effort here may be to find out from the sail developers what needs they have in their most recent sail designs for power and data transfer between the center and the boom tips, what sensors they are interested in, what concepts they are considering, and whether a 4-wire link weighing <1 g/m should be compatible with their boom design and not too hard to integrate. For the L’Garde design, we should find out whether a total ohmic heating of order 1W along a 50m wire is acceptable inside or in close proximity to their temperature-sensitive boom.

We should also look to see what commercial wiring might be available in this mass range. If none is available, it may be worth having a sample made for handling tests. (Using a robust polyimide coating should keep the costs well below those of the ProSEDS wire.) In parallel with this, we need to see what short-range wireless concepts may be most feasible and attractive, and

what the “overhead” is for providing power for wireless concepts. Then we should take a close look at the costs and risks of each option and recommend a wired or wireless solution.

In the area of sensors, we should take a fresh look at what will be most complementary to the imaging sensors and useful for understanding sail loads and dynamics and anomalies, to the extent we can predict the key issues and observables. Then we should purchase, evaluate, and test candidate sensors, first by themselves and then with candidate signal conditioning. Then we should make arrangements to have tests done with the sail booms to see whether there are any problems with deployment snagging (with wired concepts) or communication obstruction (in the case of wireless concepts). One sensor concept that we have not considered seriously but may be worth some attention is sensors and wiring concepts that are either inherent in or can be built into the membrane. For example, the resistance of the metal coating(s) between two regions may change with temperature, cumulative sputtering, or gross tearing. It may conceivably be worth measuring the resistance if a fairly low-risk way can be found to do that.

Another step is to integrate the sensors, communication links, and signal conditioning and do a variety of tests, hopefully including tests associated with the ABLE and L’Garde booms. We may want to consider circuit concepts that allow use of redundant separated cables in case one is damaged.

In parallel with this, we should look for radiation test data on candidate MEMS sensors. Such sensors are being considered for a wide variety of other programs, and radiation testing may be underway or planned. If we are very interested in a sensor that has not yet been tested, we should discuss it with radiation effects specialists to see whether there is any known reason for not using this sensor, and plan tests if it still seems prudent to use it. One final area is to periodically review progress in “Smart Dust” and other “local wireless network” concepts to see what new aspects may be relevant to distributed sensing on solar sails or other gossamer spacecraft.

11.9 Avionics

In addition to the technology tasks just discussed relating to distributed systems, the technology gaps in the avionics area are mostly associated with high-throughput imaging. The key issues are controlling 6 clusters of 4 SXGA imagers, capturing 80 frames/sec, or perhaps more if reviews of sail dynamics and transient effects suggest a need for that, and figuring out how to do near-real-time JPEG2000 compression and centroiding using low-power, low-mass flight-qualifiable hardware.

The main key TRL gap is verifying that we can do JPEG2000 compression at a sustained rate of ~80 SXGA frames/second. JPEG2000 does not use frame-to-frame similarity, so repeatedly dumping a single frame from a single high-speed buffer may be adequate unless send/receive re-synchronization after switching channels is an issue. We need to determine:

1. Whether we can download stored SXGA images fast enough over ~7m (LVDS or ?)
2. How long compression takes (which may vary with the image and compression ratio)
3. How easily we can double-buffer, to download one image while compressing another.

Careful analysis of hardware specifications may eliminate most risk. But if JPEG2000 compression time varies with the image content or compression ratio, we need tests on suitable images. And we do need good tests eventually (including radiation tests) to verify that there are no problems that may require our switching to raw-image capture plus later compression at lower rates or possibly switching to MPEG compressors if they allow higher throughput or compression.

The centroiding task should be easier, but may not be able to take advantage of optimized single-purpose hardware the way JPEG2000 may be able to. Centroiding is mature technology, but doing it at 80 frames/second on “noisy” solar sail images is not. We need to develop and test suitable algorithms, first on PCs and then on more flight-like hardware. It may be feasible to do the centroiding using mostly the same hardware used for conventional image compression if a “mostly software” solution is used for the JPEG2000 compression.

Note: The fact that the avionics subsection is shorter than that for several other topics does not mean that avionics tasks are less important or require less effort. The high-TRL areas are just somewhat better defined so it doesn't take as long to describe what needs to be done about them.

11.10 Interface issues and integration planning

The list below is copied from Section 10.1. These items are known interface issues that are common to both Cycle 1 sail designs (ABLE and L'Garde).

- Front vs back cameras and/or thermography: we need to study options overlooked in Phase 1
- Camera mast: design, ODS integration with mast, stability and knowledge of length
- Effects of ODS and camera mast on sail center of mass, static stability, and dynamics
- Stability and accuracy of knowledge of other sail dimensions ODS cannot estimate precisely
- Sail targets: number, pattern, design, attachment, location relative to folds, location accuracy
- Boom targets: same issues as sail targets, plus ensuring visibility over wide range of cases
- Visible and thermal appearance of membrane to ODS, and detectability of known anomalies
- Visible and thermal appearance of other interesting sail features, over a range of sun angles
- Sail slewing philosophy (affects glare: tilt same corner or quadrant towards sun, vs variable)
- Distributed wiring: protected or exposed, how attached, mass, possible need for redundancy
- Or tip/center wireless links: possible obstructions, need during deployment, redundancy
- Integration of distributed sensors with sail: accelerometers, load cells, strain, temperature, etc.
- Overall electrical integration of distributed ODS system with sail (power, data, grounding)
- Interfaces (if any) between ODS and sail during large-scale ground tests
- Possible schedule incompatibilities (we or they need decisions made before they are feasible)
- Implications of any required late design changes of sail or ODS on each other

REPORT DOCUMENTATION PAGE

*Form Approved
OMB No. 0704-0188*

The public reporting burden for this collection of information is estimated to average 1 hour per response, including the time for reviewing instructions, searching existing data sources, gathering and maintaining the data needed, and completing and reviewing the collection of information. Send comments regarding this burden estimate or any other aspect of this collection of information, including suggestions for reducing this burden, to Department of Defense, Washington Headquarters Services, Directorate for Information Operations and Reports (0704-0188), 1215 Jefferson Davis Highway, Suite 1204, Arlington, VA 22202-4302. Respondents should be aware that notwithstanding any other provision of law, no person shall be subject to any penalty for failing to comply with a collection of information if it does not display a currently valid OMB control number.
PLEASE DO NOT RETURN YOUR FORM TO THE ABOVE ADDRESS.

1. REPORT DATE (DD-MM-YYYY) 01- 12 - 2004		2. REPORT TYPE Technical Memorandum		3. DATES COVERED (From - To)	
4. TITLE AND SUBTITLE Optical Diagnostic System for Solar Sails: Phase 1 Final Report				5a. CONTRACT NUMBER	
				5b. GRANT NUMBER	
				5c. PROGRAM ELEMENT NUMBER	
6. AUTHOR(S) Pappa, Richard S.; Blandino, Joseph R.; Caldwell, Douglas W.; Carroll, Joseph A.; Jenkins, Christopher H. M.; and Pollock, Thomas C.				5d. PROJECT NUMBER	
				5e. TASK NUMBER	
				5f. WORK UNIT NUMBER 23-800-92-62	
7. PERFORMING ORGANIZATION NAME(S) AND ADDRESS(ES) NASA Langley Research Center Hampton, VA 23681-2199				8. PERFORMING ORGANIZATION REPORT NUMBER L-19069	
9. SPONSORING/MONITORING AGENCY NAME(S) AND ADDRESS(ES) National Aeronautics and Space Administration Washington, DC 20546-0001				10. SPONSOR/MONITOR'S ACRONYM(S) NASA	
				11. SPONSOR/MONITOR'S REPORT NUMBER(S) NASA/TM-2004-213511	
12. DISTRIBUTION/AVAILABILITY STATEMENT Unclassified - Unlimited Subject Category: 39 Availability: NASA CASI (301) 621-0390					
13. SUPPLEMENTARY NOTES An electronic version can be found at http://techreports.larc.nasa.gov/ltrs/ or http://ntrs.nasa.gov					
14. ABSTRACT NASA's In-Space Propulsion program recently selected AEC-ABLE Engineering and L'Garde, Inc. to develop scale-model solar sail hardware and demonstrate its functionality on the ground. Both are square sail designs with lightweight diagonal booms (<100 g/m) and ultra-thin membranes (<10 g/m2). To support this technology, the authors are developing an integrated diagnostics instrumentation package for monitoring solar sail structures such as these in a near-term flight experiment. We refer to this activity as the "Optical Diagnostic System (ODS) for Solar Sails" project. The approach uses lightweight optics and photogrammetric techniques to measure solar sail membrane and boom shape and dynamics, thermography to map temperature, and non-optical sensors including MEMS accelerometers and load cells. The diagnostics package must measure key structural characteristics including deployment dynamics, sail support tension, boom and sail deflection, boom and sail natural frequencies, sail temperature, and sail integrity. This report summarizes work in the initial 6-month Phase 1 period (conceptual design phase) and complements the final presentation given in Huntsville, AL on January 14, 2004.					
15. SUBJECT TERMS Solar Sails, Optical Diagnostics, In-Space Propulsion Program, Photogrammetry, Thermography, Space Flight Experiments, Instrumentation					
16. SECURITY CLASSIFICATION OF:			17. LIMITATION OF ABSTRACT	18. NUMBER OF PAGES	19a. NAME OF RESPONSIBLE PERSON
a. REPORT	b. ABSTRACT	c. THIS PAGE			STI Help Desk (email: help@sti.nasa.gov)
U	U	U	UU	146	19b. TELEPHONE NUMBER (Include area code) (301) 621-0390



An Updated Zero Boil-Off Cryogenic Propellant Storage Analysis Applied to Upper Stages or Depots in an LEO Environment

David Plachta
Glenn Research Center, Cleveland, Ohio

Peter Kittel
Ames Research Center, Moffett Field, California

The NASA STI Program Office . . . in Profile

Since its founding, NASA has been dedicated to the advancement of aeronautics and space science. The NASA Scientific and Technical Information (STI) Program Office plays a key part in helping NASA maintain this important role.

The NASA STI Program Office is operated by Langley Research Center, the Lead Center for NASA's scientific and technical information. The NASA STI Program Office provides access to the NASA STI Database, the largest collection of aeronautical and space science STI in the world. The Program Office is also NASA's institutional mechanism for disseminating the results of its research and development activities. These results are published by NASA in the NASA STI Report Series, which includes the following report types:

- **TECHNICAL PUBLICATION.** Reports of completed research or a major significant phase of research that present the results of NASA programs and include extensive data or theoretical analysis. Includes compilations of significant scientific and technical data and information deemed to be of continuing reference value. NASA's counterpart of peer-reviewed formal professional papers but has less stringent limitations on manuscript length and extent of graphic presentations.
- **TECHNICAL MEMORANDUM.** Scientific and technical findings that are preliminary or of specialized interest, e.g., quick release reports, working papers, and bibliographies that contain minimal annotation. Does not contain extensive analysis.
- **CONTRACTOR REPORT.** Scientific and technical findings by NASA-sponsored contractors and grantees.

- **CONFERENCE PUBLICATION.** Collected papers from scientific and technical conferences, symposia, seminars, or other meetings sponsored or cosponsored by NASA.
- **SPECIAL PUBLICATION.** Scientific, technical, or historical information from NASA programs, projects, and missions, often concerned with subjects having substantial public interest.
- **TECHNICAL TRANSLATION.** English-language translations of foreign scientific and technical material pertinent to NASA's mission.

Specialized services that complement the STI Program Office's diverse offerings include creating custom thesauri, building customized databases, organizing and publishing research results . . . even providing videos.

For more information about the NASA STI Program Office, see the following:

- Access the NASA STI Program Home Page at <http://www.sti.nasa.gov>
- E-mail your question via the Internet to help@sti.nasa.gov
- Fax your question to the NASA Access Help Desk at 301-621-0134
- Telephone the NASA Access Help Desk at 301-621-0390
- Write to:
NASA Access Help Desk
NASA Center for AeroSpace Information
7121 Standard Drive
Hanover, MD 21076



An Updated Zero Boil-Off Cryogenic Propellant Storage Analysis Applied to Upper Stages or Depots in an LEO Environment

David Plachta
Glenn Research Center, Cleveland, Ohio

Peter Kittel
Ames Research Center, Moffett Field, California

Prepared for the
38th Joint Propulsion Conference and Exhibit
cosponsored by AIAA, ASME, SAE, and ASEE
Indianapolis, Indiana, July 7-10, 2002

National Aeronautics and
Space Administration

Glenn Research Center

Acknowledgments

The authors want to acknowledge Robert Christie and Dale Robinson of ZIN Technologies, Inc. for their design integration work on the Protoflight ZBO Development Test Article, and Ken Mellott and Steve Geng of NASA GRC for their radiator analysis.

This report is a formal draft or working paper, intended to solicit comments and ideas from a technical peer group.

This report contains preliminary findings, subject to revision as analysis proceeds.

Available from

NASA Center for Aerospace Information
7121 Standard Drive
Hanover, MD 21076

National Technical Information Service
5285 Port Royal Road
Springfield, VA 22100

Available electronically at <http://gltrs.grc.nasa.gov>

AN UPDATED ZERO BOIL-OFF CRYOGENIC PROPELLANT STORAGE ANALYSIS APPLIED TO UPPER STAGES OR DEPOTS IN AN LEO ENVIRONMENT

David Plachta

National Aeronautics and Space Administration
Glenn Research Center
Cleveland, Ohio 44135

Peter Kittel

National Aeronautics and Space Administration
Ames Research Center
Moffet Field, California 94035

Abstract

Previous efforts have shown the analytical benefits of zero boil-off (ZBO) cryogenic propellant storage in launch vehicle upper stages of Mars transfer vehicles for conceptual Mars Missions. However, recent NASA mission investigations have looked at a different and broad array of missions, including a variety of orbit transfer vehicle (OTV) propulsion concepts, some requiring cryogenic storage. For many of the missions, this vehicle will remain for long periods (greater than one week) in low earth orbit (LEO), a relatively warm thermal environment. Under this environment, and with an array of tank sizes and propellants, the performance of a ZBO cryogenic storage system is predicted and compared with a traditional, passive-only storage concept. The results show mass savings over traditional, passive-only cryogenic storage when mission durations are less than one week in LEO for oxygen, two weeks for methane, and roughly 2 months for LH2. Cryogenic xenon saves mass over passive storage almost immediately.

Introduction

NASA has redirected the Integrated In-Space Transportation Program (IISTP) from Code R management to Code S; accordingly, the propulsion elements under development are aligned with science and exploration mission concepts. Several propulsion concepts being studied for these missions could involve cryogenic propellant storage; specifically, advanced chemical, nuclear bi-modal, solar thermal, and perhaps solar electric propulsion, particularly if it is combined with an advanced chemical propulsion assist. In addition to these concepts for IISTP, a propellant depot called the Hybrid Propulsion Module (HPM) led by NASA Langley Research Center, includes cryogenic propellants. These concepts would all involve orbit transfer from LEO, some to higher earth orbits and most to other planets or destinations. The duration of the storage for all of these concepts varies from minutes to years; the

purpose of this paper is to estimate the durations where the ZBO storage approach begins to reduce mass of the OTV. This estimation is based on scaling parameters determined from testing as well as analysis and design. The ZBO design work referenced is from a Protoflight ZBO Development Test Article (configuration shown in figure 1), which includes a flight cryocooler integrated with a propellant tank and a radiator, in a LEO simulated thermal environment.

The designs and estimations are guides for propulsion and mission design engineers in their evaluations and trade-studies involving cryogenic propellant usage. Besides helping them, this paper advances several details of the ZBO storage concept from previous studies.^{1,2} First, a detailed cryocooler integration design is shown and associated temperature drops are included, as they represent losses that require the cryocooler to operate at a lower temperature. Secondly, a tank mixer has been added to force flow across the heat exchanger coupled to the cryocooler. In addition, a radiator and associated thermal analysis is incorporated to reject the heat from the cryocooler. Finally, a look into the appropriate number of MLI layers for a ZBO tank is described.

Thermal Model

The following discussions on the analysis form the basis of the thermal model used in the analysis. Several parts are repeated from reference 1 for clarity, but the bulk of the work is based on additional research and design.

Cryocooler Model

The cryocooler model used is updated from reference 1. While the hydrogen cryocooler is again modeled using two cryocoolers (for simplicity), in this approach the first cryocooler is used to reduce the temperature of a tank shield to a typical intermediate value of a first stage of a two-stage cooler; the second cryocooler removes the remaining heat that enters the tank through that shield. Reference 1, on the other

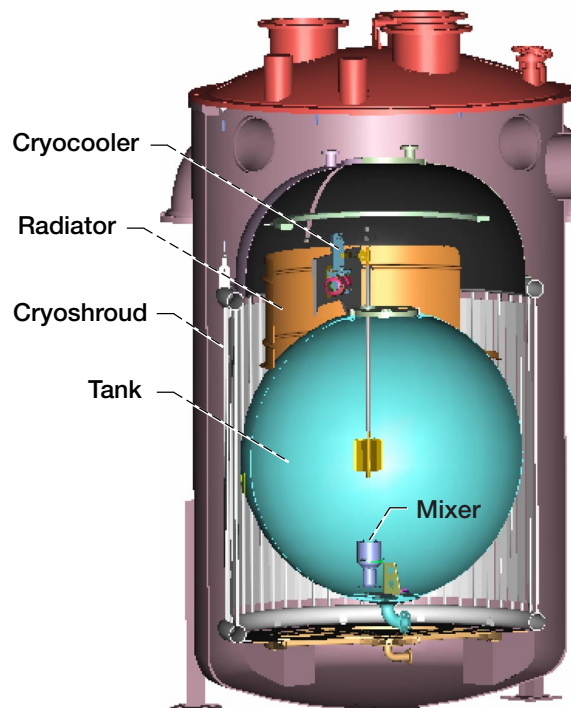


Figure 1.—Three-dimensional drawing of Proto-flight Development ZBO Test Article.

hand, incorporated a shield cryocooler in addition to a second cryocooler that removes all the heat entering the tank. The reference 1 advantage is the independence of each stage, while its disadvantage is somewhat heavier second cryocooler and more power. The revised approach disadvantage is that the stages are dependent on one another, and a high thermal load on the first stage could dwindle the performance of the second stage. Accordingly, we are assuming that the cryocooler stages and integration could be designed to match the OTV cryogenic propellant stage performance.

Unchanged from reference 1, the cryocooler sizing relationships are based on Strobridge, with modifications to account for advances in the last 25 years³ are as follows:

$$\dot{Q}_{ip} = \dot{Q}_c (T_h - T_c) (T_c \eta 10^\Sigma)^{-1} \quad (1)$$

where

$$\Sigma = -1.7359 + 0.59998 \log(\dot{Q}_c) - 0.14740 \log(\dot{Q}_c)^2 + 0.021323 \log(\dot{Q}_c)^3 - 0.0012502 \log(\dot{Q}_c)^4 \quad (2)$$

wherein \dot{Q}_{ip} is the electrical input power, \dot{Q}_c is the cooling power, T_h is the cryocooler heat rejection

temperature, T_c is the cryocooler coldhead temperature, and η is the improvement factor. The values used for η were 2.5 for CH₄ and O₂ tanks and 2.0 for H₂ tanks. These factors are estimated based on current and projected near term capabilities.^{4,5} Similarly, the mass of cryocooler is based on Strobridge's correlations adjusted by a factor of 0.2 to account for recent advances:

$$m = 0.2 \dot{Q}_c^{0.7} [(T_h - T_c) / T_c]^{1.45} \quad (3)$$

Additionally, cryocooler controller mass is included for the first time. It is estimated to be 1.4 times that of the cryocooler itself, based upon existing flight controllers.

Integration Loss and Vapor Cooled Shield

Assumption

Another update to the thermal model is the addition of an integration loss, due to physical integration of the cryocooler into the propellant tank. The loss used is based on the integration design of the flight cryocooler in the Protoflight ZBO Development Test Article, which uses liquid nitrogen as the working fluid and transfers 6.8 watts of heat to the cryocooler. The temperature drop was 8.5K (see figure 2 and table 1).

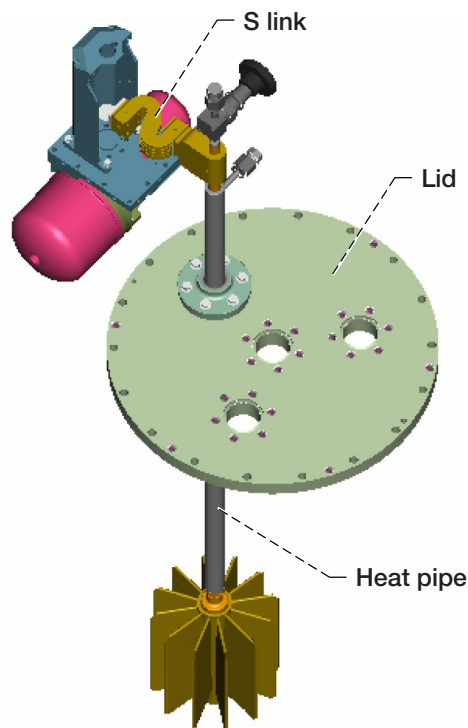


Figure 2.—Integration design connects cryocooler to propellant tank lid.

Integration Element	Temperature Drop, K
Convection drop	0.28
Fin conduction	0
Fin-wall interface	<i>0.5</i>
Evaporator wall	0.005
Evaporator	1.3
Condenser	0.98
Condenser wall	0.004
Wall-saddle interface	<i>0</i>
Saddle	0.34
Saddle-s-link interface	<i>0.5</i>
S-link	4.08
S-link to coldhead interface	<i>0.5</i>
Total	8.5

Table 1. A listing of the components and interfaces with their calculated or assumed (in italics) temperature drops for integration into a LN2 propellant tank for a protoflight test with an estimated 6.8 watts heating rate.

This drop causes the cryocooler coldhead to operate that much below the propellant bulk liquid temperature, as follows:

$$T_c = T_{\text{bulk}} - T_{\text{drop}} \quad (4)$$

This is represented as inefficiency according to the following equation:

$$(1-\eta) = (T_{\text{bulk}} - T_c) * (T_h/T_{\text{bulk}}) / (T_h - T_{\text{bulk}}) \quad (5)$$

For the Protoflight ZBO Development Test Article, (1-η) is 12%, which is used in this analysis. While this term would vary slightly with T_{bulk} depending on the fluid, those variations were not included.

The loss for integrating a cryocooler with a liquid hydrogen propellant tank has an additional part because of liquid hydrogen cryocooler's two stages, the intermediate stage (first stage) in addition to the cold head (second stage). The second stage loss is 12%, as discussed above. The first stage loss is more uncertain as it will be integrated differently, perhaps with a heat pipe to cool an oxidizer tank or tank penetrations such as feed lines or tank support struts, or in conjunction with a vapor-cooled shield to reduce the temperature of the insulation. A check on the analysis shows a vapor-cooled shield to be quite heavy, yet it slightly reduces the overall system mass and we have assumed its use around the tank. Because it is much larger and the heat travels further

than the heat exchanger attached to the second stage, it will have a greater temperature drop. Correspondingly, a larger loss of 20% was arbitrarily assumed to integrate the shield with the first stage.

The shield mass used is based on a vapor-cooled shield design. Shield valving and controls were not considered.

Mixer Heat Assumption

A mixer, which is integrated into the tank to de-stratify the propellant and force convective heat transfer across the heat exchanger (as shown in figure 1), is also represented in the analysis and is an upgrade from reference 1. Heat inputs from de-stratification mixers for existing flight and ground designs and tests were investigated. Analysis for the COLD-SAT⁶ flight experiment, and the analysis for our Protoflight ZBO Development Test Article test show that much less jet momentum (and, correspondingly, mixer power) is needed for flight applications. Analyses published by Poth and Van Hook⁷ supports this conclusion. They showed that jet momentum for low Bond numbers, which occur in low gravity environments, is a function of jet inertial surface tension forces. For ground tests with the comparatively much higher acceleration force of gravity, large Bond numbers ($N_{Bo} > 10$) occur. In this case, jet momentum is a function of jet inertia forces and body forces caused by gravity.

Applying that analysis to 2.2 meter diameter tanks (additional assumptions include 97% full tank with 0.18 m jet nozzle height), the jet momentum for LO₂ ground applications is 64 times that for flight, and for LH₂ propellants it is 42 times greater. Therefore, the mixer heat added to the tank for flight applications is assumed to be 1/64th (for O₂) and 1/42nd (for H₂) that of our ZBO ground demonstration, which was found to be 16% of the total heat added to the tank. Correspondingly, the submerged mixer heat added for this analysis is assumed to be 0.25% (O₂, CH₄, and Xe) and 0.38% (for H₂) of the heat entering the tank.

Heat Rejection Assumption

The mixer heat (which is almost insignificant) is added to the environmental heat entering the tank and must be removed by the cryocooler and ultimately rejected by its radiator. The lower the rejection temperature is, the higher the Carnot efficiency of the system. The radiator design, cryocooler input power, environmental temperature, vehicle orientation, and the propellant tank heat load directly affect this temperature.

For the Protoflight ZBO Development Test Article, an ANSYS thermal model found the heat rejection temperature to be 50K above the environmental temperature for the radiator design used. Flight radiator designs will be more efficient and, according to the cryocooler manufacturer,⁸ this design temperature could be improved for flight to roughly 30K, which was used in this analysis.

MLI Assumption

Another variation from reference 1 is that the number of MLI layers used was eliminated as a variable. This was done to present the results more simply; also, by using a spreadsheet analysis it was possible to narrow in on the appropriate number of layers for each propellant studied. This was found by adding up the predicted passive and ZBO thermal storage mass, that is, the tank, insulation, propellant, and boil-off mass for the passive case and the tank, insulation, propellant, solar array, and radiator mass for the ZBO case for a given number of MLI layers, then vary the quantity of layers and narrow in on the lowest mass results at the point where the passive and ZBO masses were equal. This was done for the average tank diameter used for each propellant. For the LH2 case, the layers were divided up such that 2/3rds (or 30 layers) covered the vapor-cooled shield attached to the 1st stage and the rest blanketed the propellant tank. This proportion was chosen because the MLI layer 2/3rds the way through the thickness is estimated to be close to the temperature of the shield. These results are shown in table 2.

Propellant	MLI Layers Used
LH ₂	45
LO ₂	30
LCH ₄	30
LXe	15

Table 2. The initialization of the number of MLI layers that result in the lowest thermal storage mass for a given propellant.

Passive Analysis Algorithm

The reference 1 algorithm used for tank mass and volume growth estimating was also rewritten, to eliminate a program bug that made it difficult to run.

This algorithm determines the necessary tank growth to accommodate boil-off. This solution was iterative, that is, as the tank grew to accommodate boil-off tank volume and surface area increased, causing the boil-off to increase a little more. A small portion (1/100th) of the volume for that boil-off was added to the tank volume and iterated upon as long as it still increased. When it stopped increasing, the tank was at the appropriate size to accommodate boil-off and the iteration stopped.

Variables

The most significant variable in the study was tank diameter (note that all tanks are assumed spherical). The diameters used have been typical propellant tank sizes used in HEDS analysis and in various transportation studies. They are shown in table 3.

Tank Diameters Considered, meters			
LO ₂	LCH ₄	LXe	LH ₂
1.2	1.2	1.2	1.2
2.2	2.2	2.2	2.2
3.3	3.3		3.3
4.4	4.4		4.4
			5.5

Table 3. The tank diameters considered in the trade space, shown for each propellant. Larger tank sizes for higher density fluids were not considered.

Another variable was the power and heat rejection system mass. It is possible and likely for some missions that this mass would be coupled with other much larger vehicle power and heat rejection requirements, thus, results are shown with and without it.

The last variable discussed is tank growth, necessary to accommodate boil-off. For passive solutions, larger tanks mean more tank and insulation mass. This effect is shown in bar graph form. A literature search found no previous analysis that included this very significant mass.

Summary of Assumptions

Because of the many parameters used and the significant changes from reference 1, table 4 is included to summarize the analysis approach.

Parameter	Assumed Value	Basis	Variation from Ref. 1
Tank Mass per Surface Area	5.4 kg/m ² for H ₂ , O ₂ , CH ₄ , 20 kg/m ² for Xe	Analysis by MSFC mission analyst. Reflects a 25% mass reduction in present tank designs.	Xe not previously analyzed. Its high tank density was assumed because of Xe's high density.
Insulation Mass per Surface Area	0.02 kg/m ² /layer	Based on actual design for flight at MSFC ⁹	Includes mass for purge bag for LH2 and LO2
Tank Ullage	3%	Prevent tank rupture	None
Tank Residual	2%	Inaccessible propellant	None
Fluid Properties		Sat. liquid at 0.2 MPa	None
Environmental LEO Temperature	243K	Avg. temp. of Earth and Sun oriented orbits. From radiation analysis of a representative vehicle.	250K
Margin	5%	Cryocooler sized to remove 5% more heat than enters tank.	0%
Heat Rejection Temperature	273K	See text.	250K
Insulation Heating Rate	Lockheed Equation (include equation) times 1.8	1.8 is a compensating factor, which correlates with reference 3 testing results.	Thicker MLI blankets not considered
Penetration Heating	$\dot{Q} = 1.28 \times 10^{-4} (f/35)^2 (T/250)^{2.3}$ m for O ₂ , CH ₄ , and Xe tanks, $\dot{Q} = 2.70 \times 10^{-4} (f/35)^2 (T/250)^{1.6}$ m for H ₂ tanks f = frequency T = heat rejection temp.	S glass epoxy struts ¹⁰	None
Mixer Heat	0.25% of tank heating for LO ₂ , LCH ₄ , LXe; 0.38% for LH ₂	See text	Not included
Integration Loss	12% or 20%	See text	Not included
Cryocooler controller	1.4 times cryocooler mass	Existing flight controllers	Not included

Table 4. A summary of assumptions used in analysis.

Results

All results shown use the thermal storage mass, which is defined as follows:

Passive: Tank, insulation, propellant, boil-off, and tank/insulation growth.

ZBO: Tank, insulation, propellant, cryocooler, solar array, radiator.

The first graph (figure 3) includes passive and ZBO thermal storage mass predictions for oxygen as a function of storage duration, or the days in LEO with cryogens, regardless of the number of engine burns.

That graph is repeated twice more, for methane (fig. 4) and hydrogen (fig. 5). From those graphs and additional runs with xenon, the equal mass lines were constructed and are shown (fig. 6). These are the storage duration's where the passive and ZBO masses are equal; durations longer than these are predicted to reduce mass for ZBO; durations shorter would benefit if passive storage was used.

The bar graph in figure 7 shows the effect if power systems were available to power the cryocooler. Eliminating that mass from the trade reduces the

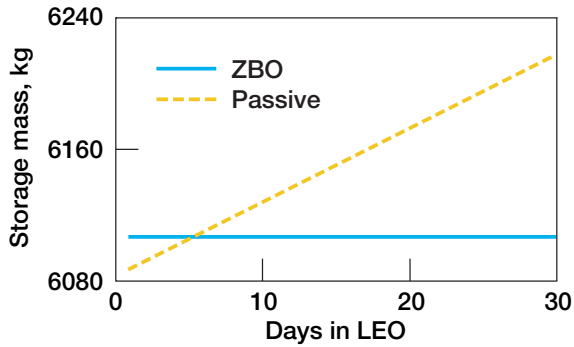


Figure 3.—Passive and ZBO cryogenic thermal storage mass versus duration for LO₂ storage in 2.2-m-diam tank.

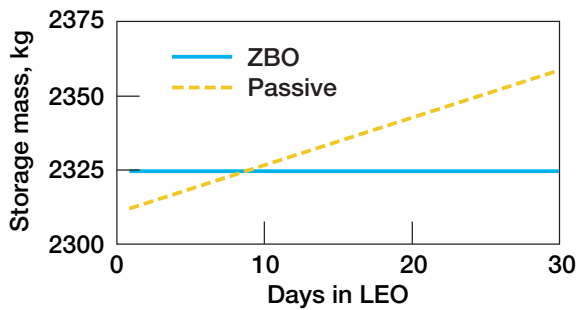


Figure 4.—Passive and ZBO cryogenic thermal storage mass versus duration for LCH₄ storage in 2.2-m-diam tank.

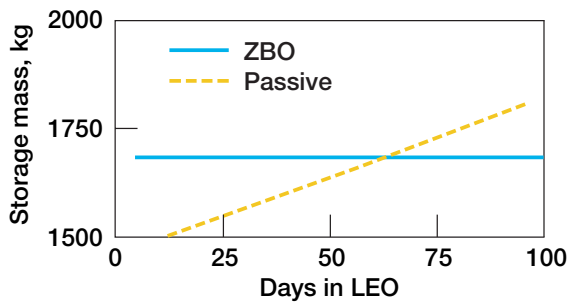


Figure 5.—Passive and ZBO cryogenic thermal storage mass versus duration for LH₂ storage in 3.3-m-diam tank.

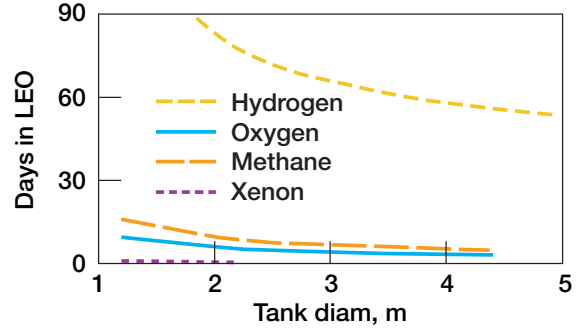


Figure 6.—Graphical composite that shows duration at which ZBO and passive storage mass is equal for a given tank size. Durations longer than these are predicted to save mass if ZBO is incorporated.

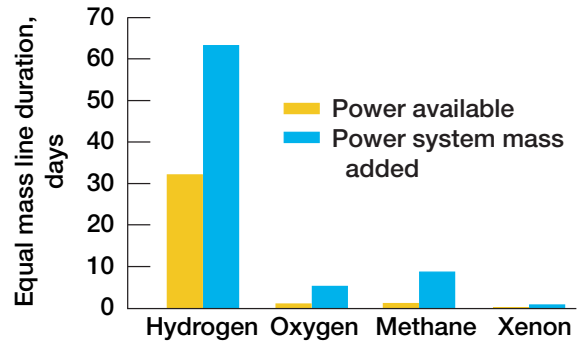


Figure 7.—Equal mass variation if power system is available and mass not included. If so, ZBO applicable for much shorter durations.

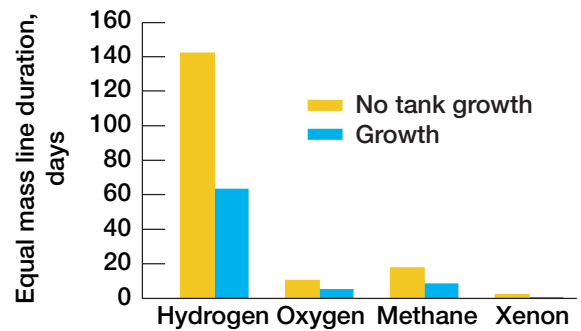


Figure 8.—Equal mass variation if tank growth to accommodate boil-off is not considered. If not, passive thermal control mistakenly appears to reduce mass to much longer storage duration than it should.

equal mass line's days in LEO substantially. Next, figure 8 shows the effect if tank growth was not considered. If not, then ZBO would not nearly be so beneficial.

Discussion

The results are surprising. The durations in LEO where ZBO starts to reduce mass are surprisingly low, which could lead to more applications for cryogenic propellants.

The first chart developed, figure 3, is for 2.2m diameter LO₂ tanks. This shows that ZBO storage durations as low as 5 days in LEO save mass when compared to the traditional passive storage approach. The results for methane storage (figure 4) are a little different in that more days are required before ZBO storage reduces mass, 8.5 days, compared to the 5 days for oxygen storage. At first glance, this is not obvious as methane's boiling point is higher than oxygen's, reducing its cooling requirements. However, boil-off mass is also dependent on the inverse of the heat of vaporization; methane's is 2.4 times that of oxygen.

Hydrogen storage takes quite a bit more days in LEO before ZBO is beneficial and also presents a challenge to cryocooler technology and the integration of two-stage cryocoolers. Still, if missions require storage times in excess of 64 days in LEO, ZBO is predicted to save mass (see figure 5).

Liquid xenon storage begins to save mass almost immediately over gaseous xenon storage. Even so, the relatively high density of xenon gas and low quantities needed for electric propulsion complicate the storage design decision.

Figure 6 compiles the results of all propellants considered and shows the effect of size--the larger the tank, the fewer days in LEO when ZBO has reduced mass. While that is the prediction, beware that this analysis uses floating point cryocooler designs and fewer large cryocoolers exist.

One cryocooler issue that could improve the ZBO results is its design. Existing flight cryocooler designs (one of which was incorporated in this analysis) include a small coldhead that cools a plate that mounts to an instrument. As shown herein, the temperature difference between coldhead and the bulk liquid is substantial, causing larger cryocoolers to be used. A design made specifically for cooling-fluid in a propellant tank could reduce this integration

loss. It could involve submersion of the cold portion of the working fluid tube directly into the propellant, eliminating the coldhead and associated loss. Another variation could be the use of the propellant itself as the cryocooler working fluid. Such designs were not considered here but were explored in reference 11.

Summary

NASA is investigating an array of exploration missions and propulsion technologies for our future. Many of those concepts include cryogenic propellants, possibly involving long storage durations. This analysis addresses the storage duration effect on cryogenic thermal storage system performance, with the purpose of possibly minimizing the storage issue. One method worthy of consideration is zero boil-off storage, which has become more interesting because of the tremendous advances in cryocooler technology. This was applied to oxygen, methane, hydrogen, and xenon propellants in tank sizes of 1.2, 2.2, 3.3, 4.4, and 5.5m in diameter. This technology provides mass savings over traditional, passive- only cryogenic storage when mission durations are as short as one week in LEO for oxygen, two weeks for methane, and roughly 2 months for LH2. Cryogenic xenon saves mass over passive storage almost immediately.

References

1. P. Kittel, D. Plachta, "Propellant Preservation for Mars Missions," Advances in Cryogenic Engineering, Vol. 45, presented at the Cryogenic Engineering Conference, Montreal, Canada, July 12-16, 1999.
2. P. Kittel, L. Salerno, D. Plachta, "Cryocoolers for Human and Robotic Missions to Mars," Cryocoolers 10, presented at the 10th International Cryocooler Conference, Monterey, California, May, 1998.
3. T.R.Strobridge, "Cryogenic Refrigeration—An Updated Survey," NBS Tech Note 655 (1974).
4. D.S. Glaister, M. Donabedian, D.G.T. Curran, and T. Davis, "An Overview of the Performance and Maturity of Long Life Cryocoolers for Space Applications," The Aerospace Corp, El Segundo, Report No. TOR-98(1057)-3 (1998).
5. E. Tward, T. Nast, W. Swift, S. Castles, and T. Davis, private communications.
6. E. Kramer, "Cryogenic On-Orbit Liquid Depot-Storage, Acquisition, and Transfer (COLD-SAT) Experiment Conceptual Design and Feasibility Study," NASA TP-3523 (1998).

7. L.J. Poth, J.R. Van Hook, "Control of the Thermodynamic State of Space-Stored Cryogens by Jet Mixing," *J. Spacecraft*, Vol. 9, No.5, May, 1972.
8. C.K. Chan, TRW, private communications.
9. L.J. Hastings, J.J. Martin, "Large-Scale Liquid Hydrogen Testing of a Variable Density Multi-layer Insulation with a Foam Substrate," NASA/TM—2001-211089, June 2001.
10. R.T. Parmley, W.C. Henninger, S.A. Katz, and I. Spradley, "Test and Evaluate Passive Orbital Disconnect Struts," NASA CR-177368 (1985).
11. P.Kittel, "Propellant Preservation Using Re-liquefiers, *Cryogenics* 41 (2001) 841.

REPORT DOCUMENTATION PAGEForm Approved
OMB No. 0704-0188

Public reporting burden for this collection of information is estimated to average 1 hour per response, including the time for reviewing instructions, searching existing data sources, gathering and maintaining the data needed, and completing and reviewing the collection of information. Send comments regarding this burden estimate or any other aspect of this collection of information, including suggestions for reducing this burden, to Washington Headquarters Services, Directorate for Information Operations and Reports, 1215 Jefferson Davis Highway, Suite 1204, Arlington, VA 22202-4302, and to the Office of Management and Budget, Paperwork Reduction Project (0704-0188), Washington, DC 20503.

1. AGENCY USE ONLY (Leave blank)		2. REPORT DATE June 2003	3. REPORT TYPE AND DATES COVERED Technical Memorandum	
4. TITLE AND SUBTITLE An Updated Zero Boil-Off Cryogenic Propellant Storage Analysis Applied to Upper Stages or Depots in an LEO Environment			5. FUNDING NUMBERS WU-706-87-13-00	
6. AUTHOR(S) David Plachta and Peter Kittel				
7. PERFORMING ORGANIZATION NAME(S) AND ADDRESS(ES) National Aeronautics and Space Administration John H. Glenn Research Center at Lewis Field Cleveland, Ohio 44135-3191			8. PERFORMING ORGANIZATION REPORT NUMBER E-13421	
9. SPONSORING/MONITORING AGENCY NAME(S) AND ADDRESS(ES) National Aeronautics and Space Administration Washington, DC 20546-0001			10. SPONSORING/MONITORING AGENCY REPORT NUMBER NASA TM-2003-211691 AIAA-2002-3589	
11. SUPPLEMENTARY NOTES Prepared for the 38th Joint Propulsion Conference and Exhibit cosponsored by AIAA, ASME, SAE, and ASEE, Indianapolis, Indiana, July 7-10, 2002. David Plachta, NASA Glenn Research Center, and Peter Kittel, NASA Ames Research Center, Moffett Field, California 94035-1000. Responsible person, David Plachta, organization code 5870, 216-977-7126.				
12a. DISTRIBUTION/AVAILABILITY STATEMENT Unclassified - Unlimited Subject Categories: 16, 20 and 28 Available electronically at http://gltrs.grc.nasa.gov This publication is available from the NASA Center for AeroSpace Information, 301-621-0390.			12b. DISTRIBUTION CODE	
13. ABSTRACT (Maximum 200 words) Previous efforts have shown the analytical benefits of zero boil-off (ZBO) cryogenic propellant storage in launch vehicle upper stages of Mars transfer vehicles for conceptual Mars Missions. However, recent NASA mission investigations have looked at a different and broad array of missions, including a variety of orbit transfer vehicle (OTV) propulsion concepts, some requiring cryogenic storage. For many of the missions, this vehicle will remain for long periods (greater than one week) in low earth orbit (LEO), a relatively warm thermal environment. Under this environment, and with an array of tank sizes and propellants, the performance of a ZBO cryogenic storage system is predicted and compared with a traditional, passive-only storage concept. The results show mass savings over traditional, passive-only cryogenic storage when mission durations are less than one week in LEO for oxygen, two weeks for methane, and roughly 2 months for LH ₂ . Cryogenic xenon saves mass over passive storage almost immediately.				
14. SUBJECT TERMS Cryogenics; Cryocoolers; Thermosyphons; Zero boil-off; Low-earth orbit; Orbit transfer vehicles; Propellant depots; Long-term propellant storage			15. NUMBER OF PAGES 14	
			16. PRICE CODE	
17. SECURITY CLASSIFICATION OF REPORT Unclassified	18. SECURITY CLASSIFICATION OF THIS PAGE Unclassified	19. SECURITY CLASSIFICATION OF ABSTRACT Unclassified	20. LIMITATION OF ABSTRACT	



Spray Bar Zero-Gravity Vent System for On-Orbit Liquid Hydrogen Storage

*L.J. Hastings
Alpha Technology, Inc., Huntsville, Alabama*

*R.H. Flachbart, J.J. Martin, A. Hedayat, and M. Fazah
Marshall Space Flight Center, Marshall Space Flight Center, Alabama*

*T. Lak and H. Nguyen
The Boeing Company, Huntington Beach, California*

*J.W. Bailey
Sverdrup Technology, Inc., Huntsville, Alabama*

The NASA STI Program Office...in Profile

Since its founding, NASA has been dedicated to the advancement of aeronautics and space science. The NASA Scientific and Technical Information (STI) Program Office plays a key part in helping NASA maintain this important role.

The NASA STI Program Office is operated by Langley Research Center, the lead center for NASA's scientific and technical information. The NASA STI Program Office provides access to the NASA STI Database, the largest collection of aeronautical and space science STI in the world. The Program Office is also NASA's institutional mechanism for disseminating the results of its research and development activities. These results are published by NASA in the NASA STI Report Series, which includes the following report types:

- **TECHNICAL PUBLICATION.** Reports of completed research or a major significant phase of research that present the results of NASA programs and include extensive data or theoretical analysis. Includes compilations of significant scientific and technical data and information deemed to be of continuing reference value. NASA's counterpart of peer-reviewed formal professional papers but has less stringent limitations on manuscript length and extent of graphic presentations.
- **TECHNICAL MEMORANDUM.** Scientific and technical findings that are preliminary or of specialized interest, e.g., quick release reports, working papers, and bibliographies that contain minimal annotation. Does not contain extensive analysis.
- **CONTRACTOR REPORT.** Scientific and technical findings by NASA-sponsored contractors and grantees.

- **CONFERENCE PUBLICATION.** Collected papers from scientific and technical conferences, symposia, seminars, or other meetings sponsored or cosponsored by NASA.
- **SPECIAL PUBLICATION.** Scientific, technical, or historical information from NASA programs, projects, and mission, often concerned with subjects having substantial public interest.
- **TECHNICAL TRANSLATION.** English-language translations of foreign scientific and technical material pertinent to NASA's mission.

Specialized services that complement the STI Program Office's diverse offerings include creating custom thesauri, building customized databases, organizing and publishing research results...even providing videos.

For more information about the NASA STI Program Office, see the following:

- Access the NASA STI Program Home Page at <http://www.sti.nasa.gov>
- E-mail your question via the Internet to help@sti.nasa.gov
- Fax your question to the NASA Access Help Desk at (301) 621-0134
- Telephone the NASA Access Help Desk at (301) 621-0390
- Write to:
NASA Access Help Desk
NASA Center for AeroSpace Information
7121 Standard Drive
Hanover, MD 21076-1320



Spray Bar Zero-Gravity Vent System for On-Orbit Liquid Hydrogen Storage

L.J. Hastings
Alpha Technology, Inc., Huntsville, Alabama

R.H. Flachbart, J.J. Martin, A. Hedayat, and M. Fazah
Marshall Space Flight Center, Marshall Space Flight Center, Alabama

T. Lak and H. Nguyen
The Boeing Company, Huntington Beach, California

J.W. Bailey
Sverdrup Technology, Inc., Huntsville, Alabama

National Aeronautics and
Space Administration

Marshall Space Flight Center • MSFC, Alabama 35812

TRADEMARKS

Trade names and trademarks are used in this report for identification only. This usage does not constitute an official endorsement, either expressed or implied, by the National Aeronautics and Space Administration.

Available from:

NASA Center for AeroSpace Information
7121 Standard Drive
Hanover, MD 21076-1320
(301) 621-0390

National Technical Information Service
5285 Port Royal Road
Springfield, VA 22161
(703) 487-4650

TABLE OF CONTENTS

1. INTRODUCTION	1
1.1 Background	1
1.2 Requirements	2
1.3 Thermodynamic Vent System Spray Bar Concept	2
1.4 Objectives	3
2. TEST ARTICLE ELEMENTS	4
2.1 Multipurpose Hydrogen Test Bed Tank	4
2.2 Environmental Shroud	5
2.3 Cryogenic Insulation Subsystem	6
2.4 Multipurpose Hydrogen Test Bed Instrumentation	6
3. SPRAY BAR THERMODYNAMIC VENT SYSTEM DESIGN DEFINITION	8
3.1 Heat Exchanger	8
3.2 Operating Pressures	11
3.3 Spray Bar Orifice Sizing	14
3.4 Control Logic	15
4. THERMODYNAMIC VENT SYSTEM DESIGN AND HARDWARE SELECTION	17
4.1 Recirculation Pump	17
4.2 Joule-Thompson Vent Valve	17
4.3 Spray Bar Heat Exchanger Assembly	19
4.4 Recirculation and Vent System Assembly	20
4.5 Thermodynamic Vent System Instrumentation	22
4.6 Component Box Assembly	23
4.7 Support Ring Assembly	23
5. SUBSYSTEM AND COMPONENT TESTING	24
5.1 Liquid Hydrogen Spray Injection	24
5.2 Recirculation Pump	26
5.3 Other Component and Subsystem Testing	27

TABLE OF CONTENTS (Continued)

6. SPRAY BAR THERMODYNAMIC VENT SYSTEM PERFORMANCE ANALYTICAL MODEL	31
6.1 Heat Exchanger	31
6.2 Spray Manifold and Injection Tube	35
6.3 Recirculation Pump	41
6.4 Tank Thermodynamics	43
7. TEST FACILITY AND PROCEDURES	58
7.1 Facility Description	58
7.2 Test Procedures	61
8. TEST RESULTS	65
8.1 Tank Heat Leak Data Reduction	65
8.2 Tank Heat Leak	66
8.3 Thermodynamic Vent System Performance	66
8.4 Test Facility and Hardware Performance	74
9. THERMODYNAMIC VENT SYSTEM ANALYTICAL MODEL CORRELATIONS	75
9.1 Series 1, Low Heat Leak Tests	75
9.2 Series 2, High Heat Leak Tests	86
10. SUMMARY AND RECOMMENDATIONS	95
APPENDIX A—MULTIPURPOSE HYDROGEN TEST BED TANKING TABLE	98
APPENDIX B—MULTIPURPOSE HYDROGEN TEST BED TEST ARTICLE INSTRUMENTATION	106
APPENDIX C—ANALYTICAL CORRELATIONS WITH TEST SEGMENT P263981E	131
REFERENCES	135

LIST OF FIGURES

1.	Spray bar TVS schematic	2
2.	MHTB test tank and supporting hardware schematic	4
3.	Manhole cover sealing arrangement	5
4.	Environmental shroud assembly	5
5.	MHTB internal instrumentation rakes	7
6.	TVS coil heat exchanger—option (1)	9
7.	TVS single-tube heat exchanger—option (2)	10
8.	TVS multitube heat exchanger configuration—option (3)	11
9.	Effects of liquid vapor pressure and vent back pressure on heat absorption	12
10.	Sensible heat absorption by vent flow versus liquid vapor pressure and vent back pressure	13
11.	Total heat absorbed by vent flow versus liquid vapor pressure and back pressure	13
12.	Effects of liquid droplet diameter on ullage pressure decay rate	14
13.	Injection velocity versus distance from spray bar top at 0.136 kg/s flow rate	15
14.	TVS baseline pressure control concept	16
15.	Two-phase flow rate versus J-T vent orifice diameter	18
16.	Vent flow rate versus liquid subcooling at 137.8 kPa/m ² vapor pressure	18
17.	TVS heat exchanger and spray injection assembly	19
18.	TVS spray bar assembly MHTB installation—top	19
19.	TVS spray bar assembly MHTB installation—bottom	20

LIST OF FIGURES (Continued)

20.	Recirculation pump and vent assembly	21
21.	Recirculation pump and vent assembly—MHTB installation	21
22.	TVS instrumentation schematic	22
23.	GRC ullage pressure collapse test setup	24
24.	GRC test data for ullage temperature	25
25.	GRC test data for tank wall temperature	25
26.	Comparison of predicted ullage pressure and GRC test results	26
27.	LH ₂ recirculation pump predicted and measured performance	26
28.	Spray injection tube water flow pressure drop test results	27
29.	Spray injection tube measured water flow loss coefficients	27
30.	Water flow pressure drop in spray tubes and heat exchanger assembly	28
31.	Predicted and measured LH ₂ spray injection system pressure loss based on water flow test results	29
32.	Spray bar LN ₂ test	29
33.	Vent tube loss coefficient prediction and test comparison	30
34.	Spray manifold analytical model	36
35.	Spray injection tube analytical model	38
36.	LH ₂ recirculation pump head-flow curve	42
37.	Tank thermal analytical model	43
38.	Ullage thermal analytical model	44
39.	Tank wall thermal analytical model	46
40.	Tank wall liquid thermal analytical model	47

LIST OF FIGURES (Continued)

41.	Bulk liquid thermal analytical model	49
42.	Droplet evaporation analytical model	56
43.	Ullage condensation analytical model	57
44.	MSFC east test area thermal vacuum facility, test stand 300	58
45.	MHTB and test stand 300 simplified flow schematic	59
46.	MHTB installation in test stand 300 vacuum chamber	59
47.	Spray bar TVS instrumentation schematic	61
48.	Tank stratification/destratification, 50-percent fill level during series 1	68
49.	Spray bar performance at 90-percent fill level during series 1	69
50.	Spray bar performance at 50-percent fill level during series 1	69
51.	Spray bar performance at 25-percent fill level during series 1	70
52.	Bulk liquid saturation pressure reduction at 25-percent fill level	72
53.	TVS operation cycles with GHe in ullage, 50-percent fill level during series 2	73
54.	Ullage pressure modeling comparison with 1996 tests P263968E and P263968F— self-pressurization and mixing with 90-percent fill	76
55.	Ullage temperature modeling comparison with 1996 tests P263968E and P263968F—self-pressurization and mixing with 90-percent fill	77
56.	Bulk liquid saturation pressure modeling comparison with 1996 tests P263968E and P263968F—self-pressurization and mixing with 90-percent fill	77
57.	Bulk liquid saturation temperature modeling comparison with 1996 tests P263968E and P263968F—self-pressurization and mixing with 90-percent fill	78
58.	Ullage pressure modeling comparison with 1996 test P263968G—mixing and venting with 90-percent fill	79
59.	Ullage temperature modeling comparison with 1996 test P263968G—mixing and venting with 90-percent fill	79

LIST OF FIGURES (Continued)

60.	Bulk liquid saturation pressure modeling comparison with 1996 test P263968G— mixing and venting with 90-percent fill	80
61.	Bulk liquid saturation temperature modeling comparison with 1996 test P263968G— mixing and venting with 90-percent fill	80
62.	Ullage pressure modeling comparison with 1996 test P263968K—mixing and venting with 50-percent fill	81
63.	Ullage temperature modeling comparison with 1996 test P263968K—mixing and venting with 50-percent fill	82
64.	Bulk liquid saturation pressure modeling comparison with 1996 test P263968K— mixing and venting with 50-percent fill	82
65.	Bulk liquid saturation temperature modeling comparison with 1996 test P263968K— mixing and venting with 50-percent fill	83
66.	Ullage pressure modeling comparison with 1996 tests P263968K and P263968L— mixing and venting with 25-percent fill	84
67.	Ullage pressure modeling comparison with 1996 test P263968L—mixing and venting with 25-percent fill	84
68.	Ullage temperature modeling comparison with 1996 test P263968L—mixing and venting with 25-percent fill	85
69.	Bulk liquid saturation pressure modeling comparison with 1996 test P263968L —mixing and venting with 25-percent fill	85
70.	Bulk liquid saturation temperature modeling comparison with 1996 test P263968L —mixing and venting with 25-percent fill	86
71.	Ullage pressure modeling comparison with 1998 test P263981D— self-pressurization and mixing with 90-percent fill	87
72.	Ullage temperature modeling comparison with 1998 test P263981D— self-pressurization and mixing with 90-percent fill	87
73.	Bulk liquid saturation pressure modeling comparison with 1998 test P263981D— self-pressurization and mixing with 90-percent fill	88

LIST OF FIGURES (Continued)

74.	Bulk liquid saturation temperature modeling comparison with 1998 test P263981D—self-pressurization and mixing with 90-percent fill	88
75.	Unshifted ullage pressure modeling comparison with 1998 test P263981T—self-pressurization, mixing, and venting with 50-percent fill	89
76.	Shifted ullage pressure modeling comparison with 1998 test P263981T—self-pressurization, mixing, and venting with 50-percent fill	90
77.	Shifted ullage temperature modeling comparison with 1998 test P263981T—self-pressurization, mixing, and venting with 50-percent fill	90
78.	Shifted bulk liquid saturation pressure modeling comparison with 1998 test P263981T—self-pressurization, mixing, and venting with 50-percent fill	91
79.	Shifted bulk liquid saturation temperature modeling comparison with 1998 test P263981T—self-pressurization, mixing, and venting with 50-percent fill	91
80.	Shifted ullage pressure modeling comparison with 1998 test P263981X—tank pressurization, mixing, and venting with 50-percent fill, GHe and GH ₂ ullage	92
81.	Shifted ullage temperature modeling comparison with 1998 test P263981X—tank pressurization, mixing, and venting with 50-percent fill, GHe and GH ₂ ullage	93
82.	Shifted bulk liquid saturation pressure modeling comparison with 1998 test P263981X—tank pressurization, mixing, and venting with 50-percent fill, GHe and GH ₂ ullage	94
83.	Shifted bulk liquid saturation temperature modeling comparison with 1998 test P263981X—tank pressurization, mixing, and venting with 50-percent fill, GHe and GH ₂ ullage	94
84.	General MHTB tank schematic	109
85.	MHTB tank instrumentation top view	111
86.	MHTB tank instrumentation side view	112
87.	MHTB tank instrumentation bottom view	113
88.	Typical insulation instrumentation profile	115

LIST OF FIGURES (Continued)

89.	Leg No. 1 instrumentation locations	117
90.	MHTB tank vent penetration instrumentation	118
91.	MHTB tank fill/drain penetration instrumentation	119
92.	MHTB tank pressurization penetration instrumentation	120
93.	MHTB MLI probe instrumentation	121
94.	MHTB manhole cover and pump-out port instrumentation	122
95.	MHTB instrumentation rake silicon diode attachment	123
96.	MHTB tank rake instrumentation layout	124
97.	MHTB typical top environmental shroud panels	126
98.	MHTB typical side wall environmental shroud panels	127
99.	MHTB typical lower environmental shroud panels	128
100.	MHTB TVS instrumentation layout	130
101.	Ullage pressure modeling comparison with 1998 test P263981E— self-pressurization and mixing with 90-percent fill	132
102.	Ullage temperature modeling comparison with 1998 test P263981E— self-pressurization, mixing, and venting with 90-percent fill	132
103.	Bulk liquid saturation pressure modeling comparison with 1998 test P263981E— self-pressurization, mixing, and venting with 90-percent fill	133
104.	Bulk liquid saturation temperature modeling comparison with 1998 test P263981E—self-pressurization, mixing, and venting with 90-percent fill	133

LIST OF TABLES

1.	Barber-Nichols pump (BNHP-08) operating characteristics	17
2.	Measured MHTB tank heat leak	66
3.	Representative mixing cycle durations	67
4.	Representative times between mixing cycles	67
5.	Liquid saturation pressure rise rates after tank lockup	69
6.	Derived TVS heat extraction data	71
7.	TVS test conditions compared with analytical model	75
8.	MHTB tanking table	99

LIST OF ACRONYMS, SYMBOLS, AND ABBREVIATIONS

ASME	American Society of Mechanical Engineers
CFM	cryogenic fluid management
GH ₂	gaseous hydrogen
GHe	gaseous helium
GN ₂	gaseous nitrogen
GRC	Glenn Research Center
HEX	heat exchanger
J-T	Joule-Thompson
LAD	liquid acquisition device
LH ₂	liquid hydrogen
LN ₂	liquid nitrogen
MHTB	multipurpose hydrogen test bed
MLI	multilayer insulation
MSFC	Marshall Space Flight Center
RGA	residual gas analyzer
SOFI	spray-on foam insulation
TVS	thermodynamic vent system
TYP	typical

NOMENCLATURE

A	area
A_S/A_T	ratio of the spray orifice to the tank area
A_{SI}	flow area of an injection tube
A_{SM}	flow area of spray manifold
$(A_S)_n$	spray orifice area at node n
$a = \frac{g}{g_c}$	acceleration ratio; ratio of environmental to Earth's gravitational constant
C	specific heat
C_d	discharge coefficient
CdA	effective orifice flow area
C_L	liquid specific heat
c_p	specific heat at constant pressure
c_{pL}	liquid specific heat at constant pressure
c_{pWL}	wall liquid specific heat at constant pressure
c_{VU}	ullage specific heat at constant volume
D	diameter
D_{CHAR}	a characteristic length determined empirically
D_D	droplet diameter
D_m	impeller diameter
D_{SI}	spray injection tube inside diameter
D_{SM}	spray manifold inside diameter

NOMENCLATURE (Continued)

$ENTH_U$	energy added to ullage
F	Reynolds number factor
f_{SM}	friction coefficient in the spray manifold
G	mass flow rate per unit area
g	acceleration
g_c	Earth's gravitational constant
H	pump head
HP_I	input power to the pump
HP_O	fluid horsepower
h	convection heat transfer coefficient; latent heat of vaporization
h_{FC}	forced convection heat transfer coefficient
h_{NB}	nucleate boiling heat transfer coefficient
h_{fg}	heat of vaporization or condensation
$(h_{fg})_L$	heat of vaporization in liquid
$(h_{fg})_U$	heat of condensation in ullage
h_{gsat}	saturated vapor enthalpy of the ullage
h_I	inlet total enthalpy
h_{in}	TVS inlet enthalpy
$(h_L)_o$	outlet liquid enthalpy
h_{LS}	heat transfer coefficient between bulk liquid and (submerged) spray bar

NOMENCLATURE (Continued)

$(h_L)_{SM}$	head loss in spray manifold
h_o	outlet total enthalpy
h_{out}	TVS outlet enthalpy
h_{satvap}	saturated vapor enthalpy
h_{UD}	forced convection heat-transfer coefficient between ullage and liquid droplets
h_{UL}	heat transfer coefficient between ullage and bulk liquid
h_{US}	heat transfer coefficient between ullage and (unsubmerged) spray bars
h_{UW}	heat transfer coefficient between ullage and wall
h_{UWL}	heat transfer coefficient between ullage and wall liquid
$(h_V)_O$	outlet vapor enthalpy
h_{vent}	vent gas enthalpy
h_{WL}	heat transfer coefficient between wall and liquid
IC	initial condition
I_p	polar moment of inertia of the pump
i	inlet
J	unit conversion constant
$(K_b)_{SI}$	90° bend resistance
$(K_b)_{SM}$	spray manifold frictional loss coefficient
$(K_c)_{SM}$	spray manifold 90° bend loss coefficient
$(K_f)_{SM}$	spray manifold sudden contraction loss coefficient
K_f	frictional loss coefficient

NOMENCLATURE (Continued)

K_S	loss coefficient of an orifice in duct
K_{SM}	total loss coefficient of an orifice in spray manifold
k	thermal conductivity
k_F	fluid thermal conductivity
k_L	liquid thermal conductivity
L	liquid; length
L_c	characteristic length
L_e	equivalent length of bend
L_{SM}	spray manifold length
M_U	ullage mass
$(M_U)_{IC}$	ullage mass with initial conditions
M_L	liquid mass
$(M_L)_{IC}$	initial liquid mass
M_{WL}	wall liquid mass
$(M_{WL})_{IC}$	initial wall liquid mass
m	mass
\dot{m}	mass flow rate
\dot{m}_{bW}	mass boiling rate of liquid on tank wall
\dot{m}_{COND}	liquid surface condensation mass flow rate
\dot{m}_{DU}	liquid droplet evaporation rate in ullage
\dot{m}_i	mass flow rate at inlet

NOMENCLATURE (Continued)

$(\dot{m}_i)_n$	mass flow rate at node n
\dot{m}_{LU}	liquid boiloff rate
$(\dot{m}_o)_n$	mass flow rate at node center
\dot{m}_S	pump flow rate
\dot{m}_{SL}	liquid spray mass flow rate into bulk liquid
$(\dot{m}_S)_n$	spray mass flow rate at node n
\dot{m}_{SU}	spray flow rate into the ullage
$(\dot{m}_{SU})_i$	spray flow rate into the ullage from orifice i
\dot{m}_{SUL}	liquid spray unevaporated droplet flow rate; liquid spray falling into bulk liquid
\dot{m}_{SW}	spray flow rate reaching tank wall
\dot{m}_{UL}	ullage condensation flow rate
\dot{m}_V	overboard vent flow rate
\dot{m}_{vent}	vent mass flow rate
N	last node; pump rotation speed
N_D	pump design speed
$(N)_{IC}$	initial rotation speed
Nu	Nusselt number
n	node number; node center
n_{drop}	number of droplets

NOMENCLATURE (Continued)

$(n_{\text{drop}})_i$	number of droplets from orifice i
o	outlet
$(p_D)_o$	dynamic pressure, outlet
p_o	outlet pressure
$(p_S)_o$	static pressure at outlet
P_T	tank pressure
p	pressure
p_i	inlet pressure
$(p_i)_n$	inlet pressure at node n
p_L	liquid vapor pressure
p_n	pressure at node n
$(p_o)_n$	outlet pressure at node n
p_{sat}	saturation pressure
$(p_{SM})_i$	spray manifold inlet pressure
$(p_{SM})_o$	spray manifold outlet pressure
$(p_T)_n$	tank pressure at node n
p_U	ullage pressure
p_{WL}	wall liquid vapor pressure
\dot{Q}	total heat-transfer rate
\dot{Q}_{ave}	average value of vent heat extraction
\dot{Q}_{boiloff}	total energy vented as boiloff

NOMENCLATURE (Continued)

$\dot{Q}_{\text{conduction}}$	heat flow through tank support legs, vent assembly, and other fluid lines
Q_D	pump design flow rate
$\dot{Q}_{\text{insulation}}$	heat input through insulation
\dot{Q}_{vent}	energy extraction rate while vent is open
q_{drop}	droplet heat transfer rate
$(q_{\text{drop}})_i$	droplet heat transfer rate from orifice i
q_{EL}	heat added to the liquid by environment
q_{EW}	heat input to the wall from environment
q_i	inlet dynamic pressure
$(q_i)_n$	inlet dynamic pressure at node n
q_L	heat transfer rate to the liquid
q_{LS}	heat transfer rate between liquid and (submerged) spray bars
$(q_o)_n$	outlet dynamic pressure
q_{SM}	dynamic pressure in spray manifold
q_U	heat transfer to ullage
q_{UD}	heat transfer rate between the ullage and liquid droplet
p_n	pressure at node n
$(p_o)_n$	node n outlet pressure
p_{sat}	saturation pressure
q_{UL}	heat transfer rate between ullage and liquid
q_{US}	heat transfer rate between ullage and (unsubmerged) spray bar

NOMENCLATURE (Continued)

q_{UWL}	heat transfer rate between ullage and wall liquid
q_{WL}	heat transfer rate between wall and liquid on the wall
q_{WU}	heat transfer rate between tank wall and ullage
Ra	Rayleigh number
Re	Reynolds number
Re_L	liquid Reynolds number
S	suppression factor
$(S_L)_O$	outlet liquid entropy
$(S)_O$	outlet total entropy
$(S_V)_O$	outlet vapor entropy
T	orifice inlet temperature
T_d	droplet temperature
T_f	film temperature
T_L	liquid temperature
$(T_L)_{IC}$	initial liquid temperature
T_S	spray temperature
T_{sat}	saturation temperature
T_{sw}	sprayed wall liquid temperature
T_U	ullage temperature
$(T_U)_{IC}$	initial ullage temperature
T_{Usat}	ullage saturation temperature

NOMENCLATURE (Continued)

T_W	wall temperature
T_{WL}	wall liquid temperature
$(T_{WL})_{IC}$	initial wall liquid temperature
t_{total}	total time
t_{open}	valve open time
U	ullage; tip velocity
V	volume
$(V_D)_i$	droplet volume from orifice i
Vel_D	droplet velocity in ullage
$(Vel_D)_i$	droplet velocity from orifice i
V_L	liquid volume
V_o	outlet fluid velocity
$(V_L)_{IC}$	initial liquid velocity
V_{SM}	velocity in the spray manifold
V_T	tank volume
V_U	ullage volume
V_{WL}	wall liquid volume
$(V_{WL})_{IC}$	initial wall liquid volume
W	tank wall; watts
WL	wall liquid
w_U	work done on the ullage

NOMENCLATURE (Continued)

X	Martinelli parameter
\bar{Y}	average total liquid quality between the inlet and outlet
Y_o	outlet fluid quality
z_i, z_o	inlet and outlet elevations
z_n	distance from liquid surface to node n
β	thermal expansion coefficient
ΔH	change in height
ΔP	pressure difference
ΔP_f	pressure loss due to frictional forces
ΔP_m	pressure loss due to momentum change
ΔP_p	pump pressure rise
ΔP_T	total pressure loss
ΔT	temperature difference between heat source and sink
$\frac{\Delta U_{\text{system}}}{\Delta t}$	energy flow rate into or out of test tank wall, insulation, and fluid mass
Δz	nodal length
ε	roughness
η_p	pump mechanical efficiency
λ	latent heat of vaporization
μ	viscosity
μ_L	liquid viscosity

NOMENCLATURE (Continued)

$\bar{\mu}_L$	average liquid viscosity between inlet and outlet
$\bar{\mu}_V$	average vapor viscosity between inlet and outlet
ρ	density
ρ_D	droplet density
ρ_L	liquid density
$\bar{\rho}_L$	average liquid density between inlet and outlet
$(\rho_L)_o$	outlet liquid density
ρ_o	outlet total density
ρ_{sat}	density at saturation conditions
ρ_{satliq}	saturated liquid density
ρ_{satvap}	saturated vapor density
$\bar{\rho}_V$	average vapor density between inlet and outlet
$(\rho_V)_o$	outlet vapor density
ρ_{WL}	wall liquid density
σ	surface tension
Φ_L	Lockhart-Martinelli correlation factor
ϕ	flow coefficient
ψ	head coefficient



TECHNICAL MEMORANDUM

SPRAY BAR ZERO-GRAVITY VENT SYSTEM FOR ON-ORBIT LIQUID HYDROGEN STORAGE

1. INTRODUCTION

1.1 Background

The development of high-energy cryogenic upper stages is necessary for delivery of large payloads to various orbital destinations, such as the geosynchronous orbit and Mars missions. Also, many advanced propulsion systems, including solar thermal and nuclear fission, use hydrogen as the propellant. A key technology challenge for all of these applications is cryogenic fluid management (CFM), including the long-term storage of cryogenics in space. In response to this challenge, NASA has initiated an advanced development/technology program to broaden the CFM experience/database. Due to constrained opportunities for orbital experiments, ground testing must be employed to the fullest extent possible. Therefore, a major objective of the NASA technology program has been to perform ground-based advanced development testing on CFM systems for space transportation applications.

A system-level test bed—the multipurpose hydrogen test bed (MHTB)—representative in size and shape of a fully integrated space transportation vehicle liquid hydrogen (LH₂) propellant tank, was established for use at Marshall Space Flight Center (MSFC). The MHTB 18-m³ (639-ft³) hydrogen tank was designed to accommodate various CFM concepts as updated or alternative versions become available. The first technology element evaluated with the MHTB was a cryogenic thermal protection concept for ground-based upper stages¹ and the second element addressed the on-orbit control of tank pressure.

Maintaining propellant tank pressure control while minimizing propellant boiloff loss is a significant challenge associated with the storage of cryogenics in the near zero-gravity environment of space. Traditionally, auxiliary thrusters are used to settle the propellants in order to accomplish tank venting. However, such systems incur weight penalties associated with the propellant and hardware required to perform the settling burns that increase with the number of settling sequences. In addition, tank venting/resettling may become necessary at inopportune times in a mission timeline, thereby increasing mission complexity. The thermodynamic vent system (TVS) concept enables tank pressure control through venting without resettling. A TVS typically includes a Joule-Thompson (J-T) expansion device, a two-phase heat exchanger, and a mixing pump to destratify and extract thermal energy from the tank contents without significant liquid losses. Implementation of TVSs has been delayed by the lack of opportunities for on-orbit experience, primarily due to funding constraints. Analytical modeling of such systems is difficult due to the complex combination of microgravity heat transfer, thermodynamic, and fluid mechanic phenomena involved. Model correlations are further complicated by the lack of on-orbit data. The TVS design requirements, a description of the concept evaluated, and test program objectives and goals are presented in sections 1.2 through 1.4.

1.2 Requirements

The overall TVS requirement was to maintain the MHTB tank ullage pressure within a 6.9-kPa (1-psi) control band for extended periods of time. The TVS was designed to accommodate tank heat leaks up to 55 W, liquid levels of 10 to 95 percent, and to operate without dependence on a capillary liquid acquisition device (LAD). In addition, there were the general requirements of simplicity, low weight, low power, high efficiency, and mission flexibility.

1.3 Thermodynamic Vent System Spray Bar Concept

The spray bar TVS concept, developed by Rockwell Aerospace (now The Boeing Company), was selected for testing in the MHTB because of some unique features relative to concepts previously tested. This concept is described in reference 2 and is illustrated in figure 1. The major advantage of this concept is that the longitudinal spray bar can be used to thermally destratify both liquid and ullage, independent of liquid-vapor positions in zero gravity. Therefore, the spray bar concept is conducive to verification in normal gravity and minimizes dependence on costly orbital experimentation. A second advantage is that active TVS components; i.e., J-T expansion valve, subsystem pump, and isolation valve, are located outside the tank. Such an approach simplifies component installation and enables modification or change-out of TVS components without entering the tank. Also, this configuration can support feedline and engine thermal conditioning during microgravity coast periods.

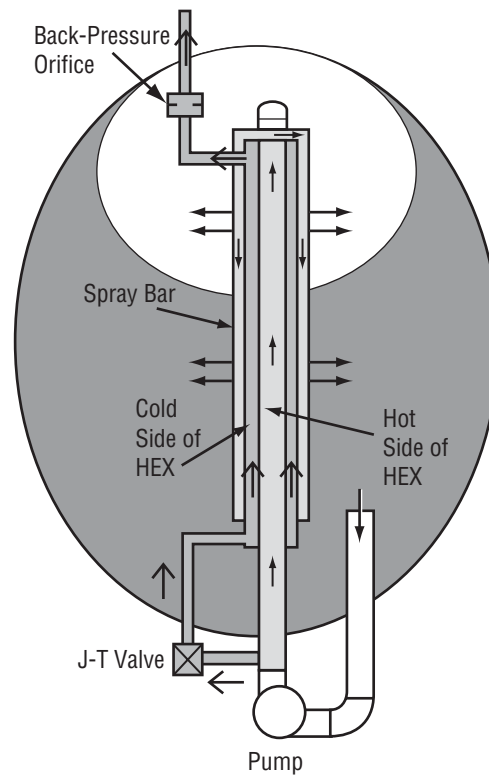


Figure 1. Spray bar TVS schematic.

In the mixing mode, fluid is withdrawn from the tank by the pump and flows back into the tank through the spray bar positioned along or near the tank longitudinal axis. The fluid is expelled radially back into the tank through the spray bar, which forces circulation and mixing of the tank contents regardless of liquid and ullage position, assuring destratification and minimum pressure rise rate. For missions lasting from a few days to weeks, depending on the insulation performance and the degree of bulk liquid subcooling, tank mixing may be sufficient to control the tank pressure with no propellant loss. When pressure control can no longer be achieved with mixing alone (the bulk liquid saturation condition corresponds to the ullage pressure), a portion of the circulated liquid is passed through the J-T valve where it is expanded to a lower temperature and pressure, passed through the heat exchanger element of the spray bar, and finally is vented to space. The vented fluid thereby removes thermal energy from, and thus cools, the bulk fluid circulated through the mixing element of the spray bar. If ullage, instead of liquid, enters the recirculation line in zero gravity, then vapor is vented through the J-T valve and ullage depressurization occurs much as it would in a normal gravity environment.

In an orbital propellant transfer scenario, the spray bar concept can be used to assist tank refill. By filling through the spray bar/heat exchanger, the in-flowing fluid can be cooled and used to mix the tank contents, thus enabling a no-vent fill process with minimal propellant losses. Additionally, if capillary LADs are used for microgravity propellant expulsion, the liquid within the LAD can be conditioned by the spray bar TVS. By withdrawing liquid from the capillary LAD, cooling it through the J-T device, and returning it to the LAD, thermal conditioning of the LAD liquid can be achieved. Thus, the effects of heat entrapment within the LAD can be minimized or perhaps eliminated.

1.4 Objectives

The primary overall objective was to evaluate the effectiveness of a spray bar mixer TVS concept for maintaining ullage pressure control within the MHTB LH₂ tank. Design and test goals included the following:

- Verify that the TVS can maintain the ullage pressure within the 6.9-kPa (1-psi) control band for extended periods of time, independent of fill level.
- Verify that reasonable variations in orbital heat leak can be accommodated with the automated control logic.
- Evaluate the spray bar mixer destratification performance.
- Evaluate the effects of gaseous helium (GHe) pressurant within the ullage.
- Analytically model the spray bar heat exchanger and vent system performance.
- Correlate the measured TVS data with analytical modeling results.

2. TEST ARTICLE ELEMENTS

The major test article elements consist of the test tank with supporting equipment, including an environmental shroud, cryogenic insulation subsystem, and test article instrumentation. Technical descriptions of each of these elements are presented in sections 2.1 through 2.4.

2.1 Multipurpose Hydrogen Test Bed Tank

The MHTB 5083 aluminum tank is cylindrical in shape with a height of 3.05 m (10 ft), a diameter of 3.05 m (10 ft), and 2:1 elliptical domes as shown in figure 2. It has an internal volume of 18.09 m³ (639 ft³) and a surface area of 35.74 m² (379 ft²), with a resultant surface area-to-volume ratio of 1.92 1/m (0.58 1/ft) that is reasonably representative of a full-scale vehicle LH₂ tank. The tank is ASME pressure vessel coded for a maximum operational pressure of 344 kPa (50 psid) and was designed to accommodate various CFM technology and advanced concepts as updated versions become available. Major accommodations include a 60.9-cm- (24-in-) diameter manhole, pressurization and vent ports, fill/drain line through tank top, 15.24- and 7.5-cm (6- and 3-in) general purpose penetrations with flanges on top, the zero-gravity pressure control subsystem (thermodynamic vent subsystem) penetration provisions on the tank bottom (one each 5.08-, 3.81-, and 1.27-cm tube) and an enclosure external to the tank, a 7.62-cm- (3-in-) diameter drain at the tank bottom for future growth, a continuous liquid level

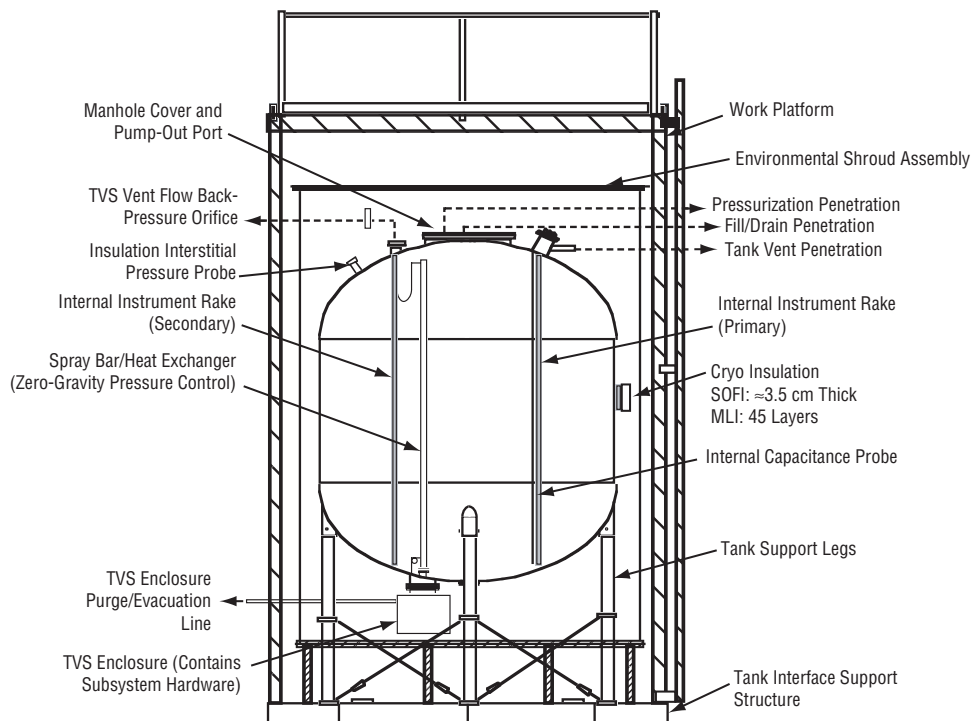


Figure 2. MHTB test tank and supporting hardware schematic.

capacitance probe, two vertical temperature rakes, wall temperature measurements at selected locations, ullage pressure sensors, pressure control/relief safety provisions, internal mounting brackets for future equipment and structural “hard points” for temporary scaffolding and ladder, and low heat leak composite structural supports. Each of the penetrations is equipped with a LH₂ heat guard to intercept heat leak, thereby enabling more accurate measurement of the tank insulation performance as required.

Fluid connections are welded wherever possible and all mechanical seals are the knife-edge/copper gasket (Conflat[®]) design. The exception is the primary manhole cover design (fig. 3), which incorporates a soft, crushable indium wire as a seal material and Invar[®] expansion collars on the stainless steel bolts to offset thermal expansion effects. The secondary manhole cover is equipped with a pump-out port so that any primary seal leakage can be intercepted and routed to a facility vacuum pump. Appendix A contains an MHTB tanking table with information regarding fill height, percent liquid/ullage volume, and LH₂ mass.

2.2 Environmental Shroud

The MHTB tank is enclosed within an environmental shroud which enables simulation of a ground hold conditioning purge, similar to that in a payload bay, and the imposition of a range of uniform temperatures on the multilayer insulation (MLI) external surfaces. The shroud (fig. 4) is 4.57 m (15 ft) high by 3.56 m (12 ft) in diameter, and contains a purge ring for distributing dry gaseous nitrogen (GN₂). The shroud heater strips/cooling loops can impose either constant or time-dependent boundary temperatures ranging from 80 K (144 °R) to 320 K (576 °R).

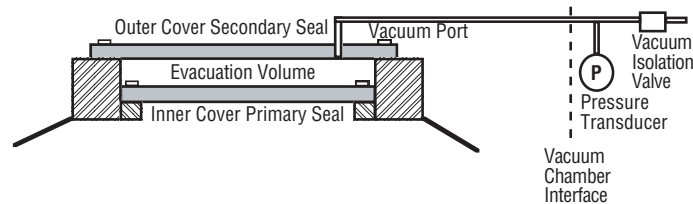


Figure 3. Manhole cover sealing arrangement.



Figure 4. Environmental shroud assembly.

2.3 Cryogenic Insulation Subsystem

The MHTB insulation concept consists of a foam/multilayer combination. The foam element enables the use of a payload bay-type GN₂ purge during ground hold periods. The 45-layer, double-aluminized mylar MLI provides thermal radiation protection while at vacuum conditions on orbit. As reported in reference 1, which describes the insulation in more detail, the combined effects of the MLI variable density, large vent hole pattern, and installation technique resulted in substantial performance improvements over conventional insulation configurations. However, in this application, the insulation system performance was compromised by the thermodynamic vent system hardware installation and by electing, in one series, to not operate the vacuum chamber cold walls.

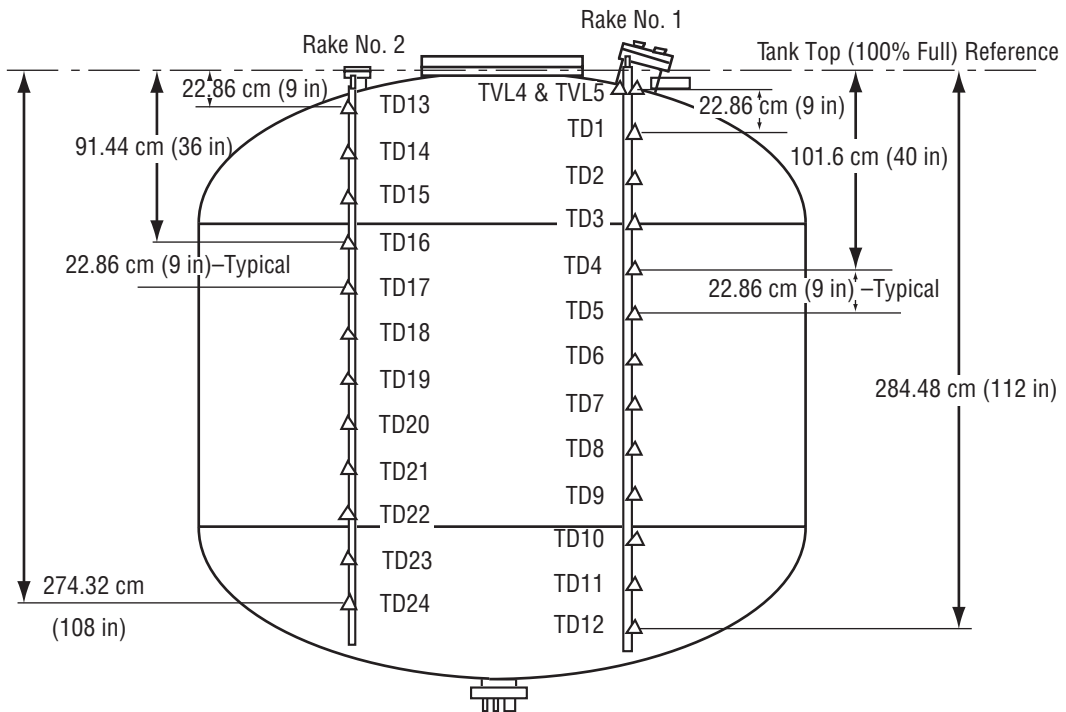
2.4 Multipurpose Hydrogen Test Bed Instrumentation

The test article and environmental shroud instrumentation details are presented in appendix B; however, the instrumentation arrangement for each primary segment is summarized in this section. The test article instrumentation consists primarily of thermocouple and silicon diodes to measure insulation, fluid, and tank wall temperatures. Typically, silicon diode (Lakeshore type DT-470-11A) temperature transducers are positioned in areas of lowest temperatures, which provide higher accuracy as compared to thermocouples. MLI temperature profiles or gradients are measured at seven positions with one silicon diode and four thermocouples placed at each of the seven measurement positions. The MLI interstitial pressure is measured at the foam/MLI interface and a sampling port for both dewpoint and gas species is provided.

The tank is internally equipped with two instrumentation rakes and a capacitance liquid level probe, all supported from the top of the tank (fig. 5). The rakes, constructed from a fiberglass epoxy channel section, are equipped with silicon diodes attached at 22.9-cm (9-in) intervals using nylon rod offsets and cryogenic compatible epoxy. The instrumentation rakes provide temperature-gradient measurements within both ullage and liquid, and serve as a backup to the continuous liquid level capacitance probe. Two of the four composite legs, vent, fill/drain, pressurization, pressure sensor probe, and manhole pump-out penetrations are instrumented to determine the solid conduction component of heat leak.

During the TVS performance testing, the bulk liquid temperature relative to ullage saturation conditions was monitored using silicon diode TD23 on rake 2 (fig. 5) and ullage pressure sensor P1 (see sec 7.1). TD23 is at the 11.5-percent fill level or 53.3 cm (21 in) above the tank bottom and is considered to be representative of the bulk liquid temperature. As described in section 7.2.3, the TD23 temperature output was converted to an equivalent saturation pressure (termed PSA1) and compared with the ullage pressure (P4). P4 is an MKS Instruments, Inc., Baratron 0-666 kPa (0-96 psia) absolute pressure transducer with an accuracy of ± 0.02 percent. TVS-specific instrumentation on the MHTB and test facility is discussed in sections 4.5 and 7.1, respectively.

The environmental shroud is composed of 17 individual panels, each equipped with a minimum of two thermocouples attached to the inner surfaces and placed beneath the electrical heating strips. These thermocouples are used with a closed-loop control system to regulate each shroud panel temperature.



Note: All Diodes Spaced at Intervals of 22.86 cm (9 in)

Figure 5. MHTB internal instrumentation rakes.

3. SPRAY BAR THERMODYNAMIC VENT SYSTEM DESIGN DEFINITION

The TVS was designed to accommodate tank heat leaks up to 55 W and liquid levels ranging from 10 to 95 percent. The four major elements are the heat exchanger, spray injection and recirculation system, controller, and instrumentation. Design selection details regarding each of the TVS elements are presented in reference 2 and are summarized in sections 3.1 through 3.4.

3.1 Heat Exchanger

The heat exchanger is a critical element since its function is to ensure optimal heat transfer between the vented and recirculating fluids. The exchanger design must be capable of rejecting the maximum environmental heat leak rate anticipated and simultaneously reduce the liquid bulk temperature within a reasonable timeframe. To ensure accommodation of a maximum projected heat leak of 55 W without excessive pump and valve operational cycles, the heat exchanger was designed to reject ≈ 844 W or ≈ 15 times the maximum heat leak requirement. This reduced the projected vent cycle from a nearly continuous operation to a more reasonable average of ≈ 5 percent of the total mission time. Additionally, the large heat rejection capability accommodates growth in heat leak, analytical prediction uncertainties, and mission flexibility. Since the TVS is designed to operate in an on-off cycle, the system automatically compensates for environmental and internal performance variations. Three design options were considered in the heat exchanger design trade study:

- (1) Coil heat exchanger: Vent tubing is wrapped around the spray injection system.
- (2) Concentric single-tube exchanger: Recirculation flow is inside an inner tube with the vent flow in an annulus between the inner and outer tube diameters.
- (3) Multitube heat exchanger: Similar to option (2) except repeated vent flow paths are used to increase the total heat exchange area.

Option (1), shown in figure 6, represents the simplest configuration. The vent flow is contained within a small diameter tube wrapped around the outside of the larger liquid recirculation tube. Unfortunately, the heat rejection capability of this configuration is compromised by the reduction in liquid flow that occurs as the recirculating liquid flows from the bottom to the top of the spray bar and the flow regime transitions from highly turbulent conditions at the inlet to laminar at the outlet. To compensate for the reduced heat transfer, the vent tube contact area can be increased by increasing the vent tube length. However, vent flow pressure loss also increases with tube length. Also, the longer vent tube reduces the amount of vent liquid available for phase change and reduces the temperature difference between the vented and recirculated liquid. A sensitivity study was performed to define the heat rejection rate as a function of vent line pressure loss for various tube diameters and the results indicated that the vent line pressure losses increase rapidly with respect to the heat rejection rate. For example, to achieve a heat rejection rate of 422 W, 34.8 m (100 ft) of 0.95-cm tubing is required and incurs a 27.6 kPa (4 psid) pressure loss. However, the vent line pressure loss exceeded the design goal

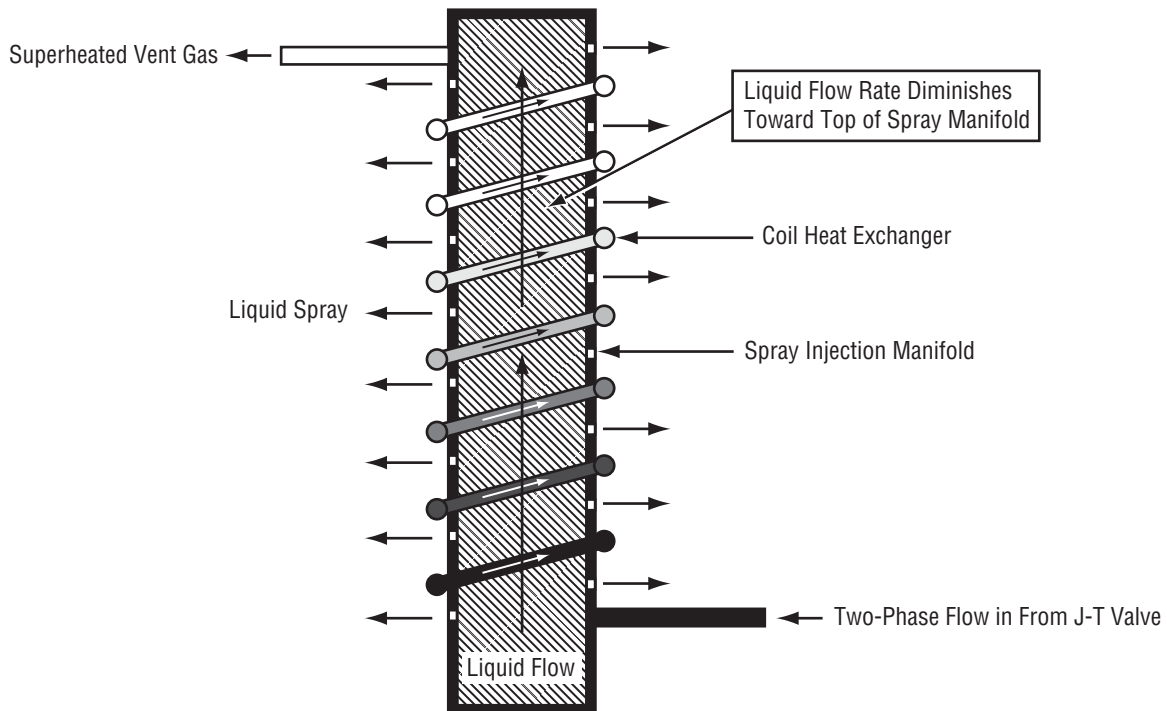


Figure 6. TVS coil heat exchanger—option (1).

of 13.8 kPa (2 psid). Since option (1) did not satisfy the heat rejection design goal of 844 W, resulted in a weight disadvantage, and incurred a risk of vent tube debonding, the concept was not selected.

Option (2), shown in figure 7, consists of two concentric tubes. The inner tube contains the recirculation flow, while the annulus between the inner and outer tubes contains the vent flow. Because the liquid flow rate is constant throughout the heat exchanger length, the hot side (recirculated liquid) heat transfer coefficient exceeds the cold side (vent fluid), unlike the coiled heat exchanger in option (1). Also, the heat transfer area is maximized since the entire length of the inner tube surface area is utilized to transfer heat between the vented and recirculated fluid. Additional energy exchange occurs between the bulk propellants and vented fluid, but was not considered in the analysis. Based on analyses of vent tube diameters ranging from 2.54 to 4.45 cm (1 to 1.75 in) with a fixed spacing of 0.635 cm (0.25 in) between the outside diameters, optimal outside (vent flow) and inside (recirculation flow) tube dimensions of 3.8 cm (1.5 in) outside diameter with a 0.147-cm (0.058-in) wall and 3.175 cm (1.25 in) outside diameter with a 0.089-cm (0.035-in) wall were selected. The design was predicted to reject ≈ 900 W, which satisfies the design goal of 844 W. Additionally, the 3.175-cm (1.25-in) inner tube diameter resulted in low recirculation flow pressure loss and pump power requirements.

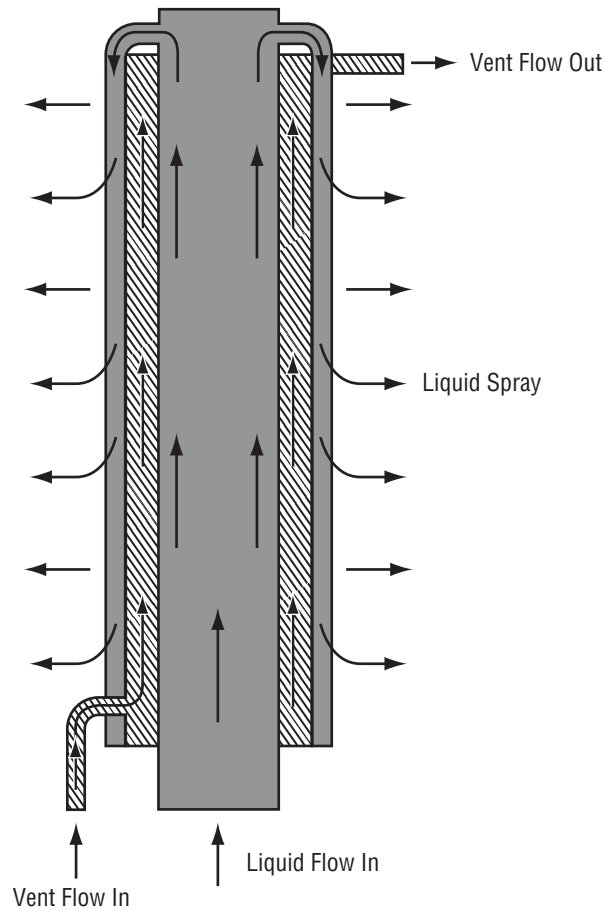


Figure 7. TVS single-tube heat exchanger—option (2).

Option (3), shown in figure 8, is similar to option (2) in that the recirculation flow is contained in the inner tube and the vent flow is in the outer tube. However, the recirculated and vent fluids are divided into a number of smaller tubes to increase both the heat transfer surface area and recirculation fluid heat transfer coefficient relative to the option (2) concept. The sensitivity analyses were based on a 0.953 cm (0.375 in) outside diameter recirculation tube. (Larger tube diameters resulted in low heat transfer coefficients due to large radial clearances on the vent side.) The results indicated that five or more tubes would be required to maintain the pressure losses and pump power below ≈ 15 percent of the total tank heat leak (8 W). With the five-tube design, a maximum heat rejection of over 2,500 W can be achieved with acceptable pressure losses. However, the multitube option is heavier, more complex to fabricate, and has more flow resistance compared to the single-tube option (option (2)).

In summary, option (2), the single-tube heat exchanger, was selected because of its low weight, fabrication simplicity, low pumping power and pressure losses, and satisfaction of the 844-W heat rejection capability.

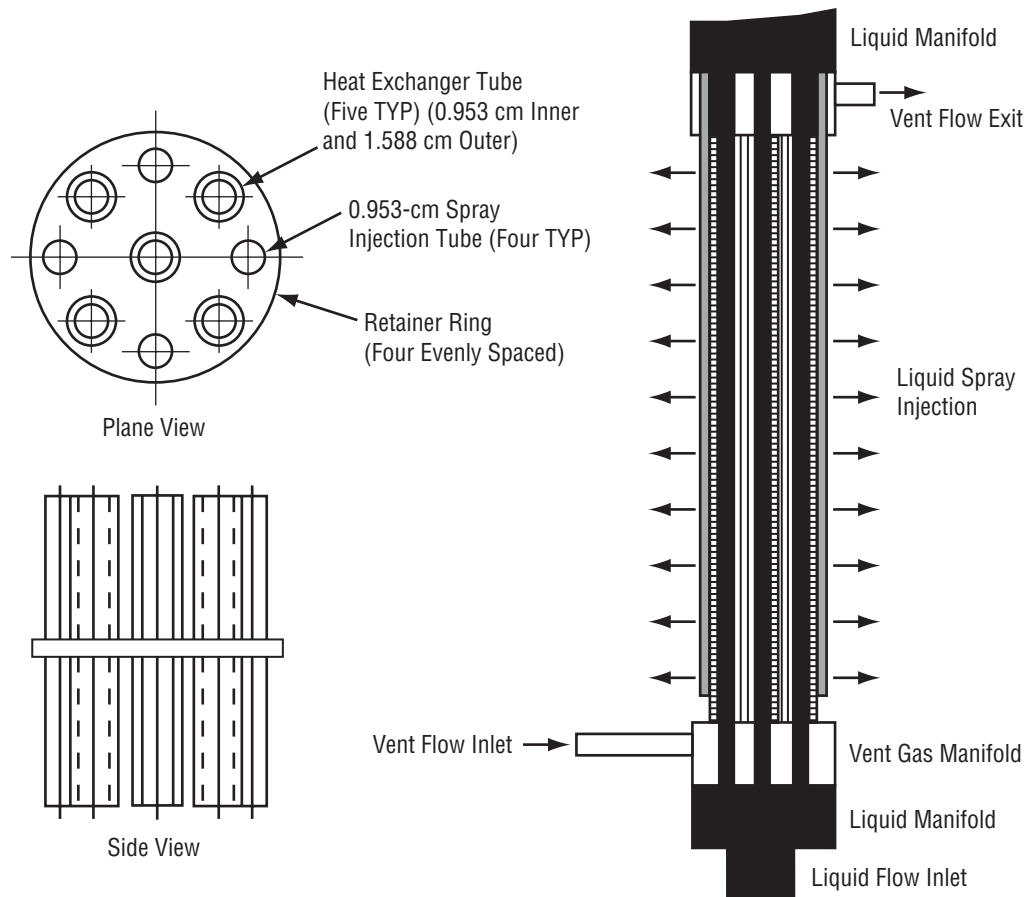


Figure 8. TVS multitube heat exchanger configuration—option (3).

3.2 Operating Pressures

A sensitivity study was performed to define the influence of propellant tank operating pressure and vent system back pressure on the TVS efficiency. The vent fluid heat absorption potential is a combination of heat required to evaporate the two-phase fluid and the sensible heat available for increasing the temperature from the saturation to the superheat condition corresponding to the propellant bulk temperature.

The heat absorbed through evaporation decreases with increasing liquid vapor pressure or tank pressure; however, the net heat absorbed by boiling increases with increasing vent line back pressure due to increasing liquid vapor fractions. The net effect is demonstrated in figure 9 which presents the heat of evaporation versus vent line back pressure for tank vapor pressures ranging from 103 to 241 kPa/m² (15 to 35 psia). At a tank pressure of 137.8 kPa/m² (20 psia), the heat of evaporation varies from 107 to 115 Whr/kg (166 to 178 Btu/lb) as the back pressure ranges from 6.89 to 34.5 kPa/m² (1 to 5 psia). At a back pressure of 34.5 kPa/m² (5 psia), the heat of evaporation ranges from 117 to 107 Whr/kg (182 to 166 Btu/lb) as tank pressure varies from 103 to 241 kPa/m² (15 to 35 psia).

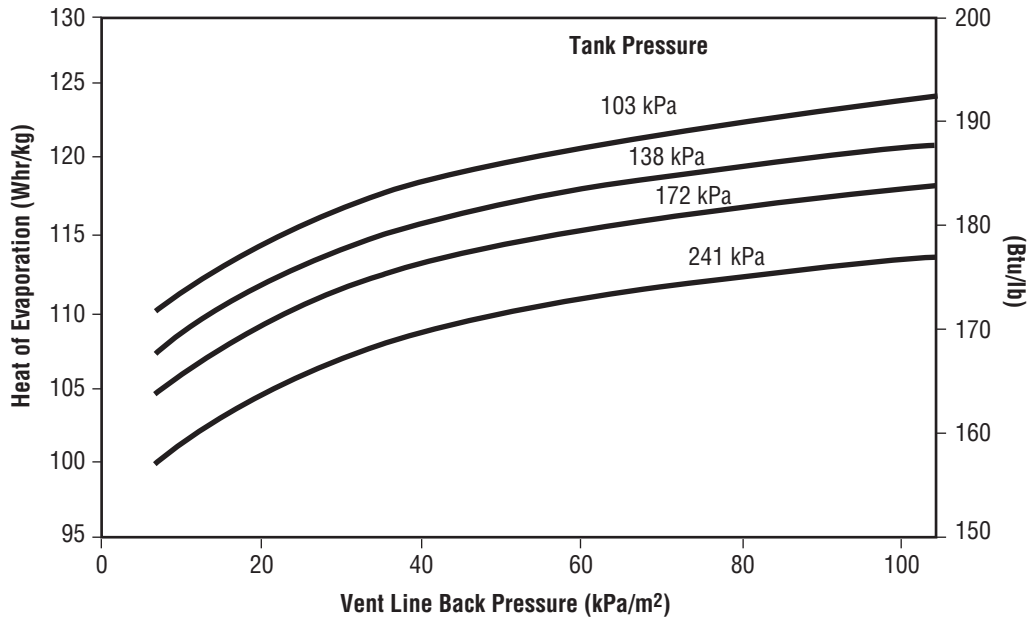


Figure 9. Effects of liquid vapor pressure and vent back pressure on heat absorption.

The effects of vent line and tank pressure on sensible heat capacity are illustrated in figure 10. The sensible heat decreases with increasing vent line back pressure, since the corresponding saturation or boiling point temperatures increase. However, the sensible heat increases as tank pressure increases at a given back pressure due to the increasing tank saturation temperature. At a back pressure of 34.5 kPa/m² (5 psia) and a 137.8-kPa/m² (20-psia) tank pressure, for example, the sensible heat and heat of evaporation are 12.9 Whr/kg (20 Btu/lb) and 115 Whr/kg (178 Btu/lb), respectively. That is, the sensible heat represents ≈ 10 percent of the vent fluid total heat absorption capability.

The combined sensible and evaporation energy effects are presented in figure 11 for tank pressures ranging from 103 to 241 kPa/m² (15 to 35 psia). The net heat absorption increases with decreasing vent line back pressure; however, a minimum practical limit of 20.7 kPa/m² (3 psia) was selected as the baseline back pressure to ensure avoidance of complications with triple-point conditions at 6.9 kPa (1 psia). At a 20.7-kPa/m² (3 psia) back pressure, the heat absorption benefits of decreasing tank pressure begin to level off at ≈ 137.8 kPa/m² (20 psia). Therefore, 137.8 kPa (20 psia) was selected as the tank pressure at which venting would be initiated. Therefore, if tank saturation conditions begin at 103 kPa (15 psia), then ≈ 4 days can be accommodated without venting due to the heat absorption involved in raising the saturation condition to 137.8 kPa/m² (20 psia), assuming a MHTB heat leak of 20 W and a homogeneous bulk liquid.

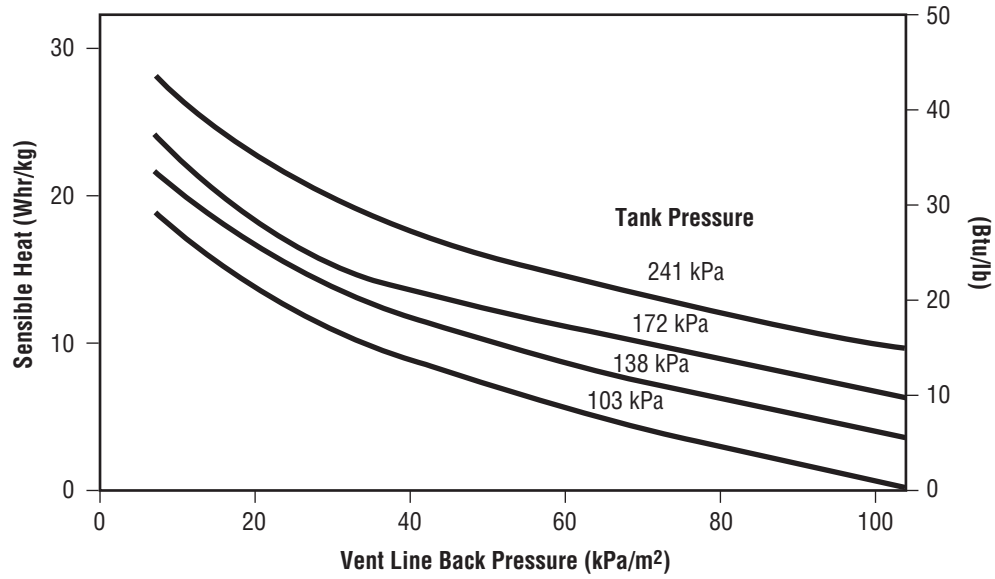


Figure 10. Sensible heat absorption by vent flow versus liquid vapor pressure and vent back pressure.

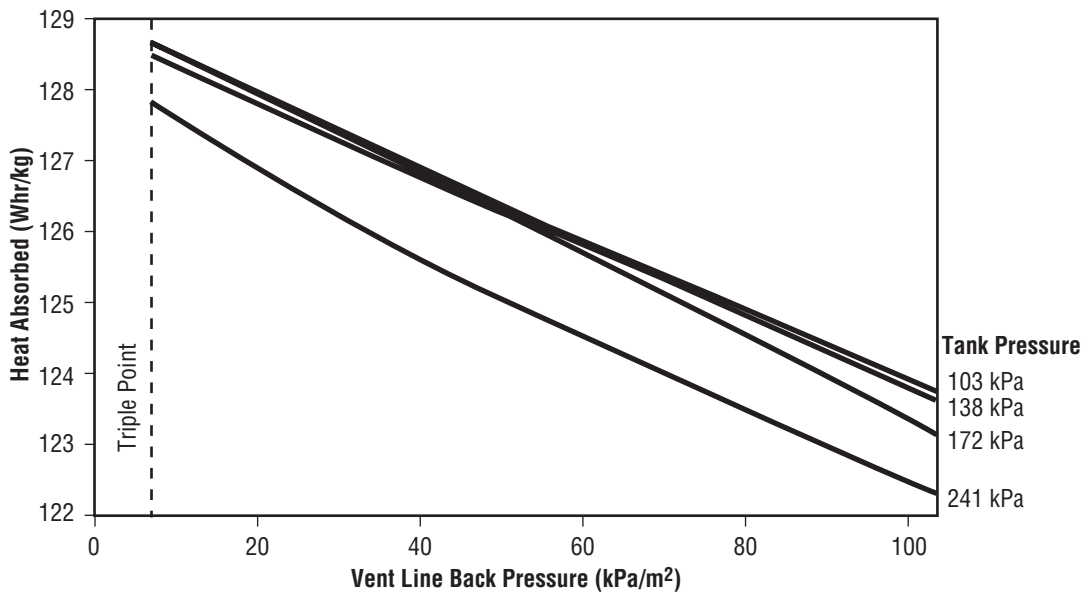


Figure 11. Total heat absorbed by vent flow versus liquid vapor pressure and back pressure.

3.3 Spray Bar Orifice Sizing

Flow from the heat exchanger outlet is manifolded into four 1.27-cm- (0.5-in-) diameter tubes which are aligned along the length of the exchanger, equally spaced radially to provide equal flow in four directions. The goal is to ensure that the spray bar provides relatively uniform flow into the ullage and bulk liquid to achieve destratification through forced convection heat transfer. The spray velocities need to be sufficient to promote good heat transfer, but without excessive pump flow rates and corresponding pressure losses. An ullage pressure decay sensitivity study was performed to guide the selection of spray injection orifice size. Assuming that the liquid droplet was equal to the orifice diameter, the number of droplets and surface area available for heat exchange with the ullage could then be calculated for a given flow rate. The ullage pressure responses computed for a 0.136-kg/s (0.3-lb/s) flow rate into an empty 18-m³ (639-ft³) tank with droplet diameters of 0.22, 0.2, and 0.1 cm (0.086, 0.08, and 0.04 in) are depicted in figure 12 and illustrate that the pressure decay rate increases with smaller droplet sizes. Analyses also were conducted to assess the injection flow rate and velocity distributions along the spray bar length. As illustrated in figure 13, 45 orifices with a diameter of 0.17 cm (0.067 in, or a standard 51 drill size) produced relatively uniform injection velocities for the design condition of a half-full tank. The velocity variations are greater with the full and empty tank conditions, but are within an acceptable range; i.e., varied from 5.2 to 7.6 m/s (17 to 25 ft/s). Similarly, the corresponding mass flow rate variations along the spray bar length were computed to be within 6 percent with the half-full tank.

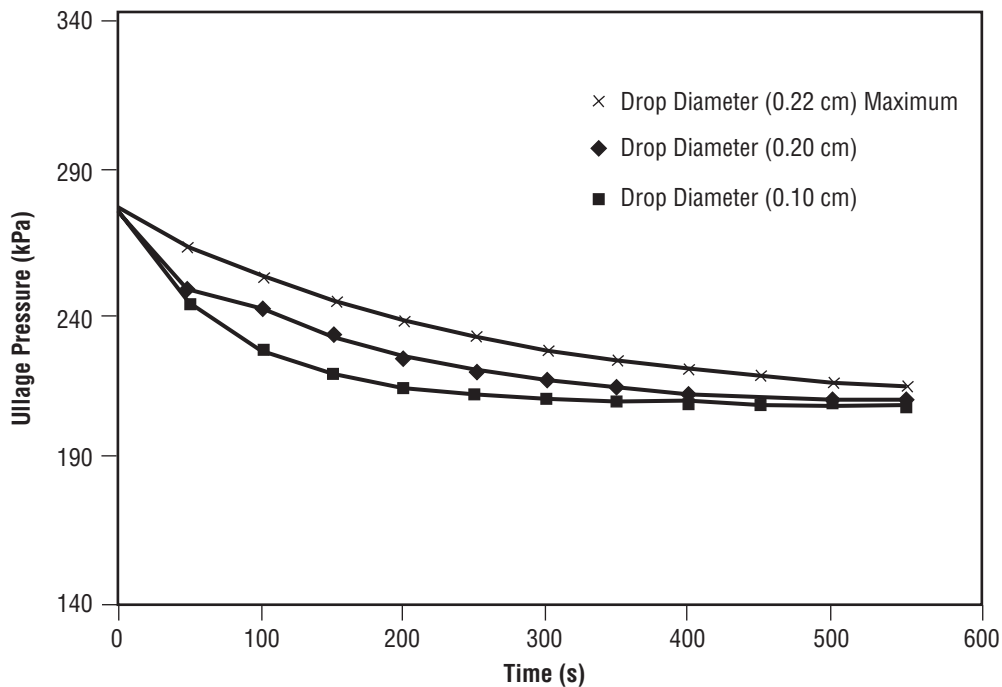


Figure 12. Effects of liquid droplet diameter on ullage pressure decay rate.

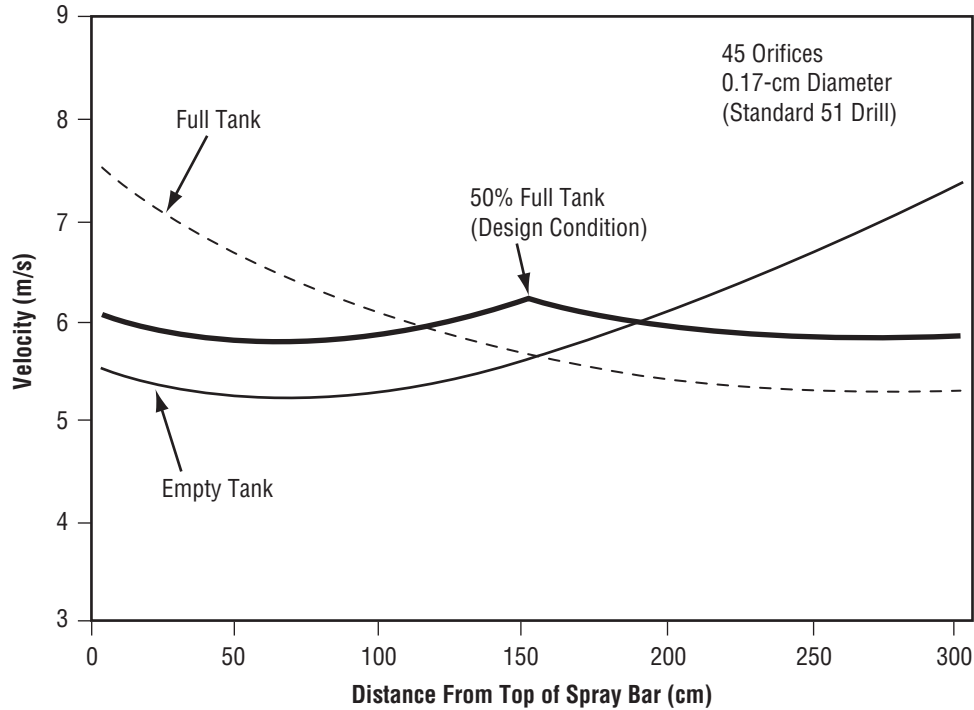


Figure 13. Injection velocity versus distance from spray bar top at 0.136 kg/s flow rate.

3.4 Control Logic

Three pressure control logic options were considered to automate the pump and vent valve operations. One option is to simultaneously activate the pump and vent valve whenever the maximum tank pressure is attained and sustain the operation until the tank pressure drops below the minimum control band level. The disadvantage is that liquid is vented even when pressure control could be achieved with mixing alone (bulk liquid is subcooled relative to the ullage pressure). Also, since bulk liquid cooling occurs with each operation, unacceptably low liquid temperatures could result. A second option is to operate the vent valve and recirculation pump independently based on measured ullage pressure. Again, the pump is activated at the upper control band pressure and is shut down when the minimum level is achieved. This mode is continued until the bulk liquid saturation pressure exceeds the upper control band limit and the vent valve is opened. The vent valve remains open until the bulk liquid saturation conditions are reduced to the minimum control band value. This control logic dictates that the pump continue to operate, adding thermal energy to the liquid, until the lower control band limit is achieved, a process that can require up to 16 hr at the maximum tank fill level. The extended pump operation is inefficient, since the added thermal energy must be removed by venting.

A third option (fig. 14), which was baselined, is to operate the pump and vent valve through separated control logic paths. The pump operation starts when the upper ullage pressure limit is reached and ceases when the lower control limit is reached. In this option, however, the vent valve control logic is based on ullage pressure and the measured bulk liquid temperature. The bulk liquid temperature is used to compute the corresponding saturation pressure, which is then compared with the measured ullage pressure. After the computed saturation pressure attains the minimum ullage pressure control band level, the vent valve is opened and closed with each subsequent recirculation pump operation cycle. The baselined option minimizes vent losses, since venting does not begin until the bulk liquid subcooling is removed; i.e., mixing cycles alone will control ullage pressure until the subcooling is removed. A minor disadvantage is that both a liquid temperature and tank ullage pressure are required, and a computation is required to convert the measured bulk liquid temperature to a corresponding vapor or saturation pressure.

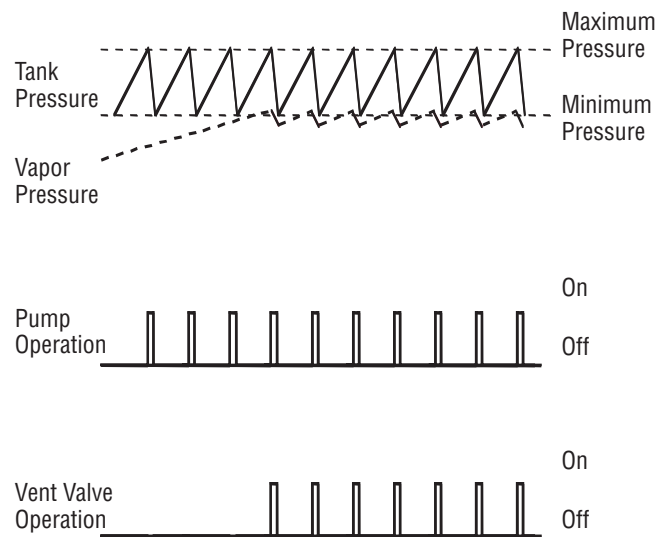


Figure 14. TVS baseline pressure control concept.

4. THERMODYNAMIC VENT SYSTEM DESIGN AND HARDWARE SELECTION

Following definition of TVS hardware design requirements, a survey of available hardware components within NASA and industry inventories was made. The design and selection processes for the recirculation pump, vent valve, heat exchanger assembly, TVS instrumentation, component box assembly, and spray bar support ring are described in detail in reference 2 and are summarized in sections 4.1 through 4.7.

4.1 Recirculation Pump

The design definition phase resulted in a 113.5-L/min (30-gal/min) nominal recirculation flow rate, with a pressure rise between 2.76 and 4.13 kPa/m² (0.4 to 0.6 psid), which represents the range corresponding to a full and empty tank. Because the TVS must operate with saturated liquid, the minimum net positive suction pressure is zero. No suitable off-the-shelf pump existed and Barber-Nichols, Inc., was selected to develop the pump. The selected pump, BNHP-08, is based on a previous Barber-Nichols design used with slush hydrogen. The centrifugal pump is powered with an electric motor (variable frequency drive) that is submerged and cooled with LH₂. As indicated in table 1, the pump motor input power requirement ranges from 0.44 to 37 W with flow rates of 18.9 and 151.4 L/min (1.3 and 40 gal/min), respectively.

Table 1. Barber-Nichols pump (BNHP-08) operating characteristics.

Flow (L/min)	Frequency (Hz)	Pump Power (W)	Motor Input Power (W)	ΔP (mBar)
18.9	18	0.04	0.44	0.9
37.8	37	0.33	1.77	3.9
56.8	55	1.10	3.47	8.6
75.7	73	2.70	6.51	15.2
113.5	110	9.00	16.75	34.5
151.4	147	21.00	37.30	61.3

4.2 Joule-Thompson Vent Valve

To assist in the vent valve selection, a two-phase pressure drop analysis was performed to determine the flow capacity of four candidate valves with orifice diameters ranging from 1.96 to 3.73 mm (0.077 to 0.147 in); the results are presented in figure 15. Although all four valves satisfied the design flow rate goal of 0.1362 kg/min (0.3 lb/min), a valve used in the Space Shuttle power reactant storage distribution system was selected because of its good working condition and flow rate capability of 0.128 kg/min. The selected Consolidated Controls Corporation valve (part number 74405-4220,

serial number 097906–CRP–0020) has an orifice diameter of 1.96 mm (0.077 in) and a pressure loss of 24 kPa/m² (3.5 psid) with GN₂ at 689 kPa/m² (100 psi) and 21 °C (70 °F). The valve, described in reference 2, is bidirectional with an electrically actuated solenoid and has a minimum life of 20,000 hr. The operating pressure range is 0.07 to 2,205 kPa/m² (0.01 to 320 psig). The effect of the bulk LH₂ subcooling on the valve vent flow rate is presented in figure 16 and indicates that the vent flow rate increases linearly from 0.128 kg/min, with no subcooling, up to 0.169 kg/min with 27.6 kPa/m² (4 psi) of subcooling.

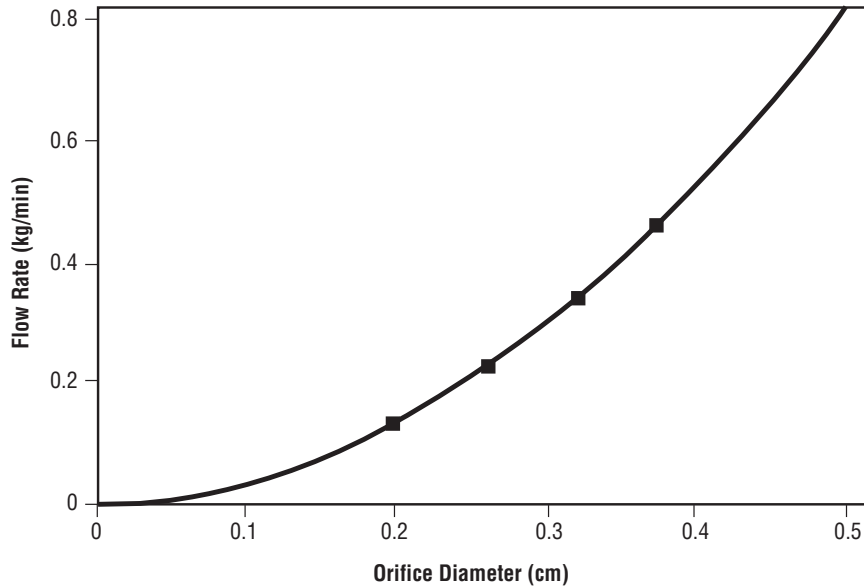


Figure 15. Two-phase flow rate versus J-T vent orifice diameter.

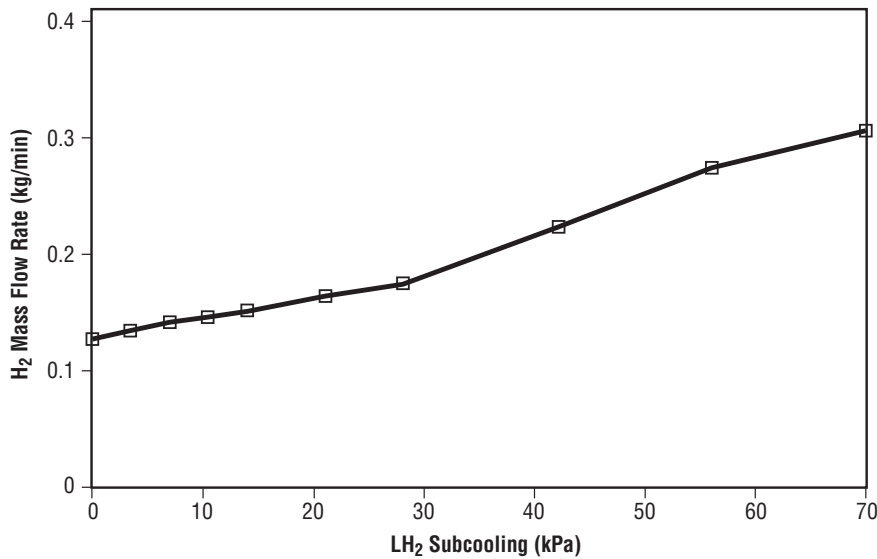


Figure 16. Vent flow rate versus liquid subcooling at 137.8 kPa/m² vapor pressure.

4.3 Spray Bar Heat Exchanger Assembly

The spray bar heat exchanger and spray injection assembly schematic is presented in figure 17 and the installation within the MHTB is pictorially presented in figures 18 and 19. The heat exchanger element consists of two concentric stainless steel tubes. The outer and inner tubes have 3.81 and 3.18 cm (1.5 and 1.25 in) outside diameters, respectively, and both have a wall thickness of 0.089 cm (0.035 in). The overall length of the assembly is 2.67 m (105 in) with an area of 0.27 m² (2.9 ft²) for energy exchange between the recirculated and vented fluids. The external area available for energy exchange between the vented and tank or bulk fluids is 0.287 m² (3.1 ft²).

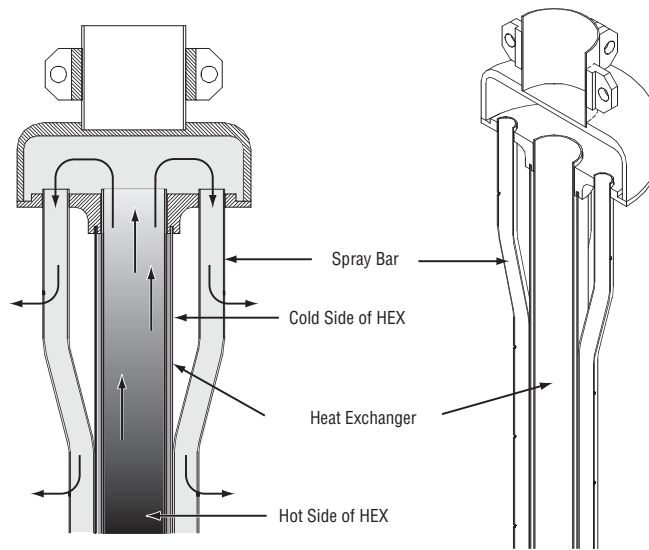


Figure 17. TVS heat exchanger and spray injection assembly.

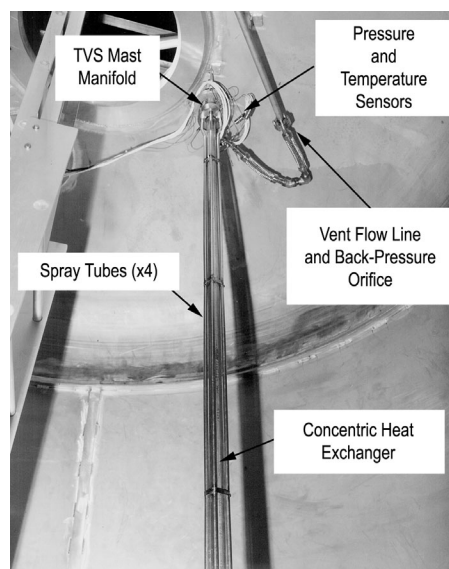


Figure 18. TVS spray bar assembly MHTB installation—top.

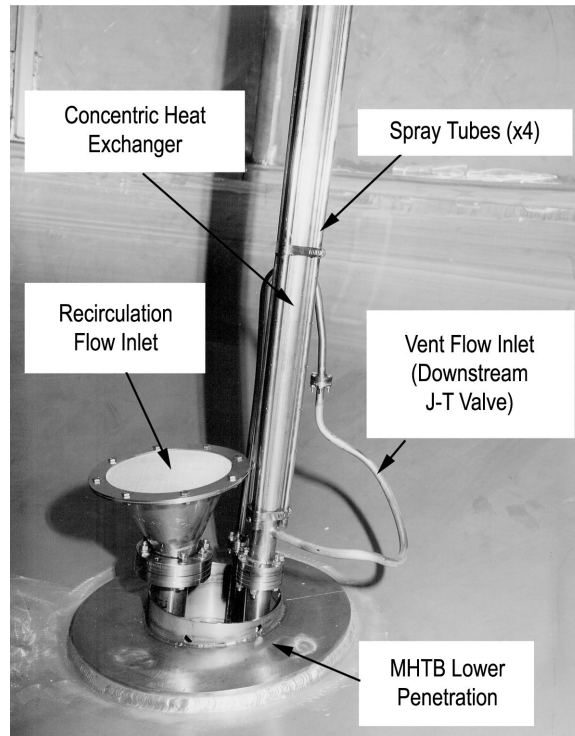


Figure 19. TVS spray bar assembly MHTB installation—bottom.

The spray injection design consists of four 1.27 cm (0.5 in) outside diameter tubes manifolded together at the heat exchanger outlet. Each tube contains 43 orifices equally spaced ≈ 6.1 cm (2.4 in) apart and enable spray injection in four directions. Additionally, eight orifices (two per axis) were included in the area above the heat exchanger outlet to increase injection cooling in the upper tank dome area.

Because the MHTB 3.2-cm- (1.25-in-) diameter interfacing line flange is 2° from vertical, the spray bar interfacing flange was adjusted to accommodate the misalignment. Additionally, the 1.27-cm (0.5-in) vent line at the top of the spray bar assembly included a 6.35-cm (2.5-in) loop to allow correction for any misalignment during installation (see ref. 2 for details).

4.4 Recirculation and Vent System Assembly

The recirculation and vent system assembly, shown in figures 20 and 21, contains the active components of the TVS; i.e., the pump, vent valve, and turbine flowmeter. As with the spray bar heat exchanger assembly, provisions were made to accommodate misalignments with the MHTB interfaces. A large U-shaped bend was included in the vent tube segment and provisions were made to add a bellows assembly downstream of the recirculation pump, subsequently deemed unnecessary. The assembly was designed to minimize intrusion in the space between the tank bottom and vacuum chamber cold walls on the floor. Additionally, the assembly had to be configured to minimize flow resistance and vapor accumulation in the recirculation pump and line. Therefore, the pump was positioned as close as possible to the tank outlet. Instrumentation provisions are described in section 4.5.

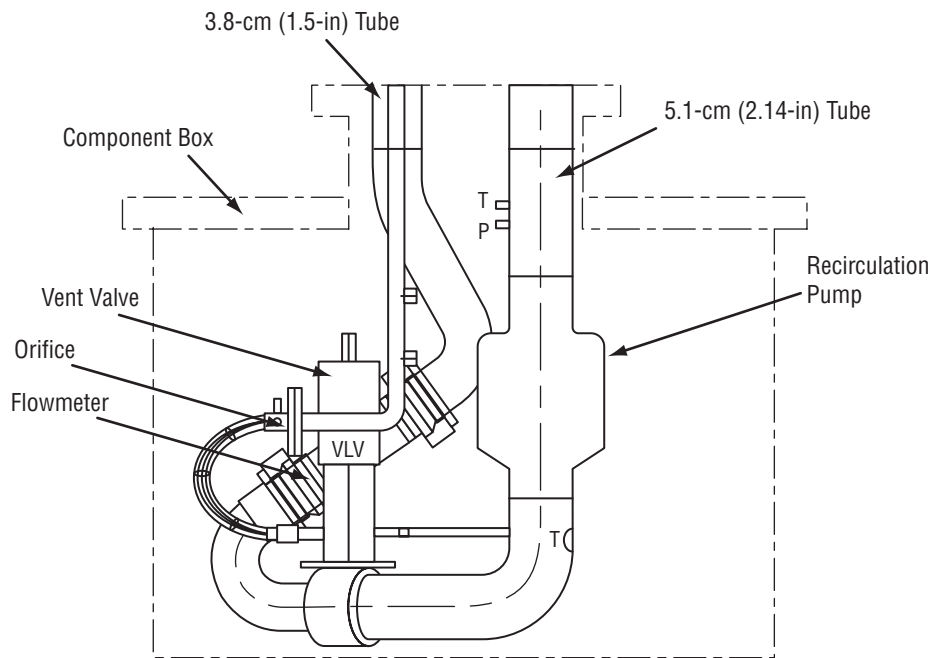


Figure 20. Recirculation pump and vent assembly.

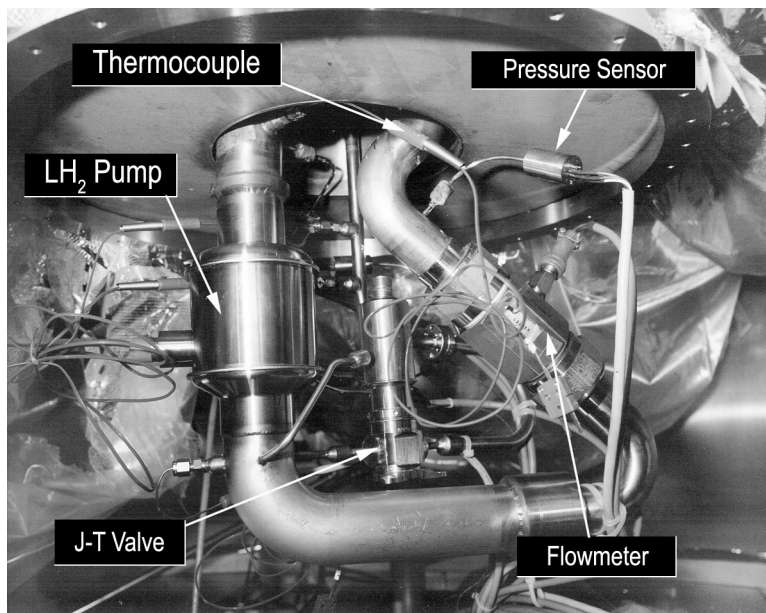


Figure 21. Recirculation pump and vent assembly—MHTB installation.

4.5 Thermodynamic Vent System Instrumentation

The TVS instrumentation presented in figure 22 is arranged to provide input to the controller and to define the TVS performance characteristics. As described in section 2.4, a bulk temperature measurement is used to monitor the bulk liquid saturation conditions relative to the measured ullage pressure and as inputs to the TVS controller. The sensor, TD23, is at the 11.5-percent fill level or 53.3 cm (21 in) above the tank bottom and is considered to be representative of the bulk liquid temperature. The TD23 temperature output is corrected to account for hydrostatic pressure, converted to a corresponding saturation pressure (termed PSA1), and compared with the ullage pressure, P4. As previously described in section 3.4, once PSA1 becomes equal to the minimum pressure control setpoint, the J-T vent valve is thereafter opened each time the mixer is activated.

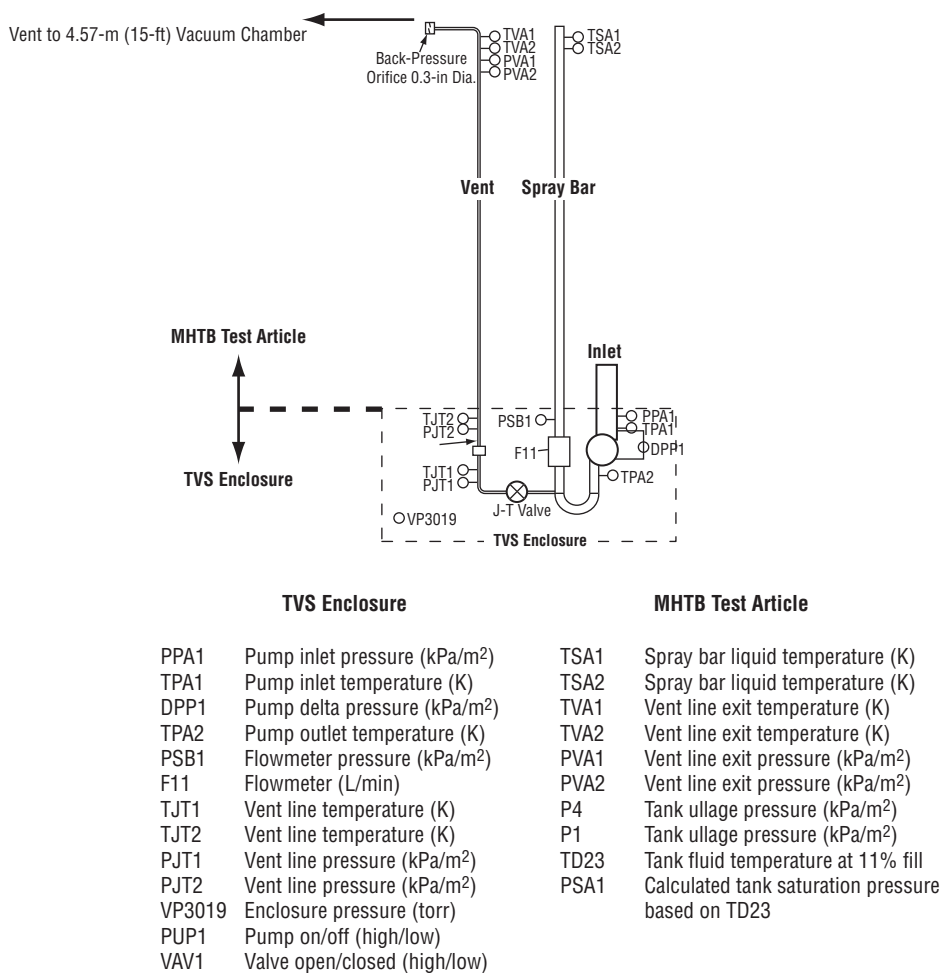


Figure 22. TVS instrumentation schematic.

The TVS performance characterization includes definition of the vent flow rate, heat exchanger performance, and recirculation spray injection flow rate. The vent flow rate is determined from choked flow calculations based on the calibrated back-pressure orifice discharge coefficient-area product, inlet pressure, and temperature measurement. Two MHTB pressure transducers are positioned upstream of the back-pressure orifice, and three temperatures are provided—two upstream and one downstream. These thermodynamic measurements provide redundancy and definition of the heat exchanger performance.

The heat exchanger performance estimate is based on the vent flow calculation (discussed above), along with the temperature measurements at the inlet and outlet of the vent side of the heat exchanger. The heat exchanger inlet temperature, along with the pump discharge pressure and vent valve inlet pressure, are used to define the heat exchanger inlet fluid two-phase quality and total enthalpy. The change in inlet to outlet enthalpy times the vent flow rate level is used to define the heat exchanger performance and the total MHTB heat extraction rate.

To define spray injection flow rate, a turbine flowmeter is positioned at the heat exchanger inlet. The recirculation flow can also be calculated based on the pump speed indication and the pump delta pressure (ΔP) measurement. The spray injection temperature exiting the heat exchanger is measured through use of the two silicone diode transducers located at the inlet to the four spray tubes. These spray injection temperature measurements can be used in the tank thermodynamic reconstruction analysis to update the liquid spray heat transfer characteristics.

4.6 Component Box Assembly

The component box function is to enclose the recirculation and vent system assembly components so that any leakage can be entrapped and pumped out without compromising the chamber vacuum levels. The cylindrical stainless steel box is 55.9 cm (22 in) in diameter by 45.7 cm (18 in) high. The pump-out or vent line has a 3.81-cm (1.5-in) diameter that is connected to a facility vacuum pump, thereby eliminating the effects of any small leaks on vacuum chamber conditions. The cylindrical section has a 0.32-cm (0.125-in) wall thickness and the top flange is 2.54 cm (1 in) thick. The top flange, used for connecting with the MHTB tank interface, contains a Conflat seal, whereas a 0.159-cm (0.0625-in) indium wire seal is used on the top and bottom box sections. The box was designed to withstand a 275.6-kPa/m² (40-psid) burst and 103.3-kPa (15-psid) crushing pressures. The ac and dc power for the pump and valve, respectively, is routed through the box pump-out line.

4.7 Support Ring Assembly

A support ring assembly is provided for horizontal support and alignment of the spray injection and heat exchanger assembly at the upper end. The support ring has three adjustable set screws, three struts, and a strut bracket. The ring assembly is attached to the three brackets inside the upper dome of the MHTB.

5. SUBSYSTEM AND COMPONENT TESTING

Component and subsystem testing of the TVS hardware was performed to verify functionality and integrity, and to anchor analytical modeling. Acceptance testing was conducted, in some cases, with simulant fluids to keep costs within funding constraints.

5.1 Liquid Hydrogen Spray Injection

Liquid hydrogen spray injection tests were performed (ref. 2) at Glenn Research Center (GRC) to verify pressure collapse analytical modeling. The test configuration (fig. 23) consisted of a 63.5-cm- (25-in-) long spray bar segment with 0.14-cm (0.055-in) orifices spaced 6.35 cm (2.5 in) apart along the spray bar length. The spray bar was mounted inside a dewar with an inside diameter of 55.9 cm (22 in), a height of 71 cm (28 in), and an internal volume of 0.178 m³ (6.3 ft³). Due to pump performance limitations, the flow rates were limited to 11.35 L/min (3 gal/min), as opposed to the 18.9 L/min (5 gal/min) desired, and to a 20-s steady-state flow duration. However, the testing provided valuable insight and was effectively utilized to anchor analytical modeling. The measured data are presented in figures 24 and 25 for the ullage temperature and wall temperature, respectively. The correlation between the predicted and measured ullage pressure, presented in figure 26, indicated that the appropriate parameters were modeled and that the spray bar would provide good pressure control during the MHTB TVS testing.

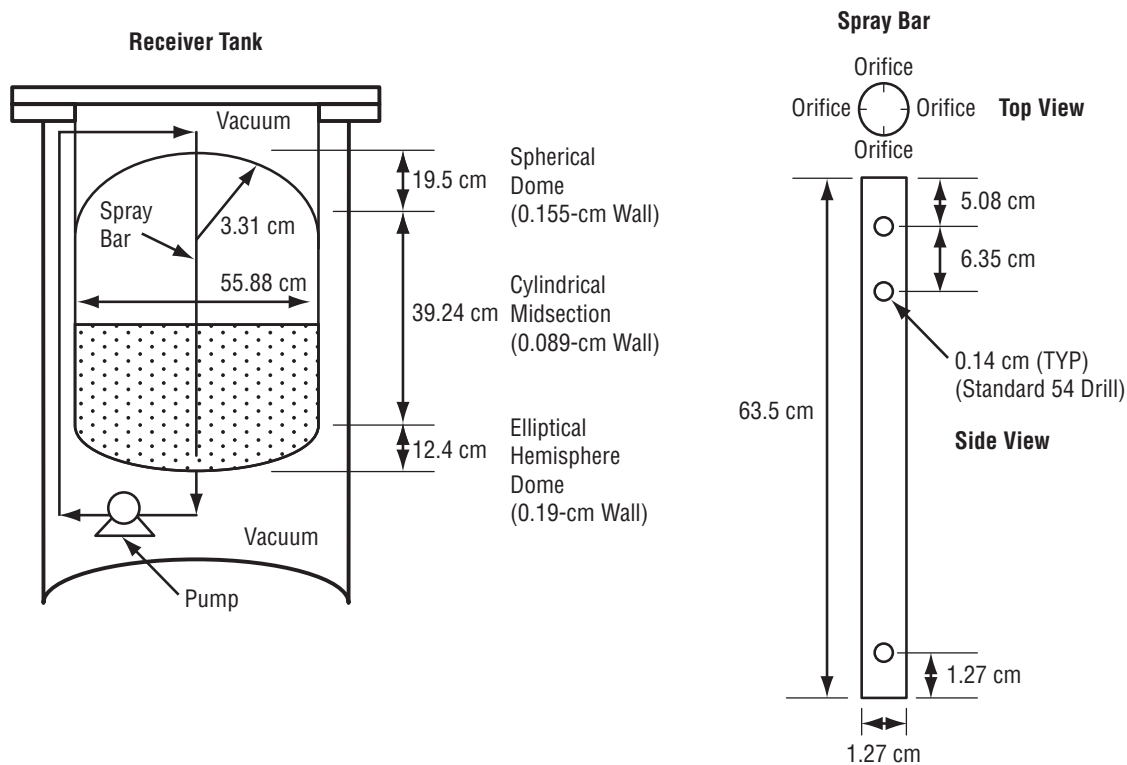


Figure 23. GRC ullage pressure collapse test setup.

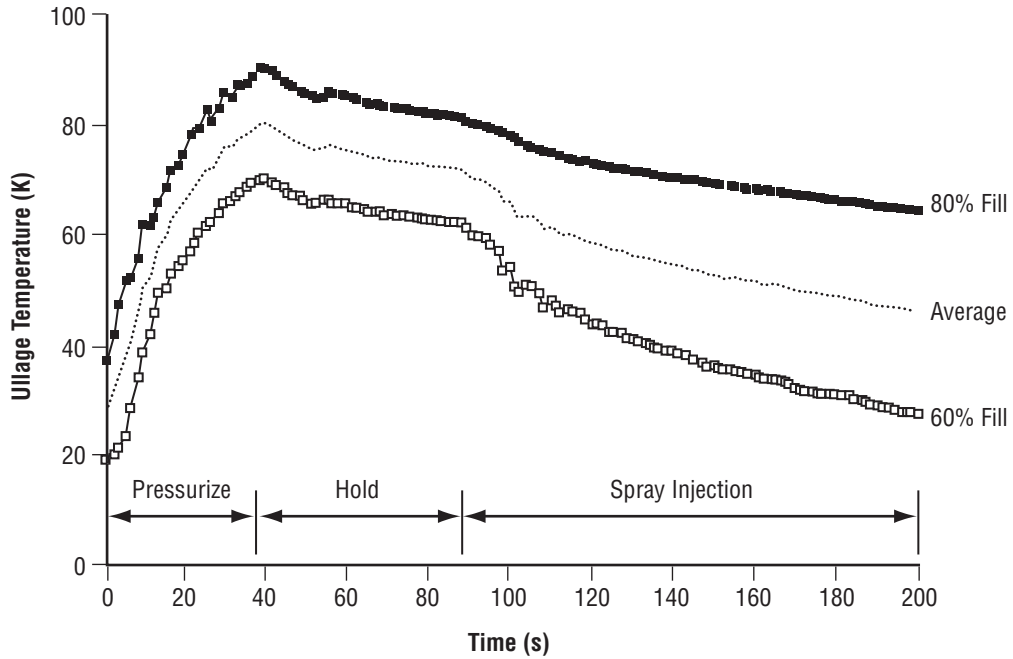


Figure 24. GRC test data for ullage temperature.

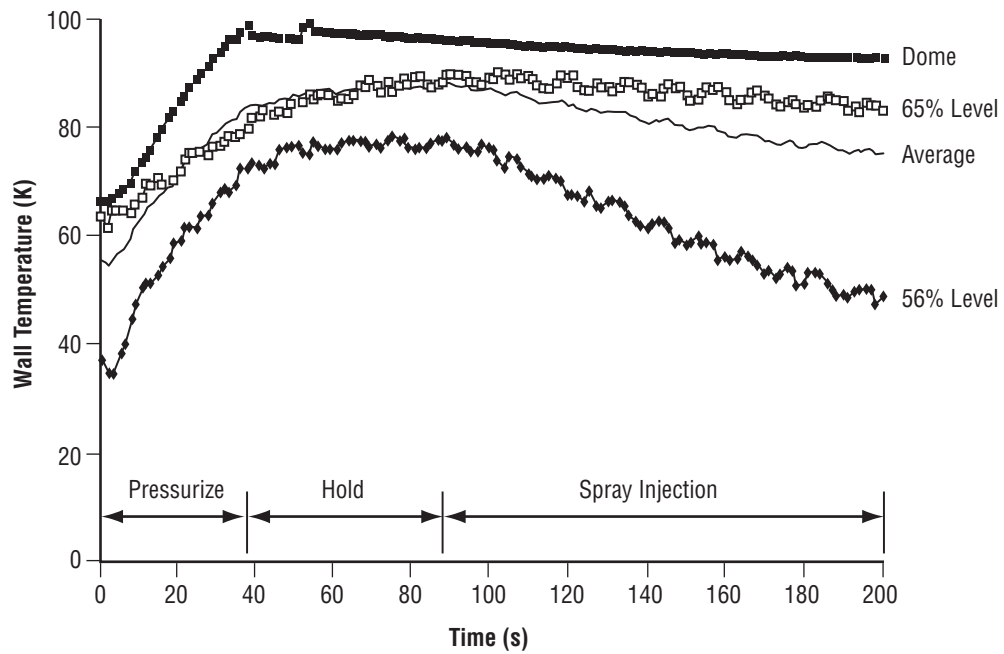


Figure 25. GRC test data for tank wall temperature.

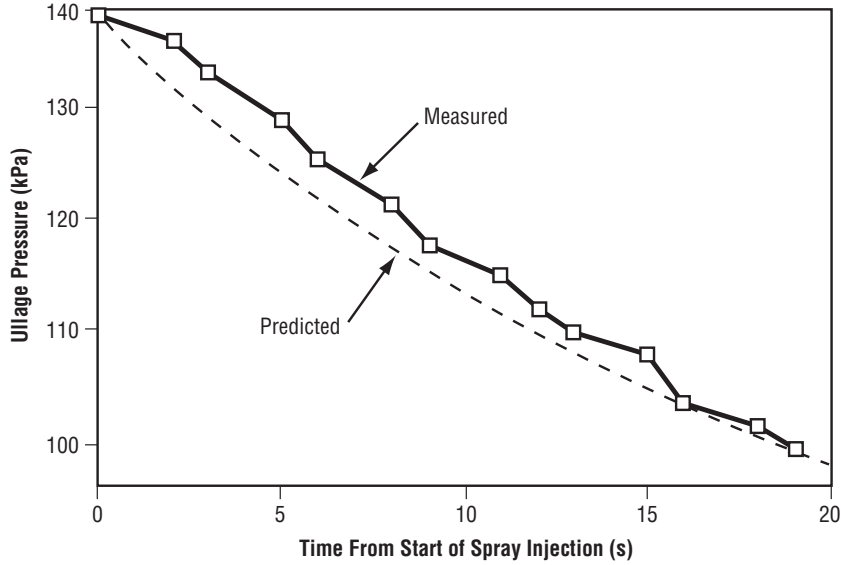


Figure 26. Comparison of predicted ullage pressure and GRC test results.

5.2 Recirculation Pump

The recirculation pump tests, performed at Barber-Nichols, measured the pump head rise versus flow rate for various operating speeds. The testing was conducted with methanol to simulate the low hydrogen density. The pump head and flow coefficients were derived from flow and delta pressure measurements, which were then used in the performance predictions. The predicted and measured flow rates versus head rise data are presented in figure 27 and indicate that the pump produces 113.5 L/min (30 gal/min) with a head rise of 3.3 kPa/m² (0.48 psid) and 6.89 kPa/m² (1 psid) at 3,134 rpm and 4,158 rpm, respectively. The pump was also operated at low speed (1,000 to 2,000 rpm) submerged in liquid nitrogen (LN₂) to verify functionality at cryogenic temperatures.

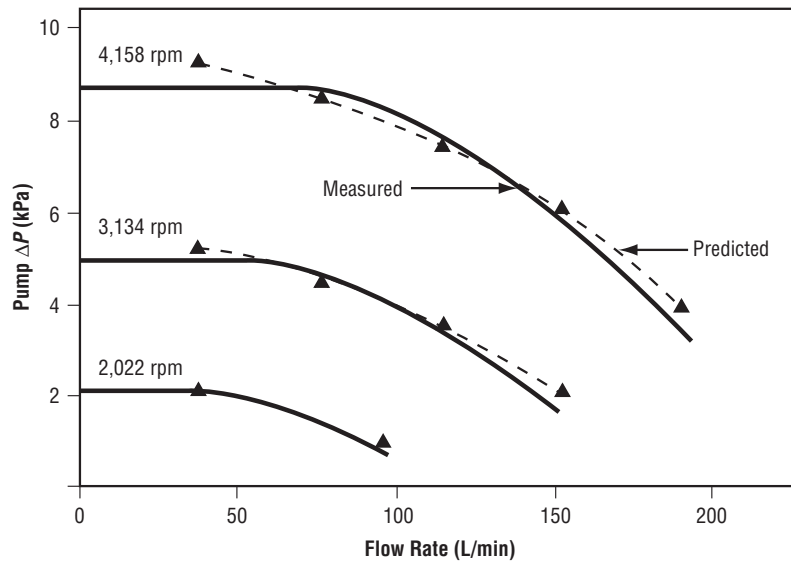


Figure 27. LH₂ recirculation pump predicted and measured performance.

5.3 Other Component and Subsystem Testing

Additional TVS component and subsystem testing included system pressure drop, flowmeter calibration, cryogenic shock, proof pressure, and leakage tests.

The spray injection tubes were individually flow tested in a horizontal position with water to measure spray orifice pressure drop. The test-derived pressure loss coefficients were compared to verify that the orifices had been uniformly drilled and deburred. The measured pressure losses and derived flow coefficients for each of the four tubes are presented in figures 28 and 29, respectively. The pressure losses ranged from about 20.67 to 227.4 kPa/m² (3 to 33 psi) with flow rates from 24.6 to 68.1 L/min (6.5 to 18 gal/min). The tube-to-tube loss coefficient variations were within 16 percent, indicating that uniform flow distributions should result.

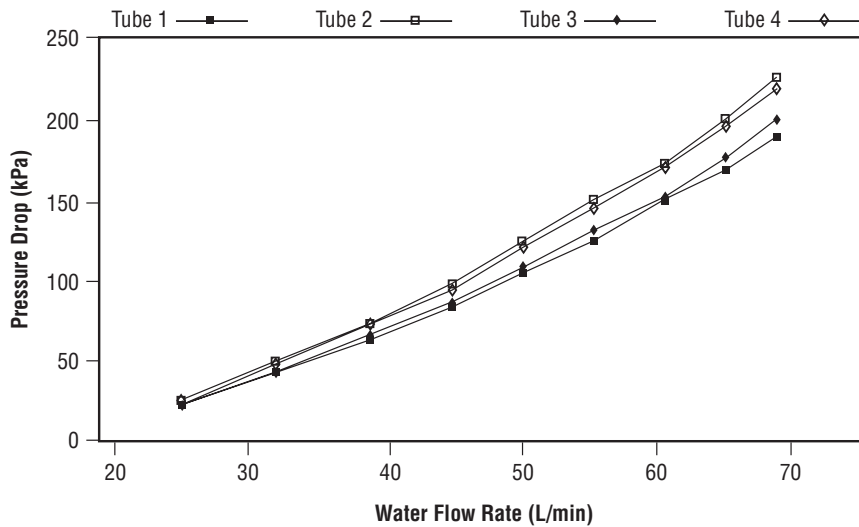


Figure 28. Spray injection tube water flow pressure drop test results.

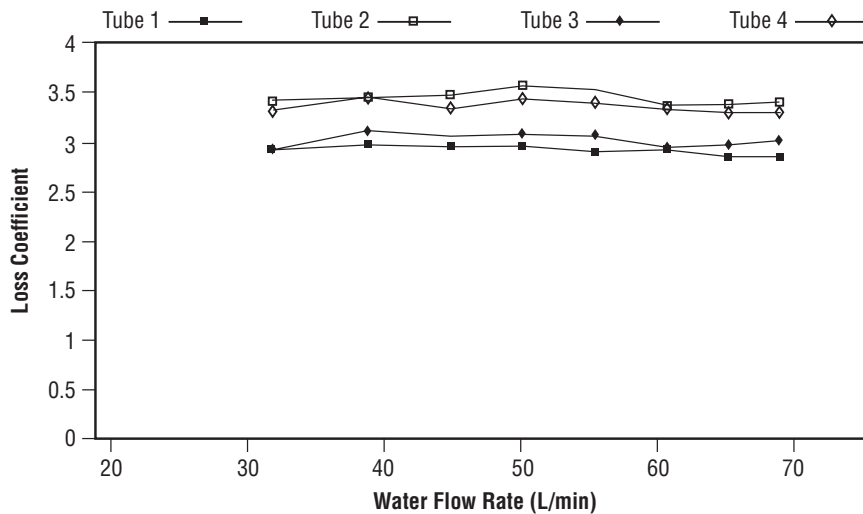


Figure 29. Spray injection tube measured water flow loss coefficients.

The spray tube and heat exchanger assembly was also tested vertically with water. The integrated spray bar and heat exchanger (hot side) pressure loss was defined, minus the hydrostatic pressure; results are presented in figure 30 and, as expected, the total pressure drop was higher than the individual tube losses due to the manifold loss effects. The water pressure loss data for the assembly was then extrapolated to LH₂ and the results are presented in figure 31. With an empty tank (worst case), the pump pressure rise is greater than the TVS pressure loss prediction based on the water data until ≈150 L/min (≈40 gal/min). For example, at 113.55 L/min (30 gal/min) and with an empty tank, the pump pressure rise is 4.134 kPa/m² (0.6 psi) and the TVS pressure loss is ≈3.24 kPa/m² (≈0.47 psi), indicating that the system should perform well. Additionally, photographic data indicated that the spray pattern exceeded 3.05 m (10 ft), assuring that the MHTB ullage will certainly be penetrated and mixed.

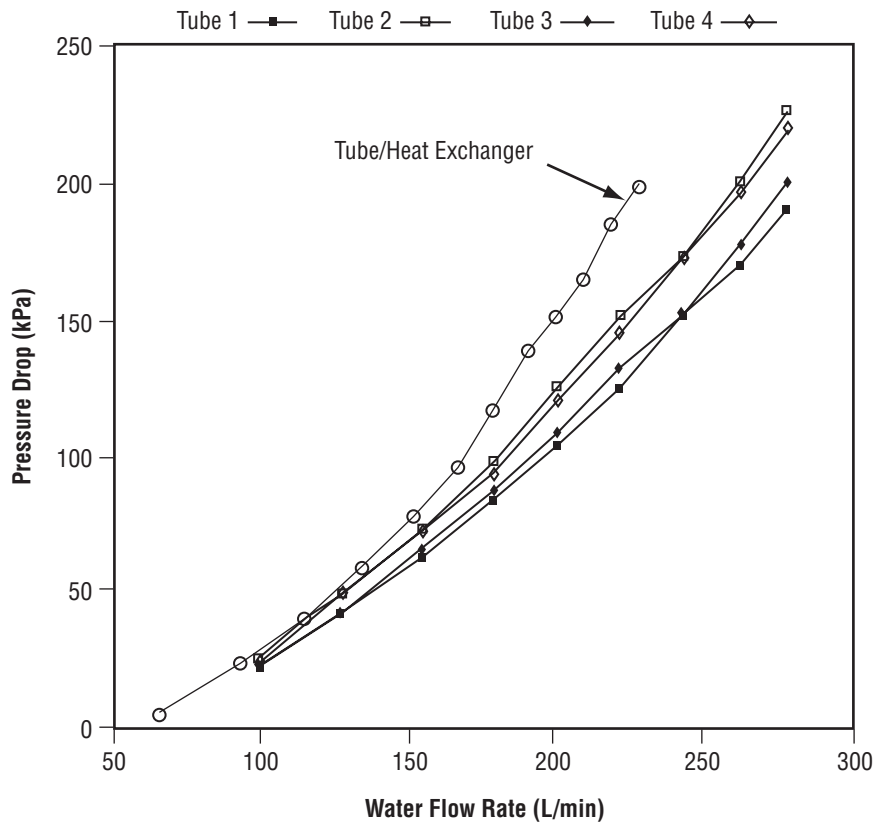


Figure 30. Water flow pressure drop in spray tubes and heat exchanger assembly.

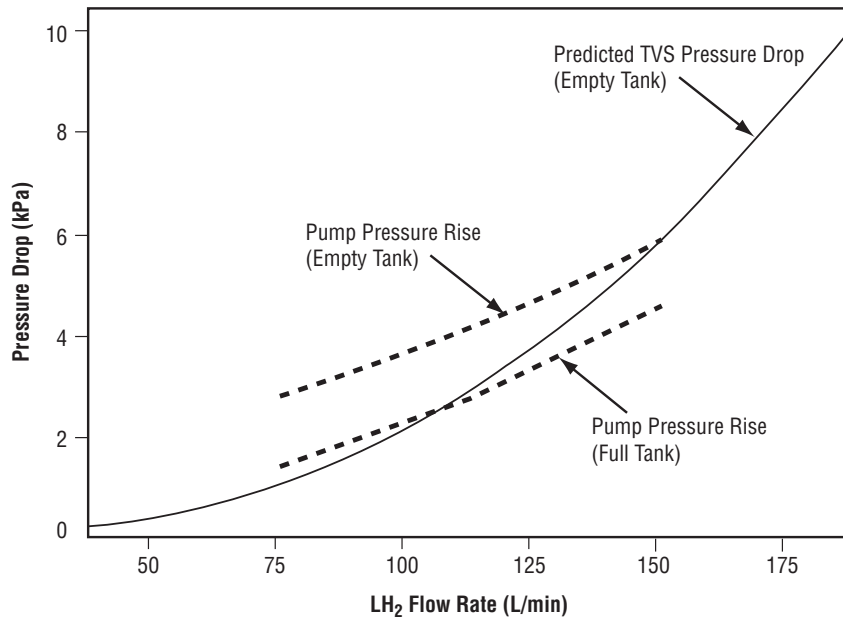


Figure 31. Predicted and measured LH₂ spray injection system pressure loss based on water flow test results.

The pressure drop on the cold side of the heat exchanger was evaluated during the cold shock testing with LN₂ (fig. 32). As LN₂ chilled the heat exchanger and spray bar (hot side), GHe was flowed through the vent or cold side and the pressure drop measured. The loss coefficient was defined based on the test data and is compared with the analytical prediction in figure 33. The measured data are 15 to 25 percent higher than predicted, probably due to entrance and exit losses not accounted for in the analytical model. There was no evidence of leakage; however, the spray tubes were displaced from the original positions due to thermal contraction. The tubing was subsequently spot welded to existing metal retainer straps to prevent further displacement.



Figure 32. Spray bar LN₂ test.

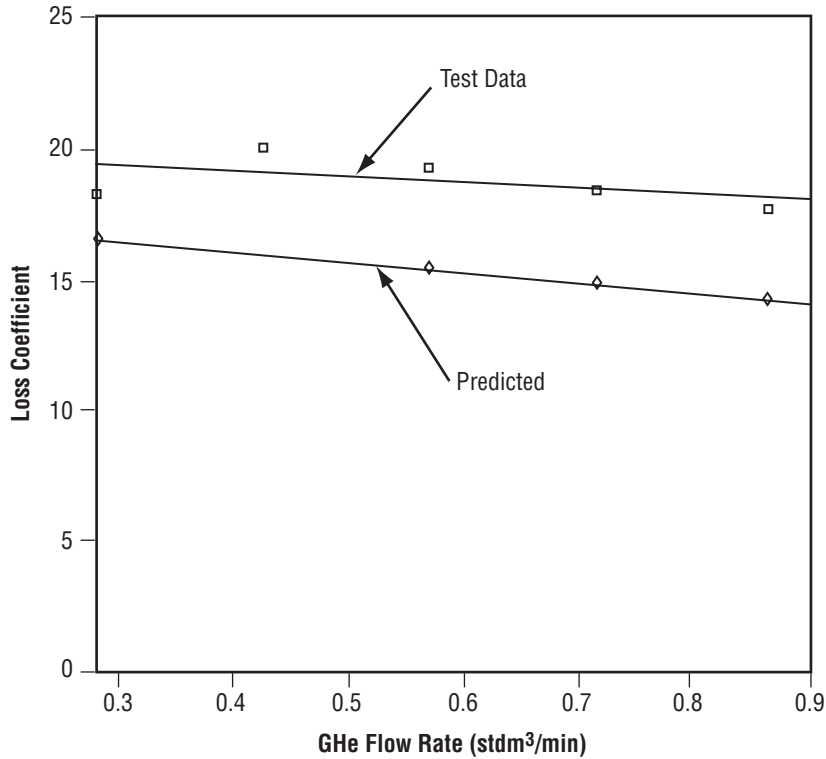


Figure 33. Vent tube loss coefficient prediction and test comparison.

Cryogenic shock and leak tests were performed on the component box assembly. The component box was filled with LN₂ and the assembly then pressurized to 413.4 kPa/m² (60 psig) proof pressure. The LN₂ was then drained; the box was returned to ambient temperature and pressurized to 275.6 kPa/m² (40 psig) with helium to measure leakage across the welds, Deutsch connectors, pipe plugs, and flange seals. No leakage was indicated by a mass spectrometer. Furthermore, no leakage into the box was observed after the internal pressure was reduced to 0.138 kPa/m² (0.02 psia).

The only instrumentation component test activity involved calibration of the recirculation line turbine flowmeter (see sec. 4.5) with water. The flowmeter testing was performed with the actual line inlet and outlet geometries (diameter, bend radii, and angle) and indicated ≈3.785 L/min (1 gal/min) per 4.45-Hz signal output.

6. SPRAY BAR THERMODYNAMIC VENT SYSTEM PERFORMANCE ANALYTICAL MODELING

A transient analytical model of the TVS within the MHTB LH₂ tank was formulated to characterize performance. The model, written in FORTRAN 77 programming language, can be run on various platforms with a FORTRAN compiler. The model is described herein; however, further details, example results, and the computer program listing are presented in reference 3. Individual thermal-fluid models of the heat exchanger, spray manifold and injection tubes, recirculation pump, and tank were developed and verified independently before being integrated into the transient TVS model. Each thermal-fluid model input is described in sections 6.1 through 6.4.

6.1 Heat Exchanger

The heat exchanger model is based on a generalized two-phase cryogenic propellant dump model developed to evaluate the Space Shuttle main propulsion system cryogenic propellant dump/vacuum inerting operations performance.⁴ It is a multinode finite difference model that simulates two-phase flow in a quasi-steady-state mode. The model uses the fluid properties at the spray manifold inlet, including total enthalpy, as the input to the first node. The total enthalpy at the exit can then be calculated based on the First Law of Thermodynamics. The total enthalpy at the exit and an assumed mass flow rate are used to determine the exit static pressure which is determined by an iterative process. With the flow assumed choked at the exit, the exit static pressure is increased incrementally until the maximum entropy is achieved (sonic flow), or until it becomes greater than the back pressure (subsonic flow). From the calculated exit pressure, the other exit fluid properties of the last node and the total pressure loss between the heat exchanger inlet and outlet can then be calculated and the inlet fluid properties determined.

Sections 6.1.1 through 6.1.3 provide the equations used in the heat exchanger model.

6.1.1 Fluid Quality at Heat Exchanger Outlet

The outlet static pressure is calculated, assuming choked or sonic flow (maximum entropy). Equations (1)–(4) are solved simultaneously for the liquid quality of the fluid at the outlet:

$$h_o = h_i + \frac{\dot{Q}}{\dot{m}} + \Delta Ha \quad (1)$$

$$V_o = \frac{\dot{m}}{\rho_o A} \quad (2)$$

$$\rho_o = \frac{1}{\frac{1}{(\rho_L)_o} + Y_o \left[\frac{1}{(\rho_V)_o} - \frac{1}{(\rho_L)_o} \right]} \quad (3)$$

$$h_o = (1 - Y_o)(h_L)_o + Y_o(h_V)_o + \frac{V_o^2}{2g_cJ} \quad (4)$$

where the following fluid properties are based on the outlet static pressure:

$(h_L)_o$ = outlet liquid enthalpy

$(h_V)_o$ = outlet vapor enthalpy

$(\rho_L)_o$ = outlet liquid density

$(\rho_V)_o$ = outlet vapor density

\dot{Q} = total heat transfer rate to a specific node

ΔH = change in height of the line between inlet and outlet

$a = \frac{g}{g_c}$ = ratio of environmental acceleration to Earth's gravitational constant

\dot{m} = mass flow rate

A = cross-section flow area

J = unit conversion constant

h_I = inlet total enthalpy

h_o = outlet total enthalpy

ρ_o = outlet total density

V_o = outlet fluid velocity

Y_o = outlet fluid quality.

With the outlet quality, the total entropy can then be calculated using the following equation:

$$\{(S)_o = (1 - Y_o)(S_L)_o + Y_o(S_V)_o\}_{\max} \quad (5)$$

where

$(S_L)_o$ = outlet liquid entropy

$(S_V)_o$ = outlet vapor entropy.

Iteration of the above outlet equations can be performed to obtain the maximum entropy and the outlet static pressure.

6.1.2 Two-Phase Pressure Loss in Heat Exchanger

To calculate the two-phase pressure loss (momentum and friction) between the heat exchanger inlet and outlet, the Lockhart-Martinelli correlation is used. The outlet pressure is

$$p_o = (p_S)_o + (p_D)_o . \quad (6)$$

The total pressure loss term is further defined as

$$\Delta p_T = \Delta p_m + \Delta p_f , \quad (7)$$

where

Δp_m = pressure loss due to momentum change

Δp_f = pressure loss due to frictional forces.

The momentum pressure loss is defined as

$$\Delta p_m = \frac{\dot{m}}{g_c A} (V_o - V_i) . \quad (8)$$

The frictional pressure loss is defined as

$$\Delta p_f = \frac{144K}{2\bar{\rho}_L g_c} \left[\frac{\dot{m}(1-\bar{Y})}{A} \right]^2 \Phi_L^2 , \quad (9)$$

where

$K = \left(f \frac{L}{D} \right)$ = line loss coefficient

$\bar{\rho}_L$ = average liquid density between the inlet and outlet

\bar{Y} = average total liquid quality between the inlet and outlet

$\Phi_L = f(X)$ = Lockhart-Martinelli correlation factor.

The Lockhart-Martinelli correlation is approximately defined as

$$\Phi_L^2 = 1 + \frac{1}{X} + \frac{1}{X^2} . \quad (10)$$

X is defined as

$$X = \left(\frac{\bar{\mu}_L}{\bar{\mu}_V} \right)^{0.1} \left(\frac{1-\bar{Y}}{\bar{Y}} \right)^{0.9} \left(\frac{\bar{\rho}_V}{\bar{\rho}_L} \right)^{0.5} , \quad (11)$$

where

$\bar{\rho}_V$ = average vapor density between the inlet and outlet
 $\bar{\mu}_L$ = average liquid viscosity between the inlet and outlet
 $\bar{\mu}_V$ = average vapor viscosity between the inlet and outlet.

6.1.3 Forced Convection Heat Transfer

The heat transfer equations used in the steady-state model are given in equations (12)–(18). Two-phase heat transfer is defined with the correlation proposed by John C. Chen:⁵

$$\frac{\dot{Q}}{A} = [h_{FC}F + h_{NB}S]\Delta T , \quad (12)$$

where

$$h_{FC} = 0.023 \left(\frac{DG}{\mu_L} \right)^{0.8} \left(\frac{\mu_L C_L}{k_L} \right)^{0.4} \left(\frac{k_L}{D} \right) \quad (13)$$

$$h_{FZ} = 0.00122 \frac{k_L^{0.79} C_L^{0.45} \rho_L^{0.49} g_c^{0.25} \Delta T^{0.24} \Delta P^{0.75}}{\sigma^{0.5} \mu_L^{0.29} \lambda^{0.24} \rho_v^{0.24}} \quad (14)$$

$$F = f(X) \quad (15)$$

$$Re_L = \frac{DG(1-Y)}{\mu_L} \quad (16)$$

$$\Delta T = T_W - T_S \quad (17)$$

$$\Delta p = \frac{\Delta T \rho_V \lambda}{T_S} , \quad (18)$$

where

- μ = viscosity
- G = mass flow rate per unit area
- C = specific heat
- Re = Reynolds number
- λ = latent heat of vaporization
- σ = surface tension
- k = thermal conductivity
- A = area
- \dot{Q} = total heat transfer rate
- F = Reynolds number factor
- h_{FC} = forced convection heat transfer coefficient
- h_{NB} = nucleate boiling heat transfer coefficient
- S = suppression factor
- X = Martinelli parameter
- T_W = wall temperature
- T_S = spray temperature
- D = line diameter.

The single-phase heat-transfer correlation used in the model (liquid and superheated gas) is

$$\frac{\dot{Q}}{A} = h\Delta T \quad (19)$$

$$h = 0.023 \left(\frac{DG}{\mu_L} \right)^{0.8} \left(\frac{\mu_L C_L}{k_L} \right)^{0.4} \left(\frac{k_L}{D} \right) . \quad (20)$$

6.2 Spray Manifold and Injection Tube

Fluid is recirculated from the MHTB tank to the spray manifold and injection tubes that spray it back into the tank ullage and liquid. A one-dimensional, incompressible fluid dynamic model was developed to determine the pressures in the spray manifold and injection tubes, and the spray flow rates and velocities exiting the injection orifices. The manifold model is described below.

6.2.1 Spray Manifold

The spray manifold model calculates the manifold pressure drop and determines the pressure at the spray injection tube inlets (fig. 34). The model accounts for the frictional pressure drop in the manifold, and pressure losses resulting from flow turning and contraction at the manifold exit. From the Bernoulli equation:

$$\frac{(p_{SM})_i}{\rho} + \frac{V_{SM}^2}{2g_c} + az_i = \frac{(p_{SM})_o}{\rho} + \frac{V_{SM}^2}{2g_c} + az_o + (h_L)_{SM} , \quad (21)$$

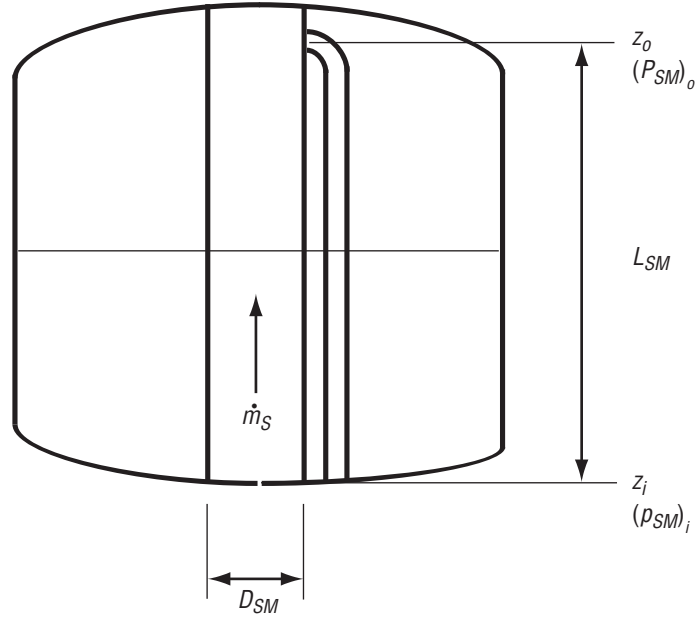


Figure 34. Spray manifold analytical model.

where

$(p_{SM})_i$ = spray manifold inlet pressure

$(p_{SM})_o$ = spray manifold outlet pressure

V_{SM} = velocity in the spray manifold

z_i, z_o = inlet and outlet elevations

$a = \frac{g}{g_c}$ = acceleration ratio.

The total head loss is defined as

$$h_{L_{SM}} = K_{SM} \frac{V_{SM}^2}{2g_c} \quad (22)$$

The total loss coefficient, K_{SM} , is given by

$$K_{SM} = (K_f)_{SM} + (K_b)_{SM} + (K_c)_{SM} \quad (23)$$

and includes

$$(K_f)_{SM} = f_{SM} \left(\frac{L}{D} \right)_{SM} \quad (\text{spray manifold frictional loss coefficient}) \quad (24a)$$

$$(K_b)_{SM} = f_{SM} \left(\frac{L_e}{D} \right) \quad (90^\circ \text{ bend resistance at manifold exit}) \quad (24b)$$

$$(K_c)_{SM} = 0.5 \left[1 - \left(\frac{D_{SI}}{D_{SM}} \right)^2 \right] \quad (\text{sudden contraction at manifold exit}), \quad (24c)$$

where

$L_{SM} = z_o - z_i =$ spray manifold length

$L_e =$ bend equivalent length

$D_{SI} =$ spray injection tube ID

$D_{SM} =$ spray manifold ID

$f_{SM} =$ friction coefficient in spray manifold is obtained from

$$f_{SM} = \frac{1}{4 \left\{ \log_{10} \left[\frac{\varepsilon / D}{3.7} + \frac{2.51}{Re \sqrt{0.0056 + \frac{0.5}{(Re)^{0.32}}}} \right] \right\}^2}, \quad Re > 3,000$$

$$f_{SM} = \frac{64}{Re}, \quad Re \leq 3,000 . \quad (25)$$

Equation (21) can be solved for the spray manifold outlet pressure:

$$(p_{SM})_o = (p_{SM})_i - K_{SM} q_{SM} - \rho a L_{SM} , \quad (26)$$

where the dynamic pressure in the spray manifold, q_{SM} , is given by

$$q_{SM} = \rho \frac{V_{SM}^2}{2g_c} = \frac{1}{2\rho g_c} \left(\frac{\dot{m}_S}{A_{SM}} \right)^2 . \quad (27)$$

6.2.2 Spray Injection Tube

The spray injection tube model is multinode, which assigns a node to each orifice (fig. 35). The Bernoulli equation is first applied to determine the pressure downstream of the 90° inlet bend (at the straight section inlet):

$$p_i = (p_{SM})_o - q_i (K_b)_{SI} . \quad (28)$$

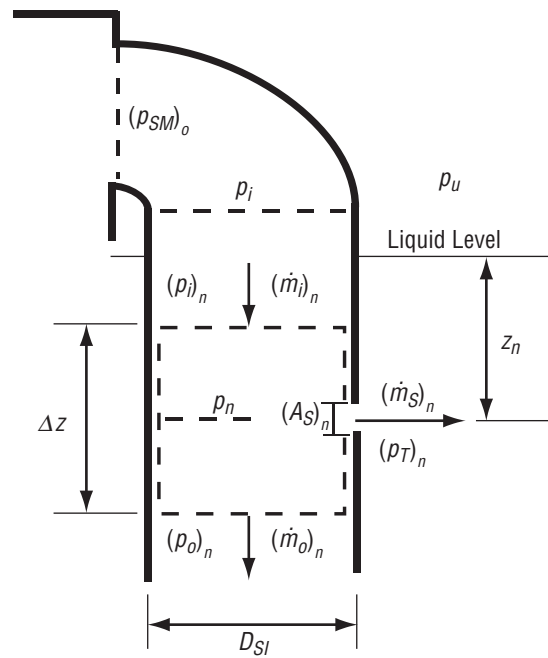


Figure 35. Spray injection tube analytical model.

In equation (28), $(K_b)_{SI}$ is the 90° bend resistance and q_i is the inlet dynamic pressure given by

$$q_i = \frac{1}{2\rho g_c} \left(\frac{\dot{m}_i}{A_{SI}} \right)^2 , \quad (29)$$

where

A_{SI} = flow area of an injection tube

\dot{m}_i = mass flow rate in each tube (equal to the flow rate in the manifold divided by the number of tubes).

The spray injection tube straight section is divided into 45 equal nodes corresponding to the 45 spray orifices. Each node has a pressure and a mass flow rate at the inlet (i), center (n), and outlet (o) of the node. The outlet pressure and mass flow rate of one node is therefore the inlet pressure and mass flow rate from the preceding node:

$$(p_i)_n = (p_o)_{n-1} \quad (29a)$$

$$(\dot{m}_i)_n = (\dot{m}_o)_{n-1} . \quad (29b)$$

The Bernoulli equation is applied successively from inlet to center and from center to outlet to determine the pressure at the center and outlet of a node n .

From inlet to center,

$$p_n = (p_i)_n + \rho a \frac{\Delta z}{2} - K_f (q_i)_n , \quad (30)$$

where

Δz = nodal length

K_f = frictional loss coefficient.

From center to outlet,

$$(p_o)_n = p_n + \rho a \frac{\Delta z}{2} - K_f (q_o)_n , \quad (31)$$

where the outlet dynamic pressure $(q_o)_n$ of node n is given by

$$(q_o)_n = \frac{1}{2\rho g_c} \left[\frac{(\dot{m}_o)_n}{A_{SI}} \right]^2 . \quad (32)$$

The mass flow rate at node n outlet, $(\dot{m}_o)_n$, is obtained from

$$(\dot{m}_o)_n = (\dot{m}_i)_n - (\dot{m}_S)_n . \quad (33)$$

$(\dot{m}_S)_n$ in equation (33) is the spray flow rate calculated from an incompressible flow relation

$$(\dot{m}_S)_n = (A_S)_n \sqrt{\frac{2\rho g_c [p_n - (p_T)_n]}{K_S}} . \quad (34)$$

In equation (34), K_S is the loss coefficient of an orifice in a duct given by

$$K_S = \left[\frac{1}{C_d} - \frac{A_S}{A_T} \right]^2 , \quad (35)$$

where

$$\begin{aligned} C_d &= \text{discharge coefficient } (C_d = 0.8) \\ A_S/A_T &= \text{ratio of the orifice to the tank area } (A_S/A_T = 0). \end{aligned}$$

Thus, K_S is determined to be 1.56.

The tank pressure $(p_T)_n$ at node n is calculated as

$$\begin{aligned} (p_T)_n &= p_U \quad (\text{ullage nodes}) \\ &= p_U + p_L g z_n, \quad (\text{liquid nodes}) , \end{aligned} \quad (36)$$

where

$$z_n = \text{distance from the liquid surface to node } n.$$

6.2.3 Spray Manifold and Injection Tube Model Algorithm

The computer model flow chart of the spray manifold and injection tube is given in section 3.2.2 of reference 3. The model is initiated with an estimated pump flow rate and then calculates the pressures and mass flow rates at each node. Using the computed pressure and spray flow rate of the last node N , the model then calculates the tank pressure corresponding to that last node by solving the incompressible flow relation of equation (34):

$$(p_T)_{N, calc} = p_N - \frac{K_S}{2\rho g_c} \left(\frac{\dot{m}_s}{A_s} \right)_N^2 \quad (37)$$

Next, $(p_T)_{N, calc}$ is compared with $(p_T)_N$ obtained from the ullage pressure and hydrostatic head (eq. (36)). If the pressures are not equal within a specified tolerance (0.00689 kPa or 0.001 psi), a new pump flow rate is estimated and the process repeated until convergence on $(p_T)_N$ is achieved.

6.3 Recirculation Pump

The TVS LH₂ recirculation is provided by a centrifugal pump that is a constant output pressure device since it imparts kinetic pressure to the fluid due to rotation. Consequently, the pump pressure rise (Δp_p) is only a function of rotation speed (N) and tip velocity (U):

$$U = \frac{\pi D_m N}{720} \quad (38)$$

where

D_m = impeller diameter.

The fluid horsepower required by the pump flow (\dot{m}), raised to Δp_p pressure, is

$$HP_o = \frac{\dot{m} \Delta p_p}{\eta_p \rho} \quad (39)$$

where

η_p = pump mechanical efficiency.

The pump operating speed then changes as a result of the energy absorbed by the fluid and the power supplied to the pump through a power source. The instantaneous rate of change in pump operating speed is

$$\frac{dN}{dt} = \left(\frac{HP_I - HP_o}{I_p N} \right) 6.0185 \times 10^5 \quad (40)$$

where

I_p = polar moment of inertia of the pump
 HP_I = input power to the pump.

Integration of the pump acceleration results in the pump speed at any given time:

$$N = (N)_{IC} + \int \left(\frac{dN}{dt} \right) dt . \quad (41)$$

By specifying the initial pump speed at zero, a pump-start transient can be simulated.

The pump head versus flow rate data presented in figure 36 were provided by the pump manufacturer, Barber-Nichols. The curve was fitted with a polynomial function to provide the head coefficient (ψ) as a function of the flow coefficient (ϕ):

$$\psi = 0.52889 - 1.4956\phi + 47.819\phi^2 - 485.93\phi^3 + 1,633.9\phi^4 - 1,833.5\phi^5 . \quad (42)$$

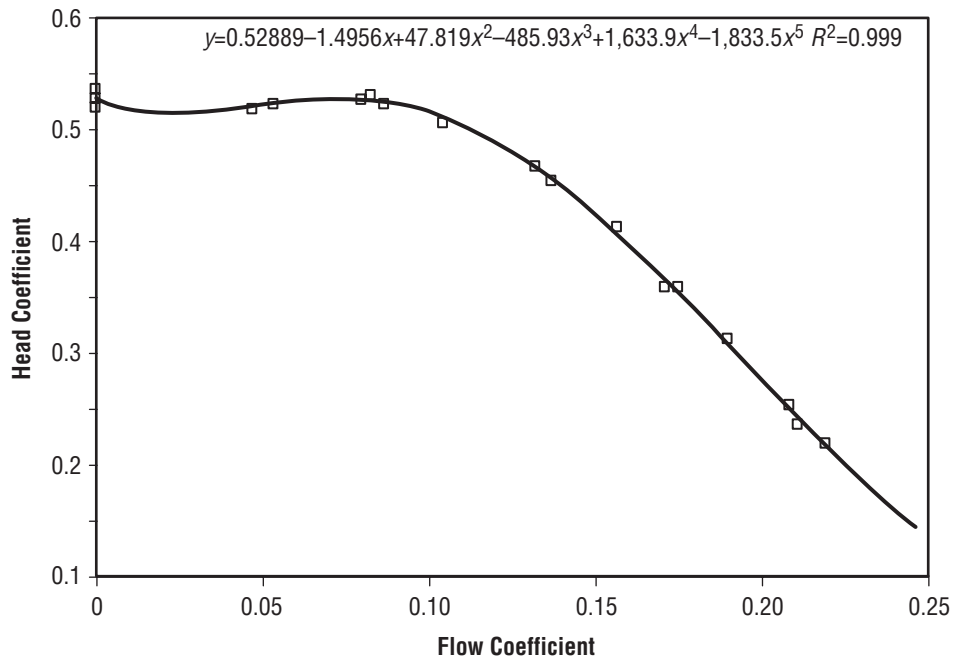


Figure 36. LH₂ recirculation pump head-flow curve.

The flow coefficient (ϕ) is obtained from test data in terms of the flow rate (in gallons per minute) and the pump speed as

$$\phi = \frac{\text{gal/min}}{0.0531N} . \quad (43)$$

The pump head is calculated from the pump speed and head coefficient:

$$H = 4.507 \times 10^{-6} N^2 \psi . \quad (44)$$

The pump pressure rise is then obtained as

$$\Delta p_p = \frac{\rho H}{144} . \quad (45)$$

The integrated pump model requires the pump design flow rate (Q_D) and speed (N_D) in order to define the other operating characteristics (HP_p, I_p) required by the model.

6.4 Tank Thermodynamics

The tank model is a lumped model consisting of four control volumes (fig. 37): (1) Ullage, (2) tank wall, (3) liquid on the tank wall, and (4) bulk liquid. The thermal model of each control volume is described in sections 6.4.1 through 6.4.4.

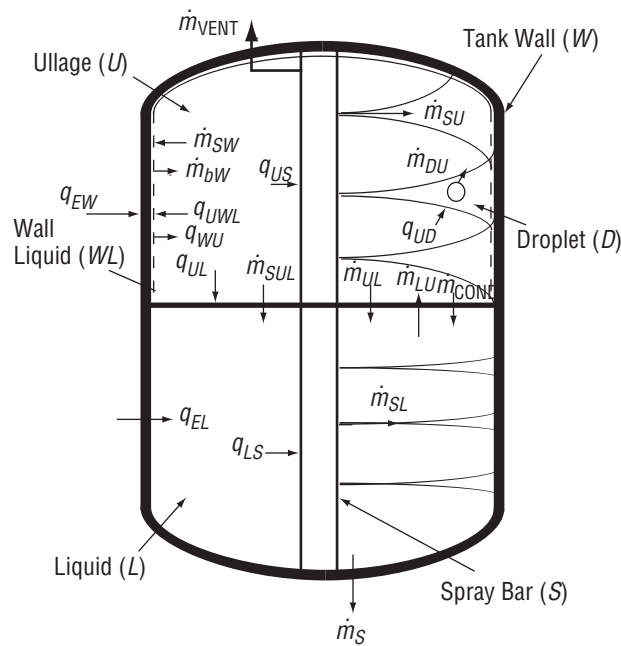


Figure 37. Tank thermal analytical model.

6.4.1 Ullage

The ullage thermal model applies conservation of mass and energy to determine the ullage pressure, temperature, and mass (fig. 38). From conservation of mass, the change in the ullage mass (M_U) is due to all masses entering and leaving the ullage control volume:

- (1) Droplet evaporation rate in the ullage (\dot{m}_{DU})
- (2) Boiling rate of the liquid on the tank wall (\dot{m}_{bW})
- (3) Bulk liquid boiling rate (\dot{m}_{LU}), or ullage condensation (\dot{m}_{UL})
- (4) Liquid surface condensation (\dot{m}_{COND}):

$$\frac{dM_U}{dt} = \dot{m}_{DU} + \dot{m}_{bW} + \dot{m}_{LU} - \dot{m}_{UL} - \dot{m}_{COND} . \quad (46)$$

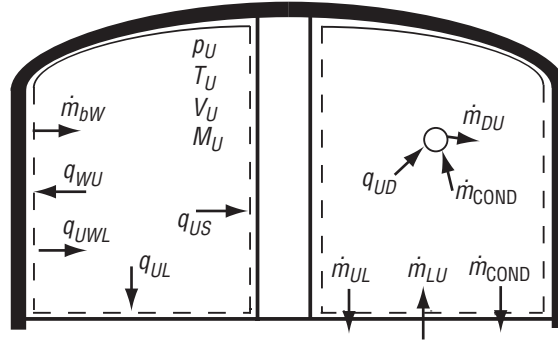


Figure 38. Ullage thermal analytical model.

These mass flow rates are defined in section 6.4.6. The ullage mass is obtained by integrating its time rate of change with respect to time:

$$M_U = (M_U)_{IC} + \int \left(\frac{dM_U}{dt} \right) dt . \quad (47)$$

From conservation of energy, the change in the ullage temperature (T_U) is the result of

- (1) Heat transfer to the ullage (q_U)
- (2) Work done on the ullage (w_U)
- (3) Energy added to the ullage by incoming and leaving masses ($ENTH_U$):

$$\frac{dT_U}{dt} = \frac{q_U - w_U - ENTH_U - c_{VU} T_U \frac{dM_U}{dt}}{M_U c_{VU}} . \quad (48)$$

The terms in equation (48) are defined as follows:

- (1) $q_U = q_{WU} - q_{UWL} - q_{UL} - q_{UD} - q_{US}$ (heat transfer to ullage),

where

q_{WU} = heat transfer rate between the tank wall and ullage:

$$\begin{aligned} |q_{WU}| &> 0 \text{ for a dry wall} \\ &= 0 \text{ for a wet wall} \end{aligned}$$

q_{UWL} = heat transfer rate between the ullage and wall liquid:

$$\begin{aligned} |q_{UWL}| &= 0 \text{ for a dry wall} \\ &> 0 \text{ for a wet wall} \end{aligned}$$

q_{UL} = heat transfer rate between the ullage and bulk liquid

q_{UD} = heat transfer rate between the ullage and liquid droplet

q_{US} = heat transfer rate between the ullage and (unsubmerged) spray bar.

The above heat transfer rates are defined in section 6.4.5.

$$(2) \quad w_U = p_U \frac{dV_U}{dt} \quad (\text{work done on ullage}),$$

where the change in the ullage volume $\left(\frac{dV_U}{dt}\right)$ is equal and opposite to the change in the liquid and wall liquid volumes:

$$\frac{dV_U}{dt} = -\frac{dV_L}{dt} - \frac{dV_{WL}}{dt} . \quad (49)$$

$$(3) \quad \text{ENTH}_U = \left(\frac{dM_U}{dt}\right) h_{gsat} ,$$

where

$$h_{gsat} = h_{sat}(p_U) = \text{saturated vapor enthalpy of the ullage.}$$

The ullage volume is obtained as the difference between the tank volume and the bulk liquid and wall liquid volumes:

$$V_U = V_T V_L - V_{WL} \quad . \quad (50)$$

Equation (48) is integrated with respect to time to obtain the ullage temperature:

$$T_U = (T_U)_{IC} + \int \left(\frac{dT_U}{dt} \right) dt \quad . \quad (51)$$

With the ullage mass, temperature, and volume determined, the ullage pressure is calculated from the equation of state:

$$p_U = \frac{M_U R_U T_U}{V_U} \quad . \quad (52)$$

6.4.2 Ullage Tank Wall

The tank wall is divided into two sections—one submerged under the liquid and the other facing the ullage. The tank wall facing the bulk liquid is assumed to be at the same temperature as the liquid. Thus, the tank wall thermal model described herein applies to the dry wall section facing the ullage (fig. 39). Since liquid can form on the tank wall as a result of spraying, the model must account for both

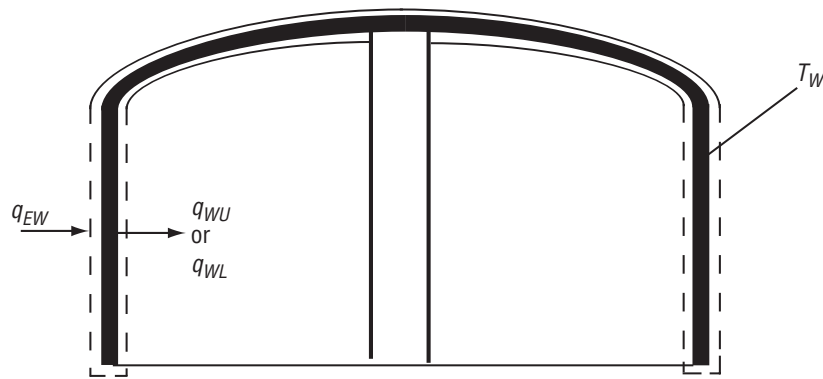


Figure 39. Tank wall thermal analytical model.

dry and wet wall cases.

From conservation of energy, the change in the tank wall temperature is due to:

- (1) Heat input to the wall from the environment (q_{EW})
- (2) Heat transfer rate between the wall and ullage (q_{WU})

$$\begin{aligned} |q_{WU}| &> 0 \text{ for a dry wall} \\ &= 0 \text{ for a wet wall} \end{aligned}$$

(3) Heat transfer rate between the wall and liquid on the wall (q_{WL}),

$$\begin{aligned} |q_{WL}| &= 0 \text{ for a dry wall} \\ &> 0 \text{ for a wet wall} \end{aligned}$$

$$\frac{dT_W}{dt} = \frac{q_{EW} - q_{WU} - q_{WL}}{M_W c_{pW}} . \quad (53)$$

Section 6.4.5 defines the heat transfer rate computations. Equation (53) can be integrated with respect to time to obtain the tank wall temperature:

$$T_W = (T_W)_{IC} + \int \left(\frac{dT_W}{dt} \right) . \quad (54)$$

6.4.3 Wetted Wall Liquid

The wetted wall liquid thermal model is also governed by the laws of conservation of mass and energy (fig. 40). From conservation of mass, the change in the wall liquid mass (M_{WL}) is equal to the difference between the liquid mass reaching the wall and the liquid mass boiled off from the wall:

$$\frac{dM_{WL}}{dt} = \dot{m}_{SW} - \dot{m}_{bW} , \quad (55)$$

where

\dot{m}_{SW} = spray flow rate reaching the wall

\dot{m}_{bW} = liquid boiloff rate from the wall.

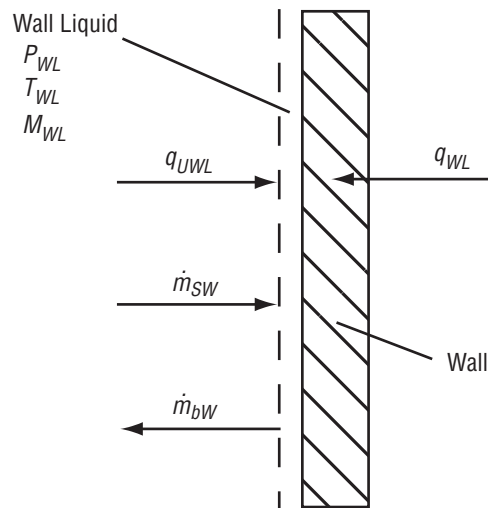


Figure 40. Tank wall liquid thermal analytical model.

These mass flow rate computations are defined in section 6.4.6. Equation (55) can be integrated to obtain the wall liquid mass:

$$M_{WL} = (M_{WL})_{IC} + \int \left(\frac{dM_{WL}}{dt} \right) dt . \quad (56)$$

From conservation of energy, the change in the wall liquid temperature (T_{WL}) is the result of heat transfer to the wall liquid and sensible energy added to the spray to raise its temperature (T_{SW}) to the wall liquid temperature. Heat transfer to the wall liquid includes the heat transfer rate between the wall and wall liquid (q_{WL}), and heat transfer rate between the ullage and wall liquid (q_{UWL}):

$$\frac{dT_{WL}}{dt} = \frac{q_{WL} + q_{UWL} - \dot{m}_{SW} c_{pL} (T_{WL} - T_{SW})}{M_{WL} c_{pWL}} . \quad (57)$$

These heat transfer rates are defined in section 6.4.5. Equation (57) can be integrated to obtain the wall liquid temperature:

$$T_{WL} = (T_{WL})_{IC} + \int \left(\frac{dT_{WL}}{dt} \right) dt . \quad (58)$$

The wall liquid vapor pressure is then obtained from the thermodynamic database as

$$p_{WL} = p_{sat}(T_{WL}) . \quad (59)$$

The volume rate of change of the wall liquid is determined from equation (55) as

$$\frac{dV_{WL}}{dt} = \frac{1}{\rho_{WL}} \frac{dM_{WL}}{dt} , \quad (60)$$

where

$$\rho_{WL} = \rho_{sat}(T_{WL}) = \text{wall liquid density.}$$

Equation (60) is integrated to obtain the wall liquid volume

$$V_{WL} = (V_{WL})_{IC} + \int \left(\frac{dV_{WL}}{dt} \right) dt . \quad (61)$$

6.4.4 Bulk Liquid

The bulk liquid thermal model is a single node, as opposed to a multinode model, since (1) mixing will destratify the liquid and create a uniform bulk, and (2) the uncertainties in heat transfer modeling do not seem to justify the added complexities of a multinode model. Like the previously described modeling, the liquid thermal model is based on the laws of conservation of mass and energy. From conservation of mass, the change in the liquid mass must be balanced by a change in the ullage mass and any mass vented overboard (fig. 41):

$$\frac{dM_L}{dt} = \dot{m}_{SL} + \dot{m}_{SUL} + \dot{m}_{COND} + \dot{m}_{UL} - \dot{m}_{LU} - \dot{m}_S - \dot{m}_V, \quad (62)$$

where

- \dot{m}_{SL} = liquid spray flow rate into the bulk liquid
- \dot{m}_{SUL} = liquid spray unevaporated droplet flow rate
- \dot{m}_{COND} = liquid surface condensation flow rate
- \dot{m}_{UL} = ullage condensation flow rate
- \dot{m}_{LU} = liquid boiloff rate
- \dot{m}_S = pump flow rate
- \dot{m}_V = overboard vent flow rate.

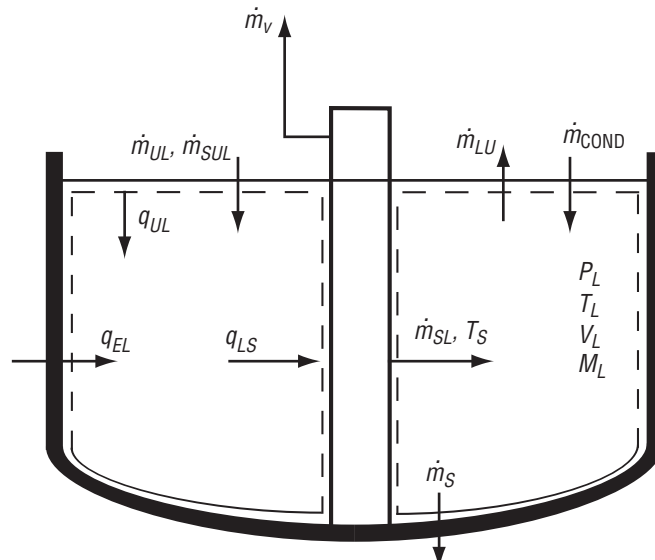


Figure 41. Bulk liquid thermal analytical model.

The liquid mass is obtained by integrating its time rate of change:

$$M_L = (M_L)_{IC} + \int \left(\frac{dM_L}{dt} \right) dt . \quad (63)$$

From conservation of energy, the change in liquid temperature is caused by

- (1) Heat transfer to the liquid
- (2) Heat added by the unevaporated droplets
- (3) Sensible energy added to the liquid spray to raise its temperature (T_S) to the liquid temperature
- (4) Latent heat of vaporization of the liquid:

$$\frac{dT_L}{dt} = \frac{q_L + \dot{m}_{SUL} c_{pL} (T_d - T_L) - \dot{m}_{LU} (h_{fg})_L - \dot{m}_{SUC} c_{pL} (T_L - T_S)}{M_L c_{pL}} . \quad (64)$$

The heat transfer rate to the liquid (q_L) is given by

$$q_L = q_{EL} + q_{UL} - q_{LS} , \quad (65)$$

where

q_{EL} = heat added to the liquid by the environment

q_{UL} = heat transfer rate between the ullage and liquid

q_{LS} = heat transfer rate between the liquid and (submerged) spray bars.

These heat transfer rates are defined by the equations in section 6.4.5. Equation (64) is integrated with respect to time to give the liquid temperature

$$T_L = (T_L)_{IC} + \int \left(\frac{dT_L}{dt} \right) dt . \quad (66)$$

The liquid vapor pressure is obtained from the thermodynamic database as

$$p_L = p_{\text{sat}} @ T_L . \quad (67)$$

The liquid volume rate of change is determined from the rate of change of the liquid mass:

$$\frac{dV_L}{dt} = \frac{1}{\rho_L} \frac{dM_L}{dt} , \quad (68)$$

where

$\rho_L = \rho_{\text{sat}} @ T_L$ = liquid density.

Equation (68) is integrated to give the liquid volume:

$$V_L = (V_L)_{IC} + \int \left(\frac{dV_L}{dt} \right) dt . \quad (69)$$

6.4.5 Heat Transfer

This section defines the heat transfer rates that are determined from the energy balances defined in sections 6.4.1 to 6.4.4. These heat transfer rates can be divided into two groups—free convection and forced convection. Free convection is the dominant heat transfer mode in the ullage and liquid, while forced convection characterizes liquid droplet heat transfer in the ullage.

The convection heat transfer rate is generally defined as

$$q = hA\Delta T , \quad (70)$$

where

h = convection heat transfer coefficient

A = heat transfer surface area

ΔT = temperature difference between the heat source and sink.

The heat transfer coefficient is obtained from the Nusselt number (Nu) as

$$h = \left(\frac{k_F}{L_c} \right) Nu , \quad (71)$$

where

k_F = fluid thermal conductivity

L_c = surface characteristic length.

The Nusselt number is a function of the Rayleigh number (Ra) defined as

$$Ra = \frac{g\beta\Delta TL_c^3 \rho^2 c_p}{\mu k} , \quad (72)$$

where

g = acceleration

β = thermal expansion coefficient

$\beta = \frac{1}{T_f}$ for gas and $\frac{1}{\rho} \left(\frac{\partial \rho}{\partial T} \right)_p$ for liquid

L_c = characteristic length

ρ = density

c_p = specific heat at constant pressure

μ = dynamic viscosity

k = thermal conductivity.

All properties must be evaluated at the film temperature (T_f), which is defined as the average of the fluid and surface temperatures.

6.4.5.1 Free Convection. Two free convection heat transfer correlations are used in the model. The first is a free convection correlation for interior surfaces of vertical ducts, vertical plates and cylinders, and horizontal cylinders:⁶

$$Nu = 0.555Ra^{0.25} + 0.447 . \quad (73)$$

This correlation is used to calculate the heat transfer coefficients:

- (1) Between the ullage and wall (h_{UW})
- (2) Between the ullage and bulk liquid (h_{UL})
- (3) Between the ullage and wall liquid (h_{UWL})
- (4) Between the ullage and (unsubmerged) spray bars (h_{US})
- (5) Between the bulk liquid and (submerged) spray bars (h_{LS}).

The characteristic length for h_{UW} , h_{UL} , and h_{UWL} is the internal tank diameter while that of h_{US} and h_{LS} is the spray bar diameter.

The second correlation is the McAdams correlation for free convection of vertical surfaces in the turbulent range:⁷

$$Nu = 0.13Ra^{1/3} . \quad (74)$$

This correlation is used to calculate the heat transfer coefficient between the wall and liquid (h_{WL}). Because of the one-third power in Ra , h_{WL} can be obtained without defining the characteristic length, thereby removing the uncertainty in determining the wall liquid layer.

6.4.5.2 Forced Convection. The forced convection heat transfer coefficient between the ullage and liquid droplets (h_{UD}) is based on a McAdams recommended correlation for flow over a sphere:⁸

$$Nu = 0.3125 Re^{0.602} \quad (75)$$

The Reynolds number (Re) of the spray flow is defined as

$$Re = \frac{\rho Vel_D D_D}{\mu} \quad (76)$$

where

- Vel_D = droplet velocity in the ullage
- D_D = droplet diameter, assumed to be equal to the orifice diameter
- ρ = density of the ullage gas
- μ = viscosity of the ullage gas.

Since the droplet diameter and velocity vary with the orifice size, the droplet heat transfer coefficient must be determined for each orifice. The total droplet heat transfer rate is obtained by summing the droplet heat transfer rates from each orifice:

$$q_{\text{drop}} = \sum_{i=1}^n (n_{\text{drop}})_i (q_{\text{drop}})_i \quad (77)$$

where

$(n_{\text{drop}})_i$ = number of droplets sprayed from orifice i into the ullage. This is given by

$$(n_{\text{drop}})_i = \frac{(\dot{m}_{SU})_i D_{\text{CHAR}}}{2\rho_D (V_D)_i (Vel_D)_i} \quad (78)$$

where

- $(\dot{m}_{SU})_i$ = spray flow rate into the ullage from orifice i
 $(V_D)_i$ = droplet volume from orifice i
 $(Vel_D)_i$ = droplet velocity from orifice i
 ρ_D = droplet density
 D_{CHAR} = a characteristic length determined empirically.

By correlating the TVS model with the GRC subscale ullage pressure collapse data (see sec. 3.1 of ref. 2), the characteristic length was determined to be one-fourth of the tank diameter.

6.4.6 Mass Transfer

This section defines the mass-transfer rates computed with the mass balance equations of section 6.4.1 through 6.4.4, which includes:

- (1) Bulk liquid boiling (\dot{m}_{LU})
- (2) Liquid boiling from the tank wall (\dot{m}_{bW})
- (3) Liquid droplet evaporation in the ullage (\dot{m}_{DU})
- (4) Liquid spray falling into the bulk liquid (\dot{m}_{SUL}) or accumulating on the tank wall (\dot{m}_{SW})
- (5) Ullage condensation (\dot{m}_{UL})
- (6) Liquid surface condensation (\dot{m}_{COND}).

6.4.6.1 Bulk Liquid Boiling. Bulk liquid boiling occurs when the liquid vapor pressure is equal to the tank ullage pressure. It can be the result of heat transfer to the liquid and/or pressure decay in the ullage. It must also include sensible energy added to the liquid spray to increase its temperature to the liquid temperature.

If $p_L = p_U$,

$$\begin{aligned}
 \dot{m}_{LU} &= \frac{1}{(h_{fg})_L} [q_L - \dot{m}_{SLC} p_L (T_L - T_S)], \quad \frac{dp_U}{dt} > 0 \\
 &= \frac{1}{(h_{fg})_L} \left[q_L - \dot{m}_{SLC} p_L (T_L - T_S) - M_{LC} p_L \left(\frac{\partial T}{\partial p} \right)_{\text{sat}} \left(\frac{dp_U}{dt} \right) \right], \quad \frac{dp_U}{dt} < 0 . \quad (79)
 \end{aligned}$$

A polynomial fit of the LH₂ saturation temperature versus pressure curve was obtained and its derivative taken to give an expression for $\left(\frac{\partial T}{\partial p} \right)_{\text{sat}}$:

$$\left(\frac{\partial T}{\partial p}\right)_{sat} = 0.37781 - 4.9170 \times 10^{-3} p_L + 21.7623 \times 10^{-6} p_L^2 . \quad (80)$$

If the ullage pressure increases above the liquid vapor pressure, boiling stops, $\dot{m}_{LU} = 0$, if $p_L < p_U$.

6.4.6.2 Wall Liquid Boiling. Wall liquid boiling from the tank wall follows the same mechanism as bulk liquid boiling.

If $p_{WL} = p_U$,

$$\begin{aligned} \dot{m}_{bW} &= \frac{1}{(h_{fg})_L} [q_{WL} + q_{UWL} - \dot{m}_{SW} c_{pL} (T_{WL} - T_{SW})], \quad \frac{dp_U}{dt} > 0 \\ &= \frac{1}{(h_{fg})_L} \left[q_{WL} + q_{UWL} - \dot{m}_{SW} c_{pL} (T_{WL} - T_{SW}) - M_{WL} c_{pL} \left(\frac{\partial T}{\partial p}\right)_{sat} \left(\frac{dp_U}{dt}\right) \right], \quad \frac{dp_U}{dt} < 0 . \end{aligned} \quad (81)$$

where

$$\left(\frac{\partial T}{\partial p}\right)_{sat} = 0.37781 - 4.9170 \times 10^{-3} p_{WL} + 21.7623 \times 10^{-6} p_{WL}^2 . \quad (82)$$

If $p_{WL} < p_U$, $\dot{m}_{bW} = 0$.

As with bulk boiling, wall liquid boiling includes heat transfer to the wall liquid and sensible energy added to the spray liquid to increase its temperature to the wall liquid temperature.

6.4.6.3 Liquid Droplet Evaporation in the Ullage. Liquid droplets in the ullage start boiling once the subcooled liquid spray attains saturation. From an energy balance on the liquid droplets, an expression for the liquid droplet boiling is obtained:

$$\dot{m}_{DU} = \frac{1}{(h_{fg})_U} [q_{UD} - \dot{m}_{SU} c_{pL} (T_{U_{sat}} - T_S)] , \quad (83)$$

where

$T_{U_{sat}} = T_{sat}(p_U)$ = ullage saturation temperature.

6.4.6.4 Liquid Spray Falling Into Bulk Liquid or Accumulating on Tank Wall. The unevaporated sprayed mass in the ullage is assumed to fall into the bulk liquid with normal gravity, or to accumulate on the tank wall with zero gravity (fig. 42); i.e.,

$$\begin{aligned} \dot{m}_{SUL} &= \dot{m}_{SU} - \dot{m}_{DU} \quad (\text{for normal gravity}) \\ \dot{m}_{SW} &= \dot{m}_{SU} - \dot{m}_{DU} \quad (\text{for zero gravity}). \end{aligned} \quad (84)$$

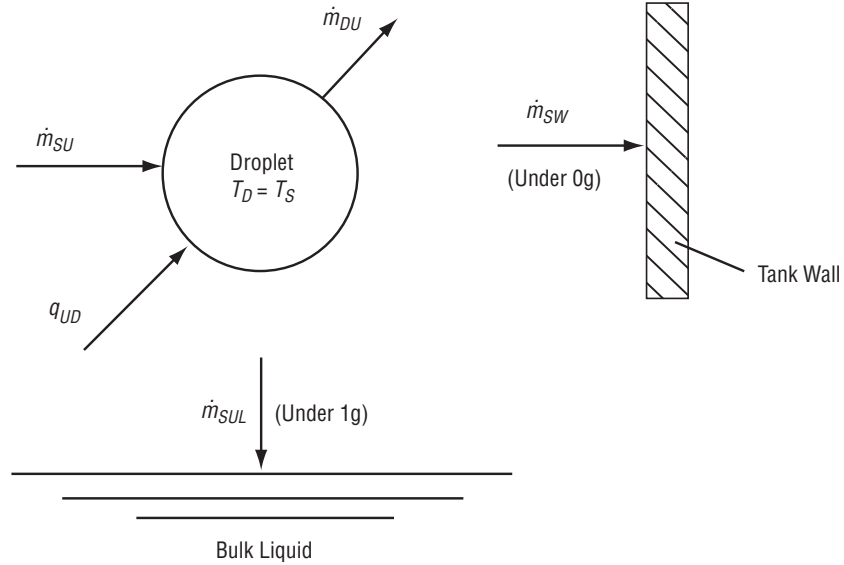


Figure 42. Droplet evaporation analytical model.

6.4.6.5 Ullage Condensation. Ullage condensation occurs whenever the ullage temperature is equal to the saturation temperature corresponding to the ullage pressure. It is the result of ullage heat removal by the liquid droplet, when there is spraying, and by the wall liquid (fig. 43):

$$\dot{m}_{UL} = \frac{q_{UD} + q_{UL} + q_{UWL}}{(h_{fg})_U} \quad T_U = T_{sat}(p_U) . \quad (85)$$

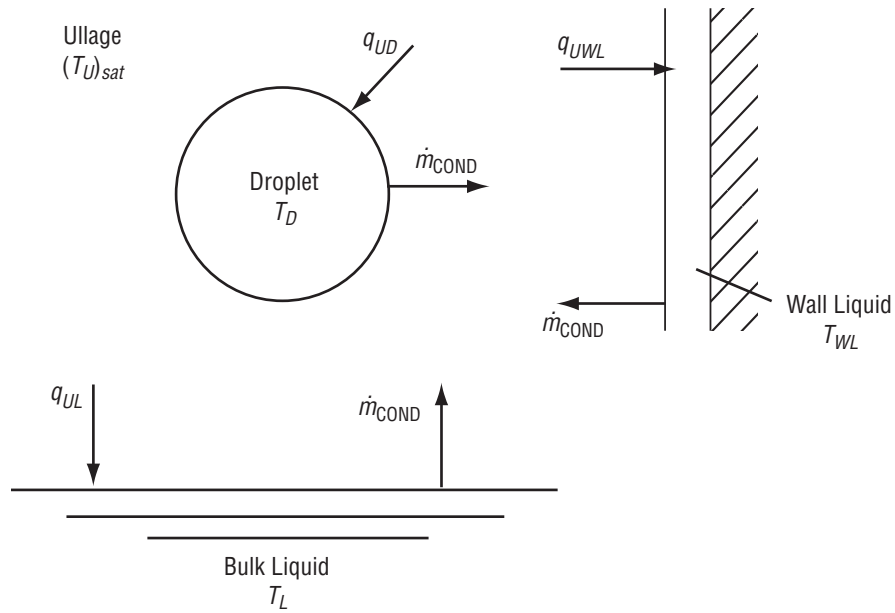


Figure 43. Ullage condensation analytical model.

6.4.6.6 Liquid Surface Condensation. When helium is not present to act as a barrier to mass transfer, bulk liquid mixing during pump operation induces condensation on the liquid surface. This condensation rate is controlled by the heat transfer rate from the ullage to the liquid:

$$\dot{m}_{\text{COND}} = \frac{q_{UL}}{(h_{fg})_U} . \quad (86)$$

7. TEST FACILITY AND PROCEDURES

7.1 Facility Description

Testing was performed at the MSFC east test area thermal vacuum facility, test stand 300 (fig. 44). The test article and facility flow schematic is presented in figure 45. The primary vacuum chamber is cylindrical in shape and has usable internal dimensions of 5.5 m (18 ft) in diameter and 7.9 m (26 ft) in height. Personnel access is through a small side-entry door, but the chamber lid is removable for installation of large test articles (fig. 46). The chamber pumping train consists of a single-stage GN₂ ejector, three mechanical roughing pumps (rated at 140 L/s (300 ft³/min each) with blowers rated at 610 L/s (1,300 ft³/min each), and two 1.2-m (48-in) oil diffusion pumps rated at 95,000 L/s (200,000 ft³/min N₂ each). LN₂ cold walls provide cryopumping and thermal conditioning capability and are comprised of five parallel zones, which totally surround the usable chamber volume with a surface emissivity of ≈ 0.95 . The facility systems in combination with the test article shroud enable simulation of orbit environmental conditions by providing vacuum levels of 10^{-8} torr and a temperature range of 80 to 320 K (140 to 576 °R) on test article exterior surfaces.

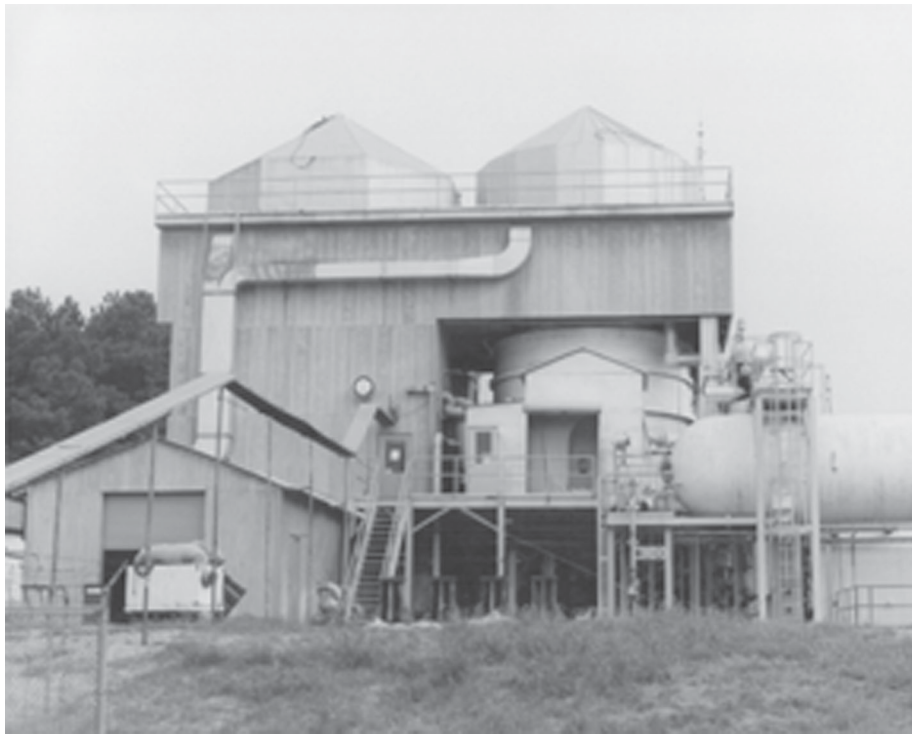


Figure 44. MSFC east test area thermal vacuum facility, test stand 300.

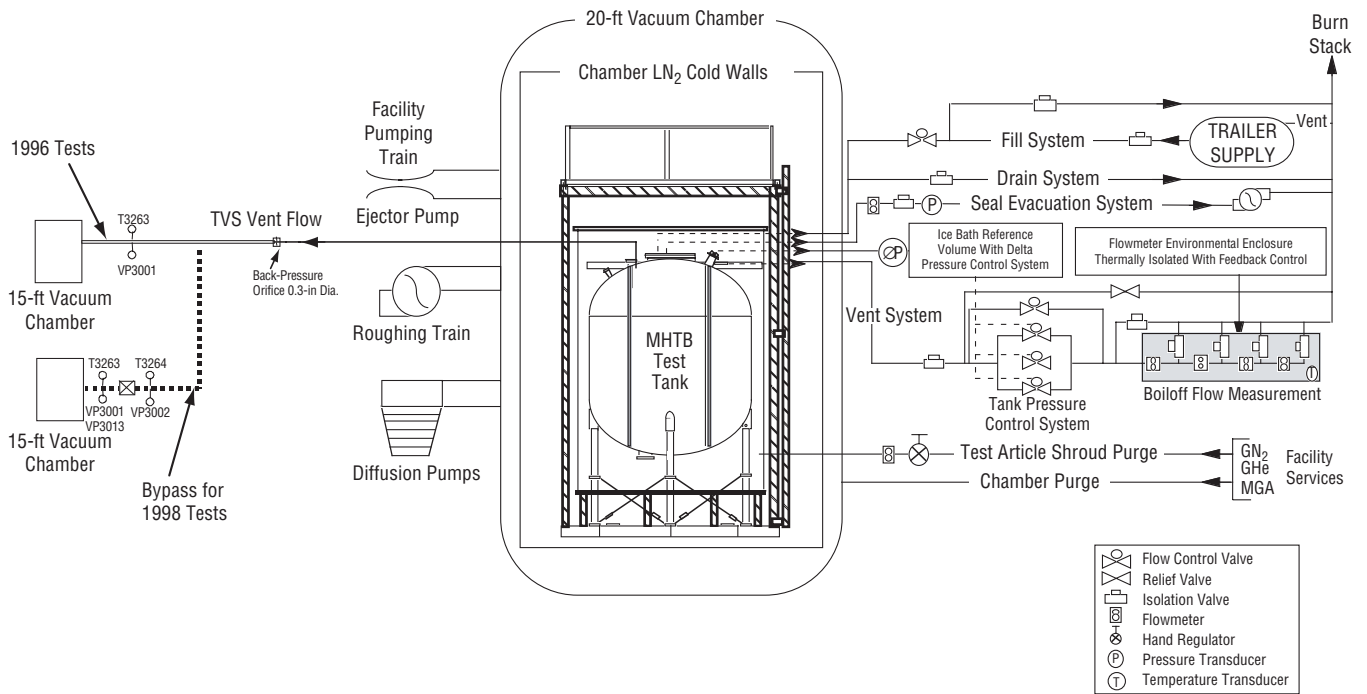


Figure 45. MHTB and test stand 300 simplified flow schematic.

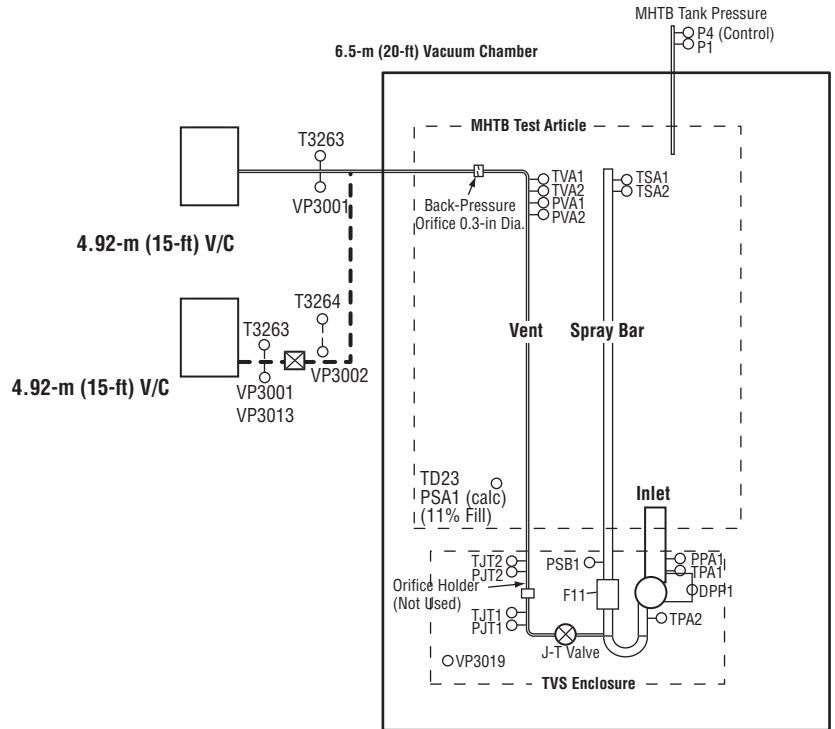


Figure 46. MHTB installation in test stand 300 vacuum chamber.

A vacuum-jacketed fill and drain system provides cryogenic fluid servicing to and from the test article. All facility lines have welded construction to ensure that vacuum conditions are not compromised by leakage. During the heat leak measurement phases of the testing, conditions within the MHTB were controlled utilizing the facility subsystems described below:

- A tank pressure control subsystem maintained the MHTB ullage pressure at the required steady-state conditions. The system was composed of several flow control valves, located in the vent line, each of which was regulated through a closed-loop control system. This control loop manipulated the valve positions based on a comparison of the measured tank ullage pressure and the desired setpoint. An MKS Instruments, Inc., Baratron 0–133 kPa (0–19 psia) absolute pressure transducer (accuracy of ± 0.02 percent) and an MKS ΔP transducer (1 torr or 133 Pa head with an accuracy of ± 0.04 percent) located outside the vacuum chamber were used to measure ullage pressure. The system can maintain setpoints ranging from 110–124 kPa (16–18 psia) with a tolerance of ± 0.00689 kPa (± 0.001 psi) for the orbital simulation conditions.
- Hydrogen boiloff flow instrumentation was located in the vent downstream of the flow control valves. During orbit hold simulations, one of three mass flowmeters (MKS model 258C, Hastings model 200, and Hastings model H–3MS) was used. These meters spanned flow ranges of zero to 280 stdL/min, zero to 50 stdL/min, and zero to 1 stdL/min with accuracies of ± 0.8 , ± 1 , and ± 1 percent of full scale, respectively. To minimize ambient temperature effects on measurement accuracy, the flowmeter system was placed within a containment box and equipped with a temperature-controlled purge, which maintained the box interior at constant temperature, typically 306 K (550 °R).
- A seal evacuation system—MKS model 258 with a range of zero to 1,000 stdcm³/min or zero to 61 stdcm³/min—captured and measured any boiloff gases leaked past the 61-cm (24-in) primary tank seal. This setup was required to prevent degradation of vacuum levels during orbit simulation and ensure boiloff measurement accuracy. The vacuum system, connected to the volume between the tank’s primary and secondary seals, maintained a seal volume pressure of 133 Pa (1 torr) or less.

During TVS testing, the hydrogen vented out of the MHTB through the J-T valve and was routed into an adjacent 4.57-m (15-ft) vacuum chamber, which enabled venting into a moderate vacuum (fig. 45). Additionally, the facility and MHTB instrumentation that directly supported the TVS operation is shown in figure 47.



TVS Enclosure		MHTB Test Article		Vent	
PPA1	Pump inlet pressure (kPa/m ²)	TSA1	Spray bar liquid temperature (K)	T3263	Vent line pressure 4.92-m V/C (K)
TPA1	Pump inlet temperature (K)	TSA2	Spray bar liquid temperature (K)	VP3001	Vent line pressure at T3263(torr); also 4.93 V/C pressure during nonventing periods
DPP1	Pump delta pressure (kPa/m ²)	TVA1	Vent line exit temperature (K)	HSA17	4.92-m V/C volume temperature (K)
TPA2	Pump outlet temperature (K)	TVA2	Vent line exit temperature (K)		
PSB1	Flowmeter pressure (kPa/m ²)	PVA1	Vent line exit pressure (kPa/m ²)		
F11	Flowmeter (L/min)	PVA2	Vent line exit pressure (kPa/m ²)		
TJT1	Vent line temperature (K)	P4	Tank ullage pressured (kPa/m ²)		
TJT2	Vent line temperature (K)	P1	Tank ullage pressured (kPa/m ²)		
PJT1	Vent line pressure (kPa/m ²)	TD23	Tank fluid temperature at 11% fill		
PJT2	Vent line pressure (kPa/m ²)	PSA1	Calculated tank saturation pressure based on TD23		
VP3019	Enclosure pressure (torr)				
PUP1	Pump on/off (high/low)				
VAV1	Valve open/closed (high/low)				

Figure 47. Spray bar TVS instrumentation schematic.

7.2 Test Procedures

The procedures and approaches utilized for test preparations, orbital heat leak measurement, TVS performance evaluation, and posttest operations are summarized in sections 7.2.1 through 7.2.4.

7.2.1 Pretest Operations

Prior to testing, the vacuum chamber and environmental shroud were purged at a trickle rate with dry GN₂ for ≈5 days to reduce the MLI dewpoint to acceptable levels. Prior to tanking, the environmental shroud purge ring was operated at a GN₂ flow rate of 5 kg/min (11.2 lb/min) with a dewpoint not to exceed -54 °C (-65 °F). Also, the seal evacuation system was activated and held steady

at a level of 2×10^{-2} torr or less. Approximately 2 hr prior to tanking, dry GN_2 (followed by gaseous hydrogen (GH_2)) with a dewpoint of -54 °C (-65 °F) was used for the internal purge/conditioning operations of the test tank, fill/drain line, and vent line. This purge and conditioning process was accomplished using charge-vent cycles during which the tank was pressurized to ≈ 103 kPa (15 psig) with GH_2 , held for ≈ 1 min, and then vented back down to near atmospheric pressure. This sequence was typically repeated 15–20 times prior to loading LH_2 into the MHTB. The test tank is designed to withstand an internal vacuum against external atmospheric pressure enabling vacuum cycling with GH_2 pressurization, a much more efficient method of conditioning. However, the vacuum cycling approach was not implemented during this test program.

The vacuum chamber was pumped down to a steady-state vacuum level (10^{-6} torr or less) and the MLI allowed time to evacuate prior to initiating tank fill. The test article was then filled with LH_2 to the 85-percent level while maintaining the ullage pressure ≈ 103.4 torr (2 psi) above the required setpoint pressure. Completion of fill to the 95-percent level was then accomplished with the automated pressure control subsystem activated to control the ullage ≈ 25.8 torr (0.5 psi) above the setpoint. Once filling was completed, the transition to the test setpoint pressure occurred over a period of 10–20 min. Several hours were required to saturate and equilibrate the tanked LH_2 at the setpoint pressure.

7.2.2 Tank Heat Leak Testing

Boiloff testing was conducted to determine the ambient heat leak into the MHTB tank and to set up consistent initial conditions for each of the TVS tests. The first test series (series 1) was conducted with the vacuum chamber LN_2 cold walls operating to produce a minimum heat leak condition. The second series (series 2) was conducted without the LN_2 cold walls, thereby providing a high ambient heat leak condition and reducing test costs. Also, additional hardware (an axial jet mixer/TVS system), was installed, which also added heat leak in the second series. The heat leak test procedures are summarized herein and further details are presented in reference 1.

Steady-state vacuum and thermal conditions, within both the chamber and MLI, were achieved before the on-orbit heat leak test phase. The four criteria that had to occur simultaneously for steady-state thermal conditions were as follows:

(1) Interstitial MLI pressures had to be 10^{-5} torr or less to preclude a transient convective heat transfer effect as the insulation pressure continues to drop. A vacuum chamber pressure of 10^{-6} torr or less was required to ensure an adequate vacuum within the insulation.

(2) Insulation temperatures (MLI and SOFI) had to be in a steady-state condition with the MLI surface temperature at the prescribed setpoint (305 K for the TVS testing) imposed by the environmental shroud. Insulation equilibrium was assumed to exist once temperature transients of no more than 0.55 K in 6 hr are measured in any section of the insulation system.

(3) Thermal equilibrium of the LH_2 had to be maintained through precise ullage pressure control during the low heat leak orbital simulation. Ullage pressure was maintained at a setpoint in the range of 110.316 to 124.106 kPa (16 to 18 psia) with a tolerance of ± 0.00689 kPa (± 0.001 psi). In the TVS testing, the boiloff rate was recorded for 6 hr after steady state was achieved.

(4) The vented ullage gas temperature had to increase with time (positive slope), indicating that the tank dome was in thermal equilibrium; i.e., the dome was no longer cooling and contributing to the vented gas enthalpy.

When performing the heat leak cryogenic storage testing, either a loss of ullage pressure control or the chamber vacuum can significantly increase unproductive test time. Each 6.89 kPa (1 psi) of LH₂ subcooling, due to a sudden reduction in ullage pressure, requires 30 hr for recovery to saturation, due to the low heat leak conditions. Similarly, a sudden increase in vacuum chamber pressure (10⁻⁴ torr or above) can dramatically alter the MLI temperatures, necessitating several days to recover the steady-state temperature profile. Therefore, great care was taken to ensure tight control of the tank ullage and vacuum chamber pressures.

An RGA (residual gas analyzer) system was used to record vacuum chamber and MLI interstitial gas composition periodically during steady-state simulated orbit hold periods. RGA sampling intervals varied depending on the vacuum chamber pressure stability and assisted in determining the source of any chamber pressure variations; e.g., test article or chamber leakage, or outgassing. Species possibilities included H₂O, N₂, O₂, CO₂, and the foam-blowing agent CFC-11 (CCL₃F molecular weight of 137.4).

7.2.3 Thermodynamic Vent System Performance Testing

The TVS spray bar was evaluated at MHTB tank fill levels of 90, 50, and 25 percent. As mentioned earlier, two test series were conducted—series 1 with a low heat leak condition and series 2 with an elevated heat leak. For each fill level, after the heat leak testing was completed, the tank was locked up and allowed to self-pressurize until the ullage pressure attained the maximum tank pressure setpoint of 138 kPa (20 psia). Upon reaching this pressure, the recirculation pump was turned on and mixing continued until the ullage pressure reached 131 kPa (19 psia), the minimum setpoint. After the pump was turned off at the minimum setpoint, the tank was allowed to self-pressurize and the cycle began again. As depicted in figure 14, this automated operation cycle continued until the bulk liquid saturation condition (PSA1) attained the lower setpoint. The J-T vent valve was then opened and the spray bar heat exchanger utilized to extract thermal energy from the tank contents. Thereafter, the J-T valve was opened each time the pump cycled on and the spray bar heat exchanger was used to extract thermal energy from the bulk liquid.

As described in section 2.4, a liquid temperature sensor was used to monitor the bulk liquid saturation conditions relative to the measured ullage pressure and as inputs to the TVS controller. The sensor, TD23, is at the 11.5-percent fill level or 53.3 cm (21 in) above the tank bottom and is considered to be representative of the bulk liquid temperature. The TD23 temperature output was converted to an equivalent saturation pressure (termed PSA1) and compared with the ullage pressure, P4.

Most of the TVS testing was conducted with a GH₂ ullage; however, helium pressurization is frequently considered to provide appropriate conditions for engine restart sequences. Furthermore, the amount of GHe could increase with each pressurization cycle since primarily GH₂ is vented through the TVS in multiple engine restart missions. The partial pressure effects of the GHe would be expected to influence the number and duration of the TVS cycles. Therefore, at the end of the second test series, GHe was injected into the ullage and the effects of a noncondensable gas on TVS performance were evaluated.

7.2.4 Posttest Operations

Chamber repressurization conditions after the TVS tests were selected primarily to protect the test article and facility. Also, following a test, the MHTB was not held under vacuum conditions for needlessly long periods. The chamber and test article were warmed and repressurized within 8–12 hr after testing was concluded. Chamber repressurization occurred slowly (≈ 30 min) with dry GN₂ (dew-point -54 °C (-65 °F)) in the 4 – 27 °C (40 – 80 °F) temperature range. To prevent water condensation, repressurization was initiated only after the vacuum chamber cold walls and all test article insulation (SOFI/MLI) had reached ≈ 15.5 °C (60 °F). The dry GN₂ was also used to accomplish purge and inerting operations for the test article volume and all service lines. These operations were designed so that the test article was not subjected to a positive differential pressure in excess of 344 kPa (50 psid). Typically, the GN₂ shield purge remained on for 24 hr after completion of testing.

8. TEST RESULTS

8.1 Tank Heat Leak Data Reduction

As mentioned earlier, boiloff testing was conducted to determine the heat leak into the MHTB tank and to establish consistent conditions prior to each of the two TVS test series. During the heat leak test periods, digital data were recorded at sample rates ranging from 1 to 0.017 Hz. These raw data were then time averaged over the steady-state period of interest to obtain measurement values required to calculate thermal performance. The heat input was expressed as an energy balance across the tank boundary by equating the total measured boiloff with the sum of heat flow through the insulation, the penetrations, and the rate of energy storage, if any:

$$\dot{Q}_{\text{boiloff}} = \dot{Q}_{\text{insulation}} + \dot{Q}_{\text{conduction}} + \frac{\Delta U_{\text{system}}}{\Delta t} . \quad (87)$$

The terms \dot{Q}_{boiloff} and $\dot{Q}_{\text{conduction}}$ were defined using the measured test data. The thermal storage term $\frac{\Delta U_{\text{system}}}{\Delta t}$ (energy flow into or out of the test tank wall, insulation, and fluid mass) is driven by the fluid saturation temperature which varies as ullage pressure fluctuates. The storage term was eliminated since the ullage pressure was maintained within a tight control band about the setpoint ($\pm 9 \times 10^{-4}$ kPa). The insulation performance term, $\dot{Q}_{\text{insulation}}$, could then be determined from the other measured quantities.

The \dot{Q}_{boiloff} term represents the total energy vented as boiloff and includes both the evaporated fluid latent heat and the sensible heat absorbed while the vented gas passes through the ullage space, also known as ullage superheat:

$$\dot{Q}_{\text{boiloff}} = \dot{m} h_{fg} \left(\frac{\rho_{\text{satliq}}}{\rho_{\text{satliq}} - \rho_{\text{satvap}}} \right) + \dot{m} (h_{\text{vent}} - h_{\text{satvap}}) . \quad (88)$$

The latent heat term of the above equation contains a density ratio that accounts for the increased volume of gas, and hence remaining energy, resulting from the decrease in liquid volume due to boiloff losses.

The solid conduction term, $\dot{Q}_{\text{conduction}}$, represents the heat flow through the tank support legs, vent assembly, and other fluid lines. Solid conduction was evaluated by using the Fourier heat transfer equation (ref. 8) with known structural geometry, material properties, and a measured temperature difference as follows:

$$\dot{Q}_{\text{conduction}} = \left(\frac{A}{L}\right) \int_{T_{\text{cold}}}^{T_{\text{hot}}} k(T) dT . \quad (89)$$

The heat input through the insulation, $\dot{Q}_{\text{insulation}}$, was then assessed using experimental data, fluid properties, and the assumption that energy storage in tank material and fluid are defined as follows:

$$\dot{Q}_{\text{insulation}} = \dot{Q}_{\text{boiloff}} - \dot{Q}_{\text{conduction}} . \quad (90)$$

8.2 Tank Heat Leak

The results from the heat leak (boiloff) testing are presented in table 2 for the three fill levels utilized in the TVS testing (90, 50, and 25 percent). As expected, the heat leak was slightly less with reduced fill levels. The high heat leak series 2 testing (51–54 W) was ≈ 2.7 times greater than in the low heat leak series 1 (19–20 W) due to the installation of additional hardware for testing of an axial jet mixer, and because the vacuum chamber LN₂ cold walls were not operated. As one would expect, increasing the heat leak had a significant influence on the vent cycle operation, which is described in section 8.3.

Table 2. Measured MHTB tank heat leak.

Fill Level (%)	Low Heat Leak Test, Series 1 (W)	High Heat Leak Test, Series 2 (W)
90	20.2	54.1
50	18.7	51.0
25	18.8	–

8.3 Thermodynamic Vent System Performance

The TVS was evaluated at 90-, 50-, and 25-percent fill levels in the first test series with low heat leak and at 90- and 50-percent fill levels in the second series with the high heat leak condition. Test results involving destratification, energy extraction, and the presence of noncondensable gases are discussed in sections 8.3.1 through 8.3.4.

8.3.1 Destratification and Pressure Control

Both the low and high heat leak test data confirmed that the spray bar was effective in destratifying both the ullage and liquid for all conditions. The mixer durations for the entire range of conditions tested are presented in table 3. Generally, the mixing durations were shorter when venting occurred due to the heat extraction effect. Also, the mixing durations clearly increased with decreasing fill level at the low heat leak with venting conditions. However, the data at the high heat leak condition were less consistent, and are believed to be due to sometimes erratic J-T valve operation coupled with limited test durations at given conditions. For all tests, the mixer cycle durations ranged from 43 to 535 s, depending on the test conditions. The mixer durations prior to the initiation of venting gradually

increased with time after lockup due to the increasing saturation pressure/temperature. For example, at the 90-percent fill level, the mixer operation duration per cycle increased from 134 s at the beginning to 535 s at the time just prior to the initiation of venting. Representative times between mixing cycles, with and without venting, are listed in table 4. With the low heat leak, the time interval between cycles increased from 57 min at 90-percent fill level to 173 min at 25-percent fill level; i.e., increased with increasing ullage size. With the high heat leak condition, the time between cycles was 25 and 83 min at 90- and 50-percent fill, respectively. In summary, the trends with the low heat leak condition are more reliable and once the J-T venting began, the average TVS duty cycle ranged from 1.25 percent at 90-percent fill level to 1.5 percent at 25-percent fill level.

Table 3. Representative mixing cycle durations.

Fill Level (%)	Tank Heat Leak (W)	Mixing Duration (s)	
		With Venting	Without Venting
90	20.2	43	134–535
50	18.7	71–89	111*
25	18.8	89–167	–
90	54.1	144**	120–470
50	51.0	97*	42–78

* Limited Data Available

** J-T Valve Operated Intermittently

Table 4. Representative times between mixing cycles.

Fill Level (%)	Tank Heat Leak (W)	Minutes Between Mixing Cycles	
		With Venting	Without Venting
90	20.2	57	80–96
50	18.7	145	158
25	18.8	173	–
90	54.1	25	32
50	51.0	83	70

Example temperature-time stratification data for the 50-percent fill level, low heat leak condition is presented in figure 48. Note that the percentages listed with each silicon diode designation represent the fill level corresponding to that sensor position. As expected, during tank lockup, the ullage became significantly stratified. Upon mixer startup, both the liquid and gas temperatures were reduced to within 0.4 K of each other within 86 s.

The preceding results are significant since buoyancy effects impede mixing in normal gravity. In zero gravity, the spray bar would be an even more efficient ullage mixer since there would be no significant gravitational force to pull the sprayed fluid out of the ullage. Also, due to the absence of buoyancy forces within the liquid, liquid mixing would be more effective. The spray bar is also effective in chilling down warm tank walls regardless of propellant position, which would be beneficial in tank fill operations. For example, during the 50-percent fill test illustrated in figure 48, the tank dome cooled ≈ 2 K during spray bar operation.

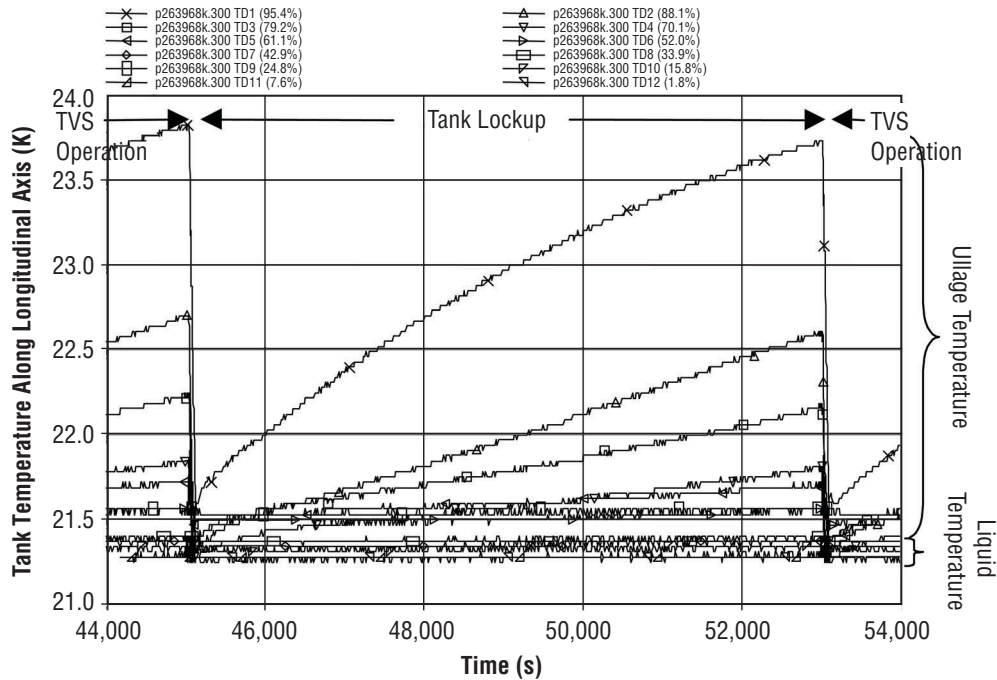


Figure 48. Tank stratification/destratification, 50-percent fill level during series 1.

8.3.2 Liquid Saturation Pressure Rise Rates

As mentioned earlier, tank mixing alone is sufficient to maintain pressure control until the thermal energy absorbed by the propellant increases the saturation pressure to the lower limit of the TVS control band. The rate of increase in liquid saturation pressure is summarized for all test conditions in table 5. This gradual increase in saturation pressure (indicated as PSA1) for the low heat leak series 1 testing is illustrated in figures 49–51 for fill levels of 90, 50, and 25 percent, respectively. For example, in the 90-percent fill test, the propellant was saturated at a pressure level of 112 kPa when the tank was locked up and ≈ 61 hr or 2.5 days elapsed before the saturation pressure increased to the lower vent control limit of 131 kPa and venting began. In the 50-percent fill test tank, lockup occurred with the tank saturated at 122 kPa and ≈ 33 hr or 1.4 days elapsed before the lower vent control limit of 131 kPa was reached. At the 25-percent level, the saturation pressure started at 122 kPa, and 19.4 hr or 0.81 days elapsed before the lower limit of 131 kPa was reached. Thus, the low heat leak saturation pressure rise rates were ≈ 0.3 kPa/hr at the 90- and 50-percent fill levels and ≈ 0.50 kPa/hr at 25-percent fill. Although the low heat leak magnitude varied only slightly with fill level, the saturation level increased much more rapidly at the 25-percent level due to the relatively low liquid mass available to absorb the thermal energy. Also, as illustrated in figure 51, there apparently is a minimum liquid level below which tank mixing alone will not reduce tank pressure beginning with the first mixing cycle; i.e., both the pump and J-T valve begin operation simultaneously.

The high heat leak effects on pressure rise rates are also shown in table 5. The high heat leak saturation pressure rise rates were 2.9 and 3.1 times as fast as in the low heat leak tests at the 90- and 50-percent fill levels, respectively. Since the high heat leak series was ≈ 2.7 times that in low heat leak series, the relative pressure rise rates are reasonable.

Table 5. Liquid saturation pressure rise rates after tank lockup.

Fill Level (%)	Tank Heat Leak (W)	Liquid Saturation Pressure Rise Rate (kPa/hr)
90	20.2	0.31
50	18.7	0.29
25	18.8	0.50
90	54.1	0.89
50	51.0	0.96

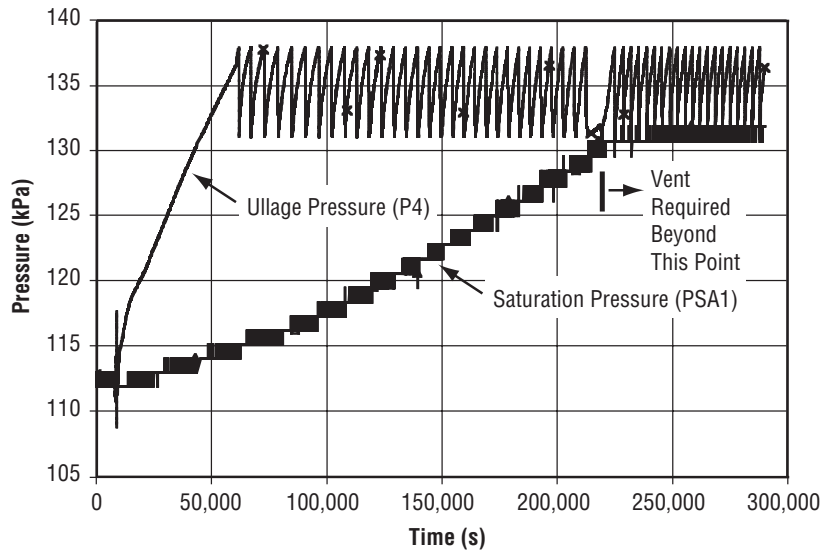


Figure 49. Spray bar performance at 90-percent fill level during series 1.

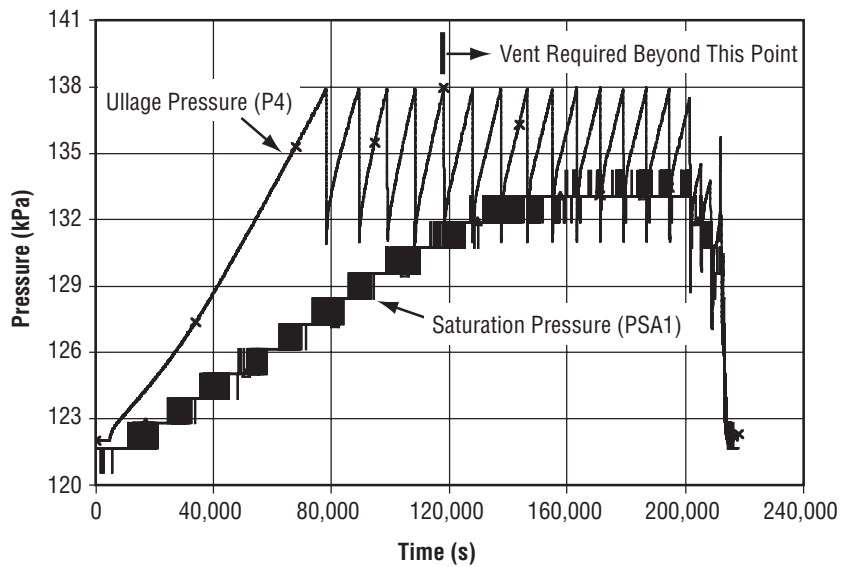


Figure 50. Spray bar performance at 50-percent fill level during series 1.

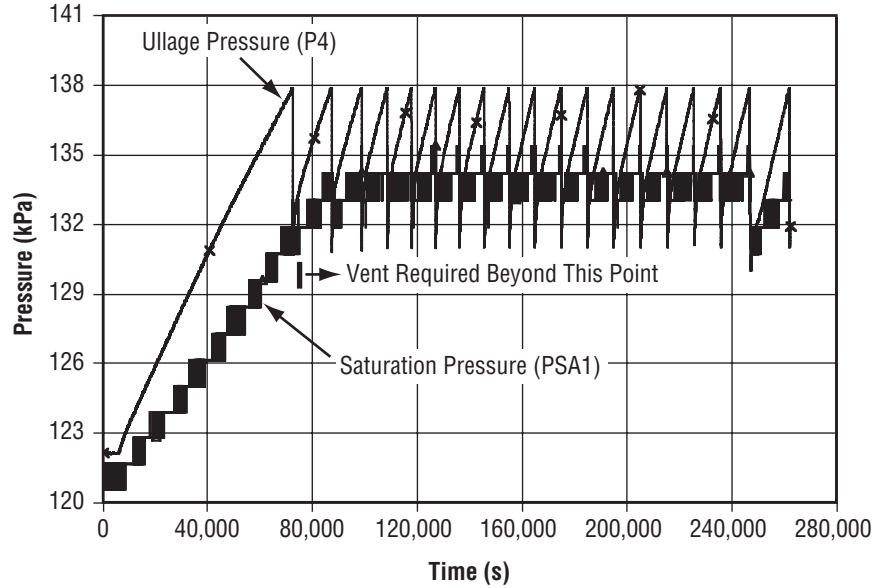


Figure 51. Spray bar performance at 25-percent fill level during series 1.

8.3.3 Heat Energy Extraction

The most important measure of TVS performance is the capability to extract thermal energy from the propellant. Once the propellant is saturated at the lower limit of the TVS pressure control band, the TVS must begin to extract enough energy to offset the tank heat leak into the tank and maintain pressure control. The heat extracted by the vent flow was calculated or derived from the test data using the following equations:

$$\dot{Q}_{\text{vent}} = \dot{m}_{\text{vent}} (h_{\text{out}} - h_{\text{in}})$$

$$\dot{Q}_{\text{ave}} = \dot{Q}_{\text{vent}} \left(\frac{t_{\text{open}}}{t_{\text{total}}} \right), \quad (91)$$

where

- \dot{Q}_{vent} = energy extraction rate while the vent is open
- \dot{m}_{vent} = vent mass flow rate
- h_{out} = TVS outlet enthalpies
- h_{in} = TVS inlet enthalpies.

Given the TVS duty cycle interval (valve open time, t_{open} , divided by the sum of valve open plus valve closed time or t_{total}) for a particular test, the average value of vent heat extraction (\dot{Q}_{ave}) could be computed for each test and enabled a comparison of TVS performance from test to test. The vent mass

flow rate was calculated using the compressible flow equation for a gas through a sonic orifice (the back-pressure orifice) as follows:

$$\dot{m}_{\text{vent}} = \frac{0.14(CdA)p}{\sqrt{T}}, \quad (92)$$

where

- T = orifice inlet temperature
- p = orifice inlet pressure
- CdA = effective orifice flow area.

The assumption that gas was flowing through the back-pressure orifice was verified with the test data which indicated that the heat exchanger completely vaporized the two-phase mixture exiting the J-T valve; i.e., measured inlet temperature at the orifice was always well above tank saturation temperature corresponding to the pressure. Table 6 summarizes the average heat extraction rates for all testing conducted. When comparing the derived heat extraction (\dot{Q}_{ave}) values to the tank heat leak for the same test (table 2), the \dot{Q}_{ave} value is 7- to 21-percent lower than the corresponding tank heat. In reality, the thermal energy removed by the TVS equaled the heat leak into the tank. Otherwise, the tank pressure would not have remained within the prescribed pressure control band and the liquid saturation pressure would have continued to rise.

Table 6. Derived TVS heat extraction data.

Test Series	Fill Level (%)	\dot{Q}_{vent} (W)	\dot{Q}_{ave} (W)	\dot{m}_{vent} (kg/s)
1	90	1,444	15.9	0.0034
1	50	1,486	16.3	0.0035
1	25	1,507	17.5	0.0036
2	90	*	*	*
2	50	2,108	40.6	0.0048

* Hardware problem; not enough J-T cycles to calculate heat extracted

Potential sources for the difference between the derived TVS heat extraction rate and the measured tank heat leak were investigated. One source considered, but ruled out, was instrumentation uncertainties. The error in measured quantities would have to have been much larger than the instrumentation uncertainties to yield the additional enthalpy necessary to increase the derived heat extraction rate to the measured tank heat leak. The most likely candidate involved the method of calculating vent mass flow rate, \dot{m}_{vent} . As seen from table 6, the vent mass flow rate was extremely small, averaging ≈ 0.0035 kg/s for the low heat leak series 1 tests; a gain of only ≈ 0.0009 kg/s would eliminate the delta between the ambient heat leak and the derived TVS heat extraction values. The equation for mass flow rate is extremely sensitive to the magnitude of CdA , and to the coefficient,

$C=0.14$, which was actually calculated from the ratio of specific heats and other terms in a more general form of the compressible flow equation. Thus, the differences between the tank heat leak and the TVS heat extraction are most likely due to the computational sensitivity of the extremely small mass flow rate.

Propellant conditioning, such as reducing the saturation pressure, could prove useful in increasing propellant storage durations and improving on-orbit propellant transfer efficiencies in future applications. Therefore, an additional test at the 25-percent fill level was conducted to evaluate the ability of the TVS to reduce the saturation conditions of the bulk LH_2 by continually extracting thermal energy. In this case, the J-T valve was allowed to remain open and the mixer operated continuously for 118 min, which reduced the saturation conditions from 133 to 70 kPa (19.3 to 10 psia) in 118 min (fig. 52). About 25.5 kg (56 lb) of vented LH_2 were required to achieve the saturation pressure reduction.

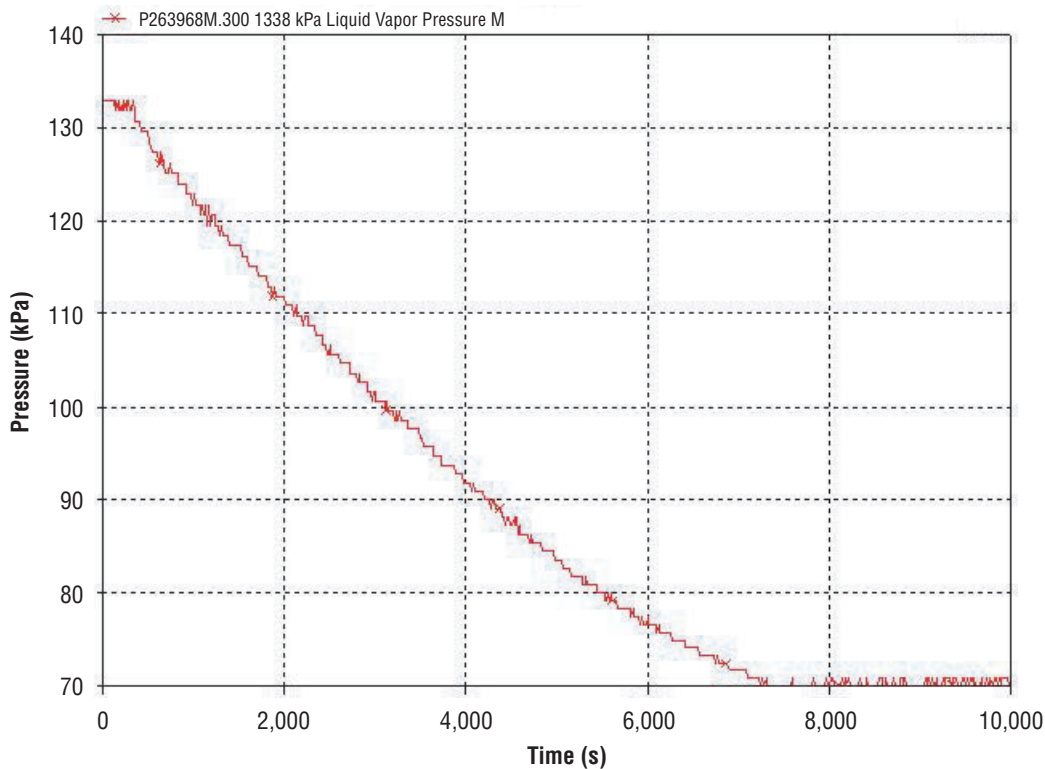


Figure 52. Bulk liquid saturation pressure reduction at 25-percent fill level.

8.3.4 Helium Pressurization Gas Effects

In a multiple engine restart scenario, for example, the GHe quantity in the ullage can increase with the number of prepressurization cycles performed, since only vaporized hydrogen is vented whenever liquid is at the TVS pump inlet. Additionally, GHe is frequently considered for hydrogen expulsion in orbital propellant transfer scenarios. Therefore, limited testing was conducted to evaluate the spray bar TVS performance with a noncondensable gas, GHe, in the ullage. Testing with helium was first attempted during the series 1 low heat leak testing at the 25-percent fill level; however, J-T valve

plugging occurred due to small amounts of moisture within the facility-provided GHe and testing was terminated. Subsequently, the GHe was dried prior to injection into the MHTB and GHe pressurization testing was repeated during the series 2 testing.

It is estimated that there was ≈ 9.3 kg (20.5 lbm) of GHe in the ullage during the series 2 test, which was conducted at the 50-percent fill level and with a heat leak of 51 W. The injected GHe initially elevated the ullage pressure to above the upper control limit of 213 kPa. Then the ullage was vented to the lower pressure control limit of 206.84 kPa whereupon the tank was locked up and testing began. At this point, the tank liquid was saturated at ≈ 165 kPa (24 psia) and the helium partial pressure was ≈ 43 kPa which resulted in the total pressure of 206.8 kPa. After the tank self-pressurized to an upper setpoint of 213.7 kPa, the mixer cycled on. As can be seen in figure 53, the mixer operated alone until the ullage pressure decay slope became positive, at which point the J-T valve was manually opened to further reduce the tank pressure.

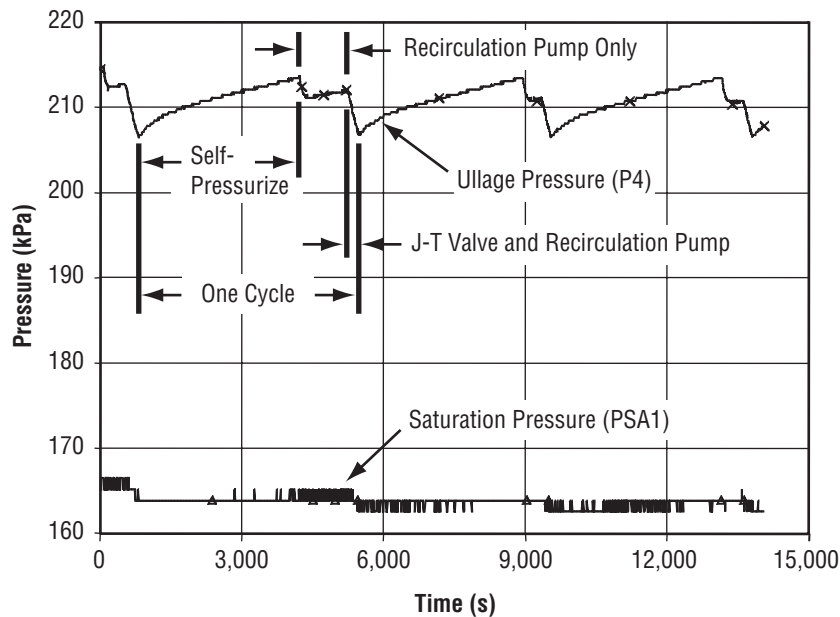


Figure 53. TVS operation cycles with GHe in ullage, 50-percent fill level during series 2.

It was apparent that mixing alone could not reduce the pressure below ≈ 211 kPa. Since the mass of helium remained constant throughout the vent/mixing cycles, the helium and hydrogen partial pressure to total pressure ratios also remained constant (Dalton's Law). Therefore, an error in injected helium mass or in helium partial pressure could not have been a factor in the incomplete pressure reduction during the mixing-only phase. Thus, it was concluded that the helium presence constrained the energy exchange between the sprayed hydrogen droplets and the ullage, thereby reducing condensation. Furthermore, the density of GHe is about twice that of hydrogen and ≈ 10 hr were required after initial helium injection to establish the initial conditions. Hence, it is believed that helium, with its larger than hydrogen density (factor of 2 larger), settled on the liquid-vapor interface and significantly reduced the mass and energy exchange between the ullage and bulk LH_2 (see sec. 6.4.6.6). Only when the J-T vent valve was used to inject cooler hydrogen into the ullage did condensation continue and a further

reduction in ullage pressure occurred. Furthermore, it was noted that the pressure reduction magnitude with the mixing-only phase became slightly more effective with each of the subsequent two cycles. Thus, the trend was toward more effective mixing with each succeeding cycle, and it is possible that the pressure leveling-off effect would have eventually disappeared with more mixing cycles. However, since test time was limited for this phase of testing, insufficient data exist to validate definite conclusions.

As expected, the presence of helium increased the mixing duration, but quantitative observations must be qualified due to the limited test duration. The time for TVS one cycle averaged ≈ 63 min with a self-pressurization time of ≈ 58 min. The mixer operated an average of 187 s before the pressure reduction leveled off, and then the mixer/J-T combination period averaged 129 s. The leveling-off duration varied since it was manually controlled, and therefore is not included in the total duty cycle time; this would be automated in a flight application. Thus, the mixer duty cycle was ≈ 9 percent and the J-T duty cycle ≈ 3.7 percent of the total cycle period.

It can be concluded from the helium testing that the spray bar TVS maintained the tank ullage pressure within a prescribed control band with helium pressurant. However, changes in the automated control system logic would be necessary to accommodate the presence of helium in future testing or applications. Further testing is required to ascertain the effects of helium on TVS performance; however, it is expected that the effects in reduced gravity would be less since helium settling on the liquid-vapor interface would not occur.

8.4 Test Facility and Hardware Performance

Overall, the test facility performed very well, especially during the critical orbital simulations. For the low heat leak series 1 tests, the vacuum chamber pressure was maintained in the low 10^{-6} torr range with LN_2 cold walls engaged. During the high heat leak series 2 testing, the vacuum level was in the low 10^{-5} torr range without the cold walls operating. During each of the two test series, the warm boundary temperatures on the MLI surfaces were successfully controlled to 305 K by the environmental shroud. The facility back-pressure control system was especially effective in maintaining the tight ullage pressure control requirements during the tank heat leak testing and controlled ullage pressures to within ± 0.00689 kPa (0.001 psi) of the setpoint. During testing with TVS venting into the adjacent 4.6-m- (15-ft-) diameter vacuum chamber, the 4.6-m chamber maintained pressure levels below 75 torr (1.4 psia).

The MHTB continuous liquid level capacitance probe served as a guide for determining propellant level; however, the silicon diode sensors on the instrumentation rake became the primary means for determining liquid level and ullage volume. Several TVS transducers failed during the second test series and somewhat compromised the data analyses. Specifically, both pressure transducers (PVA1 and PVA2) upstream of the back-pressure orifice, a vent line temperature, TJT2, and PJT1, a vent line pressure, failed. Erratic J-T valve operation compromised test results on two occasions; i.e., stuck open for a few seconds on one test and remained open on another, necessitating test termination. During one test instrumentation noise or false signal spikes on the bulk temperature sensor (TD23) caused the control system to briefly activate the J-T vent valve. A more reliable valve is recommended for future testing and component redundancy would be necessary in an actual flight application.

9. THERMODYNAMIC VENT SYSTEM ANALYTICAL MODEL CORRELATIONS

As mentioned previously, eight TVS tests were performed with various test conditions. Using the previously described analytical model (sec. 6) correlations with the measured ullage pressure and temperature and with the bulk liquid saturation pressure and temperature were developed for the eight test segments presented in table 7. Correlations for seven representative test segments are presented in figures 49 through 73 and discussed below. The remaining test segment is discussed in appendix C. Further details regarding analytical modeling correlations with the test data are reported in reference 9.

Table 7. TVS test conditions compared with analytical model.

Ullage	Fill Level (%)	Heat Leak (W)	Year, Test No.	Discussion
GH ₂	90	20.2	1996, P263968E,F	Section 9.1
GH ₂	90	20.2	1996, P263968G	Section 9.1
GH ₂	50	18.7	1996, P263968K	Section 9.1
GH ₂	25	18.8	1998, P263968L	Section 9.1
GH ₂	90	54.1	1998, P263981D	Section 9.2
GH ₂	50	51.0	1998, P263981T	Section 9.2
GH ₂ and GHe	50	51.0	1996, P263981X	Section 9.2
GH ₂	90	54.1	1998, P263981E	Appendix C

9.1 Series 1, Low Heat Leak Tests

Analytical correlations for segments from all four of the series 1 tests were performed. Test segments discussed herein include P263968E, P263968F; P263968G; P263968K; and P263968L. In each case the upper and lower tank pressure control limits were 137.9 kPa (20 psia) and 131 kPa (19 psia), respectively, and the vent flow rates ranged from 0.0036 to 0.0034 kg/s. All analytically modeled periods were initialized using measured conditions.

9.1.1 Test Segments P263968E and P263968F—Self-Pressurization and Mixing, 90-Percent Fill Level

Correlations for self-pressurization and mixing were performed using test segments P263968E and P263968F, with a 90-percent fill level and 20.2-W tank heat leak. Results are presented in figures 54–57 for the ullage pressure, ullage temperature, bulk liquid saturation pressure, and bulk liquid saturation temperature, respectively. As illustrated in figure 54, tank lockup occurred at 2.2 hr (8,000 s) and the long-term self-pressurization proceeded until the mixing cycles began and continued throughout the remainder of the test segment without venting. The model is in good agreement with the test data in the early stages of self-pressurization after tank lockup at 111.5 kPa (16.2 psia); however, the analytical pressure begins to deviate after ≈ 1.7 hr (at 14,000 s) and rises more rapidly than the measured values. The computed and measured ullage pressures reached the upper pressure limit of 137.9 kPa (20 psia)

Test and Model Conditions

- 90% Fill, GH₂ Ullage
- Test and Model: No Venting
- Tank Heat Leak: 20.2 W
- P4 Upper Limit: 137.9 kPa
- P4 Lower Limit: 131.0 kPa

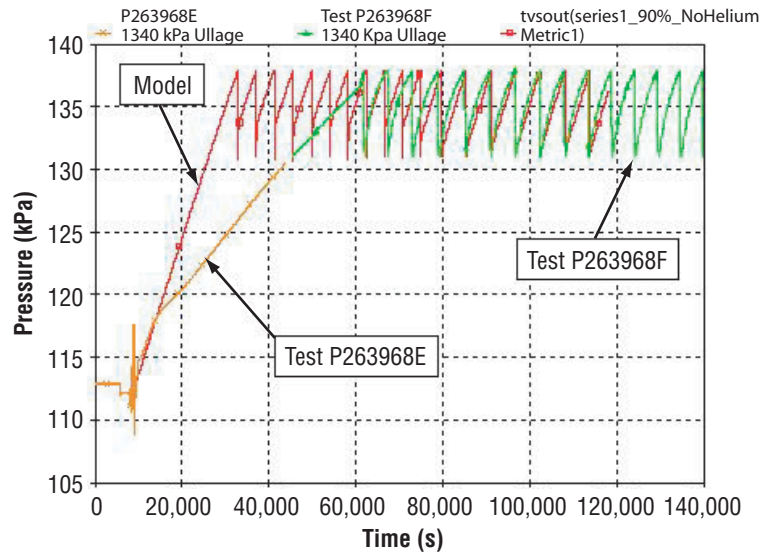


Figure 54. Ullage pressure modeling comparison with 1996 tests P263968E and P263968F—self-pressurization and mixing with 90-percent fill.

after ≈ 6.8 hr (at 32,500 s) and 14.7 hr (at 61,000 s), respectively. It is believed the analytical modeling, which assumes that the liquid and ullage are each represented by a single node, did not simulate the complex energy exchange that actually occurred at the liquid-vapor interface. Examination of modeled ullage pressure rise rate sensitivity to various parameters suggested that mass was added to the ullage across the liquid-vapor interface beginning at 14,000 s into the test, whereas the model assumed that thermal energy continued to be added at a constant rate with no mass addition. Thus, during the test, the low-temperature mass transfer across the liquid-vapor interface began to suppress the ullage pressure rise rate, whereas the modeled energy transfer and pressure rise rate remained relatively constant. Therefore, the analytical pressure rise rate after tank lockup is conservative relative to the measured data, and the modeled mixing cycles began earlier.

With mixing, the stratification effects are minimized and the energy exchange across the liquid surface is more predictable during the relatively short self-pressurization periods (≈ 40 min) between mixing cycles. Therefore, once the mixing and pressure rise cycles began, the analytical and measured data closely matched; however, it was noted that the measured pressure rise rates were slightly steeper than analytically modeled, whereas the pressure reduction rates were practically identical. Consequently, the measured cycle rate was ≈ 11 percent higher; i.e., one cycle per 1.34 hr (0.75 cycles/hr) and 1.49 hr (0.67 cycles/hr) occurred with the test and model data, respectively.

The analytical and measured ullage temperatures are presented in figure 55. Since the mixing cycles began earlier with the analytical model, the test data initially indicates higher ullage temperatures. However, after mixing began in the test, good agreement between the modeled and measured data was achieved. The bulk liquid saturation pressure and temperature correlations, presented in figures 56 and 57, respectively, indicate higher temperatures and pressures with the model. The calculated bulk liquid saturation conditions exceeded the measured pressures and temperatures by up to 15 kPa (2.2 psia) and 0.45 K, respectively. These temperature and pressure differences, however, were not factors in the pressure rise rate correlations.

Test and Model Conditions

- 90% Fill, GH₂ Ullage
- Test and Model: No Venting
- Tank Heat Leak: 20.2 W
- P4 Upper Limit: 137.9 kPa
- P4 Lower Limit: 131.0 kPa

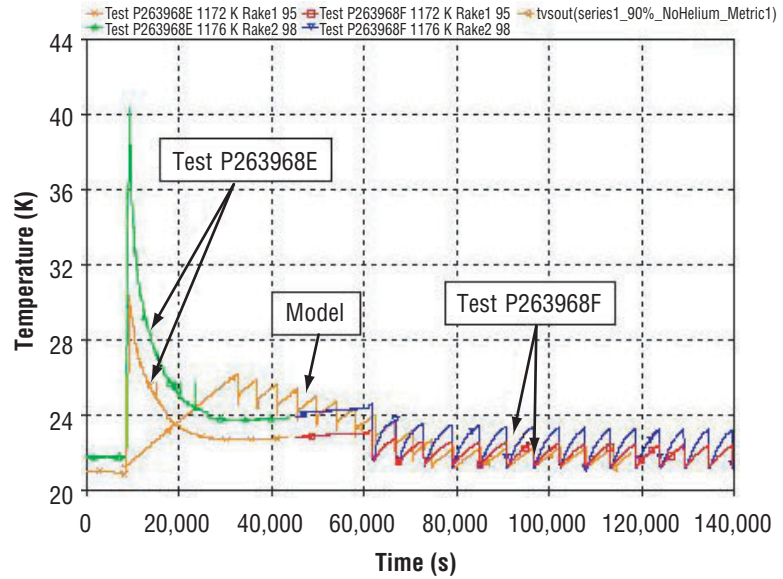


Figure 55. Ullage temperature modeling comparison with 1996 tests P263968E and P263968F—self-pressurization and mixing with 90-percent fill.

Test and Model Conditions

- 90% Fill, GH₂ Ullage
- Test and Model: No Venting
- Tank Heat Leak: 20.2 W
- P4 Upper Limit: 137.9 kPa
- P4 Lower Limit: 131.0 kPa

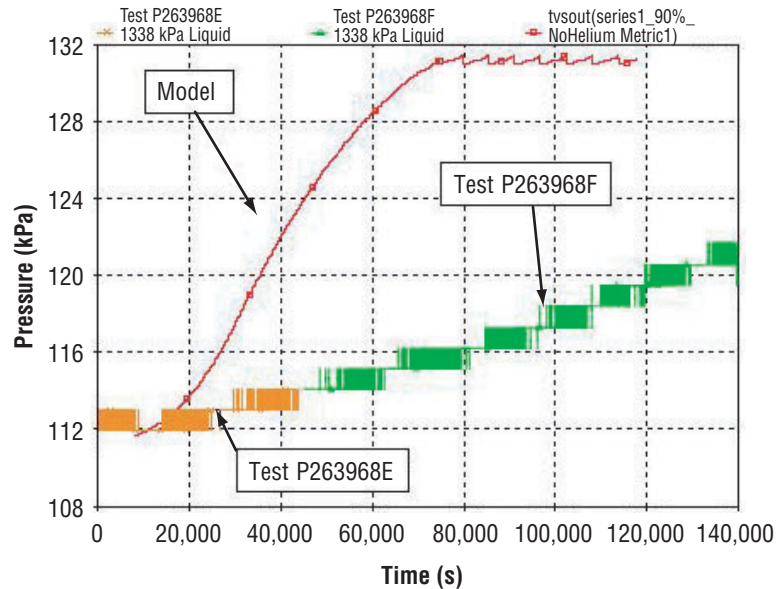


Figure 56. Bulk liquid saturation pressure modeling comparison with 1996 tests P263968E and P263968F—self-pressurization and mixing with 90-percent fill.

Test and Model Conditions

- 90% Fill, GH₂ Ullage
- Test and Model: No Venting
- Tank Heat Leak: 20.2 W
- P4 Upper Limit: 137.9 kPa
- P4 Lower Limit: 131.0 kPa

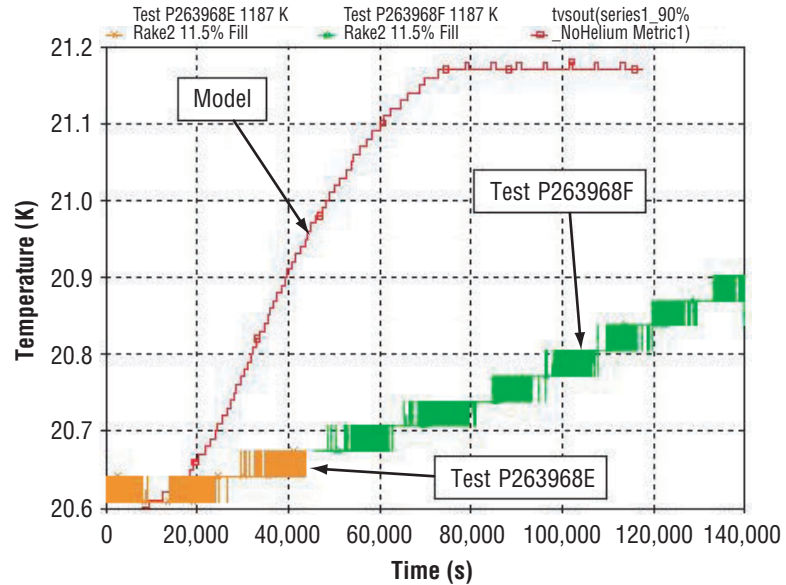


Figure 57. Bulk liquid saturation temperature modeling comparison with 1996 tests P263968E and P263968F—self-pressurization and mixing with 90-percent fill.

9.1.2 Test Segment P263968G—Mixing and Venting, 90-Percent Fill Level

Correlations for the venting and mixing operation were performed using test segment P263968G, with a 90-percent fill level and 20.2-W tank heat leak. The ullage pressure comparison is presented in figure 58. Although the timing of the first J-T valve opening event was somewhat obscured in the test data, the analytical modeling was initialized at 12,829 s and allowed to self-pressurize to the 137.9 kPa (20 psia) upper limit, whereupon the J-T valve (with a vent flow of 0.0034 kg/s) and mixer pump were activated. The data comparison indicates that the analytical model tracks the measured data very well initially; however, the model cycles about once per 1.58 hr (0.63 cycles/hr) compared with 1.06 hr (0.94 cycles/hr) in the test (computed rate is \approx 33-percent lower). As with the mixing cycles-only data (no venting), the measured pressure rise rates are steeper than the modeled data, whereas the pressure reduction rates again closely match. The ullage temperature comparison in figure 59 indicates that the averaged measured and computed ullage temperatures are 22.15 and 21.75 K, respectively; i.e., deviate by <2 percent. Similarly, the modeled and measured bulk liquid saturation pressure and temperature, presented in figures 60 and 61, respectively, are practically identical. A sensitivity analysis concluded that the differences in the short-term pressure rise rates between cycles are most likely due to errors in modeling the stratification effects on the ullage energy exchange across the liquid-vapor interface.

Test Conditions

- 90% Fill, GH₂ Ullage
- Tank Heat Leak: 20.2 W
- P4 Upper Limit: 137.9 kPa
- P4 Lower Limit: 131.0 kPa
- Vent Flow Rate: 0.0034 kg/s

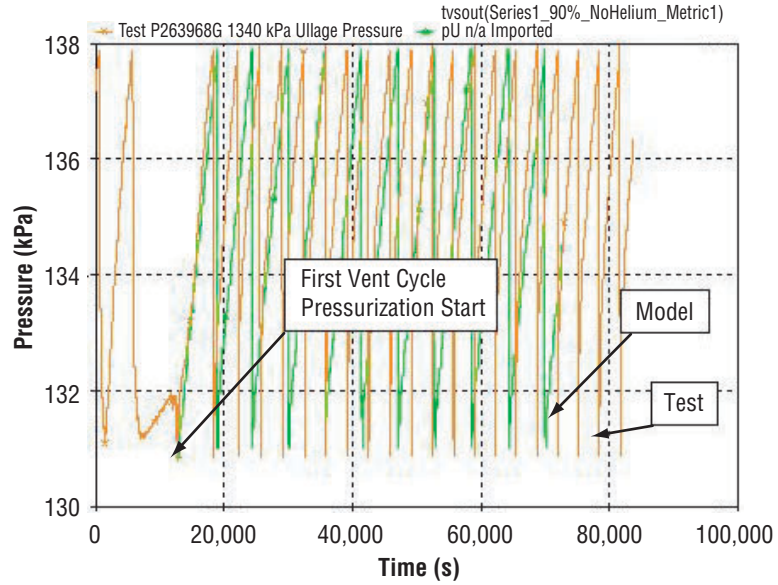


Figure 58. Ullage pressure modeling comparison with 1996 test P263968G—mixing and venting with 90-percent fill.

Test Conditions

- 90% Fill, GH₂ Ullage
- Tank Heat Leak: 20.2 W
- P4 Upper Limit: 137.9 kPa
- P4 Lower Limit: 131.0 kPa
- Vent Flow Rate: 0.0034 kg/s

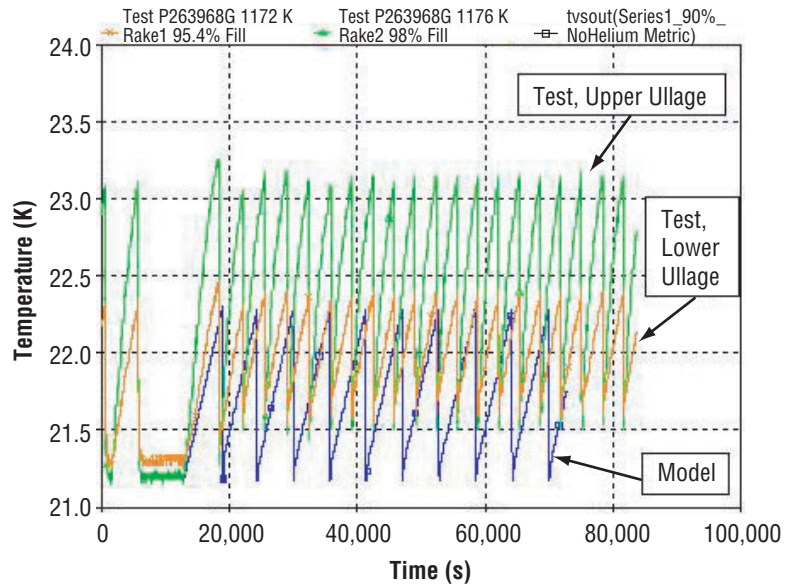


Figure 59. Ullage temperature modeling comparison with 1996 test P263968G—mixing and venting with 90-percent fill.

Test Conditions

- 90% Fill, GH₂ Ullage
- Tank Heat Leak: 20.2 W
- P4 Upper Limit: 137.9 kPa
- P4 Lower Limit: 131.0 kPa
- Vent Flow Rate: 0.0034 kg/s

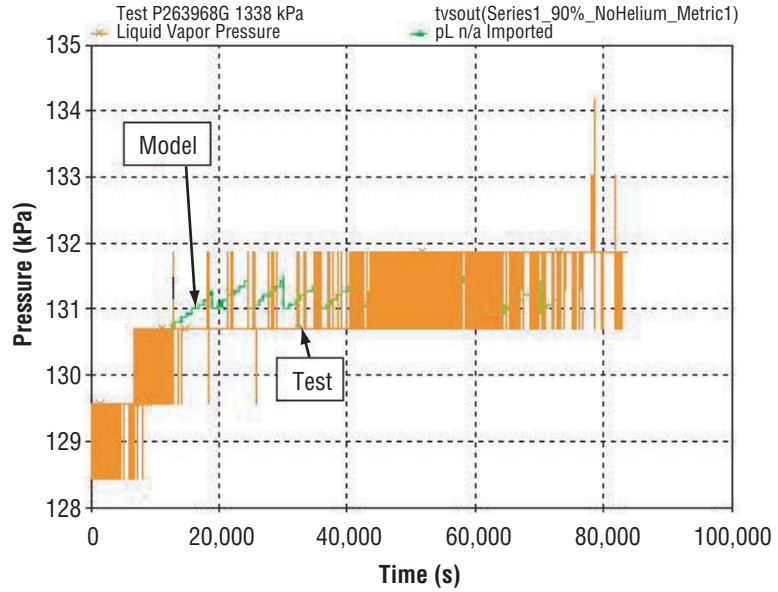


Figure 60. Bulk liquid saturation pressure modeling comparison with 1996 test P263968G—mixing and venting with 90-percent fill.

Test Conditions

- 90% Fill, GH₂ Ullage
- Tank Heat Leak: 20.2 W
- P4 Upper Limit: 137.9 kPa
- P4 Lower Limit: 131.0 kPa
- Vent Flow Rate: 0.0034 kg/s

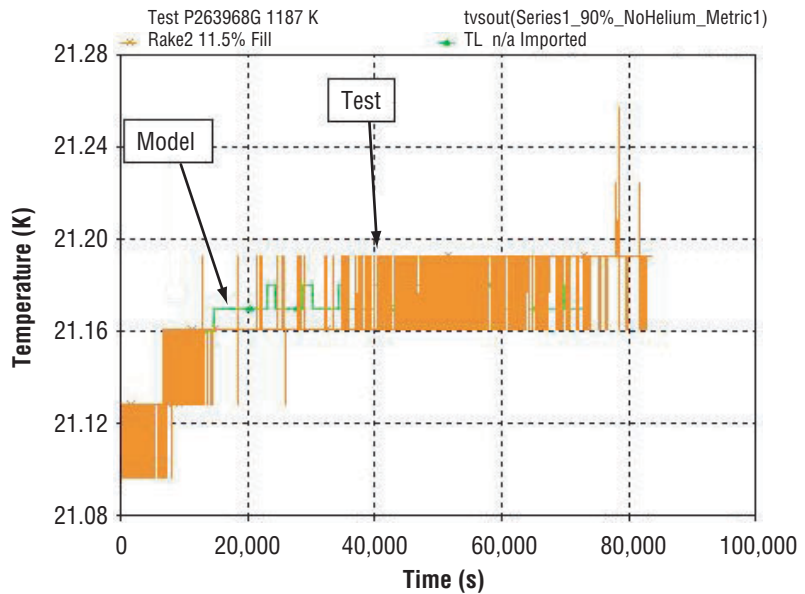


Figure 61. Bulk liquid saturation temperature modeling comparison with 1996 test P263968G—mixing and venting with 90-percent fill.

9.1.3 Test Segment P263968K—Mixing and Venting, 50-Percent Fill Level

Model and measured comparisons for mixing and venting operations in test segment P263968K, with a 50-percent fill level and 18.7-W heat leak, are presented in figures 62–65. The ullage pressure comparison, presented in figure 62, illustrates relatively good correlation until the tank draining begins shortly after 80,000 s in preparation for the next test series. As expected, the measured vent-mixer cycle rate was slower than with the 90-percent fill level; i.e., the measured TVS cycle durations were approximately 1 and 2 hr at 90 and 50 percent, respectively. However, as with the 90-percent fill level testing, the cycle rate with the model is slower than in the testing. One cycle occurred per 2.4 hr (0.417 cycles/hr) in the testing, whereas one cycle per 3.3 hr (0.3 cycles/hr) occurred in the modeling. Therefore, the modeled cycle rate is ≈ 28 percent below that measured and, again, is attributed to stratification effects.

The ullage temperature correlation is presented in figure 63, which indicates good agreement; i.e., the averaged model temperatures are within 1 K or ≈ 4 percent of the averaged measured temperatures. The bulk liquid saturation pressure and temperature correlations, presented in figures 64 and 65, respectively, indicate good agreement. Compared to the test data, the averaged modeled saturation pressures and temperatures are within 1.5 kPa and 0.06 K, respectively, except for slightly more deviation on the first cycle.

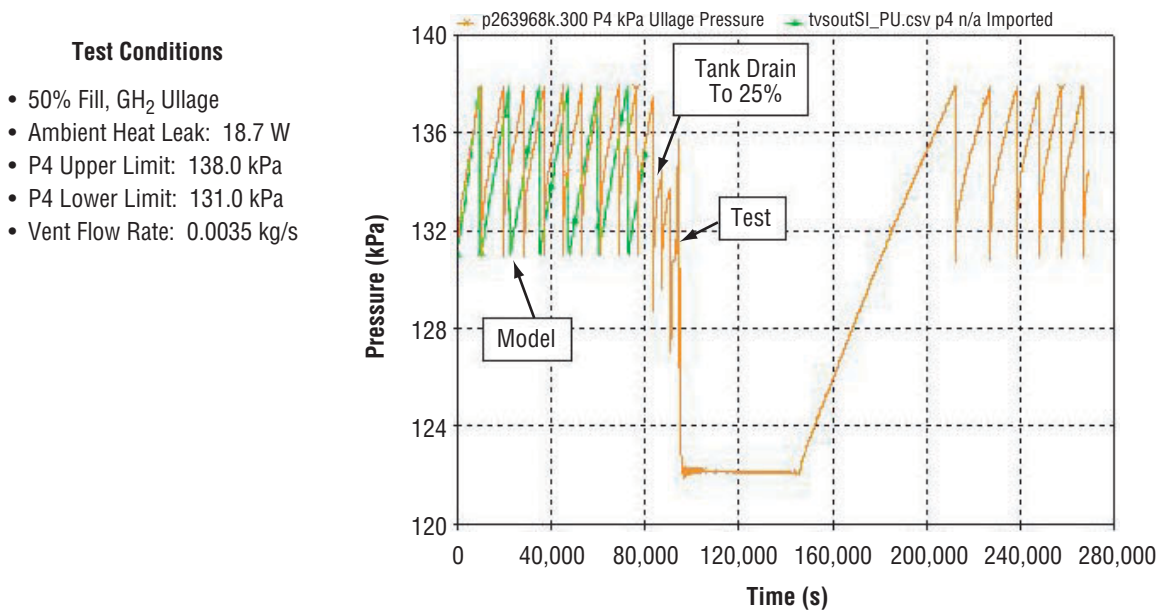


Figure 62. Ullage pressure modeling comparison with 1996 test P263968K—mixing and venting with 50-percent fill.

Test Conditions

- 50% Fill, GH₂ Ullage
- Ambient Heat Leak: 18.7 W
- P4 Upper Limit: 138.0 kPa
- P4 Lower Limit: 131.0 kPa
- Vent Flow Rate: 0.0035 kg/s

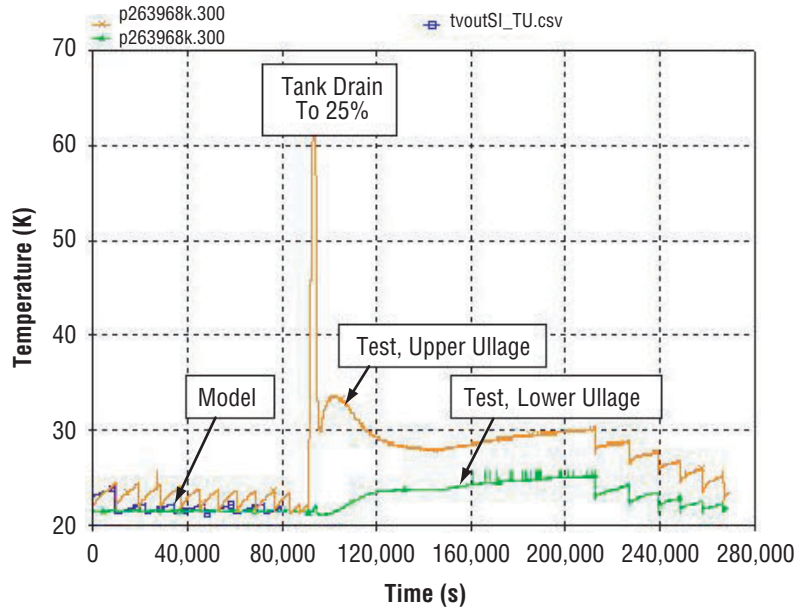


Figure 63. Ullage temperature modeling comparison with 1996 test P263968K—mixing and venting with 50-percent fill.

Test Conditions

- 50% Fill, GH₂ Ullage
- Ambient Heat Leak: 18.7 W
- P4 Upper Limit: 138.0 kPa
- P4 Lower Limit: 131.0 kPa
- Vent Flow Rate: 0.0035 kg/s

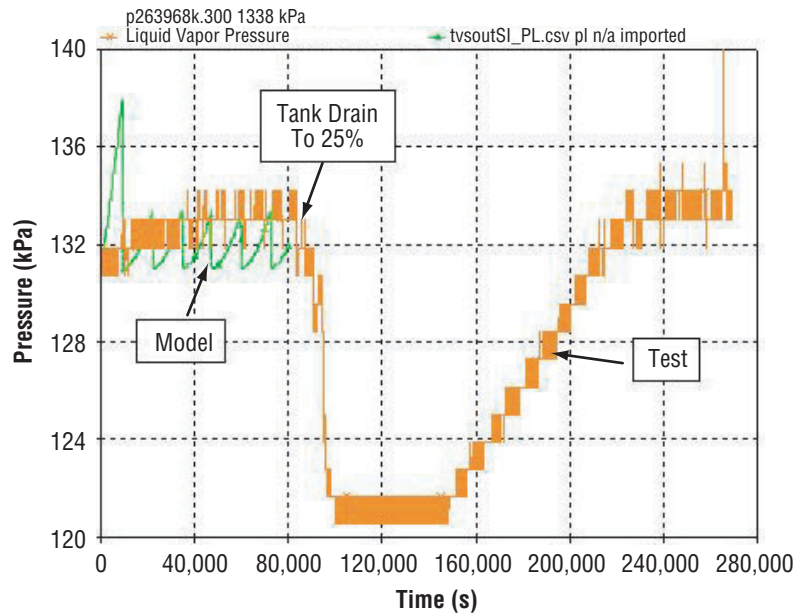


Figure 64. Bulk liquid saturation pressure modeling comparison with 1996 test P263968K—mixing and venting with 50-percent fill.

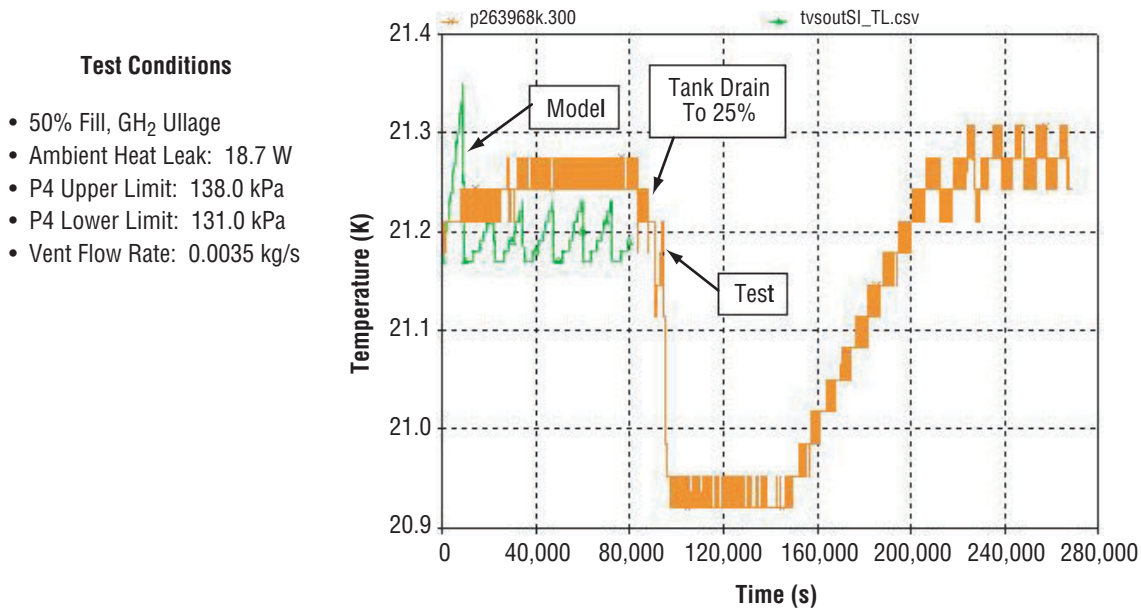


Figure 65. Bulk liquid saturation temperature modeling comparison with 1996 test P263968K—mixing and venting with 50-percent fill.

9.1.4 Test Segments P263968K and P263968L—Self-Pressurization, Mixing and Venting, 25-Percent Fill Level

Model correlations with test data for self-pressurization, mixing, and venting with a 25-percent fill level and an 18.8-W heat leak were performed using a combination of test segments P263968K and P263968L. Figure 66 presents the self-pressurization period after tank lockup at 122 kPa and indicates computed and measured pressure rise rates of 4.32 and 0.86 kPa/hr, respectively. When the mixing cycle began (fig. 67), the modeling results indicate generally good agreement with the test data. The increased ullage volume resulted in extending the measured cycle duration to 2.8 hr compared with 2.4 hr with 50-percent fill. However, the model cycle duration of 3.8 hr was again longer than that measured; i.e., the measured cycle rate (0.35 cycles/hr) was \approx 26 percent higher than that computed (0.26 cycles/hr). As with the data previously discussed, the modeled and measured pressure reduction rates correlate very well, whereas the measured pressure rise rates between mixing cycles are higher than those computed.

The ullage temperature correlation is presented in figure 68, which indicates that the average measured temperatures are generally not more than 0.5 K above the model temperatures until \approx 80,000 s, when the measured temperature began to drift upward until the J-T valve briefly remained open longer than usual for one cycle at \approx 117,000 s. The average measured and calculated bulk liquid saturation pressures (fig. 69) correlated closely; i.e., were within 0.75 kPa. The average bulk liquid saturation temperatures (fig. 70) correlated within 0.04 K.

- Test Conditions**
- 25% Fill, GH₂ Ullage
 - Tank Heat Leak: 18.8 W
 - P4 Upper Limit: 138.0 kPa
 - P4 Lower Limit: 131.0 kPa
 - Vent Flow Rate: 0.0036 kg/s

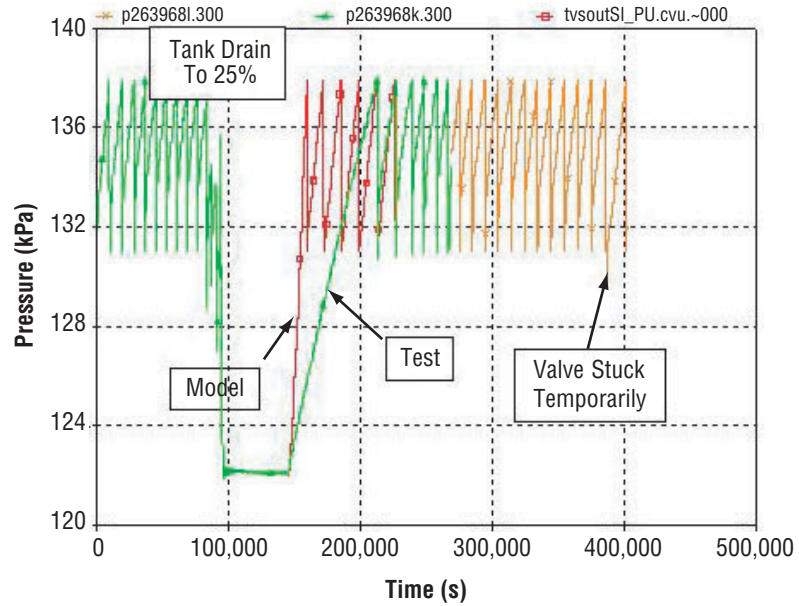


Figure 66. Ullage pressure modeling comparison with 1996 tests P263968K and P263968L—mixing and venting with 25-percent fill.

- Test Conditions**
- 25% Fill, GH₂ Ullage
 - Tank Heat Leak: 18.8 W
 - P4 Upper Limit: 138.0 kPa
 - P4 Lower Limit: 131.0 kPa
 - Vent Flow Rate: 0.0036 kg/s

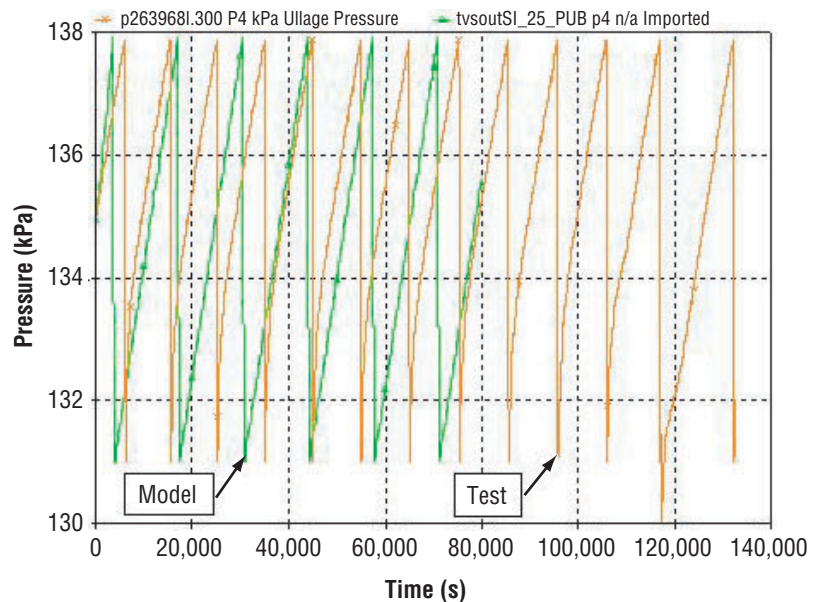


Figure 67. Ullage pressure modeling comparison with 1996 test P263968L—mixing and venting with 25-percent fill.

Test Conditions

- 25% Fill, GH₂ Ullage
- Tank Heat Leak: 18.8 W
- P4 Upper Limit: 138.0 kPa
- P4 Lower Limit: 131.0 kPa
- Vent Flow Rate: 0.0036 kg/s

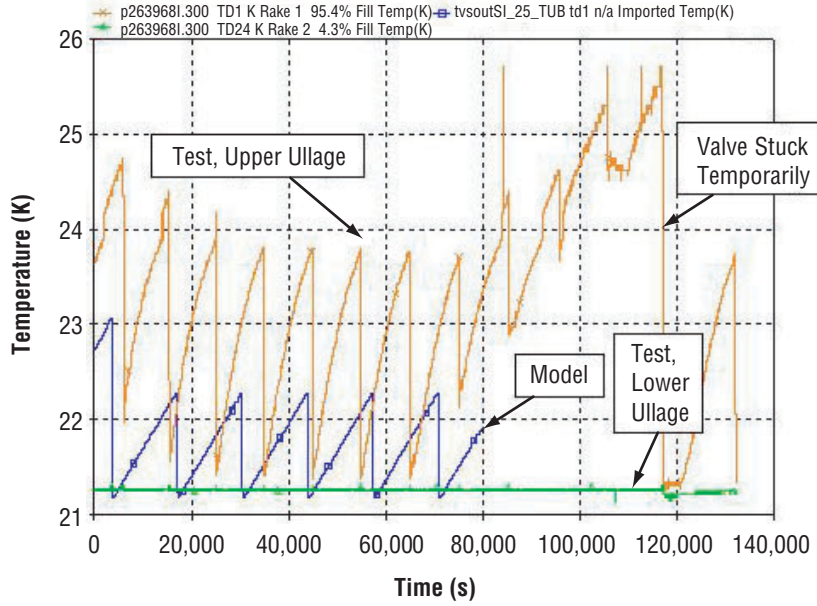


Figure 68. Ullage temperature modeling comparison with 1996 test P263968L—mixing and venting with 25-percent fill.

Test Conditions

- 25% Fill, GH₂ Ullage
- Tank Heat Leak: 18.8 W
- P4 Upper Limit: 138.0 kPa
- P4 Lower Limit: 131.0 kPa
- Vent Flow Rate: 0.0036 kg/s

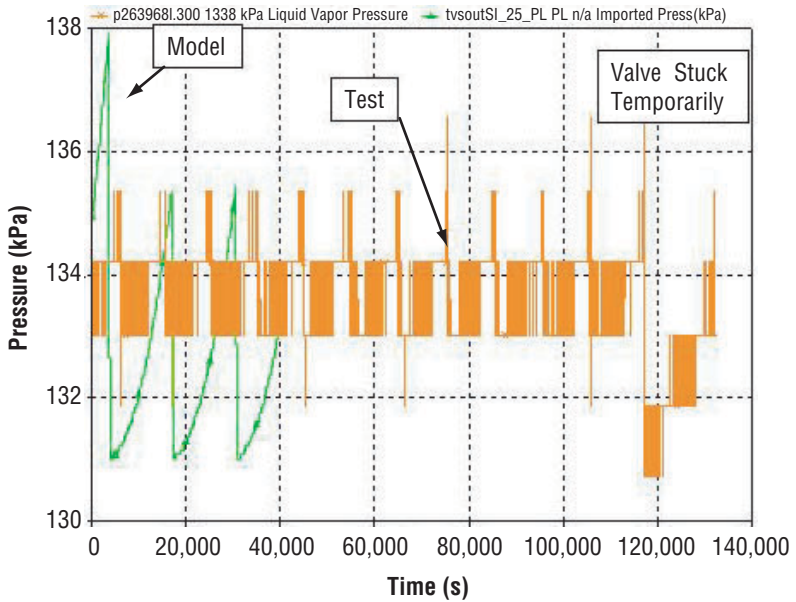


Figure 69. Bulk liquid saturation pressure modeling comparison with 1996 test P263968L—mixing and venting with 25-percent fill.

- Test Conditions**
- 25% Fill, GH₂ Ullage
 - Tank Heat Leak: 18.8 W
 - P4 Upper Limit: 138.0 kPa
 - P4 Lower Limit: 131.0 kPa
 - Vent Flow Rate: 0.0036 kg/s

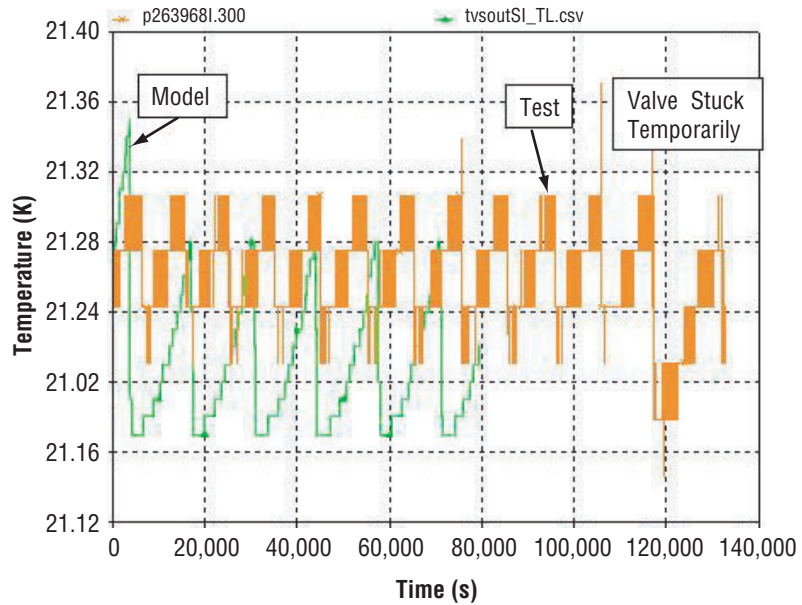


Figure 70. Bulk liquid saturation temperature modeling comparison with 1996 test P263968L—mixing and venting with 25-percent fill.

9.2 Series 2, High Heat Leak Tests

Analytical correlations for segments from all four of the series 2 tests segments were performed. Segments from three tests (P263981D, P263981T, P263981X) are discussed below, and to avoid repetition, data for P263981E is presented in appendix C. The third test was performed with GHe injected in the ullage (test segment P263981X) with a 50-percent fill level. The other two test segments—P263981D and P263981T—were performed with GH₂ only in the ullage with 90- and 50-percent fill levels, respectively. In the GH₂ ullage cases, the upper and lower tank pressure control limits were 137.9 kPa (20 psia) and 131 kPa (19 psia), respectively, and the vent flow rates ranged from 0.0036 to 0.0034 kg/s. As with previous correlations, the modeled periods were initialized using measured conditions.

9.2.1 Test Segment P263981D—Self-Pressurization and Mixing, 90-Percent Fill Level

Correlations for self-pressurization and mixing were performed using test segment P263981D, with a 90-percent fill level and 54.1-W tank heat leak. As illustrated in figure 71, tank lockup occurred at 10,380 s and self-pressurization proceeded until the mixing cycles began and continued throughout the remainder of the test segment without venting. The model is in good agreement with the test data in the early stages of self-pressurization after tank lockup at 111.5 kPa (16.2 psia). However, similar to the lower heat leak case, the analytical pressure data begins to deviate after ≈ 1.14 hr (14,500 s) and rises more rapidly than the measured values. The computed and measured ullage pressures reached the upper pressure limit of 137.9 kPa (20 psia) after ≈ 2.7 hr (20,000 s) and 5.5 hr (30,000 s), respectively. However, once the mixing cycles begin, both the pressure rise and reduction rates correlated very well. The measured and computed cycle rates were 1.83 and 1.76 cycles/hr, respectively; i.e., the measured rate was <4 percent higher. The ullage temperature correlations presented in figure 72 are consistent with the ullage pressure comparison data. During the self-pressurization period after tank lockup the modeled

Test Conditions

- 90% Fill, GH₂ Ullage
- No Venting
- Ambient Heat Leak: 54.1 W
- P4 Upper Limit: 137.9 kPa
- P4 Lower Limit: 131.0 kPa

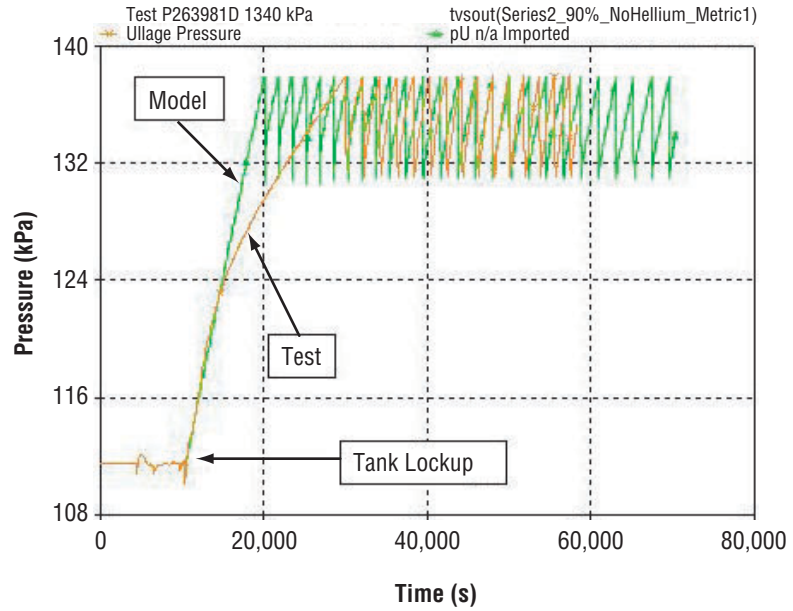


Figure 71. Ullage pressure modeling comparison with 1998 test P263981D—self-pressurization and mixing with 90-percent fill.

Test Conditions

- 1998 Test P263981D, 90% Fill, GH₂ Ullage, Tank Pressurization

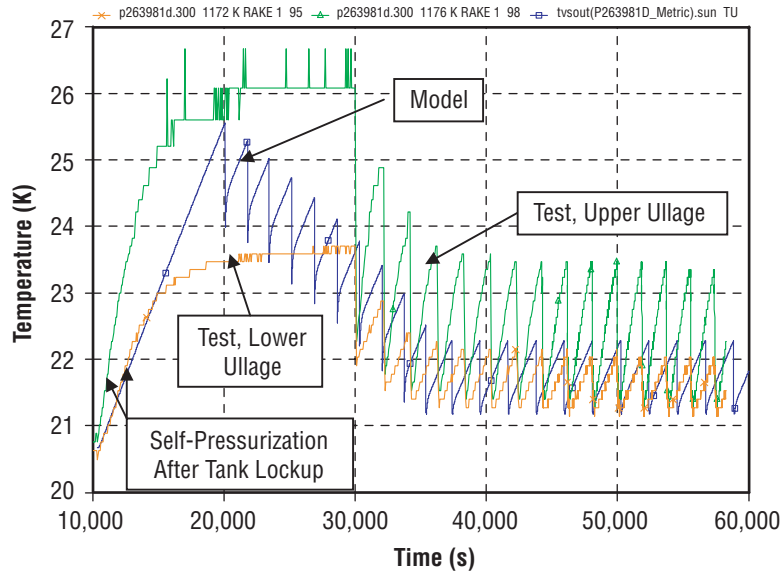


Figure 72. Ullage temperature modeling comparison with 1998 test P263981D—self-pressurization and mixing with 90-percent fill.

Test Conditions

- 90% Fill, GH₂ Ullage
- Ambient Heat Leak: 54.1 W
- P4 Upper Limit: 137.9 kPa
- P4 Lower Limit: 131.0 kPa
- Vent Flow Rate: 0.0048 kg/s

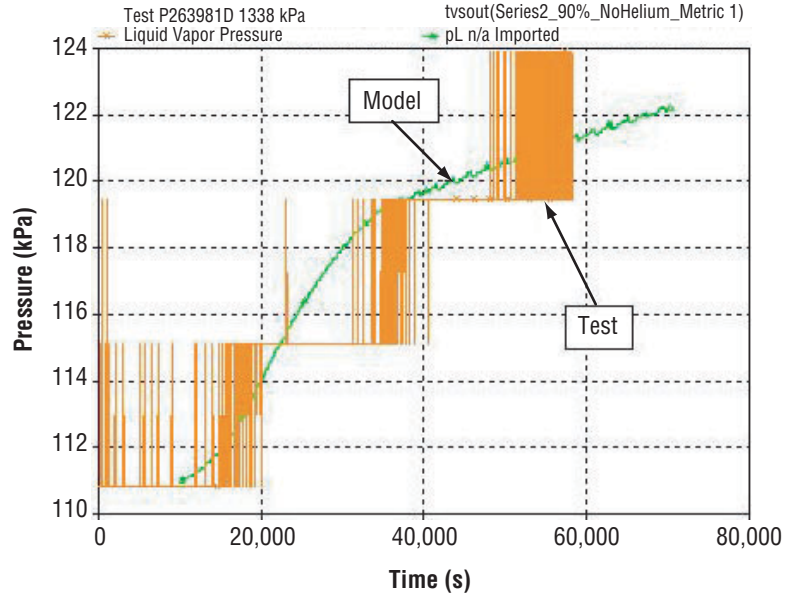


Figure 73. Bulk liquid saturation pressure modeling comparison with 1998 test P263981D—self-pressurization and mixing with 90-percent fill.

Test Conditions

- 90% Fill, GH₂ Ullage
- Ambient Heat Leak: 54.1 W
- P4 Upper Limit: 137.9 kPa
- P4 Lower Limit: 131.0 kPa
- Vent Flow Rate: 0.0048 kg/s

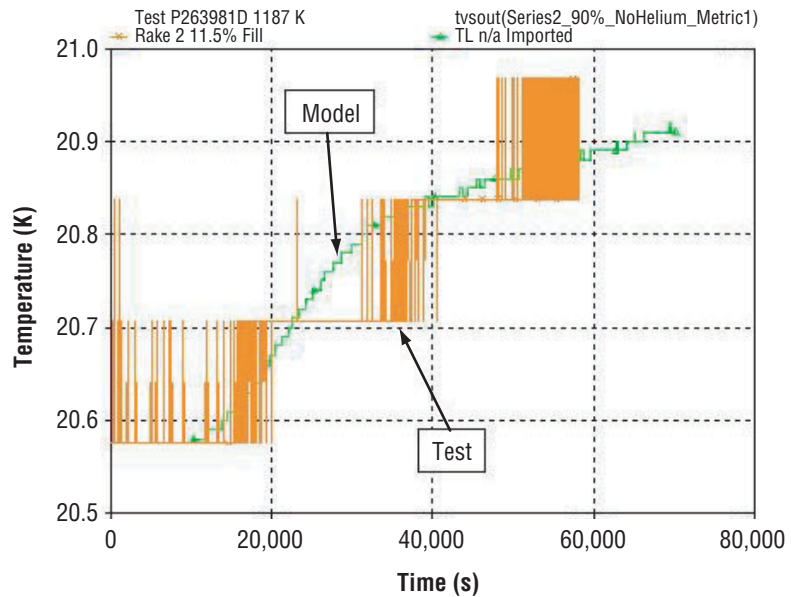


Figure 74. Bulk liquid saturation temperature modeling comparison with 1998 test P263981D—self-pressurization and mixing with 90-percent fill.

ullage temperatures initially followed the measured data in the lower portion of the ullage. However, after ≈ 1.14 hr (14,500 s) the analytical temperatures begin to rise more rapidly than measured in the lower ullage, but remain below temperatures measured in the upper ullage. The modeled temperatures begin to decrease when mixing begins at 2.7 hr (200,000 s) and very closely follow the measured lower ullage temperatures after the test data indicate that the mixing cycles have begun at 5.5 hr (30,000 s). The average measured and calculated bulk liquid saturation pressures (fig. 73) correlated closely; i.e., were within 2 kPa. The averaged bulk liquid saturation temperatures (fig. 74) correlated within 0.075 K.

9.2.2 Test Segment P263981T—Self-Pressurization and Venting, 50-Percent Fill Level

Correlations for self-pressurization, mixing, and venting were performed using test segment P263981T, with a 50-percent fill level and 51-W tank heat leak. As illustrated in figure 75, tank lockup at 111.5 kPa (16.2 psia) occurred at 127,110 s and self-pressurization proceeded until the mixing cycles began. The model pressure rise rate exceeded that measured. The modeled data indicated that the first mixing cycle began ≈ 2.8 hr (137,000 s) after lockup whereas mixing occurred ≈ 13.9 hr (177,000 s) after lockup in the test. Also, the venting began on the fifth cycle in the test, whereas it began on the first model cycle. Therefore, the trend was the same as observed in previous testing and the model again indicated conservative mixing and vent cycle start times.

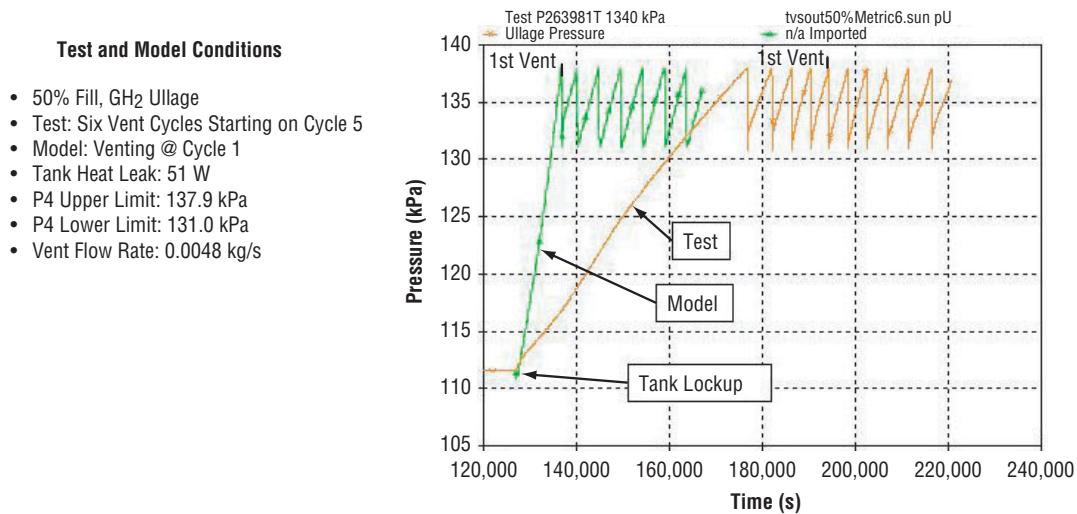


Figure 75. Unshifted ullage pressure modeling comparison with 1998 test P263981T—self-pressurization, mixing, and venting with 50-percent fill.

In order to correlate the mixing/vent cycle characteristics, the model start time with venting, was shifted by 60,350 s (to 187,460 s) to better align with the test data (fig. 71). At the beginning, both the pressure rise and reduction rates correlated reasonably well and the measured cycle rate was about 14 percent higher than computed. Once venting began in the test data, the model and test cycle rates became identical at 1.2 cycles/hr. The corresponding ullage temperature comparison (fig. 77) indicates good correlation in the upper ullage. Once venting began in the test (at 195,000 s), the measured and shifted modeled temperatures both averaged ≈ 22 K. Similarly, the liquid saturation pressure correlation (fig. 78) indicates close correlation after venting began in the test. Similarly, the liquid saturation temperature correlation (fig. 79) indicated modeled temperatures averaged ≈ 0.2 K lower than the measured values.

Test and Model Conditions

- 50% Fill, GH₂ Ullage
- Test: Six Vent Cycles Starting on Cycle 5
- Model: Venting @ Cycle 1
- Tank Heat Leak: 51 W
- P4 Upper Limit: 137.9 kPa
- P4 Lower Limit: 131.0 kPa
- Vent Flow Rate: 0.0048 kg/s

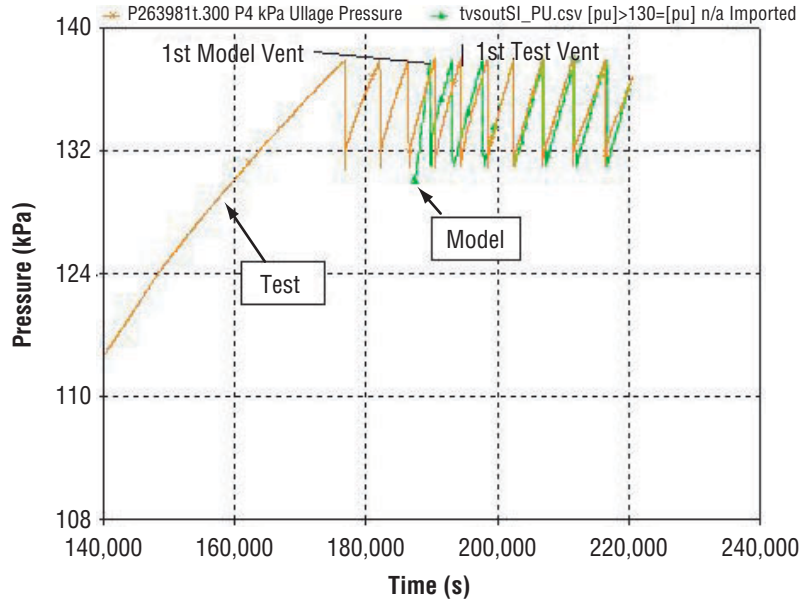


Figure 76. Shifted ullage pressure modeling comparison with 1998 test P263981T—self-pressurization, mixing, and venting with 50-percent fill.

Test and Model Conditions

- 50% Fill, GH₂ Ullage
- Test: Vent Cycles Starting @ Pressurization Cycle 5
- Model: Start Time Shifted, Venting Begins @ Cycle 1
- Tank Heat Leak: 51 W
- P4 Upper Limit: 137.9 kPa
- P4 Lower Limit: 131.0 kPa
- Vent Flow Rate: 0.0048 kg/s

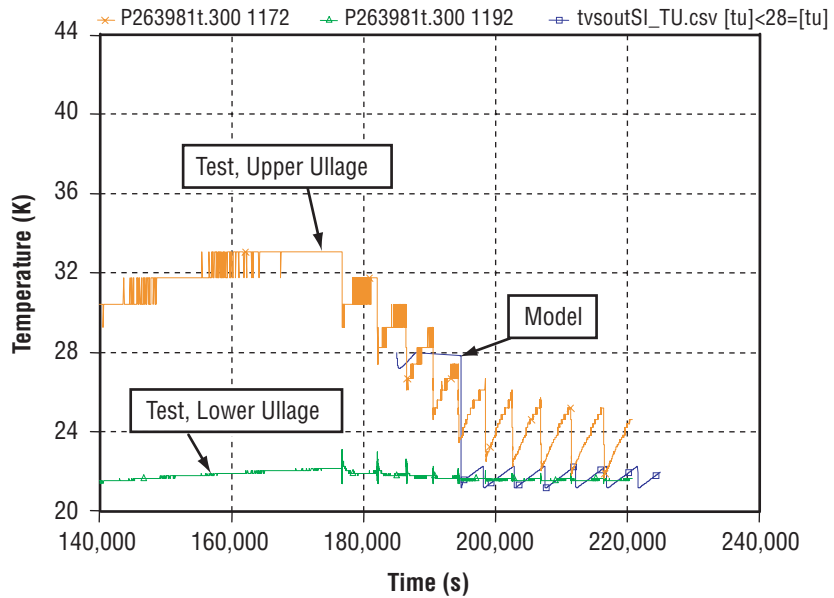


Figure 77. Shifted ullage temperature modeling comparison with 1998 test P263981T—self-pressurization, mixing, and venting with 50-percent fill.

Test and Model Conditions

- 50% Fill, GH₂ Ullage
- Test: Vent Cycles Starting @ Pressurization Cycle 5
- Model: Start Time Shifted, Venting Begins @ Cycle 1
- Tank Heat Leak: 51 W
- P4 Upper Limit: 137.9 kPa
- P4 Lower Limit: 131.0 kPa
- Vent Flow Rate: 0.0048 kg/s

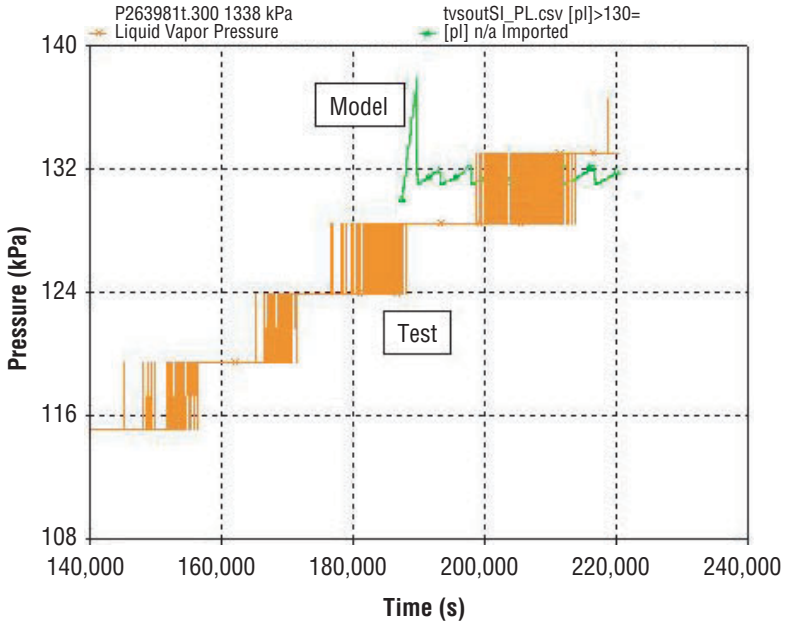


Figure 78. Shifted bulk liquid saturation pressure modeling comparison with 1998 test P263981T—self-pressurization, mixing, and venting with 50-percent fill.

Test and Model Conditions

- 50% Fill, GH₂ Ullage
- Test: Vent Cycles Starting @ Pressurization Cycle 5
- Model: Start Time Shifted, Venting Begins @ Cycle 1
- Tank Heat Leak: 51 W
- P4 Upper Limit: 137.9 kPa
- P4 Lower Limit: 131.0 kPa
- Vent Flow Rate: 0.0048 kg/s

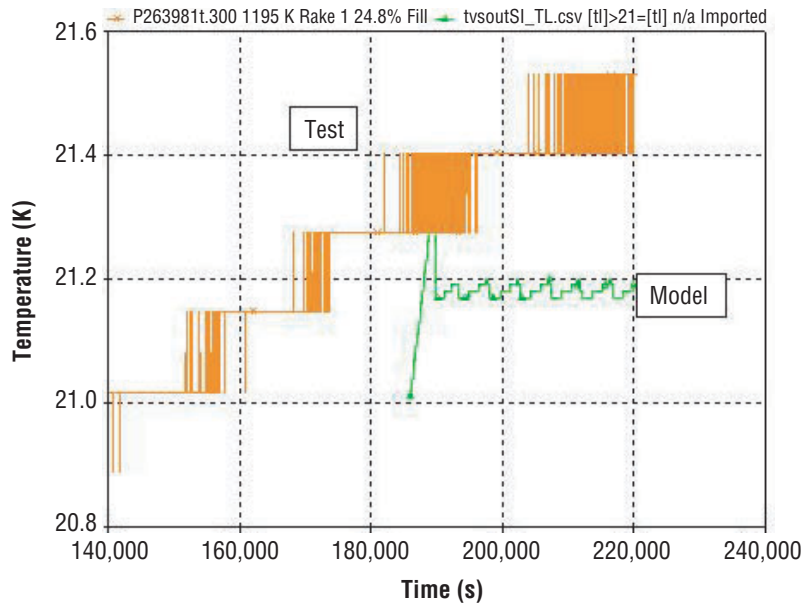


Figure 79. Shifted bulk liquid saturation temperature modeling comparison with 1998 test P263981T—self-pressurization, mixing, and venting with 50-percent fill.

9.2.3 Test Segment P263981X—Self-Pressurization and Venting, 50-Percent Fill Level, GHe and GH₂ Ullage

Correlations for self-pressurization, mixing, and venting were performed using test segment P263981X, with a 50-percent fill level, 51-W tank heat leak, and with GHe injected into the ullage at the beginning of tank lockup. As mentioned earlier, the injected GHe initially elevated the ullage pressure to above the upper control limit of 213 kPa and then the ullage was vented to the lower control limit of 206.84 kPa, whereupon the tank was locked up and the testing began. After the tank self-pressurized to 213 kPa, the mixer started and decreased the ullage pressure to \approx 211 kPa, where the pressure leveled off and began to rise. The vent was manually cycled on and the ullage pressure then decreased to the lower limit, 206.8 kPa. The sequence was repeated for two more cycles before the testing was terminated. As described in section 8.3.4, it is believed that the helium acted as a barrier to the mass transfer and to condensation on the liquid surface, thereby constraining the effectiveness of the mixing-only phase and necessitating use of the J-T venting to further cool the ullage and reduce the pressure to the lower setpoint pressure. The analytical and test ullage pressure modeling comparison with the test data is presented in figure 80. The model start time was shifted to match the first vent cycle (6,200 s), but was initiated with measured conditions at the start of tank lockup. The GH₂ and GHe partial pressures used in the model were 165.5 (24 psia) and 41.4 kPa (6 psia), respectively. The model cycle rate was slightly faster than the test data reflected, primarily because the model did not reflect the leveling-off effect observed in the mixer-only testing. Also, since the analytical bulk liquid conditions never indicated saturation, venting did not occur with the model.

Test and Model Conditions

- 50% Fill, GHe and GH₂ Ullage
- P_{H₂}=165.48 kPa, P_{H_e}=41.37 kPa
- Test: Three Manual Vent Cycles
- Model: No Venting, Start Time Shifted
- Tank Heat Leak: 51 W
- P4 Upper Limit: 213.7 kPa
- P4 Lower Limit: 206.8 kPa
- Test Vent Flow Rate: 0.0048 kg/s

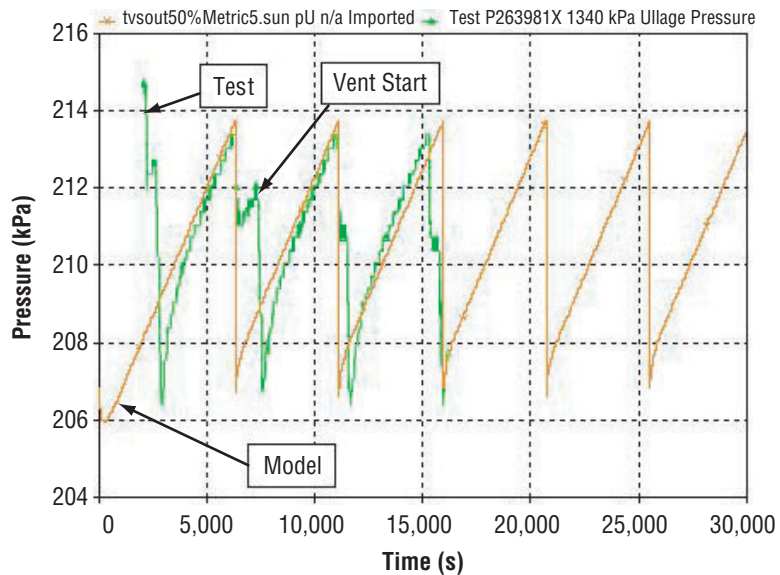


Figure 80. Shifted ullage pressure modeling comparison with test P263981X—tank pressurization, mixing, and venting with 50-percent fill, GHe and GH₂ ullage.

The shifted ullage temperature modeling comparison with the test data is presented in figure 81. The averaged model and test ullage temperatures were about 22.6 and 23 K, respectively; i.e., were within 0.4 K. The shifted bulk liquid saturation pressure and temperature correlations are presented in figures 82 and 83, respectively. The model indicated that the saturation pressure and temperature continued to rise throughout the test segment, whereas the measured saturation conditions remained relatively constant. Longer duration testing definitely is required to better define and analytically correlate the effects of helium pressurant on TVS operation and long-term trends.

Test and Model Conditions

- 50% Fill, GHe and GH₂ Ullage
- P_{H₂}=165.48 kPa, P_{He}=41.37 kPa
- Test: Three Manual Vent Cycles
- Model: No Venting, Start Time Shifted
- Tank Heat Leak: 51 W
- P4 Upper Limit: 213.7 kPa
- P4 Lower Limit: 206.8 kPa
- Test Vent Flow Rate: 0.0048 kg/s

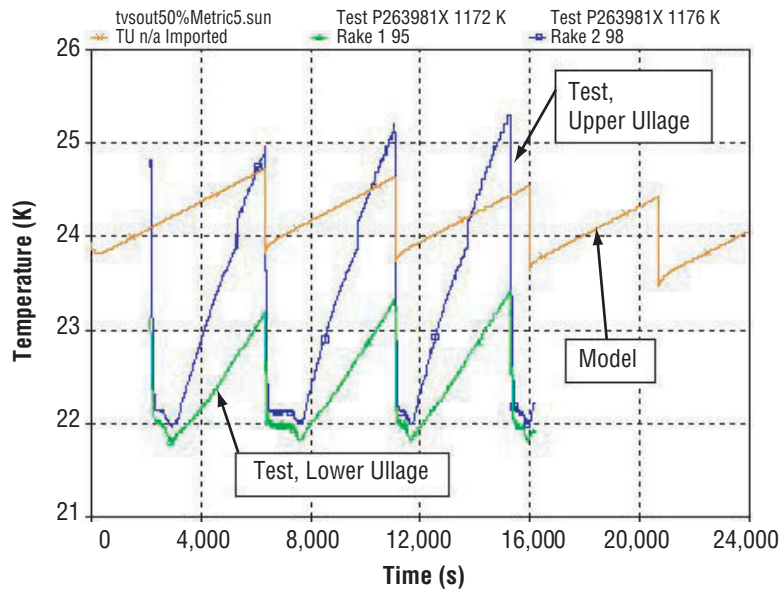


Figure 81. Shifted ullage temperature modeling comparison with 1998 test P263981X—tank pressurization, mixing, and venting with 50-percent fill, GHe and GH₂ ullage.

Test and Model Conditions

- 50% Fill, GHe and GH₂ Ullage
- P_{H₂}=165.48 kPa, P_{He}=41.37 kPa
- Test: Three Manual Vent Cycles
- Model: No Venting, Start Time Shifted
- Tank Heat Leak: 51 W
- P4 Upper Limit: 213.7 kPa
- P4 Lower Limit: 206.8 kPa
- Test Vent Flow Rate: 0.0048 kg/s

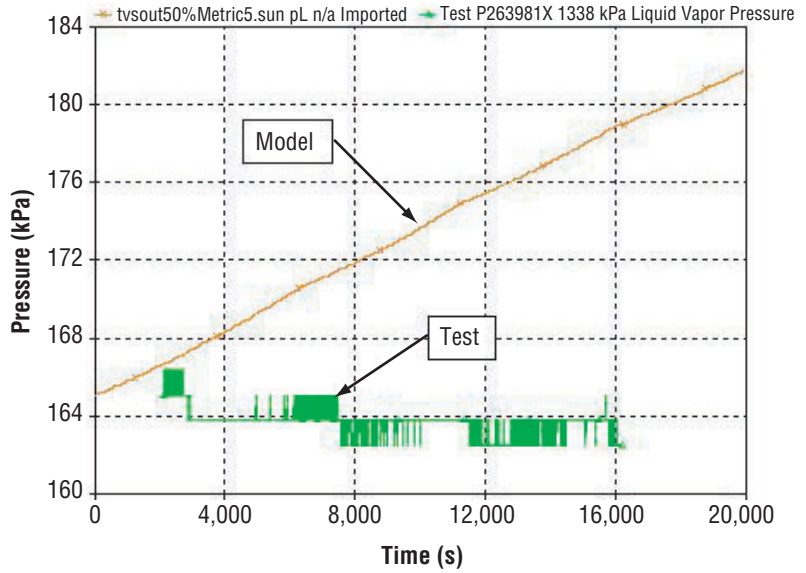


Figure 82. Shifted bulk liquid saturation pressure modeling comparison with 1998 test P263981X—tank pressurization, mixing, and venting with 50-percent fill, GHe and GH₂ ullage.

Test and Model Conditions

- 50% Fill, GHe and GH₂ Ullage
- P_{H₂}=165.48 kPa, P_{He}=41.37 kPa
- Test: Three Manual Vent Cycles
- Model: No Venting, Start Time Shifted
- Tank Heat Leak: 51 W
- P4 Upper Limit: 213.7 kPa
- P4 Lower Limit: 206.8 kPa
- Test Vent Flow Rate: 0.0048 kg/s

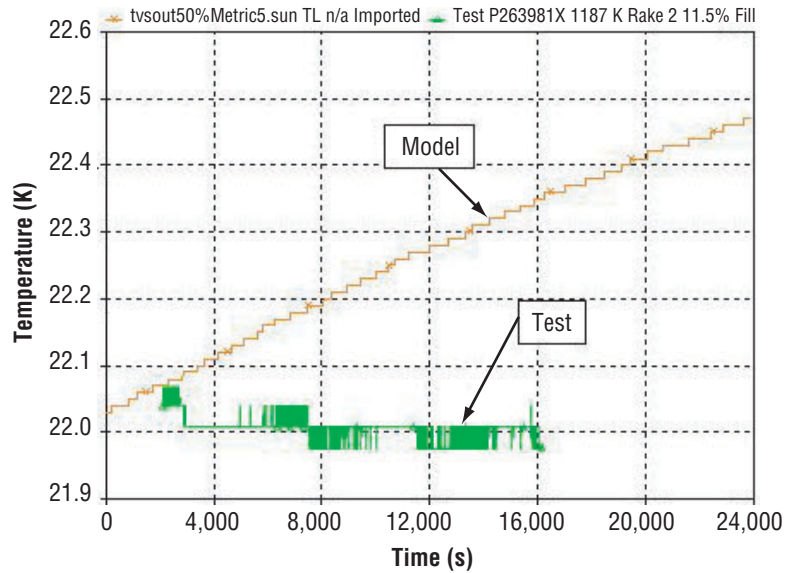


Figure 83. Shifted bulk liquid saturation temperature modeling comparison with 1998 test P263981X—tank pressurization, mixing, and venting with 50-percent fill, GHe and GH₂ ullage.

10. SUMMARY AND RECOMMENDATIONS

The program objective was to design, develop, and demonstrate with ground testing a system that can maintain LH₂ tank pressure control in zero gravity without liquid resettling while minimizing boiloff losses. A spray bar TVS concept by The Boeing Company (formerly Rockwell Aerospace) was selected to demonstrate ullage pressure control within a ± 3.45 kPa (± 0.5 psi) control band within MSFC's 18-m³ MHTB LH₂ tank. The longitudinal spray bar was designed to thermally destratify both liquid and ullage, independent of liquid-vapor positions in zero gravity. The basic design requirements were that the TVS accommodate tank heat leaks of up to 55 W, liquid levels of 10 to 95 percent, and operation without dependence on a capillary device.

The spray bar design definition and hardware selection activities resulted in the following:

- A 2.67-m- (105-in-) long spray bar concentric tube heat exchanger assembly with a heat exchange area of 0.27 m² between the vented and recirculated fluid. Forty-five 0.17-cm- (0.067-in-) diameter orifices equally spaced in each of four longitudinal tubes enable spray injection in four directions and optimum ullage pressure decay.
- Initiate venting at or near a tank pressure of 137.8 kPa (20 psia) to optimize heat absorption, and vent to a J-T valve with an orifice diameter of 1.96 mm (0.077 in) and flow rate capability of 0.0021 kg/s (0.0047 lb/s).
- Barber-Nichols pump which produces 113.5 L/min (30 gal/min) with a head rise of 6.89 kPa/m² at 4,158 rpm.

Component and subsystem testing performed included: LH₂ spray injection testing within a 55.9-cm- (22-in-) diameter dewar to verify ullage pressure collapse analytical modeling, recirculation pump testing with methanol to define pump head and flow coefficients, full-scale spray bar flow tests with water to measure pressure losses and verify uniform flow distributions, heat exchanger cold side pressure drop testing with LN₂, and pump flowmeter water calibration testing using actual line inlet and outlet geometries.

A transient analytical model was formulated to characterize TVS performance within the MHTB. Individual thermal-fluid models of the heat exchanger, spray manifold and injection tubes, recirculation pump, and tank were developed and verified before being integrated into the transient TVS model. The heat exchanger model is a multinode finite difference model that simulates two-phase flow in a quasi-steady-state mode. A one-dimensional, incompressible fluid dynamic model characterizes flow within and exiting the spray manifold and injection tubes. The recirculation pump performance model is based on the pump head versus flow rate data provided by the manufacturer combined with standard analytical equations for a centrifugal pump. The tank model consists of four control volumes: (1) Ullage, (2) tank wall, (3) liquid on the tank wall, and (4) bulk liquid.

The MSFC vacuum facility and associated controls performed very well, producing over 420 hr of testing. During the orbital simulation periods with cold walls, the vacuum was successfully maintained at 10^{-6} torr or less. Without the chamber cold walls operating, vacuum levels were 10^{-5} torr or less. During the steady-state heat leak or boiloff testing, the facility ullage pressure control system maintained LH₂ tank pressure within ± 0.00689 kPa (± 0.001 psi) of the prescribed setpoint. During TVS testing when the J-T venting was routed into an adjacent 4.6-m- (15-ft-) diameter vacuum chamber, the supporting chamber maintained pressure levels below 75 torr (1.4 psia). Also, the MHTB environmental shroud successfully maintained multilayer insulation exterior boundaries at the prescribed level of 305 K throughout the testing.

Boiloff testing established the tank heat leak prior to TVS testing at the 90-, 50-, and 25-percent fill levels. One TVS test series was with a low heat leak (19–20 W), and another test series with a high heat leak (51–54 W). Both the low and high heat leak test data confirmed the spray bar to be effective in destratifying both the ullage and liquid for all conditions. Generally, the mixing durations were shorter when venting occurred due to the heat extraction effect. The mixing durations clearly increased with decreasing fill levels with the mixing cycle durations ranging from 43 to 535 s, depending on the test condition. For example, at the 90-percent fill level, the mixer operation duration per cycle increased from 134 s at the beginning to 535 s as saturation was approached prior to the initiation of venting. The time between mixing cycles ranged from 25 to 173 min for all fill levels and conditions tested.

The automated TVS control system successfully maintained tank pressure within the selected control band of ± 3.45 kPa (± 0.5 psia) throughout the testing with a GH₂ ullage. Tank mixing alone maintained pressure control until the saturation pressure increased to the lower limit of the TVS control band. At the 90-percent fill level with a 20 W heat leak, for example, 2.5 days elapsed before J-T venting was necessitated. The low heat leak saturation pressure rise rates were ≈ 0.3 kPa/hr (0.044 psi/hr) at the 90- and 50-percent fill levels and ≈ 0.50 kPa/hr (0.073 psi/hr) at the 25-percent fill. Mixing and venting began simultaneously at the 25-percent fill level. Therefore, there apparently is a minimum liquid level below which tank mixing alone is insufficient to reduce tank pressure beginning with the first mixing cycle. TVS heat extraction rates were computed based on the TVS instrumentation data. When comparing the computed or derived heat extraction values to the measured tank heat leak for the same test, the extraction rates were 7 to 21 percent lower than the corresponding tank heat. In reality, the thermal energy removed by the TVS equaled the heat leak into the tank. The differences between the measured heat leak and heat extraction calculation are most likely due to the sensitivity of the extremely small vent flow rates (0.0035 to 0.0048 kg/s) derived from the measured data. Also, erratic J-T valve operation compromised test results on two occasions; i.e., it stuck open for a few seconds on one test and remained open on another, necessitating test termination. A more reliable valve is recommended for future testing.

To support future mission scenarios or options involving orbital propellant storage and transfer, an additional test at the 25-percent fill level was conducted to evaluate the ability of the TVS to reduce the saturation conditions of the bulk LH₂. In this case, the J-T valve was allowed to remain open and the mixer operated continuously, which successfully reduced the saturation conditions from 133 to 70 kPa (19.3 psia to 10 psia) in 118 min. About 25.5 kg (56 lb) of vented LH₂ were required to achieve the saturation pressure reduction.

Limited testing with the 50-percent fill level, 51-W heat leak condition was conducted to evaluate TVS performance with a noncondensable gas, helium, in the ullage. Even though the ullage pressures were above saturation, mixing alone did not sufficiently reduce ullage pressure. It was concluded that helium constrained the energy exchange between the GH_2 and LH_2 , reducing the condensation effects of both the sprayed droplets and convection at the bulk liquid-vapor interface. The trend was toward more effective mixing with each succeeding cycle, and it is possible that the pressure “leveling off” effect would have eventually disappeared with more mixing cycles. Further testing is required to ascertain the long-term effects of helium on TVS performance, but it is evident that the TVS control system logic would have to be modified to accommodate the presence of helium.

Using the MHTB TVS analytical model, correlations with the measured ullage pressure and temperature, and with the bulk liquid saturation pressure and temperature were developed for eight representative test segments. Correlations for the extended self-pressurization periods after each tank lockup indicated that the model pressure rise rates exceeded those measured by factors of ≈ 2 at the 90-percent fill level, and a factor of 5 at the 50- and 25-percent levels. It is believed the analytical modeling, which assumes that the liquid and ullage are each represented by single nodes, did not simulate the complex energy exchange that actually occurred at the liquid-vapor interface. Indications are that the model assumed thermal energy addition to the ullage at a constant rate; whereas in reality, a low-temperature mass transfer across the liquid-vapor interface began after 1–2 hr to suppress the ullage pressure rise rate.

Once the mixing and venting cycles began, the analytical and measured data more closely matched. With the low heat leak condition, it was noted that the measured pressure rise rates were slightly steeper than analytically modeled, whereas the pressure reduction rates were practically identical. The low heat leak-modeled TVS cycle rates ranged from 11- to 33-percent lower than the measured cycle rates. However, the cycle rate correlations improved with the higher heat leak condition, and the measured rates were 4 to 14 percent higher than the modeled rates for the mixing “without venting” cases, and almost identical in the “with venting” cases. As expected, the cycle rates did decrease with increasing ullage volume level. The correlations for ullage pressure and temperature, and the bulk liquid saturation pressure and temperature, indicated relatively good agreement for the entire range of conditions tested.

When helium was present in the ullage, the model indicated that mixing alone reduced the ullage pressure to the lower setpoint (no venting) since the bulk liquid was below saturation. In reality, manual use of the J-T venting became necessary to achieve the lower setpoint. Therefore, the effectiveness of the mixing-only phase was compromised by the helium presence. Furthermore, the modeled saturation pressure and temperature continued to rise throughout the test segment, whereas the measured saturation conditions remained relatively constant. Longer duration testing definitely is required to better define and analytically correlate the effects of helium pressurant on TVS operation and long-term trends.

APPENDIX A—MULTIPURPOSE HYDROGEN TEST BED TANKING TABLE

A tanking table (table 8) has been calculated based on the design geometry of the MHTB test tank. This table provides volume, ullage, and mass estimates based on the fluid level as referenced to the tank bottom. The tank fluid level is measured with a capacitance probe mounted such that its active length begins 10 cm above the tank bottom and continues for 2.878 m (113.3125 in) or to a height 2.978 m (117.25 in) above the tank bottom. Therefore, all capacitance probe height data must be corrected by adding 10 cm (3.9375 in) to the recorded height value to obtain the actual liquid height inside the tank.

Table 8. MHTB tanking table.

Total Tank Volume = 639.34 ft ³ 18.10 m ³ LH ₂ Density = 4.419 lbm/ft ³ 70.786 kg/m ³ Note: Height is measured from the bottom of the tank.							
Height (in)	Height (cm)	Volume (ft ³)	Volume (m ³)	Ullage (%)	Liquid (%)	Liquid Mass (lbm)	Liquid Mass (kg)
0.00	0.00	0.00	0.0000	100.00	0.00	0.00	0.0000
0.50	1.27	0.05	0.0015	99.99	0.01	0.24	0.1087
1.00	2.54	0.22	0.0061	99.97	0.03	0.95	0.4324
1.50	3.81	0.48	0.0137	99.92	0.08	2.13	0.9673
2.00	5.08	0.85	0.0242	99.87	0.13	3.77	1.7098
2.50	6.35	1.33	0.0375	99.79	0.21	5.86	2.6560
3.00	7.62	1.90	0.0537	99.70	0.30	8.38	3.8025
3.50	8.89	2.57	0.0727	99.60	0.40	11.34	5.1453
4.00	10.16	3.33	0.0944	99.48	0.52	14.73	6.6809
4.50	11.43	4.19	0.1187	99.34	0.66	18.53	8.4055
5.00	12.70	5.15	0.1457	99.20	0.80	22.74	10.3154
5.50	13.97	6.19	0.1753	99.03	0.97	27.35	12.4068
6.00	15.24	7.32	0.2073	98.85	1.15	32.36	14.6762
6.50	16.51	8.54	0.2419	98.66	1.34	37.74	17.1198
7.00	17.78	9.85	0.2788	98.46	1.54	43.51	19.7338
7.50	19.05	11.23	0.3181	98.24	1.76	49.64	22.5146
8.00	20.32	12.70	0.3597	98.01	1.99	56.13	25.4585
8.50	21.59	14.25	0.4035	97.77	2.23	62.97	28.5618
9.00	22.86	15.88	0.4495	97.52	2.48	70.15	31.8207
9.50	24.13	17.58	0.4977	97.25	2.75	77.67	35.2316
10.00	25.40	19.35	0.5480	96.97	3.03	85.52	38.7907
10.50	26.67	21.20	0.6003	96.68	3.32	93.68	42.4943
11.00	27.94	23.12	0.6546	96.38	3.62	102.16	46.3388
11.50	29.21	25.10	0.7109	96.07	3.93	110.94	50.3204
12.00	30.48	27.16	0.7690	95.75	4.25	120.01	54.4354
12.50	31.75	29.28	0.8290	95.42	4.58	129.37	58.6801
13.00	33.02	31.46	0.8907	95.08	4.92	139.00	63.0509
13.50	34.29	33.70	0.9542	94.73	5.27	148.91	67.5439
14.00	35.56	36.00	1.0193	94.37	5.63	159.08	72.1556
14.50	36.83	38.36	1.0861	94.00	6.00	169.50	76.8821
15.00	38.10	40.77	1.1545	93.62	6.38	180.16	81.7198
15.50	39.37	43.24	1.2243	93.24	6.76	191.06	86.6650

Table 8. MHTB tanking table (Continued).

Height (in)	Height (cm)	Volume (ft ³)	Volume (m ³)	Ullage (%)	Liquid (%)	Liquid Mass (lbm)	Liquid Mass (kg)
16.00	40.64	45.76	1.2957	92.84	7.16	202.19	91.7140
16.50	41.91	48.32	1.3684	92.44	7.56	213.55	96.8630
17.00	43.18	50.94	1.4425	92.03	7.97	225.11	102.1084
17.50	44.45	53.60	1.5179	91.62	8.38	236.88	107.4464
18.00	45.72	56.31	1.5946	91.19	8.81	248.84	112.8734
18.50	46.99	59.06	1.6724	90.76	9.24	261.00	118.3856
19.00	48.26	61.85	1.7515	90.33	9.67	273.33	123.9794
19.50	49.53	64.68	1.8316	89.88	10.12	285.83	129.6510
20.00	50.80	67.55	1.9128	89.43	10.57	298.50	135.3967
20.50	52.07	70.45	1.9949	88.98	11.02	311.32	141.2128
21.00	53.34	73.39	2.0780	88.52	11.48	324.29	147.0957
21.50	54.61	76.35	2.1620	88.06	11.94	337.40	153.0415
22.00	55.88	79.35	2.2469	87.59	12.41	350.64	159.0467
22.50	57.15	82.37	2.3325	87.12	12.88	364.00	165.1074
23.00	58.42	85.42	2.4188	86.64	13.36	377.48	171.2200
23.50	59.69	88.49	2.5059	86.16	13.84	391.06	177.3808
24.00	60.96	91.59	2.5935	85.67	14.33	404.74	183.5861
24.50	62.23	94.71	2.6818	85.19	14.81	418.51	189.8321
25.00	63.50	97.84	2.7705	84.70	15.30	432.36	196.1152
25.50	64.77	100.99	2.8598	84.20	15.80	446.29	202.4317
26.00	66.04	104.16	2.9494	83.71	16.29	460.28	208.7778
26.50	67.31	107.34	3.0394	83.21	16.79	474.32	215.1498
27.00	68.58	110.53	3.1298	82.71	17.29	488.42	221.5441
27.50	69.85	113.73	3.2204	82.21	17.79	502.56	227.9569
28.00	71.12	116.93	3.3112	81.71	18.29	516.73	234.3845
28.50	72.39	120.15	3.4021	81.21	18.79	530.92	240.8233
29.00	73.66	123.36	3.4932	80.70	19.30	545.14	247.2695
29.50	74.93	126.58	3.5843	80.20	19.80	559.36	253.7193
30.00	76.20	129.80	3.6755	79.70	20.30	573.58	260.1718
30.50	77.47	133.02	3.7666	79.19	20.81	587.80	266.6225
31.00	78.74	136.23	3.8577	78.69	21.31	602.02	273.0731
31.50	80.01	139.45	3.9489	78.19	21.81	616.24	279.5237
32.00	81.28	142.67	4.0400	77.68	22.32	630.47	285.9743
32.50	82.55	145.89	4.1311	77.18	22.82	644.69	292.4250
33.00	83.82	149.11	4.2222	76.68	23.32	658.91	298.8756
33.50	85.09	152.33	4.3134	76.17	23.83	673.13	305.3262
34.00	86.36	155.54	4.4045	75.67	24.33	687.35	311.7768
34.50	87.63	158.76	4.4956	75.17	24.83	701.57	318.2275
35.00	88.90	161.98	4.5868	74.66	25.34	715.79	324.6781
35.50	90.17	165.20	4.6779	74.16	25.84	730.01	331.1287

Table 8. MHTB tanking table (Continued).

Height (in)	Height (cm)	Volume (ft ³)	Volume (m ³)	Ullage (%)	Liquid (%)	Liquid Mass (lbm)	Liquid Mass (kg)
36.00	91.44	168.42	4.7690	73.66	26.34	744.24	337.5793
36.50	92.71	171.63	4.8601	73.15	26.85	758.46	344.0300
37.00	93.98	174.85	4.9513	72.65	27.35	772.68	350.4806
37.50	95.25	178.07	5.0424	72.15	27.85	786.90	356.9312
38.00	96.52	181.29	5.1335	71.64	28.36	801.12	363.3818
38.50	97.79	184.51	5.2247	71.14	28.86	815.34	369.8325
39.00	99.06	187.73	5.3158	70.64	29.36	829.56	376.2831
39.50	100.33	190.94	5.4069	70.13	29.87	843.78	382.7337
40.00	101.60	194.16	5.4980	69.63	30.37	858.00	389.1843
40.50	102.87	197.38	5.5892	69.13	30.87	872.23	395.6350
41.00	104.14	200.60	5.6803	68.62	31.38	886.45	402.0856
41.50	105.41	203.82	5.7714	68.12	31.88	900.67	408.5362
42.00	106.68	207.03	5.8626	67.62	32.38	914.89	414.9868
42.50	107.95	210.25	5.9537	67.11	32.89	929.11	421.4375
43.00	109.22	213.47	6.0448	66.61	33.39	943.33	427.8881
43.50	110.49	216.69	6.1359	66.11	33.89	957.55	434.3387
44.00	111.76	219.91	6.2271	65.60	34.40	971.77	440.7893
44.50	113.03	223.13	6.3182	65.10	34.90	986.00	447.2400
45.00	114.30	226.34	6.4093	64.60	35.40	1000.22	453.6906
45.50	115.57	229.56	6.5005	64.09	35.91	1014.44	460.1412
46.00	116.84	232.78	6.5916	63.59	36.41	1028.66	466.5918
46.50	118.11	236.00	6.6827	63.09	36.91	1042.88	473.0425
47.00	119.38	239.22	6.7738	62.58	37.42	1057.10	479.4931
47.50	120.65	242.43	6.8650	62.08	37.92	1071.32	485.9437
48.00	121.92	245.65	6.9561	61.58	38.42	1085.54	492.3943
48.50	123.19	248.87	7.0472	61.07	38.93	1099.76	498.8450
49.00	124.46	252.09	7.1384	60.57	39.43	1113.99	505.2956
49.50	125.73	255.31	7.2295	60.07	39.93	1128.21	511.7462
50.00	127.00	258.53	7.3206	59.56	40.44	1142.43	518.1968
50.50	128.27	261.74	7.4117	59.06	40.94	1156.65	524.6475
51.00	129.54	264.96	7.5029	58.56	41.44	1170.87	531.0981
51.50	130.81	268.18	7.5940	58.05	41.95	1185.09	537.5487
52.00	132.08	271.40	7.6851	57.55	42.45	1199.31	543.9993
52.50	133.35	274.62	7.7763	57.05	42.95	1213.53	550.4500
53.00	134.62	277.83	7.8674	56.54	43.46	1227.76	556.9006
53.50	135.89	281.05	7.9585	56.04	43.96	1241.98	563.3512
54.00	137.16	284.27	8.0496	55.54	44.46	1256.20	569.8018
54.50	138.43	287.49	8.1408	55.03	44.97	1270.42	576.2525
55.00	139.70	290.71	8.2319	54.53	45.47	1284.64	582.7031
55.50	140.97	293.93	8.3230	54.03	45.97	1298.86	589.1537

Table 8. MHTB tanking table (Continued).

Height (in)	Height (cm)	Volume (ft ³)	Volume (m ³)	Ullage (%)	Liquid (%)	Liquid Mass (lbm)	Liquid Mass (kg)
56.00	142.24	297.14	8.4142	53.52	46.48	1313.08	595.6043
56.50	143.51	300.36	8.5053	53.02	46.98	1327.30	602.0550
57.00	144.78	303.58	8.5964	52.52	47.48	1341.53	608.5056
57.50	146.05	306.80	8.6875	52.01	47.99	1355.75	614.9562
58.00	147.32	310.02	8.7787	51.51	48.49	1369.97	621.4068
58.50	148.59	313.23	8.8698	51.01	48.99	1384.19	627.8575
59.00	149.86	316.45	8.9609	50.50	49.50	1398.41	634.3081
59.50	151.13	319.67	9.0521	50.00	50.00	1412.63	640.7587
60.00	152.40	322.89	9.1432	49.50	50.50	1426.85	647.2093
60.50	153.67	326.11	9.2343	48.99	51.01	1441.07	653.6600
61.00	154.94	329.33	9.3254	48.49	51.51	1455.29	660.1106
61.50	156.21	332.54	9.4166	47.99	52.01	1469.52	666.5612
62.00	157.48	335.76	9.5077	47.48	52.52	1483.74	673.0118
62.50	158.75	338.98	9.5988	46.98	53.02	1497.96	679.4625
63.00	160.02	342.20	9.6900	46.48	53.52	1512.18	685.9131
63.50	161.29	345.42	9.7811	45.97	54.03	1526.40	692.3637
64.00	162.56	348.63	9.8722	45.47	54.53	1540.62	698.8143
64.50	163.83	351.85	9.9633	44.97	55.03	1554.84	705.2650
65.00	165.10	355.07	10.0545	44.46	55.54	1569.06	711.7156
65.50	166.37	358.29	10.1456	43.96	56.04	1583.29	718.1662
66.00	167.64	361.51	10.2367	43.46	56.54	1597.51	724.6168
66.50	168.91	364.73	10.3278	42.95	57.05	1611.73	731.0675
67.00	170.18	367.94	10.4190	42.45	57.55	1625.95	737.5181
67.50	171.45	371.16	10.5101	41.95	58.05	1640.17	743.9687
68.00	172.72	374.38	10.6012	41.44	58.56	1654.39	750.4193
68.50	173.99	377.60	10.6924	40.94	59.06	1668.61	756.8700
69.00	175.26	380.82	10.7835	40.44	59.56	1682.83	763.3206
69.50	176.53	384.03	10.8746	39.93	60.07	1697.06	769.7712
70.00	177.80	387.25	10.9657	39.43	60.57	1711.28	776.2218
70.50	179.07	390.47	11.0569	38.93	61.07	1725.50	782.6725
71.00	180.34	393.69	11.1480	38.42	61.58	1739.72	789.1231
71.50	181.61	396.91	11.2391	37.92	62.08	1753.94	795.5737
72.00	182.88	400.13	11.3303	37.42	62.58	1768.16	802.0243
72.50	184.15	403.34	11.4214	36.91	63.09	1782.38	808.4750
73.00	185.42	406.56	11.5125	36.41	63.59	1796.60	814.9256
73.50	186.69	409.78	11.6036	35.91	64.09	1810.82	821.3762
74.00	187.96	413.00	11.6948	35.40	64.60	1825.05	827.8268
74.50	189.23	416.22	11.7859	34.90	65.10	1839.27	834.2775
75.00	190.50	419.43	11.8770	34.40	65.60	1853.49	840.7281
75.50	191.77	422.65	11.9682	33.89	66.11	1867.71	847.1787

Table 8. MHTB tanking table (Continued).

Height (in)	Height (cm)	Volume (ft ³)	Volume (m ³)	Ullage (%)	Liquid (%)	Liquid Mass (lbm)	Liquid Mass (kg)
76.00	193.04	425.87	12.0593	33.39	66.61	1881.93	853.6293
76.50	194.31	429.09	12.1504	32.89	67.11	1896.15	860.0800
77.00	195.58	432.31	12.2415	32.38	67.62	1910.37	866.5306
77.50	196.85	435.53	12.3327	31.88	68.12	1924.59	872.9812
78.00	198.12	438.74	12.4238	31.38	68.62	1938.82	879.4318
78.50	199.39	441.96	12.5149	30.87	69.13	1953.04	885.8824
79.00	200.66	445.18	12.6061	30.37	69.63	1967.26	892.3331
79.50	201.93	448.40	12.6972	29.87	70.13	1981.48	898.7837
80.00	203.20	451.62	12.7883	29.36	70.64	1995.70	905.2343
80.50	204.47	454.83	12.8794	28.86	71.14	2009.92	911.6849
81.00	205.74	458.05	12.9706	28.36	71.64	2024.14	918.1356
81.50	207.01	461.27	13.0617	27.85	72.15	2038.36	924.5862
82.00	208.28	464.49	13.1528	27.35	72.65	2052.58	931.0368
82.50	209.55	467.71	13.2440	26.85	73.15	2066.81	937.4874
83.00	210.82	470.93	13.3351	26.34	73.66	2081.03	943.9381
83.50	212.09	474.14	13.4262	25.84	74.16	2095.25	950.3887
84.00	213.36	477.36	13.5173	25.34	74.66	2109.47	956.8393
84.50	214.63	480.58	13.6085	24.83	75.17	2123.69	963.2899
85.00	215.90	483.80	13.6996	24.33	75.67	2137.91	969.7406
85.50	217.17	487.02	13.7907	23.83	76.17	2152.13	976.1912
86.00	218.44	490.23	13.8819	23.32	76.68	2166.35	982.6418
86.50	219.71	493.45	13.9730	22.82	77.18	2180.58	989.0924
87.00	220.98	496.67	14.0641	22.32	77.68	2194.80	995.5431
87.50	222.25	499.89	14.1552	21.81	78.19	2209.02	1001.9937
88.00	223.52	503.11	14.2464	21.31	78.69	2223.24	1008.4443
88.50	224.79	506.33	14.3375	20.80	79.20	2237.46	1014.8949
89.00	226.06	509.54	14.4286	20.30	79.70	2251.68	1021.3456
89.50	227.33	512.76	14.5198	19.80	80.20	2265.90	1027.7962
90.00	228.60	515.98	14.6108	19.30	80.70	2280.12	1034.2433
90.50	229.87	519.19	14.7019	18.79	81.21	2294.33	1040.6895
91.00	231.14	522.41	14.7929	18.29	81.71	2308.52	1047.1282
91.50	232.41	525.61	14.8837	17.79	82.21	2322.69	1053.5559
92.00	233.68	528.81	14.9743	17.29	82.71	2336.83	1059.9687
92.50	234.95	532.00	15.0646	16.79	83.21	2350.93	1066.3630
93.00	236.22	535.18	15.1546	16.29	83.71	2364.98	1072.7350
93.50	237.49	538.35	15.2443	15.80	84.20	2378.97	1079.0811
94.00	238.76	541.50	15.3335	15.30	84.70	2392.89	1085.3976
94.50	240.03	544.63	15.4223	14.81	85.19	2406.74	1091.6807
95.00	241.30	547.75	15.5105	14.33	85.67	2420.51	1097.9267
95.50	242.57	550.84	15.5982	13.84	86.16	2434.19	1104.1320

Table 8. MHTB tanking table (Continued).

Height (in)	Height (cm)	Volume (ft ³)	Volume (m ³)	Ullage (%)	Liquid (%)	Liquid Mass (lbm)	Liquid Mass (kg)
96.00	243.84	553.92	15.6852	13.36	86.64	2447.78	1110.2928
96.50	245.11	556.97	15.7716	12.88	87.12	2461.25	1116.4054
97.00	246.38	559.99	15.8572	12.41	87.59	2474.61	1122.4661
97.50	247.65	562.99	15.9420	11.94	88.06	2487.85	1128.4713
98.00	248.92	565.95	16.0260	11.48	88.52	2500.96	1134.4171
98.50	250.19	568.89	16.1091	11.02	88.98	2513.93	1140.3000
99.00	251.46	571.79	16.1913	10.57	89.43	2526.75	1146.1161
99.50	252.73	574.66	16.2724	10.12	89.88	2539.42	1151.8618
100.00	254.00	577.49	16.3526	9.67	90.33	2551.92	1157.5334
100.50	255.27	580.28	16.4316	9.24	90.76	2564.26	1163.1272
101.00	256.54	583.03	16.5095	8.81	91.19	2576.41	1168.6394
101.50	257.81	585.73	16.5861	8.38	91.62	2588.37	1174.0664
102.00	259.08	588.40	16.6615	7.97	92.03	2600.14	1179.4044
102.50	260.35	591.01	16.7356	7.56	92.44	2611.71	1184.6498
103.00	261.62	593.58	16.8084	7.16	92.84	2623.06	1189.7988
103.50	262.89	596.10	16.8797	6.76	93.24	2634.19	1194.8478
104.00	264.16	598.57	16.9496	6.38	93.62	2645.09	1199.7930
104.50	265.43	600.98	17.0179	6.00	94.00	2655.76	1204.6307
105.00	266.70	603.34	17.0847	5.63	94.37	2666.18	1209.3572
105.50	267.97	605.64	17.1498	5.27	94.73	2676.34	1213.9689
106.00	269.24	607.88	17.2133	4.92	95.08	2686.25	1218.4619
106.50	270.51	610.06	17.2751	4.58	95.42	2695.88	1222.8327
107.00	271.78	612.18	17.3350	4.25	95.75	2705.24	1227.0774
107.50	273.05	614.23	17.3932	3.93	96.07	2714.31	1231.1924
108.00	274.32	616.22	17.4494	3.62	96.38	2723.09	1235.1740
108.50	275.59	618.14	17.5037	3.32	96.68	2731.57	1239.0185
109.00	276.86	619.99	17.5560	3.03	96.97	2739.73	1242.7221
109.50	278.13	621.76	17.6063	2.75	97.25	2747.58	1246.2812
110.00	279.40	623.46	17.6545	2.48	97.52	2755.10	1249.6921
110.50	280.67	625.09	17.7005	2.23	97.77	2762.28	1252.9510
111.00	281.94	626.64	17.7444	1.99	98.01	2769.13	1256.0543
111.50	283.21	628.11	17.7860	1.76	98.24	2775.62	1258.9981
112.00	284.48	629.49	17.8253	1.54	98.46	2781.75	1261.7790
112.50	285.75	630.80	17.8622	1.34	98.66	2787.51	1264.3930
113.00	287.02	632.02	17.8967	1.15	98.85	2792.90	1266.8366
113.50	288.29	633.15	17.9288	0.97	99.03	2797.90	1269.1060
114.00	289.56	634.19	17.9583	0.80	99.20	2802.51	1271.1974
114.50	290.83	635.15	17.9853	0.66	99.34	2806.72	1273.1073
115.00	292.10	636.01	18.0097	0.52	99.48	2810.52	1274.8319
115.50	293.37	636.77	18.0313	0.40	99.60	2813.91	1276.3675

Table 8. MHTB tanking table (Continued).

Height (in)	Height (cm)	Volume (ft ³)	Volume (m ³)	Ullage (%)	Liquid (%)	Liquid Mass (lbm)	Liquid Mass (kg)
116.00	294.64	637.44	18.0503	0.30	99.70	2816.87	1277.7103
116.50	295.91	638.01	18.0665	0.21	99.79	2819.40	1278.8567
117.00	297.18	638.49	18.0799	0.13	99.87	2821.48	1279.8030
117.50	298.45	638.86	18.0904	0.08	99.92	2823.12	1280.5455
118.00	299.72	639.12	18.0979	0.03	99.97	2824.30	1281.0804
118.50	300.99	639.28	18.1025	0.01	99.99	2825.01	1281.4041
119.00	302.26	639.34	18.1040	0.00	100.00	2825.25	1281.5128

APPENDIX B—MULTIPURPOSE HYDROGEN TEST BED TEST ARTICLE INSTRUMENTATION

Appendix B contains the instrumentation database document that describes the MHTB instrumentation used in the spray bar performance testing. Some of the information repeats that presented in the main body of this Technical Memorandum and some is applicable only to previously performed thermal insulation testing. However, in the interest of completeness, the entire document is presented.

Multipurpose Hydrogen Test Bed (MHTB) Instrumentation Data Base

James Martin/EP25

This document details the instrumentation use on the Multipurpose Hydrogen Test Bed hardware. This includes instrumentation used on the tank interior/exterior, tank insulation/penetrations, tank support system and environmental shroud. This document is dedicated primarily to instrumentation which was installed during fabrication and assembly of test hardware, however, some facility instrumentation is noted if it is mounted in close proximity to the test hardware.

The breakdown of test article instrumentation is outlined by the following categories:

- 1) MHTB Program Over View and Hardware Description
- 2) MHTB Tank General Instrumentation Layout
- 3) MHTB Thermal Control System Instrumentation
- 4) MHTB Support Leg Penetration Instrumentation
- 5) MHTB Vent Penetration Instrumentation
- 6) MHTB Fill / Drain Penetration Instrumentation
- 7) MHTB Pressurization Penetration Instrumentation
- 8) MHTB MLI Interstitial Pressure Probe Instrumentation
- 9) MHTB Manhole Cover and Pump Out Penetration Instrumentation
- 10) MHTB Internal Rake and Fluid Instrumentation
- 11) MHTB Environmental Shroud Instrumentation
- 12) MHTB Zero-g Thermodynamic Vent System Instrumentation

Related Documents

- 1) MHTB Test Requirements Document (EP25 (93-25))
- 2) MHTB Thermal Control Subsystem (TCS) Test Plan (EP25 (94-04))
- 3) MHTB Pre-Installation Operations Document (EP25(94-13))
- 4) MHTB Thermodynamic Vent System (TVS) Test Plan (EP25(94-12))
- 5) MHTB Thermodynamic Vent System Installation Procedure

1) MHTB Program Over View and Hardware Description

The MSFC has established a technology/advanced development program to address the area of Cryogenic Fluid Management (CFM) for orbital applications, an area common to practically all future space programs. As part of this activity a test bed, termed the multipurpose hydrogen test bed (MHTB), was devised such that a variety of CFM subsystems could be integrated and evaluated in a ground based test environment. To minimize the reliance on scaling analyses in extrapolating overall performance data, the test bed is representative in both size and shape to that of a full scale space transfer vehicle liquid hydrogen tank. Current plans baseline testing of two key technology needs in representative spacecraft thermal and vacuum environments. The first involves evaluation of a foam multilayer insulation (FMLI) thermal control concept. This concept incorporates a spray on foam insulation (SOFI) attached to the surface of the test bed tank and is in turn covered with a 45 layer variable density multi-layer insulation (MLI) blanket. This blanket is constructed of double aluminized mylar (DAM) sheets separated by Dacron netting. The second, an active tank pressure control system, is referred to as a zero-g thermodynamic vent system (TVS). This hardware will be installed after completion of the TCS test phase and consists of a tank internal spray bar/heat exchanger and tank external recirculation pump, Joule Thompson valve and back pressure orifice. More information regarding exact details of each test program can be found in the respective subsystem test plans.

The MHTB tank is constructed of aluminum 5083 and has a cylindrical shape with both a height and diameter of 3.05 m (10 ft) and elliptical domes as shown in figure 84. The tank has an internal volume of 18.09 m³ (639 ft³) with a surface area to volume ratio of 1.92 l/m (0.58 l/ft). The tank was designed and constructed per the ASME code (section VIII, Division 1) for a working differential pressure of 344 kPa (50 psig). The tank's total weight is 1270 kg (2800 lbm). The tank is equipped with a variety of penetrations, supporting hardware, and technology subsystems illustrated in figure 84.

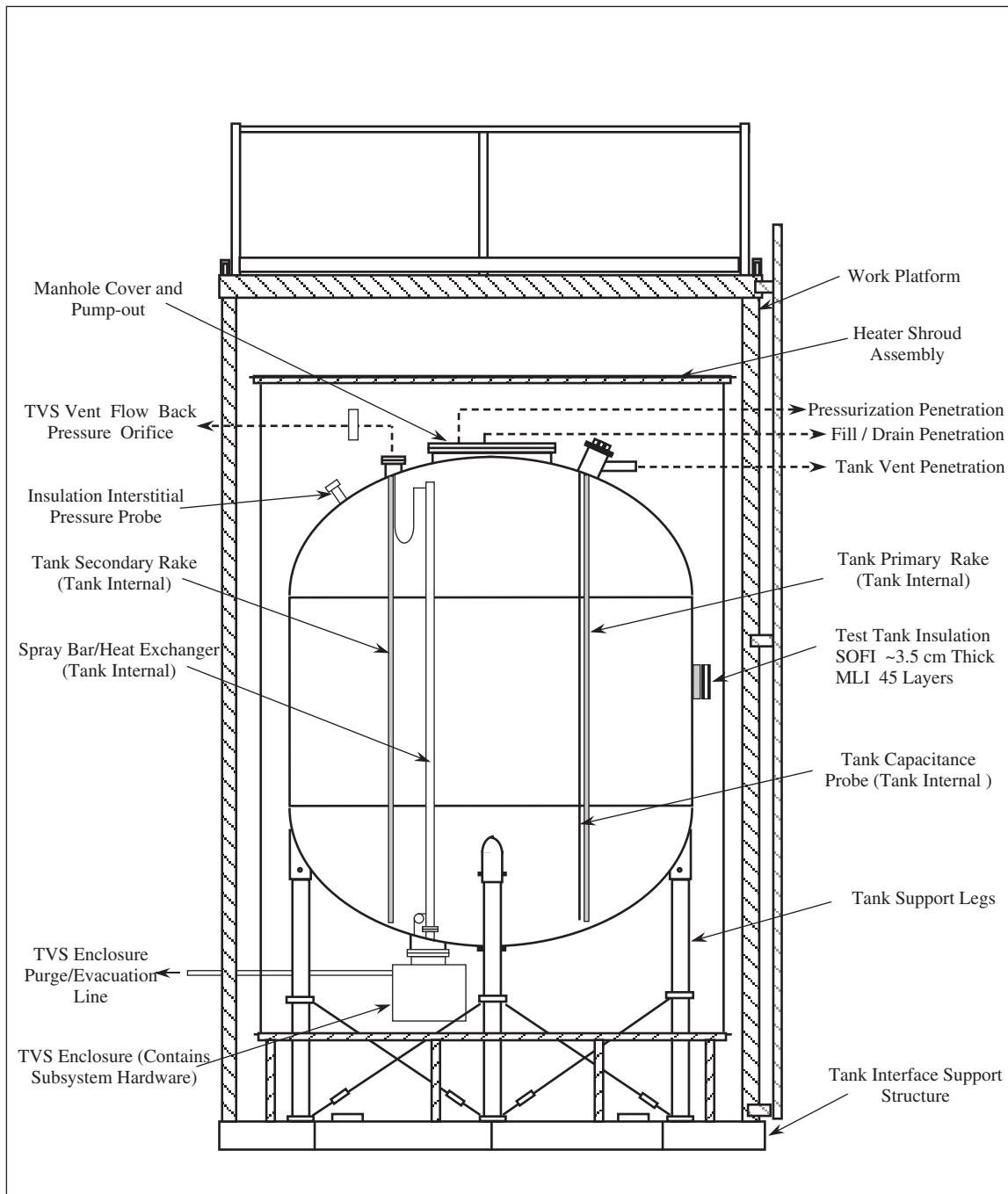


Figure 84. General MHTB tank schematic.

2) General MHTB Tank Instrumentation Layout

The general layout of instrumentation on the test bed is illustrated in figures 85–87. These figures represent the top, front and bottom views of the test tank without insulation to avoid confusion. However, the seams between major MLI blanket assemblies are indicated by dotted lines. A detailed description of instrumentation numbers and profiles shown on these figures is discussed in later document sections and Appendix A. Most of the instrumentation is composed of silicon diodes and thermocouples for measurement of thermal gradients (several pressure transducers are present). Typically, silicon diodes (Lakeshore type DT-470-11A) temperature transducers are placed in areas of lowest temperatures because they possess a higher accuracy at these temperatures when compared to thermocouples. Typical low temperature areas include the tank aluminum shell and SOFI material covering the tank. Thermocouples (Type E) are used in regions of higher temperature, such as within the MLI or on surfaces somewhat distant from the test tank contact point, where their accuracy becomes somewhat improved. The bulk of the instrumentation leads for components residing on the upper bulkhead and barrel section were routed toward the tank vent flange, while those on the lower bulkhead were routed out leg #1. There were some exceptions to this rule. Some of the penetration instrumentation was easier to route out along the respective penetration rather than snaking it to the vent or leg #1 area.

The tank orientation with respect to the vacuum chamber is such that the 0° reference is directed from the test tank center through the secondary instrumentation rake penetration toward the chamber door. Positive angle measurement from this reference is taken in a clockwise location from a vacuum chamber perspective looking down on top of the test article. The complete MHTB instrumentation data base is included in Appendix A of this document.

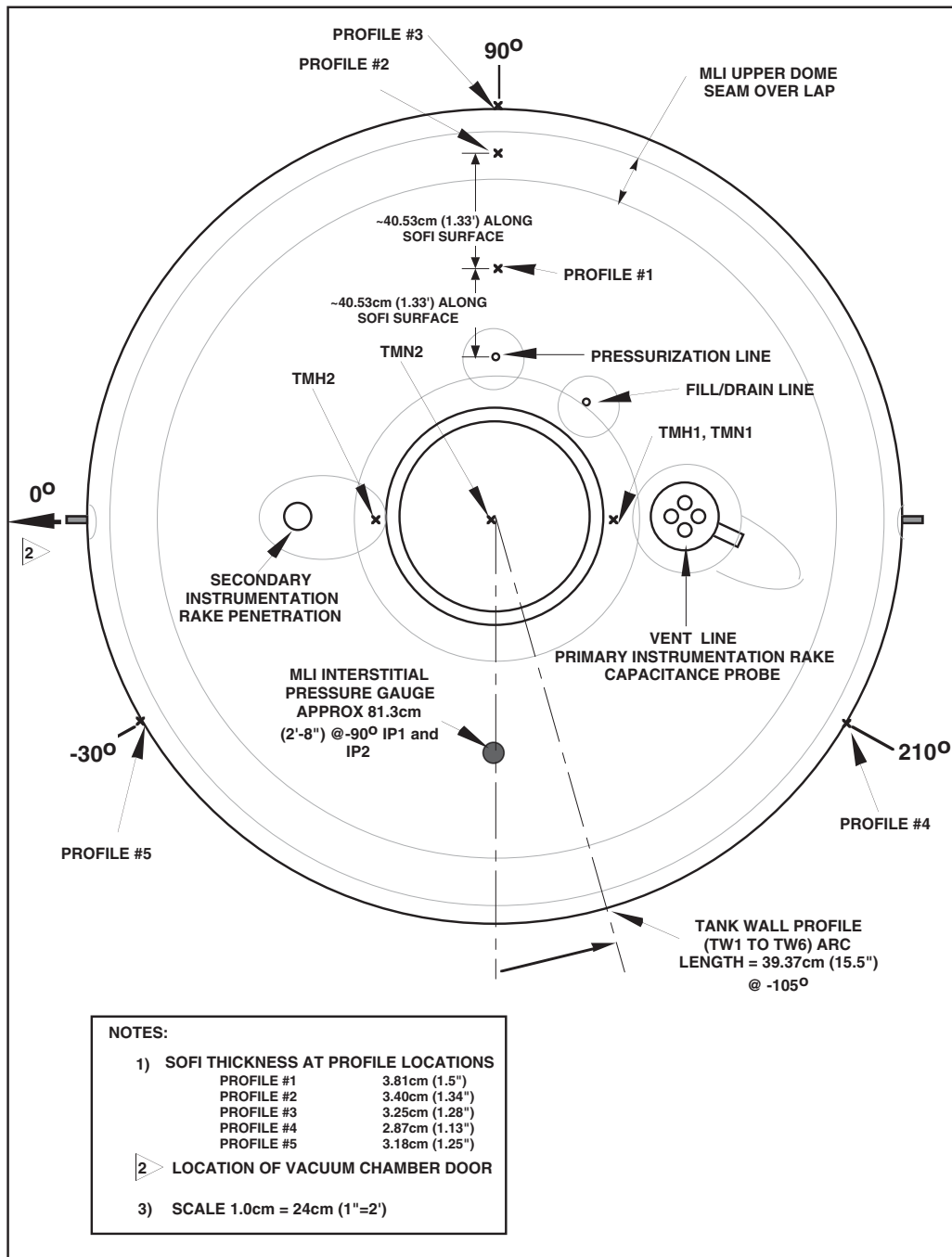


Figure 85. MHTB tank instrumentation top view.

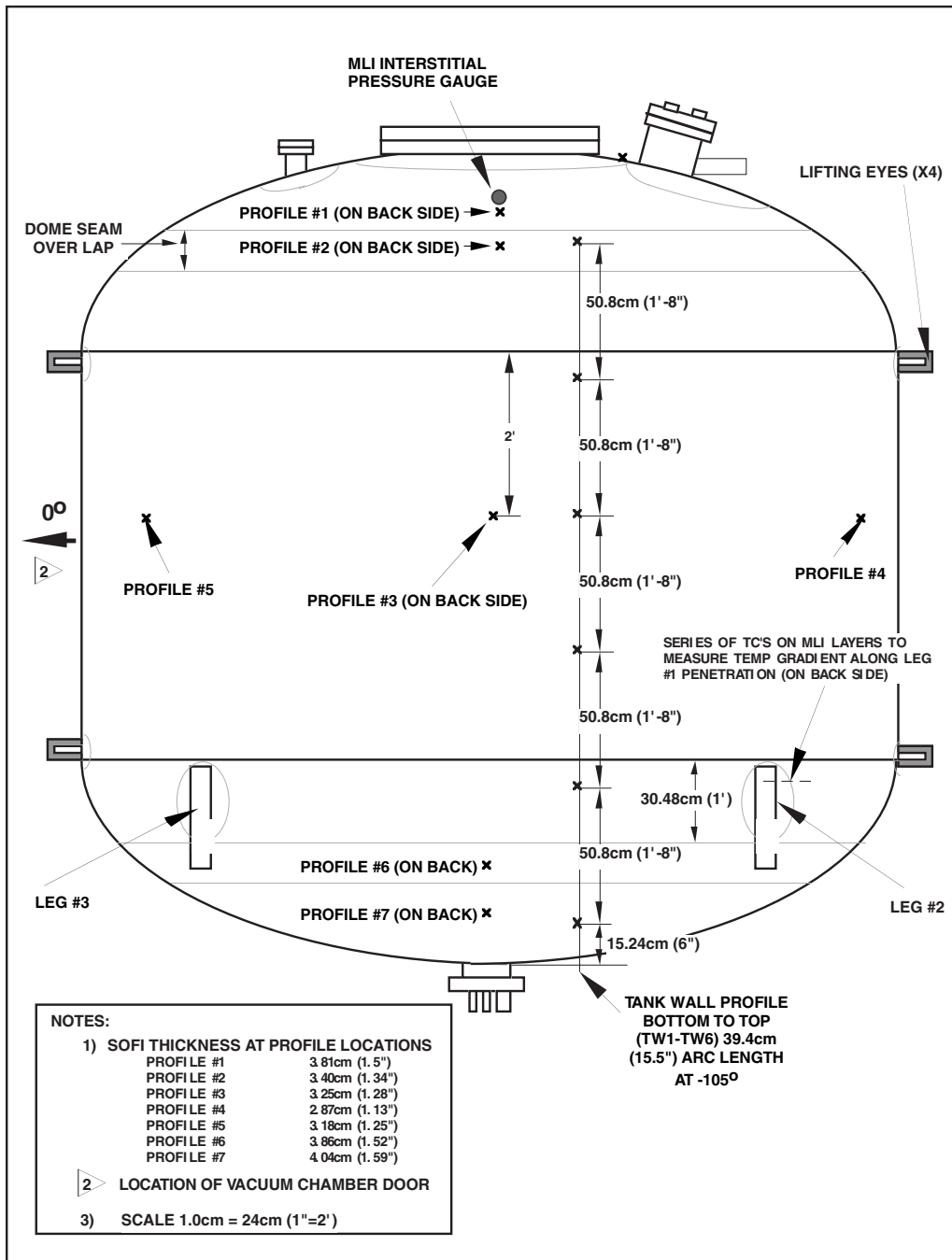


Figure 86. MHTB tank instrumentation side view.

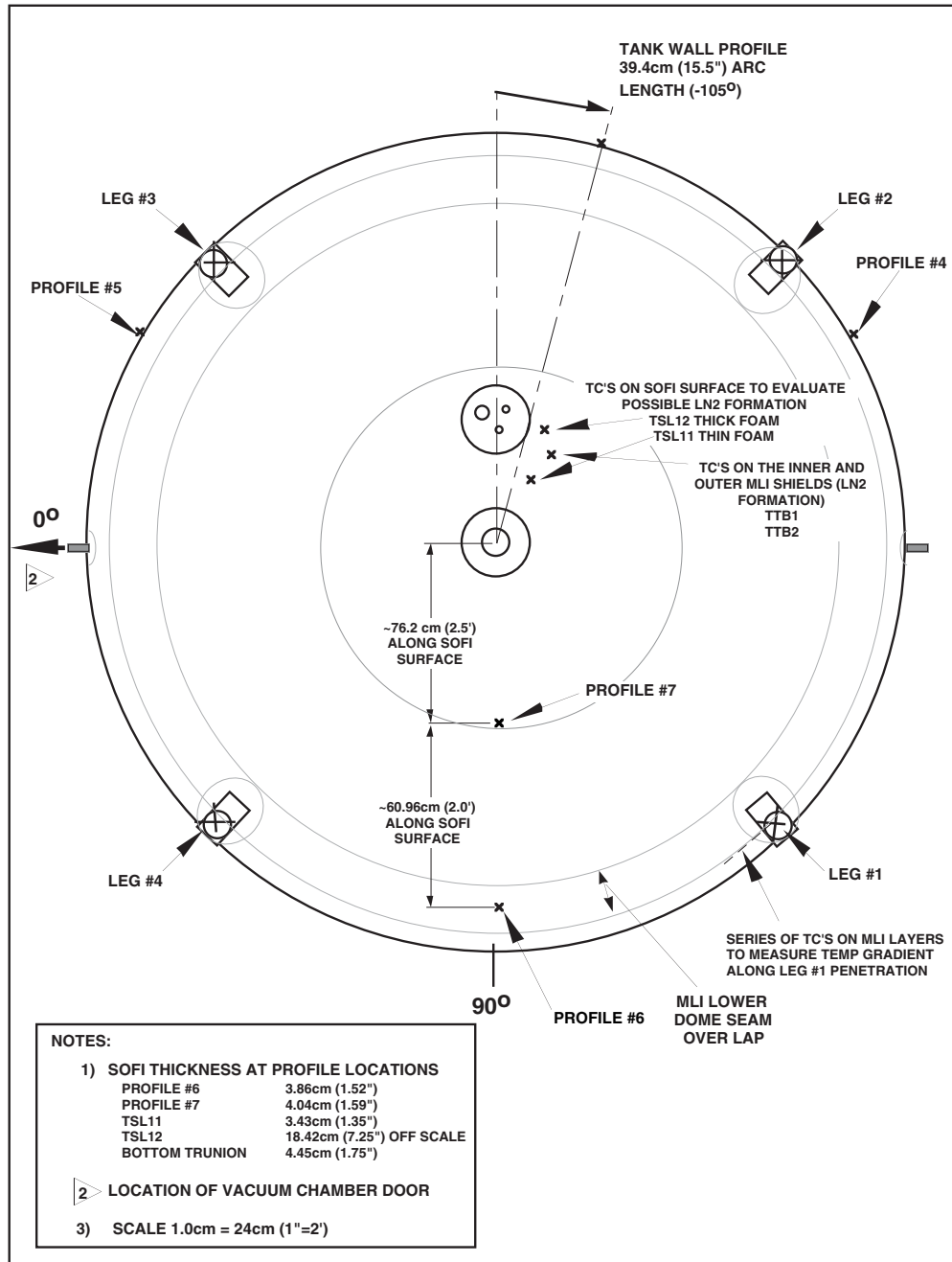


Figure 87. MHTB tank instrumentation bottom view.

3) MHTB Thermal Control System Instrumentation

A total of seven instrumentation profiles are incorporated into the test tank FMLI insulation with each profile composed of one silicon diode and four thermocouples. Figure 88 illustrates the typical location of each piece of instrumentation within the insulation layers. The diode (TSF#) was attached to the foam surface using a cryogenic epoxy (Lakeshore Stycast) while the thermocouples (TM#, TMI#, TMM# and TMO#) were attached to the MLI shields by using a piece of aluminized tape. In an effort to limit heat leak along the thermocouple leads toward the bead attachment point, approximately 5.08cm (2") of lead wire was spiraled around the bead (and placed under the tape). Additionally, each thermocouple lead was routed out (toward the exit point) along the same MLI shield to which it was attached. The thermocouples TM# were attached to the outer surface of the inner most MLI shield. The thermocouples TMI# were attached to the outer surface of the 10 MLI shield (interface between low and medium density MLI spacing). The thermocouples TMM# were attached to the outer surface of the 25 MLI shield (interface between medium and high density MLI spacing). The thermocouples TMO# were attached to the outer surface of the outer most MLI shield (shield 45 of the high density MLI spacing). The aluminized tape used to attach the thermocouples was manufactured by Lamart Corporation and was type #326L. This tape is electrically conductive on the exterior surface and has the same approximate surface emissivity as the DAM. The tape was purchased from:

Can-Do Incorporated
P.O. Box 4366
Nashville, Tn 37204
Tele. (615) 383-1775

At each instrumentation profile the SOFI thickness was measured using a Kaman eddy current device. Figures 85–87 indicate the SOFI thickness measured at each profile location. These thicknesses will be used in determining the thermal performance of the foam insulation. Data concerning each piece of instrumentation attached to the tank insulation is included in Appendix A.

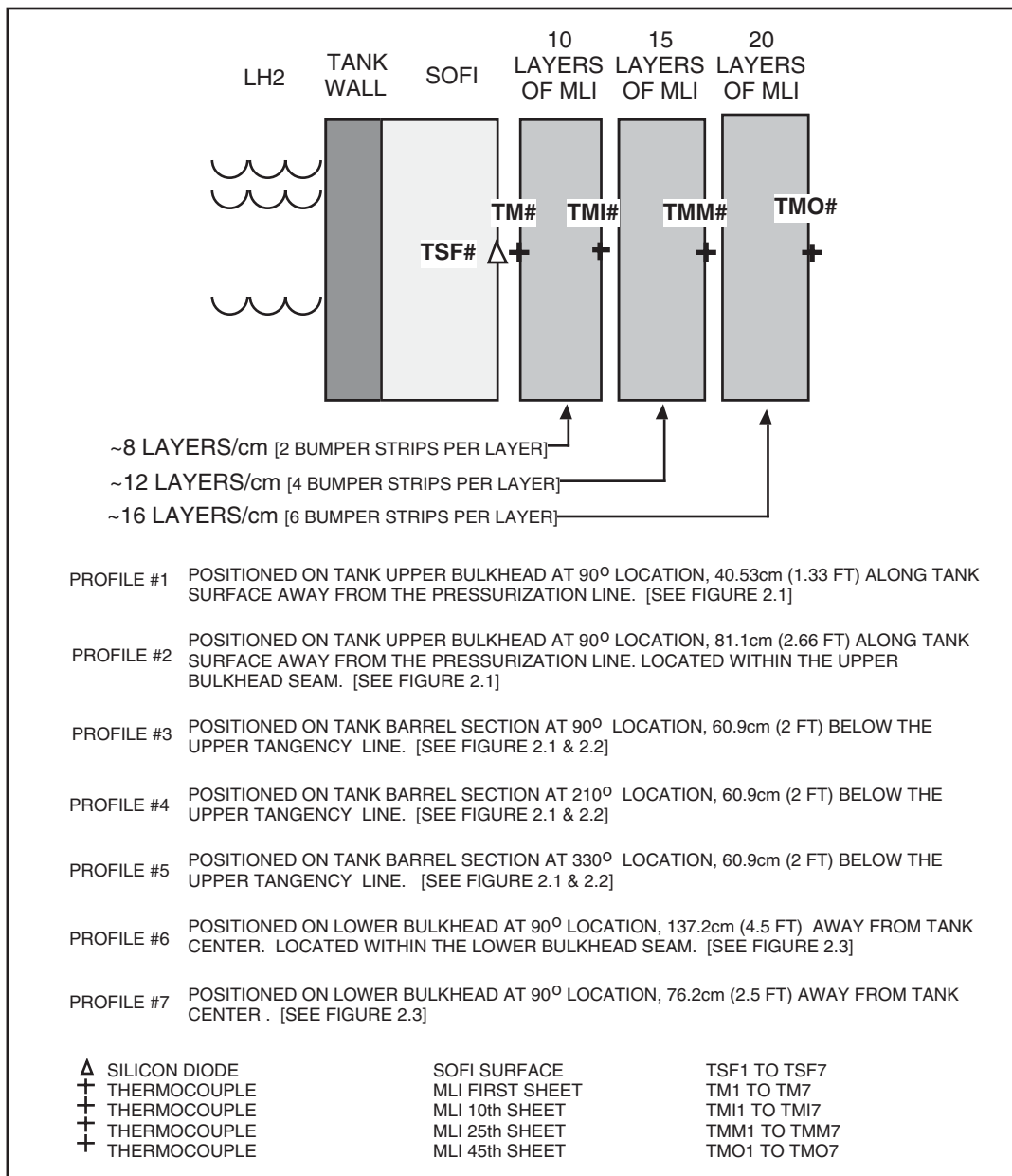


Figure 88. Typical insulation instrumentation profile.

4) MHTB Support Leg Penetration Instrumentation

The MHTB is supported by four legs as shown in figures 86 and 87. Each leg is comprised of two composite sections joined in the center by a stainless steel union. Each leg end is also equipped with stainless steel end caps which mount to the test tank and interface support structure. Two of the four tank legs are instrumented one of which, leg #1, is heavily instrumented as shown in figure 89. Silicon diodes (TSL1 and TSL2) and thermocouples (TSL5 through TSL10) are attached to the composite material (diodes closest to the tank) for determination of heat input along the support. Diodes TSL3 and TSL4 have been placed on leg #3. Each leg is equipped with a heat guard to reduce the amount of heat input. Legs #1 and #3 are instrumented with diodes (HG1 and HG3, respectively) to measure the heat guard boundary temperature. The SOFI surface (TSL17, TSL18 and TSL19) and MLI (TL13 through TL19) are also instrumented for determination of the insulation temperature profile. There are also thermocouples (TSL14 on leg #1 and TSL15 on leg #3) attached to the innermost layer of crumpled MLI (against foam) which occupies the hollow interior of the legs. These measurements will be used to determine if condensation of the insulation gaseous nitrogen (GN_2) purge gas occurs within the legs. A foam plug approximately 10.16cm (4") thick was poured into the top section of each leg's interior (above the MLI) to prevent potential condensation. The outer surface of each leg was also closed out with pour foam starting at the tank SOFI and extending out over the composite to a distance of approximately 15.24 cm (6"). Average foam thickness was based on the applied foam circumference measurements and determined to be 3.81 cm (1.5") for legs 1, 3 and 4 and 4.445 cm (1.75") for leg #2. The leg stainless steel center joint and interface support structure attachment point were instrumented with thermocouples for legs #1 (TLB1 and ISS1) and #3 (TLB3 and ISS3). Appendix A contains, in a data base format, additional information concerning the tank leg instrumentation.

5) MHTB Vent Penetration Instrumentation

The MHTB tank internal volume is vented through a 5.08 cm (2") diameter tube connected to a 20.32 cm (8") tank penetration (Conflat type flange) as illustrated in figure 90. The vent tube transitions to a vacuum jacketed pipe assembly approximately 30.48 cm (12") from the tank penetration. The penetration and tube are closed out with foam extending out over the vacuum jacketed pipe section approximately 40.64 cm (16") from the tank penetration. Average thickness of this foam based on the measured circumference is 6.98 cm (2.75"). Three silicon diodes are placed along the length of the tube for determination of heat input (TVL1 and TVL2) and evaluation of the heat guard (HG7) operation. The vent tube foam surface is instrumented with two thermocouples (TVL6 and TVL7) to assist in evaluation of heat input through the foam. The vent penetration top flange contains a tank ullage pressure measurement port and 1.27 cm (0.5") diameter sampling tube which is equipped with two thermocouples (TUP1 and TUP2). The surface temperature of the top flange is measured by a silicon diode (TVL3). Internal to the tank, the vent flange supports a capacitance probe (CAP1) and an instrumentation rake. Two diodes (TVL4 and TVL5) are supported by the rake at the 99.4% tank fill location. These diodes are positioned just below the vent penetration (inside the test tank) and provide a measurement of the out flowing gas temperature. Details regarding the instrumentation rakes will be described in a later section. Appendix A contains, in a data base format, additional information regarding this instrumentation.

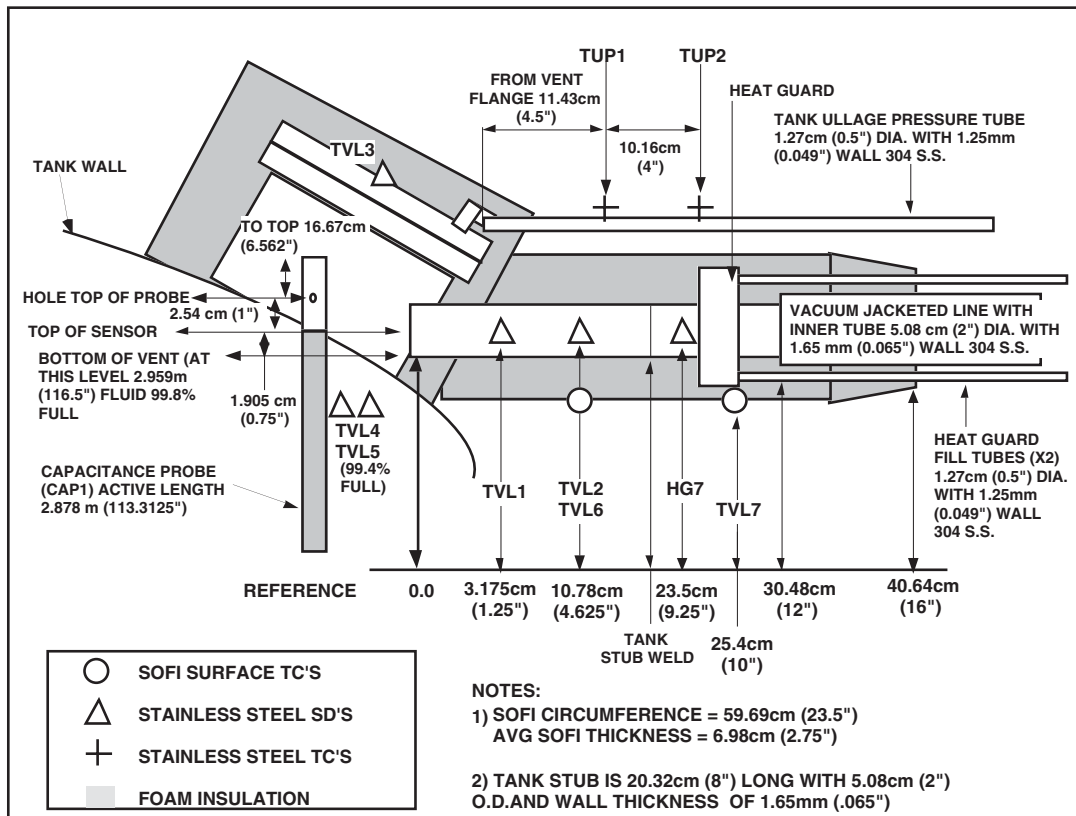


Figure 90. MHTB tank vent penetration instrumentation.

6) MHTB Fill/Drain Penetration Instrumentation

The MHTB LH₂ fluid service is provided through a 2.54 cm (1") diameter fill/drain tube attached to the test tank with an aluminum to stainless steel transition joint as illustrated in figure 91. The fill/drain tube transitions to a vacuum jacketed pipe assembly 16.51cm (6.5") from the tank penetration. A foam close-out is applied to the line and extends out over the vacuum jacketed pipe section approximately 35.56 cm (14") from the tank penetration. The average foam thickness around the fill/drain line is 6.604cm (2.6") based on the measured circumference. The tube is instrumented with three silicon diodes placed along its length to determine heat input (TFD1 and TFD2) and operation of the heat guard (HG6). The outer surface of the foam is also instrumented with two thermocouples (TFD3 and TFD4) to assist in evaluation of heat input through the foam. Appendix A contains, in a data base format, additional information regarding this instrumentation.

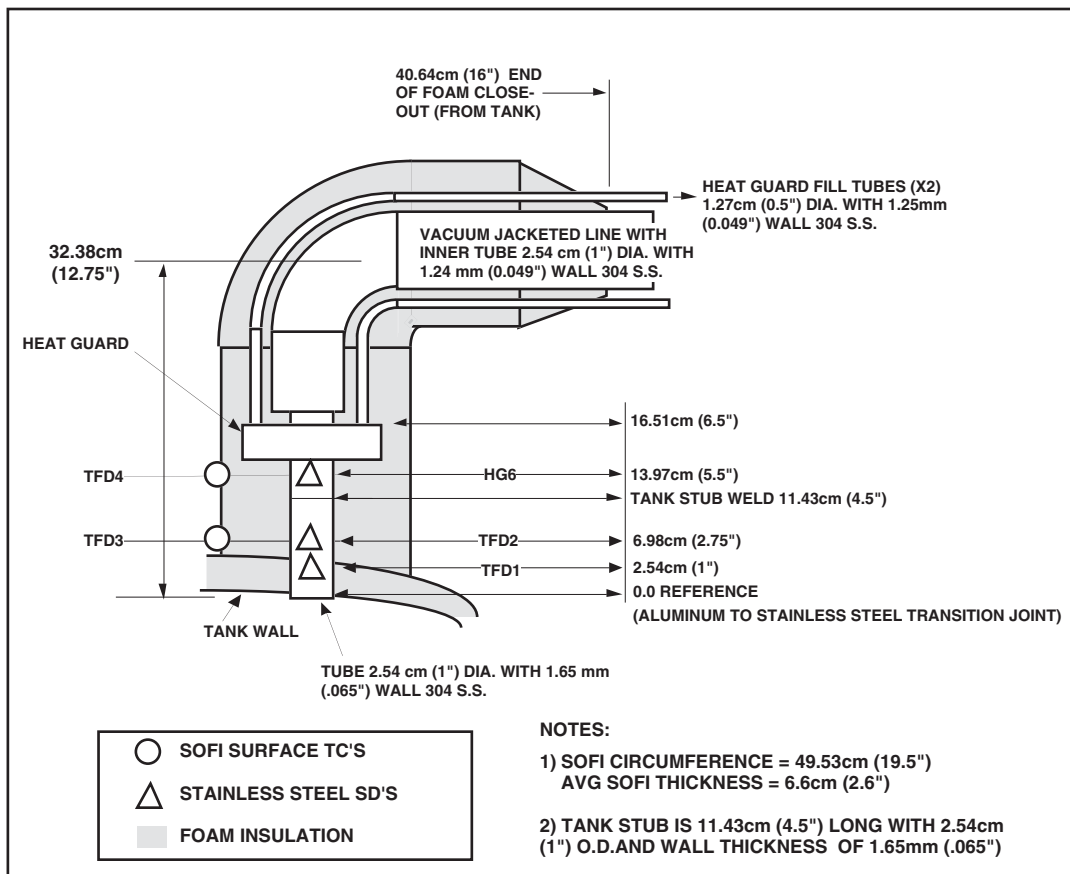


Figure 91. MHTB tank fill/drain penetration instrumentation.

7) MHTB Pressurization Penetration Instrumentation

The MHTB tank internal volume is pressurized using a 2.54 cm (1") diameter tube attached to the tank with an aluminum to stainless steel transition joint as illustrated in figure 92. The pressurization tube transitions to a double walled jacketed pipe assembly (used for gas conditioning purposes) 32.385 cm (12.75") from the tank wall. A foam close-out extends out over the jacketed pipe section approximately 40.64 cm (16") from the tank penetration. The average foam thickness around the pressurization line is 3.556 cm (1.4") based on the measured circumference. Three silicon diodes are placed along the length of the tube, between the tank and heat guard, for determination of heat input (TPL1 and TPL2) and evaluation of the heat guard (HG5) operation. The line is also equipped with two thermocouples, (TPS1) used to measure the temperature of the pressurant gas flow within the line, and (TPS2) used to measure the pressurization line outer jacket temperature. The outer surface of the foam close-out is also instrumented with two thermocouples (TPL3 and TPL4) to assist in evaluation of heat input through the foam. Appendix A contains, in a data base format, additional information regarding this instrumentation.

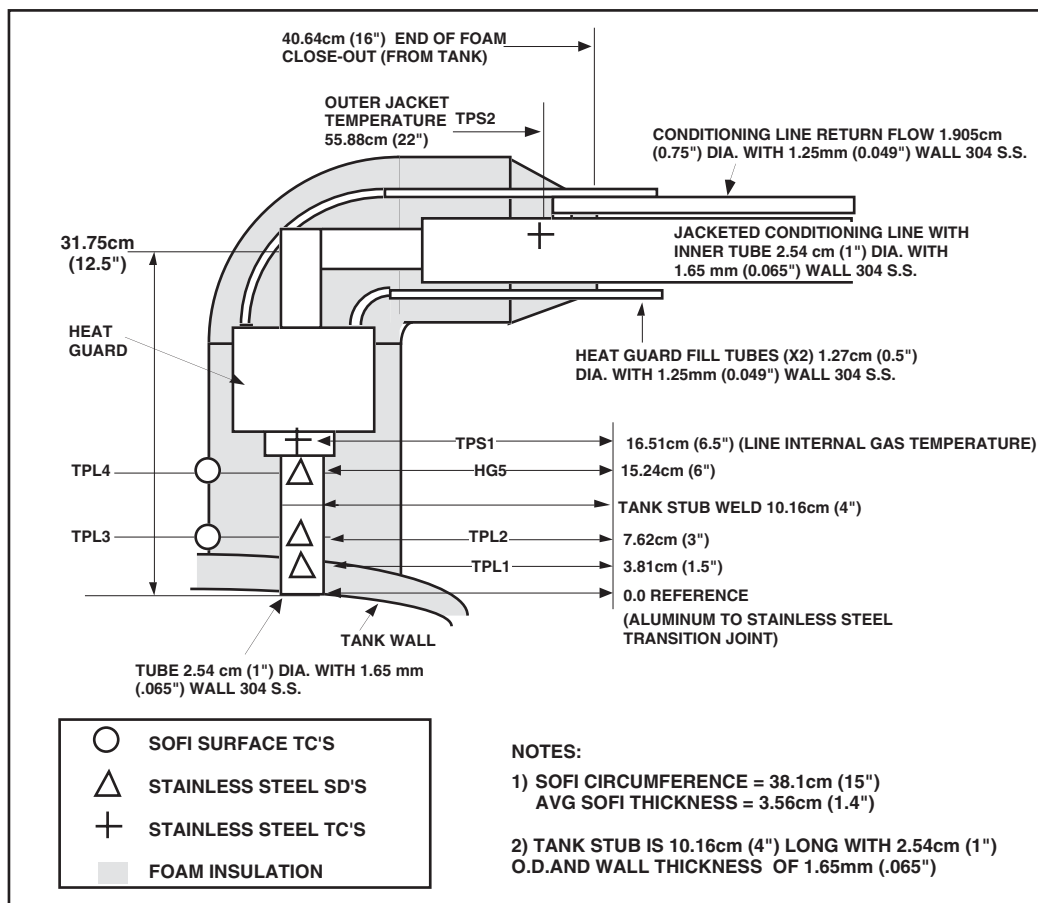


Figure 92. MHTB tank pressurization penetration instrumentation.

8) MHTB MLI Interstitial Pressure Probe Instrumentation

The gas pressure at the foam/MLI interface is measured with two pressure sensors mounted on top of a 5.08 cm (2") diameter thin wall probe that has a length of 22.86 cm (9") as illustrated in figure 93. This probe rests on the tank SOFI surface and is supported by the MLI which is taped out layer by layer to the surrounding MLI and to the probe body so as to prevent leakage of trapped MLI gases. The probe is also equipped with a 6.35mm (0.25") diameter sampling port for obtaining both dew point levels (using a hydrometer) and gas species samples (using a residual gas analyzer) from within the MLI. The two pressure transducers, a Gran Philips 275 (IP1) and a cold cathode (IP2), cover a complete pressure range from 760 to 10^{-7} torr. The Gran Philips gauge is remote mounted (for easier access) on top of the heater shroud and connected to the probe body using a flex hose. The probe body tube is equipped with three thermocouples placed along its length (IPP1, IPP2 and IPP3) to determine heat input through the probe. This probe, if necessary, shall be supported off of the tank heater shroud structure using stainless steel wire and springs to absorb transportation loads. The dew point measurement within the MLI is taken with a facility supplied Endress Hauser Model #2200 Hydrometer (DEW1). The sensing head for this unit is located in the MLI gas sample tube. Appendix A contains, in a data base format, additional information regarding this instrumentation.

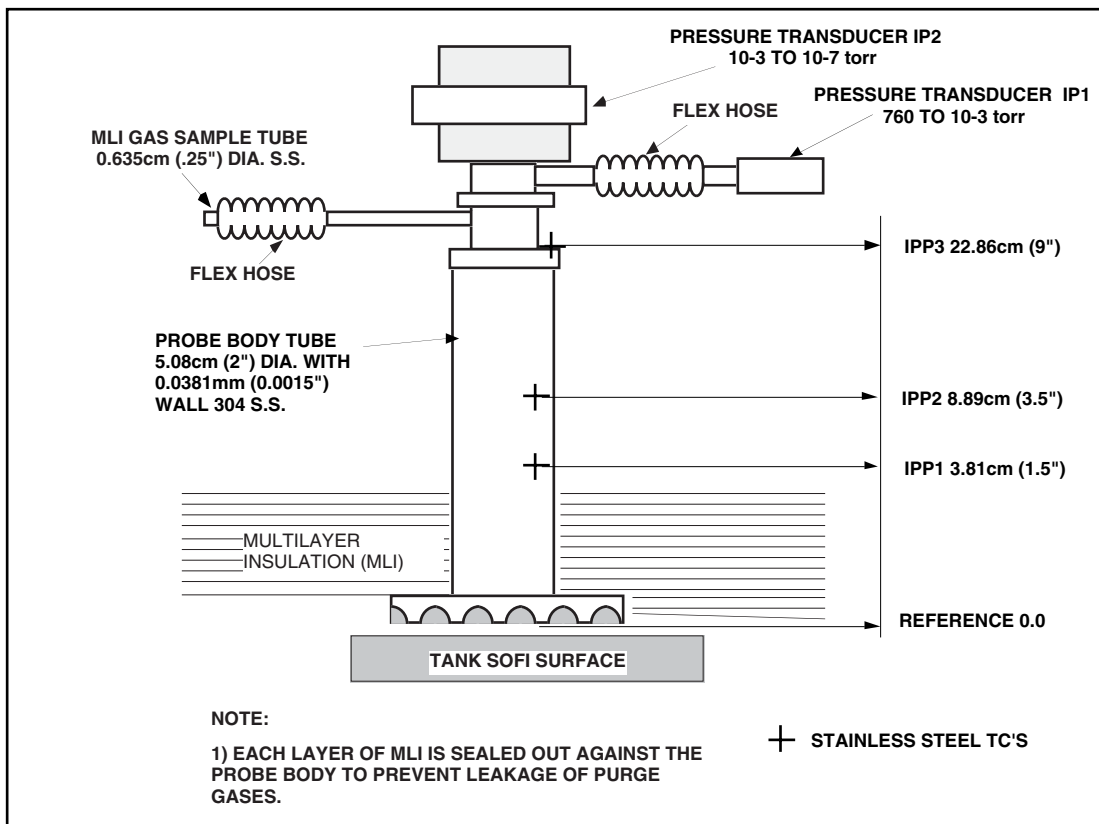


Figure 93. MHTB MLI probe instrumentation.

9) MHTB Manhole Cover & Pump Out Penetration Instrumentation

The MHTB tank is equipped with two manhole covers (inner and outer) to control potential leakage resulting in the degradation of insulation performance. Figure 94 illustrates the manhole cover set-up. The inner cover is equipped with two silicon diodes (TMN3 and TMN4) adhesively bonded to its inner surface with cryogenic epoxy (Lakeshore Stycast). The outer manhole cover exterior surface is equipped with a silicon diode (TMN2) bonded to its center with a single diode (TMN1) and two thermocouples (TMH1 and TMH2) bonded to its flange area. These temperature measurements will be used to assess the total thermal capacitance carried by the massive tank manhole system. The gas volume trapped between the inner and outer manhole covers is connected to a stainless steel evacuation line (flex hose) which is used to intercept potential leakage from the inner cover if it should occur. This flex line is equipped with two thermocouples (TCP1 and TCP2) attached to determine heat input. The spatial distance between the thermocouples is 5.08 cm (2"), however, the flex hose has a 3 to 1 contraction ratio yielding a material length of 15.24 cm (6"). The entire surface of the outer manhole cover is covered with foam insulation at an approximate thickness of 3.175cm (1.25"). The evacuation line is routed along the vent line and as such, is buried beneath the vent line foam insulation. Appendix A contains, in a data base format, additional information regarding this instrumentation.

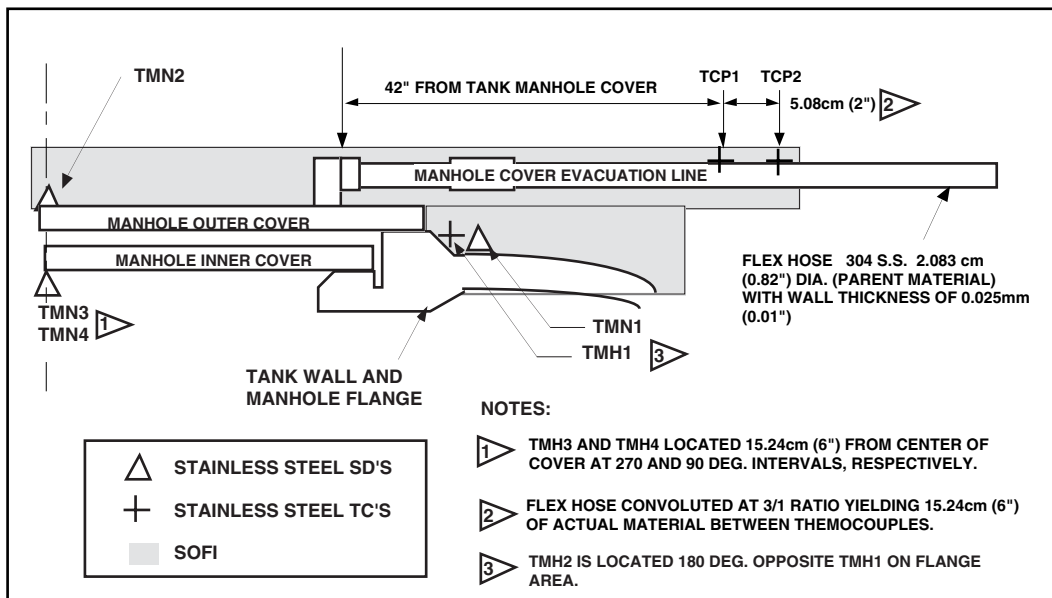


Figure 94. MHTB manhole cover and pump-out port instrumentation.

10) MHTB Internal Rake and Fluid Instrumentation

The MHTB tank is equipped internally with two instrumentation rakes and a capacitance probe which are supported from the top of the tank and extend downward. The rakes are constructed from a Fiberglass Epoxy channel section and are equipped with silicon diodes attached at given intervals using nylon rod offsets and cryogenic epoxy as illustrated in figure 95. The purpose of the rakes is to provide measurement of the temperature gradient within both the tank ullage and liquid masses in addition to providing a rough check of the liquid level to verify the capacitance probe operation. The primary rake (TD1 through TD12) positioned at 180 degrees is connected to the vent flange, while the secondary rake (TD13 through TD24) is positioned at 0 degrees as illustrated in figure 85 and 96. The capacitance probe (CAP1) provides continuous liquid level measurement and is mounted to the vent flange at the 180 degree position beside the primary rake. All tank internal instrumentation is passed through the 20.32cm (8") vent flange using four 37 pin Deutsch connectors. The exception is the capacitance probe which is equipped with its own co-axial feed through mounted in a 1.27cm (0.5") conflat type connector and attached to the center of the 20.32cm (8") vent flange. Appendix A contains, in a data base format, additional information regarding this instrumentation. Appendix B contains an MHTB tanking table with information regarding fill height, percent liquid/ullage volume and LH₂ mass.

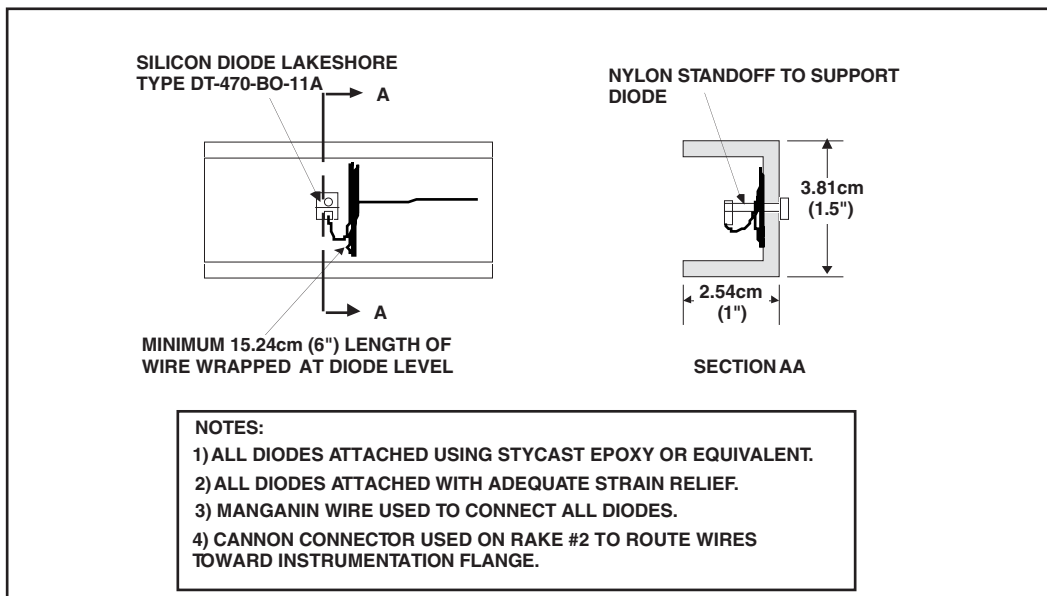


Figure 95. MHTB instrumentation rake silicon diode attachment.

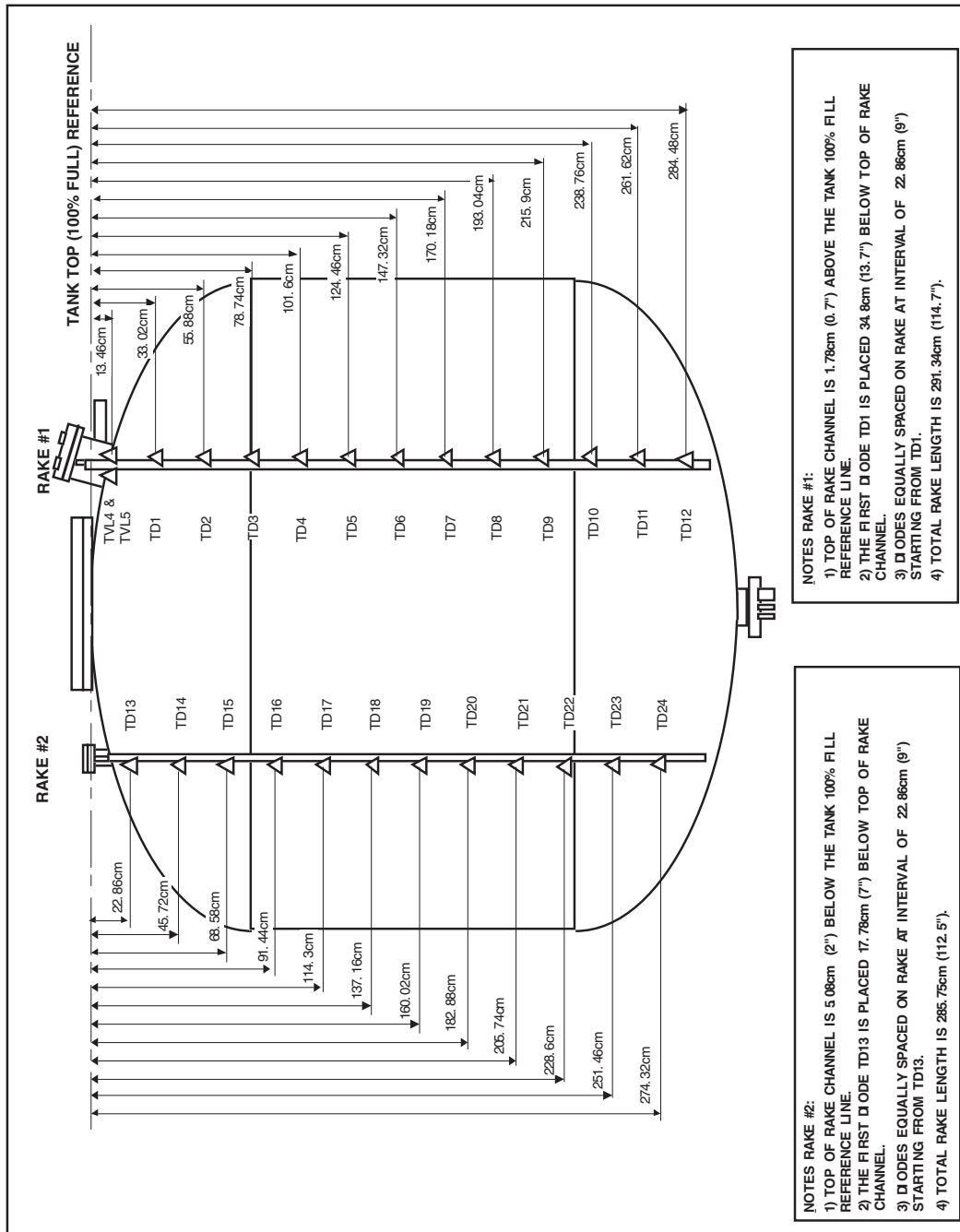


Figure 96. MHTB tank rake instrumentation layout.

11) MHTB Environmental Shroud Instrumentation

The MHTB tank and insulation systems are contained within a shroud structure that completely surrounds them and provides a warm boundary condition for which performance can be measured during testing. This structure is made completely of aluminum and is supported by the interface support structure as shown in figure 84. The shroud is composed of 17 individual panels each equipped with thermocouples attached to the inner surface of the shroud and placed beneath the electrical heating strip. These thermocouples are used with a closed loop control system to regulate each shroud panel's temperature. A minimum of two thermocouples are applied to each panel providing a primary and a backup in case of failure. Two panels #5 and #11 are equipped with additional thermocouples to provide data concerning shroud temperature gradients. Panel #11 has six thermocouples while panel #5 is heavily instrumented with 13 thermocouples since it was used during evaluation of the techniques used to assemble the shroud panels (documented in EP25(94-03)). The top shroud panels #1 through #4 are illustrated in figure 97. The typical side wall panel (5 through 12) instrumentation layout is provided in figure 98. The lower shroud panel layout (13 through 17) is illustrated in figure 99.

A series of 5 thermocouples are also placed within the annular region created between the vertical shroud panel #6 and the test tank insulation, at the 90 degree location. These thermocouples (HS18 through HS22) are spaced vertically along the panel at an interval of 60.96cm (24") with the thermocouple bead positioned approximately half way into the annular region. This instrumentation is used for measuring purge gas temperatures within the annulus. Vacuum chamber free air space temperatures are measured with facility provided thermocouples (CFA1, CFA2 and CFA3) mounted vertically at the 90 location and external to the test article shroud. These thermocouples are placed at 1.525m (5') intervals above the chamber floor. Purge gas dew point within the environmental shroud is measured with a facility supplied Endress Hauser Model #2200 Hydrometer (DEW2). The sensing head for this unit is located internal to the shroud and mounted on the lower shroud panel. Appendix A contains, in a data base format, additional information regarding this instrumentation.

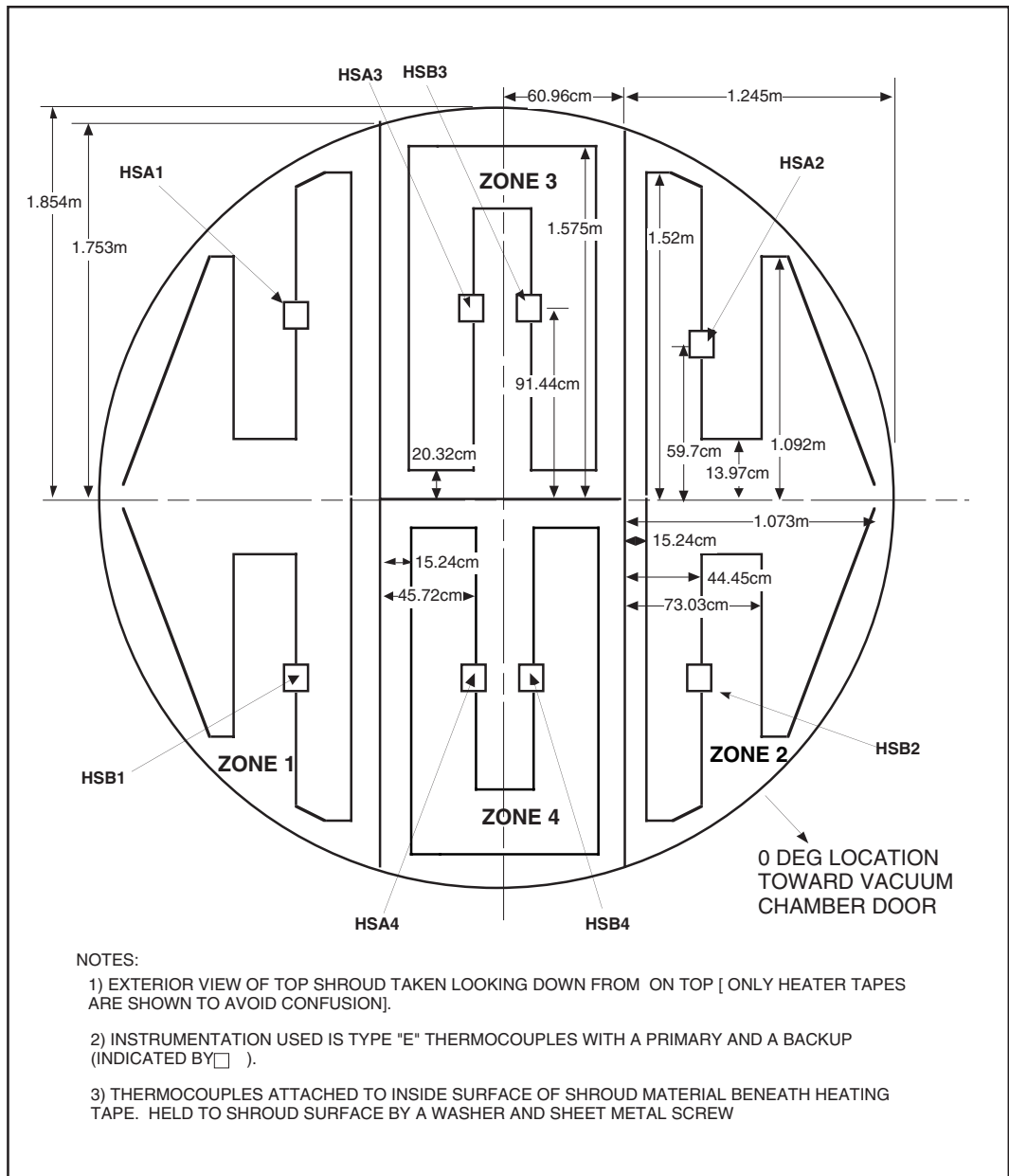


Figure 97. MHTB typical top environmental shroud panels.

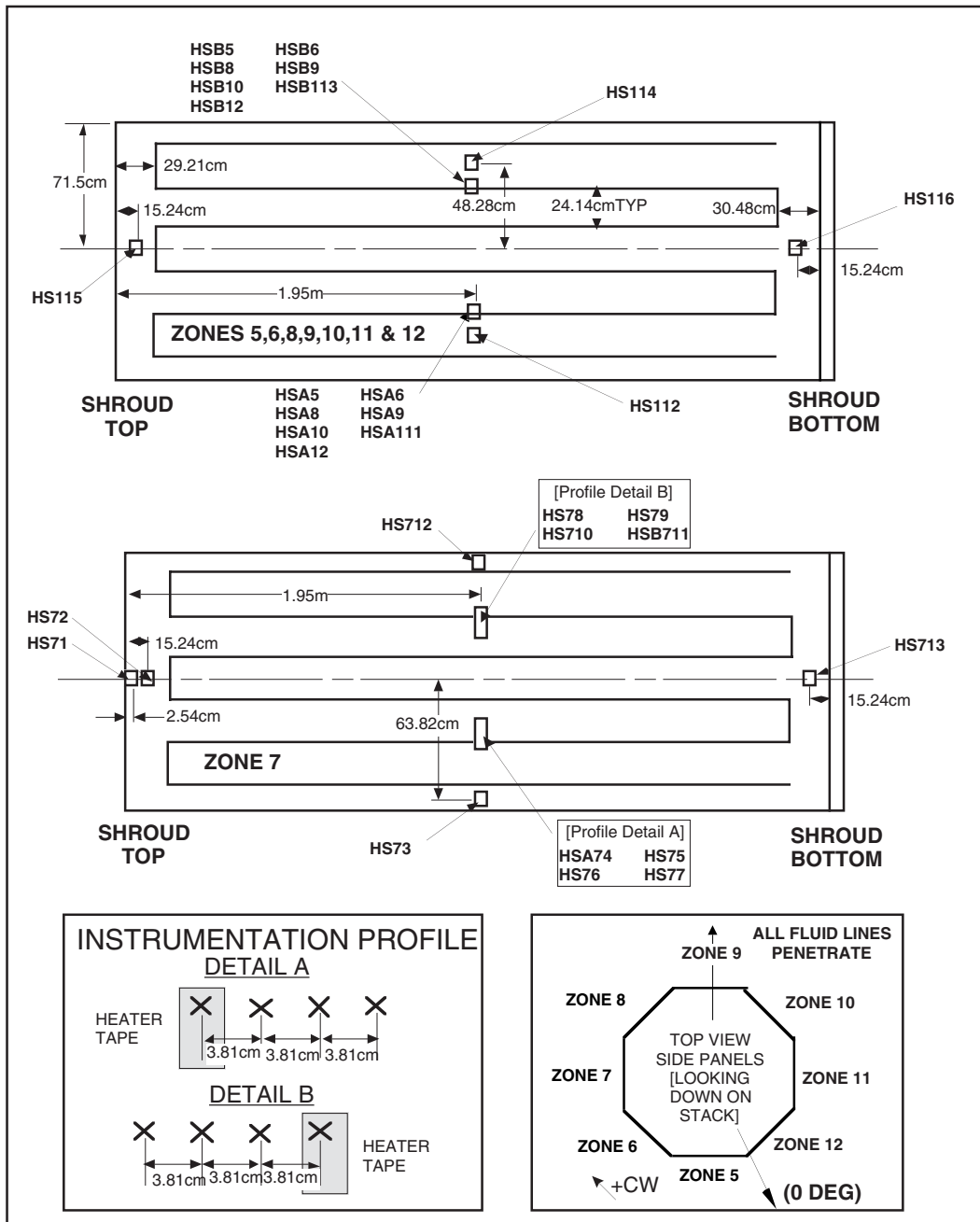


Figure 98. MHTB typical side wall environmental shroud panels.

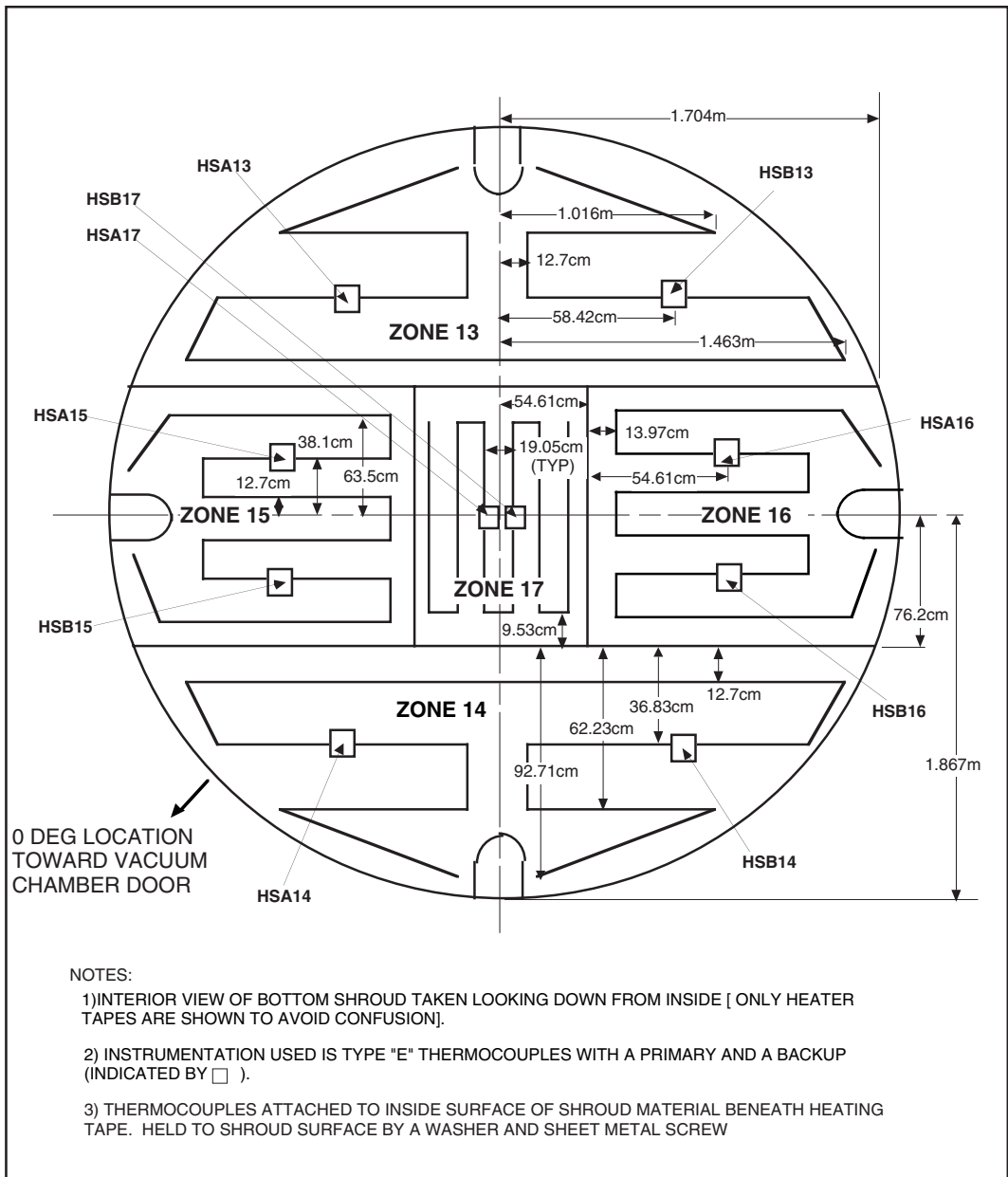


Figure 99. MHTB typical lower environmental shroud panels.

12) MHTB Zero-g Thermodynamic Vent System Instrumentation

The spray bar MHTB test phase requires that hardware related to the zero-g TVS be installed both internal and external to the MHTB test tank. Figure 84 illustrates the general hardware placement on the test tank while instrumentation placement on the hardware is outlined in figure 100. Attached to the lower MHTB tank bulkhead flange (external to the tank) is the vacuum tight TVS enclosure which contains the system control valving and recirculation pump. Instrumentation within the enclosure consists of thermocouples (T411, T412, T415, T416 and T417) pressure transducers (P402, DP400, P403, P404 and P405) and a flow meter (F401). Internal to the test tank is the heat exchanger/spray bar and a back pressure orifice. The spray bar is equipped with two silicon diodes (T413 and T414) and the orifice is instrumented with two diodes (T418 and T419) and two pressure transducers (P406 and P407). External to the MHTB tank, but still within the vacuum chamber, are temperature (diode T420) and pressure (P408) measurements on the TVS vent line to quantify the properties of the exiting gas flow. Instrumentation internal to the MHTB test tank will be routed through the 20.32cm (8") vent flange with the other internal instrumentation. The instrumentation within the TVS enclosure shall be routed through two Deutsch feed throughs and two thermocouple pull throughs. All thermocouples utilize an infinity meter for signal conditioning. The TVS enclosure shall be equipped externally with three thermocouples (T421, T422 and T423) mounted on the top, bottom and side of the enclosure, respectively. The enclosure internal pressure will be measured by two pressure transducers (P409 and P410). Appendix A contains, in a data base format, additional information regarding this instrumentation.

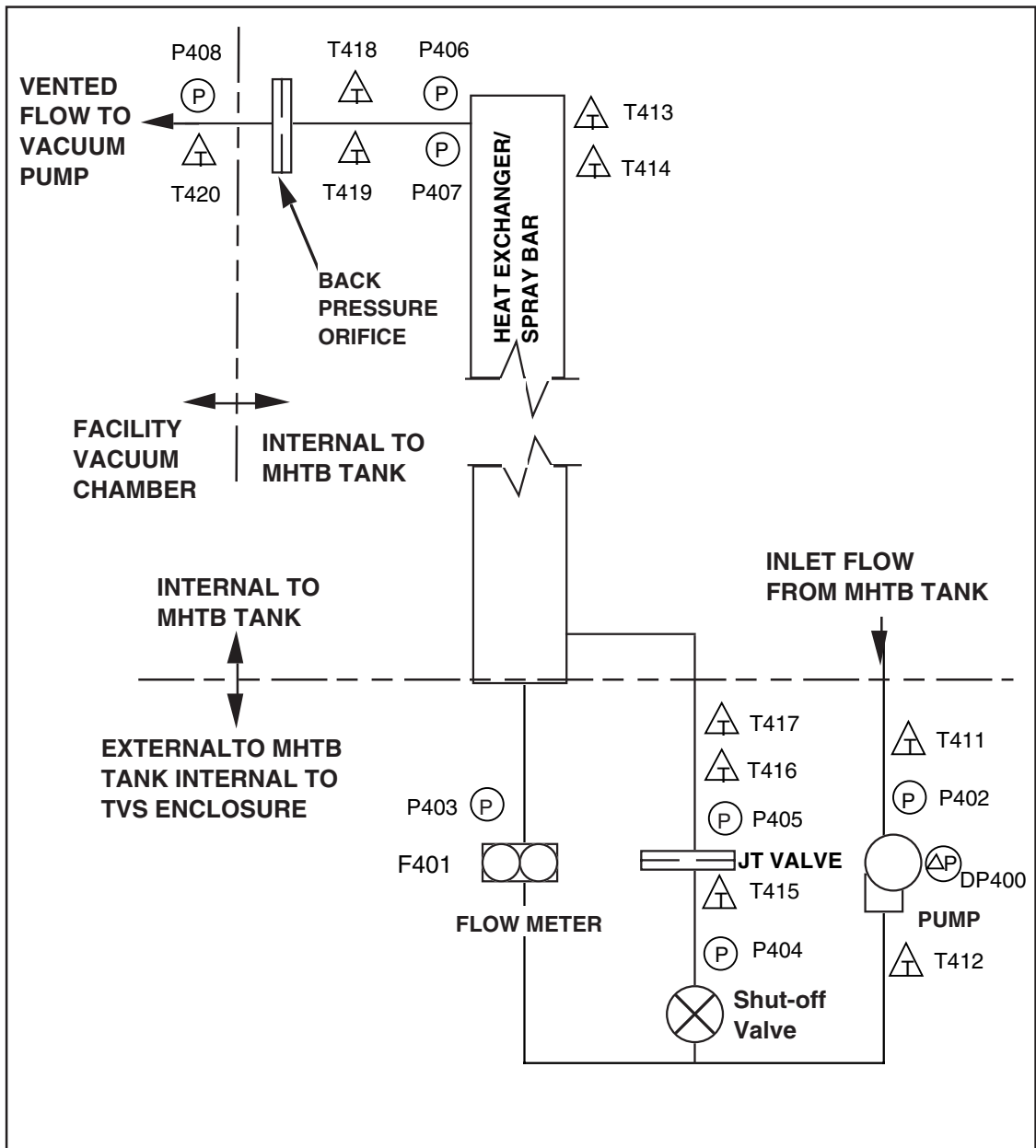


Figure 100. MHTB TVS instrumentation layout.

APPENDIX C—ANALYTICAL CORRELATIONS WITH TEST SEGMENT P263981E

Correlations for the venting and mixing operation were performed using test segment P263981E, with a 90-percent fill level and 54.1-W tank heat leak. The ullage pressure comparison is presented in figure 101. To enable a more realistic comparison of the mixing/venting cycle characteristics, the initial conditions for the analytical model were based on measured conditions at 22,595 s. Venting did not occur with the analytical model since the computed bulk liquid saturation approached, but did not reach, the lower pressure control band limit. During the test, however, the J-T valve opened at 24,108 s. Apparently the bulk liquid did not attain the lower pressure control setpoint during the test, and venting should not have occurred. However, erratic signals from the temperature sensor used to indicate bulk liquid saturation conditions (TD23) caused the J-T vent valve to temporarily open four times. Unfortunately, during the test, the J-T vent valve stuck open on the fourth vent cycle and therefore the correlation period was limited to only about three cycles. The ullage temperature comparison in figure 102 indicates that the average measured and computed ullage temperatures were 21.85 and 21.5 K, respectively; i.e., deviated by <2 percent. The modeled and measured bulk liquid saturation pressure and temperature, presented in figures 103 and 104, respectively, were comparable until the vent valve remained open on the fourth cycle and the measured values began to decrease.

Test and Model Conditions

- 90% Fill, GH₂ Ullage
- Test: Four Vent Cycles
- Model: No Venting
- Tank Heat Leak: 54.1 W
- P4 Upper Limit: 137.9 kPa
- P4 Lower Limit: 131.0 kPa
- Vent Flow Rate: 0.0048 kg/s

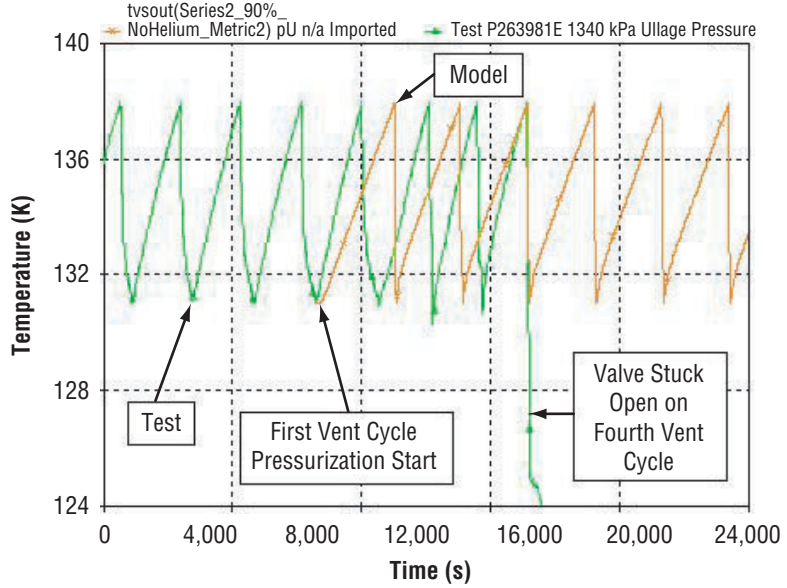


Figure 101. Ullage pressure modeling comparison with 1998 test P263981E—self-pressurization and mixing with 90-percent fill.

Test and Model Conditions

- 90% Fill, GH₂ Ullage
- Test: Four Vent Cycles
- Model: No Venting
- Tank Heat Leak: 54.1 W
- P4 Upper Limit: 137.9 kPa
- P4 Lower Limit: 131.0 kPa
- Vent Flow Rate: 0.0048 kg/s

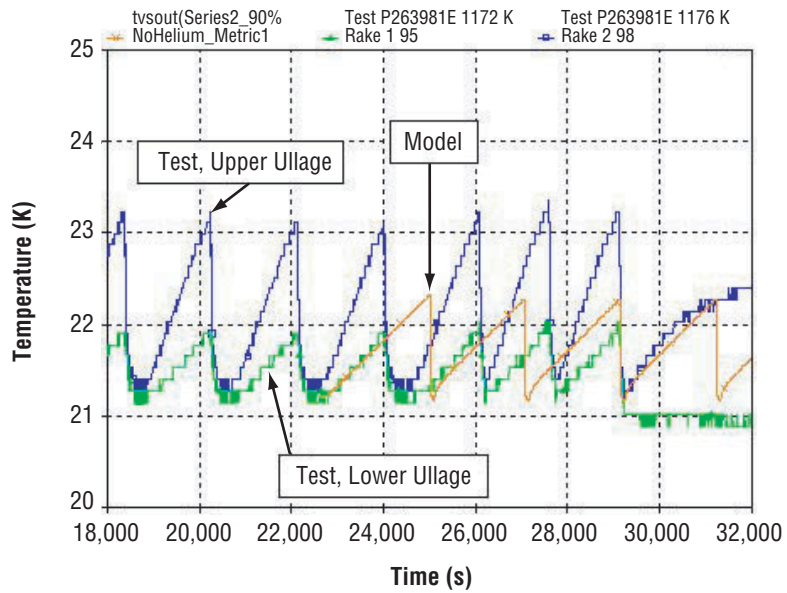


Figure 102. Ullage temperature modeling comparison with 1998 test P263981E—self-pressurization, mixing, and venting with 90-percent fill.

Test and Model Conditions

- 90% Fill, GH₂ Ullage
- Test: Four Vent Cycles
- Model: No Venting
- Tank Heat Leak: 54.1 W
- P4 Upper Limit: 137.9 kPa
- P4 Lower Limit: 131.0 kPa
- Vent Flow Rate: 0.0048 kg/s

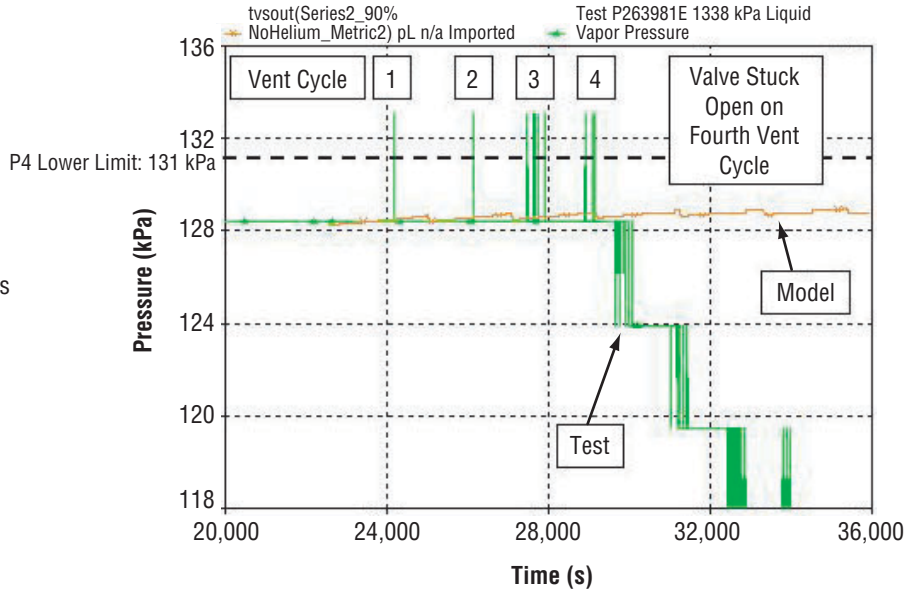


Figure 103. Bulk liquid saturation pressure modeling comparison with 1998 test P263981E—self-pressurization, mixing, and venting with 90-percent fill.

Test and Model Conditions

- 90% Fill, GH₂ Ullage
- Test: Four Vent Cycles
- Model: No Venting
- Tank Heat Leak: 54.1 W
- P4 Upper Limit: 137.9 kPa
- P4 Lower Limit: 131.0 kPa
- Vent Flow Rate: 0.0048 kg/s

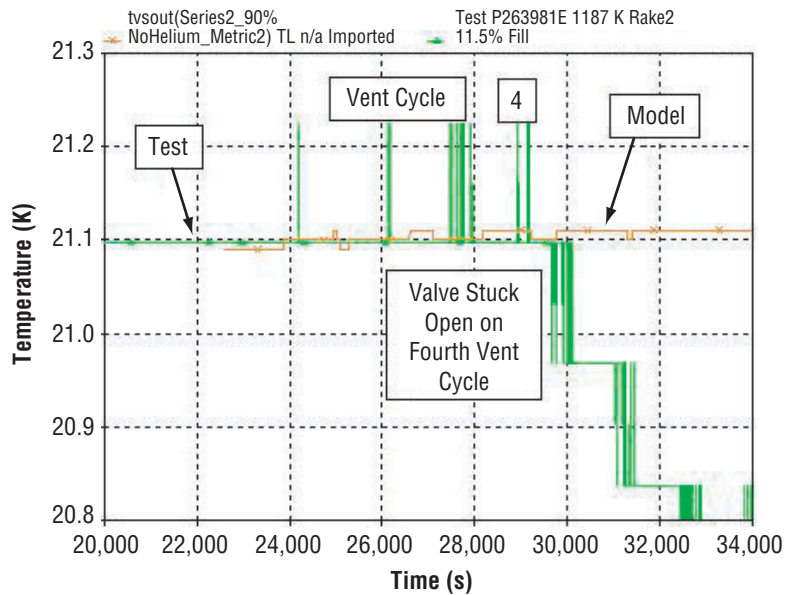


Figure 104. Bulk liquid saturation temperature modeling comparison with 1998 test P263981E—self-pressurization, mixing, and venting with 90-percent fill.

REFERENCES

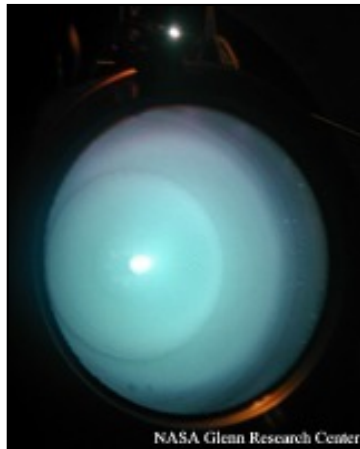
1. Martin, J.; and Hastings, L.: "Large-Scale Liquid Hydrogen Testing of a Variable Density Multilayer Insulation With a Foam Substrate," *NASA/TM-2001-211089*, Marshall Space Flight Center, AL, June 2001.
2. Cryogenic Fluid Management Technologies for Space Transportation, Zero G Thermodynamic Vent System Final Report, Rockwell Aerospace Report No. SSD 94M0038, Contract NAS8-39202, 1994.
3. Nguyen, H.: Zero-G Thermodynamic Venting System (TVS) Performance Prediction Program, Rockwell Aerospace, Contract NAS8-39202, May 24, 1994.
4. "MPS Propellant Dump and Vacuum Inerting (The Generalized Two-Phase Cryogenic Propellant Dump Model), Program No. MPS-17, 287-104-91-MPS-017, Rockwell International, June 1991.
5. Chen, J.: A Correlation for Boiling Heat Transfer to Saturated Fluids in Convective Flow, ASME Paper No. 63-HT-34, ASME-AICHe Heat Transfer Conference and Exhibit, Boston, MA, August 1963.
6. Generic Fluid Transfer Model, Computer Model Description Document, Rockwell International, December 1987.
7. Ring, E.: *Rocket Propellant and Pressurization Systems*, Prentice-Hall, Inc., Englewood Cliff, NJ, p. 218, 1964.
8. Kreith, H.: *Principles of Heat Transfer*, 4th ed., Harper & Row, New York, pp. 4-6, p.360, 1986.
9. Bailey, J.; and Hedayat, A.: "Thermodynamic Venting System (TVS) Performance Prediction Program Modification and Comparison With Test Data," Sverdrup MSFC Group Report No. MG-02-660, September 2002.

REPORT DOCUMENTATION PAGE			Form Approved OMB No. 0704-0188	
Public reporting burden for this collection of information is estimated to average 1 hour per response, including the time for reviewing instructions, searching existing data sources, gathering and maintaining the data needed, and completing and reviewing the collection of information. Send comments regarding this burden estimate or any other aspect of this collection of information, including suggestions for reducing this burden, to Washington Headquarters Services, Directorate for Information Operation and Reports, 1215 Jefferson Davis Highway, Suite 1204, Arlington, VA 22202-4302, and to the Office of Management and Budget, Paperwork Reduction Project (0704-0188), Washington, DC 20503				
1. AGENCY USE ONLY (Leave Blank)	2. REPORT DATE October 2003	3. REPORT TYPE AND DATES COVERED Technical Memorandum		
4. TITLE AND SUBTITLE Spray Bar Zero-Gravity Vent System for On-Orbit Liquid Hydrogen Storage			5. FUNDING NUMBERS	
6. AUTHORS L.J. Hastings,* R.H. Flachbart, J.J. Martin, A. Hedayat, M. Fazah, T. Lak,** H. Nguyen,** and J.W. Bailey***				
7. PERFORMING ORGANIZATION NAME(S) AND ADDRESS(ES) George C. Marshall Space Flight Center Marshall Space Flight Center, AL 35812			8. PERFORMING ORGANIZATION REPORT NUMBER M-1091	
9. SPONSORING/MONITORING AGENCY NAME(S) AND ADDRESS(ES) National Aeronautics and Space Administration Washington, DC 20546-0001			10. SPONSORING/MONITORING AGENCY REPORT NUMBER NASA/TM-2003-212926	
11. SUPPLEMENTARY NOTES Prepared by the Vehicle and Systems Development Department, Space Transportation Directorate *Alpha Technology, Inc. **The Boeing Company ***Sverdrup Technology, Inc.				
12a. DISTRIBUTION/AVAILABILITY STATEMENT Unclassified-Unlimited Subject Category 16 Availability: (301)621-0390			12b. DISTRIBUTION CODE	
13. ABSTRACT (Maximum 200 words) During zero-gravity orbital cryogenic propulsion operations, a thermodynamic vent system (TVS) concept is expected to maintain tank pressure control without propellant resettling. In this case, a longitudinal spray bar mixer system, coupled with a Joule-Thompson (J-T) valve and heat exchanger, was evaluated in a series of TVS tests using the 18-m ³ multipurpose hydrogen test bed. Tests performed at fill levels of 90, 50, and 25 percent, coupled with heat tank leaks of about 20 and 50 W, successfully demonstrated tank pressure control within a 7-kPa band. Based on limited testing, the presence of helium constrained the energy exchange between the gaseous and liquid hydrogen (LH ₂) during the mixing cycles. A transient analytical model, formulated to characterize TVS performance, was used to correlate the test data. During self-pressurization cycles following tank lockup, the model predicted faster pressure rise rates than were measured; however, once the system entered the cyclic self-pressurization/mixing/venting operational mode, the modeled and measured data were quite similar. During a special test at the 25-percent fill level, the J-T valve was allowed to remain open and successfully reduced the bulk LH ₂ saturation pressure from 133 to 70 kPa in 188 min.				
14. SUBJECT TERMS orbital cryogenic fluid management, orbital cryogenic storage, zero-gravity cryogenic pressure control, thermodynamic vent systems			15. NUMBER OF PAGES 160	
			16. PRICE CODE	
17. SECURITY CLASSIFICATION OF REPORT Unclassified	18. SECURITY CLASSIFICATION OF THIS PAGE Unclassified	19. SECURITY CLASSIFICATION OF ABSTRACT Unclassified	20. LIMITATION OF ABSTRACT Unlimited	

[Home > NEXT](#)

NASA's Evolutionary Xenon Thruster (NEXT)

Overview



40 cm ion thruster in operation

NASA's [Office of Space Science](#) selected [Glenn Research Center](#) to develop a next generation ion propulsion system called NASA's Evolutionary Xenon Thruster (NEXT) system. This advanced system has capabilities beyond conventional chemical propulsion and will revolutionize the way we send science missions deeper in to the solar system. NEXT will use xenon gas and

[Overview](#)[Accomplishments](#)**Development Activities** [coming]**Technical Details** [offsite]• [Ion Propulsion Overview](#)• [Ion Propulsion History](#)• [Current Ion Propulsion Programs & Projects](#)• [Future Applications of Ion Propulsion](#)[Ion Thruster Images](#) [offsite FTP][Publications](#)

electrical power to drive future spacecraft.

The NEXT project is a joint effort led by the [Power and Propulsion Office](#) and the [On-Board Propulsion Branch](#) of the [Power and On Board Propulsion Technology Division](#) at the NASA Glenn Research Center. It is a two-part effort, with Phase 1 consisting of a one-year undertaking to design, build and test initial laboratory components. The second phase, dependent upon NASA's exercise of an option, would complete engineering hardware development and integrate components into a full-scale system.

The major feature of NEXT is a thruster that utilizes design knowledge gained from the ion thruster that successfully propelled the [Deep Space 1](#) to a flyby of asteroid Braille and the comet Borrelly. NEXT will have a significant increase in power compared to that of Deep Space 1's ion thruster while increasing efficiency and system performance characteristics. Advanced power processing, xenon propellant management and thruster gimbal technologies will also be developed by the team to complete the NEXT ion propulsion system.

NEXT was selected for award from the [Research Opportunities in Space Science 2001 NASA Research Announcement](#), under the [In-Space Transportation Program](#) in the [Solar System Exploration Division](#) of NASA's Office of Space Science. The In-Space Propulsion Program is managed by the Office of Space Science at NASA Headquarters in Washington D.C. and implemented by

the [Marshall Space Flight Center](#) in
Huntsville, Ala.

[Home](#) • [Highlights](#) • [About P&PO](#) • [Technology](#) • [Projects](#) • [Publications](#) • [Related Links](#) • [Site Map](#)



Responsible NASA Official: Sandra Reehorst,
Sandra.T.Reehorst@grc.nasa.gov
[NASA WebSite Privacy & Security Notices & Web Site Disclaimer](#) | [NASA Accessibility Statement](#)
Site Curator: Karen Tuttle, Karen.L.Tuttle@grc.nasa.gov
Site Construction: Joe Banks, joe.banks@zin-tech.com



[NASA Glenn Research Center](#)

Cleveland, Ohio

Page Last Updated: May 13, 2003

This site makes available documents in Adobe Portable Document Format (PDF). Please visit [Adobe.com](#) to download the free [Acrobat Reader](#) or [accessibility utility](#).



Solar System Exploration



Galileo Legacy Site

Sitemap

SSE Home > Galileo Legacy Site

Search

Home

News & Events

Planets

Missions

Science & Technology

Multimedia

People

Kids

Education

History

Overview

Mission

Images

Explorations

News

Education

Galileo plunged into Jupiter's crushing atmosphere on Sept. 21, 2003. The spacecraft was deliberately destroyed to protect one of its own discoveries - a possible ocean beneath the icy crust of the moon Europa.

Galileo changed the way we look at our solar system. The spacecraft was the first to fly past an asteroid and the first to discover a moon of an asteroid. It provided the only direct observations of a comet colliding with a planet.

Galileo was the first to measure Jupiter's atmosphere with a descent probe and the first to conduct long-term observations of the Jovian system from orbit. It found evidence of subsurface saltwater on Europa, Ganymede and Callisto and revealed the intensity of volcanic activity on Io.

Read on to learn more about the historic legacy of the Galileo mission.



Quick Facts

Launch: 10.18.89

End of Mission: 9.21.03

Jupiter Orbits: 34

Total Distance Traveled: 4,631,778,000 km

Weight: 2,223 kg

Height: 5.3 meters

More Facts 

Mission Highlights

Find out how the Galileo spacecraft changed the way we look at our solar system:

- **Discovery Highlights**
- **Top 10 Science Images**
- **Jupiter Exploration Timeline**
- **Legacy of Galileo Animation (RealPlayer) (QuickTime)**
- **Galileo Legacy Powerpoint (4.90 MB)**

Resources

▪ **Solar System Bodies: Jupiter**

▪ **Solar System Bodies: Jupiter's Moons**

▪ **Sky & Telescope: Jupiter Observing Guide**

More Resources 

▪ **Sounds of Jupiter**

▪ **Cassini and Galileo: Joint Jupiter Observations in 2000**

▪ **NASA's Jet Propulsion Laboratory**

Explore more of NASA on the Web:



- + Awards & Recognition
- + Send to a Friend
- + The Vision for Space Exploration
- + NASA Solar System Exploration Roadmap
- + NASA Privacy Statement, Disclaimer and Accessiblity Certification
- + Copyright/Image Use Policy



Acting Editor: Kirk Munsell
Webmaster: David Martin
NASA Official: Orlando Figueroa
Last Updated: 08.31.05

- + FAQ
- + Dictionary
- + Contact Us



Solar System Exploration

Missions

Sitemap

SSE Home > Missions > By Target > Venus > Past > Pioneer Venus

Search

Home

News & Events

Planets

Missions

By Target

By Letter

By Year

Programs

Science & Technology

Multimedia

People

Kids

Education

History

Missions to Venus

Past

Present

Future

Pioneer Venus:

Overview

The Pioneer Venus mission had two components: an orbiter and a multiprobe. These spacecraft were launched separately, the orbiter arriving at [Venus](#) just a few days ahead of the multiprobe. The orbiter carried 17 experiments, including instruments to see through the clouds and map the surface, as well as measure cloud distribution, atmospheric composition, the magnetic field, the solar wind, properties of the ionosphere of Venus, the gravity field, and gamma ray bursts. The multiprobe spacecraft was actually four separate atmospheric probes hitching a ride on a spacecraft bus. The probes separated from the bus 12.9 million kilometers (8 million miles) before arrival at Venus and entered the atmosphere in different regions of the planet at the same time. The probes made measurements of the structure and composition of the atmosphere all the way to the surface. Meanwhile, the probe bus made measurements in the upper atmosphere, and the Orbiter simultaneously made measurements for comparison.



Key Dates

05.20.78: Orbiter Launch
08.08.78: Multiprobes Launch
12.04.78: Orbiter Arrival
12.09.78: Multiprobes Arrival
10.08.92: Burned Up in Venus' Atmosphere
Status: Mission Complete

Headlines

07.24.01: COSMOS 1 Test Flight Update
07.11.01: Cosmos 1 Solar Sail Sub-Orbital Test Flight: All Systems Go for July 19th Launch
04.11.01: Sub-orbital Test Flight of Solar Sail Delayed Due to Spacecraft Accident

More Headlines 

Links

- [Solar System Bodies: Venus](#)
- [National Space Science Data Center, Pioneer Venus Project Information](#)
- [NASA Spacelink, Pioneer Venus](#)
- [Starchild site, Space Probes to Venus](#)

Explore more of NASA on the Web:



- + Awards & Recognition
- + Send to a Friend
- + The Vision for Space Exploration
- + NASA Solar System Exploration Roadmap
- + NASA Privacy Statement, Disclaimer and Accessibility Certification
- + Copyright/Image Use Policy



Acting Editor: Kirk Munsell
Webmaster: David Martin
NASA Official: Orlando Figueroa
Last Updated: 09.23.02

- + FAQ
- + Dictionary
- + Contact Us